

CRITICAL METALS IN NORTHWEST CHINA

EDITED BY: Xiaohua Deng, Yan-Jing Chen, Leon Bagas and Chang-Zhi Wu
PUBLISHED IN: Frontiers in Earth Science



frontiers

Frontiers eBook Copyright Statement

The copyright in the text of individual articles in this eBook is the property of their respective authors or their respective institutions or funders. The copyright in graphics and images within each article may be subject to copyright of other parties. In both cases this is subject to a license granted to Frontiers.

The compilation of articles constituting this eBook is the property of Frontiers.

Each article within this eBook, and the eBook itself, are published under the most recent version of the Creative Commons CC-BY licence.

The version current at the date of publication of this eBook is CC-BY 4.0. If the CC-BY licence is updated, the licence granted by Frontiers is automatically updated to the new version.

When exercising any right under the CC-BY licence, Frontiers must be attributed as the original publisher of the article or eBook, as applicable.

Authors have the responsibility of ensuring that any graphics or other materials which are the property of others may be included in the CC-BY licence, but this should be checked before relying on the CC-BY licence to reproduce those materials. Any copyright notices relating to those materials must be complied with.

Copyright and source acknowledgement notices may not be removed and must be displayed in any copy, derivative work or partial copy which includes the elements in question.

All copyright, and all rights therein, are protected by national and international copyright laws. The above represents a summary only. For further information please read Frontiers' Conditions for Website Use and Copyright Statement, and the applicable CC-BY licence.

ISSN 1664-8714

ISBN 978-2-88974-510-4

DOI 10.3389/978-2-88974-510-4

About Frontiers

Frontiers is more than just an open-access publisher of scholarly articles: it is a pioneering approach to the world of academia, radically improving the way scholarly research is managed. The grand vision of Frontiers is a world where all people have an equal opportunity to seek, share and generate knowledge. Frontiers provides immediate and permanent online open access to all its publications, but this alone is not enough to realize our grand goals.

Frontiers Journal Series

The Frontiers Journal Series is a multi-tier and interdisciplinary set of open-access, online journals, promising a paradigm shift from the current review, selection and dissemination processes in academic publishing. All Frontiers journals are driven by researchers for researchers; therefore, they constitute a service to the scholarly community. At the same time, the Frontiers Journal Series operates on a revolutionary invention, the tiered publishing system, initially addressing specific communities of scholars, and gradually climbing up to broader public understanding, thus serving the interests of the lay society, too.

Dedication to Quality

Each Frontiers article is a landmark of the highest quality, thanks to genuinely collaborative interactions between authors and review editors, who include some of the world's best academicians. Research must be certified by peers before entering a stream of knowledge that may eventually reach the public - and shape society; therefore, Frontiers only applies the most rigorous and unbiased reviews. Frontiers revolutionizes research publishing by freely delivering the most outstanding research, evaluated with no bias from both the academic and social point of view. By applying the most advanced information technologies, Frontiers is catapulting scholarly publishing into a new generation.

What are Frontiers Research Topics?

Frontiers Research Topics are very popular trademarks of the Frontiers Journals Series: they are collections of at least ten articles, all centered on a particular subject. With their unique mix of varied contributions from Original Research to Review Articles, Frontiers Research Topics unify the most influential researchers, the latest key findings and historical advances in a hot research area! Find out more on how to host your own Frontiers Research Topic or contribute to one as an author by contacting the Frontiers Editorial Office: frontiersin.org/about/contact

CRITICAL METALS IN NORTHWEST CHINA

Topic Editors:

Xiaohua Deng, Beijing Institute of Geology for Mineral Resources, China

Yan-Jing Chen, Peking University, China

Leon Bagas, University of Western Australia, Australia

Chang-Zhi Wu, Chang'an University, China

Citation: Deng, X., Chen, Y.-J., Bagas, L., Wu, C.-Z., eds. (2022). Critical Metals in Northwest China. Lausanne: Frontiers Media SA. doi: 10.3389/978-2-88974-510-4

Table of Contents

- 05 Editorial: Critical Metals in Northwest China: Characters, Genesis and Tectonic Settings**
Chang-Zhi Wu, Xiaohua Deng, Leon Bagas, Matthew J. Brzozowski and Yan-Jing Chen
- 08 Mineralogy of Nickel and Cobalt Minerals in Xiarihamu Nickel–Cobalt Deposit, East Kunlun Orogen, China**
Yixiao Han, Yunhua Liu and Wen Yuan Li
- 22 Newly Discovered Triassic Lithium Deposits in the Dahongliutan Area, North West China: A Case Study for the Detection of Lithium-Bearing Pegmatite Deposits in Rugged Terrains Using Remote-Sensing Data and Images**
Yongbao Gao, Leon Bagas, Kan Li, Moushun Jin, Yuegao Liu and Jiaxin Teng
- 46 Columbite-Tantalite Group Mineral U–Pb Geochronology of Chaqiabeishan Li-Rich Granitic Pegmatites in the Quanji Massif, NW China: Implications for the Genesis and Emplacement Ages of Pegmatites**
Tong Pan, Qing-Feng Ding, Xuan Zhou, Shan-Ping Li, Jie Han and Long Cheng
- 63 Fluid Inclusions and H–O–C–S–Pb Isotopic Systematics of the Jinba Gold Deposit, NW China: Implications for Ore Genesis**
Shun-Da Li, Chuan Chen, Ling-Ling Gao, Fang Xia, Xue-Bing Zhang and Ke-Yong Wang
- 79 The Genesis of the Askartor Be–Mo Deposit in the North Xinjiang, Northwest China: Evidence From Geology, Geochemistry, U–Pb, and Re–Os Geochronology**
Tang Yong, Zhang Hui and Lv Zheng-Hang
- 98 Enrichment of Platinum Group Elements in Lower Cambrian Polymetallic Black Shale, SE Yangtze Block, China**
Yong Fu, Zhen Yang, Chao Li and Peng Xia
- 111 Geochronological and Geochemical Constraints on the Petrogenesis of Permian Dolerite Dyke Swarms in the Beishan Orogenic Belt, NW China**
Gang Xu, Jun Duan, Wenbin Gao, Rongmin Wang, Zhen Shi, Bocheng Ma and Jia Sun
- 125 The Metallogeny of the Lubei Ni–Cu–Co Sulfide Deposit in Eastern Tianshan, NW China: Insights From Petrology and Sr–Nd–Hf Isotopes**
Ping Li, Ting Liang, Yonggang Feng, Tongyang Zhao, Jiangtao Tian, Dahai Li, Jian Li, Gang Chen and Changzhi Wu
- 142 Compositional Variation of Amphiboles During Magma Mixing: A Case Study of Huangyangshan A-Type Granite in Kalamaili Metallogenic Belt, East Junggar, China**
Chenyang Ye, Yonggang Feng, Ruxiong Lei and Gaoxue Yang

- 159 ***Geochronological Constraint on the Evolution of the Aktyuz Terrane, Kyrgyz North Tianshan, and the Fate of the Taldybulak Levoberezhny Gold Deposit***
Wei Xi, Nuo Li, Xiaohong Xia, Xiaoxiao Ling and Yanshuang Wu
- 175 ***Geochronology and Geochemistry of Late Paleozoic Volcanic Rocks and Their Relationship With Iron and Molybdenum Deposits in Xilekuduk Area, Northern Margin of Junggar***
Xiaofeng Wei, Hao Wei, Zhen Liao, Zhiwei Wang, Dong Li, Qigui Mao and Xiao Li
- 192 ***Zircon Genesis and Geochronology for the Zhangbaoshan Super-Large Rubidium Deposit in the Eastern Tianshan, NW China: Implication to Magmatic-Hydrothermal Evolution and Mineralization Processes***
Jun Zhi, Ruxiong Lei, Boyang Chen, M. N. Muhtar, Zhijie Feng, Kai Zhang, Yuanfeng Cai and Changzhi Wu
- 211 ***Mineralization of the Tuwu Porphyry Cu Deposit in Eastern Tianshan, NW China: Insights From In Situ Trace Elements of Chlorite and Pyrite***
Wei Tan, Qigui Mao, Mingjie Yu, Yan Sun and Xiaoqiang Lv
- 237 ***Gem-Grade Garnet With Metamorphic Origin in the Tiemurt Orogenic-Type Deposit, Chinese Altay Orogen: Texture, Chemistry, and Physicochemical Condition***
Zhaobin Hu, Yi Zheng, Pengpeng Yu, Yihan Wu and Chengming Wang
- 253 ***Genesis of the Heiyanshan Tungsten Skarn Deposit in the East Tianshan, NW China: Insights From Geology, Fluid Inclusion, Isotopic Geochemistry and Geochronology***
Dong Xue, Xiao-Hua Deng, Leon Bagas, Xu-An Chen, Yan-Shuang Wu and Xiao Jiang
- 269 ***Petrology, Geochemical Characteristics, Tectonic Setting, and Implications for Chromite and PGE Mineralization of the Hongshishan Alaskan-Type Complex in the Beishan Orogenic Collage, North West China***
Zhaolin Wang, Xiaoming Zheng, Guixiang Meng, Hejun Tang and Tonghui Fang



Editorial: Critical Metals in Northwest China: Characters, Genesis and Tectonic Settings

Chang-Zhi Wu^{1*}, Xiaohua Deng^{1,2}, Leon Bagas³, Matthew J. Brzozowski⁴ and Yan-Jing Chen⁵

¹School of Earth Science and Resources, Chang'an University, Xi'an, China, ²Beijing Institute of Geology for Mineral Resources Co., Ltd., Beijing, China, ³Centre for Exploration Targeting (CET), The University of Western Australia, Crawley, WA, Australia, ⁴Department of Geology, Lakehead University, Thunder Bay, ON, Canada, ⁵Key Laboratory of Orogenic Belts and Crustal Evolution, Peking University, Beijing, China

Keywords: critical metals, petrogenesis, metallogenesis, exploration, Northwest China

Editorial on the Research Topic

Critical Metals in Northwest China: Characters, Genesis and Tectonic Settings

Critical metals are strategic mineral resources that are indispensable to our global high-tech industry. Having a robust understanding of how critical metal deposits form and the criteria that can be used for their exploration is, therefore, of great importance to the international mineral resources industry. Northwest China is one of the most important mineral exploration and mining regions in China. It formed by the multi-phase accretion of variably mineralized Paleozoic–Mesozoic terranes caused by the closure of the Paleo-Asian and Paleo-Tethys oceans. Recently, a number of important breakthroughs have been made in the petrogenesis, metallogenesis, and exploration for critical metal deposits in Northwest China, including rare metal, precious-metal, and rare-earth element deposits.

OPEN ACCESS

Edited and reviewed by:

David R. Lentz,
University of New Brunswick, Canada

*Correspondence:

Chang-Zhi Wu
wucz@njnu.edu.cn

Specialty section:

This article was submitted to
Economic Geology,
a section of the journal
Frontiers in Earth Science

Received: 09 January 2022

Accepted: 12 January 2022

Published: 27 January 2022

Citation:

Wu C-Z, Deng X, Bagas L,
Brzozowski MJ and
Chen Y-J (2022) Editorial: Critical
Metals in Northwest China:
Characters, Genesis and
Tectonic Settings.
Front. Earth Sci. 10:851360.
doi: 10.3389/feart.2022.851360

DIVERSE TECTONIC SETTINGS

Critical-metal mineralization occurs in diverse tectonic settings and in different geologic units throughout Northwest China. Chromite and platinum-group element (PGE) mineralization of the Hongshishan Alaskan-type complex in the Beishan area is characterized by cumulate and layering textures, with mineral, petrological, and geochemical characteristics that differ from typical ophiolites, and resemble Alaskan-type complexes related to subduction or arc magmatism in the Late Devonian (Z. Wang et al., this issue). During the Permian, extensive mafic dyke swarms and Ni–Cu–Co-mineralized mafic–ultramafic intrusions formed in the Beishan area, all of which are related to the extensional tectonics that dominated this area at this time (G. Xu et al., this issue; P. Li et al., this issue). In the Late Permian to Middle Triassic, the Chaqianbeishan area of the Qianji Massif was affected by the southward subduction of the Zongwulong oceanic plate (T. Pan et al., this issue), while the tectonic setting of the Eastern Tianshan transferred from a subduction to an intraplate environment (J. Zhi et al., this issue).

TYPICAL DEPOSITS AND THEIR GENESIS

Four different types of deposits located in the Chinese Altay Orogen were characterized in detail in this issue. Y. Tang et al. (this issue) combined zircon U–Pb and molybdenite Re–Os

dating methods to constrain the mineralization age of the Askartor Be–Mo deposit to the Triassic. This mineralized two-mica granite exhibits highly fractionated geochemical characteristics, suggesting that it is the product of multistage fractional crystallization of an initially Be-enriched magma, and that fluid exsolution occurred late in the evolution of this magma. S.D. Li et al. (this issue) conducted a systematic fluid inclusion and H–O–C–S–Pb isotope study of the Jinba Au deposit, constraining it as an orogenic deposit and establishing its genetic model. Z. Hu et al. (this issue) characterized the textures and major–trace element chemistry of six garnet grains from the Tiemurt Cu–Pb–Zn(–Au) deposit. They found that the fluids related to the formation of this base-metal mineralization are CO₂-rich, mesothermal, mildly acidic, and reduced, analogous to metamorphic fluids generated during orogenesis. X. Wei et al. (this issue) conducted a geochronologic and geochemical study of volcanic rocks related to Fe–Cu–Mo mineralization in the Xilekuduk area. The magnetite-related mineralization was divided into Devonian magmatic stratiform-type and Carboniferous hydrothermal vein-type, with the latter being closely related to porphyry Mo mineralization.

Four deposits in the Chinese Eastern Tianshan and one in the Kyrgyz North Tianshan have been well documented in this issue. D. Xue et al. (this issue) characterized the mineralogy, fluid inclusions, H–O isotopes, and age of a newly discovered skarn W deposit. The Heiyanshan W deposit is hosted at the contact between a Carboniferous biotite monzogranite pluton, and Mesoproterozoic metamorphosed clastic and carbonate rocks, and formed from hydrothermal fluids characterized by moderate to low temperatures and salinities. Using the trace-element composition of pyrite and chlorite in the Tuwu porphyry Cu deposit, W. Tan et al. (this issue) identified three stages of mineralization related to magmatic, hydrothermal, and metamorphic processes. P. Li et al. (this issue) conducted a systematic petrological, geochronological, and geochemical analysis of the Lubei Ni–Cu–Co deposit, and demonstrated that it formed from a magma that experienced fractional crystallization, crustal contamination, and sulfide segregation in a post-collisional extensional geodynamic setting. Using magmatic and hydrothermal zircons, J. Zhi et al. (this issue) determined the ages of five lithological zones in the Baishitouquan pluton, which hosts the large, newly discovered Zhangbaoshan Rb deposit. The ages of the magmatic and mineralization events that formed this deposit are Triassic, which is a critical period for granitic magmatism and rare-metal mineralization in the Eastern Tianshan. Based on zircon U–Pb and Lu–Hf isotopes, W. Xi et al. (this issue) constrained the ages of the auriferous monzogranite porphyry of the Taldybulak Levoberezhny gold deposit and the host Kemin Complex in Kyrgyzstan. The deposit is demonstrated to have formed in the Silurian and derived from the Precambrian basement rocks back to the Archean.

Apart from deposits in the Tianshan and Altay, four deposits from the West and East Kunlun Orogenic Belts,

the Quanji Massif, and the Southwest Yangtze Block were described in this issue. Using Zircon U–Pb and muscovite Ar–Ar isotope dating methods, Y. Gao et al. (this issue) determined the age of Li mineralization in the Bayankala Fold Belt, West Kunlun. Y. Han et al. (this issue) characterized the mineralogy of nickel and cobalt minerals, and established a mineralization model for the Xiarihamu deposit in East Kunlun, the second largest Ni–Co deposit in China. T. Pan et al. (this issue) characterized the U–Pb isotope and trace-element composition of columbite–tantalite group minerals to determine the ages of emplacement and hydrothermal metasomatism of a typical Li-rich pegmatite in the Chaqianbeishan area of the Quanji Massif. Y. Fu et al. (this issue) described two outcrop sections of lower Cambrian black shales in Southwest Yangtze that contain thin polymetallic layers with elevated Ni, Mo, V, PGEs, and rare Earth elements. They proposed that these polymetallic layers formed in a hypoxic oceanic environment during the Sinian–Cambrian transition, and that metal enrichment was enhanced during diagenesis.

MINERAL EXPLORATION AND PROSPECTING

Y. Gao et al. (this issue) used a combination of geologic mapping, geochemical methods, and high-resolution remotely sensed multispectral imagery to pinpoint potential locations of pegmatite-hosted Li occurrences in areas adjacent to the recently discovered Li deposits in the Dahongliutan area, West Kunlun Orogen. This contribution led to the discovery of several large Li-mineralized occurrences in the Bayankala Fold Belt, with a combined resource of over 1.7 million tonnes (Mt).

ELEMENT PARTITIONING

C. Ye et al. (this issue) characterized the major- and trace-element composition of amphiboles from the Huangyangshan alkalic granite and associated enclaves to estimate the crystallization temperature and pressure of these amphibole, and the partition coefficients of trace elements between these amphiboles and the granitic magma. They found that the high field strength elements and rare Earth elements are more compatible in sodic amphiboles than in calcic amphiboles.

Summary

This special Topic focuses on the most common types of deposits in Northwest China, as well as newly discovered deposits in this region, with the aim of understanding their characteristics, mineralization ages, mineralization mechanisms, and metallogenesis. We believe that these articles will provide a wealth of knowledge to a broad readership that has been fundamental to the enhancement

of our understanding of critical-metal mineralization in Northwest China.

AUTHOR CONTRIBUTIONS

C-ZW wrote the primary paper, MB revised the paper, all authors had reviewed the paper.

FUNDING

This study was supported by the National Natural Science Foundation of China (No. 91962214).

ACKNOWLEDGMENTS

We are grateful to all of the authors who responded to our call to participate in the compilation of this issue. Our gratitude is

also extended to all reviewers who kindly reviewed one or more of the manuscripts submitted to this Special Issue, and provided valuable comments and recommendations.

Conflict of Interest: XD was employed by Beijing Institute of Geology for Mineral Resources Co., Ltd.

The remaining authors declare that the research was conducted in the absence of any commercial or financial relationships that could be construed as a potential conflict of interest.

Publisher's Note: All claims expressed in this article are solely those of the authors and do not necessarily represent those of their affiliated organizations, or those of the publisher, the editors and the reviewers. Any product that may be evaluated in this article, or claim that may be made by its manufacturer, is not guaranteed or endorsed by the publisher.

Copyright © 2022 Wu, Deng, Bagas, Brzozowski and Chen. This is an open-access article distributed under the terms of the Creative Commons Attribution License (CC BY). The use, distribution or reproduction in other forums is permitted, provided the original author(s) and the copyright owner(s) are credited and that the original publication in this journal is cited, in accordance with accepted academic practice. No use, distribution or reproduction is permitted which does not comply with these terms.



Mineralogy of Nickel and Cobalt Minerals in Xiarihamu Nickel–Cobalt Deposit, East Kunlun Orogen, China

Yixiao Han^{1,2}, Yunhua Liu^{1*} and Wenyuan Li²

¹School of Earth Sciences and Resources, Chang'an University, Xi'an, China, ²Key Laboratory for the Study of Focused Magmatism and Giant Ore Deposits, Ministry of Natural Resources, Xi'an Center of China Geological Survey, Xi'an, China

OPEN ACCESS

Edited by:

Xiaohua Deng,
Beijing Institute of Geology for Mineral
Resources, China

Reviewed by:

Yun Zhao,
China University of Geosciences,
China

Shenghong Yang,
University of Oulu, Finland

*Correspondence:

Yunhua Liu
Zyyhliu@chd.edu.cn

Specialty section:

This article was submitted to
Petrology,
a section of the journal
Frontiers in Earth Science

Received: 21 August 2020

Accepted: 26 October 2020

Published: 10 December 2020

Citation:

Han Y, Liu Y and Li W (2020)
Mineralogy of Nickel and Cobalt
Minerals in Xiarihamu Nickel–Cobalt
Deposit, East Kunlun Orogen, China.
Front. Earth Sci. 8:597469.
doi: 10.3389/feart.2020.597469

Located in the East Kunlun Orogen, China, the Xiarihamu magmatic nickel–cobalt sulfide deposit is the country's second largest deposit of this type. It was formed in special early Paleozoic with low copper grade (0.14 wt%) compared with other deposits of the same type. The mineralogy of nickel and cobalt minerals, which are direct carriers of these elements, can clearly reflect their behavior in the process of mineralization; however, such information for this deposit remains unreported. In the present study, we use an electron microscope and electron probe microanalyzer to delineate and analyze many nickel and cobalt minerals such as maucherite, nickeline, cobaltite, violarite, gersdorffite, parkerite, and arsenohauchecornite in various rocks and ores. With the increase in crustal material contamination, it can reach arsenide saturation locally in sulfide melt, then a separate Ni-rich arsenide (bismuth) melt exsolves somewhere. This melt will crystallize into nickeline, parkerite, arsenohauchecornite, and maucherite first. Second, most of nickel and cobalt tend to enter cobaltite and pentlandite phases, rather than existing in chalcopyrite and pyrrhotite phases as isomorphism during sufficient fractional crystallization of sulfide melt, which gathered nickel and cobalt elements widely. Also, more than one magma might result in the superposition of ore-forming elements. Later, the ore-forming elements redistribute limitedly through a hydrothermal process. The metallogenic mechanism model of nickel and cobalt established in the present study not only explains the process of nickel–cobalt mineralization in Xiarihamu but also can be applied to similar deposits and has a wide universal replicability.

Keywords: morphology, mineralogy, nickel–cobalt minerals, Xiarihamu, chemical compositions, mineralization model

INTRODUCTION

The strategic nickel and cobalt mineral resources in China play important roles in both civil and military fields. Although there are abundant magmatic sulfide deposits in China, they are mainly rich in copper and nickel, which are similar to large–superlarge magmatic sulfide deposits in the world. Cobalt occurs mostly as an accessory element and has not been the focus of significant attention (Zhao et al., 2019). This omission has caused a lack of systematic research in nickel–cobalt metallogenesis, which is inadequate considering the increased demand of these elements. The discovery of the Xiarihamu magmatic nickel–cobalt sulfide deposit, as the second largest nickel deposit in China, gives us an excellent opportunity to study occurrence states, genetic types, and metallogenesis of nickel and cobalt in minerals.

Globally, magmatic Ni–Cu–(PGE) sulfide deposits has occurred in a large range of periods, such as Archean, Paleoproterozoic, Mesoproterozoic, Neoproterozoic, and Paleozoic. But they have occurred mainly in early Neoproterozoic (1,000–800 Ma) and late Paleozoic (295–250 Ma) in China (Lü et al., 2007). Especially, the Xiarihamu magmatic nickel–cobalt sulfide deposit has special early Paleozoic (406–423 Ma) metallogenic age (Li et al., 2015; Song et al., 2016; Qian et al., 2020), representing a new metallogenic epoch of magmatic sulfide in China. The proven nickel metal reserve of the Xiarihamu deposit amounts to 1.18 Mt, with a grade of 0.23–3.48% and averaging 0.65 wt%, and that of cobalt metal is 40,300 t, with a grade of 0.012–0.079% and averaging 0.028 wt% (No. 5 Geological and Mineral Survey Institute of Qinghai Province, 2014). It has low copper grade (0.14 wt%) and lacks platinum group elements (Du et al., 2014). These characteristics attract us to explore the special enrichment process of nickel and cobalt in metallogenic evolution.

Previous studies have reported its geological characteristics (Yi et al., 2015), geochemistry of ore-bearing rocks (Jiang et al., 2015; Zhang Z.W. et al., 2016), various isotopes (Tang et al., 2017; Wang et al., 2018), rock and metallogenic ages (Wang et al., 2013; Ao et al., 2014; Wang et al., 2014b), and tectonic setting (Jiang et al., 2015; Li et al., 2015). The major elements of chromite, olivine, and pyroxene; rare earth elements; trace elements; and isotopes of bulk rocks indicate that the parental magma originated from partial melting of the asthenospheric mantle that was modified by melts derived from the subduction slab and subsequently underwent multiple-epoch silicate fractional crystallization and liquation of sulfides and silicates (Wang et al., 2014; Feng et al., 2016; Zhang Z.B. et al., 2016; Du, 2018; Song et al., 2020). Regarding the distribution, morphology, and geochemistry of pentlandite, pyrrhotite, and chalcopyrite in ores revealed that nickel occurs mainly as sulfides, whereas cobalt is usually isomorphically substituted for Ni^{2+} in pentlandite and violarite (Wang et al., 2014a; Feng et al., 2016).

Although strong positive correlation among nickel, copper, and cobalt has been reported, high-grade nickel ores are often closely correlated with cobalt, rather than copper, ores. Moreover, as direct carriers of ore-forming elements, nickel and cobalt minerals can be easily enriched through magma evolution, hydrothermal process, and weathering (Zhao et al., 2019). Identification of various mineralization stages is helpful in understanding the mineralization processes of nickel and cobalt.

In this study, we delineate the petrographic and textural characteristics of host rocks and sulfides of the Xiarihamu nickel–cobalt sulfide deposit. Based on these characteristics, the distribution, morphology, chemical compositions, and evolution history of the nickel and cobalt minerals are examined in detail to study the original ore-forming processes. The results reveal the enrichment mechanism of nickel and cobalt in the deposit and provide a strong clue to indicate the direction of prospecting high-grade ores in the future.

GEOLOGY OF THE XIARIHAMU DEPOSIT

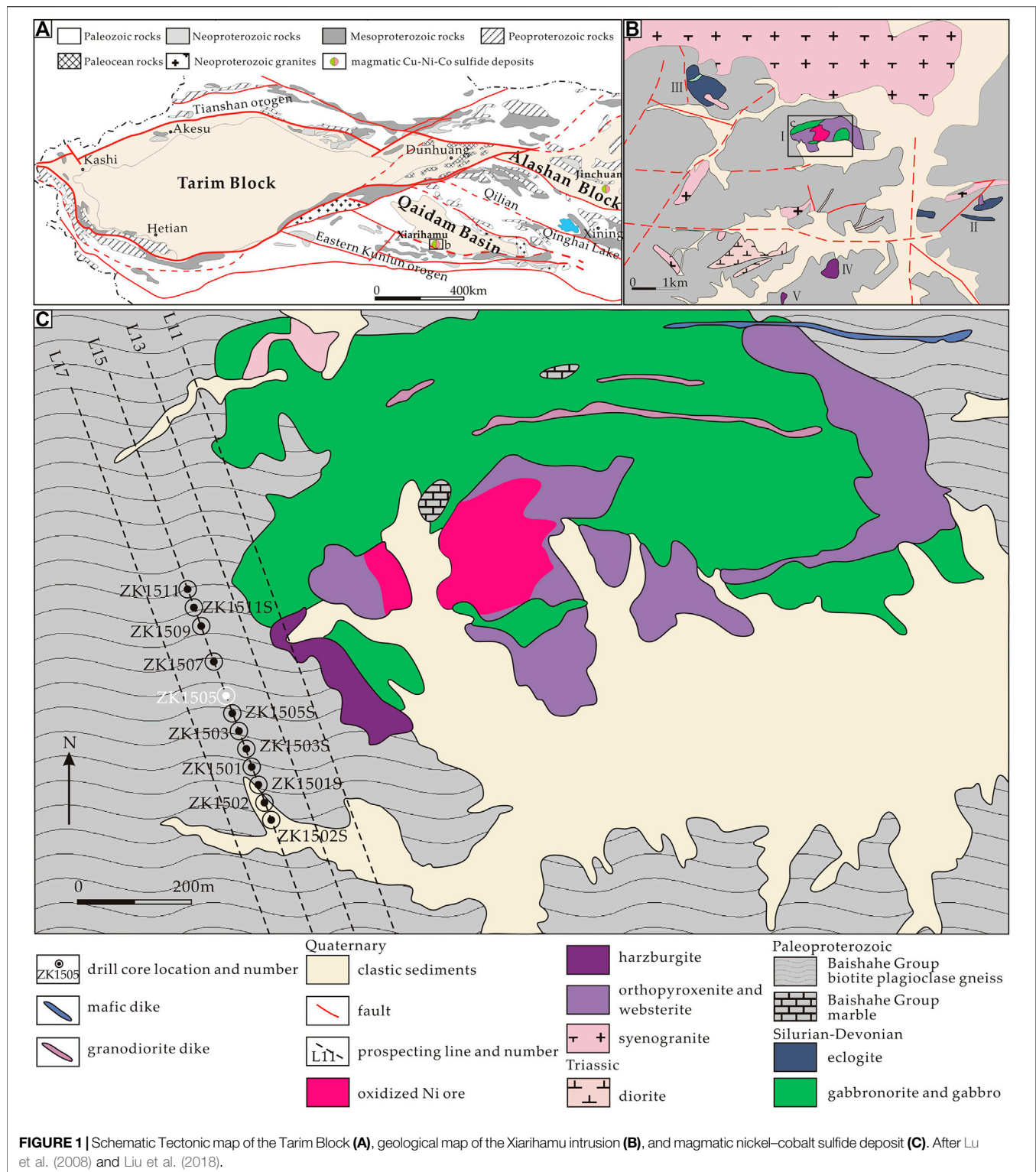
The Xiarihamu mafic–ultramafic complexes are situated in the northern east/west-trending East Kunlun Orogen at the southern margin of the Qaidam Block, as a part of the Tarim Block in geological history (Li, 2018; Li et al., 2020) (**Figure 1A**). Five mafic–ultramafic complexes labeled I, II, III, IV, and V have been discovered in the Xiarihamu area (**Figure 1B**). The complexes were in the form of the lopolith that intruded metamorphic Jinshuikou group strata, which is composed of biotite granite gneiss, quartz schist, plagioclase amphibolite, marble, and Neoproterozoic granitic gneiss. And, they have a small exposed area presently. The faults are highly developed in this area in the east–west, northwest, and northeast directions. Diorite, syenogranite, and monzonite of various ages are also present.

The Xiarihamu magmatic nickel–cobalt sulfide deposit is hosted within the Xiarihamu I complex, which is located in the northern part of the central mining area. The Xiarihamu I mafic–ultramafic complex is irregularly shaped with an approximate length, width, and area of 1,600 m, 900 m, and 1.33 km², respectively, and a northeast–east strike of approximately 60°. The altitude of the complex is high in the east and low in the west. The middle and eastern parts of the Xiarihamu I complex are exposed at the surface, whereas the western part is concealed beneath the Jinshuikou group. The exposed complex is composed of dunite, pyroxenite, harzburgite, wehrlite, gabbro, and gabbro as well as sporadic oxidized ore (**Figure 1C**). The ore bodies, which occur in the peridotite and pyroxenite facies as well as part of the gabbro facies, are generally about 100–700 m long and 1.5–80 m thick and are mostly thick-layered and lenticular with a few funnel-shaped and irregular forms.

PETROLOGY OF INTRUSIONS

The No.15 exploration line is located in the western part of the mining area (**Figure 1**). The rocks have the integral lithofacies type of mafic–ultramafic rocks: dunite, harzburgite, wehrlite, pyroxenite, and gabbro (**Figure 2**). The ores are completely buried underground and show good mineralization. The characteristics of the mafic–ultramafic rocks vary among drill cores, as indicated by the lithofacies distribution and ore bodies observed in a cross section of this exploration line. Generally, compared with the rocks occurring in the south, the mafic–ultramafic rocks in the north have relatively simple lithology, deep buried, and low thickness, with local thickness of only 50 m, which is rich in high-grade ores (Ni > 1 wt%; Co > 0.03 wt%; Cu > 0.4 wt%).

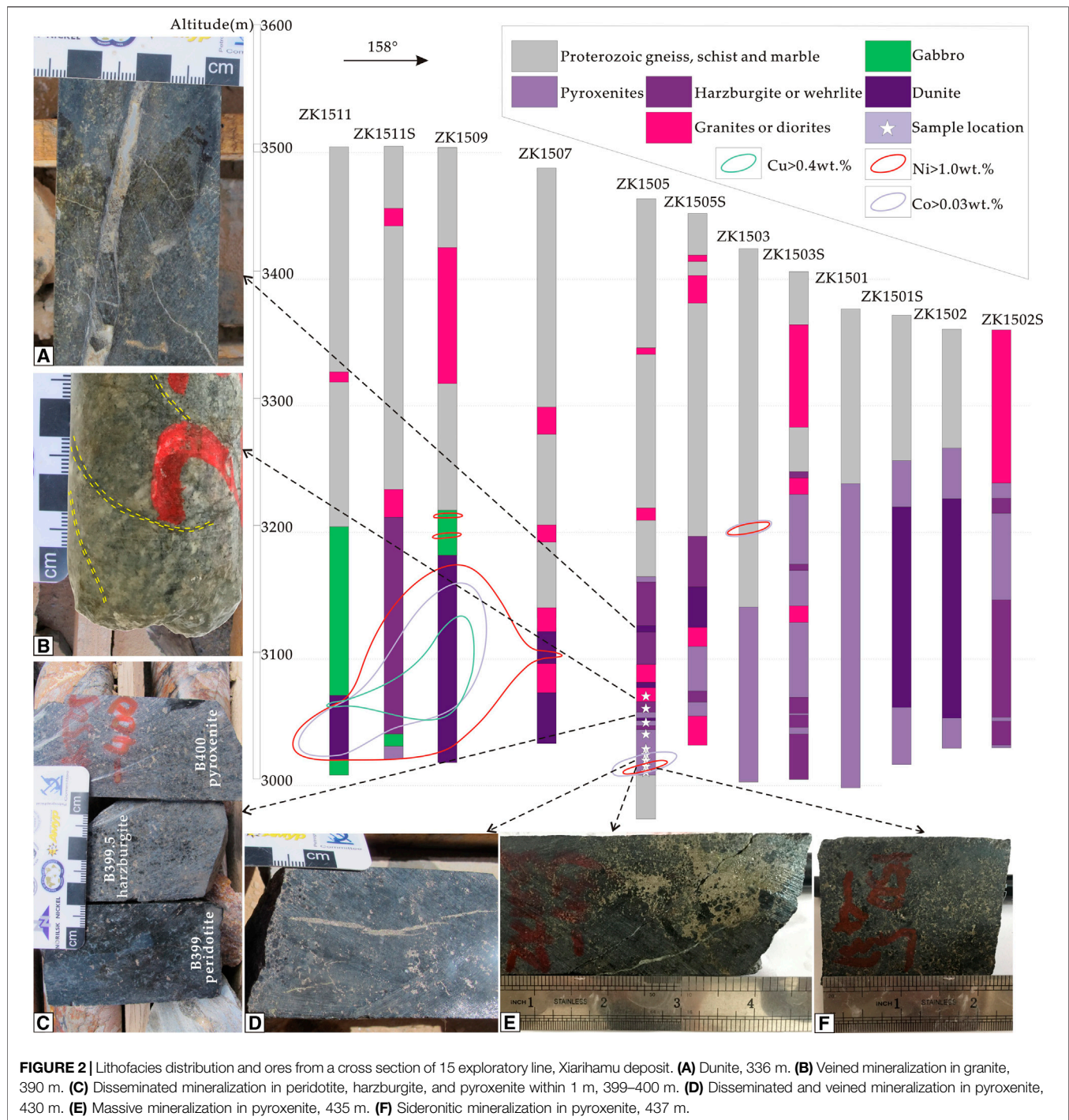
More interestingly, a strong correlation is present between the grades of nickel and cobalt, rather than between those of nickel and copper. That is, a higher nickel grade corresponds with a richer cobalt grade (nickel > 1 wt%; cobalt > 0.03 wt%; **Figure 2**), which is also found in other exploration lines in this deposit (No. 5 Geological and Mineral Survey Institute of Qinghai Province, 2015). This phenomenon also occurs in



large copper–nickel–cobalt sulfide deposits such as Jinchuan deposit (Cao et al., 2010). To study the behavior of nickel and cobalt in the ore-forming processes, a ZK1505 drill hole was selected as the object of this research owing to its different

lithofacies and ore-forming types as well as the strong correlation of cobalt and nickel grades.

Approximately 300-m-thick granitic gneiss of the Jinshui Kou group is located in the upper part of ZK1505 drill core, and the



mafic-ultramafic complex occurs mainly in the lower part, with some scattered granites in the drill core locally. In general, the distribution of mafic-ultramafic rocks and mineralization shows obvious trend. The upper part is composed of peridotite facies including dunite (Figure 2A), harzburgite, and wehrlite (Figure 3A), and the lower part is composed of pyroxenite facies including orthopyroxenite (Figure 3B) and websterite (Figure 3C). The mineralization types change

gradually from top to bottom. At 300–400 m, there are mainly spotted, veined (Figures 2B,D), and disseminated (Figure 2C) mineralization, while massive (Figure 2E) and sideronitic mineralization (Figure 2F) occurs at 400–448 m. A gradual transition occurs between different rock types of a single lithofacies, and structural fracture zones or vein rocks often appear at the point of lithofacies change. In particular, veinlet mineralized granite (Figure 2A) occurs at 370–390 m,

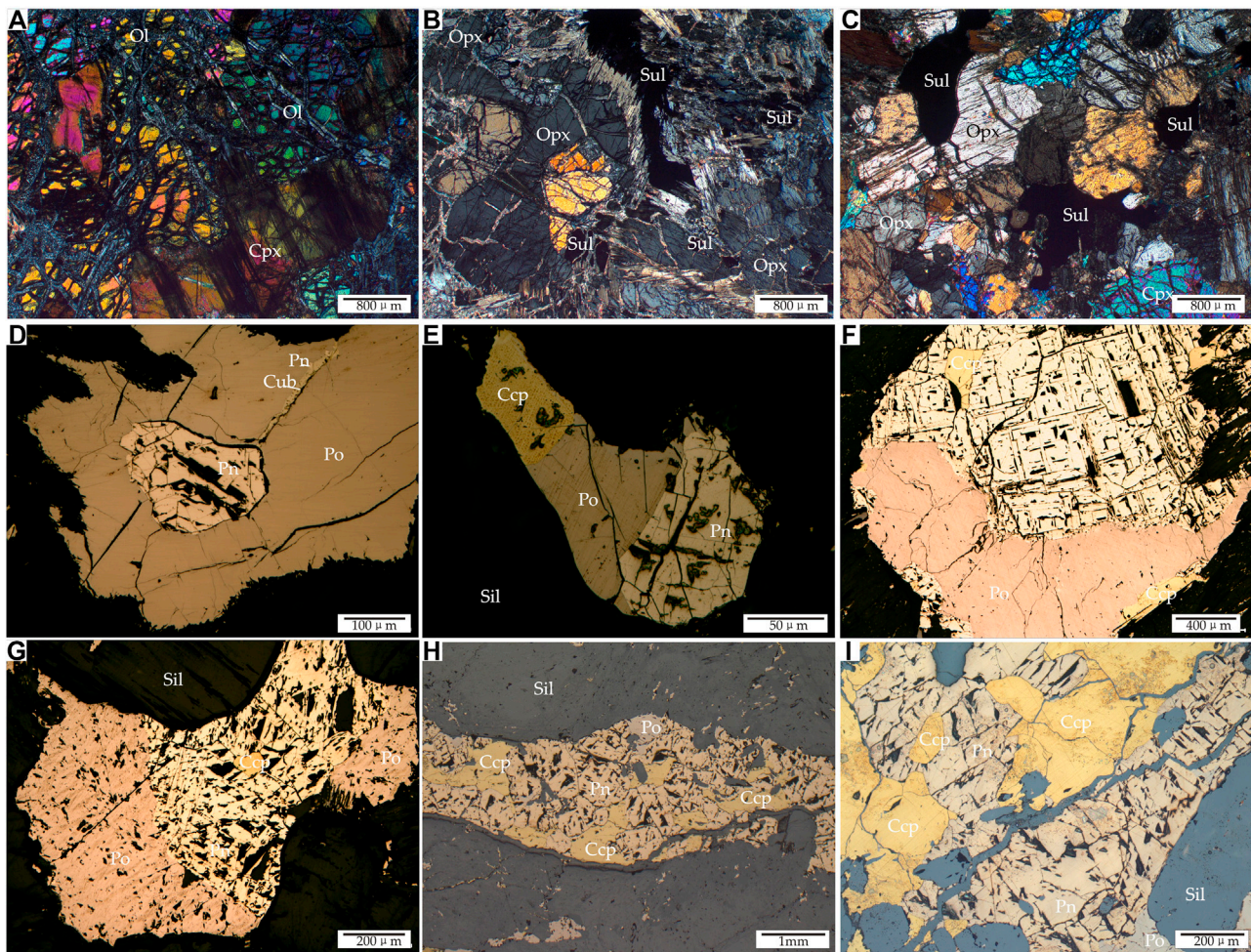


FIGURE 3 | Photomicrographs of sampling locations in main rock types (transmitted-light images) and sulfides (reflected-light images). **(A)** Wehrlite, 399.5 m. **(B,C)** Disseminated mineralization in orthopyroxenite and websterite, 400 and 427 m. **(D)** Po, filled with Cub vein in crack, encased Pn in pyroxenite, 406 m. **(E)** Ccp, Po, and Pn with straight borders in pyroxenite, 406 m. **(F,G)** Pn encased Ccp and contact with Po, in coarse disseminated mineralized pyroxenite, 418 and 427 m. **(H)** An increased quantity of Ccp in veined mineralized pyroxenite, 430 m. **(I)** More Ccp in massive mineralized pyroxenite, 442 m. Cpx, clinopyroxene; Ol, olivine; Opx, orthopyroxenite; Pn, pentlandite; Po, pyrrhotite; Ccp, chalcopyrite; Cub, cubanite; Sul, sulfide; Sil, silicate minerals.

where the lithofacies change. Within 1 m, at about 400 m, peridotite, harzburgite, and pyroxenite show transitional changes (**Figures 2C, 3A,B**). Below 400 m, the rock is essentially pyroxenite.

Pyrrhotite, pentlandite, and chalcopyrite are the main sulfides in the ores. Among them, pyrrhotite is the most abundant and chalcopyrite is the least. Pyrrhotite usually encloses pentlandite (**Figure 3D**) or occurs in a micrometer scale at the contact between chalcopyrite and pentlandite (**Figures 3E,F**). The chalcopyrite is in contact with pyrrhotite or enclosed by pentlandite (**Figures 3F,G**) in disseminated mineralization, and it coexists with pyrrhotite and pentlandite in veined and massive mineralization (**Figures 3H,I**). In addition, cubanite is observed in pyrrhotite cracks with pentlandite flames (**Figure 3D**).

EXPERIMENTAL METHODS

Although both nickel and cobalt minerals are visible in the 11, 13, 15, and 17 exploration lines, drill core ZK1505 includes different representative lithofacies and mineralization types (**Figure 2**). Therefore, it is considered as a suitable research object for studying the occurrence states and evolution behaviors of nickel and cobalt. For this study, 20 samples were collected from drill core ZK1505 in the central part of the ultramafic zone (**Figure 1C**). We conducted backscattering image observation, mineral chemical composition analysis, and element surface scanning analysis of ore minerals, particularly nickel and cobalt minerals and their associated minerals, using a JEOL JXA-8230 electron probe microanalyzer (EPMA) at Xi'an Center of China Geological Survey, Ministry of Natural

Resources. The analytical conditions for component analysis were 20 kV, 20 nA beam current, 1 μm beam size, 10 s peak-counting time, and 5 s upper and lower background counting time. In addition, the ZAF (atomic number, absorption, and fluorescence) correction method was used. The mineral standards of gallium arsenide (As 243), selenium (Se 97), chromium (Cr 145), pyrite (Fe 139, S 41), copper (Co 132), nickel (Ni 140), chalcopyrite (Cu 187), sphalerite (Zn 211), bismuth (Bi 231), cadmium (Cd 89), tellurium (Te 99), and stibnite (Sb 112) were used for calibration. The analytical conditions for element surface scanning were 20 kV, 100 nA, 0.3 μm step size, and 100 ms dwell time.

RESULTS

Distribution and Morphology of Nickel–Cobalt Minerals

The main ore minerals in the mining area are pyrrhotite, pentlandite, and chalcopyrite. Some nickel–cobalt minerals occur as accessory phases, as represented by nickel–arsenide, including maucherite ($\text{Ni}_{11}\text{As}_8$) and nickeline (NiAs), and sulpharsenides of nickel and cobalt such as gersdorffite (NiAsS) and cobaltite (CoAsS). In addition, nickel can also form minerals with some complex anions containing bismuth, arsenic, and sulfur. Parkerite ($\text{Ni}_3\text{Bi}_2\text{S}_2$) and arsenohauchecornite ($\text{Ni}_{18}\text{Bi}_3\text{AsS}_{16}$), which have been described in other superlarge copper–nickel deposits such as Sudbury (Michener and Peacock, 1943; Springer, 1989) and Noril'sk (Ponomarenko et al., 1987; Spiridonov et al., 2008), have not been described in magmatic copper–nickel sulfides in China. However, they are reported for the first time in the present study. Here, we delineate the microstructural characteristics of these minerals according to the different mineralization types, as shown in the backscattered electron images in **Figure 4**.

In the spotted mineralized peridotite above 399 m, there are pyrrhotite, pentlandite, and chalcopyrite locally and no other microscopically visible other nickel–cobalt minerals (except for pentlandite) appear. Below the depth of 399 m, xenomorphic maucherites ($10 \times 10\text{--}100 \times 150 \mu\text{m}$) are encased in pentlandite and pyrrhotite in the disseminated mineralized pyroxenite (**Figures 4A,B**). Euhedral nickelines and parkerites, with sizes of $10 \times 20\text{--}30 \times 80 \mu\text{m}$, are encased in pentlandite and pyrrhotite (**Figures 4C,D**). The ores have sideronitic texture—massive texture at the bottom of the drill core at about 435–446 m. Euhedral–subhedral granular cobaltites, with sizes of $20 \times 40\text{--}80 \times 100 \mu\text{m}$, always occur in the pyrrhotite margin and in contact with other sulfides or oxides in pyrrhotite–magnetite (**Figure 4E**), pyrrhotite–pentlandite–chalcopyrite (**Figure 4F**), pyrrhotite–pentlandite (**Figures 4G,H**), and pyrrhotite–chalcopyrite assemblages (**Figure 4I**). Several maucherites are dispersed in silicate minerals near the sulfides in this area (**Figure 4E**). They usually contain numerous inclusions of parkerite and arsenohauchecornite and display skeletal crystals (**Figures 4G–I**). Parkerites occur as $30 \times 30 \mu\text{m}$ xenomorphic granular inclusions (**Figure 4I**) and scattered microparticles (**Figure 4F**) in the center of cobaltites in both primary

pyrrhotite–pentlandite–chalcopyrite and pyrrhotite–pentlandite assemblages. Arsenohauchecornites, like some parkerites, occur as scattered microparticles in cobaltites in a primary pyrrhotite–pentlandite assemblage (**Figure 4G**).

Numerous veinlets (1–3 mm) are developed in the granites at 370–390 m (**Figure 2B**). Pyrrhotite–chalcopyrite–violarite veins are identified at 390 m, with maucherite, nickeline, and gersdorffite. The violarite, a less common iron–nickel sulfide, exhibits typical shrinkage characteristics of an exsolution product, which is dense at the core and clean at the edges (**Figure 4J**). Gersdorffite replaced pyrrhotite or chalcopyrite and displays a tight cluster now. A hackly erosion boundary was formed along fractures, and a few irregular metasomatic relict texture pyrrhotites and chalcopyrites occur inside during the metasomatism (**Figure 4K**). The enlarged image clearly shows the metasomatic structure of gersdorffite (**Figure 4L**). Granular nickelines are encased in pyrrhotite and violarite. Numerous xenomorphic granular maucherites developed in the cracks of pyrrhotite at the remote end of the metasomatic veined gersdorffite (**Figure 4K**), whereas others are nickelines with no metasomatic alteration.

Chemical Compositions of Nickel–Cobalt Minerals

The major and trace elements of the nickel and cobalt minerals are shown in **Table 1**. According to the above observations and EPMA data, the characteristics of the maucherites are different between the disseminated and vein mineralization types. The scattered xenomorphic granular maucherites in disseminated mineralization contain 45.52–46.80 wt% arsenic, 49.16–52.20 wt% nickel, and small amounts of iron and copper. In particular, cobalt replaced nickel by 0.25–0.33 wt%. In contrast, the maucherites contain 46.14–46.89 wt% arsenic and 51.13–52.27 wt% nickel with little fluctuation and substantially no cobalt in the veined mineralization. The major element (nickel, copper, cobalt, arsenic, and sulfur) maps of veined mineralization (**Figure 5**) clearly show that the maucherites experienced metasomatism together with pyrrhotite and chalcopyrite and are enclosed in a cobalt-bearing gersdorffite cluster.

The nickelines are composed of 4.26–44.48 wt% nickel, 53.3–54.53 wt% arsenic, and minute quantities of iron and copper. Tellurium replaced up to 1.16 wt% of arsenic.

The cobaltites contain 17.59–27.17 wt% cobalt, 5.84–13.01 wt% nickel, 45.58–43.04 wt% arsenic, 19.33–20.10 wt% sulfur, 3.41–5.24 wt% iron, and a small amount of tellurium, all belonging to various cobaltite–nickel cobaltites. The contents of cobalt and nickel show obvious inverse correlation in **Figure 6A**, which might be attributed to the form of cobaltite–gersdorffite solid solution or the varying degrees of pyrrhotite metasomatism.

The parkerites are composed of 25.38–28.11 wt% nickel, 61.88–64.98 wt% bismuth, and 9.80–10.03 wt% sulfur. The arsenohauchecornites are composed of 24.86 wt% arsenic, 15.63 wt% iron, 17.30 wt% cobalt, 5.66 wt% nickel, 21.89 wt% sulfur, and 16.32 wt% bismuth. Compared with the ideal formula

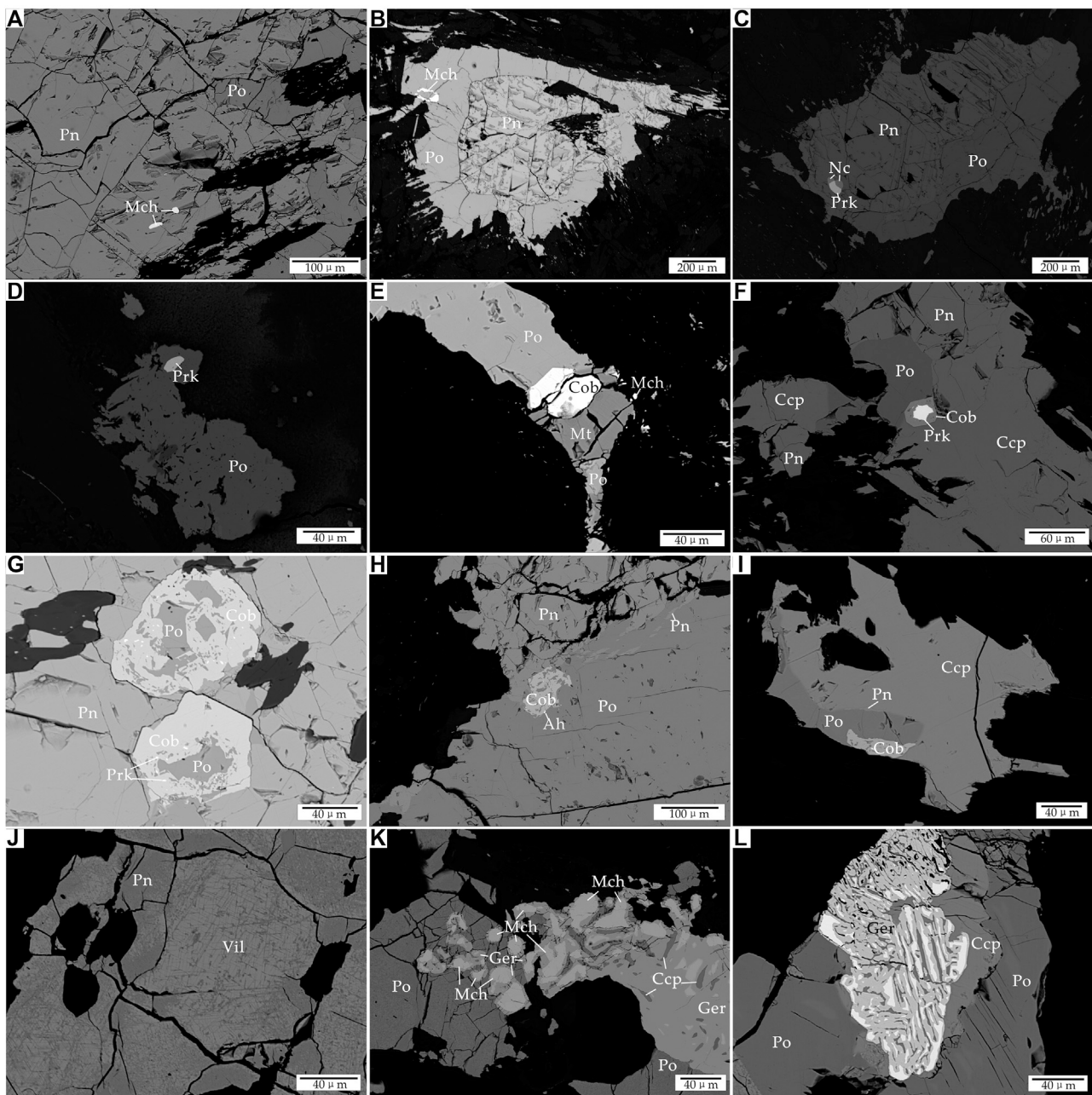


FIGURE 4 | Backscattered electron images of nickel-cobalt minerals and relevant minerals in ZK1505, Xiarihamu deposit. **(A,B)** Xenomorphic granular Mch are encased in Po and Pn, 399.5 m. **(C,D)** Euhedral Nc and Prk were encased in Pn and Po, 418 and 427 m. **(E)** Xenomorphic granular Mch dispersedly grows in silicate minerals near sulfide, 437 m. **(F)** Xenomorphic granular parkerite in the center of euhedral cobaltite, enclosed in Po, 444 m. **(G,H)** Skeletal crystals of cobaltites in Pn-Po assemblages, contained numerous inclusions of parkerite and arsenohauchecornite, 440 and 442 m. **(I)** Skeletal crystals of cobaltites in Po-Ccp assemblages, 442 m. **(J-L)** Violarite, subhedral-xenomorphic granular maucherites, grew in the crack of Po and metasomatic gersdorffite cluster in the veinlets of granites, 390 m. Po, pyrrhotite; Pn, pentlandite; Ccp, chalcocopyrite; Nc, nickeline; Mch, maucherite; Cob, cobaltite; Ger, gersdorffite; Vil, violarite; Mt, magnetite; Prk, parkerite; Ah, arsenohauchecornite.

of arsenohauchecornite ($\text{Ni}_{18}\text{Bi}_3\text{AsS}_{16}$), the isomorphs of iron and cobalt substituted nickel in large quantities. The analyzed parkerite and arsenohauchecornite grains are too small to support physical characterization, which would result in inaccurate content data; however, the mineral identification is not affected.

The composition of the violarites is 24.08–26.15 wt% iron, 35.22–36.59 wt% nickel, 35.64–38.03 wt% sulfur, and >1 wt% nickel/iron. However, this composition is different from that of its ideal composition, which is 18.52 wt% iron, 38.94 wt% nickel, and 42.54 wt% sulfur; in the former, the iron is higher, while the sulfur content is lower.

TABLE 1 | Electron probe microanalyzer data of nickel–cobalt minerals in ZK1505, Xiarihamu deposit.

	No.	As	Fe	Co	Ni	Cu	Zn	S	Bi	Cd	Se	Cr	Sb	Te	Total	Formula
Nickeline (NiAs)	B-418-12	54.53	0.66	0.10	44.31	—	—	0.23	—	0.01	—	—	—	0.97	100.80	Ni _{1.03} As
	B-418-13	54.12	0.40	0.12	44.26	—	—	0.24	—	0.01	—	—	—	0.18	99.32	Ni _{1.04} As
	B-390-13	53.94	0.43	0.05	44.19	0.26	—	0.19	—	0.01	—	—	0.17	0.35	99.58	Ni _{1.05} As
	B-390-10	53.37	0.44	0.02	44.45	0.04	—	0.23	—	—	—	—	0.14	0.30	98.98	Ni _{1.06} As
	B-390-24	54.51	0.58	0.05	43.97	0.41	—	0.21	—	—	—	—	0.11	1.16	100.99	Ni _{1.03} As
	B-390-27	54.53	0.38	—	44.48	0.20	—	0.20	—	—	—	—	0.20	0.20	100.20	Ni _{1.04} As
Cobaltite (CoAsS)	B-440-27	53.97	3.23	0.14	43.26	0.05	—	0.25	—	0.01	—	—	—	0.98	101.89	Ni _{1.02} As
	B437-1	44.86	3.99	23.76	8.37	—	—	19.76	—	—	—	—	—	0.09	100.82	Co _{0.65} Fe _{0.12} Ni _{0.23} As _{0.97} S
	B442-1	44.14	3.82	23.17	8.79	—	—	19.86	—	—	—	—	—	0.19	99.98	Co _{0.63} Fe _{0.11} Ni _{0.24} As _{0.95} S
	B442-2	44.41	3.88	24.16	8.77	—	—	19.96	—	—	—	—	—	0.06	101.24	Co _{0.66} Fe _{0.11} Ni _{0.24} As _{0.95} S
	B442-10	43.96	5.24	22.19	9.68	0.08	0.02	19.76	0.01	0.01	—	—	—	0.10	101.06	Co _{0.61} Fe _{0.15} Ni _{0.27} As _{0.95} S
	B442-14	44.61	3.94	27.17	5.84	—	—	19.74	—	0.02	—	—	—	0.08	101.40	Co _{0.75} Fe _{0.11} Ni _{0.16} As _{0.97} S
	B442-18	44.00	5.18	20.94	9.74	—	—	19.83	0.36	—	—	—	—	0.12	100.16	Co _{0.57} Fe _{0.15} Ni _{0.27} As _{0.95} S
	B442-20	44.63	3.81	24.17	8.27	—	—	20.10	—	—	—	—	—	0.16	101.14	Co _{0.65} Fe _{0.11} Ni _{0.22} As _{0.95} S
	B442-21	45.24	3.72	24.75	7.63	—	0.10	19.94	0.03	0.01	—	—	—	0.06	101.48	Co _{0.68} Fe _{0.11} Ni _{0.21} As _{0.97} S
	B442-23	44.51	3.41	23.02	9.69	—	—	19.71	0.02	—	—	—	—	0.21	100.58	Co _{0.64} Fe _{0.10} Ni _{0.27} As _{0.97} S
	B444-1	44.48	4.43	23.02	8.80	—	—	19.85	—	0.04	—	—	—	0.15	100.78	Co _{0.63} Fe _{0.13} Ni _{0.24} As _{0.96} S
	B444-2	43.61	4.44	25.28	7.05	—	0.02	20.07	—	—	—	—	—	0.04	100.51	Co _{0.69} Fe _{0.13} Ni _{0.19} As _{0.93} S
	B444-3	45.34	5.20	17.59	13.01	0.44	—	19.69	—	—	—	—	—	0.11	101.37	Co _{0.49} Fe _{0.15} Ni _{0.36} As _{0.99} S
	B446-1	45.16	5.02	22.38	8.47	—	—	19.77	0.03	—	—	—	—	0.18	101.00	Co _{0.62} Fe _{0.15} Ni _{0.23} As _{0.98} S
	B446-2	45.58	3.41	19.45	12.62	—	—	19.41	—	0.01	—	—	—	0.20	100.68	Co _{0.55} Fe _{0.10} Ni _{0.36} As _{1.01} S
Gersdorffite (NiAsS)	B-390-1	44.39	1.14	0.35	34.54	0.09	—	19.21	—	—	—	—	0.22	0.77	100.70	Ni _{0.98} Fe _{0.03} Co _{0.01} As _{0.99} S
	B-390-2	45.12	1.98	0.34	34.09	0.07	—	19.23	—	—	—	—	0.34	0.14	101.31	Ni _{0.97} Fe _{0.06} Co _{0.01} AsS
	B-390-3	43.96	1.22	0.23	33.37	0.02	—	19.27	—	0.03	—	—	0.57	0.08	98.73	Ni _{0.95} Fe _{0.04} Co _{0.01} As _{0.98} S
	B-390-4	44.98	2.60	0.26	33.18	0.41	—	19.10	—	—	—	—	0.34	0.10	100.96	Ni _{0.95} Fe _{0.08} Co _{0.01} As _{1.01} S
	B-390-5	43.89	1.86	0.67	32.94	0.15	—	18.87	—	—	—	—	0.31	0.79	99.48	Ni _{0.95} Fe _{0.06} Co _{0.02} AsS
	B-390-6	43.44	1.63	1.20	32.28	—	—	19.44	—	—	—	—	0.12	0.20	98.29	Ni _{0.91} Fe _{0.05} Co _{0.03} As _{0.96} S
	B-390-7	45.34	1.86	1.74	32.55	0.18	—	19.43	—	—	—	—	0.00	0.73	101.83	Ni _{0.91} Fe _{0.05} Co _{0.05} AsS
	B-390-8	44.22	2.83	2.78	30.70	0.01	—	19.65	—	—	—	—	0.13	0.16	100.48	Ni _{0.85} Fe _{0.08} Co _{0.08} As _{0.96} S
	B-390-9	44.82	2.51	2.34	30.98	0.10	—	19.46	—	—	—	—	0.25	0.86	101.30	Ni _{0.87} Fe _{0.07} Co _{0.07} As _{0.99} S
Violarite (FeNi ₂ S ₄)	B390-10	0.06	24.08	0.13	35.22	0.07	—	38.03	—	—	0.01	—	—	0.29	97.89	Fe _{1.45} Ni _{2.02} S ₄
	B390-11	0.12	25.21	0.05	35.67	0.01	—	36.78	—	0.03	—	—	—	0.73	98.60	Fe _{1.57} Ni _{2.12} S ₄
	B390-12	—	26.15	0.06	35.83	0.03	—	35.64	—	—	—	—	—	0.81	98.51	Fe _{1.69} Ni _{2.20} S ₄
	B-390-13	—	24.93	0.15	36.59	—	—	37.43	—	—	—	0.03	—	0.72	99.85	Fe _{1.53} Ni _{2.14} S ₄
Maucherite (Ni ₁₁ As ₈)	B-399.5-10	46.80	0.91	0.25	52.20	—	—	0.12	—	0.04	—	—	—	0.34	100.67	Ni _{11.39} As ₈
	B-399.5-13	45.52	2.28	0.33	51.00	0.07	—	0.24	—	—	—	—	—	1.14	100.58	Ni _{11.44} As ₈
	B-406-10	45.64	3.35	0.30	49.16	0.23	—	0.36	—	0.03	—	—	—	0.37	99.44	Ni ₁₁ As ₈
	B-406-12	46.18	2.81	0.30	51.25	0.06	—	0.18	—	0.03	—	—	—	0.48	101.28	Ni _{11.33} As ₈
	B-390-14	46.89	0.62	0.00	52.27	0.04	—	0.15	—	0.06	—	—	—	1.13	101.15	Ni _{11.38} As ₈
	B-390-15	46.14	1.12	0.01	51.13	0.15	—	0.18	—	—	—	—	—	1.07	99.80	Ni _{11.32} As ₈
	B-390-16	46.17	0.12	0.00	51.95	0.05	—	0.16	—	—	—	—	—	0.33	98.79	Ni _{11.49} As ₈
	B-390-17	46.78	0.33	0.02	52.03	0.09	—	0.13	—	—	—	—	—	1.34	100.72	Ni _{11.36} As ₈
Parkerite (Ni ₃ Bi ₂ S ₂)	B-442-11	—	0.70	0.01	25.38	0.71	—	10.03	61.88	—	0.02	1.15	—	0.17	100.05	—
	B-446-3	—	0.43	—	26.88	0.28	—	9.80	63.65	—	—	1.10	0.31	0.67	103.11	—
	B-444-25	—	0.52	0.21	28.11	0.13	—	9.91	64.98	—	0.01	1.03	0.26	0.86	106.01	—
	B-399.5-28	—	0.83	0.02	27.50	0.42	—	10.03	64.67	—	0.04	1.15	0.89	—	105.53	—
Arsenohauchecornite (Ni ₁₈ Bi ₃ AsS ₁₆)	B-440-24	24.86	15.63	17.30	5.66	—	—	21.89	16.32	—	—	—	—	0.01	101.67	—

Notes: “—”, below the detection limit; blanks, unanalyzed or not calculated.

The gersdorffite compositions are as follows: 0.225–2.782 wt% cobalt, 30.70–34.54 wt% nickel, 43.44–45.34 wt% arsenic, 18.87–19.65 wt% sulfur, 1.14–2.83 wt% iron, and trace amounts of tellurium, antimony, and copper. The nickel content ranges from 0.85 to 0.98 atoms per formula unit (apfu). As shown in **Figure 5B**, the contents of cobalt and nickel exhibit obvious inverse correlation. The abnormality of individual points might be related to the degree of metasomatism. In the major element (nickel, copper, cobalt, arsenic, and sulfur) maps shown in **Figure 6B**, the cobalt content of gersdorffites is not evenly distributed at the edges of nickeline and the central vein.

DISCUSSION

Due to the special cobalt and nickel mineralization in the Xiarihamu magmatic sulfide deposit, whether there exist a special enrichment and evolution mechanism of nickel and cobalt is particularly important. The previous study proposes hydrothermal genesis of cobaltites (Wang, 2014), which is inconsistent with our study. The extensive appearances of nickel and cobalt minerals including cobaltites are closely related to high-grade ores in the deposit. So, it is necessary to interpret the genesis clearly.

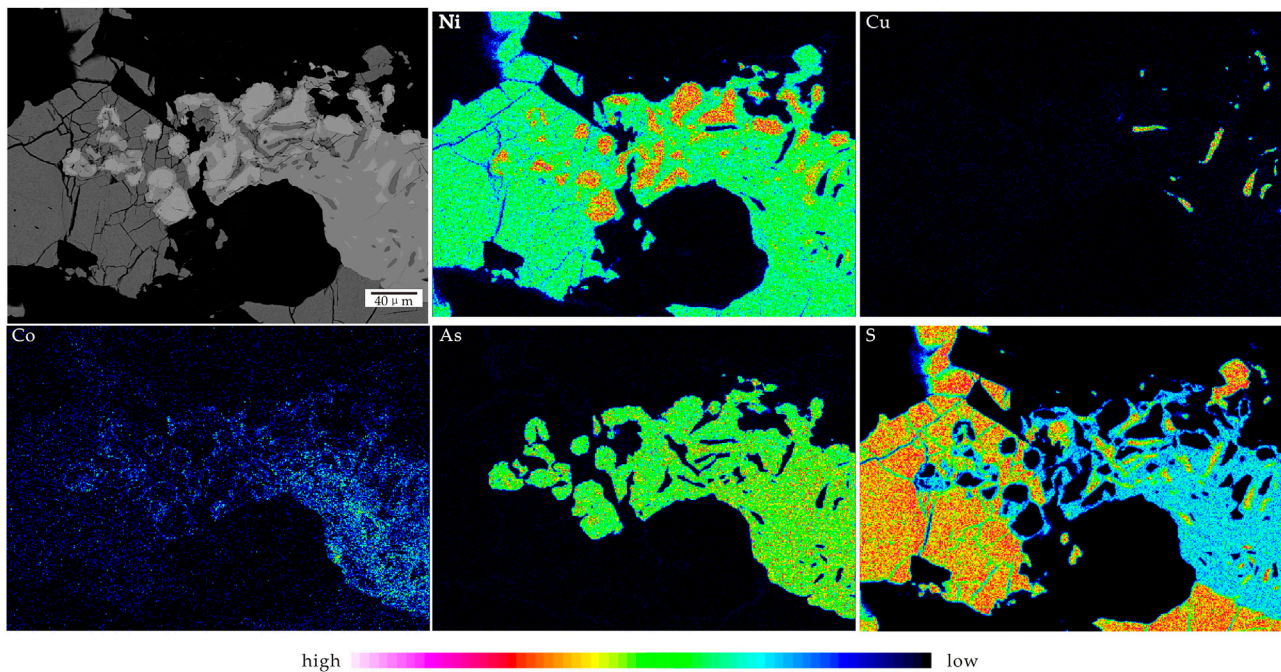


FIGURE 5 | Major element (Ni, Cu, Co, As, and S) maps of vein mineralization in ZK1505, Xiarihamu deposit.

Enrichment of Nickel and Cobalt

Previous studies indicated that when a natural sulfide melt reaches arsenide saturation (and probably many other chalcogens and metalloids in magmatic melts), a separate Ni-PGE-rich arsenide (bismuth) melt exsolves (Helmy et al., 2013). And, the affinities of the chalcophile metals for an immiscible arsenide melt follow the order $\text{Pt} > \text{Pd} > \text{Ni} \gg \text{Fe} \approx \text{Cu}$. This phenomenon conceivably occurs in nature (Fleet, 1973; Piña et al., 2014) and plays an important role in the mineralization of many cobalt deposits. Thus, if they reach arsenide (bismuth) saturation, we cannot simply explain the

formation of such kind of minerals as forming at the late stage of sulfide melt fractionation because of the low partition coefficients between the monosulfide solid solution (MSS) and the melt (Helmy et al., 2010; Helmy et al., 2013; Liu and Brenan, 2015). Small subhedral-xenomorphic granular arsenic- or bismuth-bearing minerals (nickeline, parkerite, arsenohauchecornite, and maucherite) were enclosed in base metal sulfides in sideronitic massive ores rather than spot-disseminated ores in Xiarihamu. Hence, it reveals that sulfide saturation occurs in the magma during a large amount of crustal material contamination (Liu et al., 2018).

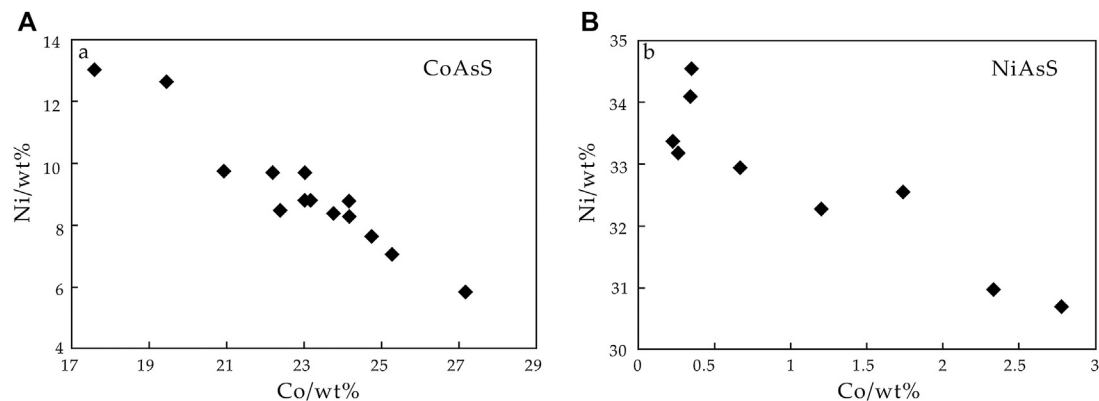


FIGURE 6 | Co-Ni (wt%) diagram of cobaltite (A) and gersdorffite (B).

TABLE 2 | Grade of nickel and cobalt in ZK1505, Xiarihamu deposit.

	Depth/m	Ni/wt%	Co/wt%
H1	295–296.8	0.023	0.0014
H2	296.8–298	0.16	0.0079
H3	298–300	0.12	0.0072
H4	300–302	0.13	0.0083
H5	302–304	0.12	0.0084
H6	304–306	0.13	0.0093
H7	306–308	0.13	0.0078
H8	308–310	0.14	0.0092
H9	310–312	0.15	0.0099
H10	312–314	0.17	0.01
H11	314–316	0.16	0.0095
H12	316–318	0.16	0.01
H13	318–320	0.17	0.011
H14	320–322	0.17	0.01
H15	322–324	0.17	0.01
H16	324–326	0.18	0.011
H17	326–328	0.19	0.011
H18	328–329.83	0.25	0.012
H19	329.83–331	0.34	0.012
H20	331–333	0.26	0.012
H21	333–335	0.31	0.012
H22	335–337	0.32	0.012
H23	337–339	0.43	0.014
H24	339–341	0.28	0.011
H25	341–343	0.17	0.01
H26	343–345	0.1	0.0066
H27	345–347	0.067	0.003
H28	347–349	0.24	0.01
H29	349–351	0.17	0.0095
H30	351–353	0.18	0.011
H31	353–355	0.18	0.011
H32	355–357	0.21	0.012
H33	357–359	0.25	0.013
H34	359–360.56	0.22	0.011
H35	360.56–362	0.17	0.0088
H36	375–376.56	0.0056	0.0004
H37	376.56–378	0.39	0.013
H38	378–380	0.52	0.016
H39	380–381.18	0.16	0.0073
H40	381.18–383	0.022	0.0005
H41	389–390.84	0.19	0.0044
H42	390.84–392	0.64	0.012
H43	392–394	0.57	0.017
H44	394–396	0.39	0.014
H45	396–398	0.51	0.014
H46	398–400	0.58	0.016
H47	400–402	0.9	0.019
H48	402–404	0.87	0.018
H49	404–406	0.72	0.017
H50	406–408	0.82	0.019
H51	408–410	0.82	0.018
H52	410–412	0.72	0.019
H53	412–414	0.73	0.02
H54	414–416	0.57	0.015
H55	416–418	0.79	0.018
H56	418–420	0.76	0.019
H57	420–422	0.66	0.02
H58	422–424	0.39	0.016
H59	424–426	0.43	0.02
H60	426–428	0.5	0.023
H61	428–430	0.57	0.025
H62	430–432	0.73	0.03
H63	432–434	0.64	0.026
H64	434–436	0.66	0.027

(Continued in next column)

TABLE 2 | (Continued) Grade of nickel and cobalt in ZK1505, Xiarihamu deposit.

	Depth/m	Ni/wt%	Co/wt%
H65	436–438	0.89	0.034
H66	438–440	0.68	0.027
H67	440–442	0.77	0.03
H68	442–444	1.25	0.044
H69	444–446	0.87	0.031
H70	446–447.14	1.13	0.038
H71	447.14–449	0.065	0.0024
H72	449–451	0.0075	0.0009

With the increase in crustal material contamination, it can reach arsenide saturation locally in sulfide melt, then a separate Ni-rich arsenide (bismuth) melt exsolves somewhere. Arsenic, bismuth, and little sulfur could potentially combine with nickel and cobalt to form these Ni- and Co-bearing accessory minerals because of PGE depletion in magma during sulfide liquation. Also, previous studies have shown that maucherites, as very common accessory phases, often occur in magmatic environments of 600–830°C (Yund, 1961; Roseboom, 1962; Singleton and Nash, 1987; Shvedov and Barkov, 2017). We propose that it might represent the crystallization temperature of Ni-rich arsenide (bismuth) melt, after the crystallization of olivine and pyroxene. These minerals mostly occur in base metal sulfides and just a little in silicate minerals (**Figure 4E**) which reveals that they are easy to move forward in sulfide melt rather than separating out like olivine and pyroxene. Since the arsenide melt crystallizes first and then the sulfide melt crystallizes, base metal sulfides contain a large number of arsenic- or bismuth-bearing minerals.

It can be inferred that sulfide melts have sufficient fractional crystallization because the boundaries among pentlandite, pyrrhotite, chalcopyrite, and cobaltite are mostly straight. Nickel usually enters pentlandite phase. And, most of cobalt tends to enter cobaltite phase with arsenic and sulfur, rather than existing in chalcopyrite and pyrrhotite as isomorphs when temperature slowly decreases, which can gather cobalt to a great extent.

The crystallization of Ni-rich arsenide (bismuth) melt and sufficient crystallization of sulfide melt largely gathered nickel and cobalt in nickel–cobalt minerals instead of being scattered as isomorphs in extensive pyrrhotite or chalcopyrite; that is the special metallogenic process of the Xiarihamu deposit.

Nickel and Cobalt Behavior in the Magma System

Based on whole-rock nickel and cobalt contents of the deposit (No. 5 Geological and Mineral Survey Institute of Qinghai Province, 2014), the grades of nickel and cobalt in ZK1505 significantly increased below 400 m, up to 1.25 (wt%) and 0.045 (wt%), respectively (**Table 2; Figure 7**). As mentioned previously, the rock type changes from peridotite in the upper part to pyroxenite in the lower part at about 400 m, regardless of the depth of the upper surrounding rock, while the ore type

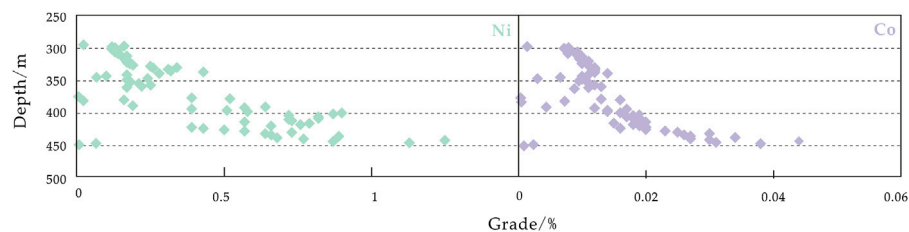


FIGURE 7 | Variation diagram of ZK1505 Ni and Co grades with depth in ZK1505, Xiarihamu deposit.

changes from spotted to sideronitic massive. More importantly, some cobalt and nickel minerals (nickeline, maucherite, and cobaltite) appear in large quantities below 400 m and are not present above that depth (only appearing pentlandite, pyrrhotite, and chalcopyrite), except for the vein at 390 m. From macroscopic to microcosmic observation, we consider that the position at which the nickel and cobalt grades are significantly increased are also the locations in which numerous nickel and cobalt minerals (nickeline, maucherite, and cobaltite) are developed. And in the low-grade ores, cobalt mainly exists in the form of isomorphism substitution of some nickel in pentlandites. Therefore, the formation of abundant nickel–cobalt minerals in the magmatic system greatly improves the ore grade.

When sulfide saturation occurs in the magma, nickel and cobaltite tend to enrich in sulfide melt due to high partition coefficient between sulfide and silicate melts (Crocket and Fleet, 1997; Li and Audétat, 2012). Cobaltite is a primary mineral. It is formed at the edge of pyrrhotite and other minerals and also contains pyrrhotite. It seems that it is formed by replacing pyrrhotite. But it shows euhedral or subhedral structure and has straight boundaries with other base metal sulfides, indicating symbiotic combination of them. In theory, when MSS

and intermediate solid solutions (ISS) crystallized, the semimetal-rich melt remained liquid (Helmy et al., 2007). Thus, it can easily move to the edges of the cobalt- and nickel-rich MSS. Then, the semimetal-rich melt the remained liquid provides arsenic, and sulfide melt provides nickel, cobalt, and sulfur, which causes the combination to cobaltite during temperature reduction. Due to the large amount of pyrrhotites crystallized at this time, cobaltites experienced insufficient nucleation. It causes that cobaltites are enclosed in pyrrhotites and located at the boundaries between pyrrhotites and other minerals, and also some pyrrhotites are enclosed in cobaltites. Based on the FeAsS–CoAsS–NiAsS diagram (Klemm, 1965), the data almost plot in the 500–600°C isotherms, indicating 500–600°C formation temperature of cobaltites (Figure 8). Such textural relationships and formation temperature both indicate that cobaltites and base metal sulfides approximately formed at the same time. Most nickel, iron, sulfur, and little isomorphism cobalt form pentlandite, while most cobalt, some nickel, arsenic, and sulfur form cobaltite.

In particular, pyrrhotite–chalcopyrite–pentlandite–violarite mineral assemblage occurs in veined mineralization at 390 m. Many researchers have concluded that violarite progressively replaces pentlandite as an outer rim of the coarse grains in the pentlandite as a result of hydrothermal alteration or weathering, as indicated by the fine-grained, porous, and finely cracked features (Craig, 1971; Tenaillé et al., 2006; Xia et al., 2009). However, the texture of the violarite in the present study (Figure 3B) is quite different, which is dense at the core and clean at the edges. Violarites are distributed along crystal face (111) of the early generation pentlandites, and it shows special shrinkage characteristics of an exsolution product. Violarites are formed by the decomposition of stable pentlandite solid solution in sulfide melt at lower temperature (Luo, 1994). In addition, the experiments revealed that violarites are stable below $461 \pm 3^\circ\text{C}$ and can form as a hypogene phase by primary direct crystallization or by secondary exsolution from an initially homogeneous MSS phase in the iron–nickel–sulfur system (Craig, 1971). The abnormally high iron content in the violarites indicates that its crystallization might not have been direct; rather, secondary exsolution from an initially homogeneous MSS phase might have occurred instead. Hence, it belongs to primary violarite here based on the above studies. The veined mineralization might be formed in lower temperature below $461 \pm 3^\circ\text{C}$.

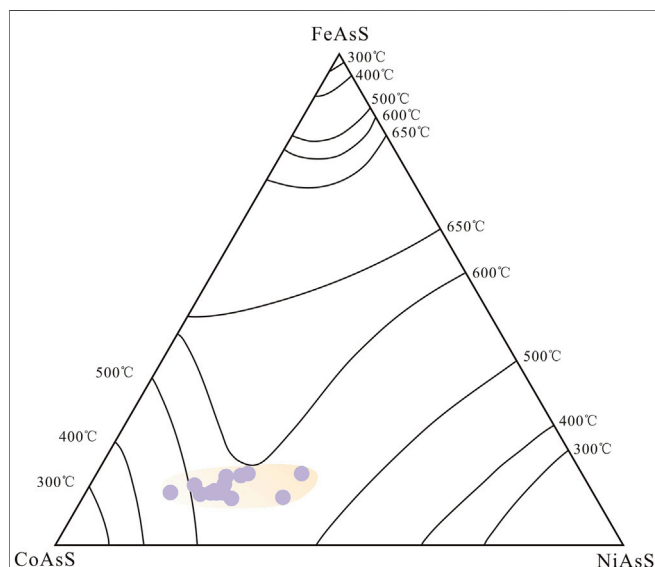
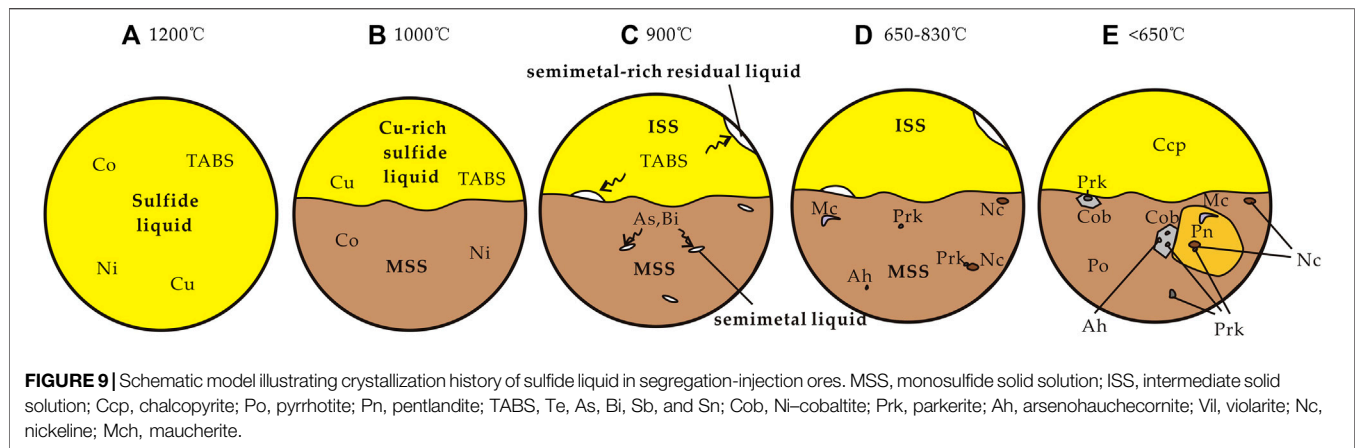


FIGURE 8 | Composition of cobaltites of the Xiarihamu deposit (isotherms data after Klemm, 1965).



Moreover, maucherites also grew in the cracks of earlier pyrrhotites and were enclosed in the gersdorffites in veined mineralization. These high-temperature Co-poor maucherites (Yund, 1961; Roseboom, 1962; Singleton and Nash, 1987; Shvedov and Barkov, 2017) here are different with those Co-rich maucherites occurred during early magmatism in occurrence and composition characteristics. It implies another magma invaded this location prior to hydrothermal mineralization (in the next section), which might lead to changes in the early rock sequence at about 400 m (Figure 2C) and additional rapid nickel and cobalt mineralization.

Mineralization Model of Nickel and Cobalt

There are three different types of ore: *in situ* liquation (spot-disseminated ores), deep segregation-injection (sideronitic massive veined ores), and hydrothermal superposition (veined ore added secondary metasomatism) (Tang and Li, 1995). Among them, the segregation-injection ores are the most important type in the deposit. So the following nickel-cobalt evolution model is proposed, based on their textural relationships and geochemical behavior.

Figure 9 schematically shows the behavior of cobalt and nickel during arsenic and sulfide saturation from magmatic temperatures in segregation-injection ores. At magmatic temperatures of about 1,200°C, the sulfide liquid contained dissolved nickel, cobalt, copper, iron, tellurium, arsenic, bismuth, antimony, and tin (Figure 9A). Upon cooling to about 1,000°C, partial cobalt and nickel were concentrated in MSS, while tellurium, arsenic, bismuth, antimony, and tin partitioned into the copper-rich residual liquid after MSS crystallization (Figure 9B). Upon further cooling to about 900°C, ISS crystallized out of the residual liquid, and the semimetal-rich melt remained liquid (Figure 9C) (Helmy et al., 2007). At about 650–830°C, Ni-rich arsenide (bismuth) melt exsolved occasionally and formed parkerite, arsenohauchecornite, maucherite, and nickeline with nickel and cobalt because of arsenide saturation locally (Figure 9D). At low temperatures, when MSS and

intermediate solid solutions (ISS) exsolved into pyrrhotite, pentlandite, and chalcopyrite below 650°C (Mansur et al., 2019), arsenic derived from the semimetal-rich residual liquid and combined with nickel, cobalt, and sulfur to form cobaltite (Figure 9E). They contained early parkerite, arsenohauchecornite, maucherite, and nickeline during crystallization. Then, the residual nickel formed in the pyrrhotite-chalcopyrite-pentlandite-violarite veins, which occur in structural weakness zones under a temperature of about 461°C.

Nickel and Cobalt Behavior in the Hydrothermal System

The primary vein mineralization was magmatic as mentioned above. But the pyrrhotite and chalcopyrite were not completely metasomatized by the gersdorffite cluster along the fracture in the granite and formed a hackly erosion boundary along fractures (Figures 4K,L, 5K), which might support their hydrothermal origin (Raič and Mogessie, 2015; Hazen et al., 2017; Moroni et al., 2017; Manuel et al., 2018; Stefan et al., 2018; Liang et al., 2019; Huang et al., 2020). During hydrothermal processes, nickel and cobalt in the silicate mineral lattice or earlier minerals were extracted or dissolved. In the process of migration to the structural weakness zones, the gersdorffite cluster redeposited and metasomatized the early minerals along the granite fractures. Although the hydrothermal source cannot be explained by the existing phenomena and data, its contribution to the deposit is extremely limited.

CONCLUSION

Almost all nickel-cobalt minerals are primary minerals, except gersdorffite. Only limited ore-forming elements redistribute during hydrothermalism. The crystallization of Ni-rich arsenide (bismuth) melt and sufficient crystallization of sulfide melt together constitute the special enrichment and evolution mechanism of nickel and cobalt in the Xiarihamu deposit.

DATA AVAILABILITY STATEMENT

The original contributions presented in the study are included in the article; further inquiries can be directed to the corresponding author.

AUTHOR CONTRIBUTIONS

YH: investigation, methodology, analysis, writing, and original draft preparation; YL and WL: writing, review, and editing; YH and YL: funding acquisition.

REFERENCES

- Ao, C., Sun, F. Y., Li, B. L., Li, S. J., and Wang, G. (2014). Geochemistry, zircon U-Pb dating and geological significance of diorite porphyrite in Xiarihamu deposit, East Kunlun Orogenic Belt, Qinghai. *Northwest. Geol.* 47, 96–106 [in Chinese with English Abstract]. doi:10.3969/j.issn.1009-6248.2014.01.007
- Cao, Z. H., Luo, X. R., and Wang, P. P. (2010). Geoelectro-chemical extraction method for prospecting nickel – cobalt deposit in south Jinchua. *J. Guilin Univ. Technol.* 30, 47–51 [in Chinese with English Abstract]. doi:10.3969/j.issn.1674-9057.2010.01.007
- Craig, J. R. (1971). Violarite stability relations. *Am. Mineral.* 56, 1303–1311.
- Crocket, J. H., and Fleet, M. E. (1997). Implications of composition for experimental partitioning of platinum-group elements and gold between sulfide liquid and basalt melt: the significance of nickel content. *Geochem. Cosmochim. Acta* 61, 4139–4149. doi:10.1016/s0016-7037(97)00234-2
- Du, W. (2018). *Study on two kinds of mafic ultramafic rocks and nickel sulfide deposit in East Kunlun island arc zone*. Xi'an, China: Chang'an University [in Chinese with English Abstract].
- Du, W., Ling, J. L., Zhou, W., Wang, Z. X., Xia, Z. D., Xia, M. Z., et al. (2014). Geological characteristics and genesis of Xiarihamu nickel deposit in East Kunlun. *Miner. Depos.* 33, 713–726 [in Chinese with English Abstract]. doi:10.3969/j.issn.0258-7106.2014.04.004
- Feng, C. Y., Zhao, Y. M., Li, D. X., Liu, J. N., and Liu, C. Z. (2016). Mineralogical characteristics of the Xiarihamu nickel deposit in the Qiman Tagh mountain, East Kunlun, China. *Geol. Rev.* 62, 215–228 [in Chinese with English Abstract]. doi:10.16509/j.georeview.2016.01.017
- Fleet, M. E. (1973). The crystal structure of maucherite (Ni₁₁As₈). *Am. Mineral.* 58, 203–210.
- Hazen, R. M., Hystad, G., Golden, J. J., Hummer, D. R., Liu, C., Downs, R. T., et al. (2017). Cobalt mineral ecology. *Am. Mineral.* 102, 108–116. doi:10.2138/am-2017-5798
- Helmy, H. M., Ballhaus, C., Berndt, J., Bockrath, C., and Wohlgemuth-Ueberwasser, C. (2007). Formation of Pt, Pd and Ni tellurides: experiments in sulfide-telluride systems. *Contrib. Mineral. Petrol.* 153, 577–591. doi:10.1007/s00410-006-0163-7
- Helmy, H. M., Ballhaus, C., Fonseca, R. O. C., and Nagel, T. J. (2013). Fractionation of platinum, palladium, nickel, and copper in sulfide-arsenide systems at magmatic temperature. *Contrib. Mineral. Petrol.* 166, 1725–1737. doi:10.1007/s00410-013-0951-9
- Helmy, H. M., Ballhaus, C., Wohlgemuth-Ueberwasser, C., Fonseca, R. O. C., and Laurenz, V. (2010). Partitioning of Se, As, Sb, Te and Bi between monosulfide solid solution and sulfide melt – application to magmatic sulfide deposits. *Geochem. Cosmochim. Acta* 74, 6174–6179. doi:10.1016/j.gca.2010.08.009
- Huang, W. T., Wu, J., Liang, H. Y., Chen, X. L., Zhang, J., and Ren, L. (2020). Geology, geochemistry and genesis of the Longhua low-temperature hydrothermal Ni-Co arsenide deposit in sedimentary rocks, Guangxi, South China. *Ore Geol. Rev.* 120, 103393. doi:10.1016/j.oregeorev.2020.103393
- Jiang, C. Y., Ling, J. L., Zhou, W., Du, W., Wang, Z. X., Fan, Y. Z., et al. (2015). Petrogenesis of the Xiarihamu Ni-bearing layered mafic-ultramafic intrusion,

FUNDING

This work was jointly supported by the Fundamental Research Funds for the Central Universities, CHD (300102278711), the National Natural Science Foundation of China (211027180410), and the National Key R&D Program of China (2017YFC0601205).

ACKNOWLEDGMENTS

The authors thank the reviewers for providing critical comments and suggestions.

- East Kunlun: implications for its extensional island arc environment. *Acta Petrol. Sin.* 31, 1117–1136 [in Chinese with English Abstract]. doi:CNKI:SUN:YsXB.0.2015-04-019
- Klemm, D. D. (1965). Synthesen und analysen in den Dreiecks-diagrammen FeAsS–CoAsS–NiAsS und FeS₂–CoS₂–NiS₂. *Neues Jahrbuch Mineral. Abhand.* 103, 205–255.
- Li, C., Zhang, Z., Li, W., Wang, Y., Sun, T., and Ripley, E. M. (2015). Geochronology, petrology and Hf-S isotope geochemistry of the newly-discovered Xiarihamu magmatic Ni-Cu sulfide deposit in the Qinghai-Tibet plateau, western China. *Lithos* 216–217, 224–240. doi:10.1016/j.lithos.2015.01.003
- Li, W. Y. (2018). The primary discussion on the relationship between Paleo-Asian ocean and Paleo-Tethys ocean. *Acta Petrol. Sin.* 34, 3–12 [in Chinese with English Abstract]. doi:CNKI:SUN:YsXB.0.2018-08-001
- Li, W. Y., Wang, Y. L., Qian, B., Liu, Y. G., and Han, Y. X. (2020). The discussion on the formation of the magmatic Cu-Ni-Co sulfide deposits in the margin of the Tarim Block. *Earth Sci. Front.* 27, 276–293. [in Chinese with English Abstract]. doi:10.13745/j.esf.sf.2020.3.22
- Li, Y., and Audétat, A. (2012). Partitioning of V, Mn, Co, Ni, Cu, Zn, As, Mo, Ag, Sn, Sb, W, Au, Pb, and Bi between sulfide phases and hydrous basanite melt at upper mantle conditions. *Earth Planet Sci. Lett.* 355–356, 327–340. doi:10.1016/j.epsl.2012.08.008
- Liang, Q.-L., Song, X.-Y., Wirth, R., Chen, L.-M., and Dai, Z.-H. (2019). Implications of nano- and micrometer-size platinum-group element minerals in base metal sulfides of the Yangliuping Ni-Cu-PGE sulfide deposit, SW China. *Chem. Geol.* 517, 7–21. doi:10.1016/j.chemgeo.2019.04.015
- Liu, Y., and Brennan, J. (2015). Partitioning of platinum-group elements (PGE) and chalcogens (Se, Te, As, Sb, Bi) between monosulfide-solid solution (MSS), intermediate solid solution (ISS) and sulfide liquid at controlled fO₂-fS₂ conditions. *Geochem. Cosmochim. Acta* 159, 139–161. doi:10.1016/j.gca.2015.03.021
- Liu, Y., Li, W., Jia, Q., Zhang, Z., Wang, Z., Zhang, Z., et al. (2018). The dynamic sulfide saturation process and a possible slab break-off model for the giant Xiarihamu magmatic nickel ore deposit in the East Kunlun orogenic belt, northern Qinghai-Tibet plateau, China. *Econ. Geol.* 113, 1383–1417. doi:10.5382/econgeo.2018.4596
- Lü, L. S., Liu, J., Zhang, Z. H., and Xie, G. Q. (2007). Temporal-spatial distribution and geodynamic settings of magmatic Ni-Cu-(PGE) sulfide deposits in China. *Acta Petrol. Sin.* 23 (10), 2561–2594. doi:10.3969/j.issn.1000-0569.2007.10.024
- Lu, S., Li, H., Zhang, C., and Niu, G. (2008). Geological and geochronological evidence for the Precambrian evolution of the Tarim Craton and surrounding continental fragments. *Precambrian Res.* 160, 94–107. doi:10.1016/j.precamres.2007.04.025
- Luo, H. B. (1994). Mineralogical Study on the genesis of violarite in magmatic copper nickel deposits. *Geol. Prospect.* 1, 38–40 [in Chinese]. doi:CNKI:SUN:DZKT.0.1994-01-008
- Mansur, E. T., Barnes, S.-J., and Duran, C. J. (2019). Textural and compositional evidence for the formation of pentlandite via peritectic reaction: implications for the distribution of highly siderophile elements. *Geology* 47, 351–354. doi:10.1130/g45779.1
- Manuel, J., Subías, I., Fanlo, I., Arranz, E., and Gervilla, F. (2018). Multi-isotope survey on the metallogenesis of the hydrothermal Co-Ni deposits in the Alpine

- Central Pyrenees of Spain. *Ore Geol. Rev.* 94, 225–238. doi:10.1016/j.oregeorev.2018.01.030
- Michener, C., and Peacock, M. (1943). Parkerite ($\text{Ni}_3\text{Bi}_2\text{S}_7$) from Sudbury, Ontario: redefinition of the species. *Am. Mineral.* 28, 343–355.
- Moroni, M., Caruso, S., Barnes, S. J., and Fiorentini, M. L. (2017). Primary stratigraphic controls on ore mineral assemblages in the Wannaway komatiite-hosted nickel-sulfide deposit, Kambalda camp, Western Australia. *Ore Geol. Rev.* 90, 634. doi:10.1016/j.oregeorev.2017.05.031
- No. 5 Geological and Mineral Survey Institute of Qinghai Province (GMSQH). (2014). Investigation report on HS26 abnormal zone in the Xiarihamu Co-Ni mining area in Golmud City, Qinghai Province, 1–189 (in Chinese).
- Piña, R., Gervilla, F., Barnes, S.-J., Ortega, L., and Lunar, R. (2014). Liquid immiscibility between arsenide and sulfide melts: evidence from a LA-ICP-MS study in magmatic deposits at Serranía de Ronda (Spain). *Miner. Depos.* 50, 265–279. doi:10.1007/s00126-014-0534-3
- Ponomarenko, A., Kovalenko, V., and Troneva, N. (1987). Parkerite. *Tr. Mineral. Muzeya Akad. Nauk SSSR* 34, 108–114.
- Qian, Y., Li, H. R., Sun, F. Y., Sun, J. L., and Wang, G. (2020). Zircon U-Pb dating and sulfide Re-Os isotopes of the Xiarihamu Cu-Ni sulfide deposit in Qinghai province, NW China. *Can. J. Earth Sci.* 57, 8. doi:10.1139/cjes-2019-0107
- Raič, S., and Mogessie, A. (2015). Arsenic-enriched Cu-Ni-PGE mineralization in Wetlegs, Duluth complex, St. Louis county, Minnesota, USA. *Can. Mineral.* 53, 105–132. doi:10.3749/canmin.1400053
- Roseboom, E. H., Jr. (1962). Skutterudites (Co, Ni, Fe) $\text{As}_3\text{-x}$: composition and cell dimensions. *Am. Mineral.* 47, 310–327.
- Shvedov, G., and Barkov, A. (2017). Primary and alteration assemblages of platinum-group minerals from the Ognit complex, Irkutskaya oblast, Eastern Sayans, Russia. *N. Jb. Miner. Abh.* 194, 35–48. doi:10.1127/njma/2016/0038
- Singleton, M., and Nash, P. (1987). The As–Ni (arsenic–nickel) system. *J. Phase Equil.* 8, 419–422. doi:10.1007/bf02893150
- Song, X.-Y., Wang, K.-Y., Barnes, S. J., Yi, J.-N., Chen, L.-M., and Schoneveld, L. E. (2020). Petrogenetic insights from chromite in ultramafic cumulates of the Xiarihamu intrusion, northern Tibet Plateau, China. *Am. Mineral.* 105, 479–497. doi:10.2138/am-2020-7222
- Song, X.-Y., Yi, J.-N., Chen, L.-M., She, Y.-W., Liu, C.-Z., Dang, X.-Y., et al. (2016). The Giant Xiarihamu Ni-Co sulfide deposit in the East Kunlun orogenic belt, northern Tibet plateau, China. *Econ. Geol.* 111, 29–55. doi:10.2113/econgeo.111.1.29
- Spiridonov, E. M., Gritsenko, Y. D., and Ponomarenko, A. I. (2008). Metamorphic-hydrothermal parkerite and associated minerals in the Noril'sk ore field. *Geol. Ore Depos.* 50, 755–762. doi:10.1134/s1075701508080126
- Springer, G. (1989). Chlorine-bearing and other uncommon minerals in the strathcona deep copper zone, Sudbury district, Ontario. *Can. Mineral.* 27, 311–313. doi:10.1007/BF01164492
- Stefan, K., Axel, G., Benjamin, F. W., Udo, N., Thomas, W., and Gregor, M. (2018). Reconstruction of a >200 Ma multi-stage “five element” Bi-Co-Ni-Fe-As-S system in the Penninic Alps, Switzerland. *Ore Geol. Rev.* 95, 746–788. doi:10.15496/publikation-24256
- Tang, Q. Y., Li, J. P., Zhang, M. J., Song, Z., Dang, Y. X., and Du, L. (2017). The volatile conditions of ore-forming magma for the Xiarihamu Ni-Cu sulfide deposit in East Kunlun orogenic belt, western China: constraints from chemical and carbon isotopic compositions of volatiles. *Acta Petrol. Sin.* 33, 104–114 [in Chinese with English Abstract]. doi:CNKI:SUN:YXSB.0.2017-01-009
- Tang, Z. L., and Li, W. Y. (1995). *Metallogenic model and geological comparison of Jinchuan Cu-Ni-(Pt-bearing) sulfide deposit*. Beijing: Geological Publishing House, 43–51.
- Tenaillieu, C., Pring, A., Etschmann, B., Brugger, J., Grguric, B., and Putnis, A. (2006). Transformation of pentlandite to violarite under mild hydrothermal conditions. *Am. Mineral.* 91, 706–709. doi:10.2138/am.2006.2131
- Wang, G. (2014). *Metallogenesis of nickel deposits in eastern Kunlun orogenic belt, Qinghai Province*. Changchun, China: Jilin University [in Chinese with English Abstract].
- Wang, G., Sun, F. Y., Li, B. L., Li, S. J., Zhao, J. W., Ao, C., et al. (2014a). Petrography, zircon U-Pb geochronology and geochemistry of the mafic-ultramafic intrusion in Xiarihamu Cu-Ni deposit from East Kunlun, with implications for geodynamic setting. *Earth Sci. Front.* 21, 381–401 [in Chinese with English Abstract]. doi:10.13745/j.esf.2014.06.036
- Wang, G., Sun, F. Y., Li, B. L., Li, S. J., Zhao, J. W., Yang, Q. A., et al. (2013). Zircon U-Pb geochronology and geochemistry of the early devonian syenogranite in the Xiarihamu ore district from East Kunlun, with implications for the geodynamic setting. *Geotect. Metal.* 37, 685–697 [in Chinese with English Abstract]. doi:10.16539/j.ddgzyckx.2013.04.015
- Wang, G., Sun, F. Y., Li, B. L., Li, S. J., Zhao, J. W., and Yang, Q. A. (2014b). Zircon U-Pb geochronology and geochemistry of diorite in Xiarihamu ore district from East Kunlun and its geological significance. *J. Jilin Univ. (Earth Sci. Ed.)* 44, 876–891 [in Chinese with English Abstract]. doi:10.13278/j.cnki.jjuese.201403113
- Wang, X. D., Zhang, M. J., Fu, J. R., Zhang, J. W., Li, L. W., Tang, Q. Y., et al. (2018). The magmatic intrusive direction constrains from noble gas isotopic compositions: a case study of the Xiarihamu Ni-Cu sulfide deposit in East Kunlun orogenic belt, China. *Acta Petrol. Sin.* 34, 3433–3444 [in Chinese with English Abstract]. doi:CNKI:SUN:YXSB.0.2018-11-022
- Xia, F., Brugger, J., Chen, G., Ngothai, Y., O'Neill, B., Putnis, A., et al. (2009). Mechanism and kinetics of pseudomorphic mineral replacement reactions: a case study of the replacement of pentlandite by violarite. *Geochem. Cosmochim. Acta* 73, 1945–1969. doi:10.1016/j.gca.2009.01.007
- Yi, J. N., Song, X. Y., Chen, L. M., and She, Y. W. (2015). Geological characteristics of Xiarihamu superlarge Cu-Ni-Co sulfide deposit in East Kunlun orogen. *Acta Mineral. Sin.* S1, 450, 2015 [in Chinese].
- Yund, R. A. (1961). Phase relations in the system Ni-As. *Econ. Geol.* 56, 1273–1296. doi:10.2113/gsecongeo.56.7.1273
- Zhang, Z. B., Li, W. Y., Zhang, Z. W., Liu, Y. G., Qian, B., Wang, Y. L., et al. (2016). Characteristics of chromian spinels from the Xiarihamu magmatic Ni-Cu sulfide ore deposit in the eastern Kunlun Orogenic Belt, northwest China and their implication. *Bull. China Soc. Mineral Petrol. Geochem.* 35, 966–975 [in Chinese with English Abstract]. doi:10.3969/j.issn.1007-2802.2016.05.017
- Zhang, Z. W., Qian, B., Wang, Y. L., Li, S. J., and Liu, C. Z. (2016). Petrogeochemical characteristics of the Xiarihamu magmatic Ni-Cu sulfide deposit in Qinghai province and its study for olivine. *Northwest Geol.* 49, 45–58 [in Chinese with English Abstract]. doi:10.3969/j.issn.1009-6248.2016.02.005
- Zhao, J., Li, G., Qin, K., and Tang, D. (2019). A review of the types and ore mechanism of the cobalt deposits. *Chin. Sci. Bull.* 64, 2484–2500 [in Chinese]. doi:10.1360/n972019-00134

Conflict of Interest: The authors declare that the research was conducted in the absence of any commercial or financial relationships that could be construed as a potential conflict of interest.

Copyright © 2020 Han, Liu and Li. This is an open-access article distributed under the terms of the Creative Commons Attribution License (CC BY). The use, distribution or reproduction in other forums is permitted, provided the original author(s) and the copyright owner(s) are credited and that the original publication in this journal is cited, in accordance with accepted academic practice. No use, distribution or reproduction is permitted which does not comply with these terms.



Newly Discovered Triassic Lithium Deposits in the Dahongliutan Area, NorthWest China: A Case Study for the Detection of Lithium-Bearing Pegmatite Deposits in Rugged Terrains Using Remote-Sensing Data and Images

Yongbao Gao^{1*}, Leon Bagas^{1,2}, Kan Li¹, Moushun Jin¹, Yuegao Liu³ and Jiaxin Teng¹

OPEN ACCESS

Edited by:

Ignacio Gonzalez-Alvarez,
Commonwealth Scientific and
Industrial Research Organisation
(CSIRO), Australia

Reviewed by:

Dalton McCaffrey,
University of Nevada, United States
Kathryn Goodenough,
British Geological Survey, United
Kingdom

*Correspondence:

Yongbao Gao
gaoyongbao2006@126.com

Specialty section:

This article was submitted to
Economic Geology,
a section of the journal
Frontiers in Earth Science

Received: 05 August 2020

Accepted: 26 October 2020

Published: 10 December 2020

Citation:

Gao Y, Bagas L, Li K, Jin M, Liu Y and
Teng J (2020) Newly Discovered
Triassic Lithium Deposits in the
Dahongliutan Area, NorthWest China:
A Case Study for the Detection of
Lithium-Bearing Pegmatite Deposits in
Rugged Terrains Using Remote-
Sensing Data and Images.
Front. Earth Sci. 8:591966.
doi: 10.3389/feart.2020.591966

¹Key Laboratory for the Study of Focused Magmatism and Giant Ore Deposits of Ministry of Natural Resources, Xi'an Center of China Geological Survey, Xi'an, China, ²Centre for Exploration Targeting (CET), The University of Western Australia, Crawley, WA, Australia, ³CAS Key Laboratory for Experimental Study Under Deep-sea Extreme Conditions, Institute of Deep-sea Science and Engineering, Chinese Academy of Sciences, Sanya, China

Rare metals, such as lithium and cobalt used in rechargeable batteries, have increased in value as demands for them escalates. Concentrations of lithium-bearing minerals are found in closed-basin brines, granitic pegmatites, and associated granitic rocks containing spodumene ($\text{LiAl}(\text{SiO}_3)_2$) and various other economic minerals. The recently discovered Dahongliutan Li mineral occurrences are hosted by a pegmatite dyke swarm in NW China, in an area that is also prospective for Be, Rb, Nb, and Ta mineralisation. However, the high altitude and steep topography in the area make it extremely difficult to explore for mineralisation. A combination of geochemical methods, geological mapping, and high-resolution remotely sensed multispectral imagery has been used in this study to pinpoint potential locations of pegmatite-hosted Li occurrences. The exploration method developed has led to the discovery many large Li mineral occurrences in the Bayankala Fold Belt, including the 505, 507, north 509, and South Fulugou 1# and 2# mineral occurrences (documented here) with a combined resource of over 1.7 million tonnes (Mt). The laser ablation multi-receiver inductively coupled plasma mass spectrometer (LA-MC-ICP-MS) $^{206}\text{Pb}/^{207}\text{Pb}$ - $^{238}\text{U}/^{207}\text{Pb}$ isochron age of the mineralised pegmatite is 223 ± 11 Ma ($N = 44$, $\text{MSWD} = 2.1$). The $^{40}\text{Ar}/^{39}\text{Ar}$ plateau age of muscovite in the mineralised pegmatite dates between 197 ± 1 and 185 ± 1 Ma. These dates show that these granitic pegmatites (with a monzogranitic composition) were emplaced during the Late Triassic coeval with magmatism in the region. Our data show that the Li mineralisation in the Dahongliutan area has a similar age and genesis as the pegmatite-hosted deposits of the Jiajika area in the western Sichuan Province. This indicates that the Dahongliutan area is highly prospective of various pegmatite-hosted mineral deposits.

Keywords: dahongliutan area, U-Pb and Ar-Ar dating, triassic, Li-bearing pegmatite, satellite remote sensing, resource potential

INTRODUCTION

Lithium compounds are widely used in the aerospace, chemical, pharmaceutical, and new energy industries (Li et al., 2007; Li et al., 2014). With continued breakthroughs in the research and development of rechargeable batteries, lithium has become a significant commodity (Wang et al., 2018). Lithium deposits can be divided into the common brine- and less common pegmatite-, granite-, and clay-hosted types (Munk et al., 2018; Wang et al., 2019). Of these, the brine types are the largest in size, but the pegmatite-hosted deposits can be more valuable and easier to mine, especially if they include combinations of high-grade Be, Nb, Ta, Rb or Cs deposits (Linnen et al., 2012; Li et al., 2014; Munk et al., 2018; Goodenough et al., 2019; Wang et al., 2019). The Li-bearing minerals in pegmatites include silicates, spodumene, mica accumulates in pegmatite veins, and in the late stages of magmatic crystallisation accompanied by volatile-rich hydrothermal fluids (London, 2018). Many of these deposits have been discovered with geological mapping, geochemical sampling and interpretation of remote sensing (satellite) images in terrains that are not mountainous.

The method of using satellite images for mineral exploration begins with the compilation of information, which is commonly done in a Geographic Information System (GIS) environment. This includes available records of exploration, geo-referenced geological maps, and initial interpretations of satellite images and orthorectified aerial photographs (where available) (Dimmell et al., 2005; Selway et al., 2005; Scogings et al., 2016; Steiner, 2018; Cardoso-Fernandes et al., 2019a; Cardoso-Fernandes et al., 2019b; Steiner, 2019a; Steiner, 2019b; Cardoso-Fernandes et al., 2020a; Cardoso-Fernandes et al., 2020b). This data is initially used to define areas that might be prospective for economic concentrations of minerals, where regional geochemistry sampling and initial geological mapping is commenced. However, these methods are not always viable in mountainous terranes such as in the Tibetan Plateau at elevations around 4,000 km above sea level. In a favourable environment, the geochemical sampling involves rock, stream-sediment, and soil sampling, which are generally considered important tool for defining vectors towards LCT pegmatites (c.f. Steiner, 2019b), but this is not easily achieved in steep mountainous terrains such as the Tibetan Plateau, and other, safer, techniques must be applied.

Remote sensing data obtained from Advanced Spaceborne Thermal Emission and Reflection Radiometer (ASTER), Sentinel-2, Landsat-5 and Landsat-8 satellites, are commonly used to detect Li-bearing pegmatites (Mendes et al., 2017; Cardoso-Fernandes et al., 2018; Cardoso-Fernandes et al., 2019a). These methods aimed to detect hydrothermally altered zones associated with mineralisation and Li-bearing minerals directly (Cardoso-Fernandes et al., 2019a). The results were often indecisive because of the limitations of the band ratios used, except for the ASTER sensor that can detect clays associated with alteration zones, and vegetation often masked the location of mineralised zones (Cardoso-Fernandes et al., 2019b). Remote sensing technology has been refined significantly in recent years with the rapid development of new, high-resolution sensors in, for example, IKONOS; DigitalGlobeQuickBird; SPOT-5; Worldview-2;

Worldview-3; Gaofen-1; Gaofen-2; and Gaofen-7 satellites (Table 1). The application of remote sensing technology is becoming increasingly widespread in distinguishing the nature of the geology and mineral exploration in remote regions. This includes the recognition of alteration assemblages associated with mineral deposits in remote sensing data at a high-resolution allowing the recognition of pegmatites at a metre-scale, whereas the tradition methods dealt with resolutions at a 10-m scale (Moradi et al., 2014; Pour and Hashim, 2015).

Northwestern China is beginning to be recognised as a highly prospective part of China for various mineral commodities, including sedimentary and metamorphic Fe, porphyry Cu-Mo, skarn polymetallic deposits, and lithium deposits (Yang et al., 2003; Chen et al., 2009; Yao et al., 2009). The two known types of lithium deposit are: 1) those associated with granites and pegmatites; and 2) those in arid environments found in brine lakes and salt pans containing soluble carbonate and chloride salts of lithium (e.g. deposits in Chile). The most common lithium deposits hosted by granite and pegmatite contain spodumene ($\text{LiAl}(\text{SiO}_3)_2$), such as at the Greenbushes mine in Western Australia. Previous studies targeted spodumene with remote sensing involving spectroscopic tests on ore-forming minerals related to pegmatite in the Jiajika region of western Sichuan Province (Dai et al., 2017; Dai et al., 2018). The application of remote sensing has not been applied on pegmatite dykes and veins in the Dahongliutan area of the Bayankala Fold Belt until now (Figure 1A).

This contribution documents a new method for identifying prospective regions containing spodumene-bearing granitic pegmatite veins. This involves processing high-resolution remote-sensing and multispectral remote sensing images including Worldview-2, Worldview-3 and ASTER images, and regional geochemical and geological data in the mountainous Dahongliutan area (Figure 1). The technique has led to the discovery of many large Li occurrences with a resource of over 1.7 Mt, which includes the 505, 507, north 509, and South Fulugou 1# and 2# mineral occurrences (Figure 1). The method is a breakthrough in allowing for a rapid and efficient exploration for pegmatite-type mineral deposits in deeply incised terrains with high-altitudes, which can be of great interest to exploration and mining companies. This paper introduces our new exploration method, evaluates its effectiveness, introduces the geological characteristics of newly discovered Li deposits, and explores the potential of regional resources in the West Kunlun and Karakoram regions. Furthermore, knowing the timing of these pegmatites and their spatially associated granitic hosts are also important, because this allows us to better constrain the tectonic setting involved, and answer the following questions. Have these intrusions been emplaced in a subduction, collisional or post-collisional setting, and how does this relate to the Li prospectivity in other regions in China?

GEOLOGICAL SETTING

The recently discovered Dahongliutan mineralised zone is in the Bayankala Fold Belt, which comprises the West Kunlun Orogen

TABLE 1 | The basic information of different remote sensing satellites.

No	Satellite name	Spectral range (nm)	Number of bands	Spatial resolution (m)
1	Landsat5	450–2,350	7	30
2	Landsat7	450–2,350	7	15
3	Landsat8	450–2,350	8	15
4	Sentinel-2	443–2,190	13	10–60
5	ASTER	520–2,430	14	15
6	SPOT-5	490–1780	4	2.5
7	GF-1	450–890	4	2
8	IKONOS	450–850	4	1
9	QUICKBIRD	450–900	4	0.6
10	GF-2	450–890	4	1
11	Worldview-2	400–1,040	8	0.5
12	Worldview-3	400–2,365	16	0.3

and Tashkurgan-Tianshuihai terranes in the southern part of the Xinjiang Province (**Figure 1A**). The combined area borders the Tibetan Plateau to the south and Tarim Block to the north (**Figure 1A**). The region includes Precambrian to Cenozoic units recording a complex geological evolution, such as subduction of oceanic plates, and collisional tectonics involving the West Kunlun and Tashkurgan-Tianshui terranes and Tarim Block during the early Paleozoic and Mesozoic (Mattern and Schneider, 2000; Xiao et al., 2003; Jiang et al., 2013; Wang et al., 2017; Yan et al., 2018).

There is a wide variety of mineral deposits in the region, including: 1) sedimentary Mn and volcanogenic massive sulfide deposits in the West Kunlun Orogen (Jia et al., 1999; Gao et al., 2017; Gao et al., 2018); 2) sedimentary Fe in banded iron-formation and giant Zn-Pb non-sulfide deposits in the Tashkurgan-Tianshui terranes (Chen et al., 2019; Gao et al., 2019; Zhang et al., 2019; Gao et al., 2020); and 3) pegmatite-hosted Li(-Be) deposits in the Bayankala Fold Belt (Li et al., 2019). This multi-element mineralised zone in the study area extends for over 50 km with a width of over 5 km and is structurally controlled by the Dahongliutan-Guozhacuo and Kangxiwa faults (**Figure 1B**).

The exposed rocks in the study area are assigned to the Paleoproterozoic Kangxiwa Complex, Permian Huangyangling Group, and Triassic Bayankala Formation (Qiao et al., 2015; Teng and Gao, 2019). The Kangxiwa Complex includes a sequence of biotite schist, biotite-plagioclase gneiss, and marble metamorphosed up to granulite facies. The Huangyangling Group consists of fine-grained clastic and minor carbonate and intermediate to mafic volcanic rocks. The Bayankala Formation is a deep-water turbiditic succession of clastic units and minor carbonate rocks, which host spodumene-bearing pegmatite veins and dykes. The formation is subdivided into: 1) an early member consisting of lithic sandstone, gravel beds and shale; 2) a central member consisting of quartz (-feldspar) sandstone, shale, and marlstone; and 3) a late member consisting of feldspathic quartz sandstone, and siltstone.

Major faults in the region trend SE including the Kangxiwa, Dahongliutan-Guozhacuo, and Qitaidaban faults (**Figure 1B**). The steep (65°–85°) NE-dipping and long-lived Kangxiwa Fault forms the boundary between the Bayankala Fold Belt to the south and South Kunlun Terrane to the north (Liu et al., 2003). Xu et al.

(2007) and He et al. (2009) note that dextral ductile strike-slip movement along the fault developed between ca. 445–428 Ma, and sinistral strike-slip movement developed during ca. 250, 203, 102–125 and 10 Ma. The fault has controlled the deposition of sedimentary successions and the emplacement of magmatic rocks during the Paleozoic to Mesozoic.

The SE-trending Dahongliutan-Guozhacuo Fault forms the boundary between the Bayankala Fold Belt and Tashkurgan-Tianshuihai terranes (**Figure 1A**). Chen et al. (2010) observe that the fault dips between 50° and 75° NE, was active as a ductile strike-slip fault during ca. 150, 122, and 106 Ma, and might be the western extension of the Altyn-Tagh Fault. Reactivation of the fault included SE-trending thrusting and eastward trending sinistral strike-slip movement depending on the orientation of the fault zone (**Figure 1B**).

The SSE-trending Qitaidaban Fault forms the boundary between the Huangyangling Group and Bayankala Formation. The foliation in the fault zone dips 40°–60° SW and NE, and has been active as an early ductile strike-slip fault and reactivated as a brittle strike-slip fault. Mesozoic and SE-trending intermediate to felsic intrusive rocks are widespread subparallel to the Kangxiwa Fault. This includes Cambrian monzogranite, ca. 223–209 Ma fine-to medium-grained biotite monzogranite, diorite, granodiorite, biotite-quartz diorite, and muscovitic diorite containing garnet and tourmaline (**Supplementary Table S1**; Qiao et al., 2015; Wei et al., 2017).

The Li deposits and occurrences in the Dahongliutan area are hosted by pegmatite dykes along the margin of the Triassic Dahongliutan Granite (**Figure 1**). The dykes form a series of clusters or swarms up to 50-km-long at the Aktas, Kalaka, 509, 505, 507, north 509, and South Fulugou 1# and 2# Li deposits (**Figure 1B**). Of these, the medium-size Aktas Li-Be-Ta-Nb pegmatite-hosted deposit is in schist on the northeastern side of the Dahongliutan Granite and has been studied in detail (Yan et al., 2018). The Aktas deposit includes 10 pegmatites containing Li-Be-Nb-Ta mineralisation in the “90” and “91” vein clusters have been evaluated. Detailed diamond drilling has been used to estimate a resource of 0.085 Mt averaging 1.5% Li₂O, 0.04% BeO, 0.09% Rb₂O, and 0.024% (Nb + Ta)₂O₅ (Teng and Gao, 2019).

The Aktas deposit yields LA-ICP-MS U–Pb columbite-(Fe) and cassiterite ages of ca. 215 Ma (Yan et al., 2018). Many

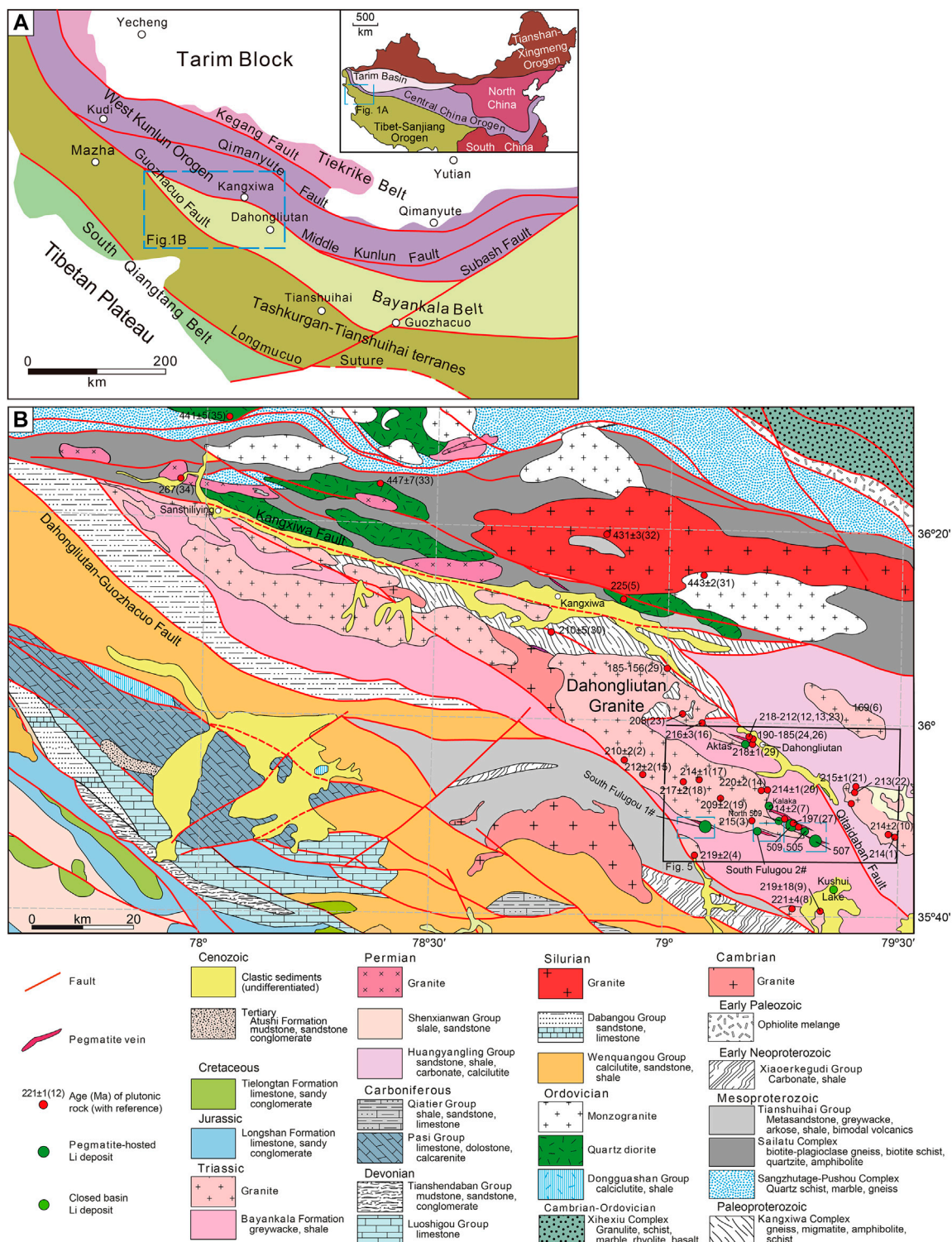


FIGURE 1 | The geological map in the Dahongliutan area, NW China: **(A)** Tectonic units of the West Kunlun Orogen and Bayankala Fold Belt (modified after Xiao and Gao 2015); and **(B)** the geological map and distribution of the spodumene-bearing pegmatites in the Dahongliutan area (from data collected during this study).

pegmatite veins and dykes around the deposit are anomalous in Li-Be-Ta-Nb, but only 10 have been found to economic with lengths between 180 and 300 m long and up to 40 m wide. The

dykes and veins trend southeast and dip steeply (60–80°) SW around the Dahongliutan Granite forming zones with barren muscovite-microcline-type pegmatites in the central zone

followed outward by Be-mineralised muscovite-microcline-albite-type pegmatites to a Li-Ta-Nb-mineralised zone containing quartz-albite-spodumene-type pegmatites (Zhou et al., 2011; Yan et al., 2018; Teng and Gao 2019; Cao et al., 2020).

The 509 deposit includes 13 pegmatite-hosted orebodies with a combined resource of 0.24 Mt averaging 1.75% Li₂O, 0.14% BeO and 0.12% Rb₂O hosted by pegmatite veins in the Bayankala Formation and along the edge of the Dahongliutan Granite (Peng et al., 2018). The Sixth Geological Brigade of the Xinjiang Geological and Mineral Bureau evaluated the Kalaka Li deposit with a ~0.1 Mt resource averaging 0.92% Li₂O, 0.06% BeO and 0.10% Rb₂O hosted by 18 pegmatites. To date, the Dahongliutan pegmatite field has an estimated resource of over 2 Mt averaging 1.5% Li₂O in a swarm of pegmatite dykes extending over 50 km in a northward to northwest direction (Teng and Gao, 2019).

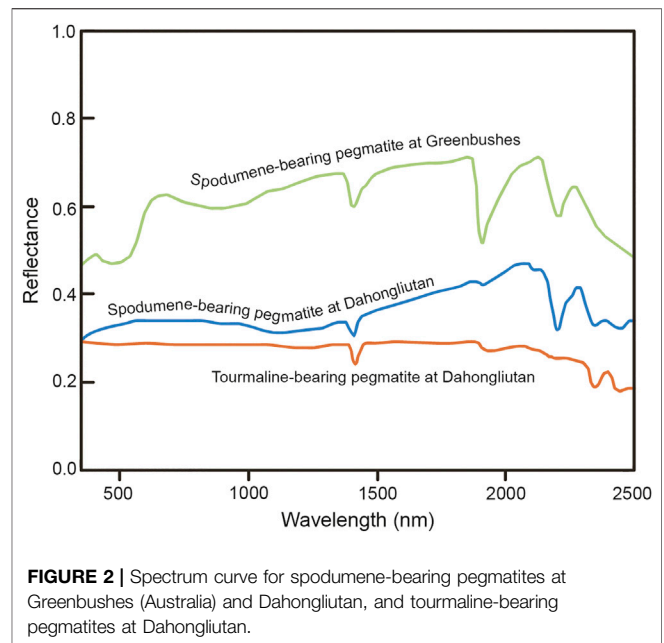
METHODS USED FOR DISCOVERING THE LITHIUM MINERALISATION

Geological and Spectral Basis

Reflectance spectra were acquired from samples on the ground surface using an Analytical Spectral Device (ASD) FieldSpec spectrometer with a spectral range of 350–2,500 nm and a nominal resolution of 1 nm. Spodumene-bearing pegmatites were collected from Greenbushes in Western Australia, and spodumene-bearing pegmatites and tourmaline-mica pegmatites from the Dahongliutan area in the Kunlun region of NW China for spectroscopic testing and comparison. The country rocks in both areas are sedimentary rocks, which were not sampled.

All samples were photographed for reference prior to analyses and the illumination of samples provided by a halogen lamp positioned at an incidence angle of approximately 10°. The radiance spectrum from the sample was collected with the ASD pointing at a normal viewing angle to the sample surface and sensing a sample footprint of approximately 30 mm in diameter at a 20 mm standoff distance. The sample radiance spectrum was normalised to that of a standard 99% white reference panel collected before measurement of each sample (Liu et al., 2017a; Liu et al., 2017b). The surface reflectance measurements were taken at 20 spots over each plot, and for each measurement, the ASD spectrometer was kept stationary and ~100 consecutively acquired spectra were recorded to reduce the noise level. The reflectance spectra for minerals are typically unique, and some minerals have distinct bands of absorption and reflection corresponding to remote-sensing image bands. The correlation between the image bands and minerals can be enhanced and extracted by mathematical operations to provide relevant information for exploration (e.g. Kendall, 1975; Hunt and Ashley, 1979; Gan et al., 2003).

We found that the spodumene crystals hosted by pegmatites in the Dahongliutan study area are: 1) columnar, granular, or forms plates; 2) vary from hoary, grey-green, emerald, purple, or yellow in colour; 3) have a hardness of 6.5–7; and 4) have a density of



3.03–3.22 g/cm³. We also found that the spodumene-bearing pegmatite veins typically exhibit a strong first-order absorption value of ~2,200 nm, a second-order absorption value of 2,350 nm, and reflective characteristics between 560 and 760 nm (Figure 2). Tourmaline-mica pegmatite dykes in the area do not contain spodumene and locally contain beryl. The dykes are characterised by a strong first-order absorption value of ~2,350 nm without an obvious second-order absorption signature.

Spodumene in the Jiajika area of northern Sichuan Province has the same characteristics, but the spodumene-bearing pegmatites cannot be directly distinguished from barren ones, and the granites (*sensu lato*) in the area have a first-order absorption signature of 1,413 and second-order absorption signature of 2,197 nm (Dai et al., 2017). Country rocks such as sandstone and shale do not have absorption signatures at 2,200 and 2,350 nm.

The Remote Sensing Interpretation Method

Low-resolution remote sensing satellites include Landsat5, Landsat7 and ASTER, which are characterised by high spectral-resolution. The spectral range includes visible light, near-infrared, and short-wave infrared, with low spatial resolution (15–30 m). Medium-resolution remote sensing satellites include SPOT-5 and Gaofen-1, which are characterised by a resolution of 2–2.5 m and four bands. The spectral range includes visible light, near-infrared, and does not include short-wave infrared. High-resolution remote sensing satellites include IKONOS, QUICKBIRD, GF-2, Worldview-2 and Worldview-3, with a resolution better than 1 m. The IKONOS, QUICKBIRD, and GF-2 have four bands, Worldview-2 has eight bands, and Worldview-3 has 16 bands. The spectrum of Worldview-3 includes visible light, near-infrared, and short-wave infrared. Other high-resolution remote sensing satellites only include visible light and near-

infrared, excluding short-wave infrared. The basic information of various satellites is shown in **Table 1**.

As mentioned above, the spectral ranges of Landsat5, Landsat7, ASTER, and Worldview-3 remote sensing satellites include visible light, near-infrared, and short-wave infrared, which is suitable for the detection of mineral anomalies using remote-sensing data. The spatial resolution of Worldview-3 is two orders of magnitude higher than that of several other remote sensing satellites. Therefore, ASTER and Worldview-3 remote sensing images are better for locating mineral anomalies. The combination of the Worldview-2 and other high-resolution imagery are used to highlight the distribution of pegmatite dykes, and the Worldview-3 data allows us to better identify the location of pegmatite dykes than other satellite data. The handicap, however, is the limited data available for the whole of our study area. It is for this reason we used the combined Worldview-2 and ASTER remote sensing images to pinpointing areas prospective for pegmatite veins.

The WorldView-2 multispectral data acquired during November 3, 2016 were used in this study. According to its manufacturer of the WorldView-2 multispectral sensor, there are the six spectral bands ranging from blue to the near infrared parts of the electromagnetic spectrum, including the Coastal Blue (400–450 nm; B1), Blue (400–510 nm; B2), Green (510–580 nm; B3), Yellow (585–625 nm; B4), Red (630–69 nm; B5), Red-Edge (705–745 nm; B6), Near infrared (770–895; B7) and NearIR-2 (860–1,040 nm; B8) bands, with 0.5 m spatial resolution making it possible to reflect information more clearly from pegmatites. The ASTER multispectral data was acquired during May 2, 2003. The spectral bands detected by modern ASTER remote sensors are now subdivided into the near-infrared and short-spectrum infrared bands giving 14 bands with a resolution of 15 m. ASTER measures reflected radiation in three bands between 520 and 860 nm (i.e. in the visible and near-infrared region, and the VNIR B1-B3) and in six bands from 1,600 to 2,430 nm (i.e. the short-wave infrared region, and SWIR B4-B9). In addition, the emitted radiation is measured at a 90 m spatial resolution in five bands in the 8,120–11,650 nm wavelength region (i.e. the thermal infrared region, and TIR B10-B11) (Bedini, 2011). ASTER images have a high spectral resolution, with six bands in the short-wave infrared spectrum, and it is easy to obtain information from mineralised areas (Jin et al., 2015; Mendes et al., 2017).

The absorption characteristics of spodumene-bearing pegmatites could correspond to each band of remote sensing in Worldview-2 and ASTER images. Spodumene-bearing pegmatites display a reflection feature in the Band 4 (B4) of the Worldview-2 data. In the ASTER bands, the Li-bearing pegmatites are characterised by reflection in B2, strong absorption in B5, and secondary absorption in B8. Using these criteria, the Worldview-2 remote sensing images were enhanced, making it easier to identify the presence of pegmatite clusters through different band combinations and principal component transformations, and the remote sensing anomalies related to the ASTER remote sensing images are extracted to identify the ore-bearing pegmatite veins.

The prospective areas are then ground-proofed with field work and geochemical sampling. The process, which is summarised in **Figure 3**, allows us to quickly focus the exploration activities. This involves a mineral system approach using detailed satellite images to identify pegmatite clusters potentially containing the mineral assemblage spodumene-muscovite-albite-quartz, however this does not guarantee that all the pegmatite clusters host economic concentrations of spodumene. Nonetheless, the method allows us to focus on prospective areas.

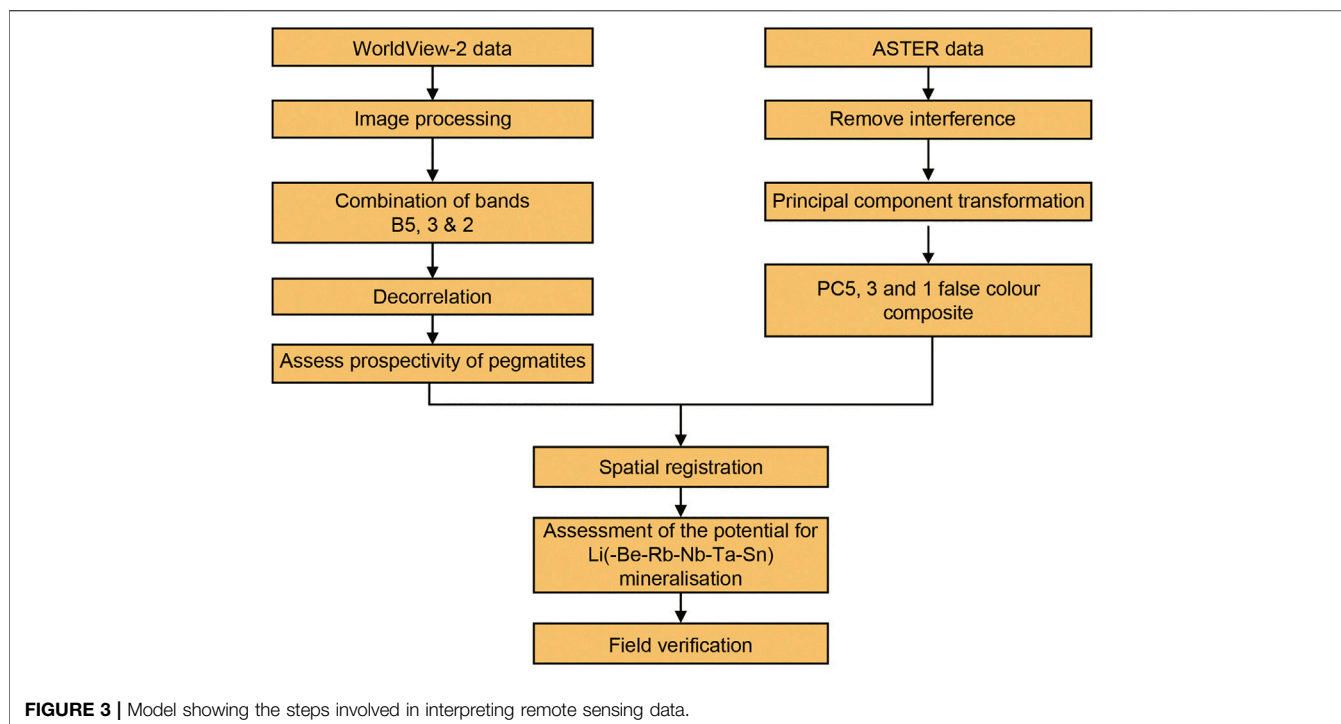
The Recognition of Pegmatite Dykes and Veins in High-Resolution Images

The PCI, ENVI and ERDAS software are used to image remote data from satellites such as Worldview-2 (Zhao, 2003). The PCI software is used for orthographic correction of the WorldView-2 remote sensing images to eliminate geometric position distortions in the remote sensing images caused by surface elevation differences. The ERDAS software is used for multi-spectral and panchromatic band fusion of the WorldView-2 remote sensing images and Mosaic of multi-landscape WorldView-2 remote sensing images. The ENVI software has strong transformation operation functions, which are used to extract remote sensing anomalies from ASTER remote sensing images.

Ortho-rectified images were developed using data from Worldview-2 sensor using bands 5, 3, and 2 (also see *Geological and Spectral Basis*). The Worldview-2 remote sensing image B5 is in the R band, B3 is in the G band, and B2 is in the B band (as part of the red-green-blue spectrum). The combination of the WorldView-2 remote sensing image 532 band is used for enhancement processing. This makes the information content rich and the combined image forms a natural true colour image, which is conducive to visual identification of pegmatites.

Decorrelation analysis was performed using the images with the B5, B3, and B2 combinations to highlight the location of areas prospective for pegmatites. This type of analysis is a process of contrast stretching of the main components of the image. This method can effectively reduce the correlation between different bands and increase the contrast between different geological units (Zhang et al., 2011; Jin et al., 2014). The procedure involves: 1) a principal component forward transformation; 2) a linear enhancement; and 3) a principal component inverse transformation.

The principal component forward transformation statistical analyses combined B5, B3, and B2 images from Worldview-2, then performs the principal component transformation. The linear enhancement involves linear stretching of each principal component obtained by the principal component transformation using the grey value of 0–255 to improve the contrast between distinctive features. The principal component inverse transformation enhances the principal component transform images. Since each principal component has been linearly stretched, it is restored to a band 5-3-2 composite image after the principal component inverse transformation is completed. An informative image is formed when the correlation between the three bands is small. The processed image using these transformations highlights the location of pegmatite dykes as



white areas with the country rocks represented by red and fawn coloured areas (**Figures 4,5A**). These prospective pegmatites are small and can only be recognised using detailed images, as discussed in *The Rapid Exploration Method Using Remote Sensing Data*.

Lithology and Structural Interpretation

The images formed with the combined ASTER B7, B4, and B1 data were used to interpret the lithology and structures hosting pegmatite-type rare metal deposits. The sedimentary rocks are characterised by banding representing bedding, which is discordant at faults or are truncated by granites. The ore-bearing Bayankala Formation is a weakly metamorphosed (up to lower greenschist facies) flysch succession that includes sandstone and shale. The formation is banded in variations of grey on the remote sensing images (**Figures 4, 5B**).

Intrusive rocks are planar, annular, elliptical, lenticular, have an irregular spatial form, have different geomorphologic combinations, and are discordant with the country rocks. The Dahongliutan Granite intrudes the Bayankala Formation, forms high mountains circumscribed by creeks and rivers, and has a pinkish-red colour on the remote sensing images (**Figure 5B**).

The location of faults is indicated by discordant boundaries between units, and the faults are in or near axial planes of antiformal folds. The structures include normal, reverse, translational and mixed types of faults, and trend northwestern in the Dahongliutan area where they transect areas with subdued topography with a rectangular bend along a river (**Figure 5B**). These structures host the NW-trending pegmatites that form pegmatite-rich clusters (**Figure 5B**).

Delineation of Pegmatites on Remote-Sensing Images

Features masking the characteristics of prospective geochemical anomalies and geological features on the images include dry rivers, alluvial fans, ice, snow, clouds, lakes, wetlands around snowfields, and swamps. If these features are not accommodated for during the image processing, the signatures for alteration zones are obscured. The purpose of interference removal is to observe different spectral characteristics and more easily choose different mathematical functions, such as ratio analysis and high- and low-end thresholding. The non-target areas and non-target ground objects are included in “interference windows” through digital processing aiming to highlight prospective area. The routine helps develop a basic image for the principal component analysis minimising the influence of interference from non-mineralised rocks and highlighting areas that are anomalous.

Principal component analysis of specific bands can remove the correlation between bands, reduce the data dimension, and concentrate it as much useful information as possible into a small number of image bands. Each principal component often represents unique geological features that do not overlap with each other (Zhang and Yao, 2009).

ASTER bands 1–9 are used in this study for principal component transformations to obtain the nine principal components PC1–9. The principal components PC1 and PC3 in the processed image contain a wealth of information and less noise, and B5 in PC5 participate to a larger extent. Thus, PC5, PC3, and PC1 were used to perform pseudo-colour synthesis producing RGB colour images. Multi-band monochromatic images were synthesised into false colour images highlighting the potential target areas for mineralised pegmatite dykes and veins (**Figures 4, 5**).

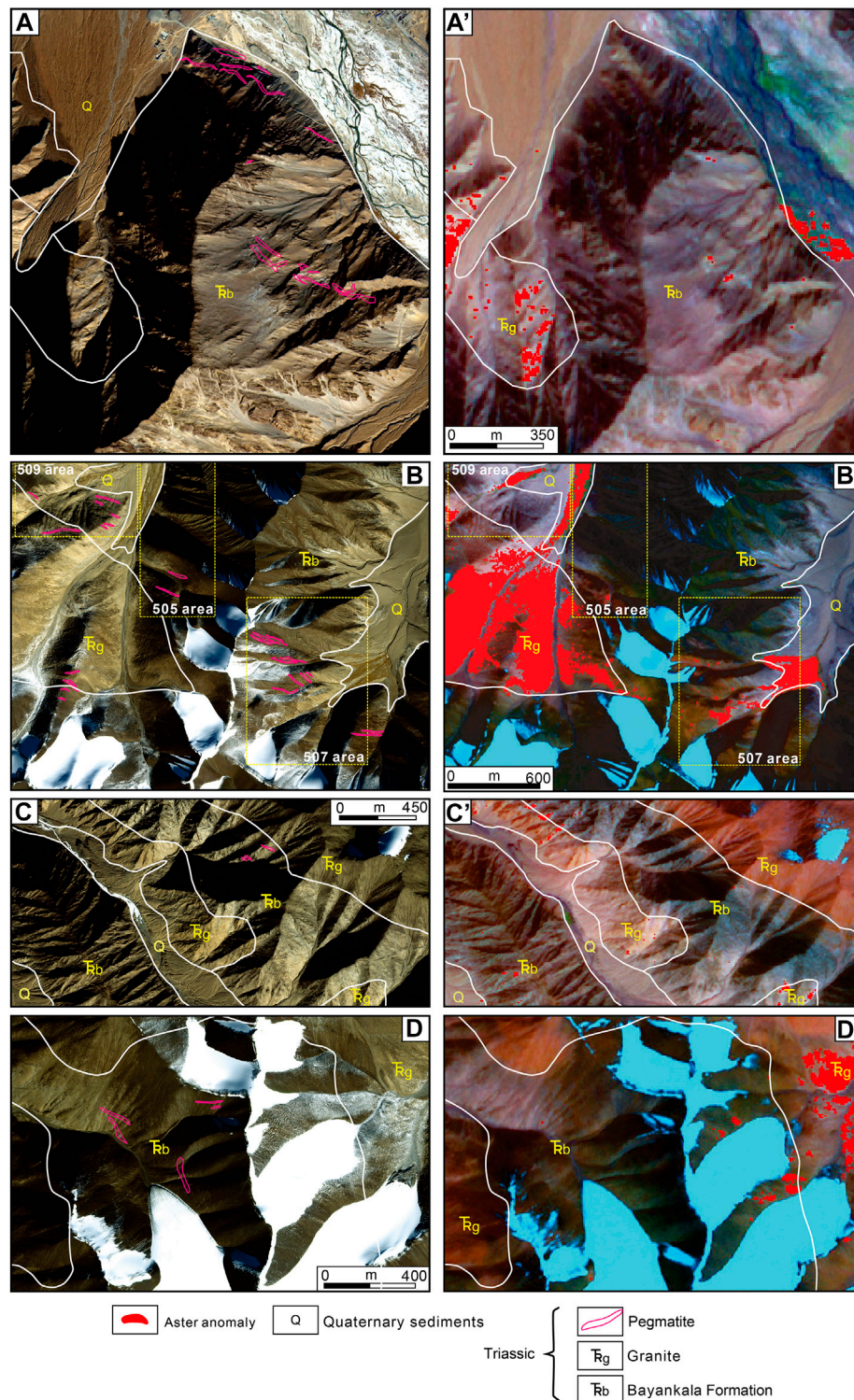


FIGURE 4 | Remote sensing images of the Aktas, 505, 507, and South Fulugou 1# and 2# Li deposits: **(A, A')** Worldview-2 image and Aster image of the Aktas Li deposit; **(B, B')** Worldview-2 image and Aster image of the 505 and 507 Li deposits; **(C, C')** Worldview-2 image and Aster image of the South Fulugou 1# Li deposit; **(D, D')** Worldview-2 image and Aster image of the South Fulugou 2# Li deposit.

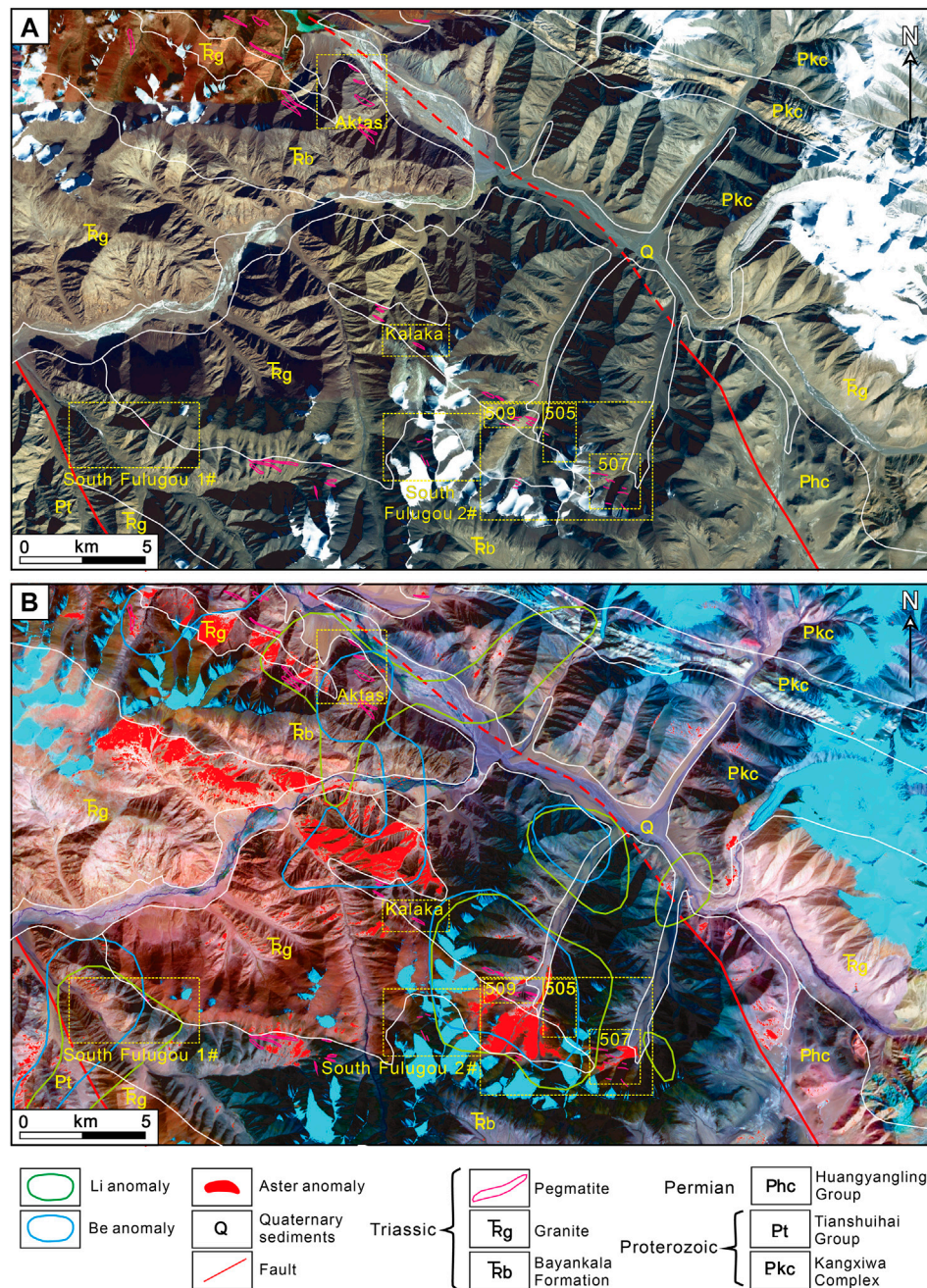


FIGURE 5 | Remote sensing images and prospective sites of Li mineralisation in the Dahongliutan area: **(A)** Worldview-2 image; and **(B)** Aster image, and geochemical anomalies of Li and Be.

The Worldview-2 and ASTER images are spatially registered, so that the interpreted location of pegmatite veins spatially overlap on the Worldview-2 image and the rare metal minerals highlighted on the ASTER image. The overlap areas including the 505, 507, and South Fulugou 1# and 2# deposits are designated as highly potential ore-bearing pegmatite locations comprising parts of two or more zones prospective for mineralisation (Figure 5).

Based on the comprehensive analysis of available geological information, the ore-forming process and structural controls are compiled. The location of potential ore-bearing pegmatites are then delineated using the combined remote sensing, geological mapping and sampling, which are combined delineating prospective target areas, such as the 505, 507, and South Fulugou 1# and 2# areas (Figures 4, 5).

The areas delineated as being prospective for ore-bearing pegmatites are field checked to determine the reliability and accuracy of the modelled data (Figure 3). ASTER remote sensing images were used to extract remote sensing anomalies related to the pegmatite-type rare metal deposits in the study area. These areas were verified in the field (Figure 5).

Sample Collection and Geochemical Analyses

Over 156 geochemical samples weighing a minimum of 1 kg were collected from trenches and diamond-drillhole core in the area considered prospective using satellite images. The samples from the trenches measured around 1 m long, 50 mm deep and 100 mm wide and those from 800 m long half diamond-drillhole core measuring 1 m long and ~70 mm in diameter were collected every 1 m. This ensured complete sampling across pegmatites logged in the core and trenches. The samples were crushed in a steel crusher, “splitted,” and then grounded to a 200 mesh (<74 μm). Sample splitting is the necessary step during the crushing, which ensures the analyses are representative of the rocks sampled.

The rock powder (~100 mg) was dissolved in a Teflon bomb using a mixture of 1 ml HNO_3 and 2 ml HF. The Teflon bomb was dried on a hotplate, and then dissolved in 1 ml HNO_3 . The Teflon bomb was put in a stainless-steel pressure jacket and heated to 180°C in an oven for 36 h. After cooling, the Teflon bomb was opened and placed on a hotplate and evaporated to dryness. The dried sample was refluxed with 1.5 ml of HNO_3 and evaporated to dryness again. A further 4 ml of HNO_3 was added to the sample and the close bomb was placed in an oven heated to 150°C for 12 h. After cooling, the final solution was diluted to ~50 ml in a polyethylene bottle and prepared for analyses. The analyses of these standards have analytical errors of $\pm 2\%$ for Li, $\pm 2.5\%$ for Rb, and $\pm 5\%$ for low concentrations of Be, Cs, Nb, and Ta. The element compositions were determined using an iCAP RQ ICP-MS at the MNR Key Laboratory for the Study of Focused Magmatism and Giant Ore Deposits, Xi'an Center of China Geological Survey.

Dating of Mineralisation

Cassiterite coexisting with spodumene was extracted from the centre of the No. 18 orebody (sample 505–2) at the 505 Li deposit for U-Pb isotope dating. The cassiterite measuring 80–150 μm across was selected under a binocular microscope, is reddish brown in colour under transmitted light, and cracks were observed under the reflected light. Cassiterite samples without cracks and inclusions were selected for U-Pb dating using a laser ablation multi-receiver inductively coupled plasma mass spectrometer (LA-MC-ICP-MS) at the Isotope Laboratory of the Tianjin Center of China Geological Survey. The multi-collector inductively coupled plasma mass spectrometer is a Neptune manufactured by Thermo Fisher Company, and the laser is a UP193-FX ArF Excimer Laser produced by the ESI Company in the USA. Li et al. (2009), Hao et al. (2016),

and Cui et al. (2017) describe the operating conditions of the laser ablation system, the ICP-MS instrument, and the data reduction process.

A 193 nm FX laser was used to ablate the cassiterites with a beam spot diameter of 75 μm . The energy density was 10–11 J/ cm^2 at a frequency of 20 Hz. The laser ablated material was then sent to the MC-ICP-MS with He as the carrier gas, and the U-Pb isotopes with very different mass numbers were received at the same time for the U-Pb measurement by expanding the dispersion with dynamic zoom adjustment. The laboratory internal standard AY-4 with the $^{206}\text{Pb}/^{238}\text{U}$ ID-TIMS age 158.2 ± 0.4 Ma was used as the measurement external standard. Every five cassiterite sample points were measured, and the standard samples were measured twice alternately to correct the analysis process and errors in the laser ablation process. The $^{206}\text{Pb}/^{207}\text{Pb}$ – $^{238}\text{U}/^{207}\text{Pb}$ isochron method was used to correct ordinary lead in cassiterite at the same time (Hao et al., 2016; Cui et al., 2017). The ICPMSDataMSCal software of Liu et al. (2010) and Isoplot program of Ludwig (2003) were used for data processing and mapping.

Muscovite was extracted from the spodumene-bearing pegmatite from the Aktas Li deposit (sample HLT-1) and the 509 Li deposit (sample 509X-1) for Ar-Ar dating. Hand-picked grains were cleaned in de-ionised water and acetone. The samples were weighed and loaded into aluminium packets for irradiation. The packets were placed in a silicate glass tube (Can UM# 86), interleaved with packets containing the flux monitor Mount Dromedary Biotite (dated at 99.125 ± 0.076 Ma [0.077%]; Phillips et al., 2017). The canister was irradiated for 60 MWh (Mega Watt hours) at the CLICIT facility of the Oregon State University TRIGA reactor, United States.

After irradiation, the mineral separates were removed from their packaging and placed in tin foil packets. The $^{40}\text{Ar}/^{39}\text{Ar}$ step-heating analyses were carried out on a conventional double-vacuum Ta-resistance furnace attached to a VG3600 mass spectrometer with Daly and Faraday detector. Samples were outgassed at 450°C for 2 h. Following initial outgassing, aliquots were incrementally heating between 500° and 1350°C. It takes about 3 min to reach the desired temperature and the duration for each heating step was 20 min. The extracted gas was purified using multiple SAES Zr-Al getters before expansion into a VG3600 mass spectrometer. Extraction line blanks were measured before the analysis of each sample. After each sample analysis, the furnace was outgassed at 1500°C. High-temperature (1450°C) furnace blanks contained low levels of the measured isotopes and the blank corrections have a minimal impact on the measured data.

The mass discrimination and detector intercalibration were monitored by analysis of standard air volumes. The correction factors for interfering reactions, as determined by irradiation of high-purity K-glass and Ca-salt included in Can UM# 86, are indicated in the dataset, and the reported data have been corrected for system backgrounds, mass discrimination, fluence gradients, and atmospheric contamination, assuming the atmospheric argon composition of Lee et al. (2006). Unless otherwise stated, errors associated with the age determinations are one standard deviation and exclude uncertainties in the

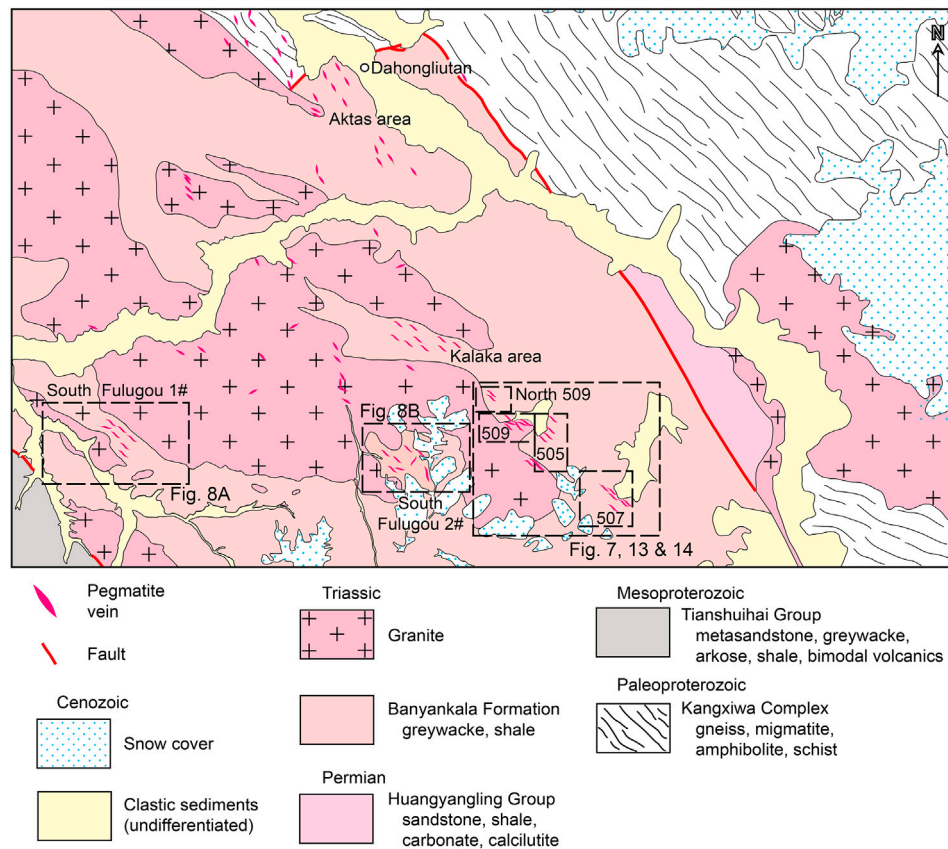


FIGURE 6 | Geological map of the Dahongliutan area.

J-value, age of the fluence monitor and the decay constants. Ages have been calculated using the decay constants of Steiger and Jager (1977), and the $^{40}\text{Ar}/^{39}\text{Ar}$ dating technique is described in detail by McDougall and Harrison (1999).

LITHIUM DEPOSITS DISCOVERED BY THIS STUDY

As outlined above, ore-bearing pegmatites have been delineated using a combination of remote sensing images, geological maps and geochemical anomalies, and were field checked following the procedure outline in **Figure 3**, which led to the discovery of the 505, 507, north 509, and South Fulugou 1# and 2# Li deposits (**Figure 6**). The Li_2O grades of the anomalies are between 1.1 and 3.8%, based on the sampling of trenches and diamond-drillhole core, and the analyses indicate a combined resource of over 1.7 Mt Li_2O , but this is only an estimate given that exploration is still at an early stage. As a comparison, the Greenbushes deposit in Western Australia has an estimated contained Li resource of over 2.9 Mt Li_2O (Geological Survey of Western Australia, Lithium Commodity Flyer, 2017).

Geology of the Newly Discovered 505, 507, South Fulugou 1# and South Fulugou 2# Lithium Deposits

The 505 and 507 deposits are hosted by hornfelsed units of the Bayankala Formation near the contact with the southern part of the Dahongliutan Granite and have similar geological features as the 509 Li deposit (**Figure 7**). The Worldview-2 satellite images were used to interpret some of the pegmatite veins represented as NW-trending white hue and strip-like patterns and can be interpreted as sheeted veins (**Figure 4B**). The anomalies extracted using the ASTER sensing images were distributed at the contact with the Bayankala Formation and monzogranite (**Figure 4B'**).

The 505 deposit assays 0.02–0.04% BeO , 0.04–0.26% Rb_2O , and 0.02–0.04% $(\text{Nb} + \text{Ta})_2\text{O}_5$, and the 507 deposit assays 0.02–0.05% BeO , 0.05–0.16% Rb_2O , and 0.01–0.02% $(\text{Nb} + \text{Ta})_2\text{O}_5$. The exposed rocks at the 505 and 507 Li deposits are in the central and upper parts of the Bayankala Formation consisting of variably deformed grey to brown, thinly layered, and fine-grained feldspar-quartz sandstone interbedded with grey to black siltstone. The formation is cleaved subparallel to the NE-trending bedding. The beds are also folded plunging shallowly to moderately to the SE.

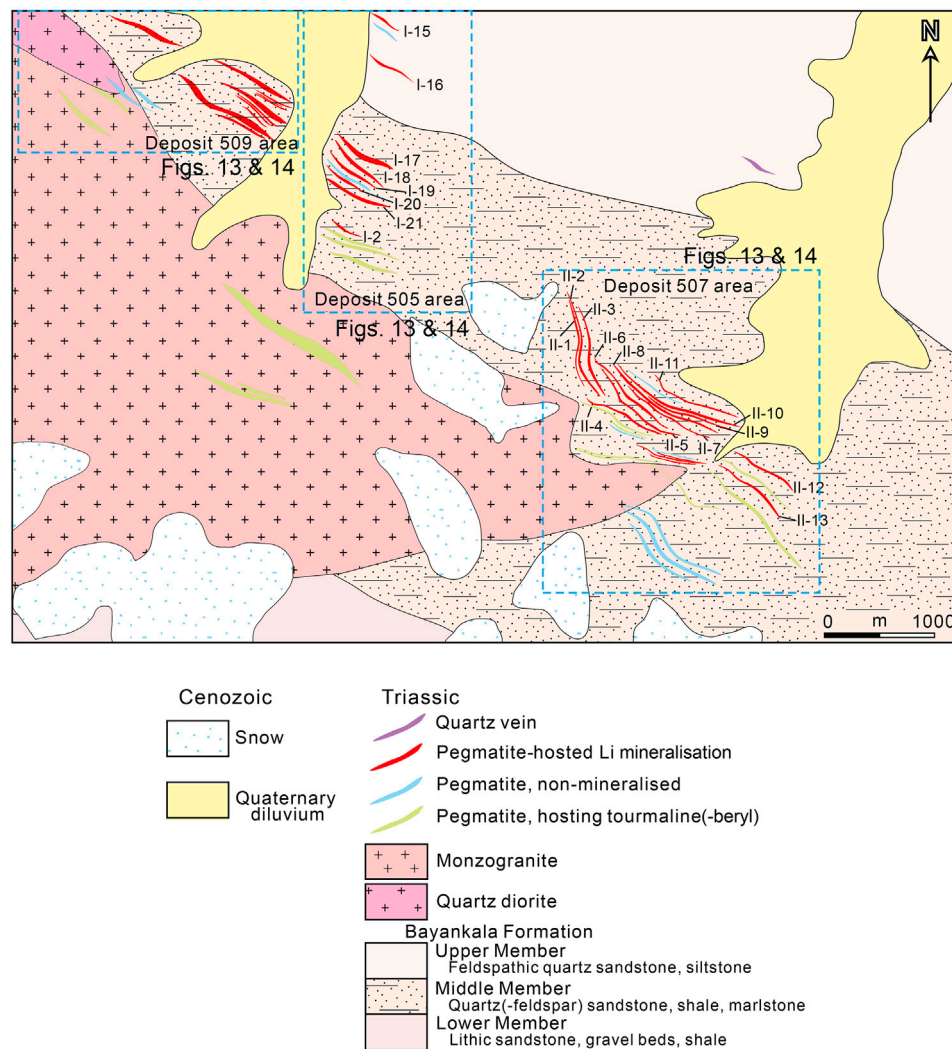


FIGURE 7 | Geological maps of the 505 Li deposit and 507 Li deposit.

A total of 20 pegmatite veins were found at 505 forming 11 orebodies that are 1.5–4 m wide and 50–260 m long with an estimated Li resource is 0.01 Mt assaying 1.1–3.3% Li_2O (**Supplementary Table S2**). Granodiorite and quartz diorite are present in the western part of the deposit intruding the Bayankala Formation. The contact alteration is up to 30 m wide and progresses from cordierite hornfels near the granite to andalusite hornfels further away. Some pegmatite veins were distributed at the contact zone.

The spodumene-pegmatite veins trend NW and parallel to the Qitaidaban Fault (**Figure 1B**), and are regionally zoned and are strongly associated with the andalusite-bearing hornfels (**Figures 10I,J, 11**). The country rocks are brittle-ductile deformed and strongly cleaved, forming a series of lensoidal shears within the fault. The structure provides a good conduct for the pegmatite veins and associated mineralisation. Twenty-eight 300–1,200 m long and 1–9 m thick pegmatite veins were found at the 507 deposit, and 13 orebodies have been delineated. The orebodies

trend NW dipping moderately either to the northeast or southwest with an estimated resource of 0.44 Mt averaging 2.5% Li_2O (**Supplementary Table S2**).

The South Fulugou pegmatite vein group is located on the south part of the Dahongliutan Granite where at least 110 pegmatite veins were highlighted on the satellite images. The central part of the group contains the South Fulugou 1# and 2# Li deposits, where the discovered mineralised pegmatites appear greyish to white on the satellite images. The mineralised pegmatite veins at South Fulugou 1# trend NW near the contact between the Dahongliutan Granite and Bayankala Formation in the western part of the study area (**Figure 8A**). Large shadows cast in valleys from adjoining mountains exist in the area on the Worldview-2 satellite images, making the accurate delineation of the pegmatite veins subtle (**Figure 4C**). The delineated remote sensing anomalies are in granite on the ASTER satellite images (**Figure 4C'**). The host rocks consist of greenschist to

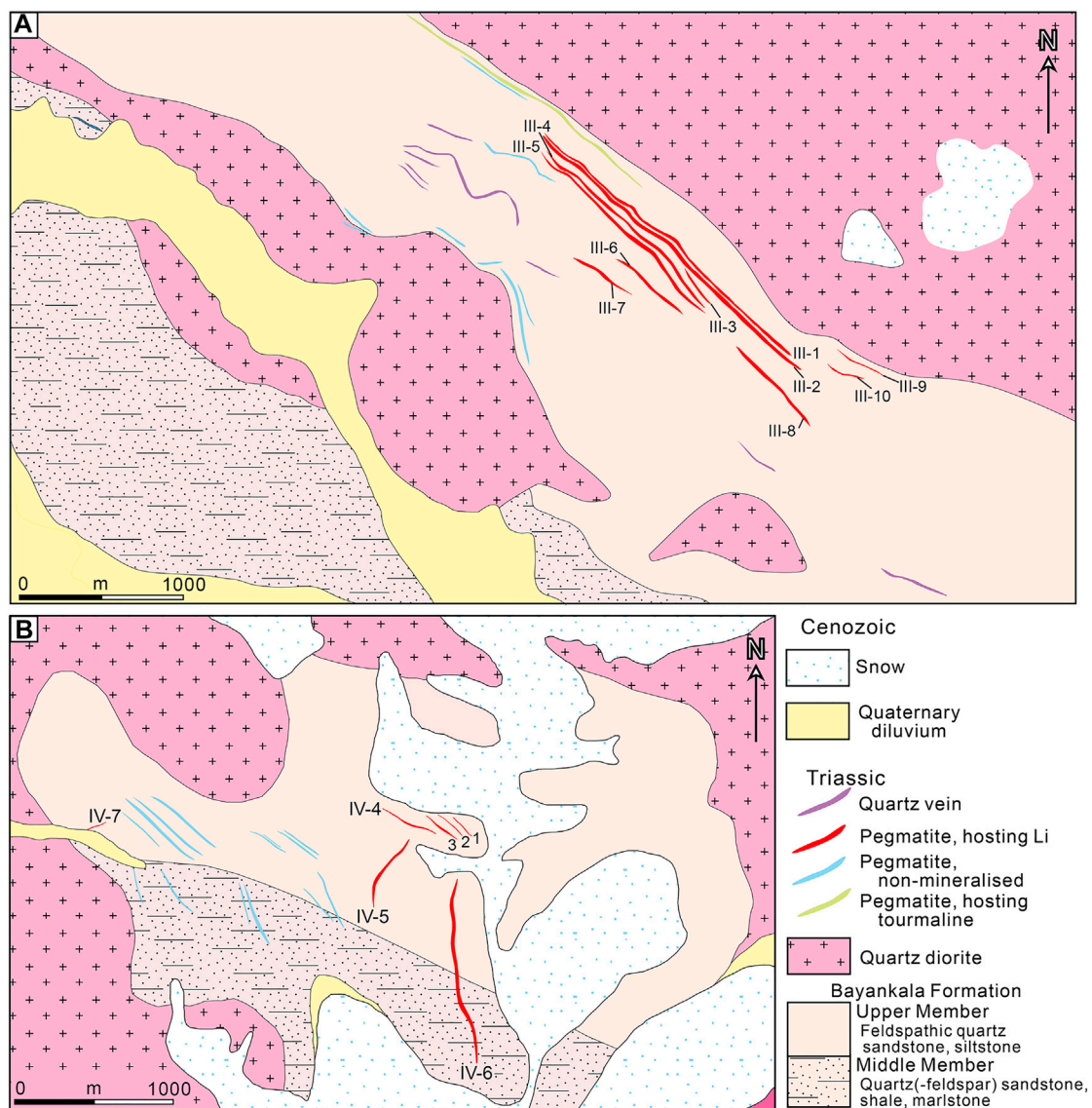


FIGURE 8 | Geological maps of: **(A)** the South Fulugou 1# Li deposit; and **(B)** the South Fulugou 2# Li deposit.

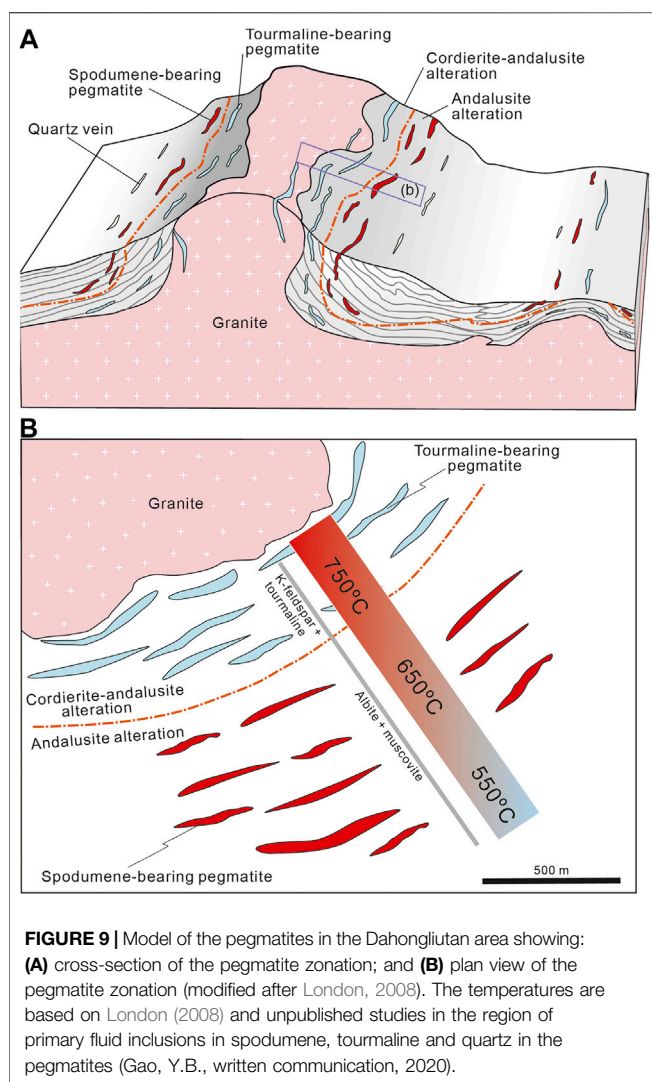
amphibolite facies light grey, fine-grained feldspar-quartz sandstone interbedded with grey, thinly layered siltstone, and biotite-quartz schist. The sequence dips moderately to the northeast (**Figure 8A**).

The exposed magmatic rocks include light grey to white, fine- to medium-grained and non-mineralised tonalite. There are two granitic outcrops in the area, which are located on the north and south sides of the Bayankala Formation. The country rocks progress from cordierite-andalusite hornfels, andalusite hornfels to sericite schist. The deposit is located on the northern limb of the South Dahongliutan antiform.

Twenty-one pegmatite veins were found in the South Fulugou 1# Li deposit hosted by the Bayankala Formation, and a small amount of pegmatite veins are present on the southern side of the

tonalite intrusion. The deposit includes ten lenticular Li orebodies dipping to the northeast subparallel to the layering (**Figure 8A**). The orebodies are up to 18 m wide and up to 2,400 m long with an estimated resource of 0.58 Mt averaging 1.2–3.9% Li_2O , 0.03–0.08% BeO , 0.01–0.09% Rb_2O , and 0.01–0.02% $(\text{Nb} + \text{Ta})_2\text{O}_5$ (**Supplementary Table S2**).

The South Fulugou 2# Li deposit is located at an elevation of 5,300–6,200 m to the east of the South Fulugou 1# deposit, west of the 509 Li deposit, and south of the Dahongliutan Granite (**Figure 4**). Both of the South Fulugou deposits are similar with pegmatite veins trending NW in the Bayankala Formation, although a small number of veins trend eastward. The pegmatites are represented by grey to white strips on the Worldview-2 satellite images (**Figure 4D**), and the delineated



ASTER remote sensing anomalies are distributed within the granite (Figure 4D').

The South Fulugou 2# deposit has an estimated resource of 0.14 Mt averaging 0.9–2.6% Li_2O , 0.02–0.05% BeO , 0.04–0.34% Rb_2O , and 0.01–0.02% $(\text{Nb} + \text{Ta})_2\text{O}_5$ (Supplementary Table S2) (Figure 8B). The deposit is hosted by the Bayankala Formation that consists of thinly layered, metamorphosed, fine-grained feldspar-quartz(-garnet-sericite) sandstone and light grey biotite-quartz schist. Light grey, fine-to medium-grained quartz diorite is exposed to the east, west, and north of the deposit. The diorite contains mafic xenocrysts and is locally foliated in biotite forming a gneissic texture. The deposit contains seven mineralised pegmatite veins (Figure 8B), which are 120–1,100 m long and 2–12 m wide. In addition, a ~680 m long and 2 m wide mineralised pegmatite vein is present in faulted quartz diorite at the western part of the deposit, where the vein dips shallowly towards the NE. This contact relationship is rarely exposed, but where exposed shows that the pegmatite is younger than the quartz-diorite.

Pegmatite Zonation

The kinds of granitic pegmatites present are spodumene-bearing, and tourmaline-bearing. The composition of the pegmatite veins change from quartz-K-feldspar-tourmaline(-muscovite) proximal to the Dahongliutan Granite to spodumene-bearing plagioclase-quartz-muscovite(-microcline-garnet) distal from the granite (Figure 9). The spodumene-bearing pegmatite veins are present 200–1,500 m from the Dahongliutan Granite in the Bayankala Formation (Figures 10A and 9). The veins trend NW, dip moderately to steeply NE and their location is structurally controlled by joints and shears (Figures 10B,C). The spodumene is grey, up to 0.15 m long (larger than other minerals in the veins), and constitute between 5 and 30% of the veins, although the highest content can reach 70% of the veins (Figure 10D–F). The veins are small and not commonly zoned, and where present contains barren edges and mineralised cores containing spodumene as the Li-bearing mineral. The location of the mapped mineralised pegmatite veins are shown in Figures 6, 7, 8.

The tourmaline-bearing pegmatites contain long columnar or needle-shaped black tourmaline with spherical, triangular or banded cross-sections, and are orientated perpendicular to the pegmatite vein (Figure 10G). The pegmatites in the Dahongliutan Granite contain quartz occupying spaces between K-feldspar and muscovite (Figure 10H). Also present are jointed, lenticular quartz-muscovite veins that cut the spodumene-bearing pegmatites and trend subparallel and oblique to the metasedimentary host rocks (Figure 10E–I). The metasedimentary rocks near the Dahongliutan Granite are strongly hornfelsed containing cordierite and andalusite near the granite progressing outward to andalusite and sericite-rich hornfels at the edge of the contact metamorphism. The spodumene-bearing pegmatites are not internally zoned and are strongly associated with the andalusite-bearing hornfels (Figure 10M,N).

Several types of pegmatites are presented in the area that include massive, patchy, and dendritic textures. The massive texture is fine-to medium-grained monoclinic, although two or more minerals can be massive in the form of banding and seriate textures. The long axis of the spodumene and tourmaline are lineated perpendicular to the strike of the pegmatite veins. The patchy texture is characterised by minerals such as spodumene, quartz, plagioclase, and sodium plagioclase with different grain sizes. The dendritic texture is common in the mineralised pegmatites and characterised by elongated and wedge-shaped dendritic crystals including spodumene-niobium-tantalum minerals, cassiterite, and triphylite (LiFePO_4) in feldspar and quartz. The association of Li-Nb-Ta-Sn in these pegmatites places them in the Li-Cs-Ta (LCT) - type, as defined by Cerný and Ercit (2005).

The main ore mineral is grey-white to green spodumene with lesser amounts of amblygonite $(\text{Li,Na})\text{AlPO}_4(\text{F,OH})$, lithium muscovite, beryl, and niobite also known as columbite $(\text{Fe, Mn})\text{Nb}_2\text{O}_6$. The spodumene is idiomorphic, fine-to coarse-grained and is larger than other minerals in the pegmatite (Figures 11A,B). The long axis is between 30 and 150 mm,

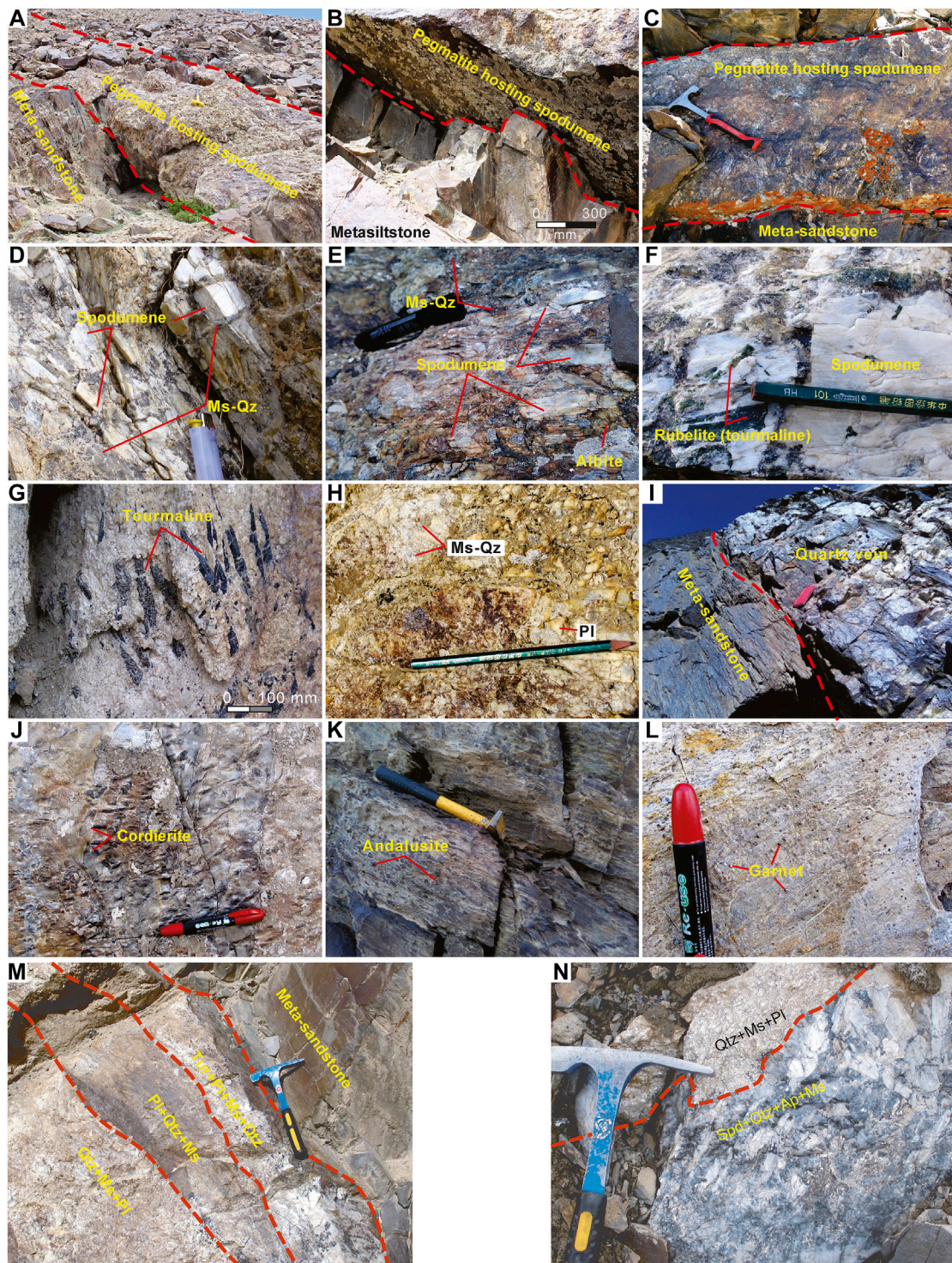


FIGURE 10 | Photographs of rocks in the Dahongliutan area: **(A)** spodumene-bearing pegmatite intruding meta-sandstone in the Bayankala Formation; **(B)** spodumene-bearing pegmatite subparallel to layering in the host rocks; **(C)** an example of spodumene-bearing pegmatite cross-cutting layering in the country rocks; **(D)** long, grey to white spodumene crystals intergrown with muscovite and quartz hosted by a fault; **(E)** pegmatite consisting of muscovite, albite, quartz, and spodumene; **(F)** green rubellite (tourmaline) coexisting with spodumene in pegmatite; **(G)** tourmaline-bearing pegmatite consisting of black tourmaline, plagioclase, muscovite and quartz; **(H)** non-mineralised pegmatite consisting of plagioclase, muscovite and quartz; **(I)** an example of quartz veining in meta-sandstone; **(J)** hornfelsed greysiltstone containing cordierite; **(K)** dark grey andalusite in hornfelsed siltstone; and **(L)** garnet-bearing hornfelsed siltstone located near a spodumene-bearing pegmatite. Zoned pegmatite dykes in the Dahongliutan area containing: **(M)** black tourmaline-plagioclase-muscovite-quartz, plagioclase-quartz-muscovite, and quartz-muscovite-plagioclase; and **(N)** quartz-muscovite-plagioclase, and spodumene-quartz-albite-muscovite. Abbreviations: Spd, spodumene; Qtz, quartz; Ms, muscovite; Pl, plagioclase; Ab, albite; Tur, tourmaline.

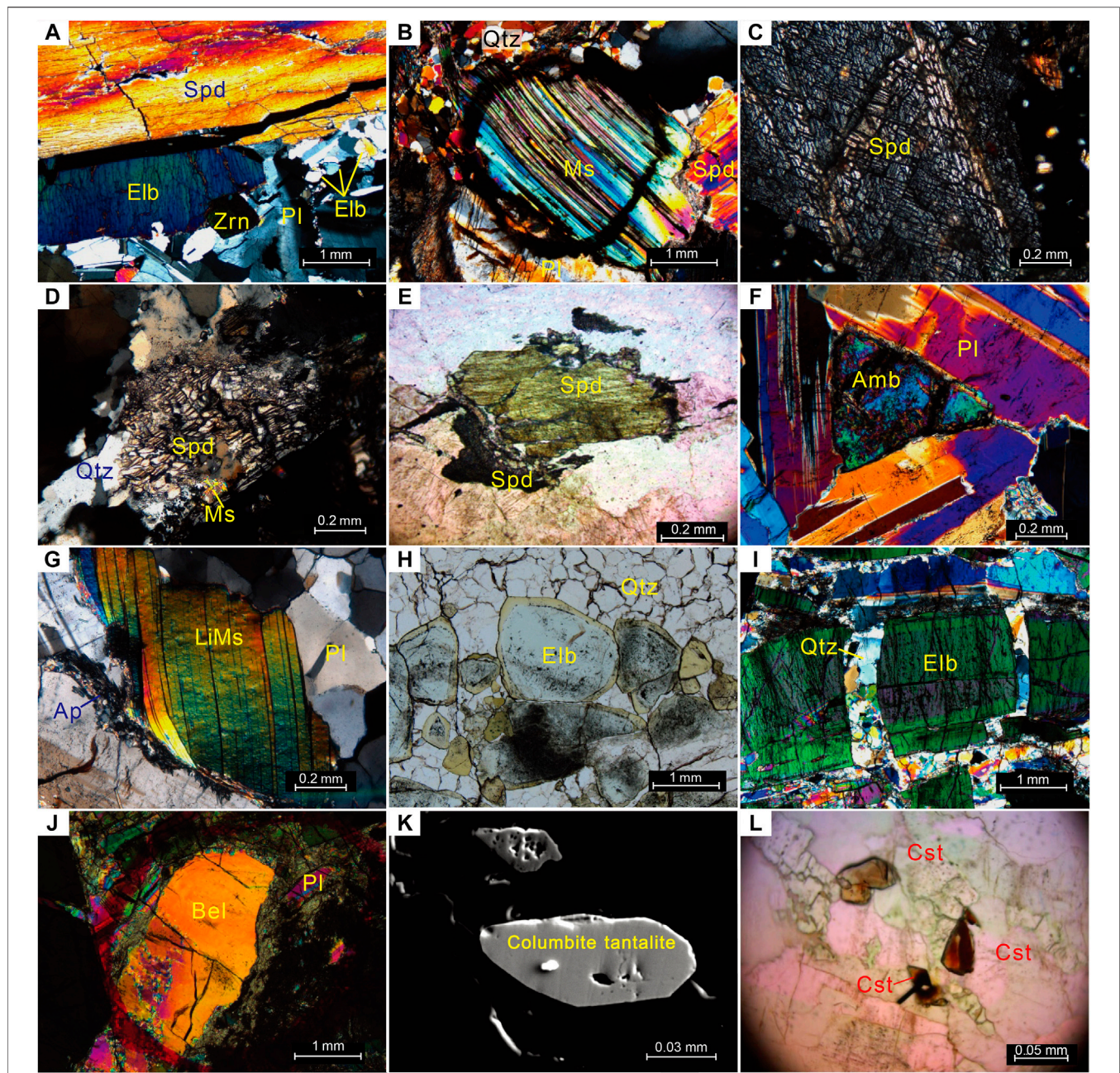
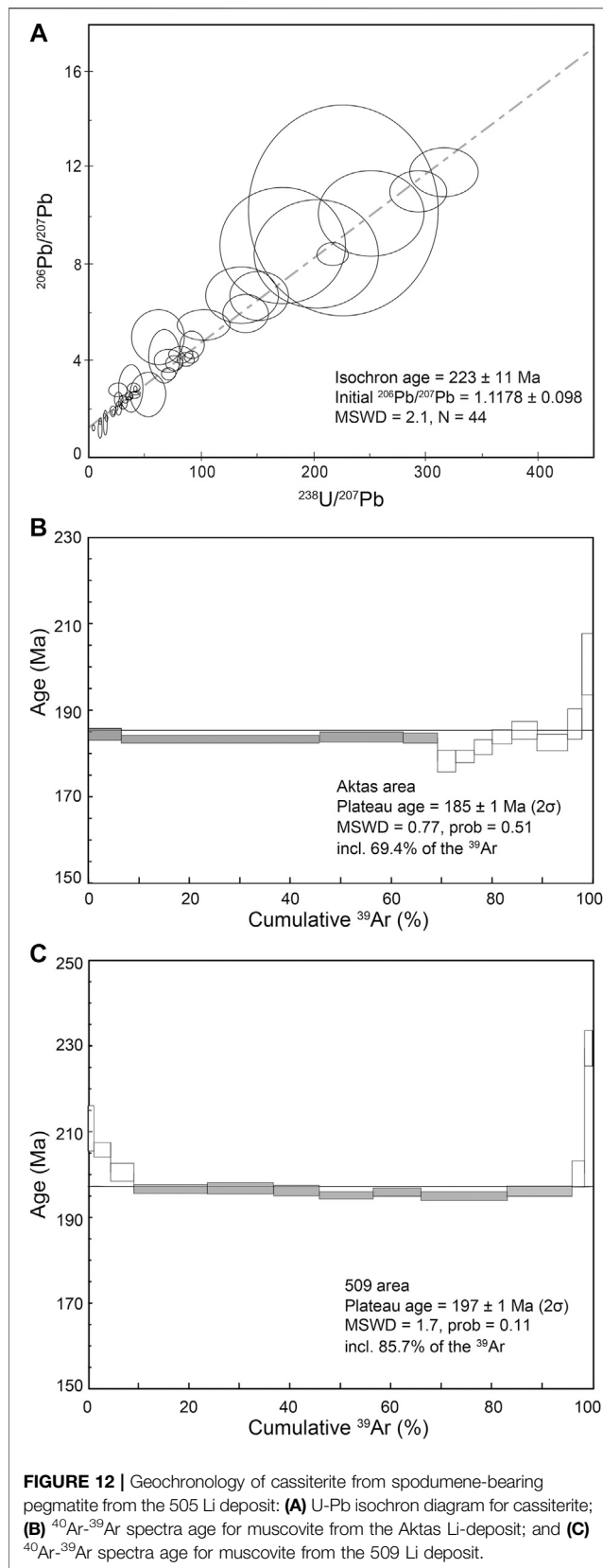


FIGURE 11 | Photomicrographs of samples from the Dahongliutan area showing: **(A)** example of spodumene-bearing pegmatite containing, elbaite, plagioclase and minor zircon; **(B)** spodumene-bearing pegmatite dykes consisting of muscovite, plagioclase and quartz; **(C)** cleaved spodumene; **(D)** quartz and muscovite filling fractures in spodumene; **(E)** late fibrous spodumene crystallised on the edge of early columnar spodumene; **(F)** a small amount of 0.2 -1 mm wide allomorphous and granular amblygonite associated with spodumene and plagioclase; **(G)** lithium-bearing, 1 and 5 mm long muscovite with a low and high refractive index; **(H)** two forms of light green elbaite; **(I)** dark green and columnar elbaite crossed by quartz and muscovite; **(J)** example of rare beryl; **(K)** back-scatter electron (BSE) image of tabular, 0.04 -0.20 mm long irregular and granular columbite-tantalite with a semi metallic luster; and **(L)** semi-automorphic to allomorphous granular 0.1 and 0.2 mm long cassiterite associated with the early spodumene. Abbreviations: Spd, spodumene; Qtz, quartz; Ms, muscovite; LiMs, lithium-bearing muscovite; Pl, plagioclase; Ab, albite; Amb, amblygonite; Zrn, zircon; Ap, apatite; Tur, tourmaline; Elb, elbaite; Bel, beryl; Cst, cassiterite.

and has cleavage orientated in two directions at close to right angles (**Figure 11C**). Partings within the spodumene are locally filled by quartz and muscovite veining, showing that the quartz-muscovite veins are late in the paragenesis of the veining

(**Figure 11D**). Furthermore, hair-like spodumene is also present along the edge of idiomorphic spodumene exists at the edge of the pore-existing spodumene, showing that there are two spodumene generations (**Figure 11E**).



The amblygonite in the mineralised pegmatite is 0.2–1 mm across, and it is often associated with spodumene and albite, and the lithium muscovite ranges from 2 to 5 mm long (**Figure 11F–G**). The spherical triangle of elbaite ($\text{Na}(\text{Li}_{1.5}\text{Al}_{1.5})\text{Al}_6\text{Si}_6\text{O}_{18}(\text{BO}_3)_3(\text{OH})_4$) is observed in cross section, with cracks were filled by later quartz and mica (**Figure 11H–I**). The beryl is rare, and the columbite-tantalite crystals are between 0.04 and 0.2 mm across (**Figure 11J–K**). The cassiterite is typically hypidiomorphic (**Figure 11L**), with a grain size of 0.1–0.2 mm. It is associated with the early spodumene, and some columbite and columbite-tantalite crystals are 0.04–0.2 mm long and co-existing cassiterite.

Age of the Lithium Mineralisation

Cassiterite co-existing with spodumene was collected from the 505 deposit for dating. The LA-MC-ICP-MS cassiterite U-Pb dating obtained 44 valid points (**Supplementary Table S3**). The $^{238}\text{U}/^{207}\text{Pb}$ ratio is between 3.388 and 315.89, the $^{238}\text{U}/^{206}\text{Pb}$ ratio ranges from 2.864 to 28.758, and the $^{206}\text{Pb}/^{207}\text{Pb}$ value is 1.159–11.837. The $^{206}\text{Pb}/^{207}\text{Pb}$ - $^{238}\text{U}/^{207}\text{Pb}$ isochron age is 223 ± 11 Ma (MSWD = 2.1) (**Figure 12A**).

Sample HLT-1 of primary muscovite co-existing with spodumene from Aktas was analysed using 12 stages with $^{40}\text{Ar}/^{39}\text{Ar}$ step-by-step heating experiments from 650° to 1,450°C (**Supplementary Table S4**). A relatively flat plateau age of 185 ± 1 Ma formed during the temperature stage from 650° to 800°C (**Figure 12B**), including 69.4% of the released ^{39}Ar . Sample 509X-1 of primary muscovite co-existing with spodumene from the 509 deposit was also analysed using 12-stages $^{40}\text{Ar}/^{39}\text{Ar}$ step-by-step heating experiments from 650° to 1,450°C, and a relatively flat plateau age of 197 ± 1 Ma formed during temperature stage from 730° to 1,050°C (**Figure 12C**), including 85.7% of the released ^{39}Ar .

DISCUSSION

The Rapid Exploration Method Using Remote Sensing Data

As mentioned earlier, spectroscopic tests show that the spodumene-bearing pegmatite exhibits strong absorption (~2,200 nm), second-order absorption (~2,350 nm), and reflection characteristics (~560 and 760 nm). The absorption and reflection characteristics correspond to each band of remote sensing images originating from Worldview-2 and ASTER data. The spodumene-bearing pegmatite veins and dykes display reflection in B4 of the Worldview-2 data, and B4 and B2 of the ASTER data. In addition, the spodumene-bearing pegmatites display strong absorption in the ASTER B5 and secondary absorption in the ASTER B8 data. Based on these characteristics of the pegmatites, the principal component transformation method is used to extract remote sensing anomalies related to rare metal concentrations. Most of the Li mineralisation, however, was discovered at the periphery of

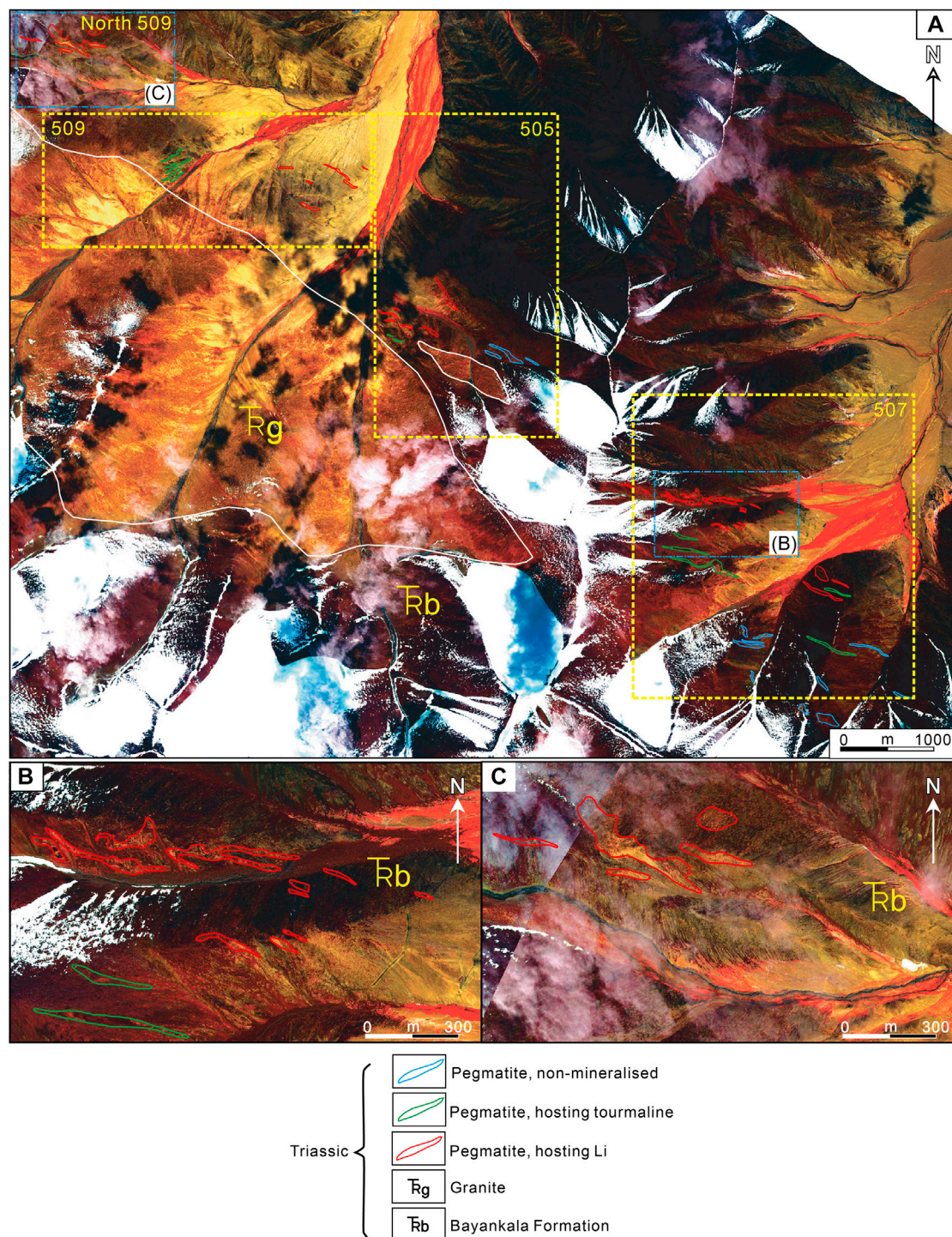


FIGURE 13 | Worldview-3 remote sensing images with an 841-band combination and enhanced processing for the 505, 507 Li deposits and surrounding areas showing: **(A)** the whole area; **(B)** the 507 Li-deposit; and **(C)** the potential area for Li deposits in the North 509 area. Pegmatite veins with widths of at least 1 m appear white on the images and the Bayankala Formation host is red and greyish brown in colour in parts **(B, C)**. The increased resolution of the Worldview-3 images resulted in an increase in the recognition of mineralised pegmatite dykes in part **14C**.

remote sensing anomalies. Furthermore, given that the resolution of the ASTER images is 15 m, the spodumene-bearing pegmatite display mixed pixels on the ASTER remote sensing images,

making it difficult to accurately pin-point the location of these pegmatites that are commonly less than 15 m wide. This is also limited by the Sentinel-2, Landsat-5 and Landsat-8 images

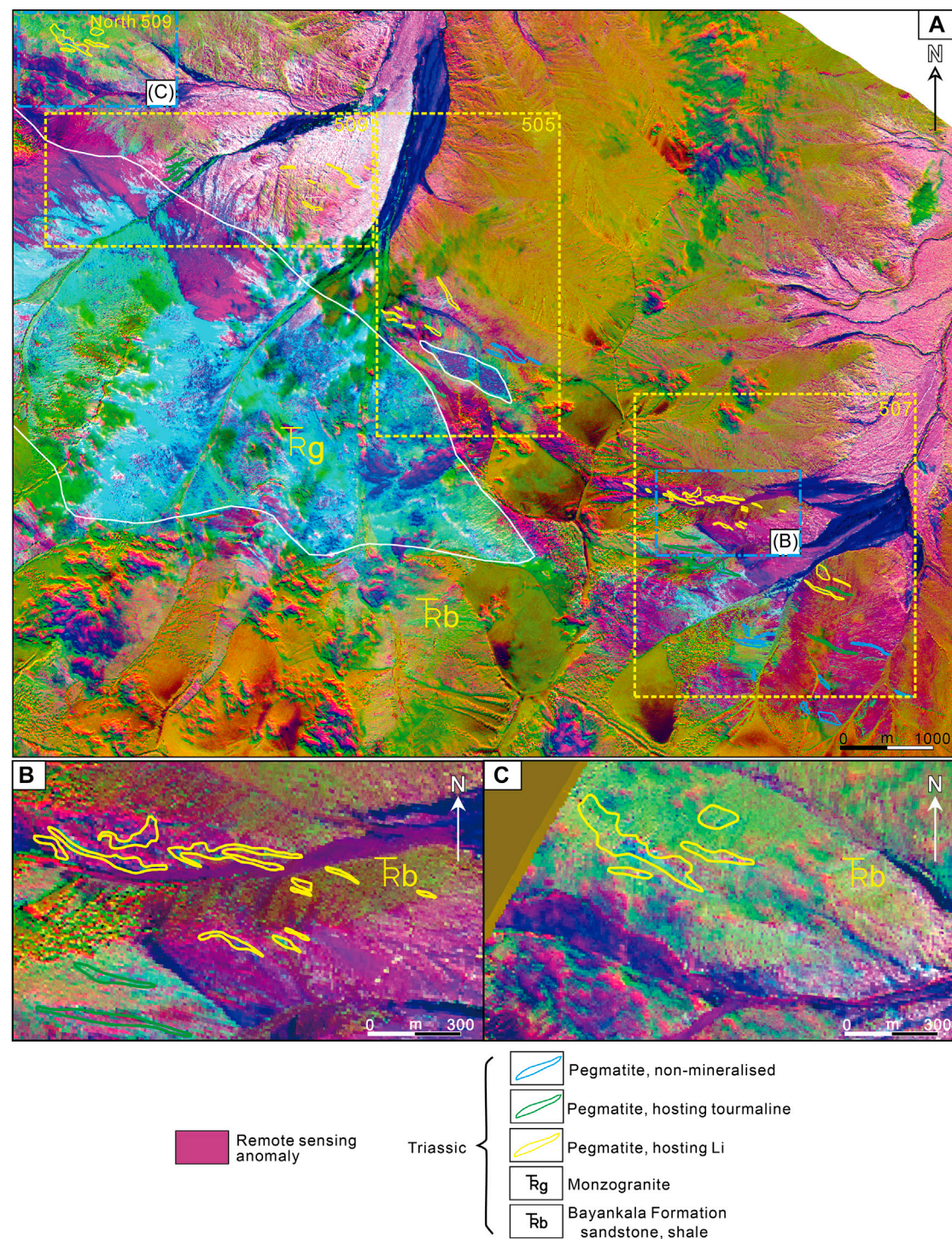


FIGURE 14 | Worldview-3 Remote sensing anomalies in the 505 and 507 Li deposits and surrounding areas: **(A)** the whole area; **(B)** the 507 Li deposit; and **(C)** the potential area for Li mineralisation in the North 509 area.

(Mendes et al., 2017; Cardoso-Fernandes et al., 2018; Cardoso-Fernandes et al., 2019a). In contrast, the location of pegmatites less than 1 m wide can be recognised using high-resolution Worldview-2 images. The ASTER images highlight the

presence of muscovite enriched in pegmatites, granitic rocks, and the widespread hydrothermal alteration around spodumene-bearing pegmatites at a metre-scale. The alteration is the result of the subsolidus reactions with residual pegmatitic fluid.

Consequently, the combination of Worldview-2 and ASTER images forms a key tool in discovering mineral occurrences, especially in the West Kunlun and Karakoram regions where more rocks are exposed. The application of this exploration method in the mountainous Dahongliutan area of the Bayankala Fold Belt has led to the discovery of large Li deposits at the 505, 507, South Fulugou 1#, and 2# deposits.

It is emphasised that the newly launched Worldview-3 remote sensing satellite has 16 bands. The spectrum range includes visible light to short-wave infrared. The spatial resolution of the visible light to near-infrared is 0.3 m and short-wave infrared is 3.7 m. It solves the shortcomings of the low spatial resolution images developed from the ASTER data, and the narrow spectral range available from the Worldview-2 data. Thus, the Worldview-3 enhanced remote sensors potentially make easier to recognise the location of pegmatite veins.

New Worldview-3 remote sensing images were adopted with an 8-4-1 band combination and enhanced processing for the 505 and 507 Li deposits and surrounding areas (**Figure 13A**). Pegmatite veins with widths of at least 1 m appear white on the images and the Bayankala Formation is red and greyish brown in colour (**Figures 13A,B**). The increased resolution of the Worldview-3 images resulted in an increase in the recognition of mineralised pegmatite dykes (**Figure 13C**). Four principal components (PC 1–4) were obtained by applying the principal component transformation of four bands (B1, B2, B14 and B16) from the Worldview-3 images. The PC3, PC4 and PC1 principal components were used to generate RGB pseudo-colour synthesis, which is a multi-band monochromatic image combination. The PC4 principal component and rare metal mineral mineralisation presents high values in the transformed image, which is obviously different from the values corresponding to granite and supracrustal wallrocks (**Figure 14A**). The false colour image for the host granite is blue area, the metasedimentary wall rocks appear as yellow-green, and the Li-bearing pegmatites are marked by a purple-red colour, which is located outside the contact zone (**Figures 14A,B**). These criteria were used north of the 509 Li deposit highlighting the potential areas for Li mineralisation (**Figure 14C**). Lithium-bearing pegmatites were also found during geological mapping and exploration trenching. As a result, a Li resource of 0.5 Mt averaging 1.7% Li₂O, 0.05% BeO, 0.25% Rb₂O, 0.027% (Nb + Ta)₂O₅ and 0.065% Cs₂O have been found. The largest mineralised pegmatite is 1,140 m long and 58 m wide.

Interpretation of the Cassiterite U-Pb and Muscovite ⁴⁰Ar/³⁹Ar Ages

Our LA-MC-ICP-MS cassiterite U-Pb and ⁴⁰Ar/³⁹Ar muscovite dating of cassiterite and muscovite associated with spodumene show that the mineralisation is between ca. 223 and 185 Ma. Given the Ar-Ar date corresponds to the muscovite's closure temperature of ~425°C (Harrison et al., 2009), the ca. 185 Ma date is the lowest age limit, and the ca. 223 Ma (Late Triassic) date is closest to the age of the mineralisation. It can be suggested from these dates that the metamorphism associated with the

emplacement of the granite, lasted for 40 million years. The regional implications of the ca. 223 Ma age of the granitic pegmatites are discussed below.

Tectonic Setting and Resource Potential

The regional Triassic granites are distributed on the north and south sides of the Kangxiwa Fault in the West Kunlun Orogen, and the Tashkurgan and Tianshuihai terranes (**Figure 1**). The genesis of the granites are thought to be related to subduction and closure of the Paleo-Tethys Oceanic Plate, with the ca. 228 Ma granite in the Kudi area being emplaced in the suture between the West Kunlun Orogen and Tashkurgan-Tianshuihai terranes during late orogenesis (Jiang and Yang, 2000). The age of the protolith for the gneissic granite at the Bulunkou village at the northern edge of Western Kunlun Orogen is 241 ± 2 Ma, which is interpreted as being emplaced in a compressional setting (Zhang et al., 2005). A younger (228 ± 1 Ma) amphibole-bearing monzogranite located about 400 km to the southeast near the Kudi Village is interpreted as being emplaced in an extension setting following the collision between the South Kunlun and Tianshuihai terranes (Zhang et al., 2005).

Jiang et al. (2013) propose that the Paleo-Tethys Oceanic Plate subducted northward during ca. 338 to 251 Ma, and the South Kunlun Terrane collided with the Tianshuihai Terrane at ca. 243 Ma. This was followed by the emplacement of high-K calc-alkaline granites during ca. 234–227 Ma (Jiang et al., 2013). Yang (2013) proposes that the subduction of the oceanic crust during ca. 251 Ma was followed by continent-continent collision during ca. 242 Ma, and over-thickening of the continental-crust during ca. 231–223 Ma. This was succeeded by post-collisional extension and the emplaced of granites during ca. 215–185 Ma. The non-mineralised pegmatite veins and dykes in the Dahongliutan area were emplaced during ca. 224–218 Ma (Liang et al., 2019), and the spodumene-bearing pegmatite veins were emplaced during ca. 223–209 Ma (Qiao et al., 2015; Wei et al., 2017; Yan et al., 2018; Wang et al., 2020). This latter age is consistent with the age of granites being emplaced during a post-collisional extension between the South Kunlun and Tianshuihai terranes (c.f. Qiao et al., 2015; Wei et al., 2017; Zhang et al., 2018). Based on the geological constraints discussed above, we propose that the LCT-type pegmatite veins and dykes in the Dahongliutan area originate from fractionating granites during a ca. 223 Ma post-collisional extensional setting.

The understanding of the orogenesis of the Dahongliutan Granite and its associated Li mineralisation is at an early stage and requires further studies. It is currently proposed that the Dahongliutan mineralised pegmatites are genetically associated with the Triassic Dahongliutan Granite, and the regional zonation of the pegmatites around the granite (**Figures 6–9**). The zonation is related to mineral fractionation from the parental magma, as mentioned above. These characteristics are similar to the classical model of a zoned LCT-type deposit (Černý, 1989), which is consistent with the Dahongliutan pegmatite dykes and veins evolving from highly fractionated granitic magma (Wang et al., 2020). The crystal fractionation leads to progressive enrichment of incompatible ore-forming elements and volatile components, such as Li, Rb, Be, Cs, P, Cl, and F in

the residual fluid or melt (Thomas and Davidson, 2016). The high-volatility content of a magma can reduce its viscosity and liquidus temperature (Baker and Vaillancourt, 1995), which further delays the crystallisation of the evolved magma explaining the presence of the regional zonation of the Dahongliutan Granite (Mulja and Williams-Jones, 2018). The crystal-fluid interaction in the Li-mineralised pegmatites' parental magma related to a closed magmatic-hydrothermal system (Fan et al., 2020). This led to the final precipitation of spodumene associated with cassiterite and muscovite, which we dated. The widespread Li mineralisation in the Dahongliutan area can be compared to the giant Yajiang-Maerkang Li deposits in the Songpan-Ganzi Orogen in China (Xu et al., 2018). The Li deposits at Dahongliutan also compares closely to the Jiajika Li deposit in western Sichuan Province in terms of its geological setting, age (ca. 223–216 Ma), and country rocks (Hao et al., 2015; Liu et al., 2015).

The newly discovered Li deposits in the Dahongliutan area are along the edges and southeastern exposures of Triassic granites, but the intervening mountainous areas that are difficult to explore are here regarded as having high prospectivity. An analogue is the No. X03 orebody at the Jiajika Li deposit that bifurcates and thickens in places, where lamellar and lenticular spodumene-bearing pegmatites extend at depth following the hornfels bordering the associated granite (Fu et al., 2015).

The remote sensing interpretation of the distribution of pegmatite veins on a regional scale shows that many pegmatite veins are present in areas such as the Kangxiwa-Aksayi River north of Dahongliutan where muscovite alteration is extensive. Furthermore, some late Triassic pegmatite veins contain beryllium, niobium, and tantalum mineralisation (Zhang et al., 2019). Thus, the Dahongliutan Li-mineralised area has potential for Be, Nb, and Ta deposits.

CONCLUSIONS

Remote sensing accompanied by fieldwork and geochemistry are the main focus of this manuscript. This led to the discovery of mineralised pegmatites in the Dahongliutan area at a high altitude. The mineralised are classified as the LCT-type and interpreted as being relating to granitic fractionation. The distribution of the pegmatites in the area is structurally controlled by joints and shears within the Bayankala Formation and Dahongliutan Granite. The spodumene-bearing pegmatite dykes and veins are located broadly between tourmaline-bearing pegmatites near granites, and feldspar-rich pegmatites and quartz veining outside the contact hornfels zone. The spodumene-bearing pegmatite dykes and veins are associated with relatively elevated assays of Be, Rb, Nb and Ta.

The LA-MC-ICP-MS $^{206}\text{Pb}/^{207}\text{Pb}$ - $^{238}\text{U}/^{207}\text{Pb}$ isochronal age of 223 ± 11 Ma for cassiterite from the spodumene-bearing pegmatite shows that the pegmatites in the Kangxiwa-Dahongliutan area are Late Triassic in age. The date also shows that the pegmatites were emplaced in a post-

collisional extensional setting coeval with the age of the Dahongliutan Granite (indicating a probable genetic relationship between the granite and pegmatite veins). The $^{40}\text{Ar}/^{39}\text{Ar}$ plateau age of 197 ± 1 to 185 ± 1 Ma for muscovite from the mineralised pegmatite is interpreted as the minimum age of the hydrothermal alteration.

The exploration strategy developed for locating spodumene-bearing pegmatites in the rugged Bayankala Fold Belt includes the recognition of Li-bearing pegmatites in sedimentary horizons. This was followed by the identification of pegmatite veins on high-resolution hyperspectral remote sensing images and anomalies related to pegmatite-type Li deposits using multispectral remote sensing images. The metre-wide Li-bearing pegmatites in the study area are associated with rare metal geochemical anomalies, as determined from the geochemistry of rock samples from trenches and diamond-drillhole core.

The method established for the Dahongliutan area proved successful in discovering several significant Li and Be deposits in the region, such as 505, 507, north 509, South Fulugou 1#, and 2#. This new technique incorporating geological mapping, geochemistry and interpretation of high-resolution remote sensing has proven to be an important breakthrough for the rapid discovery of pegmatite deposits in the rugged West Kunlun and Karakoram terrains of China. This exploration method can be also developed in the areas with good outcrops and less rugged terrains. Finally, there is now a significant potential for identifying the location of Li-bearing pegmatites using hyperspectral remote sensing with a better spatial and spectral resolution.

DATA AVAILABILITY STATEMENT

The original contributions presented in the study are included in the article/**Supplementary Material**, further inquiries can be directed to the corresponding author.

AUTHOR CONTRIBUTIONS

YG, LB, KL, and MJ contributed to the conception and design of the study. YG wrote the first draft of the manuscript and led the data analysis and interpreted the results with LB, MJ, YL, and JT. All authors contributed to manuscript revision, read and approved it for publication.

FUNDING

This research was financially supported by the National Key Research and Development Project (Grant No. 2019YFC0605201), Second Tibetan Plateau Scientific Expedition and Research (STEP; Grant No. 2019QZKK0806), China Geological Survey (Projects DD20160004 and DD20190143), and the China Scholarship Council awarded to YG.

ACKNOWLEDGMENTS

We thank the editor and the three reviewers who have contributed to improve this work with their insightful comments and suggestions.

REFERENCES

- Baker, D. R., and Vaillancourt, J. (1995). The low viscosities of F+H₂O-bearing granitic melts and implications for melt extraction and transport. *Earth Planet. Sci. Lett.* 132, 199–211. doi:10.1016/0012-821x(95)00054-g
- Bedini, E. (2011). Mineral mapping in the Kap Simpson complex, central East Greenland, using HyMap and ASTER remote sensing data. *Adv. Space Res.* 47 (1), 60–73. doi:10.1016/j.asr.2010.08.021
- Cao, R., Gao, Y. B., Chen, B., Bagas, L., Yan, S. C., Zhao, H., et al. (Forthcoming 2020). Pegmatite magmatic evolution and rare metal mineralisation of the Dahongliutan pegmatite field, Western Kunlun Orogen: constraints from the B isotopic composition and mineral-chemistry. *International Geology Review*.
- Cardoso-Fernandes, J., Lima, A., Roda-Robles, E., and Teodoro, A. C. (2019b). Constraints and potentials of remote sensing data/techniques applied to lithium (Li)-pegmatites. *Can. Mineral.* 57 (5), 72–725. doi:10.3749/canmin.ab00004
- Cardoso-Fernandes, J., Lima, A., and Teodoro, A. C. “Potential of sentinel-2 data in the detection of lithium (Li)-bearing pegmatites: a study case,” in Proceedings of the SPIE 10790, Earth Resources and Environmental Remote Sensing/GIS Applications IX. Bellingham, WA, October 15, 2018.
- Cardoso-Fernandes, J., Teodoro, A. C., Lima, A., Perrotta, M., and Roda-Robles, E. (2020a). Detecting Lithium (Li) mineralizations from space: current research and future perspectives (Review). *Appl. Sci.* 10 (5), 1785. doi:10.3390/app10051785
- Cardoso-Fernandes, J., Teodoro, A. C., and Lima, A. (2019a). Remote sensing data in lithium (Li) exploration: a new approach for the detection of Li-bearing pegmatites. *Int. J. Appl. Earth Obs. Geoinformation*. 76, 10–25. doi:10.1016/j.jag.2018.11.001
- Cardoso-Fernandes, J., Teodoro, A. C., Lima, A., and Roda-Robles, E. (2020b). Semi-automatization of support vector machines to map lithium (Li) bearing pegmatites. *Rem. Sens.* 12, 2319. doi:10.3390/rs12142319
- Cerny, P. (1989). “Characteristics of pegmatite deposits of tantalum”, in Lanthanides, Tantalum and Niobium. (Berlin, Germany: Springer-Verlag), 195–239.
- Cerný, P., and Ercit, T. S. (2005). The classification of granitic pegmatites revisited. *Can. Mineral.* 43 (6), 2005–2026. doi:10.2113/gscanmin.43.6.2005
- Chen, D. H., Sui, Q. L., Zhao, X. J., Li, X. T., Gao, Y. B., and Wang, Z. H. (2019). Geochemical characteristics of magnetite from Zankan iron deposit in Tashen-Kuergan orefield and its constraint on mineralization. *Miner. Deposits*. 38 (2), 426–438 [in Chinese with English abstract].
- Chen, J. P., Wang, Q., Dong, Q. J., and Cong, Y. (2009). Extraction of remote sensing alteration information in Tuotuohe, Qinghai Province. *Earth Sci. J. China Univ. Geosci.* 34 (2), 314–318 [in Chinese with English abstract].
- Chen, Y. T., Zhang, G. W., Lu, R. K., and Zhang, Y. Q. (2010). ⁴⁰Ar/³⁹Ar geochronology of the Guozhuo fault in the northwestern margin of Qinghai-Tibet Plateau—new evidence for the western extension of Altyn Tagh fault. *Geol. Bull. China*. 29 (8), 1129–1137 [in Chinese with English abstract].
- Cui, Y. R., Tu, J. R., Chen, F., Hao, S., Ye, L. J., Zhou, H. Y., et al. (2017). The research advances in LA-(MC)-ICP-MS U-Pb dating of cassiterite. *Acta Geol. Sin.* 91 (6), 1386–1399 [in Chinese with English abstract].
- Dai, J. J., Wang, D. H., Dai, H. Z., Liu, L. J., and Ling, T. Y. (2018). Reflectance spectral characteristics of rocks and minerals in Jiajika lithium deposits in west sichuan. *Miner. Anal.* 37 (5), 507–517 [in Chinese with English abstract].
- Dai, J. J., Wang, D. H., Dai, H. Z., Liu, L. J., and Wu, Y. N. (2017). Geological mapping and ore-prospecting study using remote sensing technology in Jiajika area of Western Sichuan Province. *Chin. Geol.* 44 (2), 389–398 [in Chinese with English abstract].
- Dimmell, P. M., and Morgan, J. A. (2005). The aubry pegmatites: exploration for highly evolved lithium-cesium-tantalum pegmatites in northern Ontario. *Explor. Min. Geol.* 14, 45–59. doi:10.2113/gsemg.14.1-4.45
- Fan, J. J., Tang, G. J., Wei, G. J., Wang, H., Xu, Y. G., Wang, Q., et al. (2020). Lithium isotope fractionation during fluid exsolution: implications for Li mineralization of the Bailongshan pegmatites in the West Kunlun, NW Tibet. *Lithos* 105236 (6), 352–353. doi:10.1016/j.lithos.2019.105236
- Fu, X. F., Yuan, L. P., Wang, D. H., Hou, L. W., Pan, M., Hao, X. F., et al. (2015). Mineralization characteristics and prospecting model of newly discovered X03 rare metal vein in Jiajika orefield, Sichuan. *Miner. Deposits*. 34 (6), 1172–1186 [in Chinese with English abstract].
- Gan, F. P., Wang, R. S., and Ma, A. N. (2003). Spectral identification tree (sit) for mineral extraction based on spectral characteristics of minerals. *Earth Sci. Front.* 10 (2), 445–454 [in Chinese with English abstract].
- Gao, Y. B., Li, K., Teng, J. X., Zhao, X. M., Zhao, X. J., Yan, Z. Q., et al. (2019). Mineralogy, geochemistry and genesis of giant huoshayun Zn-Pb deposit in Karakoram area, Xinjiang, NW China. *Northwestern Geol.* 52 (4), 152–169 [in Chinese with English abstract].
- Gao, Y. B., Teng, J. X., Chen, D. H., and Sui, Q. L. (2017). Metallogenic geological characteristics and prospecting direction of maerkansu manganese ore belt in west Kunlun, Xinjiang. *Northwestern Geol.* 50 (1), 261–269 [in Chinese with English abstract].
- Gao, Y. B., Teng, J. X., Li, W. Y., Chen, D. H., Sui, Q. L., Jing, D. L., et al. (2018). Geology, geochemistry and ore genesis of the aertuokanashi manganese deposit, West Kunlun, Xinjiang, northwest China. *Acta Petrol. Sinica*. 34 (8), 2341–2358 [in Chinese with English abstract].
- Gao, Y. B., Zhao, X. M., Zhao, X. J., Li, K., Teng, J. X., Yan, Z. Q., et al. (2020). Mineralogy, geochemistry and genesis of duobaoshan Zn-Pb deposit in Karakoram, Xinjiang. *Northwestern Geol.* 53 (1), 122–137 [in Chinese with English abstract].
- Goodenough, K. M., Shaw, R. A., Smith, M., Estrade, G., Marqu, E., Bernard, C., et al. (2019). Economic mineralization in pegmatites: comparing and contrasting NYF and LCT examples. *Can. Mineral.* 57 (5), 753–755. doi:10.3749/canmin.ab00013
- Hao, S., Li, H. M., Li, G. Z., Geng, J. Z., Zhou, H. Y., Xiao, Z. B., et al. (2016). The comparison of the principle and applicability between two methods of deducting the initial common lead for *in situ* LA-ICP-MS U-Pb isotope dating of cassiterite. *Geol. Bull. China*. 35 (4), 622–632 [in Chinese with English abstract].
- Hao, X. F., Fu, X. F., Liang, B., Yuan, L. P., Pan, M., and Tang, Y. (2015). Formation ages of granite and X03 pegmatite vein in Jiajika, western Sichuan, and their geological significance. *Miner. Deposits*. 34 (6), 1199–1208 [in Chinese with English abstract].
- Harrison, T. M., Célériér, J., Aikman, A. B., Hermann, J., and Heizler, M. T. (2009). Diffusion of ⁴⁰Ar in muscovite. *Geochim. Cosmochim. Acta*. 73 (4), 1039–1051. doi:10.1016/j.gca.2008.09.038
- He, Z. F., Li, D. P., Liu, J., and Zhao, Y. (2009). Late Cenozoic tectono-geomorphic features of the Kangxiwa fault zone, northwestern Tibetan plateau, and its tectonic implication. *Quat. Sci.* 29 (3), 616–624 [in Chinese with English abstract].
- Hunt, G. R., and Ashley, R. P. (1979). Spectra of altered rocks in the visible and near infrared. *Econ. Geol.* 74, 1613–1629. doi:10.2113/gsecongeo.74.7.1613
- Jia, Q. Z., Li, W. M., and Yu, P. S. (1999). *The Metallogenic condition and prognosis of massive sulfide deposits in west Kunlun: Beijing*. Beijing, China: Geological Publishing House, 1–130 [in Chinese].
- Jiang, Y.-H., Jia, R.-Y., Liu, Z., Liao, S.-Y., Zhao, P., and Zhou, Q. (2013). Origin of middle Triassic high-K calc-alkaline granitoids and their potassic microgranular enclaves from the Western Kunlun orogen, northwest China: a record of the closure of Paleo-Tethys. *Lithos*. 156–159, 13–30. doi:10.1016/j.lithos.2012.10.004
- Jiang, Y. H., and Yang, W. Z. (2000). Discovery of A-type granite zone and its geodynamic significance in the western Kunlun mountains: China. *Geol. Rev.* 46 (3), 235–244 [in Chinese with English abstract].

SUPPLEMENTARY MATERIAL

The Supplementary Material for this article can be found online at: <https://www.frontiersin.org/articles/10.3389/feart.2020.591966/full#supplementary-material>.

- Jin, M. S., Wang, H., Qiao, G. B., and Zhang, S. P. (2014). The discovery of heiqia iron mineralization belt in west Kunlun by high resolution remote sensing technology and its. *Geological Significance. Northwestern. Geol.* 47 (4), 221–226 [in Chinese with English abstract].
- Jin, M. S., Wang, H., Zhang, W., and Wang, X. (2015). Method for extraction of ferric contamination anomaly from high-resolution remote sensing data and its applications. *Remote Sensing For Land and Resources.* 27 (3), 122–127 [in Chinese with English abstract].
- Kendall, M. (1975). *Multivariate analysis*. London, UK: Charles Griffin and Co. Ltd.
- Lee, J.-Y., Marti, K., Severinghaus, J. P., Kawamura, K., Yoo, H.-S., Lee, J. B., et al. (2006). A redetermination of the isotopic abundances of atmospheric Ar. *Geochem. Cosmochim. Acta.* 70 (17), 4507–4512. doi:10.1016/j.gca.2006.06.1563
- Li, H. K., Geng, J. Z., Hao, S., Zhang, Y. Q., and Li, H. M. (2009). Zircon U-Pb dating technique using LA-MC-ICP-MS. *J. Mineral. Petrol.* S1, 600–601 [in Chinese].
- Li, J. K., Liu, X. F., and Wang, D. H. (2014). The metallogenetic regularity of lithium deposit in China. *Acta Geol. Sin.* 88 (12), 2269–2283 [in Chinese with English abstract].
- Li, J. K., Wang, D. H., Zhang, D. H., and Fu, X. F. (2007). *Mineralization mechanism and continental geodynamic of pegmatite type deposits in western Sichuan*. Beijing, China: Atomic Energy Press, 1–187 [in Chinese].
- Li, K., Gao, Y. B., Teng, J. X., Jin, M. S., and Li, W. (2019). Metallogenic geological characteristics, mineralization age and resource potential of the granite-pegmatite-type rare metal deposits in Dahongliutan area, Hetian County, Xinjiang. *Northwestern. Geol.* 52 (4), 206–221 [in Chinese with English abstract].
- Liang, T., Wang, Y., Zhang, Z., Feng, Y., Yang, X., Zhou, Y., et al. (2019). *Study of the zonation of pegmatite veins in the Dahongliutan area, Xinjiang Province*. Xi'an, China: Chang'an University Report, 250 [in Chinese].
- Linnen, R. L., Van Lichtenvelde, M., and Černý, P. (2012). Granitic pegmatites as sources of strategic metals. *Elements.* 8, 275–280. doi:10.2113/gselements.8.4.275
- Liu, L., Feng, J., Benoit, B., Xu, X., Zhou, J., Han, L., et al. (2017a). Mapping alteration using imagery from the Tiangong-1 hyperspectral spaceborne system: example for the Jintanzi gold province, China. *Int. J. Appl. Earth Obs. Geoinf.* 59, 31–41. doi:10.1016/j.jag.2017.02.023
- Liu, L. J., Fu, X. F., Wang, D. H., Hao, X. F., Yuan, L. P., and Pan, M. (2015). Geological characteristics and metallogeny of Jiajika-style rare metal deposits. *Miner. Deposits.* 34 (6), 1187–1198 [in Chinese with English abstract].
- Liu, L. J., Wang, D. H., Liu, X. F., Li, J. K., Dai, H. Z., and Yan, W. D. (2017b). The main types, distribution features and present situation of exploration and development for domestic and foreign lithium mine. *Chin. Geol.* 44 (2), 263–278. doi:10.1016/s1876-3804(17)30024-1 [in Chinese with English abstract].
- Liu, Q., Yang, K. G., Zhang, C. L., Dong, Y. G., and Guo, K. Y. (2003). The micro-structure feature and its geological significance of Kangxiwa Fracture zone, West Kunlun. *J. Mineral. Petrol.* 23 (3), 26–30 [in Chinese with English abstract].
- Liu, Y., Gao, S., Hu, Z., Gao, C., Zong, K., and Wang, D. (2010). Continental and oceanic crust recycling-induced melt-peridotite interactions in the Trans-North China Orogen: U-Pb Dating, Hf Isotopes and trace elements in zircons from mantle xenoliths. *J. Petrol.* 51 (1–2), 537–571. doi:10.1093/petrology/egp082
- London, D. (2008). *Pegmatites*. The Canadian Mineralogist, Mineralogical Association of Canada, Special Publication 10, 347.
- London, D. (2018). Ore-forming processes within granitic pegmatites. *Ore Geol. Rev.* 101, 349–383. doi:10.1016/j.oregeorev.2018.04.020
- Ludwig, K. R. (2003). *User's manual for Isoplot 3.00 A geochronological toolkit for Microsoft excel*, 4. Berkeley, CA: Berkeley Geochronology Center, 70.
- Mattern, F., and Schneider, W. (2000). Suturing of the proto- and paleo-tethys oceans in the western Kunlun (Xinjiang, China). *J. Asian Earth Sci.* 18, 637–650. doi:10.1016/s1367-9120(00)00011-0
- McDougall, I., and Harrison, T. M. (1999). *Geochronology and thermochronology by the ⁴⁰Ar/³⁹Ar method*. 2nd Edn. New York, NY: Oxford University Press, 269.
- Mendes, D., Perrotta, M. M., Costa, M. A. C., and Paes, V. J. C. Mapeamento espectral para identificação de assinaturas espectrais de minerais de lítio em imagens ASTER (NE/MG). in Proceedings Anais do XVIII simpósio brasileiro de sensoriamento remoto, Santos, Brazil, November 2017, 5273–5280.
- Moradi, M., Basiri, S., Kananian, A., and Kabiri, K. (2014). Fuzzy logic modeling for hydrothermal gold mineralization mapping using geochemical, geological, ASTER imageries and other geo-data, a case study in Central Alborz, Iran. *Earth Sci. India.* 8 (1), 197–205. doi:10.1007/s12145-014-0151-9
- Mulja, T., and Williams-Jones, A. E. (2018). The physical and chemical evolution of fluids in rare-element granitic pegmatites associated with the Lacorne pluton, Québec, Canada. *Chem. Geol.* 493, 281–297. doi:10.1016/j.chemgeo.2018.06.004
- Munk, L. A., Boutt, D. F., Hynek, S. A., and Moran, B. J. (2018). Hydrogeochemical fluxes and processes contributing to the formation of lithium-enriched brines in a hyper-arid continental basin. *Chem. Geol.* 493, 37–57. doi:10.1016/j.chemgeo.2018.05.013
- Peng, H. L., He, N. Q., Wang, M. C., Du, B., Li, W. J., and Liu, Y. Q. (2018). Geological characteristics and metallogenic regularity of West Trace 509 rear polymetallic deposit in Dahongliutan region, Hetian, Xinjiang. *Northwestern Geol.* 51 (3), 146–154 [in Chinese with English abstract].
- Phillips, D., Matchan, E. L., Honda, M., and Kuiper, K. F. (2017). Astronomical calibration of ⁴⁰Ar/³⁹Ar reference minerals using high-precision, multi-collector (ARGUSVI) mass spectrometry. *Geochem. Cosmochim. Acta.* 196, 351–369. doi:10.1016/j.gca.2016.09.027
- Pour, A. B., and Hashim, M. (2015). Hydrothermal alteration mapping from Landsat-8 data, Sar Cheshmeh copper mining district, south-eastern Islamic Republic of Iran. *J. Taibah Univ. Sci.* 9 (2), 155–166. doi:10.1016/j.jtusci.2014.11.008
- Qiao, G. B., Zhang, H. D., Wu, Y. Z., Jin, M. S., Du, W., Zhao, X. J., et al. (2015). Petrogenesis of the Dahongliutan monzogranite in western Kunlun: constraints from SHRIMP zircon U-Pb geochronology and geochemical characteristics. *Acta Geol. Sin.* 89 (7), 1180–1194 [in Chinese with English abstract].
- Scogings, A., Porter, R., and Jeffress, G. (2016). Reporting exploration results and mineral resources for lithium mineralised pegmatites. *AIG News Issue.* 125, 32–36.
- Selway, J. B., Breaks, F. W., and Tindle, A. G. (2005). A review of rare-element (Li-Cs-Ta) pegmatite exploration techniques for the superior province, Canada, and large worldwide tantalum deposits. *Explor. Min. Geol.* 14, 1–30. doi:10.2113/gsemg.14.1-4.1
- Steiger, R. H., and Jäger, E. (1977). Subcommission on geochronology: convention on the use of decay constants in geo- and cosmochronology. *Earth Planet Sci. Lett.* 36, 359–362. doi:10.1016/0012-821x(77)90060-7
- Steiner, B. M. (2018). Using Tellus stream sediment geochemistry to fingerprint regional geology and mineralisation systems in southeast Ireland. *Ir. J. Earth Sci.* 36, 45–61. doi:10.3318/ijes.2018.36.4
- Steiner, B. M. (2019a). W and Li-Cs-Ta signatures in I-type granites—a case study from the Vosges Mountains, NE France. *J. Geochem. Explor.* 197, 238–250. doi:10.1016/j.gexplo.2018.12.009
- Steiner, B. M. (2019b). Tools and workflows for grassroots Li-Cs-Ta (LCT) pegmatite exploration. *Minerals.* 9, 499. doi:10.3390/min9080499
- Teng, J. X., and Gao, Y. B. (2019). *Investigation and exploration demonstration second-level project of the Fe, Pb and Zn Resource Base in the Western Kunlun area*, Xi'an, China: Xi'an Center of China Geological Survey Report, 526 [in Chinese].
- Thomas, R., and Davidson, P. (2016). Revisiting complete miscibility between silicate melts and hydrous fluids, and the extreme enrichment of some elements in the supercritical state - consequences for the formation of pegmatites and ore deposits. *Ore Geol. Rev.* 72, 1088–1101. doi:10.1016/j.oregeorev.2015.10.004
- Wang, D. H., Sun, Y., Liu, X. F., Tian, S. H., Dai, J. J., Liu, L. J., et al. (2018). Deep exploration technology and prospecting direction for lithium energy metal. *Geol. Surv. China.* 5 (1), 1–9 [in Chinese with English abstract].
- Wang, D., Sun, Y., Dai, H., Guo, W., Zhao, Z., Zhao, T., et al. (2019). Characteristics and exploitation of rare earth, rare metal and rare-scattered element minerals in China. *Chin. J. Chem. Eng.* 21 (1), 119–127. doi:10.15302/j-sscae-2019.01.017 [in Chinese with English abstract].
- Wang, H., Gao, H., Zhang, X.-Y., Yan, Q.-H., Xu, Y., Zhou, K., et al. (2020). Geology and geochronology of the super-large Bailongshan Li-Rb-(Be) rare-metal pegmatite deposit, West Kunlun orogenic belt, NW China. *Lithos.* 360–361, 105449. doi:10.1016/j.lithos.2020.105449

- Wang, H., Li, P., Ma, H. D., Zhu, B. Y., Qiu, L., and Zhang, X. Y. (2017). Discovery of the Bailongshan superlarge lithium-rubidium deposit in Karakorum, Hetian, Xinjiang, and its prospecting implication. *Geotect. Metallogenia*. 41, 1053–1062 [in Chinese with English abstract].
- Wei, X. P., Wang, H., Hu, J., Mu, S. L., Qiu, Z. W., Yan, Q. H., et al. (2017). Geochemistry and geochronology of the Dahongliutan two-mica granite pluton in Western Kunlun orogen: geotectonic implications. *Geochimica*. 46 (1), 66–80 [in Chinese with English abstract].
- Xiao, P. X., and Gao, X. F. (2015). *Regional geological survey reports of critical areas in Western Kunlun and Altyn*. Xi'an, China: Xi'an Center of China Geological Survey Reports, 51–68 [in Chinese].
- Xiao, W., Han, F., Windley, B. F., Yuan, C., Zhou, H., and Li, J. (2003). Multiple accretionary orogenesis and episodic growth of continents: insights from the western Kunlun Range, Central Asia. *Int. Geol. Rev.* 45, 303–328. doi:10.2747/0020-6814.45.4.303
- Xu, Z. Q., Qi, X. X., Yang, J. S., Ji, S. C., Li, H. B., and Chen, F. Y. (2007). Senses and timings of two kinds of shear in the Kangxiwar strike-slip shear zone, West Kunlun, and their tectonic significance. *Geol. Bull. China*. 26 (10), 1252–1261 [in Chinese with English abstract].
- Xu, Z. Q., Wang, R. C., Zhao, Z. B., and Fu, X. F. (2018). On the structural backgrounds of the large-scale “hard-rock type” lithium ore belts in China. *Acta Geol. Sin.* 92 (6), 1091–1106 [in Chinese with English abstract].
- Yan, Q.-H., Qiu, Z.-W., H., Wang, M., Wei, X.-P., Li, P., et al. (2018). Age of the Dahongliutan rare metal pegmatite deposit, West Kunlun, Xinjiang (NW China): constraints from LA-ICP-MS U-Pb dating of columbite-(Fe) and cassiterite. *Ore Geol. Rev.* 100, 561–573. doi:10.1016/j.oregeorev.2016.11.010
- Yang, J. J., Fang, H. B., Zhang, Y. J., and Chen, W. (2003). Remote sensing anomaly extraction in important metallogenic belts of western China. *Remote Sensing For Land and Resources*. 57 (3), 50–53 [in Chinese with English abstract].
- Yang, W. Q. (2013). The Indosinian metamorphism, magmatism and formation age of Bunlunkuole rock group. *Taxkorgan-kangxiwar tectonic belt, western Kunlun*. PhD thesis. Kirkland (WA): Northwest University, 155 [in Chinese with English abstract].
- Yao, F. J., Yang, J. M., Zhang, Y. J., and Geng, X. X. (2009). Extraction of remote sensing alteration anomalies of three types of ore deposits and its application. *Acta Petrol. Sinica*. 25 (4), 971–976 [in Chinese with English abstract].
- Zhang, C. L., Yu, H. F., Wang, A. G., and Guo, K. Y. (2005). Dating of triassic granites in the western Kunlun mountains and its tectonic significance. *Acta Geol. Sin.* 79 (5), 645–652 [in Chinese with English abstract].
- Zhang, Q., Liu, Y., Wu, Z., Huang, H., Li, K., and Zhou, Q. (2018). Late Triassic granites from the northwestern margin of the Tibetan Plateau, the Dahongliutan example: petrogenesis and tectonic implications for the evolution of the Kangxiwa Palaeo-Tethys. *Int. Geol. Rev.* 61 (2), 175–194. doi:10.1080/00206814.2017.1419444
- Zhang, W., Zhang, W., Liu, S. Y., Yang, J. Z., and Mao, S. Y. (2011). Automatic interpretation of high resolution remotely sensed images by using kernel method. *Remote Sensing For Land and Resources*. 90 (3), 82–87 [in Chinese with English abstract].
- Zhang, Y. J., and Yao, F. J. (2009). Application study of multi-spectral ASTER data for determination of ETM remote sensing anomaly property: taking Wulonggou region of eastern Kunlun mountain range as example. *Acta. Petrol. Sinica*. 25 (4), 963–970 [in Chinese with English abstract].
- Zhang, Z., Liang, T., Feng, Y. G., Yang, X. Q., Li, K., Ding, K., et al. (2019). Geologic feature and chronology study of Kangxiwa beryl-bearing muscovite pegmatite in West Kunlun orogenic belt, Xinjiang. *Northwestern Geol.* 52 (1), 75–88 [in Chinese with English abstract].
- Zhao, Y. S. (2003). *Principles and methods of remote sensing application analysis*. Beijing, China: Science Press, 155–259 [in Chinese].
- Zhou, B., Sun, Y. X., and Kong, D. Y. (2011). Geological features and prospecting potential of rare metallic deposits in the Dahongliutan region, Xinjiang. *Acta Geol. Sichuan*. 31 (3), 288–292 [in Chinese with English abstract].

Conflict of Interest: The authors declare that the research was conducted in the absence of any commercial or financial relationships that could be construed as a potential conflict of Interest.

Copyright © 2020 Gao, Bagas, Li, Jin, Liu and Teng. This is an open-access article distributed under the terms of the Creative Commons Attribution License (CC BY). The use, distribution or reproduction in other forums is permitted, provided the original author(s) and the copyright owner(s) are credited and that the original publication in this journal is cited, in accordance with accepted academic practice. No use, distribution or reproduction is permitted which does not comply with these terms.



Columbite-Tantalite Group Mineral U-Pb Geochronology of Chaqiabeishan Li-Rich Granitic Pegmatites in the Quanji Massif, NW China: Implications for the Genesis and Emplacement Ages of Pegmatites

Tong Pan¹, Qing-Feng Ding^{2*}, Xuan Zhou², Shan-Ping Li³, Jie Han³ and Long Cheng²

¹Bureau of Geological Exploration and Development of Qinghai Province, Xining, China, ²College of Earth Sciences, Jilin University, Changchun, China, ³Qinghai Geological Survey Institute, Xining, China

OPEN ACCESS

Edited by:

Chang-Zhi Wu,
Chang'an University, China

Reviewed by:

Rongqing Zhang,
Nanjing University, China
Yonggang Feng,
Chang'an University, China

*Correspondence:

Qing-Feng Ding
dingqf@jlu.edu.cn

Specialty section:

This article was submitted to
Economic Geology,
a section of the journal
Frontiers in Earth Science

Received: 16 September 2020

Accepted: 16 November 2020

Published: 14 January 2021

Citation:

Pan T, Ding Q-F, Zhou X, Li S-P, Han J
and Cheng L (2021) Columbite-
Tantalite Group Mineral U-Pb
Geochronology of Chaqiabeishan
Li-Rich Granitic Pegmatites in the
Quanji Massif, NW China:
Implications for the Genesis and
Emplacement Ages of Pegmatites.
Front. Earth Sci. 8:606951.
doi: 10.3389/feart.2020.606951

The Chaqiabeishan area is characterized by small Li-rich granitic pegmatites in the Quanji Massif (QM), northwest China. In this study, the columbite-tantalite group minerals (CGMs) from a typical Li-rich pegmatite dike were analyzed for major element contents using an EMPA (electron microprobe analyzer), for trace element contents using LA-ICP-MS (laser ablation-inductively coupled plasma mass spectrometry), and for ages using LA-ICP-MS U-Pb dating, respectively. The CGMs from the sample can be divided into two types, i.e., magmatic Type 1 and metasomatic Type 2. Although these two types of CGMs do not exhibit distinct major and trace element variations from core to rim within an individual grain, the Ta# values, Mn# values, and some trace element contents (such as Zr, Hf, W, and Sr) of Type 1 CGMs are distinct from those of Type 2 CGMs. The overall compositional changes from Type 1 CGMs to Type 2 CGMs are consistent with the typical evolutionary trend described for many lithium-cesium-tantalum (LCT) pegmatites and the complex spodumene trend described by Černý and Ercit (Bull. Mineral., 1989, 108, 499–532). The Type 2 CGMs have formed later and must be a metasomatic product of Type 1 CGMs. Eighteen Type 1 CGMs yielded a weighted mean $^{206}\text{Pb}/^{238}\text{U}$ age of 240.6 ± 1.5 Ma. The slight oscillatory zoning and/or sector zoning suggest that the dated Type 1 columbites have a magmatic origin. Thus, the crystallization ages of Type 1 columbites represent the emplacement ages of Li-rich pegmatites. One of the Type 2 CGMs yielded a $^{206}\text{Pb}/^{238}\text{U}$ age of 211.0 ± 4.7 Ma, which is hardly interpreted to be an age representing the later hydrothermal metasomatism, because one dataset has no apparent statistical significance. Therefore, our dating results can only indicate that the Li-rich pegmatite-forming melts were emplaced at approximately 240.6 Ma. Based on these results and previous studies of the 240–254 Ma granitoids in the QM, we conclude that the 240.6 Ma Li-rich granitic pegmatites, as well as 240–254 Ma granitoids in the QM, were both emplaced during the southward subduction of the Zongwulong Ocean Plate in the Late Permian to Middle Triassic.

Keywords: columbite-tantalite group minerals, U-Pb dating, Li-rich pegmatite, Chaqiabeishan, Quanji Massif

INTRODUCTION

The Chaqiabeishan area in Tianjun County in Qinghai Province is tectonically located in the Quanji Massif (QM) and is one of the most important granitic pegmatite fields for rare element (Li and minor amounts of Be, Nb, and Ta) resources in Western China. Recently, these Li-rich pegmatites have attracted increasing amounts of attention because of the global demand for lithium and the Li prospecting potential in this area. The exotic granitic pegmatite group, including spodumene-bearing granitic pegmatites, tourmaline-bearing granitic pegmatites, beryl-bearing granitic pegmatites, and barren granitic pegmatites, was likely formed through fractional crystallization of a granitic magma (Wang et al., 2020). Yet, recently reported 235.9 and 217.0 Ma U-Pb ages of zircons within pegmatites by Wang et al. (2020) indicate amphibolous ages as well as an amphibolous genetic link between the rare-element pegmatites and the nearby Triassic granitic pluton. Nevertheless, the interpretation of the U-Pb zircon ages reported for the rare-element pegmatites remains ambiguous due to radioactive damage to the mineral structure and the disturbance of the U-Pb isotope systematics by the high U and Th contents of the zircons within the granitic pegmatites (Yan et al., 2018). Thus, the development of a precise dating alternative for the granitic pegmatites is vital for achieving a more thorough understanding of the tectono-metallogenic evolution of these pegmatites and a better exploration of the presence of rare-element-bearing minerals. Therefore, the emplacement ages of the Li-rich pegmatites in the Chaqiabeishan region need to be robustly determined to reconstruct the timeframe of the pegmatite emplacement and to explore the genesis of the Li-rich pegmatites.

Columbite-tantalite group minerals (CGMs) are important sources of critical elements, i.e., Nb and Ta, in highly evolved granites and granitic pegmatites (Linnen et al., 2012; Linnen et al., 2014). CGMs are suitable for dating granitic pegmatites (Romer and Wright, 1992; Romer et al., 1996; Smith et al., 2004; Che et al., 2015; Kaeter et al., 2018; Yan et al., 2018; Feng et al., 2019; Che et al., 2019) because the compatibility of U is sufficiently high and that of Pb is very low in CGM lattices. Recent studies have shown that CGMs are mainly crystallized from pegmatite-forming melts or during metasomatism (e.g., Van Lichtervelde et al., 2007). Therefore, U-Pb dating of CGMs can provide reliable emplacement ages for granitic pegmatites while the problems regarding zircon U-Pb dating need better explanation for pegmatites (Feng et al., 2019). In particular, in situ dating techniques such as laser ablation inductively coupled plasma mass spectrometry (LA-ICP-MS) and SIMS (secondary ion mass spectrometer) are being increasingly applied to U-Pb dating of CGMs (Che et al., 2015; Kaeter et al., 2018; Yan et al., 2018; Feng et al., 2019; Che et al., 2019) because they can avoid uranium-rich inclusions (e.g., uraninite) that are commonly present in CGMs (Che et al., 2015).

In this study, we dated representative CGM-bearing Li-rich pegmatite dikes in the Chaqiabeishan area using LA-ICP-MS CGM U-Pb dating. Then, the U-Pb ages obtained for the CGMs were compared with the U-Pb zircon ages obtained in previous studies and were used to reconstruct the evolution and timing of

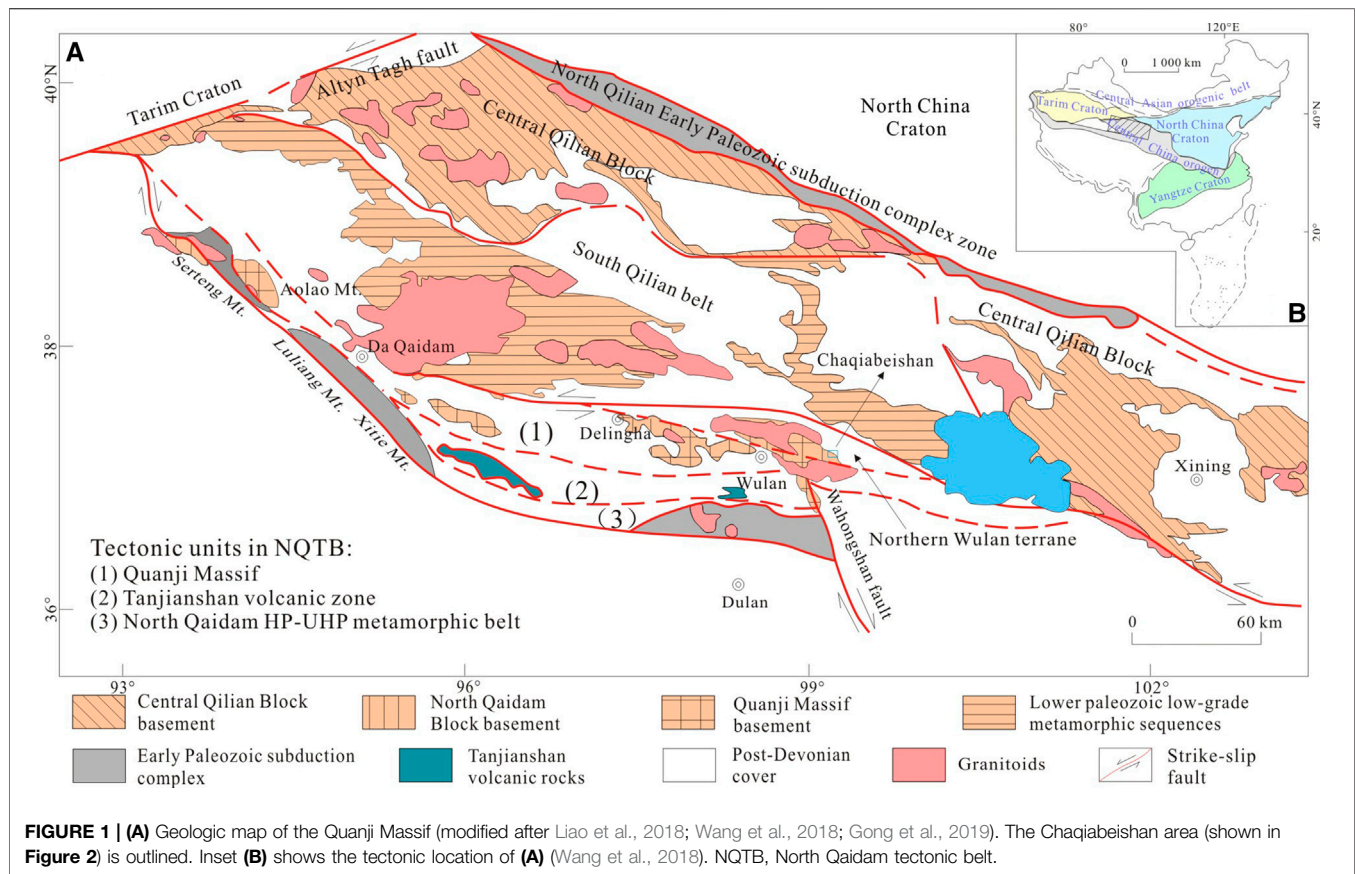
the Li-rich pegmatites in the Chaqiabeishan area. Based on the new age data, the genesis of the Li-rich pegmatites was also discussed according to the (electron microprobe analysis) EMPA and LA-ICP-MS trace element analysis results for the studied CGMs.

GEOLOGIC BACKGROUND AND GEOLOGY OF PEGMATITES

Geologic Background

The Chaqiabeishan area is tectonically located in the Quanji Massif in the North Qaidam tectonic belt (NQTB) (Wang et al., 2020). The NQTB, which is a tectonic terrane located between the Qaidam Block to the south and the Qilian Block to the north, consists of three tectonic units: the QM to the north, the Tanjianshan volcanic zone in the middle, and the North Qaidam high pressure to ultrahigh pressure (HP-UHP) metamorphic belt to the south (**Figure 1A**) (Wang et al., 2018). The latter two units are collectively referred to as the Early Paleozoic northern subduction-collision complex, which is related to the Proto-Tethys Ocean (e.g., Liao et al., 2018; Wu et al., 2019). The 540–500 Ma Tanjianshan volcanic zone has been suggested to have formed from volcanic island-arc magmatism related to northward oceanic subduction (Song et al., 2014; Zhang et al., 2014a; Zhang et al., 2017; Song et al., 2018). Continuous northward subduction of the lower plate between 500 Ma and 440 Ma (Song et al., 2018) gave rise to further island-arc magmatism in the QM and formed a continental arc. The Proto-Tethys Ocean was most likely completely closed by approximately 440 Ma when the continent-continent collision became the dominant tectonic movement in the NQTB (Wang et al., 2018). The closure of the Proto-Tethys Ocean at this time is supported by the intrusion of a postcollisional gabbroic dike at approximately 423 Ma (Wang et al., 2018). To the north, the QM is bordered by the Qinghai Lake fault (e.g., Liao et al., 2014; Zhang et al., 2014b; Mustafa et al., 2016) and the Zongwulong tectonic belt (e.g., Wang et al., 2016; Pang et al., 2019; Wang et al., 2019; Wu et al., 2019), which separates the QM from the Paleozoic South Qilian belt. Then, the Zongwulong oceanic basin was developed along the Zongwulong tectonic belt during the Middle Carboniferous to Early Permian in response to the continental rifting of the northern margin of the QM (Peng et al., 2018). By the Late Permian to Middle Triassic, the Zongwulong oceanic plate had subducted obliquely southward under the QM, forming I-type granitoids with ages of 240–254 Ma in the Tianjun and Wulan areas (Guo et al., 2009; Peng et al., 2016; Peng et al., 2018; Wu et al., 2019). Concurrently, the Paleo-Tethys oceanic plate was subducted northward, forming numerous granitic intrusions with ages of 240–254 Ma in the eastern Kunlun area (Ding et al., 2014; Xiong et al., 2014; Ding et al., 2015). Finally, the Zongwulong oceanic basin was closed during an intracontinental collisional orogeny in the Late Triassic (Guo et al., 2009; Peng et al., 2016; Peng et al., 2018).

The QM is nearly NW-SE-trending, but is E-W trending locally. It is a long and narrow small remnant continental



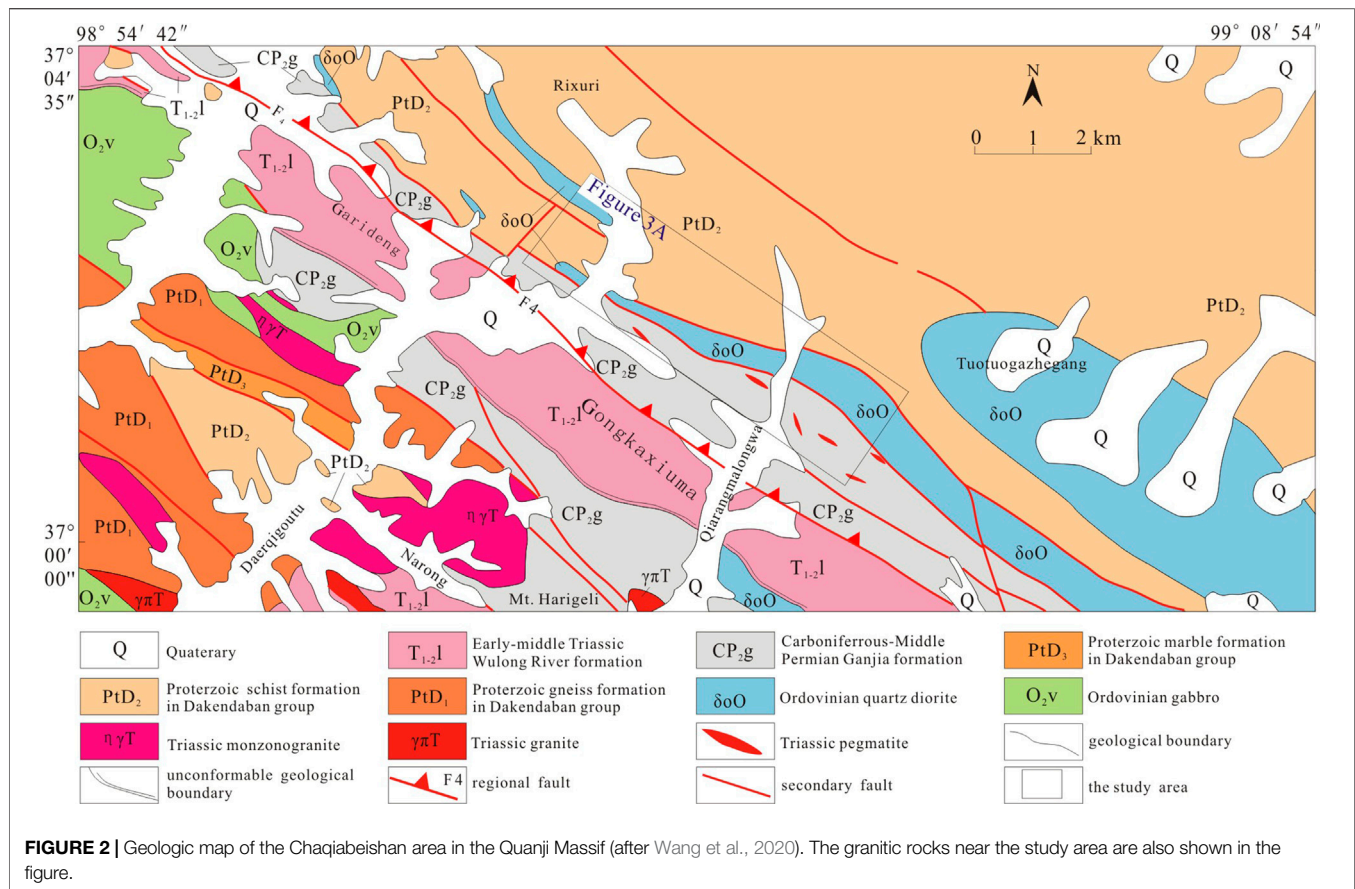
fragment, which was detached from the Tarim Craton (TC); so, the QM has had a geological history similar to that of the TC since the middle Neoproterozoic (Zhang et al., 2012). The QM is characterized by the components of a double-layered structure. The basement is composed of early Paleoproterozoic granitic gneisses and medium- to high-grade metamorphic rocks (e.g., Gong et al., 2012; Gong et al., 2014; Zhang et al., 2014b; Liao et al., 2018; Wang et al., 2018), and the cover is composed of Mesoproterozoic–Phanerozoic sedimentary rocks (Zhao et al., 2000; Lu et al., 2006; Lu et al., 2008; Zhang et al., 2012; Wang et al., 2016; Wang et al., 2018; Wang et al., 2019). The metamorphic basement of the QM is mainly composed of the early Paleoproterozoic Delingha complex and the amphibolite facies of the Paleoproterozoic Dakendaban Group paragneisses (Lu et al., 2008; Chen et al., 2012; Gong et al., 2012; Zhang C. L. et al., 2014; Gong et al., 2014; He et al., 2018; Gong et al., 2019), which is unconformably overlain by the sedimentary strata of the approximately 1.73–1.64 Ga Quanji Group (Zhang et al., 2017), and Upper Neoproterozoic and Lower Paleozoic to Mesozoic strata (Lu et al., 2008; Zhang et al., 2012; Zhang et al., 2016).

This study area is located in the eastern segment of the QM (**Figure 1A**). Some researchers have argued that the North Wulan terrane (NWT) can be separated from the northern QM (Wang et al., 2016; Pang et al., 2019; Wang et al., 2019; Wu et al., 2019). The NWT is bounded to the north by the Zongwulong tectonic belt, and it is separated from the QM to the south by a Cenozoic

thrust fault (**Figure 1A**) (Xu et al., 2006; Chen et al., 2009; Guo et al., 2009; Xiao et al., 2009).

Geology of Chaqiabeishan Pegmatites

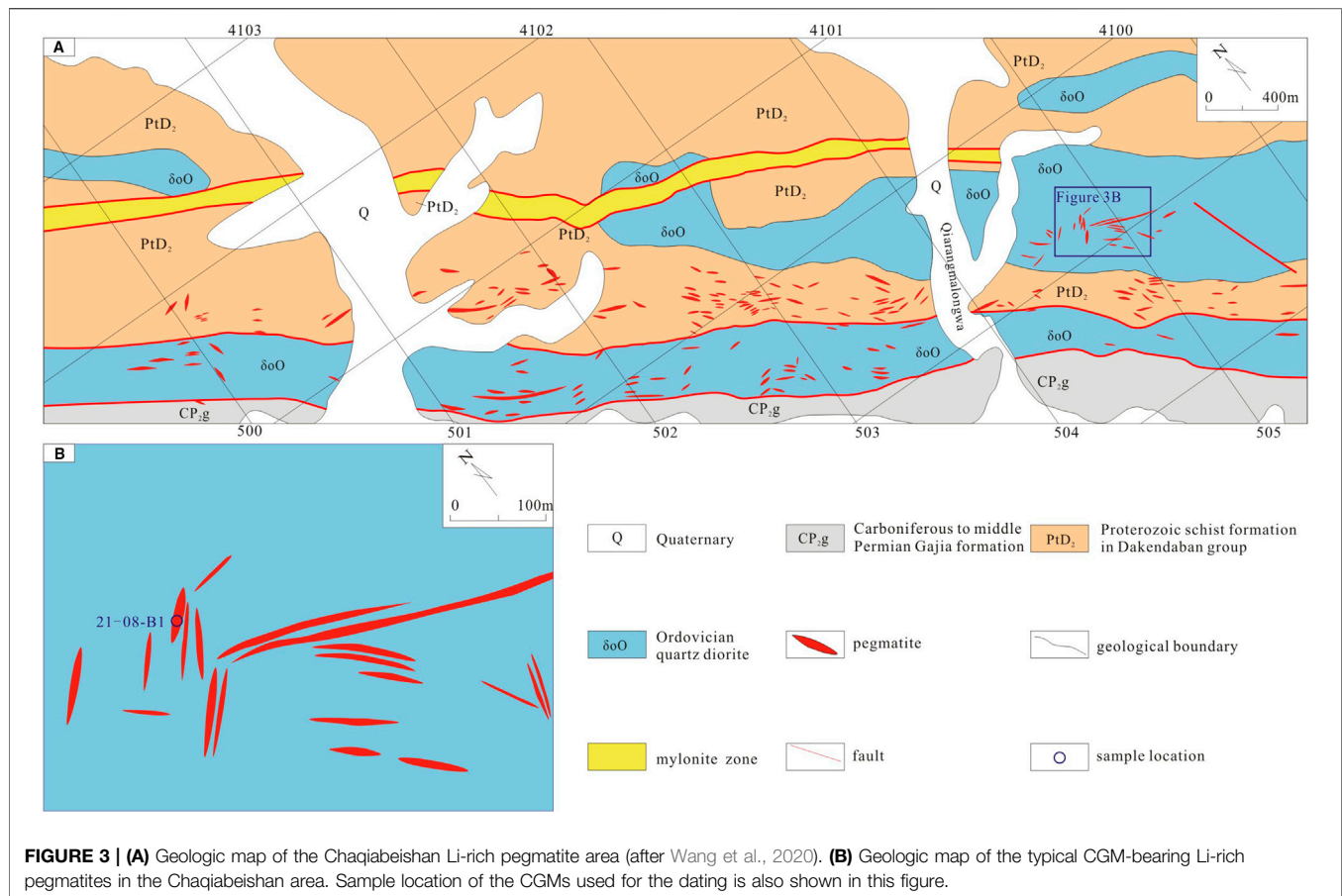
The Chaqiabeishan Li-rich pegmatites are located in the NWT within the QM (**Figure 1A**). The metamorphic basement of the study area is mainly composed of the Paleoproterozoic Dakendaban Group, which consists of the gneiss formation, the schist formation, and the marble formation. The basement is unconformably overlain by the unmetamorphosed Carboniferous–Early Permian Ganjia Formation and the Early–Middle Triassic Zongwulong River Formation (Wang et al., 2020). The Gneiss Formation in the Dakendaban Group, which is located to southwest of the South Zongwulong Mountain fault (F4; **Figure 2**) (Wang et al., 2020), consists of amphibolite-facies felsic gneiss interbedded with minor mica schist and plagioclase amphibolite. Meanwhile, the schist formation in the Dakendaban Group, which is located to the northeast of fault F4, is composed of green-schist-facies mica schist. This schist is considered to be part of the Dakendaban Group by Wang et al. (2020), but there are some minor differences between the lithological assemblage and metamorphic degree of the schist and those of the Dakendaban Group in the southwestern part of the study area (Wang et al., 2020). The Carboniferous–Early Permian Ganjia Formation and the Early–Middle Triassic Zongwulong River Formation are distributed from northwest



to southeast in the central region of the study area (**Figure 2**) (Wang et al., 2020). The Ganjia Formation is composed of lower sandstone and upper limestone, while the Zongwulong River Formation consists of a marine clastic-facies turbidite. Regional fault F4 strikes southeast and dips northeast, across the study area (**Figure 2**) (Wang et al., 2020). A series of secondary faults and milolite zones are developed in the hanging wall of fault F4, and they are pegmatite-controlling structures in the study area. The intermediate-mafic intrusions include Ordovician gabbro and quartz diorite, with the gabbros mostly occurring in the northwestern part of the study area and the quartz diorites occurring in the southeastern part (**Figure 2**) (Wang et al., 2020). The quartz diorites were emplaced along the regional fault at approximately 440 Ma (QGS, 2020), and they mostly strike northwest. Some of the granitic rocks in the southwestern part of the study area are considered to be emplaced in the Triassic or earlier. No previous studies have been conducted on these granitic rocks in the study area (**Figure 2**).

Numerous granitic pegmatite dikes were emplaced along the northwest-southeast-trending milolite zones and the secondary faults within the quartz diorites and Dakendaban Group strata (**Figures 3, 4A,B**) (Pan et al., 2020). These granitic pegmatites are lentoid or banded, are 5–60 m long and 0.2–20 m wide, and include spodumene-bearing pegmatites, tourmaline-bearing

pegmatites, beryl-bearing pegmatites, and other barren pegmatites. Usually, the granitic pegmatites have a massive unzoned structure and a granitic composition, and they do not exhibit internal fractionation, zoning, or quartz cores (**Figures 4C,D**). Estimates of the pegmatite bulk compositions indicate that they are granitic, and that the abundances of the fluxing components (B, P, and F), rare alkalis (Li), alkaline earth metals (Be), and high field strength elements (HFSE) (Nb, Ta, and U) are significantly higher than in common granites (e.g., London, 2018). Some of the pegmatites have extremely high Li_2O values (>2.15 wt.%) and relatively high Be, Nb, and Ta contents. The mineralized pegmatites are Li-rich or Be-rich, among which 58 Li-Be ore bodies and 130 Li-Be mineralized bodies (i.e., the ore grades are lower than the cut-off grade) have been delineated (QGS, 2020). Evidence in support of a petrogenetic link among the granites is not provided by the field relationships. The granitic pegmatites are usually coarse-grained to pegmatitic (i.e., crystals mostly up to 10 cm long) and consist of 20–40% quartz, 5–25% plagioclase (primarily albite), 10–30% potassium feldspar (primarily perthite), 5–30% spodumene, 5–15% tourmaline, <5% muscovite (and/or lepidolite), <5% beryl, and <5% garnet (**Figures 4C–F**). The accessory minerals include zircon, phosphorite, and CGMs.



SAMPLING AND METHODS

Sampling and Imaging

The Li-rich pegmatites in the southwestern part of the Chaqiabeishan area (**Figure 3A**) have relatively high Nb and Ta contents, and we believe that CGMs occur in such Li-rich pegmatites. Doubly polished thin sections were made from the rock samples collected from ten typical pegmatite dikes in the study area for the petrographic study. CGMs grains were successfully separated from the sample CQBS21-08-B1, which was collected from a typical Li-rich pegmatite dike in the study area (**Figure 3B**). The CGMs grains were mounted in epoxy resin and polished for EMPA analysis, LA-ICP-MS dating, and LA-ICP-MS trace element analysis. Back-scattered electron (BSE) images of the doubly polished thin sections were obtained using the TESCAN MIRA 3 LMH scanning electron microscope (SEM) at Nanjing Hongchuang Exploration Technology Service Co., Ltd.

Electron Microprobe Analyzer

The mineral compositions were analyzed at the Wuhan Microbeam Analysis Technology Co., Ltd., using a JEOL JXA-8230 electron microprobe analyzer equipped with five wavelength-dispersive spectrometers (WDS). First, the samples

were coated with a thin conductive carbon film prior to analysis. The precautions suggested by Zhang and Yang (2016) were used to minimize the variations in the carbon film thickness between the samples and to obtain an approximately 20 nm thick, uniform coating. The operating conditions for the quantitative WDS analyses involved an accelerating voltage of 15 kV, a beam current of 20 nA, and a spot size of 1.0 μm. The peak counting time was 10 s for W, Ca, Ti, Ta, Nb, Al, and Sn and 20 s for Fe and Mn. The background counting time was 1/2 of the peak counting time for the high- and low-energy background positions. The following standards were used: tungsten (W), diopside (Ca), ilmenite (Ti), tantalum (Ta), niobium (Nb), tin (Sn), pyrope garnet (Fe and Al), and rhodonite (Mn).

Laser Ablation-Inductively Coupled Plasma Mass Spectrometry U-Pb Dating and Trace Element Analysis

The LA-ICP-MS U-Pb dating and in situ trace element analysis of the CGMs were simultaneously conducted at the State Key Laboratory for Mineral Deposits Research, Nanjing University, China, using the analytical procedures described in detail by Che et al. (2015). A Photon Machines Excite laser ablation system



FIGURE 4 | Photographs and photomicrographs showing the morphology and textural features of the spodumene-rich pegmatites in the Chaqiabeishan area. **(A)** The pegmatite dike was intruded along the bedding of the gneiss strata. **(B)** Sharp contacts between pegmatites and quartz diorites. **(C)** The spodumene in the pegmatite dikes is characterized by pegmatitic texture. **(D)** Coexistence of pegmatitic spodumene, tourmaline, plagioclase, and quartz in the pegmatite specimen. **(E)** Coexisting pegmatitic euhedral spodumene, subhedral plagioclase, and coarse-grained anhedral quartz under plane-polarized transmitted light. **(F)** Coexisting pegmatitic euhedral spodumene, subhedral plagioclase, and coarse-grained anhedral quartz under perpendicular polarized transmitted light. Spd, spodumene; Qz, quartz; Pl, plagioclase; Tur, tourmaline.

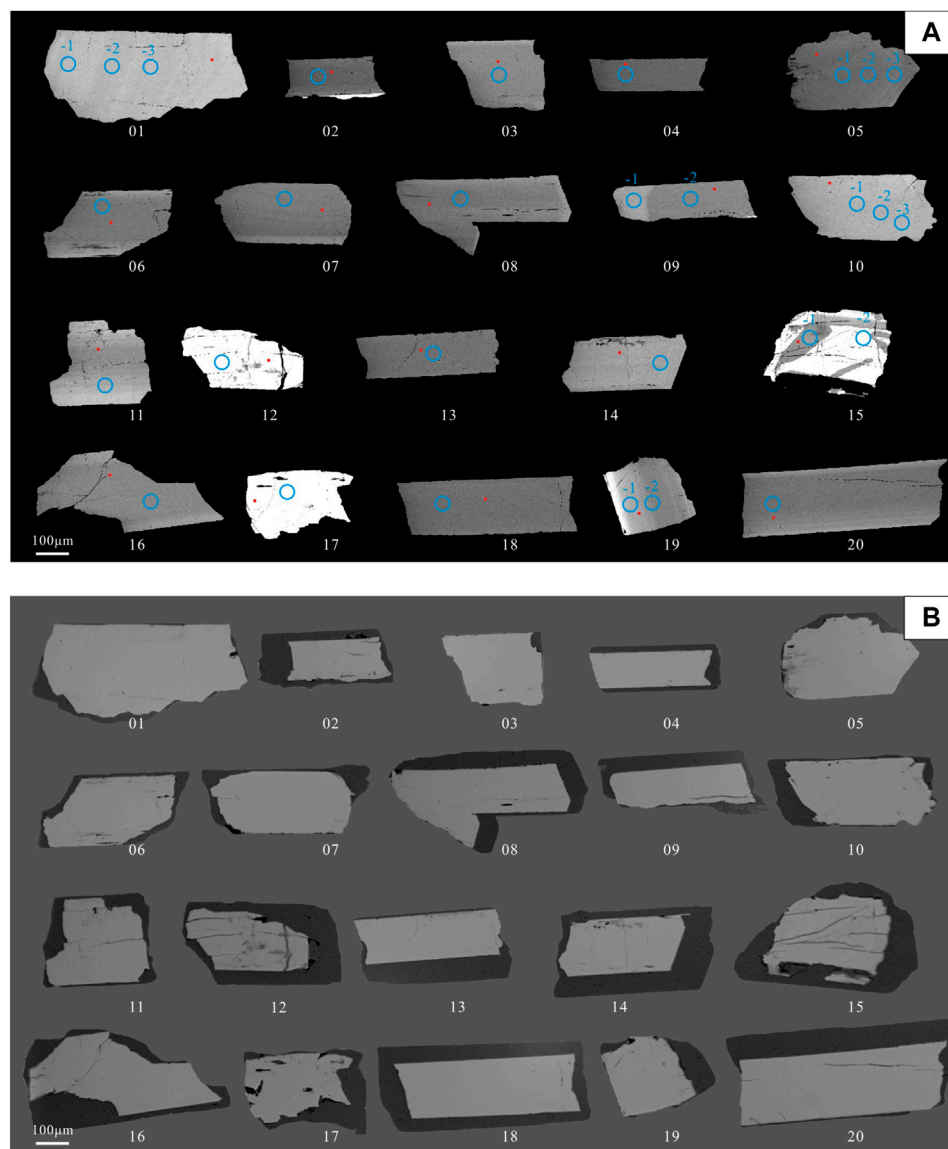


FIGURE 5 | (A) BSE images and **(B)** plane-polarized reflected light photomicrographs of representative analyzed CGM separates from the Li-rich pegmatites in the Chaqiabeishan area. The blue circles represent the positions of the 43 μm ablation spots from the LA-ICP-MS dating and trace element analysis. The red dots represent the positions of the 1.0 μm EMPA spots. The scale bars are 100 μm long.

(RESolution S-155) integrated with an inductively coupled plasma-mass spectrometer (Thermo Fisher Scientific i-CAP-Q) was used for the analyses. The ablation protocol included a spot diameter of 43 μm and a repetition rate of 4 Hz for 40 s. Helium was applied as the carrier gas to efficiently transport the aerosol into the ICP-MS. Coltan 139 with a weighted mean $^{207}\text{Pb}/^{206}\text{Pb}$ age of 506 ± 2.3 Ma (obtained by isotope dilution thermal ionization mass spectrometry) and an LA-ICP-MS U-Pb age of 506.2 ± 5.0 Ma (Che et al., 2015 and references therein) was used as the external standard for calibrating the U, Th, and Pb isotopic ratios. US National Institute of Standards and Technology (NIST) standard reference materials NIST-610 and NIST-612 and US Geological Survey basaltic glasses BCR-2G and GSE-1G were used as additional external

standards to plot the calibration curve (Gao et al., 2013). ^{55}Mn was used as an internal standard for calibrating trace element concentrations (Che et al., 2015). Every eight analyses were followed by the analysis of two NIST SRM 610 measurements, one GSE-1G measurement, one BCR-2G measurement, and two Coltan139 measurements. Each spot analysis consisted of approximately 20 s of background acquisition, 50 s of sample data acquisition, and up to 20 s of gas blank acquisition to flush the sample. The offline data processing was performed using the ICPMSDataCal program (Liu et al., 2008). The concordia U-Pb ages were calculated using the Isoplot 3.0 software (Ludwig, 2003). The estimated precision is better than $\pm 5\%$ for the major elements and $\pm 10\%$ for the trace elements (Xie et al., 2019).

TABLE 1 | Results of EPMA for CGMs in the Chagabaishean area.

Spot no.	B1-1	B1-2	B1-3	B1-4	CB1-5	-B1-6	B1-7	B1-8	B1-9	B1-10	B1-11	B1-12	B1-13	B1-14	B1-15-1	B1-15-2	B1-16	B1-17	B1-18	B1-19	B1-20
CGM type	Type 1	Type 1	Type 1	Type 1	Type 1	Type 1	Type 1	Type 1	Type 1	Type 1	Type 1	Type 2	Type 1	Type 1	Type 1	Type 2	Type 1	Type 2	Type 1	Type 1	Type 1
Al ₂ O ₃ wt. %	0.003	0.027	0.001	b.d.l.	b.d.l.	0.032	b.d.l.	0.009	b.d.l.	0.012	0.009	0.027	b.d.l.	b.d.l.	b.d.l.	b.d.l.	b.d.l.	b.d.l.	b.d.l.	0.006	0.010
WO ₃	1.386	0.849	1.023	0.824	1.068	1.200	0.800	0.887	1.200	1.110	1.039	1.871	1.195	1.067	0.955	1.860	1.213	2.119	0.897	0.814	0.998
TiO ₂	2.203	1.703	1.848	1.771	1.818	2.008	1.597	1.704	1.138	1.766	2.181	1.069	1.972	1.860	1.506	0.730	2.002	0.941	2.074	1.828	1.578
Ta ₂ O ₅	36.505	23.782	27.469	23.281	26.278	27.255	27.274	24.506	27.512	32.026	28.813	54.353	22.745	27.997	26.986	53.610	26.421	57.196	23.007	30.149	25.339
FeO	3.966	5.834	4.412	5.919	5.172	4.467	4.767	5.852	4.608	3.721	4.183	2.214	5.596	4.841	4.686	2.310	4.477	2.868	5.437	4.321	5.288
CaO	0.005	0.035	0.005	0.016	b.d.l.	0.010	0.018	0.013	0.062	0.061	0.000	0.138	0.014	0.262	0.018	0.070	0.004	b.d.l.	0.008	0.015	0.017
MnO	13.767	13.224	14.383	13.259	13.506	14.193	13.997	13.080	13.791	14.015	13.670	13.780	12.636	13.679	13.677	14.230	14.337	13.465	12.700	14.629	13.503
SnO ₂	0.605	0.708	0.670	0.778	0.490	0.670	0.457	0.640	0.378	0.503	0.558	0.525	0.584	0.438	0.521	0.340	0.626	0.711	0.814	0.689	0.460
Nb ₂ O ₅	40.905	52.366	49.423	53.003	51.375	50.103	51.162	53.536	50.348	45.838	47.791	25.659	53.490	49.582	50.738	26.740	49.844	22.914	53.324	46.484	52.225
Total	99.345	98.528	99.234	98.851	99.707	99.938	100.072	100.227	99.037	99.052	98.244	99.636	98.232	99.726	99.087	99.890	98.924	100.214	98.261	98.935	99.418
Based on 6 O atoms																					
Al apfu	0.000	0.002	0.000	0.000	0.000	0.002	0.000	0.001	0.000	0.001	0.001	0.002	0.000	0.000	0.000	0.000	0.000	0.000	0.000	0.000	0.001
W	0.024	0.014	0.017	0.013	0.017	0.020	0.013	0.014	0.020	0.019	0.017	0.035	0.019	0.017	0.016	0.035	0.020	0.040	0.015	0.014	0.016
TiO ₂	0.109	0.081	0.088	0.083	0.086	0.095	0.075	0.079	0.055	0.086	0.106	0.058	0.093	0.088	0.072	0.039	0.095	0.052	0.098	0.089	0.074
Ta	0.655	0.407	0.474	0.396	0.448	0.466	0.465	0.413	0.477	0.564	0.504	1.067	0.388	0.481	0.465	1.047	0.456	1.135	0.392	0.529	0.432
Fe	0.219	0.307	0.234	0.310	0.271	0.235	0.250	0.303	0.246	0.202	0.225	0.134	0.294	0.256	0.248	0.139	0.237	0.175	0.285	0.233	0.277
Ca	0.000	0.002	0.000	0.001	0.000	0.001	0.001	0.001	0.004	0.004	0.000	0.011	0.001	0.018	0.001	0.005	0.000	0.000	0.001	0.001	0.001
Mn	0.770	0.705	0.773	0.703	0.718	0.755	0.744	0.686	0.744	0.769	0.745	0.842	0.671	0.732	0.734	0.866	0.770	0.832	0.674	0.799	0.717
Sn	0.016	0.018	0.017	0.019	0.012	0.017	0.011	0.016	0.010	0.013	0.014	0.015	0.015	0.011	0.013	0.010	0.016	0.021	0.020	0.018	0.012
Nb	1.220	1.490	1.418	1.500	1.457	1.424	1.451	1.498	1.450	1.343	1.390	0.837	1.516	1.416	1.454	0.868	1.429	0.756	1.512	1.356	1.481
O	6.000	6.000	6.000	6.000	6.000	6.000	6.000	6.000	6.000	6.000	6.000	6.000	6.000	6.000	6.000	6.000	6.000	6.000	6.000	6.000	6.000
Mn#	77.853	69.655	76.751	69.405	72.561	76.290	74.833	69.358	75.191	79.228	76.795	86.307	69.574	74.103	74.720	86.185	76.432	82.622	70.287	77.419	72.113
Ta#	34.931	21.457	25.056	20.900	23.529	24.655	24.281	21.590	24.738	29.591	26.614	56.029	20.368	25.354	24.239	54.669	24.177	60.024	20.606	28.065	22.592
A	1.138	1.129	1.130	1.130	1.104	1.125	1.095	1.100	1.078	1.094	1.108	1.097	1.093	1.122	1.085	1.094	1.139	1.120	1.093	1.154	1.099
B	1.876	1.898	1.892	1.896	1.905	1.889	1.917	1.911	1.927	1.908	1.895	1.904	1.904	1.897	1.920	1.915	1.884	1.891	1.904	1.885	1.913

Note: b.d.l., below detection limit. "CQBS21-08-B1" within spot no. was abbreviated as "B1" in each one.

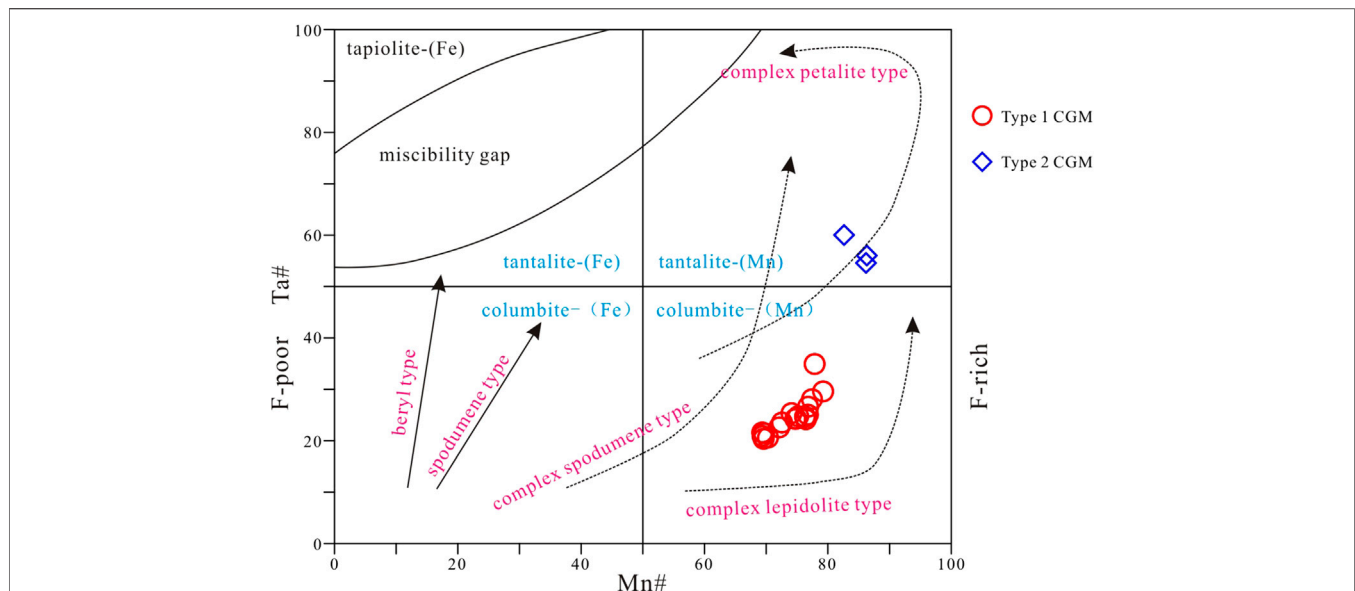


FIGURE 6 | Ta# vs. Mn# quadrilateral diagram (Černý and Ercit, 1989) for the CGMs from the Li-rich pegmatites in the Chaqiabeishan area. The Ta and Mn enrichment trends of CGMs in fluorine-rich and fluorine-poor pegmatites are also based on Černý and Ercit (1989).

RESULTS

Petrography and Classification of CGMs

CGMs were not directly observed within two of the doubly polished thin sections of the investigated pegmatites perhaps because the small CGMs had grain sizes of 150–500 μm . However, many CGM grains were successfully separated from the pegmatite sample CQBS21-08-B1 whose Nb and Tb abundances are up to 144.5 ppm and 79.9 ppm, respectively (unpublished data). We believe that CGMs are paragenetic with the other rare-element-rich minerals in the Li-rich pegmatites because recent studies have shown that CGMs mainly crystallize from pegmatite-forming melts or during metasomatism (Van Lichterfelde et al., 2007). The CGM separates were generally euhedral to subhedral and gray in plane-polarized reflected light (Figure 5B). The BSE images showing all of the analytical spots for the in situ LA-ICP-MS dating, trace element analysis, and EMPA are presented in Figure 5A. Two types of CGMs were identified based on their morphology and BSE images (Figure 5). The BSE images show that most of the Type 1 CGMs have dark BSE images and weak sector zoning or minor oscillatory zoning (Figure 5A), indicating that they are typical magmatic CGMs (Badanina et al., 2015; Van Lichterfelde et al., 2007; Timofeev et al., 2017), since oscillatory zoning is believed to be the result of the slow diffusion of Ta and Nb in the melt relative to the rate of crystal growth (Van Lichterfelde et al., 2007). The Type 2 CGMs have irregular or complicated internal textures, some of which have both bright patches and dark patches in the BSE images (e.g., nos. 12, 15, and 17 in Figure 5A), indicating that they are perhaps related to late-stage metasomatic replacement caused by highly reactive fluids exsolved from the residual melts (Černý and Ercit, 1985; Tindle and Breaks, 2000; Badanina et al., 2015).

Electron Microprobe Analyzer

All of the analyzed CGMs contain 2.214–5.919 wt.% FeO, 12.636–14.629 wt.% MnO, 0.730–2.203 wt.% TiO₂, and 0.0800–2.119 wt.% WO₃. The Al₂O₃, CaO, and SnO₂ contents are mostly less than 0.800 wt.% (Table 1). However, their Nb₂O₅ and Ta₂O₅ contents are variable. Eighteen of the analyzed spots on the CGMs separates with dark BSE images (including a residual dark patch in CGM grain no. 15-1), i.e., Type 1 CGMs, are compositionally columbite-(Mn) with relatively similar low Ta# values; while three of the CGMs (nos. 12, 15-2, and 17) with bright BSE images, i.e., the Type 2 CGMs, are compositionally tantalite-(Mn) with higher Ta# values (Table 1, Figures 5 and 6).

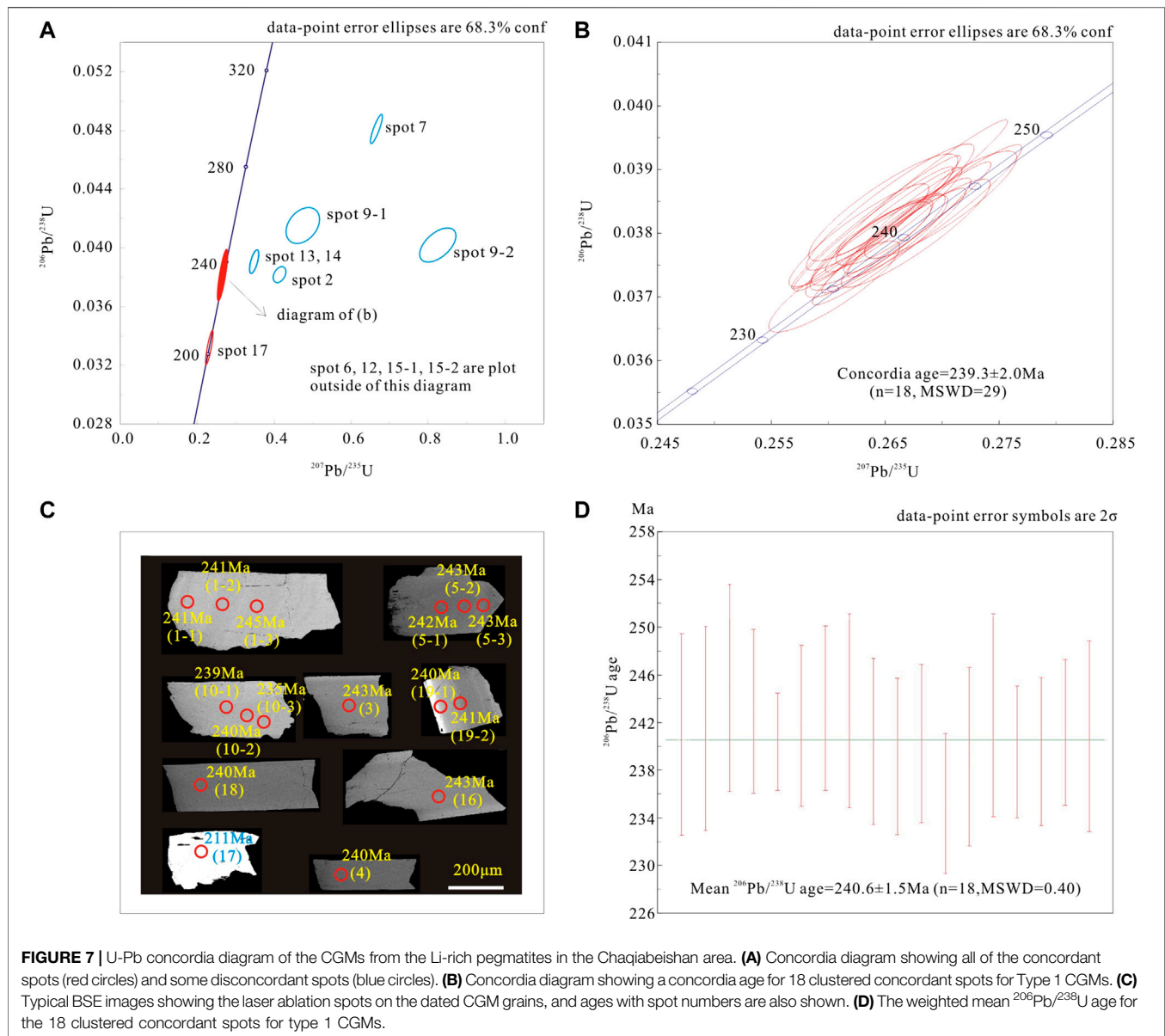
Laser Ablation-Inductively Coupled Plasma Mass Spectrometry U-Pb Dating

The LA-ICP-MS U-Pb dating data for the CGMs are presented in Table 2. Twenty-nine spots on 20 CGM grains from the same Li-rich pegmatite (sample CQBS21-08-B1) were analyzed. Figure 5 shows all of the dated CGM grains and analytical spots. Some of the data points plot below the concordia line, suggesting potential Pb loss, which could be caused by metamictization (Romer, 2003). Most discordant dating analyses show extremely high common Pb concentrations (up to 5,981.35 ppm; Table 2), indicating that the influence of common Pb is also very significant and that microscale U-rich inclusions (e.g., feldspar) is possibly present in some of the CGMs analyzed (e.g., Romer, 2003; Legros et al., 2019). Certainly, other reasons for high common Pb in CGMs may be possible. Moreover, the BSE images show that the discordant ages are likely caused by the presence of microfractures close to

TABLE 2 | LA-ICP-MS dating results for CGMs in the Chaqiabeishan area.

Spot no.	²³² Th	²³⁸ U	Total Pb	Common Pb	Isotopic ratios						Isotopic ages (Ma)						Concordance
	(ppm)	(ppm)	(ppm)	(ppm)	²⁰⁷ Pb/ ²⁰⁶ Pb	1 σ	²⁰⁷ Pb/ ²³⁵ U	1 σ	²⁰⁶ Pb/ ²³⁸ U	1 σ	²⁰⁷ Pb/ ²⁰⁶ Pb	1 σ	²⁰⁷ Pb/ ²³⁵ U	1 σ	²⁰⁶ Pb/ ²³⁸ U	1 σ	
B1-1-1	77.8	7478.0	289.5	0.8	0.050895	0.000310	0.266870	0.004915	0.038091	0.000681	235.3	14.8	240.2	3.9	241.0	4.2	99%
B1-1-2	75.5	7080.4	277.8	0.8	0.050279	0.000321	0.264209	0.004903	0.038173	0.000691	209.3	19.4	238.1	3.9	241.5	4.3	98%
B1-1-3	93.1	7597.8	302.1	0.0	0.050332	0.000301	0.268238	0.004967	0.038721	0.000700	209.3	17.6	241.3	4.0	244.9	4.3	98%
B1-2	23.7	2279.9	100.8	13.8	0.078636	0.001782	0.413782	0.010412	0.038174	0.000362	1164.8	45.2	351.6	7.5	241.5	2.2	62%
B1-3	27.9	2632.4	104.2	1.0	0.050070	0.000431	0.264841	0.004322	0.038406	0.000554	198.2	13.9	238.6	3.5	242.9	3.4	98%
B1-4	53.1	4614.0	183.2	0.7	0.050611	0.000350	0.264879	0.002763	0.037995	0.000328	233.4	16.7	238.6	2.2	240.4	2.0	99%
B1-5-1	77.5	4951.5	195.4	0.0	0.050510	0.000315	0.265755	0.003963	0.038210	0.000544	216.7	10.2	239.3	3.2	241.7	3.4	98%
B1-5-2	76.7	4564.6	180.9	0.4	0.050845	0.000309	0.269870	0.004414	0.038448	0.000557	235.3	17.6	242.6	3.5	243.2	3.5	99%
B1-5-3	73.5	4028.5	159.8	1.2	0.050150	0.000346	0.265448	0.004865	0.038410	0.000655	211.2	14.8	239.0	3.9	243.0	4.1	98%
B1-6	41.9	1727.5	294.4	208.1	0.345648	0.011731	3.829526	0.197022	0.074317	0.002299	3688.0	51.8	1599.0	41.4	462.1	13.8	-11%
B1-7	25.7	2444.9	147.9	26.0	0.100916	0.001213	0.666591	0.010256	0.048106	0.000659	1642.6	22.2	518.6	6.3	302.9	4.1	47%
B1-8	38.5	3437.4	136.3	0.7	0.051094	0.000355	0.267687	0.004323	0.037999	0.000561	255.6	16.7	240.8	3.5	240.4	3.5	99%
B1-9-1	72.5	4829.0	227.9	27.7	0.077165	0.003487	0.474811	0.028543	0.041528	0.000805	1125.6	90.3	394.5	19.7	262.3	5.0	59%
B1-9-2	14.2	1687.7	95.4	34.4	0.145555	0.003498	0.824982	0.030801	0.040188	0.000762	2294.1	40.6	610.8	17.1	254.0	4.7	17%
B1-10-1	29.1	2724.6	108.7	0.6	0.050688	0.000376	0.264255	0.004130	0.037796	0.000530	233.4	16.7	238.1	3.3	239.2	3.3	99%
B1-10-2	36.9	3090.4	123.3	0.4	0.050182	0.000385	0.262699	0.004055	0.037967	0.000535	211.2	16.7	236.8	3.3	240.2	3.3	98%
B1-10-3	30.3	2799.3	112.3	0.9	0.050828	0.000435	0.260533	0.003798	0.037161	0.000473	231.6	20.4	235.1	3.1	235.2	2.9	99%
B1-11	91.2	7000.7	280.3	0.8	0.050864	0.000303	0.265347	0.004449	0.037791	0.000604	235.3	17.6	239.0	3.6	239.1	3.8	99%
B1-12	123.6	6869.2	6468.2	5981.3	0.640544	0.005138	25.237050	0.828989	0.280119	0.007536	4602.8	11.7	3317.4	32.2	1592.0	38.0	29%
B1-13	34.0	3075.4	133.7	7.5	0.063114	0.000973	0.337117	0.004577	0.039537	0.000667	722.2	33.3	295.0	3.5	250.0	4.1	83%
B1-14	71.2	4792.2	212.0	16.3	0.065040	0.001426	0.347764	0.007549	0.039061	0.000528	775.9	46.3	303.0	5.7	247.0	3.3	79%
B1-15-1	20.9	2150.8	918.5	659.4	0.382842	0.003684	10.105341	0.389113	0.185729	0.006127	3843.1	14.5	2444.5	35.6	1098.2	33.3	23%
B1-15-2	21.2	2227.6	889.9	620.5	0.372084	0.003211	8.934694	0.344283	0.169723	0.005412	3800.0	13.1	2331.4	35.2	1010.6	29.8	20%
B1-16	40.0	3262.0	132.1	0.7	0.050932	0.000379	0.269343	0.005053	0.038351	0.000686	239.0	16.7	242.2	4.0	242.6	4.3	99%
B1-17	14.2	1355.0	46.8	0.3	0.050783	0.000754	0.232737	0.005856	0.033269	0.000749	231.6	35.2	212.5	4.8	211.0	4.7	99%
B1-18	32.4	2895.3	115.8	0.3	0.050545	0.000383	0.263861	0.003518	0.037858	0.000446	220.4	13.9	237.8	2.8	239.5	2.8	99%
B1-19-1	40.1	3913.4	155.0	1.2	0.050610	0.000377	0.264336	0.003918	0.037862	0.000501	233.4	16.7	238.2	3.2	239.6	3.1	99%
B1-19-2	41.3	3668.3	146.9	1.0	0.050808	0.000384	0.266954	0.003686	0.038120	0.000493	231.6	18.5	240.3	3.0	241.2	3.1	99%
B1-20	61.4	4115.8	164.9	0.8	0.050276	0.000358	0.263977	0.004632	0.038068	0.000645	209.3	21.3	237.9	3.7	240.8	4.0	98%

Note: "CQBS21-08-B1" within spot no. was abbreviated as "B1" in each one.



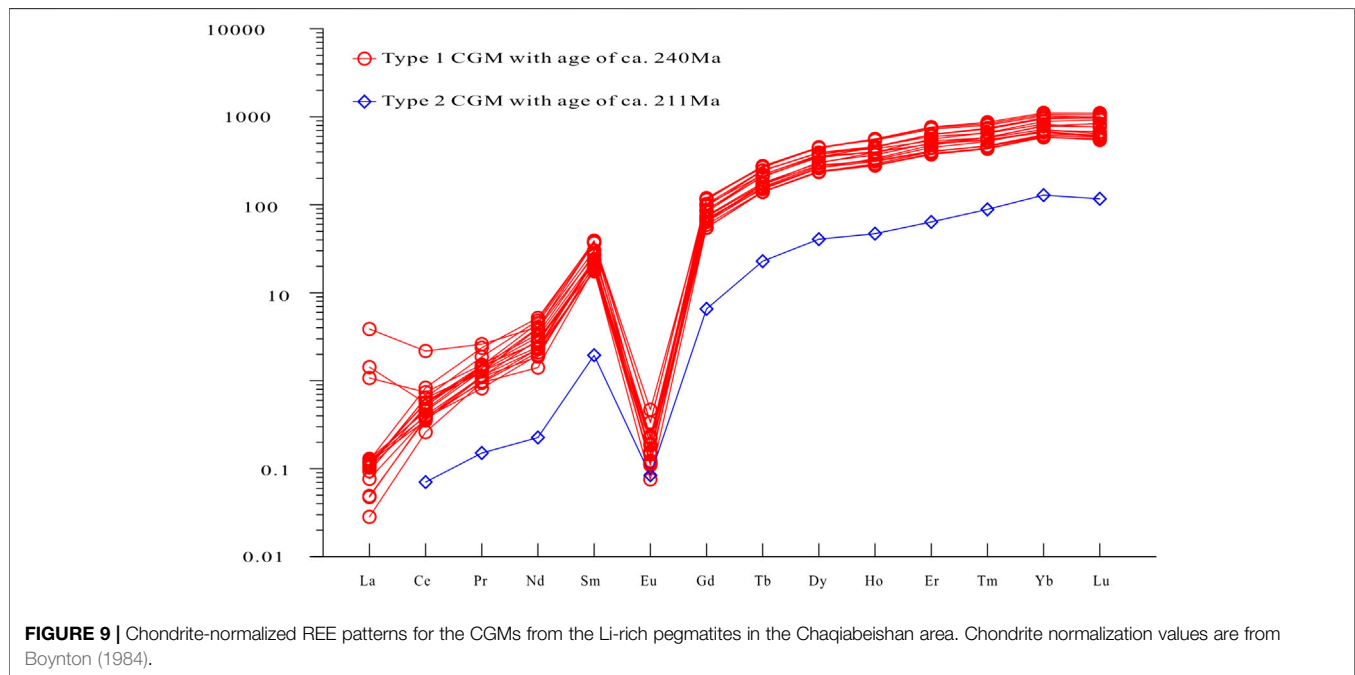
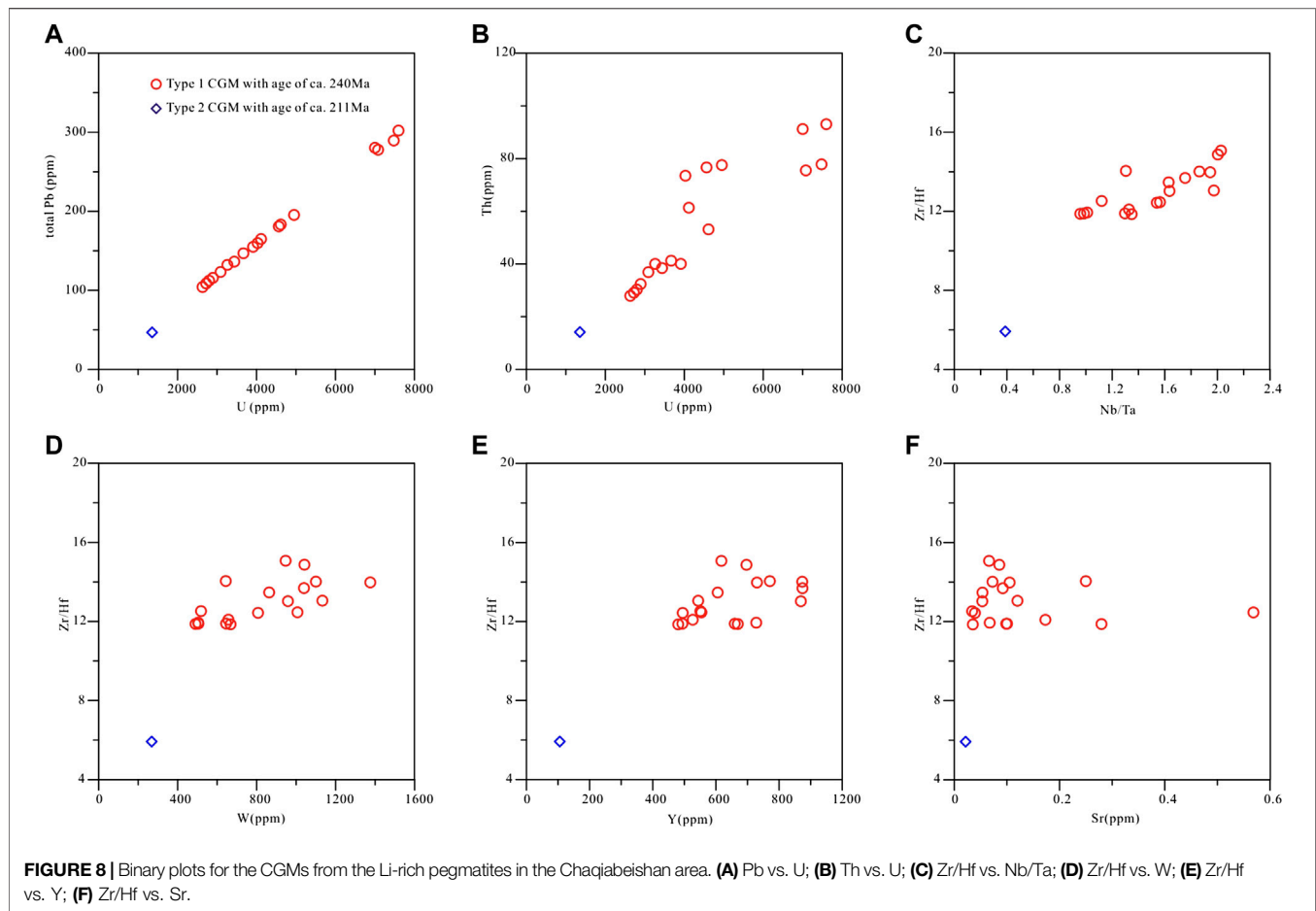
the analyzed spots within the CGMs (Figure 5). Thus, we excluded the discordant dating analyses that were possibly affected by the presence of microscale inclusions, possible metamictization, or microfractures from concordia age calculation. All of the concordant dating analyses had sufficiently high U contents (1,355.0–7,597.8 ppm; Table 2) and very low common Pb concentrations (0.0–1.2 ppm; Table 2), indicating that the influence of common Pb is likely insignificant and that the U-Pb dating of such CGMs grains can provide reliable ages.

Nineteen data points with an age concordance of >98% were plotted on the U-Pb concordia diagram (Figure 7A). Eighteen of the data points (i.e., spots 1-1, 1-2, 1-3, 3, 4, 5-1, 5-2, 5-3, 8, 10-1, 10-2, 10-3, 11, 16, 17, 18, 19-1, 19-2, and 20) for the Type 1 CGMs have close $^{206}\text{Pb}/^{238}\text{U}$ ages ranging from 235.2 Ma to 244.9 Ma,

and spot no. 17 on a Type 2 CGM has a younger $^{206}\text{Pb}/^{238}\text{U}$ age of 211.0 ± 4.7 Ma. Moreover, among these eighteen Type 1 columbite spots, the $^{206}\text{Pb}/^{238}\text{U}$ ages of the rims of the individual columbite are similar to those of the core. For example, 241.0 Ma, 241.5 Ma, and 244.9 Ma ages of spots 1-1, 1-2, and 1-3, respectively, are similar within an individual columbite grain (no. 1), indicating that there is no age variation within an individual CGM grain.

Laser Ablation-Inductively Coupled Plasma Mass Spectrometry Trace Element Analysis

All of the spots on the LA-ICP-MS dated CGM separates were simultaneously analyzed for trace element concentrations. The results are presented in Supplementary Table S1. Because the



discordant dating analyses (i.e., spots 2, 6, 7, 9-1, 9-2, 12, 13, 14, 15-1, and 15-2) were obviously affected by the presence of microscale inclusions, microfractures, or possible metamictization, the results of the LA-ICP-MS trace element analysis are not considered to be reliable and were excluded in this study. The nineteen trace element data points with U-Pb age concordance of >98% are discussed in this study. Overall, the U and Pb concentrations of the analyzed CGMs show an excellent positive correlation (**Figure 8A**), and the U and Th concentrations also exhibit a positive correlation (**Figure 8B**). The chondrite-normalized rare earth element (REE) patterns for the CGMs invariably show depleted light rare earth elements (LREEs), strongly negative Eu anomalies, and enriched heavy rare earth element (HREE) patterns (**Figure 9**). All of the analyzed CGMs are characterized by relatively low Rb (0.0–2.0 ppm), Sr (0.0–0.6 ppm), Pb (46.8–302.1 ppm), and total REE contents and relatively high Y (105.6–874.2 ppm), Zr (1,460.8–5,483.7 ppm), U (3,913.4–3,668.3 ppm), and Th (14.2–93.1 ppm). Moreover, all of the trace element contents are basically invariable from the rim to the core within an individual CGM grain (i.e., nos. 1, 5, 10, and 19).

DISCUSSION

Genetic and Geochemical Evolutions of CGMs

The lower Mn# values and relatively low Ta# values are indicated by a dark BSE response for the analyzed CGMs grains (**Figures 5 and 6**) (Xie et al., 2019). According to the Ta# vs. Mn# quadrilateral diagram in **Figure 6**, Type 1 CGMs are columbite (Mn), the bright patches in Type 2 CGMs are tantalite (Mn), and the dark patches in Type 2 CGMs are also columbite (Mn) (e.g., spot no. 15-2). The bright patches in Type 2 CGMs are generally richer in Mn and Ta than Type 1 CGMs (**Figure 6**). The overall compositional change from Type 1 CGMs to Type 2 CGMs is consistent with the typical evolutionary trend described for many lithium-cesium-tantalum (LCT) pegmatites; e.g., Separation Rapids Tindle and Breaks, 2000), Jálama (Llorens and Moro, 2012), and Kolmozero (Badanina et al., 2015), are similar to the complex spodumene trend described by Černý and Ercit (1989) and shown in **Figure 6**. Generally, the increase in the Ta# values documents a local evolution or a magmatic/hydrothermal transition within the system (Breiter et al., 2017). Therefore, Type 2 CGMs should have formed later than Type 1 CGMs, and Type 2 CGMs may be a metasomatic product of certain Type 1 CGMs which may have suffered the late hydrothermal metasomatism of boundary layer liquids excluded from original pegmatitic melt proposed by London (2018). The irregular bright patches indicate metasomatic replacement processes (e.g., Badanina et al., 2015).

Moreover, based on the LA-ICP-MS trace element analysis (**Supplementary Table S1**), Type 1 CGMs do not show distinct trace element content variations from core to rim within an individual grain (**Figure 8**). According to the only one set of trace element data available for Type 2 CGMs (i.e., no. 17), it is roughly thought that the bright BSE image patches in Type 2 CGMs

(i.e., no. 17) have lower U, Th, Pb, and W, Y, and Sr contents, lower Nb/Ta and Zr/Hf ratios (**Figure 8**), and lower total REE contents (**Figure 9**) than those of Type 1 CGMs. Moreover in both types, Nb and Zr are enriched in the least fractionated rocks, and Ta and Hf predominate in the most fractionated pegmatites (Černý and Ercit, 1985; Linnen and Cuney, 2005; Stepanov et al., 2014). Thus, it was roughly argued that Type 2 CGMs represent the later hydrothermal metasomatism products of Type 1 CGMs. The decreasing concentrations of U and Pb in the late-stage CGMs were explained as the crystallization of microlite by Badanina et al., (2015) (**Figures 8A,B**), although we did not observe any microlite in the pegmatites we studied. Perhaps, there are other reasons for the depletion of U and Pb in Type 2 CGMs. The main trend in the REE variation from the early Type 1 CGMs to the late Type 2 CGMs exhibits decreasing total REE contents and decreasing negative Eu anomalies, which is typical of late differentiates of a granitic volatile-rich magma. The variations in the chemical compositions of the different generations of CGMs can be explained by the evolution of the mineral-forming environment from a magmatic melt to a hydrothermal-metasomatic fluid (e.g., Badanina et al., 2015). According to the argument of London (2018), the boundary layer liquid is the last silicate liquid in the pegmatite-forming environment. And at their most fractionated stage, this aqueous fluid is enriched with weight-percent levels of incompatible volatile elements such as Li, Rb, Cs, and B for the LCT family and then might disperse these elements within the pegmatites (London, 2018). So, it must be reasonable that some minerals of rare elements, such as spodumene, tourmaline, and even Type 2 CGMs, are products from hydrothermal metasomatism.

Unfortunately, only one set of trace element data for Type 2 CGMs has no any statistical significance. More detailed LA-ICP-MS trace element analyses of Type 2 CGMs should be conducted in future in order to compare Type 1 and Type 2 CGMs. There is insufficient evidence for our argument regarding the chemical evolution of Type 2 CGMs.

Metallogenic Ages of Pegmatites

The data for 18 Type 1 CGM spots with an age concordance of >98% have similar $^{206}\text{Pb}/^{238}\text{U}$ ages (ranging from 235.2 Ma to 244.9 Ma). The 18 data points yield a concordant age of 239.3 ± 2.0 Ma (MSWD = 29, $n = 18$; **Figure 7B**) and a weighted mean $^{206}\text{Pb}/^{238}\text{U}$ age of 240.6 ± 1.5 Ma (MSWD = 0.4, $n = 18$; **Figure 7D**). We believe that the weighted mean $^{206}\text{Pb}/^{238}\text{U}$ age of 240.6 ± 1.5 Ma for the CGMs likely represent the magmatic emplacement age of the CGM-bearing pegmatite (**Figure 8**). Moreover, spot no. 17 on a Type 2 CGMs belongs to tantalite (Mn) rather than columbite (Mn) according its Ta# value. Type 2 CGM no. 17 experienced a different petrogenetic path than the Type 1 CGMs, but one dataset has no apparent statistical significance, and the age of 211.0 ± 4.7 Ma for grain no. 17 (Type 2 CGM) hardly represents the age of the later hydrothermal metasomatism. More detailed LA-ICP-MS dating of Type 2 CGMs should be completed in future in order to constrain the emplacement age and hydrothermal metasomatism age of the Li-rich pegmatites in the Chaqiabeishan area. But the stage of

the Middle Triassic metallogenesis of the Li-rich pegmatites (ca. 240.6 Ma) in the study area within the QM or even within the NQTB are similar to the major metallogenic stages of the Northern Tibet Li ore belt to the south and the Altay Li ore belt to the north (e.g., Hao et al., 2015; Liu et al., 2017; Wang et al., 2017; Dai et al., 2018; Xu et al., 2018; Yang et al., 2018; Tu et al., 2019), indicating that the Middle Triassic Li ore-forming potential in the study area is reasonable.

Tectonic Implications of CGM-Bearing Li-Rich Pegmatites

It is widely accepted that granitic pegmatites are the products of a highly-fractionated, volatile-rich residual magma (Jahns and Burnham, 1969; Norton, 1983; Jolliff et al., 1992; London, 1992; Webber et al., 1997; Fuentes-Fuente et al., 2000; London, 2008; London, 2018). This argument strongly relies on the granite-pegmatite relationship and the regional zonation of pegmatite groups that can reflect the distinct differentiation of granitic magmas. Although no granites are spatially linked to the Li-rich pegmatites in the Chaqiabeishan area, a granitic intrusion (I-type Narong granitic porphyry) to the south of the study area has an age approximately 245 Ma (unpublished data) similar to that of the weighted mean U-Pb age of approximately 240.6 Ma obtained for the Type 1 CGMs in this study. Thus, the CGM-bearing Li-rich pegmatites may exhibit a possible genetic link to the nearby 245 Ma granite in the Chaqiabeishan area. However, the LCT pegmatites are affiliated with S-type granites in Černý's (1991) classification, and Černý and Ercit (2005) noted that the LCT pegmatites are derived "less commonly from I-type granites." Therefore, it was hardly possible that Li-rich pegmatites were directly derived from fractional crystallization of parental magma of I-type Narong granitic porphyry. Alternatively, an anatectic origin has been proposed by several authors (Martin and De Vito, 2005; Konzett et al., 2018a; Konzett et al., 2018b; London, 2018; Feng et al., 2019) to explain the formation of LCT pegmatites without parental granitic plutons, although more detailed research studies regarding the genesis of the pegmatites should be accomplished in future.

In addition, it has been proposed that the formation of rare metal-enriched pegmatites may be related to orogenic processes (Černý, 1991) and can be used to trace the geotectonic evolution of a region (Lv et al., 2012). In many cases, LCT pegmatites are likely formed in a late/postorogenic regime (e.g., Černý, 1991; London, 2018; Zhai et al., 2019), so the Li-rich pegmatites in the Chaqiabeishan area were likely formed after the collision of the QM and the south Qilian block. And the Zongwulong oceanic basin between the QM and the South Qianli block was considered to be finally closed in the Late Triassic during an intracontinental collisional orogeny (Guo et al., 2009; Peng et al., 2016; Peng et al., 2018). However, the age of 240.6 Ma for the Type 1 CGMs, which likely represents the magmatic emplacement age of the CGM-bearing pegmatite, is the Middle Triassic rather than the Late Triassic. From the Late Permian to the Middle Triassic (240–254 Ma), a series of island arc granitoids were emplaced in the Tianjun and Wulan areas from the central to the eastern parts of the QM, including the 246 Ma Tianjunnanshan granites

(Guo et al., 2009), the 254 Ma Xugeigou granite, the 251 Ma Qiluoshan granodiorite, the 249 Ma Chahannuo hornblende diorite, the 248 Ma Chahannuo granite, the 240 Ma Chahanhe granite, and the 250–244 Ma Shailekeguolei granodiorite (Wu et al., 2009; Wu et al., 2019), and 245 Ma Narong granitic porphyry (unpublished data). This stage of granitic plutonism (240–254 Ma) was considered to be related to the southward subduction of the Zongwulong oceanic plate (Wu et al., 2019). Therefore, it would be possibly accepted that the Li-rich granitic pegmatites and the 240–254 Ma granitoids are both tectonically controlled by the southward subduction of the Zongwulong oceanic plate because the magmatic emplacement of 240.6 Ma Li-rich granitic pegmatites in the study area was almost coeval with those of the 240–254 Ma granitoids in the QM. However, the tectonic event regarding the hydrothermal metasomatism of the Li-rich pegmatites needs further investigation, as Type 2 CGMs merely yielded only one dataset of U-Pb age and trace elements.

CONCLUSIONS

The results of the LA-ICP-MS CGMs U-Pb dating and trace element analysis, as well as EMPA analysis for CGMs from a Li-rich pegmatite dyke in the Chaqiabeishan area suggest the following conclusions.

The CGMs within the Li-rich pegmatites in the Chaqiabeishan area can be divided into magmatic Type 1 and hydrothermal metasomatic Type 2 CGMs. The Type 1 CGMs commonly have lower Ta# values, Mn# values, U, Th, Pb, W, Y, and Sr contents, Nb/Ta ratios, and Zr/Hf ratios than the Type 2 CGMs.

The Type 1 CGMs yielded an LA-ICP-MS U-Pb weighted a mean $^{206}\text{Pb}/^{238}\text{U}$ age of 240.6 ± 1.5 Ma based on 18 concordant ages, which represents the magmatic emplacement age of the Li-rich pegmatites; meanwhile, one spot on a Type 2 CGM yielded a $^{206}\text{Pb}/^{238}\text{U}$ age of 211.0 ± 4.7 Ma, which has no any statistical significance and hardly represents the hydrothermal metasomatism age of the Li-rich pegmatites. Data regarding Type 2 CGMs are reported in this study for future research studies.

Based on these results and the results of previous studies, it is concluded that the 240.6 Ma Li-rich granitic pegmatites in the Chaqiabeishan area, as well as the 240–254 Ma granitoids in the QM, were both emplaced during the southward subduction of the Zongwulong Ocean Plate in the Late Permian to Middle Triassic.

DATA AVAILABILITY STATEMENT

The original contributions presented in the study are included in the article/**Supplementary Material**, further inquiries can be directed to the corresponding author.

AUTHOR CONTRIBUTIONS

TP is responsible for writing original manuscript. Q-FD is responsible for copyright and revising the manuscript. XZ is responsible for drawing figures and data arrangement. S-PL

is responsible for basic data and maps. JH is responsible for sampling. LC is responsible for field work and lab work.

FUNDING

This work was supported by the Special Funding for Qinghai scholars (Grant Number QHS201802), National Natural Science Foundation of China (Grant Number 41572056) and Opening Foundation of Key Laboratory of Mineral Resources Evaluation in Northeast Asia, Ministry of Natural Resources of the People's Republic of China.

ACKNOWLEDGMENTS

We are grateful to Mr. Zhen-Hui Cao at the Wuhan Microbeam Analysis Technology Co., Ltd. for his help with

the EPMA work and Prof. Chang-Zhi Wu from the State Key Laboratory for Mineral Deposits Research, Department of Earth Sciences in Nanjing University for their help with LA-ICP-MS CGMs dating and the trace element analysis. We also want to thank Jian-Ping Zheng for his assistance during field work. We thank the Editor-in-Chief and two reviewers for their thoughtful reviews. His constructive, stimulating and valuable comments and suggestions helped improve the manuscript significantly. We thank LetPub (www.letpub.com) for its linguistic assistance during the preparation of this manuscript.

SUPPLEMENTARY MATERIAL

The Supplementary Material for this article can be found online at: <https://www.frontiersin.org/articles/10.3389/feart.2020.606951/full#supplementary-material>.

REFERENCES

- Badanina, E. V., Sitnikova, M. A., Gordienko, V. V., Melcher, F., Gäbler, H. E., Lodziak, J., et al. (2015). Mineral chemistry of columbite-tantalite from spodumene pegmatites of Kolmozero, Kola Peninsula (Russia). *Ore Geol. Rev.* 64, 720–735. doi:10.1016/j.oregeorev.2014.05.009
- Boynton, W. V. (1984). "Geochemistry of the rare earth elements: meteorites studies, Henderson, P.," in *Rare earth element geochemistry*. Editor P. Henderson (New York, NY: Elsevier), 63–114.
- Breiter, K., Vaňková, M., Galiová, M. V., Korbelová, Z., and Kanický, V. (2017). Lithium and trace-element concentrations in triotahedral micas from granites of different geochemical types measured via laser ablation ICP-MS. *Mineral. Mag.* 81 (1), 15–33. doi:10.1180/minmag.2016.080.137
- Černý, P., and Ercit, T. S. (1989). "Mineralogy of niobium and tantalum: crystal chemical relationships, paragenetic aspects and their economic implications," in *Lanthanides, tantalum and niobium*. Editors P. Möller, P. Černý, and F. Saupé (Berlin, Germany: Springer), 27–79.
- Černý, P., and Ercit, T. S. (1985). Some recent advances in the mineralogy and geochemistry of Nb and Ta in rare-element granitic pegmatites. *Bull. Mineral.* 108, 499–532. doi:10.3406/bulmi.1985.7846
- Černý, P., and Ercit, T. S. (2005). The classification of granitic pegmatites revisited. *Can. Mineral.* 43, 2005–2026. doi:10.2113/gscanmin.43.6.2005
- Černý, P. (1991). Rare-element granitic pegmatites. Part II: regional to global environments and petrogenesis. *Geosci. Can.* 18, 2.
- Che, X. D., Wang, R. C., Wu, F. Y., Zhu, Z. Y., Zhang, W. L., Hu, H., et al. (2019). Episodic Nb-Ta mineralisation in South China: constraints from *in situ* LA-ICP-MS columbite-tantalite U-Pb dating. *Ore Geol. Rev.* 105, 71–85. doi:10.1016/j.oregeorev.2018.11.023
- Che, X. D., Wu, F. Y., Wang, R. C., Gerdes, Axel., Ji, W. Q., Zhao, Z. H., et al. (2015). *In situ* U-Pb isotopic dating of columbite-tantalite by LA-ICP-MS. *Ore Geol. Rev.* 65, 979–989. doi:10.1016/j.oregeorev.2014.07.008
- Chen, N. S., Gong, S. L., Sun, M., Li, X. Y., Long, X. P., Wang, Q. Y., et al. (2009). Precambrian evolution of the Quanji block, northeastern margin of Tibet: insights from zircon U-Pb and Lu-Hf isotope compositions. *J. Asian Earth Sci.* 35, 367–376. doi:10.1016/j.jseas.2008.10.004
- Chen, N. S., Zhang, L., Sun, M., Wang, Q. Y., and Kusky, T. M. (2012). U-Pb and Hf isotopic compositions of detrital zircons from the paragneisses of the Quanji Massif, NW China: implications for its early tectonic evolutionary history. *J. Asian Earth Sci.* 55, 110–130. doi:10.1016/j.jseas.2012.04.006
- Dai, H. Z., Wang, D. H., Liu, L. J., Yu, Y., Dai, J. J., and Fu, X. F. (2018). Geochronology, geochemistry and their geological significance of No. 308 pegmatite vein in the Jiajika deposit, western Sichuan, China. *Earth Sci.* 43 (10), 3664–3681. doi:10.3799/dqkx.2018.528
- Ding, Q. F., Jiang, S. Y., and Sun, F. Y. (2014). Zircon U-Pb geochronology, geochemical and Sr-Nd-Hf isotopic compositions of the Triassic granite and diorite dikes from the Wulonggou mining area in the Eastern Kunlun Orogen, NW China: petrogenesis and tectonic implications. *Lithos.* 205, 266–283. doi:10.1016/j.lithos.2014.07.015
- Ding, Q. F., Liu, F., and Yan, W. (2015). Zircon U-Pb geochronology and Hf isotopic constraints on the petrogenesis of early triassic granites in the wulonggou area of the eastern Kunlun orogen, northwest China. *Int. Geol. Rev.* 57, 1735–1754. doi:10.1080/00206814.2015.1029541
- Feng, Y. G., Liang, T., Zhang, Z., Wang, Y. Q., Zhou, Y., Yang, X. Q., et al. (2019). Columbite U-Pb geochronology of kalu'an lithium pegmatites in northern Xinjiang, China: implications for genesis and emplacement history of rare-element pegmatites. *Minerals* 9, 456. doi:10.3390/min9080456
- Fuertes-Fuente, M., Martin-Izard, A., Boiron, M. C., and Vinuela, J. M. (2000). P-T path and evolution in the franquiera granitic pegmatite, central galicia, northwestern Spain. *Can. Mineral.* 38, 1163–1175. doi:10.2113/gscanmin.38.5.1163
- Gao, J. F., Zhou, M. F., Lightfoot, P. C., Wang, C. Y., Qi, L., and Sun, M. (2013). Sulfide saturation and magma emplacement in the formation of the Permian Huangshandong Ni-Cu sulfide deposit, Xinjiang, Northwestern China. *Econ. Geol.* 108, 1833–1848. doi:10.2113/econgeo.108.8.1833
- Gong, S., He, C., Wang, X., Chen, N., and Kusky, T. (2019). No plate tectonic shutdown in the early Paleoproterozoic: constraints from the ca. 2.4 Ga granitoids in the Quanji Massif, NW China. *J. Asian Earth Sci.* 172, 221–242. doi:10.1016/j.jseas.2018.09.011
- Gong, S. L., Chen, N.-S., Geng, H. Y., Sun, M., Zhang, L., and Wang, Q. Y. (2014). Zircon Hf isotopes and geochemistry of the early paleoproterozoic high-Sr low-Y quartz-diorite in the quanji massif, NW China: crustal growth and tectonic implications. *J. Earth Sci.* 25 (1), 74–86. doi:10.1007/s12583-014-0401-2
- Gong, S. L., Chen, N. S., Wang, Q. Y., Kusky, T. M., Wang, L., Ba, J., et al. (2012). Early paleoproterozoic magmatism in the quanji massif, northeastern margin of the Qinghai Tibet plateau and its tectonic significance: LA-ICPMS U-Pb zircon geochronology and geochemistry. *Gondwana Res.* 21 (1), 152–166. doi:10.1016/j.gr.2011.07.011
- Guo, A. L., Zhang, G. W., Qiang, J., Sun, Y. G., Li, G., and Yao, A. P. (2009). Indosinian Zongwulong orogenic belt on the northeastern margin of the Qinghai Tibet plateau. *Acta Petrol. Sin.* 25, 1–12. (in Chinese with English abstract)
- Hao, X. F., Fu, X. F., Liang, B., Yuan, L. P., Pan, M., and Tang, Y. (2015). Formation ages of granite and X03 pegmatite vein in Jiajika, western Sichuan, and their geological significance. *Miner. Deposits.* 34 (6), 1199–1208. (in Chinese with English abstract)
- He, C., Gong, S. L., Wang, L., Chen, N. S., Santosh, M., and Wang, Q. Y. (2018). Protracted postcollisional magmatism during plate subduction shutdown in

- early Paleoproterozoic: insights from post-collisional granitoid suite in NW China. *Gondwana Res.* 55, 92–111. doi:10.1016/j.gr.2017.11.009
- Jahns, R. H., and Burnham, C. W. (1969). Experimental studies of pegmatite genesis: I. A model for the derivation and crystallization of granitic pegmatites. *Econ. Geol.* 64, 843–864. doi:10.2113/gsecongeo.64.8.843
- Jolliffe, B. L., Papike, J. J., and Shearer, C. K. (1992). Petrogenetic relationships between pegmatite and granite based on geochemistry of muscovite in pegmatite wall zones, Black Hills, South Dakota, USA. *Geochim. Cosmochim. Acta.* 56, 1915–1939. doi:10.1016/0016-7037(92)90320-I
- Kaeter, D., Barros, R., Menuge, J. F., and Chew, D. M. (2018). The magmatic–hydrothermal transition in rare-element pegmatites from southeast Ireland: LA-ICP-MS chemical mapping of muscovite and columbite–tantalite. *Geochim. Cosmochim. Acta.* 240, 98–130. doi:10.1016/j.gca.2018.08.024
- Konzett, J., Schneider, T., Nedyalkova, L., Hauzenberger, C., Melcher, F., Gerdes, A., et al. (2018a). Anatectic granitic pegmatites from the eastern Alps: a case of variable rare-metal enrichment during high-grade regional metamorphism—I: mineral assemblages, geochemical characteristics, and emplacement ages. *Can. Mineral.* 56, 555–602. doi:10.3749/canmin.1800008
- Konzett, J., Hauzenberger, C., Ludwig, T., and Stalder, R. (2018b). Anatectic granitic pegmatites from the eastern Alps: a case of variable rare metal enrichment during high-grade regional metamorphism. II: pegmatite staurolite as an indicator of anatectic pegmatite parent melt formation—a field and experimental study. *Can. Mineral.* 56, 603–624. doi:10.3749/canmin.1800011
- Legros, H., Mercadier, J., Villeneuve, J., Romer, R. L., Deloule, E., Van Lichtervelde, M., et al. (2019). U–Pb isotopic dating of columbite–tantalite minerals: development of reference materials and *in situ* applications by ion microprobe. *Chem. Geol.* 512, 69–84. doi:10.1016/j.chemgeo.2019.03.001
- Liao, F., Wang, Q., Chen, N., Santosh, M., Xu, Y., and Mustafa, H. A. (2018). Geochemistry and geochronology of the ~0.82 Ga high–Mg gabbroic dykes from the Quanji Massif, southeast Tarim Block, NW China: implications for the Rodinia supercontinent assembly. *J. Asian Earth Sci.* 157, 3–21. doi:10.1016/j.jseas.2017.06.021
- Liao, F., Zhang, L., Chen, N., Sun, M., Santosh, M., Wang, Q., et al. (2014). Geochronology and geochemistry of meta-mafic dykes in the Quanji Massif, NW China: Paleoproterozoic evolution of the Tarim Craton and implications for the assembly of the Columbia supercontinent. *Precambrian Res.* 249, 33–56. doi:10.1016/j.precamres.2014.04.015
- Linnen, R. L., and Cuney, M. (2005). “Granite-related rare-element deposits and experimental constraints on Ta–Nb–W–Sn–Zr–Hf mineralization,” in *Rare-element geochemistry and mineral Deposits*. Editors R. L. Linnen and I. M. Samson (St. John’s, Newfoundland, Canada: Geological Association of Canada), 45–68.
- Linnen, R. L., Samson, I. M., Williams-Jones, A. E., and Chakhmouradian, A. R. (2014). “Geochemistry of the rare-earth element, Nb, Ta, Hf, and Zr deposits,” in *Treatise on geochemistry*. 2nd Edn. Editors K. Holland and Turekian (Oxford, UK: Elsevier), 543–564.
- Linnen, R. L., Van Lichtervelde, M., and Černý, P. (2012). Granitic pegmatites as sources of strategic metals. *Elements*. 8, 275–280. doi:10.2113/gselements.8.4.275
- Liu, L. J., Wang, D. H., Hou, K. J., Tian, S. H., Zhao, Y., Fu, X. F., et al. (2017). Application of lithium isotope to Jiajika new No.3 pegmatite lithium polymetallic vein in Sichuan. *Earth Sci. Front.* 24 (5), 167–171. doi:10.13745/j.esf.yx.2017-1-16
- Liu, Y. S., Hu, Z. C., Gao, S., Gunther, D., Xu, J., Gao, C. G., et al. (2008). *In situ* analysis of major and trace elements of anhydrous minerals by LA-ICP-MS without applying an internal standard. *Chem. Geol.* 257 (1–2), 34–43. doi:10.1016/j.chemgeo.2008.08.004
- Llorens, T., and Moro, M. C. (2012). Oxide minerals in the granitic cupola of the Jálama Batholith, Salamanca, Spain. Part I: accessory Sn, Nb, Ta and Ti minerals in leucogranites, aplites and pegmatites. *J. Geosci.* 57, 25–43. doi:10.3190/jgeosci.113
- London, D. (2018). Ore-forming processes within granitic pegmatites. *Ore Geol. Rev.* 101, 349–383. doi:10.1016/j.oregeorev.2018.04.020
- London, D. (2008). *The Canadian mineralogist*. London, UK: Special Publication, 347.
- London, D. (1992). The application of experimental petrology to the genesis and crystallization of granitic pegmatites. *Can. Mineral.* 30, 499–540.
- Lu, S. N., Li, H. K., Zhang, C. L., and Niu, G. H. (2008). Geological and geochronological evidence for the precambrian evolution of the Tarim Craton and surrounding continental fragments. *Precambrian Res.* 160 (1/2), 94–107. doi:10.1016/j.precamres.2007.04.025
- Lu, S. N., Yu, H. F., Li, H. K., Guo, K. Y., Wang, H. C., Jin, W., et al. (2006). Research on Precambrian major problems in Chinese. (Beijing: Geological Publishing House), 1–197. (in Chinese).
- Ludwig, K. R. (2003). User’s manual for isoplot/ex, version 3.00: a geochronological toolkit for microsoft Excel. *Berkeley Geochronol. Cent. Spec. Publ.* 4, 1–70.
- Lv, Z. H., Zhang, H., Tang, Y., and Guan, S. J. (2012). Petrogenesis and magmatic–hydrothermal evolution time limitation of Kelumute No. 112 pegmatite in Altay, Northwestern China: evidence from zircon U Pb and Hf isotopes. *Lithos.* 154, 374–391. doi:10.1016/j.lithos.2012.08.005
- Martin, R. F., and De Vito, C. (2005). The patterns of enrichment in felsic pegmatites ultimately depend on tectonic setting. *Can. Mineral.* 43, 2027–2048. doi:10.2113/gscanmin.43.6.2027
- Mustafa, H. A., Wang, Q., Chen, N., Liao, F., Sun, M., and Salih, M. A. (2016). Geochemistry of metamafic dykes from the Quanji massif: petrogenesis and further evidence for oceanic subduction, late paleoproterozoic, NW China. *J. Earth Sci.* 27, 529–544. doi:10.1007/s12583-015-0659-z
- Norton, J. J. (1983). Sequence of mineral assemblages in differentiated granitic pegmatites. *Econ. Geol.* 78, 854–874. doi:10.2113/gsecongeo.78.5.854
- Pan, T., Li, S. P., Ren, H., and Wang, B. Z. (2020). Metallogenic conditions and prospecting potential of lithium polymetallic deposits in north Qaidam basin. *Miner. Explor.* 11 (6), 1101–1116. (in Chinese with English abstract)
- Pang, J. Z., Yu, J. X., Zheng, D. W., Wang, W. T., Ma, Y., Wang, Y. Z., et al. (2019). Neogene expansion of the qilian Shan, north Tibet: implications for the dynamic evolution of the Tibetan plateau. *Tectonics*. 38, 1018–1032. doi:10.1029/2018TC005258
- Peng, Y., Ma, Y. S., Liu, C. L., Sun, J. P., and Shao, P. C. (2016). Geological characteristics and tectonic significance of the Indosinian granodiorites from the Zongwulong tectonic belt in North Qaidam. *Earth Sci. Front.* 23, 206–221. doi:10.13745/j.esf.2016.02.020
- Peng, Y., Zhang, Y. S., Sun, J. P., Xing, E. Y., and Yu, H. T. (2018). Geochemistry of Late Carboniferous sedimentary rocks from the Zongwulong structural belt and adjacent areas, Qaidam Basin, China: implications for provenance and tectonic setting. *Geosci. J.* 22 (2), 287–301. doi:10.1007/s12303-017-0032-6
- QGS (2020). *Internal reports of ore exploration of Li-rich pegmatites in chaqiabeishan area in Tianjun county, Qinghai Province*.
- Romer, R. L. (2003). Alpha-recoil in U–Pb geochronology: effective sample size matters. *Contrib. Mineral. Petrol.* 145, 481–491. doi:10.1007/s00410-003-0463-0
- Romer, R. L., Smeds, S. A., and Černý, P. (1996). Crystal-chemical and genetic controls of U–Pb systematics of columbite–tantalite. *Mineral. Petrol.* 57, 243–260. doi:10.1007/BF01162361
- Romer, R. L., and Wright, J. E. (1992). U–Pb dating of columbites: a geochronologic tool to date magmatism and ore deposits. *Geochim. Cosmochim. Acta.* 56, 2137–2142. doi:10.1016/0016-7037(92)90337-I
- Smith, S. R., Foster, G. L., Romer, R. L., Tindle, A. G., Kelley, S. P., Noble, S. R., et al. (2004). U–Pb columbite–tantalite chronology of rare-element pegmatites using TIMS and laser ablation multi collector–ICP–MS. *Contrib. Mineral. Petrol.* 147, 549–564. doi:10.1007/s00410-003-0538-y
- Song, S. G., Niu, Y. L., Su, L., Zhang, C., and Zhang, L. F. (2014). Continental orogenesis from ocean subduction, continent collision/subduction, to orogen collapse, and orogen recycling: the example of the north Qaidam UHPM belt, NW China. *Earth Sci. Rev.* 129, 59–84. doi:10.1016/j.earscirev.2013.11.010
- Song, S. G., Niu, Y. L., Zhang, G. B., and Zhang, L. F. (2018). *Two epochs of eclogite metamorphism link ‘cold’ oceanic subduction and ‘hot’ continental subduction, the north Qaidam UHP belt, NW China*. London, UK: Geological Society Special Publications, 474.
- Stepanov, A., Mavrogenes, J. A., Meffre, S., and Davidson, P. (2014). The key role of mica during igneous concentration of tantalum. *Contrib. Mineral. Petrol.* 167, 499–1009. doi:10.1007/s00410-014-1009-3
- Timofeev, A., Migdisov, A. A., and Williams-Jones, A. E. (2017). An experimental study of the solubility and speciation of tantalum in fluoride-bearing aqueous

- solutions at elevated temperature. *Geochem. Cosmochim. Acta*. 197, 294–304. doi:10.1016/j.gca.2016.10.027
- Tindle, A. G., and Breaks, F. W. (2000). Columbite–tantalite mineral chemistry from rare-element granitic pegmatites: Separation Lake area, N.W. Ontario, Canada. *Mineral. Petrol.* 70, 165–198. doi:10.1007/s007100070002
- Tu, Q. J., Li, J. K., Wang, G., and Ma, H. C. (2019). Mineralization comparisons of the major pegmatite type spodumene deposits and their prospecting potential in West China. *Geological Surv. China*. 6 (6), 35–47. (in Chinese with English abstract)
- Van Lichtervelde, M., Salvi, S., Beziat, D., and Linnen, R. L. (2007). Textural features and chemical evolution in tantalum oxides: magmatic versus hydrothermal origins for Ta mineralization in the Tanco Lower pegmatite, Manitoba, Canada. *Econ. Geol.* 102, 257–276. doi:10.2113/gsecongeo.102.2.257
- Wang, B. Z., Han, J., Xie, X. L., Chen, J., Wang, T., Xue, W. W., et al. (2020). Discovery of the indosinian (Beryl-bearing) spodumene pegmatitic dike swarm in the chakaibeishan area in the northeastern margin of the Tibetan plateau: implications for Li-Be mineralization. *Geotect. Metallogenia*. 44 (1), 69–79. (in Chinese with English abstract)
- Wang, D. H., Liu, L. J., Dai, H. Z., Liu, S. B., Hou, J. L., and Wu, X. S. (2017). Discussion on particularity and prospecting direction of large and super-large spodumene deposits. *Earth Sci.* 42 (12), 2243–2257. doi:10.3799/dqkx.2017.142
- Wang, L., Johnston, S. T., and Chen, N. S. (2019). New insights into the Precambrian tectonic evolution and continental affinity of the Qilian block: evidence from geochronology and geochemistry of metasupracrustal rocks in the North Wulan terrane. *Geol. Soc. Am. Bull.* 131, 1723–1743. doi:10.1130/B35059.1
- Wang, L., Wang, H., He, C., Chen, N. S., Santosh, M., Sun, M., et al. (2016). Mesoproterozoic continental breakup in NW China: evidence from gray gneisses from the North Wulan terrane. *Precambrian. Res.* 281, 521–536. doi:10.1016/j.precamres.2016.06.016
- Wang, Q. Y., Dong, Y. J., Pan, Y. M., Liao, F. X., and Guo, X. W. (2018). Early paleozoic granulite-facies metamorphism and magmatism in the northern wulan terrane of the quanji massif: implications for the evolution of the Proto-Tethys ocean in northwestern China. *J. Earth Sci.* 29, 1081–1101. doi:10.1007/s12583-018-0881-6
- Webber, K. L., Falster, A. U., Simmons, W. B., and Foord, E. E. (1997). The role of diffusion controlled oscillatory nucleation in the formation of line rock in pegmatite-aplite dikes. *J. Petrol.* 38, 1777–1791.
- Wu, C. L., Wooden, J. L., Robinson, P. T., Gao, Y. H., Wu, S. P., Chen, Q. L., et al. (2009). Geochemistry and zircon SHRIMP U-Pb dating of granitoids from the west segment of the North Qaidam. *Sci. China Earth Sci.* 52, 1771–1790. doi:10.1007/s11430-009-0147-3
- Wu, C. L., Wu, D., Mattinson, C., Lei, M., and Chen, H. J. (2019). Petrogenesis of granitoids in the Wulan area: magmatic activity and tectonic evolution in the North Qaidam, NW China. *Gondwana Res.* 67, 147–171. doi:10.1016/j.gr.2018.09.010
- Xiao, W. J., Windley, B. F., Yong, Y., Yan, Z., Yuan, C., Liu, C. Z., et al. (2009). Early paleozoic to devonian multiple-accretionary model for the qilian Shan, NW China. *J. Asian Earth Sci.* 35, 323–333. doi:10.1016/j.jseas.2008.10.001
- Xie, L., Liu, Y., Wang, R. C., Hu, H., Che, X. D., and Xiang, L. (2019). Li-Nb-Ta mineralization in the Jurassic Yifeng granite-aplite intrusion within the Neoproterozoic Jiuling batholith, south China: a fluid-rich and quenching ore-forming process. *J. Asian Earth Sci.* 185, 104047. doi:10.1016/j.jseas.2019.104047
- Xiong, F., Ma, C., Zhang, J., Liu, B., and Jiang, H. (2014). A reworking of old continental lithosphere: an important crustal evolution mechanism in orogenic belts, as evidenced by Triassic I-type granitoids in the East Kunlun orogen, Northern Tibetan Plateau. *J. Geol. Soc.* 171, 847–863. doi:10.1144/jgs2013-038
- Xu, Z. Q., Wang, R. C., Zhao, Z. B., and Fu, X. F. (2018). On the structural backgrounds of the large-scale “hard-rock type” lithium ore belts in China. *Acta Geol. Sin.* 92 (6), 1091–1106. (in Chinese with English abstract)
- Xu, Z. Q., Yang, J. S., Wu, C. L., Li, H. B., Zhang, J. X., Qi, X. X., et al. (2006). Timing and mechanism of formation and exhumation of the Northern Qaidam ultrahigh-pressure metamorphic belt. *J. Asian Earth Sci.* 28, 160–173. doi:10.1016/j.jseas.2005.09.016
- Yan, Q., Qiu, Z., Wang, H., Wang, M., Wei, X., Li, P., et al. (2018). Age of the Dahongliutan rare metal pegmatite deposit, West Kunlun, Xinjiang (NW China): constraints from LA-ICP-MS U-Pb dating of columbite-(Fe) and cassiterite. *Ore Geol. Rev.* 100, 561–573. doi:10.1016/j.oregeorev.2016.11.010
- Yang, F. Q., Zhang, Z. L., Wang, R., Li, Q., Ding, J. G., Su, Z. H., et al. (2018). Geological characteristics and metallogenesis of rare metal deposits in Altay, Xinjiang. *Geotect. Metallogenia*. 42 (6), 1010–1026. (in Chinese with English abstract)
- Zhai, M. G., Wu, F. Y., Hu, R. Z., Jiang, S. Y., Li, W. C., Wang, R. C., et al. (2019). Critical metal mineral resources: current research status and scientific issues. *Bull. Natl. Sci. Found. China*. 2, 106–111. (in Chinese with English abstract)
- Zhang, H. J., Wang, X. L., Wang, X., and Zhou, H. R. (2016). U-Pb zircon ages of tuff from the Hongzaoshan Formation, Quanji Group, in the north margin of Qaidam Basin, NW China, and their geological significances. *Earth Sci. Front.* 23, 202–218. doi:10.13745/j.esf.2016.06.014
- Zhang, J. X., Mattinson, C. G., Yu, S. Y., and Li, Y. S. (2014a). Combined rutile-zircon thermometry and U-Pb geochronology: new constraints on early paleozoic HP/UHT granulite in the south altyn tagh, north Tibet, China. *Lithos*. 200/201, 241–257. doi:10.1016/j.lithos.2014.05.006
- Zhang, J. X., Yu, S. Y., and Mattinson, C. G. (2017). Early paleozoic polyphase metamorphism in northern Tibet, China. *Gondwana Res.* 41, 267–289. doi:10.1016/j.gr.2015.11.009
- Zhang, L., Ba, J., Chen, N. S., Wang, Q. Y., Liao, F. X., and Li, X. Y. (2012). U-Pb age spectra and trace elements of detrital zircon from quanji group: implications for thermal events and early evolution in the basement. *J. Earth Sci.* 37, 28–42. doi:10.3799/dqkx.2012.S1.004
- Zhang, L., Wang, Q. Y., Chen, N. S., Sun, M., Santosh, M., and Ba, J. (2014b). Geochemistry and detrital zircon U-Pb and Hf isotopes of the paragneiss suite from the quanji massif, SE Tarim Craton: implications for paleoproterozoic tectonics in NW China. *J. Asian Earth Sci.* 95, 33–50. doi:10.1016/j.jseas.2014.05.014
- Zhang, R. X., and Yang, S. Y. (2016). A mathematical model for determining carbon coating thickness and its application in electron probe microanalysis. *Microsc. Microanal.* 22, 1374–1380. doi:10.1017/S143192761601182X
- Zhao, F. Q., Lu, S. N., and Li, H. K. (2000). “The geochemical characteristics of the Mes-Neoproterozoic granite belt in the dakendaban complex rocks of the Qaidam block,” in Abstracts of the second cross strait: Qilian Mountains and its adjacent areas. Beijing, 95–97 (in Chinese).

Conflict of Interest: The authors declare that the research was conducted in the absence of any commercial or financial relationships that could be construed as a potential conflict of interest.

Copyright © 2021 Pan, Ding, Zhou, Li, Han and Cheng. This is an open-access article distributed under the terms of the Creative Commons Attribution License (CC BY). The use, distribution or reproduction in other forums is permitted, provided the original author(s) and the copyright owner(s) are credited and that the original publication in this journal is cited, in accordance with accepted academic practice. No use, distribution or reproduction is permitted which does not comply with these terms.



Fluid Inclusions and H–O–C–S–Pb Isotopic Systematics of the Jinba Gold Deposit, NW China: Implications for Ore Genesis

Shun-Da Li, Chuan Chen*, Ling-Ling Gao, Fang Xia, Xue-Bing Zhang and Ke-Yong Wang

Xinjiang Key Laboratory for Geodynamic Processes and Metallogenic Prognosis of the Central Asian Orogenic Belt, College of Geology and Mining Engineering, Xinjiang University, Urumqi, China

OPEN ACCESS

Edited by:

Chang-Zhi Wu,
Chang'an University, China

Reviewed by:

Qing-Feng Ding,
Jilin University, China
Guoguang Wang,
Nanjing University, China

*Correspondence:

Chuan Chen
xjzycc2017@163.com

Specialty section:

This article was submitted to
Economic Geology,
a section of the journal
Frontiers in Earth Science

Received: 06 December 2020

Accepted: 18 January 2021

Published: 22 February 2021

Citation:

Li S-D, Chen C, Gao L-L, Xia F,
Zhang X-B and Wang K-Y (2021) Fluid
Inclusions and H–O–C–S–Pb Isotopic
Systematics of the Jinba Gold Deposit,
NW China: Implications for
Ore Genesis.
Front. Earth Sci. 9:638375.
doi: 10.3389/feart.2021.638375

The Jinba gold deposit is located in the Maerkakuli Shear Zone of the south Altay Orogenic Belt, NW China. Mineralization types are classified as altered rock– and quartz vein–type. Orebodies occur as veins or lenses controlled by NW–trending faults, and are hosted in phyllite (Early–Middle Devonian Ashele Formation) and plagiogranite (Early Devonian Habahe Pluton). Three paragenetic stages were identified: early quartz–pyrite–gold (Stage 1), middle quartz–chalcopyrite (Stage 2), and late calcite–quartz–galena–sphalerite (Stage 3). Fluid inclusions within the deposit are liquid–rich aqueous (LV–type), vapor–rich aqueous (VL–type), carbonic–aqueous (LC–type), and purely carbonic (C–type) Fls. Homogenization temperatures for stages 1–3 Fls were 373–406 °C, 315–345 °C, and 237–265 °C, respectively. Fluid salinities for stages 1–3 were 2.1–13.6 wt%, 3.2–6.1 wt% and 3.9–6.0 wt% NaCl equivalent, respectively. The ore–forming fluids evolved from a CO₂–NaCl–H₂O ± CH₄ to a NaCl–H₂O system from stage 1–3. Oxygen, hydrogen, and carbon isotopic data ($\delta^{18}\text{O}_{\text{fluid}} = 1.7\text{‰}–8.1\text{‰}$, $\delta\text{D}_{\text{fluid}} = -104.1\text{‰}$ to -91.7‰ , $\delta^{13}\text{C}_{\text{fluid}} = -0.4\text{‰}–6.3\text{‰}$) indicate that ore–forming fluids were metamorphic hydrothermal origin with the addition of a late meteoric fluid. Sulfur and lead isotope data for pyrite ($\delta^{34}\text{S}_{\text{py}} = 3.3\text{‰}–5.3\text{‰}$, $^{206}\text{Pb}/^{204}\text{Pb} = 17.912.3–18.495$, $^{207}\text{Pb}/^{204}\text{Pb} = 15.564–15.590$, $^{208}\text{Pb}/^{204}\text{Pb} = 37.813–38.422$) show that the ore–forming materials were mainly derived from diorite and the Ashele Formation. Mineralization, Fls, and isotope studies demonstrate that the Jinba deposit is an orogenic gold deposit.

Keywords: fluid inclusion, isotope, orogenic gold deposit, xinjiang, altay orogenic belt

INTRODUCTION

Orogenic gold deposits (OGDs) comprise over 30% of global gold reserves (Frimmel, 2008). These deposits share a number of common features, namely: relative timing in the evolution of orogenic processes, low–medium NaCl–H₂O ± CO₂ ± CH₄ ± N₂ ore–forming fluids, structural controls exerted by second–order ductile shear zones, host rocks with greenschist facies metamorphism, and emplacement at convergent plate margins. OGDs are widely distributed throughout the world, with examples such as the Abitibi Greenstone Belt in Canada, the Yilgarn Craton in Australia, and the Chinese Altay Orogenic Belt (CAOB) (Ayer, 2008; Deng and Wang, 2016). The CAOB is part of the Central Asian Orogenic Belt and lies at the junction of the Siberian Plate, the Kazakhstan Plate, and the Junggar Plate (Groves et al., 1998). It is

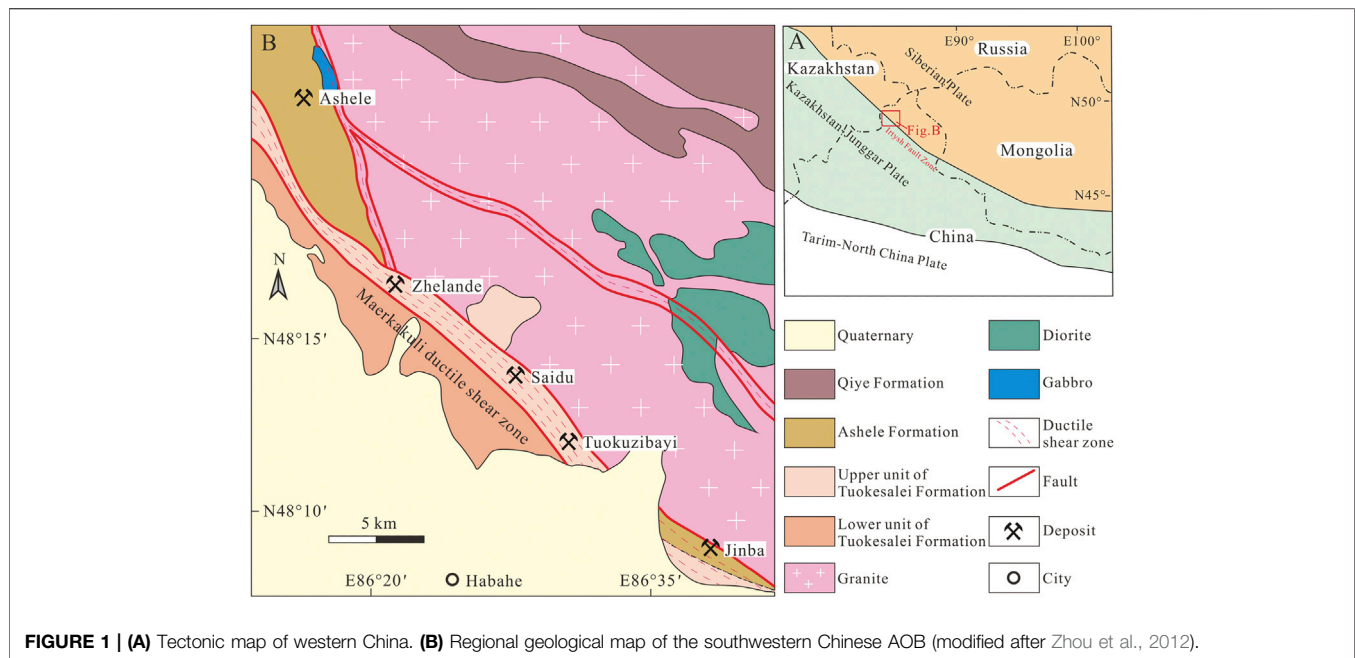


FIGURE 1 | (A) Tectonic map of western China. **(B)** Regional geological map of the southwestern Chinese AOB (modified after Zhou et al., 2012).

connected to the Kazakhstan Altay metallogenic belt to the west and borders the Mongolian metallogenic belt in the east (**Figure 1A**). This region has experienced a long geodynamic evolution, including the oceanic plate subduction, continental accretion, and collisional orogenesis (Xiao et al., 2009; Kröner et al., 2013).

The Jinba gold deposit is located in the southwestern CAOB. The deposit was discovered in 1997 by the 11th Geological Party of the Xinjiang Bureau of Geology and Mineral Exploration. Ongoing exploration has provided 15,311 m of drill core from over 50 holes, and has led to the development of 964 m of underground tunnels and 2,581 m³ of trenches. The results of this exploration revealed a 2.3 t gold reserves with a grade of 2.6 g/t Au. Previous studies of this deposit have focused on its geological features, geochemistry, geochronology, and geological exploration. However, most of the literature is in Chinese (Chen et al., 2010; Deng, 2011; Zhou et al., 2012). The nature and sources of ore-forming fluids have not yet been investigated in detail. In addition, the deposit's genetic classification is controversial. While some scholars suggest that the Jinba deposit is a ductile shear zone-type gold deposit (Chen et al., 2003), others consider it to be a middle-to low-temperature hydrothermal deposit (Wang et al., 2018). In addition, it has also been classified as an altered rock gold deposit (Li and Chen, 2004). However, many features of the Jinba deposit are typical of OGDs.

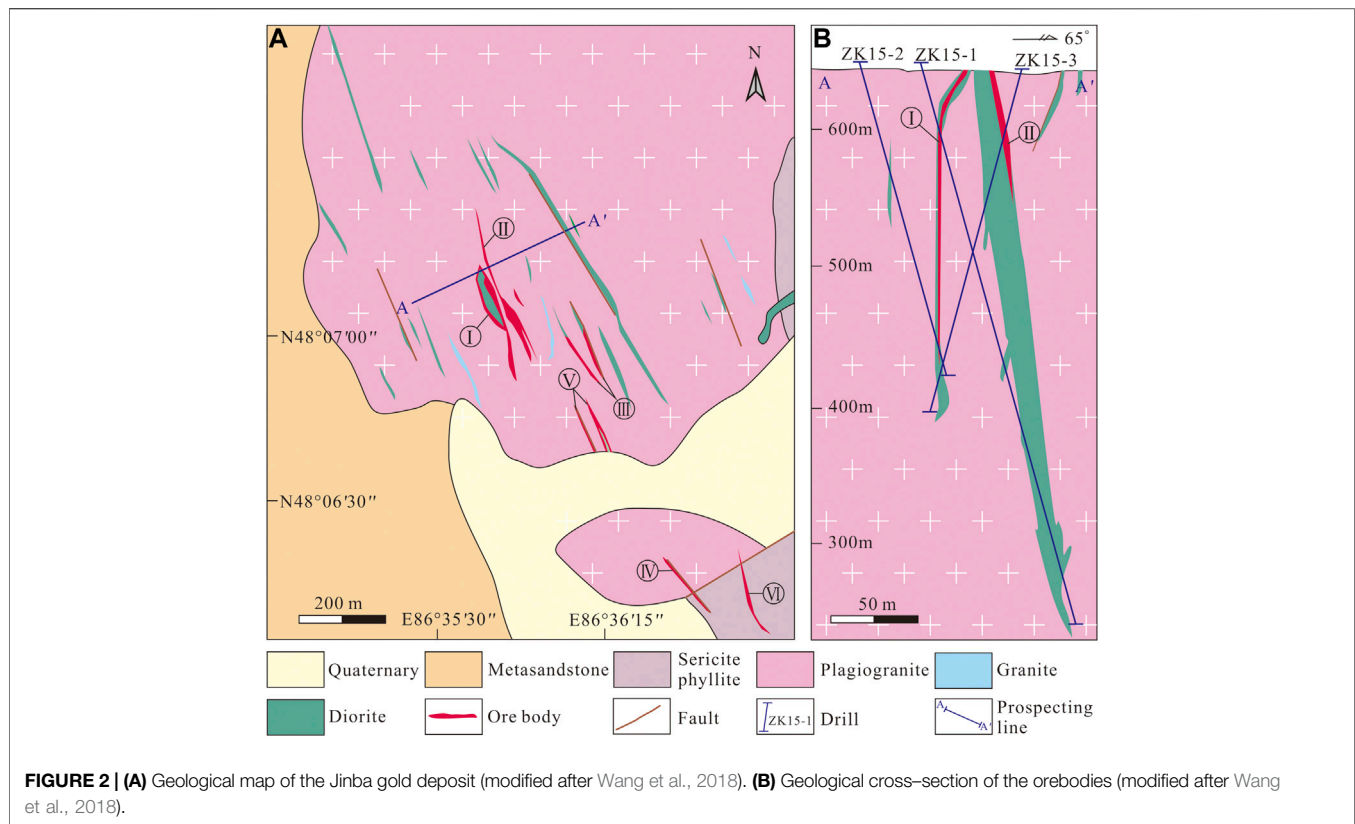
In the present work, based on fieldwork focused on geology and mineralization styles, we present new fluid inclusion (FI) and isotope (H-O-C-S-Pb) data. The main aims of this study are to: 1) determine the source and evolution of the ore-forming fluids, 2) clarify the origin of ore-forming materials, and 3) propose a genetic model for the deposit.

REGIONAL GEOLOGY

The study area is located in the southwestern CAOB (**Figure 1A**). Terranes in this region are mainly comprised of the Lower–Middle Devonian Tuokesalei Formation, the Lower–Middle Devonian Ashele Formation, the Upper Devonian Qiyé Formation, and Quaternary sediments (**Figure 1B**). The Tuokesalei Formation is a sequence of marine terrigenous clastic, metasedimentary, and carbonate rocks. The lower unit is comprised of metamorphic sandstone and metamorphic siltstone, whereas the upper unit includes sandstone, argillaceous siltstone, and limestone. The Ashele Formation is a sequence of marine volcanic rocks, metasedimentary rocks, sericite phyllite and carbonate rocks. The predominant lithologies in the sequence are tuff, tuffaceous siltstone, and metamorphic sandstone, with limestone lenses. The Qiyé Formation is a sequence of intermediate–mafic volcanic rocks, with pyroclastic–sedimentary units. These rocks are composed of andesite, breccia tuff, and tuffaceous sandstone. These Devonian strata were generally folded and metamorphosed to greenschist facies (Laurent et al., 2002; Wei et al., 2007). The Irtysch Fault Zone (**Figure 1A**)—considered to be a suture zone between the Siberian Plate and the Kazakhstan–Junggar Plate—is the largest structure in the region (Yakubchuk, 2004; Pirajno et al., 2011). The Maerkakuli Shear Zone (**Figure 1B**)—which controls the distribution of intrusive rocks and deposits in the area—is a second-order fault system of the Irtysch Fault Zone. Most of the ore deposits in this area distributed along this shear zone, such as the Ashele, Zhelände, Saidu, Tuokuzibayi and Jinba deposits.

GEOLOGY AND MINERALIZATION

The Jinba gold deposit is located 16 km northeast of the city of Habahe, Xinjiang Uygur Autonomous Region (**Figure 1B**). The



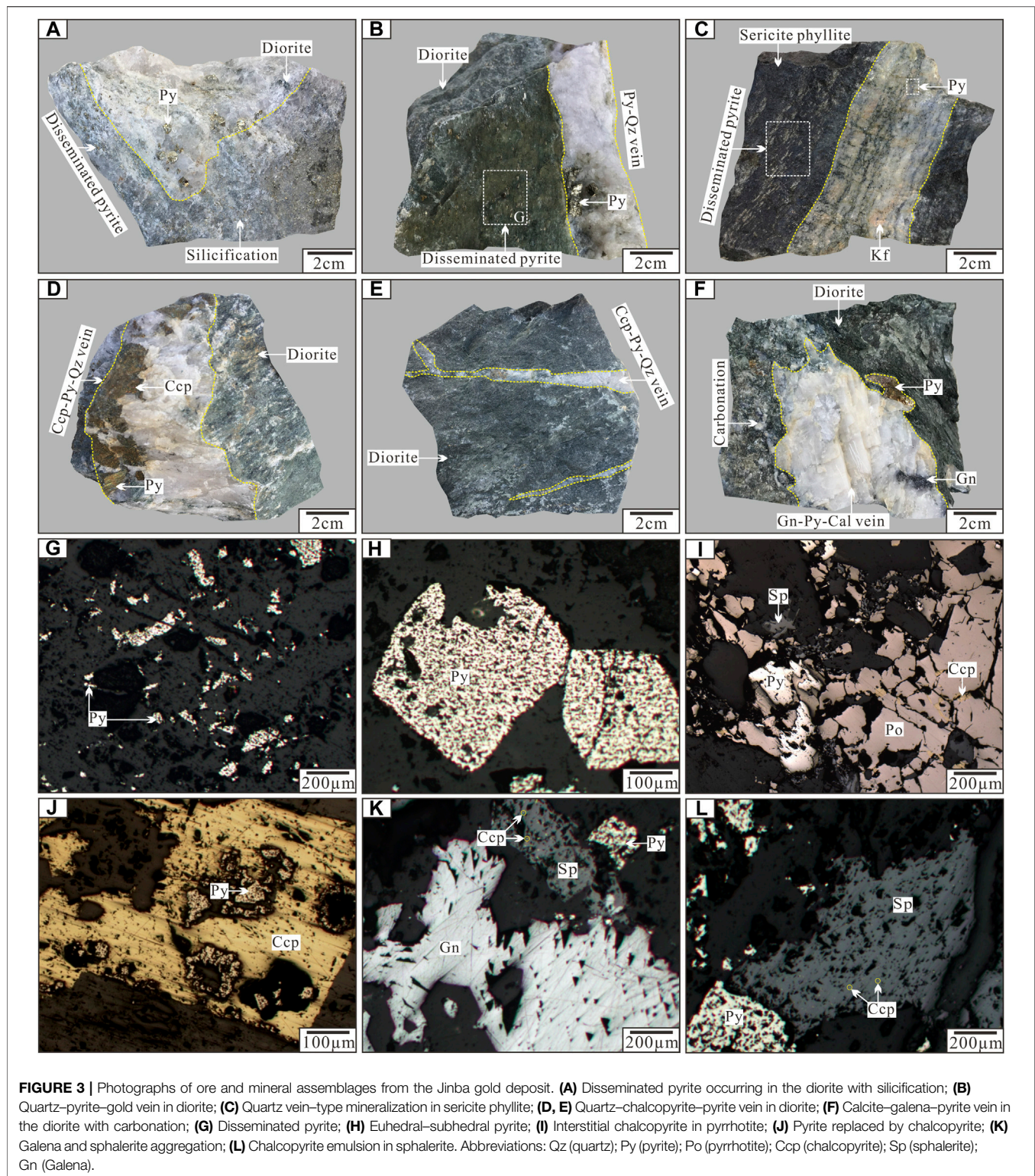
strata exposed in the mining area correspond to the Ashele Formation. Outcropping lithologies include metasandstone and sericite phyllite (**Figure 2A**). Dominant structures include NW–SE trending faults, along with minor NE–SW trending faults. The NW–SE trending faults were formed before or during mineralization, with some orebodies occurring along these faults. The NE–SW trending faults—which crosscut the orebodies—were formed after mineralization. Plagiogranite (Habahe Pluton), yielding zircon U–Pb ages of 406.3 ± 2.1 Ma (Li et al., 2012), is widely exposed in the northern part of the Jinba deposit. Granite and diorite, yielding zircon U–Pb ages of 384.5 ± 1.2 Ma and 393.9 ± 3.5 Ma (Gao, 2020), respectively, occur as dykes or stocks scattered across the deposit.

Six orebodies have been identified at the Jinba deposit prior to 2018 (Wang et al., 2018). Mineralization types are classified as altered rock– and quartz vein–type. The altered rock–type orebodies are comprised of altered diorite, and occur as veins or lenses, including orebodies I, II, III, and V (**Figure 2B**). Silicification, chloritization, epidotization and carbonation are common in diorite dykes and adjacent plagiogranite. Pyrite occurs in diorite as fine-grained crystals and disseminated veinlets (**Figures 3A,B,G**). Orebody I—which is the largest and has an average Au grade of 2.6 g/t—was selected as a representative example to study altered rock–type mineralization. This economically significant orebody is 120 m long with an average thickness of 1.8 m, striking $138\text{--}155^\circ$, and dipping $68\text{--}80^\circ$ NE (Wang et al., 2018).

Quartz vein–type orebodies, controlled by NW–trending faults, occur as veins, and are hosted in plagiogranite and sericite phyllite of the Ashele Formation. These include orebodies IV and VI (**Figure 2B**). There is a clear boundary between the ore veins and the surrounding rock (**Figure 3C**). The width of quartz veins varies from a few centimeters to several meters. Mineralization is also occasionally found in strongly fractured wall rocks along the edges of quartz veins. Wall rock alteration is characterized by silicification and potassic alteration. Orebody IV—with an average Au grade of 3.1 g/t—was selected as a representative example to study quartz vein–type orebodies. It is 140 m long with an average thickness of 1.7 m, striking $122\text{--}144^\circ$, and dipping $62\text{--}74^\circ$ NE (Wang et al., 2018).

Ore mineral assemblages mainly include pyrite, chalcopyrite, sphalerite, galena, and native Au, with minor pyrrhotite and gold telluride (calaverite). Gangue minerals include quartz, calcite, K-feldspar, biotite, sericite, chlorite, and epidote. The major ores of the deposit have a disseminated, vein, veinlet and stockwork structure. Ore microstructure is characterized by euhedral to subhedral grains, anhedral grains, emulsion and replacement textures (**Figures 3G–L**).

Based on the mineral assemblages, paragenetic sequences, and crosscutting relationships between ore veins, the following three stages of mineralization have been identified. Early-stage mineralization (stage 1), which is comprised of quartz–pyrite–gold veins, is widespread and accounts for most of the deposit's Au. Characteristic minerals of this stage are milky white quartz and pyrite with minor pyrrhotite



(Figures 3A,B,H–I). Euhedral pyrite is the most abundant ore mineral and varies in size from 0.2 mm up to 10 mm. Gold is observed between pyrite and quartz crystals, and is coeval with pyrite based on microstructural relationships. Intermediate-stage mineralization (stage 2) is characterized by quartz–chalcopyrite

veins with minor pyrite and gold (Figures 3D,E,J). Ore veins have straight boundaries and vary in size from 0.2 mm up to 5 mm. The content of Cu in the ore has no economic value for it is lower than the minimum industrial grade. Late-stage mineralization (stage 3) produced

TABLE 1 | Sample information of the Jinba gold deposit.

Sample no	Mineral	Stage	Host rock	Sampling position	Elevation (m)
J-01	Quartz	1	Quartz–pyrite–gold ore	ZK15-3	590
J-02	Quartz	1	Quartz–pyrite–gold ore	ZK15-3,	600
J-05	Quartz	1	Quartz–pyrite–gold ore	ZK15-2	455
J-08	Quartz	1	Quartz–pyrite–gold ore	Surface	650
J-10	Quartz	1	Quartz–pyrite–gold ore	ZK15-1	590
J-11	Quartz	1	Quartz–pyrite–gold ore	ZK15-1	605
J-15	Quartz	1	Quartz–pyrite–gold ore	ZK15-3	590
J-16	Quartz	2	Quartz–chalcopyrite ore	ZK15-2	450
J-22	Quartz	2	Quartz–chalcopyrite ore	ZK15-1	590
J-25	Quartz	2	Quartz–chalcopyrite ore	ZK15-1	605
J-30	Quartz	2	Quartz–chalcopyrite ore	ZK15-3	615
J-31	Quartz	2	Quartz–chalcopyrite ore	Surface	650
J-38	Quartz	3	Calcite–quartz–galena–sphalerite ore	ZK15-1	585
J-42	Quartz	3	Calcite–quartz–galena–sphalerite ore	ZK15-3	620
J-45	Quartz	3	Calcite–quartz–galena–sphalerite ore	ZK15-2	460
JB-1	Pyrite	1	Quartz–pyrite–gold ore	ZK15-3	590
JB-3	Pyrite	1	Quartz–pyrite–gold ore	ZK15-3	600
JB-5	Pyrite	1	Altered diorite	ZK15-2	450
JB-6	Pyrite	1	Quartz–pyrite–gold ore	Surface	650
JB-8	Pyrite	1	Altered diorite	Surface	650
JB-9	Pyrite	1	Quartz–pyrite–gold ore	ZK15-1	610

calcite–quartz–galena–sphalerite veins that contain small amounts of chalcopyrite and pyrite (**Figures 3F,K–L**). These veins have a limited distribution near the outer edge of the deposit, suggesting later formation within the mineralization sequence.

SAMPLES AND ANALYTICAL METHODS

Fresh ores were sampled from the drill holes (ZK15-1, ZK15-2, and ZK15-3) and surface outcrops in the Jinba deposit. Samples are divided into three groups: 1) Forty-six samples of quartz and calcite from stages 1–3 for FI petrography study. Fifteen representative quartz samples of the above were chosen for FI microthermometry. Ore-stage quartz and calcite occurred in assemblage with metallic minerals, indicating that the gangue and ore minerals were coeval; 2) Twelve quartz samples representative of mineralization stages 1–3 for H–O isotopic analyses; 3) Six pyrite samples from stage 1 for S–Pb isotopic analyses. Sulfides from stage 2 and 3 were not analyzed, since they held limited economic value and the pyrite was not abundant enough to be separated. Detailed sample information is shown in **Table 1**.

Fluid Inclusions

Forty-six samples of quartz and calcite were doubly polished to a thickness of 0.20–0.25 mm, soaked in acetone for 3–4 h, rinsed with clean water, and dried thoroughly. FI petrography involved careful observation of shapes, spatial distribution, genetic and compositional types, and vapor–liquid ratios. Fifteen samples with abundant and representative FIs were selected for microthermometric measurements.

FI analyses were carried out at the Geological Fluid Laboratory, Xinjiang University, Urumqi, China, using the

fluid inclusion assemblage (FIA) methodology of Goldstein and Reynolds (1994). An Olympus BX–50 microscope was used for petrographic analysis. Microthermometry was performed using a Linkam THMS600 heating–freezing stage with a temperature range of –196 to 600 °C. Calibration of the stage was completed using the following standards: pure water inclusions (0 °C), pure CO₂ inclusions (–56.6 °C), and potassium bichromate (398 °C). This yielded an accuracy of ±0.2 °C during freezing and ±2 °C for heating at temperatures between 100 and 600 °C. Salinities of NaCl–H₂O FIs were calculated using the final melting temperature of ice (Bodnar, 1993). For LC–type FIs, the salinities of the fluids were calculated on the basis of CO₂ clathrate melting temperatures in the NaCl–H₂O–CO₂ system (Roedder, 1984). FI density was calculated using the FIncor software (Brown, 1989). FI volatiles were analyzed using a Renishaw RM1000 Raman microprobe and an Ar ion laser. Operating conditions for the Raman microprobe were the following: surface power of 5 mW and exciting radiation of 514.5 nm; surface area of 20 μm² for the detector charge–coupled device; scanning range of 1,000–4,000 cm^{–1} for spectra; and an accumulation time of 30 s per scan.

H–O–C–S–Pb Isotopes

Quartz and pyrite grains of the different ore-forming stages were handpicked from crushed and sieved (40–60 mesh) samples under a binocular microscope (purity >99%). Isotope analyses of 6 pyrite samples and 12 quartz samples were performed on a MAT–253 mass spectrometer at the Analytical Laboratory of the Beijing Research Institute of Uranium Geology, China National Nuclear Corporation, Beijing, China. The analytical uncertainties in this study are <0.2‰.

Oxygen isotope analyses were performed on 10–20 mg quartz samples using the BrF₅ method of Clayton and Mayeda (1963), converted to CO₂ on a platinum–coated carbon rod. For

hydrogen isotope analyses, samples were placed under vacuum and heated at 150 °C for 3 h to degas labile volatiles. Water was released from FIs by heating to ~500 °C in an induction furnace, and then converted to H₂ through interaction with Zn powder at 410 °C (Friedman, 1953). Results of oxygen and hydrogen isotope analyses are reported in relation to Vienna Standard Mean Ocean Water (VSMOW). Prior to carbon isotopic analyses, quartz-hosted FIs (bearing trace amounts of carbon) were treated with H₃PO₄ at 50 °C for 24 h to generate CO₂ (Zhou et al., 2013). Results are reported as $\delta^{12}\text{C}$ with respect to the Pee Dee Belemnite standard (PDB). Sulfide isotopic analyses were carried out following the procedures of Robinson and Kusakabe (1975). Pyrite samples were reacted with Cu₂O to obtain pure SO₂. Results are reported as $\delta^{34}\text{S}$ relative to the Vienna Canyon Diablo Troilite standard (VCDT). Lead isotopic analyses were carried out following the procedures of Zhao et al., 2007. Pyrite samples were dissolved with concentrated HCl + HNO₃. A two-column AG 1-X8 anion resin method was then used to separate and purify the Pb. Data obtained were corrected using the ANBS-981 standard for analytical error correction.

RESULTS

Fluid Inclusions

Fluid Inclusion Petrography

FIs in stage 1–3 quartz grains were analyzed by microthermometry. The criteria of Roedder (1984) and Hollister and Burruss (1976) were used to distinguish different generations of FIs in hydrothermal quartz. FIs occurring as isolated inclusions, random distributions, or in clusters are interpreted as primary features (Goldstein and Reynolds, 1994; Goldstein, 2003). Each cluster or group of FIs along growth zones was considered to represent a FIA (Goldstein and Reynolds, 1994). FIs occurring in linear arrays along fractures or grain boundaries were considered to be secondary features. These secondary FIs were not analyzed by microthermometry, given the possibility that they formed later with respect to mineralization. Different types of FIs were recognized from their room-temperature phase relationships and phase transitions during heating and cooling and laser Raman microprobe analyses. Four types of FIs were identified using the classification of Shepherd et al. (1985): liquid-rich aqueous (LV-type), vapor-rich aqueous (VL-type), carbonic-aqueous (LC-type), and purely carbonic (C-type) FIs.

LV-type FIs consist of a water vapor bubble and a liquid water phase at room temperature (Figure 4A). These FIs are typically rectangular or elliptical and 5–15 μm in size. Vapor bubbles account for 10–25% of the total volume. These FIs are present in stages 2–3 and commonly occur as planar arrays restricted to the interior of quartz grains. However, some LV-type FIs fill microfractures in quartz, which indicated a secondary origin (Figure 4L).

VL-type FIs consist of liquid water with a vapor water bubble that accounts for 50–70% of the volume (Figure 4B). This type of FI is typically elliptical to sub-rounded and 8–12 μm in size. These FIs are only observed in stage 1 quartz grains.

LC-type FIs contain two phases (liquid H₂O + vapor CO₂) (Figure 4C) or three phases (liquid H₂O + liquid CO₂ + vapor CO₂) (Figure 4D) at room temperature. Two-phase LC-type FIs change into three-phase FIs with the appearance of vapor CO₂ when cooling around ~10 °C. The carbonic phase accounts for 30–70% of the total FI volume. This FI-type is usually circular or elliptical, 8–16 μm in size, and commonly observed in stages 1–2 quartz grains (absent in stage 3 samples).

C-type FIs consist of monophase CO₂ (mainly vapor) at room temperature (Figure 4E), which splits into two phases (liquid CO₂ + vapor CO₂) when cooling to 10 °C. These FIs are elliptical, appear as clusters or scattered, and are mostly less than 12 μm in size. C-type FIs commonly coexist with LC-type FIs in stage 1 quartz grains, which indicates fluid immiscibility (Lu et al., 2004).

Fluid Inclusion Microthermometry

Microthermometry was performed on FIs from 15 quartz samples of stages 1–3. Primary FIs with sizes >5 μm , regular shapes, and without evidence of necking (Roedder, 1984) were chosen for microthermometry (Table 2; Figure 5).

Stage-1 quartz veins contain LC-, C-, LV-, and VL-type FIs (Figures 4F–H), which account for about 60, 20, 10, and 10% of total primary FIs, respectively. The final melting temperatures of solid CO₂ in LC-type FIs range from –58.2 to –56.9 °C, slightly below the triple-phase point for pure CO₂ (–56.6 °C), indicating the presence of small amounts of CH₄ and/or N₂ (Lu et al., 2004). Final melting temperatures of clathrate are in the range of 7.3–8.8 °C, with corresponding salinities of 2.4–5.2 wt% NaCl equivalent, and CO₂ partial homogenization temperatures range between 25.4 and 30.2 °C. Most LC-type FIs decrepitated before homogenization during heating. Only part of the FIs with low vapor-liquid ratios achieved total homogenization. Total homogenization temperatures of these FIs to the liquid phase range from 376 to 406 °C. For C-type FIs, the final melting temperatures of solid CO₂ range from –58.2 to –57.1 °C. Final ice melting temperatures are in the range of –2.7 to –1.2 °C, corresponding to salinities of 2.1–4.5 wt% NaCl equivalent. FI homogenization to the vapor phase occurred at temperatures of 382–403 °C. Eutectic temperatures of LV-type FIs range from –25 to –22 °C. Final ice melting temperatures of FIs in stage 1 quartz grains range from –9.7 to –6.7 °C, corresponding to salinities of 10.1–13.6 wt% NaCl equivalent. Total homogenization of FIs to the liquid phase occurred at 373–399 °C.

Stage 2 quartz veins contain LC- and LV-type FIs (Figures 4I–K), which account for about 40 and 60% of total primary FIs, respectively. Final melting temperatures of solid CO₂ in LC-type FIs range from –58.1 to –56.8 °C. Final melting temperatures of clathrate range from 6.8 to 8.4 °C, with corresponding salinities of 3.2–6.1 wt% NaCl equivalent. CO₂ partial homogenization temperatures range from 25.9 to 29.8 °C. FIs were homogenized to the liquid phase at temperatures of 319–345 °C. Eutectic temperatures of LV-type FIs range from –25 to –23 °C. Final ice melting temperatures of these FIs in stage 2 quartz grains are in the range of –3.5 to –2.8 °C, corresponding to salinities of 3.7–5.7 wt% NaCl equivalent. Total homogenization of LV-type FIs to the liquid phase occurred at temperatures of 315–336 °C.

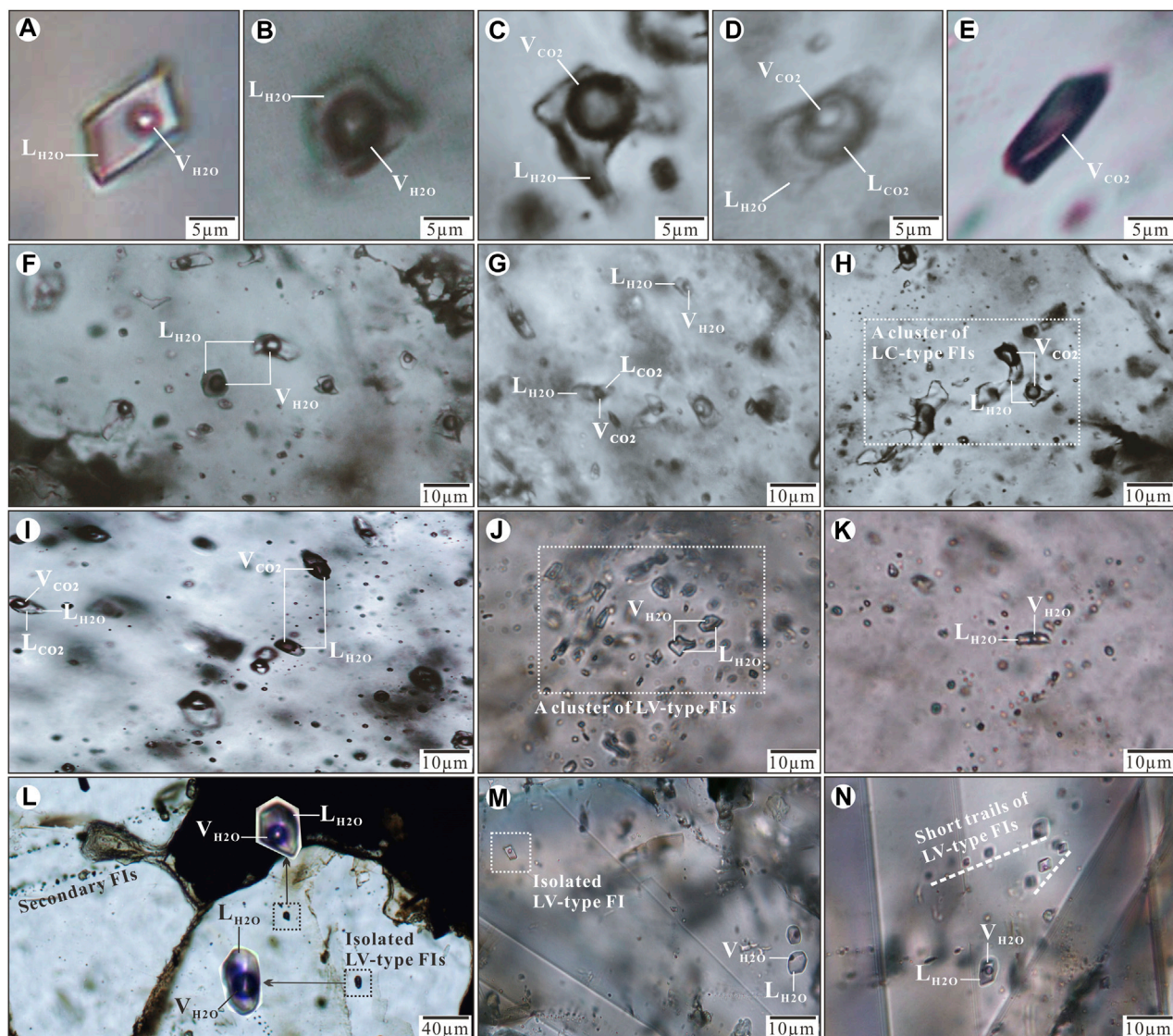


FIGURE 4 | Photomicrographs of FIs in quartz and calcite from stages 1–3 of the Jinba gold deposit. **(A)** LV-type FI; **(B)** VL-type FI; **(C)** Two phase LC-type FI; **(D)** Three phase LC-type FI; **(E)** monophasic C-type FI; **(F)** VL- and LV-type FIs in stage 1 quartz; **(G)** LV- and LC-type FIs in stage 1 quartz; **(H)** A cluster of two phase LC-type FIs in stage 1 quartz; **(I)** Two phase and three phase LC-type FIs in stage 2 quartz; **(J)** A cluster of two phase LV-type FIs in stage 2 quartz; **(K)** LV-type FIs in stage 2 quartz; **(L)** Primary isolated FI and secondary FIs in stage 3 quartz; **(M)** Isolated LV-type FI in stage 3 calcite; **(N)** Short trails of LV-type FIs in stage 3 calcite. Abbreviations: L_{H_2O} (liquid H_2O), V_{H_2O} (vapor H_2O), L_{CO_2} (liquid CO_2), V_{CO_2} (vapor CO_2).

Stage 3 quartz and calcite grains contain only LV-type FIs (**Figures 4L–N**). Eutectic temperatures of FIs range from -26 to -23°C . Homogenization to the liquid phase occurred at 237 – 265°C , and final ice melting happened at -3.7 to -2.3°C , corresponding to salinities of 3.9 – 6.0 wt% NaCl equivalent.

Laser Raman Microprobe Analysis

Typical FIs were selected for laser Raman analysis. Laser Raman spectroscopic detection revealed that the vapor phase in LC- and C-type FIs is dominated by CO_2 with minor CH_4 (**Figures 6A–C**). This is in agreement with our microthermometric results, which show that melting temperatures of solid CO_2

are slightly lower than 56.6°C . The vapor phase of LV-type FIs mainly contains H_2O (**Figure 6D**), with minor CO_2 , which is not consistent with any CO_2 phase transition in FIs. The fluid system evolved from a CO_2 -rich fluid to an aqueous solution end-member.

Oxygen, Hydrogen, and Carbon Isotopes

Isotopic data for 12 quartz samples representing mineralization stages 1–3 of the Jinba deposit are listed in **Table 3**.

Data ranges are the following: $\delta^{18}O_{qz} = 10.2\text{‰}$ – 12.5‰ , $\delta D_{fluid} = -104.1\text{‰}$ – -91.7‰ , $\delta^{13}C_{fluid} = -0.4\text{‰}$ – 6.3‰ (**Table 3**). Values for $\delta^{18}O_{fluid}$ (1.7‰ – 8.1‰) were calculated using the following

TABLE 2 | Microthermometric data from FIs in hydrothermal quartz of the Jinba gold deposit.

Sample	Host mineral	FIA	Number	Gas-liquid ratio	T_m , CO ₂ (°C)	T_e , (°C)	T_m , CO ₂ (°C)	T_m , cal (°C)	T_h , CO ₂	Salinity (NaCl wt%)	T_h , fluid (°C)	ρ , g/cm ³
J-01	Quartz from stage 1	C	5	> 95	–58.2 to –57.1		28.3–29.2					0.64–0.66
J-02		C	3	> 90	–58.0 to –57.2		28.4–29.5					0.63–0.66
		LC	8	30–40	–57.8 to –57.0			7.6–8.3	25.7–28.9	3.4–4.7	388–406	0.65–0.70
J-05		LC	10	30–40	–57.8 to –56.9			7.5–7.9	26.3–29.4	4.1–4.9	382–403	0.63–0.70
J-08		LC	9	50–60	–58.2 to –57.0			7.5–8.8	26.9–30.2	2.4–4.3	381–399	0.61–0.69
J-10		LC	12	20–30	–58.1 to –56.9			7.3–8.1	25.4–29.2	3.8–5.2	376–402	0.64–0.71
J-11		VL	4	50–70		–25 to –22	–2.7 to –1.2			2.1–4.5	382–403	0.55–0.57
J-15		LV	15	10–20		–25 to –23	–9.7 to –6.7			10.1–13.6	373–399	0.71–0.72
J-16	Quartz from stage 2	LC	12	30–40	–57.7 to –56.8			6.8–8.4	25.9–29.8	3.2–6.1	322–345	0.62–0.70
J-22		LC	10	20–30	–58.1 to –57.0			7.6–8.2	26.7–28.6	3.6–4.7	319–341	0.53–0.69
J-25		LV	3	15–25			–2.8 to –3.3			4.6–5.4	328–335	0.70–0.71
J-30		LV	16	15–25			–2.2 to –3.1			3.7–5.1	321–333	0.70–0.71
J-31		LV	10	10–20			–2.5 to –3.5			4.2–5.7	315–336	0.70–0.72
J-38	Quartz from stage 3	LV	16	15–20			–2.9 to –3.7			4.8–6.0	238–263	0.83–0.85
J-42		LV	12	15–20			–2.3 to –3.4			3.9–5.6	237–265	0.82–0.85
J-45		LV	9	10–15			–2.8 to –3.2			4.6–5.4	242–261	0.83–0.85

FIA -fluid inclusion assemblage; C, LC, LV and VL -fluid inclusion types; T_m , CO₂ -final solid CO₂ melting temperatures; T_m , ice -final ice melting temperature; T_m , cal -melting temperature of clathrate; T_h , CO₂ -partial homogenization temperature of CO₂; T_h , fluid—total homogenization temperature; T_e -eutectic temperatures.

equation: $1000\ln\alpha_{\text{qz-water}} = 3.38 \times 10^6 T^{-2} - 3.4$ (Clayton et al., 1972). Since our homogenization temperature data plot within a narrow range and correspond to the minimum trapping temperatures, we selected the highest homogenization temperature value as an estimate of the trapping temperature. The carbon isotope data obtained are unique, being the first C isotopes measured in the vapor phase of FIs from hydrothermal quartz of stages 1–3 of the Jinba deposit.

Sulfur and Lead Isotopes

S and Pb isotope compositions of 6 pyrite samples are listed in Table 4. $\delta^{34}\text{S}$ values in pyrite range from 3.3 to 5.3‰, with an average value of 4.4‰ ($n = 6$). Pb isotope compositions in pyrite yielded $^{206}\text{Pb}/^{204}\text{Pb}$ ratios of 17.912.3 to 18.495, with an average of 18.194; $^{207}\text{Pb}/^{204}\text{Pb}$ ratios of 15.564–15.590, with an average of 15.579; and $^{208}\text{Pb}/^{204}\text{Pb}$ ratios of 37.813–38.422, with an average of 38.083.

DISCUSSION

Sources of Ore-forming Materials

$\delta^{34}\text{S}$ values for 6 pyrite samples from stage 1 mineralization range from 3.9‰ to 5.3‰. The stage 1 quartz–pyrite–gold assemblage shows reduced $f\text{O}_2$ and consequently low $\text{SO}_4^{2-}/\text{H}_2\text{S}$ ratios (Bastrakov et al., 2007). Pyrite $\delta^{34}\text{S}_{\text{H}_2\text{S}}$ values are therefore consistent with fluid $\Sigma\delta^{34}\text{S}$ values. Calculated equilibrium

$^{34}\text{S}_{\text{H}_2\text{S}}$ values range from 2.4‰ to 4.4‰ (average = 3.5‰) using the following formula: $A \times 10^6 / T^2 = \delta^{34}\text{S}_{\text{VCDT}} - \delta^{34}\text{S}_{\text{H}_2\text{S}}$ (Ohmoto and Goldhaber, 1997) (T = mineralization temperature, $A_{\text{pyrite}} = -0.40$). We consider that such a narrow range of $\delta^{34}\text{S}$ in fluid H_2S has a deep origin and is probably derived from mantle or lower crust (Ohmoto and Rye, 1979). The $\delta^{34}\text{S}$ values of sulfides from gold deposits in the Maerkaluli Shear Zone are generally low positive (Figure 7A). These data are similar to the $\delta^{34}\text{S}$ values of sulfides from the majority of OGDs (Figure 7B), such as Bendigo gold deposit in Australia (1.4 to 9.3‰, Bierlein et al., 2004), Awanda gold deposit in China (–3.6 to 6.2‰, Ding et al., 2014) and Cononish gold deposit in Scotland (–2.0 to 11.4‰, Spence-Jones et al., 2018). The sources of sulfur for OGDs are commonly considered derived from host wall rocks (Kerrick et al., 2000; Chen et al., 2001). If the sulfur in wall rocks comes from deep source, the sulfur isotopes will not change significantly during the mineralization process. We speculate that sulfur from the deeper source rocks to be subsequently concentrated by metamorphism and hydrothermal processes, forming Jinba gold deposits at higher crustal levels (Large et al., 2011).

Pb isotopic compositions can also constrain ore deposit material sources (Bierlein and McNaughton, 1998). Pb isotopic data for pyrite samples from the Jinba gold deposit show values of 17.912–18.495 for $^{206}\text{Pb}/^{204}\text{Pb}$, 15.564–15.590 for $^{207}\text{Pb}/^{204}\text{Pb}$, and 37.813–38.422 for $^{208}\text{Pb}/^{204}\text{Pb}$ (Table 4). These values indicate that the samples are relatively rich in uranogenic Pb,

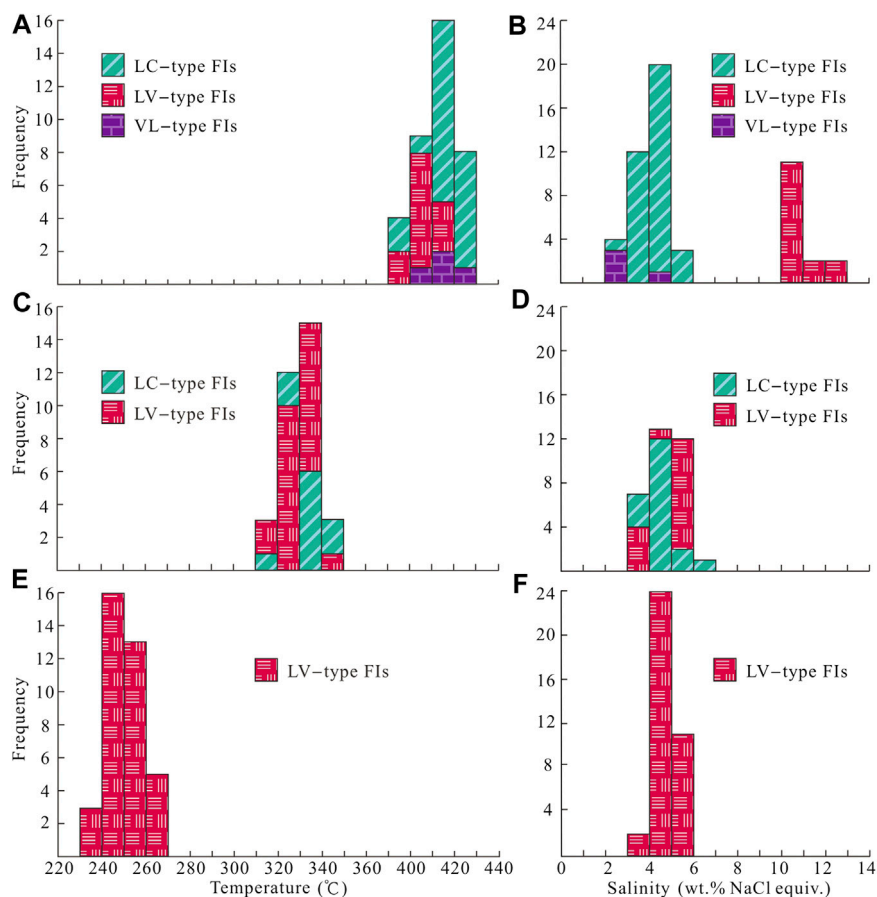


FIGURE 5 | Histograms of microthermometric data for FIs in quartz of the Jinba gold deposit. **(A)** Homogenization temperatures for LC-, VL- and LV-type FIs of stage 1. **(B)** Salinity for LC-, VL- and LV-type FIs of stage 1. **(C)** Homogenization temperatures for LC- and LV-type FIs of stage 2. **(D)** Salinity for LC- and LV-type FIs of stage 2. **(E)** Homogenization temperatures for LV-type FIs of stage 3. **(F)** Salinity for LV-type FIs of stage 3.

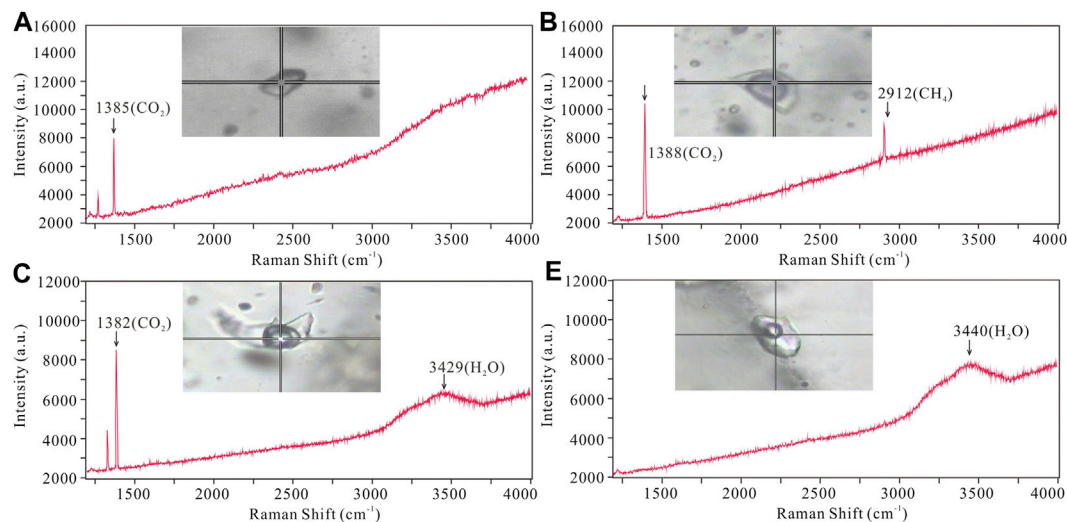


FIGURE 6 | Representative Raman spectra of FIs from the Jinba gold deposit. **(A)** C-type FI showing major CO₂ peak; **(B)** Two phase LC-type FI showing major CO₂ with minor CH₄ peak; **(C)** Three LC-type FI showing major CO₂ peaks; **(D)** LV-type FI showing major H₂O peak.

TABLE 3 | Oxygen, hydrogen, and carbon isotope data from hydrothermal quartz, stages 1–3 of the Jinba gold deposit.

Sample no	Stage	Mineral	$\delta^{18}\text{O}_{\text{qtz}}/\text{‰}$	$\delta\text{D}_{\text{fluid}}/\text{‰}$	T_h (°C)	$\delta^{18}\text{O}_{\text{fluid}}/\text{‰}$	$\delta\text{C}_{\text{fluid}}/\text{‰}$
J-05	1	Quartz	12.0	−91.7	406	8.1	6.3
J-08	1	Quartz	11.5	−95.6	406	7.6	5.9
J-10	1	Quartz	11.7	−92.5	406	7.8	4.2
J-11	1	Quartz	10.8	−94.3	406	6.9	3.7
J-16	2	Quartz	11.9	−99.9	345	6.5	3.8
J-22	2	Quartz	10.7	−101.4	345	5.3	3.3
J-25	2	Quartz	11.6	−102.7	345	6.2	1.9
J-30	2	Quartz	11.3	−97.3	345	5.9	1.7
J-38	3	Quartz	11.3	−101.6	265	3.0	1.9
J-42a	3	Quartz	12.3	−103.5	265	4.0	0.6
J-42b	3	Quartz	10.6	−100.6	265	2.3	1.2
J-45	3	Quartz	10.0	−104.1	265	1.7	−0.4

and poor in thorogenic Pb. Pb isotopic data for the samples plot close to the orogenic growth line on both the uranium and thorogenic plots, which suggests that the formation of the deposit was closely related to orogenic activity (Stacey and Kramers, 1975; Doe and Zartman, 1979). We interpret these data to reflect a hybrid crustal–mantle lead source. In addition, the Pb isotope data show a linear distribution on the uranium and thorogenic plots (Figures 8A,B). This trend suggests a mixture of two end-members components (Ding et al., 2014). One end-member must be highly radiogenic, and the other end-member must be less radiogenic. The highly radiogenic end-member is similar to the plagiogranite (Habahe Pluton) reservoir (Figure 8B), and possibly represented by magmatic rocks formed under sulfidic oxidizing condition. The less radiogenic end-member might correspond to the Ashele Formation reservoir (Figure 8B), and possibly represented by sedimentary strata with organic matter formed under nonsulfidic anoxic condition. Similar Pb isotope compositions are found in ore and diorite, suggesting the same source of Pb.

In terms of ore content, geochemical analyses for regional lithologic units indicate that the Ashele Formation, plagiogranite (Habahe Pluton) and diorite have average Au contents of 6.02, 9.45, and 11.90 ppb, respectively (Xiao et al., 2003). The Au contents of the Ashele Formation, Habahe Pluton, and diorite are much higher than the crustal abundance of Au (1.10 ppb).

Thus, the ore-forming material sources of the Jinba gold deposit were mostly diorite and Ashele Formation rocks, with minor contamination from the Habahe Pluton.

Source and Evolution of Hydrothermal Fluids

The FI microthermometric data obtained—as well as the presence of different types of FIs in gangue minerals from stages 1–3 of the Jinba gold deposit—highlight distinct changes in the hydrothermal system with time. In addition, we have identified the influence of at least two types of source fluids with contrasting composition and temperature. In this section, we analyze the hypothesis involving hydrothermal source fluids with different origins using H, O, and C isotope data.

Stage 1 samples plot below the box representing primary magmatic and metamorphic water on the δD vs $\delta^{18}\text{O}$ plot (Figure 8C). Eutectic temperatures of LV-type FIs range from −26 to −23 °C, indicating that the fluids were dominated by NaCl solutions with other minor components (such as MgCl_2 or KCl). FI microthermometric and laser Raman spectroscopic data suggest that the ore-forming fluids can be estimated as a $\text{H}_2\text{O}-\text{CO}_2-\text{NaCl} \pm \text{CH}_4$ system; which is different from a fluid exsolved from a magma with high salinity and low CO_2 content. These features are typical of metamorphic fluids as reported in many research studies (Phillips and Powell, 2015; Martinek, et al., 2016). In addition, chronological data (Li et al., 2012; Gao, 2020) show that intrusions such as the Habahe Pluton (406.3 ± 2.1 Ma), granite intrusions (393.9 ± 3.5 Ma), and diorite intrusions (384.5 ± 1.2 Ma) exposed in the mining area were all emplaced before gold mineralization (300–270 Ma) in the region (Li et al., 2007; Deng, 2011). These intrusions may provide the ore-forming materials required, however, the source of ore-forming fluids were derived from elsewhere. Carbon isotope data for FIs in quartz veins are also useful to determine the source of ore-forming fluids. The limited variation of $\delta^{13}\text{C}_{\text{fluid}}$ values ($\delta^{13}\text{C}_{\text{fluid}} = 3.7\text{--}6.3\text{‰}$) for stage 1 indicates a single source of metamorphic CO_2 (Figure 7C). CO_2 and CH_4 may have been produced from carbonaceous sediments during metamorphism through the following reaction: $2\text{C} + \text{H}_2\text{O} = \text{CO}_2 + \text{CH}_4$ (Roedder, 1984). In contrast, O–H isotope data for paragenetically younger stage 2 quartz define a trend toward the meteoric water line (Figure 8C). $\delta^{13}\text{C}_{\text{fluid}}$ values ($\delta^{13}\text{C}_{\text{fluid}} = 1.7\text{--}3.8\text{‰}$) for stage 2 reveal a mixed source of metamorphic CO_2 and meteoric CO_2 (Figure 7C). Stage 2 samples are characterized by the appearance of vast LV-type FIs and decreased LC-type FIs, as well as absent C- and VL-type FIs. Two sources of fluid have been inferred: 1) inherited $\text{CO}_2-\text{H}_2\text{O}-\text{NaCl}$ fluids, and 2) foreign $\text{H}_2\text{O}-\text{NaCl}$ fluids. LC-type FIAs were inherited from the earlier stage, while the

TABLE 4 | Sulfur and lead isotope data for pyrite from the Jinba gold deposit.

Sample no	Mineral	Stage	$\delta^{34}\text{S}_{\text{py}}/\text{‰}$	$\delta^{34}\text{S}_{\text{H}_2\text{S}}/\text{‰}$	T_h (°C)	$^{206}\text{Pb}/^{204}\text{Pb}$	$^{207}\text{Pb}/^{204}\text{Pb}$	$^{208}\text{Pb}/^{204}\text{Pb}$
JB-1	Pyrite	1	5.3	4.4	405	17.912	15.564	37.813
JB-3	Pyrite	1	5.1	4.2	405	18.314	15.585	38.207
JB-5	Pyrite	1	3.3	2.4	405	18.261	15.576	38.083
JB-6	Pyrite	1	4.6	3.7	405	18.143	15.579	38.045
JB-8	Pyrite	1	3.7	2.8	405	18.038	15.578	37.928
JB-9	Pyrite	1	4.2	3.3	405	18.495	15.590	38.422

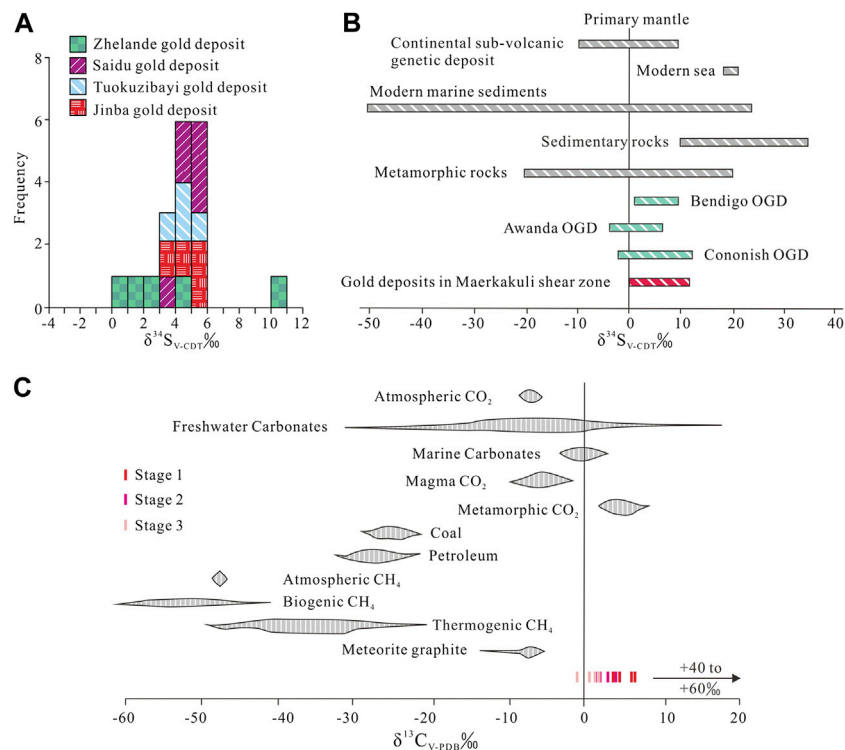


FIGURE 7 | (A) Histogram showing $\delta^{34}\text{S}$ values of pyrites from gold deposits in Maerkakuli Shear Zone (data from Xu et al., 2009; Deng, 2011; Zhan et al., 2016; Gao, 2020). **(B)** $\delta^{34}\text{S}$ values from pyrites of gold deposits in Maerkakuli Shear Zone compared to the values in important geological reservoirs (data from Ohmoto and Goldhaber, 1997; Bierlein et al., 2004; Ding et al., 2014; Spence-Jones et al., 2018). **(C)** $\delta^{13}\text{C}$ values from quartz of the Jinba gold deposit compared to the values in important geological reservoirs (data from Clark and Fritz, 1997).

occurrence of vast LV-type FIAs provides important evidence of meteoric water mixing. The mixing of metamorphic water with meteoric water caused phase separation of CO_2 fluids, resulting in the release of a large amount of CO_2 gas phase components. With temperature reduction and pressure release, VL-type inclusions were recondensed into LV-type inclusions (Heinrich et al., 2004). On the other hand, stage-3 samples plot closer to the meteoric water line (Figure 8C) and the meteoric CO_2 field (Figure 7C), and only LV-type FIAs are present. These characteristics may suggest an increasing meteoric-water influence over time. In summary, based on FI and H-O-C isotope data, the ore-forming fluids that sourced the Jinba gold deposit may have an initial metamorphic origin, followed by the introduction of meteoric water.

δD values for quartz of stages 1–3 are lighter than metamorphic water δD (Ohmoto, 1972), and plot beneath the range of metamorphic water (plotted alongside calculated $\delta^{18}\text{O}_{\text{H}_2\text{O}}$ values). Low and/or variable δD values of quartz samples may result from magmatic degassing, fluid boiling, fluid mixing, or water-rock interaction. 1) Magmatic degassing can produce wide ranges of δD values through fractionation (Li et al., 2017). However, the ore-forming fluids in the Jinba deposit have an initial metamorphic origin, followed by the introduction of meteoric water. There is no magmatic water involved in the mineralization system, excluding the impact of magmatic degassing. 2) Fluid boiling can influence H isotopic

composition, since vapor separation results in a relative depletion of δD in the remaining ore-forming fluid (Koděra et al., 2005). Abundant vapor-rich aqueous (VL-type) FIAs and/or high salinity brine FIAs are commonly trapped during the process of fluid boiling (Goldstein, 2003). However, in the case of the Jinba deposit, only minor VL-type FIAs were trapped and high salinity brine FIAs were absent in quartz grains. These characteristics reflect no obvious fluid boiling occurred during mineralization process. 3) Meteoric water has a low δD value (Taylor, 1974), and mixing of metamorphic water and meteoric water could explain the δD depletion observed in the present study. From stage I to III, the δD values define a downward trend (Figure 8C), which may reflect the increasing contribution of meteoric water to the system over time. 4) Water-rock interaction is widespread in Jinba mine confirmed by the occurrence of disseminated pyrite in the wall rocks (Figures 3A–C) and the isotope studies. The ore-forming fluid exchanged ^{13}C , ^{34}S , D, and Pb isotopes, as well as Au and Fe, among other elements, with the wall rocks. During this process, mixture of secondary or primary FIAs from devolatilization of organic matter in wall rocks can contribute to apparently lighter bulk δD values of quartz (Taylor, 1974; Sheppard, 1986). Thus, we suggest that fluid mixing and water-rock interaction may be the most likely factors for the δD depletion.

The ore-forming fluids of the Jinba gold deposit belong to the $\text{H}_2\text{O}-\text{CO}_2-\text{NaCl} \pm \text{CH}_4$ system. Temperatures and pressures can

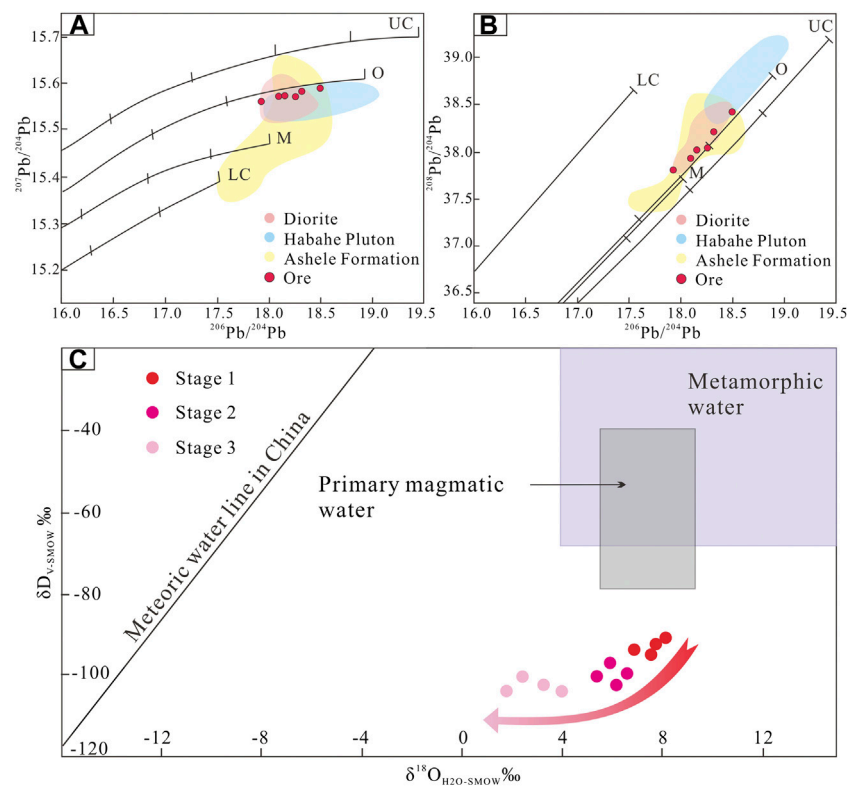


FIGURE 8 | (A) $^{207}\text{Pb}/^{204}\text{Pb}$ vs. $^{206}\text{Pb}/^{204}\text{Pb}$ plot and **(B)** $^{208}\text{Pb}/^{204}\text{Pb}$ vs. $^{206}\text{Pb}/^{204}\text{Pb}$ plot for sulfides in the Jinba gold deposit and associated host rocks. The average growth curve is from Zartman and Doe (1981). **(C)** Diagram showing δD vs. $\delta^{18}\text{O}$ for quartz, representing different stages of mineralization in the Jinba gold deposit.

be determined by using the P–T diagram of C-type and coeval LV-type FIs (Roedder and Bodnar, 1980). We obtained temperatures of 373–406 °C and pressures of 1,020–1,320 bars, which correspond to depths of 3.8–4.9 km (lithostatic pressure) (Figure 9).

Genesis and Metallogenic Model for the Jinba Deposit

The Jinba gold deposit shares many characteristics of typical OGDs. 1) Firstly, the deposit was formed near the Irtysh Fault Zone in the Altay collisional orogenic belt and is controlled by the second-order Maerkakuli Shear Zone. 2) In addition, orebodies were formed in the greenschist facies, with alteration combinations such as carbonation, sericitization and chloritization. 3) Ore-forming fluids evolved from the $\text{CO}_2\text{--NaCl--H}_2\text{O} \pm \text{CH}_4$ system to the $\text{NaCl--H}_2\text{O}$ system. 4) The ore has a low sulfide content. 5) Veins were generally formed at medium to low pressures (1–5 kbar) and at low to medium temperatures (200–600 °C), corresponding to depths of 3–20 km (Groves, 1993).

Maerkakuli Shear Zone is an important gold concentration area in the Altay Orogenic Belt. More than 50 t gold reserves have been proved in the region. Typical gold deposits include Tuokuzibayi (reserves 20.7 t @ 3.81 g/t gold), Saidu (reserves 2.4 t @ 4.61 g/t gold),

Zhelande (reserves 3.6 t @ 3.62 g/t gold) and Jinba gold deposit. These deposits are all emplaced in Devonian strata and within the Maerkakuli Shear Zone (Figure 1B), which is controlled by NW-trending faults. They all have similar mineralization types (quartz vein + altered rock types), mineral assemblages, fluid character, and isotope composition (Table 5); suggesting the same geodynamic setting and metallogenic timing. There is no accurate mineralization age data for the Jinba gold deposit to date. However, a lot of chronological data has been reported for other gold deposits in the region. The interpreted age of gold mineralization is based on Rb–Sr, K–Ar, and Ar–Ar ages of alteration minerals and FIs in ore-bearing quartz veins (Li and Chen, 2004; Yan et al., 2004; Li et al., 2007; Deng, 2011; Liu et al., 2018). Mineralization in the region is interpreted to have occurred between ca. 300 and 270 Ma with a peak value of ~290 Ma, which is consistent with the period of orogenic events in the region during the Late Carboniferous–Early Permian.

In the Late Carboniferous–Early Permian, the ancient Asian Ocean closed and the Junggar–Kazakhstan Plate collided with the Siberian Plate (Xiao et al., 2009; Kröner et al., 2013). Sedimentary terranes folded due to orogenic processes and produced a large-scale northwest-trending left-slip ductile shear zone (Xu et al., 2009; Zhan et al., 2016). Dehydration of the surrounding metalliferous and organic-bearing metasedimentary rocks in the deep source could have generated CO_2 -rich metamorphic fluids (Ding et al., 2014).

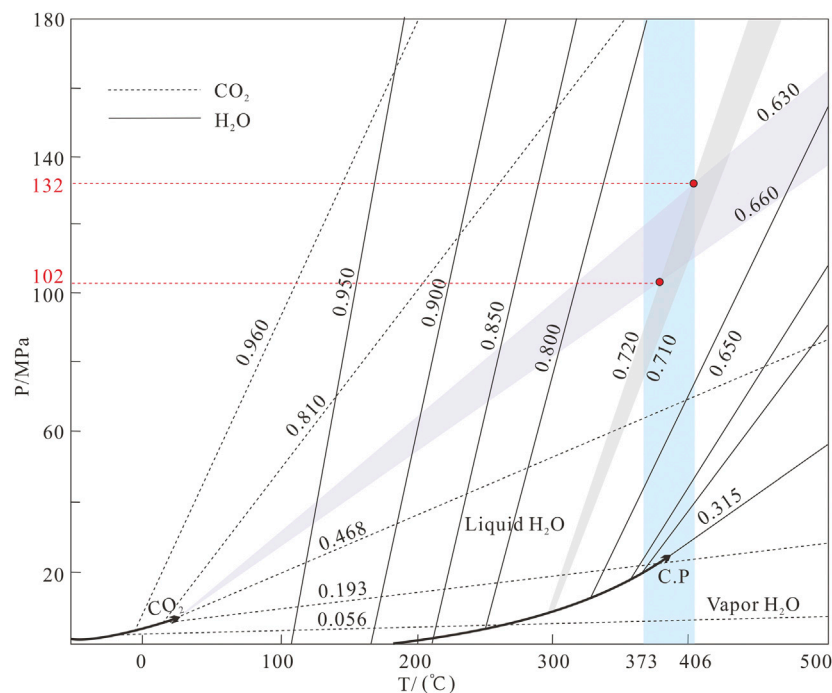


FIGURE 9 | Pressure estimates for FIs of the Jinba gold deposit (after Roedder and Bodnar, 1980).

TABLE 5 | Comparison of general features of gold deposits in the Maerkaluli Shear Zone.

Features	Tuokuzibayi deposit	Saidu deposit	Zhelande deposit	Jinba deposit
Host rocks	Metamorphic sandstone, sericite phyllite, metamorphic quartz siltstone of the devonian tuokesalei formation; plagiogranite of habahe pluton	Metamorphic sandstone, sericite phyllite and volcanic rocks of the devonian tuokesalei formation; plagiogranite of habahe pluton	Metamorphic sandstone and sericite phyllite of the devonian tuokesalei formation; plagiogranite of habahe pluton	Phyllite of the devonian ashele formation; plagiogranite of habahe pluton
Structural style	NW–SE trending shear zone, brittle–ductile faults	Brittle–ductile faults, strike–slip faults	Folds, brittle–ductile faults	NW–SE trending brittle–ductile faults, strike–slip faults
Ore minerals	Native gold, pyrite, chalcopyrite, pyrrhotite, galena, sphalerite, magnetiteetc.	Native gold, pyrite, chalcopyrite, galena, sphaleriteetc.	Native gold, pyrite, chalcopyrite, galena, sphalerite, magnetite, ilmenite, calaveriteetc.	Native gold, pyrite, chalcopyrite, sphalerite, galena, pyrrhotite, calaveriteetc.
Alteration of wall rock	Silicification, sericitization and chloritization	Silicification, sericitization, chloritization and carbonation	Silicification, sericitization and chloritization	Silicification, chloritization, epidotization, carbonation and potassic alteration
Fluid property	NaCl–H ₂ O–CO ₂	NaCl–H ₂ O–CO ₂ –N ₂	NaCl–H ₂ O–CO ₂ ±CO	NaCl–H ₂ O–CO ₂ ±CH ₄
Homogenization temperatures	191–324 °C	252–408 °C	191–325 °C	237–406 °C
Salinities	6.0 to 9.4 wt% NaCl equivalent	0.4 to 9.9 wt% NaCl equivalent	6.0 to 9.2 wt% NaCl equivalent	2.1 to 13.6 wt% NaCl equivalent
δD of fluid	–126.3 to –79.0‰	–126.3 to –107.0‰	–127.5 to –103.0‰	–104.1 to –91.7‰
δ ¹⁸ O of fluid	–9.2 to 6.3‰	–0.2–6.3‰	–0.3–6.2‰	1.7–8.1‰
δ ³⁴ S of sulfides	0.5–5.6‰	3.5–5.9‰	0.3–10.9‰	3.3–5.3‰
References	Li et al. (2007), Zheng et al. (2010), Zhan et al. (2016), Gao (2020)	Xu et al. (2009), Mi et al. (2010)	Deng (2011), Xue (2018)	This study

Gold, sulfur, lead and other ore-forming elements found in the wall rocks was mobilized and migrated by the metamorphic fluid along the Maerkakuli Shear Zone (Figure 10). A large number of ductile and brittle structures formed during the process of regional shear deformation. The shallow brittle structures provided a channel for

the upward migration of ore-forming fluids and downward-flowing meteoric water (Sibson et al., 1988). Upon reaching these structures, depressurization and fluid mixing changed the physicochemical conditions and composition of the ore-forming fluids, depositing ore-forming elements rapidly (Houghton et al., 2004), and

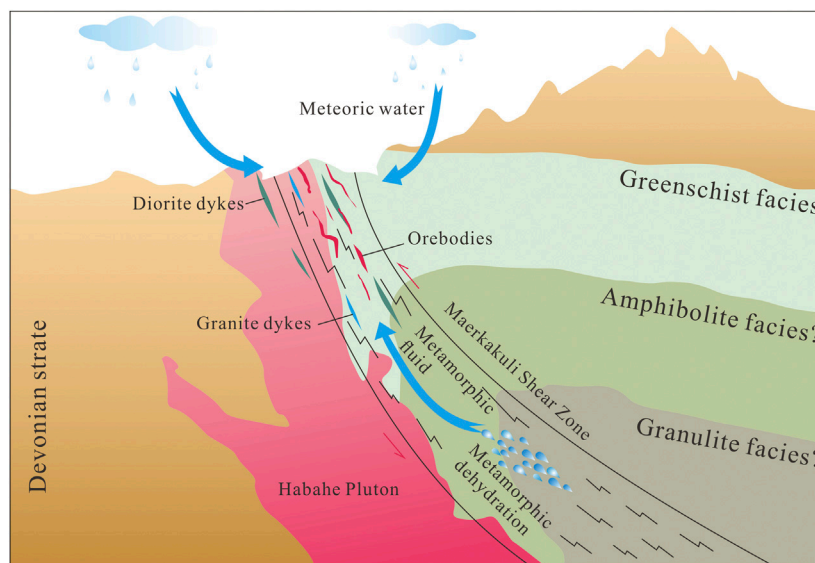


FIGURE 10 | Metallogenic model of the Jinba gold deposit.

thus resulting in intensive mineralization in the area of the Jinba mine.

CONCLUSION

- (1) The ore-forming fluids of the Jinba gold deposit evolved from medium temperature, middle-low salinity, $\text{NaCl-H}_2\text{O-CO}_2 \pm \text{CH}_4$ fluids to low temperature, low salinity, $\text{NaCl-H}_2\text{O}$ fluids. These fluids were initially derived from metamorphic water, followed by the addition of meteoric water.
- (2) The ore-forming materials of the Jinba gold deposit were most likely derived from diorite and rocks of the Ashele Formation, with some influence from the Habahe Pluton.
- (3) Based on the mineralization characteristics, source, and the evolution of ore-forming fluids and materials, we conclude that Jinba corresponds to an orogenic gold deposit.

DATA AVAILABILITY STATEMENT

The original contributions presented in the study are included in the article/Supplementary Material, further inquiries can be directed to the corresponding author.

REFERENCES

Ayer, J. A., Thurston, P. C., and Lafrance, B. (2008). A special issue devoted to base metal and gold metallogeny at regional, camp, and deposit scales in the Abitibi Greenstone belt: preface. *Econ. Geol.* 103 (6), 1091–1096. doi:10.2113/gsecongeo.103.6.1091

AUTHOR CONTRIBUTIONS

S-DL, CC, and K-YW designed the model and wrote the manuscript. S-DL, FX, L-LG, and X-BZ conducted the experiments. S-DL managed and directed the project. All authors contributed to the article and approved the submitted version.

FUNDING

This work was supported by the Natural Science Foundation of the Xinjiang Uygur Autonomous Region (Project no. 2020D01C075).

ACKNOWLEDGMENTS

We are grateful to Liu for his assistance with stable isotope analyses and chromatography analyses at the Analytical Laboratory of the Beijing Research Institute of Uranium Geology. Anonymous reviewers are thanked for their constructive comments and reviews regarding the manuscript, as well as Changzhi Wu for editorial handling.

- Bastrakov, E. N., Skirrow, R. G., and Davidson, G. J. (2007). Fluid evolution and origins of iron oxide Cu-Au prospects in the olympic dam district, gawler Craton, south Australia. *Econ. Geol.* 102, 1415–1440. doi:10.2113/gsecongeo.102.8.1415
- Bierlein, F. P., Arne, D. C., and Cartwright, I. (2004). Stable isotope (C, O, S) systematics in alteration haloes associated with orogenic gold mineralization in the Victorian gold province, SE Australia. *Geochem. Explor. Environ. Anal.* 4, 191–211. doi:10.1144/1467-7873/04-201

- Bierlein, F. P., and McNaughton, N. J. (1998). Pb isotope fingerprinting of mesothermal gold deposits from central Victoria, Australia: implications for ore genesis. *Miner. Deposita* 33, 633–638. doi:10.1007/s001260050178
- Bodnar, R. J. (1993). Revised equation and table for determining the freezing point depression of H₂O–NaCl solutions. *Geochem. Cosmochim. Acta* 57, 683–684. doi:10.1016/0016-7037(93)90378-a
- Brown, P. E. (1989). FLINCOR: a microcomputer program for the reduction and investigation of fluid inclusion data. *Am. Mineral.* 74, 1390–1393.
- Chen, H. Y., Chen, Y. J., and Liu, Y. L. (2001). Metallogenetic process of the Ergis gold ore belt in Xinjiang and relationship with the Central Asian orogeny. *Science in China (Series D)* 30, 38–44 [In Chinese with English abstract].
- Chen, K. Q., Dang, Y. X., Dong, Y. G., and Ding, R. F. (2010). Zircon U–Pb age of the Au-bearing quartz veins in Saidu gold deposit and its geological implications. *Miner. Explor.* 1 (3), 229–233 [In Chinese with English abstract].
- Chen, Y. C., Ye, Q. T., and Wang, J. B. (2003). *Geological, metallogenetic regularity and technical economic evaluation of the ore deposit in the Altai ore belt, Xinjiang*, Beijing, China: Geological Publishing House, 190–216 [In Chinese with English abstract].
- Clark, I. D., and Fritz, P. (1997). *Environmental isotopes in hydrogeology*. New York, NY: Lewis Publishers.
- Clayton, R. N., and Mayeda, T. K. (1963). The use of bromine pentafluoride in the extraction of oxygen from oxides and silicates for isotopic analysis. *Geochem. Cosmochim. Acta* 27, 43–52. doi:10.1016/0016-7037(63)90071-1
- Clayton, R. N., O'Neil, J. R., and Mayeda, T. K. (1972). Oxygen isotope exchange between quartz and water. *J. Geophys. Res.* 77, 3057–3067. doi:10.1029/jb077i017p03057
- Deng, J., and Wang, Q. (2016). Gold mineralization in China: metallogenetic provinces, deposit types and tectonic framework. *Gondwana Res.* 36, 219–274. doi:10.1016/j.gr.2015.10.003
- Deng, S. L. (2011). Mineralization of ductile shear belt gold deposit of Maerkakuli in Habahe, Xinjiang. Master's Thesis. Chengdu (China): Chengdu Unieversity of Technology [In Chinese with English abstract].
- Ding, Q.-F., Wu, C.-Z., Santosh, M., Fu, Y., Dong, L.-H., Qu, X., et al. (2014). H–O, S and Pb isotope geochemistry of the Awanda gold deposit in southern Tianshan, Central Asian orogenic belt: implications for fluid regime and metallogeny. *Ore Geol. Rev.* 62 (62), 40–53. doi:10.1016/j.oregeorev.2014.02.017
- Doe, B. R., and Zartman, R. E. (1979). “Plumbotectonics, the phanerozoic,” in *Geochemistry of hydrothermal ore deposits*. Editor H. L. Barnes Second Edn (New York, NY: John Wiley), 509–567.
- Friedman, I. (1953). Deuterium content of natural waters and other substances. *Geochem. Cosmochim. Acta* 4, 89–103. doi:10.1016/0016-7037(53)90066-0
- Frimmel, H. E. (2008). Earth's continental crustal gold endowment. *Earth Planet Sci. Lett.* 267, 45–55. doi:10.1016/j.epsl.2007.11.022
- Gao, L. L. (2020). The Metallogenetic regularity and metallogenetic prediction of Au and Cu–Zn polymetallic deposits in the south margin of western Altay Range, Xinjiang. Doctor's Thesis. Changchun (China): Jilin Unieversity [In Chinese with English abstract].
- Goldstein, R. H. (2003). “Petrographic analysis of fluid inclusions,” in *Fluid inclusions: analysis and interpretation* (Ottawa, ON, Canada: Mineralogical Association of Canada), 32, 9–53.
- Goldstein, R. H., and Reynolds, T. J. (1994). Systematics of fluid inclusions in diagenetic minerals. *SEPM Short. Course* 31, 199. doi:10.2110/scn.94.31
- Groves, D. I., Goldfarb, R. J., Gebre-Mariam, M., Hagemann, S. G., and Robert, F. (1998). Orogenic gold deposits: a proposed classification in the context of their crustal distribution and relationship to other gold deposit types. *Ore Geol. Rev.* 13, 7–27. doi:10.1016/s0169-1368(97)00012-7
- Groves, D. I. (1993). The crustal continuum model for late-Archaean lode-gold deposits of the Yilgarn Block, Western Australia. *Miner. Deposita* 28 (6), 366–374. doi:10.1007/bf02431596
- Heinrich, C. A., Driesner, T., Stefánsson, A., and Seward, T. M. (2004). Magmatic vapor contraction and the transport of gold from the porphyry environment to epithermal ore deposits. *Geol.* 32, 761–764. doi:10.1130/g20629.1
- Hollister, L. S., and Burruss, R. C. (1976). Phase equilibria in fluid inclusions from the Khtada Lake metamorphic complex. *Geochem. Cosmochim. Acta* 40, 163–175. doi:10.1016/0016-7037(76)90174-5
- Houghton, J. L., Shanks, W. C., and Seyfried, W. E. (2004). Massive sulfide deposition and trace element remobilization in the Middle Valley sediment-hosted hydrothermal system, northern Juan de Fuca Rdge. *Geochem. Cosmochim. Acta* 68, 2863–2873. doi:10.1016/j.gca.2003.12.023
- Kerrick, R., Goldfarb, R., Groves, D., Garwin, S., and Jia, Y. (2000). The characteristics, origins, and geodynamic settings of supergiant gold metallogenetic provinces. *Sci. China Earth Sci.* 43, 1–68. doi:10.1007/bf02911933
- Koděra, P., Lexa, J., Rankin, A. H., and Fallick, A. E. (2005). Epithermal gold veins in a caldera setting: banská Hodruša, Slovakia. *Miner. Deposita* 39, 921–943. doi:10.1007/s00126-004-0449-5
- Kröner, A., Alexeev, D. V., Rojas-Agramonte, Y., Hegner, E., Wong, J., Xia, X., et al. (2013). Mesoproterozoic (Grenville-age) terranes in the Kyrgyz North Tianshan: zircon ages and Nd–Hf isotopic constraints on the origin and evolution of basement blocks in the southern Central Asian Orogen. *Gondwana Res.* 23, 272–295. doi:10.1016/j.gr.2012.05.004
- Large, R. R., Bull, S. W., and Maslennikov, V. V. (2011). A carbonaceous sedimentary source-rock model for Carlin-type and orogenic gold deposits. *Econ. Geol.* 106, 331–358. doi:10.2113/econgeo.106.3.331
- Laurent, S., Charvet, J., Shu, L. S., Ma, R. S., and Lu, H. F. (2002). Palaeozoic late collisional strike-slip deformations in Tianshan and Altay, Eastern Xinjiang, NW China. *Terra. Nova* 14, 249–256. doi:10.1046/j.1365-3121.2002.00417.x
- Li, G. M., Shen, Y. C., Liu, T. B., Shen, P., and Zhou, N. W. (2007). Metallogenetic evolution of Tuokuzibayi gold deposit in southern Altay, north Xinjiang: evidence from characteristics of quartz vein systems, isotopic geochemistry and Ar–Ar chronology. *Miner. Deposits* 1, 15–32 [In Chinese with English abstract].
- Li, H. Q., and Chen, F. W. (2004). *Chronology of regional mineralization in Xinjiang*. Beijing, China: Geological Publishing House, 40–45 [In Chinese with English abstract].
- Li, S., Wang, K., Wang, Y., Zhang, X., and Quan, H. (2017). Genesis of the bairendaba Ag–Zn–Pb deposit, southern great xing'an range, NE China: a fluid inclusion and stable isotope study. *Geofluids* 2017, 1–18. doi:10.1155/2017/1206587
- Li, Y., Zhou, G., and Chai, F. M. (2012). LA–ICP–MS U–Pb ages and geological implications of the Habahe Pluton at the southern margin of the Altay, Xinjiang. *Xinjiang Geol.* 30, 146–151 [In Chinese with English abstract].
- Liu, G. R., Li, Y., Wang, R., Wang, H. P., Yang, C. D., Chen, Q., et al. (2018). ⁴⁰Ar/³⁹Ar dating of muscovite from the Zhelände Au deposit, Irtysh Tectonic Zone, Xinjiang and its geological implication. *Rock Miner. Anal.* 37 (6), 705–712 [In Chinese with English abstract].
- Lu, H. Z., Fan, H. R., Ni, P., Ou, X. G., Shen, K., and Zhang, W. H. (2004). *Fluid inclusion*. Beijing, China: Science Press, 1–487 [In Chinese with English abstract].
- Martinek, K. R., Wagner, T., Walle, M., Heinrich, C. A., and Arlt, T. (2016). Chemical evolution of metamorphic fluids in the Central Alps, Switzerland: insight from LA–ICPMS analysis of fluid inclusions. *Geofluids* 16 (5), 877–908. doi:10.1111/gfl.12194
- Mi, D. J., Su, D. Y., Zou, C. H., and Tang, X. D. (2010). Geological characteristics of Saidu gold deposit in Habahe county of Xinjiang autonomous region. *Contrib. Geol. Miner. Resour. Res.* 25 (4), 331–335 [In Chinese with English abstract].
- Ohmoto, H., and Goldhaber, M. (1997). “Sulphur and carbon isotopes,” in *Geochemistry of hydrothermal ore deposits*. Editor H. L. Barnes (New York, NY: Wiley), 517–611.
- Ohmoto, H., and Rye, R. O. (1979). *Isotopes of sulfur and carbon*. New York, NY: John Wiley and Sons.
- Ohmoto, H. (1972). Systematics of sulfur and carbon isotopes in hydrothermal ore deposits. *Econ. Geol.* 67, 551–578. doi:10.2113/gsecongeo.67.5.551
- Phillips, G. N., and Powell, R. (2015). Hydrothermal alteration in the Witwatersrand goldfields. *Ore Geol. Rev.* 65, 245–273. doi:10.1016/j.oregeorev.2014.09.031
- Pirajno, F., Seltmann, R., and Yang, Y. (2011). A review of mineral systems and associated tectonic settings of northern Xinjiang, NW China. *Geoscience Frontiers* 2, 47–75. doi:10.1016/j.gsf.2011.03.006
- Robinson, B. W., and Kusakabe, M. (1975). Quantitative preparation of sulfur dioxide, for sulfur-34/sulfur-32 analyses, from sulfides by combustion with cuprous oxide. *Anal. Chem.* 47, 1179–1181. doi:10.1021/ac60357a026
- Roedder, E. (1984). Fluid inclusions. *Rev. Mineral.* 12, 644.
- Roedder, E., and Bodnar, R. J. (1980). Geologic Pressure determinations from fluid inclusion studies. *Annu. Rev. Earth Planet Sci.* 8, 263–301. doi:10.1146/annurev.ea.08.050180.001403

- Taylor, H. P. (1974). The application of oxygen and hydrogen isotope studies to problems of hydrothermal alteration and ore deposition. *Econ. Geol.* 69, 843–883. doi:10.2113/gsecongeo.69.6.843
- Stacey, J. S., and Kramers, J. D. (1975). Approximation of terrestrial lead isotope evolution by a two-stage model. *Earth Planet Sci. Lett.* 26, 207–221. doi:10.1016/0012-821x(75)90088-6
- Shepherd, T. J., Rankin, A. H., and Alderton, D. (1985). *A practical guide to fluid inclusion studies*. Glasgow, Scotland: Blackie and Son, 239.
- Sheppard, S. M. F. (1986). Chapter 6. Characterization and isotopic variations in natural waters. *Rev. Mineral.* 16, 165–184. doi:10.1515/9781501508936-011
- Sibson, R. H., Robert, F., and Poulsen, K. H. (1988). High-angle reverse faults, fluid-pressure cycling, and mesothermal gold-quartz deposits. *Geol.* 16, 551–555. doi:10.1130/0091-7613(1988)016<0551:harffp>2.3.co;2
- Spence-Jones, C. P., Jenkin, G. R. T., Boyce, A. J., Hill, N. J., and Sangster, C. J. S. (2018). Tellurium, magmatic fluids and orogenic gold: an early magmatic fluid pulse at Cononish gold deposit, Scotland. *Ore Geol. Rev.* 102, 894–905. doi:10.1016/j.oregeorev.2018.05.014
- Wang, Y., Xu, J., Wei, X., and Ding, R. (2018). The mineralization of the Jinba gold deposit, Xinjiang, China: evidence from geology and fluid inclusions. *J. China Univ. Geosci.* 43, 3112–3125 [In Chinese with English abstract].
- Wei, C., Clarke, G., Tian, W., and Qiu, L. (2007). Transition of metamorphic series from the Kyanite- to andalusite-types in the Altai orogen, Xinjiang, China: evidence from petrography and calculated KFMASH and KFMASH phase relations. *Lithos* 96, 353–374. doi:10.1016/j.lithos.2006.11.004
- Xiao, H. L., Zhou, J. Y., Wang, H. N., Dong, Y. G., Ji, J. F., and Zhao, Y. (2003). Geochemical characteristics and source of ore-forming fluid of Duolanasayi gold deposit, Xinjiang. *Chin. J. Geochem.* 22, 74–82 [In Chinese with English abstract].
- Xiao, W. J., Windley, B. F., Huang, B. C., Han, C. M., Yuan, C., Chen, H. L., et al. (2009). End-Permian to mid-Triassic termination of the accretionary processes of the southern Altaids: implications for the geodynamic evolution, Phanerozoic continental growth, and metallogeny of Central Asia. *Int. J. Earth Sci.* 98, 1189–1217. doi:10.1007/s00531-008-0407-z
- Xu, J. H., Zhang, G. R., Xie, Y. L., Shan, L. H., Zhang, S. J., Wang, P. H., et al. (2009). The evolution of tectonic-metallogenic fluids in the Saidu gold deposit, Southern Altai. *Acta Petrol. Mineral.* 28 (2), 141–151 [In Chinese with English abstract].
- Xue, X. L. (2018). Geological characteristics and genesis of Zanlander gold deposit, Habahe county, Xinjiang. *World Nonferrous Metal* 4, 150, 2018 [In Chinese with English abstract].
- Yakubchuk, A. (2004). Architecture and mineral deposit settings of the Altaid orogenic collage: a revised model. *J. Asian Earth Sci.* 23, 761–779. doi:10.1016/j.jseas.2004.01.006
- Yan, S. H., Chen, W., Wang, Y. T., Zhang, Z. C., and Chen, B. L. (2004). $^{40}\text{Ar}/^{39}\text{Ar}$ dating and its significance of the extir gold metallogenic belt in the Altai orogen, Xinjiang. *Acta Geol. Sin.* 4, 500–506 [In Chinese with English abstract].
- Zartman, R. E., and Doe, B. R. (1981). Plumbotectonics-the model. *Tectonophysics* 75, 135–162. doi:10.1016/0040-1951(81)90213-4
- Zhan, S., Tian, Z. F., Song, M. Y., and Qi, Y. (2016). Stable isotope of the typical deposits in Habahe gold ore belt, Xinjiang. *Xinjiang Geol.* 34 (4), 476–480 [In Chinese with English abstract].
- Zhao, K.-D., Jiang, S.-Y., Ni, P., Ling, H.-F., and Jiang, Y.-H. (2007). Sulfur, lead and helium isotopic compositions of sulfide minerals from the Dachang Sn-polymetallic ore district in South China: implication for ore genesis. *Mineral. Petrol.* 89, 251–273. doi:10.1007/s00710-006-0148-2
- Zheng, Y., Lv, X. B., and Cheng, Y. (2010). Geology and genesis of Tuokuzibayi gold deposit, Xinjiang. *Geol. Sci. Technol. Inf.* (29), 123–129 [In Chinese with English abstract].
- Zhou, J., Huang, Z., Zhou, M., Li, X., and Jin, Z. (2013). Constraints of C-O-S-Pb isotope compositions and Rb-Sr isotopic age on the origin of the Tianqiao carbonate-hosted Pb-Zn deposit, SW China. *Ore Geol. Rev.* 53, 77–92. doi:10.1016/j.oregeorev.2013.01.001
- Zhou, N. W., Guo, X. C., and He, G. L. (2012). LA-ICP-MS Zircon U-Pb Ages of two types of ore-bearing dykes in the Tuokuzibayi gold ore district in Habahe area of Xinjiang and geological significance. *Geol. Bull. China* 31 (5), 707–715 [In Chinese with English abstract].

Conflict of Interest: The authors declare that the research was conducted in the absence of any commercial or financial relationships that could be construed as a potential conflict of interest.

Copyright © 2021 Li, Chen, Gao, Xia, Zhang and Wang. This is an open-access article distributed under the terms of the Creative Commons Attribution License (CC BY). The use, distribution or reproduction in other forums is permitted, provided the original author(s) and the copyright owner(s) are credited and that the original publication in this journal is cited, in accordance with accepted academic practice. No use, distribution or reproduction is permitted which does not comply with these terms.



The Genesis of the Askartor Be-Mo Deposit in the North Xinjiang, Northwest China: Evidence From Geology, Geochemistry, U-Pb, and Re-Os Geochronology

Tang Yong*, Zhang Hui* and Lv Zheng-Hang

Key Laboratory for High Temperature and High-Pressure Study of the Earth's Interior, Institute of Geochemistry, Chinese Academy of Sciences, Guiyang, China

OPEN ACCESS

Edited by:

Chang-Zhi Wu,
Chang'an University, China

Reviewed by:

Fuquan Yang,
Chinese Academy of Geological
Sciences (CAGS), China
Rui Wang,
China University of Geosciences,
China

*Correspondence:

Tang Yong
tangyong@vip.gyig.ac.cn
Zhang Hui
zhanghui@vip.gyig.ac.cn

Specialty section:

This article was submitted to
Economic Geology,
a section of the journal
Frontiers in Earth Science

Received: 28 December 2020

Accepted: 03 February 2021

Published: 16 March 2021

Citation:

Yong T, Hui Z and Zheng-Hang L
(2021) The Genesis of the Askartor Be-
Mo Deposit in the North Xinjiang,
Northwest China: Evidence From
Geology, Geochemistry, U-Pb, and
Re-Os Geochronology.
Front. Earth Sci. 9:646772.
doi: 10.3389/feart.2021.646772

The Askartor Be-Mo deposit is located in the southeastern area of the Chinese Altay orogenic belt in Xinjiang, NW China. Zircon U-Pb data show that there are two periods of magmatic activities in the Askartor Be-Mo ore district, namely, the Devonian granodiorite (386.8 ± 2.6 Ma) and biotite granite (385.4 ± 4.4 Ma), and the Triassic two-mica granite (247.5 ± 2.2 Ma) and muscovite granite (231.4 ± 2.0 Ma). The zircon U-Pb age of pegmatoid orebody is 220.6 ± 1.6 Ma which coincides with the molybdenite Re-Os isochron age of 228.7 ± 7.1 Ma. The two-mica and muscovite granites belong to the high-K Calc-alkaline series with peraluminous features, and are characterized by high SiO_2 (71.92–75.41 wt%), and Al_2O_3 (13.43–15.98 wt%), and low TiO_2 (0.01–0.25 wt%), Fe_2O_3 (0.11–1.14 wt%) and CaO (0.07–0.76 wt%). The highly fractionated element ratios of Y/Ho, Zr/Hf and Nb/Ta, and the rare earth element tetrad effect occur in the muscovite granite, indicating the fluid exsolution occurs at the late stage of magma evolution, and the muscovite granite experienced the strong self-metasomatism. Rayleigh fractional calculations show that the Askartor Be-Mo deposit is the product of multistage fractional crystallization of initial Be-enriched magma.

Keywords: Askartor Be deposit, U-Pb age, tetrad effect, melt-fluid interaction, NW China

INTRODUCTION

Because of its unique physical and chemical properties, beryllium (Be) is widely used in many important industrial products used in the aerospace, computer, defense, medical, nuclear, and telecommunications industries. The two most important Be ores are bertrandite [$\text{Be}_2\text{Si}_2\text{O}_7(\text{OH})_2$] and beryl [$\text{Be}_3\text{Al}_2\text{Si}_6\text{O}_{18}$]. At present, 90% of the source mineral of the world's beryllium produce comes from bertrandite, but industrial beryl is critical for the production of the very high purity beryllium metal needed for some strategic applications (Foley et al., 2017). At present, two distinct classes of deposits currently account for most beryllium ores (Barton and Young, 2002; London and Evensen, 2002): they are 1) volcanic and carbonated-hosted deposits that contain the mineral bertrandite, and 2) pegmatite-type deposits that have an abundance of the mineral beryl.

The Chinese Altay orogen, located in Northwest China, is the most important beryllium ore belt in China. Its deposit is mainly pegmatite type. The geological characteristics (Zou and Li, 2006; Qin et al., 2013; Yang et al., 2018; Zhang et al., 2019), geochronology (Wang et al., 2007; Chen, 2011; Ren

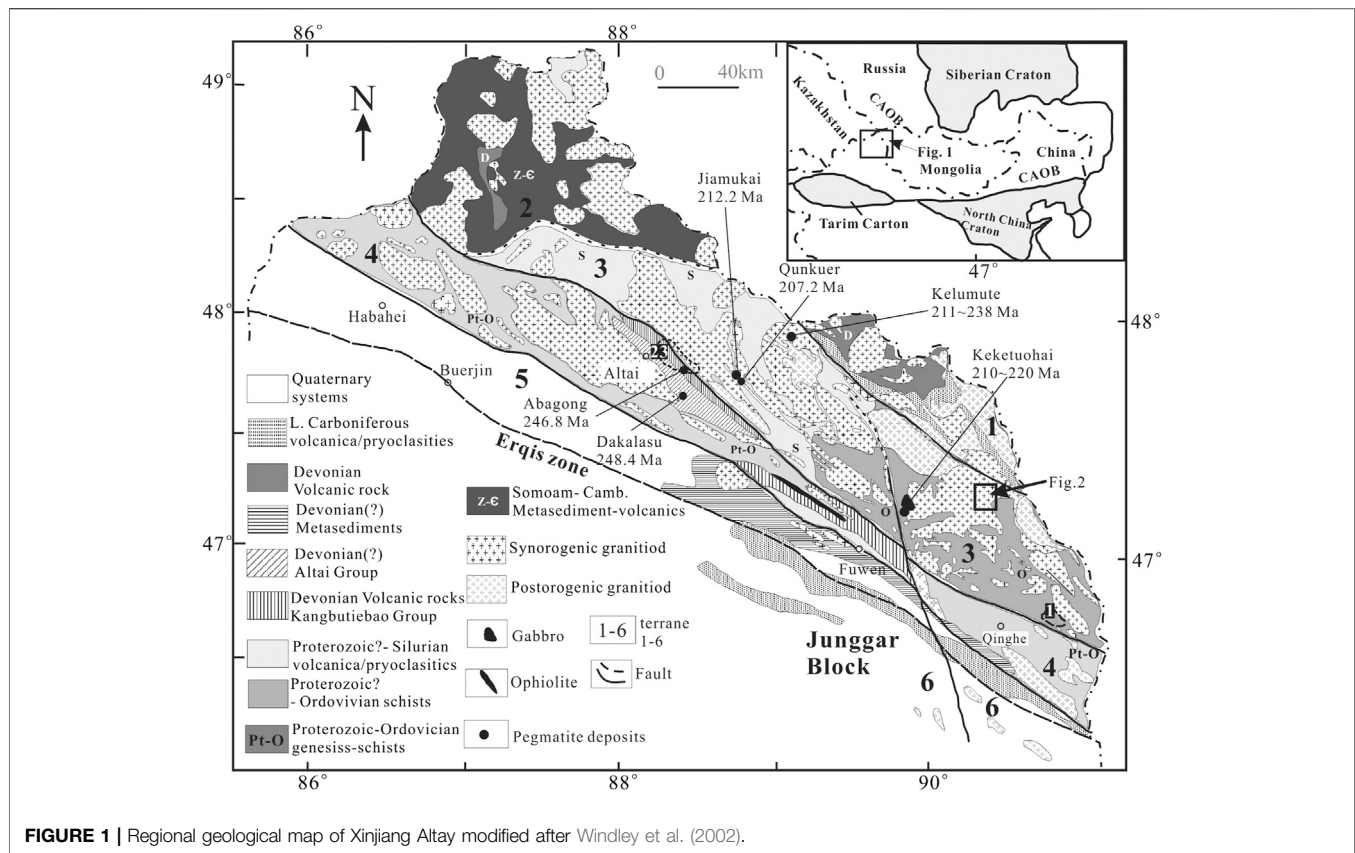


FIGURE 1 | Regional geological map of Xinjiang Altay modified after Windley et al. (2002).

et al., 2011; Lv et al., 2012) and internal evolution (Zhang et al., 2008; Lv et al., 2012; Stepanov and Hermann, 2013; Yin et al., 2013) of pegmatites in this area have been studied systematically. However, the mechanism of extraordinary enrichment of beryllium in pegmatites is not clear. Based on the solubility of beryl and the partition coefficient of Be, Evensen and London (2002) considered that extended fractionation beyond 90% total solidification by at least a three-step process is required to achieve beryl saturation in granitic magma systems, but there is a lack of factual evidence.

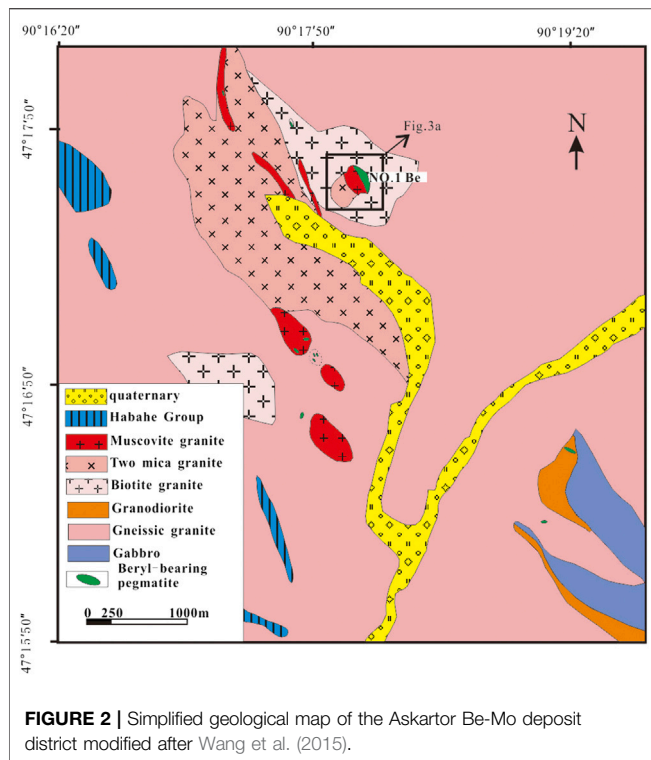
The Askartor deposit is the only granite-related Be-Mo deposit in the Chinese Altay orogen. The Askartor granite pluton is a composite rock body with obvious vertical zoning, from bottom to top, the rock types change from two-mica granite, through muscovite granite, to pegmatite. In addition, there are granodiorite and biotite granite in the ore district. Zou and Li (2006) presented the geological features, and ore body morphology. The ages of different rock types have been presented by Wang et al. (2015), Ding et al. (2016), Zhang et al. (2017). However, the processes that might have contributed to the genesis of this deposit have not been noticed. Therefore, in this study, we have carried out a systemic study of the geology, geochronology, and geochemistry, in order to establish the mineralization model of the Askartor Be-Mo deposit, and identify the key factors restricting the enrichment of Be.

GEOLOGICAL BACKGROUND

Regional Geology

The Altay orogen, which is the southernmost part of the Central Asian Orogenic Belt (CAOB), is situated between the south Siberian Craton to the north and the Junggar Block to the south. According to Windley et al. (2002), the Altay orogen in China is composed of the following six terranes, and details of the terranes can be found in Windley et al. (2002). The rare metal deposits are mainly distributed in Terrane 3 and Terrane 4 (Figure 1).

Recent studies have showed that the Chinese Altay orogen belt is a subduction-related accretionary orogen belt. The tectonic setting of the Chinese Altay varied from a passive continental margin to active continental margin during the Middle Cambrian, and then, it underwent a prolonged subduction process from Ordovician to Carboniferous, characterized by massive magma activities, and high-temperature metamorphism (e.g., Sun et al., 2008; Jiang et al., 2010; Cai et al., 2010; Cai et al., 2011a; Cai et al., 2012a; Cai et al., 2011b). During the Permian period, the Chinese Altai converged consecutively with the East and West Junggar arcs because of the closure of the Paleo-Asian Ocean (e.g., Cai et al., 2012b; Li et al., 2015; Cai et al., 2016; Broussolle et al., 2018). Since the Triassic period, the Chinese Altai has entered into a post-orogenic stage After the amalgamation of the Siberia and Tarim



cratons (e.g., Xiao et al., 2008; Xiao et al., 2009; Xiao et al., 2015; Cai et al., 2016; Xiao et al., 2018).

The granitoids occupy over ~40% of the Chinese Altay orogen (Zou et al., 1988). High precision U-Pb dating results of LA-ICPMS, SHRIMP, and SIMS shows that most of the granitoids were emplaced during the Early to Middle Paleozoic time, with minor ones in the Permian period (Zou et al., 1988; Chen and Jahn, 2002; Wang et al., 2006; Yuan et al., 2007; Sun et al., 2008). The Early Middle Paleozoic I and S-type granitoid, which is emplaced from 507 to 360 Ma, display arc-related geochemical characters (Yuan et al., 2007; Wang et al., 2009; Cai et al., 2011a, Cai et al., 2011b). They are usually deformed and partly metamorphosed to become foliated (Wang et al., 2009). In contrast, the A or I-type granitoids emplaced at ca. 290–250 Ma are mostly undeformed and possess within-plate geochemical characteristics (Tong et al., 2014).

The Chinese Altay orogen is an important rare metal metallogenic belt in China, and its deposit is mainly pegmatite. Approximately 100,000 pegmatite dykes exposed in the Chinese Altay (Zou and Li, 2006). These pegmatite dykes formed during the Devonian synorogenic to Jurassic post-orogenic to anorogenic stage, and mostly concentrated in Triassic (e.g., Ren et al., 2011; Lv et al., 2021 and references therein). The Askartor Be-Mo deposit is the only rare metal deposit related to granite.

Geology of the ore District

The Askartor Be deposit is located in the southeastern of the Central Altay, and about 80 km north of the Qinghe County (Figure 1). This deposit has mined since 1954, and a total of

11,200 tons of ore, which occupy only 2% of the total reserves, have been produced until 1996.

The Upper Ordovician Habahe subgroup sporadically crops out in the mining area, and is composed of biotite-quartz schist and biotite gneiss. Magmatic rocks develop well and make up 95% of the whole mining area, including granodiorites, biotite granites, two mica granites, and medium-fine grain muscovite granites (Figure 2). Granodiorites are the most voluminous of these intrusive rocks. These rocks are grey-black, fine to medium-grained, with a massive texture. They are composed of quartz (20–25 vol%), plagioclase (50 vol%), K-feldspar (± 10 vol%), and biotite (10–15 vol%). Accessory minerals include zircon, apatite, titanite, and magnetite. Biotite granites are the ore-hosting rock, with an outcrop area of about 0.9 km². These biotite granites are grey-white, and have an unequal-particle hypidiomorphic structure with a massive texture. Petrographic observation shows that the mineral compositions mainly involve quartz (30–35 vol%), plagioclase (± 40 vol%), K-feldspar (± 15 vol%), biotite (5–10 vol%), and muscovite (± 2 vol%). Biotite granites are intruded by two mica granites, and the boundary between those two intrusions is sharp and clear. The surface outcrop of the two mica granites is up to 5 km². They are grey-white, and have a medium-to coarse grain granitic structure with a massive texture. The two mica granites are mainly composed of quartz (35 vol%), plagioclase (~35 vol%), K-feldspar (20 vol%), biotite (± 5 vol%), and muscovite (± 5 vol%). Muscovite granites occur in the upper portion of the two mica granites, and the transition between both granite types is gradational. The Muscovite granites have a fine-to medium-grain granitic structure. These rocks are mainly composed of quartz (30–35 vol%), plagioclase (35 vol%), K-feldspar (± 20 vol%), and muscovite (5–10 vol%).

The Askartor Be-Mo deposit is composed of primary ore and placer. The primary ore consists of pegmatoid-type beryllium ore body in the upper part and granite-type beryllium ore body in the lower part, and the two parts show a gradual transitional relationship. Detailed surface geological mapping, underground mining workings and drill holes demonstrate that the following six zones are successively encountered from bottom to top (Figure 3):

- (1) medium-to fine-grain muscovite granite. These rocks are mainly composed of quartz (30–35 vol%), plagioclase (35 vol%), K-feldspar (± 20 vol%), and muscovite (5–10 vol%).
- (2) beryl-bearing fine-grain albitized muscovite granite. They are grey-white, and have a fine-grain granitic structure with a massive texture. These rocks are mainly composed of quartz (30–35 vol%), albite (± 40 vol%), K-feldspar (± 20 vol%), and muscovite (± 10 vol%). Beryl sporadically occurs in these rocks.
- (3) banded muscovite-quartz-albite zone (Figures 4A,B). This zone is usually 4–5 m wide, 0.1–2 m long and spans 10 m at its widest place. Meanwhile, it has a strong Be-mineralization and a gradual transition relationship with fine-grained albitization muscovite granite zone. Albite, microcline, quartz, muscovite, and beryl formed the zone's clear banded structure.

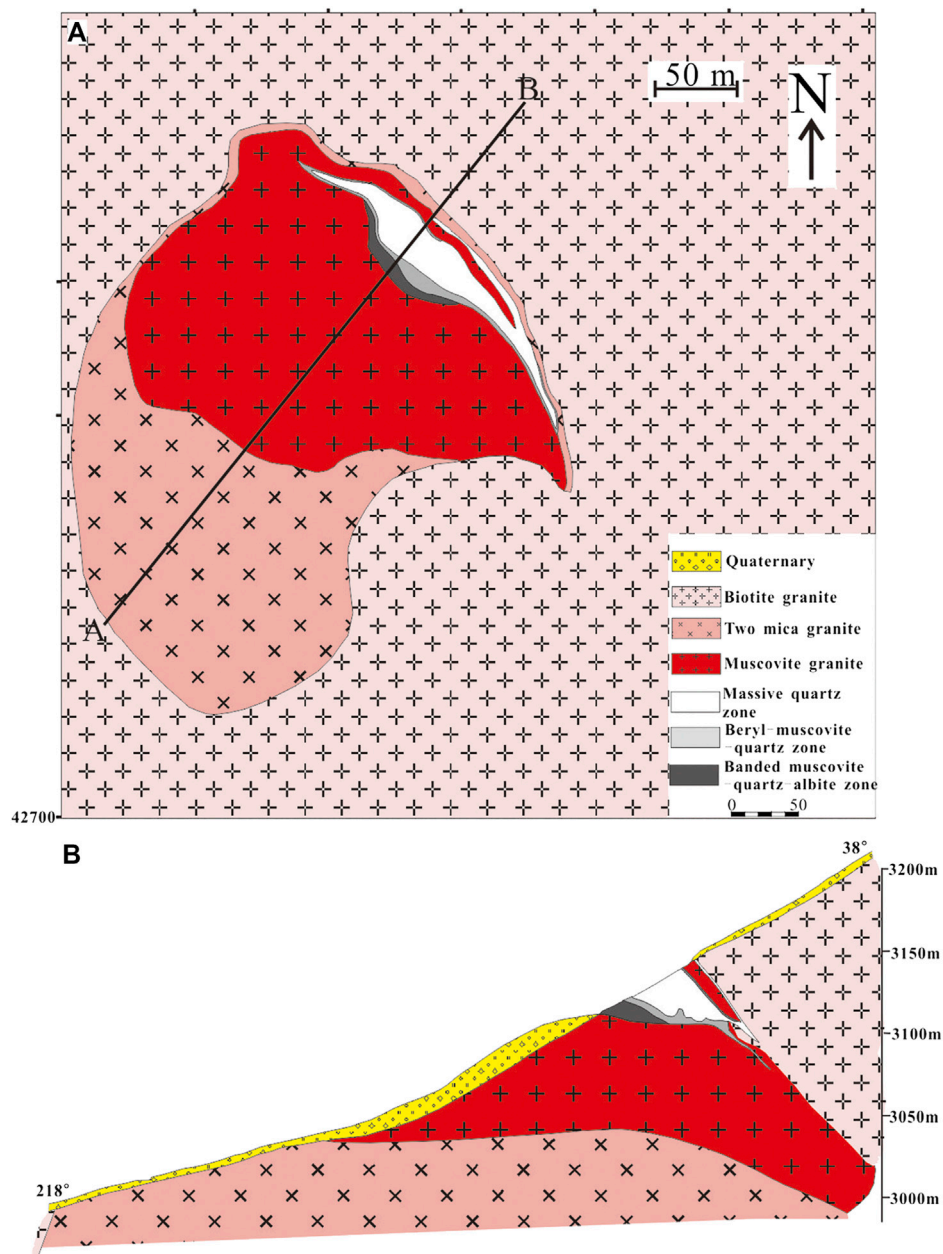


FIGURE 3 | Cross sections of the Askartor No.1 Be-Mo deposit.

- (4) **Massive quartz zone (Figure 4D).** This zone mainly consists of quartz, the colors of which are ivory, rosy, and transparency with dense block structure and the widest place of the core quartz reaches 32 m. Beryl only appears along the marginal areas, reflecting a weak Be-mineralization. There is pyrite, blende, bismuthinite, nesting of gypsum and barite vein in this zone, besides quartz, and the molybdenite appears in the inside of quartz vein's edge with little content.
- (5) **Beryl-bearing muscovite-quartz zone (Figure 4C).** This zone, showing circular distribution around the massive quartz with

0.1–5 m wide, is the primary Be-mineralization zone. The main mineral compositions are muscovite (20–30 vol%), quartz (10–20 vol%), beryl (3–5 vol%), and microcline (2–20 vol%). The molybdenite presents star-dotted lamellar and laminated shapes, coexisting with pyrite, bismuthinite, blende, spessartite, apatite, spodumene, and niobite.

- (6) **muscovite-microcline-albite zone:** This zone, which is 2–10 m thick with weak Be-mineralization, is in the top side of the deposit, contacting the biotite granite wall-rock directly. The main mineral compositions are quartz

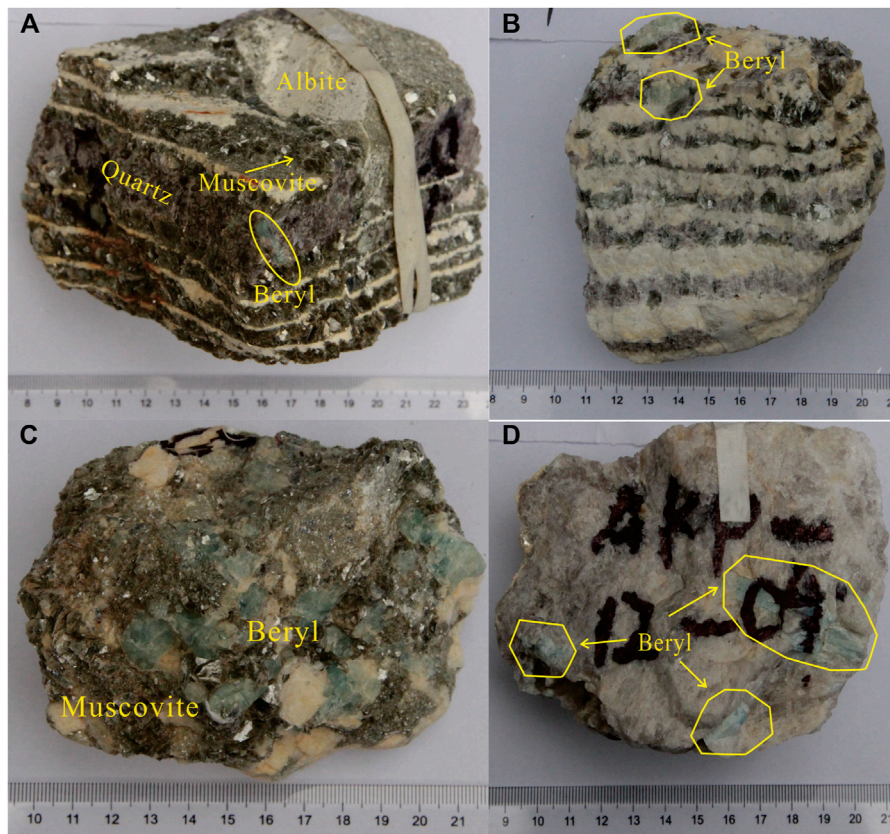


FIGURE 4 | Examples of beryl in different zones of the No.1 orebody.

(30 vol%), microcline (39 vol%), plagioclase (20 vol%), and muscovite (10 vol%), and the accessory minerals are spessartite, pyrite and molybdenite.

SAMPLES AND ANALYTICAL METHODS

Samples

Rock samples were examined by optical microscopy, and unaltered or least altered samples were selected for geochemical analysis. These samples were cleaned with deionized water, crushed, and powered with an agate mill. Five samples were selected for zircon U-Pb dating in this study. These samples are granodiorite (sample name: AKG01, Location: N47°17'32", E90°17'38"), biotite granite (sample name: AKG02, location: N47°18'21", E90°17'39"), two-mica granite (sample name: AKG04, N47°17'33", E90°17'34"), fine-grain muscovite (sample name: AKG05, location: N47°18'19", E90°17'43"), and the banded pegmatite (sample name: AKG06, N47°18'20", E90°17'45"), respectively. Seven molybdenite samples were collected from fine-grain muscovite granite and pegmatite.

Major and Trace Elements Analysis

Major and trace elements were determined at the State Key Laboratory of Ore Deposit Geochemistry, Chinese Academy of

Sciences (SKLOG, CAS). Major elements were analyzed by standard X-ray fluorescence (XRF). Samples were prepared as glass discs, formed by mixing 0.70 g of rock powder (dried at 110°C) with 7.0 g of lithium tetraborate for 15 min at 1,100°C in 95%P-5%Au crucibles. Analyses were performed on a PANalytical Axios PW4400 X-ray fluorescence spectrometer. The analytical precision, as determined on the Chinese National Standards GSR-1 and GSR-3, was better than 5%. Loss on ignition (LOI) was obtained using 1 g power heated to 1,100°C for 1 h.

Trace elements were analyzed with a Finnigan MAT ELEMENT magnetic sector ICP-MS. 50 mg of powdered granite sample were dissolved in a high-pressure PolyTetraFluoroEthylene (PTFE) bomb for 48 h using HF + HNO₃. Rh was used as an internal standard to monitor signal drift during counting. The USGS and Chinese National Standards BCR-1, BHVO-1, and GSR-3 were chosen for calibrating element concentrations. The discrepancy between the triplicates is less than 5% for all the elements (Qi et al., 2000).

Zircon U-Pb Dating

The zircon U-Pb dating samples were crashed, and grinded, and then separated by heavy liquid and magnetic separation methods. Zircons were picked by hand under a binocular microscope and mounted in epoxy resin. Before U-Pb dating analysis, The

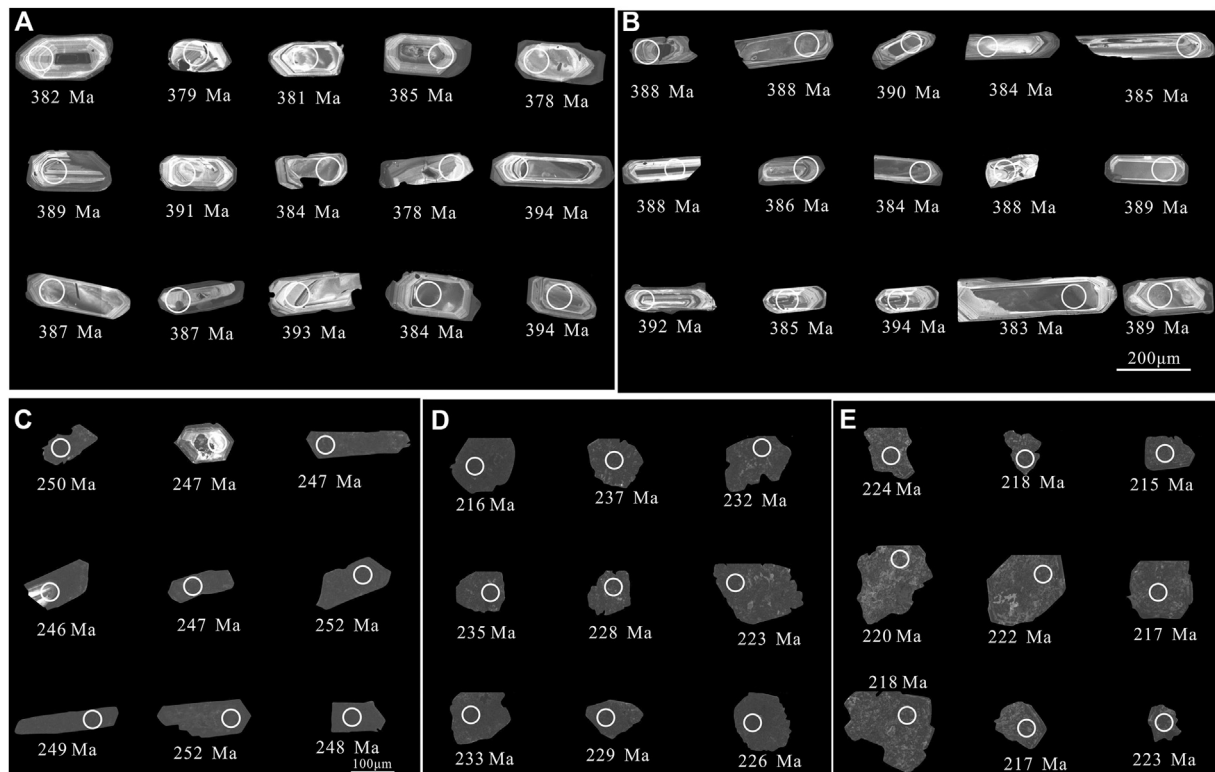


FIGURE 5 | Representative cathodoluminescence (CL) images of zircons from the different intrusions with analytical spots of the Askartor deposit. **(A)** granodiorite; **(B)** biotite granite; **(C)** two-mica granite; **(D)** muscovite granite; **(E)** pegmatite.

Cathodoluminescence (CL) images were used to assess the zircon at the Beijing zircon dating navigation technology limited company, and CL images performed at JSM6510 scanning electron microscope produced by JEOL Corporation (Japan).

Zircon U-Pb dating was done by an Elan DRC-e ICP-MS coupled with a GeoLasPro 193 nm Laser-Ablation System at SKLOGD, CAS. The conditions were summarized as follows: the laser frequency was 8 Hz with an energy of 34–40 mJ; the beam diameter was 30 μm ; and the acquisition was 30 s for background and 60 s for signal. Helium was used as a carrier gas to transport the ablated materials from the laser-ablation cell to the ICP-MS torch. The external standard is Zircon 91,500, and the internal standard to calculate U, Th, and Pb concentrations of unknowns was NIST610. Glass was used as an internal standard to

Raw data were processed using the ICPMSDataCal program (Liu et al., 2008). Uncertainties of individual analyses and weighted mean ages are reported within 1σ errors; Common Pb correction used the ^{204}Pb methods of Andersen (2002). The weighted mean U-Pb ages and Concordia plots were processed using ISOPLOT software (Ludwig 2003).

Molybdenite Re-Os Dating

Seven molybdenite samples were collected from fine-grain granite and pegmatite. Molybdenite with a purity of >99% were carefully handpicked under a binocular microscope. Re-Os isotope

analyses were done at SKLOGD, CAS. The analysis procedures are similar to that provided by Du et al. (2004). The ISOPLOT program (Ludwig, 2003) was used to calculate the Re-Os isochron age. The decay constant used in this calculation was $\lambda^{187}\text{Re} = 1.666 \times 10^{-11} \text{ year}^{-1}$ (Smoliar et al., 1996). Uncertainty in Re-Os model ages was 1.02% uncertainty. The uncertainty includes the ^{187}Re decay constant and uncertainty in Re and Os concentrations.

RESULTS

Zircon U-Pb Ages

Granodiorite (AKG01): the zircon grains from granodiorite are mostly light-yellow brown, transparent, and short prismatic. Their sizes are between 100 and $\sim 300 \mu\text{m}$. Almost all grains show clear oscillatory zoning (Figure 5A). The contents of Th and U are respectively 8–253 ppm and 172–326 ppm, and the Th/U ratios are between 0.41 and ~ 0.85 (Table 1), indicating that these zircons are of magmatic origin. Twenty spots were selected for U-Pb analysis and these points were tightly grouped, yielding a $^{206}\text{Pb}/^{238}\text{U}$ age of $386.8 \pm 2.6 \text{ Ma}$ (MSWD = 0.54) (Figure 6A), representing the crystallization age of the pluton.

Biotite granite (AKG02): the feature of zircon grains from biotite granite is similar to that in granodiorite (Figure 5B). The contents of Th and U are 73–453 ppm and 102–646 ppm,

TABLE 1 | LA-ICPMS U-Pb data of zircons from the Askaetor Be deposit.

Sample	Concentration (ppm)		Th/U	Isotopic ratio		$^{207}\text{Pb}/^{235}\text{U}$	1σ	$^{206}\text{Pb}/^{238}\text{U}$	1σ	Ages (Ma)			
	Th	U		$^{207}\text{Pb}/^{206}\text{Pb}$	1σ					$^{207}\text{Pb}/^{235}\text{U}$	1σ	$^{206}\text{Pb}/^{238}\text{U}$	1σ
AKG01.01	114	189	0.60	0.05164	0.00273	0.43061	0.02071	0.06106	0.00112	364	15	382	7
AKG01.02	116	233	0.50	0.04802	0.00216	0.40546	0.01694	0.06058	0.00096	346	12	379	6
AKG01.03	123	241	0.51	0.04695	0.00319	0.39674	0.02423	0.06084	0.00132	339	18	381	8
AKG01.04	120	222	0.54	0.05362	0.00220	0.46003	0.01773	0.06159	0.00098	384	12	385	6
AKG01.05	146	212	0.69	0.05318	0.00242	0.45116	0.02016	0.06043	0.00094	378	14	378	6
AKG01.06	160	277	0.58	0.05267	0.00247	0.45924	0.02003	0.06214	0.00102	384	14	389	6
AKG01.07	153	287	0.53	0.04878	0.00217	0.42531	0.01754	0.06251	0.00099	360	12	391	6
AKG01.08	130	222	0.58	0.05370	0.00250	0.46034	0.02064	0.06139	0.00105	384	14	384	6
AKG01.09	210	263	0.80	0.05074	0.00258	0.42444	0.02039	0.06044	0.00116	359	15	378	7
AKG01.10	112	185	0.60	0.04680	0.00249	0.41514	0.02213	0.06297	0.00120	353	16	394	7
AKG01.11	176	219	0.80	0.05420	0.00233	0.46224	0.01759	0.06187	0.00097	386	12	387	6
AKG01.12	149	326	0.46	0.04624	0.00185	0.39560	0.01460	0.06182	0.00090	338	11	387	5
AKG01.13	129	215	0.60	0.05190	0.00443	0.45338	0.03755	0.06280	0.00142	380	26	393	9
AKG01.14	112	219	0.51	0.05318	0.00301	0.45134	0.02534	0.06144	0.00135	378	18	384	8
AKG01.15	108	172	0.62	0.04750	0.00261	0.41188	0.02123	0.06300	0.00129	350	15	394	8
AKG01.16	127	308	0.41	0.04889	0.00225	0.42556	0.01818	0.06292	0.00106	360	13	393	6
AKG01.17	185	281	0.66	0.04605	0.00232	0.39918	0.01924	0.06253	0.00123	341	14	391	7
AKG01.18	124	188	0.66	0.05419	0.00273	0.47174	0.02214	0.06299	0.00116	392	15	394	7
AKG01.19	102	206	0.50	0.05198	0.00273	0.44181	0.02155	0.06250	0.00121	372	15	391	7
AKG01.20	157	249	0.63	0.05019	0.00234	0.43714	0.01953	0.06235	0.00104	368	14	390	6
AKG01.21	91	196	0.46	0.05867	0.00322	0.50699	0.02966	0.06161	0.00122	416	20	385	7
AKG01.22	184	282	0.65	0.05268	0.00212	0.45656	0.01764	0.06186	0.00095	382	12	387	6
AKG01.23	232	311	0.75	0.05240	0.00225	0.45382	0.01851	0.06205	0.00106	380	13	388	6
AKG01.24	253	297	0.85	0.05368	0.00227	0.46268	0.01870	0.06178	0.00105	386	13	386	6
Sample	Concentration (ppm)		Th/U	Isotopic ratio		$^{207}\text{Pb}/^{235}\text{U}$	1σ	$^{206}\text{Pb}/^{238}\text{U}$	1σ	Ages (Ma)			
	Th	U		$^{207}\text{Pb}/^{206}\text{Pb}$	1σ					$^{207}\text{Pb}/^{235}\text{U}$	1σ	$^{206}\text{Pb}/^{238}\text{U}$	1σ
AKG01.01	73	102	0.72	0.06418	0.00470	0.53331	0.03401	0.06208	0.00151	434	23	388	9
AKG01.02	182	337	0.54	0.05139	0.00192	0.44326	0.01562	0.06212	0.00089	373	11	388	5
AKG01.03	155	178	0.87	0.05423	0.00264	0.47109	0.02247	0.06244	0.00106	392	16	390	6
AKG01.04	109	242	0.45	0.05391	0.00258	0.45821	0.02113	0.06130	0.00090	383	15	384	5
AKG01.05	301	339	0.89	0.05167	0.00198	0.44134	0.01561	0.06155	0.00086	371	11	385	5
AKG01.06	339	363	0.93	0.05158	0.00183	0.44679	0.01488	0.06199	0.00077	375	10	388	5
AKG01.07	85	163	0.52	0.05297	0.00276	0.45214	0.02318	0.06173	0.00114	379	16	386	7
AKG01.08	82	181	0.45	0.06687	0.00316	0.57185	0.02548	0.06135	0.00113	459	16	384	7
AKG01.09	81	156	0.52	0.05182	0.00308	0.43671	0.02144	0.06210	0.00109	368	15	388	7
AKG01.10	122	207	0.59	0.05923	0.00266	0.51857	0.02309	0.06226	0.00100	424	15	389	6
AKG01.11	123	140	0.88	0.05480	0.00266	0.47020	0.02110	0.06266	0.00105	391	15	392	6
AKG01.12	453	497	0.91	0.05195	0.00153	0.45040	0.01274	0.06154	0.00078	378	9	385	5
AKG01.13	218	320	0.68	0.05196	0.00201	0.45766	0.01591	0.06303	0.00083	383	11	394	5
AKG01.14	221	420	0.53	0.04953	0.00187	0.42675	0.01517	0.06117	0.00075	361	11	383	5
AKG01.15	174	211	0.83	0.05082	0.00227	0.44076	0.01884	0.06214	0.00093	371	13	389	6
AKG01.16	273	329	0.83	0.05443	0.00199	0.47273	0.01595	0.06174	0.00080	393	11	386	5
AKG01.17	93	161	0.58	0.05384	0.00261	0.45893	0.01995	0.06235	0.00112	384	14	390	7
AKG01.18	208	328	0.63	0.05005	0.00333	0.42699	0.02773	0.06047	0.00134	361	20	379	8
AKG01.19	149	191	0.78	0.05056	0.00220	0.42830	0.01684	0.06143	0.00095	362	12	384	6
AKG01.20	251	646	0.39	0.05066	0.00148	0.44541	0.01285	0.06221	0.00074	374	9	389	4
AKG01.21	137	269	0.51	0.05317	0.00245	0.46259	0.02204	0.06240	0.00104	386	15	390	6
AKG01.22	97	182	0.53	0.05282	0.00245	0.44924	0.02006	0.06178	0.00103	377	14	386	6
AKG01.23	120	304	0.40	0.05901	0.00223	0.44341	0.01598	0.05430	0.00074	373	11	341	5
AKG01.24	343	435	0.79	0.05139	0.00176	0.41835	0.01375	0.05813	0.00073	355	10	364	4
Sample	Concentration (ppm)		Th/U	Isotopic ratio		$^{207}\text{Pb}/^{235}\text{U}$	1σ	$^{206}\text{Pb}/^{238}\text{U}$	1σ	Ages (Ma)			
	Th	U		$^{207}\text{Pb}/^{206}\text{Pb}$	1σ					$^{207}\text{Pb}/^{235}\text{U}$	1σ	$^{206}\text{Pb}/^{238}\text{U}$	1σ
AKG04.01	1,592	11,768	0.14	0.04965	0.00161	0.28534	0.00956	0.03956	0.00066	255	8	250	4
AKG04.02	1,680	12,157	0.14	0.05605	0.00187	0.32628	0.01686	0.03903	0.00123	287	13	247	8
AKG04.03	1,160	8,796	0.13	0.05658	0.00171	0.31940	0.00928	0.03910	0.00047	281	7	247	3
AKG04.04	60,118	15,458	3.89	0.06415	0.00178	0.36682	0.01357	0.03885	0.00082	317	10	246	5
AKG04.05	1,486	10,054	0.15	0.05197	0.00164	0.29778	0.01214	0.03901	0.00089	265	9	247	6

(Continued on following page)

TABLE 1 | (Continued) LA-ICPMS U-Pb data of zircons from the Askaetor Be deposit.

Sample	Concentration (ppm)		Th/U	Isotopic ratio		$^{207}\text{Pb}/^{235}\text{U}$	1σ	$^{206}\text{Pb}/^{238}\text{U}$	1σ	Ages (Ma)			
	Th	U		$^{207}\text{Pb}/^{206}\text{Pb}$	1σ					$^{207}\text{Pb}/^{235}\text{U}$	1σ	$^{206}\text{Pb}/^{238}\text{U}$	1σ
AKG04.06	772	9,875	0.08	0.05248	0.00161	0.30379	0.00996	0.03984	0.00054	269	8	252	3
AKG04.07	911	8,517	0.11	0.04810	0.00175	0.28231	0.01325	0.03942	0.00093	252	10	249	6
AKG04.08	2066	15,936	0.13	0.04504	0.00167	0.25770	0.01127	0.03992	0.00154	233	9	252	10
AKG04.09	1,507	10,554	0.14	0.05904	0.00163	0.34457	0.01288	0.03914	0.00092	301	10	248	6
AKG04.10	1,040	9,661	0.11	0.05247	0.00162	0.29513	0.00845	0.03839	0.00062	263	7	243	4
AKG04.11	617	9,999	0.06	0.04926	0.00144	0.27990	0.00824	0.03841	0.00068	251	7	243	4
AKG04.12	772	11,048	0.07	0.05071	0.00159	0.29490	0.00942	0.03907	0.00074	262	7	247	5
AKG04.13	1,561	8,696	0.18	0.05884	0.00191	0.36347	0.01064	0.04147	0.00058	315	8	262	4
AKG04.14	1,187	11,746	0.10	0.05119	0.00172	0.29746	0.01073	0.03867	0.00084	264	8	245	5
AKG04.15	482	10,083	0.05	0.05817	0.00180	0.33289	0.01242	0.03852	0.00089	292	9	244	6
AKG04.16	455	7,250	0.06	0.04612	0.00146	0.26626	0.00815	0.03939	0.00054	240	7	249	3
AKG04.17	1,080	7,121	0.15	0.05212	0.00227	0.29562	0.01312	0.03980	0.00085	263	10	252	5
AKG05.01	466	8,360	0.06	0.05887	0.00396	0.27643	0.01825	0.03406	0.00046	248	15	216	3
AKG05.02	1,539	9,060	0.17	0.07022	0.00370	0.36196	0.01832	0.03739	0.00055	314	14	237	3
AKG05.03	1,385	32,709	0.04	0.05839	0.00128	0.30657	0.00648	0.03672	0.00050	272	5	232	3
AKG05.04	2,175	9,735	0.22	0.06268	0.00175	0.33484	0.00922	0.03708	0.00051	293	7	235	3
AKG05.05	1,244	7,222	0.17	0.06124	0.00281	0.30387	0.01322	0.03599	0.00053	269	10	228	3
AKG05.06	4,544	24,671	0.18	0.07573	0.00706	0.36702	0.03374	0.03515	0.00053	317	25	223	3
AKG05.07	1,453	6,478	0.22	0.05318	0.00213	0.28493	0.00935	0.03679	0.00068	255	7	233	4
AKG05.08	515	10,428	0.05	0.04876	0.00215	0.25751	0.01019	0.03616	0.00056	233	8	229	3
AKG05.09	1,048	6,806	0.15	0.05874	0.00285	0.28896	0.01335	0.03568	0.00052	258	11	226	3
AKG05.10	12,226	6,492	1.88	0.14124	0.00673	0.84036	0.04060	0.04005	0.00079	619	22	253	5
AKG05.11	4,420	8,378	0.53	0.09897	0.00833	0.54416	0.04485	0.03988	0.00069	441	29	252	4
AKG05.12	2,713	9,038	0.30	0.06395	0.00301	0.34327	0.01609	0.03606	0.00060	300	12	228	4
AKG05.13	1,671	18,199	0.09	0.05063	0.00322	0.23443	0.01453	0.03358	0.00047	214	12	213	3
AKG05.14	971	6,915	0.14	0.05554	0.00366	0.27971	0.01792	0.03652	0.00055	250	14	231	3
AKG05.15	1,130	25,526	0.04	0.05239	0.00243	0.28043	0.01268	0.03597	0.00060	251	10	228	4
AKG05.16	858	7,029	0.12	0.05235	0.00356	0.26304	0.01704	0.03645	0.00074	237	14	231	5
AKG05.17	2,947	5,148	0.57	0.07749	0.00518	0.44492	0.02590	0.03994	0.00093	374	18	252	6
AKG05-18	1,217	7,419	0.16	0.07066	0.00401	0.35344	0.01911	0.03628	0.00062	307	14	230	4
AKG06.01	3,936	6,450	0.61	0.0778	0.0030	0.3940	0.0135	0.0353	0.0008	337	10	224	5
AKG06.02	3,533	6,229	0.57	0.0623	0.0024	0.3125	0.0117	0.0344	0.0007	276	9	218	4
AKG06.03	1,124	5,935	0.19	0.0456	0.0015	0.2249	0.0070	0.0339	0.0006	206	6	215	3
AKG06.04	2,150	4,780	0.45	0.0495	0.0019	0.2630	0.0098	0.0364	0.0006	237	8	230	4
AKG06.05	952	4,751	0.20	0.0474	0.0019	0.2396	0.0091	0.0348	0.0006	218	7	220	4
AKG06.06	1,603	4,578	0.35	0.0494	0.0019	0.2522	0.0093	0.0350	0.0006	228	8	222	3
AKG06.07	2,383	5,664	0.42	0.0443	0.0016	0.2227	0.0078	0.0342	0.0006	204	7	217	4
AKG06.08	796	6,841	0.12	0.0434	0.0016	0.2183	0.0076	0.0343	0.0006	201	6	218	4
AKG06.09	1867	4,985	0.37	0.0557	0.0019	0.2807	0.0096	0.0342	0.0006	251	8	217	4
AKG06.10	811	6,042	0.13	0.0391	0.0015	0.2009	0.0071	0.0352	0.0006	186	6	223	4
AKG06.11	1,594	7,267	0.22	0.0419	0.0016	0.2116	0.0075	0.0345	0.0006	195	6	219	4
AKG06.12	291	5,837	0.05	0.0432	0.0014	0.2148	0.0066	0.0341	0.0005	198	6	216	3
AKG06.13	2075	7,608	0.27	0.0395	0.0016	0.1959	0.0081	0.0340	0.0006	182	7	215	4
AKG06.14	890	5,567	0.16	0.0400	0.0015	0.2030	0.0068	0.0351	0.0007	188	6	223	4
AKG06.15	576	4,896	0.12	0.0353	0.0012	0.1814	0.0059	0.0353	0.0005	169	5	224	3
AKG06.16	372	4,870	0.08	0.0354	0.0013	0.1807	0.0063	0.0354	0.0005	169	5	224	3
AKG06.17	2,609	5,378	0.49	0.0387	0.0016	0.1992	0.0082	0.0355	0.0007	184	7	225	4
AKG06.18	1,122	5,172	0.22	0.0404	0.0014	0.2084	0.0071	0.0355	0.0005	192	6	225	3
AKG06.19	1743	6,841	0.25	0.0375	0.0012	0.1916	0.0059	0.0349	0.0005	178	5	221	3
AKG06.20	1953	4,277	0.46	0.0458	0.0026	0.2348	0.0131	0.0353	0.0008	214	11	224	5
AKG06.21	2,160	4,034	0.54	0.0474	0.0017	0.2434	0.0090	0.0348	0.0006	221	7	221	4
AKG06.22	538	4,539	0.12	0.0436	0.0015	0.2278	0.0076	0.0351	0.0005	208	6	223	3
AKG06.23	459	4,607	0.10	0.0449	0.0020	0.2320	0.0099	0.0350	0.0007	212	8	222	4
AKG06.24	3,936	6,450	0.61	0.0778	0.0030	0.3940	0.0135	0.0353	0.0008	337	10	224	5

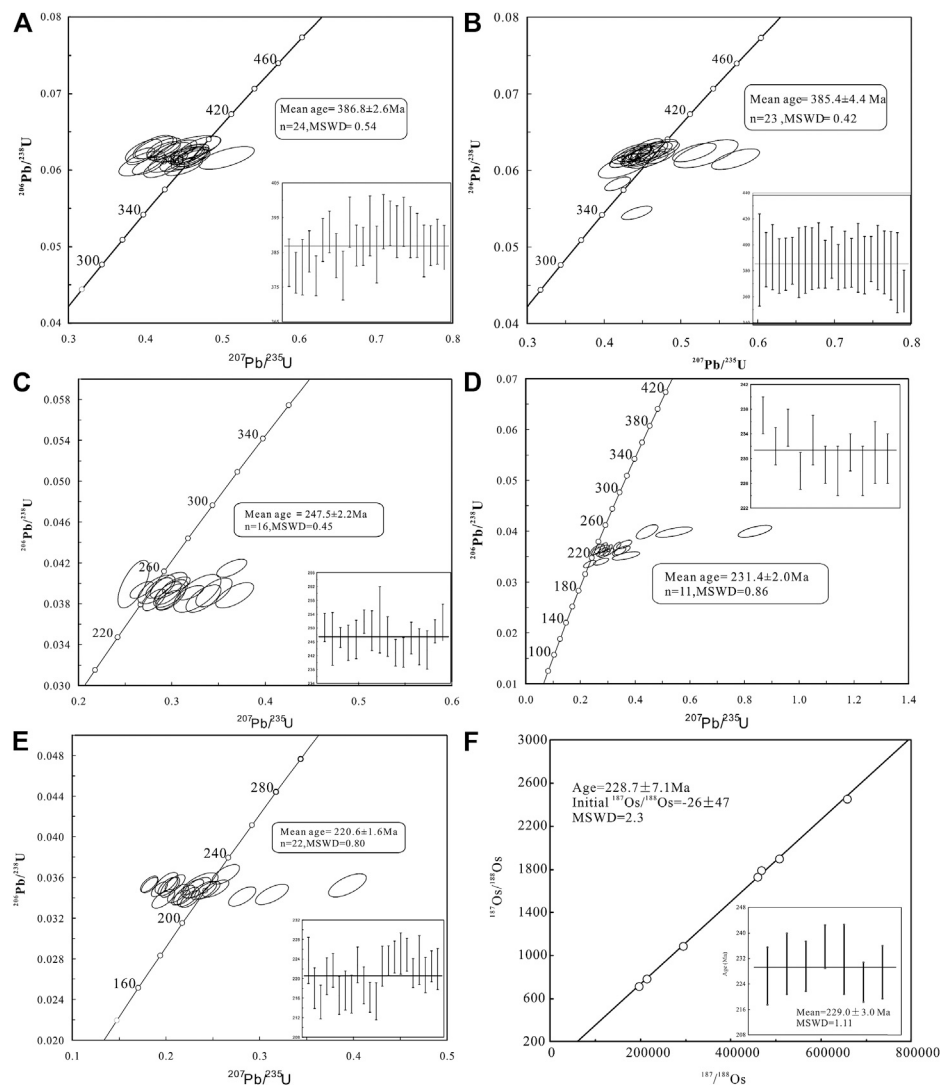


FIGURE 6 | Zircon U-Pb age of the different intrusions from the Askartor Be-Mo deposit. **(A)** granodiorite; **(B)** biotite granite; **(C)** two-mica granite; **(D)** muscovite granite; **(E)** pegmatite, and **(F)** Re-Os isochron age of molybdenites.

respectively, and the Th/U ratios ranged from 0.39 to 0.93. Twenty-three yielded concordant $^{206}\text{Pb}/^{238}\text{U}$ ages with a weighted mean age of 385.8 ± 4.4 Ma (MSWD = 0.42, $n = 23$) (**Figure 6B**), representing the crystallization age of this rock. One point showed a younger age of 341 ± 5 Ma (**Table 1**, AKG02.23), which may be affected by minor Pb loss.

Two-mica granite (AKG04): The zircon grains separated from two-mica granite are mostly brown and opaque, and varying in size of 80–220 μm , with euhedral habit featuring tetragonal dipyrmaid \pm prism. They show weak and intense luminescences in CL photos, with reservation of primary oscillatory zone in some zircons (**Figure 5C**). The CL features indicate that the zircons have suffered from low degree of recrystallization induced by metamictization due to high contents of U (7,121–15,936 ppm) and Th (mostly fall in range of 455–2066 ppm) and fluid alteration after crystallization from

melting. The zircons mostly have low Th/U ratios of 0.1–0.2. Seventeen analytical points were conducted on the zircons with legible oscillatory zones, and sixteen of them yielded consistent and concordant $^{206}\text{Pb}/^{238}\text{U}$ ages with a weighted mean age of 247.5 ± 2.2 Ma (MSWD = 0.45) (**Figure 6C**), which represents the crystallization time of the muscovite granite. The rest one analytical point yielded an older $^{206}\text{Pb}/^{238}\text{U}$ age of 262 ± 3.6 Ma (**Table 1**, AKG04.16), which may reflect the incorporation of common lead after crystallization.

Fine-grain muscovite granite (AKG05): Zircons from fine-grain muscovite granite generally exhibit euhedral tetragonal-dipyramid or stubby tetragonal prism shapes and range from 80 to 180 μm in size. Most of them are opaque and brown to dark brown in color, with weak oscillatory zoning structure (**Figure 5D**). Th and U contents of the zircon grain are 466–4,544 ppm and 5,148–32,709 ppm, respectively, with Th/U

TABLE 2 | The whole-rock compositions of different intrusions from Anskartor Be deposit.

Rock type	Two-mica granite												Muscovite granite	
	Sample	AKG-12-04K-A	AKG-12-03A-A	AKG-12-03B-D	AKG-12-03C	AKG-12-03D	AKG-12-03E	AKG-12-04D-A	AKG-12-04E-A	AKG-12-04F	AKG-12-04G-D	AKG-12-04C	Sample	AKG-12-04C
	SiO ₂	74.77	73.87	73.37	73.10	73.05	74.25	75.06	74.58	74.21	73.70	74.40		
	TO2	0.07	0.09	0.24	0.19	0.20	0.16	0.09	0.05	0.15	0.25	0.04		
	Al ₂ O ₃	14.47	14.38	13.43	14.86	14.04	14.16	14.06	14.16	14.40	13.61	14.71		
	TFe ₂ O ₃	0.76	0.83	0.92	1.11	1.14	0.97	0.71	0.49	0.90	0.97	0.35		
	MnO	0.03	0.04	0.04	0.05	0.04	0.05	0.02	0.02	0.05	0.02	0.02		
	MgO	0.17	0.20	0.27	0.27	0.29	0.22	0.17	0.12	0.19	0.04	0.05		
	CaO	0.36	0.53	0.60	0.74	0.76	0.42	0.48	0.58	0.56	0.60	0.10		
	Na ₂ O	4.28	4.21	3.47	3.72	3.06	3.41	4.06	4.58	3.64	3.31	4.85		
	K ₂ O	3.89	4.11	3.99	4.39	4.12	4.01	4.13	3.83	4.46	4.12	3.81		
	P ₂ O ₅	0.17	0.19	0.16	0.18	0.19	0.18	0.17	0.14	0.18	0.18	0.07		
	LOI	0.87	0.94	1.32	0.54	1.23	1.63	0.72	0.66	0.97	1.09	1.12		
	Total	99.84	99.39	99.91	99.15	98.12	99.45	99.67	99.21	99.69	97.89	99.53		
	A/CNK	1.22	1.17	1.21	1.22	1.29	1.32	1.17	1.11	1.22	1.24	1.20		
	Li	107.0	148.0	148.0	183.0	211.0	236.0	100.0	75.1	151.0	97.8	59.7		
	Be	12.6	12.8	19.5	12.6	21.7	15.3	9.1	9.0	12.7	13.8	13.9		
	Rb	345.0	401.0	386.0	343.0	345.0	350.0	309.0	271.0	364.0	369.0	338.0		
	Sr	21.7	32.8	48.4	52.8	47.8	43.2	19.2	14.7	24.1	25.7	18.3		
	Y	6.8	5.9	8.0	8.6	9.1	5.6	4.0	3.4	5.8	3.2	2.4		
	Zr	59.8	67.4	83.9	106.0	119.0	92.3	54.0	33.3	83.8	60.0	16.7		
	Nb	19.7	20.3	17.6	18.9	19.9	21.2	14.4	12.1	17.2	13.1	16.0		
	Ba	58.4	88.7	135.0	131.0	104.0	115.0	26.2	15.2	50.7	77.3	16.4		
	La	4.86	11.60	13.70	23.50	19.90	12.90	8.57	5.76	10.90	8.07	0.67		
	Ce	15.00	26.20	28.80	50.50	41.90	19.30	11.00	11.00	23.10	21.40	1.30		
	Pr	3.08	3.08	3.52	6.23	5.27	3.39	2.22	1.49	2.97	2.10	0.16		
	Nd	5.31	11.10	13.40	23.10	19.60	12.60	8.08	5.43	11.30	7.59	0.50		
	Sm	1.09	1.89	2.28	3.89	3.61	2.14	1.43	1.04	2.05	1.34	0.16		
	Eu	0.13	0.25	0.32	0.41	0.36	0.25	0.16	0.11	0.20	0.16	0.02		
	Gd	0.89	1.19	1.55	2.35	2.20	1.41	0.98	0.58	1.30	0.77	0.14		
	Tb	0.17	0.19	0.23	0.35	0.33	0.21	0.14	0.10	0.21	0.13	0.03		
	Dy	1.04	0.95	1.20	1.53	1.54	1.00	0.64	0.52	0.98	0.55	0.24		
	Ho	0.22	0.18	0.24	0.28	0.28	0.18	0.12	0.10	0.17	0.09	0.05		
	Er	0.69	0.54	0.82	0.82	0.85	0.54	0.37	0.33	0.56	0.30	0.20		
	Tm	0.12	0.09	0.15	0.12	0.12	0.08	0.05	0.06	0.08	0.05	0.04		
	Yb	0.78	0.67	1.23	0.80	0.83	0.60	0.38	0.35	0.54	0.30	0.35		
	Lu	0.13	0.10	0.19	0.11	0.12	0.10	0.05	0.05	0.08	0.04	0.05		
	Hf	2.3	2.3	2.6	3.0	3.6	2.9	1.9	1.3	2.8	1.9	1.0		
	Ta	3.3	2.1	2.6	2.6	3.1	2.1	1.7	1.5	3.0	2.6	2.1		
	Th	11.1	11.1	12.2	21.1	19.8	13.6	8.5	4.8	15.3	9.6	1.4		
	U	1.8	4.6	1.9	40.1	11.3	2.1	4.9	0.9	13.3	1.5	1.5		
	Nb/Ta	6.0	9.8	6.8	7.2	6.3	9.9	8.2	8.0	5.7	5.1	7.7		
	Zr/Hf	26.3	30.0	32.0	34.9	32.8	31.4	28.9	26.0	30.0	31.1	16.4		
	Y/Ho	30.5	32.7	33.4	31.2	30.6	30.2	34.1	32.6	33.6	34.4	48.6		
	Sr/Eu	172.8	131.7	143.8	129.2	131.4	170.8	123.7	128.1	121.5	158.0	877.8		
	ΣREE	31.77	58.03	67.63	113.98	96.91	69.40	42.48	26.92	54.44	42.89	3.91		
	δEu	0.39	0.50	0.52	0.41	0.39	0.44	0.40	0.45	0.37	0.49	0.42		
	δCe	1.05	1.05	0.99	1.00	0.98	1.23	1.06	0.90	0.97	1.25	0.96		
	TE3.4	1.03	1.04	1.02	1.02	1.00	0.99	0.98	1.03	1.03	1.06	1.16		
Rock type sample	Muscovite granite												Beryl-bearing muscovite granite	
	Sample	AKG-12-04G	AKG-12-04J	AKG-12-04M	AKG-12-04N	AKY-12-04L	AKG-12-04O	AKG-12-04B	AKG-12-04H	AKG-12-04R-A	AKG-12-04S	AKG-12-04I	Sample	AKG-12-04I
	SiO ₂	74.33	74.85	75.41	74.87	74.86	74.04	72.64	75.05	71.92	74.13	75.04		
	TO2	0.06	0.05	0.04	0.03	0.04	0.03	0.01	0.01	0.01	0.01	0.03		
	Al ₂ O ₃	14.70	14.81	13.78	14.61	14.51	15.00	15.34	14.15	15.98	15.19	15.41		
	TFe ₂ O ₃	0.51	0.42	0.27	0.33	0.34	0.41	0.17	0.43	0.22	0.11	0.32		
	MnO	0.02	0.02	0.01	0.02	0.02	0.08	0.02	0.04	0.01	0.04	0.08		
	MgO	0.09	0.04	0.03	0.02	0.04	0.02	0.00	0.04	0.03	0.00	0.00		

(Continued on following page)

Rock type	Two-mica granite										Muscovite granite
	Sample	AKG-12-04K-A	AKG-12-03A-A	AKG-12-03B-D	AKG-12-03C	AKG-12-03D	AKG-12-03E	AKG-12-04D-A	AKG-12-04E-A	AKG-12-04F	
	0.19	0.26	0.25	0.16	0.25	0.22	0.07	0.33	0.15	0.09	0.09
	4.04	4.36	3.77	4.49	4.53	4.76	5.51	5.41	5.96	6.03	4.52
	4.47	4.14	4.80	3.87	3.77	3.96	3.90	2.92	4.39	3.07	3.38
	0.11	0.09	0.11	0.11	0.11	0.14	0.11	0.19	0.15	0.13	0.10
	0.55	0.74	0.55	0.91	1.00	0.84	1.04	0.69	0.89	0.75	0.89
	99.08	99.77	99.46	99.42	99.47	99.51	98.80	99.26	99.31	99.69	99.72
	1.24	1.22	1.16	1.23	1.21	1.20	1.14	1.12	1.08	1.13	1.37
						ppm					
	70.8	66.2	45.5	56.5	45.5	37.5	30.4	23.5	23.7	29.7	36.3
	10.0	10.5	9.7	10.3	11.0	10.5	200.6	311.9	300.8	355.9	175.2
	359.0	323.0	349.0	344.0	317.0	431.0	448.0	587.0	454.0	318.0	385.0
	34.6	6.8	7.7	5.0	15.0	8.3	14.6	21.0	21.1	12.4	5.9
	2.8	2.3	2.9	4.4	3.0	3.9	5.3	5.8	5.6	5.6	2.5
	Y										
	15.1	18.2	15.5	33.2	14.6	23.0	26.7	23.0	20.8	21.4	22.5
	Nb	14.4	8.6	13.9	15.5	21.4	98.7	96.7	110.0	105.0	60.6
	6.6	7.2	5.2	3.1	4.0	13.6	15.4	32.3	19.5	39.5	5.9
	Ba	7.2	1.89	1.79	1.05	1.18	0.41	0.68	1.04	0.90	0.58
	La	1.35	1.82	1.79	1.05	1.18	0.41	0.68	1.04	0.90	0.58
	Ce	3.54	3.74	3.36	2.26	2.20	0.79	1.56	2.05	1.51	1.16
	Pr	0.43	0.49	0.42	0.24	0.27	0.10	0.19	0.21	0.11	0.13
	Nd	1.35	1.58	1.41	0.70	0.84	0.32	0.68	0.66	0.40	0.41
	Sm	0.32	0.38	0.37	0.21	0.23	0.08	0.16	0.20	0.10	0.10
	Eu	0.05	0.04	0.03	0.04	0.03	0.01	0.02	0.03	0.02	0.02
	Gd	0.25	0.26	0.31	0.18	0.20	0.09	0.18	0.15	0.12	0.10
	Tb	0.06	0.05	0.08	0.04	0.05	0.04	0.06	0.05	0.06	0.03
	Dy	0.35	0.30	0.37	0.58	0.39	0.40	0.53	0.44	0.53	0.21
	Ho	0.07	0.07	0.07	0.12	0.08	0.12	0.14	0.09	0.12	0.06
	Er	0.22	0.21	0.26	0.45	0.32	0.35	0.39	0.47	0.22	0.22
	Tm	0.04	0.04	0.04	0.09	0.06	0.09	0.12	0.08	0.08	0.06
	Yb	0.27	0.30	0.33	0.66	0.46	0.77	0.88	0.70	0.81	0.59
	Lu	0.04	0.05	0.04	0.07	0.07	0.11	0.11	0.11	0.11	0.10
	Hf	0.8	0.9	0.7	1.7	0.8	4.3	4.1	3.5	4.0	1.6
	Ta	3.2	2.2	1.3	2.0	3.4	61.4	116.0	98.2	78.8	51.2
	Th	2.8	2.7	2.1	2.9	1.6	3.4	3.9	4.8	5.4	0.8
	U	2.1	8.0	1.5	3.2	2.0	18.4	16.6	10.8	5.8	2.3
	Nb/Ta	5.4	6.6	6.8	6.9	6.2	1.6	0.8	1.1	1.3	1.6
	Zr/Hf	18.5	19.3	21.8	19.2	15.1	6				

ratios in the range of 0.06–0.30 (**Table 1**). Seventeen spots were selected from domains of homogenous composition and clear oscillatory zoning for U-Pb analysis. Of these, eleven yield an age population with a weighted mean $^{206}\text{Pb}/^{238}\text{U}$ age of 231.4 ± 2.0 Ma (**Figure 6D**), representing the crystallization age of zircons. Four spots yield younger ages (213–226), deviating from the concordia due to a small amount of Pb loss or inclusions. The remaining spot yields an older age of 252 Ma, most likely representing the formation age of xenocrysts.

Pegmatite (AKG06): The zircon grains from the banded pegmatite collected for U-Pb dating are similar to those from sample AKG05 in color, transparency, crystal habit, and grain size. Some zircons show metasomatic relict textures in CL photos, and are characterized by microtextured mantle-core with nonuniform luminescences and relict rim with uniform luminescence, indicating evident metasomatic alteration after crystallization. The primary zircon domains are featured by weak and uniform luminescences, embayed texture, and regular or irregular shapes, and are enclosed by spongy domains (**Figure 5E**). All these features suggest that the zircons have suffered from metamictization, metasomatism, and recrystallization to different extents. The zircons have Th and U contents of 291–3,936 ppm and 4,034–7,608 ppm, respectively, with varying Th/U ratios from 0.05 to 0.61. Twenty-four analytical points were conducted on the primary zircon domains and twenty-two of them yielded consistent and concordant $^{206}\text{Pb}/^{238}\text{U}$ ages with a weighted mean age of 220.6 ± 1.6 Ma (MSWD = 0.80) (**Figure 6E**), which represents the crystallization time of the pegmatite. The other two points yielded inconcordant ages, indicating the incorporation of common lead after crystallization or influence of mineral inclusion in zircon.

Molybdenite Re-Os Ages

The Re-Os isotope results of the 7 molybdenite samples are shown in **Table 2**. The Re content of molybdenite is between 38 and 56 ppm with an average of 47 ppm. The Re-Os model ages of 7 molybdenite samples range from 224.6 ± 3.1 to 235 ± 3.4 Ma, with a weighted mean age of 229.0 ± 3.0 Ma (**Table 3**). ISOPLOT software was used to calculate the isochron age for the seven data points, and derived an isochron age of 228.7 ± 7.1 Ma (**Figure 6D**). The isochron age represents the time of molybdenite crystallization.

Geochemical Characteristic

The two-mica granite, muscovite granite, and beryl-bearing muscovite granite are rich in SiO_2 (71.92–75.41 wt%), Al_2O_3 (13.43–15.98 wt%), and total alkali $\text{Na}_2\text{O} + \text{K}_2\text{O}$ (7.18–10.35 wt %), poor in CaO (0.07–0.76 wt%), TFe_2O_3 (0.11–1.14 wt%), and TiO_2 (0.01–0.25 wt%) (**Table 2**). In the TAS diagram, all the samples fall in the granite area (**Figure 7A**); on the K_2O - SiO_2 diagram, most of the samples fall in the range of high-K calc alkaline series (**Figure 7B**); the A/CNK index varies from 1.1 to 1.3 (**Figure 7C**), with strong peraluminous characteristics. Compared with the former two, beryl-bearing muscovite granite has higher $\text{Na}_2\text{O}/\text{K}_2\text{O}$ ratio ($\text{Na}_2\text{O}/\text{K}_2\text{O} = 1.2$ –2.0). The REE content decreases gradually from two mica granite

($\sum \text{REE} = 27$ –114.0 ppm), medium fine-grained muscovite granite ($\sum \text{REE} = 4$ –10 ppm) to beryl-bearing muscovite granite ($\sum \text{REE} = 4$ –6 ppm); The rock samples all have negative Eu anomalies ($\delta \text{Eu} = 0.27$ –0.61). the Lanthanide tetrad effects in the REE patterns are observed in muscovite granite. The degrees of the tetrad effects ($\text{TE}_{3,4}$) in the muscovite and beryl-bearing muscovite granite are in the range of 1.08–1.19 and 1.24–1.34, respectively, (**Table 2**; **Figures 8A,B**).

In the normalized spider web diagram of trace element primitive mantle, all of the rock samples show enrichment of large ion lithophile elements, and have obvious negative anomalies of Ba, Sr, and Ti (**Figures 8C,D**).

DISCUSSION

The Formation age of Be Deposit in Altay

The zircon U-Pb age of pegmatoid orebody is 220.6 ± 1.6 Ma which coincides with the molybdenite Re-Os isochron age of 228.7 ± 7.1 . This age is slightly younger than that of muscovite granite (231.4 ± 2.0 Ma). The zircon U-Pb age of the Askartor Be-Mo deposit obtained in this paper is consistent with that of the previous study (Wang et al., 2015) (**Table 4**).

Recent studies have revealed that the geodynamic change in the Triassic period played a key role in the formation of rare-metal deposits in Altay, NW China. These deposits include (see **Table 4**): Koktokay No.3 pegmatite-type Li-Be-Ta-Nb-Cs deposit (220–209 Ma, Chen, 2011; Wang et al., 2007); Koktokay No.1 and Koktokay No.11 pegmatite-type Li-Be-Ta-Nb (208 and 212 Ma, respectively, Ren et al., 2011); Kelumute No.112 pegmatite-type Li-Be-Nb-Ta deposit (238–211 Ma, Lv et al., 2012), and Fuhai No.11 pegmatite-type Li-Be-Nb-Ta deposit (203 Ma, Lv et al., 2012). Some medium-scale Be-Nb-Ta deposits and small-scale pegmatite-type Be in Altay, such as Kalaerqisi, Qiebielin-xiaokalasus, and Jiamanhaba pegmatites were dated at 250–209 Ma (Ren et al., 2011; Ma et al., 2015).

Thus, the formation of Askartor Be-Mo deposit is not an accidental metallogenic event, but is representative of the Triassic rare metal metallogenic event in Altay.

The Genesis of Askartor Be-Mo Deposit

The two-mica granite, muscovite granite, beryl-bearing muscovite granite, and pegmatoid shell have a close spatial and temporal relationship, with similar zircon Hf isotopic composition (Wang et al., 2015). These features indicate that these rocks may be the products of the same magmatic system at different evolution stages.

As shown in **Figure 9**, although the beryl-bearing muscovite granite has higher Na_2O content and $\text{Na}_2\text{O}/\text{K}_2\text{O}$ ratio, the evolutionary relationship among the major elements of the three types of granites is not obvious. The proportion of rock-forming minerals (such as quartz and feldspars) of the three types of granites is basically the same, which is close to the proportion of the minimum composition, $\text{Ab}_{37}\text{Ms}_{10}\text{Or}_{20}\text{Qtz}$ (Icenhower and London, 1995). Therefore, these rocks can be the products of

TABLE 3 | Re-Os data of molybdenite from the Askartor Be deposit.

Sample	Re (ppm)		¹⁸⁷ Re (ppm)		¹⁸⁷ Os (ppb)		Ages (Ma)	
	Measured	1σ	Measured	1σ	Measured	1σ	Measured	1σ
QHA12-02	49.7	2.3	31.1	1.4	117.1	2.3	226.5	4.5
QHA12-03	43.3	2.0	27.1	1.3	103.8	2.2	230.4	4.8
QHA12-04	45.7	0.7	28.6	0.4	109.3	1.9	229.6	3.9
QHA12-05	38.3	0.7	24.0	0.4	93.90	1.4	235.7	3.4
QHA12-07	56.4	0.7	35.3	0.4	136.2	3.2	231.8	5.5
QHA12-08	46.8	0.8	29.3	0.5	109.4	1.5	224.6	3.1
QHA12-10	50.9	1.5	31.7	1.0	120.1	2.2	227.8	4.2

model continuous fractional crystallization in the same magmatic systems.

One consequence of Goldschmidt's Rule is that isovalent trace elements of equal or very similar ionic radii should remain tightly coupled in geological processes. If, however, in certain geological systems other properties become important, this coherency is likely to break down. In octahedral coordination, Y^{3+} , Ho^{3+} , Zr^{4+} , Hf^{4+} , Nb^{5+} , and Ta^{5+} show effective ionic radii of 1.04, 1.04, 0.86, 0.85, 0.78, and 0.78, respectively, (Shannon, 1976). Hence, the element pairs Y-Ho, Zr-Hf, and Nb-Ta are geochemical twin pairs. The fractionation of these trace element pairs occurred in muscovite granites, with the increase degree of the tetrad effect (Figure 10). The fractionation of isovalent trace element and the lanthanide tetrad are known to indicate magmatic-hydrothermal transition environments (e.g., Bau, 1996; Irber, 1999; Monecke et al., 2002; Monecke et al., 2007; Ballouard et al., 2016). The characteristics of trace elements indicate that muscovite granites have undergone self-metasomatism. This self-metasomatism refers to the reaction between the fluid, excluding from the granitic magma, and incompletely crystallized granite.

Based on the partition coefficients of Be and the results of this study, we preliminarily established the mineralization model of Askartor Be-Mo deposit (Figure 11). The model is mainly established on the basis of the Rayleigh fractional crystallization equation:

$$C^{RL} = C^L f^{D^S-1} \quad (1)$$

$$\overline{C^S} = C^L \times \frac{(1 - f^{D^S})}{1 - f} \quad (2)$$

C^L : concentration of Be in initial magma.

C^{RL} : instant concentration of Be in residual magma.

C^S : average concentration of Be in crystalline solid.

D^S : The total partition coefficient of Be

f : ratio of residual magma to initial magma.

The inclusion data show that the emplacement pressure and temperature of the initial magma of the Askartor Be-Mo deposit are 500 MPa and $750 \pm 50^\circ\text{C}$ (Ding, 2016). At these temperature and pressure conditions, the minimum and maximum water contents in the initial magma are 4 wt% and 10 wt%, respectively, (Holtz et al., 2001). When we assume that the water content of the initial is 4%, according to the balance calculation: $4 \text{ wt}\% = (1-f) \times 0 \text{ wt}\% + f \times 10 \text{ wt}\%$

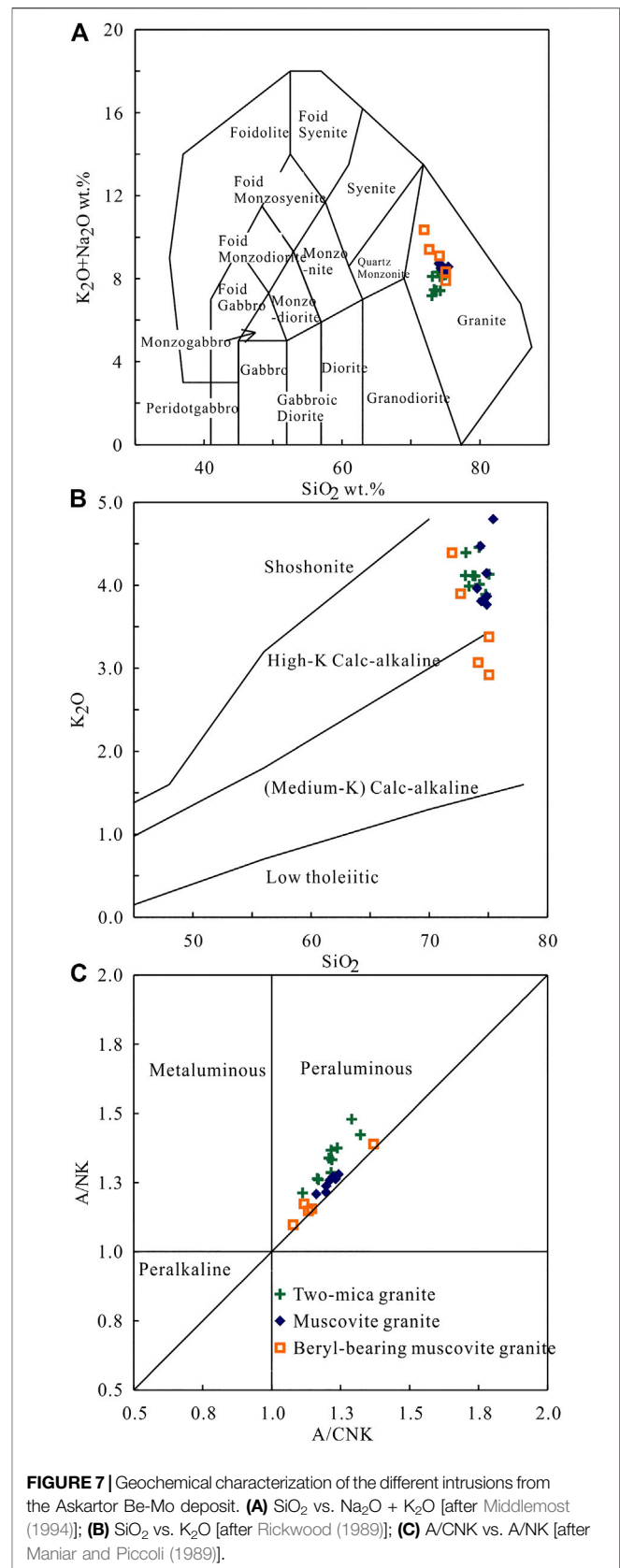


FIGURE 7 | Geochemical characterization of the different intrusions from the Askartor Be-Mo deposit. (A) SiO_2 vs. $Na_2O + K_2O$ [after Middlemost (1994)]; (B) SiO_2 vs. K_2O [after Rickwood (1989)]; (C) A/NK vs. A/CNK [after Maniar and Piccoli (1989)].

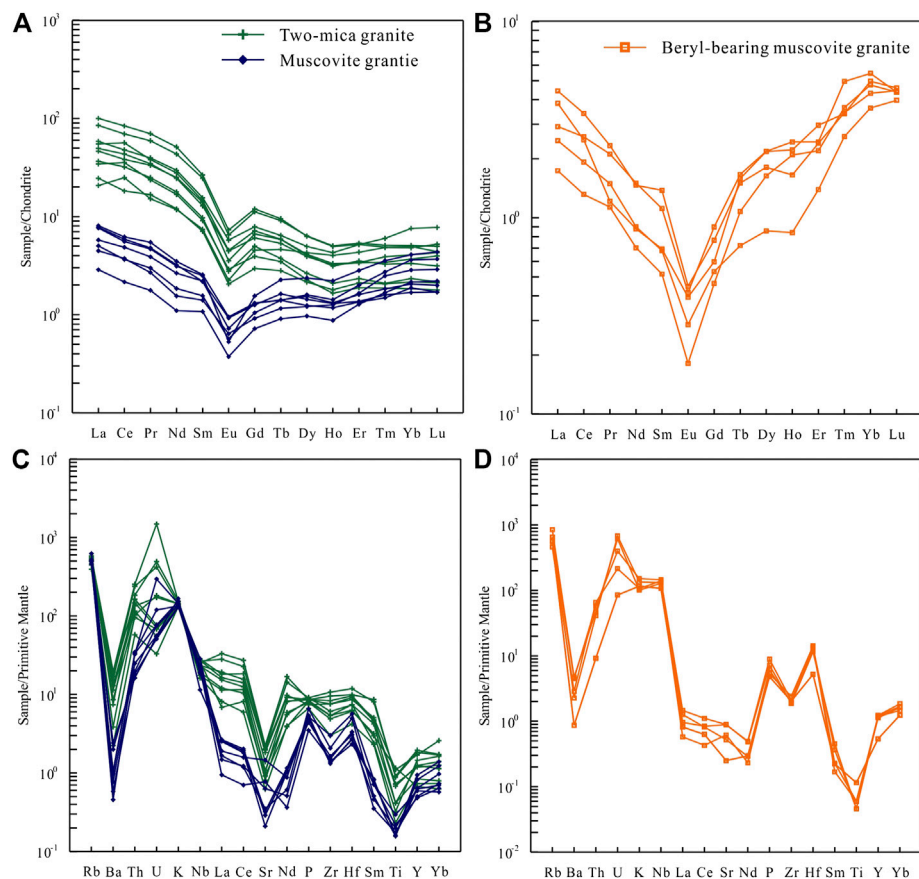


FIGURE 8 | The Chondrite-normalized rare earth element (REE) patterns and Primitive-mantle-normalized spider diagram of the different intrusions from the Askartor Be-Mo deposit. **(A, C)** two-mica and muscovite granite; **(B, D)** beryl-bearing muscovite granite. Symbols are as in **Figure 7**. Chondrite and primitive-mantle values are from Sun and McDonough (1989).

TABLE 4 | Age of rare metal deposit in the Chinese Altay orogenic belt.

Location	Deposit type	Deposit name	Mineralization type	Age (Ma)	Dating method	Reference
Koktokay	Pegmatite	KKT03	Li-Be-Ta-Nb-Cs	220–209	U-Pb	Chen (2011)
	Pegmatite	KKT01	Li-Be-Ta-Nb	208.1 ± 0.8	U-Pb	Wang et al. (2007)
	Pegmatite	KKT11	Li-Be-Ta-Nb	212.7 ± 2.5	U-Pb	Ren et al. (2011)
Kelumute-jideke	Pegmatite	FH11	Be-Ta-Nb	202.9 ± 0.8	U-Pb	Ren et al. (2011)
	Pegmatite	KLMT112	Li-Be-Ta-Nb	238–211	U-Pb	Lv et al. (2012)
Kalaerqisi	Pegmatite	KKLG650	Li-Be-Ta-Nb	228–211	U-Pb	Ren et al. (2011)
	Pegmatite	JMK02	Li-Be-Ta-Nb	212.2 ± 1.7	U-Pb	Ma et al. (2015)
	Pegmatite	QK02	Be-Ta-Nb	206.8 ± 1.6	U-Pb	Ren et al. (2011)
	Pegmatite	FH08	Be-Ta-Nb	244.3 ± 1.1	U-Pb	
	Pegmatite	ALT01	Be-Ta-Nb	246.8 ± 1.2	U-Pb	
Qiebielin-xiakalasu	Pegmatite	BRJ10	Be	249.7 ± 0.7	U-Pb	
	Pegmatite	BRJ07	Be	240.5 ± 1.4	U-Pb	
Jiamanhaba	Pegmatite	HB07	Be	237.5 ± 2.6	U-Pb	
Askartor	Granite ± pegmatite	Askartor	Be-Mo	220.6 ± 1.6	U-Pb	This study
				218.2 ± 3.9	U-Pb	Wang et al. (2015)
				228.7 ± 7.1	Re-Os	This study
				218.6 ± 1.3	Re-Os	Wang et al. (2015)

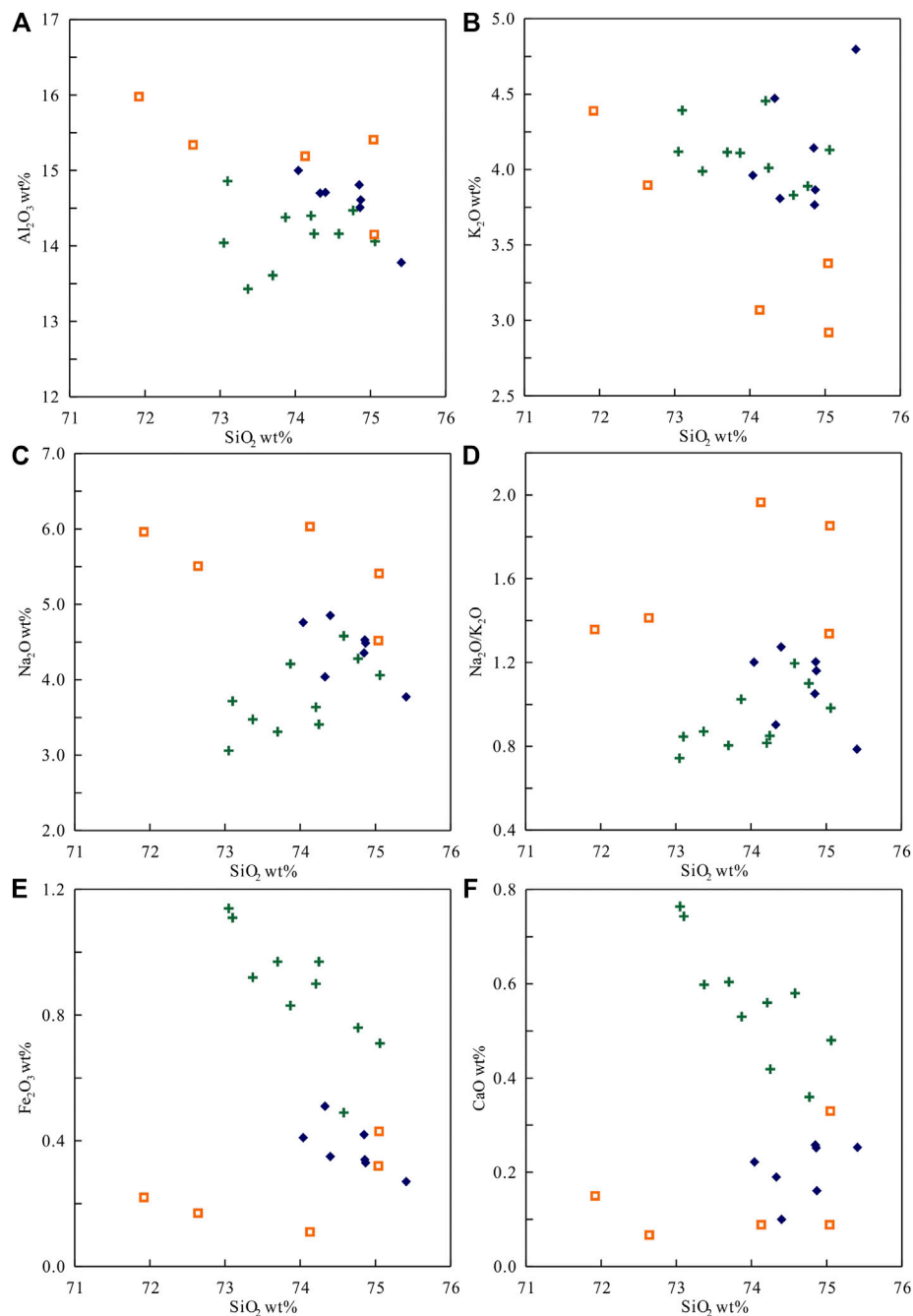


FIGURE 9 | Bivariate plots of the oxides Al_2O_3 , K_2O , Na_2O , Fe_2O_3 , CaO , and $\text{Na}_2\text{O}/\text{K}_2\text{O}$ ratios vs. SiO_2 of the different intrusions from the Askartor Be-Mo deposit.

%, when the water content in magma will reach 10 wt%, the f equals to 0.4. Even if we consider hydrous minerals like mica, because the content of mica is low, it has little effect on the results. Trace element data show that the two-mica granite should be the product of pure magmatic crystallization, so at this stage, the fractional degree of initial magma will not exceed 0.6. The Be content in two-mica granite is ~ 13 ppm. If $f = 0.4$, from Eq. 2, we can calculate that the Be content in the initial magma is ~ 30 ppm, and then we can work out that the Be content in residual magma is ~ 60 ppm based on Eq. 1. Then we can

use the Be content in the beryl-bearing muscovite granite to calculate the fractional degree in the second stage. The mass of the fluid and the Be content in fluid are gained via the mass balance. Rayleigh fractional calculations show that:

- the content of Be in the initial magma forming the Askartor deposit is as high as 30 ppm, which is 10 times of the average Be content in the upper crust (Be ~ 3 ppm in upper crust, Taylor and McLennan, 1995). This value is similar to the Be

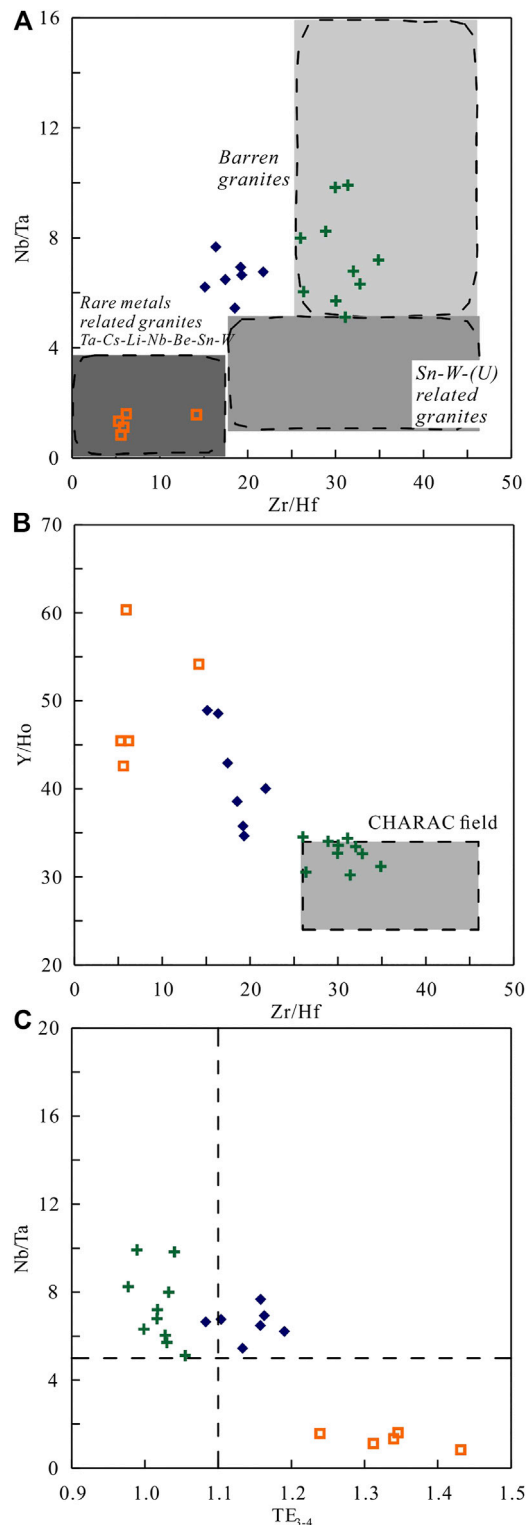


FIGURE 10 | The fractionation of isovalent trace elements of the different intrusions from the Askartor Be-Mo deposit. **(A)** Zr/Hf vs Nb/Ta, the different rare metal mineralization zones are defined by Ballouard et al. (2016); **(B)** Zr/Hf vs Y/Ho, the "CHARAC field with $24 < Y/Ho < 34$ and $26 < Zr/Hf < 46$ " is defined by Bau (1996); **(C)** TE_{3-4} vs Nb/Ta, Degree of tetrad effect (TE_{3-4}) has been calculated using equation of Irber (1999).

content of the less-altered tuffs and pumices from the Macusani Province, Peru (28 ± 9 ppm, with a high of 37 ppm, Noble et al., 1984). These rhyolites are S-type in overall chemical character with high $^{87}\text{Sr}/^{86}\text{Sr}$, strongly peraluminous composition, and trace element patterns that follow from an abundance of argillic or micaceous material at the source (Pichavant et al., 1988). Partial melting of a typical pelitic mica schist with 3 ppm Be, which is composed of muscovite, biotite, plagioclase, and quartz, will yield a content of 4–6 ppm Be in melt (Evensen and London, 2002), so, the pre-enrichment of Be in the source will restrict the mineralization of Be.

- b. The initial magma is fluid saturated after the crystallization of 60%, and the residual magma contains ~60 ppm Be. After that, the system changed from pure magma (+crystal) stage to magma-hydrothermal transition stage.

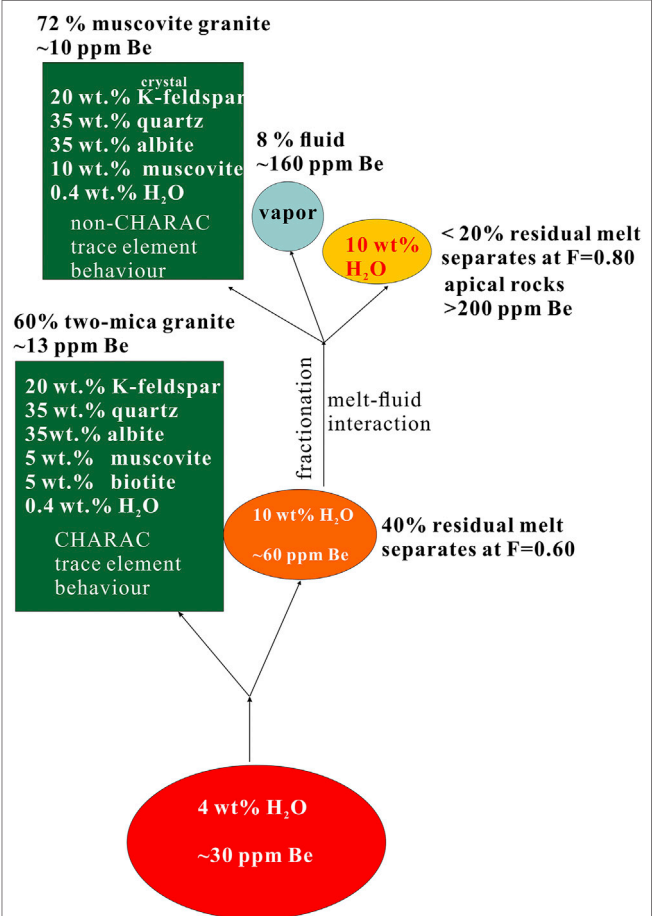


FIGURE 11 | A simple mineralization model for Askartor Be-Mo deposit. This model is based on the fractionation crystallization. The partition coefficients of Be between minerals and melts are cited from Evensen and London (2002): $D^{\text{K-feldspar/melt}} = 0.14$; $D^{\text{quartz/melt}} = 0.24$; $D^{\text{albite/melt}} = 0.19$; $D^{\text{muscovite/melt}} = 1.35$; $D^{\text{biotite/melt}} = 0.54$; the mineral proportions are close to the real mineral proportions of rocks, which are typical of mica granite systems. Based on the inclusions, the emplacement pressure and temperature of the rocks from Askartor Be-Mo deposit are ~500 MPa and 800°C Ding (2016), so the H_2O content in the initial magma was ~4 wt% and the H_2O solubility in melt at this condition was 10 wt% Holtz et al. (2001).

- c. When this smaller volume of magma has reached ~80% solidification, then the residual magma could achieve beryl saturation ($\text{Be} > 200 \text{ ppm}$), assuming that it could be efficiently extracted to produce beryl-bearing muscovite granite and its overlying pegmatoid shell.
- d. The Be content of the exsolution fluid is as high as 160 ppm. The partition coefficient of Be in coexisting fluid and melt is 0.8, which is consistent with that obtained from the inclusion data (e.g., 0.37 ± 0.43 , Zajacz et al., 2008).

CONCLUSION

- (1) the zircon U-Pb ages of the granodiorite, biotite granite, two-mica granite, muscovite granite and pegmatoid are 386.8 ± 2.6 , 385.4 ± 4.4 , 247.5 ± 2.2 , 231.4 ± 2.0 , and $220.6 \pm 1.6 \text{ Ma}$, respectively. The molybdenite Re-Os isochron age is 228.7 ± 7.1 , which coincides with the zircon U-Pb age of $220.6 \pm 1.6 \text{ Ma}$ of the pegmatoid orebody. The two-mica granite, muscovite granite, beryl-bearing muscovite granite and pegmatoid shell have close spatial and temporal relationships.
- (2) The highly fractionated element ratios of Y/Ho, Zr/Hf and Nb/Ta, plus the REE tetrad effect indicate the fluid exsolution occurs at the late stage of magma evolution and the muscovite granite experienced strong self-metasomatism.

REFERENCES

- Andersen, T. (2002). Correction of common lead in U-Pb analyses that do not report ^{204}Pb . *Chem. Geol.* 192 (1), 59–79. doi:10.1016/S0009-2541(02)00195-X
- Ballouard, C., Poujol, M., Boulvais, P., Branquet, Y., Tartèse, R., and Vigneresse, J.-L. (2016). Nb-Ta fractionation in peraluminous granites: a marker of the magmatic-hydrothermal transition. *Geology* 44 (3), 231–234. doi:10.1130/G37475.1
- Barton, M. D., and Young, S. (2002). Non-pegmatitic deposits of beryllium: mineralogy, geology, phase equilibria and origin. *Rev. Mineral. Geochem.* 50 (1), 591–691. doi:10.2138/rmg.2002.50.14
- Bau, M. (1996). Controls on the fractionation of isovalent trace elements in magmatic and aqueous systems: evidence from Y/Ho, Zr/Hf, and lanthanide tetrad effect. *Contrib. Mineral. Petrol.* 123 (3), 323–333. doi:10.1007/s004100050159
- Brousse, A., Aguilar, C., Sun, M., Schulmann, K., Štípská, P., Jiang, Y., et al. (2018). Polycyclic Palaeozoic evolution of accretionary orogenic wedge in the southern Chinese Altai: evidence from structural relationships and U-Pb geochronology. *Lithos* 314–315, 400–424. doi:10.1016/j.lithos.2018.06.005
- Cai, K., Sun, M., Yuan, C., Zhao, G., Xiao, W., Long, X., et al. (2010). Geochronological and geochemical study of mafic dykes from the northwest Chinese Altai: implications for petrogenesis and tectonic evolution. *Gondwana Res.* 18 (4), 638–652. doi:10.1016/j.gr.2010.02.010
- Cai, K., Sun, M., Yuan, C., Zhao, G., Xiao, W., Long, X., et al. (2011a). Geochronology, petrogenesis and tectonic significance of peraluminous granites from the Chinese Altai, NW China. *Lithos* 127 (1), 261–281. doi:10.1016/j.lithos.2011.09.001
- Cai, K., Sun, M., Yuan, C., Zhao, G., Xiao, W., Long, X., et al. (2011b). Prolonged magmatism, juvenile nature and tectonic evolution of the Chinese Altai, NW China: evidence from zircon U-Pb and Hf isotopic study of Palaeozoic granitoids. *J. Asian Earth Sci.* 42 (5), 949–968. doi:10.1016/j.jseas.2010.11.020
- Cai, K., Sun, M., Yuan, C., Zhao, G., Xiao, W., and Long, X. (2012a). Keketuohai mafic-ultramafic complex in the Chinese Altai, NW China: petrogenesis and geodynamic significance. *Chem. Geol.* 294–295, 26–41. doi:10.1016/j.chemgeo.2011.11.031
- (3) Rayleigh fractional calculations show that the Askartor Be-Mo deposit is the product of multistage fractional crystallization of initial Be-enriched magma.

DATA AVAILABILITY STATEMENT

The original contributions presented in the study are included in the article/Supplementary Material, further inquiries can be directed to the corresponding authors.

AUTHOR CONTRIBUTIONS

TY, ZH, and LZ-H designed the study and Participated in field work, TY and LZ-H analyze the sample and acquired the data, All authors contributed to the writing of the manuscript, and read and approved the final version.

FUNDING

The study is supported by the National Science Foundation of China (No. 91962222).

- Cai, K., Sun, M., Yuan, C., Xiao, W., Zhao, G., Long, X., et al. (2012b). Carboniferous mantle-derived felsic intrusion in the Chinese Altai, NW China: implications for geodynamic change of the accretionary orogenic belt. *Gondwana Res.* 22 (2), 681–698. doi:10.1016/j.gr.2011.11.008
- Cai, K., Sun, M., Jahn, B.-M., Xiao, W., Long, X., Chen, H., et al. (2016). Petrogenesis of the permian intermediate-mafic dikes in the Chinese Altai, northwest China: implication for a postaccretion extensional scenario. *J. Geol.* 124 (4), 481–500. doi:10.1086/686464
- Chen, B., and Jahn, B.-M. (2002). Geochemical and isotopic studies of the sedimentary and granitic rocks of the Altai orogen of Northwest China and their tectonic implications. *Geol. Mag.* 139 (1), 1–13. doi:10.1017/S0016756801006100
- Chen, J.-F. (2011). Geochemistry of the plate part in Altai No.3 pegmatite and its formation and evolution. Master's thesis. Beijing (China): University of Chinese Academy of Sciences.
- Ding, X., Li, J.-K., Ding, J.-G., Wang, S., Liu, Y.-C., and Wang, X. (2016). Molybdenite Re-Os isochron age and geological implication in Asikaerte Be-Nb-Mo deposit of Xinjiang. *J. Guilin Univ. Technol.* 36 (1), 60–65. doi:10.3969/j.issn.1674-9057.2016.01.009 [in Chinese, with English summary].
- Ding, X. (2016). Ore-forming mechanism of Askartor granite type beryllium deposit in Xinjiang, China. Master's thesis. Wuhan (China): China University of Geosciences.
- Du, A., Wu, S., Sun, D., Wang, S., Qu, W., Markey, R., et al. (2004). Preparation and certification of Re-Os dating reference materials: molybdenites HLP and JDC. *Geostand. Geoanal. Res.* 28 (1), 41–52. doi:10.1111/j.1751-908X.2004.tb01042.x
- Evensen, J. M., and London, D. (2002). Experimental silicate mineral/melt partition coefficients for beryllium and the crustal Be cycle from migmatite to pegmatite. *Geochim. et Cosmochim. Acta* 66 (12), 2239–2265. doi:10.1016/S0016-7037(02)00889-X
- Foley, N. K., Jaskula, B. W., Piatak, N. M., and Schulte, R. F., II (2017). "Beryllium," in *Critical mineral resources of the United States-economic and environmental geology and prospects for future supply*. Editors K. J. Schulz, J. H. DeYoung, R. R. Jr Seal, and D. C. Bradley (Reston, VA: U.S. Geological Survey Professional Paper), 797.
- Holtz, F., Johannes, W., Tamic, N., and Behrens, H. (2001). Maximum and minimum water contents of granitic melts generated in the crust: a

- reevaluation and implications. *Lithos* 56 (1), 1–14. doi:10.1016/s0024-4937(00)00056-6
- Icenhower, J., and London, D. (1995). An experimental study of element partitioning among biotite, muscovite, and coexisting peraluminous silicic melt at 200 MPa (H₂O). *Am. Mineral.* 80 (11–12), 1229–1251. doi:10.2138/am-1995-11-1213
- Irber, W. (1999). The lanthanide tetrad effect and its correlation with K/Rb, Eu/Eu*, Sr/Eu, Y/Ho, and Zr/Hf of evolving peraluminous granite suites. *Geochim. et Cosmochim. Acta* 63 (3–4), 489–508. doi:10.1016/s0016-7037(99)00027-7
- Jiang, Y., Sun, M., Zhao, G., Yuan, C., Xiao, W., Xia, X., et al. (2010). The 390 Ma high-T metamorphic event in the Chinese Altai: a consequence of ridge-subduction? *Am. J. Sci.* 310 (10), 1421–1452. doi:10.2475/10.2010.08
- Li, P., Yuan, C., Sun, M., Long, X., and Cai, K. (2015). Thermochronological constraints on the late Paleozoic tectonic evolution of the southern Chinese Altai. *J. Asian Earth Sci.* 113, 51–60. doi:10.1016/j.jseas.2014.11.004
- Liu, Y., Hu, Z., Gao, S., Günther, D., Xu, J., Gao, C., et al. (2008). *In situ* analysis of major and trace elements of anhydrous minerals by LA-ICP-MS without applying an internal standard. *Chem. Geol.* 257 (1), 34–43. doi:10.1016/j.chemgeo.2008.08.004
- London, D., and Evensen, J. M. (2002). Beryllium in silicic magmas and the origin of beryl-bearing pegmatites. *Rev. Mineral. Geochem.* 50 (1), 445–486. doi:10.2138/rmg.2002.50.11
- Ludwig, K. (2003). *User's manual for Isoplot 3.00: a geochronological toolkit for microsoft excel*. Berkeley, CA: Berkeley Geochronology Center Special Publication, 74.
- Lv, Z.-H., Zhang, H., and Tang, Y. (2021). Anatexis origin of rare metal/earth pegmatites: evidences from the Permian pegmatites in the Chinese Altai. *Lithos* 380–381, 105865. doi:10.1016/j.lithos.2020.105865
- Lv, Z.-H., Zhang, H., Tang, Y., and Guan, S.-J. (2012). Petrogenesis and magmatic-hydrothermal evolution time limitation of Kelumute No. 112 pegmatite in Altay, Northwestern China: evidence from zircon U-Pb and Hf isotopes. *Lithos* 154 (0), 374–391. doi:10.1016/j.lithos.2012.08.005
- Ma, Z.-L., Zhang, H., Tang, Y., Lv, Z.-H., Zhang, X., and Zhao, J.-Y. (2015). Zircon U-Pb geochronology and Hf isotopes of pegmatites from the Kaluan mining area in the Altay, Xinjiang and their genetic relationship with the Halong granite. *Geochimica* 44 (1), 9–26. doi:10.19700/j.0379-1726.2015.01.002 [in Chinese, with English summary].
- Maniar, P. D., and Piccoli, P. M. (1989). Tectonic discrimination of granitoids. *Geol. Soc. Am. Bull.* 101, 635–643. doi:10.1130/0016-7606(1989)101<0635:tdog>2.3.co;2
- Middlemost, E. A. K. (1994). Naming materials in the magma/igneous rock system. *Earth Sci. Rev.* 37 (3), 215–224. doi:10.1016/0012-8252(94)90029-9
- Monecke, T., Dulski, P., and Kempe, U. (2007). Origin of convex tetrads in rare earth element patterns of hydrothermally altered siliceous igneous rocks from the Zinnwald Sn-W deposit, Germany. *Geochim. et Cosmochim. Acta* 71 (2), 335–353. doi:10.1016/j.gca.2006.09.010
- Monecke, T., Kempe, U., Monecke, J., Sala, M., and Wolf, D. (2002). Tetrad effect in rare earth element distribution patterns: a method of quantification with application to rock and mineral samples from granite-related rare metal deposits. *Geochim. et Cosmochim. Acta* 66 (7), 1185–1196. doi:10.1016/s0016-7037(01)00849-3
- Noble, D. C., Vogel, T. A., Peterson, P. S., Landis, G. P., Grant, N. K., Jezek, P. A., et al. (1984). Rare-element-enriched, S-type ash-flow tuffs containing phenocrysts of muscovite, andalusite, and sillimanite, southeastern Peru. *Geology* 12 (1), 35–39. doi:10.1130/0091-7613(1984)12<35:rsatcp>2.0.co;10
- Pichavant, M., Kontak, D. J., Herrera, J. V., and Clark, A. H. (1988). The miocene-pliocene Macusani volcanics, SE Peru. *Contrib. Mineral. Petrol.* 100 (3), 300–324. doi:10.1007/BF00379741
- Qi, L., Hu, J., and Gregoire, D. C. (2000). Determination of trace elements in granites by inductively coupled plasma mass spectrometry. *Talanta* 51 (3), 507–513. doi:10.1016/s0039-9140(99)00318-5
- Qin, K.-Z., Guo, Z.-L., Shen, M.-D., Tang, D.-M., Zhou, Q.-F., Wang, C.-L., et al. (2013). Typer, intrusive and mineralization ages of pegmatite rare-element deposits in Chinese Altay. *Xinjiang Geol.* 31, 1–7. [in Chinese, with English summary].
- Ren, B.-Q., Zhang, H., Tang, Y., and Lv, Z.-H. (2011). LA-ICPMS U-Pb zircon geochronology of the Altai pegmatites and its geological significance. *Acta Mineral. Sin.* 31 (3), 587–596. doi:10.16461/j.cnki.1000-4734.2011.03.041 [in Chinese, with English summary].
- Rickwood, P. C. (1989). Boundary lines within petrologic diagrams which use oxides of major and minor elements. *Lithos* 22 (4), 247–263. doi:10.1016/0024-4937(89)90028-5
- Shannon, R. D. (1976). Revised effective ionic radii and systematic studies of interatomic distances in halides and chalcogenides. *Acta Cryst. Sect. A* 32 (5), 751–767. doi:10.1107/s0567739476001551
- Smoliar, M. I., Walker, R. J., and Morgan, J. W. (1996). Re-Os ages of group IIA, IIIA, IVA, and IVB iron meteorites. *Science* 271 (5252), 1099–1102. doi:10.1126/science.271.5252.1099
- Stepanov, A. S., and Hermann, J. (2013). Fractionation of Nb and Ta by biotite and phengite: implications for the “missing Nb paradox”. *Geology* 41 (3), 303–306. doi:10.1130/g33781.1
- Sun, M., Yuan, C., Xiao, W., Long, X., Xia, X., Zhao, G., et al. (2008). Zircon U-Pb and Hf isotopic study of gneissic rocks from the Chinese Altai: progressive accretionary history in the early to middle Palaeozoic. *Chem. Geol.* 247 (3), 352–383. doi:10.1016/j.chemgeo.2007.10.026
- Sun, S.-S., and McDonough, W. F. (1989). Chemical and isotopic systematics of oceanic basalts: implications for mantle composition and processes. *Geol. Soc. London Spec. Publ.* 42 (1), 313–345. doi:10.1144/gsl.sp.1989.042.01.19
- Taylor, S. R., and McLennan, S. M. (1995). The geochemical evolution of the continental crust. *Rev. Geophys.* 33 (2), 241–265. doi:10.1029/95rg00262
- Tong, Y., Wang, T., Jahn, B.-M., Sun, M., Hong, D.-W., and Gao, J.-F. (2014). Post-accretionary permian granitoids in the Chinese Altai orogen: geochronology, petrogenesis and tectonic implications. *Am. J. Sci.* 314 (1), 80–109. doi:10.2475/01.2014.03
- Wang, C.-L., Qin, K.-Z., Tang, D.-M., Zhou, Q.-F., Shen, M.-D., Guo, Z.-L., et al. (2015). Geochronology and Hf isotope of zircon for the Arskartor Be-Nb-Mo deposit in Altay and its geological implication. *Acta Petrol. Sin.* 31 (8), 2337–2352.
- Wang, T., Hong, D. W., Jahn, B. M., Tong, Y., Wang, Y. B., Han, B. F., et al. (2006). Timing, petrogenesis, and setting of Paleozoic synorogenic intrusions from the Altai Mountains, Northwest China: implications for the tectonic evolution of an accretionary orogen. *J. Geol.* 114 (6), 735–751. doi:10.1086/507617
- Wang, T., Jahn, B.-M., Kovach, V. P., Tong, Y., Hong, D.-W., and Han, B.-F. (2009). Nd-Sr isotopic mapping of the Chinese Altai and implications for continental growth in the central asian orogenic belt. *Lithos* 110 (1), 359–372. doi:10.1016/j.lithos.2009.02.001
- Wang, T., Tong, Y., Jahn, B.-M., Zou, T.-R., Wang, Y.-B., Hong, D.-W., et al. (2007). SHRIMP U-Pb Zircon geochronology of the Altai No. 3 Pegmatite, NW China, and its implications for the origin and tectonic setting of the pegmatite. *Ore Geol. Rev.* 32 (1–2), 325–336. doi:10.1016/j.oregeorev.2006.10.001
- Windley, B. F., Kröner, A., Guo, J., Qu, G., Li, Y., and Zhang, C. (2002). Neoproterozoic to Paleozoic geology of the Altai orogen, NW China: new zircon age data and tectonic evolution. *J. Geol.* 110 (6), 719–737. doi:10.1086/342866
- Xiao, W., Han, C., Yuan, C., Sun, M., Lin, S., Chen, H., et al. (2008). Middle cambrian to permian subduction-related accretionary orogenesis of northern Xinjiang, NW China: implications for the tectonic evolution of central asia. *J. Asian Earth Sci.* 32 (2), 102–117. doi:10.1016/j.jseas.2007.10.008
- Xiao, W. J., Windley, B. F., Huang, B. C., Han, C. M., Yuan, C., Chen, H. L., et al. (2009). End-Permian to mid-Triassic termination of the accretionary processes of the southern Altaids: implications for the geodynamic evolution, Phanerozoic continental growth, and metallogeny of Central Asia. *Int. J. Earth Sci.* 98 (6), 1189–1217. doi:10.1007/s00531-008-0407-z
- Xiao, W., Windley, B. F., Han, C., Liu, W., Wan, B., Zhang, J. e., et al. (2018). Late Paleozoic to early Triassic multiple roll-back and oroclinal bending of the Mongolia collage in Central Asia. *Earth Sci. Rev.* 186, 94–128. doi:10.1016/j.earscirev.2017.09.020
- Xiao, W., Windley, B. F., Sun, S., Li, J., Huang, B., Han, C., et al. (2015). A tale of amalgamation of three permo-triassic collage systems in central asia: oroclinal sutures, and terminal accretion. *Annu. Rev. Earth Planet. Sci.* 43 (1), 477–507. doi:10.1146/annurev-earth-060614-105254
- Yang, F.-Q., Zhang, Z.-L., Wang, R., Li, Q., Ding, J.-G., Su, Z.-h., et al. (2018). Geological characteristics and metallogenesis of rare metal deposits in Altay, Xinjiang. *Geotecton. et Metallog.* 42 (6), 1010–1026. doi:10.16539/j.ddgzycx.2018.06.006 [in Chinese, with English summary].

- Yin, R., Wang, R. C., Zhang, A.-C., Hu, H., Zhu, J. C., Rao, C., et al. (2013). Extreme fractionation from zircon to hafnon in the Koktokay No. 1 granitic pegmatite, Altai, Northwestern China. *Am. Mineral.* 98 (10), 1714–1724. doi:10.2138/am.2013.4494
- Yuan, C., Sun, M., Xiao, W., Li, X., Chen, H., Lin, S., et al. (2007). Accretionary orogenesis of the Chinese Altai: insights from paleozoic granitoids. *Chem. Geol.* 242 (1), 22–39. doi:10.1016/j.chemgeo.2007.02.013
- Zajacz, Z., Halter, W. E., Pettke, T., and Guillon, M. (2008). Determination of fluid/melt partition coefficients by LA-ICPMS analysis of co-existing fluid and silicate melt inclusions: controls on element partitioning. *Geochim. et Cosmochim. Acta* 72 (8), 2169–2197. doi:10.1016/j.gca.2008.01.034
- Zhang, A., Wang, R., Li, Y., Hu, H., Lu, X., Ji, J., et al. (2008). Tourmalines from the Koktokay No.3 pegmatite, Altai, NW China: spectroscopic characterization and relationships with the pegmatite evolution. *EJM* 20 (1), 143–154. doi:10.1127/0935-1221/2008/0020-1779
- Zhang, H., Lv, Z.-H., and Tang, Y. (2019). Metallogeny and prospecting model as well as prospecting direction of pegmatite-type rare metal ore deposits in Altay orogenic belt, Xinjian. *Mineral. Deposits* 38 (4), 792–814. doi:10.16111/j.0258-7106.2019.04.008 [in Chinese, with English summary].
- Zhang, Y.-F., Lin, X.-W., Zhao, Y.-M., Guo, Q.-M., and Zhao, D.-C. (2017). Geochronology and geochemistry of granitoids of Asfalt beryllium deposit in Qinghe County, Northern Xinjiang. *Mineral. Deposits* 36 (3), 643–658. doi:10.16111/j.0258-7106.2017.03.007 [in Chinese, with English summary].
- Zou, T.-R., Chao, H.-Z., and Wu, B.-Q. (1988). Orogenic and anorogenic granitoids of Altay Mountains of Xinjiang and their discrimination criteria. *Acta Geol. Sin.* 2 (1), 45–64. doi:10.1111/j.1755-6724.1989.mp2001005.x
- Zou, T.-R., and Li, Q.-C. (2006). *Rare and rare earth metallic deposits in Xinjiang*. Beijing, China: Beijing: Geological Publishing House [in Chinese, with English summary].

Conflict of Interest: The authors declare that the research was conducted in the absence of any commercial or financial relationships that could be construed as a potential conflict of interest.

Copyright © 2021 Yong, Hui and Zheng-Hang. This is an open-access article distributed under the terms of the Creative Commons Attribution License (CC BY). The use, distribution or reproduction in other forums is permitted, provided the original author(s) and the copyright owner(s) are credited and that the original publication in this journal is cited, in accordance with accepted academic practice. No use, distribution or reproduction is permitted which does not comply with these terms.



Enrichment of Platinum Group Elements in Lower Cambrian Polymetallic Black Shale, SE Yangtze Block, China

Yong Fu^{1*}, Zhen Yang^{1,2*}, Chao Li^{3,4} and Peng Xia¹

¹College of Resources and Environmental Engineering of Guizhou University, Guiyang, China, ²College of Eco-Environmental Engineering of Guizhou Minzu University, Guiyang, China, ³Key Laboratory of Metallogeny and Mineral Assessment, Ministry of Natural Resources of the PRC, Institute of Mineral Resources, Chinese Academy of Geological Sciences, Beijing, China, ⁴National Research Center for Geoanalysis, Beijing, China

OPEN ACCESS

Edited by:

Xiaohua Deng,
Beijing Institute of Geology for Mineral
Resources, China

Reviewed by:

Yiguan Lu,
Tianjin Center, China Geological
Survey, China
Yayun Liang,
University of Science and Technology
Beijing, China

*Correspondence:

Yong Fu
byez1225@126.com
Zhen Yang
cugbyzh@163.com

Specialty section:

This article was submitted to
Economic Geology,
a section of the journal
Frontiers in Earth Science

Received: 11 January 2021

Accepted: 11 February 2021

Published: 18 March 2021

Citation:

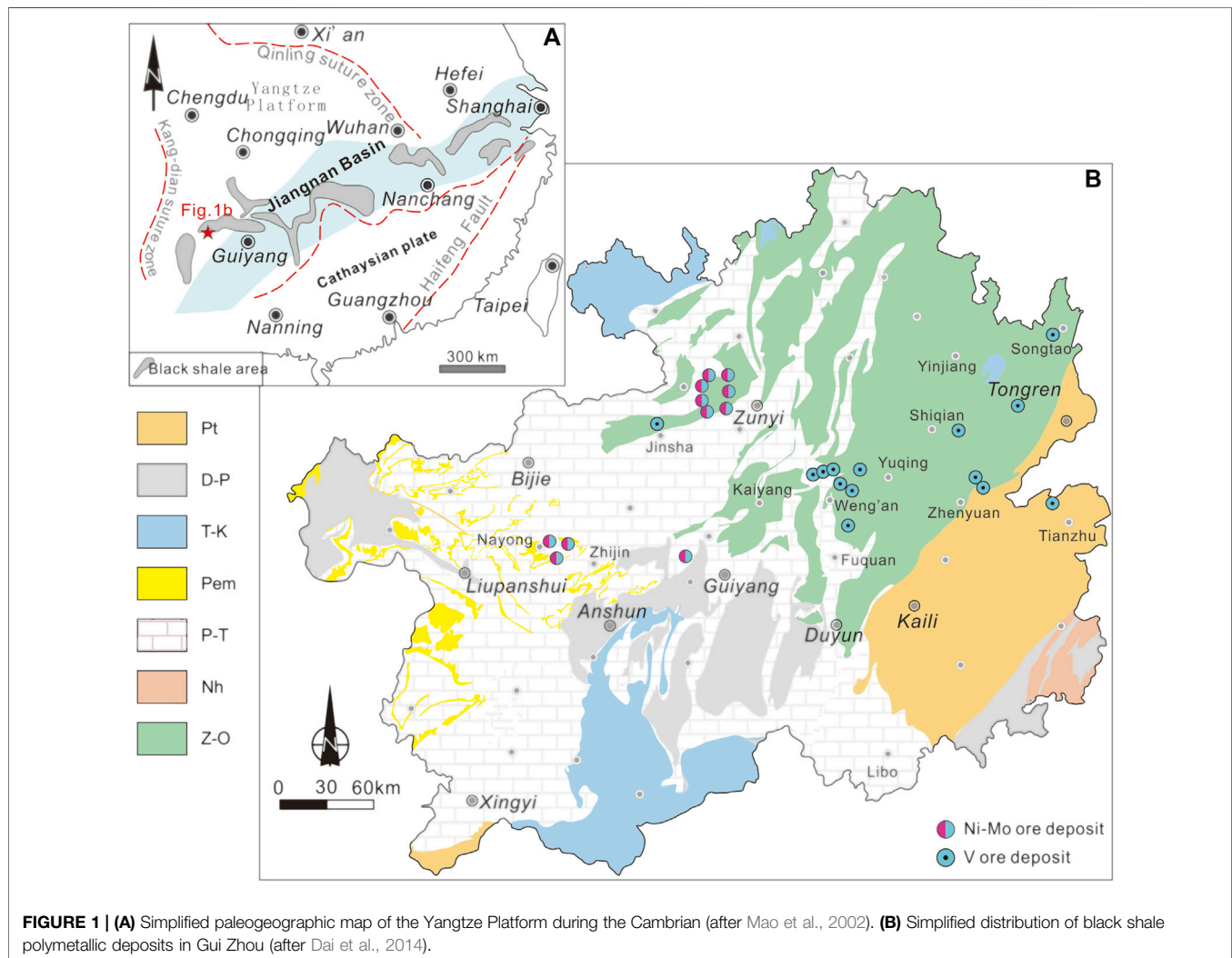
Fu Y, Yang Z, Li C and Xia P (2021)
Enrichment of Platinum Group
Elements in Lower Cambrian
Polymetallic Black Shale, SE Yangtze
Block, China.
Front. Earth Sci. 9:651948.
doi: 10.3389/feart.2021.651948

Platinum group elements (PGEs) occur mainly in basic-ultrabasic igneous rocks and are concentrated by the differentiation and crystallization of magma. Thin polymetallic layers including Ni, Mo, V, PGEs, and rare-earth elements are widely developed in lower Cambrian black shales in southern China. The PGE contents in such layers may not be economically significant but are still unusually enriched. PGE enrichment mechanisms have not been widely studied, but here the PGE compositions of polymetallic layers in the Shuidong (Nayong) and Niuchang (Weng'an) sections of the SE Yangtze block in China were determined, and results compared with published data for the region. Results indicate that PGEs are enriched in the polymetallic layers, whereas the surrounding country rocks are barren. The Σ PGE contents in the Shuidong Ni-Mo deposits are generally lower than in the Niuchang V deposits. PGE distribution patterns in the polymetallic layers are similar to those in basic-ultrabasic rocks, indicating that such rocks played a role in the PGE enrichment. Oceanic hypoxia during the Sinian-Cambrian transition resulted in the production of large amounts of organic matter and H₂S in the ocean. When high-salinity brine reached the ocean bottom, rapid changes in Eh-pH conditions caused enrichment of metals at the sediment-seawater interface, and this enrichment was later enhanced during diagenesis.

Keywords: enrichment, black shale, platinum group element, lower cambrian, south China

INTRODUCTION

Lower Cambrian black shales contain important ore-bearing strata worldwide, including large and super-large deposits of Ni-Mo-V-PGE, rare-earth elements (REEs), barite, P, and stone coal (Fan et al., 1984; Fan et al., 1987; Mao et al., 2002; Xu et al., 2012; Paava et al., 2019). In China, such shales are distributed mainly on the southeastern margin of the Yangtze Block, in Yunnan, Guizhou, Sichuan, Shanxi, Hubei, Hunan, Guangdong, Guangxi, Zhejiang, and Jiangxi provinces (Figure 1A). Large-scale deposits are distributed mainly in Guizhou and Hunan provinces (Figure 1B). Nickel, REE, and platinum group elements (PGEs) have recently been listed as strategic key minerals in the “National Mineral Resources Planning (2016–2020) of China” and the “Draft List of Crisis Minerals”



issued by the United States Department of the Interior (Jiang et al., 2019). Study of the formation mechanisms and metallogenic characteristics of polymetallic mineralization in lower Cambrian black shales is thus important to meet the strategic needs of various countries.

Several formation mechanisms have been proposed for lower Cambrian black-shale polymetallic deposits, including biogenesis (Jewell, 2000; Lu et al., 2004), a Ba-rich cold-spring origin (Paytan et al., 2002; Griffith and Paytan, 2012; Zhou et al., 2016), and hydrothermal origins (Wang and Li, 1991; Wu et al., 1999; Clark et al., 2004; Yang et al., 2007; Wu et al., 2009; Gao et al., 2018). The sources of Mo and Ni are possibly seawater (Mao et al., 2002; Lehmann et al., 2007; Xu et al., 2013) submarine hot water (Coveney, 2003; Jiang et al., 2006, Jiang et al., 2007; Han et al., 2017), and mixed sources of seawater and terrestrial hot water (Pašava et al., 2008). Vanadium sources include terrestrial environments, marine biogenesis, and deep-sea hot water (Fan et al., 1984; Fan

et al., 1987). PGE deposits generally occur in basic-ultrabasic igneous rocks and are formed by the differentiation and crystallization of magma (Barnes and Lightfoot, 2005; Qi et al., 2008; Duan et al., 2016). However, this proposal is difficult to reconcile with the above mechanisms of PGE enrichment in black shale, with the PGEs likely being derived from multiple sources (Jiang et al., 2003). Ni-Mo sulfide ores in black shale of the Niutitang Formation, South China, have a submarine hydrothermal origin, and the extreme metal enrichment is likely to have occurred in an anoxic environment with abundant organic matter in an ocean basin (Jiang et al., 2007). PGE enrichment in black shale is similar to that in marine oil shale, with contributions by terrigenous and seawater sources (Han et al., 2015). Thus, the enrichment mechanism of PGE in black shale remains unclear and it can promote the understanding of the enrichment mechanism of polymetallic layers, and then guide the regional prospecting. This study aimed to improve our understanding of the genetic

types of PGE deposit and to constrain the genesis of black-shale polymetallic deposits.

GEOLOGICAL SETTING

Lower Cambrian black shales are commonly enriched in unusual combinations of elements including Mo, Ni, Se, Re, Os, REE, and PGE (Fan et al., 1984; Steiner et al., 2001; Mao et al., 2002; Jiang et al., 2007; Xu et al., 2013; Shi et al., 2020). Such enrichment occurs sporadically along a 1600 km NE-striking facies belt in South China (**Figure 1A**). However, economically mineable ores are exposed only in Guizhou and Hunan provinces, including the Zunyi, Nayong, and Zhenyuan districts of Guizhou Province, and the Dayong and Zhangjiajie districts of Hunan Province. In Guizhou during the early Cambrian, deep-sea sedimentary rocks were enriched mainly in Mo, V, and barite, while the shallow-sea carbonate platform was enriched mainly in Ni, Mo, V, and P (**Figure 1B**), forming one of the few economically viable Ni–Mo and V black-shale polymetallic deposits (Fan et al., 1984; Fan et al., 1987). Globally, it is rare for such Ni–Mo and V deposits to be economic (Coveney, 2003; Orberger et al., 2003).

The host sequence is a diachronous, transgressive black shale sequence of the Niutitang Formation. A conformable Ni–Mo polymetallic sulfide horizon occurs in the lowermost few centimeters of this succession. The linear geographic trend of Ni–Mo polymetallic sulfide ores in South China suggests the possibility of structural control by a major deep fault zone in the Neoproterozoic back-arc-basin/platform transition zone (Steiner et al., 2001). Alternatively, as the trend is parallel to the reconstructed Cambrian shoreline, it is also possible that water depth, distance from shore, sunlight availability, or other features of the paleo-environment controlled ore deposition (Xu et al., 2012; Pagès et al., 2018; Sarwar et al., 2019). The Niutitang Formation lies unconformably on dolomite of the Neoproterozoic Dengying Formation, which in turn is underlain by black shale, chert, phosphorite, and dolomite of the Doushantuo Formation (Fan et al., 1992). The Ni–Mo and V deposits have distinct spatial distributions, with the former being distributed mainly in the Bozhou and Huichuan districts of Zunyi City, and west of Meitan–Weng'an, Nayong, and Zhijin in Bijie City (**Figure 1B**). The combined Mo and Ni reserves of the known deposits in Guizhou are 897 kilotonne (kt) and 621 kt, respectively. These deposits include three large, three medium, and nine small ore deposits, and four ore-rich regions. Vanadium deposits are distributed mainly in the Tongren–Songtao–Wanshan, Shibing–Zhenyuan–Tianzhu, and Weng'an–Yuqing–Fuquan areas (**Figure 1B**). One large-scale, 15 medium-sized, and 43 small-scale V deposits have been found in Guizhou. Ni–Mo deposits, distributed mainly in the Yangtze area, occur in black carbonaceous mudstone at the base of the Niutitang Formation. Vanadium ore is distributed mainly in the transition zone of slope to basin and occurs in black carbonaceous mudstone, the lower part of the Niutitang Formation, and in siliceous rock of the Laobao Formation.

SECTION AND SAMPLES

The early Cambrian black-shale Ni–Mo and V polymetallic deposits have clearly defined distributions in Guizhou, with the Nayong–Zunyi area containing predominantly Ni–Mo deposits and the Weng'an–Tongren area V deposits. The XJ4 exploration well profile in Shuidong, and the Moshi profile in Niuchang, were chosen for study. The polymetallic layer and black shale were analyzed for PGE composition in the two study areas, with results being compared with published data for Ni–Mo–V–PGE polymetallic layers in black shales in South China. Sampling locations are shown in **Figure 2**.

Shuidong Section XJ4, Nayong

Lower Cambrian black shale in the Nayong area occurs in the western area of Guizhou Province and the southwestern area of the Yangtze Platform. The Shuidong Ni–Mo–polymetallic deposit lies ~20 km southeast of Nayong County. Strata exposed in the mining area include the upper Sinian Dengying Formation; lower Cambrian Niutitang Formation; Mingxinsi Formation; upper Carboniferous Dapu, Huanglong, and Maping formations; Permian Liangshan, Qixia, Maokou Formation; and clastic of Quaternary. The ore-bearing rock is within the first member of the lower Cambrian Niutitang Formation (0.5–18.0 m thick), and is in unconformable contact with the underlying Sinian Dengying Formation. The ore-bearing rock includes siliceous rock, banded dolomitic phosphorite, siliceous phosphorous rock, carbonaceous argillaceous siltstone, siliceous sandstone, carbonaceous mudstone, pyrite-bearing carbonaceous siltstone, and a Ni–Mo deposit (**Figure 2A**). The Ni–Mo deposit, which occurs on top of the ore-bearing rock group, is a dark-gray to gray-black shale layers. It has a scaly structure post-weathering. The deposit base is comprised siliceous siltstone and carbonaceous mudstone (0.05–0.10 m thick). The ore containing 0.50–7.40 wt% Mo (average 4.32 wt%) and 0.33–5.78 wt% Ni (average 2.37 wt%). The Mo and Ni contents tend to be negatively correlated.

Niuchang Section, Weng'an

The main Sinian–Cambrian strata in the Weng'an area include phosphorite of the Doushantuo Formation, dolomite of the Dengying Formation, black shale of the Niutitang Formation, and mudstone and sandstone of the Mingxinsi Formation. The Niuchang section shows that the stratum could be divided into seven sub-layers according to their lithology and mineralization from top to bottom, namely during the Sinian–Cambrian transition period (**Figure 2B**).

- (1) Gray massive dolomite (~1.2 m thick) of the Dengying Formation, locally containing dissolution pores.
- (2) Fe–Mn oxide claystone (0.2 m thick), has a characteristic of typical paleo-weathering crust. It is discontinuous lens shape generally and distributed on concave and convex surfaces of the underlying dolomite of Sinian.
- (3) A Gy P-bearing dolomite layer, with a relatively high P content (0.2 m thick). It is the same age with the

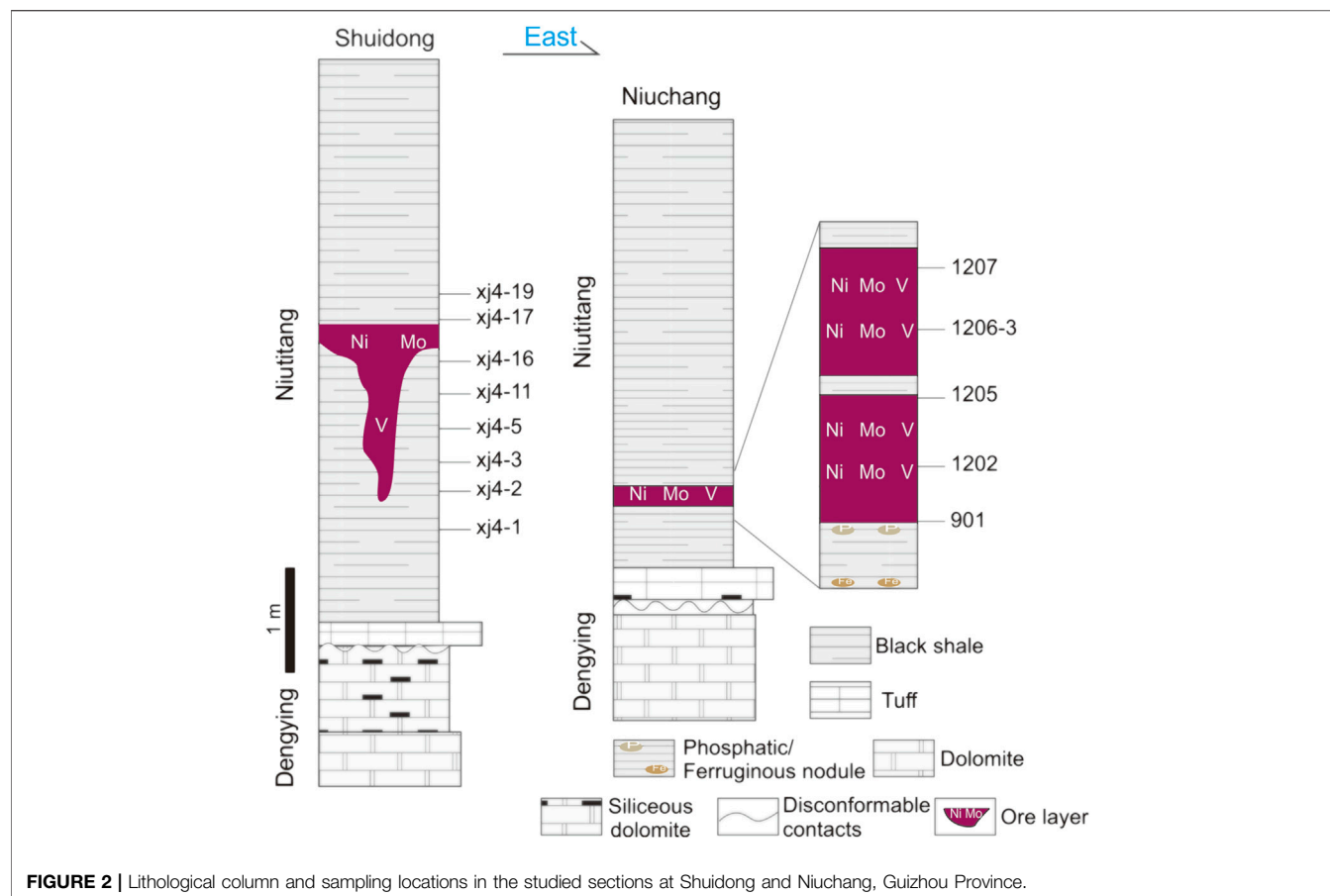


FIGURE 2 | Lithological column and sampling locations in the studied sections at Shuidong and Niuchang, Guizhou Province.

phosphorite in Zhijin of Guizhou and Kunyang of western Yunnan.

- (4) Carbonaceous silty hydromica claystone intercalated with lenticular phosphorite, total thickness 0.25 m.
- (5) Carbonaceous shale deposits containing Ni, Mo, and V. The metal sulfides are worm-like, bamboo-leaf-like and colloidal-like, distributed in a matrix of carbonaceous mica and silty sand. The ore bed is layered, lamella-like and lenticular. The boundary between the mineralized layer and the carbonaceous shale is clearly defined. The ore bed is generally 0.30 m thick.
- (6) A carbonaceous shale layer (0.1 m) containing V. The lamination is well developed and the bedding surface is smooth with a relatively high degree of cementation.
- (7) Carbonaceous hydromica claystone and silty claystone, total thickness >2 m.

ANALYTICAL METHODS

PGE analyses were undertaken at the National Research Center for Geoanalysis (NRCG), Beijing, China. A digestion technique involving 100 ml Teflon beakers and stainless-steel pressure bomb was used (Qi et al., 2011). Powdered sample (2–3 g) was

dissolved in HF + HNO₃ in a 120 ml Teflon beaker to remove silicates and sulfides. The dried residue, with an appropriate amount of isotopic spike solution containing ¹⁰¹Ru, ¹⁹³Ir, ¹⁰⁵Pd, and ¹⁹⁴Pt was digested with 5 ml HF + 15 ml HNO₃ in a sealed beaker in the pressure bomb at 190°C for 48 h, and the resulting solution evaporated to dryness. HCl (5 ml) was added to remove residual HF and HNO₃ during evaporation to dryness. The residue was dissolved in 40 ml 2 mol L⁻¹ HCl and centrifuged. PGEs were preconcentrated from the supernate by coprecipitation with Te. The main interfering elements (Cu, Ni, Zr, and Hf) were removed by ion-exchange chromatography with Dowex 50 W X8 cation exchange resin and a P507 Levextrel resin. The eluate was analyzed by inductively coupled plasma–mass spectrometry (ELAN DRC-e), with detection limits ranging from 0.004 ppb for Ir to 0.014 ppb for Pt.

RESULTS

PGE analysis results are listed in **Table 1**. The total PGE (ΣPGE) content of the polymetallic layer in the Weng'an area is in the range 538.87–989.59 ppb (average 773.18 ppb) with Os = 50.41–79.99 ppb; Ir = 1.82–3.09 ppb; Ru = 5.39–13.58 ppb; Rh = 1.56–6.19 ppb; Pt = 216.87–381 ppb; and Pd = 263–380.82 ppb. The ΣPGE of the polymetallic layer in the Nayong area is in the

TABLE 1 | PGE contents (ppb) of black shales in the lower Cambrian Nutitang Formation at Shuidong and Niuchang, Guizhou Province.

Location	Sample No.	Sample characteristic	Os	Ir	δIr	Ru	δRu	Rh	Pt	δPt	Pd	δPd	Ni	Cu	La	Ce	ΣPGE	Pt+Pd/(Os+Ir+Ru+Rh)	Pt/Pd	Ru/Ir	Os/Ir	Pt/Pt*	Ce/La	Ni/Pd	Cu/Ir	Pd/Ir	Ni/Cu		
Nayong	Xj4-1	Carbonaceous	0.87	0.01	0.10	0.00	1.76	0.02	6.38	0.05	4.48	0.06	946.80	43.60	41.40	87.30	13.64	3.91	1.42	63.80	17.60	8.70	2.82	2.12	211.34	436.00	44.80	21.72	
	Xj4-2	shale	0.47	0.01	0.13	0.00	1.92	0.05	6.16	0.07	2.75	0.01	454.30	38.00	23.50	28.50	11.49	3.45	2.24	47.38	14.77	3.62	4.38	1.21	165.20	292.31	21.15	11.96	
	Xj4-3	Ni-Mo layer	52.05	0.53	3.42	0.29	6.42	0.88	4.32	370.28	3.84	356.95	7.04	19830.00	1249.00	69.90	125.10	793.44	10.98	1.04	108.27	1.88	15.22	2.05	55.55	365.20	104.37	55.88	
	Xj4-3		51.87	0.48	4.03	0.94	6.66	0.65	3.98	365.96	4.82	351.61	7.31	18941.00	1132.00	58.80	116.30	794.11	10.78	1.04	90.81	1.65	12.87	2.06	1.98	53.02	280.89	87.25	16.47
	Xj4-5		50.93	0.38	2.52	0.07	2.90	0.16	2.62	297.81	3.34	288.36	6.28	22210.00	1244.00	64.70	83.50	645.14	9.94	1.03	118.18	1.15	20.21	2.09	80.49	493.65	114.43	18.66	
Weng'an	Xj4-5		51.69	0.49	2.76	0.03	2.98	0.41	2.96	294.47	3.56	290.56	5.40	22624.00	1033.00	63.80	82.20	645.42	9.69	1.01	106.69	1.08	18.73	2.01	78.55	374.28	105.28	22.09	
	Xj4-11	V layer	21.68	0.23	1.52	0.11	1.99	0.11	1.47	147.67	1.13	215.76	31.75	10410.00	586.80	48.10	85.90	388.65	14.41	0.88	97.15	1.31	14.26	1.37	48.25	386.05	141.95	17.74	
	Xj4-11		21.07	0.20	1.54	0.15	1.93	0.12	1.42	142.67	0.90	205.76	28.75	11103.00	593.20	46.20	84.10	373.00	14.18	0.69	92.64	1.25	13.68	1.39	53.96	385.19	133.61	18.72	
Xj4-16	Carbonaceous shale	18.37	1.39	0.94	0.01	1.75	0.15	2.70	98.96	5.14	161.20	5.71	10920.00	671.10	19.70	6.40	283.92	10.95	0.61	105.28	1.86	19.54	1.21	0.32	65.26	713.94	171.49	15.68	
Xj4-17	Black shale	1.35	0.01	0.08	0.00	0.82	0.02	0.18	5.11	0.06	5.32	0.05	825.20	62.10	13.40	21.60	12.86	4.29	0.96	63.88	10.25	16.88	1.86	1.61	155.11	776.25	66.50	13.29	
Weng'an	Xj4-19		0.65	0.01	0.13	0.00	0.49	0.01	0.19	5.89	0.08	6.35	0.06	960.50	50.70	17.90	22.60	13.70	8.38	0.93	45.31	3.77	5.00	1.80	1.26	390.00	48.85	18.94	
	901	V layer	68.47	0.61	2.72	0.11	6.44	0.82	2.73	331.14	2.31	373.22	6.19	9120.00	1656.00	25.70	33.80	794.72	8.77	0.89	121.74	2.37	25.17	1.76	2.09	606.82	137.21	5.51	
	1202		79.39	0.64	2.94	0.08	7.21	0.20	6.19	390.82	3.46	429.91	6.49	60900.00	2460.50	69.20	88.10	905.46	8.46	0.89	129.53	2.45	27.00	1.75	2.44	836.90	145.89	24.75	
	1205		50.41	0.51	1.82	0.10	4.97	0.37	1.56	216.87	1.29	263.24	1.93	13560.00	2628.30	45.20	64.00	538.87	8.17	0.82	119.16	2.73	27.70	1.64	1.42	51.51	1389.18	144.64	5.36
	1205		50.86	0.48	1.83	0.05	5.39	0.27	1.59	221.96	1.25	271.28	2.25	13421.00	2473.10	43.70	63.50	552.91	8.27	0.82	121.29	2.95	27.79	1.63	1.45	49.47	1351.42	148.24	5.43
1206-3	1206-3		69.72	0.67	3.09	0.11	8.25	0.35	2.86	367.48	5.05	416.12	6.04	42985.00	2809.50	17.70	27.20	867.52	9.34	0.88	115.93	2.67	22.56	1.75	1.54	102.34	909.22	134.67	15.16
	1207		79.99	0.60	3.05	0.05	13.58	0.78	2.88	371.79	2.50	518.30	23.66	67001.00	2740.50	70.20	87.10	989.59	8.95	0.72	121.90	4.45	26.23	1.43	1.24	129.27	886.52	169.93	24.45

range 373.00–793.44 ppb (average 604.96 ppb) with Os = 21.07–51.87 ppb; Ir = 1.52–4.03 ppb; Ru = 1.93–6.66 ppb; Rh = 0.03–4.32 ppb; Pt = 142.67–370.28 ppb; and Pd = 205.76–356.95 ppb. The Rh content of sample Nayong xj4-11 is very low, possibly because Rh has no corresponding isotopic calibration and the analytical result is inaccurate.

DISCUSSION

Regional Distribution of PGE

Analysis of the Shuidong (Nayong) section indicates that PGEs are enriched only in the polymetallic layer, with low contents in country rocks and the overlying and underlying black shale (Figure 3). The Weng'an area contains predominantly V mineralization, with the PGE content of the polymetallic layer generally being higher than in the Nayong area. This difference implies that the PGE content varies between sedimentary environments. Previous studies have shown that the PGE contents of polymetallic layers in Zhongnan Village, Zunyi, and in Guizhou and Dayong, Hunan, are in the range 551–1215 ppb (Li et al., 2003), and that the Huangjiawan polymetallic layer in the Songlin, Zunyi (Guizhou) contains 773–1187 ppb (Mao et al., 2001). The PGE content of the V-bearing black-shale layer in western Hunan is 123 ppb (Wu et al., 2001), much lower than in regional polymetallic layers.

Carbonaceous black shale in the Nayong area has ΣPGE contents of 11.5–13.7 ppb with Os = 0.47–1.35 ppb; Ir = 0.08–0.13 ppb; Ru = 0.49–1.92 ppb; Rh = 0.05–0.19 ppb; Pt = 5.1–6.4 ppb; and Pd = 2.8–6.4 ppb. Its ΣPGE content is similar to those of deep-water black shale in western Hunan (Wu et al., 2001) and Cambrian black shale in the base of the Tarim Basin (Yu et al., 2003) (Figure 4). This indicates that under anoxic conditions, the adsorption capacity of organic-rich shale is similar for all PGEs and that the formation environments of these rocks were similar.

Nayong and Weng'an black shale samples exhibit PPGE (Pt + Pd) enrichment and relative IPGE (Os + Ir + Ru + Rh) depletion. The PPGE/IPGE ratio is generally >1 (3.8–14.4), with ratios for most samples being around 9 (barring sample XJ4-11) in the polymetallic layer, much higher than that of original mantle (0.88) and upper crust (1.3) but lower than the crustal ratio (15); and also higher than the value for modern South China Sea sediments (3.45; Zhu et al., 2010) and oceanic Co-rich crusts (1.62–7.32; Yao et al., 2002; Sun et al., 2006). Sample Pt/Pd ratios are generally in the range 0.7–2.2 and <1 in the polymetallic layer (0.6–1.0), much lower than in Co-rich oceanic crust (53–439; Yao et al., 2002; Sun et al., 2006), lower than normal seawater (4.5; Hodge et al., 1985), and similar to sulfides in basic–ultrabasic rock (Pašava et al., 2003; Pašava et al., 2004). The Os/Ir ratio in the polymetallic layer is in the range 12.9–26.6, much higher than in primitive mantle (~1.1) and chondrite (~1.0; McDonough and Sun, 1995), but similar to organic-rich shale such as oil shale in Tibet (12.2–15.8; Fu et al., 2010). There is strong positive correlation between Pt and Pd contents (Figure 5A). The Pt content is also positively correlated with Os, Ir, and Ru contents (Figures 5B–D). There is a lack of correlation between Ru–Rh

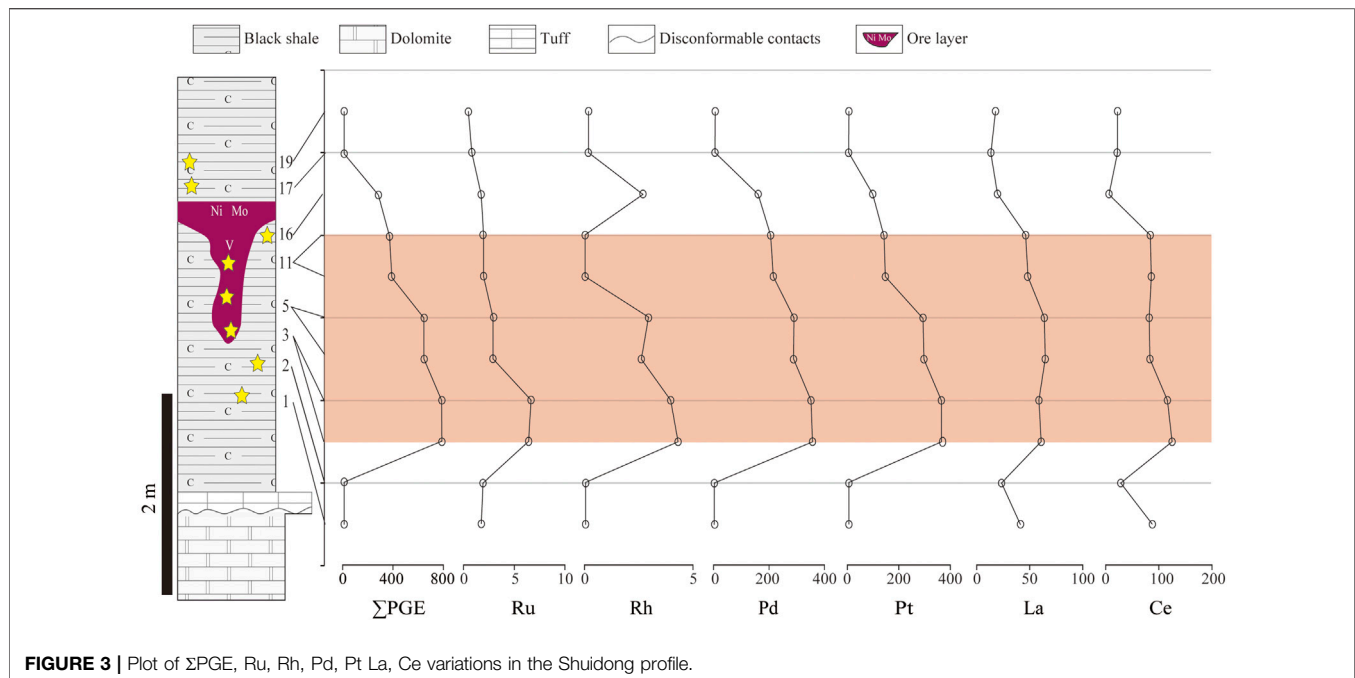


FIGURE 3 | Plot of Σ PGE, Ru, Rh, Pd, Pt La, Ce variations in the Shuidong profile.

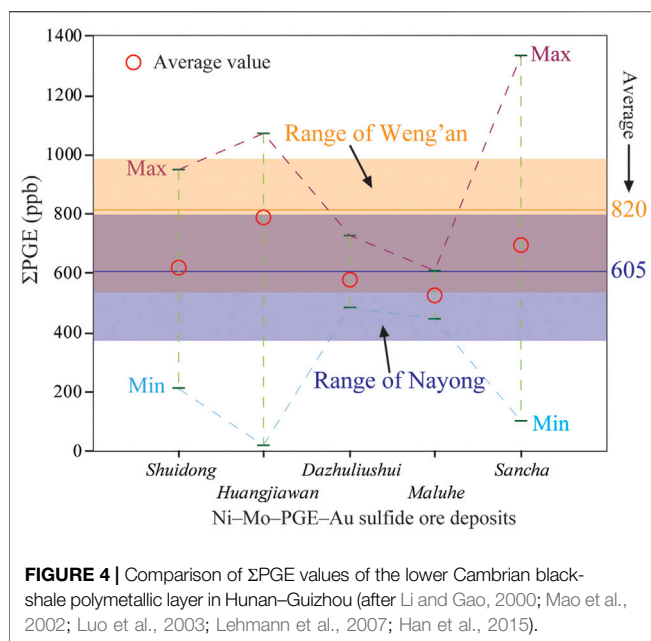


FIGURE 4 | Comparison of Σ PGE values of the lower Cambrian black-shale polymetallic layer in Hunan–Guizhou (after Li and Gao, 2000; Mao et al., 2002; Luo et al., 2003; Lehmann et al., 2007; Han et al., 2015).

and Os–Ir, among other elements (Figures 5E,F). The Ni/Cu, Ce/La, Ni/Pd, and Cu/Ir ratios are respectively 5.4–21.7, 0.3–2.1, 50–211, and 289–1384, and the Cu/Ir ratio of the polymetallic layer is much higher than that of black shale. The Ni/Pd ratio is generally lower than that of black shale (Table 1).

PGE Distribution Model

PGEs are not strongly affected by low-temperature alteration and diagenesis; consequently, their distribution pattern in rocks is

indicative of the environment in which the host rock was formed and of their source (Mao et al., 2001; Lehmann et al., 2003; Li et al., 2003; Pašava et al., 2003; Pašava et al., 2004). A PGE distribution model based on Ni–Mo–V–PGE contents of the polymetallic layer was developed for the black shales of Nayong and Weng'an. The elemental distribution curve is similar to that of the polymetallic layer in mining areas of Zunyi and west Hunan (Figure 6; Li and Gao, 2000; Wu et al., 2001; Mao et al., 2002; Yu et al., 2003; Lehmann et al., 2007; Xu et al., 2013; Han et al., 2015; Xing et al., 2015). The four regions of Nayong, Zunyi, Weng'an, and Zhangjiajie lie on the same metallogenic belt (Figures 1A, 6B) and have the same material source and metallogenetic mechanism.

The source of mineralization elements in the black-shale polymetallic layer at the base of the Niutitang Formation is considered in terms of our analytical data. Although the PGE content of seafloor Fe–Mn crusts is similar to that of the Cambrian black-shale polymetallic layer (Sun et al., 2006) and the PGE distribution model is consistent with normal oceanic sediments. PGE distributions are similar in basic–ultrabasic rocks, continental basalt, organic-rich black shale, and oil shale (Figure 6B), implying that either 1) PGEs in black shale are derived from basic–ultrabasic rocks in underlying strata (Li and Gao, 2000; Jiang et al., 2003; Jiang et al., 2007) or 2) the underlying basic–ultrabasic rocks are weathered and their contents transported to the ocean after being exposed on the surface, with extreme enrichment occurring due to changes in the Eh/pH balance of seawater (Lehmann et al., 2003; Lehmann et al., 2007).

Oil shale in Tibet and Cambrian black shale in the Tarim Basin have PGE distribution curves similar to that of the polymetallic layer in the Hunan–Guizhou area (Yu et al.,

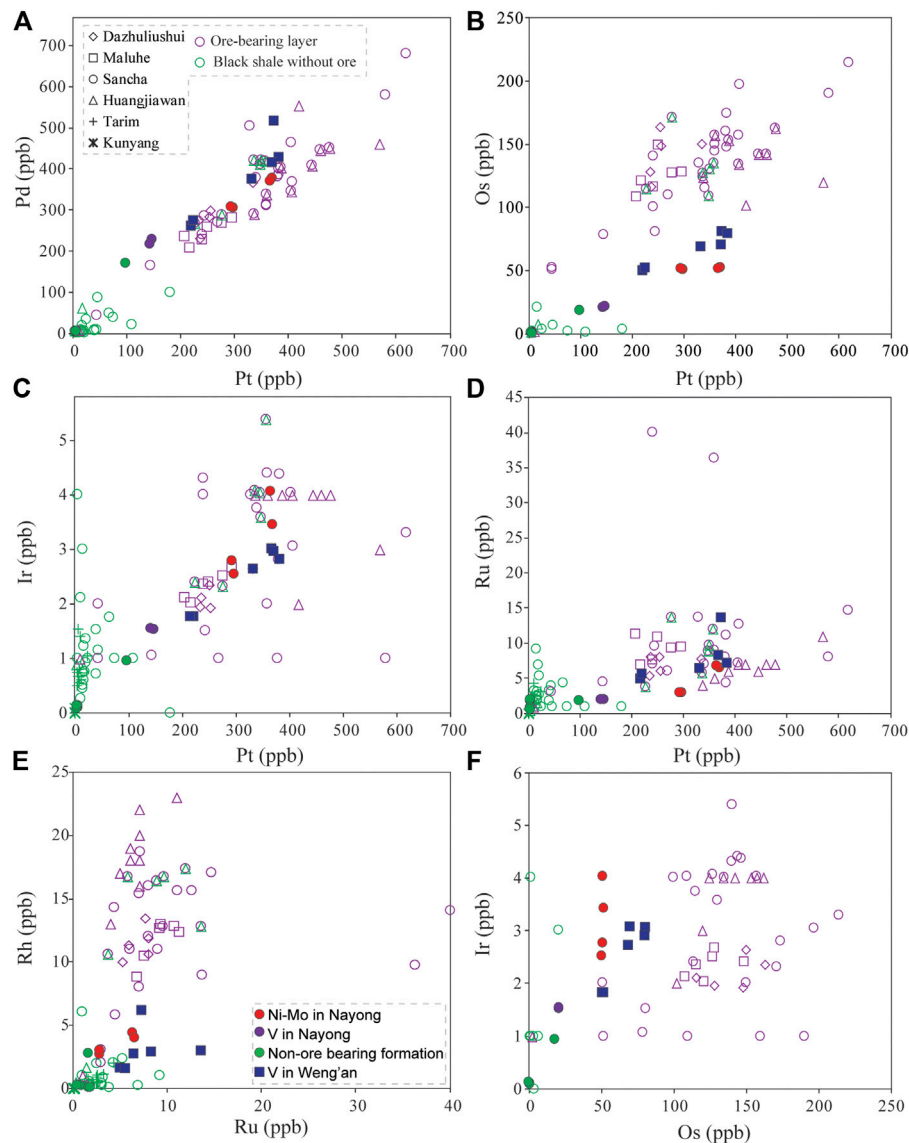


FIGURE 5 | (A) Pd–Pt; **(B)** Os–Pt; **(C)** Ir–Pt; **(D)** Ru–Pt; **(E)** Rh–Ru; and **(F)** Ir–Os diagrams for the Cambrian ore-bearing layer and black shale.

2003; Fu et al., 2010), further implying that the PGE distribution in organic-rich shale is controlled by the occurrence of PGE rocks. The PGE contents of different phases in black shales of South China indicate that PGEs are associated mainly with organic matter and sulfide phases (Wang et al., 2004). Other studies have found that Au ($1900 \mu\text{g g}^{-1}$), Pt ($600 \mu\text{g g}^{-1}$), and Pd ($1900 \mu\text{g g}^{-1}$) are highly enriched in the organic-rich clay rock of black shale. In minerals containing arsenide, uranium, and thorium, Pt and U contents are positively correlated, while Pd is enriched in As–Au–Ag-containing aggregates (Kucha, 1982; Kucha and Przybyłowicz, 1999). Adsorption by organic matter and sulfides in organic-rich shales thus affects the distribution of PGEs in black shale, meaning that not appropriate for clarifying the source of PGEs, simple according to the PGE distribution curves.

PGE Ratios in Polymetallic Layers

PGE ratios and their relationship with ore-forming elements are considered an effective geochemical method for tracing mineral sources (Li and Gao, 2000; Mao et al., 2001; Lehmann et al., 2003; Lehmann et al., 2007; Pašava et al., 2003; Pašava et al., 2004). The polymetallic layers in lower Cambrian black shales in South China contain elevated Ir contents, exceeding 10 ppb (Fan et al., 1984), similar to the Ir content of clays at the Cretaceous–Tertiary (K–T) boundary where the Os/Ir ratio of clay minerals is generally <1 (Evans et al., 1993) and different to chondrite values (McDonough and Sun, 1995). However, for the Cambrian polymetallic layer in South China the Os/Ir ratio is in the range 12–26 (Li et al., 2000; Mao et al., 2001; Jiang et al., 2007), much higher than that of the clay layer at the K–T boundary. Furthermore, the PGE distribution curve of the K–T clay layer is

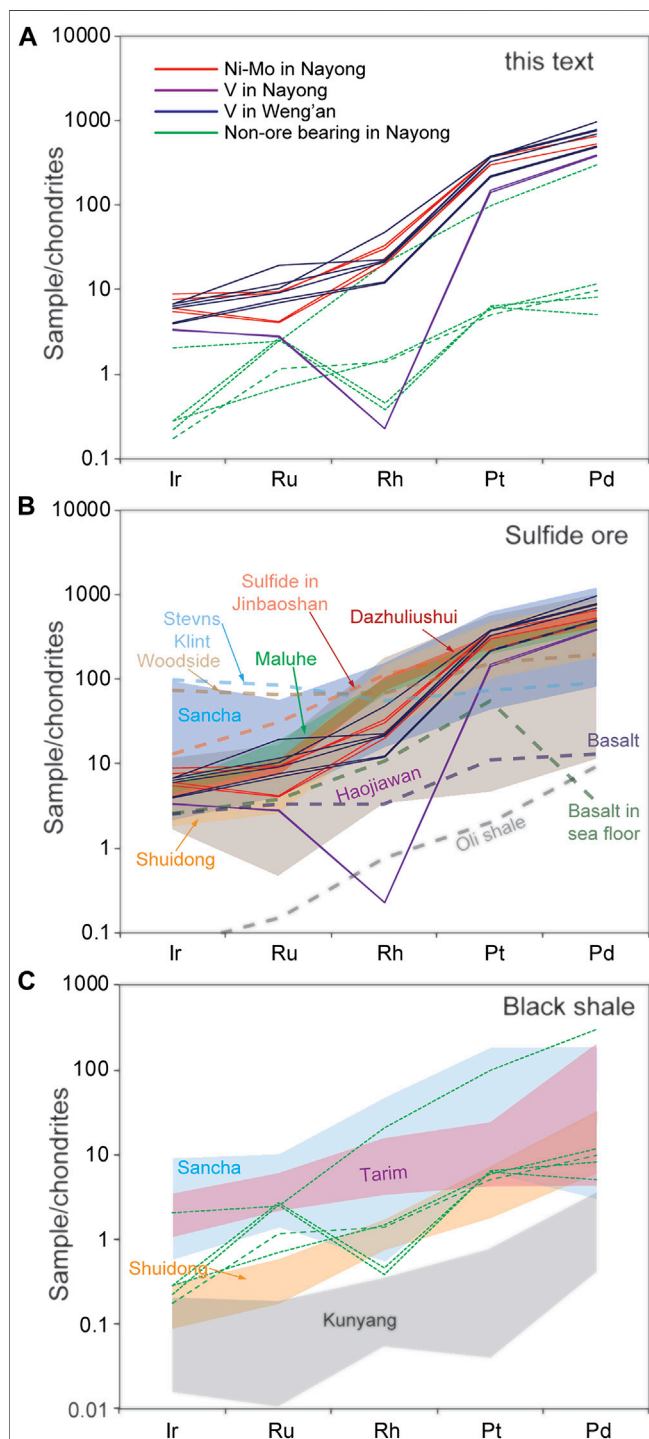


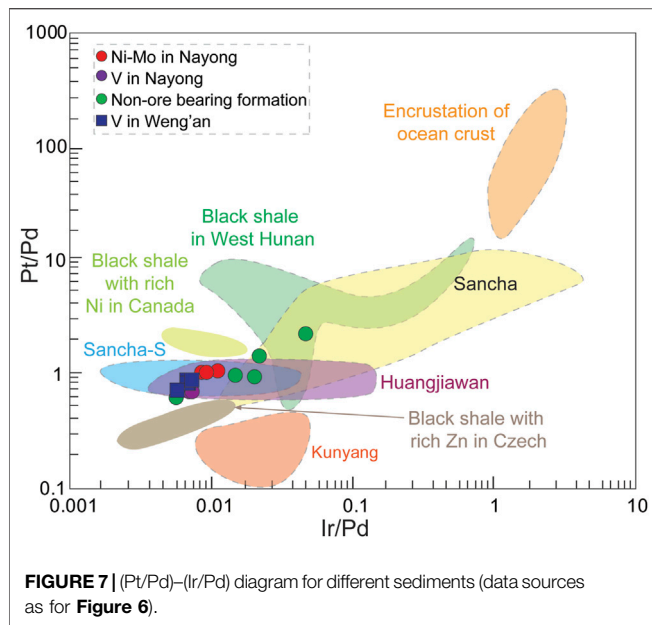
FIGURE 6 | PGE/chondrite distribution pattern of the Cambrian ore-bearing layer and black shale. Chondrite data are from McDonough and Sun (1995); Jinbaoshan basic-rock sulfide-enclave data are from Wang et al. (2010); ocean-floor basalt data are from Sun et al. (2010); K-T boundary layer clay data are from Evans et al. (1993); oil shale data are from Fu et al. (2010); other data are from Wu et al. (2001), Li and Gao (2000), Mao et al. (2001), Wu et al. (2001), Xu et al. (2013), Xing et al. (2015), and Han et al. (2015).

completely different to that of the polymetallic layer. The chondrite standard curve is near level, similar to that of the element distribution (**Figure 6B**).

Pt/Pd and Au/Pd ratios in the polymetallic layer of Cambrian black shale in South China are near unity (Lehmann et al., 2003; Lehmann et al., 2007), similar to the ratios in seawater (Nozaki, 1997). Cambrian seawater had high metal contents. The Mo isotopic studies of the PGE polymetallic layer indicating that Sinian–Cambrian-boundary seawater contained large amount of H_2S (Lehmann et al., 2003; Lehmann et al., 2007). This is the mineralization model for sedimentation from normal seawater. However, Pt/Pd ratios in many PGE deposits are near unity, as in the Jinbaoshan basic–ultrabasic deposit, the Yangliuping deposit, and Archean komatiite sulfides (Brugmann et al., 1989; Tao et al., 2007; Liang et al., 2019).

The PGE enrichment factor in the black-shale polymetallic layer can reach 10^7 – 10^9 , differing from the adjacent non-metallic layers by one to two orders of magnitude. If seawater were rich in metal elements together with excessive H_2S , the PGE content of the black shale would be high. However, the PGE content above and below the polymetallic layer is not significantly different to that of typical sediments (Zhu et al., 2010). An example of anomalously high levels of PGE in sediments is cobalt-rich Fe–Mn oceanic crusts, reaching hundreds of ppb (Yao et al., 2002; Sun et al., 2006). The enrichment of many ore-forming elements in oceanic Fe–Mn crusts is controlled mainly by the deposition rate of the crust (Puteanus and Halbach, 1988). Therefore, a low deposition rate of black shale would favor the formation of polymetallic deposits (Lehmann et al., 2003; Lehmann et al., 2007). However, some studies have indicated that the deposition rate cannot be the dominant factor in Fe–Mn crust enrichment in mineral elements (Basolo and Pearson, 1973). The Eh–pH values in the formation environment of Fe–Mn crusts may promote oxidation/reduction reactions between free PGE ions in seawater and Mn^{2+} on the contact surface of the Fe–Mn crust. Free PGE ions would also form hydroxides and be adsorbed by the Fe–Mn crust under appropriate Eh–pH conditions. The PGE enrichment of Fe–Mn crusts is thus not controlled by deposition rate; rather, it is due to the geochemical conditions of seawater and PGE properties (Sun et al., 2006). Black shale is formed at relatively low Eh–pH values (Basolo and Pearson, 1973; Gao et al., 2018); i.e., under conditions suitable for PGE adsorption by Fe–Mn crusts. However, excessive PGE enrichment is rare in black shale. Globally, PGE-rich black-shale deposits occur mainly in the Dry Valley in Russia (Distler et al., 2004), the Yukon in Canada (Pašava et al., 2003), and Palentin in the Czech Republic (Pašava et al., 2003). These deposits were controlled by organic matter and sulfides, with their metallogenic setting being rift-type basins and with their ore-forming matters are mainly derived from hydrothermal fluid. Therefore, the model of PGE enrichment and mineralization in polymetallic layers formed by normal seawater deposition should be further discussed.

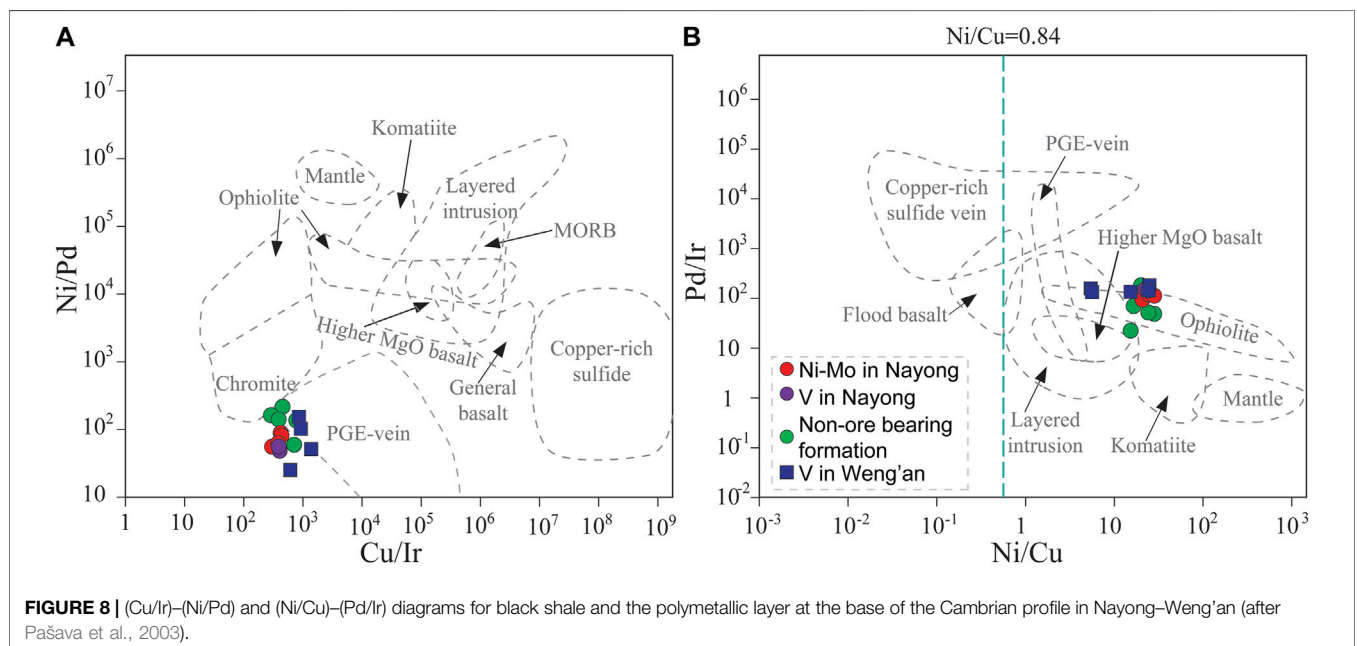
A comparison of the PGE distribution in black shales with that in modern submarine hydrothermal sulfides indicates that the polymetallic layers in black shales of South China were formed



mainly by hot brine (Li et al., 2000; Jiang et al., 2003; Pašava et al., 2003; Pašava et al., 2004; Jiang et al., 2007). The distribution curve of PGEs in the polymetallic layers is similar to that in basic and ultrabasic rocks. Zinc-rich black shale in the Czech Republic and Ni-rich black shale in Canada have Pt/Pd ratios similar to those in the South China polymetallic layer (Figure 7; Pašava et al., 2003), while the ratios in Co-rich crusts formed by seawater sedimentation are completely different, but similar with the Zn-rich black shale in the Czech Republic which was influenced by hydrothermal processes (Kucha, 1982). So the mineralogy of black shale in South China may also have been controlled by hydrothermal processes. Cu/Ir, Ni/Pd, Ni/Cu, and Pd/Ir ratios

can be used to trace the material sources of ore-forming fluids (Pašava et al., 2003). The polymetallic layer in the Nayong and Weng'an areas plots in the ophiolite and PGE-vein fields in the (Cu/Ir)–(Ni/Pd) and (Ni/Cu)–(Pd/Ir) diagrams (Figure 8), implying that the main source of PGE elements in the Nayong–Weng'an polymetallic layers was related to ultrabasic rocks. The tectonic background of the region suggests that the Nayong–Zhijin–Zunyi–Weng'an–Dayong metallogenic belt was in an extensional setting in the Hunan–Guizhou area during the Cambrian (Wu et al., 1999; Li et al., 2003), with the many extensional fractures that developed providing sites for hydrothermal activity. Sulfides in the largest modern-day submarine hydrothermal area (the Trans-Atlantic Geotraverse, Mid-Atlantic Ridge) have a Pd content of up to $1 \mu\text{g g}^{-1}$, while those in submarine black chimneys can reach 136 ppb (Wang et al., 2004). Submarine hydrothermal solutions could thus provide large amounts of PGEs. A quartz vein was found cutting the phosphorous rock layer under the black shale polymetallic layer in the Huangjiawan deposit, Guizhou, and the Daping deposit, Hunan. Fluid inclusions in this ore-bearing vein have a fluid salinity of up to 30 wt% and a trapping temperature of 70–140°C (Wang et al., 2004), indicating that the formation of the black shale was directly related to hydrothermal fluids. Many “siliceous chimneys” have been discovered in the Ganziping section at Dayong but not at Nayong. The siliceous layer is only 50–70 cm below the black-shale polymetallic layer. Banded barite is common in the siliceous rock, confirming the existence of ancient hydrothermal fluids. Fluid inclusions in siliceous rocks have also been found to contain high-salinity brine with a salinity of >35% and sealing temperatures of 110–135°C (Chen et al., 2009).

During the Sinian–Cambrian period, seawater suddenly changed from being oxygen-rich to oxygen-deficient, with large amounts of organic matter accumulating in the oceans and sulfate rock being reduced to sulfide, providing conditions



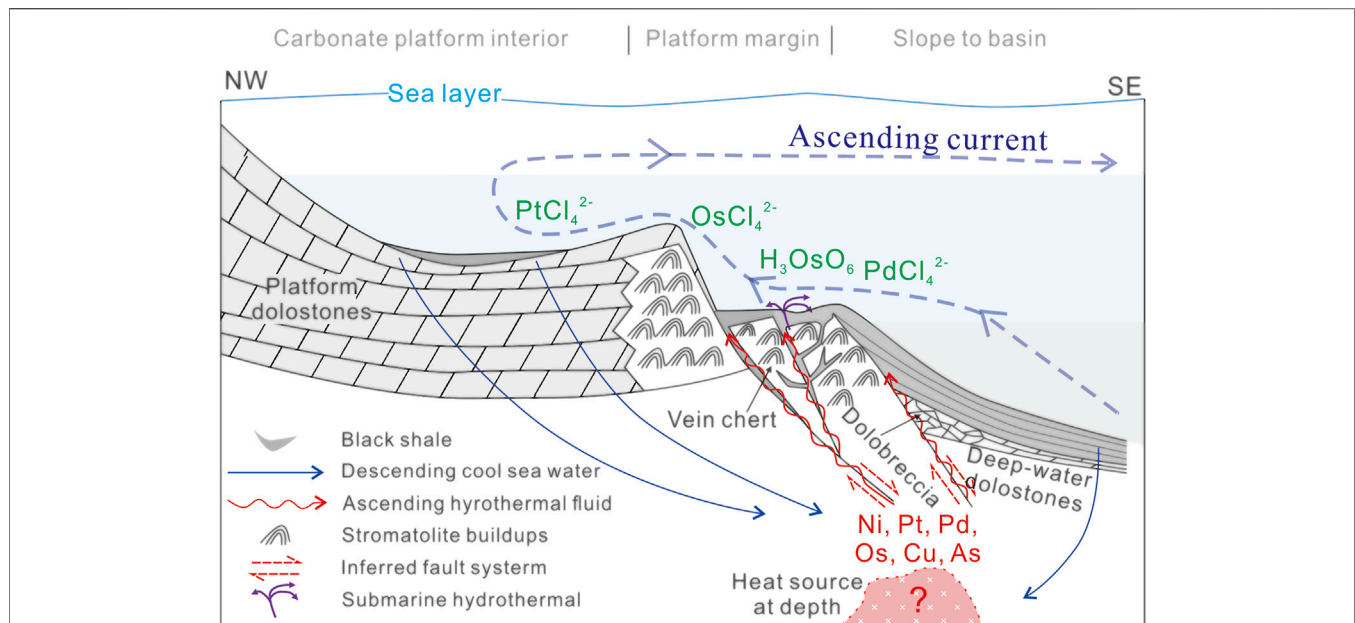


FIGURE 9 | PGE metallogenic model for the Cambrian polymetallic layer in South China (after Wang et al., 2012; Li et al., 2020).

conducive to PGE enrichment (Wu et al., 1999; Mao et al., 2002; Jiang et al., 2007; Han et al., 2015). Volcanic tuff occurs near the bottom of the Cambrian profile in the Kunyang and Songlin areas, under the Ni–Mo layer and occurring as a lens shape on the southeastern edge of the Yangtze Platform (Luo et al., 2003). The tuff contains large amounts of sulfide and organic matter, with PGE contents of up to hundreds of ppb, including Pt and Pd at up to 434 and 142 ppb, respectively. The distribution of PGEs relative to chondrites is similar to that of PGEs in the black-shale polymetallic layer (Pašava et al., 2010). At the bottom of the black shale of Niutitang Formation, a thin layer of tuff is usually developed, indicating the presence of volcanism. In other words, the PGE and polymetallic sources may be contributed by volcanic rocks. There is no direct evidence for such a direct PGE source but it does appear that the PGEs were derived mainly from basic or ultrabasic rocks rather than directly from seawater.

Enrichment of PGES in Black Shale

The mineralization of PGEs in black shale in South China is controlled mainly by their source area and seawater Eh–pH conditions. PGEs are generally considered inert, with their separation and enrichment being associated mainly with high-temperature and high-pressure magmatic activity. Previous simulations of the effects of low-temperature hydrothermal activity on PGEs indicate Pd and Pt exist as PdCl_2 and PtCl_3^- in solution, respectively, at concentrations of up to >1 ppb (Mountain and Wood, 1988; Gammons et al., 1992), and demonstrate the mobile nature of Pt and Pd in high-salinity hydrothermal fluid. Furthermore, a simulation of the solubility of PdS and PtS in H_2S + NaHS solution indicates that the amounts dissolved exceed the number of chloro complexes (Gammons and Bloom, 1993). This may explain why the Pd

sulfide content at the mouth of seafloor black chimneys can be as high as 1 ppb (Crocket, 1990), illustrating the ease with which Pt and Pd enter solution as complexes during low-temperature hydrothermal processes (Mountain, 1989; Gammons et al., 1992; Gammons and Bloom, 1993; Chen et al., 2009). We conclude that hydrothermal fluids participated during the early stages of the formation of the black-shale polymetallic layer in South China, leading to PGE enrichment.

PGEs are transported mainly in the form of chlorides (Figure 9), and when hydrothermal fluid crosses the seawater–sediment interface, Pt^{2+} and Pd^{4+} are released into the seawater. In seawater, Pt^{2+} is most stable as PtCl_4^{2-} . Only when seawater reaches a high pH and low oxygen fugacity will it exist in the form of +4 ions, as follows (Halbach et al., 1989):

$$\log \left[\frac{(\text{PtCl}_4^{2-})}{(\text{PtCl}_6^{2-})} \right] = -15.96 - \frac{1}{2} \log f_{\text{O}_2/\text{H}_2\text{O}} + 2\text{pH} \quad (1)$$

Where $\log f_{\text{O}_2/\text{H}_2\text{O}}$ represents the oxygen fugacity of seawater and the pH value is that of seawater.

Pt and Pd do not enter sediments as chlorides for the waters of South China, but are adsorbed on sediment as sulfide, and arsenide forms with the MeCl_x ($\text{Me} = \text{Pd-Pt-Os}$) + $\text{S}^{2-}/\text{As}^{2-} = \text{MeS}/(\text{As} + \text{Cl})$; MeCl_x ($\text{Me} = \text{Pd, Pt, Os}$)—ne = $\text{Me} + \text{Cl}^-$ chemical reaction on the surface of sediment. Kucha (1982) found that PGEs in Zn-rich black shale are distributed mainly in arsenide and sulfide. Pt–Cl and Pd–Cl bond energies in $\text{K}_2\text{Me}(\text{Pt, Pd})\text{Cl}_4$ are 372.6 and 347.5 kJ mol^{−1}, respectively (Basolo and Pearson, 1967). In seawater, Pd ions are reduced before entering sediments, with Pd/Pt ratios in sediments thus being >1 in reducing environments.

The PGE distribution in black shale shows a typical Pt–Pd enrichment pattern, similar to that in many basalts (Rehkämper

et al., 1999), with Pt/Ru \approx 10 and Pt/Pd \approx 1. Osmium is highly enriched (up to 100 ppb) due to its solubility in seawater where it exists mainly as H_3OsO_6^- (Sharma et al., 1997), H_2OsO_5 , or OsCl_6^{2-} (Koide et al., 1991). Osmium is therefore more soluble in seawater than are Ir, Ru, and other elements, with more being adsorbed by organic matter; this explains why the Os content of black shale is higher than the Ir and Ru contents (Ravizza et al., 2001).

In summary, PGE-rich ore in the Ni–Mo polymetallic layer of black shale in South China was formed during the development of rifts, with fractures forming in basement rocks and frequent water–rock exchange reactions. Coincidentally, the geothermal gradient in the South China metallogenic belt increased rapidly, enhancing the thermal convection velocity and causing the overflow of high-salinity brine rich in metals (Li et al., 2020). Oceanic hypoxia events occurred during the Sinian–Cambrian, producing large amounts of organic matter and H_2S in the oceans (Lehmann et al., 2003; Lehmann et al., 2007; Wang et al., 2012). When high-salinity brine reached the ocean floor as part of oceanic circulation, the rapid change in Eh–pH conditions caused many metal elements to become enriched at the sedimentary interface, ultimately enriching the ore. Metal ions were also transported in ocean circulation, resulting in distal precipitation and mineralization (Figure 9).

CONCLUSION

PGEs are enriched only in the polymetallic layer of the black shale examined here. The PGE contents in the vanadium-mining area of Niuchang are higher than in the Ni–Mo mining area of Shuidong. The accumulation of PGEs in the lower Cambrian black-shale polymetallic layer was controlled mainly by hydrothermal processes, which provided large amounts of ore-forming elements to the South China anoxic ocean basin. With ocean circulation and continuing sea-level rise, the productivity

of bio-organisms increased, enriching the ocean floor in organic matter. The degradation of this organic matter produced H_2S , changing seawater Eh–pH conditions and promoting PGE enrichment. Black-shale PGE-rich ore in South China is thus a syn-sedimentary ore formed under the action of hydrothermal fluids.

DATA AVAILABILITY STATEMENT

The original contributions presented in the study are included in the article/Supplementary Material, further inquiries can be directed to the corresponding author.

AUTHOR CONTRIBUTIONS

YF led the conception and design of the paper. ZY and PX contributed the field work, summarize and analyze the distribution regularity of PGE in the Early Cambrian black shale in the region. CL contributed the experiments to test PGE and geochemical analysis.

FUNDING

This work was jointly supported by the National Natural Science Foundation of China (Grand No. 41763006, 42063009), Mineral Geology of China Project, China Geological Survey (Grand Nos. (DD20160346, DD20190379) and Guizhou Science and Technology Fund ((2020)1Y166).

ACKNOWLEDGMENTS

We thank to Associate Editor Prof. Xiaohua Deng and two reviewers for their constructive suggestions.

REFERENCES

- Barnes, S. J., and Lightfoot, P. C. (2005). Formation of magmatic nickel-sulfide ore deposits and processes affecting their copper and platinum-group element contents. *Econ. Geology*. 100, 179–213. doi:10.5382/AV100.08
- Basolo, F., and Pearson, R. G. (1967). *Mechanisms of inorganic reactions*. New York, NY: Wiley. Chap. 3.
- Basolo, F., and Pearson, R. G. (1973). Inorganic reactions. *Nat. Phys. Sci.* 241, 88. doi:10.1038/physci241088a0
- Brugmann, G. E., Naldrett, A. J., and Macdonald, A. J. (1989). Magma mixing and constitution zone refining in the lac des iles complex, ontario; genesis of platinum-group element mineralization. *Econ. Geology*. 84 (6), 1557–1573. doi:10.2113/gsecongeo.84.6.1557
- Chen, D. Z., Wang, J. G., Qing, H. R., Yan, D. T., and Li, R. W. (2009). Hydrothermal venting activities in the early Cambrian, South China: petrological, geochronological and stable isotopic constraints. *Chem. Geology*. 258 (3–4), 168–181. doi:10.1016/j.chemgeo.2008.10.016
- Clark, S. H. B., Poole, F. G., and Wang, Z. (2004). Comparison of some sediment-hosted, stratiform barite deposits in China, the United States, and India. *Ore Geol. Rev.* 24 (1–2), 85–101. doi:10.1016/j.oregeorev.2003.08.009
- Coveney, R. M. (2003). Re–Os dating of polymetallic ni-mo-pge-au mineralization in lower cambrian black shales of south china and its geological significance-A discussion. *Econ. Geology*. 98 (3), 661–662. doi:10.2113/98.3.661
- Crocket, J. H. (1990). Noble metals in seafloor hydrothermal mineralization from the Juan de Fuca and Mid-Atlantic Ridges: a fractionation of gold from platinum metals in hydrothermal fluids. *Canadian Mineralogist* 28, 636–648.
- Dai, C. G., Chen, J. S., and Wang, X. H. (2014). A series of geological maps of Guizhou Province and a comprehensive study of the new generation of regional geological records of Guizhou Province. *Management Res. Scientific Technol. Achievements* 5, 50–55. [in Chinese]. doi:10.3772/j.issn.1673-6516.2014.05.017
- Distler, V. V., Yudovskaya, M. A., Mitrofanov, G. L., Prokofev, V. Y., and Lishnevskii, E. N. (2004). Geology, composition, and genesis of the Sukhoi Log noble metals deposit, Russia. *Ore Geology. Rev.* 24, 7–44. doi:10.1016/j.oregeorev.2003.08.007
- Duan, J., Li, C., Qian, Z., Jiao, J., Ripley, E. M., and Feng, Y. (2016). Multiple S isotopes, zircon Hf isotopes, whole-rock Sr–Nd isotopes, and spatial variations of PGE tenors in the Jinchuan Ni–Cu–PGE deposit, NW China. *Miner Deposita* 51 (4), 557–574. doi:10.1007/s00126-015-0626-8
- Evans, N. J., Gregoire, D. C., Goodfellow, W. D., I. McInnes, B., Miles, N., and Veizer, J. (1993). Ru/Ir ratios at the Cretaceous-Tertiary boundary: implications for PGE source and fractionation within the ejecta cloud.

- Geochimica Et Cosmochimica Acta* 57 (13), 3149–3158. doi:10.1016/0016-7037(93)90299-c
- Fan, D. L., Yang, R. Y., and Huang, Z. X. (1984). “The Lower Cambrian black shale series and iridium anomaly in south China,” in *Developments in geoscience, 27th international geological congress* (Moscow: Beijing Science Press), 215–224.
- Fan, D. L., Ye, J., and Liu, T. B. (1992). Black shale series-hosted silver-vanadium deposits of the upper Sinian Doushantuo formation, western Hubei province, China. *Exploration Mining Geology* 1 (1), 29–38.
- Fan, D. L., Ye, J., Yang, R. Y., and Huang, Z. X. (1987). The geological events and ore mineralization nearby the Precambrian-Cambrian boundary in Yangtze platform. *Acta Sedimentol. Sinica* 5 (3), 81–96. [in Chinese with English abstract].
- Fu, X., Wang, J., Zeng, Y., Tan, F., and He, J. (2010). Concentrations and modes of occurrence of platinum group elements in the Shengli river oil shale, northern Tibet, China. *Fuel* 89 (12), 3623–3629. doi:10.1016/j.fuel.2010.07.043
- Gammons, C. H., and Bloom, M. S. (1993). Experimental investigation of the hydrothermal geochemistry of platinum and palladium: II. The solubility of PtS and PdS in aqueous sulfide solutions to 300°C. *Geochimica et Cosmochimica Acta* 57, 2451–2467. doi:10.1016/0016-7037(93)90409-p
- Gammons, C. H., Bloom, M. S., and Yu, Y. (1992). Experimental investigation of the hydrothermal geochemistry of platinum and palladium: I. Solubility of platinum and palladium sulfide minerals in NaCl/H₂SO₄ solutions at 300°C. *Geochimica Et Cosmochimica Acta* 56 (11), 3881–3894. doi:10.1016/0016-7037(92)90003-2
- Gao, P., He, Z., Li, S., Lash, G. G., Li, B., Huang, B., et al. (2018). Volcanic and hydrothermal activities recorded in phosphate nodules from the Lower Cambrian Niutitang Formation black shales in South China. *Palaeogeogr. Palaeoclimatol. Palaeoecol.* 505 (15), 381–397. doi:10.1016/j.palaeo.2018.06.019
- Griffith, E. M., and Paytan, A. (2012). Barite in the ocean - occurrence, geochemistry and palaeoceanographic applications. *Sedimentology* 59 (6), 1817–1835. doi:10.1111/j.1365-3091.2012.01327.x
- Halbach, P., Kriete, C., Prause, B., and Puteanus, D. (1989). Mechanisms to explain the platinum concentration in ferromanganese seamount crusts. *Chem. Geology* 76 (1–2), 95–106. doi:10.1016/0009-2541(89)90130-7
- Han, T., Fan, H., Zhu, X., Wen, H., Zhao, C., and Xiao, F. (2017). Submarine hydrothermal contribution for the extreme element accumulation during the early Cambrian, South China. *Ore Geology. Rev.* 86, 297–308. doi:10.1016/j.oregeorev.2017.02.030
- Han, T., Zhu, X., Li, K., Jiang, L., Zhao, C., and Wang, Z. (2015). Metal sources for the polymetallic Ni-Mo-PGE mineralization in the black shales of the Lower Cambrian Niutitang formation, South China. *Ore Geology. Rev.* 67, 158–169. doi:10.1016/j.oregeorev.2014.11.020
- Hodge, V. F., Stallard, M., Koide, M., and Goldberg, E. D. (1985). Platinum and the platinum anomaly in the marine environment. *Earth Planet. Sci. Lett.* 72 (2–3), 158–162. doi:10.1016/0012-821x(85)90002-0
- Jewell, P. W. (2000). Bedded barite in the geologic record. *Mar. Authigenesis: Glob. Microb.* 66, 147–161. doi:10.2110/pec.00.66.0147
- Jiang, S.-Y., Chen, Y.-Q., Ling, H.-F., Yang, J.-H., Feng, H.-Z., and Ni, P. (2006). Trace- and rare-earth element geochemistry and Pb-Pb dating of black shales and intercalated Ni-Mo-PGE-Au sulfide ores in Lower Cambrian strata, Yangtze Platform, South China. *Miner Deposita* 41, 453–467. doi:10.1007/s00126-006-0066-6
- Jiang, S.-Y., Yang, J.-H., Ling, H.-F., Chen, Y.-Q., Feng, H.-Z., Zhao, K.-D., et al. (2007). Extreme enrichment of polymetallic Ni-Mo-PGE-Au in Lower Cambrian black shales of South China: an Os isotope and PGE geochemical investigation. *Palaeogeogr. Palaeoclimatol. Palaeoecol.* 254, 217–228. doi:10.1016/j.palaeo.2007.03.024
- Jiang, S., Yang, J., Ling, H., Feng, H., Chen, Y., and Chen, J. (2003). Re-Os isotopes and PGE geochemistry of black shales and intercalated Ni-Mo polymetallic sulfide bed from the Lower Cambrian Niutitang Formation, South China. *Prog. Nat. Sci.* 13, 788–794. [in Chinese with English abstract]. doi:10.1080/10020070312331344440
- Jiang, S. Y., Wen, H. J., Xu, C., Wang, Y., Su, H. M., and Sun, W. D. (2019). Earth sphere cycling and enrichment mechanism of critical metals: major scientific issues for future research. *Bull. Natl. Nat. Sci. Found. China* 33 (2), 10–16. [in Chinese with English abstract]. doi:10.16262/j.cnki.1000-8217.2019.02.003
- Koide, M., Goldberg, E. D., Niemeyer, S., Gerlach, D., Hodge, V., Bertine, et al. (1991). Osmium in marine sediments. *Geochimica et Cosmochimica Acta* 55, 1641–1648. doi:10.1016/0016-7037(91)90135-R
- Kucha, H. (1982). Platinum-group metals in the Zechstein copper deposits, Poland. *Econ. Geology* 77 (6), 1587–1591. doi:10.2113/gsecongeo.77.6.1578
- Kucha, H., and Przyłowicz, W. (1999). Noble metals in organic matter and clay-organic matrices, kupferschiefer, Poland. *Econ. Geology* 94 (7), 1137–1162. doi:10.2113/gsecongeo.94.7.1137
- Lehmann, B., Mao, J. W., Li, S. R., Zhang, G. D., and Zeng, M. G. (2003). aRe-Os dating of polymetallic Ni-Mo-PGE-Au mineralization in lower cambrian black shales of south china and its geological significance--A reply. *Econ. Geology* 98, 663–665. doi:10.2113/98.3.663
- Lehmann, B., Nögler, T. F., Holland, H. D., Wille, M., Mao, J., Pan, J., et al. (2007). Highly metalliferous carbonaceous shale and Early Cambrian seawater. *Geol* 35, 403–406. doi:10.1130/g23543a.1
- Li, C., Zhang, Z., Jin, C., Cheng, M., Wang, H., Huang, J., et al. (2020). Spatiotemporal evolution and causes of marine euxinia in the early Cambrian Nanhua Basin (South China). *Palaeogeogr. Palaeoclimatol. Palaeoecol.* 546, 109676. doi:10.1016/j.palaeo.2020.109676
- Li, S., and Gao, Z. (2000). Source tracing of noble metal elements in Lower Cambrian black rock series of Guizhou-Hunan Provinces, China. *Sci. China Ser. D-earth Sci.* 43, 625–632. doi:10.1007/bf02879506
- Li, S., Xiao, Q. Y., Shen, J. F., Sun, L., Liu, B., Yan, B. K., et al. (2003). Rhenium-osmium isotope constraints on the age and source of the platinum mineralization in the lower Cambrian black rock series of Hunan-Guizhou provinces, China. *Sci. China Ser. D* 46 (9), 919–927. doi:10.1360/01yd0277
- Liang, Q.-L., Song, X.-Y., Wirth, R., Chen, L.-M., and Dai, Z.-H. (2019). Implications of nano- and micrometer-size platinum-group element minerals in base metal sulfides of the Yangliuping Ni-Cu-PGE sulfide deposit, SW China. *Chem. Geology* 517, 7–21. doi:10.1016/j.chemgeo.2019.04.015
- Lu, Z. C., Liu, C. Q., Liu, J. J., and Wu, F. C. (2004). Geochemical studies on the lower Cambrian witherite-bearing cherts in the northern daba mountains. *Acta Geol. Sin.* 78 (3), 390–406. [in Chinese with English abstract]. doi:10.3321/j.issn:0001-5717.2004.03.013
- Luo, T. Y., Zhang, H., and Li, X. B. (2003). Mineralization characteristics of the multi-element-rich strata in the Niutitang formation black shale series, Zunyi, Guizhou, China. *Acta Mineralogica Sin.* 23 (4), 296–302. [in Chinese with English abstract]. doi:10.3321/j.issn:1000-4734.2003.04.002
- Mao, J. W., Zhang, G. D., Du, A. D., Wang, T. Y., and Zeng, M. G. (2001). Geology, geochemistry, and Re-Os isotopic dating of the Huangjiawan Ni-Mo-PGE deposit, Zunyi, Guizhou province-with a discussion of the polymetallic mineralization of basal cambrian black shales in South China. *Acta Geol. Sin.* 35 (3), 454–472. [in Chinese with English abstract]. doi:10.3321/j.issn:0001-5717.2001.02.013
- Mao, J., Lehmann, B., Du, A., Zhang, G., Ma, D., Wang, Y., et al. (2002). Re-Os dating of polymetallic Ni-Mo-PGE-Au mineralization in lower cambrian black shales of South China and its geologic significance. *Econ. Geol.* 97, 1051–1061. doi:10.2113/gsecongeo.97.5.1051
- Mcdonough, W. F., and Sun, S. S. (1995). The composition of the earth. *Chem. Geol.* 120 (3–4), 223–253. doi:10.1016/0009-2541(94)00140-4
- Mountain, B. W., and Wood, S. A. (1988). Chemical controls on the solubility, transport and deposition of platinum and palladium in hydrothermal solutions; a thermodynamic approach. *Econ. Geol.* 83 (3), 492–510. doi:10.2113/gsecongeo.83.3.492
- Mountain, R. D. (1989). Molecular dynamics investigation of expanded water at elevated temperatures. *J. Chem. Phys.* 90 (3), 1866–1870. doi:10.1063/1.456028
- Nozaki, Y. (1997). Updated (1996 version) table of the elements in seawater and its remarks. *Bull. Soc. Sea Water Sci. Jpn.* 51, 302–308. doi:10.11457/swsj1965.51.302
- Orberger, B., Pasava, J., Gallien, J. P., Daudin, L., and Pinti, D. L. (2003). Biogenic and abiogenic hydrothermal sulfides: controls of rare metal distribution in black shales (Yukon territories, Canada). *J. Geochem. Explor.* 78 (1–2), 559–563. doi:10.1016/s0375-6742(03)00141-9
- Paava, J., Chrastn, V., Loukola, R. K., and Ebek, O. (2019). Nickel isotopic variation in black shales from bohemia, China, Canada, and Finland: a reconnaissance study. *Mineralium Deposita* 54 (5), 719–742. doi:10.1007/s00126-018-0839-8
- Pages, A., Barnes, S., Schmid, S., Coveney, R. M., Schwark, L., Liu, W., et al. (2018). Geochemical investigation of the lower Cambrian mineralised black shales of South China and the late Devonian Nick deposit, Canada. *Ore Geology. Rev.* 94, 396–413. doi:10.1016/j.oregeorev.2018.02.004

- Pašava, J., Barnes, S. J., and Vymazalova, A. (2003). The use of mantle normalization and metal ratios in the identification of the sources of platinum-group elements in various metal-rich black shales. *Miner. Deposita* 38, 775–783. doi:10.1007/s00126-003-0366-z
- Pašava, J., Kříbek, B., Vymazalová, A., Sýkorová, I., Žák, K., and Orberger, B. (2008). Multiple sources of metals of mineralization in Lower Cambrian black shales of South China: evidence from geochemical and petrographic study. *Resour. Geol.* 58, 25–42. doi:10.1111/j.1751-3928.2007.00042.x
- Pašava, J., Vymazalova, A., Petersen, S., and Herzig, P. (2004). PGE distribution in massive sulfides from the PACMANUS hydrothermal field, eastern Manus basin, Papua New Guinea: implications for PGE enrichment in some ancient volcanogenic massive sulfide deposits. *Miner. Deposita* 39, 784–792. doi:10.1007/s00126-004-0442-z
- Pašava, J., Vymazalová, A. V., Košler, J., Koneev, R. I., Jukov, A. V., and Khalmatov, R. A. (2010). Platinum-group elements in ores from the kalmakyr porphyry Cu-Au-Mo deposit, Uzbekistan: bulk geochemical and laser ablation ICP-MS data. *Miner. Deposita* 45 (5), 411–418. doi:10.1007/s00126-010-0286-7
- Paytan, A., Mearon, S., Cobb, K., and Kastner, M. (2002). Origin of marine barite deposits: Sr and S isotope characterization. *Geology* 30 (8), 747–750. doi:10.1130/0091-7613(2002)030<0747:oombds>2.0.co;2
- Puteanus, D., and Halbach, P. (1988). Correlation of Co concentration and growth rate—a method for age determination of ferromanganese crusts. *Chem. Geol.* 69 (1–2), 73–85. doi:10.1016/0009-2541(88)90159-3
- Qi, L., Gao, J., Huang, X., Hu, J., Zhou, M.-F., and Zhong, H. (2011). An improved digestion technique for determination of platinum group elements in geological samples. *J. Anal. Spectrom.* 26 (9), 1900–1904. doi:10.1039/c1ja10114e
- Qi, L., Wang, C. Y., and Zhou, M.-F. (2008). Controls on the PGE distribution of permian emeishan alkaline and peralkaline volcanic rocks in longzhoushan, sichuan province, SW China. *Lithos* 106, 222–236. doi:10.1016/j.lithos.2008.07.012
- Ravizza, G., Blusztajn, J., and Prichard, H. M. (2001). Re-Os systematics and platinum-group element distribution in metalliferous sediments from the Troodos ophiolite. *Earth Planet. Sci. Lett.* 188 (3–4), 369–381. doi:10.1016/S0012-821X(01)00337-5
- Rehkämper, M., Halliday, A. N., Fitton, J. G., Lee, D.-C., Wieneke, M., and Arndt, N. T. (1999). Ir, Ru, Pt, and Pd in basalts and komatiites: new constraints for the geochemical behavior of the platinum-group elements in the mantle. *Geochim. et Cosmochim. Acta* 63 (22), 3915–3934. doi:10.1016/S0016-7037(99)00219-7
- Sarwar, A. R., Liu, C., Gong, H., Dun, C., and Chamssidini, L. G. (2019). Paleo-sedimentary environment in relation to enrichment of organic matter of early cambrian black rocks of niutitang formation from Xiangxi area China. *Mar. Pet. Geology*. 112, 104057. doi:10.1016/j.marpetgeo.2019.104057
- Sharma, M., Papanastassiou, D. A., and Wasserburg, J. G. (1997). The concentration and isotopic composition of Os in the oceans. *Geochimica et Cosmochimica Acta* 61 (16), 3287–3299. doi:10.1016/S0016-7037(97)00210-X
- Shi, C. H., Cao, J., Han, S. C., Hu, K., Bian, L. Z., and Yao, S. P. (2020). A review of polymetallic mineralization in Lower Cambrian black shales in South China: combined effects of seawater, hydrothermal fluids, and biological activity. *Palaeogeogr. Palaeoclimatol. Palaeoecol.* 561, 110073. doi:10.1016/j.marpetgeo.2019.104057
- Steiner, M., Wallis, E., Erdtmann, B. D., Zhao, Y., and Yang, R. (2001). Submarine-hydrothermal exhalative ore layers in black shales from South China and associated fossils—insights into a lower Cambrian facies and bio-evolution. *Palaeogeogr. Palaeoclimatol. Palaeoecol.* 169 (3–4), 165–191. doi:10.1016/S0031-0182(01)00208-5
- Sun, T., Qian, Z. Z., Tang, Z. L., Jiang, C. Y., He, K., Sun, et al. (2010). Zircon U-Pb chronology, platinum group element geochemistry characteristics of Hulu Cu-Ni deposit, east Xinjiang, and its geological significance. *Acta Petrologica Sinica* 26 (11), 3339–3349. (in Chinese with English abstract). doi:10.1130/G30929C.1
- Sun, X. M., Xue, T., He, G. W., Ye, X. R., Zhang, M., Lu, H. F., et al. (2006). Noble gases isotopic compositions and sources of cobalt-rich crusts from west Pacific Ocean seamounts. *Acta Petrologica Sin.* 22 (9), 2331–2340. [in Chinese with English abstract]. doi:10.3969/j.issn.1000-0569.2006.09.008
- Tao, Y., Li, C. S., Hu, R. Z., Ripley, E. M., Du, A. D., and Zhong, H. (2007). Petrogenesis of the Pt–Pd mineralized Jinbaoshan ultramafic intrusion in the Permian Emeishan large igneous province, SW China. *Contrib. Mineral. Petrol.* 153 (3), 321–337. doi:10.1007/s00410-006-0149-5
- Wang, C. Y., Zhou, M. F., and Qi, L. (2010). Origin of extremely PGE-rich mafic magma system: an example from the Jinbaoshan ultramafic sill, Emeishan large igneous province, SW China. *Lithos* 119 (1–2), 147–161. doi:10.1016/j.lithos.2010.07.022
- Wang, J., Chen, D., Wang, D., Yan, D., Zhou, X., and Wang, Q. (2012). Petrology and geochemistry of chert on the marginal zone of Yangtze Platform, western Hunan, South China, during the Ediacaran-Cambrian transition. *Sedimentology* 59, 809–829. doi:10.1111/j.1365-3091.2011.01280.x
- Wang, M., Sun, X. M., and Yang, M. M. (2004). Geochemistry of ore-forming fluid and its metallogenetic significances of PGE-polymetallic deposits in Lower Cambrian black rock series, Southern China. *Acta Scientiarum Naturalium Universitatis Sunyatseni* 43 (5), 98–102. [in Chinese with English abstract]. doi:10.3321/j.issn:0529-6579.2004.05.028
- Wang, Z. C., and Li, G. Z. (1991). Barite and witherite deposits in lower Cambrian shales of south China: stratigraphic distribution and geochemical characterization. *Econ. Geol.* 86 (2), 354–363. doi:10.2113/gsecongeo.86.2.354
- Wu, C. D., Chen, Q. Y., and Lei, J. J. (1999). The genesis factors and organic petrology of black shale series from the upper Sinian to the lower Cambrian, southwest of China. *Acta Petrologica Sin.* 15 (3), 453–462. [in Chinese with English abstract]. doi:10.3969/j.issn.1000-0569.1999.03.014
- Wu, C. D., Shen, Y. P., and Hou, Q. L. (2001). Geochemical characteristics and enrichment factors of platinum metals in black shales, West Hunan, China. *Prog. Nat. Sci.* 11 (5), 507–513. [in Chinese]. doi:10.3321/j.issn:1002-008X.2001.05.010
- Xing, L., Zhou, M., Qi, L., and Huang, Z. (2015). Discussion on the PGE anomalies and source materials of K-bentonite (bed 5) in the lower cambrian meishucun section, yunnan. *Chin. J. Geochem.* 34 (3), 346–361. doi:10.1007/s11631-015-0057-3
- Xu, L. G., Lehmann, B., and Mao, J. W. (2012). Seawater contribution to polymetallic Ni-Mo-PGE-Au mineralization in Early Cambrian black shales of South China: evidence from Mo isotope, PGE, trace element, and REE geochemistry. *Ore Geol. Rev.* 52, 66–84. doi:10.1016/j.oregeorev.2012.06.003
- Xu, L., Lehmann, B., and Mao, J. (2013). Seawater contribution to polymetallic Ni-Mo-PGE-Au mineralization in early Cambrian black shales of South China: evidence from Mo isotope, PGE, trace element, and REE geochemistry. *Ore Geol. Rev.* 52, 66–84. doi:10.1016/j.oregeorev.2012.06.003
- Yang, R. D., Wei, H. R., Bao, M., and Wang, W. (2007). Submarine hydrothermal venting—flowing sedimentary characters of the Cambrian Shanggongtang and Dahebian barite deposits, Tianzhu county, Guizhou province. *Geol. Rev.* 53 (5), 675–680. [in Chinese with English abstract]. doi:10.3321/j.issn:0371-5736.2007.05.012
- Yao, D., Zhang, L. J., Wiltshire, J. C., Chu, F. Y., Du, A. D., Liu, X. Z., et al. (2002). PGE and Re-Os isotope compositions and their significances of Co-rich ferromanganese crusts. *Mar. Geol. Quat. Geol.* 22 (3), 53–58. [in Chinese with English abstract]. doi:10.16562/j.cnki.0256-1492.2002.03.008
- Yu, B., Chen, J. Q., Li, X. W., and Lin, C. S. (2003). Geochemistry of black shale at the bottom of the Lower Cambrian in Tarim Basin and its significance for lithosphere evolution. *Sci. China Ser. D* 46 (5), 498–507. doi:10.1360/03yd9043
- Zhou, X. Q., Yu, H., Huang, T. Y., Zhang, L. Y., Zhang, G. J., Fu, Y., et al. (2016). Genetic classification of sedimentary barites and discussion on the origin of the lower Cambrian barite-rich deposits in the Yangtze block, south China. *Acta Sedimentol. Sin.* 34 (6), 1044–1056. [in Chinese with English abstract]. doi:10.14027/j.cnki.cjxb.2016.06.004
- Zhu, L. M., Shang, T., Gao, Z. Y., Li, B., and Xu, J. (2010). Geochemical distributions and their impacts of platinum group elements from surficial sediments in the South China Sea. *Acta Oceanolog. Sin.* 32 (1), 56–66. doi:10.1017/S0004972710001772

Conflict of Interest: The authors declare that the research was conducted in the absence of any commercial or financial relationships that could be construed as a potential conflict of interest.

Copyright © 2021 Fu, Yang, Li and Xia. This is an open-access article distributed under the terms of the Creative Commons Attribution License (CC BY). The use, distribution or reproduction in other forums is permitted, provided the original author(s) and the copyright owner(s) are credited and that the original publication in this journal is cited, in accordance with accepted academic practice. No use, distribution or reproduction is permitted which does not comply with these terms.



Geochronological and Geochemical Constraints on the Petrogenesis of Permian Dolerite Dyke Swarms in the Beishan Orogenic Belt, NW China

Gang Xu¹, Jun Duan^{1*}, Wenbin Gao¹, Rongmin Wang², Zhen Shi¹, Bocheng Ma¹ and Jia Sun³

¹ College of Earth Sciences and Resources, Chang'an University, Xi'an, China, ² Oilfield Development Division of Petrochina Changqing Oilfield Company, Xi'an, China, ³ Tianjin North China Geological Exploration Bureau, Tianjin, China

OPEN ACCESS

Edited by:

Xiaohua Deng,
Beijing Institute of Geology for Mineral
Resources, China

Reviewed by:

Wei Zhang,
China University of Geosciences
Wuhan, China
Joyashish Thakurta,
Western Michigan University,
United States

*Correspondence:

Jun Duan
Duanjun108@163.com

Specialty section:

This article was submitted to
Economic Geology,
a section of the journal
Frontiers in Earth Science

Received: 23 January 2021

Accepted: 26 February 2021

Published: 24 March 2021

Citation:

Xu G, Duan J, Gao W, Wang R,
Shi Z, Ma B and Sun J (2021)
Geochronological and Geochemical
Constraints on the Petrogenesis
of Permian Dolerite Dyke Swarms
in the Beishan Orogenic Belt, NW
China. *Front. Earth Sci.* 9:657716.
doi: 10.3389/feart.2021.657716

Extensive Early Permian mafic-ultramafic intrusions, doleritic dykes, and basalts crop out within the Beishan area, southern Central Asian Orogenic Belt (CAOB). We present new geochronological and geochemical data for Gubaoquan dolerite dyke swarms in the Beishan orogenic belt. Zircon U-Pb Dating of the Gubaoquan dykes indicates that they were emplaced during the Early Permian (280.7 ± 4 Ma), that was coeval with Yinaoxia and Podong mafic dykes in Beishan area. The dykes are characterized by low Mg# (47–84) in the clinopyroxene crystals, and the content of whole-rock Fe_2O_3 (t), MgO, and alkali ($\text{Na}_2\text{O} + \text{K}_2\text{O}$) range from 12.5–17.4, 4.06–5.51, and 2.8–4.4 wt.%, respectively. The samples from the Gubaoquan dykes have high and variable Ba/La (5.93–14.2) and Ba/Nb (15.0–37.3) ratios but low Th/Yb (0.17–0.24) ratios. The rocks show slightly enrichments in LREE, HFSE, Th, and Hf, and depletion in Nb and Ta. The ϵ_{Nd} ($t = 280$ Ma) values and initial $^{87}\text{Sr}/^{86}\text{Sr}$ ratios of the Gubaoquan dykes show variations ranging from 6.4 to 6.8 and 0.706240 to 0.707546, respectively. These data suggest that the parental magmas for the Gubaoquan dykes were probably derived from partially decompressed melting of upwelling depleted asthenosphere mantle that was metasomatized previously by subducted fluids.

Keywords: Zircon U-Pb dating, Sr-Nd isotopes, Early Permian dolerite dyke swarms, Beishan, Central Asian Orogenic Belt

INTRODUCTION

The Central Asian Orogenic Belt (CAOB) is the important Phanerozoic accretionary orogenic belt in the world (Figure 1A; Sengör et al., 1993; Jahn et al., 2000). It was formed by the amalgamation of accretionary complexes, magmatic arcs, arc-related basins, ophiolites, seamounts, and microcontinents during the long-lived subduction of the Paleo-Asian Ocean (Kröner et al., 2007; Windley et al., 2007; Xiao et al., 2008, 2011, 2019). The Beishan Orogenic Belt is located in the southern margin of the CAOB, and experienced a complex process of tectono-magmatic evolution during the Paleozoic. Therefore, it has become a key part to study the geological evolutionary history of the CAOB. The Early Permian was a crucial period in the evolutionary history of the CAOB, marked by the closure of the Paleo-Asian Ocean, the transition from subduction-accretion to post-collisional tectonism and the occurrence of extensive mantle-derived magmatism

(Wartes et al., 2002; Charvet et al., 2007). The Early Permian (290–270 Ma) magmatism and associated mineralization have been considered as the post-subduction byproducts after the closure of the Paleo-Asian Ocean (Han et al., 2010; Yuan et al., 2010; Song et al., 2011, 2013; Zhang et al., 2011). The petrogenesis of the Early Permian mafic-ultramafic complexes, doleritic dykes, and basalts in the Beishan orogenic belt, and is still in controversial. Zhou et al. (2004) believe that the Permian magmatic rocks in the Tarim area and the adjacent Beishan area together constitute a Large Igneous Province (LIP), which is a product of mantle plume activities (Zhou et al., 2004; Qin et al., 2011; Su et al., 2011, 2012). Zhang et al. (2011) suggest that the Permian mantle-derived coeval in the Beishan area are both products of the post-subduction extension (Zhang et al., 2011; Li et al., 2013, 2020; Zheng et al., 2014). Ao et al. (2010) believe that Permian mafic-ultramafic complexes, such as Pobei and Hongshishan, were formed by subduction process of the Paleo-Asian Ocean, representing the Late Paleozoic island arc settings in the Beishan area (Ao et al., 2010).

Previous studies have mostly focused on the investigation of the Early Permian mafic-ultramafic complex and basalt in the Beishan area, but the petrogenesis of the doleritic dykes is poorly constrained and lack of comparison between different regions, due to the limited geochemical investigations of mafic dykes in this area. As a specific product of tectono-magmatism (Hoek and Seitz, 1995), dolerite dyke swarms can be formed in the marginal areas of the mantle plume-related LIP, the back-arc extension environment and the post-subduction extension settings. The doleritic dykes are important signs of tectono-magmatic evolutionary events and can maximally retain information of mantle source (Halls, 1982; Liu et al., 2013). Thus, they are widely used in reconstructing the aggregation, extension, and breakup of ancient plates (Zhou et al., 2000). In addition, mafic dykes can serve as magma conduits, allowing the transportation of mafic magma from the mantle to the crust and potentially preserving primitive magma compositions that provide crucial information on the nature of the underlying mantle (Adams et al., 2005). Accordingly, we present new geochronological and geochemical data for Gubaoquan mafic dyke swarms in the Beishan area (Figure 1B), and investigate their petrogenesis and the dynamic background. This study aims to provide a basis for further understanding the geotectonic background in Beishan area during Early Permian.

GEOLOGICAL BACKGROUND AND SAMPLE DESCRIPTIONS

Geological Background

The Beishan orogenic belt is located in the southernmost margin of CAOB, adjacent to the Central Tianshan orogenic belt in the north, and the Tarim-North China Craton in the south (Figure 1B). The boundary between CAOB and the North China Craton is the South Tianshan–Liuyuan–Solonker suture zone (Figure 1A), which is considered to represent the final suture zone on the southern margin of CAOB. High-pressure to ultrahigh-pressure metamorphic rock belts related to the

subduction of the Paleo-Asian Ocean are distributed across the suture zone, including Akeyazi blueschist and eclogite in the southwestern Tianshan (Ar–Ar age: 315–319 Ma) (Gao and Klemd, 2003; Klemd, 2003; Klemd et al., 2015; Li et al., 2015), Gubaoquan eclogite in the south of Liuyuan (age of peak metamorphism: ~465 Ma; Liu et al., 2012; Saktura et al., 2017), and the Wenduermiao metamorphic rocks of blueschist facies in Solonker (Ar–Ar age: ~450 Ma) (Gao et al., 1990).

The Beishan orogenic belt evolved from the suturing of several island arcs located in different parts of the Paleo-Asian Ocean during the Early–Middle Paleozoic. The boundaries between the island arcs are the ophiolite belts representing the former oceanic crusts, which are Hongshishan (346.6 ± 2.8 Ma) – Baiheshan–Pengboshan ophiolitic mélange zone (Wang et al., 2014), Jijitaizi (321.2 ± 3.7 Ma) – Xiaohuangshan (336 ± 4 Ma) ophiolitic mélange zone (Li et al., 2012; Zheng et al., 2013), Hongliuhe (516.2 ± 7.1 Ma) – Niujuanzi (446.5 ± 4 Ma) – Xichangjing (536 ± 7 Ma) ophiolitic mélange zone (Zhang and Guo, 2008), and Huitongshan (446.1 ± 3 Ma) – Zhangfangshan (362.6 ± 4 Ma) ophiolitic mélange zone (Yu et al., 2012) from north to south, respectively. In the Beishan area, there are outcrops of Proterozoic to Cenozoic strata, among which, the Precambrian, Ordovician, Silurian, Carboniferous and Permian strata are relatively developed.

Available zircon U–Pb chronological data has shown that there were at least two phases of mafic-ultramafic magmatism in the Beishan area: one from the Late Ordovician to Devonian (360–450 Ma) and the other from the Late Carboniferous to Early Permian (260–305 Ma). The widely distributed ophiolite belts formed during the first stage in the Beishan area includes high-Mg diorite, Nb-rich basalt, normal-mid-oceanic ridge basalt (N-MORB), enriched-MORB (E-MORB), and island arc tholeiite, indicating that the Beishan area may have experienced oceanic crust subduction from the Late Ordovician to Early Devonian (Mao et al., 2012; Zheng et al., 2018). In the later phase, mafic-ultramafic magmatism was frequent, and several mafic-ultramafic complexes and dolerite dyke swarms were developed. These dolerite dykes are extensively distributed across the entire Beishan area and were once associated with the Tarim mantle plume (Xiao et al., 2006).

Permian Mafic Dyke Swarm

The dolerite dyke swarms in the Beishan area are concentrated in the Pobei area in the west, Gubaoquan area in the middle, and Yinwaxia area in the east. Moreover, there are scattered outcrops in other regions (Figure 1B). The dykes are generally parallel, striking toward NW ($310\text{--}355^\circ$) and NE ($10\text{--}80^\circ$), and are nearly vertical (dips of $80^\circ\text{--}90^\circ$; Figure 2E). The dyke swarms predominantly intrude the Silurian–Devonian (380–442 Ma) granodiorite and quartz diorite, as well as the Precambrian to Permian strata (Figures 2A,C,E; Mao, 2008; Mao et al., 2010) in the Liuyuan area. The contact boundaries between the dykes and country rocks and strata are conspicuous (Figures 2A,C,E). Baked edges can be seen between individual dykes and the granodiorite.

The Gubaoquan area is located in the middle section of the southern margin of Beishan in Gansu, to the north of the

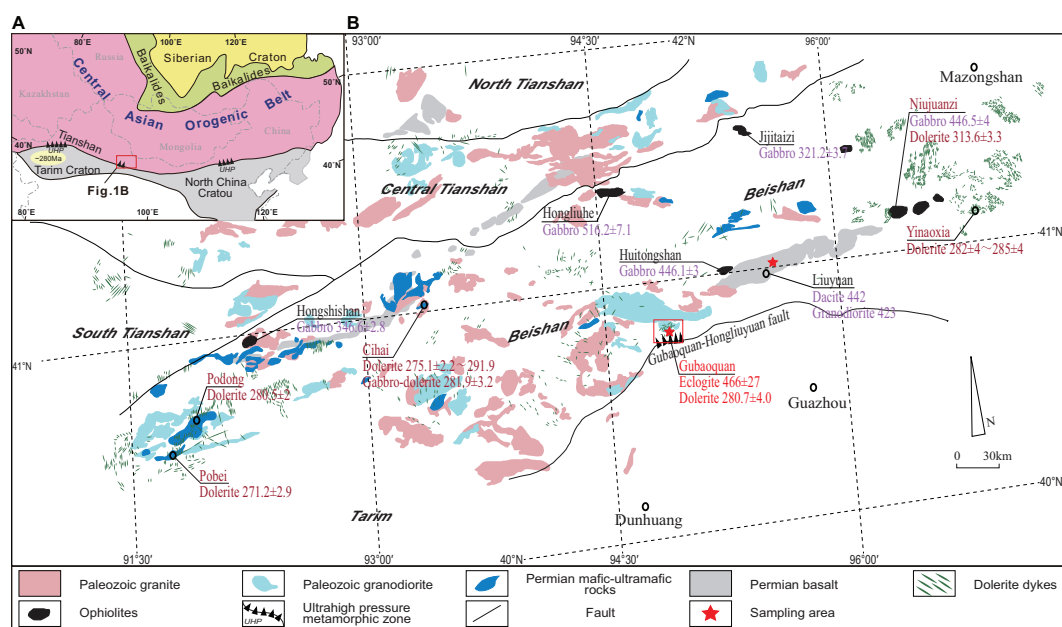


FIGURE 1 | (A) Simplified tectonic sketch map of the Central Asian Orogenic Belt (modified from Jahn, 2004). **(B)** Simplified geological map showing the distribution of Late Paleozoic dolerite dykes, mafic-ultramafic intrusions in the Beishan area modified from Xiao et al. (2004) and Xue et al. (2019). The age data (zircon U-Pb) from: Pobei dolerite (Tian, 2018), Podong dolerite (Xue et al., 2016), Hongshishan gabbro (Wang et al., 2014), Cihai dolerite (Chen et al., 2013, 2015), Cihai gabbro-dolerite (Chen et al., 2015), Hongliuhe gabbro (Zhang and Guo, 2008), Huitongshan gabbro (Yu et al., 2012), Jijitai gabbro (Li et al., 2012), Niujuanzi gabbro (Wu et al., 2012), Niujuanzi dolerite (Qi et al., 2017), Yinaoxia dolerite (Zhang et al., 2015; Peng et al., 2020), Liuyuan dacite (Mao et al., 2012), Liuyuan granodiorite (Zheng et al., 2018), and Gubaoquan eclogite (Saktura et al., 2017).

Gubaoquan–Hongliuyuan Fault. These dykes generally strike between NNE–NE and NW–SE, and are various in size, with widths ranging from 0.5 to 6 m. Dykes extend from hundreds of meters to thousands of meters, and are nearly vertical (**Figure 2E**). The Gubaoquan doleritic dykes mainly intrude the Ordovician–Devonian granodiorite, and some of them intrude the metamorphic strata of the Early Paleozoic Huaniushan Group (**Figure 1B**). The dykes are interspersed in the rock mass and cut through the strata, mostly in apophyses or stocks. The doleritic dykes exposed in the strata generally occur parallel to each other, with greenish-black to dark gray color, and have undergone weak chlorite and sericite alteration (**Figure 2F**). The dolerite dykes in the granodiorite rock mass are well preserved, mostly in dark green color, and the boundary between the dyke and country rocks is clear and flat (**Figure 2E**). These mafic dykes contain clinopyroxene (~15 vol.%) and plagioclase (~10 vol.%) phenocrysts (**Figures 2B,D**). Matrix minerals are composed of clinopyroxene and plagioclase with minor hornblende and Fe–Ti oxides (**Figure 2D**). The Gubaoquan doleritic dykes are porphyritic and fresh, with the ophitic textures (**Figures 2B,D,F**) and comprise the low proportion of Fe–Ti oxides (2 vol.% ~3 vol.%).

ANALYTICAL METHODS

Zircon crystals were separated from a fresh doleritic dyke sample (~25 kg, GBQ-04, 41°00′43.09″N, 95°00′21.52″E) using the

conventional heavy liquid and magnetic separation techniques in a commercial laboratory at Langfang, Hebei Province, China. Representative zircon crystals those were euhedral, colorless, transparent and underformed were mounted in an epoxy resin disk and then polished to analysis. Cathodoluminescence (CL) and back-scattered electron (BSE) images were obtained at the Beijing SHRIMP Center, Institute of Geology, Chinese Academy of Geological Sciences. CL and BSE images were used together to help select the zircon grains that have oscillatory or simple zoning patterns indicative of magmatic crystallization for U–Pb dating.

Zircon U–Pb dating for mafic dykes from the Gubaoquan areas was carried out using LA–ICP–MS at the Key Laboratory of Western China's Mineral Resources and Geological Engineering, Ministry of Education. Detailed descriptions of the instrumentation and analytical procedures can be found in Luan et al. (2019). A Plešovice zircon ($^{206}\text{Pb}/^{238}\text{U}$ age = 337 Ma, Sláma et al., 2008) and Qinghu zircon ($^{206}\text{Pb}/^{238}\text{U}$ age = 159 Ma, Li et al., 2009) standard were used as external standard for correcting mass discrimination and isotope fractionation, and Zircon 91500 ($^{207}\text{Pb}/^{206}\text{Pb}$ age = 1065 Ma, Wiedenbeck, 1995) was analyzed alternately with unknown zircons. Concordia diagrams and weighted mean calculations were carried out using the Isoplot 3.0 program (Ludwig, 2003). Common Pb correction was made using the measured ^{204}Pb and the values of Stacey and Kramers (1975).

Major element concentrations for clinopyroxene and plagioclase were determined by a JEOL JXA-8100 electron microprobe at Chang'an University, China. The analytical

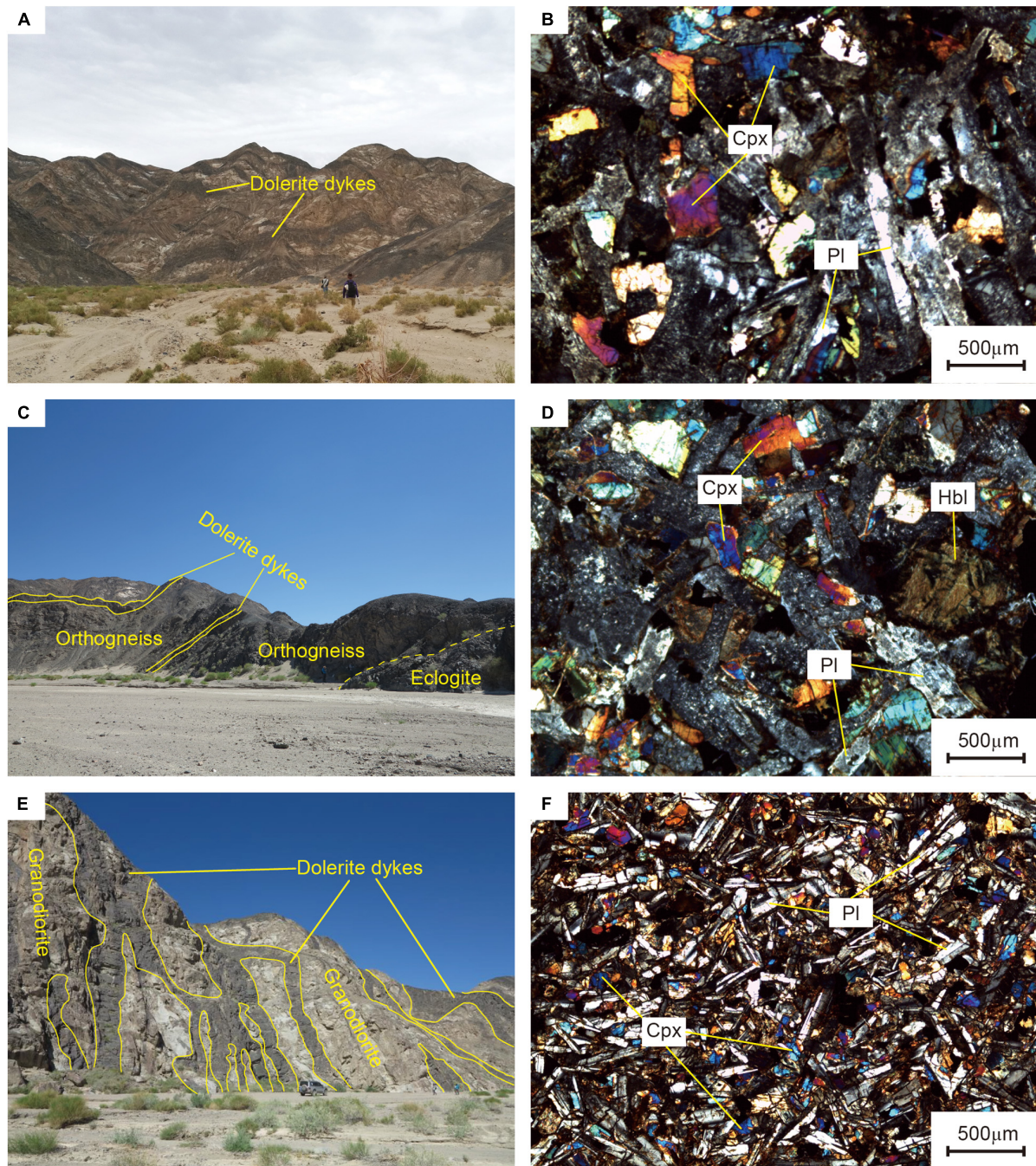


FIGURE 2 | Outcrops of dolerite dykes and photomicrographs of representative dolerite dykes from Gubaoquan. **(A)** Gubaoquan Dolerite dykes intruded into Precambrian orthogneisses. **(C)** Gubaoquan dikes between orthogneisses and eclogite. **(E)** Gubaoquan dikes intruded into Silurian-Devonian granodiorite country rocks. **(B,D)** Clinopyroxene, plagioclase and hornblende within the Gubaoquan dikes. **(F)** Showing the ophitic texture. Cpx, clinopyroxene; Pl, plagioclase; and Hbl, hornblende.

conditions were: 15-kV accelerating voltage, 20-nA beam current, 1- μ m beam size, and a 20-s peak counting time. International mineral standards were used for calibration. Analytical reproducibility was within $\pm 2\%$ relative.

Whole-rock major and trace element compositions were determined at Chang'an University, China. The major element

concentrations were measured by X-ray fluorescence (XRF) spectrometer (Shimadzu 1800) on fused glass disks, and Chinese national rock standards GBW07112 (gabbro) was used for calibration. Analytical precision for major elements was less than 3%. Whole-rock trace elements analyses were performed using a American Thermoelectric X-7 ICP-MS instrument, at

Chang'an University. Sample powder (40mg) were acid-digested with mixed HNO₃ and HF in steel-bomb coated Teflon beakers for 48 h in order to ensure complete dissolution of refractory minerals. Take the USGS basalt standard BCR-2 as external standard sample to calibrate the trace elemental concentrations of the measured samples, and analytical precision was generally better than 5%.

Whole-rock Sr–Nd isotopic analyses were undertaken using a Nu Plasma HR multi-collector (MC) ICP–MS instrument at State Key Laboratory of Continental Dynamics, Northwest University. Detailed descriptions of analytical procedures can be found in Zong (2013). The measured ¹⁴³Nd/¹⁴⁴Nd and ⁸⁷Sr/⁸⁶Sr ratios were normalized to ¹⁴⁶Nd/¹⁴⁴Nd = 0.7219 and ⁸⁶Sr/⁸⁸Sr = 0.1194, respectively. Repeated analysis of the NBS987 and Shin-Etsu JNdi-1 standards yielded ⁸⁷Sr/⁸⁸Sr and ¹⁴³Nd/¹⁴⁴Nd ratios of 0.710248 ± 0.000012 (2σ) and 0.512116 ± 0.000009 (2σ), respectively, and the reference values for these standards are ⁸⁷Sr/⁸⁸Sr_{NBS987} = 0.710241 ± 12 (Thirlwall, 1991), ¹⁴³Nd/¹⁴⁴Nd_{JNdi-1} = 0.512110 (Tanaka, 2000). The analytical precision for Sm/Nd and Rb/Sr ratios were below 1%. The total procedural blanks were < 200 pg for Sr and < 100 pg for Nd.

ANALYTICAL RESULTS

Zircon U–Pb Age

Zircon U–Pb data for the Gubaoquan mafic dykes are listed in Table 1. Sample GBQ-04 was collected from a mafic dyke in the Gubaoquan area that was intruded into Silurian–Devonian granodiorite (424–380 Ma; Mao et al., 2010) and Precambrian orthogneisses (Figures 2A,C; Yang et al., 2006; Mao, 2008; Saktura et al., 2017). The zircons separated from this sample are colorless and transparent in subhedral granular or columnar shapes, with a length of 50–100 μm and a length to width ratio of 1:1–2:1. In cathodoluminescence (CL) images, the zircon grains have flat crystal planes, and the majority of these zircons

have well-developed oscillatory zoning, indicating a magmatic origin (Figure 3a). The majority of the older zircon grains have recrystallized blurred zoning and are stubby and subhedral, whereas the three youngest zircons are elongated grain and have more developed oscillatory zoning (Figure 3a). The fourteen measured zircon ²⁰⁶Pb/²³⁸U age values vary in a wide range (Figure 3b). Four zircons yielded Precambrian ages (2044 to 897 Ma), and seven zircons yielded Silurian ages (441 to 425 Ma). In addition, the three youngest ages yield a weighted average age of 280.7 ± 4 Ma (Figure 3b). Accordingly, we interpret the age of 280.7 ± 4 Ma as the emplacement age of the Bubaoquan doleritic dykes, and all older grains as inherited zircons captured from the wall rocks.

Mineral Chemistry

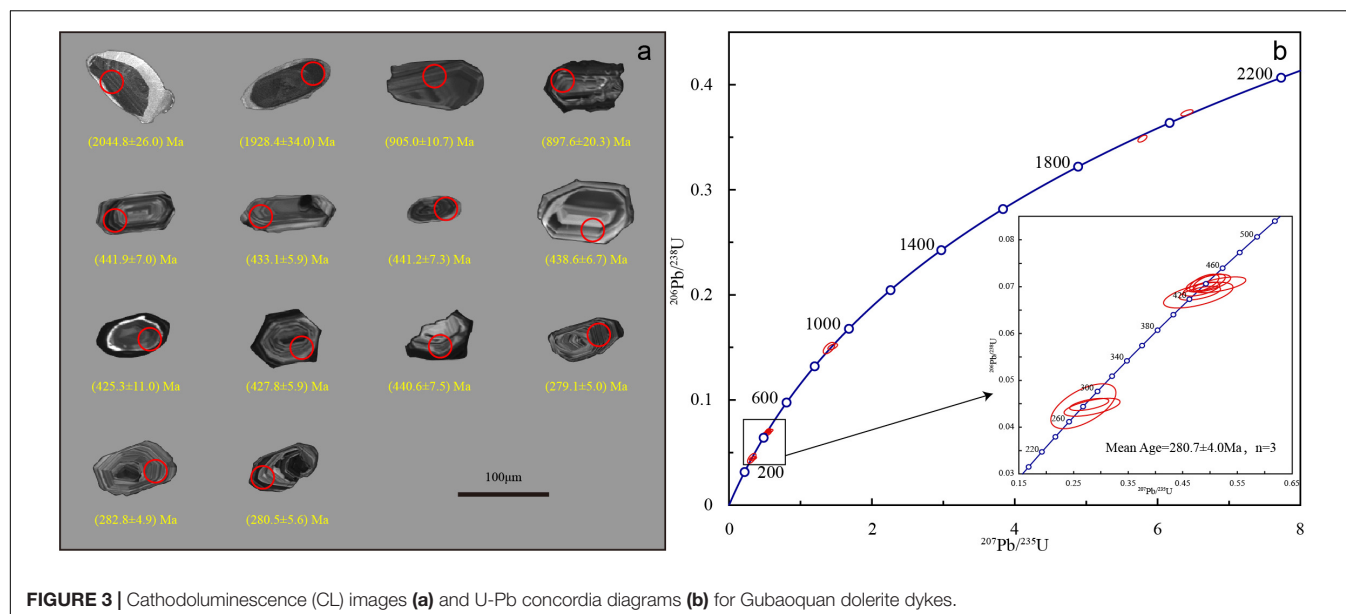
The compositions of clinopyroxene and plagioclase in the Gubaoquan doleritic dykes are given as Supplementary Table 1. Plagioclase within the mafic dykes is mainly labradorite and bytownite with An values of 46.4–74.3 mol%, indicating that plagioclase is the early crystallized mineral from the magma. Clinopyroxene (Wo_{29.6–43.3}En_{30.0–51.2}Fs_{8.8–33.5}) within the doleritic dykes is mainly consist of augite (Wo_{33–42}En_{39–50}Fs_{13–26}), with a small amount of diopside and endiopside (Figure 4). Clinopyroxene from Gubaoquan mafic dykes have the variable Mg# values (47–84), and mainly concentrated in 66 to 84.

Major and Trace Elements

Whole-rock major and trace element compositions of the mafic dykes from the Gubaoquan are given as Supplementary Table 2. The content of whole-rock SiO₂ and Fe₂O₃^T from Gubaoquan dykes ranges from 47.7 to 50.1 wt.% and from 12.5 to 17.4 wt.%, respectively, with relatively lower concentrations of MgO (4.06–5.51 wt.%) and total alkali (Na₂O + K₂O = 2.83–4.37 wt.%). The Mg# values (magnesium index of rock) of the Gubaoquan dolerite are between 41.5 and 57. These dykes are relatively rich

TABLE 1 | Concentrations of U, Th, Pb, and U–Pb isotopes of zircon crystals from a large (25 kg) dolerite sample from the Gubaoquan dolerite dyke.

Spot	U	Th	Pb	Th/U	²⁰⁷ Pb/ ²⁰⁶ Pb		²⁰⁷ Pb/ ²³⁵ U		²⁰⁶ Pb/ ²³⁸ U		²⁰⁶ Pb/ ²³⁸ U	
	ppm	ppm	ppm		Ratio	1σ	Ratio	1σ	Ratio	1σ	Age (Ma)	1σ
GBQ-04-01	482	142	38	0.30	0.055607	0.002092	0.534197	0.022213	0.069493	0.000983	433.1	5.9
GBQ-04-02	812	305	69	0.38	0.055787	0.001699	0.548701	0.019399	0.070958	0.001169	441.9	7.0
GBQ-04-03	896	296	69	0.33	0.054952	0.001661	0.539530	0.017815	0.070837	0.001207	441.2	7.3
GBQ-04-04	403	190	38	0.47	0.055594	0.003802	0.528526	0.042042	0.068207	0.001818	425.3	11.0
GBQ-04-05	649	248	55	0.38	0.055658	0.002584	0.531442	0.025080	0.068616	0.000974	427.8	5.9
GBQ-04-06	446	308	112	0.69	0.068421	0.002588	1.399316	0.053892	0.149408	0.003623	897.6	20.3
GBQ-04-07	451	120	68	0.27	0.069355	0.002308	1.451242	0.045158	0.150718	0.001913	905.0	10.7
GBQ-04-08	267	131	28	0.49	0.057753	0.003236	0.567486	0.031822	0.070407	0.001114	438.6	6.7
GBQ-04-09	434	183	39	0.42	0.055745	0.002878	0.547047	0.026929	0.070744	0.001238	440.6	7.5
GBQ-04-12	349	238	13	0.68	0.052223	0.003409	0.333921	0.033872	0.044252	0.001264	279.1	5.0
GBQ-04-14	349	83	13	0.24	0.052673	0.002826	0.328714	0.023732	0.044854	0.000854	280.5	5.6
GBQ-04-15	676	352	26	0.52	0.055816	0.003224	0.318270	0.039358	0.044471	0.003167	282.8	4.9
GBQ-04-17	488	141	156	0.29	0.124542	0.002452	6.409970	0.056531	0.373285	0.001946	2044.8	26.0
GBQ-04-18	1632	125	489	0.08	0.120357	0.002013	5.786799	0.042245	0.348710	0.002171	1928.4	34.0



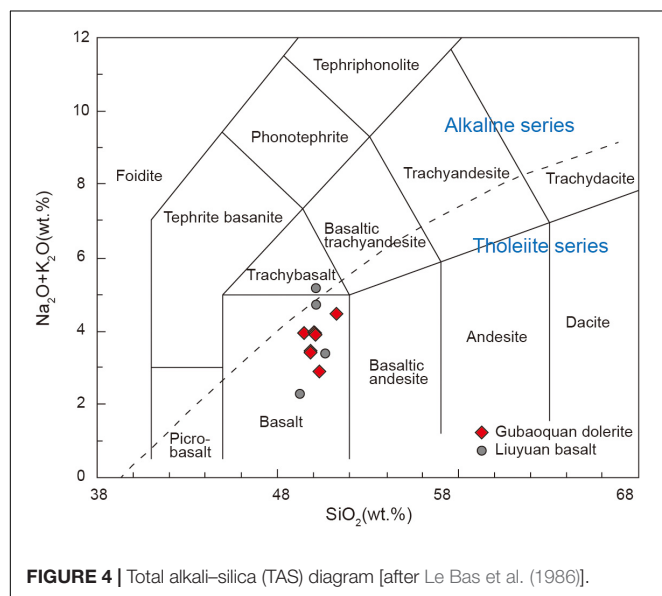
in iron and poor in magnesium thereby belonging to iron-rich mafic rock group, and are also sub-alkaline and basaltic in a TAS diagram (Figure 5; Le Bas et al., 1986), that is similar to the major element characteristics of dolerites in the Yinwaxia and Podong areas (Zhang et al., 2015; Xue et al., 2016), whereas the type of dolerite formed in the same period in the Tarim Bachu area is dominantly alkaline basalt (Yu, 2009).

The chondrite-normalized rare-earth element (REE) patterns and primitive mantle-normalized immobile incompatible element patterns are illustrated in Figures 6A,B. The Gubaoquan dykes show slightly depleted to enriched LREE patterns ($[La/Yb]_N = 0.93\text{--}1.32$) and weakly negative Eu anomalies ($\delta Eu = 0.87\text{--}0.99$; Figure 6A), which may be caused by the

distribution of Eu in the magma into the early crystallized plagioclase. The samples from the Gubaoquan doleritic dykes have lower Ni (14.9–62.9 ppm) and Cr (12–132 ppm) concentrations and lower Nb/La (0.33–0.41), Nb/Ta (10.64–14.48), Nb/Y (0.05–0.07) ratios, but higher Th/La (0.12–0.15) and Zr/Nb (48.2–56.2) ratios than the primitive mantle (McDonough and Sun, 1995). As shown in Figure 6B, the samples are characterized by pronounced Nb-Ta negative anomalies and slightly light REE enrichments relative to heavy REE, that is similar to the trace element distribution characteristics of the Mesozoic island arc basalts. Compared with the regional contemporaneous dykes and basalt, the Liuyuan basalt is relatively more enriched in LREE and HFSE, while the Gubaoquan dykes have slightly higher trace element content than that of doleritic dykes in the Yinwaxia and Podong areas. However, they have similar distribution patterns of rare earth elements and trace elements which are significantly different from the geochemical characteristics of Bachu mafic dykes of the same period in the Tarim area.

Sr-Nd Isotopes

The Rb-Sr and Sm-Nd contents and isotopic composition of the Gubaoquan dykes are listed in Table 2. The $\epsilon Nd(t = 280 \text{ Ma})$ value of the Gubaoquan dolerites ranges from 6.4 to 6.8, similar to the values of dolerites in Yinwaxia [$\epsilon Nd(t) = 9.0\text{--}9.1$; Zhang et al., 2015] and Podong [$\epsilon Nd(t) = 5.5\text{--}7.4$; Xue et al., 2016], and shows the characteristics of depleted mantle, which is different from the Bachu dolerite in the Tarim area [$\epsilon Nd(t) = -1.2\text{--}3.5$; Jiang et al., 2004b; Yu, 2009; Yu et al., 2017]. The Gubaoquan doleritic dykes have variably and higher initial $^{87}Sr/^{86}Sr$ ratios (0.706240 to 0.707626) than the ratios of dolerites in Yinwaxia (0.703622 to 0.704141; Zhang et al., 2015) and Podong (0.704042 to 0.705267; Xue et al., 2016), which may be attributed to a certain degree of crustal contamination during magma ascent and emplacement. The relatively low initial $^{87}Sr/^{86}Sr$ ratios and



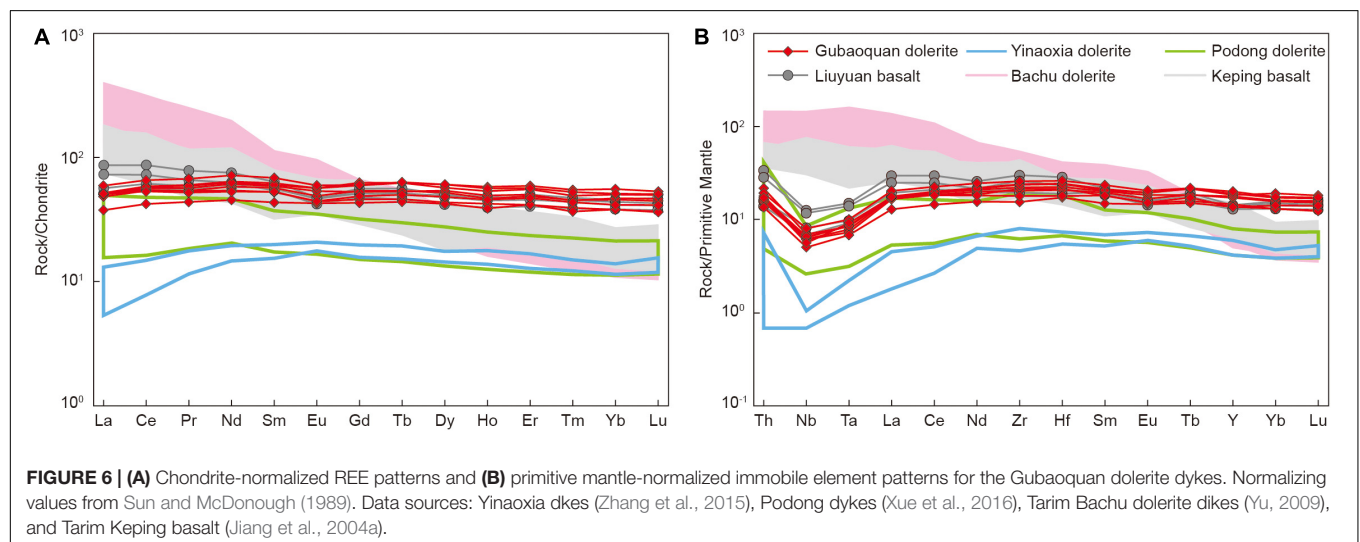
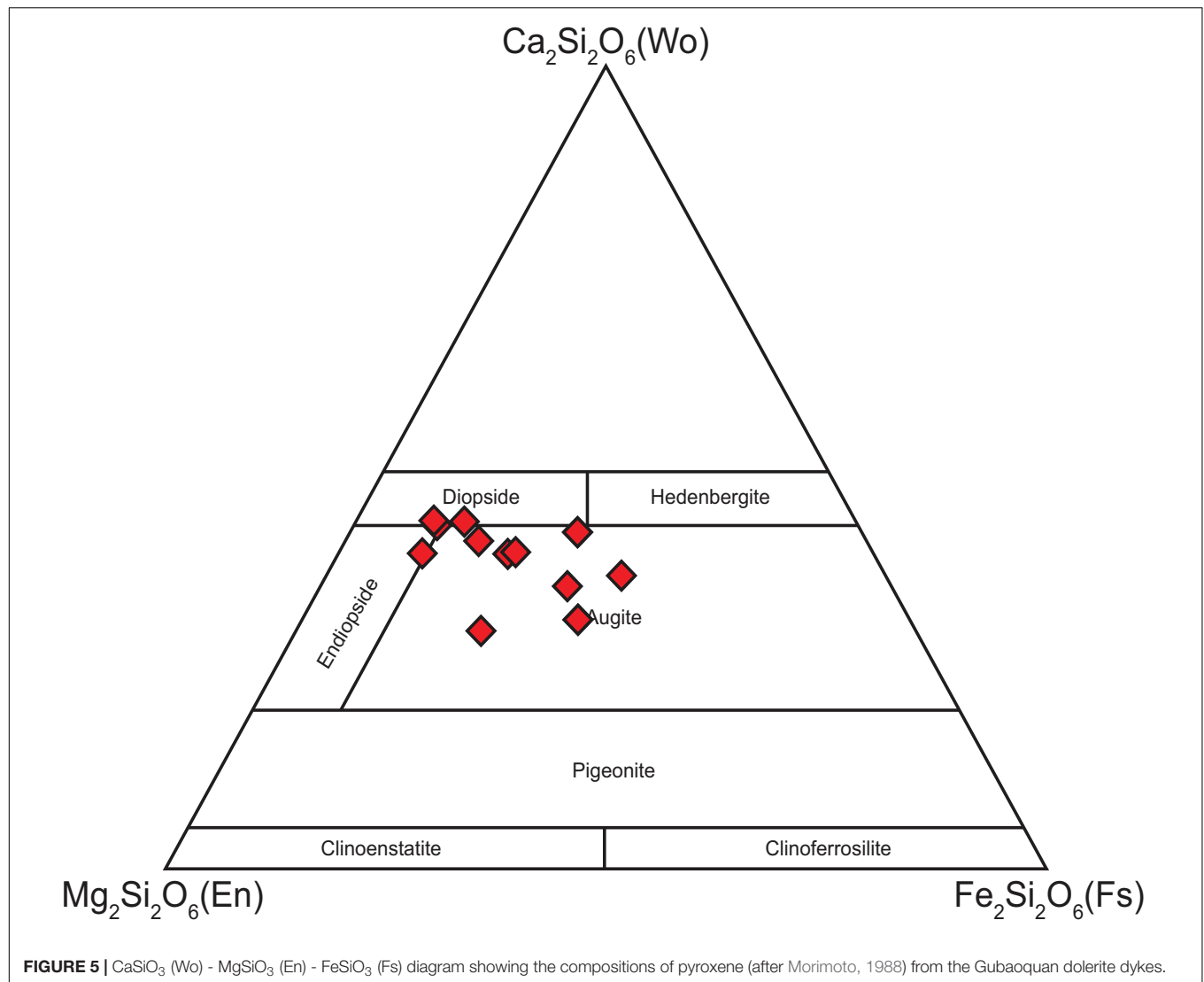


TABLE 2 | Sm-Nd and Rb-Sr isotopic analytical results of the Gubaoquan dolerite dykes in the Beishan area, NW China.

Sample	Rb (ppm)	Sr (ppm)	$^{87}\text{Rb}/^{86}\text{Sr}$	$^{87}\text{Sr}/^{86}\text{Sr}$	2 σ	$(^{87}\text{Sr}/^{86}\text{Sr})_i$	Sm (ppm)	Nd (ppm)	$^{147}\text{Sm}/^{144}\text{Nd}$	$^{143}\text{Nd}/^{144}\text{Nd}$	2 σ	$(^{143}\text{Nd}/^{144}\text{Nd})_i$	$\epsilon_{\text{Nd}}(t)$
GBQ-1b	34.8	137	0.7375	0.710174	0.000016	0.707183	9.48	29.8	0.1937	0.512964	1.1E-05	0.512602	6.5
GBQ-5a	38.1	170	0.6466	0.710168	0.000013	0.707546	8.95	28.4	0.1918	0.512971	8E-06	0.512613	6.7
GBQ-6a	43.8	157	0.8076	0.710901	0.000012	0.707626	9.17	29.2	0.1913	0.512975	6E-06	0.512618	6.8
GBQ-7a	29.2	151	0.5612	0.708516	0.000016	0.706240	6.62	21.1	0.1907	0.512966	0.00001	0.512610	6.6
GBQ-9a	36.9	160	0.6678	0.709702	0.000014	0.706994	10.5	33.4	0.1908	0.512954	9E-06	0.512598	6.4

high $\epsilon_{\text{Nd}}(t)$ values (Figure 7) are similar to the mafic dykes in Podong and Yinaoxia. It is also similar to the Liuyuan mafic-ultramafic intrusions and basalts [$\epsilon_{\text{Nd}}(t) = -1.84$ – 9.0 ; initial $^{87}\text{Sr}/^{86}\text{Sr} = 0.703390$ – 0.7098] which are thought to have been derived from a depleted asthenospheric mantle source (Zhao et al., 2006; Mao et al., 2012).

DISCUSSION

Age of Doleritic Dykes

Dolerite belongs to a mafic hypabyssal intrusive rock. The primitive magma was silica-unsaturated, and dolerite was formed during the rapid ascent and emplacement of magma. Therefore,

primary magmatic zircons are difficult to crystallize in dolerite. Considering the fact that mafic dykes are able to capture zircons from their wall rocks during ascent, the majority of these zircons can be interpreted as xenocrysts captured from wall rocks.

Previous data show that Precambrian metamorphic basement were extensively developed in Beishan area (China University of Geosciences Press, 1997; Niu et al., 2020). The doleritic dykes from Gubaoquan area mainly intruded the Silurian–Devonian granodiorite (424–380 Ma; Mao et al., 2010) and Precambrian orthogneisses (Figures 2A,C; Yang et al., 2006; Mao, 2008; Saktura et al., 2017), respectively. It is inferred that the formation age of the Gubaoquan doleritic dykes should be later than the Devonian. This means that the three youngest zircons (279.1, 280.5, and 282.8 Ma) are most likely to crystallize from the mafic magma, and their weighted average $^{206}\text{Pb}/^{238}\text{U}$ age of 280.7 ± 4 Ma can be taken as the best estimation of the emplacement age of the Gubaoquan dykes. Whereas, the older age groups (2044–897 Ma and 441–425 Ma) represent the ages of zircons captured from the basement strata (Precambrian orthogneisses) and country rocks (granodiorite) during the ascent of magma. In addition, According to the statistics of the age of doleritic dykes (Table 3) in the Beishan area, the emplacement age range of the dolerite dyke swarms is 271.2 ± 2.9 – 313.6 ± 3.3 Ma, and concentrated in 285–270 Ma, similar to that of the mafic dykes in Podong, Huaniushan, and Yinwaxia area. Moreover, the age of doleritic dykes obtained by Zhang et al. (2015) in the Liuyuan Gubaoquan area is 282 Ma, indicating that there was extensive mafic magmatism from the Late Carboniferous to Early Permian in the Beishan area.

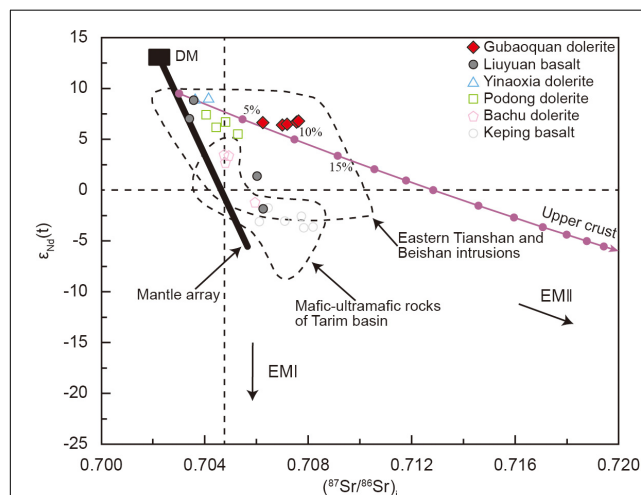


FIGURE 7 | Plot of $\epsilon_{\text{Nd}}(t)$ versus initial $^{87}\text{Sr}/^{86}\text{Sr}$ isotopic ratios for dolerite dykes and basalt in Beishan and Tarim areas. Data for intrusions within the eastern Tianshan and Beishan areas are from Zhou et al. (2004), Qin et al. (2011), Song et al. (2011), and Zhang et al. (2011). Data sources for Permian magmatism of the Tarim LIP are from Jiang et al. (2004a), Yu (2009), Zhou et al. (2009), Xie et al. (2014), and Wei et al. (2014). Data sources: Yinaoxia dykes (Zhang et al., 2015), Podong dykes (Xue et al., 2016), Tarim Bachu dolerite dykes (Yu, 2009), Tarim Keping basalt (Jiang et al., 2004a), and Liuyuan basalt (Zhao et al., 2006). Values used in the mixing calculation: (1) upper crust, 27 ppm Nd, 320 ppm Sr, $\epsilon_{\text{Nd}}(t) = -6$, $(^{87}\text{Sr}/^{86}\text{Sr})_i = 0.72$; (2) mantle-derived magma, 7.3 ppm Nd, 90 ppm Sr, $\epsilon_{\text{Nd}}(t) = 9.5$, $(^{87}\text{Sr}/^{86}\text{Sr})_i = 0.703$. Concentrations of immobile elements: Depleted mantle is from Sun and McDonough (1989), upper crust is from Rudnick and Gao (2014). The Sr-Nd isotopic array for magmas derived from oceanic mantle is from Zindler and Hart (1986).

Magma Source and Crustal Contamination

The results of the whole-rock Sr-Nd isotopic simulation reveal that the magma of the Gubaoquan doleritic dykes experienced contamination with upper-crust materials during the emplacement. In the simulation, the two-component of the magma isotopic composition are taken from the primitive mantle that is the intersection point between the sample and the mantle trend line [$\epsilon_{\text{Nd}}(t) = 9.5$, $(^{87}\text{Sr}/^{86}\text{Sr})_i = 0.703$], and the upper crust [Rudnick and Gao, 2014; $\epsilon_{\text{Nd}}(t) = 6$, $(^{87}\text{Sr}/^{86}\text{Sr})_i = 0.72$]. The magma evolved from the depleted mantle has Sr and Nd concentrations of 90 ppm and 7.3 ppm, respectively. The Sr and Nd concentrations of upper-crust contaminant end members are assumed to be 320 ppm and 27 ppm, respectively. These values lie within the mean value ranges of oceanic basalts and upper crust, respectively (Sun and McDonough, 1989; Rudnick

and Gao, 2014). The simulation calculation results show that the Gubaoquan mafic dykes have a crustal contamination degree of 5~10% (Figure 7), which is close to the Liuyuan basalts and higher than the doleritic dykes in Yinwaxia and Pobei areas. In addition, the presence of xenocrystic zircons from the Precambrian strata and granodiorite provided the evidence for crustal contamination during the magma emplacement.

Mafic magma generally originates from the asthenosphere or lithospheric mantle (Fiona et al., 2017). The Fe/Mn ratios of mafic rocks can be used to identify their parental magma composition (Liu et al., 2008). In general, MORB have the lower Fe/Mn ratios (55–58; Zhang et al., 2011) than the plume-derived basalts such as Hawaiian OIBs (about 65–71; Humayun et al., 2004) and continental flood basalts (~63.7; Wang et al., 2011). Olivine and clinopyroxene fractionation will decrease and increase Fe/Mn ratios, respectively (Liu et al., 2008). The relatively uniform Fe/Mn ratios (54.1–59.7) of the Gubaoquan doleritic dykes is similar to the MORB, and suggest that the crystallization of olivine and pyroxene has little overall impact on the Fe/Mn ratio of the magma. This reveals that the Fe/Mn ratios of the Gubaoquan dykes reflect the composition of their mantle source and imply a MORB-type parental magma. In addition, the $\epsilon\text{Nd}(t)$ value of the Gubaoquan doleritic dykes varies between 6.4 and 6.8, showing the characteristics of a depleted mantle. All of the mafic dykes plot above the MORB-OIB array on a Th/Yb versus Nb/Yb diagram, that are similar to Liuyuan basalts, Podong and Yinaoxia doleritic dykes (Figure 8), further suggesting the involvement of a subduction-related component (Pearce, 2008). However, the Bachu doleritic dykes and Keping basalts plot close to the OIB in the MORB-OIB array, with obvious different sources. Subduction components mainly include siliceous melts and slab-derived fluids, both can impose distinctive geochemical signatures on mantle sources (Pearce, 2005). Highly mobile elements (e.g., Rb, Ba, Cs, and U) are tend to partition into aqueous fluids, whereas Th and LREE are strongly partitioned into sediment-derived siliceous melts (Plank and Wade, 2005). The high and variable Ba/La (5.93–14.2) and Ba/Nb (15.0–37.3) ratios but low Th/Yb (0.17–0.24) ratios of the Gubaoquan doleritic dykes strongly suggest they were derived from a mantle source that was metasomatized by slab-derived fluids (Woodhead

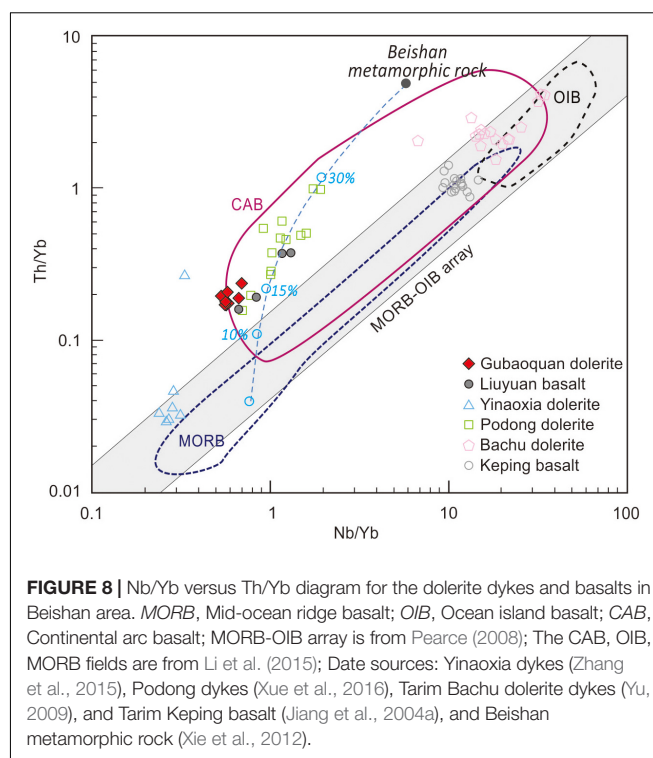


FIGURE 8 | Nb/Yb versus Th/Yb diagram for the dolerite dykes and basalts in Beishan area. MORB, Mid-ocean ridge basalt; OIB, Ocean island basalt; CAB, Continental arc basalt; MORB-OIB array is from Pearce (2008); The CAB, OIB, MORB fields are from Li et al. (2015); Date sources: Yinaoxia dykes (Zhang et al., 2015), Podong dykes (Xue et al., 2016), Tarim Bachu dolerite dykes (Yu, 2009), and Tarim Keping basalt (Jiang et al., 2004a), and Beishan metamorphic rock (Xie et al., 2012).

et al., 2001; Plank and Wade, 2005). Therefore, based on the above results, we propose that the parental magma for the Gubaoquan mafic dykes was derived from the depleted Asthenospheric mantle that metasomatized previously by the subducted fluids, and then contaminated by crustal materials.

Geodynamic Background of Magmatism

The parent magma of these dykes underwent assimilation and contamination with upper-crust materials during the emplacement process, which may have caused of the negative Nb-Ta anomalies in the Gubaoquan dolerite, because the continental crust is severely depleted in Nb and Ta (Rudnick and Gao, 2003). However, there are other possibilities to cause negative Nb-Ta anomalies. Island arc basaltic magma and the mantle-derived magma that was previously metasomatized by a subduction-related component both have the characteristics of negative Nb-Ta anomalies (Rudnick and Gao, 2003; Pearce et al., 2013).

In order to further understand the genesis of negative Nb-Ta anomalies in the Gubaoquan doleritic dykes, we use the whole-rock Nb/Yb and Th/Yb ratios to evaluate the explanations (Pearce, 2008). As shown in Figure 8, the trace element ratios represent the parental magma composition, if we assume that the negative Nb-Ta anomalies in dykes are entirely caused by the contamination with crustal, up to ~15% crustal contamination is required (Figure 8), indicating that the assimilation and contamination with more crustal materials is required to reach the current level of Nb-Ta depletion. As mentioned above, the Sr-Nd isotope compositions of the mafic dykes show significantly lower degrees of crustal contamination (< 10%, Figure 7). The contradiction rules out the possibility of crustal contamination

TABLE 3 | Compiled ages of dolerite dykes in Beishan area.

Location	Rock type	Analytical method	Age (Ma)	Error	Data source
Pobei	Dolerite	SHRIMP	271.2	2.9	Tan (2018)
Podong	Mafic dyke	SIMS	280.5	2.0	Xue et al. (2016)
Cihai	Dolerite	LA-ICP-MS	291.9		Chen et al. (2013)
	Gabbro-dolerite	SIMS	281.9	3.2	Chen et al. (2015)
	Dolerite	SIMS	275.1	2.2	Chen et al. (2015)
Gubaoquan	Dolerite	SIMS	282.0	6.0	Zhang et al. (2015)
Niujuanzi	Mafic dyke	LA-ICP-MS	313.6	3.3	Qi et al. (2017)
Yinaoxia	Dolerite	SIMS	282.0	4.0	Zhang et al. (2015)
		LA-ICP-MS	285.0	4.0	Peng et al. (2020)
Dahongshan	Dolerite	LA-ICP-MS	305.2	2.0	Yang et al. (2015)

as a major cause for the negative Nb-Ta anomalies in the dykes. And the Nb/Yb and Th/Yb ratios of Gubaoquan dykes are within the field of Cenozoic continental arc basalts. The characteristics of trace element and Sr-Nd isotopes indicate that the negative Nb-Ta anomalies probably reflect the primary signature of a mantle source. The parent magma of the Gubaoquan doleritic dykes had a certain degree of Nb-Ta depletion. This shows that the parent magma of the Gubaoquan dykes probably was the basaltic magma in island arc setting or the mantle-derived magma whose source had been metasomatized by subduction fluids before its formation.

The Beishan orogenic belt was formed by the suturing of blocks located in different places in the Paleo-Asian Ocean during the Paleozoic (Zheng et al., 2014, 2016; Chen et al., 2017; Wang et al., 2018). Available geological data have shown that the ophiolite belt in the Beishan area was formed between 330 Ma and 516 Ma (Zhang and Guo, 2008; Li et al., 2012; Zheng et al., 2013; Wang et al., 2014), which represent the upper time limit of the oceanic crust subduction between different blocks. The metamorphic age of the high-temperature and high-pressure metamorphic rock belt distributed across the South Tianshan-Liuyuan-Solonker suture zone on the southernmost margin of CAOBS was 465–315 Ma (Gao and Klemd, 2003; Klemd, 2003; Liu et al., 2012; Li et al., 2015; Saktura et al., 2017), which represents the end of oceanic crust subduction, i.e., the subduction of Paleo-Asian oceanic crust ended before the Late Carboniferous (~315 Ma), and subsequently, the stage of arc-continent collision and post-subduction extension was started.

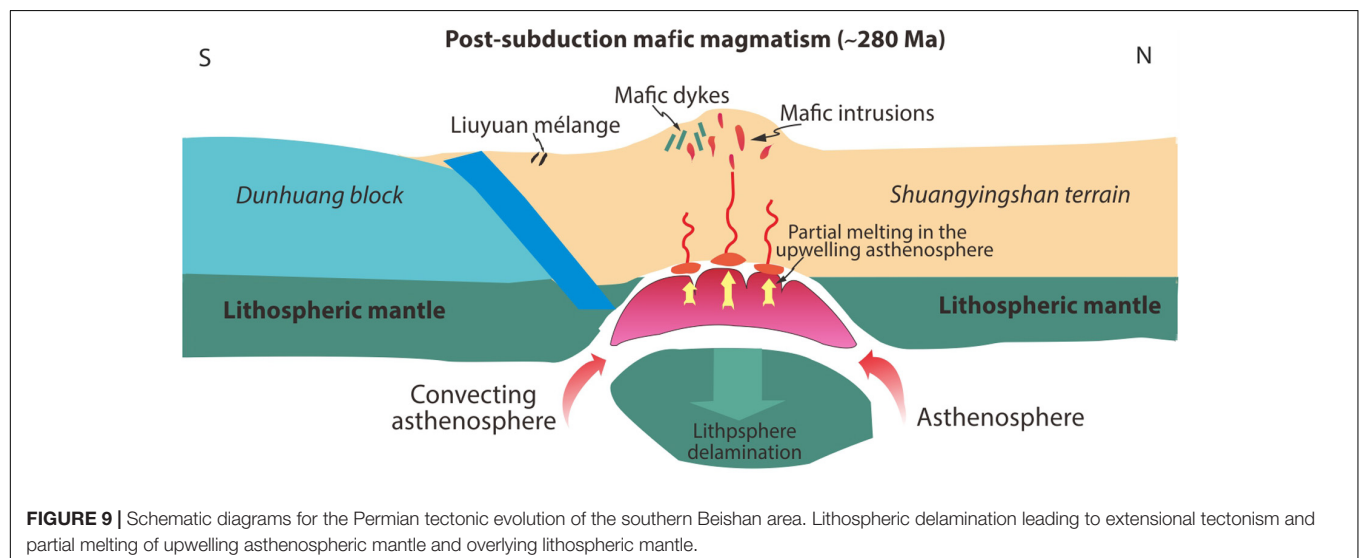
The Gubaoquan dolerite was formed in the Early Permian (~280 Ma). After the subduction of the Paleo-Asian Ocean, the Beishan area has entered the stage of intracontinental evolution. Moreover, considering that there was no arc-related magmatism in the Huaniushan arc or Shibanshan arc since Early Permian. In other words, the significant negative Nb-Ta anomalies in the dykes probably were not formed by the basaltic magma in the island arc setting. Instead, they are the combined results of metasomatism of the mantle-derived magma by fluids from

ancient subducting slab and crustal contamination. The trace rare earth elements and Sr-Nd isotopic characteristics of the Gubaoquan doleritic dykes indicate that its primary magma originated from the depleted asthenosphere mantle, and the magma experienced 5%~10% of assimilation and contamination with upper-crust materials during the emplacement. The petrological and geochemical characteristics of the Gubaoquan doleritic dykes also indicate that they formed under conditions of low water fugacity that are different from the conditions of arc-related basaltic rocks (Feig et al., 2006; Metcalf and Shervais, 2008). Therefore, during the post-subduction extension stage (~280 Ma), lithospheric delamination system was most likely responsible for the genesis of the Permian Gubaoquan mafic dykes in the Beishan area (Figure 9).

Consequently, we suggest that the Gubaoquan doleritic dykes were formed during the tectonic period after the plate subduction. The lithospheric delamination in an extensional environment led to the partial melting of upwelling asthenospheric mantle and the overlying metasomatized mantle, which consequently generated the mafic magma of dolerite. In addition, on a larger scale in Beishan, the formation age of the Gubaoquan doleritic dykes was similar to that of the widely distributed doleritic dykes in the Beishan area, and the Gubaoquan mafic dykes have similar geochemical characteristics to the dykes in the Yinwaxia in the east and Podong in the west. This indicates that the Late Carboniferous to Early Permian doleritic dykes in the Beishan orogenic belt may be controlled by a unified continental geodynamic background, i.e., the dykes are related to the post-subduction extensional setting.

CONCLUSION

Zircon U-Pb dating indicates that the Gubaoquan doleritic dykes in the Beishan orogenic belt were emplaced at ca. 280 Ma, that was the same time as the formation of the dolerite dyke



swarms extensively distribution in Beishan and the Tarim LIP. The geochemical characteristics of these dykes are obviously different from the mafic dykes related to mantle plume activity characterized by OIB-type mantle in Bachu area, Tarim. On the contrary, they are similar to the dykes in Yinaoxia and Podong area. Trace elements and Sr-Nd isotopes indicate that the parental magma for these mafic dykes was derived from the partial melting of the depleted asthenosphere mantle that metasomatized previously by the fluids from ancient subducting slab. This suggests that the dolerite dyke swarms in Beishan area were formed after the closure of the Paleo-Asian Ocean. It was a product of basaltic magmatism formed by the partial melting of the decompressed asthenosphere caused by the lithospheric delamination in a post-subduction extensional setting.

DATA AVAILABILITY STATEMENT

The original contributions presented in the study are included in the article/**Supplementary Material**, further inquiries can be directed to the corresponding authors.

AUTHOR CONTRIBUTIONS

GX: field geological investigation, ideas, formal analysis, and writing – original draft. JD: field geological investigation, validation, and writing – review and editing. WG: data curation and visualization. RW: project administration and validation.

REFERENCES

- Adams, M. G., Lentz, D. R., Shaw, C. S., Williams, P. F., Archibald, D. A., and Cousens, B. (2005). Eocene shoshonitic mafic dykes intruding the Monashee Complex, British Columbia: a petrogenetic relationship with the Kamloops Group volcanic sequence? *Can. J. Earth Sci.* 42, 11–24. doi: 10.1139/e04-091
- Ao, S. J., Xiao, W. J., Han, C. M., Mao, Q. G., and Zhang, J. E. (2010). Geochronology and geochemistry of Early Permian mafic-ultramafic complexes in the Beishan area, Xinjiang, NW China: implications for late Paleozoic tectonic evolution of the southern Altaids. *Gondwana Res.* 18, 466–478. doi: 10.1016/j.gr.2010.01.004
- Charvet, J., Shu, L. S., and Laurent-Charvet, S. (2007). Paleozoic structural and geodynamic evolution of eastern Tianshan (NW China): welding of the Tarim and Junggar plates. *Episodes* 30, 162–186.
- Chen, B., Qin, K. Z., Tang, D. M., Mao, Y. J., Feng, H. Y., Xue, S. C., et al. (2015). Lithological, chronological and geochemical characteristics of Cihai iron deposit, Eastern Xinjiang: constraints on genesis of mafic-ultramafic and syenite intrusions and mineralization. *Acta Petrol. Sin.* 31, 2156–2174.
- Chen, C., Xiu, D., Pan, Z. L., Zhang, H., Zhang, J. L., Li, Q. Z., et al. (2017). Early Paleozoic crustal extensional tectonic regime in the central part of Beishan Orogenic Belt: new evidence from geochronology and geochemistry of gabbro in Shibanjing. *Acta Geol. Sin.* 91, 1661–1673.
- Chen, J. P., Liao, Q. A., Luo, T., Zhang, X. H., Guo, D. B., Zhu, H. L., et al. (2013). Zircon U-Pb geochronology and genesis study on the mafic complex from diabase-type iron deposit in Cihai, Beishan area. *Geol. Sci. Technol. Inform.* 32, 76–83.
- China University of Geosciences Press (1997). *Bureau of Geology and Mineral Resources of Gansu Province*. Zhenkoudian: China University of Geosciences Press.
- ZS: field geological investigation and visualization. BM: data collection and software. JS: experimental test assistance and software. All authors contributed to the article and approved the submitted version.

FUNDING

This work was financially supported by the National Natural Science Foundation of China (41872076 and 41802081), Shaanxi Natural Science Basic Research Program (2019JQ-674 and 2020JQ-440), and Chang'an University (300102279203).

ACKNOWLEDGMENTS

We are very grateful to Prof. Zhuangzhi Qian, Editor XD, as well as two anonymous reviewers for their encouraging and constructive comments and suggestions in improving this work. Mr. Minwu Liu, Mr. Ke He, and Ms. Chunlei Zong are greatly appreciated for their kind help with geochemical analyses.

SUPPLEMENTARY MATERIAL

The Supplementary Material for this article can be found online at: <https://www.frontiersin.org/articles/10.3389/feart.2021.657716/full#supplementary-material>

- Feig, S. T., Jürgen, K., and Snow, J. E. (2006). Effect of water on tholeiitic basalt phase equilibria: an experimental study under oxidizing conditions. *Contrib. Mineral. Petrol.* 152, 611–638. doi: 10.1007/s00410-006-0123-2
- Fiona, C. B., Anthony, J. C., Reid, R. K., and Paul, A. P. (2017). The geology, geochemistry and Ni-Cu-PGE potential of mafic-ultramafic bodies associated with the Dido Batholith, North Queensland, Australia. *Ore Geol. Rev.* 90, 532–552. doi: 10.1016/j.oregeorev.2017.05.002
- Gao, C. L., Ji, R. S., Qin, D. Y., and Yin, Y. (1990). Blueschists in three tectonic environments in northern China. *Geol. Rev.* 36, 20–29.
- Gao, J., and Klemd, R. (2003). Formation of HP-LT rocks and their tectonic implications in the western Tianshan Orogen, NW China: geochemical and age constraints. *Lithos* 66, 1–22. doi: 10.1016/s0024-4937(02)00153-6
- Halls, H. C. (1982). The importance and potential of mafic dyke swarms in studies of geodynamic processes. *Geosci. Canada* 9, 145–154.
- Han, B. F., Guo, Z. J., Zhang, Z. C., Zhang, L., Chen, J. F., and Song, B. (2010). Age, geochemistry, and tectonic implications of a late Paleozoic stitching pluton in the North Tianshan suture zone, western china. *GSA Bull.* 122, 627–640. doi: 10.1130/b26491.1
- Hoek, J. D., and Seitz, H. M. (1995). Continental mafic dyke swarms as tectonic indicators: an example from the Vestfold Hills, East Antarctica. *Precamb. Res.* 75, 121–139. doi: 10.1016/0301-9268(95)80002-y
- Humayun, M., Qin, L. P., and Norman, M. D. (2004). Geochemical evidence for excess iron in the mantle beneath Hawaii. *Science* 306, 91–94. doi: 10.1126/science.1101050
- Jahn, B. M. (2004). The Central Asian Orogenic Belt and growth of the continental crust in the Phanerozoic. *Aspects Tectonic Evol. China* 226, 73–100. doi: 10.1144/gsl.sp.2004.226.01.05
- Jahn, B. M., Wu, F. Y., and Chen, B. (2000). Massive granitoid generation in Central Asia: Nd isotope evidence and implication for continental growth in the Phanerozoic. *Episodes* 23, 82–92. doi: 10.18814/epiugs/2000/v23i2/001

- Jiang, C. Y., Zhang, P. B., Lu, D. R., Bai, K. Y., Wang, Y. P., Tang, S. H., et al. (2004a). Petrology, geochemistry and petrogenesis of the Kalpin basalts and their Nd, Sr and Pb isotopic compositions. *Geol. Rev.* 50, 492–500.
- Jiang, C. Y., Zhang, P. B., Lu, D. X., and Bai, K. Y. (2004b). Petrogenesis and magma source of the ultramafic rocks at Wajilitag region, western Tarim Plate in Xinjiang. *Acta Petrol. Sin.* 20, 1433–1444.
- Klemd, R. (2003). Ultrahigh-pressure metamorphism in eclogites from the western Tianshan high-pressure belt (Xinjiang, western China)-comment. *Am. Mineral.* 88, 1153–1156.
- Klemd, R., Gao, J., Li, J. L., and Meyer, M. (2015). Metamorphic evolution of (ultra)-high-pressure subduction-related transient crust in the South Tianshan Orogen (Central Asian Orogenic Belt): geodynamic implications. *Gondwana Res. Int. Geosci. J.* 28, 1–25. doi: 10.1016/j.gr.2014.11.008
- Kröner, A., Windley, B. F., Badarch, G., Tomurtogoo, O., and Martínez, C. (2007). Accretionary growth and crust-formation in the Central Asian Orogenic Belt and comparison with the Arabian-Nubian shield. *Memoir Geol. Soc. Am.* 200, 181–209. doi: 10.1130/2007.1200(11)
- Le Bas, M. J., Le, M. R. W., Streckeisen, A., Zanettin, B., and Rocks, I. S. O. O. I. (1986). A chemical classification of volcanic rocks based on the total alkali-silica diagram. *J. Petrol.* 27, 745–750. doi: 10.1093/petrology/27.3.745
- Li, J. L., Klemd, R., Gao, J., Jiang, T., and Song, Y. H. (2015). A common high-pressure metamorphic evolution of interlayered eclogites and metasediments from the 'ultrahigh-pressure unit' of the Tianshan metamorphic belt in China. *Lithos* 226, 169–182. doi: 10.1016/j.lithos.2014.12.006
- Li, M., Xin, H. T., Ren, B. F., Ren, Y. W., and Liu, W. G. (2020). Early-Middle Permian post-collisional granitoids in the northern Beishan orogen, northwestern China: evidence from U-Pb ages and Sr-Nd-Hf isotopes. *Can. J. Earth Sci.* 57, 681–697. doi: 10.1139/cjes-2019-0088
- Li, S., Wilde, S. A., and Wang, T. (2013). Early Permian post-collisional high-k granitoids from Liuyuan area in southern Beishan orogen, NW China: petrogenesis and tectonic implications. *Lithos* 179, 99–119. doi: 10.1016/j.lithos.2013.08.002
- Li, X. H., Li, W. X., Wang, X. C., Li, Q. L., Liu, Y., and Tang, G. Q. (2009). Role of mantle-derived magma in genesis of early Yanshanian granites in the Nanling Range, South China: in situ zircon Hf-O isotopic constraints. *Sci. China* 52, 1262–1278. doi: 10.1007/s11430-009-0117-9
- Li, X. M., Yu, J. Y., Wang, G. Q., and Wu, P. (2012). Geochronology of Jijitai ophiolite in Beishan area, Gansu Province, and its geological significance. *Geol. Bull. China* 31, 2025–2031.
- Liu, L., Wang, C., Cao, Y. T., Chen, D. L., Kang, L., Yang, W. Q., et al. (2012). Geochronology of multi-stage metamorphic events: constraints on episodic zircon growth from the UHP eclogite in the South Altyn, NW China. *Lithos* 136, 10–26. doi: 10.1016/j.lithos.2011.09.014
- Liu, S., Feng, C. X., Jahn, B. M., Hu, R. Z., Gao, S., Coulson, L. M., et al. (2013). Zircon U-Pb age, geochemical, and Sr-Nd-Hf isotopic constraints on the origin of mafic dykes in the Shaanxi Province, North China Craton, China. *Lithos* 175, 244–254. doi: 10.1016/j.lithos.2013.04.020
- Liu, Y. S., Gao, S., Kelemen, B. P., and Xu, W. L. (2008). Recycled crust controls contrasting source compositions of Mesozoic and Cenozoic basalts in the north China craton. *Geochim. Cosmochim. Acta* 72, 2349–2376. doi: 10.1016/j.gca.2008.02.018
- Luan, Y., He, K., and Tan, X. J. (2019). In situ U-Pb dating and trace element determination of standard zircons by LA-ICP-MS. *Geol. Bull. China* 38, 1206–1218.
- Ludwig, K. R. (2003). User's Manual for Isoplot 3.00: a geochronological toolkit for microsoft excel. *Berkeley Geochronol. Center* 125, 197–218.
- Mao, Q. G. (2008). *Paleozoic to Early Mesozoic Accretionary and Collisional Tectonics of the Beishan and Adjacent Area*. Ph. D. Thesis, Chinese Academy of Sciences, Institute of Geology and Geophysics, Beijing.
- Mao, Q. G., Xiao, W. J., Fang, T. H., Wang, J. B., and Han, C. M. (2012). Late Ordovician to early Devonian adakites and Nb-enriched basalts in the Liuyuan area, Beishan, NW China: implications for early Paleozoic slab-melting and crustal growth in the southern Altai. *Gondwana Res.* 22, 534–553. doi: 10.1016/j.gr.2011.06.006
- Mao, Q. G., Xiao, W. J., Han, C. M., Sun, M., Yuan, C., Zhang, J. E., et al. (2010). Discovery of Middle Silurian adakite granite and its tectonic significance in Liuyuan area, Beishan Mountains, NW China. *Acta Petrol. Sin.* 26, 84–96.
- McDonough, W. F., and Sun, S. S. (1995). The composition of the Earth. *Chem. Geol.* 120, 223–253.
- Metcalfe, R. V., and Shervais, J. W. (2008). Suprasubduction-zone ophiolites: is there really an ophiolite conundrum? *Geol. Soc. Am. Spec. Pap.* 438, 191–222. doi: 10.1130/2008.2438(07)
- Morimoto, N. (1988). Nomenclature of pyroxenes. *Mineral. Petrol.* 39, 55–76. doi: 10.1007/bf01226262
- Niu, Y. Z., Song, B., Zhou, J. L., Xu, W., Shi, J. Z., Zhang, Y. X., et al. (2020). Lithofacies and chronology of volcano-sedimentary sequence in the southern Beishan Region, Central Asian Orogenic Belt and its paleogeographical implication. *Acta Geologica Sinica* 94, 615–633. doi: 10.19762/j.cnki.dizhixuebao.202047
- Pearce, J. A. (2005). *Element Transfer from Slab to Wedge: the Subducted Plate Perspective*. London: AGU Spring Meeting.
- Pearce, J. A. (2008). Geochemical fingerprinting of oceanic basalts with applications to ophiolite classification and the search for Archean oceanic crust. *Lithos* 100, 14–48. doi: 10.1016/j.lithos.2007.06.016
- Pearce, J. A., Stern, R. J., Bloomer, S. H., and Fryer, P. (2013). Geochemical mapping of the Mariana arc-basin system: implications for the nature and distribution of subduction components. *Geochem. Geophys. Geosyst.* 6, 1525–2027.
- Peng, R., Zhang, G. S., and Qiu, H. X. (2020). Petrogenesis and tectonic significances of the late Paleozoic mafic dykes in the Beishan area in Gansu province. *Bull. Mineral. Petrol. Geochem.* 39, 89–101.
- Plank, T., and Wade, J. (2005). *Constraints from Water on Mantle Melting and Slab Fluid Composition*. London: AUG Fall Meeting.
- Qi, Q., Wang, Y. H., Yu, J. Y., Liu, D. M., Guo, L., Ji, B., et al. (2017). Geochronology, geochemistry and tectonic significance of diabase dike swarms in Beishan, Gansu. *Xinjiang Geol.* 35, 99–106.
- Qin, K. Z., Su, B. X., Sakya, P. A., Tang, D. M., Li, X. H., Sun, H., et al. (2011). SIMS zircon U-Pb geochronology and Sr-Nd isotopes of Ni-Cu-bearing mafic-ultramafic intrusions in eastern Tianshan and Beishan in correlation with flood basalts in Tarim Basin (NW China): constraints on a ca. 280 Ma mantle plume. *Am. J. Sci.* 311, 237–260. doi: 10.2475/03.2011.03
- Rudnick, R. L., and Gao, S. (2003). Composition of the continental crust. *Treatise Geochem.* 3, 1–64. doi: 10.1016/B0-08-043751-6/03016-4
- Rudnick, R., and Gao, S. (2014). Composition of the continental crust. *Treatise Geochem.* 4, 1–51. doi: 10.1016/B0-08-043751-6/03016-4
- Saktura, W. M., Buckman, S., Nutman, A. P., Belousova, E. A., Yan, Z., and Aitchison, J. C. (2017). Continental origin of the Gubaoquan eclogite and implications for evolution of the Beishan Orogen, Central Asian Orogenic Belt, NW China. *Lithos* 294, 20–38. doi: 10.1016/j.lithos.2017.10.004
- Sengör, A. M. C., Natal'in, B. A., and Burtman, V. S. (1993). Evolution of the Altaid tectonic collage and Palaeozoic crustal growth in Eurasia. *Nature* 364, 299–307. doi: 10.1038/364299a0
- Sláma, J., Koler, J., Condon, D. J., Crowley, J. L., Gerdes, A., Hanchar, J. M., et al. (2008). Pleovite zircon—a new natural reference material for U-Pb and Hf isotopic microanalysis. *Chem. Geol.* 71, 1–35. doi: 10.1016/j.chemgeo.2007.11.005
- Song, X. Y., Chen, L. M., Deng, Y. F., and Xie, W. (2013). Syncollisional tholeiitic magmatism induced by asthenosphere upwelling owing to slab detachment at the southern margin of the Central Asian Orogenic Belt. *J. Geol. Soc.* 170, 941–950. doi: 10.1144/jgs2012-130
- Song, X. Y., Xie, W., Deng, Y. F., Crawford, A. J., Zheng, W. Q., Zhou, G. F., et al. (2011). Slab break-off and the formation of Permian mafic-ultramafic intrusions in southern margin of Central Asian Orogenic Belt, Xinjiang, NW China. *Lithos* 127, 128–143. doi: 10.1016/j.lithos.2011.08.011
- Stacey, J. S., and Kramers, J. D. (1975). Approximation of terrestrial lead isotope evolution by a two-stage model. *Earth Planet. Sci. Lett.* 26, 207–221. doi: 10.1016/0012-821x(75)90088-6
- Su, B. X., Qin, K. Z., Sakya, P. A., Li, X. H., Yang, Y. F., Sun, H., et al. (2011). U-pb ages and Hf-O isotopes of zircons from Late Paleozoic mafic-ultramafic units in the southern Central Asian Orogenic Belt: tectonic implications and evidence for an Early-Permian mantle plume. *Gondwana Res.* 20, 516–531. doi: 10.1016/j.gr.2010.11.015

- Su, B. X., Qin, K. Z., Sakyi, P. A., Tang, D. M., Liu, P. P., Malaviarachchi, S. P. K., et al. (2012). Geochronologic-petrochemical studies of the Hongshishan mafic-ultramafic intrusion, Beishan area, Xinjiang (NW China): petrogenesis and tectonic implications. *Int. Geol. Rev.* 54, 270–289. doi: 10.1080/00206814.2010.543011
- Sun, S. S., and McDonough, W. F. (1989). Chemical and isotopic systematics of oceanic basalts: implications for mantle composition and source processes. *Geol. Soc. Lond. Spec. Publ.* 42, 313–345. doi: 10.1144/gsl.sp.1989.042.01.19
- Tan, L. (2018). *The Study on Magmatic Sequence and Chronology for the Pobei Basic and Ultrabasic Complex in The Northeastern Margin of the Tarim Plate*. Ph. D. Thesis, Chang'an University, Xi'an.
- Tanaka, T. (2000). JNd1: a neodymium isotopic reference in consistency with LaJolla neodymium. *Chem. Geol.* 168, 279–281. doi: 10.1016/s0009-2541(00)00198-4
- Thirlwall, M. F. (1991). Long-term reproducibility of multicollector Sr and Nd isotope ratio analysis. *Chem. Geol.* 94, 85–104. doi: 10.1016/s0009-2541(10)80021-x
- Wang, G. Q., Li, X. M., Xu, X. Y., Yu, J. Y., Ji, B., and Zhu, T. (2018). Petrogenesis and tectonic setting of the Carboniferous and Permian volcanic rocks in the Beishan orogenic belt. *Acta Petrol. Mineral.* 37, 18–34.
- Wang, G. Q., Li, X. M., Xu, X. Y., Yu, J. Y., and Wu, P. (2014). Zircon U-Pb chronological study of the Hongshishan ophiolite in the Beishan area and their tectonic significance. *Acta Petrol. Sin.* 30, 1685–1694.
- Wang, Y., Zhao, Z. F., Zheng, Y. F., and Zhang, J. J. (2011). Geochemical constraints on the nature of mantle source for Cenozoic continental basalts in east-central China. *Lithos* 125, 940–955. doi: 10.1016/j.lithos.2011.05.007
- Wartes, M. A., Carroll, A. R., and Greene, T. J. (2002). Permian sedimentary record of the Turpan-Hami basin and adjacent regions, northwest China: constraints on postamalgamation tectonic evolution. *Geol. Soc. Am. Bull.* 114, 131–152. doi: 10.1130/0016-7606(2002)114<0131:psrott>2.0.co;2
- Wei, X., Xu, Y. G., Feng, Y. X., and Zhao, J. X. (2014). Plume-lithosphere interaction in the generation of the Tarim large igneous province, NW China: geochronological and geochemical constraints. *Am. J. Sci.* 314, 314–356. doi: 10.2475/01.2014.09
- Wiedenbeck, M. (1995). An example of reverse discordance during ion microprobe zircon dating: an artifact of enhanced ion yields from a radiogenic labile Pb. *Chem. Geol.* 125, 197–218. doi: 10.1016/0009-2541(95)00072-t
- Windley, B. F., Alexiev, D., Xiao, W. J., Kröner, A., and Badarch, A. (2007). Tectonic models for accretion of the Central Asian Orogenic Belt. *J. Geol. Soc.* 164, 31–47.
- Woodhead, J. D., Hergt, J. M., Davidson, J. P., and Eggins, S. M. (2001). Hafnium isotope evidence for 'conservative' element mobility during subduction zone processes. *Earth Planet. Sci. Lett.* 192, 331–346. doi: 10.1016/s0012-821x(01)00453-8
- Wu, P., Wang, G. Q., Li, X. M., Yu, J. Y., and Kang, L. (2012). The age of Niujuanzi ophiolite in Beishan area of Gansu Province and its geological significance. *Geol. Bull. China* 31, 2033–2037.
- Xiao, P. X., Huang, Y. H., Wang, Y. X., Wang, X. A., and Li, Y. J. (2006). Geological characteristic and tectonic environment of basic dike swarms in the Beishan area, southern Hami, Xinjiang, China. *Geol. Bull. China* 25, 189–193.
- Xiao, W. J., Han, C. M., Yuan, C., Sun, M., Lin, S. F., Chen, H. L., et al. (2008). Middle Cambrian to Permian subduction-related accretionary orogenesis of Northern Xinjiang, NW China: implications for the tectonic evolution of Central Asia. *J. Asian Earth Sci.* 32, 102–117. doi: 10.1016/j.jseas.2007.10.008
- Xiao, W. J., Huang, B. C., Han, C. M., Sun, S., and Li, J. L. (2011). A review of the western part of the Altai: a key to understanding the architecture of accretionary orogens. *Gondwana Res.* 18, 253–273. doi: 10.1016/j.gr.2010.01.007
- Xiao, W. J., Song, D. F., Han, C. M., Wan, B., Zhang, J., Ao, S. J., et al. (2019). Deep structure and metallogenic processes of the Altai-Junggar-Tianshan collage in southern Altai. *Acta Geol. Sin. Eng. Ed.* 93, 1163–1168. doi: 10.1111/1755-6724.14393
- Xiao, W. J., Zhang, L. C., Qin, K. Z., Sun, S., and Li, J. L. (2004). Paleozoic accretionary and collisional tectonics of the Eastern Tianshan (China): implications for the continental growth of central Asia. *Am. J. Sci.* 304, 370–395. doi: 10.2475/ajs.304.4.370
- Xie, W., Song, X. Y., Deng, Y. F., Wang, Y. S., Ba, D. H., Zheng, W. Q., et al. (2012). Geochemistry and petrogenetic implications of a Late Devonian mafic-ultramafic intrusion at the southern margin of the Central Asian Orogenic Belt. *Lithos* 144, 209–230. doi: 10.1016/j.lithos.2012.03.010
- Xie, W., Xu, Y. G., Feng, Y. X., and Zhao, J. X. (2014). Plume-lithosphere interaction in the generation of the Tarim large igneous province, NW China: geochronological and geochemical constraints. *Am. J. Sci.* 314, 314–356. doi: 10.2475/01.2014.09
- Xue, S. C., Li, C. S., Qin, K. Z., and Tang, D. M. (2016). A non-plume model for the Permian protracted (266–286 Ma) basaltic magmatism in the Beishan-Tianshan region, Xinjiang, Western China. *Lithos* 256, 243–249. doi: 10.1016/j.lithos.2016.04.018
- Xue, S. C., Li, C. S., Wang, Q. F., Ripley, E. M., and Yao, Z. S. (2019). Geochronology, petrology and Sr-Nd-Hf-S isotope geochemistry of the newly-discovered Qixin magmatic Ni-Cu sulfide prospect, southern Central Asian Orogenic Belt, NW China. *Ore Geol. Rev.* 111:103002. doi: 10.1016/j.oregeorev.2019.103002
- Yang, C. X., Wang, Q. H., Gao, X., Pu, W. F., and Zhao, W. (2015). Geochem characteristics and tectonic setting of dolerite in Beishan. *Gansu. Gansu Geol.* 24, 19–23.
- Yang, J. S., Wu, C. L., Chen, S. Y., Shi, R. D., Zhang, J. X., Meng, F. C., et al. (2006). Neoproterozoic eclogitic metamorphic age of the Beishan eclogite of Gansu, China. Evidence from SHRIMP U-Pb isotope dating. *Geol. China* 33, 317–325.
- Yu, J. Y., Li, X. M., Wang, G. Q., Wu, P., and Yan, Q. J. (2012). Zircon U-Pb ages of Huitongshan and Zhangfangshan ophiolite in Beishan of Gansu-Inner Mongolia border area and their significance. *Geol. Bull. China* 32, 2038–2045.
- Yu, X. (2009). *Magma Evolution and Deep Geological Processes of Early Permian Tarim Large Igneous Province*. Ph. D. Thesis, Zhejiang University, Hangzhou.
- Yu, X., Yang, S. F., Chen, H. L., Li, Z. L., and Li, Y. Q. (2017). Petrogenetic model of the permian tarim large igneous province. *Sci. China Earth Sci.* 47, 1179–1190.
- Yuan, F., Zhou, T. F., Zhang, D. Y., Fan, Y., Liu, S., Peng, M. X., et al. (2010). Source, evolution and tectonic setting of the basalts from the native copper mineralization area in eastern Tianshan, Xinjiang. *Acta Petrol. Sin.* 26, 533–546.
- Zhang, Y. Y., Dostal, J., Zhao, Z. H., Liu, C., and Guo, Z. J. (2011). Geochronology, geochemistry and petrogenesis of mafic and ultramafic rocks from Southern Beishan area, NW China: implications for crust-mantle interaction. *Gondwana Res.* 20, 816–830. doi: 10.1016/j.gr.2011.03.008
- Zhang, Y. Y., and Guo, Z. J. (2008). Accurate constraint on formation and emplacement age of Hongliuhe ophiolite, boundary region between Xinjiang and Gansu Provinces and its tectonic implications. *Acta Petrol. Sin.* 24, 803–809.
- Zhang, Y. Y., Yuan, C., Sun, M., Long, X. P., Xia, X. P., Wang, X. Y., et al. (2015). Permian doleritic dikes in the Beishan Orogenic Belt, NW China: asthenosphere-lithosphere interaction in response to slab break-off. *Lithos* 233, 174–192. doi: 10.1016/j.lithos.2015.04.001
- Zhao, Z. H., Guo, Z. J., Han, B. F., Wang, Y., and Liu, C. (2006). Comparative study on Permian basalts from eastern Xinjiang-Beishan area of Gansu province and its tectonic implications. *Acta Petrol. Sin.* 22, 1279–1293.
- Zheng, R. G., Wang, Y. P., Zhang, Z. Y., Zhang, W., Meng, Q. P., and Wu, T. R. (2016). Geochronology and geochemistry of Yinwaxia acidic volcanic rocks in the southern Beishan: new evidence for Permian continental rifting. *Acta Petrol. Mineral.* 37, 18–34.
- Zheng, R. G., Wu, T. R., Zhang, W., Meng, Q. P., and Zhang, Z. Y. (2014). Geochronology and geochemistry of late Paleozoic magmatic rocks in the Yinwaxia area, Beishan: implications for rift magmatism in the southern Central Asian Orogenic Belt. *J. Asian Earth Sci.* 91, 39–55. doi: 10.1016/j.jseas.2014.04.022
- Zheng, R. G., Wu, T. R., Zhang, W., Xu, C., and Meng, Q. P. (2013). Late Paleozoic subduction system in the southern Central Asian Orogenic Belt: evidences from geochronology and geochemistry of the Xiaohuangshan ophiolite in the Beishan orogenic belt. *J. Asian Earth Sci.* 62, 463–475. doi: 10.1016/j.jseas.2012.10.033
- Zheng, R. G., Xiao, W. J., Li, J. Y., Wu, T. R., and Zhang, W. (2018). A Silurian-early Devonian slab window in the southern Central Asian Orogenic Belt: evidence from high-Mg diorites, adakites and granitoids in the western Central Beishan

- region, NW China. *J. Asian Earth Sci.* 153, 75–99. doi: 10.1016/j.jseae.2016.12.008
- Zhou, D. W., Zhang, C. L., Liu, L., Wang, J. L., Wang, Y., and Liu, J. P. (2000). Synthetic study on Proterozoic basic dyke swarms in the Qinling Orogenic Belt and its adjacent block as well as a discussion about some questions related to them. *Acta Petrol. Sin.* 16, 22–28.
- Zhou, M. F., Leshner, C. M., Yang, Z. X., Li, J. W., and Sun, M. (2004). Geochemistry and petrogenesis of 270 Ma Ni-Cu-(PGE) sulfide-bearing mafic intrusions in the Huangshan district, Eastern Xinjiang, Northwest China: implications for the tectonic evolution of the Central Asian Orogenic belt. *Chem. Geol.* 209, 233–257. doi: 10.1016/j.chemgeo.2004.05.005
- Zhou, M. F., Zhao, J. H., Jiang, C. Y., Gao, J. F., Wang, W., and Yang, S. H. (2009). Oib-like, heterogeneous mantle sources of Permian basaltic magmatism in the western Tarim Basin, NW China: implications for a possible Permian large igneous province. *Lithos* 113, 583–594. doi: 10.1016/j.lithos.2009.06.027
- Zindler, A., and Hart, S. R. (1986). Chemical geodynamics. *Annu. Rev. Earth Planet. Sci.* 14, 493–571.
- Zong, C. L. (2013). *Chemical Separation of Pb, Sr, Nd, Hf isotopes from a Single Rock Dissolution and Its Geological Application*. Ph. D. Thesis, Northwest University, Xi'an.
- Conflict of Interest:** RW was employed by the company Petrochina Changqing Oilfield Company.
- The remaining authors declare that the research was conducted in the absence of any commercial or financial relationships that could be construed as a potential conflict of interest.
- Copyright © 2021 Xu, Duan, Gao, Wang, Shi, Ma and Sun. This is an open-access article distributed under the terms of the Creative Commons Attribution License (CC BY). The use, distribution or reproduction in other forums is permitted, provided the original author(s) and the copyright owner(s) are credited and that the original publication in this journal is cited, in accordance with accepted academic practice. No use, distribution or reproduction is permitted which does not comply with these terms.



The Metallogeny of the Lubei Ni–Cu–Co Sulfide Deposit in Eastern Tianshan, NW China: Insights From Petrology and Sr–Nd–Hf Isotopes

Ping Li^{1,2,3*}, Ting Liang^{1*}, Yonggang Feng¹, Tongyang Zhao², Jiangtao Tian², Dahai Li², Jian Li⁴, Gang Chen^{2,3} and Changzhi Wu¹

¹ College of Earth Science and Resources, Chang'an University, Xi'an, China, ² Xinjiang Bureau of Geological Mineral Exploration and Development, Urumqi, China, ³ Xinjiang Bureau of Geology and Mineral Resources, Urumqi, China, ⁴ Xinjiang Experimental Institute of Mineral Resources, Urumqi, China

OPEN ACCESS

Edited by:

Ryan Mathur,
Juniata College, United States

Reviewed by:

Yu-Feng Deng,
Hefei University of Technology, China
Rui Wang,
China University of Geosciences,
China

*Correspondence:

Ting Liang
liangt@chd.edu.cn
Ping Li
liping3731@163.com

Specialty section:

This article was submitted to
Economic Geology,
a section of the journal
Frontiers in Earth Science

Received: 31 December 2020

Accepted: 10 March 2021

Published: 01 April 2021

Citation:

Li P, Liang T, Feng Y, Zhao T, Tian J, Li D, Li J, Chen G and Wu C (2021) The Metallogeny of the Lubei Ni–Cu–Co Sulfide Deposit in Eastern Tianshan, NW China: Insights From Petrology and Sr–Nd–Hf Isotopes. *Front. Earth Sci.* 9:648122. doi: 10.3389/feart.2021.648122

The Lubei Ni–Cu–Co deposit situated in western segment of the Huangshan–Jing'erquan mafic–ultramafic rock belt in eastern Tianshan of the Central Asian Orogenic Belt (CAOB). The estimated reserve is approximately 9.11 million tons of ore resources with average grades of 0.82 wt% Ni, 0.52 wt% Cu, and 0.03 wt% Co. The Lubei intrusion is mainly composed of gabbro (phase I), peridotite (phase II), pyroxene peridotite (phase III), olivine pyroxenite (phase IV), and diorite (phase V), which intruded into the early Carboniferous tuffaceous clastic rocks. Zircon Laser Ablation–Inductively Coupled Plasma–Mass Spectrometry (LA–ICP–MS) U–Pb age of the diorite (phase V) from the edge of the intrusion is interpreted as the top-limit metallogenic age, which is consistent with the formation ages of the Huangshan and Xiangshan Ni–Cu deposits in eastern Tianshan. The roughly parallel rare earth element (REE) curves of the Lubei intrusion indicate the magma originated from a homologous source. The slightly enriched large ion lithophile elements (LILE) are compared to high field strength elements (HFSE) with negative Nb and Ta anomalies show that the Lubei intrusion has arc-affiliate geochemical characteristics. The Sr–Nd–Hf isotopes show that the magma was derived from depleted lithospheric mantle, while suffering 4–10% lower crustal contamination with slight contamination of the upper crust. Based on a comprehensive conservation of regional geological, geochemical, and geochronological evidence, the primary magma of the Lubei intrusion was identified that it was derived from the partial melting of metasomatized lithospheric mantle previously modified by subduction events. The Lubei nickel–copper–cobalt sulfide deposit was formed after the primary magma experienced fractional crystallization, crustal contamination, and sulfide segregation in a post-collisional extensional geodynamic setting after the closure of the Kanggur ocean basin in the early Permian.

Keywords: Sr–Nd–Hf isotopes, eastern Tianshan (NW China), metallogenic mechanism, Ni–Cu sulfide deposit, Lubei

INTRODUCTION

Most world-class magmatic Ni-Cu-PGE sulfide deposits were formed at cratons or at the margins in association with intraplate magmatism (Naldrett, 1999). Thus, the magmatic evolution and mineralization processes of magmatic Ni-Cu deposits within cratons have been well documented (Barnes and Lightfoot, 2005; Naldrett, 2009; Begg et al., 2010). However, relatively small magmatic sulfide deposits formed in orogenic belts have not been well studied and resulted in debates on their sulfide mineralization and magmatic conduit systems (Gao et al., 2012, 2013; Su et al., 2013b; Zhao et al., 2015; Deng et al., 2021).

The Central Asian Orogenic Belt (CAOB) is a typical accretionary orogenic belt, which contains abundant exposed mafic-ultramafic rocks (Qin et al., 2012). Eastern Tianshan located at the southern margin of the CAOB has better metallogenic conditions and it is an important base of nickel-copper resources in China based on accounting for 31.4% of the nickel resources in Xinjiang. The large-scale copper-nickel deposits formed in mafic-ultramafic rocks of the orogenic belt are one of the significant characteristics of Ni-Cu mineralization in eastern Tianshan. For example, Tulargen, Huangshan, Huangshandong, Xiangshan, Hulu, Erhongwa, and Tudun copper-nickel sulfide deposits are occurred along the Kanggur-Huangshan fault zone in eastern Tianshan and characterized by multistage intrusive bodies and distinct lithofacies (Mao et al., 2008; Qin et al., 2012; Wu et al., 2018), with a relative concentrative metallogenic age (290–275 Ma) (Sun et al., 2010, 2013b; Zhao et al., 2015; Chen et al., 2018; Feng et al., 2018). However, although the main ore-bearing mafic-ultramafic intrusions in eastern Tianshan have experienced sulfide segregation at depth, and still have different views on sulfur saturation mechanism about fractional crystallization and crustal contamination (Zhang et al., 2011; Sun et al., 2013b; Deng et al., 2014, 2015). Whether these mafic-ultramafic intrusions were related to the Tarim mantle plume (Mao et al., 2008; Pirajno et al., 2008; Qin et al., 2011; Tang et al., 2011; Zhang et al., 2017), subduction accretion (Mao et al., 2006b; Ao et al., 2010; Xue et al., 2016), or post-collisional extension setting is still being debated (Deng et al., 2011a, 2015; Gao et al., 2013; Sun et al., 2013b).

The Lubei Ni-Cu-Co deposit was newly discovered by the Geological Survey Academy of Xinjiang in 2014 during a geochemical anomaly inspection of the western segment in eastern Tianshan (Yang et al., 2017). The estimated reserve contains approximately 9.11 million tons of ore resources with an average grade of 0.82 wt% Ni, 0.52 wt% Cu, and 0.03 wt% Co. In particular, cobalt was reported as a critical metal for the first time. The Lubei intrusions were distributed in northern Kanggur fault and emplaced into the tuffaceous clastic rocks in the early Carboniferous Xiaorequanzi Formation (Yang et al., 2017; Li and Tian, 2018). The age of the zircon U-Pb from hornblende gabbro is 287.9 ± 1.6 Ma (Chen et al., 2018). However, there are few researches on the critical mechanisms of sulfur saturation and mineralization processes during migration of the magmas in their conduit system. The prospecting and exploration studies are still in progress. A great breakthrough in the northern mining area in 2020 made the systematic studies of magmatic evolution

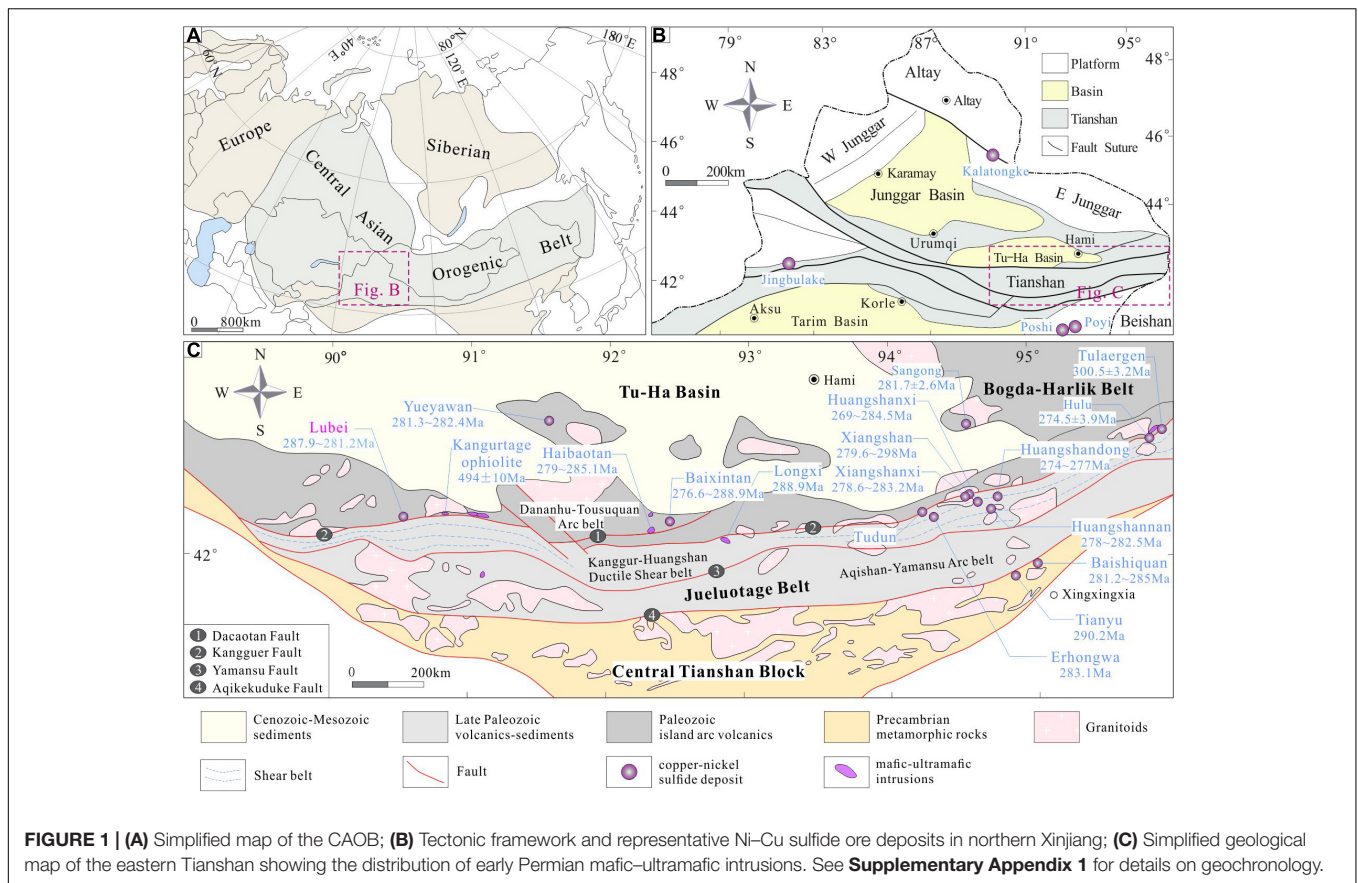
and mineralization mechanism more practical. Based on the fine identification of magmatic lithofacies, this contribution intends to restrict the metallogenic section, magma source, and sulfur saturation mechanisms in the magma conduit system using petrology and Sr-Nd-Hf isotopic evaluation of the Lubei intrusion. Combined with the regional geological data, we try to reconstructed the tectonic evolution, magmatic differentiation, and mineralization process in the magma conduit system of the Lubei Ni-Cu deposit, hope to provide the theoretical supporting for future Ni-Cu-Co deposit prospecting in eastern Tianshan.

GEOLOGICAL SETTING

The northern Xinjiang region located at the southern margin of the CAOB is adjacent to the Siberian Craton to the north and the Tarim Craton to the south (Figure 1A), which distributes different types of Ni-Cu deposits formed in orogenic belt. The Kalatongke Ni-Cu deposit related to post-collisional extension is located in southern Altay (Zhang et al., 2005), whereas the Jingbulake deposit related to the subduction of the southern Tianshan Ocean is distributed in western Tianshan (Zhang et al., 2012). The Poyi and Poshi deposits related to the Tarim mantle plume in the Permian are distributed in Beishan (Su et al., 2013a; Figure 1B). The eastern Tianshan is successively divided into the Dananhu-Tousuquan island arc, Jueluotage belt, and Central Tianshan block from north to south, bounded by the Kanggur and Aqikekuduk faults (Figure 1C).

The northern portion of the Dananhu-Tousuquan island arc is characterized by Paleozoic Kalatage arc volcanic rocks and pyroclastic rocks which intercalated with marine intermediate-felsic volcanic sedimentary rocks. Along with gradually weakened volcanic activities from Ordovician to Devonian, the magma compositions gradually transited from intermediate-basic to intermediate-acidic and accompanied by extensive granitic intrusive magmatism. In the early Carboniferous, the andesitic and dacitic tuffs of the Xiaorequanzi Formation and Qi'eshan Formation were distributed on the northern Kanggur fault. In the late Carboniferous, the gradually weakened volcanism was accompanied by shallow marine terrigenous clastic rocks. In the early Permian, bimodal volcanic rocks occurred in some areas, while the continental fluvial-lacustrine sediments were dominant in the late Permian (Long et al., 2019). In addition, mafic-ultramafic rocks were scattered and formed the Baixintan (Zhao et al., 2018), Yueyawan (Sun et al., 2019), and Lubei (Chen et al., 2018) Cu-Ni (-Co) deposits.

The Jueluotage tectonic belt in eastern Tianshan can be divided into the Kanggur-Huangshan ductile shear zone and the Aqishan-Yamansu island arc bounded by the Yamansu fault (Figure 1C). The Kanggur-Huangshan belt is influenced by the Kanggur-Huangshan ductile shear, which formed a set of disordered strata with strong deformation and metamorphism in the Carboniferous. The Aqishan-Yamansu belt is mainly composed of early Carboniferous intermediate-acidic island arc volcanic rocks, shallow marine carbonate rocks intercalated with clastic rocks, and late Carboniferous continental volcanic sedimentary rocks, with molasse formation at the top of Permian.



The ages of granites, diorite porphyrite, and mafic dykes respectively are about 349–246 Ma (Zhou et al., 2010), 315–311 Ma (Long et al., 2020), 260–290 Ma (Lin et al., 2014) within the Jueluotage tectonic belt.

The Central Tianshan Block is composed of clastic rocks, carbonate rocks, volcanic rocks, and intrusive rocks. Metamorphic rocks were developed widely, mainly include the Paleoproterozoic Tianhu Group, Mesoproterozoic Xingxingxia Group, and Kawabulake Group (Wang et al., 2017). The intrusive magmatism is dominated by granitic rocks with emplacement ages from the late Archean to Mesozoic. The Baishiquan and Tianyu Ni-Cu deposits related to the Permian mafic-ultramafic rocks were formed in the eastern part of the belt (Wu et al., 2005; Tang et al., 2011).

The mafic-ultramafic intrusions in eastern Tianshan mainly distributed along with the Kanggur-Huangshan deep fault in the form of beads. Before 2010, researchers were mainly focused on the geological background and exploration of the mafic-ultramafic complexes in the Huangshan-Tulargen metallogenic belt in the eastern part of the Jueluotage tectonic belt (Han et al., 2004; Zhou et al., 2004; Hu et al., 2008; Sun et al., 2010). More than 30 mafic-ultramafic rocks in different spatial scales were identified successively in the eastern segment of the Jueluotage tectonic belt, which hosted the Huangshan, Xiangshan, Hulu, Tulargen, Tudun, and Huangshannan Ni-Cu deposits (San et al., 2010; Qin et al., 2011; Zhao et al., 2015; **Supplementary Appendix 1**). In recent years, new Ni-Cu

(-Co) deposits have been found in the western segment of the Jueluotage tectonic belt, such as the medium-scale Lubei and Baixintan deposits (Wang et al., 2015a; Yang et al., 2017). Moreover, Yang et al. (2017) identified more than 20 outcrops of mafic-ultramafic rocks in the Lubei mining area including peridotite, pyroxene peridotite, olivine gabbro, gabbro, etc. Most of the mafic-ultramafic rocks contain pentlandite, indicating good nickel-copper (-cobalt) prospects.

ORE DEPOSIT GEOLOGY

Geology

The Lubei intrusion is situated in northern Kanggur fault and was emplaced into the tuffaceous clastic rocks of the Xiaorequanzi Formation in the early Carboniferous, which are situated in a semiring shape on the plane with an exposure area of 1.35 km². The Lubei intrusion was divided into two parts, north and south. The southern part contains mafic-ultramafic rocks that occur in high-grade orebodies, which are composed of peridotite, pyroxene peridotite, olivine pyroxenite, minor gabbro, diorite, and quartz diorite. The surface length is approximately 2,000 m, the exposed width is from 400 to 800 m with an average of 500 m, and the area is 0.89 km². The northern part was composed of mafic rocks, the host rock of the low-grade orebody, primarily lithology are gabbro, hornblende gabbro, and minor diorite

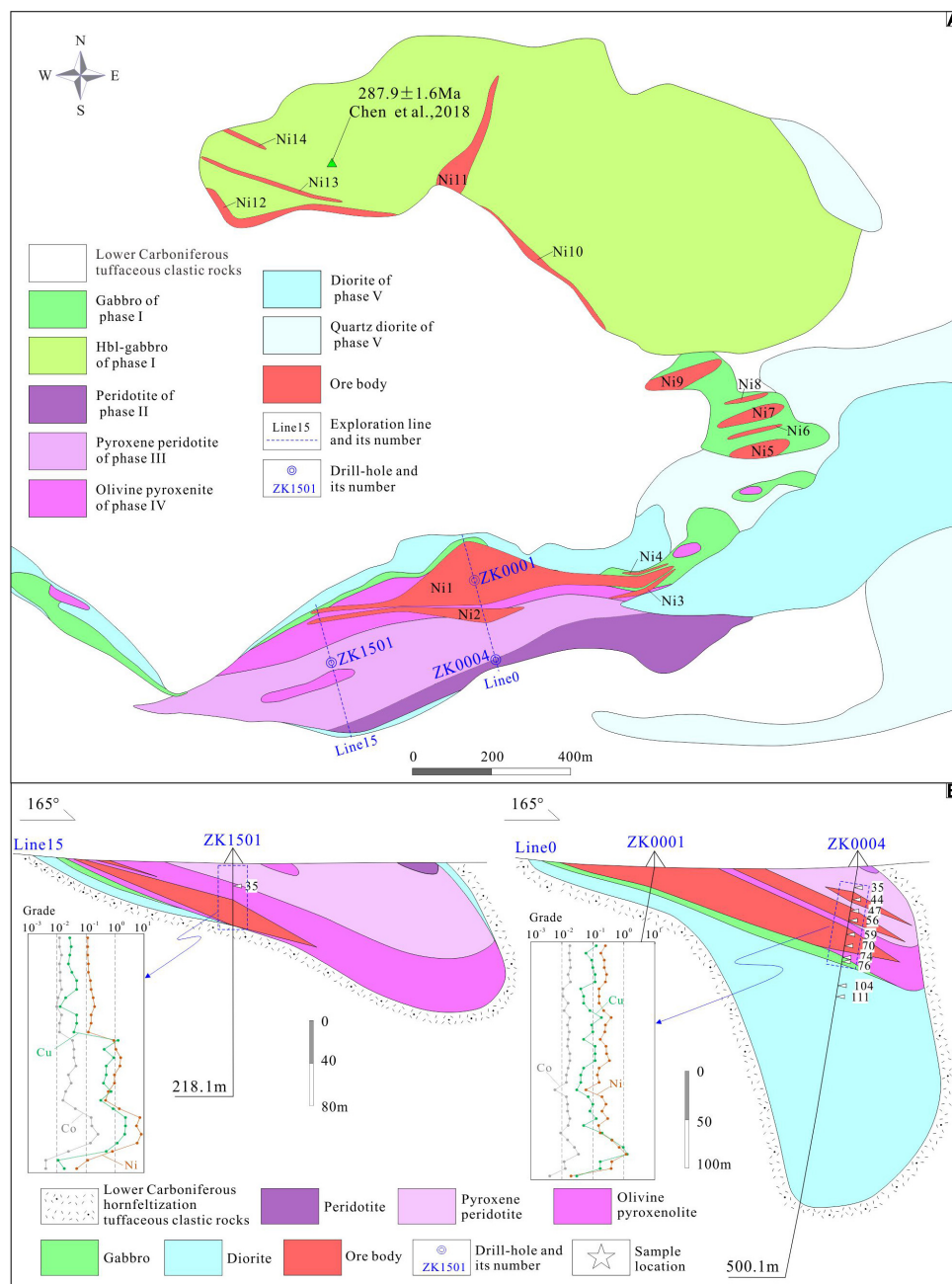


FIGURE 2 | Simplified geological map (A) and sample location (B) of the Lubei intrusion and Ni-Cu-Co orebodies.

(Figure 2A). The surrounding rocks are emplaced by the Lubei intrusion heated into hornfels.

Petrology

According to the spatial distribution, the mineral assemblage, the mineralization, and the alteration, the Lubei intrusion can be divided into five intrusive sequences: gabbro → peridotite → pyroxene peridotite → olivine pyroxenite (Figure 3A) → diorite (Figures 3B,C). The details of the characteristics for each lithology are described as follows:

The gabbro (phase I) is one of the ore-bearing rocks, includes gabbro and hornblende gabbro. Gabbro distributes at the edge of pyroxenite in the southern portion of the mining area, mainly represented by No. 4 to No. 9 orebodies with weak mineralization of nickel-copper-cobalt. The gabbro is composed of clinopyroxene ($25\% \pm$), plagioclase ($70\% \pm$), and olivine. Plagioclase with kaolinization has a particle size of 0.12–0.6 mm. Hornblende gabbro only distributes in northern part of the mining area with average of $287.9 \pm 1.6 \text{ Ma}$ (Chen et al., 2018) and mainly forms ore bodies No. 10 to No. 14.

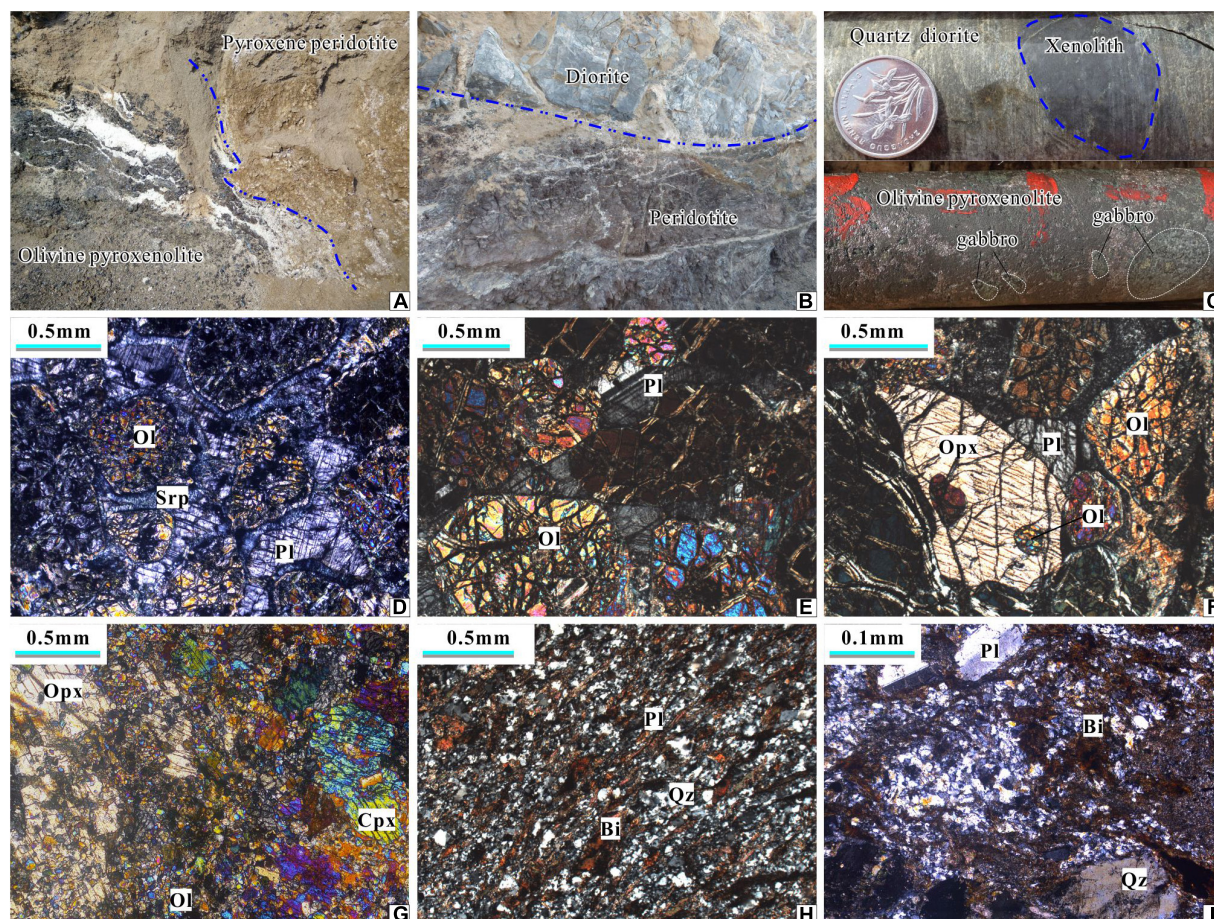


FIGURE 3 | Photos of outcrops and microphotographs of representative rocks from Lubei deposit. (A) contact relationship between olivine pyroxenite and pyroxene peridotite; (B) contact relationship between diorite and peridotite; (C) wall-rock xenoliths in quartz diorite and gabbro xenoliths in olivine pyroxenite; (D) serpentinized peridotite; (E) pyroxene peridotite; (F) pyroxene peridotite; (G) fragmented olivine pyroxenite; (H) slightly deformed quartz diorite; (I) deformed quartz diorite with porphyritic texture. Ol, olivine; Opx, orthopyroxene; Cpx, clinopyroxene; Pl, plagioclase; Srp, serpentine; Bi, Biotite; Qz, quartz.

The peridotite (phase II) only situated in southernmost part of the Lubei intrusion that intruded by the diorite (**Figure 3B**). The rock shows strong iddingsite, serpentinization (**Figure 3D**), and carbonate alteration without Ni-Cu-Co mineralization, and contains olivine (62%±), serpentine (25%±), calcite (10%±), and magnetite (3%±) (**Figure 3E**). The olivine characterized by network cracks is hypidiomorphic with a width of 0.3–1 mm and is filled with serpentine along the edge.

The pyroxene peridotite (phase III) only situated in south of the Lubei intrusion, which is obviously different from olivine pyroxenite and forms ore body No. 2. The rocks are serpentinized and glided and are mainly composed of olivine (62%±), augite (15%±), and serpentine (15%±) (**Figure 3F**). The Olivine exists in euhedral and subhedral grains, with a particle size of 0.5–1.5 mm. Augite in the form of subhedral columnar distributes between olivine, with a particle size of 0.5–1 mm. Serpentine distributes between olivine and pyroxene in fibrous form. Calcite distributes in the vein along the edges of fractures in olivine.

The olivine pyroxenite facies (phase IV) mainly situated in the southern mining area, intruded by diorite and exposed

sporadically. It is the most important ore bearing rock which is formed by the largest No.1 ore body. The rocks are mainly composed of olivine (10%±), orthopyroxene (43%±), and clinopyroxene (25%±), occasionally accompanied with olivine, amphibolite, and chloritization (**Figure 3G**). The Olivine has a xenomorphic granular structure with a particle size of 0.28 ± 2.3 mm, and the orthopyroxene is columnar with a particle size of 0.24 ± 3.2 mm.

The diorite (phase V) mainly situated at the edge and along the underpart of the Lubei intrusion, represents the latest product with wallrock xenoliths (**Figure 3C**). The rocks are composed of plagioclase (75%±), amphibole (15%±), quartz (10%±), and deformed minor biotite (**Figure 3H**), magnetite, and porphyritic textures (**Figure 3I**). Plagioclase has a euhedral plate structure, slightly kaolinized with a particle size of 0.4–2 mm. Amphibole is actinolite, distributes between plagioclase crystals. Biotite distributes between plagioclase crystals in a leaf shape. Magnetite distributes between hornblende and plagioclase in xenomorphic granular form.

Mineralization

There are 14 identified orebodies in the Lubei deposit, includes orebodies Nos. 1–4 in southern part which mainly hosted by olivine pyroxenite, orebodies Nos. 5–9 in the middle part that mainly occur in the gabbros, and orebodies Nos. 10–14 in the northern part that mainly occur in the hornblende gabbro (**Figure 2A**). The Ni–Cu–Co sulfide orebodies are bedded (**Figure 2B**) and dip south with a dip angle of 14° – 28° . The No.1 orebody, as the largest ore body in the mining area, extends about 930 m at surface and 265 m in depth, and has average grades of 0.91% Ni, 0.54% Cu, and 0.031% Co. The main ore minerals include pentlandite, chalcopyrite, pyrrhotite, magnetite, and chromite. The ores in gabbro are mainly present as disseminated, and ores in olivine pyroxenite are mainly shown as massive (**Figures 4A–C**). Pentlandite and pyrrhotite coexist with chalcopyrite (**Figures 4D,E,G**). Chromite generally coexist with magnetite (**Figure 4E**) or surround pentlandite (**Figures 4J–M,O**). Pyrrhotite shows strong oxidation (**Figures 4H,I,M,N**).

ANALYTICAL METHODS

Conducting backscattering image observation and mineral chemical composition analysis of ore minerals, using a JEOL JXA-8230 electron probe microanalyzer (EPMA) at Xinjiang Experimental Institute of Mineral Resources, the analytical conditions for component analysis were 15 kV, 10 nA beam current, 1–10 μm beam size, 10 s peak-counting time, and 5 s upper and lower background counting time.

Laser Ablation–Inductively Coupled Plasma–Mass Spectrometry (LA–MC–ICP–MS) zircon U–Pb analyses as has been completed in Nanjing FocuMS Technology Co., Ltd., by applying a laser-ablation inductively coupled plasma mass spectrometer with Agilent 7700X. The spot size was 24 μm , with standard zircon samples 91500, GJ-1, and NIST SRM 610. Weighted mean age calculations and concordia diagrams were processed by using ISOPLOT software (Ludwig, 2003).

Hf isotope analyses were conducted by using a multi-collector Thermo Electron Neptune MC–ICP–MS system at the same company as LA–MC–ICP–MS zircon U–Pb analyses. Helium was used as the carrier gas of denudation material in the experiment. Ablation protocol employed a spot diameter of 50 μm at 8 Hz repetition rate for 40 s. The zircon GJ-1 was used as external standard with the $^{176}\text{Hf}/^{177}\text{Hf}$ average value of 0.282008 ± 28 (2σ). The analysis process and correction are shown in Hou et al. (2007).

The whole-rock geochemical analysis was conducted at ALS Laboratory in Guangzhou. The main elements were analyzed by X-ray fluorescence spectrometer (pw4400), and the accuracy of analysis was better than 1%. FeO was determined by volumetric titration. Rare earth and trace elements were determined by plasma mass spectrometry (PE300D). The analytical accuracy was better than 5–10%.

The whole-rock Sr–Nd isotopic analysis was performed at Nanjing FocuMS Technology Co., Ltd., applied by a Nu plasma HR multi-collector plasma mass spectrometer. For Sr–Nd isotope analyses, rock powders (~ 100 mg) were dissolved in distilled HF–HNO₃ Savillex screwtop Teflon beakers at 150°C

overnight. Strontium and REEs were separated on columns which are made of Sr and REE resins from the Eichrom Company using 0.1% HNO₃ as eluant. Separation of Nd from the REE fractions was carried out on HDEHP columns with a 0.18 N HCl eluant. Measured Sr and Nd isotopic ratios were respectively normalized by using a $^{86}\text{Sr}/^{88}\text{Sr}$ value of 0.1194 and a $^{146}\text{Nd}/^{144}\text{Nd}$ value of 0.7219. The analyses of standards NIST SRM 987 for Sr and JNdi-1 for Nd over the measurement period respectively provided: $^{87}\text{Sr}/^{86}\text{Sr} = 0.710291 \pm 6$ (2σ), and $^{143}\text{Nd}/^{144}\text{Nd} = 0.512084 \pm 3$ (2σ).

ANALYTICAL RESULTS

Chemical Compositions of Major Minerals

The trace elements of the major minerals are shown in **Supplementary Appendix 2**. According to above observations and EPMA data, the characteristics of the maucherites are different from the disseminated and vein mineralization types. The pyrrhotite is composed of 60.176–63.394 wt% iron, 0.016–0.085 wt% cobalt, <0.078 wt% nickel, 35.76–39.263 wt% sulfur, and trace amounts of tellurium, copper, and arsenic. The pentlandite is composed of 28.443–32.981 wt% iron, 0.527–2.459 wt% cobalt, 31.307–36.737 wt% nickel, 32.843–33.803 wt% sulfur, and trace amounts of copper and arsenic. The tellurium of pentlandite from zk004–35, 44 ranges from 1.476 to 1.837 wt%. Copper and nickel minerals coexist with each other, and cobalt minerals appear in pentlandite as isomorphism.

LA–MC–ICP–MS U–Pb Zircon Dating

Because of the outcrops of the Lubei intrusion are weathered severely, the fresh diorite (phase V) sample was collected from the bottom of the Lubei intrusion in drill hole ZK004 for zircon U–Pb dating. The data are listed in **Supplementary Appendix 3**. The zircon in the diorite has 50–120 μm long and 40–60 μm width, and it was shown as a magmatic origin with oscillatory zoning. The zircon U content of 23 points ranges from 232.8×10^{-6} to 630.1×10^{-6} , and the Th content between is 130.1×10^{-6} and 509.2×10^{-6} , with a Th/U ratio of 0.53–0.85, which indicates the magmatic origin of zircon. The zircon concordant age is 281.3 ± 0.7 Ma (2σ , MSWD = 4.2), and the weighted mean age of $^{206}\text{Pb}/^{238}\text{U}$ is 281.2 ± 1.5 Ma (2σ , MSWD = 2.4) (**Figure 5A**). Therefore, the mean $^{206}\text{Pb}/^{238}\text{U}$ age is interpreted to be the crystallization age of the diorite (Li et al., 2018), and it represents the latest magmatism (phase V) of the Lubei intrusion. This age is consistent with that of mafic-ultramafic rocks in Lubei intrusion (Chen et al., 2018; Deng et al., 2020) and the typical mafic-ultramafic rocks in Huangshan, Huangshandong, and Xiangshan in the eastern Tianshan (**Figure 5B**).

Whole-Rock Geochemistry

The major and trace elements were analyzed as shown in phase I to phase V: (1) two gabbro samples (phase I), (2) two pyroxene peridotite samples (phase III), (3) five olivine pyroxenite samples (phase IV), and (4) two diorite samples

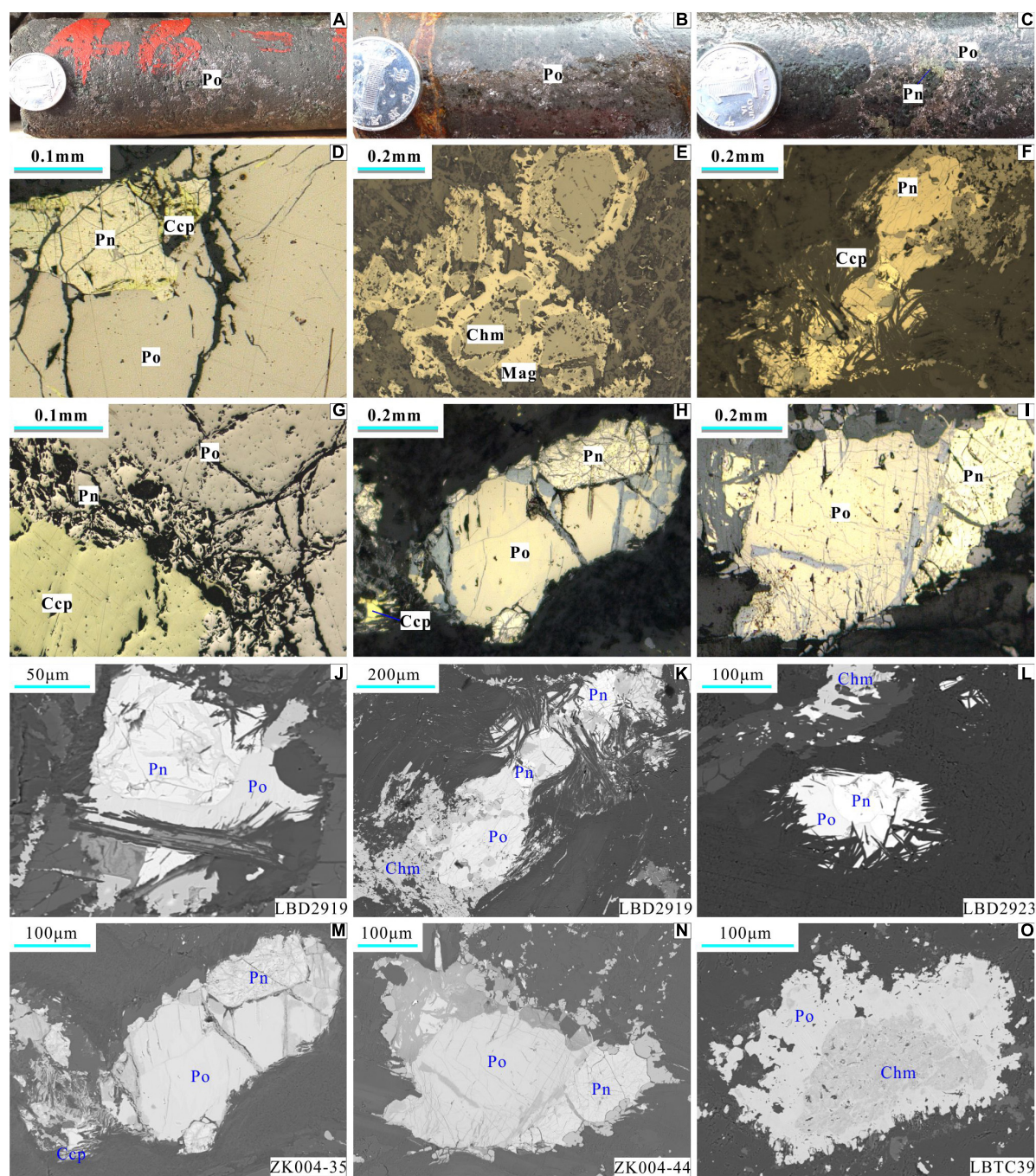
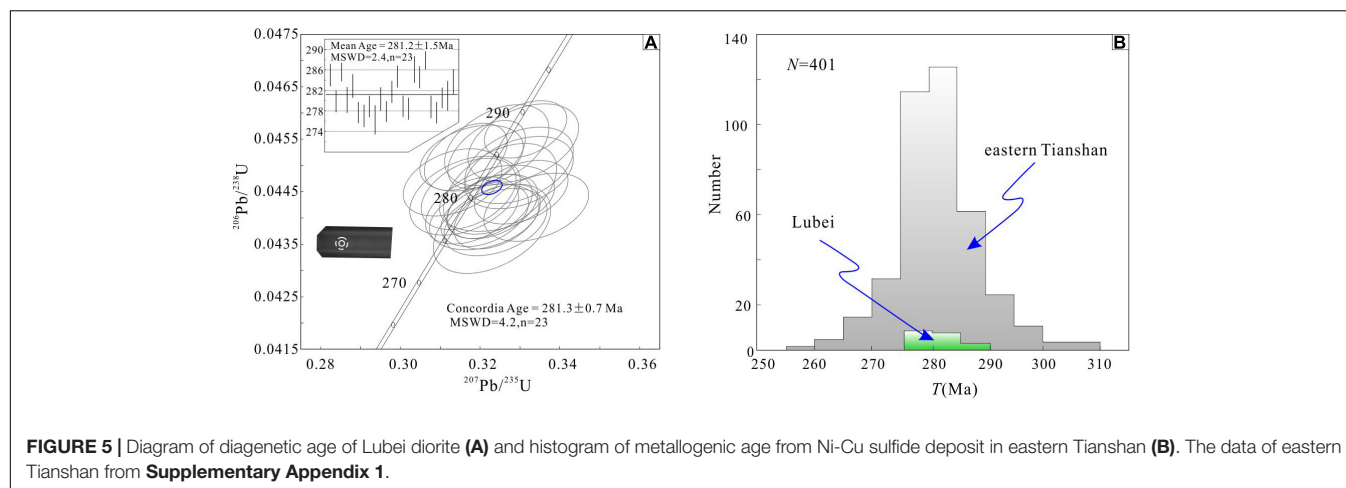


FIGURE 4 | Photos of outcrops and microphotographs of representative ores from Lubei deposit. (A) pentlandite in olivine pyroxenolite; (B) pentlandite in olivine pyroxenolite with limonitization vein; (C) Pn and Po in pyroxenolite; (D) Pn, Po, and Ccp co-occurrence; (E) Chm surrounded by Mag; (F) Pn coexisted with Ccp, and Pn in crack; (G) Pn, Po, and Ccp co-occurrence; (H) oxidized Po and Pn in crack; (I) oxidized Po; (J) Pn surrounded by Po; (K) Pn coexisted with Ccp, and Pn in crack; (L) Pn coexisted with Po; (M) oxidized Po and Pn in crack; (N) oxidized Po; (O) Chm surrounded by Po. Pn, Pentlandite; Po, Pyrrhotite; Chm, chromite; Ccp, chalcopyrite; Mag, magnetite.

(phase V) (Supplementary Appendix 4). The sample locations are shown in Figure 2B. Variable loss on ignition (LOI) values reflect variable degrees of alteration in the samples. Based on the plots and discussion below, the major element contents are normalized to 100% after the correction of LOI. Ultrabasic rocks

in phase III and IV contain the lowest SiO_2 and Al_2O_3 , and highest MgO and FeO^T contents. The Diorite of phase V exhibits the highest SiO_2 and Al_2O_3 , and lowest MgO and FeO^T contents. The composition of gabbro in phase I is between ultrabasic rocks in phase III and IV and Diorite in phase V. All samples



of the Lubei intrusion are characterized by relatively low $K_2O + Na_2O$ and TiO_2 contents. On the SiO_2 versus FeO^T/MgO diagram, the samples mainly fall into the field of tholeiite series (**Figure 6A**). On the $(Mg+Fe)/Ti$ versus Si/Ti diagram, both pyroxene peridotite in phase III and pyroxenite in phase IV are on the control line of olivine and orthopyroxene, gabbro in phase I is on the control line of orthopyroxene and clinopyroxene, and diorite in phase V is on the control line of plagioclase (**Figure 6B**), which are consistent with the petrographic observation.

Total rare earth element (ΣREE) contents of the Lubei intrusion display an increasing trend from peridotite to gabbro, then to diorite (**Supplementary Appendix 4**), reflected an increase in the volume of inter cumulus liquids. The Lubei intrusion displays enriched light rare earth elements (LREEs) relative to heavy rare earth elements (HREEs) and lower LREE/HREE ratios. All the samples have a slightly negative Eu anomalies, with an average Eu/Eu^* ratio of 0.89 (**Figure 6C**). Primitive mantle-normalized diagrams of incompatible elements also exhibit variable element concentrations (**Figure 6D**), the other notable features include the depletion of Nb and Ta relative to La and Th (**Figure 6D**). In particular, the distribution of the diorite is consistent with ultrabasic rocks, which indicates the diorite were evolved from homologous magma, and it is similar to typical Permian Ni-Cu sulfide deposits and mafic-ultramafic intrusions in the eastern Tianshan (**Figure 6D**).

Sr and Nd Isotopes

The results of the whole-rock Sr-Nd are summarized in **Supplementary Appendix 5**. The Rb concentration vary has a narrow range from 0.643×10^{-6} to 34.5×10^{-6} , whereas the Sr concentration ranges between 39.1×10^{-6} and 1171×10^{-6} . The initial $^{87}Sr/^{86}Sr$ ratios of the Lubei intrusion ranges from 0.704881 to 0.711383 with an average of 0.7073818. The value of $\epsilon Nd_{(281Ma)}$ is -2.83 to +4.37, with an average value of +1.54. The Sr and Nd isotopic compositions indicate that the Lubei intrusion is characterized by low initial $^{87}Sr/^{86}Sr$ value and positive $\epsilon Nd_{(281Ma)}$ value type magma source area (except for sample ZK004-59 with $\epsilon Nd_{(281Ma)} = -2.83$), which is characterized by depleted mantle source area. The $\epsilon Nd_{(281Ma)}$

value of -2.83 indicates the parental magma was contaminated by crustal materials.

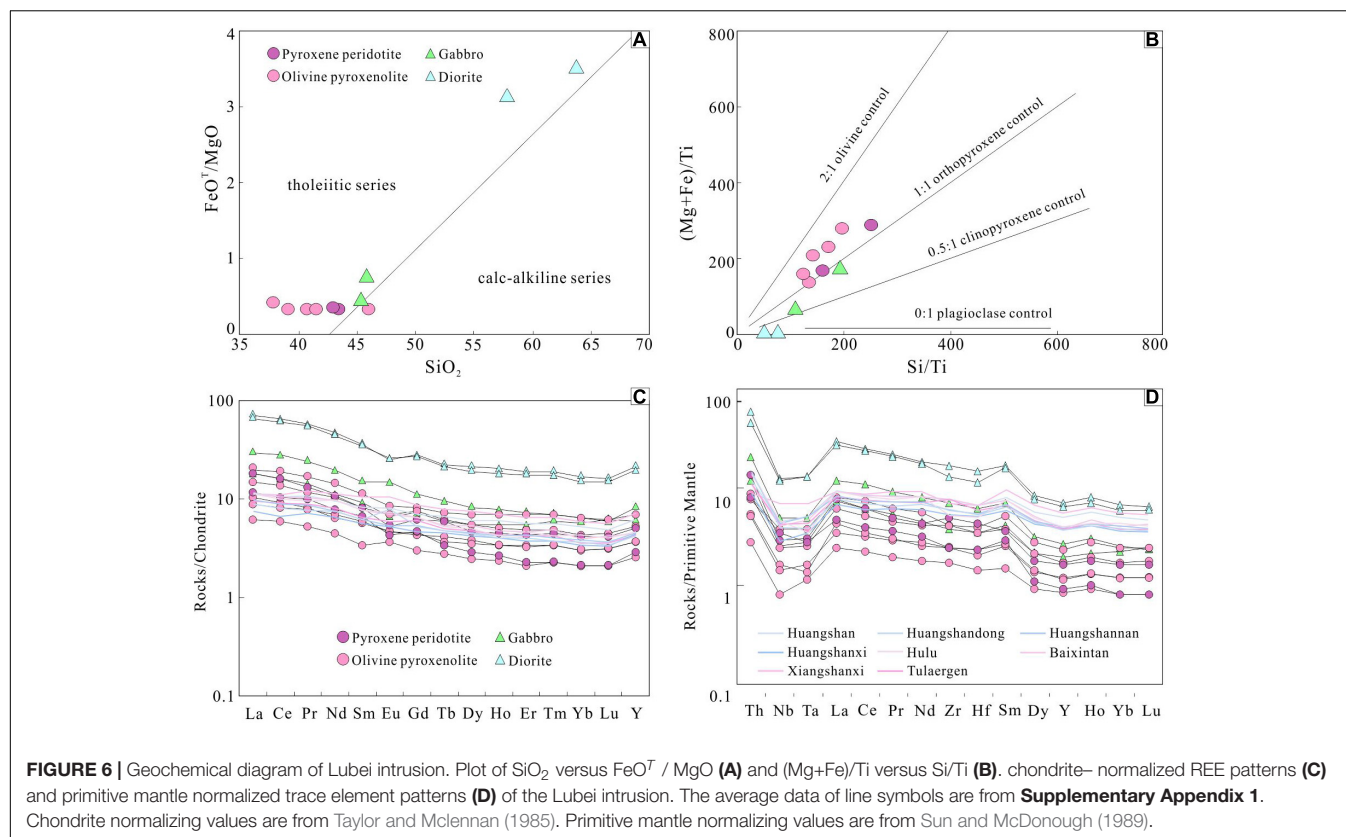
Hf Isotopes

The results of zircon Hf isotope are summarized in **Supplementary Appendix 6**. The Lu-Hf isotopic compositions of zircon in diorite could be characterized as relatively high initial $^{176}Hf/^{177}Hf$ ratios (0.282916–0.282973, with an average of 0.282938) and slightly depleted ϵHf value (11.3–13.4, with an average of 12.1). Meanwhile, the zircon has relatively young one-stage model ages ($T_{DM(Hf)}$; 393–476 Ma), correspond to the T_{DM2} model ages which from 417 to 522 Ma. The narrow range of Hf isotopic compositions and slightly depleted ϵHf value indicates that the sources of these zircon grains were derived from depleted mantle, mixed with a small amount of crustal material.

DISCUSSION

Magma Source

The contact zone between the Lubei intrusion and country rock shows the contact metamorphism, and wall-rock xenoliths, and can be observed in the late emplaced diorite (**Figure 3B**), which indicates the Lubei intrusion experiences magmatic thermal emplacement instead of the ophiolite suite. At present, the mafic-ultramafic source of the eastern Tianshan Ni-Cu metallogenic belt is related to the Tarim large igneous province has become the focus (Xia et al., 2006; Pirajno et al., 2008). Large igneous provinces (LIPs) are characterized by large-scale mantle-derived magmatism occurring within a relatively short geological period (generally several Ma), mainly includes overflow basalts and radial basic dyke swarms (Coffin and Eldholm, 1994). The magma source was dominated by relatively dry and low volatile matter (Campbell and Griffiths, 1993). Most of the scholars believe that the mantle source of the Ni-Cu bearing mafic-ultramafic intrusions was modified by slab-derived melts and fluids due to oceanic crust subduction in eastern Tianshan before the Late Permian (Mao et al., 2008; Gao et al., 2013). However, there



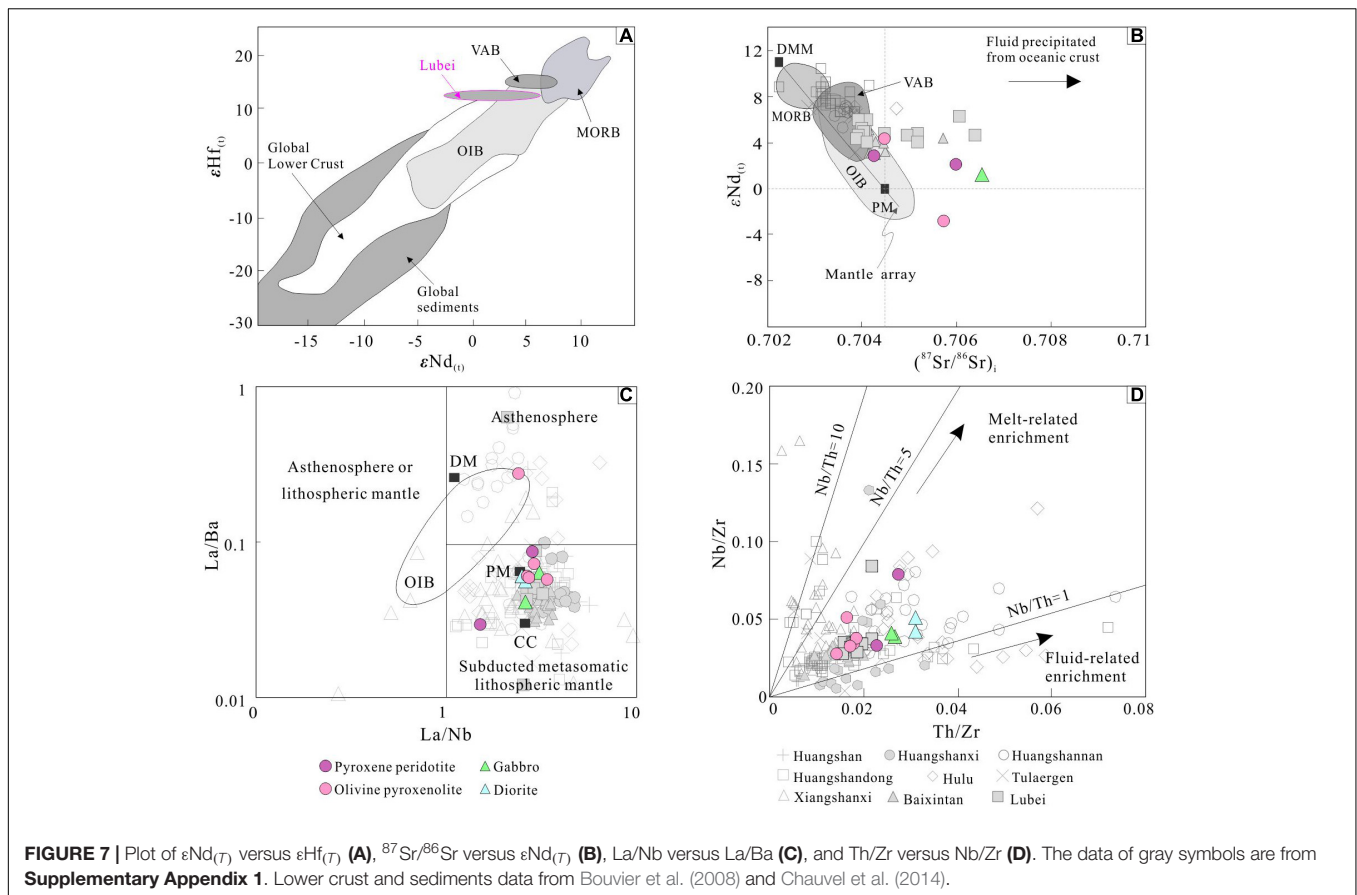
have had no reports on overflow basalts and radial basic dyke swarm assemblages related to LIPs in this area. On the contrary, amphibole, biotite, and other primary hydrous minerals are commonly found in the Lubei intrusion, which indicates that the primary magma related to subduction of Kanggur ocean basin in Late Carboniferous (Sun et al., 2020 and their references) is relatively wet.

The geochemical characteristics of the Lubei intrusion, which are relatively enriched in large ion lithophile elements (LILEs) (such as K, Rb, Ba, and Sr) and depleted in high field strength elements (HFSEs) (such as Th, Nb, Ta, and Ti), that indicate the magma suffered from fluid metasomatism during a subduction setting. In the $\epsilon\text{Nd}(T)$ versus $\epsilon\text{Hf}(T)$ diagram, the data points plot next to the ocean island basalt (OIB) and volcanic arc basalt (VAB; **Figure 7A**), which indicate the primary may be related to island arc magmatism. In the La/Nb versus La/Ba diagram, almost all samples plot in the subducted metasomatic lithospheric mantle region (**Figure 7C**). The $^{87}\text{Sr}/^{86}\text{Sr}$ versus $\epsilon\text{Nd}(T)$ diagram (**Figure 7B**) and Th/Zr versus Nb/Zr diagram (**Figure 7D**) indicate the fluids were involved in magmatic evolution. Due to the release of fluids from early altered slabs, many magmas in post-collisional extensional environments often inherits the magma source characteristics of fluid metasomatism in early subduction setting (Zhao et al., 2016), which is consistent with the low Nb and Ta concentrations of subduction-related magmas in the Lubei intrusion. All the results show that the magma source of the Lubei intrusion originated from the upwelling of the asthenosphere in a post-collisional extension setting, that led

to the partial melting of metasomatic mantle which was modified by subduction fluid in the late Carboniferous (Deng et al., 2011b), and then formed to high magnesium tholeiite basaltic magma.

Ore Formation Mechanism

Ore formation mechanism generally has four ways which are: the changes in temperature and pressure, the fractional crystallization, the magma mixing, and the crustal contamination, that make magma reach sulfur saturation (Naldrett, 1999; Li and Ripley, 2005). First, the sulfur solubility decreases with decreasing temperature and increasing pressure (Li and Ripley, 2005). Although the initial magma is sulfur saturated, the sulfur will also be unsaturated during magma rise because of the increase in sulfur solubility, which is caused by the pressure drop is much greater than the temperature drop (Mavrogenes and O'Neill, 1999; Barnes and Lightfoot, 2005). Second, the sulfur content in the magma increases after the removal of Fe-oxide in fractional crystallization. Then, the magma became sulfur saturated and resulted in sulfide segregation (Haughton et al., 1974; Irvine, 1975). Third, magma mixing could change the saturation curve of sulfur and cause sulfur to enter the saturation zone to form immiscible sulfides (Irvine et al., 1983), such as the Bushveld and Jinchuan deposits. In fact, the petrology and geochemistry of the Lubei intrusion do not show the characteristics of magma mixing. Finally, crustal contamination was considered as a necessary factor for the formation of large Ni–Cu sulfide deposits (Naldrett, 2004, Naldrett, 2010).



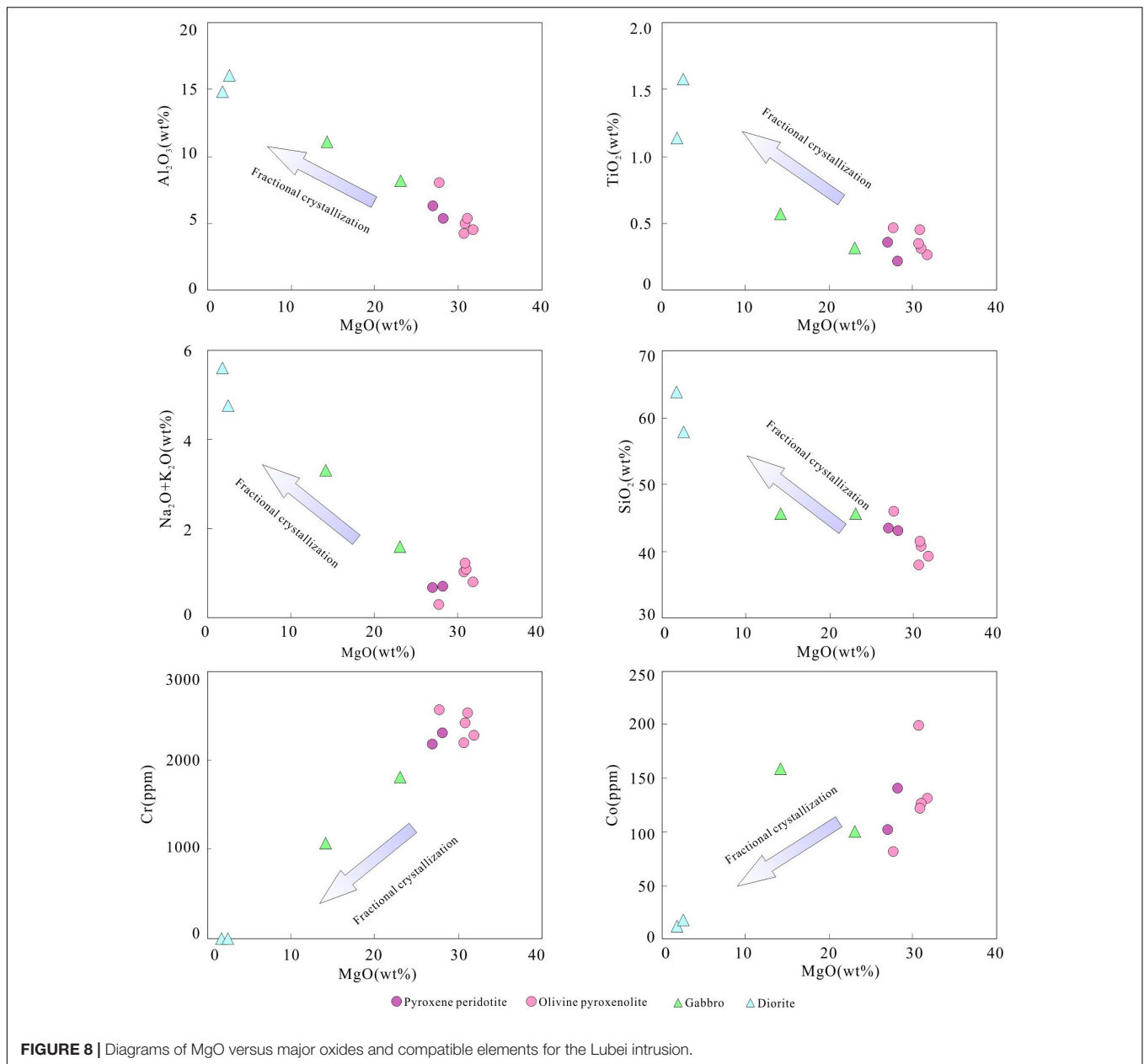
Fractional Crystallization

In addition, the gabbro at the edge was influenced by surrounding rocks in the early stage, the progressive decrease in olivine content from peridotite through orthopyroxene peridotite to olivine pyroxenite and the textures as described above indicate that the fractionation is dominated by the crystallization and accumulation of olivine, orthopyroxene and clinopyroxene, which is consistent with the mineral separation and crystallization control line (Figure 6B). The diorite samples plot on the trends are same as the other rocks of the intrusion. The diagrams of MgO versus major oxides and compatible elements (e.g., Cr and Co) illustrate the fractionation/accumulation of olivine, pyroxene, and plagioclase. For example, a negative correlation of MgO with SiO_2 , CaO, $\text{Na}_2\text{O}+\text{K}_2\text{O}$, and TiO_2 indicates the fractionation/accumulation of clinopyroxene and plagioclase; a positive correlation of MgO with compatible elements (e.g., Cr, Co, Ni, and V) is consistent with the fractionation/accumulation of olivine and orthopyroxene (Figure 8).

Crustal Contamination

In fact, it is difficult to avoid the assimilation and contamination of magma from the mantle to the crust, and the key is the degree and source of crustal contamination. The source of crustal contamination includes the addition of silicon and sulfur materials. The former can reduce the solubility of sulfur in

magma (Irvine, 1975; Lightfoot and Hawkesworth, 1997), and the latter can increase the sulfur content in magma (Leshner and Campbell, 1993). The sulfur saturation of some nickel-copper sulfide deposits is mainly caused by the addition of crustal SiO_2 , and it has nothing to do with sulfur-rich surrounding rocks, such as Norilsk (Lightfoot and Hawkesworth, 1997; Ripley et al., 2003) and Kalatongke (Zhang et al., 2003) deposits. In addition, some sulfur-rich country rocks were incorporated into the magma to trigger sulfide saturation, such as Duluth and Voisey's Bay deposits (Lambert et al., 1998). The Hf isotopes of diorite deviate significantly from the depleted mantle evolution line (Figure 9A), which indicate that the diorite may have suffered from crustal contamination. The Rb/Sr ratio (0.04 to 0.47) of the Lubei intrusion varies greatly with $\epsilon\text{Sr}(T)$ value of 0.7–33.4. The Sr–Nd isotopic magma mixing simulation shows that the magma source suffered 4–10% lower crustal contamination with slight contamination of the upper crust (Figure 9B), which is similar to Tulargen (<5%, Jiao et al., 2012), Huangshandong (5–8%, Xia et al., 2010), Erhongwa (<5%, Sun et al., 2013a), Hulu (5–10%, Xia, 2009) and Huangshannan (~5%, Mao et al., 2016). The sulfur isotope $\delta^{34}\text{S}$ (–0.3 to +1.8‰, Chen et al., 2019) of the Lubei ores was characterized by mantle sulfur (–3 to +3‰; Ohmoto, 1986), which is consistent with the Huangshannan (–0.4 to +0.8‰, Mao et al., 2017) and Huangshanxi (–0.2 to +0.8‰, Zhang et al., 2011) deposits in eastern Tianshan. Therefore, we conclude that the main mechanism of sulfur saturation in Lubei



deposit is lower crustal contamination with slight contamination of the upper crust.

Metallogenic Process

The magma conduit plays an important role in the formation of Ni-Cu sulfide deposits (Maier et al., 2001; Su et al., 2014; Barnes et al., 2016). After the sulfur-unsaturated basaltic magma melt enters the crust, along with changes in temperature and pressure, and the addition of surrounding rock, sulfur saturation of magma is achieved through fractional crystallization and crustal contamination. Then, sulfide droplets are continuously deposited and accumulate owing to gravitational forces at the bend, widening, or bifurcation of the magma conduit due to the decrease in magma velocity (Keays, 1995; Naldrett, 1999;

Lightfoot et al., 2012; Su et al., 2014). The Lubei Ni-Cu-Co sulfide deposit has undergone the following metallogenic processes (Figure 10).

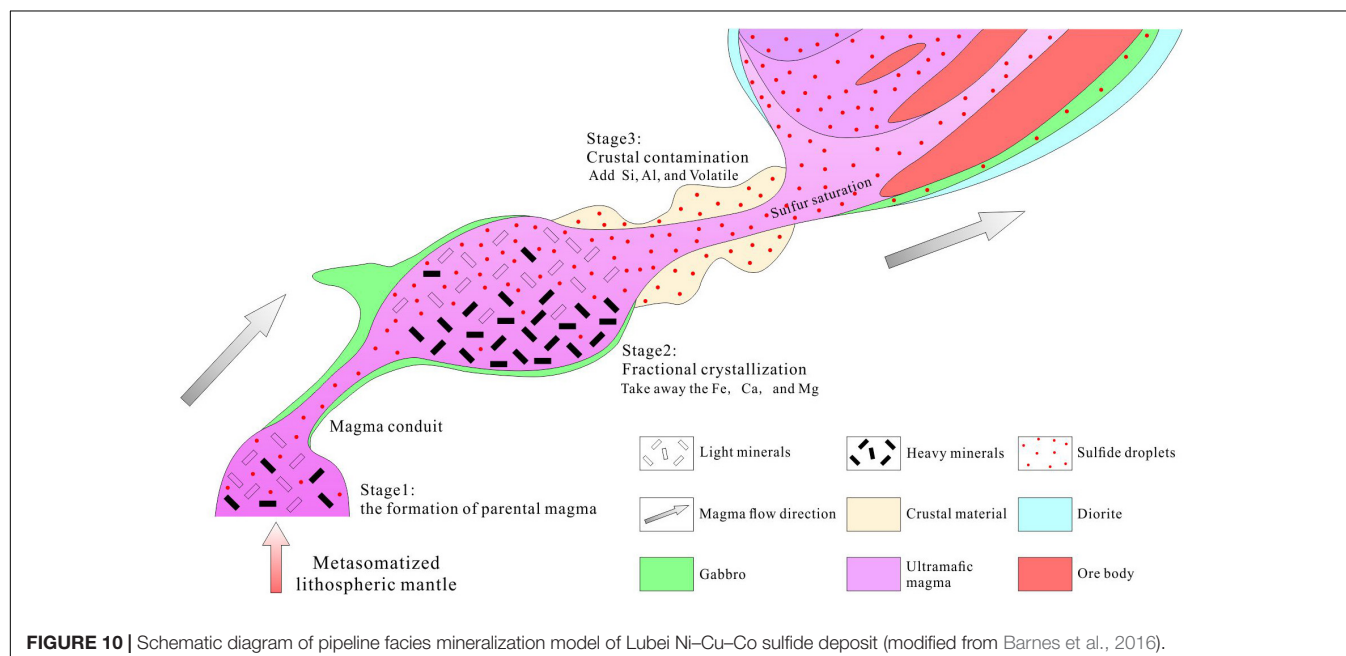
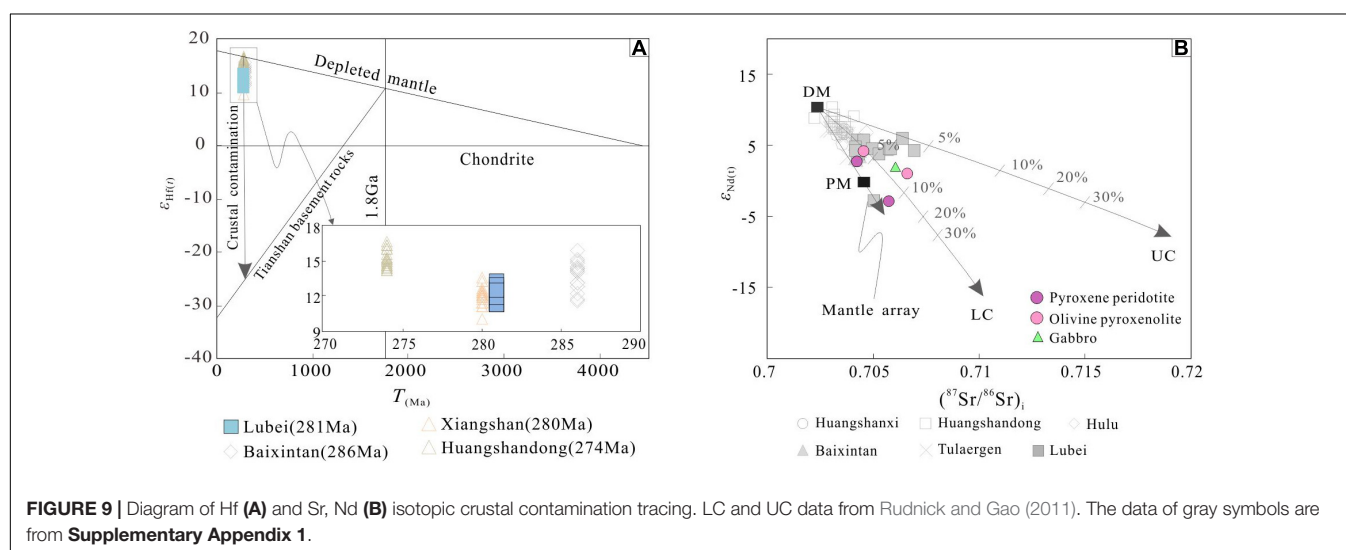
The first stage is the formation of the parent magma. The high-Mg tholeiitic basaltic magma was formed by partial melting of the metasomatic lithospheric mantle (Chen et al., 2019), which was likely derived from a hydrous mantle previously modified by a fluid phase during the dehydration of the descending slab (Chen et al., 2018). The initial magma with a small amount of sulfide droplet migrates upwards through the conduit of the early structural fracture and rapidly crystallizes to form gabbro (phase I), influenced by the relatively low-temperature country rocks. The second stage is the fractional crystallization of the silicate and oxide minerals. As the magma moves upwards

within the conduit, the temperature gradually drops, and high-temperature minerals (such as olivine, orthopyroxene, etc.) begin to crystallize, which removes a large amount of Si, Mg, and Fe. Meanwhile, the addition of a small amount of wall rock materials will change the magma viscosity, sulfur solubility, and crystallization temperature. The sulfur solubility will decrease with decreasing FeO contents and increasing Si-rich materials (Irvine, 1975; Lightfoot and Hawkesworth, 1997), which can promote more metal elements into sulfide melts to gather gradually as sulfide droplets (Barnes et al., 2016). The third stage is crustal contamination and mineralization. The addition of abundant Si materials further reduced the sulfur solubility and forms abundant sulfides. Meanwhile, due to the addition of SiO_2 , Al_2O_3 , and volatiles, the flow velocity of magma slows to ensure adequate sulfide melt enrichment. The last stage is

sulfide segregation and mineralization. Due to gravity flow and sulfide accumulation, the upper hanging ore body composed of disseminated ore generally forms in the middle of the magma, whereas the layered orebody composed of dense disseminated and dense massive ores forms in the lower part of the magma.

Geodynamic Setting

The crystallization age of the earliest emplacement of hornblende gabbro in the Lubei intrusion was 288 ± 1.8 Ma (Chen et al., 2018), and the latest emplacement diorite was 281.2 ± 1.5 Ma (Li et al., 2018), whose section (288–281 Ma) is consistent with the metallogenic ages of Huangshan, Huangshan, Xiangshan and other typical Ni-Cu-(Co) deposits in the eastern Tianshan area. At present, there are three different views of the geodynamic setting that formed the early Permian mafic-ultramafic



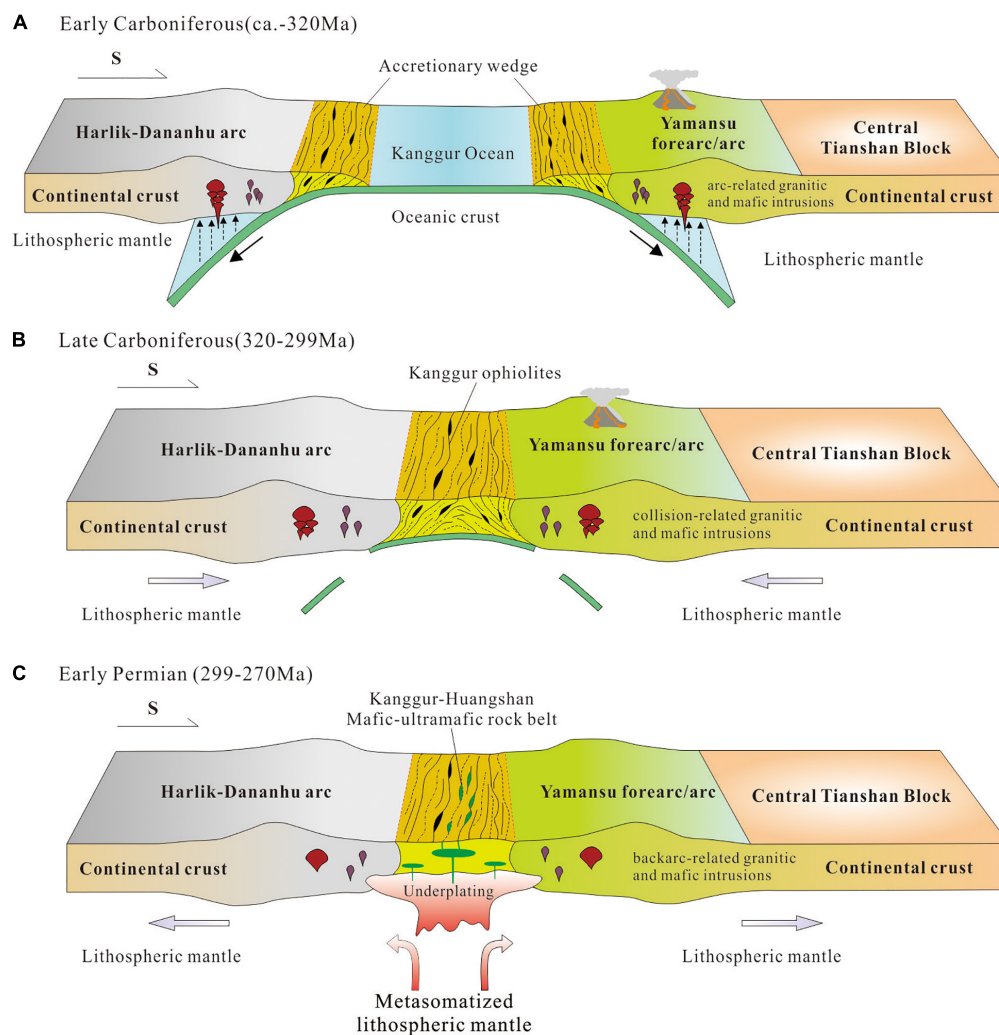


FIGURE 11 | The tectonic evolution in the late Paleozoic of eastern Tianshan. **(A)** the two-way subduction and accretion of the Kanggur ocean basin occurred in the Early Carboniferous; **(B)** closure of Kanggur ocean basin in Late Carboniferous; **(C)** post-collisional extensional environment in Early Permian.

intrusions in the Huangshan-Jingerquan belt, including an active continental margin (Xiao et al., 2004; Mao et al., 2006b), a post-collisional lithosphere extension environment (Gu et al., 2006), and a mantle plume (Mao et al., 2006a; Pirajno et al., 2008; Su et al., 2013a). The geochemical characteristics of rocks suggest that the parent magma originated from a metasomatic mantle that was modified by subduction events, which is not consistent with the characteristics of rock assemblages and magmas of the Alaskan type (Irvine, 1974; Helmy and El Mahallawi, 2003). It is also inconsistent with the large-scale mantle-derived magmatism formed by the mantle plume within a short time (1–2 Ma), tholeiitic magma series, dry mantle source, and very low volatile content (Campbell and Griffiths, 1993). Therefore, we believe that the Lubei Ni–Cu–Co deposit formed in an extensional postcollisional environment with the geochemical characteristics of an early-stage subducted metasomatic mantle, which has nothing to do with mantle

plume activity (Deng et al., 2011a). The regional tectonic-magmatic evolution and mineralization have had experienced the following processes.

The Kanggur ocean basin had already opened in the late Cambrian (494 ± 10 Ma, Li et al., 2008) and then entered the stage of ocean basin evolution. With the earliest subduction northward in the Late Ordovician (Du et al., 2018; Sun et al., 2018), the Dananhu–Tousuquan island arc belt was formed and accompanied by porphyry copper deposits (Sun et al., 2018), epithermal copper deposits (431.8 ± 2.7 Ma, Deng et al., 2016) and VMS-type zinc–copper deposits (434.2 ± 3.9 Ma, Deng et al., 2016) in the Kalatage area. The Devonian subduction continued to the north and formed basaltic–andesite volcanic rocks (Du et al., 2019). In the early Carboniferous, the Aqishan–Yamansu forearc basin or island arc belt was formed by subduction southward (Han et al., 2019; Zhao et al., 2019; Liu et al., 2020; **Figure 11A**) with iron and lead–zinc deposits related

to volcanism (Hou et al., 2014). At the same time, porphyry copper deposits were formed by subduction to the north (Wang et al., 2016; Xiao et al., 2017). In the late Carboniferous, the Kanggur ocean basin was closed (Figure 11B), and the tectonic compression environment led to the formation of volcanic iron deposits (Zhao et al., 2017; Zhang et al., 2018), as well as ductile shear zone gold deposits (Wang et al., 2015b; Muhtar et al., 2020a). The geodynamic setting in the early Permian represented post-collisional extension setting (Muhtar et al., 2020b; Figure 11C). The metasomatic lithospheric mantle produced in the early subduction stage was partially melted, and the mantle-derived magma upwelling formed beaded mafic-ultramafic rocks along the Kanggur-Huangshan regional fault, accompanied by Huangshandong, Huangshannan, Hulu, Tulargen, Baixintan, and Lubei sulfide deposits (San et al., 2010; Sun et al., 2010; Chen et al., 2013, 2018; Zhao et al., 2015; Feng et al., 2018).

CONCLUSION

1. The Lubei mafic-ultramafic intrusion was composed of five lithofacies, including gabbro (phase I), peridotite (phase II), pyroxenite (phase III), olivine pyroxenite (phase IV), and diorite (phase V). In addition to pyroxene peridotite (phase III) and gabbro (phase I), the most important ore-bearing lithology is olivine pyroxenite (phase IV).
2. The Lubei intrusion was formed at the same time as the bearing Ni-Cu-Co sulfide mafic-ultramafic rocks in eastern Tianshan, and its metallogenic age was between $288 \pm 1.8\text{Ma}$ of hornblende gabbro (phase I) and $281.3 \pm 0.7\text{Ma}$ of diorite (phase V).
3. In addition to magmatic fractional crystallization, the most important mechanism of sulfur saturation in Lubei Ni-Cu-Co deposit is crustal contamination. The Sr-Nd isotope shows that the contamination degree of lower crustal materials is 4–10% with slight contamination of the upper crust.
4. The Lubei Ni-Cu-Co deposit was formed in post-collisional extensional setting of the CAOBS during the early Permian. The primary magma derived from partial melting of metasomatized lithospheric mantle was formed Ni-Cu-Co sulfide deposit has gone through three stages,

including fractional crystallization, crustal contamination, and sulfide segregation.

DATA AVAILABILITY STATEMENT

The original contributions presented in the study are included in the article/Supplementary Material, further inquiries can be directed to the corresponding author/s.

AUTHOR CONTRIBUTIONS

PL: investigation, analysis, writing, and original draft preparation. TL: academic support and revising original version. YF: original manuscript English editing. TZ, JT, and DL: investigation and original figures editing. GC: investigation and financial support. JL: mineralogy analysis and interpretation. CW: geochemistry analysis and interpretation. All authors have contributed to the article and approved the submitted version.

FUNDING

This work was funded by the Project of China Geological Survey (Grant No. DD20190379), the National key R&D project of China (Grant No. 2018YFC0604001-04), and the second Tibetan Plateau Scientific Expedition and Research (Grant No. 2019QZKK0806).

ACKNOWLEDGMENTS

We thank Qiong Han, Liuyuan Jin, and Xiaojun Zhang from Geological Survey Academy of Xinjiang for assistance in fieldwork and thank the reviewers for providing critical comments and suggestions.

SUPPLEMENTARY MATERIAL

The Supplementary Material for this article can be found online at: <https://www.frontiersin.org/articles/10.3389/feart.2021.648122/full#supplementary-material>

REFERENCES

- Ao, S. J., Xiao, W. J., Han, C. M., Mao, Q. G., and Zhang, J. E. (2010). Geochronology and geochemistry of early Permian mafic-ultramafic complexes in the Beishan area, Xinjiang, NW China: implications for late Paleozoic tectonic evolution of the southern Altai. *Gondwana Res.* 18, 466–478. doi: 10.1016/j.gr.2010.01.004
- Barnes, S. J., Cruden, A. R., Arndt, N., and Saumur, B. M. (2016). The mineral system approach applied to magmatic Ni-Cu-PGE sulphide deposits. *Ore Geol. Rev.* 76, 296–316. doi: 10.1016/j.oregeorev.2015.06.012
- Barnes, S. J., and Lightfoot, P. C. (2005). "Formation of magmatic nickel sulfide ore deposits and processes affecting their copper and platinum group element contents," in *Economic Geology, 100th Anniversary Volume*, eds J. W. Hedenquist, J. F. H. Thompson, R. J. Goldfarb, and J. P. Richards (Littleton, CO: Society of Economic Geologists, Inc), 179–213.
- Begg, G. C., Hronsky, J. A. M., Arndt, N. T., Griffin, W. L., O'Reilly, S. Y., and Hayward, N. (2010). Lithospheric, cratonic and geodynamic setting of Ni-Cu-PGE sulfide deposits. *Econ. Geol.* 105, 1057–1070. doi: 10.2113/econgeo.105.6.1057
- Bouvier, A., Vervoort, J. D., and Patchett, P. J. (2008). The Lu-Hf and Sm-Nd isotopic composition of CHUR: constraints from unequilibrated chondrites and implications for the bulk composition of terrestrial planets. *Earth Planet. Sci. Lett.* 273, 48–57. doi: 10.1016/j.epsl.2008.06.010
- Campbell, I. H., and Griffiths, R. W. (1993). The evolution of the mantle's chemical structure. *Lithos* 30, 389–399. doi: 10.1016/0024-4937(93)90047-g
- Chauvel, C., Garçon, M., Bureau, S., Besnault, A., Jahn, B., and Ding, Z. L. (2014). Constraints from loess on the Hf-Nd isotopic composition of the upper

- continental crust. *Earth Planet. Sci. Lett.* 388, 48–58. doi: 10.1016/j.epsl.2013.11.045
- Chen, B. Y., Yu, J. J., and Liu, S. J. (2018). Source characteristics and tectonic setting of mafic-ultramafic intrusions in North Xinjiang, NW China: insights from the petrology and geochemistry of the Lubei mafic-ultramafic intrusion. *Lithos* 308–309, 329–345. doi: 10.1016/j.lithos.2018.03.016
- Chen, B. Y., Yu, J. J., Liu, S. J., and Tian, J. T. (2019). Formation of the Lubei magmatic Ni–Cu deposit in a post-subduction setting in East Tianshan, North West China. *Ore Geol. Rev.* 104, 356–372. doi: 10.1016/j.oregeorev.2018.11.017
- Chen, J. P., Liao, Q. N., Zhang, X. H., Luo, T., Guo, D. B., and Hu, Z. C. (2013). Contrast of Huangshandong and Xiangshan mafic-ultramafic complex, East Tianshan. *Earth Sci. J. China Univ. Geosci.* 38, 1183–1196. doi: 10.3799/dqkx.2013.117
- Coffin, M. F., and Eldholm, O. (1994). Large igneous provinces: crustal structure, dimensions, and external consequences. *Rev. Geophys.* 32, 1–36. doi: 10.1029/93RG02508
- Deng, X. H., Wang, J. B., Pirajno, F., Wang, Y. W., Li, Y. C., Li, C., et al. (2016). Re–Os dating of chalcopyrite from selected mineral deposits in the Kalatag district in the eastern Tianshan Orogen, China. *Ore Geol. Rev.* 77, 72–81. doi: 10.1016/j.oregeorev.2016.01.014
- Deng, Y. F., Song, X. Y., Chen, L. M., Cheng, S. L., Zhang, X. L., and Li, J. (2011a). Features of the mantle source of the Huangshanxi Ni–Cu sulfide-bearing mafic-ultramafic intrusion, eastern Tianshan. *Acta Petrol. Sin.* 27, 3640–3652. doi: 10.1080/00288306.2011.590212
- Deng, Y. F., Song, X. Y., Chen, L. M., Zhou, T. F., Pirajno, F., Yuan, F., et al. (2014). Geochemistry of the Huangshandong Ni–Cu deposit in northwestern China: implications for the formation of magmatic sulfide mineralization in orogenic belts. *Ore Geol. Rev.* 56, 181–198. doi: 10.1016/j.oregeorev.2013.08.012
- Deng, Y. F., Song, X. Y., Hollings, P., Zhou, T. F., Yuan, F., Chen, L. M., et al. (2015). Role of asthenosphere and lithosphere in the genesis of the Early Permian Huangshan mafic-ultramafic intrusion in the Northern Tianshan, NW China. *Lithos* 227, 241–254. doi: 10.1016/j.lithos.2015.04.014
- Deng, Y. F., Song, X. Y., Jie, W., Cheng, S. L., and Li, J. (2011b). Petrogenesis of the Huangshandong Ni–Cu sulfide-bearing mafic-ultramafic intrusion, northern Tianshan, Xinjiang: evidence from major and trace elements and Sr–Nd isotope. *Acta Geol. Sin.* 85, 1435–1451.
- Deng, Y. F., Song, X. Y., Jie, W., Yang, F., Zhao, Z. M., Wei, S., et al. (2021). Determination of sedimentary ages of strata in the Huangshan-Jingerquan mineralization belt and its geological significance. *Acta Geol. Sin.* 95, 362–376.
- Du, L., Long, X. P., Yuan, C., Zhang, Y. Y., Huang, Z. Y., Sun, M., et al. (2018). Early Paleozoic dioritic and granitic plutons in the Eastern Tianshan Orogenic Belt, NW China: constraints on the initiation of a magmatic arc in the southern Central Asian Orogenic Belt. *J. Asian Earth Sci.* 153, 139–153. doi: 10.1016/j.jseas.2017.03.026
- Du, L., Zhang, Y. Y., Huang, Z. Y., Li, X. P., Yuan, C., Wu, B., et al. (2019). Devonian to carboniferous tectonic evolution of the Kanggou Ocean in the Eastern Tianshan, NW China: insights from three episodes of granitoids. *Lithos* 35, 1–11. doi: 10.1016/j.lithos.2019.105243
- Feng, Y. Q., Qian, Z. Z., Duan, J., Xu, G., Ren, M., and Jiang, C. (2018). Geochronological and geochemical study of the Baixintan magmatic Ni–Cu sulphide deposit: new implications for the exploration potential in the western part of the East Tianshan nickel belt (NW China). *Ore Geol. Rev.* 95, 366–381. doi: 10.1016/j.oregeorev.2018.02.023
- Gao, J. F., Zhou, M. F., Lightfoot, P. C., Wang, C. Y., and Qi, L. (2012). Origin of PGE–poor and Cu–rich magmatic sulfides from the Kalatongke deposit, Xinjiang, Northwest China. *Econ. Geol.* 107, 481–506. doi: 10.2113/econgeo.107.3.481
- Gao, J. F., Zhou, M. F., Lightfoot, P. C., Wang, C. Y., Qi, L., and Sun, M. (2013). Sulfide saturation and magma emplacement in the formation of the Permian Huangshandong Ni–Cu sulfide deposit, Xinjiang, NW China. *Econ. Geol.* 108, 1833–1848. doi: 10.2113/econgeo.108.8.1833
- Gu, L. X., Zhang, Z. Z., Wang, Y. X., Tang, J. H., Wang, C. S., Xi, A. H., et al. (2006). Some problems on granites and vertical growth of the continental crust in the eastern Tianshan Mountains, NW China. *Acta Petrol. Sin.* 22, 1103–1120.
- Han, B. F., Ji, J. Q., Song, B., Chen, L. H., and Li, Z. H. (2004). SHRIMP zircon U–Pb ages of the Kalatongke and Huangshan East mafic complexes and their geological significance. *Sci. Bull.* 22, 2324–2328. doi: 10.1360/04wd0163
- Han, J. S., Chen, H. Y., Jiang, H. J., Zhao, L. D., Zhang, W. F., and Lai, C. (2019). Genesis of the Paleozoic Aqishan–Yamansu arc–basin system and Fe (–Cu) mineralization in the Eastern Tianshan, NW China. *Ore Geol. Rev.* 105, 55–70. doi: 10.1016/j.oregeorev.2018.12.012
- Haughton, D. R., Roeder, P. L., and Skinner, B. J. (1974). Solubility of sulfur in mafic magmas. *Econ. Geol.* 69, 451–467. doi: 10.2113/gsecongeo.69.4.451
- Helmy, H. M., and El Mahallawi, M. M. (2003). Gabbro Akarem mafic-ultramafic complex, Eastern Desert, Egypt: a late Precambrian analogue of Alaskan-type complexes. *Mineral. Petrol.* 77, 85–108. doi: 10.1007/s00710-001-0185-9
- Hou, K. J., Li, Y. H., Zou, T. R., Qu, X. M., Shi, Y. R., and Xie, G. Q. (2007). Laser ablation-MC-ICP-MS technique for Hf isotope microanalysis of zircon and its geological applications. *Acta Petrol. Sin.* 23, 2595–2604. doi: 10.3969/j.issn.0371-5736.2013.02.017
- Hou, T., Zhang, Z. C., Santosh, M., Encarnacion, J., Zhu, J., and Luo, W. J. (2014). Geochronology and geochemistry of submarine volcanic rocks in the Yamansu iron deposit, Eastern Tianshan Mountains, NW China: constraints on the metallogenesis. *Ore Geol. Rev.* 56, 487–502. doi: 10.1016/j.oregeorev.2013.03.008
- Hu, K. B., Yao, S. Z., Qu, W. J., Du, A. D., and Ao, S. J. (2008). Re–Os isotopic analysis of the Hulu Cu–Ni sulfide deposit magmatic ore system, East Tianshan, Xinjiang, NW China. *Acta Petrol. Sin.* 24, 2359–2370.
- Irvine, T. N. (1974). Petrology of the Duke Island ultramafic complex southern Alaska. *Geol. Soc. Am. Memoir* 138:240. doi: 10.1130/mem138-p1
- Irvine, T. N. (1975). Crystallization sequences in the Muskox intrusion and other layered intrusions; II, Origin of chromitite layers and similar deposits of other magmatic ores. *Geochim.; Cosmochim. Acta* 39, 991–1020. doi: 10.1016/B978-0-08-019954-2.50022-6
- Irvine, T. N., Keith, D. W., and Todd, S. G. (1983). The J–M platinum–palladium reef of the Stillwater Complex, Montana: II, Origin by double diffusive convective magma mixing and implications for the Bushveld complex. *Econ. Geol.* 78, 1287–1334. doi: 10.2113/gsecongeo.78.7.1287
- Jiao, J. G., Tang, Z. L., Qian, Z. Z., Sun, T., Duan, J., and Jiang, C. (2012). Genesis and metallogenic process of Tulargen large scale Cu–Ni sulfide deposit in eastern Tianshan area, Xinjiang. *Acta Petrol. Sin.* 28, 3772–3786.
- Keays, R. R. (1995). The role of komatiitic and picritic magmatism and S–saturation in the formation of ore deposits. *Lithos* 34, 1–18. doi: 10.1016/0024-4937(95)90003-9
- Lambert, D. D., Foster, J. G., Frick, L. R., Ripley, E. M., and Zientek, M. L. (1998). Geodynamics of magmatic Cu–Ni–PGE sulfide deposits: new insights from the Re–Os isotopic system. *Econ. Geol.* 93, 121–137. doi: 10.2113/gsecongeo.93.2.121
- Leshner, C. M., and Campbell, I. H. (1993). Geochemical and fluid dynamic controls on the composition of Komatiite-hosted nickel sulfide ores in Western Australia. *Econ. Geol.* 88, 804–816.
- Li, C., and Ripley, E. M. (2005). Empirical equations to predict the sulfur content of mafic magmas at sulfide saturation and applications to magmatic sulfide deposits. *Miner. Depos.* 40, 218–230. doi: 10.1007/s00126-005-0478-8
- Li, D. H., and Tian, J. T. (2018). Geological characteristics and Lithochemical features of Lubei Cu–Ni deposit, eastern Tianshan. *Xinjiang Geol.* 36, 423–428.
- Li, P., Zhao, T. Y., Zhu, Z. X., Tian, J. T., and Li, D. H. (2018). First report of Zircon U–Pb ages from Lubei Cu–Ni Sulfide deposit in East Tianshan of central Asian Orogenic Belt (NW China). *Acta Geol. Sin. (Eng. Edition)* 92, 855–856. doi: 10.1111/1755-6724.13559
- Li, W. Q., Ma, H. D., Wang, R., Wang, H., and Xia, B. (2008). SHRIMP dating and Nd–Sr isotopic tracing of Kangguertage ophiolite in eastern Tianshan, Xinjiang. *Acta Petrol. Sin.* 24, 773–780. doi: 10.1016/j.sedgeo.2008.03.004
- Lightfoot, P. C., and Hawkesworth, C. J. (1997). “Flood basalts and magmatic Ni, Cu and PGE sulphide mineralization: comparative geochemistry of the Noril’sk (Siberian Trap) and West Greenland Sequences,” in *Large Igneous Province*, eds J. J. Mahoney and M. F. Coffin (Washington DC: American Geophysical Union), 357–380. doi: 10.1029/GM100p0357
- Lightfoot, P. C., Keays, R. R., Evans-Lamswood, D., and Wheeler, R. (2012). S saturation history of Nain Plutonic Suite mafic intrusions: origin of the Voisey’s Bay Ni–Cu–Co sulfide deposit, Labrador, Canada. *Miner. Depos.* 47, 23–50. doi: 10.1007/s00126-011-0347-6
- Lin, Y., Tang, Q. Y., Zhang, M. J., Jiao, J. G., Chen, S. T., and Hu, X. (2014). Magmatism and dynamic settings of Permian mafic dyke swarms in the northern of Xinjiang. *J. Earth Sci. Environ.* 36, 73–82.

- Liu, B., Wu, J. H., Li, H., Mathur, R., Wu, Q. H., Zheng, H., et al. (2020). Late Paleozoic tectonic evolution of the Kangguer Shear Zone and Yamansu Arc Belt, Eastern Tianshan (NW China): constraints from structure, petrogenesis and geochronology of granitoids. *Lithos* 380–381. doi: 10.1016/j.lithos.2020.105821
- Long, L. L., Wang, J. B., Wang, Y. W., Deng, X. H., Mao, Q. G., Sun, Y., et al. (2019). Metallogenic regularity and metallogenic model of the paleo arc-basin system in eastern Tianshan. *Acta Petrol. Sin.* 35, 3161–3188. doi: 10.18654/1000-0569/2019.10.13
- Long, X. P., Wu, B., Sun, M., Yuan, C., Xiao, W. J., and Zuo, R. (2020). Geochronology and geochemistry of Late Carboniferous dykes in the AqishaneYamansu belt, eastern Tianshan: evidence for a post-collisional slab breakoff. *Geosci. Front.* 11, 347–362. doi: 10.1016/j.gsf.2019.06.003
- Ludwig, K. R. (2003). *User's Manual for Isoplot/Ex. Version 3.00: A Geochronological Toolkit for Microsoft Excel*. Berkeley, CA: Berkeley Geochronology Center Special Publication, 1–77.
- Maier, W. D., Li, C., and De Waal, S. A. (2001). Why are there no major Ni–Cu sulfide deposits in large layered mafic–ultramafic intrusions? *Can. Miner.* 39, 547–556. doi: 10.2113/gscanmin.39.2.547
- Mao, J. W., Pirajno, F., Zhang, Z. H., Chai, F. M., Wu, H., Chen, S. P., et al. (2008). A review of the Cu–Ni sulfide deposits in the Chinese Tianshan and Altay orogens (Xinjiang Autonomous Region, NW China): principal characteristics and ore-forming processes. *J. Asian Earth Sci.* 32, 184–203. doi: 10.1016/j.jseas.2007.10.006
- Mao, J. W., Pirajno, F., Zhang, Z. H., Chai, F. M., Yang, J. M., Wu, H., et al. (2006a). Late Variscan Post-collisional Cu–Ni Sulfide deposits in East Tianshan and Altay in China: principal characteristics and possible relationship with mantle plume. *Acta Geol. Sin.* 80, 925–942. doi: 10.1016/S1001-8042(06)60011-0
- Mao, Q. G., Xiao, W. J., Han, C. M., Sun, M., Yan, Z., Yong, Y., et al. (2006b). Zircon U–Pb age and the geochemistry of the Baishiquan mafic–ultramafic complex in the Eastern Tianshan, Xinjiang province: constraints on the closure of the Paleo–Asian Ocean. *Acta Petrol. Sin.* 22, 153–162. doi: 10.1016/j.sedgeo.2005.10.007
- Mao, Y. J., Qin, K. Z., Barnes, S. J., Tang, D. M., Xue, S. C., and Vaillant, M. L. (2017). Genesis of the Huangshannan high–Ni tenor magmatic sulfide deposit in the eastern Tianshan, Northwest China: constraints from PGE geochemistry and Os–S isotopes. *Ore Geol. Rev.* 90, 591–606. doi: 10.1016/j.oregeorev.2017.05.015
- Mao, Y. J., Qin, K. Z., Tang, D. M., Feng, H. Y., and Xue, S. C. (2016). Crustal contamination and sulfide immiscibility history of the Permian Huangshannan magmatic Ni–Cu sulfide deposit, East Tianshan, NW China. *J. Asian Earth Sci.* 129, 22–37. doi: 10.1016/j.jseas.2016.07.028
- Mavrogenes, J. A., and O'Neill, H. C. (1999). The relative effects of pressure, temperature and oxygen fugacity on the solubility of sulfide in mafic magmas. *Geochim. Cosmochim. Acta* 639, 1173–1180. doi: 10.1016/S0016-7037(98)00289-0
- Muhtar, M. N., Wu, C. Z., Brzozowski, M. J., Li, P., Yuan, X. C., Wang, S. M., et al. (2020a). Geochronology, geochemistry, and Sr–Nd–Pb–Hf–S isotopes of the wall rocks of the Kanggur gold polymetallic deposit, Chinese North Tianshan: implications for petrogenesis and sources of ore-forming materials. *Ore Geol. Rev.* 125:103688. doi: 10.1016/j.oregeorev.2020.103688
- Muhtar, M. N., Wu, C. Z., Santosh, M., Lei, R. X., Gu, L. X., Wang, S. M., et al. (2020b). Late Paleozoic tectonic transition from subduction to post-collisional extension in Eastern Tianshan, Central Asian Orogenic Belt. *Geol. Soc. Am. Bull.* 132, 1756–1774. doi: 10.1130/B35432.1
- Naldrett, A. J. (1999). World-class Ni–Cu–PGE deposits: key factors in their genesis. *Miner. Depos.* 34, 227–240. doi: 10.1007/s001260050200
- Naldrett, A. J. (2010). Secular variation of magmatic sulfide deposits and their source magmas. *Econ. Geol.* 105, 669–688. doi: 10.2113/gsecongeo.105.3.669
- Naldrett, A. J. (2004). *Magmatic Sulfide Deposits: Geology, Geochemistry and Exploration*. Berlin: Springer, 1–727.
- Naldrett, A. J. (2009). “Fundamentals of magmatic sulfide deposits,” in *New Developments in Magmatic Ni–Cu and PGE Deposits*, eds C. Li and E. M. Ripley (Beijing: Geological Publishing House), 1–26.
- Ohmoto, H. (1986). “Stable isotope geochemistry of ore deposits,” in *Stable isotopes in high temperature geological processes. Review in Mineralogy and Geochemistry*, 16, eds J. W. Valley, H. P. Taylor, and J. R. O'Neil (Berlin: De Gruyter), 491–559.
- Pirajno, F., Mao, J. W., Zhang, Z. C., Zhang, Z. H., and Chai, F. M. (2008). The association of mafic–ultramafic intrusions and A-type magmatism in the Tianshan and Altay orogens, NW China: implications for geodynamic evolution and potential for the discovery of new ore deposits. *J. Asian Earth Sci.* 32, 165–183. doi: 10.1016/j.jseas.2007.10.012
- Qin, K. Z., Su, B. X., Sakyi, P. A., Tang, D. M., Li, X. H., Sun, H., et al. (2011). SIMS zircon U–Pb geochronology and Sr–Nd isotopes of Ni–Cu–bearing mafic–ultramafic intrusions in eastern Tianshan and Beishan in correlation with flood basalts in Tarim Basin (NW China): constraints on a ca. 280 Ma mantle plume. *Am. J. Sci.* 311, 237–260. doi: 10.2475/03.20.11.03
- Qin, K. Z., Tang, D. M., Su, B. X., Mao, Y. J., Xue, S. C., Tian, Y., et al. (2012). The tectonic setting, style, basic feature, relative erosion degree, ore-bearing evaluation sign, potential analysis of mineralization of Cu–Ni–bearing Permian mafic–ultramafic complexes, northern Xinjiang. *Northwest. Geol.* 45, 83–116.
- Ripley, E. M., Lightfoot, P. C., Li, C., and Elswick, E. R. (2003). Sulfur isotopic studies of continental flood in the Noril'sk region: implications for the association between lavas and ore-bearing intrusions. *Geochim. Cosmochim. Acta* 67, 2805–2817. doi: 10.1016/S0016-7037(03)00102-9
- Rudnick, R. L., and Gao, S. (2011). “Composition of the continental crust,” in *Treatise on Geochemistry*, v.3: *the Crust*, ed. R. L. Rudnick (Amsterdam: Elsevier), 1–64.
- San, J. Z., Qin, K. Z., Tang, Z. L., Tang, D. M., Su, B. X., Sun, H., et al. (2010). Precise zircon U–Pb age dating of two mafic–ultramafic complexes at Tulargen large Cu–Ni district and its geological implications. *Acta Petrol. Sin.* 26, 3027–3035.
- Su, B. X., Qin, K. Z., Santosh, M., Sun, H., and Tang, D. M. (2013a). The Early Permian mafic–ultramafic complexes in the Beishan Terrane, NW China: alaskan-type intrusives or rift cumulates? *J. Asian Earth Sci.* 66, 175–187. doi: 10.1016/j.jseas.2012.12.039
- Su, B. X., Qin, K. Z., Tang, D. M., Sakyi, P. A., Liu, P. P., Sun, H., et al. (2013b). Late Paleozoic mafic–ultramafic intrusions in southern Central Asian Orogenic Belt (NW China): insight into magmatic Ni–Cu sulfide mineralization in orogenic setting. *Ore Geol. Rev.* 51, 57–73. doi: 10.1016/j.oregeorev.2012.11.007
- Su, S. G., Tang, Z. L., Luo, Z. H., Deng, J. F., Wu, G. Y., Zhou, M. F., et al. (2014). Magmatic conduit metallogenic system. *Acta Petrol. Sin.* 30, 3120–3130.
- Sun, M., Wang, Y. H., Zhang, F. F., Lin, S. Y., Xue, C. J., Liu, J. J., et al. (2020). Petrogenesis of Late Carboniferous intrusions in the Linglong area of Eastern Tianshan, NW China, and tectonic implications: Geochronological, geochemical, and zircon Hf–O isotopic constraints. *Ore Geol. Rev.* 120:103462. doi: 10.1016/j.oregeorev.2020.103462
- Sun, S. S., and McDonough, W. F. (1989). “Chemical and isotopic systematics of oceanic basalt: implications for mantle composition and processes,” in *Magmatism in the Ocean Basins*, Vol. 42, eds A. D. Saunders and M. J. Norry (London: Geological Society), 313–345.
- Sun, T., Qian, Z. Z., Deng, Y. F., Li, C., Song, X. Y., and Tang, Q. Y. (2013a). PGE and Isotope (Hf–Sr–Nd–Pb) constraints on the origin of the Huangshandong magmatic Ni–Cu sulfide deposit in the Central Asian Orogenic Belt, Northwestern China. *Econ. Geol.* 108, 1849–1864. doi: 10.2113/econgeo.108.8.1849
- Sun, T., Qian, Z. Z., Li, C. S., Xia, M. Z., and Yang, S. H. (2013b). Petrogenesis and economic potential of the Erhongwa mafic–ultramafic intrusion in the Central Asian Orogenic Belt, NW China: constraints from olivine chemistry, U–Pb age and Hf isotopes of zircons, and whole-rock Sr–Nd–Pb isotopes. *Lithos* 182–183, 185–199. doi: 10.1016/j.lithos.2013.10.004
- Sun, T., Qian, Z. Z., Tang, Z. L., Jiang, C. Y., He, K., Sun, Y. L., et al. (2010). Zircon U–Pb chronology, platinum group element geochemistry characteristics of Hulu Cu–Ni deposit, East Xinjiang, and its geological significance. *Acta Petrol. Sin.* 26, 3339–3349.
- Sun, Y., Wang, J. B., Li, Y. C., Wang, Y. W., Yu, M. J., Long, L. L., et al. (2018). Recognition of Late Ordovician Yudai porphyry Cu (Au, Mo) mineralization in the Kalatag district, Eastern Tianshan terrane, NW China: constraints from geology, geochronology, and petrology. *Ore Geol. Rev.* 100, 220–236. doi: 10.1016/j.oregeorev.2017.07.011
- Sun, Y., Wang, J. B., Lv, X. P., Yu, M. J., Li, Y. C., Mao, Q. G., et al. (2019). Geochronology, petrogenesis and tectonic implications of the newly discovered Cu–Ni sulfide–mineralized Yueyawan gabbroic complex, Kalatag district, northwestern Eastern Tianshan, NW China. *Ore Geol. Rev.* 109, 598–614. doi: 10.1016/j.oregeorev.2019.05.009

- Tang, D. M., Qin, K. Z., Li, C., Qi, L., Su, B. X., and Qu, W. J. (2011). Zircon dating, Hf-Sr-Nd-Os isotopes and PGE geochemistry of the Tianyu sulfide-bearing mafic-ultramafic intrusion in the Central Asian orogenic belt, NW China. *Lithos* 126, 84–98. doi: 10.1016/j.lithos.2011.06.007
- Taylor, S. R., and McLennan, S. M. (1985). *The Continental Crust: Its Composition and Evolution*. London: Blackwell Scientific Publications, 1–312.
- Wang, X. S., Gao, J., Klemm, R., Jiang, T., Li, J. L., Zhang, X., et al. (2017). The Central Tianshan Block: A microcontinent with a Neoproterozoic-Paleoproterozoic basement in the southwestern Central Asian Orogenic Belt. *Precambrian Res.* 295, 130–150. doi: 10.1016/j.precamres.2017.03.030
- Wang, Y. H., Xue, C. J., Zhang, F. F., Liu, J. J., Gao, J. B., and Qi, T. J. (2015b). SHRIMP zircon U-Pb geochronology, geochemistry and H-O-Si-S-Pb isotope systematics of the Kanggur gold deposit in Eastern Tianshan, NW China: implication for ore genesis. *Ore Geol. Rev.* 68, 1–13. doi: 10.1016/j.oregeorev.2015.01.009
- Wang, Y. H., Zhang, F. F., Liu, J. J., and Que, C. Y. (2016). Genesis of the Fuxing porphyry Cu deposit in Eastern Tianshan, China: evidence from fluid inclusions and C-H-O-S-Pb isotope systematics. *Ore Geol. Rev.* 79, 46–61. doi: 10.1016/j.oregeorev.2016.04.022
- Wang, Y. L., Zhang, Z. W., You, M. X., Li, X., Li, K., and Wang, B. L. (2015a). Chronological and geochemical characteristics of the Baixintan Ni-Cu deposit in Eastern Tianshan Mountains, Xinjiang, and their implications for Ni-Cu mineralization. *Geol. China* 42, 452–467.
- Wu, C. Z., Xie, S. W., Gu, L. X., Samson, I. M., Yang, T., Lei, R. X., et al. (2018). Shear zone-controlled post-magmatic ore formation in the Huangshandong Ni-Cu sulfide deposit, NW China. *Ore Geol. Rev.* 100, 545–560. doi: 10.1016/j.oregeorev.2017.02.015
- Wu, H., Li, H. Q., Mo, X. H., Chen, F. W., Lu, Y. F., Mei, Y. P., et al. (2005). Age of the Baishiquan mafic-ultramafic complex, Hami, Xinjiang and its geological significance. *Acta Geol. Sin.* 79, 498–502.
- Xia, L. Q., Li, X. M., Xia, Z. C., Xu, X. Y., Ma, Z. P., and Wang, L. S. (2006). Carboniferous-permian rift-related volcanism and mantle plume in the Tianshan, northwestern China. *Northwest. Geol.* 39, 1–49.
- Xia, M. Z. (2009). *The Mafic-ultramafic Intrusions in the Huangshan Region Eastern Tianshan, Xinjiang: Petrogenesis and Mineralization Implication*. Doctor's thesis. Xi'an: Chang'an University.
- Xia, M. Z., Jiang, C. Y., Qian, Z. Z., Xia, Z. D., Wang, B. Y., and Sun, T. (2010). Geochemistry and petrogenesis of Huangshandong intrusion, East Tianshan, Xinjiang. *Acta Petrol. Sin.* 26, 2413–2430. doi: 10.1016/j.sedgeo.2010.06.014
- Xiao, B., Chen, H. Y., Hollings, P., Han, J. S., Wang, Y. F., Yang, J. T., et al. (2017). Magmatic evolution of the Tuwu-Yandong porphyry Cu belt, NW China: constraints from geochronology, geochemistry and Sr-Nd-Hf isotopes. *Gondwana Res.* 43, 74–91. doi: 10.1016/j.gr.2015.09.003
- Xiao, W. J., Zhang, L. C., Qin, K. Z., Sun, S., and Li, J. L. (2004). Paleozoic accretionary and collisional tectonics of the eastern Tianshan (China): implication for the continental growth of central Asia. *Am. J. Sci.* 304, 370–395. doi: 10.2475/ajs.304.4.370
- Xue, S. C., Qin, K. Z., Li, C., Tang, D. M., Mao, Y. J., Qi, L., et al. (2016). Geochronological, petrological and geochemical constraints on Ni-Cu sulfide mineralization in the Poyi ultramafic-troctolitic intrusion in the NE rim of Tarim Craton, Western China. *Econ. Geol.* 111, 1465–1484. doi: 10.2113/econgeo.111.6.1465
- Yang, W. Z., Ren, Y., Tian, J. T., She, J. Z., and Yang, G. G. (2017). The discovery of Lubei Cu-Ni Sulfide deposit in Eastern Tianshan, NW China and its significant. *Bull. Miner. Petrol. Geochem.* 36, 112–120. doi: 10.3969/j.issn.1007-2802.2017.01.013
- Deng, Y. F., Yuan, F., Hollings, P., Song, X. Y., Zhou, T. F., Fu, B., et al. (2020). Magma generation and sulfide saturation of Permian mafic-ultramafic intrusions from the western part of the Northern Tianshan in NW China: implications for Ni-Cu mineralization. *Miner. Depos.* 55, 515–534. doi: 10.1007/s00126-019-00890-8
- Zhang, J. W., Zhang, Z. W., Li, W. Y., Xie, D. S., Gao, Y. B., Wang, Y. L., et al. (2012). Chronology and geochemistry of jingbulake complex containing Cu-Ni mineralization, West Tianshan Mountain, NW China. *Northwest. Geol.* 45, 302–313. doi: 10.1007/s11783-011-0280-z
- Zhang, M. J., Li, C., Fu, P. E., Hu, P. Q., and Ripley, E. M. (2011). The Permian Huangshanxi Cu-Ni deposit in western China: intrusive-extrusive association, ore genesis, and exploration implications. *Miner. Depos.* 46, 153–170. doi: 10.1007/s00126-010-0318-3
- Zhang, M. J., Tang, Q. Y., Cao, C. H., Li, W. Y., Wang, H., Li, Z. P., et al. (2017). The origin of Permian Pobei ultramafic complex in the northeastern Tarim craton, western China: evidences from chemical and C-He-Ne-Ar isotopic compositions of volatiles. *Chem. Geol.* 469, 85–96. doi: 10.1016/j.chemgeo.2017.06.006
- Zhang, W. F., Chen, H. Y., Peng, L. H., Zhao, L. D., Lu, W. J., Zhang, Z. J., et al. (2018). Ore genesis of the Duotoushan Fe-Cu deposit, Eastern Tianshan, NW China: constraints from ore geology, mineral geochemistry, fluid inclusion and stable isotopes. *Ore Geol. Rev.* 100, 401–421. doi: 10.1016/j.oregeorev.2017.02.021
- Zhang, Z. C., Yan, S. H., Chen, B., He, L. X., He, Y. S., and Zhou, G. (2003). Geochemistry of the Kalatongke basic complex in Xinjiang and its constraints on genesis of the deposit. *Acta Petrol. Miner.* 22, 217–224.
- Zhang, Z. H., Chai, F. M., Du, A. D., Zhang, Z. C., Yan, S. H., Yang, J. M., et al. (2005). Re-Os dating and ore-forming material tracing of the Karatungku Cu-Ni sulfide deposit in northern Xinjiang. *Acta Petrol. Miner.* 24, 285–293. doi: 10.1360/gso50303
- Zhao, B. B., Deng, Y. F., Zhou, T. F., Yuan, F., Zhang, D. Y., Deng, G., et al. (2018). Petrogenesis of the baixintan Ni-Cu sulfide-bearing mafic-ultramafic intrusion, East Tianshan: evidence from geochronology, petrogeochemistry and Sr-Nd isotope. *Acta Petrol. Sin.* 34, 2733–2753.
- Zhao, L. D., Chen, H. Y., Hollings, P., and Han, J. S. (2019). Late Paleozoic magmatism and metallogenesis in the Aqishan-Yamansu belt, Eastern Tianshan: constraints from the Bailingshan intrusive complex. *Gondwana Res.* 65, 68–85. doi: 10.1016/j.gr.2018.08.004
- Zhao, L. D., Chen, H. Y., Zhang, L., Xia, X. P., Zhang, W. F., Li, D. F., et al. (2017). Geology and ore genesis of the late Paleozoic Heijianshan Fe oxide-Cu (-Au) deposit in the Eastern Tianshan, NW China. *Ore Geol. Rev.* 91, 110–132. doi: 10.1016/j.oregeorev.2017.10.014
- Zhao, Y., Xue, C. J., Zhao, X. B., Yang, Y. Q., and Ke, J. J. (2015). Magmatic Cu-Ni sulfide mineralization of the Huangshannan mafic-ultramafic intrusion, Eastern Tianshan, China. *J. Asian Earth Sci.* 105, 155–172. doi: 10.1016/j.jseae.2015.03.031
- Zhao, Y., Yang, Y. Q., and Ke, J. J. (2016). Origin of Cu- and Ni-bearing magma and sulfide saturation mechanism: a case study of Sr-Nd-Pb-S isotopic composition and element geochemistry on the Huangshannan magmatic Ni-Cu sulfide deposit, Xinjiang. *Acta Petrol. Sin.* 32, 2086–2098.
- Zhou, M. F., Leshar, C. M., Yang, Z. X., Li, J. W., and Sun, M. (2004). Geochemistry and petrogenesis of 270 Ma Ni-Cu-(PGE) sulfide-bearing mafic intrusions in the Huangshan district, Eastern Xinjiang, Northwest China: implications for the tectonic evolution of the Central Asian orogenic belt. *Chem. Geol.* 209, 233–257. doi: 10.1016/j.chemgeo.2004.05.005
- Zhou, T. F., Yuan, F., Zhang, D. Y., Fan, Y., Liu, S., Peng, M. X., et al. (2010). Geochronology, tectonic setting and mineralization of granitoids in Jueluotage area, eastern Tianshan, Xinjiang. *Acta Petrol. Sin.* 26, 478–502.

Conflict of Interest: The authors declare that the research was conducted in the absence of any commercial or financial relationships that could be construed as a potential conflict of interest.

Copyright © 2021 Li, Liang, Feng, Zhao, Tian, Li, Li, Chen and Wu. This is an open-access article distributed under the terms of the Creative Commons Attribution License (CC BY). The use, distribution or reproduction in other forums is permitted, provided the original author(s) and the copyright owner(s) are credited and that the original publication in this journal is cited, in accordance with accepted academic practice. No use, distribution or reproduction is permitted which does not comply with these terms.



Compositional Variation of Amphiboles During Magma Mixing: A Case Study of Huangyangshan A-Type Granite in Kalamaili Metallogenic Belt, East Junggar, China

Chenyang Ye^{1,2,3,4,5}, Yonggang Feng^{1,2*}, Ruxiong Lei^{1,2} and Gaoxue Yang^{1,2}

¹ School of Earth Science and Resources, Chang'an University, Xi'an, China, ² Laboratory of Mineralization and Dynamics, Chang'an University, Xi'an, China, ³ State Key Laboratory of Lithospheric Evolution, Institute of Geology and Geophysics, Chinese Academy of Sciences, Beijing, China, ⁴ College of Earth and Planetary Sciences, University of Chinese Academy of Sciences, Beijing, China, ⁵ Innovation Academy for Earth Science, Chinese Academy of Sciences, Beijing, China

OPEN ACCESS

Edited by:

Xiaohua Deng,
Beijing Institute of Geology for Mineral
Resources, China

Reviewed by:

Huan Li,
Central South University, China
Fuquan Yang,
Chinese Academy of Geological
Sciences (CAGS), China
Ewa Slaby,
Institute of Geological Sciences,
Polish Academy of Sciences, Poland

*Correspondence:

Yonggang Feng
ygfeng@chd.edu.cn

Specialty section:

This article was submitted to
Economic Geology,
a section of the journal
Frontiers in Earth Science

Received: 06 January 2021

Accepted: 29 March 2021

Published: 16 April 2021

Citation:

Ye C, Feng Y, Lei R and Yang G
(2021) Compositional Variation
of Amphiboles During Magma Mixing:
A Case Study of Huangyangshan
A-Type Granite in Kalamaili
Metallogenic Belt, East Junggar,
China. *Front. Earth Sci.* 9:650014.
doi: 10.3389/feart.2021.650014

The Huangyangshan A-type granitic pluton, distributed along the thrust fault in the Kalamaili region of East Junggar, Xinjiang, China, consists of alkaline granite containing abundant dioritic enclaves that formed via magma mixing. Both the host granite and the enclaves contain sodic amphiboles. The textural evidence indicates that amphiboles crystallized as a magmatic phase in both units. We determined major and trace element contents of amphiboles from both units to investigate the compositional variation of the amphiboles during the magma mixing process. The results show that cations of W- and C-site are influenced by chemical compositions of the magma whereas cations of A-, B- and T-site and Al^{3+} are controlled by crystal structure. Therefore, the variations of W- and C-site cations can reflect magma evolution. The core and rim of the amphiboles show similar trace element patterns, which also suggests that the amphiboles are late-stage phases. Furthermore, the amphibole-only thermometers yield reasonable estimates that are consistent with petrographic evidence. However, thermometers based on partition coefficients and all the currently available amphibole-based barometers that rely on Al contents or D_{Al} cannot be applied to Fe-rich and Al-poor amphiboles.

Keywords: amphibole, A-type granite, dioritic enclave, magma mixing, Sn mineralization, Huangyangshan

INTRODUCTION

Magma mixing is a common magmatic process during formation of granitoids (Kumar et al., 2004; Liu et al., 2013; Xiong et al., 2020). Previous studies suggest that magma mixing can be important for formation of critical metal deposits (e.g., Ma et al., 2013). If mafic magma injects into felsic magma during magma mixing, microgranular mafic enclaves (MMEs) would likely form. During this process, amphiboles are usually the major rock-forming minerals.

The amphibole-group are complex in chemical composition but share a general chemical formula expressed as $AB_2C_5T_8O_{22}W_2$, where A, B, C, and T represent different crystal sites (Leake et al., 1997). The T site is commonly occupied by Si^{4+} , Al^{3+} , Ti^{4+} , and the like and is tetrahedrally coordinated, forming a double chain of tetrahedra. The A site occurs in the center of space between the double-chains of the structure. The C site is octahedrally coordinated and occupied by cations including Mg^{2+} , Fe^{2+} , Mn^{2+} , Al^{3+} , Fe^{3+} , Mn^{3+} , Ti^{4+} , etc. Cations on the B-site situate at the periphery of the strip of the octahedra C-cations occupy. Anions including OH^- , F^- , Cl^- , and O^{2-} dominate the W-site. This complexity gives rise to a complicated classification for amphiboles (Hawthorne et al., 2012). Owing to the complexity, amphiboles are capable of accommodating a variety of elements with variable ionic charges and radii, including alkali elements, rare earth elements (REE), high field strength elements (HFSE), and large ion lithophile elements (LILE) (Siegel et al., 2017). Therefore, amphiboles are sensitive to chemical compositions of the crystallizing melts and may record some processes during magma evolution.

The Huangyangshan A-type granite located in the Kalamaili metallogenic belt, Xinjiang, is alkaline and contains abundant mafic microgranular enclaves (MMEs) (Yang et al., 2011). The reported ages for both units were 311–305 Ma and 300 ± 6 Ma, respectively (Su et al., 2008; Yang et al., 2011). The consistent ages along with the gradational contact between the host granite and MMEs and the presence of acicular apatite indicate magma mixing during the formation of the Huangyangshan A-type granite (Yang et al., 2009, 2010, 2011). In both units, Na-rich amphiboles are a common mineral phase. Therefore, in this paper, we choose amphiboles from the MMEs and their host granite to explore the compositional variations during magma mixing. Also, due to their sensitivity, amphiboles are potential geo-thermometer and barometer. For this reason, we tested whether they could yield proper estimates on the crystallization temperature and pressure of the amphiboles in the Huangyangshan A-type granite.

GEOLOGICAL SETTING

The Huangyangshan A-type granite, distributed along the Kalamaili thrust fault, is situated in the central part of the Kalamaili region in East Junggar, Xinjiang (Figure 1). This region represents the northern margin of East Junggar, part of the Junggar terrane that belongs to the Central Asian Orogenic Belt (CAOB) (Sengor et al., 1993; Xiao et al., 2003). The NW-SE trending Huangyangshan A-type granite covers an area of ~ 230 km² and is intruded into the early Carboniferous strata, showing sharp contact (Yang et al., 2011). Contact metamorphism has also been observed, which implies shallow depth for emplacement (Yang et al., 2011). The granites consist of 40–55% alkali-feldspar, 5–15% plagioclase, 20–30% quartz, 5–10% mafic minerals (biotite and/or amphibole) and accessory minerals (< 1%) including apatite, zircon, and fluorite. Based on the content of mafic minerals, four main phases can be distinguished. A great number of MMEs

with variable sizes are present in the granite. The MMEs exhibit sharp to diffuse contact with their host granite and chilled margins or biotite-rich reaction rims are locally present (Figure 2), indicating hybridization between MMEs and host granites (e.g., Yang et al., 2010). These MMEs are dioritic in composition and composed of 5–15% amphibole, 20–30% alkali-feldspar, 30–40% plagioclase, 5% biotite, and < 1% acicular apatite.

The Kalamaili region defines an important metallogenic belt in the East Junggar terrane. According to previous studies, Au and Cu mineralization are mainly distributed at the margins of calcic-alkaline granitoids, whereas tin mineralization mainly occurs at the margins of alkaline granitoids including the Huangyangshan granite (Yang et al., 2011).

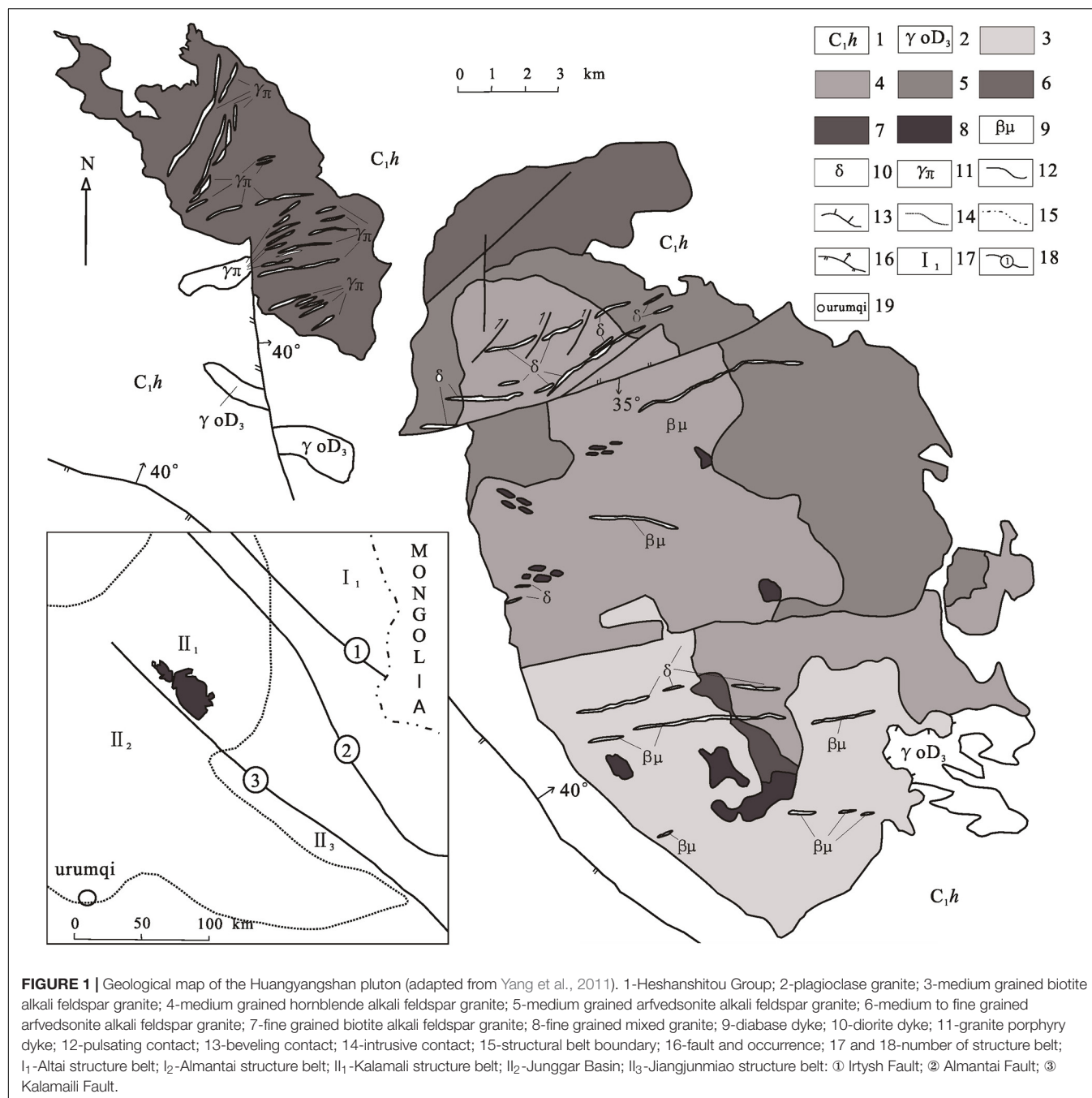
ANALYTICAL METHODS

Petrographic and Electron-Microprobe Analyses

Doubly polished thin sections were made for rock samples collected from the Huangyangshan granite and the hosted MMEs. Petrographic observations were performed using optical microscopy and scanning electron microscope (SEM). All polished thin sections were carbon-coated and major element contents of amphiboles were determined using a JEOL JXA-8100 electron microprobe (Tokyo, Japan) at the Laboratory of Mineralization and Dynamics, Chang'an University. During EPMA analysis, the accelerating voltage, sample current, and beam diameter were 15 kV, 10 nA, and 5 μ m, respectively. Fourteen elements in total were analyzed. The standards for calibrating element contents include: synthetic $MnTiO_3$ (for Mn K α), plagioclase (Na K α , Ca K α , and Al K α), magnetite (Fe K α), sanidine (K K α), zirconium metal (Zr L α), olivine (Mg K α and Si K α), synthetic Nb-Ta alloy (Nb L α and Ta L α), synthetic rutile (Ti K α), and fluorite (F K α). The analytical precision (expressed as relative standard deviation) for major element oxide contents > 1 wt.% are better than 3%. Summary of EPMA data for amphiboles is given in Table 1 and the complete EPMA dataset for amphiboles is presented in Supplementary Material S1.

Laser-Ablation ICP-MS Analysis

Trace elements of amphiboles were analyzed using a Photon Machines 193 nm excimer laser ablation system coupled with an Agilent 7700 ICP-MS (Santa Clara, CA, United States) at the Laboratory of Mineralization and Dynamics, Chang'an University. The analyzed elemental isotopes included 7Li , ^{27}Al , ^{29}Si , ^{35}Cl , ^{45}Sc , ^{49}Ti , ^{55}Mn , ^{63}Cu , ^{66}Zn , ^{69}Ga , ^{85}Rb , ^{88}Sr , ^{89}Y , ^{90}Zr , ^{93}Nb , ^{118}Sn , ^{137}Ba , ^{139}La , ^{140}Ce , ^{141}Pr , ^{146}Nd , ^{147}Sm , ^{153}Eu , ^{157}Gd , ^{159}Tb , ^{163}Dy , ^{165}Ho , ^{166}Er , ^{169}Tm , ^{172}Yb , ^{175}Lu , ^{177}Hf , ^{181}Ta , ^{206}Pb , ^{232}Th , and ^{238}U . Helium gas was used as the carrier gas. The diameter, energy density, and repetition rate of the laser beam were 35 μ m, 5.9 J/cm², and 8 Hz, respectively. For each analysis, signals on the gas background and samples or standards were collected for 10 s and 40 s, respectively. NIST SRM 610 and NIST SRM 612 were used as



the primary and secondary external standards, respectively. The LA-ICP-MS data were processed using Iolite v.3.71 (Paton et al., 2011) and the Si concentrations of the amphiboles obtained by EMPA was the internal standard for calculating trace element concentrations. The accuracy based on the test on NIST SRM 612 (expressed as relative difference between measured and reference values) was < 15% for most analyzed elements. The precision test on NIST SRM 612 indicated that the precision (expressed as relative standard deviation) was better than 10% for most analyzed elements except for Ti that showed analytical precision of 15.6%. The results are summarized in **Table 2** and

the complete dataset of trace element concentrations is provided in **Supplementary Material S2**.

RESULTS

Petrography

The granite mainly exhibits medium- to fine-grained texture and vermicular texture and mantling texture are locally present. The major rock-forming minerals are alkaline feldspar (mainly perthite) and quartz, with minor plagioclase (An₂₃ to An₂₉,



FIGURE 2 | Field photos of the enclaves in the Huangyangshan alkaline granite. **(a–c)** Both sharp and transitional boundaries exist indicating the rheology of magma during magma mixing. **(d)** Alkali feldspar of the host granites crosscuts the boundaries of the MME.

TABLE 1 | Major element contents of amphiboles from the host granite and enclaves.

Amphibole	Granite Mean (n = 13)	Enclaves Mean (n = 2)	Amphibole	Granite Mean (n = 13)	Enclaves Mean (n = 2)
Na ₂ O	7.00	9.17	Al ³⁺	0.16	0.05
FeO	31.11	27.07	Fe ³⁺	0.14	0.03
K ₂ O	1.44	0.38	Mn ²⁺	0.05	0.04
F	0.79	0.27	Fe ²⁺	4.17	3.64
MnO	0.35	0.30	Mg ²⁺	0.04	0.16
CaO	3.00	4.86	C-site	4.75	4.11
SiO ₂	48.83	50.90	Mn ²⁺	0.00	-
Ta ₂ O ₅	0.04	0.04	Fe ²⁺	0.00	-
ZrO ₂	0.07	0.57	Ca ²⁺	0.54	0.84
Al ₂ O ₃	1.11	0.25	Na ⁺	1.45	1.16
SnO ₂	0.00	0.01	B-site	2.00	2.00
MgO	0.16	0.65	Na ⁺	0.79	1.72
Nb ₂ O ₅	0.01	0.03	K ⁺	0.30	0.08
TiO ₂	1.63	1.26	A-site	1.09	1.80
Total	95.47	95.76	OH ⁻	1.09	1.56
Si	8.08	8.24	F ⁻	0.53	0.14
Al	0.05	—	O ²⁻	0.37	0.30
T-site	8.15	8.24	W-site	2.00	2.00
Ti	0.18	0.15	Fe#	0.97	0.99
Zr	0.01	0.05			

Fe# = Fe³⁺/(Fe²⁺ + Fe³⁺). The apfu values are calculated based on 24 oxygen atoms.

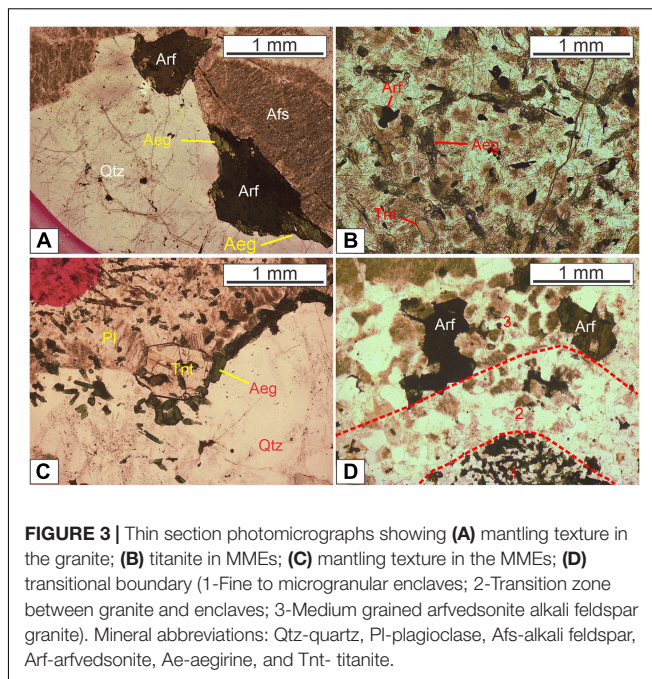
TABLE 2 | Average trace element concentrations (in ppm) of the amphiboles from the host granite and MMEs.

Comment	Granite		Enclaves	
	Core	Rim	Core	Rim
	Mean (n = 7)	Mean (n = 8)	Mean (n = 2)	Mean (n = 4)
Li	1627.0	1375.1	480.8	1155.7
Al	6758.7	7339.8	1621.3	1802.0
Cl	7795.7	762.8	2122.9	4466.3
Sc	8.3	13.2	13.4	7.8
Ti	10054.3	7797.8	7177.9	8312.5
Mn	3007.1	2767.4	2395.9	3183.1
Cu	18.8	8.6	20.0	48.7
Zn	3153.1	2611.0	1129.6	1774.4
Ga	10.4	11.0	4.9	3.8
Rb	16.3	15.5	4.5	28.7
Sr	30.3	14.9	28.6	42.4
Y	169.8	81.8	346.8	278.9
Zr	461.7	364.1	4154.1	2843.7
Nb	74.5	36.4	20.7	65.4
Sn	14.3	9.2	39.8	35.7
Ba	2.7	2.9	2.2	3.9
La	18.9	13.0	22.5	12.6
Ce	58.5	46.6	172.6	79.4
Pr	10.3	8.3	14.8	7.7
Nd	53.8	43.3	82.9	38.7
Sm	16.7	12.7	31.4	14.3
Eu	0.1	0.1	0.3	0.2
Gd	16.5	11.0	38.6	19.8
Tb	2.6	1.8	7.1	4.0
Dy	17.3	11.8	49.6	31.3
Ho	4.7	3.3	12.3	8.7
Er	21.4	15.8	44.6	36.5
Tm	5.6	4.3	9.2	8.1
Yb	64.1	48.4	80.2	71.6
Lu	13.8	10.8	14.4	12.7
Hf	15.3	13.6	113.7	73.3
Ta	0.9	0.6	0.6	1.6
Pb	17.9	25.1	17.3	17.8
Th	0.9	0.4	4.7	1.9
U	0.5	0.5	2.2	1.6

b,d, represent the element content is below detection limit.

oligoclase), biotite, and arfvedsonite (**Figure 3A**). Most aegirine occurs along the boundaries of amphibole grains in the host granite, indicating that arfvedsonite crystallize earlier than aegirine (**Figure 3A**), which may also imply the magma evolved toward more oxidized trend (Scaillet and MacDonald, 2001). The accessory minerals mainly include zircon, fluorite, and apatite. The presence of fluorite indicates that the granitic magma is likely F-saturated.

The MMEs mainly show subhedral granular texture and porphyritic texture and mantling texture locally occurs. Compared with the granite, the MMEs contain relatively abundant plagioclase and mafic minerals (mainly alkaline amphibole and aegirine), whereas the amounts of quartz and



alkali feldspar are less than those of the host granite. The accessory minerals in the MMEs include titanite, apatite, and zircon. Apatite shows an acicular habit (**Figure 3B**), indicating a quench process. The amphibole crystallizes in a shape with excessively long *c*-axis and is semi-oriented (**Figures 3B,C**), suggesting that MMEs remained their rheology to some extent during formation. Typical transitional zone (diffuse contact) between the MMEs and the host granite can be observed under microscope (**Figure 3D**). It is also noted that quartz is mantled by a mineral assemblage consisting of aegirine and titanite (**Figures 3C, 4a,b**). This texture is similar to quartz ocellus texture described in previous studies (e.g., Baxter and Feely, 2002; Renna et al., 2006). Back-scattered electron imaging shows that the early arfvedsonite is enclosed by the aegirine rimming the quartz xenocryst (**Figure 4b**). The replacement of arfvedsonite by aegirine can also be observed (**Figure 4c**), indicating that the aegirine postdates the arfvedsonite. Other mafic minerals including biotite are only present in minor quantities. Zircon as an accessory phase is often subject to hydrothermal alteration (**Figure 4d**).

Major Element Compositions of Amphiboles and Formula Assignments

The average major and trace element compositions of amphiboles are given in **Tables 1, 2**, respectively. Major and trace element compositions of the host granite and MMEs from Su et al. (2008) and Yang et al. (2011) are also listed in **Table 3** for comparison (complete dataset of bulk rock is given in **Supplementary Materials S3, S4**).

The K content of amphiboles from the host granites ranges from 0.275 to 0.371 apfu and shows a dichotomy that one group exhibits higher value (0.352–0.371 apfu) whereas the other lies

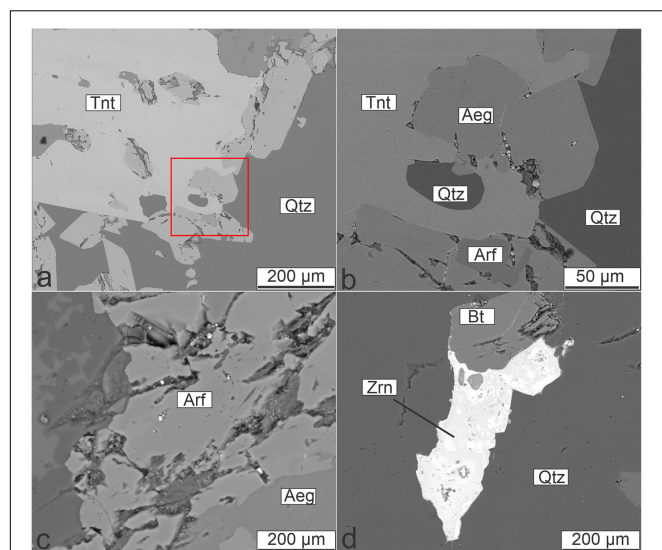


FIGURE 4 | Backscattered electron (BSE) images showing typical textures in the MMEs. **(a)** BSE image of the mantling texture showed in **Figure 3C**. **(b)** Enlargement of the area in the red box in **(a)**. **(c)** Replacement of arfvedsonite by aegirine. **(d)** Zircon associated with biotite and quartz.

below the median value (~ 0.3125 apfu), ranging from 0.215 to 0.304 apfu. The K content of amphiboles from the MMEs lies in the above-mentioned two ranges respectively. The Na content of amphiboles from both the granite and MMEs vary in a narrow range (2.185–2.488 apfu) except two analyses showing abnormally low values. The Ca content of amphibole from the host granite ranges from 0.235–0.607 apfu except one analysis showing abnormally high value (1.039 apfu), whereas the Ca content of amphibole from the MMEs is relatively low (~ 0.25 apfu). The Mg, Si and Mn^{2+} show similar patterns that the amphibole from granites have constrained Mg, Si and Mn^{2+} in relatively low values (0.004–0.120 apfu, 7.81–8.351 apfu, 0.043–0.054 apfu, respectively) whereas the amphibole from the MMEs have higher Mg, Si and Mn^{2+} (~ 0.6 apfu, ~ 8.3 apfu, ~ 0.075 apfu, respectively). Ti and Al show opposite patterns that amphiboles of granites (0.187–0.214 apfu, 0.064–0.409 apfu, respectively) have higher Ti and Al than MME-host amphiboles (0.017–0.211 apfu, 0.044–0.084 apfu, respectively). Fe^{3+} is calculated based on algorithm provided by Locock (2014) and both granite-host and MME-host amphiboles share a similar range of Fe^{3+} (0–0.620 apfu) and Fe^{2+} (3.669–4.423 apfu). Fluorine content ranges from 0.2–0.9 apfu and Cl content is below 0.1 apfu except HY5-9 which has 1.4 apfu Cl. The abnormally high value of HY5-9 may be ascribed to Cl-rich inclusions.

After analyzing the major elements of amphiboles, the chemical formula of amphibole can be calculated. Generally, the amphiboles-group minerals have a structure formula as $\text{AB}_2\text{C}_5\text{T}_8\text{O}_{22}\text{W}_2$, and the specific formula can be calculated using the spreadsheet provided by Locock (2014). The results of the formula assignment are listed in **Table 4** (the detailed formulae assignment is given in **Supplementary Material S5**). In our case, the A-site of amphiboles is occupied by Na^+ , K^+ and vacancies;

TABLE 3 | Average whole-rock major and trace element contents of the host granite and MMEs.

Unit	Host granite	MMEs
Samples	(n = 18)	(n = 2)
SiO_2 wt%	75.9	58.8
TiO_2	0.3	1.0
Al_2O_3	11.0	16.2
TFe_2O_3	2.6	7.2
MnO	0.1	0.1
MgO	0.1	2.7
CaO	0.5	3.7
Na_2O	3.8	6.0
K_2O	4.3	3.2
P_2O_5	0.1	0.2
LOI	0.5	0.5
Total	98.8	99.2
Li (ppm)	107.36	114.01
Be	5.08	1.96
Sc	3.13	14.88
V	1.05	141.43
Cr	21.03	22.59
Co	0.20	18.11
Ni	8.32	11.41
Cu	2.25	5.57
Zn	73.26	137.40
Ga	24.22	21.34
Rb	173.44	92.28
Sr	34.33	246.80
Y	68.16	48.80
Zr	341.49	166.07
Nb	14.50	10.46
Mo	0.60	0.28
Cd	0.17	0.14
In	0.22	0.17
Cs	13.05	12.68
Ba	100.73	314.72
La	31.15	23.04
Ce	69.13	53.50
Pr	9.46	7.54
Nd	38.21	31.40
Sm	9.56	7.43
Eu	0.21	1.04
Gd	10.29	7.45
Tb	1.92	1.34
Dy	11.64	8.26
Ho	2.49	1.70
Er	7.27	5.07
Tm	1.20	0.80
Yb	7.86	5.28
Lu	1.14	0.74
Hf	11.25	5.17
Ta	1.49	1.39
Pb	24.51	16.69
Bi	0.70	0.29
Th	13.78	9.49
U	4.60	2.92

The whole-rock geochemical data are cited from Tang et al. (2007), Su et al. (2008), and Yang et al. (2010).

TABLE 4 | Average calculated formulae and cation assignments (in apfu) of amphiboles based on (Locock, 2014).

Unit	Amphibole/granite	Amphibole/MMEs
Samples	(n = 12)	(n = 2)
T-site (8)	8.17	8.32
Si	8.14	8.32
Al ^{IV}	0.03	0.00
C-site (5)	4.79	4.68
Ti ^C	0.20	0.11
Al ^C	0.18	0.06
Zr	0.01	0.00
Mn ²⁺	0.05	0.07
Fe ³⁺	0.15	0.12
Fe ²⁺	4.17	3.96
Mg	0.04	0.34
B-site (2)	2.00	2.00
Na ^B	1.56	1.75
Ca	0.44	0.25
A-site (1)	1.00	0.92
Na ^A	0.70	0.60
K	0.30	0.32
W-site (2)		
F	0.41	0.56

The ideal number of each site is given in the brackets.

B-site is occupied by Na⁺ and Ca²⁺. In both sites, Na⁺ is the dominant cation. Therefore, these amphiboles belong to sodic amphiboles enriched in alkali. The octahedral C-site is occupied by various cations Ti⁴⁺, Al³⁺, Zr⁴⁺, REE³⁺, Mg²⁺, Fe²⁺, Fe³⁺, Mn²⁺, etc. The tetrahedral T-site is dominated by Si⁴⁺ with less Al³⁺. The W-site mainly contains anions F⁻, Cl⁻ and OH⁻, indicating ^W(OH, F, Cl)-dominant amphiboles. According to the formula, W-site also contains O²⁻, the amount of which is calculated by Ti in apfu (Oberti et al., 1992).

In Table 4, The C-site often shows low occupancy (< 5 apfu), whereas the A-site has an over-occupancy (> 1 apfu), although the average value seems to be in the normal range. The low occupancy of the C-site and over-occupancy of the A-site cannot be reduced, no matter how we changed calculation procedures and normalization schemes or set up different initial Fe²⁺/Fe³⁺ ratios and oxo-components. However, this issue seems to be common for alkali amphiboles in alkaline and peralkaline rocks, as reported by Hawthorne et al. (1993). The reason may be related to the misfit of B-site cations in C-site that is followed by A-site cations shifting to B-site (Siegel et al., 2017). Although cation misfit may exist, B-site cations, which determine the sub-group of amphiboles, do not show such shift in formula and still point out that most amphiboles from the Huangyangshan granite and MMEs are sodic amphiboles.

Trace Element Chemistry of Amphiboles

The chondrite-normalized amphiboles REE pattern of both MMEs and granites are generally similar (Figures 5E,F), characterized by relatively flat light and middle REE, marked negative Eu-anomaly and an enrichment in HREE (Figures 5B,D). The (La/Sm)_N, Eu/Eu* and (La/Yb)_N of

amphiboles range from 0.42–1.74, 0.004–0.028, 0.03–0.13 in MMEs and 0.45–1.43, 0.002–0.039, 0.03–0.73 in granites. Amphiboles REE pattern of MMEs shows a weakly positive Ce-anomaly (1.19–1.63) with slightly lower total REE concentration than that of amphiboles hosted in granites (Figure 5D). The abundance of REE in each amphibole varies significantly, nearly an order of magnitude.

The primitive mantle-normalized trace elements pattern of amphiboles shows a negative Ba, Eu, Sr anomalies and positive Pb anomaly (Figures 5A,C). The Ba, Sr, Pb contents of amphiboles range from 1.61–6.40 ppm, 18.45–90.10 ppm, 9.06–25.60 ppm in MMEs and 0.45–11.50 ppm, 3.43–150.60 ppm, 7.54–58.60 ppm in granites. In amphiboles of MMEs, Nb and Ta show a positive anomaly compared with adjacent U, Th and La, Ce (Figures 5A,C). Nb, Ta, U and Th contents of amphiboles range from 8.62–150.10 ppm, 0.68–5.94 ppm, 0.03–1.22 ppm and 0.08–2.69 ppm, respectively. Zr and Hf of amphiboles do not show noticeably anomaly both in MMEs and granites but with an enrichment of Hf compared with Zr. The Zr and Hf concentrations of amphiboles range from 19.4–494.00 ppm, 1.19–49.30 ppm in MMEs and 161.00–728.00 ppm, 5.50–27.10 ppm in granites. These trace elements plotted in the spidergram also vary significantly.

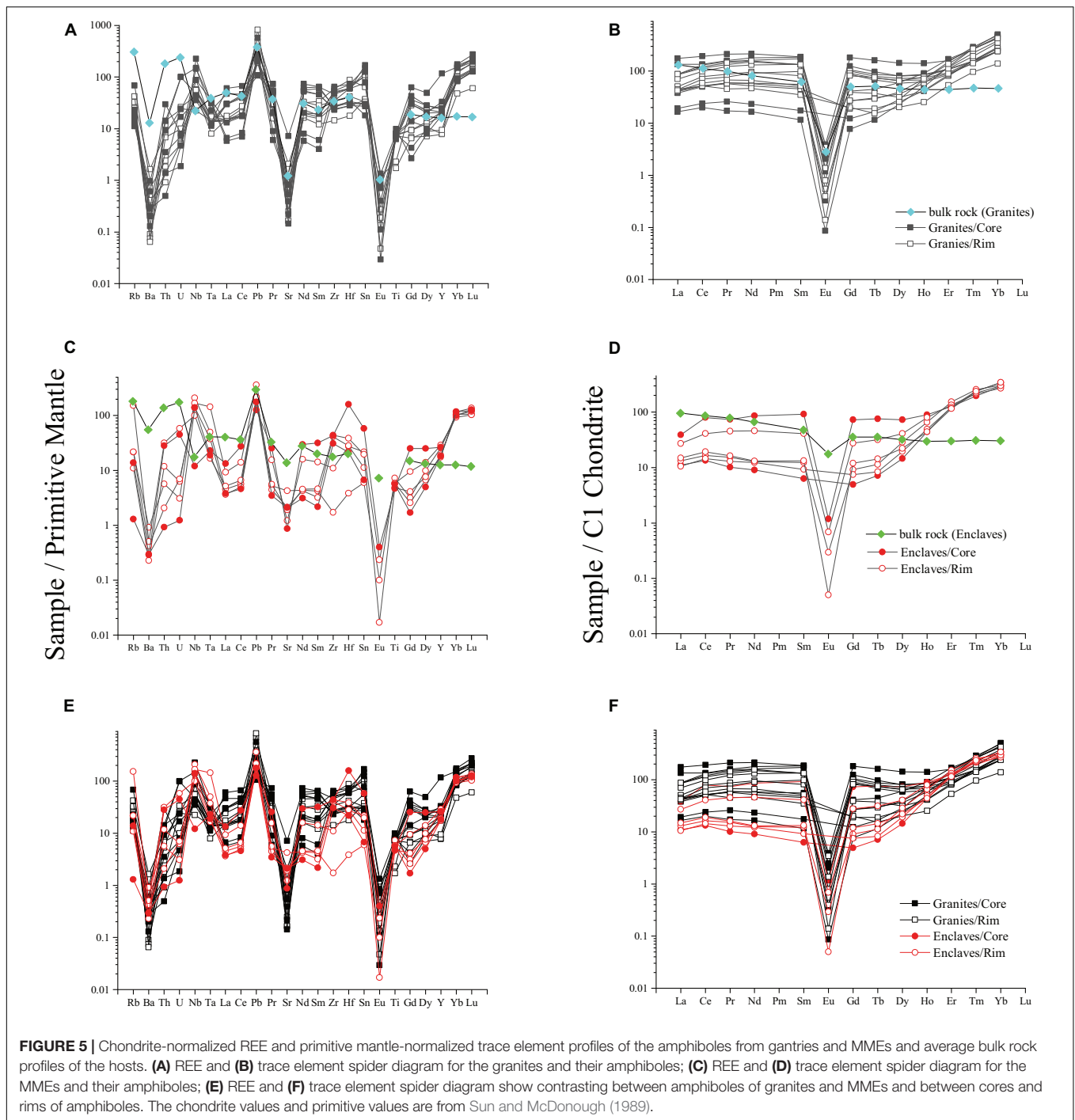
Compared with the bulk compositions of the granite and MMEs, the Nb and HREE concentrations of the amphiboles are higher than the whole-rock Nb and REE concentrations (Tables 2, 3), whereas the LILE, Th, U and LREE concentrations of the amphiboles are lower, implying that HREE and Nb are more compatible in amphiboles than LILE, Th, U and LREE.

DISCUSSION

Magma Mixing and Formation of MMEs in the Huangyangshan Granite

Petrogenesis of MMEs and A-type granites are still controversial because of their complex geochemical characteristics (Bonin, 2007). MMEs are commonly found in granitoids and are more mafic than their host rocks in chemical compositions. Due to the compositional difference and the occurrence of MMEs, the MMEs was first regarded as refractory residues of partial melting and entrained by granitoids (White and Chappell, 1977). To date, four hypotheses have been proposed to explain the genesis of MMEs:

- 1) Refractory residues of partial melting source (e.g., White and Chappell, 1977; Barbarin and Didier, 1992; White et al., 1999; Chappell et al., 2000);
- 2) Early cumulus from host magma (e.g., Dodge and Kistler, 1990; Chen et al., 2009; Shellnutt et al., 2010; Huang et al., 2014);
- 3) Xenolith of wall rocks captured by magma (e.g., Yang et al., 2004, 2006);
- 4) Magma mixing through mafic magma injected into chambers of less mafic magma (e.g., Wiebe et al., 1997; Kumar and Rino, 2006; Su et al., 2008; Guo et al., 2010; Yang et al., 2010, 2011).



5) Different crust-derived melts mixing (e.g., Roberts and Clemens, 1993; Domanska-Siuda et al., 2019).

Although the petrogenesis of MMEs is still open to debate, the magma mixing model is the most widely accepted. The mixing processes provide constraints on the petrogenesis and sources of granitoids and information about the tectonics settings (Yang et al., 2006, 2011; Kazemi et al., 2019).

In our case, major and trace elements of the MMEs and granites prove that the MMEs formed via magma mixing (Figure 6). If we assume mafic magma similar to the average oceanic crust injected into the average host granites that are little influenced by the mafic magma, this two end-members mixing in Figure 6B shows that nearly 40-70% of felsic magma added to the mafic magma. Besides, zircon U-Pb ages support magma mixing because both MMEs and host granites are contemporary and the acicular apatites resulted

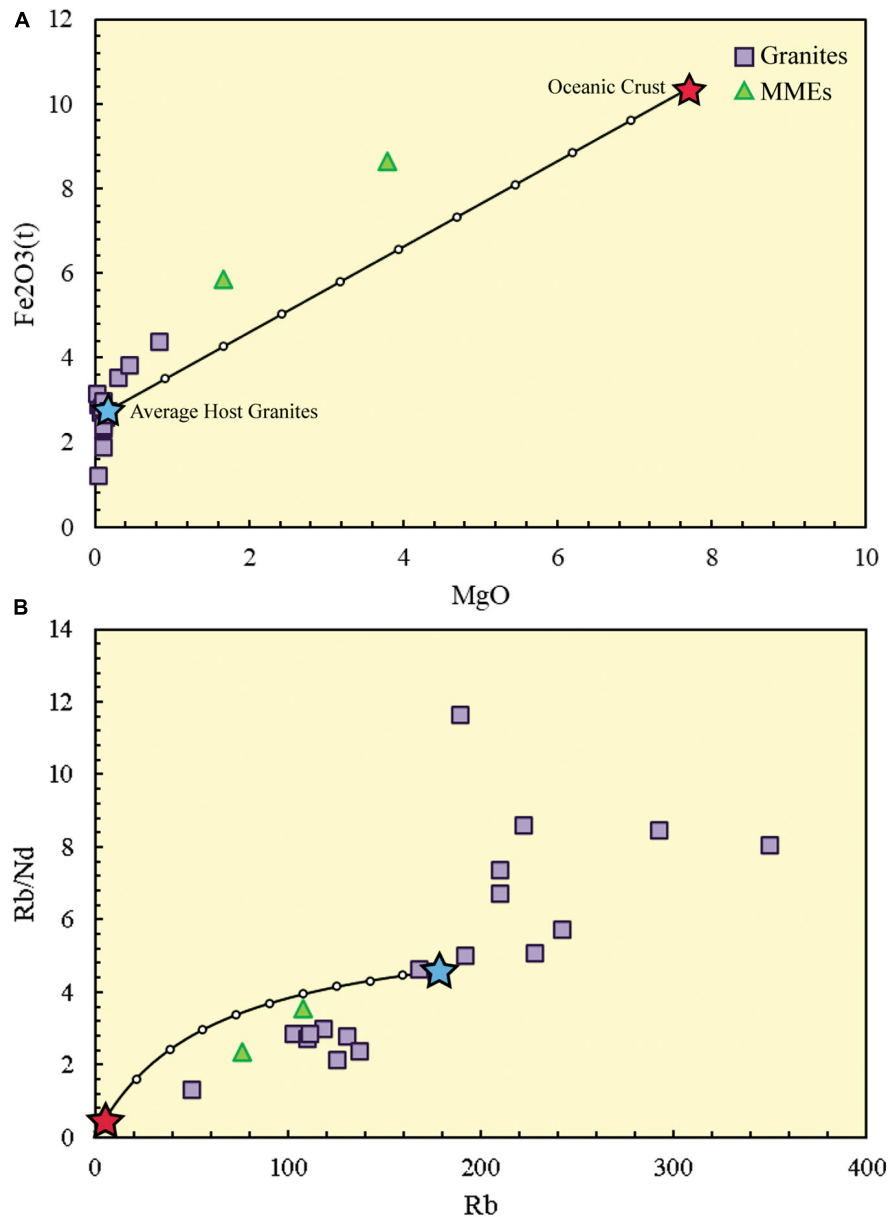


FIGURE 6 | Binary plots with magma mixing curves. **(A)** MgO versus Fe_2O_3 (Zorpi et al., 1989); **(B)** Rb/Nd - Rb (Schiano et al., 2010). The estimation shows that ~40-70% felsic magma mixed with mafic magma.

from quenching hot mafic magma within cold felsic magma (Yang et al., 2011).

Voluminous felsic magma contaminated the mafic magma rendering the trace elements pattern of the MMEs resembles that of host granites. Therefore, as a late phase, amphiboles from both units are depleted in Ba, Eu, Sr while enriched in Pb. The similar patterns of REE and other trace elements reflect homogeneous mixing in trace elements which is also supported by the absence of zonation of amphiboles. In contrast, the major element contents are not only under control of the magma composition but are also influenced by other factors like crystal structure and valence balance. Therefore, the

major elements of both amphiboles should record the chemical variation during magma mixing.

Compositional Variation of Amphiboles Halogens in W-Site of Amphiboles

A-type granites and their sodic amphiboles are usually enriched in halogens such as F and Cl. As W-site anions, F^- and Cl^- can substitute for OH^- and O^{2-} (Hawthorne et al., 2012). Substitution between $(\text{F}^-, \text{OH}^-, \text{Cl}^-)$ and O^{2-} require involvement of Ti^{4+} to maintain charge balance, i.e. $(\text{Mg, Fe})^{2+} + 2 (\text{OH, F, Cl})^- \rightarrow \text{Ti}^{4+} + 2 \text{O}^{2-}$ (Oberti et al., 1992). Therefore, if F and Cl contents are controlled by crystal

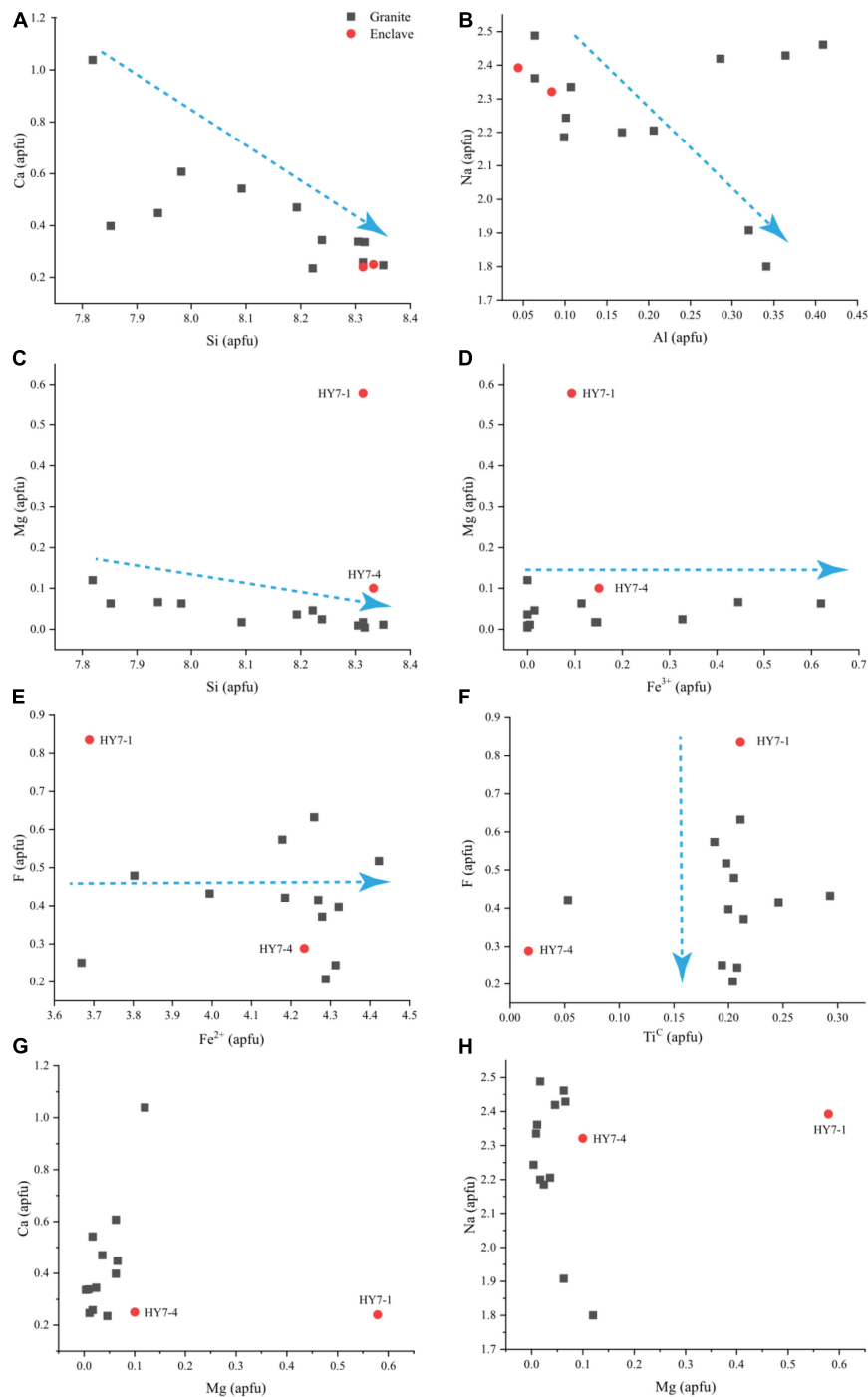


FIGURE 7 | Binary diagrams showing major elements concentrations of amphiboles in atoms per formula unit (apfu). **(A)** Ca versus Si; **(B)** Na versus Al; **(C)** Mg versus Si; **(D)** Mg versus Fe³⁺; **(E)** F versus Fe³⁺; **(F)** F versus Ti in C-site; **(G)** Ca versus Mg; and **(H)** Na versus Mg. In the plots, black squares represent chemical composition of granites-host amphiboles, red circles represent chemical composition of enclave-host amphiboles.

chemistry, they must show a negative correlation with Ti. However, **Figure 7F** shows that Ti in the amphiboles has no clear correlation with F and Cl, implying that F in the amphiboles is mainly influenced by chemical compositions of host rocks, other than crystal chemistry. Similarly, F and Cl do not show correlation with Fe (**Figure 7E**),

implying that the influence of Fe-F avoidance principle (e.g., Morrison, 1991) is negligible and also supporting the conclusion that halogens are mainly controlled by chemical compositions of melts.

Although amphiboles in our case crystallize as later phases, the variation of F still records the evolution of itself during

magma mixing. Because the chemical variation of magma is the only factor that influences F in the amphiboles, lower F content of amphiboles from F-saturated granites reflects that F decreased during evolution before magma mixing, which could be the result of fluorite crystallization. Subsequent mixing that lowered the F content of the MMEs is recorded by the amphiboles from the MMEs.

Although crystal chemistry has little influence on F content, conversely, abundance of F can control partitioning of major and trace elements that occupies other sites and further cause change in crystal chemistry (Adam et al., 1993; Iveson et al., 2017, 2018). In aluminosilicate melts, elevated silica and alumina contents normally enhance polymerization whereas addition of F would form F-Si and F-Al complexes and depolymerize the melts (Iveson et al., 2017). In addition, polymerization of melts is a key factor that controls the partition coefficients of HFSE, REE and some other economic metals (e.g., Mo, W, Nb). Generally, the lower polymerization degree of the melt is, the lower $D_{amp/melt}$ of these elements will become (Iveson et al., 2018). On the contrary, Cl prefers to form alkali-Cl complexes, resulting in higher polymerization that facilitates incorporation of trace element into amphibole. In our case, both amphiboles from the host granites and MMEs are F-rich and Cl-poor, which is consistent with the conclusion that F is compatible in amphiboles and Cl is incompatible in amphiboles (e.g., Van den Bleeken and Koga, 2015). Although lacking reliable partition coefficients that are applicable for using amphibole halogen contents to estimate the halogen contents of the melts, the influence of halogens on major and trace elements partitioning cannot be ignored.

Can Cations of A-, B-, and C-Sites Trace Magma Mixing?

A- and B-sites are mainly occupied by Na with considerable K and Ca. On B-site, Na^+ and Ca^{2+} can substitute for each other, followed by T-site substitution between Si^{4+} and Al^{3+} . This coupled substitution can be expressed using the following reaction:



Similarly, K^+ and Na^+ can also substitute for each other on A-site without any change in valence. For fluoro- sodic-amphiboles, elevated Na and F can constitute local configuration of ${}^ANa-{}^WF-{}^BNa$ to maintain the stability of amphiboles (Hawthorne et al., 1996).

In **Figures 7A,B**, negative correlations of Ca-Si and Na-Al reflect Ca and Na are under the control of substitution and thus B-site cations cannot trace chemical variation of magma. The substitution of B-site also influences the A-site and the sum of cations of A-site often exceed 1 apfu, indicating crystal chemistry dominates the behavior of K and Na^A (**Supplementary Table 5**).

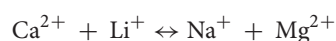
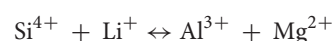
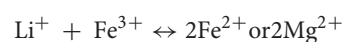
Although the bulk CaO content of the MMEs is higher than the host granite (**Table 1**), the amphibole from the MMEs contain lower CaO content than that from the host granite. The reason for such discrepancy may be ascribed to MMEs containing more plagioclase than the granite. Therefore, more Ca partitions into plagioclase other than amphibole. Different from

the CaO content, the Na_2O and K_2O contents of the amphiboles from both units are comparable, although the K_2O contents of the amphiboles are much lower than the bulk K_2O contents of both rock units. This phenomenon may be ascribed to Na having higher diffusivity than K and further imply the melt mixing cannot be fully traced by major elements of A-site either (Hawthorne et al., 2005).

As trace elements, Pb, U and Th can be incorporated into A- and B-site (Tiepolo et al., 2007; Hawthorne et al., 2012). Generally, Pb occupies the A-site, whereas U and Th occupy the B-site. Although they are expected to occur mostly as tetravalent cations which are unsuitable for A- and B-site from the perspective of charge balance, due to their small ionic radii, they prefer to occupy these sites in contrast (Tiepolo et al., 2007). Partitioning of Pb, U and Th is mainly controlled by melt compositions (i.e., polymerization of magmas). In addition, partitioning of U is also influenced by the redox state, because U^{6+} is difficult to incorporate into amphibole. In this study, the Pb contents of amphiboles is similar to their hosts, indicating Pb is not so incompatible. This is consistent with the results of Brenan et al. (1995) and Tiepolo et al. (2007). Uranium and Th also have higher partition coefficients in sodic amphiboles than calcic amphiboles (Tiepolo et al., 2007).

More interestingly, Li is commonly expected to substitute for Na. It can also replace cations such as Mg or Fe^{2+} via coupled substitution on C-site (e.g., Hawthorne et al., 1993, 1994; Oberti et al., 2003), which brings complexity in discerning the occupancy of Li.

Incorporation mechanism of Li in amphiboles includes (e.g., Hawthorne et al., 1994):



In our case, Si and Mg show a negative correlation, which indicates that C-site occupied by Li is coupled with Si incorporated in T-site (**Figure 7C**). This process may further explain why T-site shows excess Si (> 8 apfu).

Besides Li, the C-site of amphiboles is mainly occupied by Fe^{2+} and minor Mg^{2+} , Mn^{2+} , Ti^{4+} and Fe^{3+} (e.g., Hawthorne et al., 2012). Because Fe^{3+} and Fe^{2+} cannot be directly determined by EMPA, the content of Fe^{3+} is estimated through algorithm based on charge balance (Locock, 2014). Therefore, Fe^{3+}/Fe^{2+} cannot represent the redox state since no Mn^{3+} exists in the amphiboles. No correlation between Fe^{3+} and Mg^{2+} also supports this (**Figure 7D**). In our case, C-site is only partly filled (< 5 apfu), the effect of crystal chemistry is insignificant except for Al, which is allocated to both C- and T-site, the latter where Si constrain the behavior of Al. Although Si negatively correlates with Mg, implying the Li-substitution (**Figure 7C**), the

Li content of amphiboles is too low to significantly influence the variation of Mg. Also, considering amphibole is the major carrier of Mg in both MMEs and host granites, Mg in amphiboles records the evolution of magma. Therefore, the amphiboles of the MMEs and host granites prove that high MgO magma mixed with low MgO magma.

The variations of Fe and Ti of amphiboles are different from their hosts. As suggested by the mixing model, the unmixed mafic magma is higher in Fe and Ti than granites but Fe and Ti of amphiboles from the MMEs are lower than those of granites. If we assume the high MgO amphibole crystallized earlier than low MgO amphiboles, the former has lower Fe and higher Ti while the latter is opposite depicts such a scenario: when high-MgO amphibole crystallized, the crystallization of titanite and Fe-oxide had already decreased the Fe and Ti content of the mixed magma, as evidenced by the similar range of Ti content among high-MgO amphibole and amphiboles from granites; subsequent injection of felsic magma replenish the Fe to increase the Fe of low-MgO amphibole while consistently crystallizing titanite further lower the Ti of low-MgO amphibole.

Similar to Ti, other HFSE (including Nb, Ta, Zr, Hf) also occupy C-site but behave diversely. Zr^{4+} and Hf^{4+} have the same valence as Ti^{4+} but larger ionic radii (Shannon, 1976), Zr and Hf are thus sensitive to compositional change of amphiboles or melts (Tiepolo et al., 2007). In contrast, although Nb^{5+} and Ta^{5+} have higher valence and the high valence can be balanced by oxo-component introduced during Ti incorporation ($(Mg, Fe)^{2+} + 2(OH, F, Cl)^- \rightarrow Ti^{4+} + 2O^{2-}$) (Tiepolo et al., 2001, 2007). Hence, Nb and Ta in amphiboles could behave as slightly incompatible or even compatible elements with increasing Ti (Tiepolo et al., 2007). In both the Huangyangshan granite and its MMEs, Zr and Hf show different partitioning behavior between the amphibole and melt. Niobium is relatively compatible compared to Ta in the amphibole from the granite whereas both Nb and Ta behave compatibly in the amphibole from the MMEs (Figures 5A,C).

Distribution of REE

Distribution of REE in amphibole-group minerals is mainly influenced by crystal structure and melt compositions. The effect of melt compositions relates to major elements that are involved during incorporation of REE into amphiboles. The difference in substitution mechanism can be justified by different site preference between LREE and HREE (Bottazzi et al., 1999; Shimizu et al., 2017). Similarly, the size of different sites also controls the site preference of REE (Blundy and Wood, 1994). Many studies have demonstrated that LREE prefer to substitute for Ca^{2+} whereas HREE prefer to substitute for Fe^{2+} corresponding to M4-site (B-site) and M4'-site (B-site) or M2-site (C-site) respectively (e.g., Bottazzi et al., 1999; Tiepolo et al., 2007).

Due to the lower Ca content and higher Fe content of sodic amphibole, HREE are much more compatible than LREE in sodic amphibole and the $D_{amph-melt}$ of REE in our case are higher than the values reported in other studies (Table 5; e.g., Marks et al., 2004; Siegel et al., 2017). The REE partition coefficients of the amphibole from the host granites show a pattern that from La to Td and from Dy to Lu, each group

fits a specific parabolic trend that can be calculated using the model of Blundy and Wood (1994). However, REE partition coefficients of the amphibole from the MMEs do not show the same trend but monotonically increase from La to Lu instead (Figure 8). This phenomenon may indicate that in melts with different compositions, site preference of REE could be different. In addition, the partition coefficients decrease from core to rim (Table 5; complete partition coefficients of REE between amphiboles and their hosts are given in Supplementary Material S6), regardless of the hosts of amphiboles, implying that most REE are distributed into accessory minerals, such as titanite and/or zircon.

Temperature and Pressure Estimate of Sodic Amphiboles

According to major and trace elements, zircon U-Pb ages, texture, and rheology, the petrogenesis of the MMEs hosted by the Huangyangshan A-type granite requires mafic magma injection (Figure 9). If the amphiboles are the later phase during magma mixing, they may record similar temperature. Notably, most thermometers and barometers for amphibole are based on chemical compositions of calcic amphiboles. However, in our case, amphiboles are mostly sodic amphiboles that may not be suitable for these thermometers and barometers (e.g., Ridolfi et al., 2010; Ridolfi and Renzulli, 2012; Putirka, 2016). Therefore, the prerequisite is to test whether these amphiboles have intrinsic flaws that prevent them from estimating temperature or pressure and seek for a reference value to test the estimates of various thermometers.

Before testing and estimating the crystallization temperatures of the amphiboles, an "amphibole-saturation temperature" for a given liquid composition can be estimated using liquid-only thermometer provided by Molina et al. (2015). Because the chemical compositions of amphiboles are not needed for calculation, liquid-only thermometer can yield reasonable values of $1024 \pm 42^\circ\text{C}$ for MMEs and $843 \pm 42^\circ\text{C}$ for granites, regardless of the species of amphiboles.

TABLE 5 | Apparent melt-amphiboles partition coefficients ($D_{Amph-bulk}$) of rare earth element (REE).

	$D_{core-granite}$	$D_{rim-granite}$	$D_{core-MMEs}$	$D_{rim-MMEs}$
La	0.39	0.59	0.17	0.26
Ce	0.63	0.83	0.26	0.53
Pr	0.82	1.07	0.28	0.53
Nd	1.06	1.39	0.31	0.71
Sm	1.25	1.73	0.39	1.01
Gd	0.99	1.56	0.39	1.07
Tb	0.87	1.34	0.46	1.16
Dy	0.96	1.46	0.86	1.34
Ho	1.28	1.86	1.99	2.23
Er	2.13	2.86	4.29	4.12
Tm	3.62	4.57	7.42	6.97
Yb	6.17	7.93	9.80	10.15
Lu	9.48	11.81	11.65	12.58

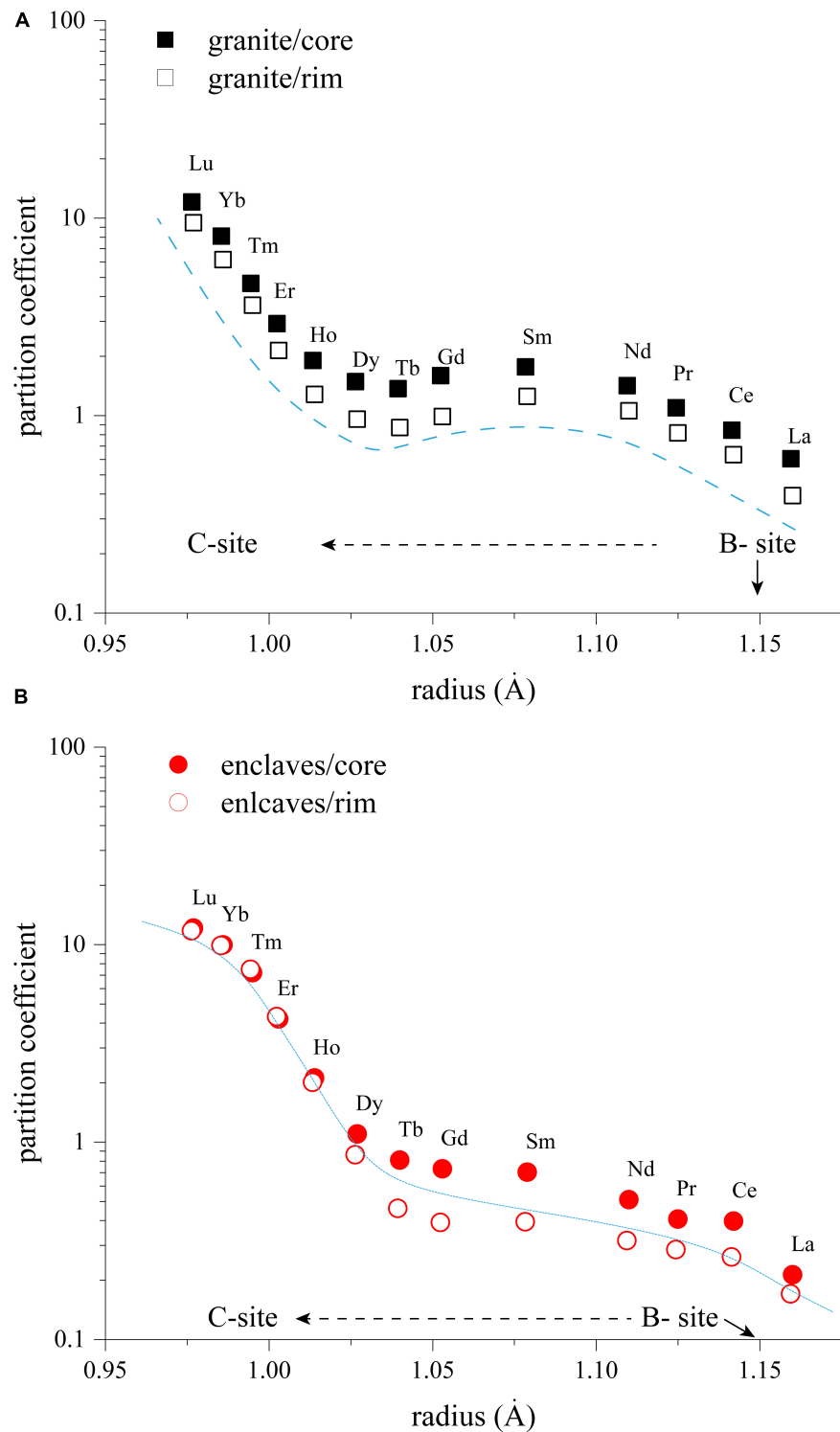


FIGURE 8 | Diagrams showing the relationship between ionic radii and apparent partition coefficient $D_{amph-melt}$ (average REE content of amphiboles/average REE content of the bulk rock) for amphiboles from the host granite **(A)** and from the enclaves **(B)**. Blue dash lines represent Lattice-Strain Theory fit through these data. Black dash lines reflect potential site preference of REE.

We then tested and estimated the crystallization temperatures of the amphiboles from the Huangyangshan granite and its MMEs using amphibole-only thermometers and thermometers based on partition coefficients. Amphibole-only thermometers are based on the correlation between temperature and chemical compositions of amphiboles that are either experimentally synthesized or natural samples (e.g., Ridolfi et al., 2010; Ridolfi and Renzulli, 2012; Putirka, 2016). Through these algorithms, the temperature estimates for the amphiboles in the MMEs and host granite are consistent within errors ($\sim 650^\circ\text{C}$), implying that the amphiboles crystallize as late phase, consistent with the fluorite, titanite, and Fe-oxide crystallized earlier than amphiboles (Price et al., 1999; Scaillet and MacDonald, 2001). As for thermometers based on partition coefficients, Molina et al. (2015) and Putirka (2016) recommend thermometers derived from correlation between temperatures and D_{Mg} or D_{Na} . Although Molina et al. (2015) emphasized that their dataset only contained amphiboles with $\text{Ca}^{\text{B}}/(\text{Ca}^{\text{B}} + \text{Na}^{\text{B}}) > 0.75$, Mg in amphiboles does not show any correlation with Ca or Na in our case (Figures 7G,H), therefore the thermometer provided by Molina et al. (2015) may be applicable to our samples. The temperature estimates are $946 \pm 45^\circ\text{C}$ for amphiboles in the MMEs and $1028 \pm 45^\circ\text{C}$ for amphiboles in the granite, respectively. However, the estimates are higher than the “amphibole saturation temperature” and the temperature of the amphibole from the host granite deviates from the amphibole stability field under most conditions (e.g., Xiong et al., 2005). On the other hand, the amphibole from the host granite crystallized earlier than that from the MMEs is unreasonable. This may be ascribed to that the Mg or Na exchange between the amphiboles and melts do not reach equilibrium, especially the Na in sodic amphiboles is under control of crystal chemistry. Thus, the temperature is more likely the closure temperature for element exchange to reach equilibrium other than the crystallization temperatures.

In summary, amphibole-only thermometers yield good results because the estimates are under “saturation temperature” but the thermometers also prove that the amphiboles crystallized as a late phase consistent with petrographic evidence. However, thermometers based on partition coefficients produce erroneous estimates.

The basis of amphiboles barometer is that Al-Tschermak exchange, which mainly involves in Al incorporation, is pressure-sensitive, so it seems to be proper to use Al to estimate pressure of crystallization (e.g., Hammarstrom and Zen, 1986; Shane and Smith, 2013; Mutch et al., 2016). However, most researchers have questioned the reliability of Al-in-amphiboles barometer, because the exchange of Al is also influenced by temperature and melt compositions, which means that variation of Al content of amphiboles is too complex to use for estimating pressure directly (e.g., Kiss et al., 2014). In order to acquire accurate pressure estimates, Anderson and Smith (1995) recommend two filters: $T < 800^\circ\text{C}$ and $\text{Fe}^{\text{Amp}}/(\text{Fe}^{\text{Amp}} + \text{Mg}^{\text{Amp}}) < 0.65$. If amphiboles fit these filters, they are suitable for Al-in-amphiboles barometer. Unfortunately, in our case, amphiboles in both the granite and MMEs are Fe-rich, far beyond the values required by the filters. On the other hand, Al content of amphiboles in our case are too low, which results in an unreasonably low pressure. In addition

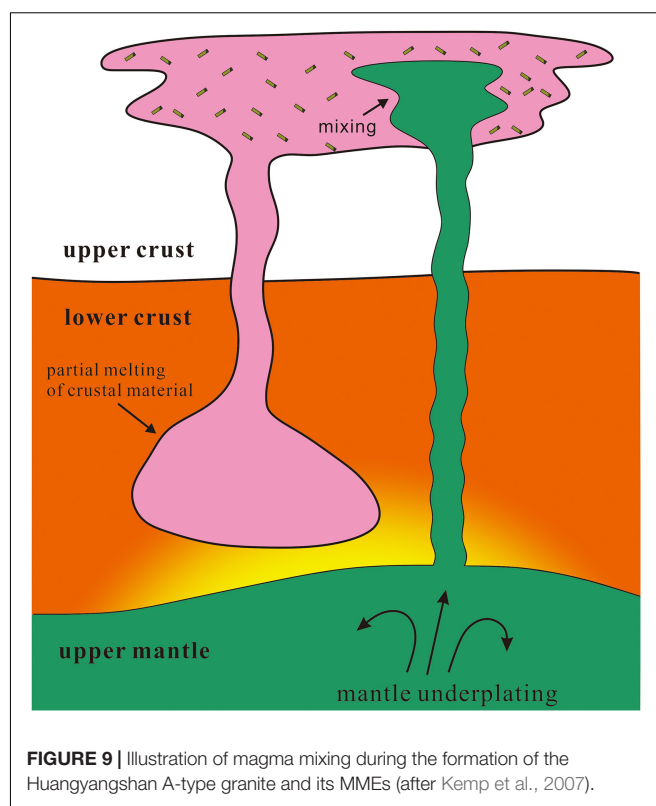


FIGURE 9 | Illustration of magma mixing during the formation of the Huangyangshan A-type granite and its MMEs (after Kemp et al., 2007).

to Al-in-amphiboles barometer, Putirka (2016) recommended D_{Al} barometer to lower the uncertainty of pressure estimates, but no reasonable estimates can be acquired (10.5 kbar for amphiboles of MMEs; 3.5 kbar for amphiboles of granites). The outstanding pressure difference between the amphiboles from the MMEs and granites may also indicate that the estimates do not reflect depths but more related to temperature variations, which is consistent with the conclusion of Erdmann et al. (2014). Therefore, sodic amphiboles cannot be used to reflect the pressure change during magma mixing.

CONCLUSION

We have shown major and trace elements variation of amphiboles of granites and MMEs during magma mixing and tentatively estimate the crystallization temperature and pressure of these amphiboles. In sodic amphiboles from both the MMEs and host granite, halogens in W-site and Mg, Fe, and Ti in C-site are only controlled by chemical compositions of magma and can potentially reflect the evolution of magma. By contrast, A-, B- and T-site cations are influenced by crystal chemistry and magma composition limiting their ability as tracers. Although F can depolymerize the melts, resulting in lower partition coefficients of trace elements, HFSE and REE behave more compatibly in sodic amphiboles than in calcic amphiboles. Also, taking “saturation temperature” as reference, amphiboles-only thermometers yield reasonable results and further prove amphiboles are later phase during magma mixing, but partition coefficient-based

thermometers show considerable deviation. All of the barometers now available rely on Al content or D_{Al} of amphiboles cannot be applied to Fe-rich and Al-poor amphiboles.

DATA AVAILABILITY STATEMENT

The original contributions presented in the study are included in the article/Supplementary Material, further inquiries can be directed to the corresponding author/s.

AUTHOR CONTRIBUTIONS

YF and CY together conceived the idea for this study. CY conducted petrographic observation, EPMA and LA-ICP-MS analyses on amphiboles, and wrote the manuscript. YF revised and finalized the manuscript. YF and RL conducted the fieldwork and collected the samples. GY provided assistance with the fieldwork. All authors contributed to the article and approved the submitted version.

REFERENCES

- Adam, J., Green, T. H., and Sie, S. H. (1993). Proton microprobe determined partitioning of Rb, Sr, Ba, Y, Zr, Nb and Ta between experimentally produced amphiboles and silicate melts with variable F content. *Chem. Geol.* 109, 29–49. doi: 10.1016/0009-2541(93)90060-v
- Anderson, J. L., and Smith, D. R. (1995). The effects of temperature and F(O₂) on the al-in-hornblende barometer. *Am. Mineral.* 80, 549–559. doi: 10.2138/am-1995-5-614
- Barbarin, B., and Didier, J. (1992). Genesis and evolution of mafic microgranular enclaves through various types of interaction between coexisting felsic and mafic magmas. *Trans. R. Soc. Edinburgh Earth Sci.* 83, 145–153. doi: 10.1017/s0263593300007835
- Baxter, S., and Feely, M. (2002). Magma mixing and mingling textures in granitoids: examples from the Galway Granite, Connemara, Ireland. *Mineral. Petrol.* 76, 63–74.
- Blundy, J., and Wood, B. (1994). Prediction of crystal-melt partition-coefficients from elastic-moduli. *Nature* 372, 452–454. doi: 10.1038/372452a0
- Bonin, B. (2007). A-type granites and related rocks: evolution of a concept, problems and prospects. *Lithos* 97, 1–29. doi: 10.1016/j.lithos.2006.12.007
- Bottazzi, P., Tiepolo, M., Vannucci, R., Zanetti, A., Brumm, R., Foley, S. F., et al. (1999). Distinct site preferences for heavy and light REE in amphibole and the prediction of D-Amph/L(REE). *Contrib. Mineral. Petrol.* 137, 36–45. doi: 10.1007/s004100050580
- Brenan, J. M., Shaw, H. F., Ryerson, F. J., and Phinney, D. L. (1995). Experimental-determination of trace-element partitioning between pargasite and a synthetic hydrous andesitic melt. *Earth Planet. Sci. Lett.* 135, 1–11. doi: 10.1016/0012-821x(95)00139-4
- Chappell, B. W., White, A. J. R., Williams, I. S., Wyborn, D., and Wyborn, L. A. I. (2000). Lachlan Fold Belt granites revisited: high- and low-temperature granites and their implications. *Aust. J. Earth Sci.* 47, 123–138. doi: 10.1046/j.1440-0952.2000.00766.x
- Chen, B., Chen, Z. C., and Jahn, B. M. (2009). Origin of mafic enclaves from the Taihang Mesozoic orogen, north China craton. *Lithos* 110, 343–358. doi: 10.1016/j.lithos.2009.01.015
- Dodge, F. C. W., and Kistler, R. W. (1990). Some additional observations on inclusions in the granitic-rocks of the sierra-nevada. *J. Geophys. Res. Solid Earth Planets* 95, 17841–17848. doi: 10.1029/jb095ib11p17841
- Domanska-Siuda, J., Slaby, E., and Szuszkiewicz, A. (2019). Ambiguous isotopic and geochemical signatures resulting from limited melt interactions in a seemingly composite pluton: a case study from the Strzegom-Sobotka Massif

FUNDING

This study is funded by the National Natural Science Foundation of China (grant numbers: 91962214 and 41902073) and Department of Science and Technology of Shaanxi Province (grant number: 2020JM-215).

ACKNOWLEDGMENTS

We are very grateful for the insightful suggestions from HL, FY, and ES that helped improve this manuscript. We would also like to thank XD for handling this manuscript.

SUPPLEMENTARY MATERIAL

The Supplementary Material for this article can be found online at: <https://www.frontiersin.org/articles/10.3389/feart.2021.650014/full#supplementary-material>

- (Sudetes, Poland). *Int. J. Earth Sci.* 108, 931–962. doi: 10.1007/s00531-019-01687-w
- Erdmann, S., Martel, C., Pichavant, M., and Kushnir, A. (2014). Amphibole as an archivist of magmatic crystallization conditions: problems, potential, and implications for inferring magma storage prior to the paroxysmal 2010 eruption of Mount Merapi, Indonesia. *Contrib. Mineral. Petrol.* 167:1016.
- Guo, F., Jiang, C., Lu, R., Xia, Z., Ling, J., and Guo, N. (2010). Petrogenesis of the Huangyangshan alkali granites in Kalamaili area, northern Xinjiang. *Acta Petrologica Sinica* 26, 2357–2373.
- Hammarstrom, J. M., and Zen, E. A. (1986). Aluminum in hornblende - an empirical igneous geobarometer. *Am. Mineral.* 71, 1297–1313.
- Hawthorne, F. C., Della Ventura, G., Oberti, R., Robert, J. L., and Iezzi, G. (2005). Short-range order in minerals: amphiboles. *Can. Mineral.* 43, 1895–1920. doi: 10.2113/gscanmin.43.6.1895
- Hawthorne, F. C., Oberti, R., and Sardone, N. (1996). Sodium at the site in clinoamphiboles: the effects of composition on patterns of order. *Can. Mineral.* 34, 577–593.
- Hawthorne, F. C., Oberti, R., Harlow, G. E., Maresch, W. V., Martin, R. F., Schumacher, J. C., et al. (2012). Nomenclature of the amphibole supergroup. *Am. Mineral.* 97, 2031–2048. doi: 10.2138/am.2012.4276
- Hawthorne, F. C., Ungaretti, L., Oberti, R., Bottazzi, P., and Czamanske, G. K. (1993). LI - AN important component in igneous alkali amphiboles. *Am. Mineral.* 78, 733–745.
- Hawthorne, F. C., Ungaretti, L., Oberti, R., Cannillo, E., and Smelik, E. A. (1994). The mechanism of 6 Li incorporation in amphiboles. *Am. Mineral.* 79, 443–451.
- Huang, H., Niu, Y. L., Nowell, G., Zhao, Z. D., Yu, X. H., Zhu, D. C., et al. (2014). Geochemical constraints on the petrogenesis of granitoids in the East Kunlun Orogenic belt, northern Tibetan Plateau: implications for continental crust growth through syn-collisional felsic magmatism. *Chem. Geol.* 370, 1–18. doi: 10.1016/j.chemgeo.2014.01.010
- Iveson, A. A., Rowe, M. C., Webster, J. D., and Neill, O. K. (2018). Amphibole-, Clinopyroxene- and Plagioclase-melt partitioning of trace and economic metals in halogen-bearing rhyodacitic melts. *J. Petrol.* 59, 1579–1604. doi: 10.1093/petrology/egy072
- Iveson, A. A., Webster, J. D., Rowe, M. C., and Neill, O. K. (2017). Major Element and Halogen (F, Cl) mineral-melt-fluid partitioning in hydrous rhyodacitic melts at shallow crustal conditions. *J. Petrol.* 58, 2465–2492. doi: 10.1093/petrology/egy011
- Kazemi, K., Kananian, A., Xiao, Y., and Sarjoughian, F. (2019). Petrogenesis of Middle-Eocene granitoids and their Mafic microgranular enclaves in central

- Urmia-Dokhtar Magmatic Arc (Iran): evidence for interaction between felsic and mafic magmas. *Geosci. Front.* 10, 705–723. doi: 10.1016/j.gsf.2018.04.006
- Kemp, A. I. S., Hawkesworth, C. J., Foster, G. L., Paterson, B. A., Woodhead, J. D., Hergt, J. M., et al. (2007). Magmatic and crustal differentiation history of granitic rocks from Hf-O isotopes in zircon. *Science* 315, 980–983. doi: 10.1126/science.1136154
- Kiss, B., Harangi, S., Ntafos, T., Mason, P. R. D., and Pal-Molnar, E. (2014). Amphibole perspective to unravel pre-eruptive processes and conditions in volcanic plumbing systems beneath intermediate arc volcanoes: a case study from Ciomadul volcano (SE Carpathians). *Contrib. Mineral. Petrol.* 167:986.
- Kumar, S., and Rino, V. (2006). Mineralogy and geochemistry of microgranular enclaves in Palaeoproterozoic Malanjhand granitoids, central India: evidence of magma mixing, mingling, and chemical equilibration. *Contrib. Mineral. Petrol.* 152, 591–609. doi: 10.1007/s00410-006-0122-3
- Kumar, S., Rino, V., and Pal, A. B. (2004). Typology and geochemistry of microgranular enclaves hosted in Malanjhand Granitoids, central India. *J. Geol. Soc. India* 64, 277–292.
- Leake, B. E., Woolley, A. R., Arps, C. E. S., Birch, W. D., Gilbert, M. C., and Grice, J. D. (1997). Nomenclature of amphiboles: report of the subcommittee on amphiboles of the international mineralogical association, commission on new minerals and mineral names. *Am. Mineral.* 82, 1019–1037.
- Liu, L., Qiu, J.-S., and Li, Z. (2013). Origin of mafic microgranular enclaves (MMEs) and their host quartz monzonites from the Muchen pluton in Zhejiang province, Southeast China: implications for magma mixing and crust-mantle interaction. *Lithos* 160, 145–163. doi: 10.1016/j.lithos.2012.12.005
- Locock, A. J. (2014). An excel spreadsheet to classify chemical analyses of amphiboles following the IMA 2012 recommendations. *Comput. Geosci.* 62, 1–11. doi: 10.1016/j.cageo.2013.09.011
- Ma, X., Chen, B., and Yang, M. (2013). Magma mixing origin for the Aolunhua porphyry related to Mo-Cu mineralization, eastern central Asian Orogenic Belt. *Gondwana Res.* 24, 1152–1171. doi: 10.1016/j.gr.2013.02.010
- Marks, M., Halama, R., Wenzel, T., and Markl, G. (2004). Trace element variations in clinopyroxene and amphibole from alkaline to peralkaline syenites and granites: implications for mineral-melt trace-element partitioning. *Chem. Geol.* 211, 185–215. doi: 10.1016/j.chemgeo.2004.06.032
- Molina, J. F., Moreno, J. A., Castro, A., Rodriguez, C., and Fershtater, G. B. (2015). Calcic amphibole thermobarometry in metamorphic and igneous rocks: new calibrations based on plagioclase/amphibole Al-Si partitioning and amphibole/liquid Mg partitioning. *Lithos* 232, 286–305. doi: 10.1016/j.lithos.2015.06.027
- Morrison, J. (1991). Compositional constraints on the incorporation of Cl into Amphiboles. *Am. Mineral.* 76, 1920–1930.
- Mutch, E. J. F., Blundy, J. D., Tattitch, B. C., Cooper, F. J., and Brooker, R. A. (2016). An experimental study of amphibole stability in low-pressure granitic magmas and a revised Al-in-hornblende geobarometer. *Contrib. Mineral. Petrol.* 171:85.
- Oberti, R., Camara, F., Ottoloni, L., and Caballero, J. M. (2003). Lithium in amphiboles: detection, quantification, and incorporation mechanisms in the compositional space bridging sodic and Li-B-amphiboles. *Eur. J. Mineral.* 15, 309–319. doi: 10.1127/0935-1221/2003/0015-0309
- Oberti, R., Ungaretti, L., Cannillo, E., and Hawthorne, F. C. (1992). the behavior of ti in amphiboles .1. 4-coordinate and 6-coordinate ti in richterite. *Eur. J. Mineral.* 4, 425–439. doi: 10.1127/ejm/4/3/0425
- Paton, C., Hellstrom, J., Paul, B., Woodhead, J., and Hergt, J. (2011). Iolite: freeware for the visualisation and processing of mass spectrometric data. *J. Anal. At. Spectrom.* 26, 2508–2518. doi: 10.1039/c1ja10172b
- Price, J. D., Hogan, J. P., Gilbert, M. C., London, D., and Morgan, G. B. (1999). Experimental study of titanite-fluorite equilibria in the A-type mount scott granite: implications for assessing F contents of felsic magma. *Geology* 27, 951–954. doi: 10.1130/0091-7613(1999)027<0951:esotfe>2.3.co;2
- Putirka, K. (2016). Amphibole thermometers and barometers for igneous systems and implications for eruption mechanisms of felsic magmas at arc volcanoes. *Am. Mineral.* 101, 841–858. doi: 10.2138/am-2016-5506
- Renna, M. R., Tribuzio, R., and Tiepolo, M. (2006). Interaction between basic and acid magmas during the latest stages of the post-collisional variscan evolution: clues from the gabbro-granite association of Ota (Corsica-Sardinia batholith). *Lithos* 90, 92–110. doi: 10.1016/j.lithos.2006.02.003
- Ridolfi, F., and Renzulli, A. (2012). Calcic amphiboles in calc-alkaline and alkaline magmas: thermobarometric and chemometric empirical equations valid up to 1,130A degrees C and 2.2 GPa. *Contrib. Mineral. Petrol.* 163, 877–895. doi: 10.1007/s00410-011-0704-6
- Ridolfi, F., Renzulli, A., and Puerini, M. (2010). Stability and chemical equilibrium of amphibole in calc-alkaline magmas: an overview, new thermobarometric formulations and application to subduction-related volcanoes. *Contrib. Mineral. Petrol.* 160, 45–66. doi: 10.1007/s00410-009-0465-7
- Roberts, M. P., and Clemens, J. D. (1993). origin of high-potassium, calc-alkaline, i-type granitoids. *Geology* 21, 825–828. doi: 10.1130/0091-7613(1993)021<0825:oohpta>2.3.co;2
- Scailliet, B., and MacDonald, R. (2001). Phase relations of peralkaline silicic magmas and petrogenetic implications. *J. Petrol.* 42, 825–845. doi: 10.1093/petrology/42.4.825
- Schiano, P., Monzier, M., Eissen, J. P., Martin, H., and Koga, K. T. (2010). Simple mixing as the major control of the evolution of volcanic suites in the Ecuadorian Andes. *Contrib. Mineral. Petrol.* 160, 297–312. doi: 10.1007/s00410-009-0478-2
- Sengor, A. M. C., Natalin, B. A., and Burtman, V. S. (1993). evolution of the altaid tectonic collage and paleozoic crustal growth in eurasia. *Nature* 364, 299–307. doi: 10.1038/364299a0
- Shane, P., and Smith, V. C. (2013). Using amphibole crystals to reconstruct magma storage temperatures and pressures for the post-caldera collapse volcanism at Okataina volcano. *Lithos* 156, 159–170. doi: 10.1016/j.lithos.2012.11.008
- Shannon, R. D. (1976). revised effective ionic-radii and systematic studies of interatomic distances in halides and chalcogenides. *Acta Crystallogr. Sec. A* 32, 751–767. doi: 10.1107/s0567739476001551
- Shellnutt, J. G., Jahn, B. M., and Dostal, J. (2010). Elemental and Sr-Nd isotope geochemistry of microgranular enclaves from peralkaline A-type granitic plutons of the Emeishan large igneous province, SW China. *Lithos* 119, 34–46. doi: 10.1016/j.lithos.2010.07.011
- Shimizu, K., Liang, Y., Sun, C., Jackson, C. R. M., and Saal, A. E. (2017). Parameterized lattice strain models for REE partitioning between amphibole and silicate melt. *Am. Mineral.* 102, 2254–2267. doi: 10.2138/am-2017-6110
- Siegel, K., Williams-Jones, A. E., and van Hinsberg, V. J. (2017). The amphiboles of the REE-rich A-type peralkaline strange lake pluton fingerprints of magma evolution. *Lithos* 288, 156–174. doi: 10.1016/j.lithos.2017.07.012
- Su, Y., Tang, H., and Cong, F. (2008). zircon u-pb age and petrogenesis of the huangyangshan alkalinegranite body in east junggar, xinjiang. *Acta Mineral. Sinica* 28, 117–126.
- Sun, S. S., and McDonough, W. F. (1989). “Chemical and isotopic systematics of oceanic basalts: implications for mantle composition and processes,” in *Magmatism in the Oceanic Basalts, Special Publication*, eds A. D. Saunders, and M. J. Norry (London: Geological Society), 313–345.
- Tang, H., Qu, W., Su, Y., Hou, G., Du, A., and Cong, F. (2007). Genetic connection of Sarehsike tin deposit with the alkaline A-type granites of saabei body in Xinjiang: constraint from isotopic ages. *Acta Petrologica Sinica* 23, 1989–1997.
- Tiepolo, M., Bottazzi, P., Foley, S. F., Oberti, R., Vannucci, R., and Zanetti, A. (2001). Fractionation of Nb and Ta from Zr and Hf at mantle depths: the role of titanite paragonite and kaersutite. *J. Petrol.* 42, 221–232. doi: 10.1093/petrology/42.1.221
- Tiepolo, M., Oberti, R., Zanetti, A., Vannucci, R., and Foley, S. F. (2007). “Trace-element partitioning between amphibole and silicate melt,” in *Amphiboles: Crystal Chemistry, Occurrence, and Health Issue*, eds F. C. Hawthorne, R. Oberti, G. Della Ventura, and A. Mottana (Berlin: De Gruyter), 417–451. doi: 10.2138/rmg.2007.67.11
- Van den Bleeken, G., and Koga, K. T. (2015). Experimentally determined distribution of fluorine and chlorine upon hydrous slab melting, and implications for F-Cl cycling through subduction zones. *Geochimica Et Cosmochimica Acta* 171, 353–373. doi: 10.1016/j.gca.2015.09.030
- White, A. J. R., and Chappell, B. W. (1977). ultrametamorphism and granitoid genesis. *Tectonophysics* 43, 7–22. doi: 10.1016/0040-1951(77)90003-8
- White, A. J. R., Chappell, B. W., and Wyborn, D. (1999). Application of the restite model to the Deddick Granodiorite and its enclaves - a reinterpretation of the observations and data of Maas et al. (1997). *J. Petrol.* 40, 413–421. doi: 10.1093/petroj/40.3.413
- Wiebe, R. A., Smith, D., Sturm, M., King, E. M., and Seckler, M. S. (1997). Enclaves in the Cadillac mountain granite (coastal Maine): samples of hybrid magma from the base of the chamber. *J. Petrol.* 38, 393–423. doi: 10.1093/petroj/38.3.393

- Xiao, W. J., Windley, B. F., Hao, J., and Zhai, M. G. (2003). Accretion leading to collision and the permian solonker suture, inner mongolia, China: termination of the central Asian orogenic belt. *Tectonics* 22. doi: 10.1029/2002tc001484
- Xiong, X. L., Adam, J., and Green, T. H. (2005). Rutile stability and rutile/melt HFSE partitioning during partial melting of hydrous basalt: implications for TTG genesis. *Chem. Geol.* 218, 339–359. doi: 10.1016/j.chemgeo.2005.01.014
- Xiong, X., Zhu, L., Zhang, G., Santosh, M., Jiang, H., Zheng, J., et al. (2020). Petrogenesis and tectonic implications of Indosinian granitoids from Western Qinling Orogen, China: Products of magma-mixing and fractionation. *Geosci. Front.* 11, 1305–1321. doi: 10.1016/j.gsf.2019.12.011
- Yang, G., Li, Y., Wu, H., Si, G., Jin, Z., and Zhang, Y. (2009). LA-ICP-MS zircon U-Pb dating of the huangyangshan pluton and its enclaves from kalamaili area eastern Junggar, Xinjiang, and geological implications. *Acta Petrologica Sinica* 25, 3197–3207.
- Yang, G., Li, Y., Wu, H., Si, G., Zhang, Y., and Jin, Z. (2010). A tentative discussion on the genesis of huangyangshan granite body in kalamaili orogen, east junggar. *Acta Geoscientia Sinica* 31, 170–182.
- Yang, G., Li, Y., Wu, H., Zhong, X., Yang, B., Yan, C., et al. (2011). Geochronological and geochemical constrains on petrogenesis of the Huangyangshan A-type granite from the East Junggar, Xinjiang, NW China. *J. Asian Earth Sci.* 40, 722–736. doi: 10.1016/j.jseas.2010.11.008
- Yang, J.-H., Wu, F.-Y., Chung, S.-L., Wilde, S. A., and Chu, M.-F. (2004). Multiple sources for the origin of granites: geochemical and Nd/Sr isotopic evidence from the gudaoling granite and its mafic enclaves, northeast China. *Geochimica Et Cosmochimica Acta* 68, 4469–4483. doi: 10.1016/j.gca.2004.04.015
- Yang, J.-H., Wu, F.-Y., Chung, S.-L., Wilde, S. A., and Chu, M.-F. (2006). A hybrid origin for the Qianshan A-type granite, northeast China: geochemical and Sr-Nd-Hf isotopic evidence. *Lithos* 89, 89–106. doi: 10.1016/j.lithos.2005.10.002
- Zorpi, M. J., Coulon, C., Orsini, J. B., and Cocirta, C. (1989). magma mingling, zoning and emplacement in calc-alkaline granitoid plutons. *Tectonophysics* 157, 315–329. doi: 10.1016/0040-1951(89)90147-9

Conflict of Interest: The authors declare that the research was conducted in the absence of any commercial or financial relationships that could be construed as a potential conflict of interest.

Copyright © 2021 Ye, Feng, Lei and Yang. This is an open-access article distributed under the terms of the Creative Commons Attribution License (CC BY). The use, distribution or reproduction in other forums is permitted, provided the original author(s) and the copyright owner(s) are credited and that the original publication in this journal is cited, in accordance with accepted academic practice. No use, distribution or reproduction is permitted which does not comply with these terms.



Geochronological Constraint on the Evolution of the Aktyuz Terrane, Kyrgyz North Tianshan, and the Fate of the Taldybulak Levoberezhny Gold Deposit

Wei Xi^{1,2,3}, Nuo Li^{1,2*}, Xiaohong Xia^{4,5*}, Xiaoxiao Ling⁶ and Yanshuang Wu^{1,2}

¹ Xinjiang Research Centre for Mineral Resources, Xinjiang Institute of Ecology and Geography, Chinese Academy of Sciences, Urumqi, China, ² Xinjiang Key Laboratory of Mineral Resources and Digital Geology, Urumqi, China, ³ University of Chinese Academy of Sciences, Beijing, China, ⁴ Sichuan Geological and Mineral Resources Group Co., Ltd., Chengdu, China, ⁵ Altynken Limited Liability Company, Zijin Mining Group, Bishkek, Kyrgyzstan, ⁶ State Key Laboratory of Lithospheric Evolution, Institute of Geology and Geophysics, Chinese Academy of Sciences, Beijing, China

OPEN ACCESS

Edited by:

Xiaohua Deng,
Beijing Institute of Geology for Mineral
Resources, China

Reviewed by:

Yin-Hong Wang,
China University of Geosciences,
China
Yi Zheng,
Sun Yat-sen University, China

*Correspondence:

Nuo Li
nuolipku@126.com
Xiaohong Xia
xiaxiaohong55555@163.com

Specialty section:

This article was submitted to
Economic Geology,
a section of the journal
Frontiers in Earth Science

Received: 05 February 2021

Accepted: 07 April 2021

Published: 20 May 2021

Citation:

Xi W, Li N, Xia X, Ling X and Wu Y
(2021) Geochronological Constraint
on the Evolution of the Aktyuz Terrane,
Kyrgyz North Tianshan, and the Fate
of the Taldybulak Levoberezhny Gold
Deposit. *Front. Earth Sci.* 9:664361.
doi: 10.3389/feart.2021.664361

The Aktyuz Terrane in Kyrgyz North Tianshan is of particular interest due to the occurrence of high and ultrahigh pressure (HP–UHP) rocks and it containing the third largest gold deposit in Kyrgyz North Tianshan, i.e., Taldybulak Levoberezhny (abbreviated to Taldybulak Lev.). To constrain the ages of the host Kemin Complex and its auriferous monzogranite porphyry, detailed zircon U–Pb dating [by laser ablation inductively coupled plasma-mass spectrometry (LA-ICPMS) and secondary ion mass spectrometry (SIMS)] and Lu–Hf isotopic analyses were carried out. The intensively altered auriferous monzogranite porphyry yielded two weighted mean ages of 444 ± 3 Ma ($n = 14$, mean squared weighted deviation (MSWD) = 0.49, by LA-ICPMS) and 440 ± 5 Ma ($n = 8$, MSWD = 0.82, by SIMS) that are indistinguishable within error ranges. Such ages are consistent with a previously reported sulfide Re–Os isochron age of 434 ± 18 Ma, supporting a Silurian porphyry gold mineralization. The granitic gneiss yielded a protolith age of 773 ± 7 Ma ($n = 7$, MSWD = 0.04) and two metamorphic ages of 514 ± 4 Ma ($n = 8$, MSWD = 0.09) and 483 ± 3 Ma ($n = 11$, MSWD = 0.04). Detrital zircons from one fuchsite schist sample yielded highly variable ages from 729 ± 13 Ma to $2,463 \pm 30$ Ma, with 12 data points weighted at 740 ± 5 Ma (MSWD = 0.95). The metamorphic overgrowth yielded a weighted mean age of 460 ± 4 Ma ($n = 4$, MSWD = 0.15). Detrital zircons in the migmatitic amphibolite are aged from 788 ± 7 Ma to $3,447 \pm 32$ Ma, with two major concentrations at 941 ± 7 Ma ($n = 13$, MSWD = 0.95) and 794 ± 5 Ma ($n = 8$, MSWD = 0.19). The metamorphic overgrowth yielded an average age of 555 ± 4 Ma ($n = 8$, MSWD = 0.65). The detrital and xenocryst zircons, and evolved $\epsilon_{\text{Hf}}(t)$ values (–20.9 to –7.8) and old two-stage Hf model ages (1,367–3,159 Ma), revealed the presence of a Precambrian basement that may be dated back to the Archean Eon. The two metamorphic ages may correlate with oceanic subduction and continental collision, respectively.

Keywords: zircon U–Pb age, Lu–Hf isotope, Aktyuz terrane, Kyrgyz North Tianshan, Taldybulak Levoberezhny gold deposit

INTRODUCTION

The Central Asia Orogenic Belt (CAOB; **Figure 1A**) is the biggest accretion-type orogen since the Phanerozoic (Windley et al., 2007; Zhu et al., 2007; Gao et al., 2009b; Xiao et al., 2012, 2013). Its southwestern area, i.e., the Tianshan Orogen in Kazakhstan, Kyrgyzstan, and northwest China, is a composite of Paleozoic island arcs, ophiolites, metamorphic complexes, and Precambrian microcontinental terranes that were wedged together during the early Paleozoic (Kröner et al., 2012). The mechanism of Paleozoic accretion, however, remains poorly constrained (Sengor and Natalin, 1994; Charvet et al., 2007, 2011; Windley et al., 2007; Kröner et al., 2012, 2013). Critical questions, such as the geometry, extent, and source of individual terranes or sutures and also the age and origin of medium- to high-grade metamorphic complexes are still unsolved (Alexeiev et al., 2011; Kröner et al., 2012; Rojas-Agramonte et al., 2013). In this context, the high and ultrahigh-pressure (HP-UHP) metamorphic belt that characterizes ancient subduction zones and sutures is of particular interest due to the important information it can provide for the reconstruction of tectonic evolution (Gao and Klemd, 2003; Klemd et al., 2005; Orozbaev et al., 2007, 2010; Gao et al., 2009a).

The Aktyuz terrane is one of two eclogite and garnet amphibolite occurrences in Kyrgyz North Tianshan (Kröner et al., 2012; Rojas-Agramonte et al., 2013). It is composed of two litho-tectonic assemblages, named the Aktyuz and Kemin Complexes. The former is outcropped in the northern area and is well studied because it contains HP-UHP rocks that can be used as a powerful tool for geodynamic reconstruction (Kröner et al., 2012; Rojas-Agramonte et al., 2013). The latter is in the southern area of the terrane and, by contrast, is poorly studied. Kröner et al. (2012) and Rojas-Agramonte et al. (2014) carried out sensitive high-resolution ion microprobe (SHRIMP) zircon U–Pb studies of granitoid gneiss and paragenesis that precisely constrained their protolith age. Nevertheless, their metamorphic timing remains to be elucidated, preventing the correlation with the metamorphism and exhumation of HP-UHP rocks in this region.

Although it does not contain UHP-HP rocks, the Kemin Complex has a giant gold endowment. The Taldybulak Levoberezhny (abbreviated to Taldybulak Lev. hereafter) deposit is the third largest gold deposit in Kyrgyz North Tianshan, with a reserve of Au 130 t and an average grade of 6.9 g/t (Zhao et al., 2015; Xi et al., 2018). Since its discovery in the 1960s, the genesis of the deposit has been hotly debated. The proposed genesis includes porphyry (Djenchuraeva et al., 2008; Trifonov, 2016), orogeny (Goldfarb et al., 2014; Xue et al., 2014), or multiple mineralization involving both orogeny and porphyry (Zhao et al., 2015, 2017). Recently, Xi et al. (2018) recognized massive sulfide ores that are typical for the volcanogenic massive sulfide (VMS) or sedimentary exhalative (SEDEX) system instead of the above-mentioned porphyry or orogenic deposits. Hence, a comprehensive geochronological study of the host rocks and the ore-causative granitic porphyry is invaluable for an improved understanding of the deposit formation and regional tectonic evolution.

In this article, we report the results obtained from an integrated *in situ* U–Pb and Hf isotope analysis of zircon for an auriferous monzogranite porphyry and metamorphic rocks of the Kemin Complex hosting the Taldybulak Lev. deposit. These data provide a well-constrained temporal framework of regional magmatic and metamorphic events. In combination with the previous work, they also shed light on regional tectonic evolution and ore formation.

GEOLOGICAL BACKGROUND

The CAO is sandwiched between blocks including the plate of Siberia, Eastern Europe, Tarim, Karakum, and North China (**Figure 1A**). It is composed of an island arc, seamount, ophiolite suite, Precambrian micro-continents, and an accretionary wedge and is attributed to the collision between Siberia and the Tarim–North China Block (Windley et al., 2007; Xiao et al., 2009; Chen et al., 2012). The Tianshan Orogen in Kyrgyzstan in the southwestern part of CAO has been traditionally grouped into three fault-bounded tectonic zones (**Figure 1B**), from south to north, i.e., South Tianshan, Middle Tianshan, and North Tianshan, with the Atbashi-Inylchek suture and Nikolaev Line as the main boundaries (Seltmann et al., 2011; Kröner et al., 2012). Kyrgyz North Tianshan is characterized by several Precambrian microcontinents (or fragments), ophiolite belts representative of a former oceanic basin (e.g., Djalair-Naiman and Kyrgyz-Terskey), and HP-UHP eclogite facies metamorphic rocks (Windley et al., 2007; Glorie et al., 2010; De Grave et al., 2013). There are abundant Andes-type early Paleozoic magmatic rocks, with the Ordovician granitoids considered as products of subduction and subsequent Silurian granitoid as products of post-collision. The Kyrgyz Middle Tianshan contains Devonian to Pennsylvanian passive margin carbonate and siliciclastic facies rocks. It is considered as the deformed southern margin of the Kazakhstan continent (Alexeiev et al., 2019). On its southwestern margin, there are well-developed continental arcs of Silurian, Devonian, and Pennsylvanian origins (Rojas-Agramonte et al., 2014; Alexeiev et al., 2016). The Kyrgyz South Tianshan is dominated by sedimentary assemblages, followed by minor volcanic, metamorphic, and ophiolitic rocks. They are stacked together by a south-facing thrust in an accretionary and collisional setting in the Late Carboniferous and Permian (Han et al., 2011; Alexeiev et al., 2019).

The Aktyuz terrane in Kyrgyz North Tianshan is considered as part of the North Tianshan microcontinent that rifted from the Tarim craton (Rojas-Agramonte et al., 2014). It is bound by the Late Cambrian–Early Ordovician Dzhair-Naiman ophiolite-bearing suture in the north, and a Grenvillian-age granitic gneiss in the south (Kröner et al., 2012; Rojas-Agramonte et al., 2014; Alexeiev et al., 2019). In this region, there is an extensively exposed Precambrian metamorphic basement including Aktyuz and Kemin Complex rocks. The Aktyuz Complex in the north has an outcropped length of more than 20 km and a width up to 5 km (Orozbaev et al., 2010). It mainly consists of well-foliated pelitic and granitic gneisses

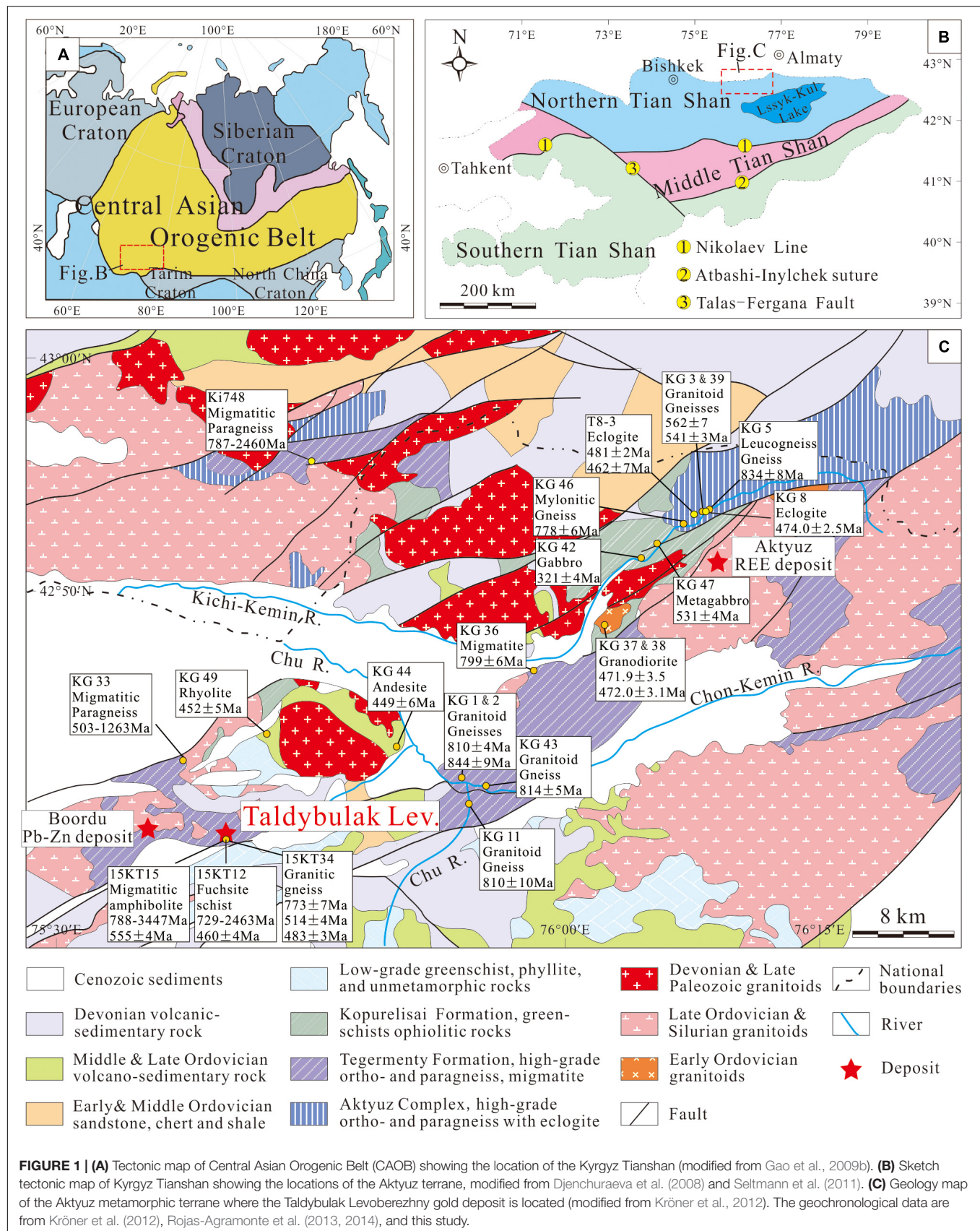


FIGURE 1 | (A) Tectonic map of Central Asian Orogenic Belt (CAOB) showing the location of the Kyrgyz Tianshan (modified from Gao et al., 2009b). **(B)** Sketch tectonic map of Kyrgyz Tianshan showing the locations of the Aktyuz terrane, modified from Djenchuraeva et al. (2008) and Seltnann et al. (2011). **(C)** Geology map of the Aktyuz metamorphic terrane where the Taldybulak Levoberezhny gold deposit is located (modified from Kröner et al., 2012). The geochronological data are from Kröner et al. (2012), Rojas-Agramonte et al. (2013, 2014), and this study.

enclosing layers or boudins of eclogite, garnet amphibolite, and amphibolite (Bakirov et al., 2003). The gneisses were previously considered to be Archean and Paleoproterozoic in age (Bakirov and Korolev, 1979; Kiselev et al., 1993), although Kröner et al. (2012) reported protolith ages of 541 – 562 and 778 – 834 Ma for granitoid gneisses. Orozbaev et al. (2010) emphasized that the Aktyuz eclogite is unusual in that they occur as remnants in mafic dykes that previously intruded the sedimentary protolith, instead of in rocks derived from oceanic crust. The eclogites had undergone peak metamorphism in the range of 550–670°C and 1.6–2.3 GPa (Orozbaev et al., 2010). Tagiri et al. (1995) obtained a mineral/whole-rock Rb–Sr isochron age of 749 ± 14 Ma for an eclogite sample, but this age is controversial. Rojas-Agramonte et al. (2013) and Klemm et al. (2014) reported Sm–Nd, Ar/Ar, and Lu–Hf ages of 462 ± 7 Ma, 481 ± 2 Ma, and 474.3 ± 2.2 Ma, respectively (Supplementary Table 4). Such ages are comparable with the muscovite Ar/Ar plateau age for the country rock gneiss (475.7 ± 5.5 and 470.6 ± 5.3 Ma; Kröner et al., 2012) and thus may be reasonable for the HP–UHP metamorphic event.

The Kemin Complex in the south of the terrane is distinguished from the Aktyuz Complex by the absence of HP–UHP metamorphic rocks. It was subdivided into three formations named Kopurelisai, Kapchigai, and Kokbulak by Bakirov et al. (2003) and Orozbaev et al. (2010) or two formations named Kopurelisai and Tegermenty (Djenchuraeva et al., 2008). In this article, the second classification scheme was adopted. The Kopurelisai Formation consists of massive but foliated isotropic hornblende gabbro, greenschist-facies metabasalt, locally with well-preserved but flattened pillows. It is in thrust contact along a serpentinite mélange zone with tectonically overlying gneiss of the Aktyuz Complex and interpreted as constituents of a dismembered ophiolite (Bakirov et al., 2003). Kröner et al. (2012) obtained a SHRIMP zircon U–Pb age of 531.2 ± 3.7 Ma for a foliated metagabbro. The Tegermenty Formation mainly consists of migmatitic paragneisses with subordinate granitoid gneisses. The matrix of some migmatites consists of amphibolitic gabbro, ultramafic rocks, and cherty schists, considered as a metamorphosed ophiolite by Bakirov et al. (2003). Previous α -Pb zircon dating yielded ages of $2,550 \pm 250$ and $2,050 \pm 200$ Ma for migmatitic gneisses (Bakirov and Korolev, 1979), whereas conventional multigrain U–Pb zircon dating of migmatitic tonalitic-trondhjemitic gneisses yielded ages of $\sim 2,050$ and $1,850 \pm 10$ Ma (Kiselev et al., 1993). More precise geochronological data reported by Kröner et al. (2012) revealed protolith ages of 799 – 844 Ma for granitic gneiss and 503 – 2,460 Ma for paragneisses.

The Ordovician volcanic-sedimentary rocks unconformably overlying on the Kemin Complex are the oldest undeformed rocks in the region (Figure 1C). One rhyolite sample from the Burubai Formation yielded a SHRIMP zircon U–Pb age of 452.2 ± 2.8 Ma, and one porphyritic basaltic andesite from the Cholok Formation is nearly contemporaneous, aged 448.9 ± 5.6 Ma (Kröner et al., 2012). Devonian volcanic-sedimentary rocks in the southwest of the terrane are distributed around the metamorphic basement. Together they constitute the Taldybulak-Boordu dome (with an area of about

10 km \times 20 km) that was subsequently intruded by the Late Paleozoic subvolcanic rocks.

DEPOSIT GEOLOGY AND SAMPLE DESCRIPTION

The Taldybulak Lev. gold deposit is located in the Taldybulak shear zone, which is an overthrust complex of highly deformed lithologies (Malyukova, 2001). The exposed strata include the Kopurelisai and Tegermenty Formations of the Kemin Complex and the volcanic-sedimentary rocks of the Devonian Barkol Formation (Figure 2A). The Kopurelisai Formation here is dominated by amphibolite, biotite amphibolite, schist, and migmatite, and the Tegermenty Formation consists mainly of mica schist with layers of gneiss and chert. The Devonian Barkol Formation unconformably covers the Tegermenty Formation metamorphic rocks. It is dominated by andesite, basaltic andesite, volcanic breccia, tuff, and sandstone (Djenchuraeva et al., 2008).

There are three shear and thrust zones in the mining area, which are successively named the Upper zone, the Middle zone, and the Taldybulak zone from west to east, with a total thickness of about 700 m (Figures 2A,B). In the shearing zone, there is a chaotic assemblage of schist, amphibolite, and gneisses that have undergone intensive quartz–calcite and quartz–sericite alteration. They were further offset by an NE-trending or nearly E–W-trending fault and intruded by numerous diorite-monzodiorite-monzogranite or dolerite dykes (Zhao et al., 2015, 2017).

Thus far, 11 gold ore bodies have been discovered, which are confined to the shear zone or around the granitic dykes (Figures 2A,B). The No. 1 orebody is a prominent entity located at the junction of the Taldybulak shear and thrust zone with a nearly E–W-trending fault. Its eastern area is vein- or pipe-shaped and decreases gradually to the west. It extends for ca. 1,300 m, and a width of 60 – 350 m and a thickness of 20 – 80 m (Xi et al., 2018). Except for Nos. I and II, other orebodies occur mainly as veins or lenses.

In this study, four samples, namely one auriferous porphyry and three wall rock samples from the Kopurelisai Formation, were selected for zircon U–Pb dating and Lu–Hf isotopic studies (Figure 3). Sample 15KT12 is a fuchsite schist collected from the No. 1582 ramp. It is dominated by quartz and fuchsite, where auriferous pyrite was associated with secondary sericite or calcite. Sample 15KT34 has little or no mineralization. It is a pink, medium-grained, finely layered granitic gneiss collected from the outcrops at the ventilation room of the deposit. It mainly consists of plagioclase, K-feldspar, biotite, quartz, and secondary sericite and epidote. Sample 15KT15 is a migmatitic amphibolite collected from the No. 1582 ramp. The matrix is gray or gray-green colored and consists mainly of hornblende, plagioclase, and biotite with volumetric percentages of 55, 40, and <5%, respectively. The hornblende was partially replaced by epidote, chlorite, calcite, and quartz. The leucosome is pink colored and contains mainly quartz, plagioclase, and K-feldspar. Sample 15KD66 is a medium-grained, reddish-colored biotite monzonite porphyry intruding the fuchsite schist. The sample

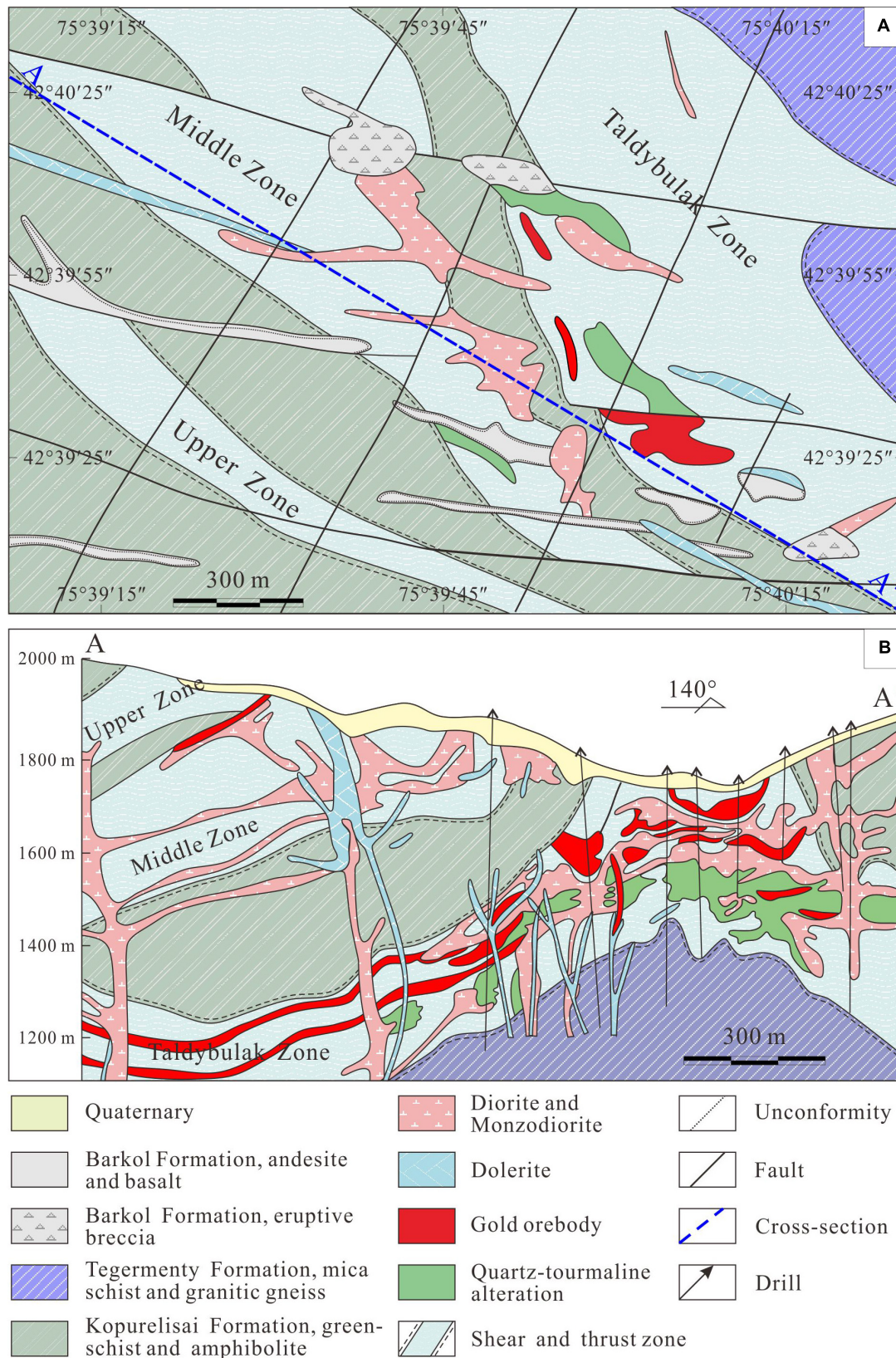


FIGURE 2 | Geological map (A) and a cross-section along A–A' (B) of the Taldybulak Levoberezhny gold deposit, modified from Malyukova (2001) and Djenchuraeva et al. (2008).

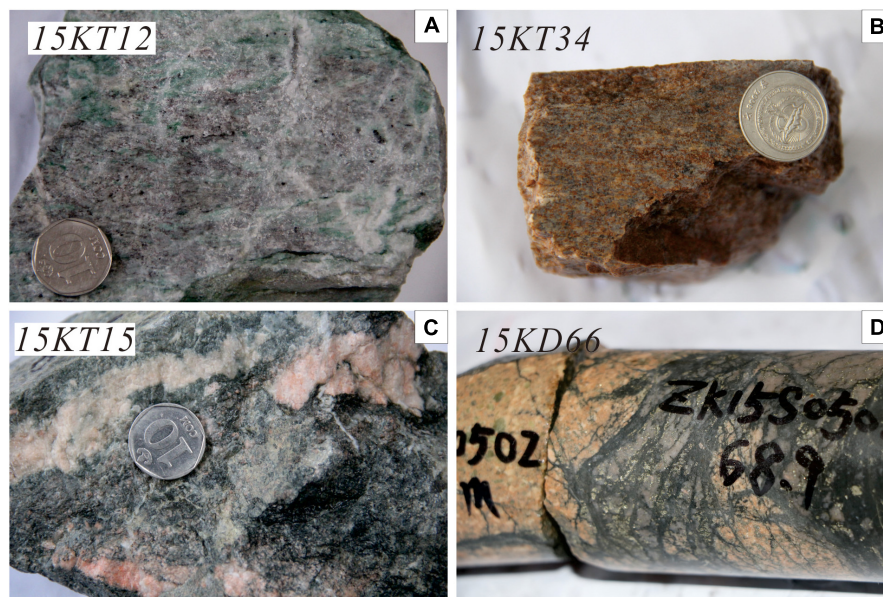


FIGURE 3 | Photographs showing samples used for geochronological study. (A) Fuchsite schist; (B) granitic gneiss; (C) migmatitic amphibolite; and (D) monzogranite porphyry.

was collected from drilling hole ZK15S0502 (with a sample depth of 68.9 m). It has a typical porphyritic texture, with plagioclase and K-feldspar phenocrysts in a groundmass of K-feldspar, plagioclase, quartz, biotite, and apatite. The auriferous porphyry was intensively altered by sericite and calcite, hosting abundant quartz–tourmaline–pyrite veins or veinlets (Figure 3D).

ANALYTICAL METHOD

In situ Zircon U–Pb Dating and Hf Isotopic Analyses

Zircon grains were extracted by magnetic techniques and conventional heavy liquids and then purified by handpicking under a binocular microscope. Representative zircon grains were mounted in epoxy resin and polished down to expose the grain center. Cathodoluminescence (CL) images of zircons were taken at the Beijing Zircon Linghang Technology Company, Beijing. The images were obtained by a MonoCL³⁺ (Gatan Company, Abingdon, England) CL spectroscopy attached to a Quanta 400 FEG Scanning Electron Microscope. The operative condition during CL imaging was 15 kV.

In situ zircon laser ablation inductively coupled plasma-mass spectrometry (LA-ICPMS) U–Pb dating, Hf isotope, and trace element analyses were conducted at the State Key Laboratory of Continental Dynamics at Northwest University, Xi'an. The laser denudation system consists of a Geolas 2005 excimer ArF laser-ablation system (Lambda Physik AG, Göttingham, Germany), Elan 6100 DRC (Dynamic Reaction Cell) Q-ICP-MS (Inductively Coupled Plasma Mass Spectrometry, Perkin Elmer Inc., United States of America), and Nu Plasma HR MC-ICP-MS (High Resolution Multiple Collector Inductively Coupled

Plasma Mass Spectrometer, Nu Instruments Ltd., Wrexham, United Kingdom), which were used for simultaneous acquisition of trace elements, Hf isotopes, and U–Pb isotopes. The zircon aerosol generated by the laser was split into two transmission tubes by a y-shaped convection device after the ablation unit and introduced into two mass spectrometers at the same time. The hafnium isotopes were measured by MC-ICP-MS, and U–Pb age and trace element composition were measured by Q-ICP-MS. An Edwards E2M80 source rotary pump was used in the interface area to improve sensitivity. The spot size was 30 μm for U–Pb dating and 40 μm for Lu–Hf analysis. Helium was used as the carrier gas to provide effective aerosol transport to ICP and to minimize aerosol deposition. The detailed analytical procedure can be found in Yuan et al. (2008).

Standard Zircon GJ-1, 91500, NIST SRM 610, and Monasteries are used as reference standards for calibration and control of analytical instrument conditions. Uranium, lead, thorium, and trace element concentrations were calibrated using ^{29}Si as an internal standard and NIST SRM 610 as an external reference standard. ^{202}Hg in Q-ICP-MS gas blank is usually < 30 . Therefore, the contribution of ^{204}Hg to ^{204}Pb is negligible and has not been adjusted. The $^{206}\text{Pb}/^{238}\text{U}$, $^{207}\text{Pb}/^{206}\text{Pb}$, $^{208}\text{Pb}/^{232}\text{Th}$, and $^{207}\text{Pb}/^{235}\text{U}$ ratios were calculated using the GLITTER 4.4 (GEMOC, Macquarie University, Sydney, Australia), and zircon 91500 was used to correct instrument mass deviations and depth-dependent element and isotope fractionation. Zircon 91500 and GJ-1 is used as an external standard. Obtained $^{206}\text{Pb}/^{238}\text{U}$ weighted mean ages of 91,500 and GJ-1 were $1,062 \pm 5.6$ Ma (2σ) and 604.8 ± 5.6 Ma (2σ), respectively, highly consistent with the recommended ages. Common lead was corrected according to the method put forward by Andersen (2002). The results were reported as one error. The Concordia plot and

weighted average U–Pb age (95% confidence) were obtained using the ISOPLOT 3.0 (Ludwig, 2003).

Interference of $^{176}\text{Lu}/^{177}\text{Hf}$ was corrected by measuring the intensity of the ^{175}Lu without interference, and the $^{176}\text{Lu}/^{177}\text{Hf}$ was calculated using the recommended ratio of $^{176}\text{Lu}/^{175}\text{Lu}$ with 0.02669 (Horn and von Blanckenburg, 2007). In the same way, we used the recommended $^{176}\text{Yb}/^{177}\text{Hf}$ ratio of 0.5586 (Hazarika et al., 2018) to correct the $^{176}\text{Yb}/^{172}\text{Yb}$ ratio to calculate the $^{176}\text{Yb}/^{177}\text{Hf}$ ratio. In the course of analysis, the ratio of $^{176}\text{Hf}/^{177}\text{Hf}$ obtained in the analysis is 0.282296 ± 50 for 91,500 and 0.282019 ± 15 for GJ-1, consistent with the recommended ratios of 0.2823075 ± 58 and 0.282015 , respectively. Analytical ratios of $^{176}\text{Hf}/^{177}\text{Hf}$, $^{176}\text{Yb}/^{177}\text{Hf}$, and $^{176}\text{Lu}/^{177}\text{Hf}$ are reported with 2σ error. The initial $^{176}\text{Lu}/^{177}\text{Hf}$ ratio is calculated based on chondrite simultaneously with zircon growth in magma. The decay constant of the chondritic ratios of $^{176}\text{Lu}/^{177}\text{Hf}$ with 0.282772, 1.867×10^{-11} for ^{176}Lu (Söderlund et al., 2004) and $^{176}\text{Lu}/^{177}\text{Hf}$ with 0.0332 are introduced by Blichert-Toft and Albarède (1997). The current ratios of 0.28325 at $^{176}\text{Lu}/^{177}\text{Hf}$ and 0.0384 at $^{176}\text{Lu}/^{177}\text{Hf}$ are used to calculate single-stage Hf model ages ($T_{\text{DM}1}$) relative to the depleted mantle. The referred $^{176}\text{Lu}/^{177}\text{Hf}$ value with 0.0093 for average upper continental crust and the $f_{\text{Lu}/\text{Hf}}$ value of -0.55 for the average continental crust are used to calculate two-stage Hf model ages ($T_{\text{DM}2}$) (Vervoort and Patchett, 1996; Vervoort and Blichert-Toft, 1999). The $f_{\text{Lu}/\text{Hf}}$ ratio equals $(^{176}\text{Lu}/^{177}\text{Hf})_{\text{s}}/(^{176}\text{Lu}/^{177}\text{Hf})_{\text{CHUR}} - 1$, where the $(^{176}\text{Lu}/^{177}\text{Hf})_{\text{CHUR}} = 0.0332$, and the $(^{176}\text{Lu}/^{177}\text{Hf})_{\text{s}}$ value is obtained from analysis of the sample.

SIMS Zircon U–Pb Dating

To better constrain the ages of the rim or cores, zircon U–Pb dating of sample 15KT15 and 15KD66 was further conducted using a Cameca IMS-1280HR SIMS at the Institute of Geology and Geophysics, Chinese Academy of Sciences in Beijing. For comprehensive descriptions of the instrument and the analytical procedure, refer to Li et al. (2009). A brief summary is provided here. The primary O_2^- ion beam spot is about $20 \mu\text{m} \times 30 \mu\text{m}$ in size, and positive secondary ions were extracted with a 10-kV potential. In the secondary ion beam optics, an energy window of 60 eV was used, together with a mass resolution of ca. 5,400 (at 10% peak height), to separate Pb^+ peaks from isobaric interferences. A single electron multiplier was used in the ion-counting mode to measure secondary ion beam intensities by peak jumping mode. Analyses of the standard zircon Plesovice were interspersed with unknown grains. Each measurement consists of seven cycles. Pb/U calibration was performed relative to zircon standard Plesovice ($^{206}\text{Pb}/^{238}\text{U}$ age = 337 Ma, Slama et al., 2008); U and Th concentrations were calibrated against zircon standard 91500 (Th = 29 ppm and U = 81 ppm; Wiedenbeck et al., 1995). A long-term uncertainty of 1.5% [1σ relative standard deviation (RSD)] for $^{206}\text{Pb}/^{238}\text{U}$ measurements of the standard zircons was propagated to the unknowns (Li et al., 2010), despite that the measured $^{206}\text{Pb}/^{238}\text{U}$ error in a specific session is generally $\leq 1\%$ (1σ RSD). The measured compositions were corrected for common Pb using non-radiogenic ^{204}Pb . Corrections are sufficiently small to be insensitive to the choice of common Pb composition, and an

average of present-day crustal composition (Stacey and Kramers, 1975) is used for the common Pb assuming that the common Pb is largely surface contamination introduced during sample preparation. Data reduction was carried out using the ISOPLOT 3.0 (Ludwig, 2003). Uncertainties in individual analyses in data tables are reported at the 1σ level; Concordia U–Pb ages are reported with 95% CI, unless otherwise stated.

To monitor the external uncertainties of SIMS U–Pb zircon dating calibrated against a Plesovice standard, a standard zircon GBW04705 (Qinghu) was alternately analyzed as an unknown together with other unknown zircons. Nine measurements on Qinghu zircon yielded a Concordia age of 160 ± 1 Ma, which is identical within error to the recommended value of 159.5 ± 0.2 Ma (Li et al., 2013).

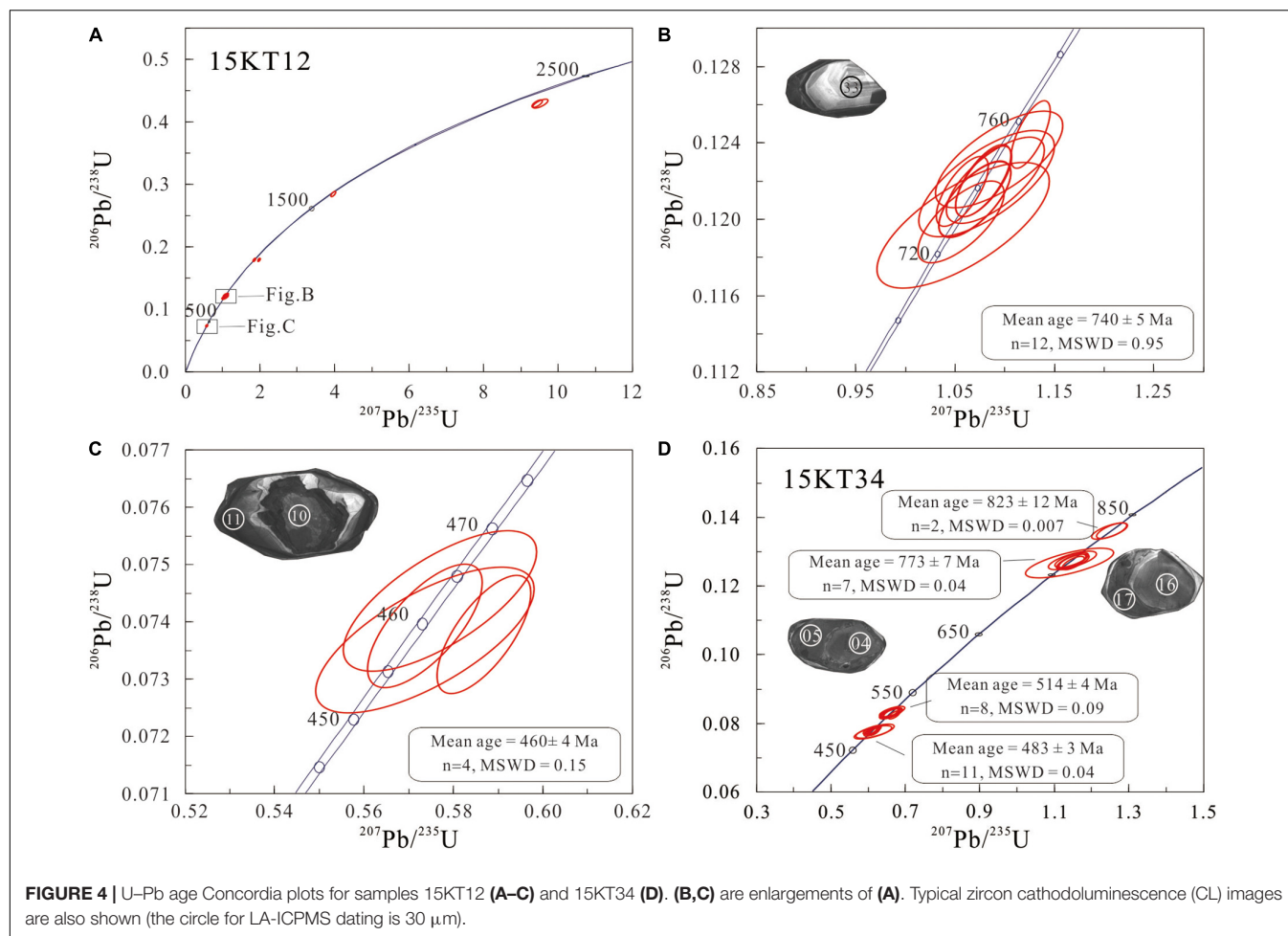
RESULTS

Zircon Morphology and U–Pb Ages

The zircon CL images, LA-ICPMS, and SIMS U–Pb data are available in **Supplementary Tables 1,2** and **Figures 4–6**. It is commonly accepted that precise dating of zircon crystals younger than 1,000 Ma is best achieved by using concordant $^{206}\text{Pb}/^{238}\text{U}$ age, whereas the older grains would be more precisely dated using $^{206}\text{Pb}/^{207}\text{Pb}$ ages due to decreasing amounts of radiogenic lead available for the measurement (Kröner et al., 2012; Rojas-Agramonte et al., 2013; Zhang et al., 2020).

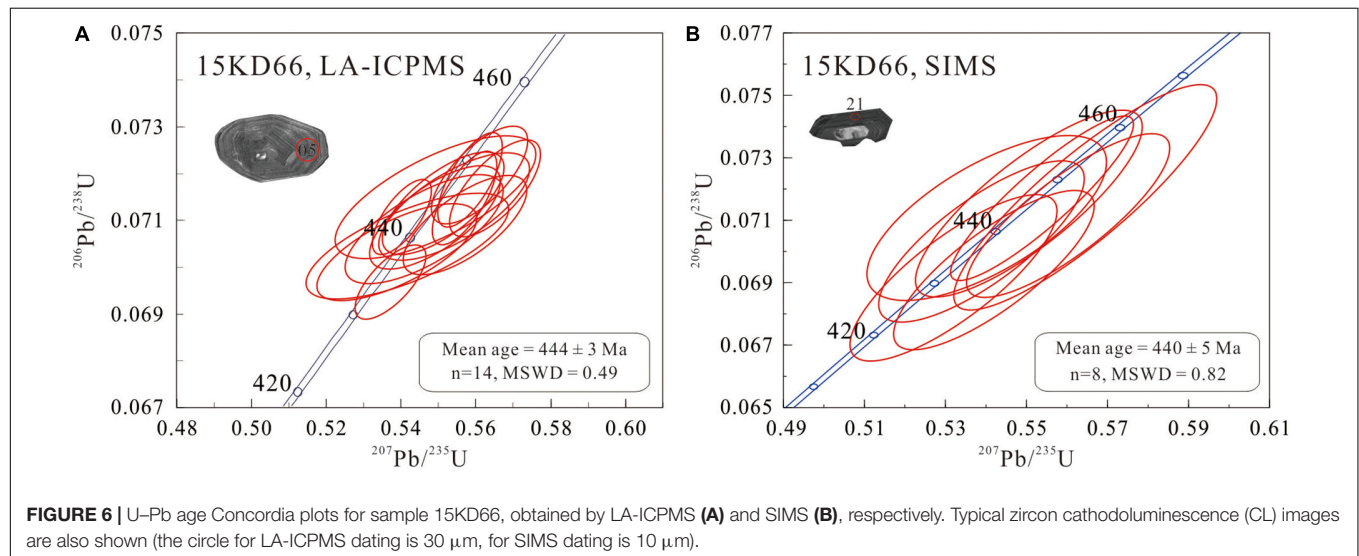
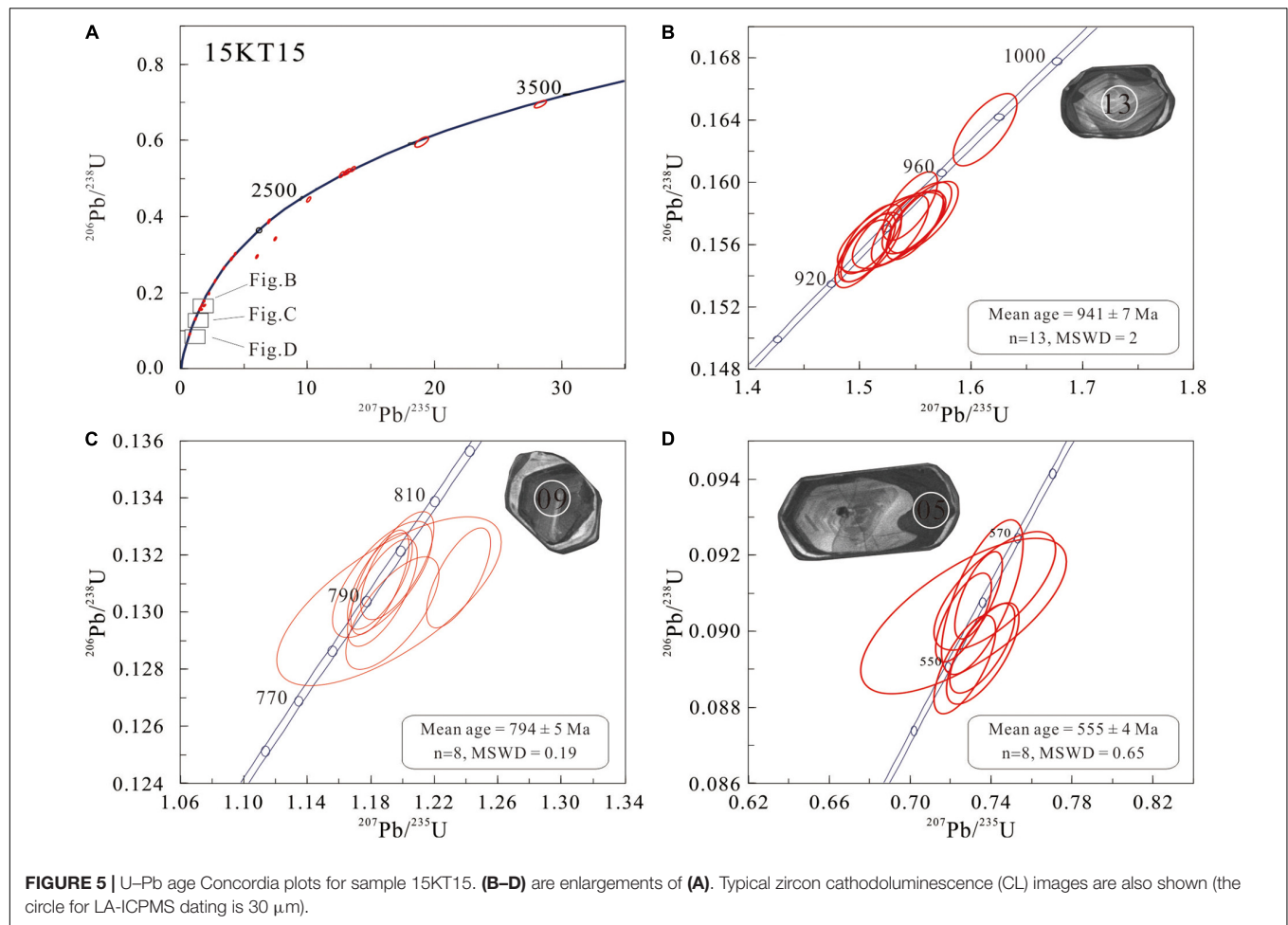
Detrital zircons collected from sample 15KT12 are mainly light black and colorless, with lengths ranging from 80 to $280 \mu\text{m}$ and length/width ratios from 1.3:1 to 3:1. They tend to have near-euhedral to subhedral shapes, indicative of rather short transport and source areas not far from the depositional sites. The CL images illustrate that the zircons generally have complex inner textures, with a bright, oscillatory zoned core overgrown by a dark, unzoned rim (**Figure 4B**). Nineteen of 23 LA-ICPMS analyses were performed on the central part. They yielded highly variable U (36 – 1,393 ppm) and Th (30 – 250 ppm) contents as well as Th/U ratios (0.07 – 1.51) and provide an array of concordant or near-concordant data corresponding to ages between 729 and 2,463 Ma (**Figure 4A**). The most prominent concentrate emanates from those with oscillatory zoning (**Figure 4B**), with 12 data points yielding a weighted mean age of 740 ± 5 Ma ($^{206}\text{Pb}/^{238}\text{U}$ age, mean squared weighted deviation (MSWD) = 0.95). Another seven spots on the core yielded $^{206}\text{Pb}/^{207}\text{Pb}$ ages of ca. 1,065 Ma, 1,190 Ma, 1,647 Ma, and ca. 2,450 Ma (**Supplementary Table 1**). The overgrowth has unambiguously lower Th (12 – 104 ppm) content and Th/U ratios (0.03 – 0.09). Four data points collectively yielded a weighted mean age of 460 ± 4 Ma ($^{206}\text{Pb}/^{238}\text{U}$ age, MSWD = 0.15). This distribution (**Figures 4A–C**) suggests a Neoproterozoic–Cambrian age (most probably between 729 and 463 Ma) of deposition and the source terrane ranges in age from Neoproterozoic to Paleoproterozoic. The rock underwent metamorphism at 460 Ma.

In sample 15KT34, the zircon crystals are gray-white-colored short prismatic or subhedral crystal, with a common length of 100–180 μm and length/width ratio of 1.3:1 to 2.5:1. The CL



imaging revealed that most zircon crystals contain inherited cores that can either be oscillatory zoned or exhibit faint zonation. Seventeen LA-ICPMS analyses on the interior reveal three populations. The older two populations have similar oscillatory zonation and overlapped U (105–299 ppm), Th (68–289 ppm), and Th/U ratios (0.46–1.16). Two analyses yielded an average of 823 ± 12 Ma ($n = 2$, MSWD = 0.007), and seven analyses yielded a younger age of 773 ± 7 Ma ($n = 7$, MSWD = 0.04). They are interpreted as the age of zircon xenocryst and the granitic protolith, respectively. The third population is easily distinguished by their unzoned or patch-zoned CL response and high U (388–558 ppm), but low Th (14–52 ppm) and Th/U ratios (0.03–0.11). They collectively give a weighted average age of 514 ± 4 Ma ($n = 8$, MSWD = 0.09) (Figure 4D and Supplementary Table 1), which may represent an important metamorphic event. Outward from the core is a dark overgrowth with little or no zonation. Eleven analyses reveal extremely low Th and Th/U ratios of 2–7 ppm and 0.01–0.03, respectively. Obtained $^{206}\text{Pb}/^{238}\text{U}$ ages vary from 481 ± 8 to 485 ± 5 Ma (1 σ error), with a weighted average of 483 ± 3 Ma ($n = 11$, MSWD = 0.04). Furthermore, there is a very bright rim that is too thin to be dated precisely (Figure 4D).

In sample 15KT15, the zircon crystals have highly variable morphologies and colors (Figures 5B–D). Some grains are dark colored, subrounded columns, or almost spherical, whereas others are brown in color and subrounded to near-euhedral in shape. They range from 100 to 120 μm in length and 70 to 100 μm in width, yielding length/width ratios of 1.2:1 to 2:1. The CL images show that most zircons exhibit a distinct core-rim texture. In some cases, an inherited core is identified on the basis of its bright and well-round appearance, with oscillatory or planar zoning indicative of a magmatic origin. Interior domain mantling cores tend to be dark and unzoned in the CL response. They are further overgrown by thin, bright, and unzoned rims. A total of 50 LA-ICPMS analyses were conducted and provided mostly concordant, but highly diverse ages (Figure 5A). Eight core analyses yielded $^{206}\text{Pb}/^{238}\text{U}$ dates of 788–797 Ma and combined to a weighted average of 794 ± 5 Ma ($n = 8$, MSWD = 0.19). A second population on the core comprises 13 dates ranging from 931 to 948 Ma, with a weighted average of 941 ± 7 Ma ($n = 13$, MSWD = 2). Other spots on the core yielded ages ranging from 975 to 3,447 Ma (Supplementary Table 1). The youngest $^{206}\text{Pb}/^{238}\text{U}$ date averaged at 555 ± 4 Ma ($n = 8$, MSWD = 0.65) emanates from the thin zircon overgrowths that have low U (245–1,384 ppm, mostly < 500 ppm), extremely



low Th (15–122 ppm, mostly < 35 ppm), and Th/U ratio (0.04–0.09). This could be regarded as the best estimate of an unbiased age for a metamorphic event. Furthermore, there is a rim, which is too thin to be dated precisely. The above

result is further verified by an additional seven SIMS analyses that yielded consistent ages of 1,021 – 1,102 Ma, 895, 689, and 556 Ma (Supplementary Table 2). The youngest two ages averaged at 558 ± 12 Ma (MSWD = 0.03) may represent the

metamorphic event, whereas other older ages represent the ages of the sedimentary protolith.

Most zircon crystals collected from sample 15KD66 have an euhedral, elongated shape with sharp facets and pointed tips. The zircon crystals are mainly colorless and transparent, with lengths ranging from 140 to 270 μm and length/width ratios from 1.5:1 to 3:1. Occasionally, the prisms are irregular, suggesting chemical corrosion or physical abrasion. The CL investigation (Figures 6A,B) revealed that most zircon crystals have oscillatory zoning. Some grains have irregular cores mantled by oscillatory-zoned magmatic rims, and the core-rim boundary is often irregular and marked by a CL-bright thin band (Figure 6B). The cores are small (50–70 μm in length), with points being analyzed by LA-ICPMS. Three analyses on the inherited cores yielded ages of 766 ± 13 , 770 ± 8 , and $2,567 \pm 35$ Ma, respectively (Supplementary Table 1). In an attempt to date the crystallization age of the porphyry, the LA-ICPMS analyses were mainly concentrated on the zircon rims. A total of 14 analyses yielded consistent $^{206}\text{Pb}/^{238}\text{U}$ ages varying from 434 ± 7 to 448 ± 4 Ma, with a weighted mean of 444 ± 3 Ma ($n = 14$, MSWD = 0.49, Figure 6A). The same sample was further analyzed by SIMS. Nine analyses on the thin overgrowth yielded a weighted mean of 440 ± 5 Ma ($n = 8$, MSWD = 0.82, Figure 6B) that is indistinguishable from the LA-ICPMS data within error. Thus, the emplacement of the monzogranite porphyry is constrained to ca. 442 Ma.

Zircon Hf Isotopes

In sample 15KT12, three zircons belonging to the 740-Ma-aged group have $^{176}\text{Lu}/^{177}\text{Hf}$ ratios of 0.000232–0.000785, $^{176}\text{Hf}/^{177}\text{Hf}$ ratios of 0.281841–0.281963, $\epsilon\text{Hf}(t)$ values of -17.0 to -12.4 , and two-stage Hf model ages ($T_{\text{DM}2}$) of 2,430–2,732 Ma. Another two zircons aged 1,193 and 2,463 Ma yielded higher $^{176}\text{Lu}/^{177}\text{Hf}$ ratios (0.001294 and 0.001248) but lower $^{176}\text{Hf}/^{177}\text{Hf}$ ratios (0.281680 and 0.280993) relative to the younger ones, with calculated $\epsilon\text{Hf}(t)$ of -13.2 and -9.8 and $T_{\text{DM}2}$ ages of 2,813 and 3,563 Ma (Figure 7 and Supplementary Table 3).

In sample 15KT34, the 773-Ma-aged zircons have $^{176}\text{Lu}/^{177}\text{Hf}$ ratios within a range between 0.000568 and 0.002407, $^{176}\text{Hf}/^{177}\text{Hf}$ ratios between 0.281681 and 0.281943, $\epsilon\text{Hf}(t)$ values between -22.8 and -12.8 and $T_{\text{DM}2}$ ages between 2,469 and 3,088 Ma, respectively (Figure 7 and Supplementary Table 3).

The zircons from the protolith of sample 15KT15 yielded a highly variable Hf isotopic composition. In general, the crystals aged 793 Ma have much lower $^{176}\text{Lu}/^{177}\text{Hf}$ ratios (0.281771–0.281963) and $\epsilon\text{Hf}(t)$ values (-18.3 to -11.5), but higher $T_{\text{DM}2}$ ages (2,407–2,826 Ma) in comparison with the older group aged 941 Ma ($^{176}\text{Lu}/^{177}\text{Hf}$ = 0.281947–0.282269, $\epsilon\text{Hf}(t)$ = -8.5 to $+2.6$, $T_{\text{DM}2}$ = 1,634–2,335 Ma) (Figure 7 and Supplementary Table 3).

Magmatic zircon rims from sample 15KD66 yielded slightly higher $^{176}\text{Lu}/^{177}\text{Hf}$ ratios (0.000730–0.002008) and $T_{\text{DM}2}$ ages (1,908–2,197 Ma), but lower $^{176}\text{Hf}/^{177}\text{Hf}$ ratios (0.282162–0.282287) and $\epsilon\text{Hf}(t)$ values (from -12.3 to -7.7 , Figure 7 and Supplementary Table 3) compared with the inherited cores. Two 770-Ma-aged cores yielded $^{176}\text{Lu}/^{177}\text{Hf}$ ratios of 0.000177 and 0.000175, $^{176}\text{Hf}/^{177}\text{Hf}$ ratios of 0.282006 and 0.282009, $\epsilon\text{Hf}(t)$

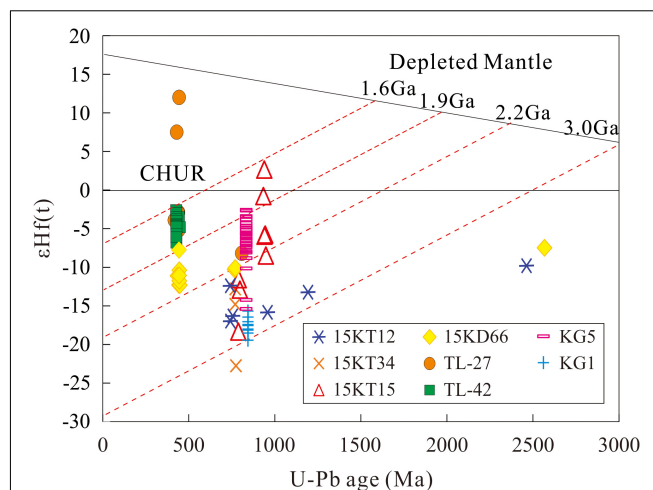


FIGURE 7 | $\epsilon\text{Hf}(t)$ vs. age plot showing most zircon samples from the Aktyuz Terrane with negative $\epsilon\text{Hf}(t)$ values. Samples: fuchsite schist (15KT12), granitic gneiss (15KT34), migmatitic amphibolite (15KT15), and gray granitoid gneiss (KG1, Kröner et al., 2012) of the Kemin Complex, well-banded leucogneiss (KG5, Kröner et al., 2012) of the Aktyuz Complex, and monzogranite porphyry (15KD66), diorite (TL-27, Zhao et al., 2017), and monzonite (TL-42, Zhao et al., 2017) outcropped in the Taldybulak Levoberezhny deposit.

values of -10.3 and -10.1 , and $T_{\text{DM}2}$ of 2,310 and 2,301 Ma. Another Archean aged core (2,567 Ma), however, has an even higher $^{176}\text{Hf}/^{177}\text{Hf}$ ratio of 0.280993, $\epsilon\text{Hf}(t)$ value of -7.5 and $T_{\text{DM}2}$ age of 3,503 Ma (Figure 7 and Supplementary Table 3).

DISCUSSION

Evidence for Porphyry-Type Gold Mineralization

Since its discovery in 1963, the ore genesis of the Taldybulak Lev. deposit has been hotly debated. Some scholars regard the deposit as a complex porphyry system (Trifonov, 1987; Malyukova, 2001; Djenchuraeva et al., 2008; Seltnann et al., 2014) based on the spatial association between the porphyritic dykes and gold mineralization revealed by extensive drilling in Soviet times (Figure 2B). Emplacement ages of these intrusions, however, are poorly constrained, with available ages varying considerably from 183 to 403 Ma (without dating error, K–Ar dating). By contrast, Xue et al. (2014) and Goldfarb et al. (2014) proposed that the deposit may be orogenic gold system considering that it is spatially controlled by the shear and thrust zones. Zhao et al. (2015, 2017) suggested a multistage mineralization involving both orogenic and porphyry events and provided two sulfide Re–Os isochron ages of 434 ± 18 Ma ($n = 6$, MSWD = 24) and 511 ± 18 Ma ($n = 5$, MSWD = 2.0). Thus, the emplacement age of the granitic dyke and its contribution to gold mineralization becomes a key point.

In this article, one monzogranite sample with crosscutting quartz–tourmaline–pyrite veinlets was collected. The rock was intensively altered, with typical porphyry-type alterations including silicic, potassic, and sericite alterations.

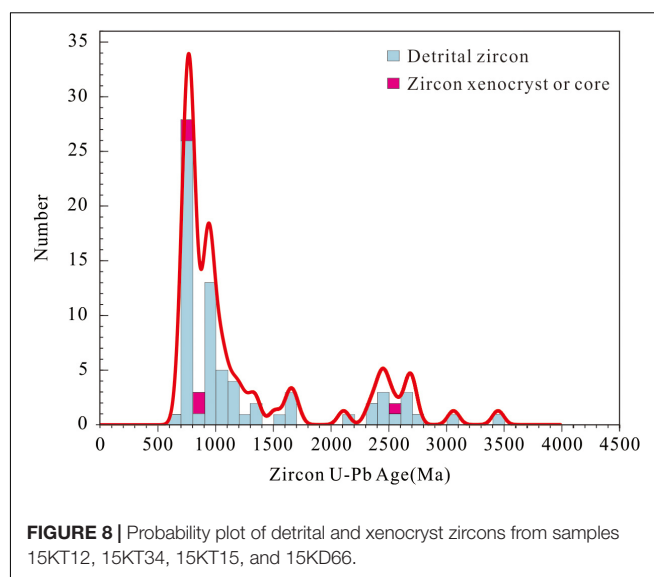
Djenchuraeva et al. (2008) further proposed a vertically zoned hydrothermal alteration surrounding the diorite–monzonite intrusion, including the argillic zone corresponding to the apical part, the quartz–carbonate, and quartz–sericite zones around the intrusion, grading at depth to potassic alteration and the quartz–tourmaline alteration. Detailed petrological studies revealed native gold and electrum (with gold contents of 76.51%) inclusions in pyrite, and the pyrite itself contains considerable invisible gold up to 0.26% (Xi et al., 2018). Our new U–Pb ages provide a robust geochronological constraint for the emplacement of the auriferous monzogranite porphyry (Supplementary Table 1), with overlapping ages of 444 ± 3 Ma ($n = 14$, MSWD = 0.93) and 440 ± 4 Ma ($n = 9$, MSWD = 6.5) revealed by LA-ICPMS and SIMS U–Pb dating, respectively. These ages are consistent with the sulfide Re–Os isochron age of 434 ± 18 Ma ($n = 6$, MSWD = 24, Zhao et al., 2015) within error, providing another line of evidence for porphyry mineralization.

The Age and Reworking of the Precambrian Basement

The Kyrgyz North Tianshan, including the Aktyuz terrane, is one of the oldest orogenic domains of the CAOB. It has a Precambrian block mainly consisting of Grenvillian-aged granitoids, whereas the subordinate Paleoproterozoic and Archean rocks crop out in its western extension to southern Kazakhstan (Kröner et al., 2014). Based on detrital and xenocryst zircon ages and comparison with published ages from the Chinese Tianshan and the Tarim Craton, Rojas-Agramonte et al. (2014) suggested that the Kyrgyz North Tianshan rifted off the Tarim craton.

In this study, the inhomogeneous population of zircons from the fuchsite schist and migmatitic amphibolite supports a detrital origin of the zircons. These zircons are mostly near-euhedral to subhedral in shape, with a few exhibiting slight rounding at their terminations, suggesting a relatively short transport and source areas not far from the depositional site. As shown in the age probability plot (Figure 8), the most prominent age frequency is bracketed between 700 and 1,200 Ma. Such a major phase of Neo- to Mesoproterozoic magmatic event is not only prevalent in North Tianshan, but also well documented in surrounding areas such as Kyrgyz Middle Tianshan, southern Kazakhstan, the Chinese Tianshan, and the Tarim Craton (Kiselev and Maksumova, 2001; Kröner et al., 2007; Zhou et al., 2017, 2018). Another main cluster of single grain U–Pb ages between 2,300 and 2,700 Ma accords well with the Paleoproterozoic to Neoproterozoic peaks revealed by detrital and xenocryst zircons from the North Tianshan, South Tianshan, and the Tarim craton (Rojas-Agramonte et al., 2014). A minor peak between 1,500 and 1,700 Ma is difficult to interpret because it corresponds to the global magmatic hiatus (Condie and Aster, 2010). The oldest zircon age is $3,447 \pm 32$ Ma, suggesting the presence of Archean crust.

The old zircon cores or xenocryst also carry a record of older geological history, signifying the existence of a Precambrian basement at depth. In the monzogranite porphyry, three zircon cores yielded concordant ages of 766, 770, and 2,567 Ma,



respectively. In the case of granitic gneiss, there are two xenocrysts aged at ca. 823 Ma. The younger ages grouped at 770–823 Ma fit well to the Neoproterozoic peak for detrital zircons, whereas the old age of 2,567 Ma corresponds to the Archean peak around 2,500 Ma (Figure 8). Zircon xenocrysts of similar ages are also reported for other rocks in this region. For instance, Zhao et al. (2017) reported two inherited zircon aged 813 and 808 Ma from a diorite outcropped in the deposit. Kröner et al. (2012) recognized zircon xenocrysts dated at 1,180 Ma in a Neoproterozoic migmatite of the Kemin Complex and at 1,263 Ma in a para-migmatite sample.

More evidence for an early Archean crustal component is presented based on our zircon Lu–Hf isotope studies of monzogranite porphyry and other detrital zircons. In the former case, 26 out of 27 zircons yielded negative $\epsilon_{\text{Hf}}(t)$ values between -22.8 and -0.8 (Figure 7), with one exceptional positive $\epsilon_{\text{Hf}}(t)$ value of 2.6. Zhao et al. (2017) carried out zircon Lu–Hf isotopic studies for one diorite (435.3 ± 3.8 Ma) and one monzogranite (427.7 ± 1.9 Ma) sample of similar ages. Their results yielded slightly higher $\epsilon_{\text{Hf}}(t)$ values (-8.2 to 12), with data varying between negative and positive. The Neoproterozoic granitoids outcropped in the Aktyuz terrane yielded even lower negative $\epsilon_{\text{Hf}}(t)$ values indicative of crustal remelting. Kröner et al. (2012) obtained zircon $\epsilon_{\text{Hf}}(t)$ values of -19.5 to -15.7 for a gray granodioritic gneiss (844 ± 9 Ma) of the Kemin Complex, and -15.4 to -2.6 for a well-banded leucogneiss (834 ± 8 Ma) of the Aktyuz Complex. Such highly evolved $\epsilon_{\text{Hf}}(t)$ values, in combination with geochemistry and whole-rock Sr–Nd isotopic data (Kröner et al., 2012; Zhao et al., 2017), reveal that at least the Paleozoic and Neoproterozoic magmatic rocks outcropped in the Aktyuz terrane mainly resulted from partial melting of continental crust or its mixing with limited juvenile or short-lived material. This supports the conclusion proposed by Kröner et al. (2013) that the production of mantle-derived or juvenile continental crust in CAOB has been overstated. The results also provide clues that there is

an extensive Precambrian basement at depth, more than the surface outcrops; the Aktyuz terrane consists of reworked crustal material, some of it with a long history, possibly dating back to the Archean Eon.

The Timing of Metamorphism and Its Geological Significance

No geochronological constraint had been available for the metamorphism of the Kemin Complex until the present study. Our work reveals zircon overgrowth with a low Th/U ratio (generally < 0.1 , **Supplementary Table 1**) and unzoned or patch-zoned CL imaging. They generally grow surrounding an oscillatory-zoned core and are attributed to a metamorphic origin according to Corfu et al. (2003) and Wu and Zheng (2004). Such overgrowths yielded a weighted mean of 460 ± 4 Ma for fuchsite schist, indicating a Middle Ordovician metamorphic event. The migmatitic amphibolite, by contrast, exhibits Neoproterozoic metamorphism at 555 ± 4 Ma, although a subsequent metamorphic event cannot be excluded since the ca. 555-Ma-aged overgrowth still has a distinct bright, thin rim (**Figure 5D**). Interestingly, the granitic gneiss experienced two metamorphic events at ca. 514 Ma and 483 Ma that can even be recorded by a single zircon grain (the left one in **Figure 5D**). Hence, the above data reveal that both a Neoproterozoic–Cambrian (514 – 555 Ma) and an Ordovician (460 – 483 Ma) metamorphism were accompanied by zircon growth. The latter matches well with the timing of HP–UHP metamorphism of the Aktyuz Complex (462–481 Ma, by Sm–Nd, Lu–Hf, and Ar/Ar dating, **Supplementary Table 4**), but no precursor metamorphic event has been reported for the Aktyuz Complex. Instead, the Neoproterozoic–Cambrian metamorphic event is in good agreement with the HP–UHP metamorphism at other complexes such as Kokchetav, Makbal, and Anrakhai.

At the Kokchetav Terrane, northern Kazakhstan, the HP–UHP metamorphism and subsequent exhumation are well confined to 530 – 540 Ma and 505 – 530 Ma by biotite Ar/Ar and zircon U–Pb dating (Claoué-Long et al., 1991; Shatsky et al., 1999; Hermann et al., 2001; Dobretsov et al., 2005, 2006; Buslov et al., 2010). The migmatites and gneisses within the terrane (Katayama et al., 2001; Ragozin et al., 2009) yielded zircon U–Pb ages of 505 – 540 Ma, with the oldest and youngest being interpreted as the timing of peak metamorphism and the timing of UHP exhumation, respectively. The subsequent collisional deformation occurred at 470–490 Ma, inducing folding, shearing, and retrograde metamorphism (De Grave et al., 2006; Dobretsov and Buslov, 2007; Zhimulev et al., 2011). At the Makbal block of the Kyrgyz North Tianshan, the HP–UHP event was constrained to 480 – 509 Ma by monazite and zircon U–Pb dating (Togonbaeva et al., 2009; Konopelko et al., 2012). In the case of the Anrakhai Complex, SHRIMP zircon U–Pb dating yielded ages of ca. 490 Ma for garnet pyroxenite, constraining a Late Cambrian HP metamorphism and exhumation (Alexeiev et al., 2011). These lines of geochronological evidence support a possible link among these terranes and support a Kokchetav–Kyrgyz North Tianshan belt (Windley et al., 2007; Kröner et al., 2012).

Tectonic Evolution and the Fate of the Gold Deposit

The current geodynamic model for the Aktyuz terrane (Alexeiev et al., 2011; Kröner et al., 2012; Rojas-Agramonte et al., 2013) favors the North Tianshan as a microcontinent sandwiched between the Dzhailair–Naiman basin in the north and the Kyrgyz–Terskey basin in the south during the Cambrian and Early Ordovician. Our new data, in combination with previous results (Kröner et al., 2012; Rojas-Agramonte et al., 2013, 2014), reveal a Precambrian basement that shows affinity to other small fragments in the Kokchetav–North Tianshan belt. The Aktyuz terrane itself, however, is not a coherent continental domain, but instead, is composed of tectonic slivers including Precambrian continental crusts and Early Paleozoic ophiolite. This is also evident in the variable Hf isotope of the Kemin and Aktyuz Complexes (**Figure 7**).

The southwest-directed subduction of the Paleo-Asian Ocean beneath the North Tianshan induced the opening of the Dzhailair–Naiman back-arc basin. The zircon U–Pb data of 531.2 ± 3.7 Ma (Kröner et al., 2012) for a leucogabbro sample from the Kopurelisai ophiolite suite confirms an Early Cambrian age (Ryazantsev et al., 2009). Although there are no available geochronological data, the massive sulfide ores of the Taldybulak Lev. deposit (Xi et al., 2018) may be the product of back-arc extension (**Figure 9**). It is hosted by the Kopurelisai Formation and underwent orogenic deformation. The sulfide Re–Os isochron of 511 ± 18 Ma that is interpreted as the timing of orogenic-type mineralization (Zhao et al., 2015, 2017) may alternatively record an initial massive sulfide precursor. The large uncertainty in this date prevents a comprehensive understanding of its geological meaning. Another response to the oceanic subduction is the granitoids with continental arc affinity. Kröner et al. (2012) reported zircon U–Pb ages of 541–562 Ma for the youngest granitoid gneisses at the Aktyuz terrane, which is comparable to a metadacite sample from the Anrakhai area. The Cambrian metamorphic zircon overgrowth recognized in our study may evidence this convergence. These rocks represent exotic slivers that share a similar metamorphic history with the Makbal or Kokchetav terranes.

Subsequent northwards subduction of the Dzhailair–Naiman basin and its final closure led to the convergence of the Anrakhai and Aktyuz microcontinents (Kröner et al., 2012). The previous passive margin of the North Tianshan microcontinent was involved in subduction underneath the Anrakhai microcontinent. Klemd et al. (2014) suggest that the HP rocks of the Aktyuz Complex represent subducted continental crust, and the eclogite and hosting metasedimentary rocks underwent metamorphism at variable depths of the subduction zone and subsequently juxtaposed during exhumation in the subduction channel. Our present study, in combination with previous stratigraphic, structural, and isotopic data (Kröner et al., 2012 and references therein), constrains the timing of the collision to Early Ordovician (most probably between 480 and 460 Ma). The Silurian (428–440 Ma) diorite and monzogranite outcropped in the Taldybulak Lev. deposit may be formed by partial melting of continental crust in a post-collision setting (Zhao et al., 2017).

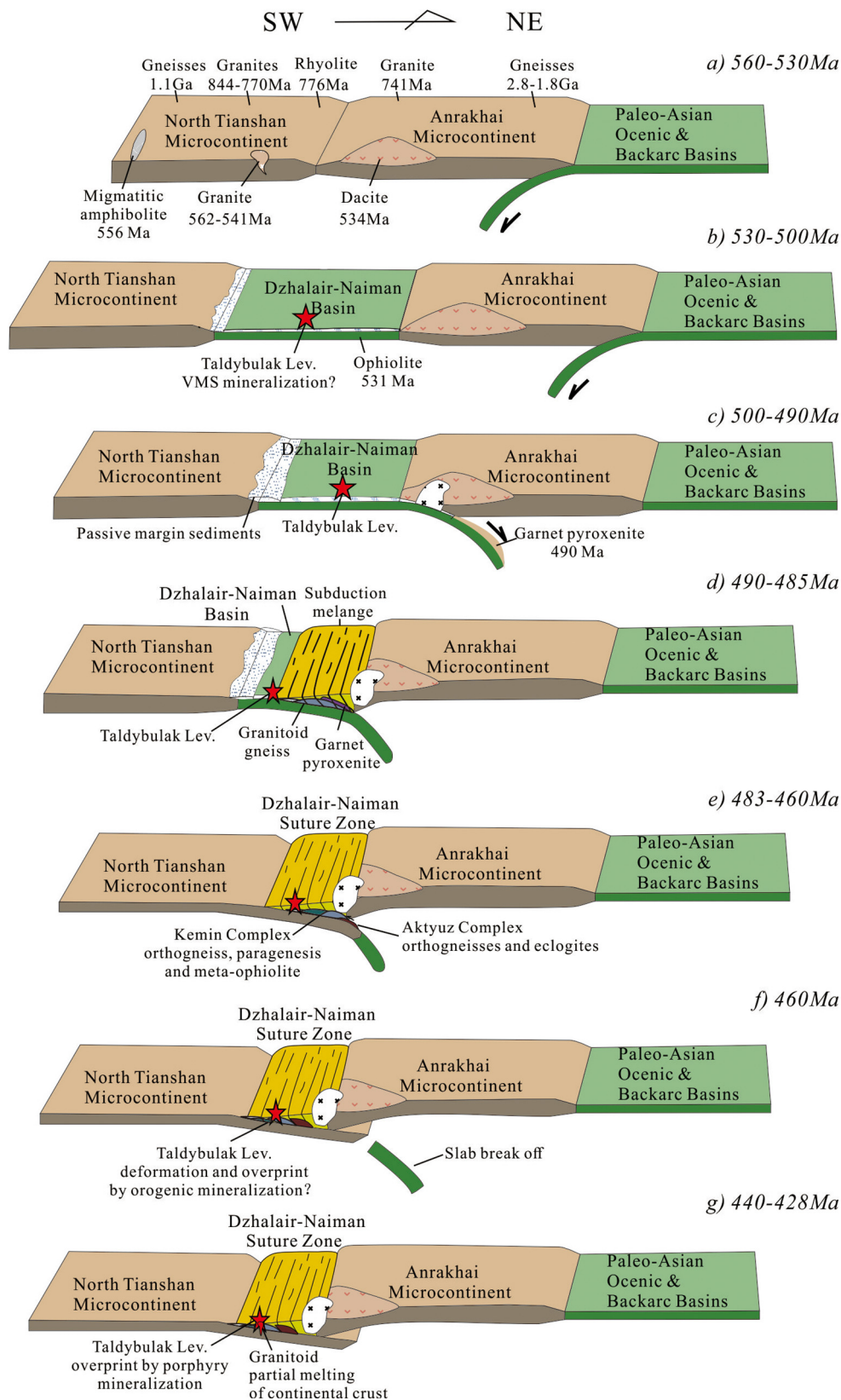


FIGURE 9 | Tectonic evolution of the Aktyuz Terrane and the fate of the Taldybulak Levoberezhny deposit (modified from Kröner et al., 2012).

They intruded into the metamorphic rocks, induced porphyry-type gold mineralization that superimposed on earlier VMS, and/or orogenic gold mineralization.

CONCLUSION

- (1) The ore-causative monzogranite porphyry at the Taldybulak Lev. deposit was dated at 440 Ma.
- (2) Three wall rock samples of the Kemin Complex yielded two episodes of metamorphic ages at 514 – 556 and 460 – 483 Ma, which may represent the age of oceanic subduction and continental collision, respectively.
- (3) The detrital and xenocryst zircons (689 – 3,447 Ma), and highly evolved $\epsilon\text{Hf}(t)$ values (– 20.9 to – 7.8) and old two-stage Hf model ages (1,367 – 3,159 Ma), reveal the presence of a Precambrian basement that may be dated back to the Archean Eon.

DATA AVAILABILITY STATEMENT

The original contributions presented in the study are included in the article/**Supplementary Material**, further inquiries can be directed to the corresponding author/s.

AUTHOR CONTRIBUTIONS

WX provided initial data as part of a Ph.D. thesis. NL and XX designed the project, and took the lead on writing the manuscript. XL and YW helped with the SIMS and LA-ICPMS dating. All authors contributed to the article and approved the submitted version.

REFERENCES

- Alexeiev, D. V., Kröner, A., Hegner, E., Rojas-Agramonte, Y., Biske, Y. S., Wong, G., et al. (2016). Middle to late Ordovician arc system in the Kyrgyz middle tianshan: from arc-continent collision to subsequent evolution of a Palaeozoic continental margin. *Gondwana Res.* 39, 261–291. doi: 10.1016/j.gr.2016.02.003
- Alexeiev, D. V., Kröner, A., Kovach, V. P., Tretyakov, A. A., Rojas-Agramonte, Y., Degtyarev, K. E., et al. (2019). Evolution of cambrian and early ordovician arcs in the Kyrgyz North Tianshan: insights from U–Pb zircon ages and geochemical data. *Gondwana Res.* 66, 93–115. doi: 10.1016/j.gr.2018.09.005
- Alexeiev, D. V., Ryazantsev, A. V., Kröner, A., Tretyakov, A. A., Xia, X., and Liu, D. Y. (2011). Geochemical data and zircon ages for rocks in a high-pressure belt of Chu–Yili mountains, southern Kazakhstan: implications for the earliest stages of accretion in Kazakhstan and the Tianshan. *J. Asian Earth Sci.* 42, 805–820. doi: 10.1016/j.jseas.2010.09.004
- Andersen, T. (2002). Correction of common lead in U–Pb analyses that do not report ^{204}Pb . *Chem. Geol.* 192, 59–79. doi: 10.1016/S0009-2541(02)00195-X
- Bakirov, A. B., and Korolev, V. G. (1979). The age of oldest rocks in Tianshan. *Izvestiya AN SSSR Geol. Ser.* 7, 15–25.
- Bakirov, A. B., Tagiri, M., Sakiev, K. S., and Ivleva, E. A. (2003). The lower precambrian rocks in the Tien Shan and their geodynamic setting. *Geotectonics* 37, 368–380.
- Blichert-Toft, J., and Albarède, F. (1997). The Lu–Hf isotope geochemistry of chondrites and the evolution of the mantle–crust system. *Earth Planet. Sci. Lett.* 148, 243–258. doi: 10.1016/S0012-821X(97)00040-X
- Buslov, M. M., Zhimulev, F. I., and Travin, A. V. (2010). New data on the structural setting and $40\text{Ar}/^{39}\text{Ar}$ age of the MP–LP metamorphism of the Dautlet formation, Kokchetav metamorphic belt, Northern Kazakhstan, and their tectonic interpretation. *Doklady Earth Sci.* 434, 1147–1151. doi: 10.1134/S1028334X10090023
- Charvet, J., Liangshu, S., and Laurent-Charvet, S. (2007). Paleozoic structural and geodynamic evolution of eastern Tianshan (NW China): welding of the Tarim and Junggar Plates. *Episodes* 30, 162–186.
- Charvet, J., Shu, L., Laurent-Charvet, S., Wang, B., Faure, M., Cluzel, D., et al. (2011). Palaeozoic tectonic evolution of the Tianshan belt, NW China. *Sci. China Earth Sci.* 54, 166–184. doi: 10.1007/s11430-010-4138-1
- Chen, Y. J., Pirajno, F., Wu, G., Qi, J. P., and Xiong, X. L. (2012). Epithermal deposits in North Xinjiang, NW China. *Intern. J. Earth Sci.* 101, 889–917. doi: 10.1007/soo531-011-0689-4
- Claoué-Long, J. C., Sobolev, N. V., Shatsky, V. S., and Sobolev, A. V. (1991). Zircon response to diamond-pressure metamorphism in the Kokchetav Massif, USSR. *Geology* 19, 710–713. doi: 10.1130/0091-7613(1991)019<0710:ZRTDPM>2.3.CO;2
- Condie, K. C., and Aster, R. C. (2010). Episodic zircon age spectra of orogenic granitoids: the supercontinent connection and continental growth. *Precamb. Res.* 180, 227–236. doi: 10.1016/j.precamres.2010.03.008
- Corfu, F., Hanchar, J. M., Hoskin, P. W., and Kinny, P. (2003). Atlas of zircon textures. *Rev. Mineral. Geochem.* 53, 469–500. doi: 10.2113/0530469
- De Grave, J., Buslov, M. M., Zhimulev, F., Vermeesch, P., McWilliams, M. O., and Metcalf, J. (2006). The Early Ordovician age of deformations in the Kokchetav

FUNDING

This research was financially supported by the National Key Research and Development Program of China (No. 2017YFC0601202) and a Xinjiang Outstanding Youth Scientific Grant (No. 2020Q006).

ACKNOWLEDGMENTS

We are grateful to XD (the handling editor) and the two reviewers for their constructive comments and suggestions.

SUPPLEMENTARY MATERIAL

The Supplementary Material for this article can be found online at: <https://www.frontiersin.org/articles/10.3389/feart.2021.664361/full#supplementary-material>

Supplementary Table 1 | LA-ICPMS zircon U–Pb data for samples from the porphyry and metamorphic rocks.

Supplementary Table 2 | SIMS zircon U–Pb data for samples from the porphyry and metamorphic rocks.

Supplementary Table 3 | Zircon Lu–Hf isotope data for samples from the porphyry and wall rocks.

The following parameters were employed in the calculation: $(^{176}\text{Lu}/^{177}\text{Hf})_{\text{CHUR}} = 0.0332$, $(^{176}\text{Hf}/^{177}\text{Hf})_{\text{CHUR},0} = 0.282772$, $(^{176}\text{Lu}/^{177}\text{Hf})_{\text{DM}} = 0.0384$, $(^{176}\text{Hf}/^{177}\text{Hf})_{\text{DM},0} = 0.28325$ (Blichert-Toft and Albarède, 1997); $^{176}\text{Lu}/^{177}\text{Hf}$ for the average upper continental crust is 0.0093 (Vervoort and Patchett, 1996; Vervoort and Blichert-Toft, 1999); ^{176}Lu decay constant $\lambda = 1.867 \times 10^{-11} \text{ a}^{-1}$ (Söderlund et al., 2004).

Supplementary Table 4 | Available geochronological data from rocks from the Aktyuz terrane.

- subduction-collision zone: new structural and Ar-40/Ar-39 data. *Russian Geol. Geophys.* 47, 441–450.
- De Grave, J., Glorie, S., Buslov, M. M., Stockli, D. F., McWilliams, M. O., Batalev, V. Y., et al. (2013). Thermo-tectonic history of the Issyk-Kul basement (Kyrgyz Northern Tien Shan, Central Asia). *Gondwana Res.* 23, 998–1020. doi: 10.1016/j.gr.2012.06.014
- Djenchuraeva, R. D., Borisov, F. I., Pak, N. T., and Malyukova, N. N. (2008). Metallogeny and geodynamics of the Aktiuz-Boordu mining District, Northern Tien Shan, Kyrgyzstan. *J. Asian Earth Sci.* 32, 280–299. doi: 10.1016/j.jseas.2007.10.019
- Dobretsov, N. L., and Buslov, M. M. (2007). Late cambrian-Ordovician tectonics and geodynamics of Central Asia. *Russian Geol. Geophys.* 48, 71–82. doi: 10.1016/j.rgg.2006.12.006
- Dobretsov, N. L., Buslov, M. M., and Zhimulev, F. I. (2005). Cambrian-Ordovician tectonic evolution of the Kokchetav metamorphic belt, northern Kazakhstan. *Russian Geol. Geophys.* 46, 785–795.
- Dobretsov, N. L., Buslov, M. M., Zhimulev, F. I., Travin, A. V., and Zayachkovy, A. A. (2006). Vendian-Early Ordovician geodynamic evolution and model for exhumation of ultrahigh- And high-pressure rocks from the Kokchetav subduction-collision zone. *Russian Geol. Geophys.* 47, 428–444.
- Gao, J., and Klemm, R. (2003). Formation of HP-LT rocks and their tectonic implications in the western Tianshan Orogen, NW China. *Geochem. Age Const. Lithos.* 66, 1–22. doi: 10.1016/S0024-4937(02)00153-6
- Gao, J., Long, L., Klemm, R., Qian, Q., Liu, D., Xiong, X., et al. (2009a). Tectonic evolution of the South Tianshan orogen and adjacent regions, NW China: geochemical and age constraints of granitoid rocks. *Intern. J. Earth Sci.* 98, 1221–1238. doi: 10.1007/s00531-008-0370-8
- Gao, J., Qian, Q., Long, L. L., Zhang, X., Li, J. L., and Su, W. (2009b). Accretionary orogenic process of Western Tianshan, China. *Geol. Bull. China* 28, 1804–1816.
- Glorie, S., De Grave, J., Buslov, M., Elburg, M., Stockli, D., and Gerdes, A. (2010). Multi-method chronometric constraints on the evolution of the Northern Kyrgyz Tien Shan granitoids (Central Asian Orogenic Belt): from emplacement to exhumation. *J. Asian Earth Sci.* 38, 131–146. doi: 10.1016/j.jseas.2009.12.009
- Goldfarb, R. J., Taylor, R. D., Collins, G. S., Goryachev, N. A., and Orlandini, O. F. (2014). Phanerozoic continental growth and gold metallogeny of Asia. *Gondwana Res.* 25, 48–102. doi: 10.1016/j.gr.2013.03.002
- Han, B. F., He, G. Q., Wang, X. C., and Guo, Z. J. (2011). Late Carboniferous collision between the Tarim and Kazakhstan-Yili terranes in the western segment of the South Tian Shan Orogen, Central Asia, and implications for the Northern Xinjiang, western China. *Earth Sci. Rev.* 109, 74–93. doi: 10.1016/j.earscirev.2011.09.001
- Hazarika, P., Mishra, B., and Lochan Pruseth, K. (2018). Trace-element geochemistry of pyrite and arsenopyrite: ore genetic implications for late Archean orogenic gold deposits in southern India. *Mineral. Magaz.* 81, 661–678. doi: 10.1180/minmag.2016.080.128
- Hermann, J., Rubatto, D., Korsakov, A., and Shatsky, V. S. (2001). Multiple zircon growth during fast exhumation of diamondiferous, deeply subducted continental crust (Kokchetav Massif, Kazakhstan). *Contribut. Mineral. Petrol.* 141, 66–82. doi: 10.1007/s004100000218
- Horn, I., and von Blanckenburg, F. (2007). Investigation on elemental and isotopic fractionation during 196 nm femtosecond laser ablation multiple collector inductively coupled plasma mass spectrometry. *Spectrochim. Acta Part B Atom. Spectrosc.* 62, 410–422. doi: 10.1016/j.sab.2007.03.034
- Katayama, I., Maruyama, S., Parkinson, C. D., Terada, K., and Sano, Y. (2001). Ion micro-probe U-Pb zircon geochronology of peak and retrograde stages of ultrahigh-pressure metamorphic rocks from the Kokchetav massif, northern Kazakhstan. *Earth Planet. Sci. Lett.* 188, 185–198. doi: 10.1016/S0012-821X(01)00319-3
- Kiselev, V., Apayarov, F. K. M., Komarev, E. N., Tsyganok, E. N., and Lukashova, E. M. (1993). “Zircon isotopic ages of crystalline complexes of Tien-Shan,” in *Early Precambrian of the Central Asian Fold Belt*, ed. I. K. Kazakov (St. Petersburg: Nauka), 99–115.
- Kiselev, V., and Maksumova, R. (2001). Geology of the Northern and Middle Tien Shan: principal outlines. Paleozoic geodynamics and Gold Deposits in the Kyrgyz Tien Shan. *IAGOD Guidebook Ser.* 9, 21–28.
- Klemm, R., Brocker, M., Hacker, B. R., Gao, J., Gans, P., and Wemmer, K. (2005). New age constraints on the metamorphic evolution of the high-pressure/low-temperature belt in the Western Tianshan Mountains, NW China. *J. Geol.* 113, 157–168. doi: 10.1086/427666
- Klemm, R., Hegner, E., Bergmann, H., Pfander, J. A., Li, J. L., and Hentschel, F. (2014). Eclogitization of transient crust of the Aktyuz Complex during late Palaeozoic plate collisions in the Northern Tianshan of Kyrgyzstan. *Gondwana Res.* 26, 925–941. doi: 10.1016/j.gr.2013.08.018
- Konopelko, D., Kullerud, K., Apayarov, F., Sakiev, K., Baruleva, O., Ravna, E., et al. (2012). SHRIMP zircon chronology of HP-UHP rocks of the Makbal metamorphic complex in the Northern Tien Shan, Kyrgyzstan. *Gondwana Res.* 22, 300–309. doi: 10.1016/j.gr.2011.09.002
- Kröner, A., Alexeiev, D., Rojas-Agramonte, Y., Hegner, E., Wong, J., Xia, X., et al. (2013). Mesoproterozoic (Grenville-age) terranes in the Kyrgyz North Tianshan: zircon ages and Nd-Hf isotopic constraints on the origin and evolution of basement blocks in the southern Central Asian Orogen. *Gondwana Res.* 23, 272–295. doi: 10.1016/j.gr.2012.05.004
- Kröner, A., Alexeiev, D. V., Hegner, E., Rojas-Agramonte, Y., Corsini, M., Chao, Y., et al. (2012). Zircon and muscovite ages, geochemistry, and Nd-Hf isotopes for the Aktyuz metamorphic terrane: evidence for an Early Ordovician collisional belt in the northern Tianshan of Kyrgyzstan. *Gondwana Res.* 21, 901–927. doi: 10.1016/j.gr.2011.05.010
- Kröner, A., Kovach, V., Belousova, E., Hegner, E., Armstrong, R., Dolgoplova, A., et al. (2014). Reassessment of continental growth during the accretionary history of the Central Asian Orogenic Belt. *Gondwana Res.* 25, 103–125. doi: 10.1016/j.gr.2012.12.023
- Kröner, A., Windley, B. F., Badarch, G., Tomurtogoo, O., Hegner, E., Jahn, B. M., et al. (2007). Accretionary growth and crust-formation in the Central Asian Orogenic Belt and comparison with the Arabian-Nubian shield. *Mem. Geol. Soc. Am.* 200:461. doi: 10.1130/2007.1200(11)
- Li, Q.-L., Li, X.-H., Liu, Y., Tang, G.-Q., Yang, J.-H., and Zhu, W.-G. (2010). Precise U-Pb and Pb-Pb dating of Phanerozoic baddeleyite by SIMS with oxygen flooding technique. *J. Analyt. Atom. Spectrom.* 25, 1107–1113. doi: 10.1039/b923444f
- Li, X., Tang, G., Gong, B., Yang, Y., Hou, K., Hu, Z., et al. (2013). Qinghu zircon: a working reference for microbeam analysis of U-Pb age and Hf and O isotopes. *Chin. Sci. Bull.* 58, 4647–4654. doi: 10.1007/s11434-013-5932-x
- Li, X. H., Liu, Y., Li, Q. L., Guo, C. H., and Chamberlain, K. R. (2009). Precise determination of Phanerozoic zircon Pb/Pb age by multicollector SIMS without external standardization. *Geochem. Geophys. Geosyst.* 10:C002400. doi: 10.1029/2009GC002400
- Ludwig, K. R. (2003). Isoplot 3.00: a geochronological toolkit for Microsoft Excel, Berkeley. *Geochronol. Cent. Spec. Publ.* 4:71.
- Malyukova, N. (2001). The Taldybulak Levoberezhny gold deposit. Paleozoic geodynamics and gold deposits in the Kyrgyz Tien Shan. *Excurs. Guidebook Ser. Annu. Newsl. IGCP* 373, 97–109.
- Orozbaev, R., Takasu, A., Bakirov, A., Tagiri, M., and Sakiev, K. (2010). Metamorphic history of eclogites and country rock gneisses in the Aktyuz area, Northern Tien-Shan, Kyrgyzstan: a record from initiation of subduction through to oceanic closure by continent-continent collision. *J. Metamorph. Geol.* 28, 317–339. doi: 10.1111/j.1525-1314.2010.00865.x
- Orozbaev, R. T., Takasu, A., Tagiri, M., Bakirov, A. B., and Sakiev, K. S. (2007). Polymetamorphism of Aktyuz eclogites (northern Kyrgyz Tien-Shan) deduced from inclusions in garnets. *J. Miner. Petrol. Sci.* 102, 150–156. doi: 10.2465/jmps.060831b
- Ragozin, A. L., Liou, J. G., Shatsky, V. S., and Sobolev, N. V. (2009). The timing of the retrograde partial melting in the Kumdy-Kol region (Kokchetav Massif, Northern Kazakhstan). *Lithos* 109, 274–284. doi: 10.1016/j.lithos.2008.06.017
- Rojas-Agramonte, Y., Herwartz, D., García-Casco, A., Kröner, A., Alexeiev, D. V., Klemm, R., et al. (2013). Early Palaeozoic deep subduction of continental crust in the Kyrgyz North Tianshan: evidence from Lu-Hf garnet geochronology and petrology of mafic dikes. *Contribut. Mineral. Petrol.* 166, 525–543. doi: 10.1007/s00410-013-0889-y
- Rojas-Agramonte, Y., Kröner, A., Alexeiev, D. V., Jeffreys, T., Khudoley, A. K., Wong, J., et al. (2014). Detrital and igneous zircon ages for supracrustal rocks

- of the Kyrgyz Tianshan and palaeogeographic implications. *Gondwana Res.* 26, 957–974. doi: 10.1016/j.gr.2013.09.005
- Ryazantsev, A. V., Degtyarev, K. E., Kotov, A. B., Sal'nikova, E. B., Anisimova, I. V., and Yakovleva, S. Z. (2009). Ophiolite sections of the Dzhailair-Nayman zone, South Kazakhstan: their structure and age substantiation. *Doklady Earth Sci.* 427, 902–906. doi: 10.1134/S1028334X09060038
- Seltmann, R., Konopelko, D., Biske, G., Divaev, F., and Sergeev, S. (2011). Hercynian post-collisional magmatism in the context of Paleozoic magmatic evolution of the Tien Shan orogenic belt. *J. Asian Earth Sci.* 42, 821–838. doi: 10.1016/j.jseae.2010.08.016
- Seltmann, R., Porter, T. M., and Pirajno, F. (2014). Geodynamics and metallogeny of the central Eurasian porphyry and related epithermal mineral systems: a review. *J. Asian Earth Sci.* 79(Part B), 810–841. doi: 10.1016/j.jseae.2013.03.030
- Sengor, A. M. C., and Natalin, B. (1994). "Paleotectonics of Asia: fragments of a syn thesis," in *The Tectonic Evolution of Asia*, eds A. Yin and T. M. Harrison (Cambridge: Cambridge University Press), 486–640.
- Shatsky, V. S., Jagoutz, E., Sobolev, N. V., Kozmenko, O. A., Parkhomenko, V. S., and Troesch, M. (1999). Geochemistry and age of ultrahigh pressure metamorphic rocks from the Kokchetav massif (Northern Kazakhstan). *Contribut. Mineral. Petrol.* 137, 185–205. doi: 10.1007/s004100050545
- Slama, J., Kosler, J., Condon, D. J., Crowley, J. L., Gerdes, A., Hanchar, J. M., et al. (2008). Plesovice zircon - A new natural reference material for U-Pb and Hf isotopic microanalysis. *Chem. Geol.* 249, 1–35. doi: 10.1016/j.chemgeo.2007.11.005
- Söderlund, U., Patchett, P. J., Vervoort, J. D., and Isachsen, C. E. (2004). The ^{176}Lu decay constant determined by Lu-Hf and U-Pb isotope systematics of Precambrian mafic intrusions. *Earth Planet. Sci. Lett.* 219, 311–324. doi: 10.1016/S0012-821X(04)00012-3
- Stacey, J. S., and Kramers, J. D. (1975). Approximation of terrestrial lead isotope evolution by a two-stage model. *Earth Planet. Sci. Lett.* 26, 207–221. doi: 10.1016/0012-821X(75)90088-6
- Tagiri, M., Yano, T., Bakirov, A., Nakajima, T., and Uchiumi, S. (1995). Mineral parageneses and metamorphic P-T paths of ultrahigh-pressure eclogites from Kyrgyzstan Tien-Shan. *ISL Arc.* 4, 280–292. doi: 10.1111/j.1440-1738.1995.tb00150.x
- Togonbaeva, A., Takasu, A., Bakirov, A. A., Sakurai, T., and Sakiev, K. (2009). CHIME monazite ages of garnet-chloritoid-talc schists in the Makbal Complex, Northern Kyrgyz Tien-Shan: first report of the age of the UHP metamorphism. *J. Mineral. Petrol. Sci.* 104, 77–81. doi: 10.2465/jmps.081022e
- Trifonov, B. (1987). "Ore controlling reverse-thrusting zones in Kyrgyzstan," in *Proceedings of the Conference: Metallogeny of the Tien Shan, Union of Soviet Socialist Republics (USSR)*, Russia, 174–176.
- Trifonov, B. (2016). Comment on "Re-Os pyrite and U-Pb zircon geochronology from the Taldybulak Levoberezhny gold deposit: insight for Cambrian metallogeny of the Kyrgyz northern Tien Shan" by Xiaobo Zhao, Chunji Xue, Guoxiang Chi, Nikolay Pak, Bo Zu [Geol. Rev. 67 (2015) 78–89]. *Ore Geol. Rev.* 106, 464–467. doi: 10.1016/j.oregeorev.2016.10.041
- Vervoort, J., and Blichert-Toft, J. (1999). Evolution of the depleted mantle: Hf isotope evidence from juvenile rocks through time. *Geochim. Cosmochim. Acta* 63, 533–556. doi: 10.1016/S0016-7037(98)00274-9
- Vervoort, J. D., and Patchett, P. J. (1996). Behavior of hafnium and neodymium isotopes in the crust: constraints from Precambrian crustally derived granites. *Geochim. Cosmochim. Acta* 60, 3717–3733. doi: 10.1016/0016-7037(96)00201-3
- Wiedenbeck, M., Alle, P., Corfu, F., Griffin, W. L., Meier, M., Oberli, F., et al. (1995). Three natural zircon standards for U-Th-Pb, Lu-Hf, trace element and REE analyses. *Geostand. Newslett.* 19, 1–23. doi: 10.1111/j.1751-908X.1995.tb00147.x
- Windley, B. F., Alexeiev, D., Xiao, W., Kröner, A., and Badarch, G. (2007). Tectonic models for accretion of the Central Asian Orogenic Belt. *J. Geol. Soc.* 164, 31–47. doi: 10.1144/0016-76492006-022
- Wu, Y., and Zheng, Y. (2004). Genesis of zircon and its constraints on interpretation of U-Pb age. *Chin. Sci. Bull.* 49, 1554–1569. doi: 10.1360/04wd0130
- Xi, W., Xia, X. H., Wu, Y. S., Ye, T., and Li, N. (2018). Geological characteristics and ore minerals of the Taldybulak Levoberezhny gold deposit, Kyrgyzstan. *Earth Sci. Front.* 25, 135–150.
- Xiao, W., Li, S., Santosh, M., and Jahn, B.-M. (2012). Orogenic belts in Central Asia: correlations and connections. *J. Asian Earth Sci.* 49, 1–6. doi: 10.1016/j.jseae.2012.03.001
- Xiao, W., Windley, B. F., Allen, M. B., and Han, C. (2013). Paleozoic multiple accretionary and collisional tectonics of the Chinese Tianshan orogenic collage. *Gondwana Res.* 23, 1316–1341. doi: 10.1016/j.gr.2012.01.012
- Xiao, W. J., Windley, B. F., Yuan, C., Sun, M., Han, C. M., Lin, S. F., et al. (2009). Paleozoic multiple subduction-accretion processes of the southern Altai. *Am. J. Sci.* 309, 221–270. doi: 10.2475/03.2009.02
- Xue, C. J., Zhao, X. B., Mo, X. X., Dong, L. H., Gu, X. X., Nurtaev, B., et al. (2014). Asian gold belt in western Tianshan and its geodynamic setting, metallogenic control and exploration. *Earth Sci. Front.* 21, 128–155.
- Yuan, H. L., Gao, S., Dai, M. N., Zong, C. L., Günther, D., Fontaine, G. H., et al. (2008). Simultaneous determinations of U-Pb age, Hf isotopes and trace element compositions of zircon by excimer laser-ablation quadrupole and multiple-collector ICP-MS. *Chem. Geol.* 247, 100–118. doi: 10.1016/j.chemgeo.2007.10.003
- Zhang, W., Lentz, D. R., Thorne, K. G., and Massawe, R. J. R. (2020). Late Silurian-Early Devonian slab break-off beneath the Canadian Appalachians: insights from the Nashwaak Granite, west-central New Brunswick, Canada. *Lithos* 2020, 358–359. doi: 10.1016/j.lithos.2020.105393
- Zhao, X., Xue, C., Chi, G., Chu, H., Li, Z., Pak, N., et al. (2017). Multi-stage gold mineralization in the Taldybulak Levoberezhny deposit, Tien Shan, Kyrgyzstan: reply to comment by Boris Trifonov on "Re-Os pyrite and U-Pb zircon geochronology from the Taldybulak Levoberezhny gold deposit: insight for Cambrian metallogeny of the Kyrgyz northern Tien Shan". *Ore Geol. Rev.* 82, 217–231. doi: 10.1016/j.oregeorev.2016.10.042
- Zhao, X., Xue, C., Chi, G., Pak, N., and Zu, B. (2015). Re-Os pyrite and U-Pb zircon geochronology from the Taldybulak Levoberezhny gold deposit: insight for Cambrian metallogeny of the Kyrgyz northern Tien Shan. *Ore Geol. Rev.* 67, 78–89. doi: 10.1016/j.oregeorev.2014.12.002
- Zhimulev, F. I., Buslov, M. M., Travin, A. V., Dmitrieva, N. V., and De Grave, J. (2011). Early-Middle Ordovician nappe tectonics of the junction between the Kokchetav HP-UHP metamorphic belt and the Stepnyak paleoisland arc (northern Kazakhstan). *Russian Geol. Geophys.* 51, 190–203. doi: 10.1016/j.rgg.2010.12.009
- Zhou, G., Liu, H., Chen, K., Gai, X., Zhao, C., Liao, L., et al. (2018). The origin of pyroelectricity in tourmaline at varying temperature. *J. Alloys Compounds* 744, 328–336. doi: 10.1016/j.jallcom.2018.02.064
- Zhou, L., McKenna, C. A., Long, D. G. F., and Kamber, B. S. (2017). LA-ICP-MS elemental mapping of pyrite: an application to the Palaeoproterozoic atmosphere. *Precamb. Res.* 297, 33–55. doi: 10.1016/j.precamres.2017.05.008
- Zhu, Y., He, G. Q., and An, F. (2007). Geological evolution and metallogeny in the core part of the central Asian metallogenic domain. *Geol. Bull. China* 26, 1167–1177.

Conflict of Interest: XX was employed by Sichuan Geological and Mineral Resources Group Co., Ltd. and by Altynken Limited Liability Company, Zijin Mining Group.

The remaining authors declare that the research was conducted in the absence of any commercial or financial relationships that could be construed as a potential conflict of interest.

Copyright © 2021 Xi, Li, Xia, Ling and Wu. This is an open-access article distributed under the terms of the Creative Commons Attribution License (CC BY). The use, distribution or reproduction in other forums is permitted, provided the original author(s) and the copyright owner(s) are credited and that the original publication in this journal is cited, in accordance with accepted academic practice. No use, distribution or reproduction is permitted which does not comply with these terms.



Geochronology and Geochemistry of Late Paleozoic Volcanic Rocks and Their Relationship With Iron and Molybdenum Deposits in Xilekuduk Area, Northern Margin of Junggar

Xiaofeng Wei¹, Hao Wei^{2*}, Zhen Liao³, Zhiwei Wang², Dong Li², Qigui Mao⁴ and Xiao Li²

¹Zhongse Zijin Geological Exploration (Beijing) Co., Ltd., Beijing, China, ²Hebei Key Laboratory of Strategic Critical Mineral Resources, Hebei GEO University, Shijiazhuang, China, ³Sinotech Minerals Exploration Co., Ltd., Beijing, China, ⁴Beijing Institute of Mineral Geology Co., Ltd., Beijing, China

OPEN ACCESS

Edited by:

Chang-Zhi Wu,
Chang'an University, China

Reviewed by:

Hao Yujie,
Jilin University, China
Fuquan Yang,
Chinese Academy of Geological
Sciences (CAGS), China

*Correspondence:

Hao Wei
ronghaiwei@163.com

Specialty section:

This article was submitted to
Economic Geology,
a section of the journal
Frontiers in Earth Science

Received: 22 January 2021

Accepted: 29 April 2021

Published: 21 May 2021

Citation:

Wei X, Wei H, Liao Z, Wang Z, Li D,
Mao Q and Li X (2021) Geochronology
and Geochemistry of Late Paleozoic
Volcanic Rocks and Their Relationship
With Iron and Molybdenum Deposits in
Xilekuduk Area, Northern Margin
of Junggar.
Front. Earth Sci. 9:657083.
doi: 10.3389/feart.2021.657083

A large number of intermediate basic volcanic rocks and porphyry Cu-Mo deposits as well as volcanic-hosted magnetite deposit have been recently discovered in the Xilekuduk area. However, no reports concerning petrogenesis and age or their relationship with mineralization have been published to date. The purpose of this study was to make up for the absence of previous studies on Devonian volcanic activities in the area and to confirm the relationship between two stages of volcanic activities and mineralization so as to provide important theoretical basis for mineral exploration. Based on research results of zircon U-Pb geochronology and element geochemistry of volcanic rocks in the area, the ages of dacite, andesite, and stomatal andesite are considered as 375.2 ± 2.9 Ma, 386.5 ± 3.0 Ma, and 317.9 ± 2.9 Ma, respectively, corresponding to the Middle Devonian and Late Carboniferous Period. The Devonian volcanic rocks belong to the high-K calc-alkaline series and island arc volcanic rocks, which are enriched in LREE, strongly enriched in large ion lithophile elements Th, Rb, Ba, and K and relatively depleted in high-field strength elements (HFSEs) Nb, Ta, and Ti. The Carboniferous volcanic rocks are enriched in LREE, as well as the large ion lithophile elements Th, Rb, Ba, and K are strongly enriched, while depleted in the HFSEs Nb, Ta, and Ti; moreover, the contents of TiO_2 and V are 0.94–0.97% and $178\text{--}183 \times 10^{-6}$, which are higher than those of island arc basalts. According to mineralogical typomorphic characteristics and geochemical analysis, magnetite mineralization is divided into two phases. The early stratiform magnetite ore MT1 has magmatic characteristics, forming a volcanic rock type magnetite deposit related to Devonian volcanic eruption and sedimentation (375–386 Ma). The magnetite MT2 in the magnetite-quartz vein is considered as hydrothermal genesis, which is a metal mineral in the early metallogenic stage of Carboniferous (317.1 ± 2.9 Ma) volcanic eruption and subvolcanism, and may be related to porphyry molybdenum mineralization. Therefore, the volcanism and Fe-Cu-Mo mineralization in this area is characterized by multistage superimposed mineralization.

Keywords: volcanic rocks, LA-ICP-MS, zircon, U-Pb, geochemistry, mineralization, northern margin of junggar

INTRODUCTION

The Xilekuduk area in Fuyun County, Xinjiang, is located in the northern margin of the Junggar Basin, in the collision suture zone of the Siberian Plate and the Junggar Plate (Sengör et al., 1993; Windley et al., 2007). A large number of Paleozoic strata were formed during the process of plate amalgamation and accretion in the Paleozoic, with crisscross faults and strong magmatic activities forming a geological unit with complex coupling of tectonics, magmatism, and mineralization, which gave birth to an important metallogenic belt of precious gold and nonferrous metals such as iron, copper, gold, nickel, and rare metals in China (Yang et al., 2009; Yang et al., 2012; Yang et al., 2014; Li et al., 2015; Wei et al., 2019).

The porphyry Cu-Mo deposit discovered in the Xilekuduk area in 2005 is of great significance in understanding mineralization and the metallogenic series in the Junggar area. The zircon U-Pb method was applied for accurately dating the granitoids of porphyry (copper) molybdenum deposit. The diagenetic age was concentrated at 340–315 Ma, which was considered as the product of tectonic magmatic evolution of plate collision—post collision (You et al., 2016; Long et al., 2009); the Re-Os isochron age of molybdenite was 327.1 ± 2.9 Ma, and the metallogenic age was determined as early stage of Middle–Late Carboniferous (Long et al., 2011). It is considered that the source of ore-forming material and granite porphyry bear the characteristics of homologous magma (Long et al., 2014). The age data of a large number of andesitic, dacitic volcanic rocks, and pyroclastic rocks exposed in the ore district are yet to be reported. It is generally speculated that they belong to the volcanic sedimentary assemblage of the Lower Carboniferous Namingshui Formation (Long et al., 2009; Ding et al., 2011; Long et al., 2011; Long et al., 2014; You et al., 2016; Wei et al., 2019). Some new scientific issues, however, have also been raised in this study:

1) The volcanic sedimentary assemblage of intermediate acid volcanic rocks–pyroclastic rocks–carbonate rocks distributed in the ore district obviously differs from that of the marine continental interactive facies clastic sedimentary rocks of the Lower Carboniferous Namingshui Formation (the Jiangbastao Formation). Are these volcanic rocks all formed in Carboniferous as previously speculated? Are the two types of sedimentary assemblages the product of the same geological event? 2) In 2015, layered magnetite bodies that occurred at the interface between volcanic rocks and clastic rocks were successively discovered more than 100 m southwest of the porphyry copper–molybdenum deposit; their coupling relationship with volcanic rocks, however, remains unclear.

The above issues hinder our understanding of volcanism and the genesis of the deposit in this area and limit the breakthrough of mineral exploration. Therefore, on the basis of detailed field investigation, the author has carried out systematic geochronology and rock geochemistry of volcanic rocks, determined the formation age and genesis of volcanic rocks, and through mineralogical studies of two periods of magnetite, combined with regional data, discussed the volcanic magmatic events and mineralization

in this area, so as to provide scientific guidance for mineral exploration in this area.

REGIONAL GEOLOGY AND DEPOSIT CHARACTERISTICS

Regional Geological Background

The tectonic location of the study area is located in the Gabosar Island Arc Belt of the East Junggar Orogenic Belt (You et al., 2016) (Figure 1A). The regional exposed strata are predominantly Paleozoic, Devonian, and Carboniferous, followed by Cenozoic tertiary and Quaternary, with local occurrence of Permian and Jurassic. Among these, the Devonian is the most widely distributed, which is a set of littoral and neritic clastic rock, volcanic lava, pyroclastic rock with carbonate rock, and terrigenous clastic rock. It is the main ore-bearing layer of iron and copper polymetallic in the area. Regional fold and fault structures are developed, mainly including the Yitieke aketas composite anticline, Sarbulak karatongke composite syncline, and Jiaposar composite anticline as well as the northwest trending Erqisi deep fault, Ulunguhe deep fault, and Kalashinger fault. Among these, the Kalashinger fault has been formed most recently as the main rock-controlling and ore-controlling fault structure in the region. The magmatic activity in the area is intense and various intrusive bodies are formed. The rock types are mainly granite. The diagenetic age is concentrated in the Early–Middle Devonian of Late Paleozoic, followed by the Early Carboniferous. The volcanic rocks mainly occur in the Devonian Tuorangekuduke, Beitashan, Yundukala, and Kashion formations, and Carboniferous Jiangbastao and Batamayineishan formations (Zhang et al., 2006; Li et al., 2015) (Figure 1B).

Geological Characteristics of the Deposit

According to previous studies, the volcanic and pyroclastic rock strata exposed in the ore district are assigned to the Lower Carboniferous Namingshui Formation (Long et al., 2009; Ding et al., 2011; Long et al., 2011; Long et al., 2014; You et al., 2016; Wei et al., 2019). Two groups of volcanic rock–clastic rock formations were decomposed in this field investigation: one group was the combination of intermediate–basic volcanic lava–sedimentary rock, while the other was the combination of intermediate–basic volcanic lava–volcanic clastic rock–clastic sedimentary rock. The two were in a fault contact relationship (Figure 1C, Figure 2). The intermediate basic volcanic lava is mainly distributed in the northeast of the ore district, with an area of about 1.1 km² and a lithology thickness of about 520 m. Intermediate basic volcanic lava–pyroclastic rocks–clastic sedimentary rocks are mainly distributed in the northwest of the ore district, with an area of 8.9 km².

It can be divided into five volcanic rhythms with a thickness of 3018 m, showing an integrated contact relationship of volcanic eruption: 1) Overflow facies andesite–erupted andesite lithic tuff, about 57 m thick. 2) Eruptive facies stomatal and esite-falling accumulation facies volcanic sedimentary tuff, with a thickness of about 110 m. 3) Overflow facies andesite–erupted andesite lithic tuff–sedimentary facies tuffaceous sandstone, about 1540 m thick.

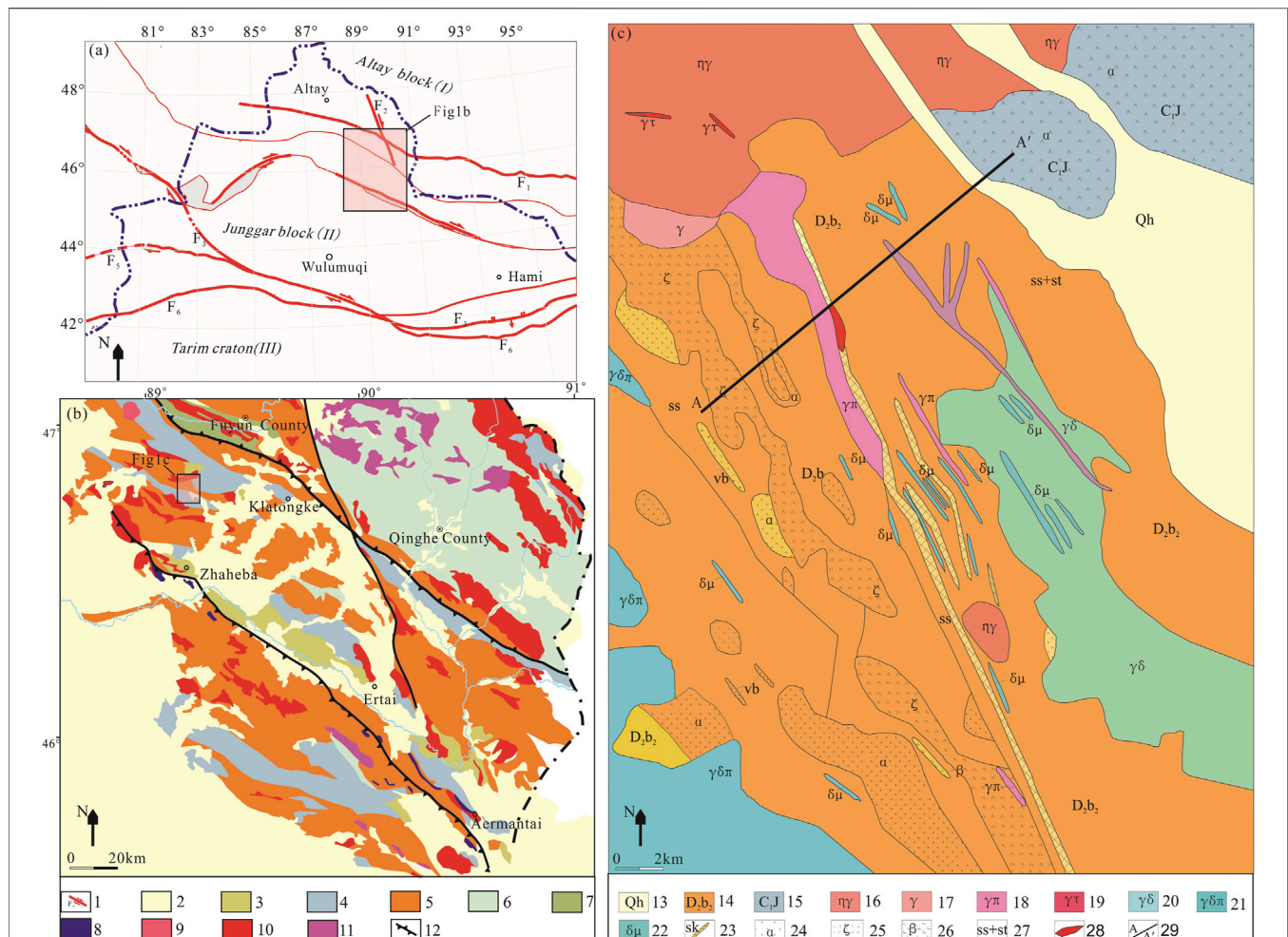


FIGURE 1 | (Mended according to Wei et al. (2019)). Tectonic location map (A), regional geological map (B), and deposit geological map (C) in the Xilekuduk area, Fuyun County, Xinjiang. 1: regional major fault; 2: Quaternary; 3: Permian; 4: Carboniferous; 5: Devonian; 6: Silurian; 7: Precambrian; 8: ophiolite; 9: Permian granite; 10: Carboniferous granite; 11: Devonian Silurian granite; 12: suture zone; 13: Quaternary; 14: Lower Carboniferous Jiangbastao Formation; 15: Middle Devonian Beitashan formation; 16: monzogranite; 17: granite; 18: granite porphyry; 19: quartz porphyry; 20: granodiorite; 21: granite porphyry; 22: diorite porphyrite; 23: skarn belt; 24: andesite; 25: dacite; 26: basalt; 27: siltstone and sandstone; 28: iron ore body; and 29: measured section position.

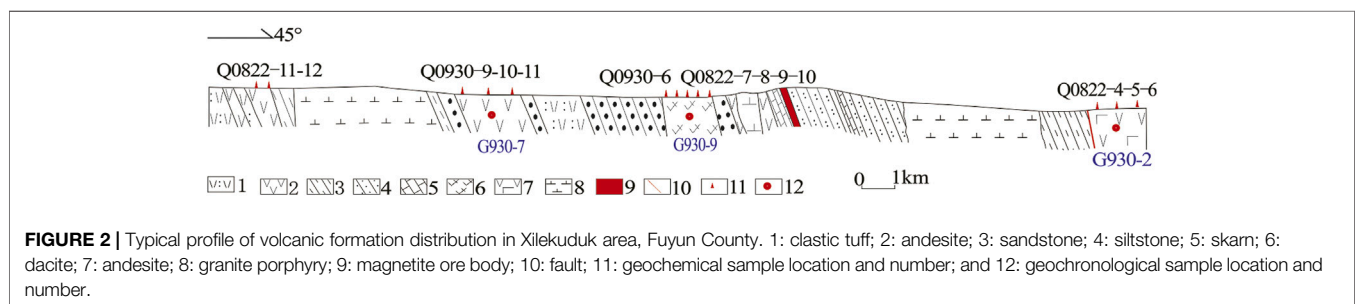
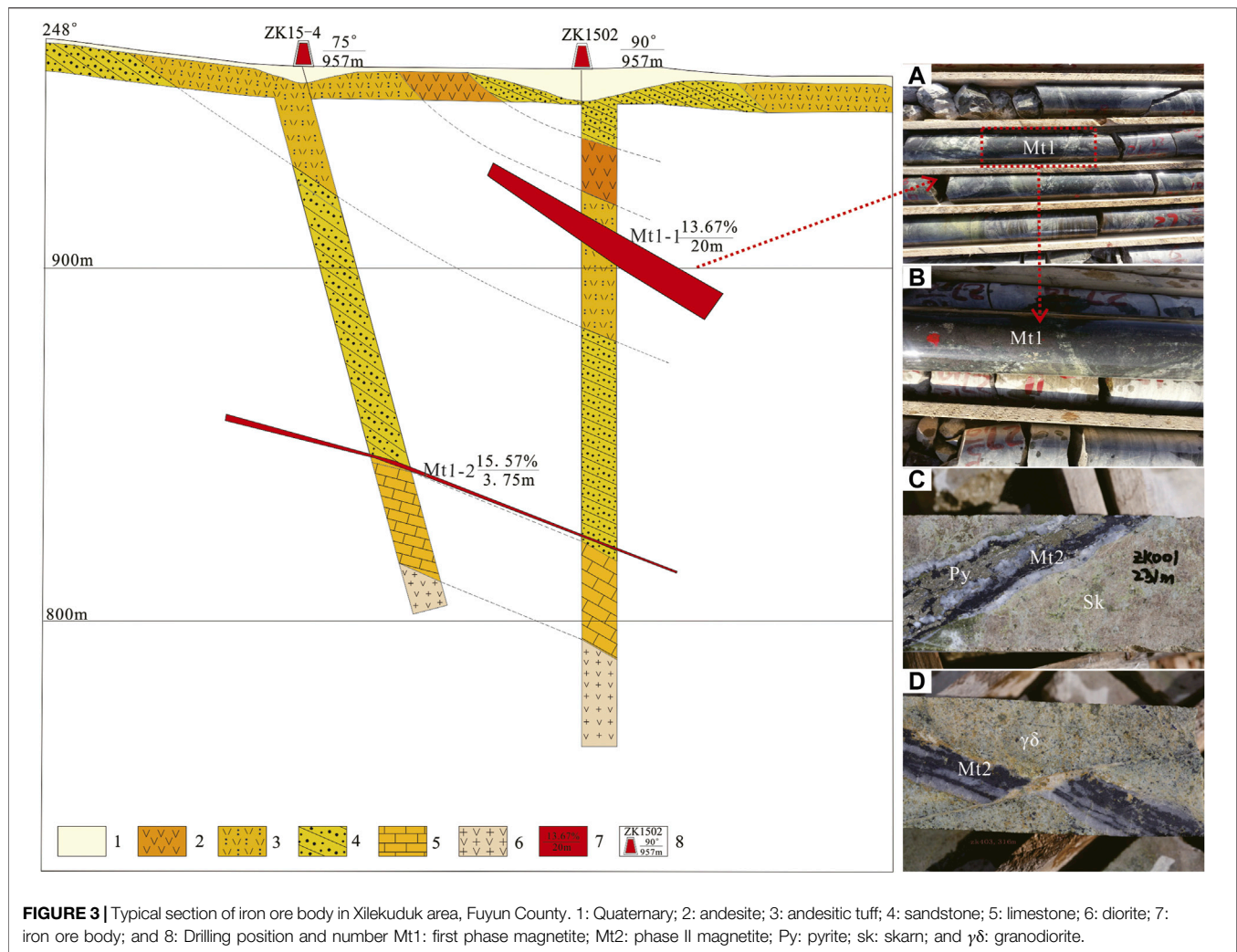


FIGURE 2 | Typical profile of volcanic formation distribution in Xilekuduk area, Fuyun County. 1: clastic tuff; 2: andesite; 3: sandstone; 4: siltstone; 5: skarn; 6: dacite; 7: andesite; 8: granite porphyry; 9: magnetite ore body; 10: fault; 11: geochemical sample location and number; and 12: geochronological sample location and number.

4) Overflow facies dacite-sedimentary facies tuffaceous sandstone, about 810 m thick. 5) Overflow facies andesite-sedimentary facies carbonate rock, sandstone, with a thickness of about 510 m, magnetite ore bodies are distributed in the skarnized zone of contact between pyroclastic rocks and

carbonate rock. On the basis of type of rock association, the volcanic rock and clastic rock association exposed in the ore district is not completely Carboniferous.

Intrusive rocks are well developed in the ore district. Monzonitic granite, quartz porphyry, diorite porphyrite, and



diorite occur successively from the north to the south of the ore district. Fault structures are extremely developed, comprising three main groups of NNW-NS, NW-EW, and NEE trending faults. Among them, NNW-NS fault is the most developed in the central part of the ore district, which is the main rock-controlling and ore-controlling fault in the ore district. It belongs to the secondary fault of the NW-trending regional Erqis south fault (Ablimit, 2017) (Figure 1C).

The Cu-Mo deposit is a concealed porphyry deposit located in the northern part of the area. It mainly occurs in the internal and external contact zone of granite porphyry, quartz diorite, and tuffaceous siltstone. The ore body is stratoid and lenticular, strikes 350° – 360° , inclines to the east with dips of 25° – 40° , and occurs in parallel with local pinch of outbranches. It is 100–300 m long, 90–380 m wide, and 0.84–30.37 m thick. The average grade of Mo ore body is 0.061–0.097%. The metal minerals are mainly molybdenite and pyrite, with a small amount of chalcopyrite and magnetite. The gangue minerals mainly include quartz, sericite, chlorite, and epidote. The iron ore body is located in the skarn zone at the lithologic interface between pyroclastic sedimentary rock and carbonate rock in the south of the ore district. The

surface mineralization chiefly comprises a beaded or lenticular shape. The exposed ore body is 1 m thick with a Cu grade of 1.57% and TFe content of 22.6%; the magnetite ore body with a thickness of 3 m is delineated by deep drilling (Figure 3), and the average TFe content is 18.54%. The main mineralization types are skarn type copper (gold) ore, skarn type copper-bearing magnetite, and skarn type copper-bearing pyrrhotite magnetite.

MATERIALS AND METHODS

Sample Collection and Preparation

Geochronology and geochemistry samples were collected from the northeastern andesite outcrop area, the southwestern dacite outcrop area, and the southwestern andesite outcrop area of the Xilekuduk copper (molybdenum) deposit. The respective coordinates are $95^{\circ}13'44''$ E and $46^{\circ}49'46''$ N, $95^{\circ}13'04''$ E and $46^{\circ}48'33''$ N, and $95^{\circ}12'20''$ E and $46^{\circ}48'00''$ N.

Selection and preparation of zircon minerals were undertaken by Langfang Regional Geological Survey Institute.

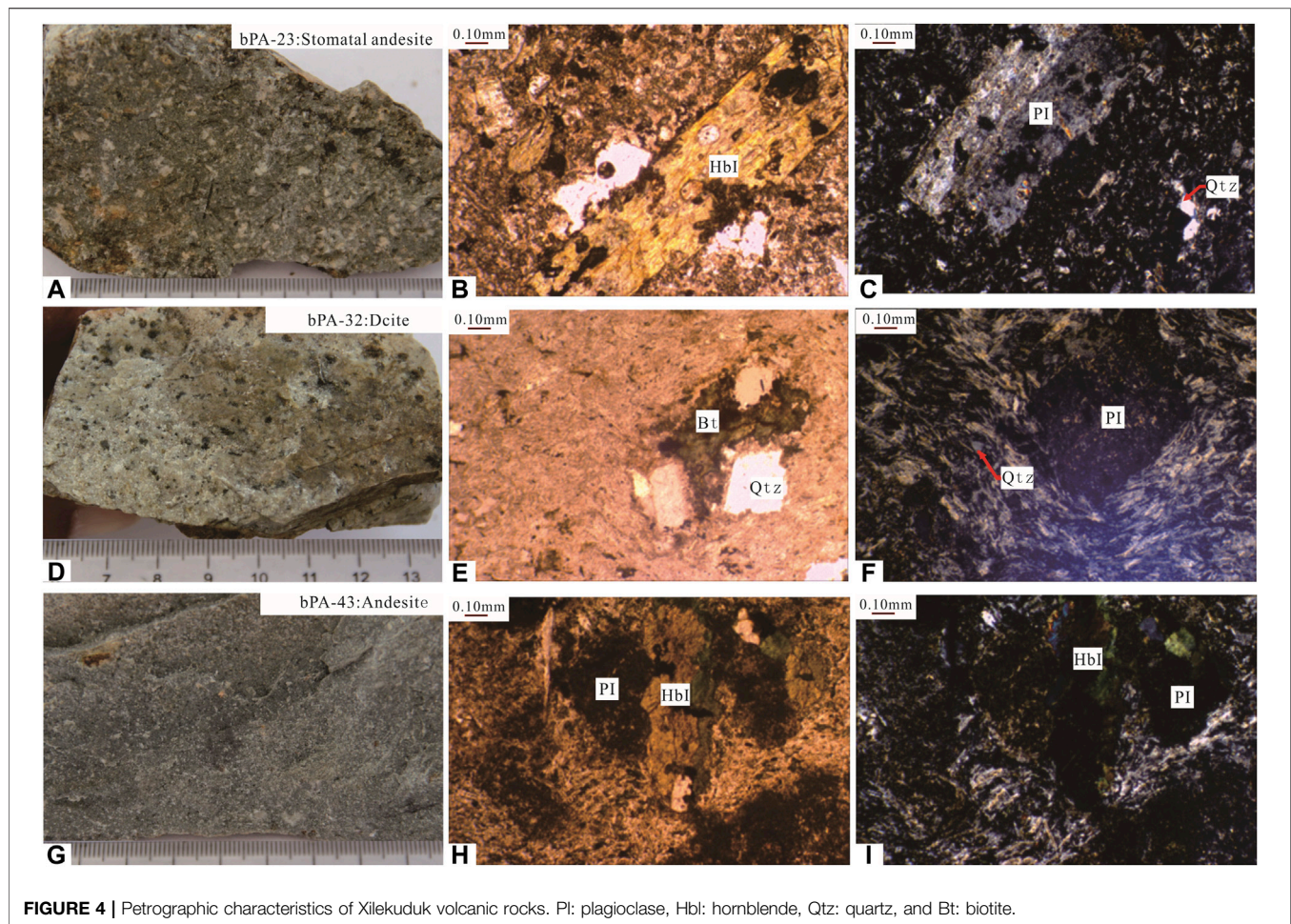


FIGURE 4 | Petrographic characteristics of Xilekuduk volcanic rocks. Pl: plagioclase, Hbl: hornblende, Qtz: quartz, and Bt: biotite.

Sample Characteristics

1) Characteristics of Volcanic Rock Samples

According to the field observation and the measured section, the volcanic lava in the southwest of the ore district includes dacite and andesite, and the volcanic lava in the northeast is mainly stomatal andesite. The specific petrographic characteristics are as follows:

Northeast stomatal andesite: the weathered surface is gray, while the fresh surface is cyan gray, in porphyritic structure; the matrix is felsic and in fine interwoven structure and massive structure; the rock is composed of phenocrysts and the matrix (**Figure 4A**). The phenocryst minerals are plagioclase (PL) and hornblende (HBL), accounting for 15–25% of the total rock mass; the matrix is microcrystalline plagioclase, hornblende, and biotite; plagioclase is arranged in a directional manner; microcrystalline quartz is in felsic interlaced structure, accounting for about 80–85% of the total rock, and the accessory mineral is magnetite (**Figures 4B,C**).

Southwest dacite: the weathered surface is gray, while the fresh surface is grayish white, in porphyritic structure; the matrix is in felsic interlaced structure and massive structure; the rock is composed of phenocrysts and matrix (**Figure 4D**). The phenocryst minerals are plagioclase (PL), biotite, and quartz

(QTZ), accounting for 8–10% of the total rock mass; the matrix is microcrystalline plagioclase, quartz, and biotite. Plagioclase is directionally arranged with quartz in felsic and fine texture, accounting for about 90–92% of the total rock mass (**Figures 4E,F**). The accessory minerals are magnetite, while the altered minerals are sericite and chlorite.

Southwest andesite: the weathered surface is grayish green while the fresh surface is greenish green (**Figure 4G**). The rocks are composed of phenocrysts and matrix. The phenocryst minerals are plagioclase (PL) and hornblende (HBL), accounting for about 10–20% of the total rock mass; the matrix is microcrystalline plagioclase, hornblende, and quartz. Plagioclase is oriented and interwoven, accounting for 85–90% of the total rock mass (**Figures 4H,I**). The accessory mineral is magnetite.

2) Characteristics of Magnetite Samples

There are two main occurrence types of magnetite in the study area: 1) MT1 type: stratiform magnetite ore occurring along the strata (**Figure 5A**). The surrounding rocks are mainly composed of andesitic volcanic tuff and tuffaceous siltstone (**Figures 3A,B, 5A**). Magnetite is mainly of euhedral and subhedral texture (**Figures 5B,C**). Intergrowth granular pyrite can be seen in

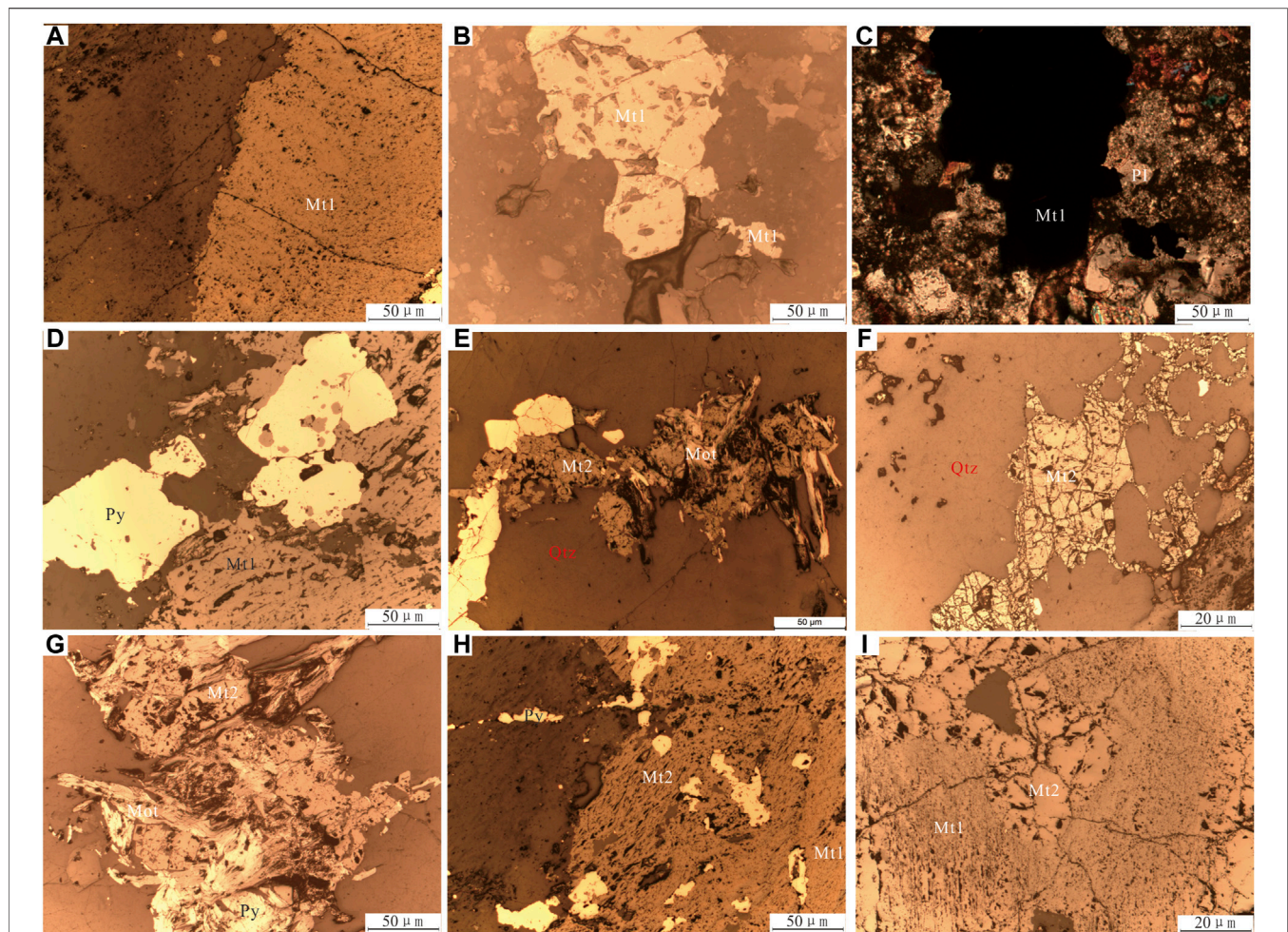


FIGURE 5 | Typical magnetite micrograph of Xilekuduk ore district. **(A):** the contact boundary between early bedding stratiform magnetite ore MT1 and Devonian volcanic rocks (reflection); **(B):** early veined euhedral-subhedral magnetite MT1 (reflection); **(C):** early vein euhedral-subhedral magnetite MT1 (reflection +); **(D):** intergrowth granular pyrite in MT1 magnetite; **(E):** anhedral magnetite MT2 in late quartz vein replaced by late pyrite and molybdenite (reflection); **(F):** anhedral magnetite MT2 in quartz veins; **(G):** anhedral magnetite MT2 in late magnetite quartz vein is replaced by late molybdenite and pyrite (reflection); **(H):** MT2 magnetite occurs along the contact zone between MT1 magnetite and volcanic strata and is cut by late pyrite veins; and **(I):** MT1 magnetite is wrapped by MT2 magnetite; Py: pyrite; Mot: molybdenite; Mt: magnetite; and Qtz: quartz.

MT1 magnetite (**Figure 5D**). 2) MT2 type: reticular vein magnetite-quartz vein (**Figures 5E–G**), are veined into the tensile fractures of skarn and diorite (**Figures 3C,D**), often replaced by late pyrite and molybdenite (**Figures 5E,G**), with poor euhedral texture and rough surface (**Figures 5F,H,I**). Some MT2 magnetite veins cut through the contact zone between MT1 magnetite and volcanic rock stratum, and are cut by late pyrite vein (**Figure 5H**). MT1 magnetite is often wrapped by MT2 magnetite, which indicates that the formation of MT2 magnetite is later than that of MT1.

Analysis Method

1) Zircon U-Pb Dating

Zircon U-Pb dating was carried out in the Chinese Academy of Sciences' Guiyang Institute of Geochemistry. The test instrument was the GeoLas2005 laser ablation system produced by Agilent, company of the United States, and Elan 6100DRC ICP-MS. The

laser spot diameter was 30 μm , the laser pulse was 10 Hz, the energy was 32–36 mJ, and the depth of laser ablation sample was 20–40 μm . The international standard zircon 91,500 was used as the external reference material for zircon age determination. For detailed analysis steps and data processing methods, please refer to the relevant literature (Yuan et al., 2003). The isotopic ratio and element content of zircon were calculated by Gitter (ver 4.0, Macquarie University) program and Andersen Tom (Andersen, 2002). LA-ICP-MS Common Lead Correction (ver 3.15) software was used for correction of common lead, and Isoplot (ver 3.0) software was used for age calculation and concordance diagram drawing.

2) Analysis of Elements

The major rare earth and trace elements were determined in the State Key Laboratory of Institute of Geology and Geophysics of the Chinese Academy of Sciences. The major elements were

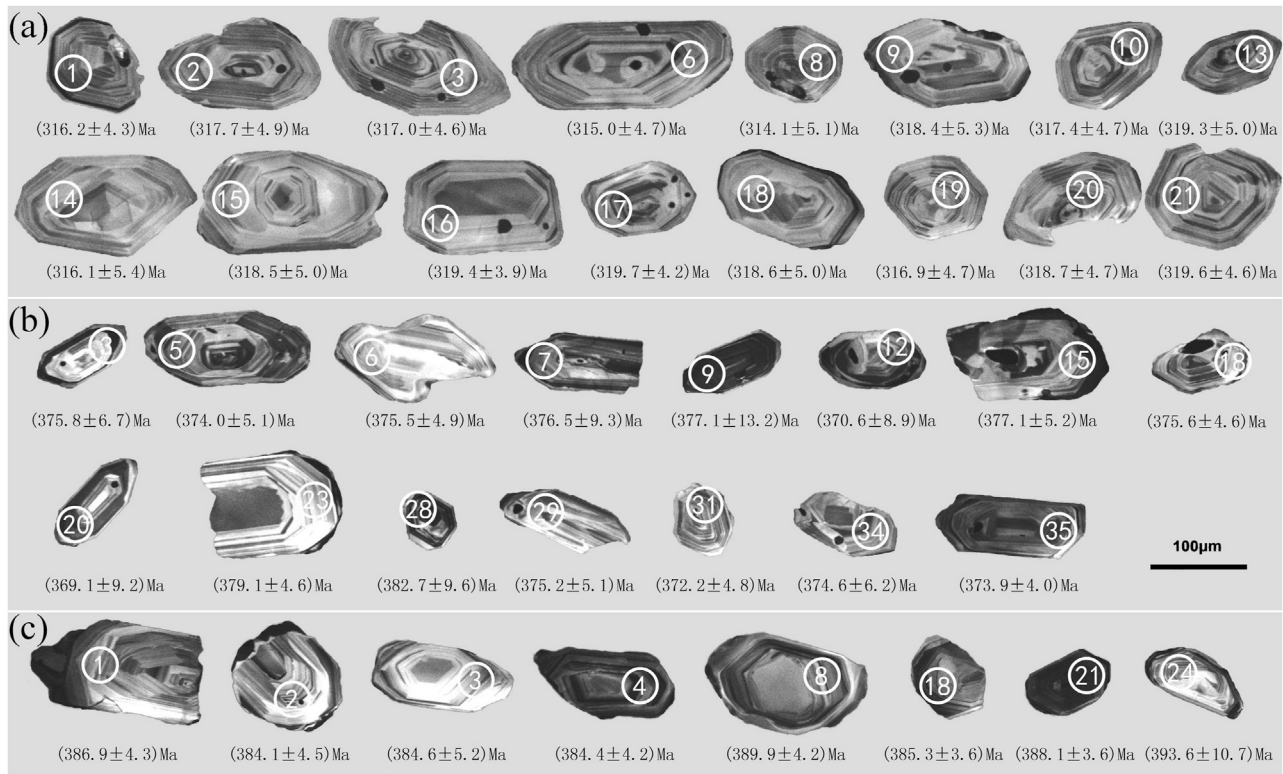


FIGURE 6 | Cathodoluminescence of zircon in volcanic lava. **(A)** Northeast stomatal andesite; **(B)** southwest dacite; and **(C)** southwest andesite.

determined with application of the melting XRF method (national standard GB/t14506.28–1993) on X-ray fluorescence spectrometer 3080 E. The contents of rare earth and trace elements were determined by double-focus high-resolution ICP-MS produced by Finnigan MAT.

RESULTS

LA-ICP-MS Geochronology of Zircon

The zircons in the stomatal andesite of the northeast area were mostly subhedral long columnar, with clear crystal edges and planes in the grains; grain lengths varied from 70 to 220 μm , while grain widths varied from 30 to 80 μm . The ratios of the grain length and width were within 1:1 to 1:10. The weight abundances of uranium (w (U)) in zircons were $(222.56\text{--}360.80) \times 10^{-6}$ and the weight abundances of thorium (w (Th)) were $(74.26\text{--}381.45) \times 10^{-6}$, while the ratio of Th/U was 0.55–0.92, further above 0.1. The zircons in dacite and andesite in the southwest area were mostly hypidiomorphic short columnar to long columnar with clear crystal edges and planes in the grains. The grain lengths varied from 50 to 120 μm , the grain widths ranged from 30 to 80 μm , and the ratios of the grain length and width were within 1:1 to 1:8. The w (U) in zircons were $(212.19\text{--}699.10) \times 10^{-6}$ and $(329.60\text{--}4273.32) \times 10^{-6}$, respectively, w (th) were $(138.62\text{--}969.58) \times 10^{-6}$ and $(161.84\text{--}4582.81) \times 10^{-6}$, respectively, Th/U ratio was 0.42–0.92 (except G930-7-2 = 1.22,

G930-7-9 = 1.10), and 0.23–0.63 (except G930-9-29 = 1.07). Combined with the cathodoluminescence image (CL) (Figure 6), these zircons have a typical oscillatory rhythmic zoning structure and belong to magmatic origin (Courfu et al., 2003).

The zircon U-Pb isotopic analysis data of volcanic rocks (Table 1) show that they are more consistent within the error range in the values of $^{207}\text{Pb}/^{235}\text{U}$ and $^{206}\text{Pb}/^{238}\text{U}$, and the data fall on and near the concordant curve, the $^{206}\text{Pb}/^{238}\text{U}$ age of andesite in the northeast area was between (311 ± 4.6) to (319 ± 4.6) Ma, and its weighted average was (317.9 ± 2.9) Ma, with the weighted mean variance (MSWD) being 0.13, which can categorize the corresponding diagenetic age to the Lower Carboniferous (Figure 7A). The $^{206}\text{Pb}/^{238}\text{U}$ ages of the dacite in the southwestern area ranged from 373 ± 5.1 Ma to 393 ± 10.7 Ma, and its weighted average was 375.2 ± 2.9 Ma (MSWD = 0.20) (Figure 7B). The $^{206}\text{Pb}/^{238}\text{U}$ ages of the southern porous andesite were between 369 ± 9.2 Ma to 382 ± 9.6 Ma, and its weighted average was 386.5 ± 3.0 Ma (MSWD = 0.30), with the diagenetic age corresponding to the Middle and Late Devonian (Figure 7C).

Petrogeochemistry

1) Major Element Geochemistry

The results of major elements of volcanic rocks are shown in Table 2. The SiO_2 content of Carboniferous stomatal andesite was between 55.01 and 55.80%, and the SiO_2 content was relatively low. The Al_2O_3 content was between 17.08 and 17.48%, the CaO content was between 5.86 and 6.11%, and the content of MgO was

TABLE 1 | Zircon isotopic analysis results of volcanic rocks in the Xilekuduk area.

Point Number	Lithology	Element content ($\times 10^{-6}$)			Th/U	Isotope ratio						Age (Ma)					
		Pb	Th	U		$^{207}\text{Pb}/^{206}\text{Pb}$	1 σ	$^{207}\text{Pb}/^{235}\text{U}$	1 σ	$^{207}\text{Pb}/^{238}\text{U}$	1 σ	$^{207}\text{Pb}/^{206}\text{Pb}$	1 σ	$^{207}\text{Pb}/^{235}\text{U}$	1 σ	$^{206}\text{Pb}/^{238}\text{U}$	1 σ
G930-2-1	Northeast stromatal andesite (Carboniferous)	32.74	223.89	335.41	0.67	0.06126	0.00445	0.39376	0.01994	0.05027	0.00070	650.0	157.4	337.1	14.5	316.2	4.3
G930-2-2		30.14	142.55	222.56	0.64	0.06257	0.00513	0.41283	0.03280	0.05052	0.00080	694.5	174.8	350.9	23.6	317.7	4.9
G930-2-3		28.79	155.32	264.16	0.59	0.06853	0.00455	0.45079	0.02548	0.05041	0.00075	884.9	137.0	377.8	17.8	317.0	4.6
G930-2-6		28.84	201.93	301.36	0.67	0.06270	0.00467	0.40463	0.02733	0.05008	0.00076	698.2	159.2	345.0	19.8	315.0	4.7
G930-2-8		34.01	310.65	381.20	0.81	0.05655	0.00343	0.36707	0.02027	0.04993	0.00082	472.3	133.3	317.5	15.1	314.1	5.1
G930-2-9		22.63	178.65	260.67	0.69	0.06437	0.00766	0.40826	0.03000	0.05064	0.00087	753.7	253.7	347.6	21.6	318.4	5.3
G930-2-10		28.49	196.88	318.45	0.62	0.04796	0.00315	0.32328	0.01850	0.05046	0.00077	98.2	157.4	284.4	14.2	317.4	4.7
G930-2-13		56.66	481.80	522.77	0.92	0.05973	0.00308	0.40840	0.01972	0.05079	0.00081	594.5	112.9	347.7	14.2	319.3	5.0
G930-2-14		33.95	241.93	315.46	0.77	0.07316	0.00552	0.45003	0.02631	0.05026	0.00088	1018.2	153.7	377.3	18.4	316.1	5.4
G930-2-15		21.21	128.09	231.39	0.55	0.05739	0.00491	0.36533	0.02392	0.05065	0.00082	505.6	188.9	316.2	17.8	318.5	5.0
G930-2-16		51.62	400.17	494.51	0.81	0.04816	0.00263	0.33496	0.01628	0.05079	0.00063	105.6	125.9	293.3	12.4	319.4	3.9
G930-2-17		50.02	381.45	480.58	0.79	0.05920	0.00317	0.41147	0.01987	0.05084	0.00068	576.0	116.7	349.9	14.3	319.7	4.2
G930-2-18		25.54	183.85	288.49	0.64	0.05914	0.00385	0.38626	0.02165	0.05066	0.00082	572.3	137.9	331.6	15.9	318.6	5.0
G930-2-19		34.90	269.07	348.05	0.77	0.07653	0.00563	0.48958	0.03078	0.05039	0.00077	1109.3	148.1	404.6	21.0	316.9	4.7
G930-2-20		32.40	224.18	360.80	0.62	0.05454	0.00339	0.37580	0.02003	0.05069	0.00077	394.5	136.1	323.9	14.8	318.7	4.7
G930-2-21		31.78	249.23	344.24	0.72	0.06441	0.00393	0.44703	0.02616	0.05082	0.00075	755.3	129.6	375.2	18.4	319.6	4.6
G930-7-3	Southwest dacite (Devonian)	38.37	235.64	370.43	0.64	0.06857	0.00463	0.54918	0.03570	0.06003	0.00111	887.0	140.7	444.5	23.4	375.8	6.8
G930-7-5		27.99	138.62	332.90	0.42	0.06251	0.00372	0.49359	0.02470	0.05973	0.00084	700.0	123.1	407.4	16.8	374.0	5.1
G930-7-6		44.07	269.86	380.11	0.71	0.06262	0.00326	0.51063	0.02258	0.05998	0.00080	694.5	305.5	418.9	15.2	375.5	4.9
G930-7-7		28.63	153.40	309.76	0.50	0.06471	0.00662	0.51567	0.06439	0.06015	0.00152	764.8	218.5	422.3	43.1	376.5	9.3
G930-7-9		100.00	810.27	666.26	1.22	0.06172	0.00597	0.52639	0.06318	0.06024	0.00218	664.8	208.2	429.4	42.0	377.1	13.2
G930-7-12		68.56	460.83	498.81	0.92	0.07179	0.00524	0.61035	0.06537	0.05917	0.00146	988.9	144.3	483.8	41.2	370.6	8.9
G930-7-15		58.33	321.77	589.25	0.55	0.05576	0.00251	0.48686	0.02026	0.06024	0.00086	442.6	100.0	402.8	13.8	377.1	5.2
G930-7-18		70.42	413.04	498.38	0.83	0.06703	0.00287	0.55371	0.02219	0.06000	0.00076	838.9	89.7	447.4	14.5	375.6	4.6
G930-7-20		71.85	508.37	699.10	0.73	0.05919	0.00330	0.49720	0.04633	0.05893	0.00151	572.3	122.2	409.8	31.4	369.1	9.2
G930-7-23		49.85	280.32	469.37	0.60	0.05771	0.00268	0.48136	0.02161	0.06057	0.00075	520.4	101.8	399.0	14.8	379.1	4.6
G930-7-28		133.48	969.58	883.65	1.10	0.06981	0.00331	0.57612	0.03283	0.06117	0.00159	924.1	97.4	462.0	21.2	382.7	9.6
G930-7-29		56.38	345.83	502.50	0.69	0.05325	0.00271	0.46401	0.02120	0.05993	0.00083	338.9	114.8	387.0	14.7	375.2	5.1
G930-7-31		62.23	369.78	527.78	0.70	0.05900	0.00276	0.47669	0.02070	0.05944	0.00079	568.6	101.8	395.8	14.2	372.2	4.8
G930-7-34		16.65	74.26	212.19	0.35	0.05803	0.00368	0.45874	0.02595	0.05984	0.00102	531.5	138.9	383.4	18.1	374.6	6.2
G930-7-35		84.87	449.63	883.47	0.51	0.05904	0.00272	0.50439	0.02495	0.05972	0.00066	568.6	100.0	414.7	16.8	373.9	4.0
G930-9-1	Southwest andesite (Devonian)	43.48	211.51	594.09	0.36	0.05516	0.00231	0.46955	0.01867	0.06185	0.00070	416.7	94.4	390.9	12.9	386.9	4.3
G930-9-2		56.25	313.88	622.97	0.50	0.05805	0.00250	0.48572	0.01961	0.06139	0.00073	531.5	99.1	402.0	13.4	384.1	4.5
G930-9-3		36.87	205.05	329.60	0.62	0.05396	0.00267	0.45539	0.02094	0.06148	0.00086	368.6	111.1	381.0	14.6	384.6	5.2
G930-9-4		155.86	909.27	1439.80	0.63	0.05363	0.00197	0.47689	0.01630	0.06144	0.00069	353.8	50.9	395.9	11.2	384.4	4.2
G930-9-8		40.05	161.84	696.38	0.23	0.05830	0.00256	0.49823	0.02077	0.06235	0.00069	542.6	96.3	410.5	14.1	389.9	4.2
G930-9-18		124.95	534.33	1281.81	0.42	0.06696	0.00228	0.57468	0.01945	0.06160	0.00059	836.7	70.4	461.0	12.5	385.3	3.6
G930-9-21		649.40	4582.81	4273.32	1.07	0.05502	0.00157	0.47922	0.01320	0.06205	0.00060	413.0	64.8	397.5	9.1	388.1	3.6
G930-9-24		86.32	339.38	1051.04	0.32	0.05886	0.00253	0.49288	0.02914	0.06296	0.00177	561.1	94.4	406.9	19.8	393.6	10.7

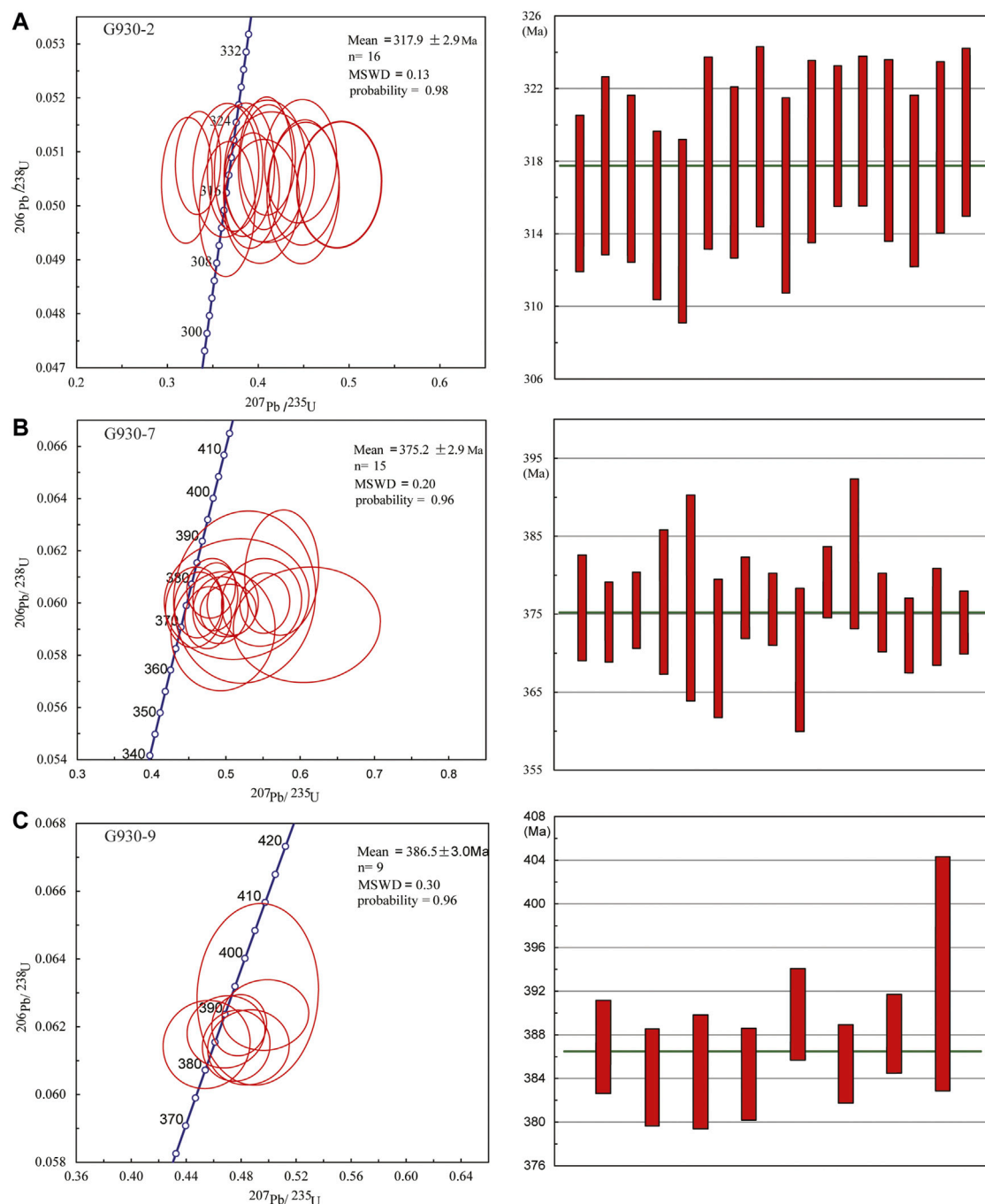


FIGURE 7 | Concordant age diagram and weighted mean age of LA-ICP-MS zircon $^{207}\text{Pb}/^{235}\text{U}$ - $^{206}\text{Pb}/^{238}\text{U}$ of volcanic lava in Xilekuduk area. **(A)** Northeast stomatal andesite; **(B)** southwest dacite; and **(C)** southwest andesite.

between 4.36 and 4.40%. The Fe_2O_3 content ranged from 3.77 to 3.82%; TiO_2 varied between 0.94 and 0.97%, and the content of TiO_2 was relatively high. The total alkali content ranged from 5.77 to 6.30% and sodium rich ($\text{Na}_2\text{O}/\text{K}_2\text{O} = 3.05\text{--}3.60$); the Mg number is 33.45–36.01, the consolidation index (SI), the feldspar index (FL), and the iron magnesium index (MF) were relatively low, as shown in **Table 3**.

The SiO_2 content of Devonian dacite ranged from 62.25 to 63.08%; the Al_2O_3 content 16.85–17.58%; the CaO content 2.57–3.64%; the MgO content 1.18–1.51%; the Fe_2O_3 content 0.84–1.04%; and the TiO_2 content 0.34–0.35%. The total alkali content was between 7.45 and 9.00%, and it was rich in sodium ($\text{Na}_2\text{O}/\text{K}_2\text{O} = 1.33\text{--}1.88$). The SiO_2 content of Devonian andesite ranged from 61.89 to 62.71%; the Al_2O_3 content

TABLE 2 | Major element analysis data of volcanic rocks in the Xilekuduk area (wt%).

Sample number	Lithology	SiO ₂	TiO ₂	Al ₂ O ₃	Fe ₂ O ₃	MgO	MnO	CaO	Na ₂ O	K ₂ O	P ₂ O ₅	FeO	LOI ¹	Total
Q0822-4	Northeast stomatal andesite (Carboniferous)	55.80	0.94	17.08	3.79	4.36	0.15	5.95	4.63	1.52	0.28	3.62	1.71	99.83
Q0822-5		55.76	0.97	17.24	3.77	4.40	0.17	6.11	4.50	1.27	0.28	3.72	1.66	99.85
Q0822-6		55.01	0.96	17.48	3.82	4.37	0.15	5.86	4.93	1.37	0.28	3.72	1.89	99.83
Q930-6	Southwest dacite (Devonian)	62.78	0.34	17.53	0.90	1.18	0.12	3.10	4.82	2.63	0.29	3.71	2.23	99.63
Q0822-7		63.08	0.35	16.85	1.04	1.44	0.11	2.57	5.14	3.86	0.23	3.14	2.01	99.82
Q0822-8		63.08	0.35	17.34	0.76	1.30	0.12	3.64	5.07	2.68	0.22	3.24	2.02	99.82
Q0822-9	Southwest andesite (Devonian)	62.85	0.35	17.58	0.96	1.32	0.11	2.93	5.24	3.30	0.23	2.95	2.00	99.81
Q0822-10		62.25	0.34	17.03	0.84	1.51	0.13	3.14	5.06	3.57	0.22	3.54	2.18	99.82
Q930-9		62.71	0.42	16.62	1.64	1.72	0.15	2.94	5.24	0.99	0.38	3.45	3.26	99.52
Q930-10		61.89	0.43	16.85	1.18	1.72	0.17	3.56	5.11	0.98	0.39	3.84	3.38	99.50
Q930-11		60.83	0.42	17.89	1.76	1.75	0.15	2.74	4.63	1.15	0.36	3.61	3.96	99.25
Q0822-11		62.16	0.47	17.82	1.54	1.76	0.14	2.76	5.59	1.31	0.36	3.29	2.67	99.87
Q0822-12		62.48	0.46	17.83	1.56	1.87	0.14	2.66	5.28	1.40	0.29	3.33	2.56	99.87

¹LOI: Loss on ignition.**TABLE 3 |** Geochemical parameters of volcanic rocks.

Sample number	Lithology	Mg# ¹	Alkali value	AR ²	A/CNK	A/NK	SI ³	FL ⁴	MF ⁵	σ ⁶
Q0822-4	Northeast stomatal andesite (Carboniferous)	35.98	1.73	0.32	2.78	19.51	50.81	73.09	2.95	2.95
Q0822-5		33.45	1.66	0.34	2.99	19.82	48.58	73.22	2.61	2.61
Q0822-6		36.01	1.74	0.33	2.78	19.21	51.78	73.44	3.30	3.30
Q930-6	Southwest dacite (Devonian)	42.50	2.13	0.29	2.35	8.64	70.62	80.97	2.81	2.81
Q0822-7		53.45	2.73	0.22	1.87	9.63	77.83	75.86	4.04	4.04
Q0822-8		44.69	2.17	0.27	2.24	9.68	68.04	77.05	2.99	2.99
Q0822-9	Southwest andesite (Devonian)	48.56	2.43	0.25	2.06	9.37	74.47	76.23	3.67	3.67
Q0822-10		50.64	2.49	0.23	1.97	10.12	73.30	76.00	3.87	3.87
Q930-9		37.48	1.93	0.42	2.67	12.81	67.94	76.09	1.97	1.97
Q930-10		36.14	1.85	0.41	2.77	12.97	63.11	76.00	1.96	1.96
Q930-11		32.31	1.78	0.46	3.10	13.16	67.84	76.73	1.87	1.87
Q0822-11		38.74	2.01	0.40	2.58	12.73	71.43	74.64	2.49	2.49
Q0822-12		37.51	1.97	0.40	2.67	13.51	71.52	73.82	2.29	2.29

¹Mg# = 100 × MolarMg²⁺ / (Mg²⁺ + Fe²⁺)²Alkalinity rate³Consolidation index⁴Feldspar quartz index⁵Iron-magnesium index⁶Rittman index.

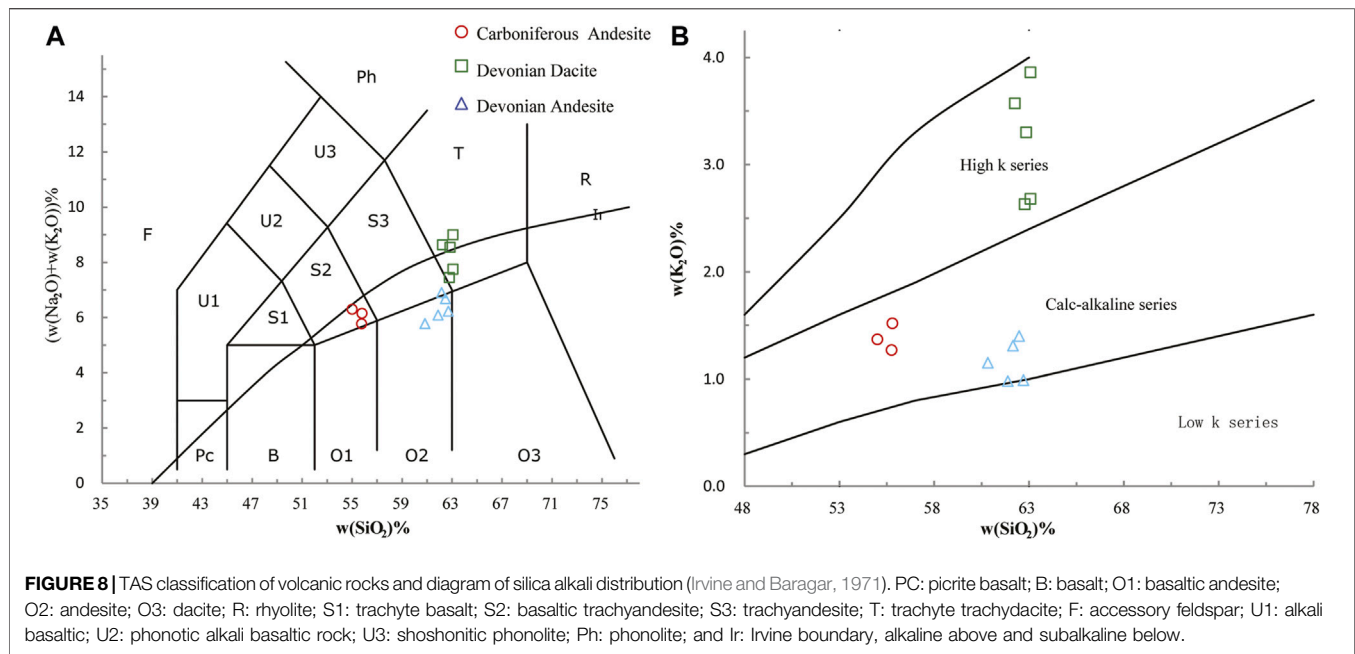
16.62–17.89%; the CaO content 2.66–3.56%; the MgO content 1.18–1.51%; the Fe₂O₃ content 0.84–1.04%; and the TiO₂ content 0.34–0.35%. The total alkali content is between 5.78 and 6.68%, and it is sodium-rich and potassium-poor (Na₂O/K₂O = 3.77–5.29), Mg number is 42.50–53.45 and 32.31–38.74, respectively. The consolidation index (SI), the felsic index (FL), and the iron-magnesium index (MF) increase compared with the non-amygdaloid ones, indicating a high degree of magmatic crystallization differentiation (**Table 3**).

On the TAS (SiO₂/(K₂O + Na₂O)) diagram of volcanic rocks (**Figure 8A**), the samples of Carboniferous mainly fall on basaltic trachyandesite, while the Devonian samples fall on the trachydacite and trachyte-andesite. On the SiO₂/K₂O diagram

(Harris et al., 1986) (**Figure 8B**), the samples fall into calc-alkaline basaltic andesite, andesite, and high-potassium series (andesite) dacite, respectively.

2) Geochemistry of Rare Earth and Trace Elements

The results of rare earth elements (REEs) and trace elements are shown in **Table 4**. The weight abundance (w (Σ REE)) of the Carboniferous stomatal andesite samples and their values of europium anomaly (δ Eu) and the values of (La)_N/(Yb)_N are (95.54–116.07) × 10⁻⁶, 1.14–1.16, and 5.93–8.35, respectively. The diagram of chondrite-normalized REE distribution curve (**Figure 9A**) shows that the rocks are slightly enriched in LREE and have no obvious Eu anomaly, implying that there was no obvious fractional crystallization of



plagioclase during the magmatic evolution. The primitive mantle standard diagram of incompatible elements (Figure 9C) shows that large ion lithophile elements (LILEs) are relatively enriched and the high-field strength elements (HFSEs) are relatively depleted.

The $w(\sum \text{REE})$ of Devonian dacite samples varies slightly $108.16\text{--}130.96 \times 10^{-6}$, $d \text{Eu}$ is $0.97\text{--}1.16$, and $w(\text{La})_{\text{N}}/(\text{Yb})_{\text{N}}$ is $5.67\text{--}7.65$. The $w(\sum \text{REE})$ of Devonian andesite is $108.26\text{--}130.02 \times 10^{-6}$, $d \text{Eu}$ is $0.84\text{--}1.09$, and $w(\text{La})_{\text{N}}/(\text{Yb})_{\text{N}}$ is $5.12\text{--}7.73$. The normalized REE distribution curve of chondrite (Figure 9B) shows right-leaning LREE enrichment type, and there is no Eu anomaly in the Devonian dacites and andesites. On the primitive mantle standard diagram of incompatible elements (Figure 9D), the LILEs are relatively enriched and the LILEs are relatively depleted.

DISCUSSION

Diagenetic Age and Tectonic Environment

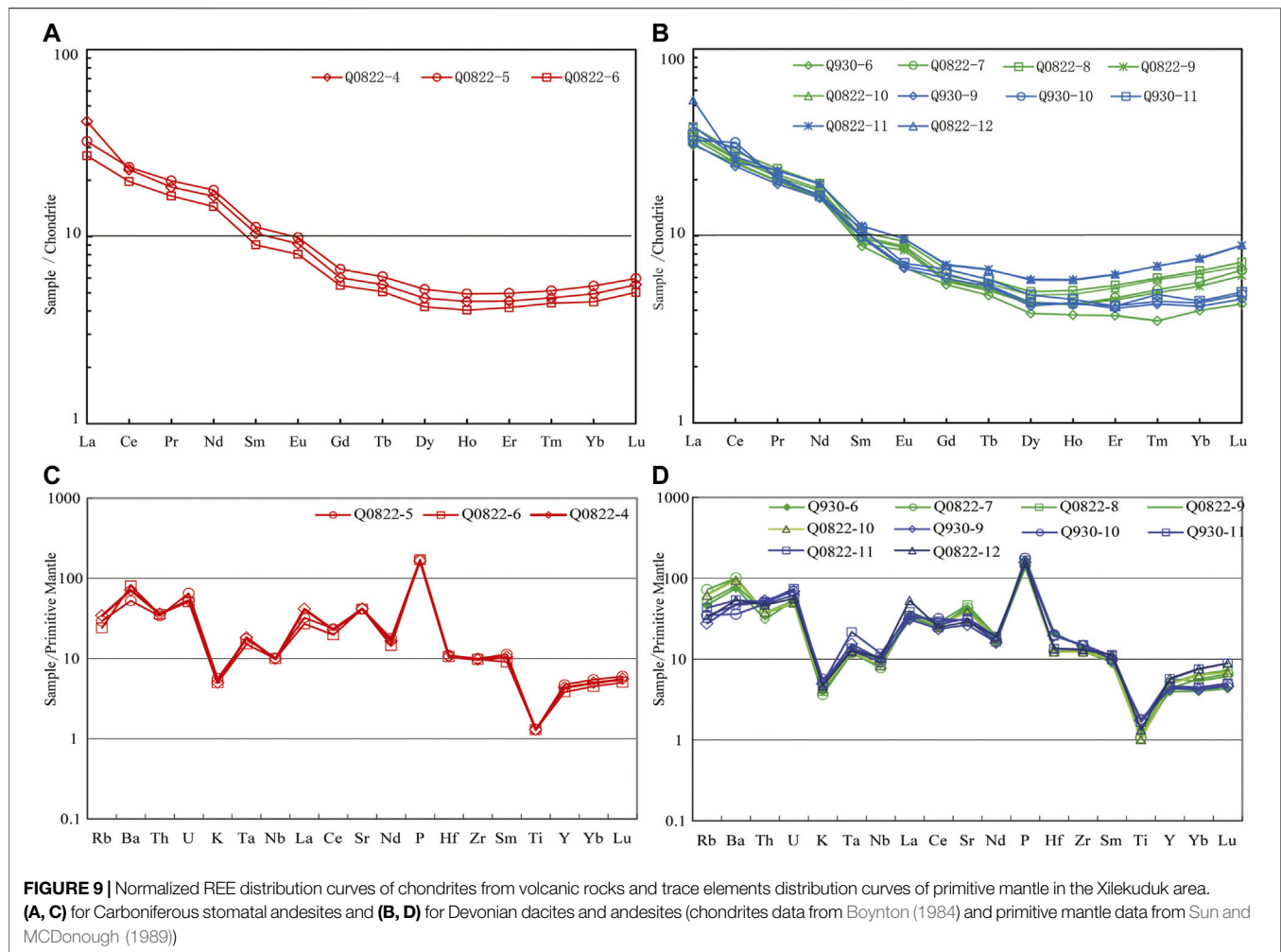
As predecessors have speculated, andesitic, dacitic volcanic rocks and pyroclastic rocks exposed in the ore district belong to the volcanic sedimentary assemblage of the Lower Carboniferous Namingshui Formation (Long et al., 2009; Ding et al., 2011; Long et al., 2011; Long et al., 2014; You et al., 2016; Wei et al., 2019). However, in this study, LA-ICP-MS zircon U-Pb data show that the diagenetic age of dacite is 375.2 ± 2.9 Ma and that of andesite is 386.5 ± 3.0 Ma, indicating that the volcanic rock was formed in the Middle Devonian and the basaltic andesite is 317.9 ± 2.9 Ma, corresponding to the early Late Carboniferous. According to the 1:250000 and 1:50000 regional geological survey data and previous studies, there is a set of Middle Devonian Beitashan Formation mainly composed of shallow and coastal volcanic

rocks, pyroclastic rocks, and carbonate rocks, and a set of Late Carboniferous Jiangbastao Formation mainly composed of marine and continental facies clastic rocks (Zhang et al., 2005; Zhang et al., 2008). Based on this, the strata in this area can be divided into two sets: the dacite-pyroclastic rocks in the southeast belong to the Beitashan Formation of Middle Devonian, and the clastic sedimentary rocks with stomatal andesite volcanic rocks in the northwest belong to the Lower Carboniferous Jiangbastao Formation.

The Devonian volcanic rock assemblage consists of andesite and dacite. The content of TiO_2 varies from 0.34 to 0.35% and from 0.42 to 0.47%, which belongs to high-K calc-alkaline series. The REE standard distribution model belongs to the LREE enrichment type and the large ion lithophile elements Rb, Ba, and K are strongly enriched, and the high-field strength elements (HFSEs) Nb, Ta, and Ti are relatively depleted. The Zr/Nb ratio is 15.38–23.90, which is close to the Zr/Nb ratio range of MORB (10–60, Davisin, 1996), and the Nb/Ta ratio is 9.41–12.14, which are lower than those of the original mantle (–17), indicating that Nb and Ta are separated by subducting fluid metasomatism of the original mantle (Othman et al., 1989). The geochemical characteristics of the volcanic rocks are similar to those of the Beitashan Formation in the region and are typical island arc volcanic rocks (Deng et al., 2009). The Carboniferous volcanic rocks are mainly stomatal andesite the REE standard distribution pattern belongs to LREE enrichment type. There is no obvious negative Ce anomaly, showing obvious continental volcanic characteristics (Zhang et al., 2006). The large ion lithophile elements Th, Rb, Ba, and K are strongly enriched, and the HFSEs Nb, Ta, and Ti are relatively depleted, which are similar to island arc basalt. However, the variation of TiO_2 content is 0.94–0.97%, and that of V content is $178\text{--}183 \times 10^{-6}$, which is higher than that of island arc basalt. The metamorphic basicity of

TABLE 4 | Analysis data of rare earth elements and trace elements in the Xilekuduk area (10^{-6}).

Lithology	Q0822-4	Q0822-5	Q0822-6	Q930-6	Q0822-7	Q0822-8	Q0822-9	Q0822-10	Q930-9	Q930-10	Q930-11	Q0822-11	Q0822-12
	Carboniferous stromatolite andesite			Devonian dacite					Devonian andesite				
La	28.36	22.20	18.60	21.00	23.57	26.33	22.87	24.48	21.40	22.30	23.80	26.47	36.62
Ce	40.46	41.71	34.94	43.40	45.91	50.26	43.81	46.52	41.90	56.20	52.30	47.09	44.00
Pr	5.07	5.49	4.55	5.40	5.71	6.32	5.46	5.90	5.23	5.50	5.66	6.16	6.18
Nd	22.27	24.03	19.60	21.70	23.60	25.90	22.58	24.20	21.60	22.20	22.20	25.65	25.76
Sm	4.62	4.99	4.01	3.92	4.30	4.65	4.08	4.41	4.36	4.42	4.85	5.03	5.01
Eu	1.54	1.66	1.35	1.14	1.45	1.57	1.40	1.49	1.13	1.16	1.20	1.62	1.62
Gd	3.59	3.99	3.26	3.27	3.46	3.95	3.40	3.66	3.53	3.73	3.96	4.19	4.16
Tb	0.60	0.66	0.55	0.52	0.57	0.63	0.55	0.60	0.58	0.59	0.63	0.72	0.71
Dy	3.45	3.85	3.11	2.84	3.26	3.72	3.20	3.56	3.11	3.24	3.56	4.28	4.32
Ho	0.74	0.81	0.66	0.62	0.71	0.84	0.71	0.80	0.72	0.71	0.75	0.95	0.96
Er	2.17	2.39	2.00	1.80	2.24	2.62	2.18	2.53	1.97	2.03	2.02	2.97	3.00
Tm	0.35	0.38	0.33	0.26	0.38	0.44	0.37	0.43	0.32	0.33	0.36	0.51	0.51
Yb	2.44	2.69	2.21	1.97	2.79	3.21	2.65	3.10	2.07	2.16	2.21	3.71	3.76
Lu	0.41	0.44	0.37	0.32	0.49	0.54	0.45	0.51	0.34	0.36	0.37	0.66	0.66
Y	19.73	21.43	17.37	18.10	19.86	23.07	25.77	22.58	19.60	20.50	21.10	25.85	26.43
Σ ree	116.07	115.30	95.54	108.16	118.44	130.96	113.70	122.18	108.26	124.93	123.87	130.02	137.27
LREE	102.32	100.09	83.05	96.56	104.55	115.03	100.20	107.00	95.62	111.78	110.01	112.03	119.19
HREE	13.75	15.21	12.49	11.60	13.89	15.93	13.50	15.18	12.64	13.15	13.86	18.00	18.08
L/HREE	7.44	6.58	6.65	8.32	7.53	7.22	7.42	7.05	7.56	8.50	7.94	6.22	6.59
La_N/Yb_N	8.35	5.93	6.04	7.65	6.06	5.90	6.20	5.67	7.42	7.41	7.73	5.12	7.00
δEu	1.16	1.14	1.14	0.97	1.15	1.12	1.16	1.13	0.88	0.87	0.84	1.08	1.09
δCe	0.83	0.93	0.93	1.00	0.97	0.96	0.96	0.95	0.97	1.24	1.11	0.90	0.72
Rb	34.11	29.28	24.08	46.77	72.60	52.43	63.40	62.13	27.56	35.12	42.99	34.82	32.28
Ba	70.95	52.34	80.64	75.69	100.76	81.11	97.72	94.82	48.08	35.91	53.80	46.52	53.86
Th	36.01	33.96	35.60	30.94	37.89	38.26	37.21	37.84	53.18	48.47	51.29	50.33	46.72
U	53.05	65.00	50.90	53.81	52.48	49.05	48.86	50.10	69.05	61.90	74.29	70.00	56.19
K	4.98	5.64	4.98	3.98	3.65	3.98	3.65	4.32	4.98	5.64	4.98	4.65	4.65
Ta	18.20	17.41	15.05	13.66	12.00	12.12	11.78	12.29	15.37	12.68	21.71	13.66	12.73
Nb	9.85	10.15	9.96	9.54	7.78	8.26	8.14	8.35	9.99	9.23	11.77	10.49	10.34
La	41.28	32.31	27.07	30.57	34.31	38.33	33.29	35.63	31.15	32.46	34.64	38.53	53.30
Ce	22.79	23.50	19.68	24.45	25.86	28.32	24.68	26.21	23.61	31.66	29.46	26.53	24.79
Sr	41.62	41.69	41.43	40.38	42.60	46.70	44.76	38.61	26.54	30.14	31.09	32.21	28.96
Nd	16.45	17.75	14.48	16.03	17.43	19.13	16.68	17.87	15.95	16.40	16.40	18.94	19.03
P	166.29	170.88	170.88	170.42	144.24	148.83	135.51	162.62	158.48	176.40	165.83	151.13	152.97
Hf	10.53	10.95	10.53	21.10	12.54	12.28	12.50	12.32	19.45	20.03	19.35	13.50	13.34
Zr	9.64	10.00	9.77	13.93	12.40	12.30	12.38	12.29	14.64	14.64	15.09	13.29	13.08
Sm	10.40	11.25	9.03	8.83	9.69	10.48	9.18	9.94	9.82	9.95	10.92	11.33	11.29
Ti	1.29	1.29	1.29	1.34	1.06	1.01	1.06	1.01	1.75	1.80	1.66	1.66	1.34
Y	4.34	4.71	3.82	4.71	4.36	5.07	5.66	4.96	4.31	4.51	4.64	5.68	5.81
Yb	4.95	5.45	4.48	4.00	5.66	6.50	5.37	6.29	4.20	4.38	4.48	7.53	7.62
Lu	5.53	5.97	5.03	4.32	6.55	7.24	6.12	6.89	4.59	4.86	5.00	8.89	8.92



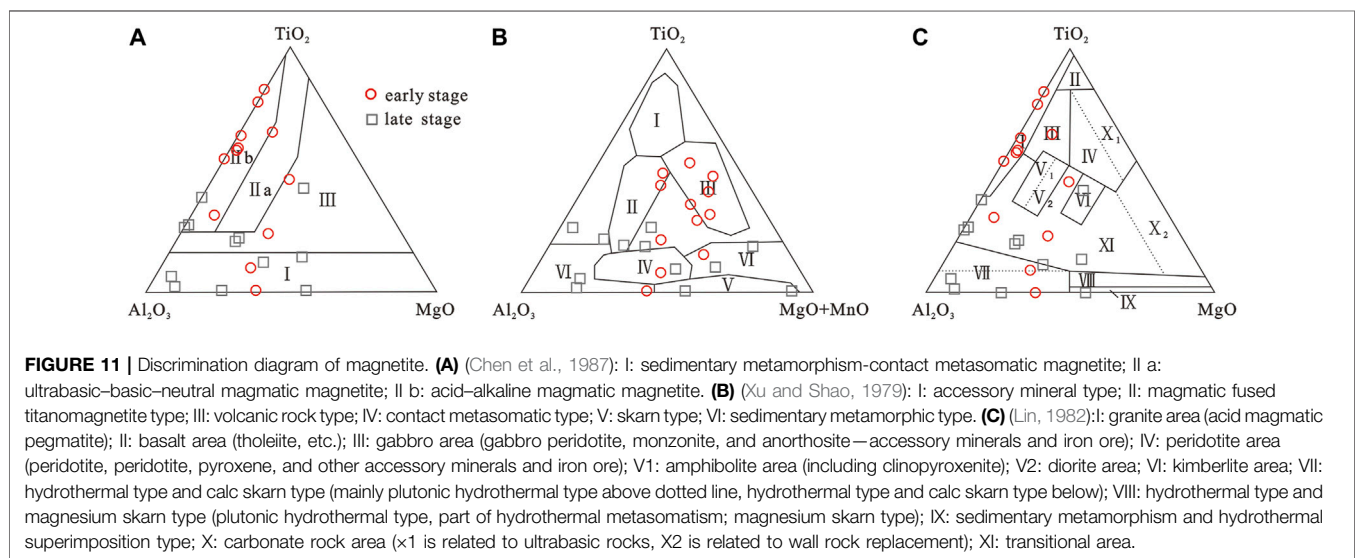
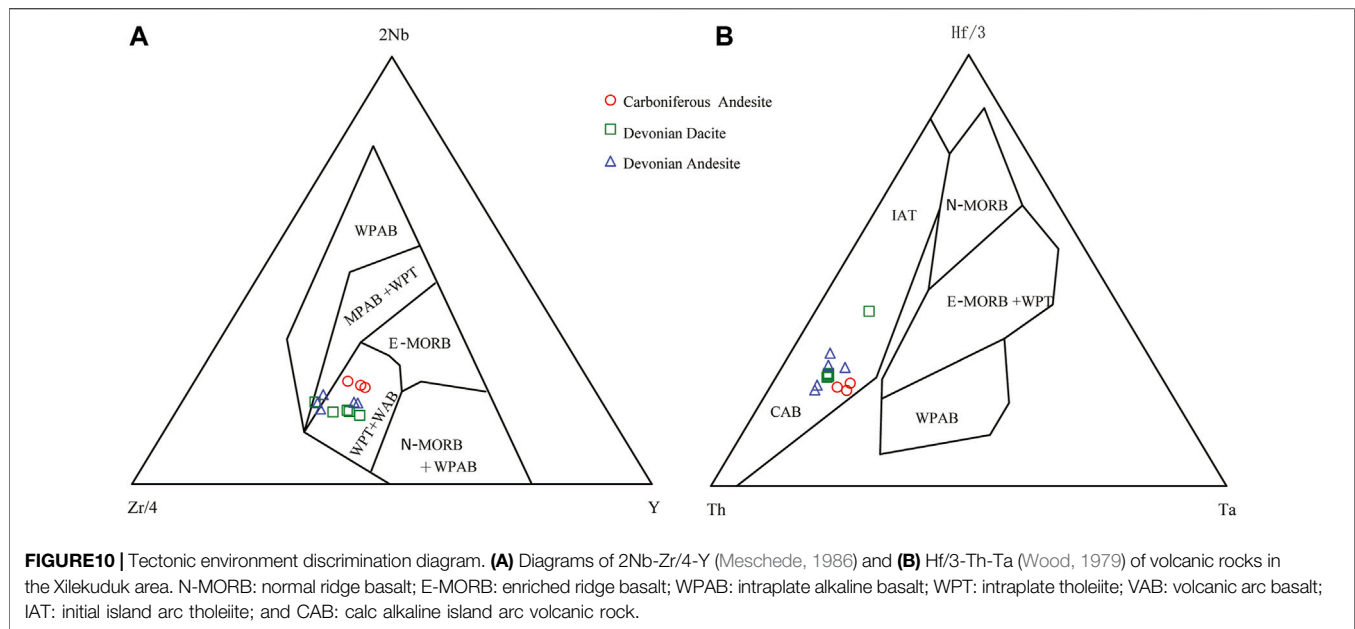
the Lower Carboniferous Jiangbastao Formation in the eastern part of the study area shows the characteristics of back arc basalts (Woodhead et al., 1993; Zhou et al., 2005). The cause of this phenomenon may be linked to the transitional environment and complex formation process; consequently, it is inferred that the diagenetic environment belongs to the early stage of plate collision.

On the Nb-Zr-Y tectonic environment discrimination diagram, Devonian and Carboniferous volcanic rock samples fall mainly in the volcanic arc basalt and the intraplate tholeiitic basalt area (Figure 10A), and all samples fall in island arc volcanic rocks on the Hf-Th-Ta diagram, showing the products of island arc environment (Figure 10B). This indicates that the diagenesis has certain transitional characteristics, and this may be related to the complex plate subduction and collision process.

Relationship Between Volcanism and Iron and Molybdenum Mineralization

Magnetite is widely distributed in various types of deposits, such as the skarn type deposit, the Kiruna type deposit, the iocg type deposit, the magmatic type deposit, the BIF type deposit, and the

porphyry type deposit (Dupuis and Beaudoin, 2011; Huberty et al., 2012; Hu et al., 2014). The content and variation range of major elements, trace elements, and rare earth elements of magnetite with different genesis differ: this can indicate different formation temperature, oxygen fugacity, sulfur fugacity, ore-forming material source, and tectonic environment, and so on (Pearce and Gale, 1977; Nadoll et al., 2012). Therefore, the mineral chemical characteristics of magnetite have certain typomorphic significance for distinguishing different types of ore deposits. For example, magnetite in skarn-type iron ore contains lower V and Ti, higher Ca, Al, and Mn contents than that in magmatic iron ore, and their REE characteristics are also obviously different (Frietsch and Perdahl, 1995; Dupuis and Beaudoin, 2011; Hu et al., 2014; Nadoll et al., 2014). The iron-bearing minerals in the Xilekuduk area are mainly magnetite. Through microscopic mineral research, it is found that MT1 magnetite is generally wrapped and metasomatized by MT2, and the contact boundary between them is clear, indicating that there are at least two stages of mineralization in this area. In recent years, some scholars have also identified two phases of magnetite in adjacent areas. For example, the Qiaoxiahala and Laoshankou iron-copper-gold



deposits in the northern margin of Junggar, Xinjiang, were divided into two phases of magnetite, and it was noted that “dissolution reprecipitation” may have occurred in the mineralization process (Shang et al., 2017). The EPMA data of two typical magnetite samples (to be published in another article) show that MT1 magnetite has higher Ti and V and lower Ca, Al, Cr than MT2 magnetite. In the genetic diagram of $\text{TiO}_2\text{-Al}_2\text{O}_3\text{-MgO}$ (Figure 11A), most of the early crystallized magnetites fall in the acid-alkaline magmatic magnetite region. The magnetite crystallized in the late stage is dispersed, and some of them fall in the area of sedimentary metamorphism-contact metasomatism. In the genetic diagram of $\text{TiO}_2\text{-Al}_2\text{O}_3\text{-MgO+MnO}$ genetic diagram (Figure 11B), magnetite crystallized in the early stage mainly falls in the volcanic rock type and the magmatic melt

separated titanomagnetite type area. The magnetite crystallized in the late stage mainly occurs in contact metasomatic and skarn type areas. In the genetic diagram of $\text{TiO}_2\text{-Al}_2\text{O}_3\text{-MgO}$ (Figure 11C), most of the early crystallized magnetites fall in the granite area (acidic magmatic pegmatite). The magnetite crystallized in the late stage mainly occurs in hydrothermal and calc skarn type areas. Therefore, the early crystallized magnetite MT1 is mostly of magmatic origin, while the late crystallized magnetite MT2 shows the characteristics of hydrothermal origin. This further confirms the existence of at least two stages of mineralization of magnetite. According to the banded occurrence characteristics of MT1 magnetite and the occurrence along with volcanic rocks in the Middle Devonian, it is inferred that the formation of MT1 magnetite is related to the

eruption and deposition of Devonian volcanoes (375–386 Ma). However, MT2 magnetite occurs in the form of magnetite quartz vein. Microscopically, it can be observed that MT2 magnetite is metasomatized by molybdenite and pyrite, which has hydrothermal characteristics. This may be similar to the “dissolution–reprecipitation” of magnetite in the surrounding the Qiaoxiahala and Laoshankou iron–copper–gold deposits. The relationship between magnetite and molybdenite in this stage is relatively close. Combined with the porphyry molybdenum metallogenic event in the ore district, it is speculated that MT2 magnetite may be related to porphyry molybdenum mineralization.

According to regional data, the study area experienced plate subduction, collision, and post-collision regional tectonic events in the late Paleozoic (Wang et al., 2006; Cai et al., 2011; Xiao and Santosh, 2014), accompanied by strong volcanism, such as volcanic eruption, eruption, and subvolcanism (Liu, 2001). According to the two stages of Late Paleozoic volcanic rock formation in the Xilekuduk area, the coupling relationship between two stages of volcanism and iron and molybdenum mineralization is sorted out:

In the early Devonian, the Junggar plate began to subduction northward and was in the tectonic environment of the plate margin. Volcanic rocks transited from tholeiitic (low-potassium) series to calc-alkaline series and then to high-potassium series of dacite, indicating that the island arc experienced the evolution process from early stage to mature stage. There are a large number of andesite dacite assemblages in the Xilekuduk area. The ages of these volcanic rock assemblages are between 375 and 385 Ma, showing typical island arc magmatic characteristics. During the intermittent period of volcanic eruption, the magmatic fluid rich in iron and copper first crystallized and precipitated between the layers of volcanic rocks, or interposed in the fissures of volcanic rocks, forming magnetite ore bodies mainly in strip and vein (Wilkinson, 2013), and a large number of banded and vein magnetite (MT1) were developed. With the crystallization differentiation of magma and the precipitation of copper element, the high background value of copper in volcanic rocks of the Beitashan Formation is formed. The Cu content of basalt is 95×10^{-6} – 25×10^{-6} , which is about 4 times of the Clark value of crust and that of andesite is 20×10^{-6} , which is roughly equivalent to the Clark value of crust, which provides material source for the formation of later copper deposits (Yang et al., 2010). In the Qiaoxiahala iron–copper–gold deposit on the northern side of the study area, iron ore body mainly occurs in the basalt-andesite volcanic rock of the Beitashan Formation of the Middle Devonian, which is derived from the early intermediate-basic volcanism (Ying, 2007). Therefore, the basalt andesite formation in the Xilekuduk area is an important iron-bearing area.

In the Early Carboniferous, the Junggar plate continued to subduction to form the Devonian–Early Carboniferous back arc ocean basin (Li, 2009). Volcanism in this stage was mainly subvolcanic facies, which was composed of intermediate–intermediate acid hypabyssal and ultrahypabyssal intrusive facies igneous rocks with different depths. The diagenetic age was concentrated in 340–318 Ma. Basaltic

andesite porphyrite xenoliths are distributed in the granodiorite in the Xilekuduk area, suggesting that the source of crust mantle mixing of acid rock mass: the upper mantle material upwelling of asthenosphere induces the melting of lower crust material, and the mantle-derived magma rises and mixes with the crust source material, resulting in large-scale magma mixing (Wang et al., 2015), forming ore-bearing magma. Subsequently, the ore-bearing magma intruded and emplaced along the extensional structure, metasomatized the Devonian overflow andesite-sedimentary carbonate formation, forming a skarn belt. At the same time, a large amount of magmatic segregation formed a small amount of magnetite quartz veins (MT2), superimposed or wrapped early stratiform magnetite ore (MT1). With the gradual evolution of fluid, a large amount of Cu–Mo precipitates to form the Xilekuduk porphyry Cu–Mo deposit.

Volcanism and Fe–Cu–Mo mineralization in this area, therefore, bear the characteristics of multistage superimposed mineralization. The andesite–dacite formation in the Middle Devonian is closely related to the formation of early-stage magnetite, and the Early Carboniferous homologous heterogeneous volcanic rock formation, such as basaltic andesite–diorite–granite porphyry, is closely related to the porphyry copper mineralization and late-stage magnetite.

CONCLUSION

- 1) The diagenetic age of dacite is 375.2 ± 2.9 Ma and that of andesite is 386.5 ± 3.0 Ma, which indicates that the volcanic rock was formed in the Middle Devonian, and the diagenetic age of stomatal andesite is 317.9 ± 2.9 Ma, it was formed in the Late Carboniferous.
- 2) The Devonian volcanic rock assemblage is composed of andesite and dacite. The content of TiO_2 varies from 0.34 to 0.35% and 0.42–0.47%, respectively. It belongs to the high-K calc-alkaline series, enriched in LREE, enriched in large ion lithophile elements Th, Rb, Ba, and K, and relatively depleted in HFSEs Nb, Ta, and Ti. The Carboniferous volcanic rocks are mainly stomatal andesite. The REE standard distribution pattern belongs to LREE enrichment type. The large ion lithophile elements Rb, Ba, and K are strongly enriched. The HFSEs Nb, Ta, and Ti are relatively depleted. The contents of TiO_2 and V are 0.94–0.97% and $178\text{--}183 \times 10^{-6}$, which are higher than those of island arc basalts. They are characterized by transitional diagenetic environment and are close to the stage of plate collision.
- 3) There are two periods of magnetite in the ore district. The stratiform magnetite ore MT1 produced along the early strata is mostly of magmatic origin. It is inferred that its formation is related to the eruption and deposition of Devonian volcano (375–386 Ma), while the magnetite MT2 of late magnetite quartz vein shows the characteristics of hydrothermal mineral, indicating the metal minerals precipitation in the early stage of the

mineralization of the Carboniferous (317.1 ± 2.9 ma) porphyry copper molybdenum deposit. Therefore, the volcanism and Fe-Cu-Mo mineralization in this area have the characteristics of multistage superimposed mineralization.

DATA AVAILABILITY STATEMENT

The original contributions presented in the study are included in the article/Supplementary Material, further inquiries can be directed to the corresponding author.

AUTHOR CONTRIBUTIONS

XW: wrote the paper and performed data treatment; HW: formulated the scientific problem, participated in writing the manuscript, and revised paper; ZL: provided natural samples and edited paper format; ZW: organized the research team and guided

the study; DL: conducted the experiment; QM and XL: funding. All authors have read and agreed to the published version of the manuscript.

FUNDING

This research was funded by the Natural Science Foundation of Hebei Province, Grant No. D2020403019; Science and Technology Research Project of University, Hebei Province, Grant No. ZD2020134; S&T Program of Hebei, Grant No. 19224205D; National Natural Science Foundation, Grant No. 41702165; the National Key R&D Program of China, Grant No. 2017YFC0601201 and 2017YFC0601204.

ACKNOWLEDGMENTS

We are grateful to reviewers for helpful comments and suggestions.

REFERENCES

- Ablimit, E. (2017). *Genesis of Ore Forming Rocks in Xilekudouke Mo Deposit and Implication for Regional Mineralization [dissertation/doctor's Thesis]*. [Beijing: China University of Geosciences].
- Andersen, T. (2002). Correction of Common Lead in U-Pb Analyses that Do Not Report 204Pb. *Chem. Geology*. 192 (1–2), 59–79. doi:10.1016/s0009-2541(02)00195-x
- Boynnton, W. V. (1984). "Cosmochemistry of the Rare Earth Elements: Meteorite Studies," in *Rare Earth Element Geochemistry*. Editor Henderson (New York: Elsevier), Vol. 2, 63–114.
- Cai, K., Sun, M., Yuan, C., Long, X., and Xiao, W. (2011). Geological Framework and Paleozoic Tectonic History of the Chinese Altai, NW China: a Review. *Russ. Geology. Geophys.* 52, 1619–1633. doi:10.1016/j.rgg.2011.11.014
- Chen, G. Y., Sun, D. S., Yin, H. A., and Davidson, J. P. (1987). *Genetic Mineralogy and Prospecting Mineralogy 1996*. in *Deciphering Mantle and Crustal Signatures in Subduction Zone Magmatism. Subduction Top to Bottom* (Chongqing Washington D. C: Chongqing Publishing Press Geophysical Monograph, American Geophysical Union), 251–262.
- Courfu, F., Hanchar, J. M., and Hoskin, P. W. O. (2003). Atlas of Zircon Textures. *Rev. Mineralogy Geochem.* 53, 469–500. doi:10.2113/0530469
- Deng, J. F., Luo, Z. H., Su, S. G., Mo, X. X., Ding, B. S., Lai, X. Y., et al. (2009). *Petrogenesis of Tectonics Environment and Metallogenesis*. Beijing: Geological Publishing Press. doi:10.1061/41039(345)179
- Ding, R. F., You, J., and Li, C. X. (2011). Selection and Evaluation of Xilekuduke Cu–Mo–Au Prospecting Target in Xinjiang. *Mineral. Exploration* 2 (6), 740–748.
- Dupuis, C., and Beaudoin, G. (2011). Discriminant Diagrams for Iron Oxide Trace Element Fingerprinting of Mineral Deposit Types. *Miner. Deposita*. 46, 319–335. doi:10.1007/s00126-011-0334-y
- Frietsch, R., and Perdahl, J.-A. (1995). Rare Earth Elements in Apatite and Magnetite in Kiruna-type Iron Ores and Some Other Iron Ore Types. *Ore Geology. Rev.* 9 (6), 489–510. doi:10.1016/0169-1368(94)00015-g
- Harris, N. B. W., Marzouki, F. M. H., and Ali, S. (1986). The Jabel Sayid Complex, Arabian Shield: Geochemical Constraints on the Origin of Peralkaline and Related Granites. *J. Geol. Soc.* 143, 287295. doi:10.1144/gsjgs.143.2.0287
- Hu, H., Li, J. W., and Lentz, D. (2014). Dissolution-reprecipitation Process of Magnetite from the Chengchao Iron Deposit: Insights into Ore Genesis and Implication for in-Situ Chemical Analysis of Magnetite. *Ore Geology. Rev.* 57, 393–405. doi:10.1016/j.oregeorev.2013.07.008
- Huberty, J. M. (2012). Silician Magnetite from the Dales Gorge Member of the Brockman Iron Formation, Hamersley Group, Western Australia. *Am. Mineral.* 97, 26–37. doi:10.2138/am.2012.3864
- Irvine, T. N., and Baragar, V. R. (1971). Aguidetothechemical Classification of the volcanic rocks. *Can. J. Earth. Sci.* 8, 523–548. doi:10.1139/e71-055
- Li, C. M. (2009). A Review on the Minerageny and Situmicroanalytical Dating Techniques of Zircons. *Geol. Surv. Researh* 33 (3), 161–174. doi:10.1007/978-3-642-01053-8_70
- Li, W. Y., Dong, F. C., Zhang, Z. W., Tan, W. J., Jiang, H. B., and Xiao, C. Y. (2015). Major Progress and Achievements in Study of the Metallogenic Prospect and Prospecting Deployment of Mineral Resources in Northwest China. *Geol. Surv. China* 2 (1), 19–24. doi:10.19388/j.zgdzdc.2015.01.004
- Lin, S. Z. (1982). Discussion on the Mineral Chemistry, Genesis and Evolution of Magnetite. *J. Mineralogy* (3), 166–174. doi:10.16461/j.cnki.1000-4734.1982.03.002
- Liu, J. Y. (2001). Continental Volcanic and Gold-Coper Metallogensis in East Junggar, Xinjiang. *Geotectonics and metallogeny* 25 (4), 1434–1438. doi:10.16539/j.ddgzycx.2001.04.010
- Long, L. L., Wang, J. B., Wang, Y. W., Wang, L. J., Liao, Z., Zhao, L. T., et al. (2014). Characteristics of REE Composition and Trace Element of the Pyrites from the Xilekuduke Cu–Mo Deposit in Xinjiang. *Mineral. Exploration* 5 (02), 169–177.
- Long, L. L., Wang, J. B., Wang, Y. W., Wang, L. J., Wang, S. L., and Pu, K. X. (2009). Geochronology and Geochemistry of the Ore-Bearing Porphyry in Xilekuduke Cu–Mo Deposit, Fuyun Area, Xinjiang, China. *Geol. Bull. China* 28 (12), 18401851
- Long, L. L., Wang, Y. W., Du, A. D., Wang, J. B., Wang, L. J., Wang, S. L., et al. (2011). Molybdenite Re–os Age of Xilekuduke Cu–Mo Deposit in Xinjiang and its Geological Significance. *Mineral. Deposits* 30 (4), 635–644. doi:10.16111/j.0258-7106.2011.04.004
- Meschede, M. (1986). A Method of Discriminating between Different Types of Mid-ocean Ridge Basalts and Continental Tholeiites with the Nb–Zr–Y Diagram. *Chem. Geol.* 56 (3/4), 207–218. doi:10.1016/0009-2541(86)90004-5
- Nadoll, P., Angerer, T., and Mauk, J. L. (2014). The Chemistry of Hydrothermal Magnetite: A Review. *Ore Geology. Rev.* 61, 1–32. doi:10.1016/j.oregeorev.2013.12.013
- Nadoll, P., Mauk, J. L., and Hayes, T. S. (2012). Geochemistry of Magnetite from Hydrothermal Ore Deposits and Host Rocks of the Mesoproterozoic Belt Supergroup, United States. *Econ. Geology*. 107, 1275–1292. doi:10.2113/econgeo.107.6.1275

- Othman, B. D., White, W. M., and Patchett, J. (1989). The Geochemistry of Marine Sediment, Island Arc Magma Genesis and Crust-Mantle Recycling. *Earth Planet. Sci. Lett.* 94, 1–24. doi:10.1016/0012-821x(89)90079-4
- Pearce, J., and Gale, G. (1977). Identification of Ore-Deposition Environment from Trace-Element Geochemistry of Associated Igneous Host Rocks. *Geol. Soc. Lond. Spec. Publications* 7 (1), 14–24. doi:10.1144/gsl.sp.1977.007.01.03
- Sengör, A. M. C., Natalin, B. A., and Burtman, V. S. (1993). Evolution of the Altaid Tectonic Collage and Paleozoic Crustal Growth in Eurasia. *Nature* 364, 299–307.
- Shang, H. J., Li, Q., Yu, X. B., and Li, Y. (2017). Analysis of Magnetite Composition and Geological Characteristics of Qiaoxiahala and Laoshankou Fe-Cu-Au Deposits in the Northern Junggar, Xinjiang. *Xinjiang Geology*. 35 (1), 43–49.
- Sun, S. S., and McDonough, W. F. (1989). “Chemical and Isotopic Systematics of Oceanic Basalts: Implications for Mantle Composition and Processes,”. *Magmaism in Oceanic Basins*. Editors A. D. Saunders and M. J. Norry (London: Spec. Publ. Geol. Soc. Lond.), 42, 313–345. doi:10.1144/gsl.sp.1989.042.01.19
- Wang, J. B., and Xu, X. (2006). Post-collisional Tectonic Evolution and Metallogenesis in Northern Xinjiang, China. *Acta geologica sinica* 80 (1), 23–31.
- Wang, Y. W., Wang, J. B., Long, L. L., Ding, R. F., Shi, Y., and Zhao, L. T. (2015). The Early Carboniferous Gold-Copper-Molybdenum Mineralization Events in the Northern Margin of Junggar Basin Xinjiang: Geochronological Evidence. *Acta Petrologica Sinica* 31 (5), 14481460
- Wei, X. F., Pan, D., Yuan, J., Liao, Z., Lu, X. Q., Shan, L. H., et al. (2019). Zircon U-Pb Age of Biotite Granite and 39Ar/40Ar Age of Sericite from Aketasi Gold Deposit in Xinjiang, and Their Geological Significance. *Mineral. Deposits* 38 (2), 251–260. doi:10.16111/j.0258-7106.2019.02.002
- Wilkinson, J. (2013). Triggers for the Formation of Porphyry Ore Deposits in Magmatic arcs. *Nat. Geosci.* 6 (11), 917–925. doi:10.1038/ngeo1940
- Windley, B. F., Alexiev, D., Xiao, W., Kroner, A., and Badarch, G. (2007). Tectonic Models for Accretion of the Central Asian Orogenic Belt. *J. Geol. Soc. Lond.* 164, 31–47. doi:10.1144/0016-76492006-022
- Wood, D. A. (1979). A Variably Veined Suboceanic Upper Mantle: Genetic Significance for Mid-ocean Ridge Basalts from Geochemical Evidence. *Geology* 7 (10), 499–503. doi:10.1130/0091-7613(1979)7<499:avsum>2.0.co;2
- Woodhead, J. D., Eggins, S. M., and Gamble, J. (1993). High Field Strength and Transition Element Systematics in Island Arc and Back Arc Basin Basalts: Evidence for Multi-phase Melt Extraction and a Depleted Mantle Wedge. *Earth Planet. Sci. Lett.* 114, 4 91–50. doi:10.1016/0012-821x(93)90078-n
- Xiao, W. J., and Santosh, M. (2014). The Western Central Asian Orogenic Belt: A Window to Accretionary Orogenesis and Continental Growth. *Gondwana Res.* 25 (4), 1429–1444. doi:10.1016/j.gr.2014.01.008
- Xu, G. F., and Shao, L. J. (1979). The Typomorphic Characteristics of Magnetite and its Practical Significance. *Geology. exploration* 3, 30–37.
- Yang, F. Q., Chai, F. M., Zhang, Z. X., Geng, X. X., and Li, Q. (2014). Zircon U-Pb Geochronology, Geochemistry, and Sr-Nd-Hf Isotopes of Granitoids in the Yulekenhalasu Copper Ore District, Northern Junggar, China: Petrogenesis and Tectonic Implications. *Lithos* 190–191, 85–103. doi:10.1016/j.lithos.2013.12.003
- Yang, F. Q., Mao, J. W., Bierlein, F. P., Pirajno, F., Zhao, C. S., Ye, H. S., et al. (2009). A Review of the Geological Characteristics and Geodynamic Mechanisms of Late Paleozoic Epithermal Gold Deposits in North Xinjiang, China. *Ore Geology. Rev.* 35, 217–234. doi:10.1016/j.oregeorev.2008.09.003
- Yang, F. Q., Mao, J. W., Pirajno, F., Yan, S. H., Liu, G. R., Zhou, G., et al. (2012). A Review of the Geological Characteristics and Geodynamic Setting of Late Paleozoic Porphyry Copper Deposits in the Junggar Region, Xinjiang Uygur Autonomous Region, Northwest China. *J. Asian Earth Sci.* 49, 80–98. doi:10.1016/j.jseae.2011.11.024
- Yang, F. Q., Yan, S. H., Liu, G. R., Zhou, G., Zhang, Z. X., Liu, F., et al. (2010). Geological Characteristics and Metallogenesis of Porphyry Copper Deposits in Junggar, Xinjiang. *Mineral. Deposits* 29 (6), 956–971. doi:10.16111/j.0258-7106.2010.06.012
- Ying, L. J. (2007). *Geology, Geochemistry and Discussion on the Origin of the Qiaoxiahala Fe-Cu-Au Deposit in Xinjiang*. [Beijing]: Chinese Academy of Geological Sciences [dissertation/master's Thesis].
- You, J., Hong, T., Wu, C., Ding, R. F., and Xu, X. W. (2016). Characteristics of Magmatic Activity in the Xilekuduk Mo-Cu Ore District, Fuyun County, Xinjiang, and its Constrains on Regional Tectonic Evolution in Late-Post Collisional Stages. 32(5), 1262–1282.
- Yuan, H. L., Wu, F. Y., Gao, S., Liu, X. M., Xu, P., and Sun, D. Y. (2003). Precise Determinations of U-Pb Age and Rare Earth Element Concentrations of Zircons from Cenozoic Intrusions in Northern China by Laser Ablation ICP-MS. *Chin. Sci. Bull.* 48 (22), 4211–4241.
- Zhang, H. X., Niu, H. C., and Sato, H. (2005). Late Paleozoic Adakites and Nb-Enriched Basalts from Northern Xinjiang, NW China: Evidence for the Southward Subduction of the Pale-Asian Oceanic Plate. *The Isl. Arc* 14 (1), 55–68. doi:10.1111/j.1440-1738.2004.00457.x
- Zhang, H. X., Niu, H. C., Shi, X. M., Ma, L., and Yu, X. Y. (2008). Late Paleozoic Tectonic Evolution and Polymetallic Ore-Forming Processes in Southern Altay and Northern Junggar. *Mineral. Deposits* 27 (5), 596–600.
- Zhang, Z. C., Yan, S. H., Chen, B. L., Zhou, G., He, Y. K., Chai, F. M., et al. (2006). SHRIMP Zircon U-Pb Dating for Subducting-Related Granitic Rocks in the Northern Part of East Junggar, Xinjiang. *Chin. Sci. Bull.* 51 (13), 1565–1574. doi:10.1007/s11434-008-0952-7
- Zhou, G., Zhang, Z. C., Yang, W. P., Gu, G. Z., Zhang, X. L., Luo, S. B., et al. (2005). Metabasic Rock on the South Side of Mayin'ebao Fault in the South Margin of Altay Mountains, Xin Jiang, and its Geological Implications. *Earth Science-Journal China Univ. Geosciences* 30 (6), 738–747.

Conflict of Interest: XW was employed by the Zhongse Zijin geological exploration (Beijing) Co., Ltd., ZL was employed by the Sinotech Minerals Exploration Co., Ltd., and QM was employed by the Beijing Institute of mineral geology Co., Ltd.

The remaining authors declare that the research was conducted in the absence of any commercial or financial relationships that could be construed as a potential conflict of interest.

Copyright © 2021 Wei, Wei, Liao, Wang, Li, Mao and Li. This is an open-access article distributed under the terms of the Creative Commons Attribution License (CC BY). The use, distribution or reproduction in other forums is permitted, provided the original author(s) and the copyright owner(s) are credited and that the original publication in this journal is cited, in accordance with accepted academic practice. No use, distribution or reproduction is permitted which does not comply with these terms.



Zircon Genesis and Geochronology for the Zhangbaoshan Super-Large Rubidium Deposit in the Eastern Tianshan, NW China: Implication to Magmatic-Hydrothermal Evolution and Mineralization Processes

Jun Zhi¹, Ruxiong Lei^{2*}, Boyang Chen¹, M. N. Muhtar¹, Zhijie Feng¹, Kai Zhang², Yuanfeng Cai¹ and Changzhi Wu^{2,3}

¹State Key Laboratory for Mineral Deposits Research, School of Earth Sciences and Engineering, Nanjing University, Nanjing, China, ²School of Earth Science and Resources, Chang'an University, Xi'an, China, ³Xinjiang Research Centre for Mineral Resources, Chinese Academy of Sciences, Urumqi, China

OPEN ACCESS

Edited by:

Massimo Chiaradia,
Université de Genève, Switzerland

Reviewed by:

Nuo Li,
Leibniz Universität Hannover,
Germany
Mohsen Rezaei,
Shahid Chamran University of
Ahvaz, Iran

*Correspondence:

Ruxiong Lei
ruxionglei@chd.edu.cn

Specialty section:

This article was submitted to
Economic Geology,
a section of the journal
Frontiers in Earth Science

Received: 19 March 2021

Accepted: 31 May 2021

Published: 15 June 2021

Citation:

Zhi J, Lei R, Chen B, Muhtar MN, Feng Z, Zhang K, Cai Y and Wu C (2021) Zircon Genesis and Geochronology for the Zhangbaoshan Super-Large Rubidium Deposit in the Eastern Tianshan, NW China: Implication to Magmatic-Hydrothermal Evolution and Mineralization Processes. *Front. Earth Sci.* 9:682720. doi: 10.3389/feart.2021.682720

The Zhangbaoshan (ZBS) super-large Rubidium deposit, located in the Eastern Tianshan, is a typical granite-type Rb deposit. The ZBS deposit is mainly hosted in the highly evolved Baishitouquan (BST) pluton enriched in F and Rb, which exhibits five lithological zones from the bottom to the top: leucogranite (zone-a), amazonite-bearing granite (zone-b), amazonite granite (zone-c), topaz-bearing amazonite granite (zone-d) and topaz albite granite (zone-e), as well as minor small lodes of amazonite pegmatite. Two types of zircon were identified from the BST pluton. Type-I zircons mainly occur in the zone-a, are characterized by obvious oscillatory zoning, high Zr contents (47.4–67.3 wt% ZrO₂) and Zr/Hf ratios (21.72–58.23), low trace element concentrations, and heavy rare earth elements (HREE)-enriched patterns with prominent positive Ce anomalies (Ce/Ce* = 1.21–385) and strong negative Eu anomalies (Eu/Eu* = 0.008–0.551), indicative of early magmatic zircon. Type-II zircons mainly occur in the upper zones (zone-c to zone-e), exhibit porous and dark Cathodoluminescence images, inhomogeneous internal structure, plenty of mineral inclusions, low Zr (38.7–51.0 wt% ZrO₂) and Zr/Hf ratios (3.35–11.00), high Hf (34,094–85,754 ppm), Th (718–4,980 ppm), U (3,540–32,901 ppm), Ta (86.7–398 ppm), Y (1,630–28,890 ppm) and rare earth elements (REEs) (3,910–30,165 ppm), as well as slightly HREE-enriched patterns and significant M-type tetrad patterns with t₃ values (quantification factor of tetrad effect) of 1.51–1.69. It is suggested that the type-II zircons are crystallized from a deuteric F-rich fluid coexisted with the highly evolved residual magma during the transition from the magmatic to the F-rich hydrothermal stage of the BST pluton. The F-rich fluid exsolution during the magmatic-hydrothermal transition is one of the most important factors controlling the modification of highly evolved granite and related Rb enrichment and mineralization. The type-I zircon samples from zone-a yield concordant ages of 250 ± 2.5 Ma and 250.5 ± 1.7 Ma, respectively, indicating that the BST pluton was emplaced

in the Early Triassic. The type-II zircons from zone-c to zone-e yield lower intercept U–Pb ages between 238 and 257 Ma, which may represent the age of F-rich fluid–melt interaction during the transition from the magmatic to the hydrothermal stage. The mineralization of the ZBS super-large Rb deposit should have occurred shortly after emplacement of the BST pluton in the Early Triassic. Combined with available data, it is suggested that the Triassic is an important period for granitic magmatism and rare metal metallogeny in the Eastern Tianshan.

Keywords: rubidium deposit, f-rich highly evolved granite, hydrothermal zircon, zircon alteration, Eastern tianshan

INTRODUCTION

As a common accessory mineral in a variety of rocks, zircon has long been recognized as an excellent geochronometer due to its high U, Th and low common Pb contents, and high closure temperature for the U–Th–Pb system (Geisler et al., 2007; Harley et al., 2007). Zircon can also incorporate considerable amounts of temperature- or process-sensitive trace elements, including Hf, Y, Ti and REEs during crystallization, which make it a useful tool to fingerprint the mineral–melt–fluid processes during crust formation and evolution, hydrothermal alteration and mineralization (Belousova et al., 2006; Geisler et al., 2007; Hanchar and Van Westrenen, 2007; Harley et al., 2007).

Zircon is ubiquitous in granitoids and has generally been considered as magmatic in origin (e.g., Hoskin, 2005; Jiang et al., 2020). However, zircons of both magmatic and hydrothermal origin commonly occur in highly evolved granite and pegmatite (e.g., Yang et al., 2014; Li H. et al., 2018; Li X.-C. et al., 2018; Huang et al., 2020). In addition, recent studies have suggested that zircons are susceptible to hydrothermal alterations (Erdmann et al. 2013; Yang et al., 2014; Li and Zhou, 2015; Takehara et al., 2018; Liu et al., 2019), and the crystal structure, chemical composition and isotopic system of zircons could be disturbed during hydrothermal alteration processes, including recrystallization, dissolution–reprecipitation and metamictization (Geisler et al., 2007; Kusiak et al., 2009). Zircon has been proved to be modified by F-rich fluids (Veksler et al., 2005; Han et al., 2019), and Zr and trace elements (e.g., REEs, Ta, Ti, Hf, Th, and U) within zircon have been suggested to be mobile in alkali- and F-rich highly evolved magmatic systems (Veksler et al., 2005; Ayers et al., 2012). Therefore, zircons in F-rich highly evolved magmatic systems are generally complex, and caution should be taken to interpret their elemental and isotopic data.

The Zhangbaoshan (ZBS) super-large rubidium deposit is a typical granite-type Rb deposit, which is mainly hosted in the highly evolved Baishitouquan (BST) pluton and partly in the other pluton around the BST in the Eastern Tianshan, Northwest China (GPGSI, 2015). The BST pluton is characterized by high SiO₂, Na₂O, K₂O, Li, Rb, Cs and F, low Ti, Fe, Ca, and Mg contents, is weakly peraluminous (A/NKC = 1.00–1.11), and has low K/Rb, Al/Ga, Y/Ho, Zr/Hf and Nb/Ta ratios (Gu et al., 2003). It can be divided into five lithological zones based on the mineral compositions, which are considered to be formed by successive fractionation crystallization and F-rich fluid–melt interaction

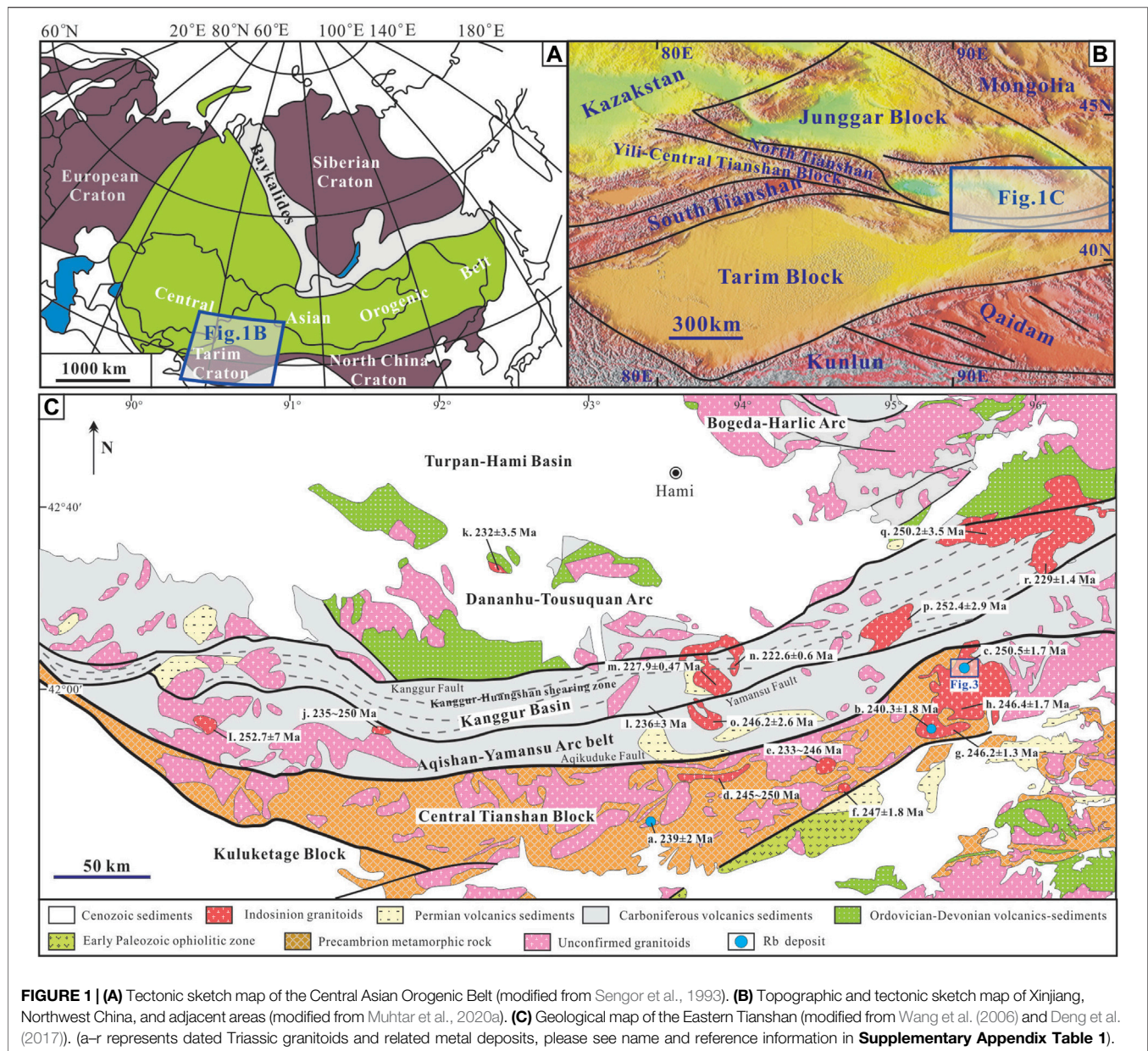
(Gu et al., 2011). Previous studies have mainly focused on the petrology and geochemical feature of the BST pluton (Gu et al., 2003; Gu et al., 2011; Wu et al., 2011), however, little attention has been paid to the associated Rb enrichment and mineralization mechanism. Although it is generally suggested that Rb mineralization is related to highly evolved granitic systems, our current understanding of the geological processes governing Rb mineralization is still limited and controversial (Han et al., 2021). Furthermore, the emplacement age of the BST pluton and the timing of the Rb mineralization are still unclear (Gu et al., 1994; Liu et al., 2008), which has hindered a better understanding of the formation of the granite and the Rb mineralization mechanism.

In this paper, we present new results of detailed petrographic characteristics, chemical composition and LA-ICP-MS U–Pb ages of zircons from each lithological zone of the BST pluton. Using these data, we identify two types of zircons and constrain their origin, which is crucial for correctly determine the age of granite emplacement and Rb mineralization. We also discuss the implications of our results for illustrating the magmatic and hydrothermal evolution process of the BST pluton and Rb deposit, which may provide new insights for the formation of Rb and F-rich highly evolved granites.

GEOLOGICAL BACKGROUND

The Central Asian Orogenic Belt (CAOB) is the world's largest Phanerozoic accretive orogenic belt, surrounded by the Siberian, European, Tarim and North China cratons (**Figure 1A**; Xiao et al., 2004; Jahn, 2004; Windley et al., 2007; Wang et al., 2014; Xiao et al., 2015; Li et al., 2017; Deng et al., 2017). The Eastern Tianshan is considered as the southernmost segment of the CAOB, located at the junction of the Junggar Block and Turfan–Hami Block (**Figure 1B**). From north to south, the Eastern Tianshan is composed of the Bogda–Harlik Arc, the Jueluotag Arc belt, and the Central Tianshan Block, respectively (**Figure 1C**; Coleman, 1989; Sengor et al., 1993; Xiao et al., 2004; Shu et al., 2011; Zhang et al., 2016).

The Bogda–Harlik Arc is mainly composed of Ordovician–Carboniferous volcanic rocks, granites and mafic–ultramafic complexes (Gu et al., 2001). The Jueluotag Arc belt can be subdivided into three subunits from north to south, which are the Dananhu–Tousuquan Arc, the Kanggur Basin, and the Aqishan–Yamansu Arc, respectively (**Figure 1C**).



The Dananhu–Tousuquan Arc, north of the Kanggur Fault, mainly consists of Ordovician–Carboniferous volcanic and pyroclastic rocks and accretionary complexes (Xiao et al., 2004; Wang Y. et al., 2018; Muhtar et al., 2020b). The Kanggur Basin, located between the Kanggur Fault and Yamansu Fault, is mainly composed of Carboniferous volcanic–sedimentary rocks, with intense ductile shearing and a large right–lateral slip throughout the basin (Xu et al., 2003; Wu et al., 2018). The Aqishan–Yamansu Arc, south of the Yamansu Fault, mainly consists of Carboniferous volcanic, volcani-clastic, terrigenous clastic sedimentary rocks and limestones (Hou et al., 2014; Wang Y. et al., 2018). The Central Tianshan Block is mainly composed of Precambrian volcano–sedimentary rocks (Chen, 1999; Shu et al., 2004; Xiao

et al., 2004; Lei et al., 2011). Most of these rocks have been metamorphosed to migmatized schists, gneisses, marbles and amphibolites (Hu et al., 1997).

The Eastern Tianshan has a wide distribution of magmatic rocks, which are mainly emplaced during the Paleozoic (e.g., Gu et al., 2006; Zhou et al., 2010; Chen et al., 2011; Zhang et al., 2014; Chen et al., 2019). Triassic granitoids have been identified in the Eastern Tianshan during the past decade and various Triassic granite–related W, Mo and Rb deposits have also been discovered in the Eastern Tianshan (shown in **Supplementary Appendix Table 1**). The mineralizing characteristics and zircon U–Pb ages of Rb-bearing granites in the Eastern Tianshan are listed in **Supplementary Appendix Table 2**. This suggests that the Triassic was an important magmatic and metallogenic period

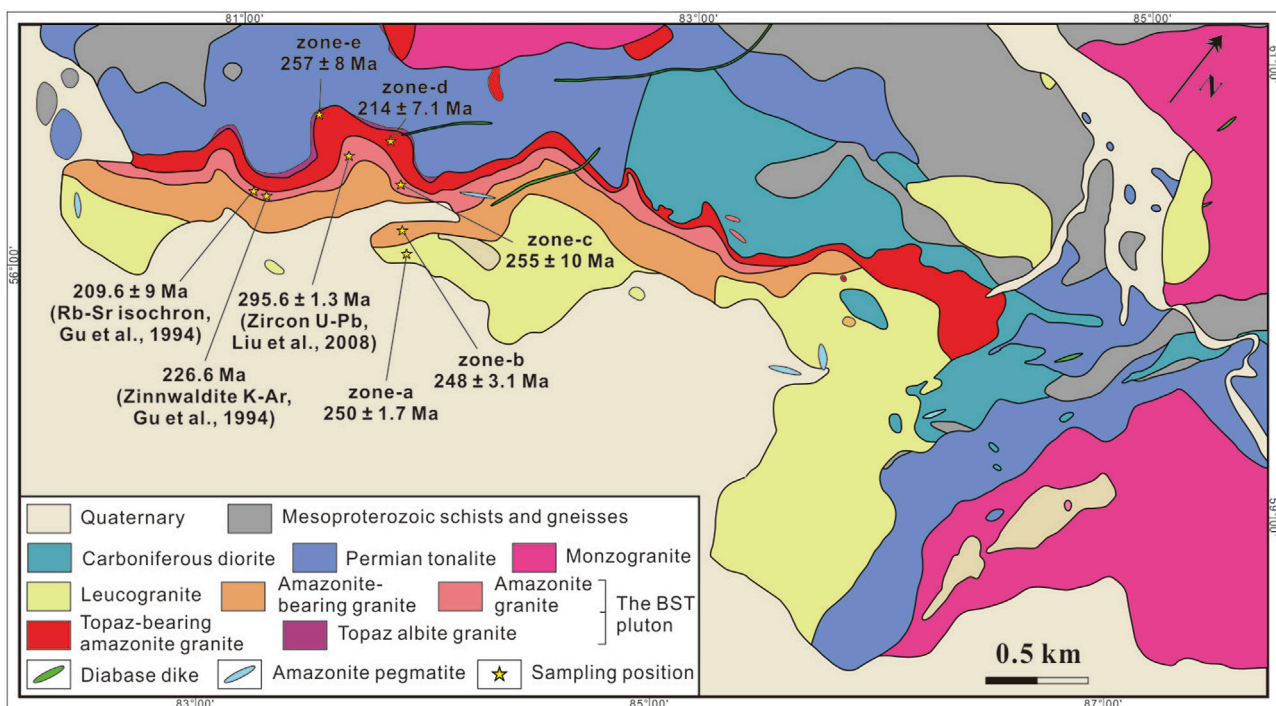


FIGURE 2 | Simplified geological map of the Baishitouquan (BST) in the Central Tianshan Block.

in the Eastern Tianshan (Wu et al., 2010; Deng et al., 2017; Zhang et al., 2017; Lei et al., 2020).

GEOLOGY OF THE ZHANGBAOSHAN RB DEPOSIT

The ZBS Rb deposit, located in the eastern section of the Central Tianshan Block, Eastern Tianshan, (**Figure 1C**), is a typical granite-type Rb deposit (GPGSI, 2015). Recent exploration identified that it is a super large Rb deposit, with ore reserves (Rb_2O) of about 67,080 tons (GPGSI, 2015). The main Rb-bearing minerals in the deposit are microcline (0.36–0.41 wt% Rb_2O) and zinnwaldite (0.35–0.67 wt% Rb_2O). The Rb deposit is mainly hosted by the BST pluton, which intruded into the Mesoproterozoic schists and gneisses and the Carboniferous diorite. The BST pluton exhibits intrusive contacts with the overlying Permian tonalite and monzogranite (**Figure 2**). Based on detailed petrological and mineralogical studies, the BST pluton can be divided into five progressive lithological zones from the bottom to the top, namely leucogranite (zone-a), amazonite-bearing granite (zone-b), amazonite granite (zone-c), topaz-bearing amazonite granite (zone-d) and topaz albite granite (zone-e) (Gu et al., 2003; Gu et al., 2011).

Leucogranite (zone-a) is weakly altered and ash gray in color, which is the main part of this pluton. This zone is mainly composed of plagioclase (22–36%), K-feldspar (25–35%), quartz (28–35%) and zinnwaldite (3–5%), exhibiting medium-to fine-grained texture and massive structure. The

main difference between zone-b and zone-a is the occurrence of amazonite (2–5%), as well as microcline (2–5%). As the content of amazonite generally increases upwards from the zone-b to zone-c (mainly 5–15%, and up to 20%), the lithology gradually evolved from amazonite-bearing granite to amazonite granite (**Figure 3A**). Correspondingly, the content of microcline increases to 5–15% in zone-c, which is generally characterized by cross-hatched twinning (**Figure 3B**). The zone-d is characterized by the appearance of topaz (1–5%) in the form of phenocrysts, and the main composition of this zone is essentially similar to the amazonite granite (**Figure 3C**). The zone-e exhibits an abrupt transition with zone-d below: this zone mainly contains phenocrysts of topaz (10–20%) and quartz (15–30%), and matrix of albite (45–60%), K-feldspar (10–15%) and zinnwaldite (5–10%). Accessory minerals of the BST pluton mainly consists of zircon, fluorite, garnet, cassiterite, magnetite, apatite, monazite and columbite-group minerals.

Veins of the topaz albite granite (zone-e) cut and replace the overlying tonalite locally (**Figure 3D**). There are several amazonite pegmatite veins cutting through both the pluton and overlying tonalite (**Figure 3E**). These amazonite pegmatite veins show compositional zoning from a marginal fine-grained muscovite-feldspar zone to a central pegmatitic muscovite-quartz-microcline zone, with a thickness of 0.3–1 m and length of 2–10 m. The high concentration of volatiles (F and H_2O) in zone-e and the appearance of amazonite pegmatite veins indicate that the magmatic-hydrothermal transition stage has played an important role in the formation of the pluton (Gu et al., 2011).

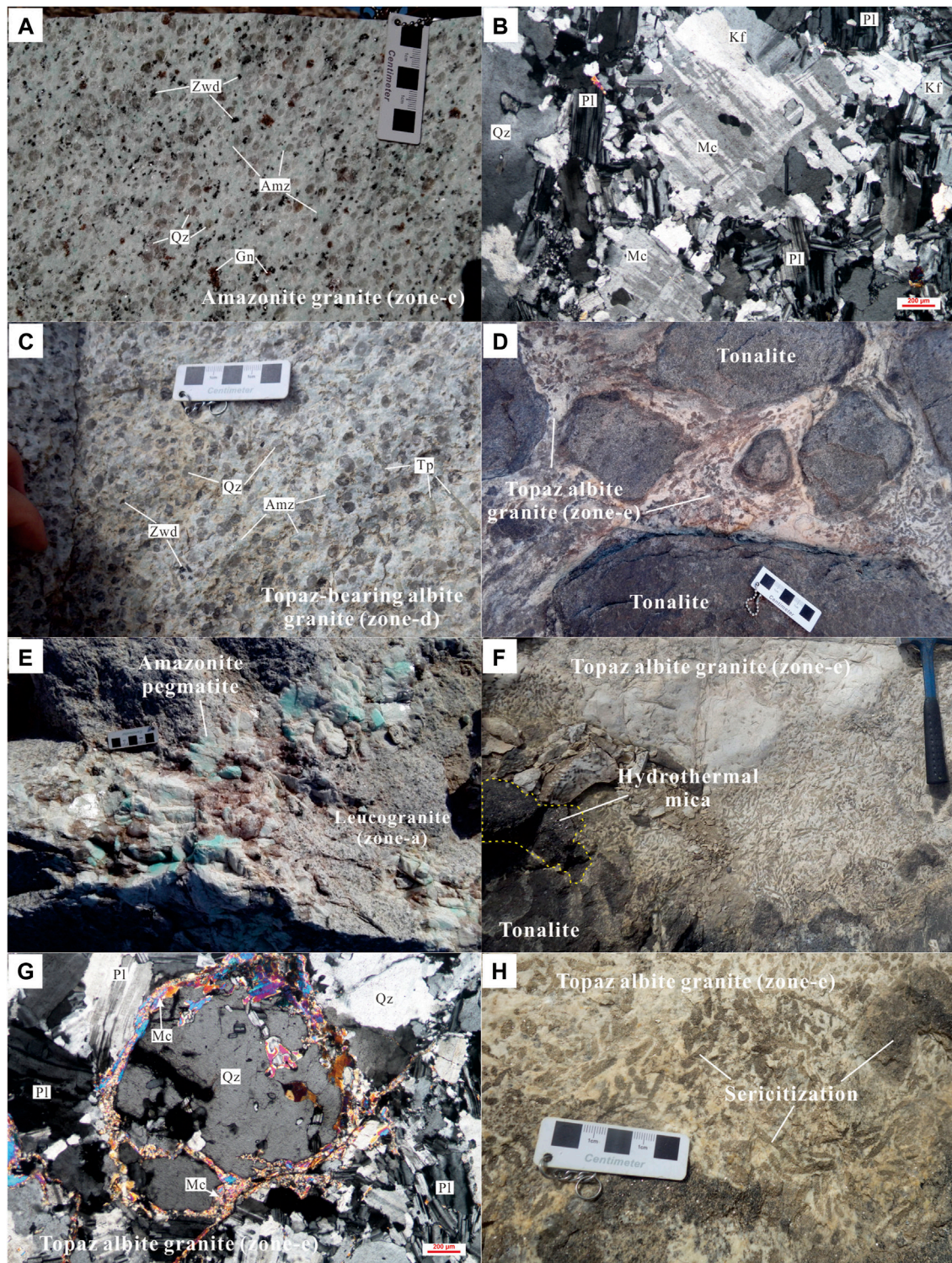


FIGURE 3 | Field photographs and microphotographs showing lithological characteristics of the BST pluton. Mineral symbols: Qz—quartz, Pl—albite, Kf—K-feldspar, Amz—amazonite, Zwd—zinnwaldite, Mc—microcline, Tp—topaz, Gn—garnets. **(A)** Porphyritic texture of amazonite granite from zone-c. Hand specimen. **(B)** Microphotograph showing the texture of amazonite granite. Microcline with cross-hatched twins has corroded K-feldspar and albite grains into optically continuous relict. Crossed polarizers. **(C)** Prismatic topaz crystals occur as a phenocrysts in zone-d. Hand specimen. **(D)** The zone-e has penetrated and replaced the overlying tonalite (country rock). **(E)** Amazonite pegmatite vein in zone-a. **(F)** Clustered crystals of hydrothermal mica occurring in the contact between the zone-e and tonalite. **(G)** White mica and twin-free albite occurring as vein along mineral grains and fractures in zone-e. **(H)** Prismatic topaz crystals were replaced by hydrothermal mica.

Hydrothermal alteration in the ZBS Rb deposit occurs mainly in zone-e, including muscovitization, sericitization, albitization, and fluoritization, which is principally represented by secondary fluorite, white mica and albite. White mica and twin-free albite replacing topaz and K-feldspar (**Figure 3F**) or occurring as veins along mineral grain and fractures in zone-e (**Figure 3G**) can be observed, indicating that they are produced by subsolidus metasomatism. Moreover, clustered crystals of hydrothermal mica with low Rb, Cs, Fe, Mn, Al and high Si, Ti, Mg contents (unpublished data) can be observed at the contact of zone-e and tonalite (**Figure 3H**), indicative of a hydrothermal origin.

SAMPLING AND ANALYTICAL METHODS

Zircons from seven samples from zone-a (BST-27, 19KH-231), zone-b (19KH-235), zone-c (19KH-238), zone-d (19KH-253), and zone-e (19KH-250, xxx-22), with sampling depth of 1,490 m, 1,498 m, 1,509 m, 1,540 m, 1,558 m, 1,521 m, 1,573 m, respectively, were extracted for zircon petrography observation, U–Pb dating, and trace element analyses.

The distribution and paragenesis of the zircons in the granite were examined in transmitted light using an optical microscope. Zircon grains from each sample were separated by gravity and magnetic methods, and mounted in one-inch epoxy resin disk. The internal structure of single zircon crystals was studied by Cathodoluminescence (CL) and Backscattered electron (BSE) imaging. The CL and BSE images were collected by using a JEOL JXA-8100 electron microprobe at the State Key Laboratory for Mineral Deposits Research (SKLMDR), Nanjing University (China), with operating conditions of 15 kV accelerating voltage and 20 nA beam current. The U–Pb isotopes (^{206}Pb , ^{207}Pb , ^{208}Pb , ^{232}Th and ^{238}U) and trace elements (^{49}Ti , ^{91}Zr , ^{93}Nb , ^{181}Ta and rare earth elements (REEs) analyses were conducted by a laser ablation–inductively coupled plasma–mass spectrometer (LA–ICP–MS) in the SKLMDR. Coherent Geolas Pro 193 nm laser ablation system and Thermal iCAP RQ inductively coupled plasma mass spectrometry (ICP–MS) were connected for the in situ dating, with a laser beam diameter of 32 μm . The zircon STDGJ (600 Ma, Jackson et al., 2004) was used as an external standard to correct mass bias of the ICP–MS and residual elemental fractionation. Mud Tank zircon (735 Ma) was analyzed to observe the stability and reproducibility of the instrument. NIST 610 and ^{91}Zr were used as external and internal standards for quantitative calculation of trace elements in all zircons. The experimental data were processed by GLITTER (Van Achterbergh et al., 2001). The concordia diagrams and weighted mean calculations were obtained using Isoplot (ver 3.70) (Ludwig, 2008).

ZIRCON PETROGRAPHY

Two types of zircon can be identified in the BST pluton. Type-I zircons are mainly distributed in the lower zone (zone-a) of the pluton embedded in K-feldspar and the amount of type-I zircons

gradually decreases upwards (**Figure 4A**). They are transparent, colorless, prismatic and euhedral under the optical microscope (**Figure 4D**), exhibiting clear oscillatory zoning in CL images (**Figure 5A**). These zircon grains are generally 100–200 μm in size, with length–width ratios of 3:1–6:1. BSE images show that type-I zircons are dark in color and show growth zoning (**Figure 6A**). The observation of distinctive alteration textures with pores and microcracks, as well as the occurrence of fluorite inclusions, show that deuteric hydrothermal overprinting (H.O. for short) occurs along the boundary of type-I zircon grains (**Figure 6A**) or restrictedly replace the growth zoning and core (**Figures 5B, 6B**).

Type-II zircons are found in the samples from upper zones (zone-c to zone-e) of the BST pluton, and are mainly in contact with or interstitial to late magmatic K-feldspar, albite and zinnwaldite grains (**Figures 4B,C**), and the content of the type-II zircons increases gradually from zone-c (10–20%) to zone-e (70–80%). They are dark brown, translucent, dirty and subhedral to anhedral under the optical microscope (**Figure 4D**). Type-II zircon grains are generally 150–300 μm in length, with length–width ratios of 2:1–3:1. They are generally characterized by extremely dark, porous, microcracks-rich and inhomogeneous structures in CL images (**Figure 5C**). Numerous mineral inclusions, including fluorite (Fl) and columbite-group minerals (CGM), in voids and microcracks were observed in these zircons (**Figure 6C**). Type-II zircons with an inhomogeneous internal structure, can be subdivided into two domains in BSE images (**Figure 6D**). The light domains (LD) show a flat and smooth zircon surface. The dark domains (DD) show a rough surface and a veinlet-disseminated structure. It is noticed that some zircons show core–rim structure with the H.O. type-I zircon core and the overgrowth of type-II zircon (**Figures 4D, 5D**).

RESULTS

Zircon U–Pb Ages

Seven groups of zircon samples from five lithological zones of the BST pluton are used for U–Pb dating, and the results are presented in **Supplementary Appendix Table 3**.

Two zircon samples from zone-a (19KH-231 and BST-27) are type-I zircon. They have Th contents of 117–2020 ppm, with a mean of 787 ppm, and U contents of 239–2,202 ppm, with a mean of 928 ppm. The Th/U ratios vary from 0.33 to 1.37. Analyses of sample 19KH-231 give closely concordant ages and all the analyzed spots fall on the concordia, yielding a weighted mean age of 250 ± 2.5 Ma ($n = 9$, MSWD = 0.082, 1σ) (**Figure 7A**). Analyses of sample BST-27 are mostly concordant and fall on the concordia. Except for five discordant spots (No. BST-27-22 to -26), the remaining concordant analyses yield a weighted mean age of 250.5 ± 1.7 Ma ($n = 21$, MSWD = 0.35, 1σ) (**Figure 7B**).

Zircons from zone-b (19KH-235) mainly belong to type-I zircon. They have low Th (157–2,487 ppm) and U (297–2,812 ppm) contents, with Th/U ratios of 0.40–1.39. All of the analyses deviate from the concordia, and fifteen analyses

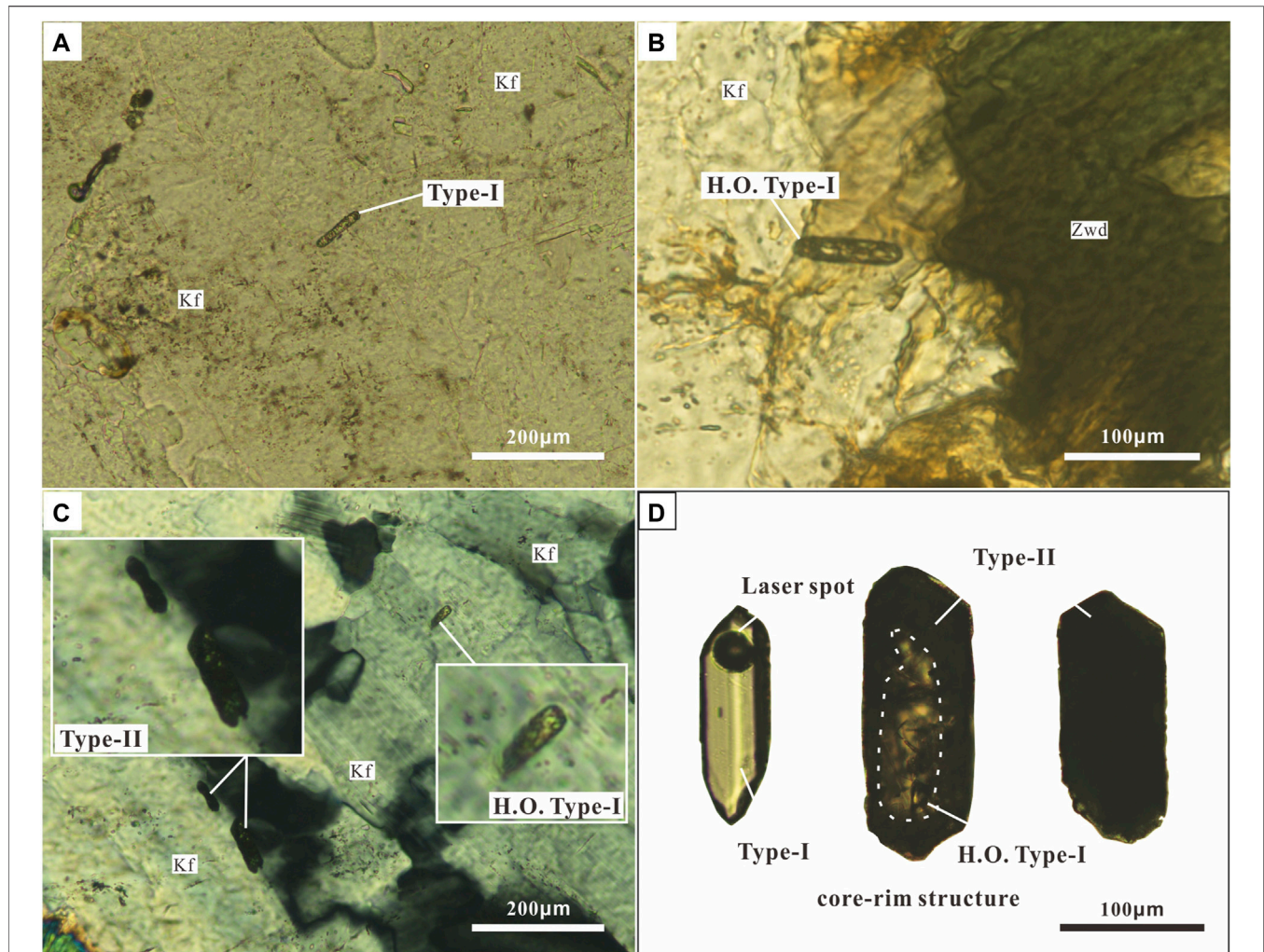


FIGURE 4 | Transmitted-light microscopic images of zircons from the BST pluton. H.O. type-I-hydrothermal overprinting type-I zircon. **(A)** Type-I zircon embedded in the K-feldspar crystal. Single polarizer. **(B)** H.O. type-I zircon contact with zinnwaldite. Single polarizer. **(C)** H.O. type-I zircon embedded in the K-feldspar and the type-II zircons contact with K-feldspar. Crossed polarizers. **(D)** Photomicrographs showing the feature of different types of zircons. The black circle in the type-I zircon is the laser spot. Single polarizer.

yield a lower intercept age of 248 ± 3.1 Ma ($n = 15$, MSWD = 0.18, 1σ) (**Figure 7C**). These results indicate that there was radiogenic Pb loss probably due to metamictization of these zircons (Nasdala et al., 1996).

Fourteen analyses were conducted on the zircons from zone-c (19KH-238), including twelve type-I zircons and two xenocrysts (according to the Miller et al., 2007). The type-I zircons show variable Th (78–4,857 ppm) and U (165–3,301 ppm) contents, with Th/U ratios of 0.29–1.48. The two xenocrysts have Th contents of 294–313 ppm, U contents of 375–698 ppm and Th/U ratios of 0.45–0.78. These xenocrysts show apparent $^{238}\text{U}/^{206}\text{Pb}$ ages of 297 Ma and 441 Ma, respectively. Notably, the apparent $^{238}\text{U}/^{206}\text{Pb}$ ages of 297 Ma is consistent with the previous zircon U–Pb age obtained from zone-c (Liu et al., 2008). All analyses of the type-I zircons deviate from concordia, yielding a well-defined lower intercept age of 255 ± 10 Ma ($n = 12$, MSWD = 3.4, 1σ) (**Figure 7D**).

Sixteen analyses were obtained from the zircons from zone-d (19KH-253), including eight type-I zircons, four type-II zircons, and four xenocrysts. The Th (260–1,237 ppm) and U (457–4,666 ppm) contents of type-I zircons are much lower than those of the type-II, which have Th and U contents of 1,138–4,976 ppm and 3,542–32,901 ppm, respectively. The xenocrysts have Th contents of 187–1,032 ppm, U contents of 254–1,247 ppm, and Th/U ratios of 0.61–0.83. Except for the xenocrysts and one analysis of type-II zircons, zircons from zone-d yield a lower intercept age of 238 ± 5.9 Ma ($n = 11$, MSWD = 0.36, 1σ). Two analyses of type-I zircons (No. 19KH-253-01 and -07) give concordant ages of 242 ± 4 Ma and 239 ± 7 Ma, respectively (**Figure 7E**). Remarkably, the xenocrysts from the zone-d show concordant apparent $^{238}\text{U}/^{206}\text{Pb}$ ages of 298–299 Ma (**Figure 7E**), which are also consistent with previous zircon U–Pb ages (Liu et al., 2008).

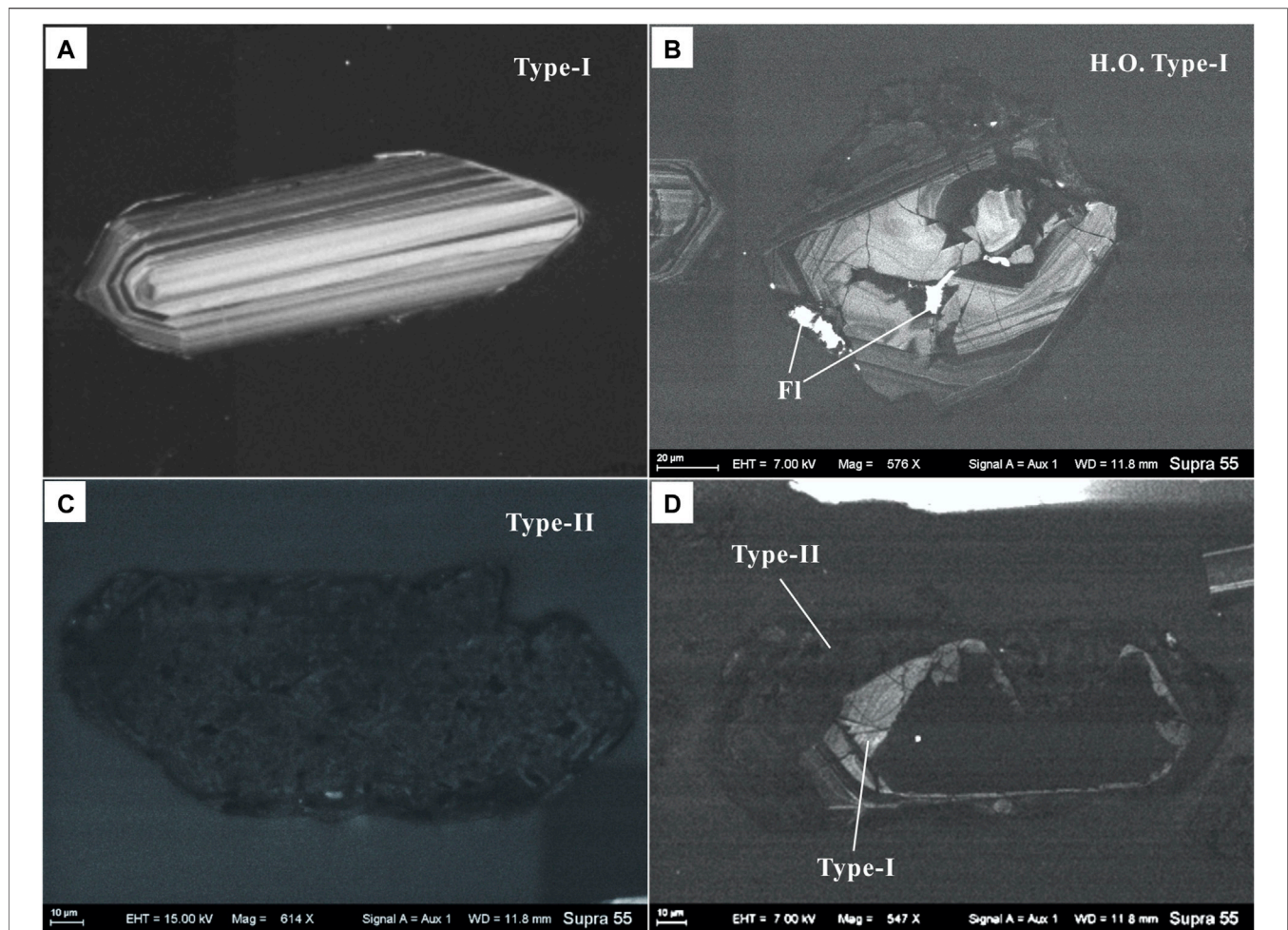


FIGURE 5 | Cathodoluminescence (CL) images of zircons from the BST pluton. **(A)** Type-I zircon with oscillatory zoning. **(B)** Type-I zircon with the hydrothermal overprinting. Fluorite inclusion occur in the microcracks of the H.O. type-I zircon. **(C)** Subhedral, dark and inhomogeneous type-II zircon grain. **(D)** Zircon grains with core-rim structure. H.O. type-I zircon in core and type-II zircon in edge.

Zircons were separated from two samples (19KH-250 and xxx-22) in zone-e. Eight analyses obtained from the 19KH-250 zircons are type-I zircon. The Th and U contents of these type-I zircons are range from 103 to 1,485 ppm and 145 to 2,182 ppm, respectively, with Th/U ratios of 0.54–1.82. They define a lower intercept age of 254 ± 13 Ma ($n = 8$, 1σ , MSWD = 0.026) with a collinear array (**Figure 7F**). Forty four analyses were conducted on the zircons of sample xxx-22 (**Figure 7G**), including thirteen type-I zircons, twenty four type-II zircons and six xenocrysts. The type-I zircon show variable Th (339–3,317 ppm) and U (516–3,688 ppm) contents, with Th/U ratios of 0.17–3.29. The type-II zircons show extremely inhomogeneous concentrations of Th (386–15,943 ppm) and U (1,485–12,380 ppm), with Th/U ratios of 0.13–5.68. The xenocrysts have Th, U contents and Th/U ratios of 112–1,385 ppm, 178–1,761 ppm and 0.16–0.79, respectively. Except for the xenocrysts, xxx-22 zircons yield a lower intercept age of 256.5 ± 8.0 Ma ($n = 38$, 1σ , MSWD = 4.5), with all the analyses deviating from the concordia (**Figure 7H**).

Type-I zircons from zone-a (19KH-231 and BST-27) in the BST pluton show weighted average ages of 250 ± 2.5 Ma and 250.5 ± 1.7 Ma, respectively, indicating that the BST pluton was intruded in the Early Triassic. The lower intercept ages of type-I zircons from 19KH-235 (zone-b), 19KH-238 (zone-c) and 19KH-250 (zone-e) are also ca. 250 Ma. Type-II zircons from 19KH-253 (zone-d) and xxx-22 (zone-e) together with coexisting type-I zircons define the lower intercept ages (238–257 Ma), which may represent an approximate crystallization age of the type-II zircons.

Chemical Composition of the Zircons

In situ LA-ICP-MS data for trace elements in zircons are listed in **Supplementary Appendix Table 4**. Type-I zircons from the BST pluton generally have high Zr contents between 350,744 and 498,235 ppm (≈ 47.4 –67.3 wt% ZrO_2 , with a mean of 61.12 wt% ZrO_2), and low Ti (1.72–69 ppm with a mean of 9.42 ppm), Y (498–6,510 ppm with a mean of 2,184 ppm), Nb (1.19–1,470 ppm with a mean of 125 ppm), Ta (0.621–219 ppm with a mean of

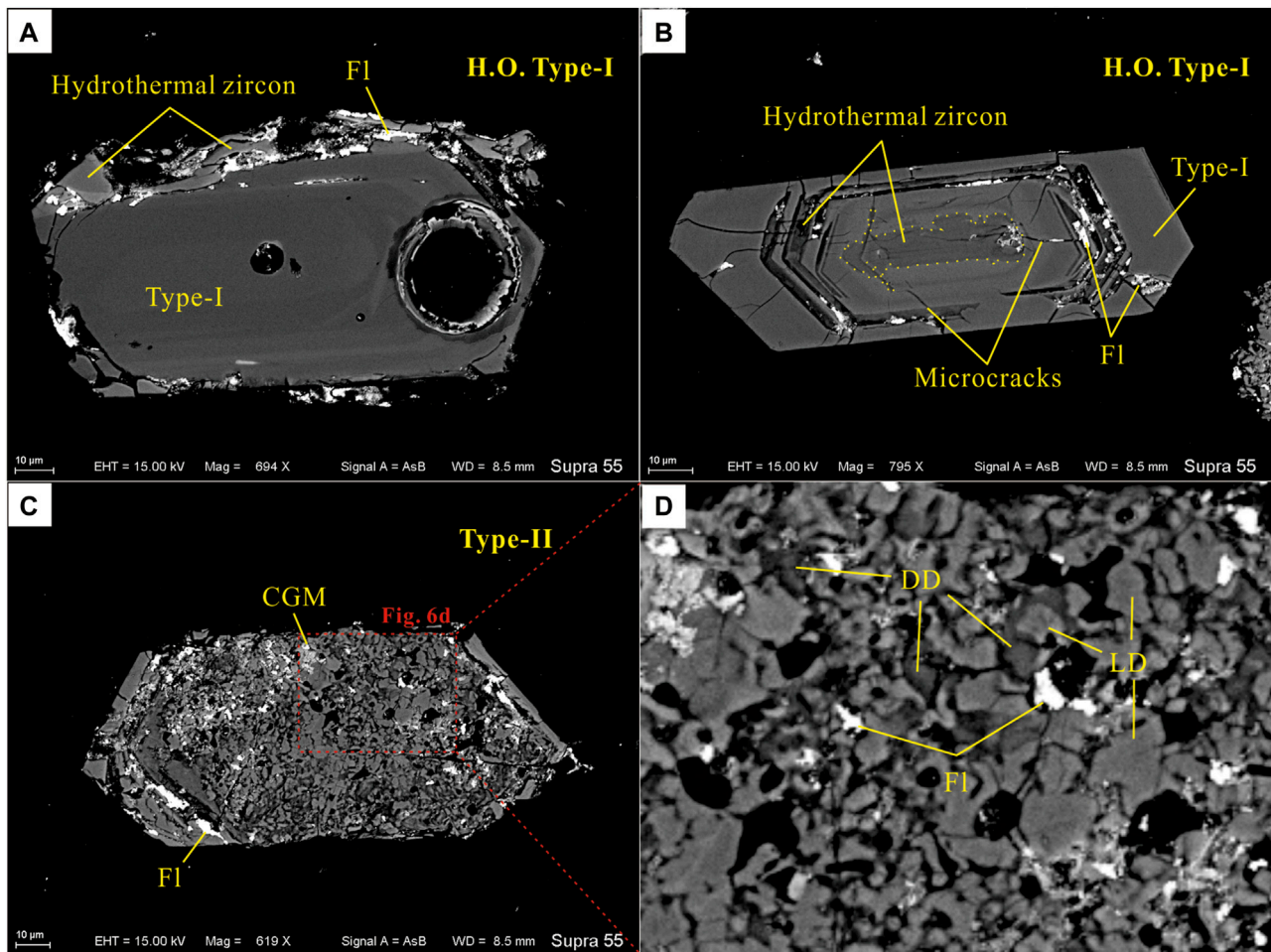


FIGURE 6 | Backscattered electron (BSE) images of zircons from the BST pluton. Fl—fluorite, CGM—columbite group minerals. **(A)** Hydrothermal zircon and fluorite occur around the type-I zircon crystal. The circle is the laser spot. **(B)** F-rich hydrothermal alteration occurs along the growth zoning and fractures in inner zone of the type-I zircon. Microcracks in the H.O. type-I zircon are partially filled with fluorite. **(C)** Type-II zircons, with a complex internal structure, contain large amount of fluorite (Fl) and columbite group mineral (CGM) inclusions in their crystals. **(D)** Closeup of the type-II zircon with the light domains (LD) and dark domains (DD). The fluorite (Fl) inclusions are embedded in microcracks and voids in type-II zircon.

12.99), Hf (7,471–20,835 ppm with a mean of 11,269 ppm), Th (78.2–2,810 ppm with a mean of 770 ppm and a median of 442 ppm), and U (165–2,810 ppm with a mean of 897 ppm and a median of 630 ppm) concentrations, as well as minor amounts of the light REE (LREE) (27–604 ppm with a mean of 110 ppm), heavy REE (HREE) (388–4,029 ppm with a mean of 1,512 ppm) corresponding to total REE of 451–4,590 ppm with a mean of 1,679 ppm. They show HREE-enriched patterns with prominent positive Ce anomalies ($Ce/Ce^* = 1.21\text{--}385$), strong negative Eu anomalies ($Eu/Eu^* = 0.008\text{--}0.551$) and low LREE/HREE ratios (0.04–0.26 with a mean of 0.10) (**Figures 8A–E**). They have Zr/Hf ratios ranging from 21.72 to 58.23 with a mean of 41.48 (**Figure 8F**) and Th/U ratios from 0.29 to 2.08 with a mean of 0.84 (**Figure 9A**).

Type-II zircons vary greatly in chemical composition and are enriched in trace elements. They have low Zr contents of 286,445–377,627 ppm ($\approx 38.7\text{--}51.0$ wt% ZrO_2 with a mean of

47.45 wt% ZrO_2), and unusually high contents of Hf (34,094–85,754 ppm with a mean of 67,983 ppm), Y (1,630–28,890 ppm with a mean of 8,434 ppm), Nb (171–2,520 ppm with a mean of 1,216 ppm), Ta (86.7–398 ppm with a mean of 167 ppm), Th (718–4,980 ppm with a mean of 2,136 ppm and a median of 1730 ppm) and U (3,540–32,901 ppm with a mean of 7,898 ppm and a median of 5,440 ppm). The concentrations of Ti (0–42.6 ppm with a mean of 12.44 ppm) are similar to those of the type-I. They have Zr/Hf ratios ranging from 3.35 to 11.00 with a mean of 5.56 (**Figure 8F**) and Th/U ratios from 0.12 to 0.57 with a mean of 0.36 (**Figure 9A**). The LREE, HREE, total REE contents and LREE/HREE ratios vary from 267 to 6,523 ppm with a mean of 2095 ppm, 3,628–23,640 ppm with a mean of 9,670 ppm, 3,909–30,163 ppm with a mean of 11,765 ppm, and 0.07–0.35 with a mean of 0.20, respectively, which are much higher than those of type-I zircon (**Figure 9B**).

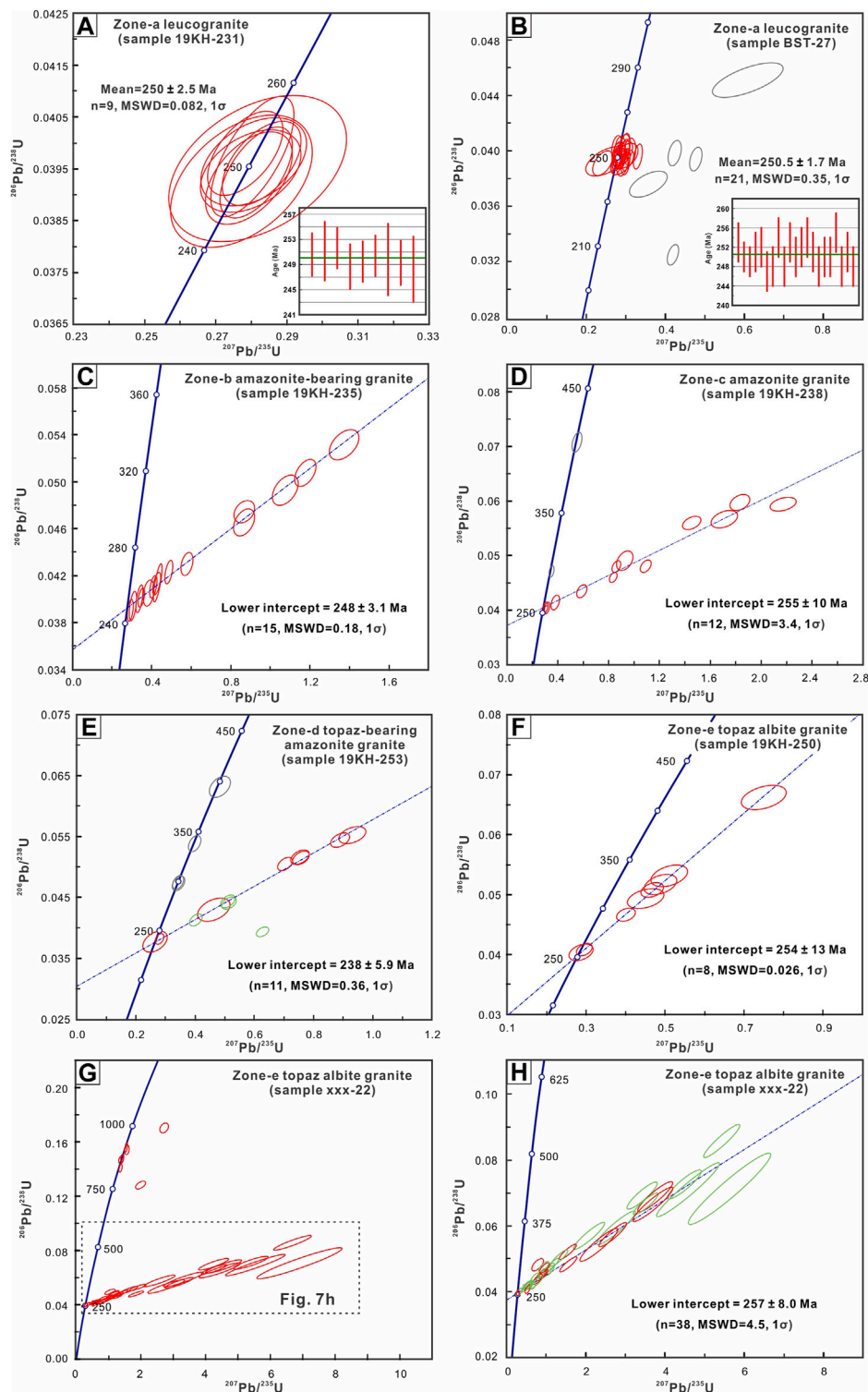
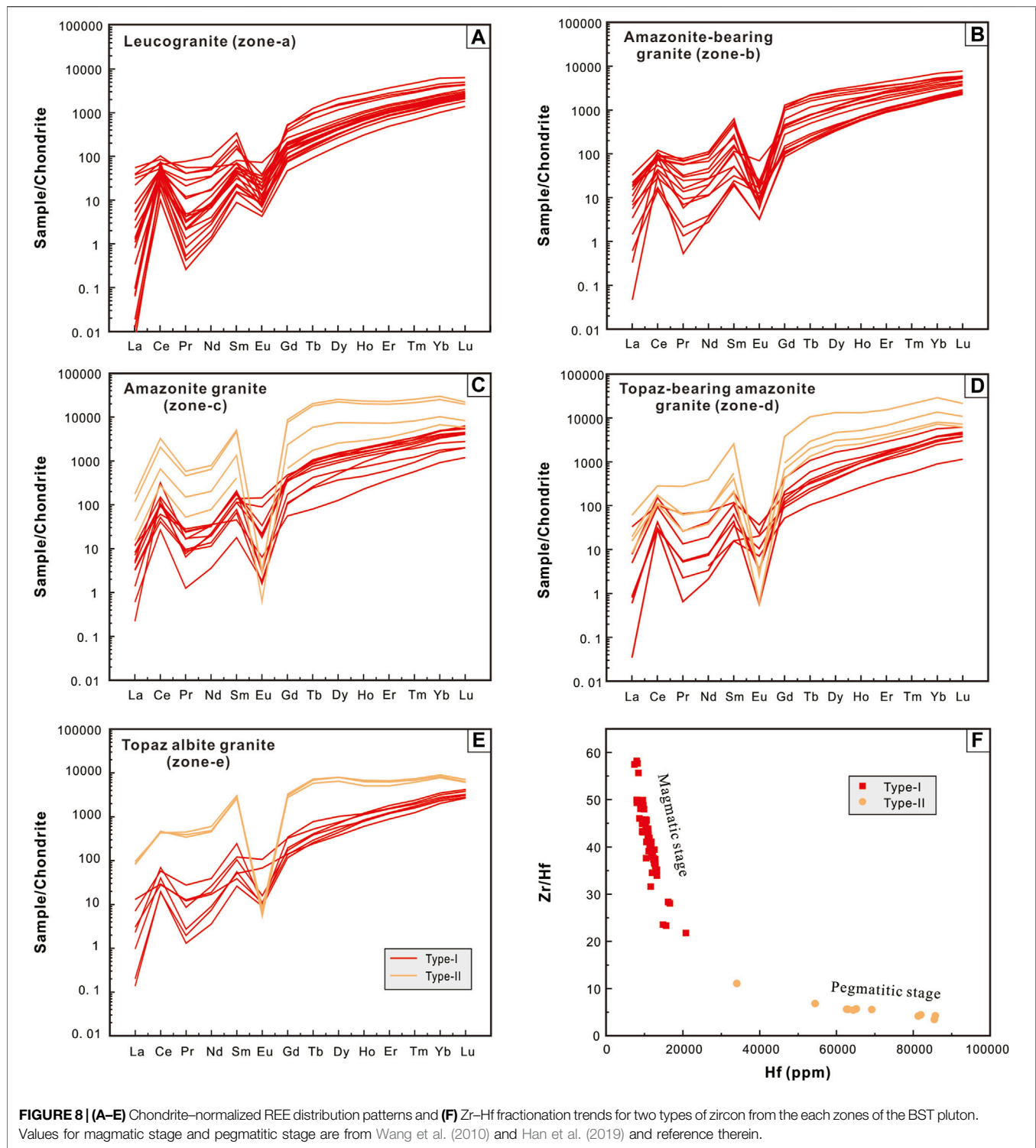


FIGURE 7 | (A,B) U–Pb concordia diagrams and weighted average ages of type-I zircon from zone-a. **(C–H)** U–Pb concordia diagrams of type-I (red circle) and type-II (green circle) zircons from the upper zones of the BST pluton.

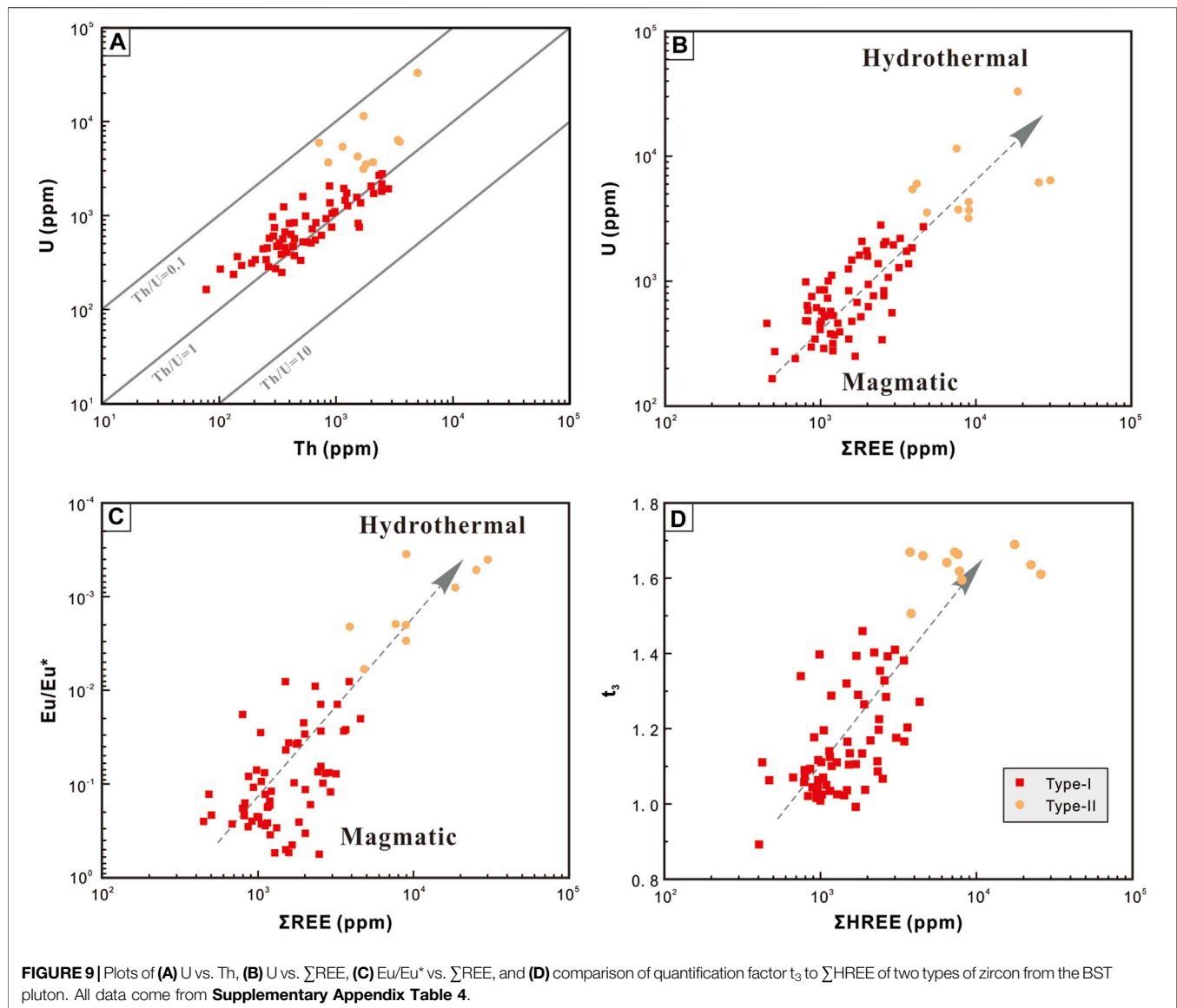
Type-II zircons exhibit gull wing-shaped, slightly HREE-enriched patterns with lower positive Ce anomalies ($Ce/Ce^* = 2.1\text{--}10.3$) and deeper Eu anomalies

($Eu/Eu^* = 0\text{--}0.006$) than those of the type-I zircons (**Figure 9C**). Chondrite-normalized REE patterns of type-II zircons display clearer tetrad effect than the type-I. The t_3 value



(quantification factor of tetrad effect) and $\sum\text{HREE}$ can be used to describe the tetrad effect of the zircons, and is calculated and listed in **Supplementary Appendix Table 4**. The t_3 value in zircons from the BST pluton are generally

greater than 1. The t_3 values of both two types of zircons have strongly positive correlation with $\sum\text{HREE}$ (**Figure 9D**), and increases from type-I zircons (0.89–1.46) to type-II zircons (1.51–1.69).



DISCUSSION

Zircon Genesis

The zircons in the BST pluton can be divided into two types: type-I and type-II, based on their distinct petrographic features, crystal structures and chemical compositions.

Type-I zircons are clean, transparent, colorless and euhedral under the optical microscope (**Figure 4D**), and are bright and show clear oscillatory zoning in CL (**Figure 5A**), consistent with a magmatic origin (Corfu et al., 2003). They are primarily distributed at the bottom of the granite (zone-a), and embedded in K-feldspar crystals (**Figure 4A**), indicating that they crystallized before K-feldspar. Chemically, the type-I zircons are characterized by high Zr and low trace element contents. They show HREE-enriched patterns with prominent positive Ce anomalies ($Ce/Ce^* = 1.21\text{--}385$) and strong negative Eu

anomalies ($Eu/Eu^* = 0.008\text{--}0.551$). The contents of LREE vary from 27 to 604 ppm and HREE from 403 to 4,320 ppm with LREE/HREE ratios of 0.04–0.26. The low concentrations of Th, U and high Th/U ratios (mostly >0.4) are comparable to those of zircons crystallized in early magmatic stages (U contents of 76–12,381 ppm with a median of 764 ppm and Th contents of 31–12,088 ppm with a median of 368 ppm, Belousova et al., 2002; UO_2 contents of 0–0.56 wt% ($\approx 0\text{--}4,936$ ppm U) with an average of 0.30 wt% ($\approx 2,644$ ppm U) and ThO_2 contents of 0–0.15 wt% ($\approx 0\text{--}1,318$ ppm Th) with an average of 0.04 wt% (≈ 352 ppm Th), Wang et al., 2011). The Hf contents of 7,471–20,835 ppm, with an average of 11,269 ppm (≈ 1.33 wt% HfO_2), and Zr/Hf ratios of 22–58 are consistent with primary granitic zircons crystallized at high temperature (<2 wt% HfO_2 and $Zr/Hf > 27$, Pupin et al., 2000; model HfO_2 contents of 1.43 wt% and Zr/Hf ratios of 38.5, Wang et al., 2010). Gu et al. (2003) indicate that the

homogenization temperatures of melt trapped in quartz phenocrysts decrease from the zone-a (810–860°C) to the zone-e (680–660°C) in the BST pluton. Type-I zircons are mainly distributed in the zone-a. Therefore, they are considered to be high temperature magmatic zircons.

Type-II zircons are dark brown, translucent, dirty and euhedral to subhedral under the optical microscope, and are porous, microcracks-rich and inhomogeneous in structures in CL and BSE images, consistent with the petrographic features of hydrothermal zircons (e.g., Wang et al., 2011; Wang X. et al., 2016; Wang and Ren, 2018). The contents of Hf, Nb, Ta, Y, Th, U, LREE and total REE in type-II zircons are much higher than in type-I. They show slightly HREE-enriched patterns with lower positive Ce anomalies ($Ce/Ce^* = 2.1\text{--}10.3$) and deeper Eu anomalies ($Eu/Eu^* = 0\text{--}0.006$) than those of the type-I zircons. The high LREE and HREE contents and LREE/HREE ratios of type-II zircons are consistent with a hydrothermal origin (LREE contents of 608–2,502 ppm with a mean of 1,303 ppm, HREE contents of 324–4,990 ppm with a mean of 2064 ppm, and LREE/HREE ratios of 0.29–5.49 with a mean of 1.20, Yang et al., 2014). The generally higher Th (718–4,980 ppm with a mean of 2,136 ppm), U (3,180–32,901 ppm with a mean of 7,898 ppm) contents and lower Th/U ratios (mostly <0.4 , **Figure 9A**) of type-II zircons are comparable to those of zircons of hydrothermal origin in highly evolved magmatic systems (U contents of 560–3,820 ppm with a mean of 1710 ppm, Th contents of 83.0–12,638 ppm with a mean of 1,594 ppm, and Th/U ratios of 0.11–0.54, Yang et al., 2014). The extremely high Hf contents (up to 10.1 wt% Hf_2O) and low Zr/Hf ratios of type-II zircons in the BST pluton (**Figure 6F**) are also comparable to zircons from the pegmatite or highly evolved granite ($>2.4\text{wt}\% HfO_2$ and Zr/Hf ratios ≤ 20 , Gbelsky, 1979; Cerny et al., 1985). The much higher Hf contents and low Zr/Hf ratios of zircons from granitic rocks (especially hydrothermal zircons) could be caused by low crystallization temperatures (Wang et al., 2010; Wang X. et al., 2016). Moreover, the positive relationship between U and $\sum REE$ (**Figure 9B**), and the increase of negative Eu anomalies from type-I to type-II zircons (**Figure 9C**), suggest the increase of hydrothermal contribution to zircon crystallization (Veksler, 2004; Hoskin, 2005). Thus, type-II zircons from the BST pluton are interpreted to be of hydrothermal origin.

The high contents of LREE and low Zr/Hf ratios in type-II zircon could be the result of non-charge-and-radius-controlled (Non-CHARAC) behavior (Bau and Dulski, 1995; Bau, 1996), which commonly occurs in volatile-rich highly evolved magmatic systems during the transition from magmatic to hydrothermal conditions (Veksler, 2004). Non-CHARAC behavior is often accompanied by the lanthanide tetrad effect of both whole-rock and minerals including zircon (Masuda and Ikeuchi, 1979; Akagi et al., 1993; Bau, 1996; Irber, 1999; Veksler et al., 2005). Type-II zircons in the BST pluton show obvious M-type tetrad patterns in chondrite-normalized REE distribution patterns with t_3 values of 1.51–1.69, consistent with the clear tetrad features of other minerals in the BST pluton, such as quartz, plagioclase, garnet and monazite (Wu et al., 2011). The lanthanide tetrad effect is generally attributed to

hydrothermal fluid-rock interaction (Monecke et al., 2002; Monecke et al., 2007; Takahashi et al., 2002; Badanina et al., 2006), and the M-type tetrad patterns are considered to be caused by F-rich magmatic fluid-melt interaction above the solidus (Wu et al., 2011). Thus, the formation of type-II zircons should represent a magmatic fluid-melt interaction during the transition from magmatic to F-rich hydrothermal conditions. At this stage, Th, U, Hf, Ta, REEs and other trace elements in the magmatic system were significantly concentrated in the magmatic fluids that coexisted with the melt.

F-Rich Fluid Exsolution and Magmatic-Hydrothermal Transition

The Rb-bearing granites in the Eastern Tianshan are characterized by high SiO_2 , Na_2O , K_2O Li, Rb, Cs and F, low Ti, Fe, Ca, Mg and P, $Na_2O > K_2O$, are weakly peraluminous ($A/NKC = 1.00\text{--}1.11$), low K/Rb, Al/Ga, Y/Ho, Zr/Hf and Nb/Ta ratios, and have low $(La/Lu)_N$ and deep Eu anomalies (Gu et al., 2003; Chen et al., 2018; Li T. G. et al., 2018; Muhtar et al., 2020a). They are generally highly evolved magmatic systems with abundant deuteric fluid exsolution and hydrothermal alteration occurring in the late magmatic stage. A previous study has suggested that several fluid exsolution events occurred during the differentiation of magma, controlling the formation and modification of the highly evolved granite (Berni et al., 2017; Berni et al., 2020).

The present study observed that $\sum HREE$ and t_3 values show linear variations between two types of zircon, with t_3 values increasing markedly from type-I to type-II zircons (**Figure 9D**). Such a trend of evolution may represent the increase of F-rich fluid-melt interaction during the differentiation of F-Rb-rich granitic magma (Wu et al., 2011). However, $\sum HREE$ and t_3 values of zircons from zone-a to zone-e do not show linear variations, and the two types of zircons of different origin occur together in the upper lithological zones. A possible explanation is that turbulence in the volatile (F)-rich magmatic-hydrothermal system disturbed the original distribution of zircons (Gu et al., 2011), and the type-I zircons were carried to the top of the granite contained by late magmatic minerals. Moreover, modification of crystallized rocks and zircons by exsolved (F-rich) fluids occurs in the BST pluton, evidenced by large amounts of fluorite in the microcracks in magmatic type-I zircons (**Figure 6B**) and in voids of some hydrothermal type-II zircons (**Figure 6D**). The hydrothermal fluorite occurs as a vein along plagioclase, K-feldspar and zinnwaldite grains and fractures (Gu et al., 2011), also indicating the existence of a F-rich hydrothermal event after the crystallization of rock-forming minerals.

Both zircon types can be found in the same grain (**Figure 5D**), which is crucial to study the F-rich fluid exsolution processes, including F-rich fluid-melt interaction and hydrothermal modification, during the magmatic-hydrothermal transition stage. The petrography observations and geochemical compositions of zircons suggest that type-I zircons crystallized earlier than type-II zircons. Some type-I zircons crystallized in the early-magmatic stage were modified by the F-rich fluids

through dissolution–reprecipitation at the edges (Figure 6A) or along defective magmatic euhedral zones (Figure 6B), consistent with petrographic features of hydrothermal overprinting of zircons (e.g., Wang and Ren, 2018; Liu et al., 2019; Han et al., 2019). This supports the mobilization of Zr in hydrothermal systems that are rich in F (Rubin et al., 1993; Aja et al. 1995; Veksler et al., 2005). Such selective alteration of zircon grains probably occurs as a result of metamictization (e.g., Geisler et al., 2007; Van Lichtenvelde et al., 2009; Liu et al., 2019). Radiation-induced metamictization can greatly enhance (two or three times compared to high crystallinity zircons) the hydrothermal alteration of zircons (Ewing et al., 2003). The alpha recoil process (i.e., recoils of the U and Th nuclei after emitting a He particle) can be a main source of damage in metamictization (Wasilewski et al., 1973; Smith et al., 1991; Weber et al., 1994; Nasdala et al., 1996, 2001; Palenick et al., 2003), which can accumulate rapidly over a period of 0.0001–1 million years in the zircon grains. Then, the deuteric F-rich fluid locally replaced some type-I zircons, from which the hydrothermal type-II zircon and fluorite crystallized as overgrowth of the type-I (Figures 4D, 5D). Gradual increase of the amount of the hydrothermal type-II zircons upward within the zoned granite (increase from 10 to 20% in zone-c to 70–80% in zone-e), as well as the intense modification of zircon in zone-e, suggest that a F-rich fluid could rise and accumulate to form a segregated fluid phase at the top of the BST magma (Burnham, 1997; Wilkinson, 2001; Gu et al., 2011), which is comparable to the magmatic to hydrothermal evolution in other highly evolved granites (e.g., Yang et al., 2014; Berni et al., 2020).

Previous studies suggested that the source of the BST magma is mica gneiss in the middle crust, partial melting of which can provide large amounts of F, Rb and Cs, based on the high $\text{Na}_2\text{O} + \text{K}_2\text{O}$, low FeO, MgO and TiO_2 contents, the weakly peraluminous character, low $\epsilon\text{Nd}(t)$ value and $\delta^{18}\text{O}$ value (9.25–9.75 in zone-a) (Gu et al., 2011). The Rb is transported in the form of complex with F in highly evolved granitic magma (Hildreth, 1981; Jia, 2016), and the hydrolysis takes place with the decrease of temperature (Webster and Holloway, 1990; Zhao et al., 2008). The homogenization temperatures of melt trapped in quartz phenocrysts and the petrographic studies suggest that the mineral composition of the zone-a can approximately represent the mineral assemblages of the early magmatic stage (Gu et al., 2003). At this stage, F tends to enter the fluid phase and form stable complexes with Li, Rb, Cs, Sn and other elements (Hildreth, 1981; Cerny et al., 1985; Bhalla et al., 2005; Sun, 2013; Jia, 2016). With the decrease of temperature hydrolysis takes place (Webster and Holloway, 1990; Zhao et al., 2008), the F⁻ and Ca^{2+} form fluorite, and Rb replaces part of the K into the lattice of the low temperature microcline and zinnwaldite, consistent with the observation of the enrichment of Rb in low temperature K-feldspar (microcline) and mica (zinnwaldite) in the highly evolved granite (e.g., Wang et al., 2009; Badanina et al., 2010; Seltmann et al., 2010; Tang and Zhang, 2015; Ostrooumov, 2015; Li T. G. et al., 2018). The coupling of F and Rb in the early magmatic stage is also consistent with the positive correlation between Rb and F from zone-a to zone-d in the BST pluton (Gu et al., 2003, 2011). Magmatic fluid from F-rich highly evolved

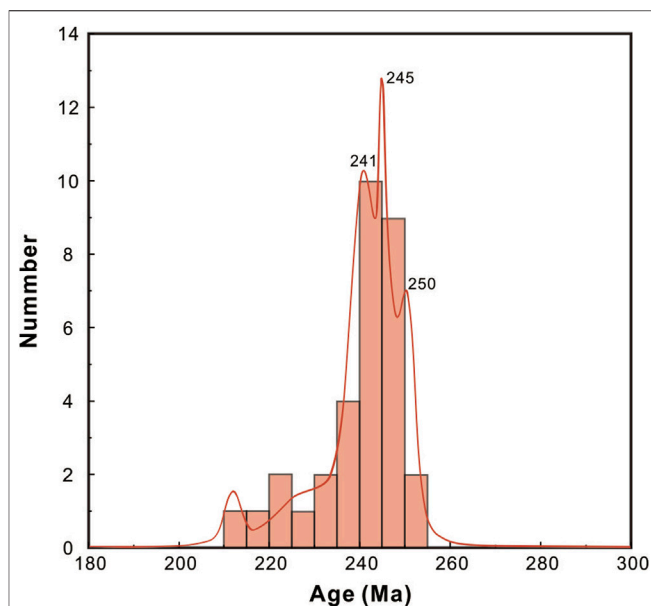


FIGURE 10 | Age data histogram of the Triassic granitic intrusions and related rare metal deposits from the Eastern Tianshan.

granite and related pegmatite contains high concentrations of trace elements including Rb (Berni et al., 2020), and the ore minerals (e.g., amazonite and zinnwaldite) in the BST pluton generally crystallized from residual magma that has experienced the F-fluid exsolution during the magmatic–hydrothermal transition (Gu et al., 2003; Gu et al., 2011), indicating that the enrichment and mineralization of Rb is closely related to the magmatic F-rich fluids.

Therefore, F-rich fluid exsolution during the magmatic–hydrothermal transitional stage is one of the important factors controlling the modification of highly evolved granites (Gu et al., 2011; Berni et al., 2017; Berni et al., 2020), as well as related Rb enrichment and mineralization.

Implication for Rb Mineralization Age of the Zhangbaoshan Super-Large Rb Deposit

The LA-ICP-MS U–Pb data for type-I zircons from the leucogranite (zone-a) show a concordant age of 250.5 ± 1.7 Ma and 250 ± 2.5 Ma (Figures 7A,B), indicating that the BST pluton was emplaced in the Early Triassic. Type-II zircons from zone-c to zone-e show lead loss on the U–Pb concordia diagrams, yielding lower intercept U–Pb ages between 238 and 257 Ma (Figures 7E–H), which could indicate the age of the F-rich fluid–melt interaction above solidus during the transition from magmatic to hydrothermal conditions. These Early Triassic ages are also consistent with the emplacement age of the BST granitic magma.

As discussed above, the rubidium mineralization of the ZBS super-large Rb deposit mainly occurred during the magmatic–hydrothermal transition stage, which was later than the crystallization of magmatic type-I zircon, and close to the

crystallization age of the hydrothermal type-II zircon. We thus suppose that the rubidium mineralization occurred shortly after the emplacement age (ca. 250 Ma) of the BST pluton.

Triassic granitoids and related rare metal deposits have been increasingly identified in the Eastern Tianshan during the past decade (**Supplementary Appendix Table 1** and **Figure 10**). The ZBS granite-type super-large Rb deposit (ca. 250 Ma) and other rare-metal granite or pegmatite deposits in the Eastern Tianshan, including the Shadong W-(Rb) deposit (239 ± 2 Ma, Chen et al., 2018), the Guobaoshan Rb deposit (240.3 ± 1.8 Ma, Li T. G. et al., 2018) and the Jing'erquanbei (Li-Be-Rb) pegmatite (250.2 ± 3.5 Ma, Muhtar et al., 2020a), likely make up a >200-km-long rare metal metallogenic belt. A summary of the rare metal deposits in the Eastern Tianshan suggests that the Triassic should be an important rare metal metallogenic period in the Eastern Tianshan, and rare metal deposits are closely related to the Triassic highly evolved leucogranite enriched in F in the Eastern Tianshan.

CONCLUSION

- 1) Zircon from the BST pluton can be divided into two genetic types. Type-I zircons are early magmatic zircons, characterized by clear oscillatory zoning, high Zr contents and Zr/Hf ratios, low trace element concentrations, and HREE-enriched patterns. Type-II zircons are hydrothermal zircons crystallized from deuteric F-rich fluid that coexisted with residual magma. They are characterized by low Zr contents and Zr/Hf ratios, high Hf, Th, U, Ta, Y and REEs concentrations, and significant M-type tetrad patterns in chondrite-normalized REE distribution patterns.
- 2) The formation of type-II zircons represents a magmatic fluid-melt interaction during the transition from the magmatic to the F-rich hydrothermal stage of the BST pluton. The F-rich fluid exsolution during the magmatic-hydrothermal transition is one of the important factors controlling the modification of highly evolved granite and related Rb enrichment and mineralization.
- 3) Type-I zircons from leucogranite (zone-a) show a concordant age of ca. 250 Ma, indicating that the BST pluton was emplaced in the Early Triassic. Type-II zircons from zone-c to zone-e yield lower intercept U-Pb ages between 238 and 257 Ma, which could indicate the age of the F-rich fluid-melt interaction during the transition stage from the magmatic to the hydrothermal conditions. The mineralization

of the ZBS super-large Rb deposit should occur shortly after emplacement of the BST pluton in the Early Triassic.

- 4) The Triassic should be an important rare metal metallogenic period of the Eastern Tianshan. The rare metal mineralization are closely related to the Triassic highly evolved F-rich leucogranite in the Eastern Tianshan.

DATA AVAILABILITY STATEMENT

The original contributions presented in the study are included in the article/**Supplementary Material**, further inquiries can be directed to the corresponding author.

AUTHOR CONTRIBUTIONS

RL and CW designed the study, leaded the field investigation and revised the manuscript, JZ, BC and MM participated in field work, JZ, FZ and KZ analyzed the sample and acquired the data, YC made great contributions in explanation of experimental results. All authors contributed to the writing of the manuscript, and reviewed the manuscript and agree to this submission.

FUNDING

This study is supported by Natural Science Foundation of China (No. 91962214) and National Key R&D Program of China (Grant No. 2018YFC0603703).

ACKNOWLEDGMENTS

We thank Tongguo Li and Youkui Zhang from Geological Survey Academy of Gansu Province, and Kai Gan, Simeng Wang and Xianglong Luo from Nanjing University for their assistance in fieldwork.

SUPPLEMENTARY MATERIAL

The Supplementary Material for this article can be found online at: <https://www.frontiersin.org/articles/10.3389/feart.2021.682720/full#supplementary-material>

REFERENCES

- Aja, S. U., Wood, S. A., and Williams-Jones, A. E. (1995). The Aqueous Geochemistry of Zr and the Solubility of Some Zr-Bearing Minerals. *Appl. Geochem.* 10 (6), 603–620. doi:10.1016/0883-2927(95)00026-7
- Akagi, T., Shabani, M. B., and Masuda, A. (1993). Lanthanide Tetrad Effect in Kimuraite [CaY₂(CO₃)₄ · 6H₂O]: Implication for a New Geochemical index. *Geochimica et Cosmochimica Acta* 57 (12), 2899–2905. doi:10.1016/0016-7037(93)90397-f
- Ayers, J. C., Zhang, L., Luo, Y., and Peters, T. J. (2012). Zircon Solubility in Alkaline Aqueous Fluids at Upper Crustal Conditions. *Geochimica et Cosmochimica Acta* 96, 18–28. doi:10.1016/j.gca.2012.08.027
- Badanina, E. V., Syritso, L. F., Volkova, E. V., Thomas, R., and Trumbull, R. B. (2010). Composition of Li-F Granite Melt and its Evolution during the Formation of the Ore-Bearing Orlovka Massif in Eastern Transbaikalia. *Petrology* 18 (2), 131–157. doi:10.1134/s0869591110020037
- Badanina, E. V., Trumbull, R. B., Dulski, P., Wiedenbeck, M., Veksler, I. V., and Syritso, L. F. (2006). The Behavior of Rare-Earth and Lithophile Trace Elements in Rare-Metal Granites: a Study of Fluorite, Melt Inclusions and Host Rocks

- from the Khangilay Complex, Transbaikalia, Russia. *Can. Mineral.* 44 (3), 667–692. doi:10.2113/gscanmin.44.3.667
- Bau, M. (1996). Controls on the Fractionation of Isovalent Trace Elements in Magmatic and Aqueous Systems: Evidence from Y/Ho, Zr/Hf, and Lanthanide Tetrad Effect. *Contrib. Mineralogy Petrol.* 123 (3), 323–333. doi:10.1007/s004100050159
- Bau, M., and Dulski, P. (1995). Comparative Study of Yttrium and Rare-Earth Element Behaviours in Fluorine-Rich Hydrothermal Fluids. *Contrib. Mineralogy Petrol.* 119 (2–3), 213–223. doi:10.1007/s004100050037
- Belousova, E. A., Griffin, W. L., and O'Reilly, S. Y. (2006). Zircon crystal Morphology, Trace Element Signatures and Hf Isotope Composition as a Tool for Petrogenetic Modelling: Examples from Eastern Australian Granitoids. *J. Petrol.* 47 (2), 329–353. doi:10.1093/ptrology/legi077
- Belousova, E., Griffin, W., O'Reilly, S. Y., and Fisher, N. (2002). Igneous Zircon: Trace Element Composition as an Indicator of Source Rock Type. *Contrib. Mineral. Petrol.* 143 (5), 602–622. doi:10.1007/s00410-002-0364-7
- Berni, G. V., Wagner, T., and Fusswinkel, T. (2020). From a F-Rich Granite to a NYF Pegmatite: Magmatic-Hydrothermal Fluid Evolution of the Kymi Topaz Granite Stock, SE Finland. *LITHOS* 364–365, 105538. doi:10.1016/j.lithos.2020.105538
- Berni, G. V., Wagner, T., Fusswinkel, T., and Wenzel, T. (2017). Magmatic-hydrothermal Evolution of the Kymi Topaz Granite Stock, SE Finland: mineral Chemistry Evidence for Episodic Fluid Exsolution. *Lithos* 292–293, 401–423. doi:10.1016/j.lithos.2017.09.015
- Bhalla, P., Holtz, F., Linnen, R. L., and Behrens, H. (2005). Solubility of Cassiterite in Evolved Granitic Melts: Effect of T, fO₂, and Additional Volatiles. *Lithos* 80 (1–4), 387–400. doi:10.1016/j.lithos.2004.06.014
- Burnham, C. W. (1997). "Magmas and Hydrothermal Fluids," in *Geochemistry of Hydrothermal Ore Deposits*. Editor H. L. Barnes. third edition (New York: John Wiley & Sons), 63–124.
- Cerny, P., Meintzer, R. E., and Andreson, A. J. (1985). Extreme Fractionation in Rare-Element Granitic Pegmatites: Selected Examples of Data and Mechanisms. *Can. Mineral.* 23, 381–421.
- Chen, C., Lü, X., Wu, C., Jiang, X., and Mao, C. (2018). Origin and Geodynamic Implications of Concealed Granite in Shadong Tungsten Deposit, Xinjiang, China: Zircon U-Pb Chronology, Geochemistry, and Sr-Nd-Hf Isotope Constraint. *J. Earth Sci.* 29 (01), 114–129. doi:10.1007/s12583-017-0808-7
- Chen, X., Shu, L., and Santosh, M. (2011). Late Paleozoic post-collisional Magmatism in the Eastern Tianshan Belt, Northwest China: New Insights from Geochemistry, Geochronology and Petrology of Bimodal Volcanic Rocks. *Lithos* 127 (3), 581–598. doi:10.1016/j.lithos.2011.06.008
- Chen, Y. (1999). *Geochemistry of Granites from the Eastern Tianshan Mountains and the Northern Qinling Belt*. Beijing: Geological Publishing House. (in Chinese).
- Chen, Y. L., and Wang, Z. G. (1993). Geochemical Characteristics of East Tianshan Granitoid Rocks, Xinjiang, China. *Geochimica* 3, 288–302. (in Chinese).
- Chen, Z. H., Wang, D. H., Gong, Y. F., Chen, Y. C., and Chen, S. P. (2006). ⁴⁰Ar-³⁹Ar Isotope Dating of Muscovite from Jingerquan Pegmatite Rare Metal deposit in Hami, Xinjiang, and its Geological Significance. *Mineral. Deposit* 25 (4), 471–476. (in Chinese).
- Chen, Z., Xiao, W., Windley, B. F., Schulmann, K., Mao, Q., Zhang, Z., et al. (2019). Composition, Provenance, and Tectonic Setting of the Southern Kangurtag Accretionary Complex in the Eastern Tianshan, NW China: Implications for the Late Paleozoic Evolution of the North Tianshan Ocean. *Tectonics* 38 (8), 2779–2802. doi:10.1029/2018tc005385
- Coleman, R. G. (1989). Continental Growth of Northwest China. *Tectonics* 8 (3), 621–635. doi:10.1029/tc008i003p00621
- Corfu, F., Hanchar, J. M., Hoskin, P. W. O., and Kinny, P. (2003). 16. Atlas of Zircon Textures. *Rev. Mineralogy Geochem.* 53, 469–502. doi:10.1515/9781501509322-019
- Deng, X.-H., Chen, Y.-J., Santosh, M., Wang, J.-B., Li, C., Yue, S.-W., et al. (2017). U-pb Zircon, Re-os Molybdenite Geochronology and Rb-Sr Geochemistry from the Xiaobaishitou W (-Mo) Deposit: Implications for Triassic Tectonic Setting in Eastern Tianshan, NW China. *Ore Geology. Rev.* 80, 332–351. doi:10.1016/j.oregeorev.2016.05.013
- Erdmann, S., Wodicka, N., Jackson, S. E., and Corrigan, D. (2013). Zircon Textures and Composition: Refractory Recorders of Magmatic Volatile Evolution?. *Contrib. Mineral. Petrol.* 165 (1), 45–71. doi:10.1007/s00410-012-0791-z
- Ewing, R. C., Meldrum, A., Wang, L., Weber, W. J., and Corrales, L. R. (2003). Radiation Effects in Zircon. *Rev. Mineralogy Geochem.* 53, 378–420. doi:10.2113/0530387
- Gansu Provincial Geological Survey Institute (GPGSI) (2015). Internal Reconnaissance Report of the Zhangbaoshan Ru-Polymetallic deposit in Hami City, Xinjiang Province. (Unpublished report (in Chinese).
- Gbel'sky, J. (1979). Electron Microprobe Determination of Zr/Hf Ratios in Zircons from Pegmatites of the Male Karpaty Mts (West Carpathians). *Geologica Carpathica* 30, 463–474.
- Geisler, T., Schaltegger, U., and Tomaschek, F. (2007). Re-equilibration of Zircon in Aqueous Fluids and Melts. *Elements* 3 (1), 43–50. doi:10.2113/gselements.3.1.43
- Gu, L. X., Gou, X. Q., Zhang, Z. Z., Wu, C. Z., Liao, J. J., Yang, H., et al. (2003). Geochemistry and Petrogenesis of a Multi-Zoned High Rb and F Granite in Eastern Tianshan. *Acta Petrologica Sinica* 19 (4), 585–600. (in Chinese). doi:10.3321/j.issn:1000-0569.2003.04.001
- Gu, L. X., Hu, S. X., Yu, C. S., Zhao, M., Wu, C. Z., and Li, H. Y. (2001). Intrusive Activities during Compression-Extension Tectonic Conversion in the Bogda Intracontinental Orogen. *Acta Petrologica Sinica* 17 (2), 187–198. (in Chinese). doi:10.3321/j.issn:1000-0569.2001.02.002
- Gu, L. X., Yang, H., Gou, X. Q., Guo, J. C., and Wang, J. Z. (1994). Geology and Genesis of the Baishitouquan High-Rubidium and Fluorine Granites in the Xingxingshia District of Hami County, Xinjiang. *Acta petrologica sinica* 10 (1), 41–53.
- Gu, L. X., Zhang, Z. Z., Wu, C. Z., Wang, Y. X., Tang, J. H., Wang, C. S., et al. (2006). Some Problems on Granites and Vertical Growth of the continental Crust in the Eastern Tianshan Mountains, NW China. *Acta Petrologica Sinica* 22 (5), 1103–1120. (in Chinese). doi:10.3321/j.issn:1000-0569.2006.05.005
- Gu, L.-x., Zhang, Z.-z., Wu, C.-z., Gou, X.-q., Liao, J.-j., and Yang, H. (2011). A Topaz- and Amazonite-Bearing Leucogranite Pluton in Eastern Xinjiang, NW China and its Zoning. *J. Asian Earth Sci.* 42 (5), 885–902. doi:10.1016/j.jseas.2010.12.010
- Han, C., Xiao, W., Su, B., Sakya, P. A., Ao, S., Zhang, J., et al. (2018). Geology, Re-Os and U-Pb Geochronology and Sulfur Isotope of the the Donggebi Porphyry Mo deposit, Xinjiang, NW China, Central Asian Orogenic Belt. *J. Asian Earth Sci.* 165, 270–284. doi:10.1016/j.jseas.2018.05.001
- Han, C., Xiao, W., Zhao, G., Sun, M., Qu, W., and Du, A. (2014). Re-Os Geochronology on Molybdenites from the Donggebi Mo Deposit in the Eastern Tianshan of the Central Asia Orogenic Belt and its Geological Significance. *Resource Geology*. 64, 136–148. doi:10.1111/rge.12033
- Han, J., Chen, H., Hollings, P., Jiang, H., Xu, H., Zhang, L., et al. (2019). The Formation of Modified Zircons in F-Rich Highly-Evolved Granites: An Example from the Shuangji Granites in Eastern Tianshan, China. *Lithos* 324–325, 776–788. doi:10.1016/j.lithos.2018.12.009
- Han, J., Chen, H., Hollings, P., Wang, J., Zhang, D., Zhang, L., et al. (2021). Efficient Enrichment of Rb during the Magmatic-Hydrothermal Transition in a Highly Evolved Granitic System: Implications from Mica Chemistry of the Tiantangshan Rb-Sn-W deposit. *Chem. Geology*. 560, 120020. doi:10.1016/j.chemgeo.2020.120020
- Hanchar, J. M., and Van Westrenen, W. (2007). Rare Earth Element Behavior in Zircon-Melt Systems. *Elements* 3 (1), 37–42. doi:10.2113/gselements.3.1.37
- Harley, S. L., Kelly, N. M., and Moller, A. (2007). Zircon Behaviour and the Thermal Histories of Mountain Chains. *Elements* 3 (1), 25–30. doi:10.2113/gselements.3.1.25
- Hildreth, W. (1981). Gradients in Silicic Magma chambers: Implications for Lithospheric Magmatism. *J. Geophys. Res.* 86 (B11), 10153–10192. doi:10.1029/jb086ib11p10153
- Hoskin, P. W. O. (2005). Trace-element Composition of Hydrothermal Zircon and the Alteration of Hadean Zircon from the Jack Hills, Australia. *Geochimica et Cosmochimica Acta* 69 (3), 637–648. doi:10.1016/j.gca.2004.07.006
- Hou, T., Zhang, Z., Santosh, M., Encarnacion, J., Zhu, J., and Luo, W. (2014). Geochronology and Geochemistry of Submarine Volcanic Rocks in the Yamansu Iron deposit, Eastern Tianshan Mountains, NW China: Constraints on the Metallogenesis. *Ore Geology. Rev.* 56, 487–502. doi:10.1016/j.oregeorev.2013.03.008

- Hu, A., Wang, Z., and Tu, G. (1997). *Geological Evolution, Petrogenesis and Metallogeny of North Xinjiang*. Beijing: Science Press. (in Chinese).
- Huang, W., Wu, J., Liang, H., Zhang, J., Ren, L., and Chen, X. (2020). Ages and Genesis of W-Sn and Ta-Nb-Sn-W Mineralization Associated with the Limu Granite Complex, Guangxi, China. *Lithos* 352–353, 105321. doi:10.1016/j.lithos.2019.105321
- Irber, W. (1999). The Lanthanide Tetrad Effect and its Correlation with K/Rb, Eu/Eu*, Sr/Eu, Y/Ho, and Zr/Hf of Evolving Peraluminous Granite Suites. *Geochimica et Cosmochimica Acta* 63 (3–4), 489–508. doi:10.1016/s0016-7037(99)00027-7
- Jackson, S. E., Pearson, N. J., Griffin, W. L., and Belousova, E. A. (2004). The Application of Laser Ablation-Inductively Coupled Plasma-Mass Spectrometry to *In Situ* U-Pb Zircon Geochronology. *Chem. Geology* 211, 47–69. doi:10.1016/j.chemgeo.2004.06.017
- Jahn, B.-M. (2004). The Central Asian Orogenic Belt and Growth of the continental Crust in the Phanerozoic. *Geol. Soc. Lond. Spec. Publications* 226 (1), 73–100. doi:10.1144/gsl.sp.2004.226.01.05
- Jia, Z. L. (2016). *Geochemical and Metallogenetical Characteristics of Nb-Ta-Rb Deposits, South Qilian-Beishan Area*. Gansu Province, China: Lanzhou University. (in Chinese).
- Jiang, W.-C., Li, H., Turner, S., Zhu, D.-P., and Wang, C. (2020). Timing and Origin of Multi-Stage Magmatism and Related W-Mo-Pb-Zn-Fe-Cu Mineralization in the Huangshaping deposit, South China: An Integrated Zircon Study. *Chem. Geology* 552, 119782. doi:10.1016/j.chemgeo.2020.119782
- Kusiak, M. A., Dunkley, D. J., Slaby, E., Martin, H., and Budzyn, B. (2009). Sensitive High-Resolution Ion Microprobe Analysis of Zircon Re-equilibrated by Late Magmatic Fluids in a Hybridized Pluton. *Geology* 37 (12), 1063–1066. doi:10.1130/g30048a.1
- Lei, R. X., Wu, C. Z., Zhang, Z. Z., Gu, L. X., Tang, J. H., and Li, G. R. (2013). Geochronology, Geochemistry and Tectonic Significances of the Yamansubei Pluton in Eastern Tianshan, Northwest China. *Acta Petrologica Sinica* 29 (8), 2653–2664. (in Chinese).
- Lei, R.-X., Brzozowski, M. J., Feng, Y.-g., Zhang, K., Muhtar, M. N., Luo, X., et al. (2020). Triassic Crust-Mantle Interaction in the Eastern Tianshan, Southern Altaids: Insights from Microgranular Enclaves and Their Host Tianhu Granitoids. *Lithos*, 105879. doi:10.1016/j.lithos.2020.105879
- Lei, R.-X., Wu, C.-Z., Gu, L.-X., Zhang, Z.-Z., Chi, G.-X., and Jiang, Y.-H. (2011). Zircon U-Pb Chronology and Hf Isotope of the Xingxingxia Granodiorite from the Central Tianshan Zone (NW China): Implications for the Tectonic Evolution of the Southern Altaids. *Gondwana Res.* 20 (2), 582–593. doi:10.1016/j.gr.2011.02.010
- Li, H., Chen, F., Lu, Y., Yang, H., Guo, J., and Mei, Y. (2005). New Chronological Evidence for Indosinian Diagenetic Mineralization in Eastern Xinjiang, NW China. *Acta Geologica Sinica* 79 (2), 264–275.
- Li, H., Wu, J.-H., Evans, N. J., Jiang, W.-C., and Zhou, Z.-K. (2018). Zircon Geochronology and Geochemistry of the Xianghualing A-type Granitic Rocks: Insights into Multi-Stage Sn-Polymetallic Mineralization in South China. *Lithos* 312–313, 1–20. doi:10.1016/j.lithos.2018.05.001
- Li, T. G., Liang, M. H., Yu, J. P., Huang, Z. B., and Zhang, X. (2018). *Geological Background of Rare (Rare-earth) Metal Mineralization in Gansu Province*. Beijing: Geological Publishing House. (in Chinese).
- Li, X.-C., Zhou, M.-F., Chen, W. T., Zhao, X.-F., and Tran, M. (2018). Uranium-lead Dating of Hydrothermal Zircon and Monazite from the Sin Quyen Fe-Cu-REE-Au-(U) deposit, Northwestern Vietnam. *Miner Deposita* 53 (3), 399–416. doi:10.1007/s00126-017-0746-4
- Li, N., Yang, F., Zhang, Z., and Yang, C. (2019). Geochemistry and Chronology of the Biotite Granite in the Xiaobaishituo W-(Mo) deposit, Eastern Tianshan, China: Petrogenesis and Tectonic Implications. *Ore Geology. Rev.* 107, 999–1019. doi:10.1016/j.oregeorev.2019.03.027
- Li, S., Chung, S. L., Wilde, S. A., Jahn, B. M., Xiao, W. J., Wang, T., et al. (2017). Early-Middle Triassic High Sr/Y Granitoids in the Southern Central Asian Orogenic Belt: Implications for Ocean Closure in Accretionary Orogens. *J. Geophys. Res. Solid Earth* 122 (3), 2291–2309. doi:10.1002/2017jb014006
- Li, W. M., Ren, B. C., Yang, X. K., Li, Y. Z., and Chen, Q. (2002). The Intermediate-Acid Intrusive Magmatism and its Geodynamic Significance in Eastern Tianshan Region. *Northwest. Geology* 35 (4), 41–64. (in Chinese).
- Li, X., and Zhou, M.-F. (2015). Multiple Stages of Hydrothermal REE Remobilization Recorded in Fluorapatite in the Paleoproterozoic Yinachang Fe-Cu-(REE) deposit, Southwest China. *Geochimica et Cosmochimica Acta* 166, 53–73. doi:10.1016/j.gca.2015.06.008
- Liu, B., and Wang, X. (2016). SIMS U-Pb Dating and Hf Isotope of Zircons from the Deep Granite Porphyry in Baishan Mo deposit, Eastern Tianshan, Northwest China, and Their Geological Significance. *Earth Sci. Front.* 23 (05), 291–300. doi:10.13745/j.esf.2016.05.028
- Liu, S. H., Wu, C. Z., Gu, L. X., Zhang, Z. Z., Tang, J. H., Li, G. R., et al. (2008). Geochronology, Petrogenesis and Tectonic Significances of the Baishitouquan Pluton in Middle Tianshan, Northwest China. *Acta Petrologica Sinica* 24, 2720–2730. (in Chinese).
- Liu, Y., Hou, Z., Zhang, R., Wang, P., Gao, J., and Raschke, M. B. (2019). Zircon Alteration as a Proxy for Rare Earth Element Mineralization Processes in Carbonatite-Nordmarkite Complexes of the Mianning-Dechang Rare Earth Element Belt, China. *Econ. Geology* 114 (4), 719–744. doi:10.5382/econgeo.4660
- Ludwig, K. W. (2008). *User's Manual for Isoplot 3.70*. In *A Geochronological Toolkit for Microsoft Excel*. California: Berkeley Geochronology Center Special Publication, 476.
- Masuda, A., and Ikeuchi, Y. (1979). Lanthanide Tetrad Effect Observed in marine Environment. *Geochem. J.* 13, 19–22. doi:10.2343/geochemj.13.19
- Miller, J. S., Matzel, J. E. P., Miller, C. F., Burgess, S. D., and Miller, R. B. (2007). Zircon Growth and Recycling during the Assembly of Large, Composite Arc Plutons. *J. Volcanology Geothermal Res.* 167 (1), 282–299. doi:10.1016/j.jvolgeores.2007.04.019
- Monecke, T., Dulski, P., and Kempe, U. (2007). Origin of Convex Tetrads in Rare Earth Element Patterns of Hydrothermally Altered Siliceous Igneous Rocks from the Zinnwald Sn-W deposit, Germany. *Geochimica et Cosmochimica Acta* 71, 335–353. doi:10.1016/j.gca.2006.09.010
- Monecke, T., Kempe, U., Monecke, J., Sala, M., and Wolf, D. (2002). Tetrad Effect in Rare Earth Element Distribution Patterns: a Method of Quantification with Application to Rock and mineral Samples from Granite-Related Rare Metal Deposits. *Geochimica et Cosmochimica Acta* 66, 1185–1196. doi:10.1016/s0016-7037(01)00849-3
- Muhtar, M. N., Wu, C. Z., Santosh, M., Lei, R. X., Gu, L. X., Wang, S. M., et al. (2020b). Late Paleozoic Tectonic Transition from Subduction to post-collisional Extension in Eastern Tianshan, Central Asian Orogenic Belt. *GSA Bull.* 132 (7–8), 1756–1774. doi:10.1130/b35432.1
- Muhtar, M. N., Wu, C. Z., Santosh, M., Lei, R. X., Feng, Y., Yang, T., et al. (2020a). Peraluminous Granitoid Magmatism from Isotopically Depleted Sources: The Case of Jing'erquanbei Pluton in Eastern Tianshan, Northwest China. *Geol. J.* 55 (1), 117–132. doi:10.1002/gj.3392
- Nasdala, L., Pidgeon, R. T., and Wolf, D. (1996). Heterogeneous Metamictization of Zircon on a Microscale. *Geochimica et Cosmochimica Acta* 60 (6), 1091–1097. doi:10.1016/0016-7037(95)00454-8
- Nasdala, L., Wenzel, M., Vavra, G., Irmer, G., Wenzel, T., and Kober, B. (2001). Metamictisation of Natural Zircon: Accumulation versus thermal Annealing of Radioactivity-Induced Damage. *Contrib. Mineral. Petrol.* 141 (2), 125–144. doi:10.1007/s004100000235
- Ostrooumov, M. (2015). *Amazonite: Mineralogy, Crystal Chemistry, and Typomorphism*. Elsevier.
- Palenik, C. S., Nasdala, L., and Ewing, R. C. (2003). Radiation Damage in Zircon. *Am. Mineral.* 88 (5–6), 770–781. doi:10.2138/am-2003-5-606
- Pupin, J. P. (2000). Granite Genesis Related to Geodynamics from Hf-Y in Zircon. *Earth Environ. Sci. Trans. R. Soc. Edinb.* 91 (1–2), 245–256. doi:10.1017/s0263593300007410
- Rubin, J. N., Henry, C. D., and Price, J. G. (1993). The Mobility of Zirconium and Other "immobile" Elements during Hydrothermal Alteration. *Chem. Geology* 110 (1–3), 29–47. doi:10.1016/0009-2541(93)90246-f
- Seltmann, R., Soloviev, S., Shatov, V., Pirajno, F., Naumov, E., and Cherkasov, S. (2010). Metallogeny of Siberia: Tectonic, Geologic and Metallogenic Settings of Selected Significant Deposits*. *Aust. J. Earth Sci.* 57 (6), 655–706. doi:10.1080/08120099.2010.505277
- Sengor, A. M. C., and Natal'in, B. A. (1996). "Paleotectonics of Asia: Fragments of Synthesis," in *The Tectonic Evolution of Asia*. Editors A. Yin and T. M. Harrison (Cambridge: Cambridge University Press), 480–640.

- Sengor, A., Natal'in, B., and Burtman, V. (1993). Evolution of the Altaid Tectonic Collage and Palaeozoic Crustal Growth in Eurasia. *Nature* 364 (6435), 299–307. doi:10.1038/364299a0
- Shu, L., Wang, B., Zhu, W., Guo, Z., Charvet, J., and Zhang, Y. (2011). Timing of Initiation of Extension in the Tianshan, Based on Structural, Geochemical and Geochronological Analyses of Bimodal Volcanism and Olistostrome in the Bogda Shan (NW China). *Int. J. Earth Sci. (Geol Rundsch)* 100 (7), 1647–1663. doi:10.1007/s00531-010-0575-5
- Shu, L., Yu, J., Charvet, J., Laurent-Charvet, S., Sang, H., and Zhang, R. (2004). Geological, Geochronological and Geochemical Features of Granulites in the Eastern Tianshan, NW China. *J. Asian Earth Sci.* 24 (1), 25–41. doi:10.1016/j.jseas.2003.07.002
- Smith, D., Jorre, L., Reed, S., and Long, J. (1991). Zonally Metamictized and Other Zircons from Thor Lae, Northwest Territories. *Can. mineral* 29, 301–309.
- Sun, H., Li, H., Danišik, M., Xia, Q., Jiang, C., Wu, P., et al. (2017). U-Pb and Re-os Geochronology and Geochemistry of the Donggebi Mo deposit, Eastern Tianshan, NW China: Insights into Mineralization and Tectonic Setting. *Ore Geology. Rev.* 86, 584–599. doi:10.1016/j.oregeorev.2017.03.020
- Sun, Y. (2013). *Research on of Typical Rubidium Deposits and Tectonic Background in China*. Beijing, China: China University of Geosciences. (in Chinese). doi:10.4324/9781315878560
- Takahashi, Y., Yoshida, H., Sato, N., Hama, K., Yusa, Y., and Shimizu, H. (2002). W- and M-type Tetrad Effects in REE Patterns for Water-Rock Systems in the Tono Uranium deposit, central Japan. *Chem. Geology*. 184 (3–4), 311–335. doi:10.1016/s0009-2541(01)00388-6
- Takehara, M., Horie, K., Hokada, T., and Kiyokawa, S. (2018). New Insight into Disturbance of U-Pb and Trace-Element Systems in Hydrothermally Altered Zircon via SHRIMP Analyses of Zircon from the Duluth Gabbro. *Chem. Geology*. 484, 168–178. doi:10.1016/j.chemgeo.2018.01.028
- Tang, Y., and Zhang, H. (2015). Lanthanide Tetrads in Normalized Rare Element Patterns of Zircon from the Koktokay No. 3 Granitic Pegmatite, Altay, NW China. *Am. Mineral.* 100 (11–12), 2630–2636. doi:10.2138/am-2015-5270
- Van Achterbergh, E., Ryan, C. G., Jackson, S. E., and Griffin, W. L. (2001). “Data Reduction Software for LA-ICP-MS: Appendix,” in *Laser Ablation-ICP-Mass Spectrometry in the Earth Sciences. Principles and Applications, Mineralogical Association of Canada (MAC) Short Course Series*. Editor P. J. Sylvester (Ottawa, Ontario: Canada), 239–243.
- Van Lichtervelde, M., Melcher, F., and Wirth, R. (2009). Magmatic vs. Hydrothermal Origins for Zircon Associated with Tantalum Mineralization in the Tanco Pegmatite, Manitoba, Canada. *Am. Mineral.* 94 (4), 439–450. doi:10.2138/am.2009.2952
- Veksler, I. V., Dorfman, A. M., Kamenetsky, M., Dulski, P., and Dingwell, D. B. (2005). Partitioning of Lanthanides and Y between Immiscible Silicate and Fluoride Melts, Fluorite and Cryolite and the Origin of the Lanthanide Tetrad Effect in Igneous Rocks. *Geochimica et Cosmochimica Acta* 69 (11), 2847–2860. doi:10.1016/j.gca.2004.08.007
- Veksler, I. V. (2004). Liquid Immiscibility and its Role at the Magmatic-Hydrothermal Transition: a Summary of Experimental Studies. *Chem. Geology*. 210 (1–4), 7–31. doi:10.1016/j.chemgeo.2004.06.002
- Wang, B., Cluzel, D., Jahn, B.-m., Shu, L., Chen, Y., Zhai, Y., et al. (2014). Late Paleozoic Pre- and Syn-Kinematic Plutons of the Kangguer-Huangshan Shear Zone: Inference on the Tectonic Evolution of the Eastern Chinese north Tianshan. *Am. J. Sci.* 314 (1), 43–79. doi:10.2475/01.2014.02
- Wang, J. B., Wang, Y. W., and He, Z. H. (2006). Ore Deposits as a Guide to the Tectonic Evolution in the East Tianshan Mountains, NW China. *Geology. China* 33, 461–469. (in Chinese).
- Wang, R., Cheng Che, X., Dong Zhang, W., Lan Zhang, A., and Cheng Zhang, H. (2009). Geochemical Evolution and Late Re-equilibration of NaCs-Rich Beryl from the Koktokay #3 Pegmatite (Altai, NW China). *ejm* 21 (4), 795–809. doi:10.1127/0935-1221/2009/0021-1936
- Wang, X., Griffin, W. L., Chen, J., Huang, P. Y., and Li, X. (2011). U and Th Contents and Th/U Ratios of Zircon in Felsic and Mafic Magmatic Rocks: Improved Zircon-Melt Distribution Coefficients. *Acta Geol. Sinica (English Edition)* 85 (1), 164–174.
- Wang, X., Chen, J., and Ren, M. (2016). Hydrothermal Zircon Geochronology: Age Constraint on Nanling Range Tungsten Mineralization (Southeast China). *Ore Geology. Rev.* 74, 63–75. doi:10.1016/j.oregeorev.2015.10.034
- Wang, X., Griffin, W. L., and Chen, J. (2010). Hf Contents and Zr/Hf Ratios in Granitic Zircons. *Geochem. J.* 44 (1), 65–72. doi:10.2343/geochemj.1.0043
- Wang, X., and Ren, M. (2018). Constraints of Hydrothermal and Magmatic Zircon on the Origin of the Yaogangxian Tungsten deposit, Southern China. *Ore Geology. Rev.* 101, 453–467. doi:10.1016/j.oregeorev.2018.07.011
- Wang, Y. H., Zhang, F. F., Liu, J. J., Xue, C. J., Wang, J. P., Liu, B., et al. (2015). Petrogenesis of Granites in Baishan Molybdenum deposit, Eastern Tianshan, Xinjiang: Zircon U-Pb Geochronology, Geochemistry, and Hf Isotope Constraints. *Acta Petrologica Sinica* 31 (7), 1962–1976. (in Chinese).
- Wang, Y. S., Zou, H., Tu, Q. J., Xu, M., Yang, C., and Fu, Y. Z. (2019). Zircon U-Pb and Molybdenite Re-os Geochronology and Whole-rock Geochemistry of the Baishan Porphyry Mo deposit: Insights into Triassic Mineralisation and Tectonic Setting in the Eastern Tianshan, NW China. *Geol. J.* 55 (6), 4057–4078. doi:10.1002/gj.3654
- Wang, Y. W., Wang, J. B., Wang, L. J., and Long, L. L. (2008). Zircon U-Pb Age, Sr-Nd Isotope Geochemistry and Geological Significances of the Weiya Mafic-Ultramafic Complex, Xinjiang. *Acta Petrologica Sinica* 24 (4), 781–792. (in Chinese).
- Wang, Y.-h., Zhang, F.-f., Liu, J.-j., Xue, C.-j., Li, B.-c., and Xian, X.-c. (2018). Ore Genesis and Hydrothermal Evolution of the Donggebi Porphyry Mo Deposit, Xinjiang, Northwest China: Evidence from Isotopes (C, H, O, S, Pb), Fluid Inclusions, and Molybdenite Re-os Dating. *Econ. Geology*. 113 (2), 463–488. doi:10.5382/econgeo.2018.4558
- Wang, Y., Chen, H., Han, J., Chen, S., Huang, B., Li, C., et al. (2018). Paleozoic Tectonic Evolution of the Dananhu-Tousuquan Island Arc belt, Eastern Tianshan: Constraints from the Magmatism of the Yuhai Porphyry Cu deposit, Xinjiang, NW China. *J. Asian Earth Sci.* 153, 282–306. doi:10.1016/j.jseas.2017.05.022
- Wang, Y., Xue, C., Liu, J., and Zhang, F. (2016). Geological, Geochronological, Geochemical, and Sr-Nd-O-Hf Isotopic Constraints on Origins of Intrusions Associated with the Baishan Porphyry Mo deposit in Eastern Tianshan, NW China. *Miner Deposita* 51 (7), 953–969. doi:10.1007/s00126-016-0646-z
- Wasilewski, P. J., Senftle, F. E., Vaz, J. E., Thorpe, A. N., and Alexander, C. C. (1973). A Study of the Natural α -recoil Damage in Zircon by Infrared Spectra. *Radiat. Effects* 17 (3–4), 191–199. doi:10.1080/00337577308232615
- Weber, W. J., Ewing, R. C., and Wang, L.-M. (1994). The Radiation-Induced Crystalline-To-Amorphous Transition in Zircon. *J. Mater. Res.* 9 (3), 688–698. doi:10.1557/jmr.1994.0688
- Webster, J. D., and Holloway, J. R. (1990). Partitioning of F and Cl between Magmatic Hydrothermal Fluids and Highly Evolved Granitic Magmas/fluids and Highly Evolved Granitic Magmas. *Geol. Soc. America Spec. Paper* 246, 21–34. doi:10.1130/spe246-p21
- Wilkinson, J. J. (2001). Fluid Inclusions in Hydrothermal Ore Deposits. *Lithos* 55 (1–4), 229–272. doi:10.1016/s0024-4937(00)00047-5
- Windley, B. F., Alexeiev, D., Xiao, W., Kröner, A., and Badarch, G. (2007). Tectonic Models for Accretion of the Central Asian Orogenic Belt. *J. Geol. Soc.* 164 (1), 31–47. doi:10.1144/0016-76492006-022
- Wu, C.-z., Liu, S.-h., Gu, L.-x., Zhang, Z.-z., and Lei, R.-x. (2011). Formation Mechanism of the Lanthanide Tetrad Effect for a Topaz- and Amazonite-Bearing Leucogranite Pluton in Eastern Xinjiang, NW China. *J. Asian Earth Sci.* 42 (5), 903–916. doi:10.1016/j.jseas.2010.09.011
- Wu, C.-Z., Xie, S.-W., Gu, L.-X., Samson, I. M., Yang, T., Lei, R.-X., et al. (2018). Shear Zone-Controlled post-magmatic Ore Formation in the Huangshandong Ni-Cu Sulfide deposit, NW China. *Ore Geology. Rev.* 100, 545–560. doi:10.1016/j.oregeorev.2017.02.015
- Wu, C.-Z., Zhang, Z.-Z., Gu, L.-X., Tang, J.-H., and Lei, R.-X. (2010). Sr, Nd and O Isotopic Characters of Quartz Syenite in the Weiya Magmatic Complex from Eastern Tianshan in NW China: Melting of the Thickened Juvenile Lower Crust. *Geochem. J.* 44 (4), 285–298. doi:10.2343/geochemj.1.0072
- Wu, Y. S., Xiang, N., Tang, H. S., Zhou, K. F., and Yang, Y. F. (2013). Molybdenite Re-os Isotope Age of the Donggebi Mo deposit and the Indosinian Metallogenic Event in Eastern Tianshan. *Acta Petrologica Sinica* 29 (1), 121–130. (in Chinese).
- Wu, Y.-S., Zhou, K.-F., Li, N., and Chen, Y.-J. (2017). Zircon U-Pb Dating and Sr-Nd-Pb-Hf Isotopes of the Ore-Associated Porphyry at the Giant Donggebi Mo deposit, Eastern Tianshan, NW China. *Ore Geology. Rev.* 81, 794–807. doi:10.1016/j.oregeorev.2016.02.007

- Xiao, W.-J., Zhang, L. C., Qin, K. Z., Sun, S. H. U., and Li, J. L. (2004). Paleozoic Accretionary and Collisional Tectonics of the Eastern Tianshan (China): Implications for the continental Growth of central Asia. *Am. J. Sci.* 304 (4), 370–395. doi:10.2475/ajs.304.4.370
- Xiao, W., Windley, B. F., Sun, S., Li, J., Huang, B., Han, C., et al. (2015). A Tale of Amalgamation of Three Permo-Triassic Collage Systems in Central Asia: Oroclines, Sutures, and Terminal Accretion. *Annu. Rev. Earth Planet. Sci.* 43 (1), 477–507. doi:10.1146/annurev-earth-060614-105254
- Xu, X.-W., Ma, T.-L., Sun, L.-Q., and Cai, X.-P. (2003). Characteristics and Dynamic Origin of the Large-Scale Jiaoluotage Ductile Compressional Zone in the Eastern Tianshan Mountains, China. *J. Struct. Geology*. 25 (11), 1901–1915. doi:10.1016/s0191-8141(03)00017-8
- Xu, Y. X., Qin, K. Z., Ding, K. S., Li, J. X., Miao, Y., Fang, T. H., et al. (2008). Geochronology Evidence of Mesozoic Metallogenesis and Cenozoic Oxidation at Hongshan HS-Epithermal Cu-Au deposit, Kalatage Region, Eastern Tianshan, and its Tectonic and Paleoclimatic Significances. *Acta Petrologica Sinica* 24 (10), 2371–2383. (in Chinese).
- Yang, W.-B., Niu, H.-C., Shan, Q., Sun, W.-D., Zhang, H., Li, N.-B., et al. (2014). Geochemistry of Magmatic and Hydrothermal Zircon from the Highly Evolved Baerzhe Alkaline Granite: Implications for Zr-REE-Nb Mineralization. *Miner Deposita* 49, 451–470. doi:10.1007/s00126-013-0504-1
- Zhang, D. Y., Zhou, T. F., Yuan, F., Fan, Y., Liu, S., and Qu, W. J. (2009). A Genetic Analysis of Baishan Molybdenum deposit in East Tianshan Area, Xinjiang. *Mineral. Deposits* 5, 152–161. (in Chinese). doi:10.3969/j.issn.0258-7106.2009.05.012
- Zhang, D., Zhou, T., Yuan, F., Fan, Y., Deng, Y., Xu, C., et al. (2014). Genesis of Permian Granites along the Kangguer Shear Zone, Jueluotage Area, Northwest China: Geological and Geochemical Evidence. *Lithos* 198–199, 141–152. doi:10.1016/j.lithos.2014.03.023
- Zhang, D., Zhou, T., Yuan, F., Xiao, W., White, N. C., Deng, Y., et al. (2015). Petrogenesis and Mineralization Potential of a Granite Porphyry Intrusion beneath the Baishan Mo deposit, Eastern Tianshan, NW China. *J. Asian Earth Sci.* 113, 254–265. doi:10.1016/j.jseas.2015.05.002
- Zhang, F., Wang, Y., Liu, J., and Wang, J. (2015). Zircon U-Pb and Molybdenite Re-Os Geochronology, Hf Isotope Analyses, and Whole-Rock Geochemistry of the Donggebi Mo deposit, Eastern Tianshan, Northwest China, and Their Geological Significance. *Int. Geology. Rev.* 57 (4), 446–462. doi:10.1080/00206814.2015.1013067
- Zhang, L., Xiao, W., Qin, K., Qu, W., and Du, A. (2005). Re-Os Isotopic Dating of Molybdenite and Pyrite in the Baishan Mo-Re deposit, Eastern Tianshan, NW China, and its Geological Significance. *Miner Deposita* 39 (8), 960–969. doi:10.1007/s00126-004-0451-y
- Zhang, W., Chen, H., Han, J., Zhao, L., Huang, J., Yang, J., et al. (2016). Geochronology and Geochemistry of Igneous Rocks in the Bailingshan Area: Implications for the Tectonic Setting of Late Paleozoic Magmatism and Iron Skarn Mineralization in the Eastern Tianshan, NW China. *Gondwana Res.* 38, 40–59. doi:10.1016/j.gr.2015.10.011
- Zhang, X., Zhao, G., Sun, M., Han, Y., and Liu, Q. (2017). Triassic Magmatic Reactivation in Eastern Tianshan, NW China: Evidence from Geochemistry and Zircon U-Pb-Hf Isotopes of Granites. *J. Asian Earth Sci.* 145, 446–459. doi:10.1016/j.jseas.2017.06.022
- Zhang, Z. Z., Gu, L. X., Wu, C. Z., Li, W. Q., Xi, A. H., and Wang, S. (2005). Zircon SHRIMP Dating for the Weiya Pluton, Eastern Tianshan: Its Geological Implications. *Acta Geologica Sinica* 79 (4), 481–490. doi:10.1111/j.1755-6724.2005.tb00914.x
- Zhao, H. G., Su, R., Liang, J. W., Wang, J., Jin, Y. X., Ou, G. X., et al. (2017). Petrology, Geochemical Characteristics and Genesis of the Tianhu Pluton in the East Section of the Middle Tianshan Mountains. *Acta Geologica Sinica* 91 (06), 1208–1226. (in Chinese). doi:10.1111/1755-6724.13405
- Zhao, L., Chen, H., Hollings, P., and Han, J. (2019). Tectonic Transition in the Aqishan-Yamansu belt, Eastern Tianshan: Constraints from the Geochronology and Geochemistry of Carboniferous and Triassic Igneous Rocks. *Lithos* 344–345, 247–264. doi:10.1016/j.lithos.2019.06.023
- Zhao, Z. H., Xiong, X. L., Wang, Q., and Qiao, Y. L. (2008). Some Aspects on Geochemistry of Nb and Ta. *Geochimica* 37 (4), 304–320. (in Chinese).
- Zhou, T. F., Yuan, F., Zhang, D. Y., Fan, Y., Liu, S., Peng, M. X., et al. (2010). Geochronology, Tectonic Setting and Mineralization of Granitoids in Jueluotage Area, Eastern Tianshan, Xinjiang. *Acta Petrologica Sinica* 26 (2), 478–502. (in Chinese).

Conflict of Interest: The authors declare that the research was conducted in the absence of any commercial or financial relationships that could be construed as a potential conflict of interest.

Copyright © 2021 Zhi, Lei, Chen, Muhtar, Feng, Zhang, Cai and Wu. This is an open-access article distributed under the terms of the Creative Commons Attribution License (CC BY). The use, distribution or reproduction in other forums is permitted, provided the original author(s) and the copyright owner(s) are credited and that the original publication in this journal is cited, in accordance with accepted academic practice. No use, distribution or reproduction is permitted which does not comply with these terms.



Mineralization of the Tuwu Porphyry Cu Deposit in Eastern Tianshan, NW China: Insights From *In Situ* Trace Elements of Chlorite and Pyrite

Wei Tan^{1,2}, Qigui Mao^{1*}, Mingjie Yu¹, Yan Sun¹ and Xiaoqiang Lv^{1,2}

¹Beijing Institute of Geology for Mineral Resources Co., Ltd., Beijing, China, ²Sino-Zijin Resources Ltd., Beijing, China

OPEN ACCESS

Edited by:

Chang-Zhi Wu,
Chang'an University, China

Reviewed by:

Wei Zhang,
China University of Geosciences
Wuhan, China
Saeed Alirezaei,
Shahid Beheshti University, Iran

*Correspondence:

Qigui Mao
qg_mao@sina.cn

Specialty section:

This article was submitted to
Economic Geology,
a section of the journal
Frontiers in Earth Science

Received: 31 December 2020

Accepted: 10 May 2021

Published: 16 June 2021

Citation:

Tan W, Mao Q, Yu M, Sun Y and Lv X
(2021) Mineralization of the Tuwu
Porphyry Cu Deposit in Eastern
Tianshan, NW China: Insights From *In*
Situ Trace Elements of Chlorite
and Pyrite.
Front. Earth Sci. 9:648177.
doi: 10.3389/feart.2021.648177

The Tuwu porphyry copper deposit is located on the Dananhu-Haerlik island arc in eastern Tianshan, NW China. Based on geology, petrology, and *in situ* trace element studies of pyrite and chlorite, we redefined the characteristics of hydrothermal fluids and the following three mineralization stages: premineralization stage (stage I), porphyry metallogenic stage (stage II), and superimposed transformation stage (stage III). Pyrite stage I (Py-I) has the highest Co/Ni ratios, and the precipitation crystallization of chlorite (Chl-I₂) has the similar rare earth element distribution patterns with those of volcanic rocks Carboniferous Qieshan (CQ), indicating intense volcanic hydrothermal activity. The Co/Ni ratios of Py-II₁ and Py-II₂ (stage II) tend to decrease over time. Moreover, the rare earth element (REE) distribution patterns of Chl-II have similar LREE enrichment, and the Eu anomalies in Chl-II₁, Chl-II₂, and Chl-II₃ range from positive to negative. The initial ore-forming fluid was mainly magmatic hydrothermal fluid, and with the late-stage addition of meteoric water and continuous sulfide precipitation, the trace element composition of the fluid changed, and the whole system became more oxidizing. Py-III (stage III) has the lowest Co/Ni ratios, and the REE distribution pattern of Chl-III is characterized by LREE enrichment. Moreover, the Chl-III shows obvious shear deformation characteristics. The results indicate that the host rocks experienced intensely superimposed reformation. By combining and integrating our results with the regional evolution processes in the eastern Tianshan, we propose that the Tuwu porphyry deposit has undergone magmatic hydrothermal and metamorphic hydrothermal processes. Volcanism (stage I) provided the space and initial conditions for the emplacement of the metallogenic body. With the emplacement of the plagiogranite porphyry (stage II), the main copper mineralization occurred in the porphyry and surrounding rocks. After porphyry mineralization (stage III), regional ductile shearing and collisional compression led to a copper reaction, and its accumulation along the faults formed an ore shoot.

Keywords: porphyry deposits, mineralization, pyrite, chlorite, LA-ICP-MS

INTRODUCTION

The eastern Tianshan orogen, which represents an important part of the tectonic evolution of the Central Asian orogenic belt, has undergone a complicated evolutionary process of stretching, multiblock merging, subduction accretion, collisional orogenesis, and postcollision processes (**Figure 1A**) (Chen et al., 2007; 2012; Pirajno, 2009, 2013; Zhai et al., 2011). Along with the multiple processes of continental accretion, crust-mantle interactions, and transformation in the eastern Tianshan orogen, numerous polygenetic mineral deposits have been formed, and most have been superimposed by late complex ore-forming processes. These deposits include the Honghai (Huangtupo) Cu-Zn deposit (Deng et al., 2016; Mao et al., 2019), Xiaorequanzi Cu-Zn deposit (Long et al., 2019; Mao et al., 2020), Yamaisu Cu-Fe deposit, Hongyuntan Cu-Fe deposit (Sun et al., 2017; Han et al., 2018; Zhang et al., 2018), and Tuwu-Yandong Cu deposit (Wang Y. F. et al., 2016; Xiao et al., 2017). Research on superimposed metallogenic systems is very important for recognizing the regional metallogenic history and guiding mineral exploration activities in the eastern Tianshan.

The Tuwu porphyry copper deposit is located at the southern part of the Dananhu-Haerlik island arc belt (**Figure 1B**). Since the Tuwu copper deposit was discovered by the No. 1 geological party of the Xinjiang Bureau of Geological Exploration in 1994, the Yandong, Fuxing, Yanxi, Linglong, and Chihu copper deposits were consecutively discovered afterward. All of these deposits formed the Tuwu-Yandong porphyry copper metallogenic belt, which has attracted extensive attention. Studies have focused on its geological characteristics (Wang et al., 2001; Rui et al., 2001, 2002; Han et al., 2006; Shen et al., 2014b), metallogenic background, metallogenic characteristics, zoning classification (Shen et al., 2012; Pan et al., 2013; Xiao et al., 2018), geochemistry, geochronology (Rui et al., 2002; Zhang et al., 2006; Han et al., 2014; Shen et al., 2014a; Wang et al., 2014), metallogenic chronology (Rui et al., 2002; Wang et al., 2014; Xiao et al., 2017), and compositions and characteristics of ore-forming fluids (Han et al., 2006; Gao et al., 2015; Wang et al., 2015, 2017). We have found that there are many differences between the porphyry metallogenic system of the Tuwu-Yandong deposit and the classical porphyry metallogenic model. For example, 1) the boundaries of the potassic zone are not obvious, 2) the morphology of the ore body is tabular rather than equiaxial, and 3) the temperature of the ore-forming fluid is obviously lower than that of a typical porphyry copper deposit. These findings indicate that the Cenozoic porphyry mineralization model may not be strictly suitable for Paleozoic porphyry deposits which experienced a multistage structural evolution.

Mineral microanalysis is an important method for defining ore-forming fluid characteristics, metallogenic physicochemical conditions, and ore-forming element migration and enrichment processes (Large et al., 2009; Zhou, et al., 2010; Ye et al., 2011; Zhang, 2011; Reich et al., 2013; Franchini et al., 2015; Zhang et al., 2020). The development of laser ablation inductively coupled plasma mass spectrometry (LA-ICP-MS) analysis technology has

allowed for the measurement of most trace elements in sulfide and oxides. Pyrite is an important sulfide in many metallogenic systems, and its chemical composition is often used to trace the genesis of ore deposits and the metallogenic environment and conditions (Cook et al., 2009; Large et al., 2009, 2011; Reich et al., 2013; Franchini et al., 2015). Chlorite is a mineral that commonly forms during diagenesis, medium- to low-temperature metamorphism and hydrothermal alterations. Due to the variability in its structure and the nonstoichiometry of its composition, chlorite and its paragenetic mineral assemblages are often used to constrain the physicochemical conditions and determine the diagenetic and metallogenic environment (Davidson et al., 2001; Bortnikov et al., 2008; Inoue et al., 2010; Fadda et al., 2012; Wilkinson et al., 2015; David et al., 2016). This study used LA-ICP-MS to analyze the composition of trace elements in pyrite and chlorite in the main alteration zone of the Tuwu copper deposit, and the combination of detailed geological surveys and petrographical studies was used to study the genesis of ore minerals and the characteristics of trace elements and further reveal characteristics of hydrothermal fluids and mineralization processes of the Tuwu porphyry deposit.

REGIONAL GEOLOGICAL BACKGROUND

A review of the regional geology and the tectonic evolution processes of the accretionary orogenic belt from the Precambrian to Triassic are given in Xiao et al. (2004). From north to south, eastern Tianshan consists of the Dananhu-Haerlik arc, Kangguer Forearc, Yamansu arc, Central Tianshan arc, and the South Tianshan (**Figure 1B**).

The Dananhu-Haerlik Ordovician-Carboniferous island arc, as an important Ordovician to Permian metallogenic belt located between the Kalameili and the Kangguer faults (**Figure 1B**), includes the Paleozoic Dananhu-Haerlik arc, the Bogda Late Paleozoic intra-arc basin, and the Kanggur forearc (Xiao et al., 2004, 2015). The Dananhu-Haerlik arc consists of Ordovician to Permian tholeiite to calc-alkaline mafic-felsic volcanic rock, volcanoclastics, tuff, and flysch sediments (Ma et al., 1997; Li et al., 2004; Xiao et al., 2004; Hou et al., 2005; Tang et al., 2006; Mao et al., 2014b, Mao et al., 2016; Deng et al., 2016; Li et al., 2016). The Ordovician to Silurian marine volcanic and volcanoclastic rocks consist of tholeiite to calc-alkaline basalts, andesite-basalts, andesite, high-Mg andesite, and volcanoclastic rocks (Ma et al., 1997; Mao et al., 2014b, 2016; Deng et al., 2016; Li et al., 2016). The Devonian to Carboniferous rocks mainly consists of tholeiite to calc-alkaline basalts, andesite, dacite rhyolite, volcanoclastic rocks, and sedimentary (Ma et al., 1997; Li et al., 2004; Xiao et al., 2004; Hou et al., 2005; Tang et al., 2006; Mao et al., 2014b). The arc-related granitic intrusions are formed from Ordovician to Permian (Song et al., 2002; Li et al., 2004; Chen et al., 2005; Hou et al., 2005; Sun et al., 2005; Wu et al., 2006; Chao et al., 2006; Guo et al., 2006; Mao et al., 2010, 2019; Long et al., 2016; Zhang et al., 2017).

The Bogda intra-arc basin, which formed within the Dananhu-Haerlik arc from the Carboniferous to Early

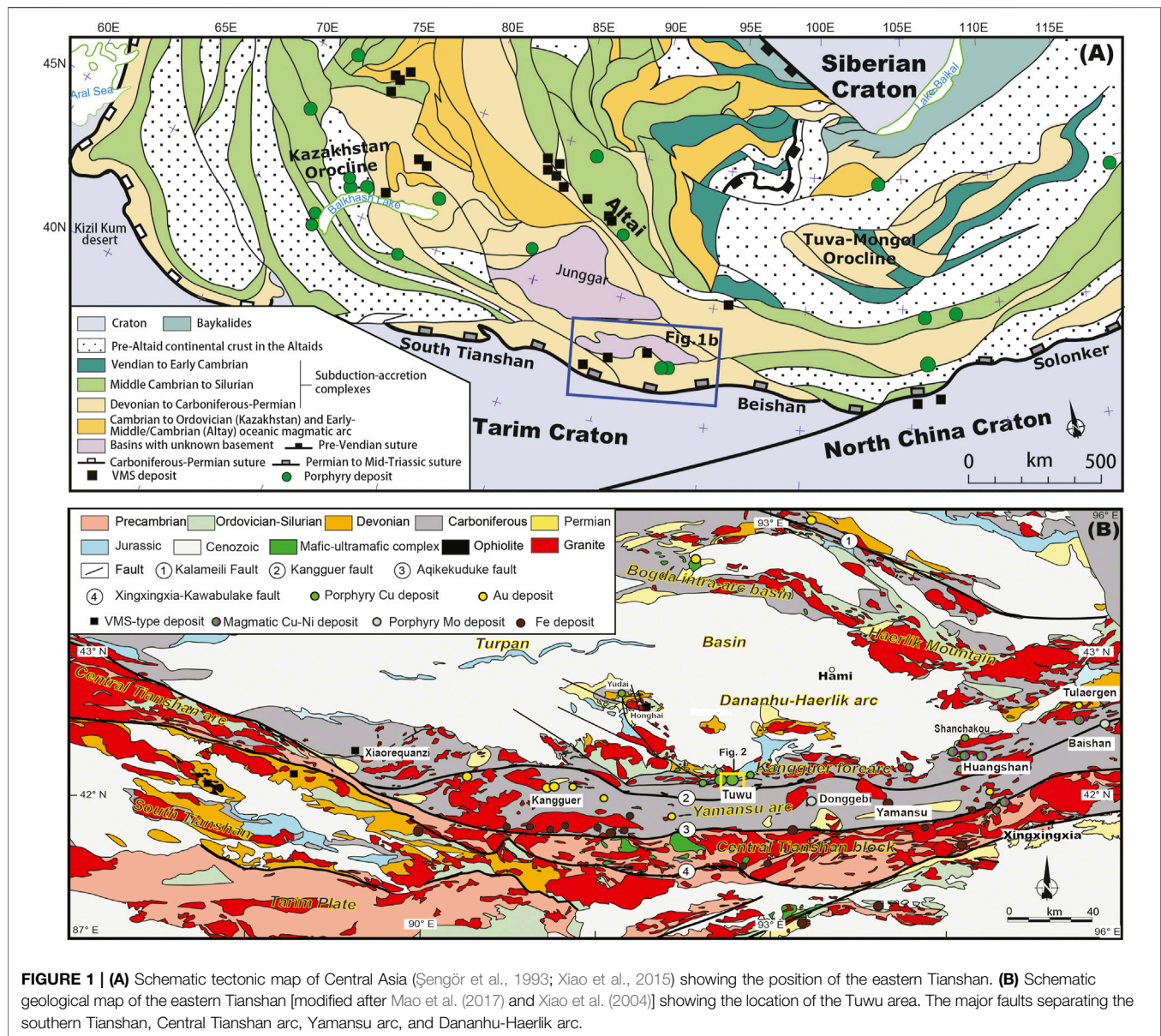


FIGURE 1 | (A) Schematic tectonic map of Central Asia (Şengör et al., 1993; Xiao et al., 2015) showing the position of the eastern Tianshan. **(B)** Schematic geological map of the eastern Tianshan [modified after Mao et al. (2017) and Xiao et al. (2004)] showing the location of the Tuwu area. The major faults separating the southern Tianshan, Central Tianshan arc, Yamansu arc, and Dananhu-Haerlik arc.

Permian, is composed of basalt, dacite, rhyolite, volcanoclastics, minor interbedded andesite, and sedimentary rocks. The mafic to granitic intrusions are mainly Early Permian (Gu et al., 2001a, Gu et al., 2001b; Li et al., 2004; Xiao et al., 2004; Li et al., 2006; Wang et al., 2010; Shu et al., 2011; Chen et al., 2013; Gao et al., 2014).

The Kanggur forearc located at the south margin of the Dananhu-Haerlik arc is made up of structurally dismembered Devonian-Carboniferous volcanic-sedimentary rocks and ophiolitic slices (Yang and Scott, 1996; Ma et al., 1997; Zhou et al., 2001; Xiao et al., 2004). The Permian granitoids are extensive, and a zone of earlier Permian mafic-ultramafic complexes is located along the Kanggur forearc terrane and stretches several hundred kilometers (Ma et al., 1997; Mao et al., 2002; Han C. M. et al., 2004; Xiao et al., 2004; Zhou et al., 2004; Qin et al., 2011). Multiple types of mineral deposits developed in

the Dananhu-Haerlik arc, including porphyry Cu (Au/Mo) deposits (Rui et al., 2002; Chen et al., 2005; Wu et al., 2006; Zhang et al., 2006; Shen et al., 2014; Wang et al., 2015; Mao et al., 2018), hydrothermal vein Cu (Au) deposits (Fang et al., 2002; Mao et al., 2014a; Yu et al., 2019), Cu-Ni sulfide deposits (Mao et al., 2002; Han B. F. et al., 2004; Xiao et al., 2004; Zhou et al., 2004; Mao et al., 2006; Han et al., 2010; Qin et al., 2011), VMS Cu-Zn-(Au/Ag) polymetallic deposits (Mao et al., 2010, 2019; Deng et al., 2016; Li et al., 2002), and Au deposits (Wang et al., 2006).

The Dananhu-Haerlik island arc, situated north of the Kanggur fault, comprises Paleozoic volcano-sedimentary rocks and Mesozoic to Cenozoic sedimentary rocks, intercalated with volcanic and pyroclastic rocks (Xiao et al., 2004; Hou et al., 2006; Qin et al., 2011). Paleozoic mafic-ultramafic complexes and granites intruded the sedimentary and volcanic rocks and are

associated with some Cu and Au mineralization (Deng et al., 2016; Gao et al., 2015). The Carboniferous rocks are mostly foliated and mylonitized and influenced by ductile shearing processes. Carboniferous acidic igneous rocks and a Permian mafic-ultramafic complex are well developed in this belt and mainly occur in the form of stocks (Han et al., 2006; Pan et al., 2013; Shen et al., 2014b). Late Paleozoic mineral deposits are developed at the southern zone of the Dananhu-Haerlik island arc. These deposits include shear zone-type gold deposits, such as the Tianmu Au deposit and Hongtan Au deposit (Yao, 2006), Cu-Ni sulfide deposits, which are associated with Permian mafic-ultramafic rocks (Wang Y. L. et al., 2016), and Carboniferous-Permian porphyry Cu (Mo) deposits, such as the Tuwu-Yandong Cu deposits (Pirajno, 2013; Shen et al., 2014b) and Sanchakou Cu deposit (Qin et al., 2009).

GEOLOGY OF THE TUWU DEPOSITS

The Tuwu copper deposit is hosted in the Carboniferous Qieshan (CQ) group, diorite porphyrite and plagiogranite porphyry at the northeastern part of the Qieshan anticline (**Figure 2A**). According to previous studies (Han et al., 2006; Shen et al., 2012; Pan et al., 2013; Shen et al., 2014b), the CQ group can be divided into five lithologic members (**Figure 2A**). The first lithologic member (CQ¹) is volcanic effusive facies distributed symmetrically around the volcanic crater. The lithology is mainly basalt, followed by andesite, tuff, dacite, breccia lava, volcanic breccia, and other volcanics. Additionally, dioritic porphyrite, which is the main ore-hosting rock, is located at the contact between the basalt in CQ¹ and the pebble-rich lithic sandstone in CQ³. The second lithologic member (CQ²), which is an explosive volcanic facies, is located in the north-central part of the mining area near the center of volcanism. The lithology is agglomerate breccia lava and minor andesite and basalt. The second lithologic group can be divided into three lithologic members. The third lithologic member (CQ³) is distributed in a nearly east-west direction in the northern part of the mining area. The lithology is mainly volcanic-sedimentary facies. CQ³ is a pebble-rich lithic sandstone that contains basalt and andesite layers. The fourth lithologic member (CQ⁴) is distributed in the southern part of the mining area in a nearly east-west direction along the northern side of the Kangguer fault. The lithology is mainly pebble-rich sandstone and minor basalt and volcanic breccia at the top. The fifth lithologic member (CQ⁵) is in angular unconformable contact with the underlying breccia lava of CQ². The lithology is mainly heterolithic conglomerate with lenticular feldspathic lithic sandstone. The volcanic rocks of the CQ Group constitute a relatively complete volcanic eruption cycle and resulted from Carboniferous magmatism in this area. The CQ group strikes nearly east-west and dips to the south at angles of approximately 40–65°. The upper Carboniferous Gandun formation (C_{2g}) is distributed in the southern part of the mining area in a nearly east-west direction along the southern side of the Kangguer fault. The lithology is phyllonite, carbonaceous phyllonite and tuff, which have been altered by regional ductile shear deformation metamorphism. The Jurassic Xishanyao formation (Jx) is covered

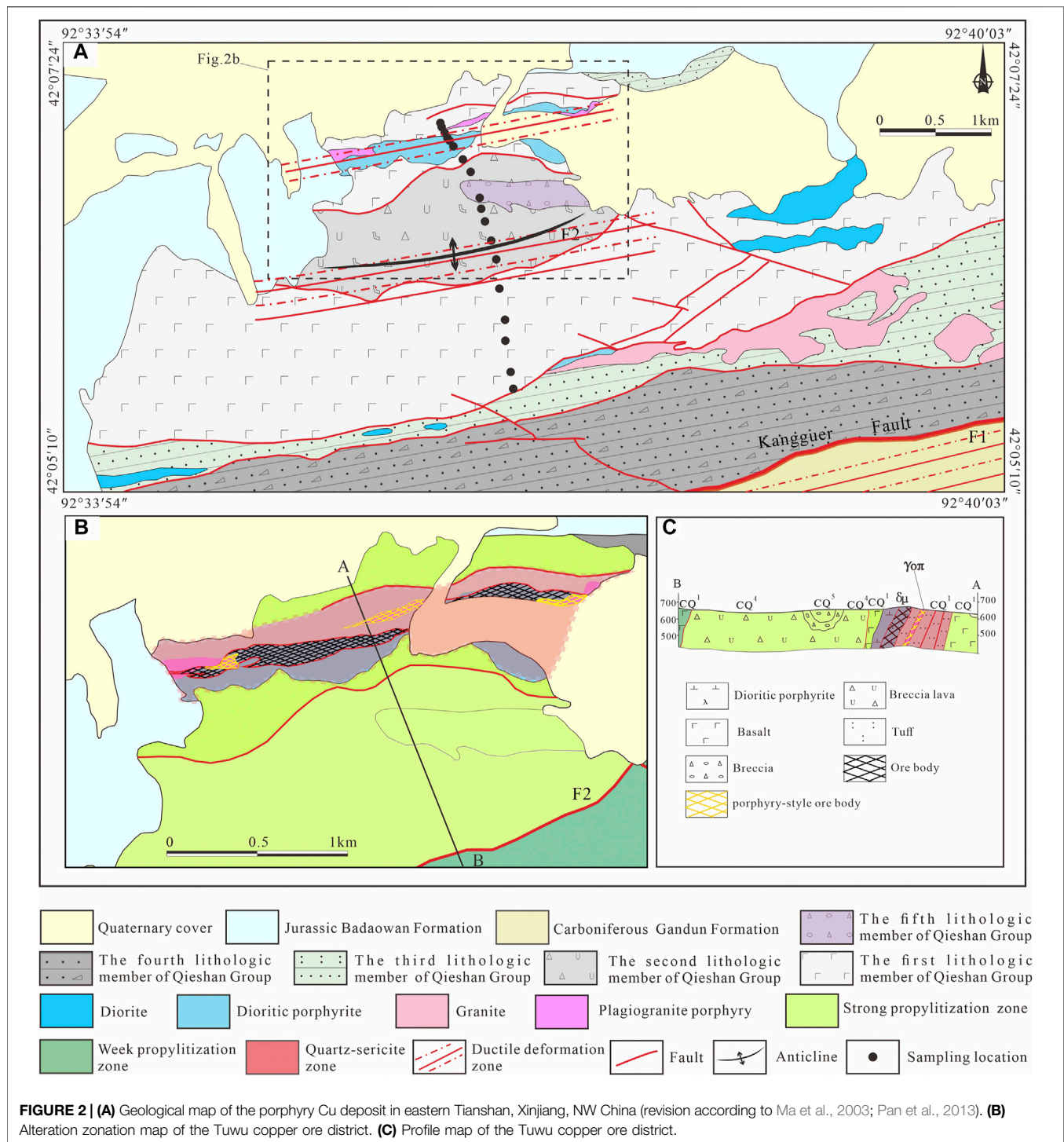
in cap rock and exposed in the northern part of the mining area. The lithology is mainly sandstone, siltstone, mudstone, and conglomerate.

The magmatism was developed quite intensely in the Tuwu-Yandong ore district. The intrusive rocks mainly include granite, plagiogranite porphyry, diorite and diorite porphyry. The Carboniferous metallogenic plagiogranite porphyry of the Tuwu deposit occurs as a small stock (Cheng et al., 2005; Wang et al., 2014; Xiao et al., 2018). The plagiogranite porphyry cut through the dioritic porphyrite and intrude into the contemporaneous volcanism-related fault with an E-W trend (Pan et al., 2013). The dioritic porphyrite is the main ore-hosting rock and belongs to subvolcanic rocks (Hou et al., 2005, 2006; Zhao et al., 2014). It cuts through the basalt in CQ¹ and the pebble-rich lithic sandstone in CQ³, thus forming an east-west-trending stock or dike (Shen et al., 2012) (**Figure 3**).

The Tuwu deposit is located in the northeastern part of the Qieshan anticlinorium (**Figure 2A**). The direction of fracture development is mainly east-west, followed by northwest-southeast. The copper ore bodies mainly occur in the dilated portion of the east-west fault. The intensity of the ductile deformation zone in the Tuwu-Yandong mining area is stronger in the south and weaker in the north. The southern part of the ore field features a continuous strong ductile zone, whereas the northern part is a weakly ductile deformation zone composed of several discretely distributed small lenticular and zonal ductile deformation zones. The copper ore body is distributed in an en echelon shape both in cross section and in map view. In general, the ore-controlling brittle-ductile shear zone is a ENE-trending tectonic belt that dips southward (Ma et al., 2003). The exploration data show that the schistosity obviously cuts the strata and ore body, indicating that the ore body suffered late brittle-ductile deformation. However, distinguishing radial and annular contemporaneous faults from the effect of brittle-ductile deformation is difficult.

The ore mainly has medium- to fine-grained hypidiomorphic-xenomorphic granular textures (**Figure 4**; **Figure 5**). The ore structure mainly includes veins and dissemination. The metallic minerals are mainly chalcocite, followed by pyrite and bornite, with minor chalcocite, covellite, magnetite, hematite, and molybdenite. Pyrite is mainly developed at the top and bottom of the ore body and it is negatively related to copper minerals. The gangue minerals are mainly quartz, sericite and chlorite, followed by biotite, epidote, actinolite, gypsum, feldspar, and calcite. The supergene minerals are malachite, atacamite, and limonite.

Propylitization is extensively developed in the volcanic-pyroclastic rocks of the CQ Group. According to systematic alteration mapping and a comprehensive laboratory study, we find that weak propylitization related to volcanic hydrothermal activity in the late volcanic activity is concentrated in the range of 1.2–3 km from the ore body while strong propylitization obviously superimposed by late hydrothermal activity is concentrated in the range of 0–1.2 km. The alteration intensity differs significantly between these zones, with the F2 fault as the dividing line. The altered minerals associated with weak



propylitization are chlorite, epidote, quartz, zoisite, calcite, and pyrite, and the rock color is dark green in general (**Figures 4A,F; Figure 5A**). Chlorite is mainly in the form of interstitial mafic minerals developed between feldspars. The formation of chlorite is related to the late hydrothermal alteration of dark minerals, such as amphibole. Epidote mainly exists discontinuously in the form of veins in faulted structures.

Pyrite grains with particle sizes of 0.01–0.05 nm exhibit a stellate distribution.

The concentric alteration zones from the interior outward in succession are the potassic zone, the quartz–sericite zone, and the propylitic zone.

The potassic zone is mainly distributed in plagiogranite porphyry and dioritic porphyrite. The alteration mineral

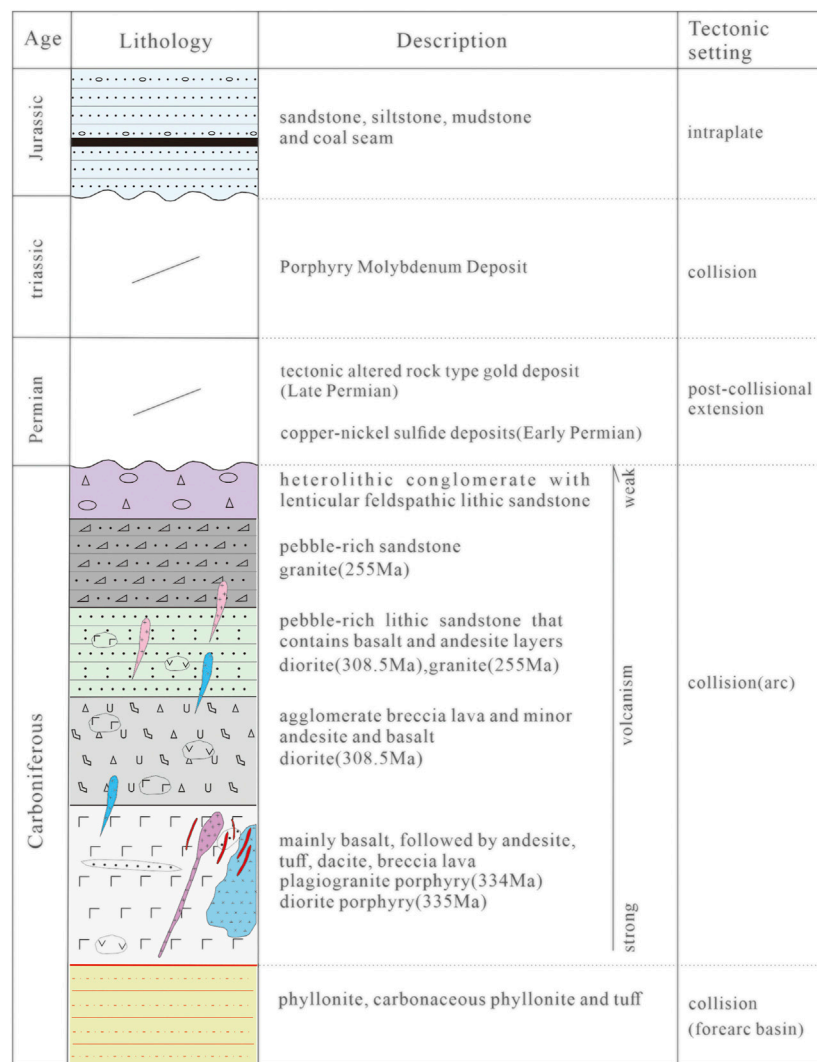


FIGURE 3 | The chronostratigraphic chart of geological events in Tuwu copper ore district.

assemblage of disseminated and vein types includes potassium feldspar, biotite, and magnetite. The fine-grained and scaly biotite originated from biotitization of hornblende and recrystallization of primary biotite. The hydrothermal biotite is poorly preserved and often altered into chlorite, ilmenite, and rutile. Identifying the potassic zone is difficult because it has been altered by later hydrothermal activity. Consequently, the boundary of the potassic zone is not clear. Pyritization, sericitization, and silicification are well developed in plagiogranite porphyry (**Figures 4C,H**). Plagioclase has been almost completely altered to sericite and fine-grained quartz. Pyrite is also widespread (**Figures 5B,C**). The alteration assemblage is mainly sericite, pyrite, quartz, chalcopryite, and calcite with net veins and disseminated forms. The dioritic porphyrite is locally developed and sericitized. Plagioclase has been altered to sericite and minor epidote and albite. The alteration assemblage is sericite, chlorite, pyrite, epidote, and quartz (**Figures 4D,I,J; Figures 5D–F**).

The strongly propylitized rocks are bright green in color and exhibit strong silicification. The alteration assemblage is mainly epidote, chlorite, quartz, calcite, and pyrite. Quartz, epidote, and chlorite are mainly distributed in dense disseminated and vein forms. The disseminated quartz is mainly associated with propylitic alteration, while the vein quartz that appears to have a hydrothermal filling genesis is an obviously younger overprinting feature. Radial and granular epidote aggregates can be seen in some veins. The basalt near the ore is altered and contains minor pyrite, epidote, chlorite, quartz, calcite, and chalcopryite veins (**Figures 4B,G**).

Alterations related to ductile shear deformation are developed in the local area and characterized by intense sericitization and chloritization. The altered minerals show obvious crumpled and directional arrangement. The rocks have augen and cataclastic structures. The plagioclase in the dioritic porphyrite has been altered to scaly sericite and fine-grained quartz. Chlorite is present in the form of blocks and stockwork and well

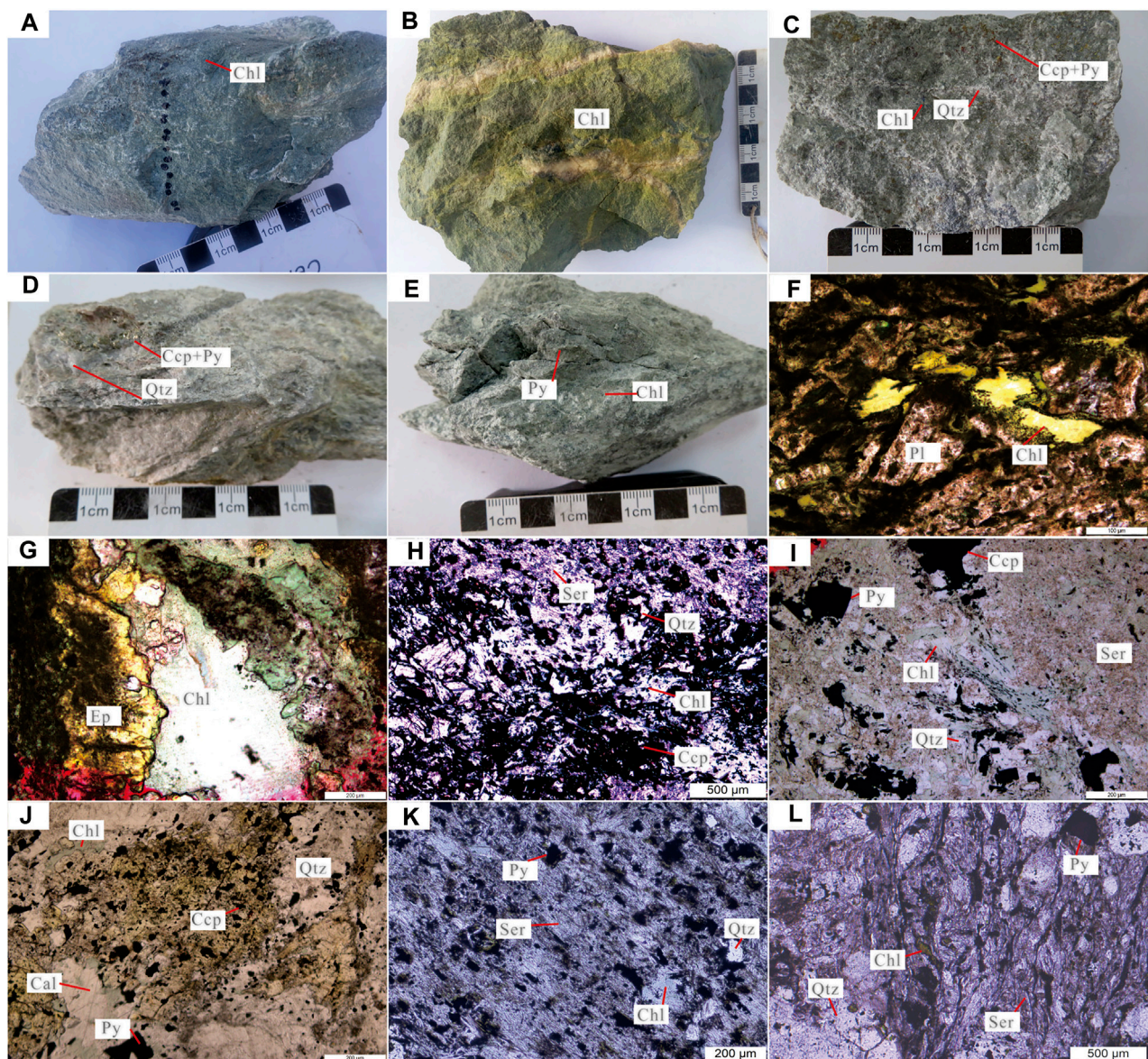


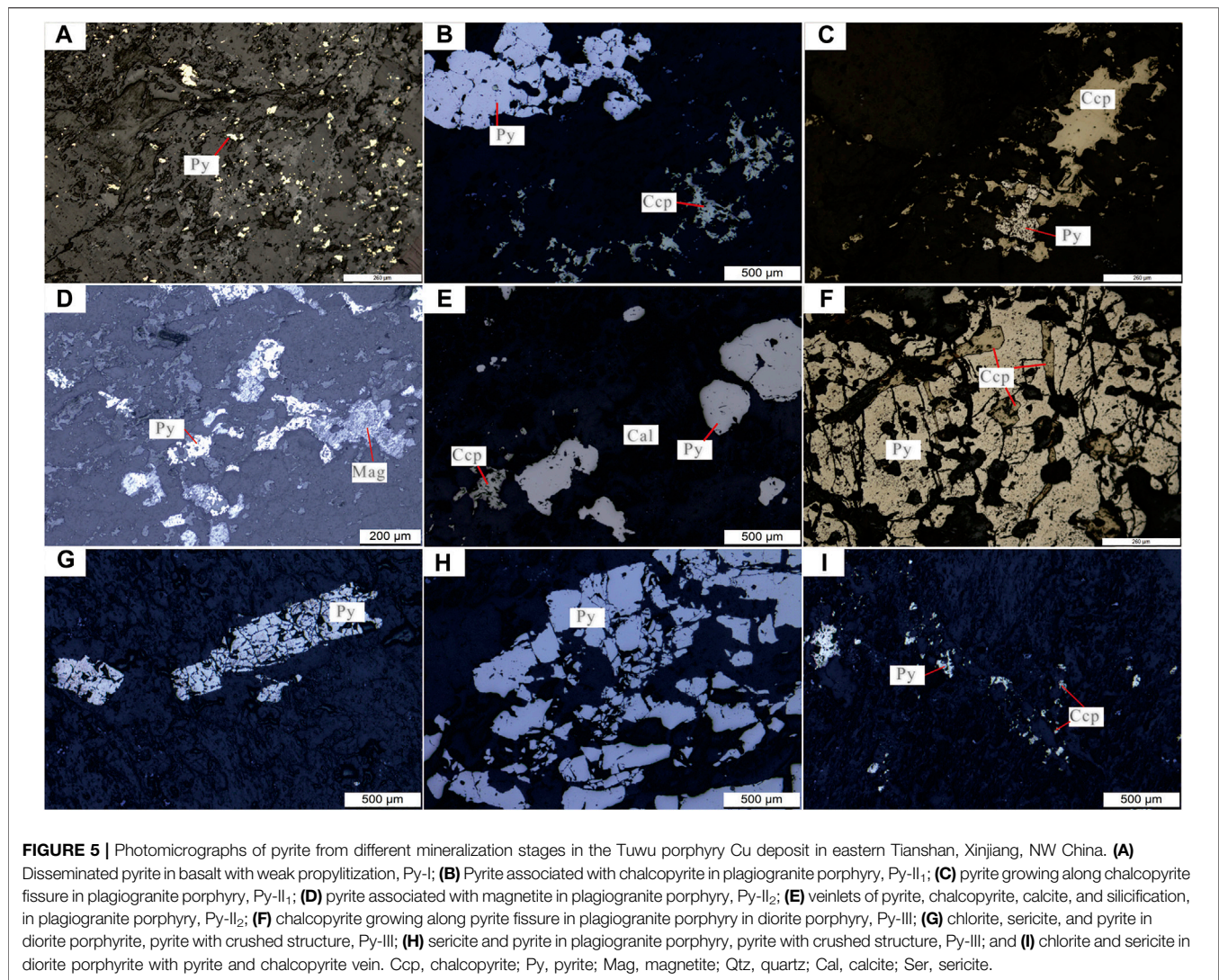
FIGURE 4 | Photomicrographs of the chlorite and specimens of typical ore samples from different mineralization stages of Tuwu porphyry Cu deposit in eastern Tianshan, Xinjiang, NW China. **(A)** Weakly propylitized basalt; **(B)** strongly propylitized basalt; **(C)** pyrite + chalcocite + chlorite + sericite in diorite porphyry; and **(D)** pyrite + chalcocite + silicification development in plagiogranite porphyry; **(E)** mylonitized diorite porphyry; **(F)** weak chlorite development in basalt, Chl-I; **(G)** strong epidote and chlorite development in basalt, Chl-II₁; **(H)** pyritization, sericitization, silicification, and chloritization of plagiogranite porphyry, Chl-II₂; **(I)** sericite, silicification, and chlorite development in plagiogranite porphyry, Chl-II₂; **(J)** chlorite, epidote, pyrite, and calcite development in plagiogranite porphyry, Chl-II₃; **(K)** chlorite, chalcocite, and sericite in diorite porphyry (chlorite, sericite, and pyrite grains have an oriented arrangement) Chl-III; and **(L)** chlorite, chalcocite, and sericite in diorite porphyry rock with an augen structure, Chl-III. Ccp, chalcocite; Py, pyrite; Pl, plagioclase; Chl, chlorite; Ep, epidote; Qtz, quartz; Cal, calcite; Ser, sericite.

developed in the local ductile shear zone (**Figures 4E,K,L**). The altered mineral assemblage is sericite, chlorite, and quartz. The metallic minerals are mainly chalcocite and pyrite, which are distributed in disseminated and vein types (**Figures 5G,H,I**). The alteration zone is related to the rich ore body in this area.

The main supergene alteration mineral assemblage is kaolinite, atacamite, malachite, and hematite.

Previous researchers have conducted a large amount of research on the alteration zonation and metallogenic timing of the Tuwu copper

deposit based on the association of alteration minerals, mineral relationships, and crosscutting relationships (Shen et al., 2012; Pan et al., 2013; Wang Y. F. et al., 2016). After extensive research on the petrography of the main rock types exposed in the Tuwu mining area (**Figures 2B,C**), this study identified four stages of hydrothermal activity, namely, alterations related to volcanic activity (stage I), alterations related to porphyry mineralization (stage II), alterations related to ductile shear deformation (stage III), and alterations related to supergenesis (stage IV) (**Figure 6**).

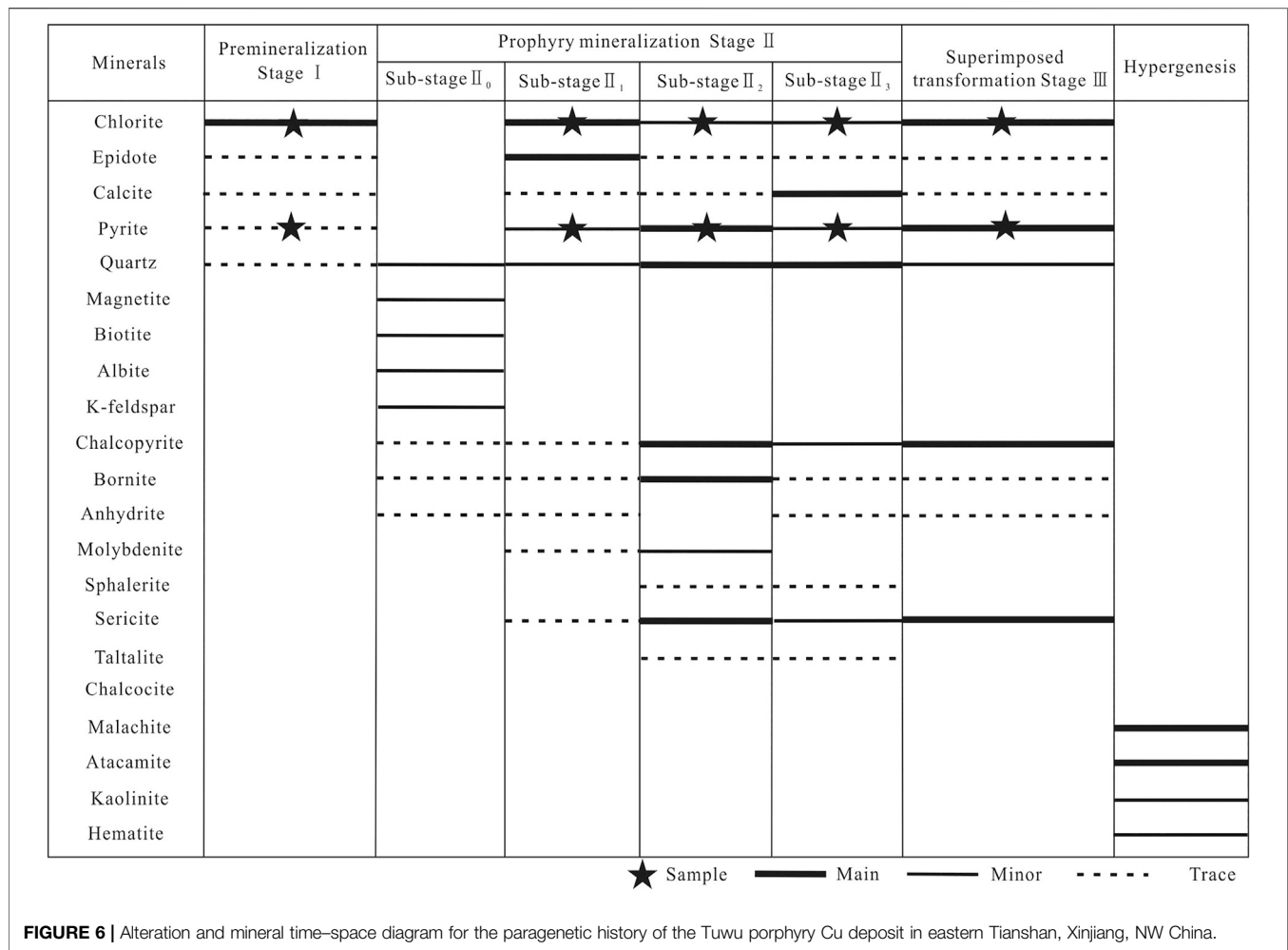


SAMPLING AND ANALYSIS METHODS

This study carried out detailed geological observations and profile surveys of outcrops, troughs, open mining pits and drilling samples from the Tuwu mining area. Typical samples of various alteration zones were collected from the area, and thin sections with a thickness of 0.8 mm were prepared. Two to three typical samples were selected from each alteration zone, and 19 samples were selected for testing and analysis. The mineral types of the tested samples are mainly pyrite Py-I, chlorite Chl-I₁ (metasomatic crystallization), and Chl-I₂ (precipitation crystallization) related to volcanic activity, pyrite Py-II, and chlorite Chl-II related to porphyry mineralization, pyrite Py-III, and chlorite Chl-III related to ductile shear deformation.

The *in situ* analysis of chlorite composition was completed in the LA-ICP-MS laboratory of the State Key Laboratory of Ore Deposit Geochemistry, Institute of Geochemistry, Chinese Academy of Sciences. The LA-ICP-MS instrument is

composed of an Agilent 7700cs quadrupole ICP-MS instrument connected to a GeoLasPro 193 nm LA system. The operating conditions of the instrument were as follows: the laser beam width was 44 nm, the frequency of the laser pulse was 6 Hz, and the pulse energy was 0.032–0.105. The analysis time was 90 s (30 s for the blank test and 60 s for the sample analysis). During testing, the LA spot coincided with the electron microprobe analysis spot. The internal standards NIST610 and NIST612 were analyzed once every nine chlorite samples to monitor the instrument deviation. The international standard samples ML3B-G and BCR-2G were used as unknown samples to monitor the data quality. Data processing was calibrated by Igor-pro software. The Si content was analyzed by electron microprobe as the internal standard to calibrate the Si content determined by LA-ICP-MS. The analysis results of GOR128-G, BIR-1G, BHVO-2G, ML3B-G, and BCR-2G were in good agreement with their reference values. The analytical error of most elements was less than 10%, although Cr, Y, and Zr had errors of 10–15%.



The analysis of pyrite was carried out in the State Key Laboratory of Ore Deposit Geochemistry, Institute of Geochemistry, Chinese Academy of Sciences. The standard sample of the LA system was NWR-213, and the experimental analysis instrument was an Agilent 7700x type quadrupole mass spectrometer. Helium (480 ml/min) was used as a transport medium for the ablated material, and it was mixed evenly with argon (900 ml/min) after leaving the ablation compartment. The mixture then entered the ICP-MS instrument, where the element contents were measured. The analysis time was 90 s (30 s for blank test and 60 s for sample analysis). The laser beam width was 44 nm, the frequency of the laser pulse was 10 Hz, and the pulse energy was 5 J/cm². The analysis method was a multiple external standard—no internal standard method, and the external standards were GSE-1G, MASS, and Py. Data processing was performed with ICPMSDataCal software.

TEST RESULTS

In Situ Trace Element Composition of Pyrite

The results of the *in situ* trace element composition of pyrite in the Tuwu copper mining area are shown in Table 1. Overall, the

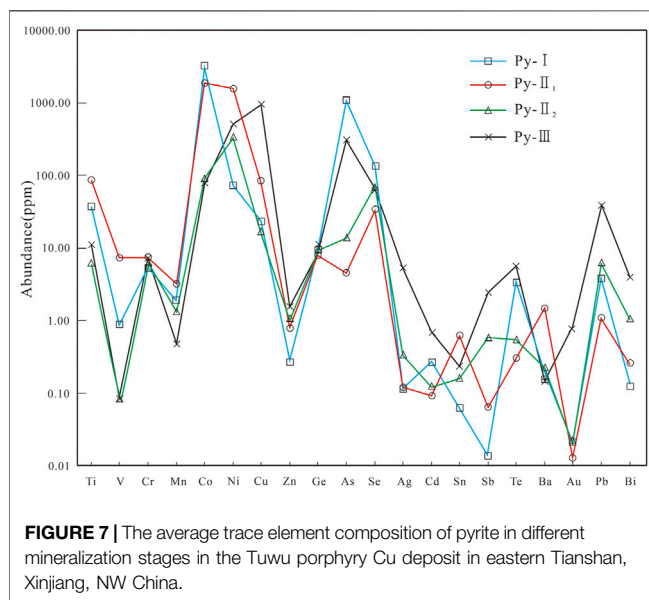
contents of chalcophile elements (Cu, Zn, Pb, As, Se, Te, Ge, and Ag), siderophile elements (Cr, Co, and Ni), V, and Ba are all above the limit of detection. The contents of Sn, Cd, Sb, Au, Bi, and other elements were mostly lower than or near the detection limit (Figures 7, 8).

The results showed that Py-I has the highest total amount of trace elements (average 4,351 ppm) and highest Co/Ni ratio (average 33). Py-I is rich in Co, Ni, and As and poor in Cu and Pb, and the Zn, Au, and Ag contents are below or near the detection limit. The total amount of trace elements of Py-II₁ (average 4,049 ppm) and Py-II₂ (average 544 ppm) displayed an obvious decrease with the occurrence of porphyry mineralization. Moreover, the Co/Ni ratio of Py-II₁ (average 3) and Py-II₂ (average 0.53) also showed a certain decrease. Py-II₁ and Py-II₂ are rich in Co, Ni, and Cu, and poor in As, Pb, Zn, Au, and Ag. The total amount of trace elements in Py-III ranges from 133 to 6,401 ppm (average 1982 ppm). Py-III has the lowest Co/Ni ratio (average 0.16). This phase features obviously higher mineralization element contents than Py-I, Py-II₁, and Py-II₂, and the contents of elements, such as Co, Ni, Cu, Pb, As, Pb, Zn, Au, and Ag, have extremely uneven distributions (Table 1).

TABLE 1 | *In situ* trace element compositions of pyrite for different metallogenic stages of the Tuwu porphyry Cu deposit in eastern Tianshan, Xinjiang, NW China (ug/g).

Trace element (ppm)	Py-I <i>n</i> = 3 (total)	Py-II ₁ <i>n</i> = 11 (total)	Py-II ₂ <i>n</i> = 10 (total)	Py-III <i>n</i> = 6 (total)
V	0.68–1.11; Av = 0.87 (<i>n</i> = 3)	0.06–32.17; Av = 7.34 (<i>n</i> = 11)	0.03–0.29; Av = 0.09 (<i>n</i> = 10)	Mostly bdl; 0.53–0.53; Av = 0.53
Cr	3.02–9.07; Av = 5.65 (<i>n</i> = 3)	1.21–27.41; Av = 7.28 (<i>n</i> = 11)	1.08–18.45; Av = 6.35 (<i>n</i> = 10)	2.25–20.96; Av = 7.56
Co	288.5–6,417.17; Av = 3,027.09 (<i>n</i> = 3)	115.7–6,339.2; Av = 2,260.87 (<i>n</i> = 11)	5.73–318.06; Av = 91.40 (<i>n</i> = 10)	0.65–415.9; Av = 75.21
Ni	25.38–105.89; Av = 71.9 (<i>n</i> = 3)	27.58–3,396.17; Av = 1,635.83 (<i>n</i> = 11)	11.19–1,623.02; Av = 325.23 (<i>n</i> = 10)	47.38–1,298.36; Av = 509.45
Cu	8.95–50.68; Av = 23.16 (<i>n</i> = 3)	0.66–336.25; Av = 86.28 (<i>n</i> = 10)	2.96–43.6; Av = 16.38 (<i>n</i> = 10)	5.94–4,133.8; Av = 950.33
Zn	0.1–0.7; Av = 0.4 (<i>n</i> = 2)	0.13–10.42; Av = 3.13 (<i>n</i> = 6)	0.29–2.61; Av = 1.17 (<i>n</i> = 8)	Mostly bdl; 8.84–8.84; Av = 8.84
Ge	7.87–11.69; Av = 9.15 (<i>n</i> = 3)	6.75–12.88; Av = 9.28 (<i>n</i> = 11)	7.23–13.85; Av = 9.24 (<i>n</i> = 10)	6.17–10.85; Av = 8.38
As	50.73–2,933.98; Av = 1,072.03 (<i>n</i> = 3)	0.27–21.14; Av = 5.03 (<i>n</i> = 10)	0.01–58.85; Av = 16.95 (<i>n</i> = 8)	10.1–1817.01; Av = 913.56
Se	87.3–167.07; Av = 133.16 (<i>n</i> = 3)	21.15–82.59; Av = 39.62 (<i>n</i> = 11)	41.95–174.06; Av = 71.49 (<i>n</i> = 10)	19.65–137.42; Av = 68.10
Ag	0.02–0.16; Av = 0.11 (<i>n</i> = 3)	0.02–0.57; Av = 0.13 (<i>n</i> = 9)	0.02–1.4; Av = 0.37 (<i>n</i> = 9)	0.02–20.22; Av = 5.21
Cd	0.22–0.33; Av = 0.27 (<i>n</i> = 3)	0.1–0.44; Av = 0.24 (<i>n</i> = 6)	0.01–0.49; Av = 0.17 (<i>n</i> = 7)	0.39–1.41; Av = 0.69
Sn	bdl	0.01–3.63; Av = 0.75 (<i>n</i> = 8)	0.01–0.49; Av = 0.26 (<i>n</i> = 6)	0.12–1.07; Av = 0.46
Sb	0.22–0.22; Av = 0.22 (<i>n</i> = 2)	0.01–0.37; Av = 0.09 (<i>n</i> = 6)	0.06–4.8; Av = 0.73 (<i>n</i> = 8)	0.08–14.34; Av = 3.66
Te	0.43–8.24; Av = 3.42 (<i>n</i> = 3)	0.02–0.74; Av = 0.42 (<i>n</i> = 8)	0.01–3.05; Av = 0.68 (<i>n</i> = 8)	0.61–12.15; Av = 5.57
Ba	0.05–0.42; Av = 0.19 (<i>n</i> = 3)	0.03–8.12; Av = 2.18 (<i>n</i> = 8)	0.06–0.91; Av = 0.25 (<i>n</i> = 9)	0.15–0.3; Av = 0.21
Au	0.03–0.03; Av = 0.03 (<i>n</i> = 2)	0.01–0.04; Av = 0.02 (<i>n</i> = 7)	0.01–0.1; Av = 0.03 (<i>n</i> = 7)	0.01–4.91; Av = 1.24
Pb	1.93–6.86; Av = 3.93 (<i>n</i> = 3)	0.02–3.41; Av = 1.16 (<i>n</i> = 11)	0.04–27.01; Av = 5.99 (<i>n</i> = 10)	0.66–164.32; Av = 48.61
Bi	0.09–0.19; Av = 0.12 (<i>n</i> = 3)	0.02–0.79; Av = 0.34 (<i>n</i> = 8)	0.01–6.2; Av = 1.28 (<i>n</i> = 8)	0.01–13.82; Av = 3.39
Co/Ni	11.37–60.60; Av = 33.37 (<i>n</i> = 3)	0.09–9.94; Av = 2.71 (<i>n</i> = 11)	0.12–2.02; Av = 0.53 (<i>n</i> = 10)	0.003–0.57; Av = 0.16
Total content	478.09–9,692.23; Av = 4,351.34 (<i>n</i> = 3)	594–7,839.08; Av = 4,049.19 (<i>n</i> = 11)	125.64–2028.18; Av = 543.68 (<i>n</i> = 10)	132.52–6,401.02; Av = 1982.41

Note: Av stands for average and bdl stands for below the detection limit.



In Situ Trace Element Composition of Chlorite

The results of the *in situ* trace element composition of chlorite in the Tuwu copper mining area are shown in Table 2. To ensure that the mineral in the experiment is chlorite, the chlorite are filtered based on the standard of ω ($\text{Na}_2\text{O} + \text{K}_2\text{O} + \text{CaO}$) < 0.5%

(Foster, 1962; Zang and Fyfe, 1995). According to the Fe-Si classification of chlorite, the chlorite samples are mainly clinocllore and pyrochlore (unpublished data).

In this study, the data show that the total rare earth element (REE) content of chlorite from different stages is above the detection limit, thus, REEs are selected for research. The content of REEs in Chl-I₁ ranges from 0.03 to 17.62 ppm, and the REE patterns are characterized by obvious enrichment of light REEs over heavy REEs (LREE/HREE = 0.12–5.95), negative Eu anomalies ($\delta\text{Eu} = 0.223$ –0.866), and no Ce anomalies ($\delta\text{Ce} = 0.53$ –2.11). The results of (La/Sm)_n (0.14–1.33) and (Gd/Yb)_n (0.95–4.70) indicate that the internal fractionation of LREEs and HREEs is weak (Figure 9A).

The content of REEs in Chl-I₂ ranges from 0.02 to 0.71 ppm, and the REE patterns are mainly characterized by the enrichment of LREEs (LREE/HREE = 0.18–3.91), positive Eu anomalies ($\delta\text{Eu} = 1.0$ –3.78), and weak Ce anomalies ($\delta\text{Ce} = 0.54$ –2.01). The results of (La/Sm)_n (0.07–1.81) and (Gd/Yb)_n (0.22–5.61) indicate that the internal fractionation of LREEs and HREEs is relatively weak (Figure 9B).

The content of REEs in Chl-II₁ ranges from 0.056 to 0.77 ppm, and the REE patterns are characterized by the relative enrichment of HREEs (LREE/HREE = 0.07–0.59), positive Eu anomalies ($\delta\text{Eu} = 1.08$ –1.62), and weakly negative Ce anomalies ($\delta\text{Ce} = 0.43$ –1.52). The results of (La/Sm)_n (0.11–0.497) and (Gd/Yb)_n (1.1–12.02) indicate that the internal fractionation of LREEs and HREEs is stronger (Figure 9C).

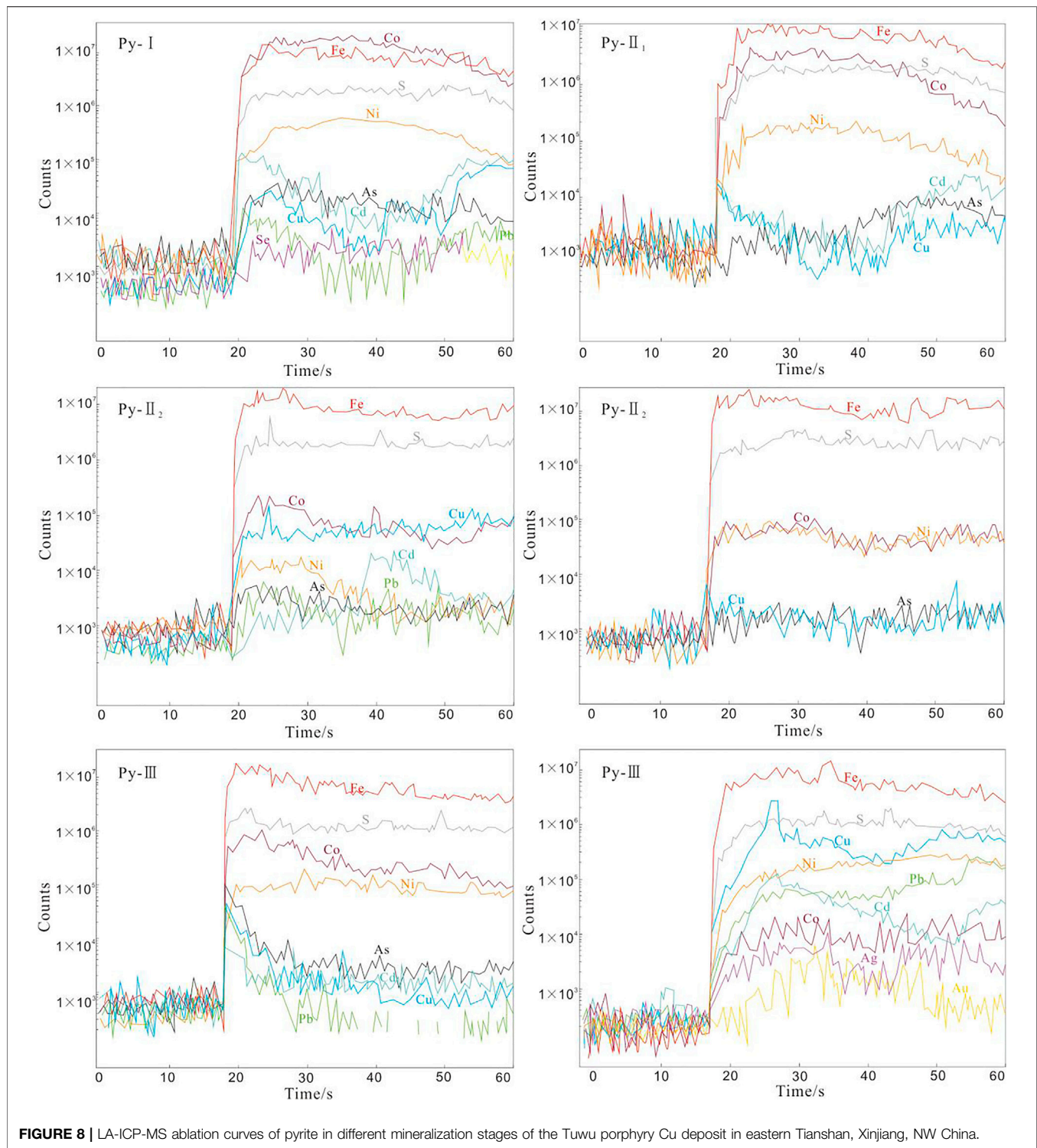


FIGURE 8 | LA-ICP-MS ablation curves of pyrite in different mineralization stages of the Tuwu porphyry Cu deposit in eastern Tianshan, Xinjiang, NW China.

The content of REEs in Chl-II₂ ranges from 0.02 to 3.42ppm, and the REE patterns are characterized by the relative enrichment of HREEs (LREE/HREE = 0.11–1.19), weak positive Eu anomalies ($\delta\text{Eu} = 1.02\text{--}2.52$), and positive Ce anomalies ($\delta\text{Ce} = 0.52\text{--}1.95$). The results of (La/Sm)_n (0.07–0.71) and (Gd/Yb)_n (0.502–11.60)

indicate that the internal fractionation of LREEs and HREEs is strong (**Figure 9D**).

The content of REEs in Chl-II₃ ranges from 0.05 to 3.34 ppm, and the REE patterns are characterized by the relative enrichment of HREEs (LREE/HREE = 0.08–0.85), negative Eu to weakly

TABLE 2 | *In situ* trace element composition and characteristic REE values of chlorite for different metallogenic stages of the Tuwu porphyry Cu deposit in eastern Tianshan, Xinjiang, NW China ($\mu\text{g/g}$).

Trace element	ChI-I ₁	ChI-I ₂	ChI-II ₁	ChI-II ₂	ChI-II ₃	ChI-III
	<i>n</i> = 17 (total)	<i>n</i> = 15 (total)	<i>n</i> = 18 (total)	<i>n</i> = 10 (total)	<i>n</i> = 13 (total)	<i>n</i> = 6 (total)
Na	76.46–1,050.02; Av = 498.1 (<i>n</i> = 17)	76.75–1,413.61; Av = 562.06 (<i>n</i> = 15)	269.87–1,274.41; Av = 637.36 (<i>n</i> = 18)	24.09–1,346.2; Av = 512.28 (<i>n</i> = 10)	20.07–864.1; Av = 202.91 (<i>n</i> = 13)	42–96.48; Av = 66.36 (<i>n</i> = 6)
K	66.64–660.13; Av = 252.8 (<i>n</i> = 17)	79.72–596.30; Av = 274.13 (<i>n</i> = 15)	27.8–398.35; Av = 180.18 (<i>n</i> = 18)	12.58–804.58; Av = 198.13 (<i>n</i> = 10)	11.51–2,164.91; Av = 337.54 (<i>n</i> = 13)	63.82–483.25; Av = 144.47 (<i>n</i> = 6)
Ca	101.30–2,525.45; Av = 828.3 (<i>n</i> = 17)	186.82–2,104.71; Av = 581.74 (<i>n</i> = 15)	219.25–1,550.54; Av = 455.25 (<i>n</i> = 18)	68.92–569.66; Av = 246.97 (<i>n</i> = 8)	10.25–849.34; Av = 203.19 (<i>n</i> = 13)	140–553.39; Av = 310.82 (<i>n</i> = 6)
Ti	12.22–159.33; Av = 29.64 (<i>n</i> = 17)	10.96–573.20; Av = 71.45 (<i>n</i> = 15)	11.07–176.09; Av = 37.54 (<i>n</i> = 18)	19–486.8; Av = 165.92 (<i>n</i> = 10)	21.64–1,055.86; Av = 334.43 (<i>n</i> = 13)	177.9–572.4; Av = 299.68 (<i>n</i> = 6)
V	44.63–210.72; Av = 115.75 (<i>n</i> = 17)	35.38–188.80; Av = 99.53 (<i>n</i> = 15)	38.78–181.6; Av = 103.62 (<i>n</i> = 18)	28.67–933.29; Av = 229.91 (<i>n</i> = 10)	127.41–780.29; Av = 363.64 (<i>n</i> = 13)	153.74–254.63; Av = 214.70 (<i>n</i> = 6)
Mn	1946.41–3,466.17; Av = 2,275.41 (<i>n</i> = 17)	1,376.12–2,973.11; Av = 2,099.84 (<i>n</i> = 15)	2,368.23–3,662.86; Av = 2,711.42 (<i>n</i> = 18)	380.31–2048.76; Av = 1,505.32 (<i>n</i> = 10)	348.55–2,715.22; Av = 1,139.89 (<i>n</i> = 13)	1951.67–2,853.68; Av = 2,247.81 (<i>n</i> = 6)
Ni	153.95–387.96; Av = 309.24 (<i>n</i> = 17)	147.21–397.03; Av = 301.59 (<i>n</i> = 15)	251.76–371.36; Av = 329.01 (<i>n</i> = 18)	80.73–477.43; Av = 325.56 (<i>n</i> = 10)	117.74–382.95; Av = 249.15 (<i>n</i> = 13)	262.68–313.44; Av = 284.64 (<i>n</i> = 6)
Cu	1.81–345.91; Av = 98.07 (<i>n</i> = 17)	3.11–215.25; Av = 106.21 (<i>n</i> = 15)	0.02–388.38; Av = 68.54 (<i>n</i> = 18)	0.05–102.99; Av = 37.96 (<i>n</i> = 7)	0.01–1.03; Av = 0.288 (<i>n</i> = 10)	0.04–1.2; Av = 0.64 (<i>n</i> = 6)
Zn	190.46–411.24; Av = 257.89 (<i>n</i> = 17)	185.61–293.06; Av = 256.57 (<i>n</i> = 15)	157.33–597.87; Av = 251.98 (<i>n</i> = 18)	40.31–395.41; Av = 192.57 (<i>n</i> = 10)	57.63–154.24; Av = 106.17 (<i>n</i> = 13)	154.04–188.16; Av = 168.21 (<i>n</i> = 6)
Ge	0.18–0.76; Av = 0.413 (<i>n</i> = 6)	0.02–1.11; Av = 0.506 (<i>n</i> = 7)	0.02–1.05; Av = 0.576 (<i>n</i> = 15)	2.98–3.66; Av = 3.33 (<i>n</i> = 3)	2.02–4.15; Av = 3 (<i>n</i> = 5)	bdl
Sr	1.79–29.16; Av = 10.94 (<i>n</i> = 17)	0.86–7.49; Av = 4.79 (<i>n</i> = 15)	1.83–7.1; Av = 4.45 (<i>n</i> = 18)	0.51–58.69; Av = 12.79 (<i>n</i> = 10)	0.37–121.19; Av = 17.18 (<i>n</i> = 13)	0.71–2.02; Av = 1.42 (<i>n</i> = 6)
Mo	0.01–0.159; Av = 0.088 (<i>n</i> = 16)	0.13–0.023; Av = 0.071 (<i>n</i> = 15)	0.024–0.13; Av = 0.082 (<i>n</i> = 18)	0.01–0.09; Av = 0.056 (<i>n</i> = 9)	0.012–0.099; Av = 0.045 (<i>n</i> = 12)	0.04–0.34; Av = 0.12 (<i>n</i> = 6)
Cd	0.053–0.107; Av = 0.062 (<i>n</i> = 6)	0.02–0.09; Av = 0.052 (<i>n</i> = 5)	0.0064–0.065; Av = 0.037 (<i>n</i> = 14)	0.07–0.11; Av = 0.09 (<i>n</i> = 2)	0.022–0.15; Av = 0.075 (<i>n</i> = 5)	bdl
In	0.002–0.025; Av = 0.012 (<i>n</i> = 6)	0.005–0.02; Av = 0.011 (<i>n</i> = 6)	0.0012–0.056; Av = 0.022 (<i>n</i> = 15)	0.007–0.013; Av = 0.01 (<i>n</i> = 3)	0.004–0.027; Av = 0.013 (<i>n</i> = 6)	bdl
Sb	0.002–0.456; Av = 0.085 (<i>n</i> = 14)	0.0004–0.62; Av = 0.193 (<i>n</i> = 12)	0.001–0.0186; Av = 0.067 (<i>n</i> = 14)	0.001–0.20; Av = 0.068 (<i>n</i> = 10)	0.003–0.0302; Av = 0.072 (<i>n</i> = 10)	0.11–0.25; Av = 0.2 (<i>n</i> = 3)
La	0.001–2.132; Av = 0.208 (<i>n</i> = 16)	0.0009–0.043; Av = 0.012 (<i>n</i> = 15)	0.0018–0.014; Av = 0.008 (<i>n</i> = 16)	0.001–0.01; Av = 0.008 (<i>n</i> = 10)	0.002–0.045; Av = 0.019 (<i>n</i> = 11)	0.0004–0.0758; Av = 0.03 (<i>n</i> = 6)
Ce	0.003–6.37; Av = 0.566 (<i>n</i> = 17)	0.0008–0.18; Av = 0.037 (<i>n</i> = 12)	0.0038–0.067; Av = 0.027 (<i>n</i> = 18)	0.002–0.1; Av = 0.03 (<i>n</i> = 10)	0.006–0.22; Av = 0.056 (<i>n</i> = 12)	0.011–0.244; Av = 0.099 (<i>n</i> = 6)
Pr	0.001–0.93; Av = 0.101 (<i>n</i> = 14)	0.0007–0.02; Av = 0.059 (<i>n</i> = 15)	0.0008–0.016; Av = 0.007 (<i>n</i> = 15)	0.001–0.01; Av = 0.005 (<i>n</i> = 10)	0.005–0.03; Av = 0.011 (<i>n</i> = 10)	0.001–0.052; Av = 0.022 (<i>n</i> = 5)
Nd	0.008–4.56; Av = 0.506 (<i>n</i> = 14)	0.0056–0.048; Av = 0.026 (<i>n</i> = 12)	0.0086–0.11; Av = 0.038 (<i>n</i> = 16)	0.008–0.12; Av = 0.047 (<i>n</i> = 8)	0.008–0.14; Av = 0.07 (<i>n</i> = 10)	0.029–0.351; Av = 0.144 (<i>n</i> = 5)
Sm	0.007–1.06; Av = 0.155 (<i>n</i> = 12)	0.0005–0.026; Av = 0.013 (<i>n</i> = 11)	0.0039–0.04; Av = 0.024 (<i>n</i> = 16)	0.006–0.05; Av = 0.02 (<i>n</i> = 8)	0.006–0.1; Av = 0.034 (<i>n</i> = 11)	0.007–0.106; Av = 0.053 (<i>n</i> = 5)
Eu	0.002–0.085; Av = 0.017 (<i>n</i> = 13)	0.002–0.021; Av = 0.01 (<i>n</i> = 12)	0.0033–0.02; Av = 0.011 (<i>n</i> = 17)	0.004–0.042; Av = 0.017 (<i>n</i> = 8)	0.002–0.04; Av = 0.015 (<i>n</i> = 11)	0.011–0.047; Av = 0.019 (<i>n</i> = 5)
Gd	0.007–0.847; Av = 0.153 (<i>n</i> = 12)	0.0022–0.064; Av = 0.026 (<i>n</i> = 15)	0.0093–0.084; Av = 0.048 (<i>n</i> = 18)	0.0001–0.125; Av = 0.045 (<i>n</i> = 7)	0.005–0.18; Av = 0.065 (<i>n</i> = 11)	0.008–0.1071; Av = 0.048 (<i>n</i> = 5)
Tb	0.0009–0.12; Av = 0.017 (<i>n</i> = 16)	0.0009–0.014; Av = 0.006 (<i>n</i> = 11)	0.0028–0.024; Av = 0.01 (<i>n</i> = 16)	0.0008–0.045; Av = 0.016 (<i>n</i> = 9)	0.0003–0.04; Av = 0.015 (<i>n</i> = 11)	0.0001–0.025; Av = 0.0068 (<i>n</i> = 6)

(Continued on following page)

TABLE 2 | (Continued) *In situ* trace element composition and characteristic REE values of chlorite for different metallogenic stages of the Tuwu porphyry Cu deposit in eastern Tianshan, Xinjiang, NW China (μg/g).

Trace element	Chl-I ₁ <i>n</i> = 17 (total)	Chl-I ₂ <i>n</i> = 15 (total)	Chl-II ₁ <i>n</i> = 18 (total)	Chl-II ₂ <i>n</i> = 10 (total)	Chl-II ₃ <i>n</i> = 13 (total)	Chl-III <i>n</i> = 6 (total)
Dy	0.0007–0.672; Av = 0.115 (<i>n</i> = 14)	0.0008–0.088; Av = 0.044 (<i>n</i> = 12)	0.039–0.11; Av = 0.078 (<i>n</i> = 17)	0.003–0.454; Av = 0.11 (<i>n</i> = 7)	0.001–0.43; Av = 0.116 (<i>n</i> = 13)	0.016–0.109; Av = 0.054 (<i>n</i> = 50)
Ho	0.002–0.139; Av = 0.028 (<i>n</i> = 15)	0.0001–0.035; Av = 0.01 (<i>n</i> = 14)	0.0085–0.042; Av = 0.021 (<i>n</i> = 16)	0.001–0.134; Av = 0.027 (<i>n</i> = 8)	0.009–0.12; Av = 0.031 (<i>n</i> = 13)	0.0076–0.033; Av = 0.013 (<i>n</i> = 5)
Er	0.002–0.43; Av = 0.085 (<i>n</i> = 16)	0.0028–0.10; Av = 0.037 (<i>n</i> = 13)	0.0058–0.145; Av = 0.071 (<i>n</i> = 18)	0.005–0.796; Av = 0.191 (<i>n</i> = 10)	0.005–0.69; Av = 0.17 (<i>n</i> = 11)	0.006–0.069; Av = 0.03 (<i>n</i> = 6)
Tm	0.0003–0.045; Av = 0.012 (<i>n</i> = 16)	0.0008–0.017; Av = 0.007 (<i>n</i> = 9)	0.0018–0.015; Av = 0.01 (<i>n</i> = 18)	0.0008–0.13; Av = 0.027 (<i>n</i> = 7)	0.0003–0.124; Av = 0.029 (<i>n</i> = 11)	0.001–0.009; Av = 0.004 (<i>n</i> = 6)
Yb	0.005–0.25; Av = 0.073 (<i>n</i> = 17)	0.0059–0.21; Av = 0.054 (<i>n</i> = 12)	0.0236–0.269; Av = 0.087 (<i>n</i> = 18)	0.0001–1.175; Av = 0.206 (<i>n</i> = 9)	0.009–1.094; Av = 0.217 (=13)	0.006–0.027; Av = 0.018 (<i>n</i> = 5)
Lu	0.001–0.034; Av = 0.011 (<i>n</i> = 14)	0.0008–0.029; Av = 0.01 (<i>n</i> = 10)	0.0007–0.037; Av = 0.013 (<i>n</i> = 18)	0.002–0.23; Av = 0.048 (<i>n</i> = 7)	0.0009–0.198; Av = 0.042 (<i>n</i> = 12)	0.0003–0.01; Av = 0.0004 (<i>n</i> = 6)
Ti	0.0008–0.011; Av = 0.006 (<i>n</i> = 5)	0.0009–0.01; Av = 0.006 (<i>n</i> = 6)	0.0003–0.0089; Av = 0.0045 (<i>n</i> = 10)	0.005–0.05; Av = 0.02 (<i>n</i> = 3)	0.004–0.125; Av = 0.029 (<i>n</i> = 6)	bdl
ΣREE	0.03–17.62; Av = 1.8	0.02–0.71; Av = 0.248	0.056–0.77; Av = 0.425	0.02–3.42; Av = 0.66	0.05–3.34; Av = 0.808	0.04–1.27; Av = 0.49
LREE/HREE	0.12–5.95; Av = 1.32	0.18–3.91; Av = 0.96	0.07–0.59; Av = 0.296	0.11–1.19; Av = 0.64	0.08–0.85; Av = 0.55	1.26–3.17; Av = 1.75
(La/Sm) <i>n</i>	0.14–1.33; Av = 0.70	0.07–1.81; Av = 0.64	0.11–0.497; Av = 0.268	0.07–0.71; Av = 0.298	0.124–0.78; Av = 0.37	0.2–0.88; Av = 0.52
(Gd/Yb) <i>n</i>	0.95–4.70; Av = 1.90	0.22–5.61; Av = 2.28	1.1–12.02; Av = 3.33	0.502–11.60; Av = 3.28	0.51–7.38; Av = 2.99	1.8–8.08; Av = 4.84
(La/Yb) <i>n</i>	0.066–6.16; Av = 1.09	0.09–1.09; Av = 0.31	0.01–0.09; Av = 0.06	0.01–8.11; Av = 1.05	0.02–1.93; Av = 0.26	0.57–12.08; Av = 3.89
δEu	0.223–0.866; Av = 0.55	1–3.78; Av = 1.83	1.08–1.62; Av = 1.15	1.02–2.52; Av = 1.36	0.385–1.49; Av = 0.87	0.8–4.27; Av = 1.61
δCe	0.53–2.11; Av = 0.915	0.54–2.01; Av = 0.99	0.43–1.52; Av = 1.03	0.52–1.95; Av = 1.24	0.64–1.5; Av = 1.06	0.73–3.92; Av = 1.53

TABLE 3 | Relationship table between the sequence of events and the chemistry of pyrite and chlorite.

Age		Permian		Carboniferous			
Tectonic setting		Post-collisional extension		Collision			
Stage		Superimposed transformation stage		Porphyry metallogenic stage		Preminalization stage	
Mineral structure		Chl-III (disseminated and vein type with shear deformation characteristics)	Chl-II ₁ (dense disseminated and stockwork type)	Chl-II ₂ (disseminated and vein type)	Chl-II ₃ (mainly disseminated type)	Chl-i ₁ (replacement remnant, pseudomorphic)	Chl-i ₂ (disseminated type)
		Py-III (disseminated and vein type with fragmentized)	Spotted (fine-grained)	Py-II ₁ (disseminated and vein type)	Py-II ₂ (disseminated and vein type)	Py-I (disseminated type)	
Pyrite (ppm)	Co/Ni	0.003–0.57; Av = 0.16	—	0.09–9.94; Av = 2.71	0.12–2.02; Av = 0.53	11.37–60.60; Av = 33.37	
	Co + Ni	313.88–6,523.06; Av = 3,098.99	—	143.28–9,735.37; Av = 3,896.7	16.92–1941.08; Av = 416.63	48.03–1714.26; Av = 584.66	
	Total content	478.09–9,692.23; Av = 4,351.3	—	594–7,839.08; Av = 4,049.19	125.64–2028.18; Av = 543.68	132.52–6,401.02; Av = 1982.41	
	Cu	8.95–50.68; Av = 23.16	—	0.66–336.25; Av = 86.28	2.96–43.6; Av = 16.38	5.94–4,133.8; Av = 950.33	
Chlorite (ppm)	REE	0.04–1.27; Av = 0.49	0.056–0.77; Av = 0.425	0.02–3.42; Av = 0.66	0.05–3.34; Av = 0.808	0.03–17.62; Av = 1.8	0.02–0.71; Av = 0.248
	LREE/HREE	1.26–3.17; Av = 1.75	0.07–0.59; Av = 0.296	0.11–1.19; Av = 0.64	0.08–0.85; Av = 0.55	0.12–5.95; Av = 1.32	0.18–3.91; Av = 0.96
	δEu	0.8–4.27; Av = 1.61	1.08–1.62; Av = 1.15	1.02–2.52; Av = 1.36	0.385–1.49; Av = 0.87	0.223–0.866; Av = 0.55	1–3.78; Av = 1.83
	δCe	0.73–3.92; Av = 1.53	0.43–1.52; Av = 1.03	0.52–1.95; Av = 1.24	0.64–1.5; Av = 1.06	0.53–2.11; Av = 0.915	0.54–2.01; Av = 0.99
	Ti	177.9–572.4; Av = 299.68	11.07–176.09; Av = 37.54	19–486.8; Av = 165.92	21.64–1,055.86; Av = 334.43	12.22–159.33; Av = 29.64	10.96–573.20; Av = 71.45
	Sr	0.71–2.02; Av = 1.42	1.83–7.1; Av = 4.45	0.51–58.69; Av = 12.79	0.37–121.19; Av = 17.18	1.79–29.16; Av = 10.94	0.86–7.49; Av = 4.79

positive anomalies ($\delta\text{Eu} = 0.385\text{--}1.49$), and negative Ce to positive anomalies ($\delta\text{Ce} = 0.64\text{--}1.5$) in general. The results of $(\text{La}/\text{Sm})_n$ (0.124–0.78) and $(\text{Gd}/\text{Yb})_n$ (0.51–7.38) indicate that the internal fractionation of LREEs and HREEs is strong (**Figure 9E**).

The content of REEs in Chl-III ranges from 0.04 to 1.27 ppm, and the REE patterns are characterized by the relative enrichment of LREEs ($\text{LREE}/\text{HREE} = 1.26\text{--}3.17$), positive to weakly negative Eu anomalies ($\delta\text{Eu} = 0.80\text{--}4.27$), and positive to weakly negative Ce anomalies ($\delta\text{Ce} = 0.73\text{--}3.92$). The results of $(\text{La}/\text{Sm})_n$ ($0.20\text{--}0.88$) and $(\text{Gd}/\text{Yb})_n$ ($1.80\text{--}8.08$) indicate that the internal fractionation of LREEs and HREEs is strong (**Figure 9F**).

The *in situ* trace element analysis of chlorite shows that the trace element with the highest content in Chl-I ~ Chl-III is Mn. The contents of Ge, Mo, Cd, In, Sb, and REEs are usually less than 1 ppm, and Mn (348.55–3,466 ppm), Ni (80.73–477.43 ppm), Cu (0.01–388.38 ppm), and Sr (0.37–121.19 ppm) vary in large ranges. The contents of V, Ni, Ti, and Zn mostly range from 100 to 500 ppm.

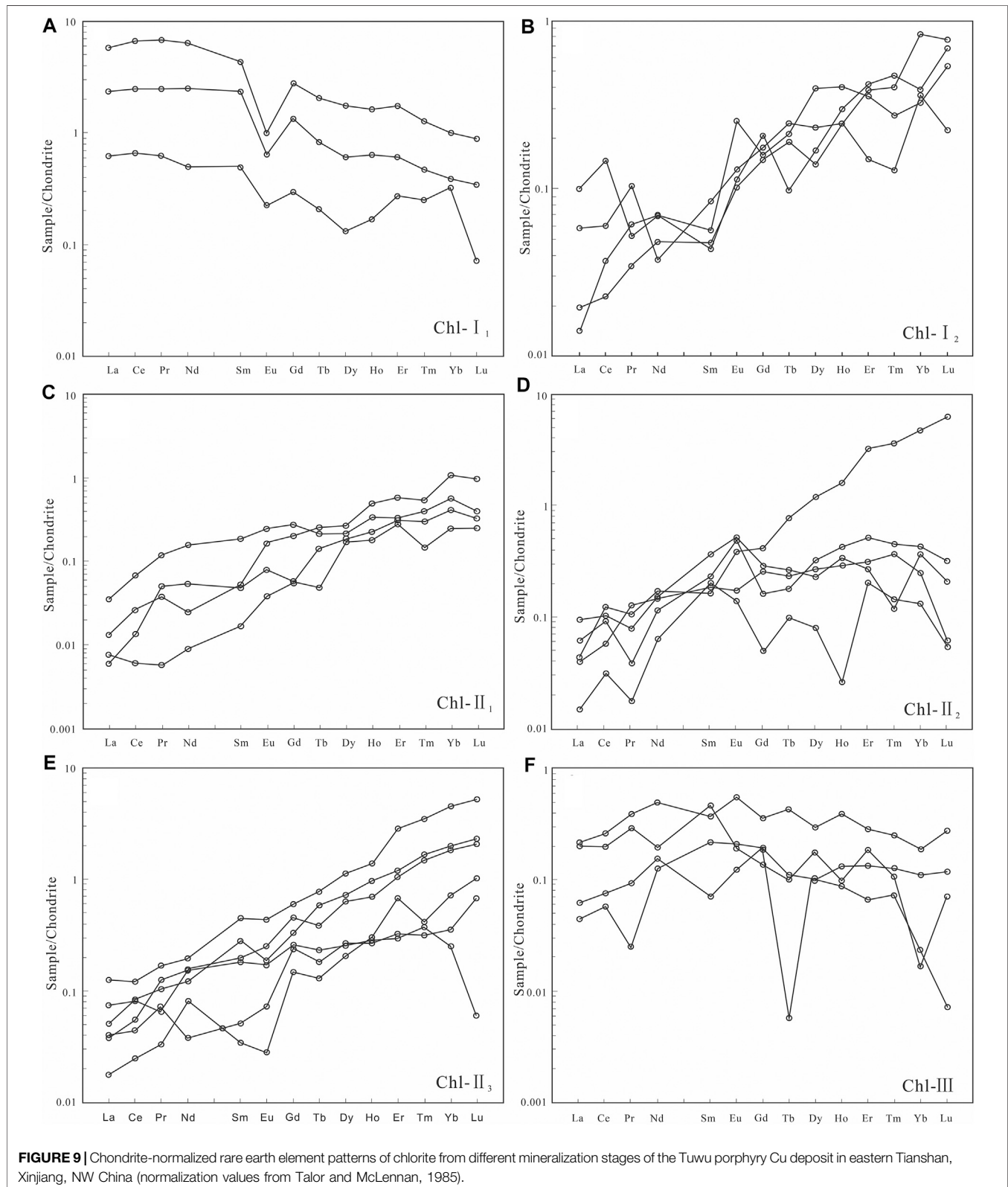
DISCUSSION

Occurrence of Trace Elements in Pyrite

The distribution of trace elements of pyrite is obviously various in the different mineralization stages in the Tuwu copper deposit. Three main occurrence forms of trace elements in pyrite and

other sulfides are observed: 1) in the mineral lattice in the form of isomorphism, 2) in visible micron-scale inclusions of other minerals, and 3) as invisible nanometer-scale mineral particles (Leng, 2017). LA-ICP-MS can not only accurately obtain the content of *in situ* trace elements but also determine the occurrence forms of elements in minerals according to the spatial variation trend of elements with depth during LA (Zhou et al., 2010; Keith et al., 2016). The trend of each element in the LA-ICP-MS time resolution profile shows that the signals of Sb, Se, Co, and Ni are generally stable and basically consistent with the signal distribution of Fe, indicating that Sb, Se, Co, and Ni may exist mainly in the form of isomorphism. Co and Ni replace Fe in pyrite, while Se and Sb can replace S. The ablation signal curves of Cu, Pb, Zn, Cu, and Au are variable and irregular, indicating that these elements mainly exist in the form of microinclusions in pyrite (**Figure 8**).

Moreover, most curves of Cu, Pb, and Ag appeared in local peaks (**Figure 8**), which indicates that Cu, Pb, and Ag elements mainly exist in pyrite in the form of microinclusions (chalcopyrite, galena, and native silver). In the correlation diagram (**Figure 10**), Cu shows a significant positive correlation with Pb and Ag. The degree of correlation was better in Py-II₁ and Py-II₂ than in Py-I and Py-III because Pb and Ag replacements of Fe are difficult by isomorphism, while Cu is known to occur as a substitution for Fe in many Fe-bearing sulfides (i.e., pyrite and pyrrhotite) and silicates (i.e., biotite and hornblende), indicating that more Cu exists in the form of



isomorphism in Py-I and Py-III than in Py-II₁ and Py-II₂. A weak positive correlation occurs between Cu and As in pyrite. The signal distribution of As is consistent with that of Fe. A local peak

of As appears in a small number of samples and corresponds to the high value point of Cu, which indicates that As not only exists in arsenopyrite but also replaces S in pyrite *via* isomorphism. The

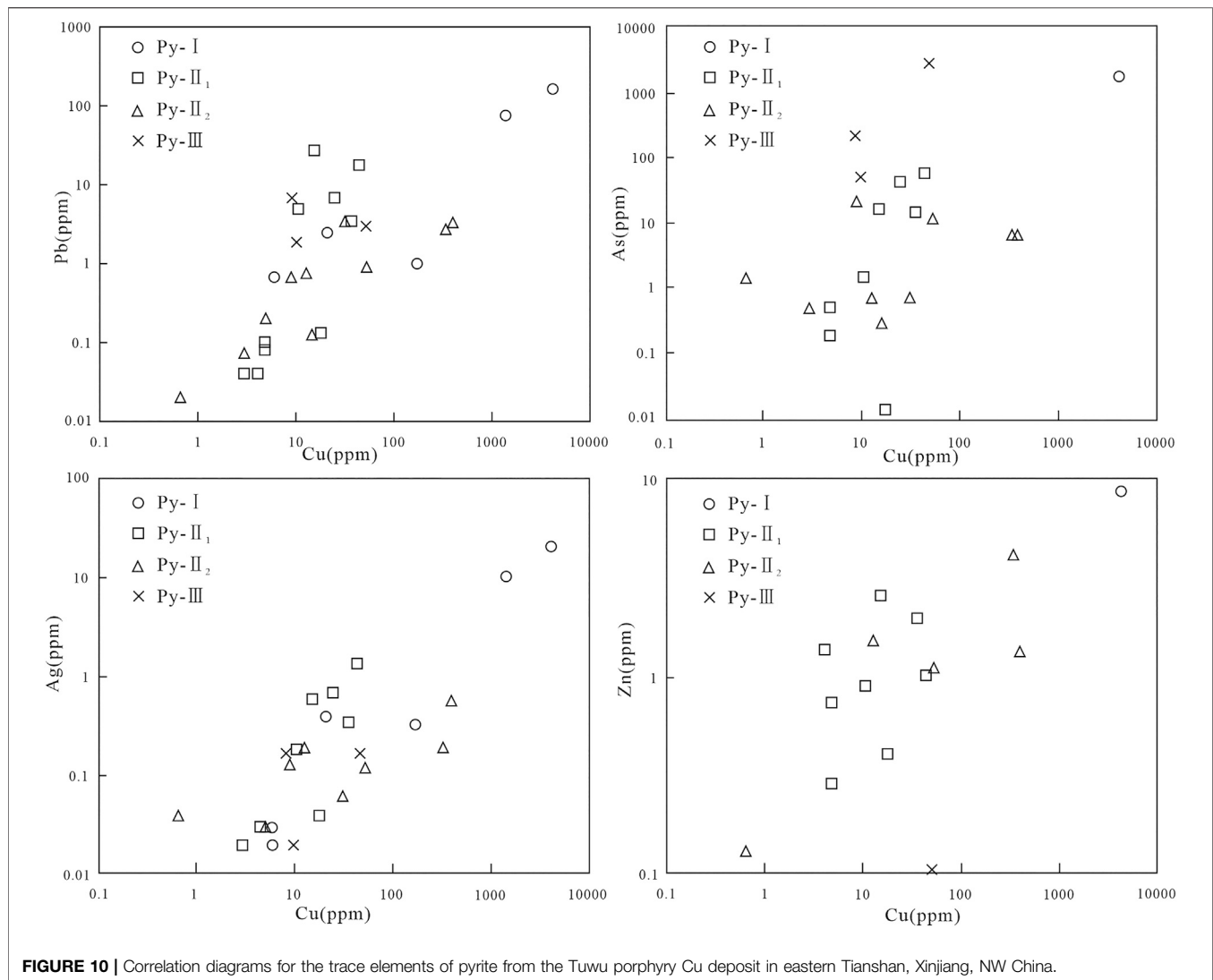


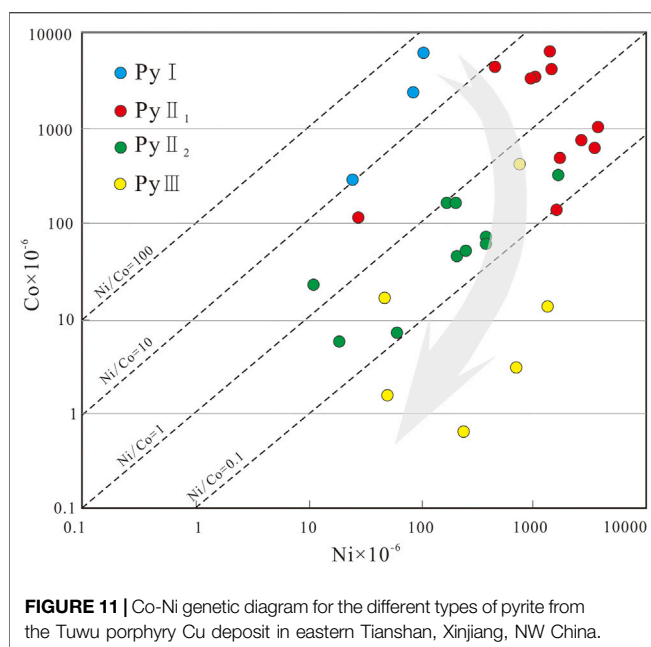
FIGURE 10 | Correlation diagrams for the trace elements of pyrite from the Tuwu porphyry Cu deposit in eastern Tianshan, Xinjiang, NW China.

mass fraction of As fluctuates greatly, with obvious high values in Py-I and Py-III. Above all, these results indicate that the content of As was greatly affected by fluid in later stages, and its content may have a certain effect on the precipitation and occurrence of Cu. Zinc appeared in local peaks (**Figure 8**), which indicates that Zn may exist in the form of sphalerite microinclusions in pyrite, and the content of Zn appears to be highly variable in Py-II1 and Py-III. Moreover, considering that the ionic radius of Zn^{2+} is 0.74 Å and Fe^{2+} is 0.76 Å, Zn may replace Fe in the pyrite lattice *via* isomorphism.

Genesis of Pyrite

Trace elements entering into the pyrite lattice in solid solution form are restricted by the chemical composition of the surrounding rock, mineral assemblage, and fluid properties. Because different hydrothermal fluids usually form under different physicochemical conditions, the contents of trace elements in pyrite vary significantly. Co and Ni are the most common trace elements in pyrite, and their

contents and the Co/Ni ratio are often used to trace the genesis, deposition environment, and formation temperature of pyrite (Bralia et al., 1979; Campbell and Ethier, 1984; Bajwah et al., 1987; Cook, 1996). Different genetic types of pyrite usually have different Co/Ni ratios (Bralia et al., 1979; Brill, 1989; Large et al., 2011). The Co/Ni ratio of synsedimentary pyrite is usually less than 1, whereas the Co/Ni ratio of hydrothermal pyrite varies widely but is generally greater than 1; in particular, the Co/Ni ratio of volcanic hydrothermal pyrite is generally between 5 and 100 (Bralia et al., 1979; Craig et al., 1998; Franchini et al., 2015; Keith et al., 2016) because of the difference in the octahedral site preference energies of Co (7.4 cal/mol) and Ni (20.6 cal/mol) (Bralia et al., 1979). With the process of magma crystallization differentiation, Ni prefers to enter minerals with a high octahedral ratio (such as olivine and orthopyroxene) during early crystallization, while Co becomes relatively enriched in minerals forming in later-stage crystallization, thus causing the Co/Ni ratio of magmatic and hydrothermal pyrite to be greater than 1. Therefore, the Co/Ni ratio of pyrite that precipitated in response to magmatic or



hydrothermal activity is generally greater than 1 (Song and Zhang, 1986; Zhou et al., 2010; Leng, 2017).

The test results show that the Co and Ni contents of pyrite in the Tuwu mining area vary greatly and tend to decrease from Py-I, Py-II₁, and Py-II₂ to Py-III, which reflects the fluid evolution characteristics of the Tuwu mining area to a certain (Figure 11). The Co/Ni ratio of the pyrite in the weakly propylitized zone (Py-I) ranges from 11.37 to 60.60. The siderophile elements Co and Ni are often enriched in basic or ultrabasic rocks. Thus, the anomalous enrichment of Co and Ni elements and high Co/Ni ratios in Py-I reflect a magmatic origin and are closely related to the formation of the CQ group volcanic rocks.

The Co/Ni ratio of the pyrite in the pyritization, sericitization, and silicification zone (Py-II₁) ranges from 0.09 to 9.94 and is generally consistent with the characteristics of magmatic or hydrothermal pyrite. However, the lower the Co/Ni ratio of Py-II₁ is, the more the fragmented pyrite is. Some studies have shown that using the Co/Ni ratio as a criterion to distinguish the boundary of different types of ore deposits is not reliable, especially for hydrothermal deposits (Song and Zhang, 1986; Wang, 1989). Geochemistry characteristics of fluid inclusions and H, O, and S isotopes show that the ore-forming fluid mainly evolved from magmatic hydrothermal fluids, meteoric water, and metamorphic fluid (Liu et al., 2009; Wang et al., 2018). Therefore, Py-II₁ may have been affected by the addition of meteoric water or other fluids in the late stage of mineralization, and the Co/Ni ratio of the pyrite shows certain characteristics of sedimentary origin. Py-II₁ is depleted in low-temperature elements such as As, Se, and Te, which is consistent with the geochemical characteristics of high-temperature hydrothermal pyrite.

The Co/Ni ratio of the pyrite in the sericitization zone (Py-II₂) ranges from 0.12 to 2.02 (average 0.53), and the corresponding data points mainly plot in the field of sedimentary-origin pyrite. The characteristics of trace elements in Py-II₂ indicate the complexity of pyrite genesis. The formation of this pyrite may

have involved the mixing of magmatic hydrothermal fluid and meteoric water. The meteoric water erased most of the magmatic-hydrothermal information. In addition, calcite, a typical low-temperature mineral, is abundant in this stage.

The Co/Ni ratio of the pyrite in the chloritization-sericitization zone (Py-III) ranges from 0.003 to 0.57. Cobalt and Ni in pyrite can form CoS₂ and NiS₂ by replacing Fe *via* isomorphism. The unit cell parameters of pyrite are lengthening because the bond lengths of Co-S and Ni-S are greater than that of Fe-S. Pyrite can form a continuous solid solution series of FeS₂-CoS₂ and a discontinuous solid solution series of FeS₂-NiS₂ (Bralia et al., 1979; Song and Zhang, 1986; Craig et al., 1998). The content of FeS₂-CoS₂ is 2-3 orders of magnitude lower than that of FeS₂-NiS₂ in Py-III. The rocks in the chloritization-sericitization zone are characterized by shear deformation, which manifests as highly schistose local ore bodies and significant elongation of minerals. Overall, the formation of pyrite in this stage appears to involve superimposed transformation by metamorphic hydrothermal fluids, which is consistent with the geochemistry of fluid inclusions and isotopes (Liu et al., 2009; Wang et al., 2018).

The temperature controls the types and contents of trace elements in pyrite. Generally, a higher temperature of formation corresponds to more trace element types in pyrite and a higher content of trace elements (Craig et al., 1998; Large et al., 2007; Keith et al., 2016). Pyrite with different total trace element contents can be divided into three different stages. Comprehensive research on the contents of different trace elements and the Co/Ni ratio in pyrite shows that the total trace element content is highest in Py-I (4,351.34 ppm), which mainly formed in the later period of volcanic activity. The high copper content may reflect the high copper background value of the volcanic rocks in the CQ Group.

The total trace element contents in PyII₁ and PyII₂ are 4,049.19 and 543.68 ppm, respectively. Combined with previous studies of fluid inclusions (Liu et al., 2009; Han et al., 2010; Wang et al., 2018), these results reflect the variation characteristics of trace elements in pyrite from the main mineralizing stage to the late stage of the porphyry mineralization period. The total trace element content in Py-III is 1982.41 ppm. The temperature of the metamorphic hydrothermal fluid is between 150°C and 300°C, and the copper is obviously enriched by the superimposed transformation of the metamorphic hydrothermal solution. This finding explains why the temperature of the main metallogenic stage in the Tuwu copper deposit was approximately 200°C (Liu et al., 2009; Han et al., 2010), which is mainly because earlier high-temperature fluid inclusions were superimposed by ductile shearing.

Rare Earth Element Geochemistry of Chlorite

The geochemical similarity of REEs allows them to be used in tracing applications, which is similar to isotopic values for the process of mineralization (Michard and Albarède, 1986; Maclean, 1988; Fulignati et al., 1999). By studying the REE composition characteristics of minerals from different metallogenic stages, we can determine the geochemical behavior of REEs during the processes of ore formation and alteration (Maclean, 1988;

Chen and Fu, 1991, 1997). Such work can effectively constrain the ore-forming material source, the metallogenic physicochemical environment, the fluid evolution process, and ore genesis (Chen and Fu, 1991; Bortnikov et al., 2008; Parsapoor et al., 2009; Tan et al., 2016, 2018). Research has shown that the geochemical behavior of REEs in minerals is mainly related to the secondary minerals formed by alteration, the content of REEs in hydrothermal fluids, the formation temperature of minerals, the pH and Eh of hydrothermal systems, the crystal chemical properties of minerals, and the partition coefficient of REEs between minerals and fluids (Michard and Albarède, 1986; Michard, 1989; Bortnikov et al., 2008). Previous studies on the REE characteristics of argillization zones (Karakaya et al., 2012), silicification zones (Terakado and Fujitani, 1998; Khalili and Malekmahmoudi, 2012), sericitization–silicification zones (Parsapoor et al., 2009), propylitization zones (Fulignati et al., 1999), and potassic zones (Taylor and McLennan, 1985) show that the contents of REEs differ among different alteration zones.

Rare Earth Element Characteristics of Chlorite in the Premineralization Period

Microstructure research has shown that there are two main formation mechanisms of chlorite in the Tuwu copper deposit: 1. metasomatic crystallization, which is chlorite formation *via* the metasomatism of biotite and hornblende, and in those rocks by late-stage hydrothermal fluids, 2. precipitation crystallization, which is the chlorite precipitated from hydrothermal fluids rich in Fe and Mg in the cracks or gaps between minerals. Metasomatic crystallization chlorite (Chl-I₁) in the weakly propylitized zone mainly formed by late hydrothermal alteration of hornblende, pyroxene, and biotite in basalt. This chlorite generally inherited the REE distribution pattern of the volcanic rocks in the CQ group in the Tuwu mining area (Hou et al., 2005, 2006; Zhao et al., 2014). The precipitation crystallization chlorite (Chl-I₂) is mainly associated with quartz, epidote, and minor pyrite. The REE patterns of Chl-I₂ are characterized by the relative enrichment of LREEs and positive Eu anomalies, which may be due to the Eu in minerals that were in equilibrium with the hydrothermal solution entering the fluid in the form of Eu²⁺ during the rock–water interaction and separated from the other REEs. As a result, Chl-I₁ has stronger negative Eu anomalies than the volcanic rocks. In contrast, Eu is enriched in the fluid, and Chl-I₂, which precipitated from the fluid, has positive Eu anomalies.

The enrichment degree of Eu in the fluid is closely related to temperature. Even in relatively oxidized environments, Eu in hydrothermal solutions mainly exists in the form of Eu²⁺ at relatively high temperatures (Bortnikov et al., 2008; Parsapoor et al., 2009; Fadda et al., 2012). Therefore, Chl-I₂ has a high crystallization temperature, and the total content of REEs in Chl-I₁ is generally 1–2 orders of magnitude higher than those in Chl-II and Chl-III, indicating the characteristics of the fluids related to Chl-I were obviously different from those of the fluids in the metallogenic epoch. The fluid likely was a volcanogenic hydrothermal solution that formed during late volcanic activity. The content of Cu in chlorite is generally high. The closer to the ore body, the higher the Cu content. This

relationship reflects that the volcanic rocks in the CQ group have a high background value of Cu. In addition, the volcanic syngenetic hydrothermal activity primarily led to the enrichment in copper.

Rare Earth Element Characteristics of Chlorite in Porphyry Metallogenic Stage

Similar LREE enrichment is observed in the REE distribution patterns of Chl-II₁, which is associated with epidote, quartz, calcite, and zoisite in the strong propylitization zone. Chl-II₂ is associated with sericite, pyrite, and chalcopyrite in the pyritization–sericitization–silicification zone, and Chl-II₃ is associated with sericite, calcite, pyrite, and chalcopyrite in the sericitization–silicification zone. In addition, the total REE content in Chl-II is significantly lower than that of Chl-I and the Eu anomalies in Chl-II₁, Chl-II₂, and Chl-II₃ range from positive to negative. The reasons for the above REE characteristics in Chl-II are as follows.

- 1) Because chloritization occurs in neutral to alkaline pH conditions with relatively low temperatures (<300°C) (Reed, 1997), the REEs in the fluid mainly form complexes with SO₄²⁻ and CO₃²⁻. While SO₄²⁻ does not preferentially bind with REEs, CO₃²⁻ does preferentially bind with REEs to form complexes (Foster, 1962; Bortnikov et al., 2008; Inoue et al., 2010). The secondary minerals formed from this fluid are relatively rich in heavy REEs.

LREEs have a larger ionic radius and smaller atomic weight than HREEs; therefore, LREEs are more easily leached from minerals (Bortnikov et al., 2008; Ye et al., 2011; Karakaya et al., 2012). The REE patterns of Chl-II are characterized by the relative enrichment of HREEs, indicating that it experienced leaching action of late hydrothermal fluids. Additionally, the similarity in REE distribution patterns indicates that Chl-II₁, Chl-II₂, and Chl-II₃ have the same material source and geochemical behavior.

- 2) Although accessory minerals exist in only very small quantities in most rocks, the REE distribution coefficients in accessory minerals are very high; therefore, they play a great role in controlling the REE content in rocks. The content of REEs in plagiogranite porphyry (24.87–55.88 ppm) is lower than that in volcanic rock (50.64–117.73 ppm) (Wang et al., 2014, 2015; Zhao et al., 2014), and the accessory minerals in plagiogranite porphyry are more than that in the volcanic rock, which causes the content of REEs in Chl-II to be lower than that in Chl-I.
- 3) The stability of Eu²⁺ is controlled not only by the temperature, pH, Eh, and oxygen fugacity of the open system but also by the supply of alteration minerals. Previous studies have found that Eu³⁺ tends to occur under low pH and high oxygen fugacity (Sverjensky, 1984; Bau, 1991; Hedenquist, 1995). The valence state of Eu will transform from Eu³⁺ to Eu²⁺ and fractionate from other REEs³⁺ in a reducing environment, and Eu²⁺ will remain in a stable state under a low oxygen fugacity environment. The Chl-II₁ in the strong propylitization zone and the Chl-II₂ in the

sericitization–silicification zone exhibit positive Eu anomalies, indicating that the hydrothermal system featured a higher temperature (>250°C), a low pH, and relatively reducing conditions and the chlorite generally inherited the REE distribution pattern of the ore-forming fluid. The stronger positive Eu anomalies in Chl-II₂ may be consistent with the large amount of sulfide that crystallized from the ore-forming fluid. With the development of mineralization and the addition of meteoric water, the metallogenic environment will transform from a relatively reducing environment to a relatively oxidizing environment. The occurrence of a large number of low-temperature minerals, such as calcite, indicates that the mineralization temperature has obviously decreased. Chl-II₃ formed at this stage shows obviously negative Eu anomalies. Eu²⁺ has an ionic radius similar to that of Ca²⁺ and often occurs in calcite *via* isomorphism. Therefore, a large amount of calcite precipitation also reduces the content of Eu in the ore-forming fluid.

Rare Earth Element Characteristics of Chlorite in the Superimposed Transformation Period

The chlorite in the rich ore bodies (Chl-III) is characterized by obvious shear deformation characteristics. The REE distribution pattern exhibits LREE enrichment, and the fractionation of HREEs and LREEs is not obvious. This result suggests that the REE distribution pattern of Chl-III is apparently different from that of Chl-I and Chl-II. The formation depth of the Tuwu copper deposit is approximately 2–3 km (Wang et al., 2018). Combined with the significant deformation characteristics of the minerals in the chloritization–sericitization zone, we can infer that the Tuwu copper deposit was located in the brittle-ductile transitional zone. As the water/rock ratio increased, the diffusion pattern of the fluids shifted from percolation to infilling. The REE distribution pattern of Chl-III was mainly controlled by the fluid properties. In addition, the fluid source is also an important factor in determining the composition of REEs. The REE distribution patterns of the plagiogranite porphyry and dioritic porphyrite are generally consistent with that of Chl-III. However, the fractionation of HREEs and LREEs in Chl-III is obviously low, which indicates that the physical and chemical conditions of the Chl-III formation are apparently different from those of Chl-I and Chl-II. The positive Eu anomalies of Chl-III may indicate that Chl-III formed in a relatively reducing environment at relatively high temperatures.

Spatial Variation Pattern of Trace Elements in Chlorite

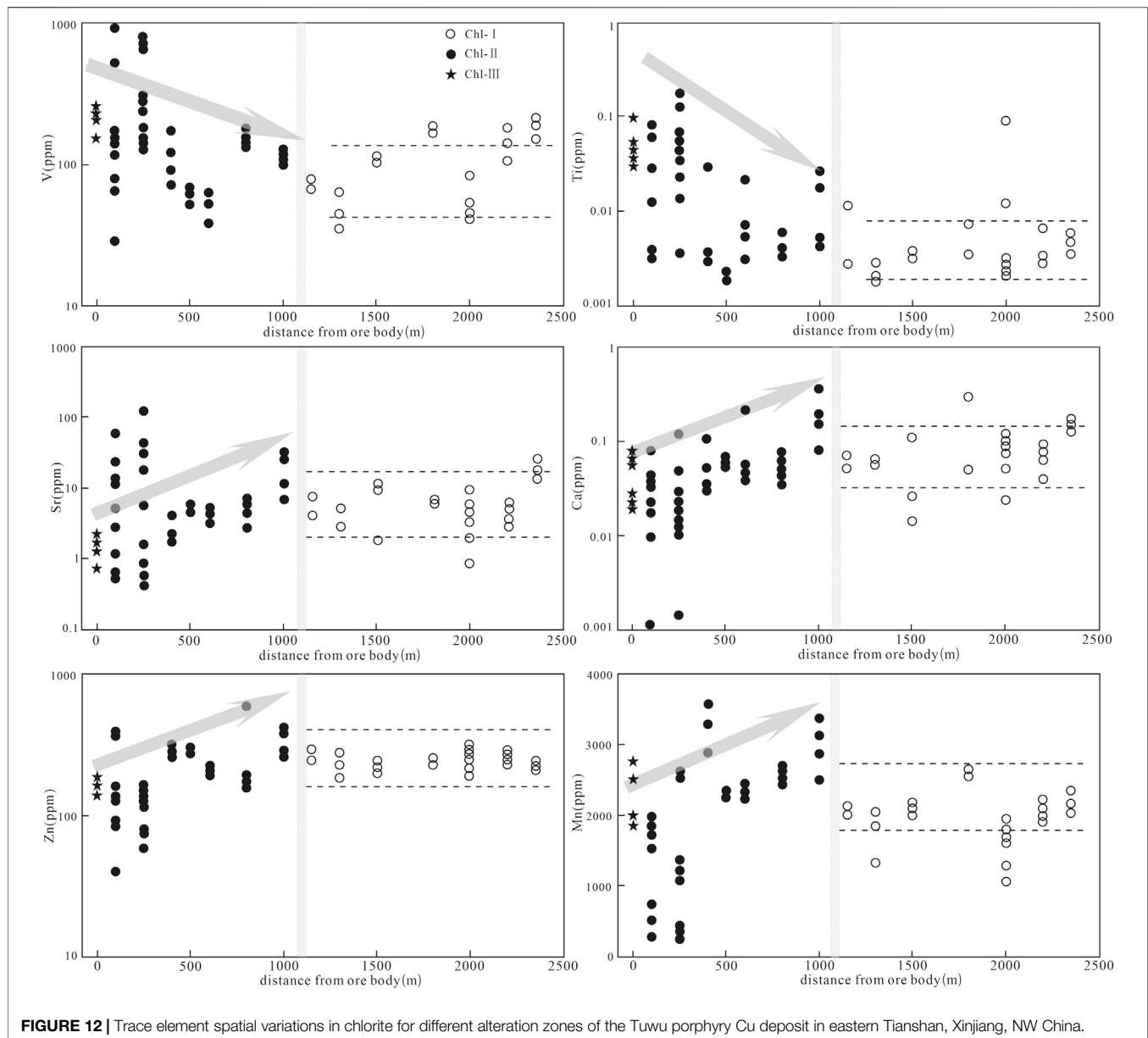
In the formation process of porphyry deposits, a large alteration halo usually occurs around the center of the ore body. In this alteration halo, the mineral association and chemical composition may show certain zonation (Lowell and Guilbert, 1970). The classical metallogenic model of porphyry copper provides theoretical support for exploring porphyry deposits on the regional scale. However, ore bodies of economic value tend to be concentrated in the range of 1 km, and there are many alterations that are irrelevant to the ore-forming process (Inoue et al., 2010; Fadda et al., 2012). Therefore, effective identification

of metallogenic and nonmetallogenic alteration systems is of great significance for the exploration of porphyry deposits. In recent years, the geochemical characteristics of altered minerals have attracted the widespread attention (Inoue et al., 2010; Cooke et al., 2014; Wilkinson et al., 2015; Xiao et al., 2018). Understanding these characteristics not only helps reveal the genesis of ore deposits but also provides technical guidance for prospecting exploration. Currently, based on electron probe and LA-ICP-MS analyses of altered minerals in porphyry systems, scholars have documented spatial variations in trace elements in altered minerals (Cooke et al., 2014; Wilkinson et al., 2015).

These achievements have been applied and verified many times in the field of exploration in China and elsewhere. They are commonly used to assist exploration. The systematic electron probe and LA-ICP-MS analysis of chlorite in the propylitization zone of the Batu Hijau superlarge porphyry copper (gold) deposit in Indonesia has shown that K, Li, Mg, Ca, Sr, Ba, Ti, V, Mn, Co, Ni, Zn, and Pb can enter the crystal lattice of chlorite. With distance from the ore body, the contents of Ti, V, and Mg decrease exponentially, while the contents of K, Li, Ca, Sr, Ba, Mn, Co, Ni, Zn, and Pb increase exponentially (Cooke et al., 2014; Wilkinson et al., 2015; Xiao et al., 2018).

The spatial variations in the trace element compositions in chlorite in the Tuwu mining area are similar to those in the Batu Hijau superlarge porphyry copper (gold) deposit. For example, the contents of high field strength elements, such as Ti and V, are higher in Chl-II and Chl-III near the ore body than in Chl-I far from the ore body. The degree of isomorphism of Ti in chlorite is mainly controlled by the temperature of mineral crystallization (Wilkinson et al., 2015). Therefore, the spatial variation in Ti content in chlorite also provides information on the thermal anomaly around the mineralization center. The variation range of Ti contents in Chl-II and Chl-III can reach 2–3 orders of magnitude within 300 m. However, the migration ability of high field strength elements, such as Ti and V, in hydrothermal fluid is quite limited. The significant differences in Ti content in chlorite in the porphyry mineralization stage in the Tuwu mining area indicate that the migration and diffusion of Ti were affected not only by temperature but also by the repeated action of hydrothermal. Moreover, the Ti contents in Chl-I vary little within a range of 1 km, which suggests that Chl-I in the volcanic rocks mainly formed in the volcanism and was scarcely affected by late hydrothermal activity.

With increasing distance from the ore body, the contents of K, Ca, Sr, Ba, and other large ion lithophile elements decrease but the degree of spatial variation is not as obvious as in a previous study (Wilkinson et al., 2015). This finding shows that the large ion lithophile elements migrated more easily in the late-stage hydrothermal solution. The content ranges of K, Ca, Sr, and Ba in Chl-I are obviously less than those in Chl-II and Chl-III, which suggests that Chl-II and Chl-III were affected by multiple phases of hydrothermal activity. The contents of Mn and Zn in chlorite gradually increase with distance from the center of the ore body, with a maximum value at a distance of approximately 1.2 km; beyond this distance, they gradually decrease until they stabilize. This pattern reflects the horizontal movement of Mn and Zn with the magmatic hydrothermal fluid in the surrounding



rock. The high contents of Mn and Zn in Chl-I reflect the high background values of Mn and Zn in the volcanic rocks in the CQ group (Figure 12).

Influence of Ductile Shearing on the Tuwu Deposit

Although the Tuwu deposit experienced intense superimposed reformation, there are many features and characteristics that match those of a porphyry system. 1) Although most of the Cu in the Tuwu deposit is hosted in the surrounding rock, the ore-bearing plagiogranite porphyries are almost wholly mineralized. 2) Although the shape of the orebodies is mainly tabular, the ore structures are disseminated and veinlet-disseminated and form stockwork. 3) Although the boundaries

of the alteration zone are not obvious, the concentric alteration zones from the interior outward in succession are the potassic zone, the quartz-sericite zone, and the propylitic zone in general.

Compared with young porphyry systems, ancient porphyry systems tend to be subjected to later superimposed transformations. However, few studies have focused on the deformation and mineralization enrichment of porphyry deposits. The following evidence is presented in this article to demonstrate that the Tuwu porphyry deposit has undergone strong deformation and transformation. 1) The Tuwu porphyry deposit has experienced regional ductile shear activity after mineralization. The mining area is located in the northern influence zone of the large Qiugemingtashi-Huangshan ductile shear zone. 2) The intensity of the ductile deformation zone in the Tuwu-Yandong mining area is stronger in the south and weaker in the north. The southern part features a

continuous strong ductile deformation zone and the northern part features a weak ductile deformation zone composed of several discretely distributed small lenticular and zonal ductile deformation zones. The ore has mylonite, augen, and fragmented structures. The mylonitic foliation developed in the ore body provides the main fine structural space for ore minerals (Ma et al., 2002, 2003). These characteristics indicate that the Tuwu mining area formed in the brittle–ductile transition zone. 3) Considerable research has already been done on fluid inclusions in the Tuwu copper deposit. Previous studies have found that the temperatures of the main ore-forming periods are approximately 200°C (Liu et al., 2009; Han et al., 2010), while others found that the temperatures are approximately 350°C (Wang et al., 2015). This discrepancy may be related to the different fluid properties of ore bodies in different positions. 4) Oriented secondary fluid inclusions are well developed in the deformation zone (Liu et al., 2009; Wang et al., 2018), indicating that the shape of the orebody changes from a disseminated low-grade to a vein high-grade orebody by tectonism. 5) The Tuwu mining area can be divided into three tectonic facies according to the characteristics of deformation. The ductile compression zone belongs to the moderately deep ductile deformation facies; the brittle–ductile shear zone belongs to the moderately shallow transition facies between ductile and brittle deformation, and the brittle fault zone belongs to the shallow structural facies. The fact that the moderately deep, moderately shallow, and shallow structures appear on the same plane indicates that they did not form at the same time but are instead the result of superimposing different structures in ore-bearing geologic bodies that have been uplifted several times and that have undergone multiple phases of structural deformation at different depths (Ma et al., 2003). 6) Closer to the ductile deformation zone, the contents of copper, sericite, chlorite, and quartz increase, and the oriented arrangement characteristics of these mineral become more obvious. There are some chalcopyrite and pyrite distributed along foliations of mylonite in the ductile deformation zone, and the chalcopyrite veins filled the fractures in the pyrite. These characteristics indicate that the ore has experienced strong deformation and the copper remobilized. 7) *In situ* trace element analysis of chlorite and pyrite in different stages shows distinctly different geochemical compositions **Table 3**.

The mineralization of the Tuwu and Yandong copper deposits occurred in the early Carboniferous at the southern belt of Dananhu-Haerlik island arc, and these deposits are separated by only 5 km. The ore-forming bodies are all plagiogranite porphyry and have similar mineralization processes (Chen et al., 2005; Hu et al., 2011; Shen et al., 2012; Pan et al., 2013). However, 80% of the Cu in the Tuwu mining area is hosted in the diorite porphyry, while 90% of the Cu in the Yandong mining area is hosted in the plagiogranite porphyry (Hu et al., 2011). The superposition and transformation of late ductile shearing on the two deposits in different spatial positions may be one of the reasons for this difference. The plagiogranite porphyry brought metallogenic materials and formed the initial mineralization of the Tuwu copper deposit, while the late ductile shear process accompanied by strong hydrothermal

activity resulted in the activation and enrichment of copper in the mining area. Moreover, the morphology of the ore bodies is mainly tabular, which is quite different from that of typical porphyry deposits.

These findings may be related to changes in the tectonic environment of the Tuwu mining area caused by ductile shearing to brittle shearing after metallogenesis, which not only led to the activation and migration of copper but also the enrichment of copper in the narrow brittle fractures. Therefore, the ore bodies are characterized by obvious tectonic control.

Mineralization of the Tuwu Copper Deposit

The Tuwu deposit is located approximately 10 km north of the Kangguer fault. The southern part of the Tuwu mining area experienced complicated subduction, island arc growth, plate collision, and ductile shearing from the Carboniferous to Permian. Finally, a faulted structural zone with complex structures and properties developed (Han et al., 2006; Wang et al., 2006; Cai et al., 2012), and the obviously superimposed mineralization characteristics of the Tuwu copper deposit developed. By combining and integrating our results with previously published data on the eastern Tianshan orogens, we suggest the following new model to interpret the evolution of the Tuwu deposit in eastern Tianshan and then provide a short discussion. Stage I: In the early Carboniferous, the northward subduction of the North Tianshan Ocean formed the CQ group volcanic rocks in the southern belt of the Dananhu-Haerlik island arc (Hou et al., 2005, 2006). A series of circular structures and radial structures around the volcanic crater were formed in the Tuwu mining area. The intersections of these structures formed dilational zones that provided the space and initial conditions for the emplacement of the plagiogranite porphyry. Typical minerals in the weakly propylitized zone, such as chlorite, epidote, dolomite, and calcite in the CQ Group volcanic rocks, were formed by volcanic hydrothermal processes. The higher contents of trace elements in pyrite and chlorite show that the mixing action of meteoric water played only a relatively minor role, while the high copper contents reflect the high copper background values of the volcanic rocks and the initial enrichment of Cu by volcanic hydrothermal processes. The volcanic rocks that were far from the ore bodies mainly suffered weakly volcanic hydrothermal process because of the undeveloped fracture system, and the trace element content of chlorite does not change obviously with the spatial position and generally inherited the REE distribution pattern of dark minerals in volcanic rocks **Table 3**.

Stage II: In the early Carboniferous, with the subduction and partial melting of the northern Tianshan oceanic plate at depth under certain physical and chemical conditions, adakitic magmas intruded into the shallow crust and formed the plagiogranite porphyry (Wang et al., 2014; Han et al., 2014; Shen et al., 2014b). The contemporaneous faults of the CQ group provided the tectonic environment for porphyry intrusion. The pyrite that formed in the early stage of porphyry mineralization under high-temperature and high-salinity

conditions has an obvious magmatic-hydrothermal origin. With the development of mineralization, the input of meteoric water, and the long-term metasomatism of fluid in the late stage, the Co/Ni ratio of pyrite continuously decreased. From the early to late stages of porphyry mineralization, the REEs in chlorite show similar distribution patterns, indicating that the fluid had a similar source of ore-forming material **Table 3**. With the addition of meteoric water in the late stage II, the metallogenic system became more open, and the fluid mixing caused mineralogical matter precipitation (Liu et al., 2009; Shen et al., 2014b; Wang et al., 2015; Gao et al., 2017; Wang et al., 2018). As a consequence, the REE composition of the fluid changed, and the metallogenic system became a relatively oxidizing environment.

Stage III: In the Late Carboniferous-Triassic, the North Tianshan oceanic basin subducted and closed along the Kangguer ductile shear zone (Xiao et al., 2004; Mao et al., 2014b; Chen et al., 2019). The Tuwu copper deposit, which underwent multiple phases of compression and shear deformation, is located in the influence zone of the Kangguer ductile deformation zone, and the ore body underwent a strong superimposed transformation. The ore body was obviously mylonitized, and the Co/Ni ratio of pyrite decreased continuously under the action of multiphase fluids. The trace element characteristics of Chl-III also show distinct differences from those of Chl-II in the porphyry metallogenic stage **Table 3**.

CONCLUSION

- 1) We redefined the altered zones and the following three mineralization stages: premineralization stage (stage I), porphyry metallogenic stage (stage II), and superimposed transformation stage (stage III). Pyrite and chlorite are widely distributed in the three mineralization stages and different altered zones. Elements in pyrite, such as Sb, Se, Co, and Ni, mainly occur in the pyrite crystal lattice *via* isomorphism. Cu has obvious positive correlations with Pb, Zn, Ag, and Au in different ore-forming stages, and these elements may occur in the form of microinclusions or nanometer-scale particles.
- 2) The trace element compositions of pyrites from three stages obviously changed, thus reflecting the evolution of fluid properties with the mineralization process. The Co/Ni ratios changed from Py-I (11.37–60.60) to Py-II₁ (0.09–9.94), Py-II₂ (0.12–2.02), and finally Py-III (0.003–0.57), indicating that the fluid evolved from a volcanic genesis to a magmatic hydrothermal genesis. The fluid was affected by meteoric water and other fluids in the late metallogenic period and experienced a superimposed complicated structural hydrothermal fluid.
- 3) The REE distribution pattern of chlorite has obviously different features in the three stages. Chl-I generally inherited the REE distribution pattern of the volcanic rocks in the CQ Group, which shows that the fluid exsolved from the products of late volcanic activity. The similar REE distribution pattern of Chl-II₁ to Chl-II₃ indicates that the fluid had a similar ore-forming material source. The different features from Chl-II₁ to Chl-II₃ show that the fluid

evolved from magmatic hydrothermal to the mixture of magmatic and meteoric fluid. The REE distribution pattern of Chl-III shows that the fluid in ductile deformation zones experienced strong water–rock interactions with the surrounding rocks.

- 4) The contents of Ti, V, and Mg in the chlorite decreased exponentially with increasing distance, whereas the contents of K, Li, Ca, Sr, Ba, Mn, Co, Ni, Zn, and Pb increased. The maximum value appears at approximately 1.2 km and the values then gradually stabilize.
- 5) The Tuwu porphyry deposit has undergone volcanic activity, porphyry metallogenesis, and structural deformation from the early Carboniferous to early Triassic.

DATA AVAILABILITY STATEMENT

The raw data supporting the conclusion of this article will be made available by the authors, without undue reservation.

AUTHOR CONTRIBUTIONS

We the undersigned declare that this manuscript entitled “Mineralization of the Tuwu porphyry Cu deposit in eastern Tianshan, NW China: Insights from *in situ* trace elements of chlorite and pyrite” is original, has not been published before, and is not currently being considered for publication elsewhere. We would like to draw the attention of the editor to the following publications of one or more of us that refer to aspects of the manuscript presently being submitted, where relevant copies of such publications are attached. We confirm that the manuscript has been read and approved by all named authors and that there are no other persons who satisfied the criteria for authorship but are not listed. We further confirm that the order of authors listed in the manuscript has been approved by all of us. We understand that the corresponding author is the sole contact for the editorial process. He is responsible for communicating with the other authors about the progress, submissions of revisions, and final approval of proofs. Signed by all authors as follows: WT, QM*, MY, YS, and XL.

FUNDING

This study was financially supported by the National Key R&D Program of China (No. 2017YFC0601201), Chinese National Basic Research 973 Program (No. 2014CB440803), Ministry of Land and Resources of China (No. 201411026), and the Chinese Geological Survey Project (No. DD20160071).

ACKNOWLEDGMENTS

Han Runsheng of the Kunming University of Science and Technology and Researcher Chen Zhengle of the Institute of Geomechanics provided valuable revision suggestions that improved this paper.

REFERENCES

- Bau, M. (1991). Rare-earth Element Mobility during Hydrothermal and Metamorphic Fluid-Rock Interaction and the Significance of the Oxidation State of Europium. *Chem. Geology*. 93, 219–230. doi:10.1016/0009-2541(91)90115-8
- Bajwah, Z. U., Seccombe, P. K., and Offler, R. (1987). Trace element distribution, Co: Ni ratios and genesis of the Big Cadia iron-copper deposit, New South Wales, Australia. *Mineralium Deposita* 22, 292–300. doi:10.1007/BF00204522
- Bortnikov, N. S., Gorelikova, N. V., Korostelev, P. G., and Gonevchuk, V. G. (2008). Rare Earth Elements in Tourmaline and Chlorite from Tin-Bearing Assemblages: Factors Controlling Fractionation of REE in Hydrothermal Systems. *Geol. Ore Deposits*. 50, 445–461. doi:10.1134/s1075701508060032
- Bralia, A., Sabatini, G., and Troja, F. (1979). A Revaluation of the Co/Ni Ratio in Pyrite as Geochemical Tool in Ore Genesis Problems. *Mineralium Deposita*. 14, 353–374. doi:10.1007/bf00206365
- Brill, B. (1989). Trace-element Contents and Partitioning of Elements in Ore Minerals from the CSA Cu-Pb-Zn deposit, Australia. *Can. Mineral.* 27, 263–274. doi:10.1007/BF01164492
- Cai, Z. H., Xu, Z. Q., He, B. Z., and Wang, R. R. (2012). Age and Tectonic Evolution of Ductile Shear Zones in the Eastern Tianshan-Beishan Orogenic belt. *Acta Petrologica Sinica*. 28, 1875–1895. [in Chinese with English abstract]
- Campbell, F. A., and Ethier, V. G. (1984). Nickel and Cobalt in Pyrrhotite and Pyrite from the Faro and Sullivan Orebodies. *Can. Mineral.* 22, 503–506. doi:10.1007/BF01082965
- Chao, F. G., Tu, Q. J., Zhang, X. M., Ren, Y., Li, G. L., and Dong, F. R. (2006). Preliminary Determination of the Early Paleozoic Magmatic Arc in the Karlik Mountains, East Tianshan, Xinjiang, China-Evidence from Zircon SHRIMP U-Pb Dating of Granite Bodies in the Tashuihe Area. *Geol. Bull. China*. 25, 923–927. doi:10.3969/j.issn.1671-2552.2006.08.004 [in Chinese with English abstract]
- Chen, F. W., Li, H. Q., Chen, Y. C., Wang, D. H., Wang, J. L., Liu, D. Q., et al. (2005). Zircon SHRIMP U-Pb Dating and its Geological Significance of Mineralization in Tuwu- Yandong Porphyry Copper Mine, East Tianshan Mountain. *Acta Geol. Sinica*. 79, 256–261. doi:10.3321/j.issn:0001-5717.2005.02.011 [in Chinese with English abstract]
- Chen, X., Shu, L., Santosh, M., and Zhao, X. (2013). Island Arc-type Bimodal Magmatism in the Eastern Tianshan Belt, Northwest China: Geochemistry, Zircon U-Pb Geochronology and Implications for the Paleozoic Crustal Evolution in Central Asia. *Lithos*. 168–169, 48–66. doi:10.1016/j.lithos.2012.10.006
- Chen, Y.-J., Chen, H.-Y., Zaw, K., Pirajno, F., and Zhang, Z.-J. (2007). Geodynamic Settings and Tectonic Model of Skarn Gold Deposits in China: An Overview. *Ore Geology. Rev.* 31, 139–169. doi:10.1016/j.oregeorev.2005.01.001
- Chen, Y. J., and Fu, S. G. (1991). Variation of REE Patterns in Early Pre-cambrian Sediments: the Oretical Study and Evidence from the Southern Margin of the Northern China Craton. *Chin. Sci. Bull.* 36, 1100–1104. doi:10.1159/000202829 [in Chinese with English abstract]
- Chen, Y. J., and Zhao, Y. C. (1997). Geochemical Characteristics and Evolution of REE in the Early Precambrian Sediments: Evidences from the Southern Margin of the North China Craton. *Episodes*. 20, 109–116.
- Chen, Z., Xiao, W., Windley, B. F., Schulmann, K., Mao, Q., Zhang, Z., et al. (2019). Composition, Provenance, and Tectonic Setting of the Southern Kangurtag Accretionary Complex in the Eastern Tianshan, NW China: Implications for the Late Paleozoic Evolution of the North Tianshan Ocean. *Tectonics*. 38, 2779–2802. doi:10.1029/2018tc005385
- Cook, N. J., Ciobanu, C. L., Pring, A., Skinner, W., Shimizu, M., Danyushevsky, L., et al. (2009). Trace and Minor Elements in Sphalerite: A LA-ICPMS Study. *Geochimica Et Cosmochimica Acta*. 73, 4761–4791. doi:10.1016/j.gca.2009.05.045
- Cook, N. J. (1996). Mineralogy of the Sulphide Deposits at Sulitjelma, Northern Norway. *Ore Geology. Rev.* 11, 303–338. doi:10.1016/s0169-1368(96)00009-1
- Cooke, D. R., Baker, M., Hollings, P., Sweet, G., Chang, Z., Danyushevsky, L., et al. (2014). “New Advances in Detecting the Distal Geochemical Footprints of Porphyry Systems: Epidote mineral Chemistry as a Tool for Vectoring and Fertility Assessments.”. *Building Exploration Capability for the 21st Century*. Editors KD Kelley and HC Golden (Colorado, USA: Society of Economic Geologists, Special Publication), 18, 127–152.
- Craig, J. R., Vokes, F. M., and Solberg, T. N. (1998). Pyrite: Physical and Chemical Textures. *Mineralium Deposita*. 34, 82–101. doi:10.1007/s001260050187
- David, R. C., Mike, B., Pete, H., Gabe, S., Zhao, S. G., Zhou, T. F., et al. (2016). New Advances in Detecting the Distal Geochemical Footprints of Porphyry Systems Epidote Mineral Chemistry as a Tool for Vectoring and Fertility Assessments. *Society of Economic Geology* 18, 127–152. doi:10.5382/SP.18.07
- Davidson, J., Tepley, F., Palacz, Z., and Meffan-Main, S. (2001). Magma Recharge, Contamination and Residence Times Revealed by *In Situ* Laser Ablation Isotopic Analysis of Feldspar in Volcanic Rocks. *Earth Planet. Sci. Lett.* 184, 427–442. doi:10.1016/s0012-821x(00)00333-2
- Deng, X.-H., Wang, J.-B., Pirajno, F., Wang, Y.-W., Li, Y.-C., Li, C., et al. (2016). Re-Os Dating of Chalcopyrite from Selected mineral Deposits in the Kalatag District in the Eastern Tianshan Orogen, China. *Ore Geology. Rev.* 77, 72–81. doi:10.1016/j.oregeorev.2016.01.014
- Fadda, S., Fiori, M., Grillo, S. M., and Prochaska, W. (2012). REE Mobilization in Complex Hydrothermal-Metasomatic Systems: Fluid Chemistry Evidence of Albitite and Chlorite-Talc Mineralisations in Central Sardinia, Italy. *Proc. 10th Int. Congress Appl. Mineralogy*, 171–178. doi:10.1007/978-3-642-27682-8_22
- Fang, T. H., Qin, K. Z., Wang, S. L., Wang, S. L., Jiang, F. Z., Gan, X. P., and Zhou, Z. J. (2002). Preliminary analysis on the geological back ground of Kalatage Cu-Au deposit, Xinjiang. *Mineral Deposits* 21, 380–384. [in Chinese with English abstract]
- Foster, M. D. (1962). Interpretation of the Composition and a Classification of the Chlorites. *U.S. Geological Surv. Prof. Paper*. 414, 33. doi:10.3133/pp414A
- Franchini, M., McFarlane, C., Maydagan, L., Reich, M., Lentz, D. R., Meinert, L., et al. (2015). Trace Metals in Pyrite and Marcasite from the Agua Rica Porphyry-High Sulfidation Epithermal deposit, Catamarca, Argentina: Textural Features and Metal Zoning at the Porphyry to Epithermal Transition. *Ore Geology. Rev.* 66, 366–387. doi:10.1016/j.oregeorev.2014.10.022
- Fulignati, P., Gioncada, A., and Sbrana, A. (1999). Rare-earth Element (REE) Behaviour in the Alteration Facies of the Active Magmatic-Hydrothermal System of Vulcano (Aeolian Islands, Italy). *J. Volcanology Geothermal Res.* 88, 325–342. doi:10.1016/s0377-0273(98)00117-6
- Gao, J.-F., Zhou, M.-F., Qi, L., Chen, W. T., and Huang, X.-W. (2015). Chalcophile Elemental Compositions and Origin of the Tuwu Porphyry Cu deposit, NW China. *Ore Geology. Rev.* 66, 403–421. doi:10.1016/j.oregeorev.2014.08.009
- Gao, J. F., Zhou, M. F., Zhang, L. C., Chen, W. T., and Huang, X. W. (2017). Chalcophile elemental compositions and origin of the Tuwu porphyry Cudeposit, NW China. *Ore Geology Reviews* 66, 403–421. doi:10.1016/j.oregeorev.2014.08.009
- Gao, J. G., Li, W. Y., Guo, X. C., Zhou, Y., and Fan, T. B. (2014). Geochemistry, Zircon U-Pb Age and Hf Isotopes of Late Carboniferous Rift Volcanics in the Sepikou Region, Eastern Bogda, Xinjiang. *Acta Petrologica Sinica*. 30, 3539–3552. [in Chinese with English abstract]
- Gu, L. X., Hu, S. X., Yu, C. S., Wu, C. Z., and Yan, Z. (2001a). Initiation and Evolution of the Bogda Subduction-torn-type Rift. *Acta Petrologica Sinica*. 17, 585–597. doi:10.3321/j.issn:1000-0569.2001.04.009 [in Chinese with English abstract]
- Gu, L. X., Hu, S. X., Yu, C. S., Zhao, M., Wu, C. Z., and Li, H. Y. (2001b). Intrusive Activities during Compression-Extension Tectonic Conversion in the Bogda Intracontinental Orogen. *Acta Petrologica Sinica*. 2, 187–198. doi:10.3321/j.issn:1000-0569.2001.02.002 [in Chinese with English abstract]
- Guo, H. C., Zhong, L., and Li, L. Q. (2006). Zircon SHRIMP U-Pb Dating of Quartz Diorite in the Koumenzi Area, Karlik Mountains, East Tianshan, Xinjiang, China, and its Geological Significance. *Geol. Bull. China* 25, 928–931. doi:10.3969/j.issn.1671-2552.2006.08.005 [in Chinese with English abstract]
- Han, B. F., Song, B., Chen, L. H., and Li, Z. H. (2004). Zircon U-Pb SHRIMP Ages of the Mafic-Ultramafic Complexes from the Halatongke and Huangshandong Cu-Ni Sulfide Deposits in Xinjiang, and Their Tectonic Significance. *Chin. Sci. Bull.* 49, 2324–2328. [in Chinese with English abstract]. doi:10.1360/04wd0163
- Han, C. M., Xiao, W. J., Zhao, G. C., Mao, J. W., and Mao, Q. G. (2004). Major Types, Characteristics and Geodynamic Mechanism of Upper Paleozoic Copper Deposits in Northern Xinjiang, Northwestern China. *Ore Geology. Rev.* 28, 308–328. doi:10.1016/j.oregeorev.2005.04.002

- Han, C. M., Xiao, W. J., Wan, B., Ao, S. J., Zhang, J. E., Song, D. F., et al. (2018). Late Palaeozoic-Mesozoic Endogenetic Metallogenic Series and Geodynamic Evolution in the East Tianshan Mountains. *Acta Petrologica Sinica*. 34, 1914–1932. [in Chinese with English abstract]
- Han, C., Xiao, W., Zhao, G., Ao, S., Zhang, J., Qu, W., et al. (2010). *In-situ* U-Pb, Hf and Re-os Isotopic Analyses of the Xiangshan Ni-Cu-Co deposit in Eastern Tianshan (Xinjiang), Central Asia Orogenic Belt: Constraints on the Timing and Genesis of the Mineralization. *Lithos*. 120, 547–562. doi:10.1016/j.lithos.2010.09.019
- Han, C., Xiao, W., Zhao, G., Mao, J., Yang, J., Wang, Z., et al. (2006). Geological Characteristics and Genesis of the Tuwu Porphyry Copper deposit, Hami, Xinjiang, Central Asia. *Ore Geology. Rev.* 29, 77–94. doi:10.1016/j.oregeorev.2005.07.032
- Han, Z. K., Han, C. M., Xiao, W. J., Zhao, G. C., Wang, Z. M., Ao, S. J., et al. (2014). Palaeozoic porphyry Cu-Au and ultramafic Cu-Ni deposits in the eastern Tianshan orogenic belt: Temporal constraints from U-Pb geochronology. *Inter. Geol. Review* 55, 842–862. doi:10.1080/00206814.2012.745977
- Hedenquist, J. W. (1995). “The Ascent of Magmatic Fluid, Discharge versus Mineralization.”. *Magma, Fluids and Ore Deposits Mineralogical Association of Canada, Short Course*. Editor JFH Thompson, 23, 263–289.
- Hou, G. S., Tang, H. F., and Liu, C. Q. (2006). Geochemical Characteristics of the Late Paleozoic Volcanics in Jueluotage Tectonic belt, Eastern Tianshan and its Implications. *Acta Petrologica Sinica*. 22, 1167–1177. doi:10.3321/j.issn:1000-0569.2006.05.009 [in Chinese with English abstract]
- Hou, G. S., Tang, H. F., Liu, C. Q., and Wang, Y. B. (2005). Geochronological and Geochemical Study on the Wallrock of Tuwu-Yandong Porphyry Copper Deposits, Eastern Tianshan Mountains. *Acta Petrologica Sinica*. 21, 1729–1736. doi:10.3969/j.issn.1000-0569.2005.06.020 [in Chinese with English abstract]
- Inoue, A., Kurokawa, K., and Hatta, T. (2010). Application of Chlorite Geothermometry to Hydrothermal Alteration in Toyoha Geothermal System, Southwestern Hokkaido, Japan. *Resource Geology*. 60, 52–70. doi:10.1111/j.1751-3928.2010.00114.x
- Karakaya, M. Ç., Karakaya, N., Küpeli, Ş., and Yavuz, F. (2012). Mineralogy and Geochemical Behavior of Trace Elements of Hydrothermal Alteration Types in the Volcanogenic Massive Sulfide Deposits, NE Turkey. *Ore Geology. Rev.* 48, 197–224. doi:10.1016/j.oregeorev.2012.03.007
- Keith, M., Häckel, F., Haase, K. M., Schwarz-Schampera, U., and Klemm, R. (2016). Trace Element Systematics of Pyrite from Submarine Hydrothermal Vents. *Ore Geology. Rev.* 72, 728–745. doi:10.1016/j.oregeorev.2015.07.012
- Khalili, M., and Malekmahmoudi, F. (2012). “Geochemical Variations during Alteration of an Andesite-Basalt to Bentonite, in Khur, East of Isfahan, Iran,” in Proceedings of the 10th International Congress for Applied Mineralogy (ICAM), 43, 361–368. doi:10.1007/978-3-642-27682-8_43
- Large, R. R., Bull, S. W., and Maslennikov, V. V. (2011). A Carbonaceous Sedimentary Source-Rock Model for Carlin-Type and Orogenic Gold Deposits. *Econ. Geology*. 106, 331–358. doi:10.2113/econgeo.106.3.331
- Large, R. R., Danyushevsky, L., Hollit, C., Maslennikov, V., Meffre, S., Gilbert, S., et al. (2009). Gold and Trace Element Zonation in Pyrite Using a Laser Imaging Technique: Implications for the Timing of Gold in Orogenic and Carlin-Style Sediment-Hosted Deposits. *Econ. Geology*. 104, 635–668. doi:10.2113/econgeo.104.5.635
- Large, R. R., Maslennikov, V. V., Robert, F., Danyushevsky, L. V., and Chang, Z. (2007). Multistage Sedimentary and Metamorphic Origin of Pyrite and Gold in the Giant Sukhoi Log Deposit, Lena Gold Province, Russia. *Econ. Geology*. 102, 1233–1267. doi:10.2113/econgeo.102.7.1233
- Leng, C. B. (2017). Genesis of Hongshan Cu Polymetallic Large deposit in the Zhongdian Area, NW Yunnan, Constraints from LA-IPC-MS of Trace Elements of Pyrite and Pyrrhotite. *Earth Sci. Front.* 24, 162–175. doi:10.13745/j.esf.yx.2016-11-61 [in Chinese with English abstract]
- Li, H. Q., Chen, F. W., Lu, Y. F., Yang, H. M., Guo, J., and Mei, Y. P. (2004). Zircon SHRIMP U-Pb Age and Strontium Isotopes of Mineralized Granitoids in the Sanchakou Copper Polymetallic Depoist, East Tianshan Mountains. *Acta Geologica Sinica*. 22, 191–195. doi:10.3321/j.issn:1006-3021.2004.02.018 [in Chinese with English abstract]
- Li, J. Y., Song, B., Wang, K. Z., Li, Y. P., Sun, G. H., and Qi, D. Y. (2006). Permian mafic-ultramafic complexes on the southern margin of the Tu-Ha basin, eastern Tianshan Mountains: geological records of vertical crustal growth in central Asia. *Acta. Geoscientica Sinica* 27, 424–446. doi:10.3321/j.issn:1006-3021.2006.05.006 [in Chinese with English abstract]
- Li, F. M., Wang, Z. S., and Hou, W. B. (2002). Synthetic prospecting model developed from Xiaorequanzi copper deposit in east Tianshan, Xinjiang. *Xinjiang Geology* 20, 38–43. doi:10.3969/j.issn.1000-8845.2002.01.009 [in Chinese with English abstract]
- Li, W., Chen, J. L., Dong, Y. P., Xu, X. Y., Li, Z. P., Liu, X. M., et al. (2016). Early Paleozoic subduction of the Paleo-Asian Ocean: Zircon U-Pb geochronological and geochemical evidence from the Kalatag high-Mg andesites, East Tianshan. *Acta Petrologica Sinica*. 32, 505–521. [in Chinese with English abstract]
- Liu, M., Wang, Z. L., Zhang, Z. H., Chen, W. S., and Yang, D. (2009). Fluid Inclusion Geochemistry of Tuwu Porphyry Copper deposit, Eastern Tianshan in Xinjiang. *Acta Geologica Sinica*. 25, 1446–1455. [in Chinese with English abstract]
- Long, L. L., Wang, J. B., Wang, Y., Deng, X. H., Mao, Q. G., Sun, Y., et al. (2019). Metallogenic Regularity and Metallogenic Model of the Paleo Arc-basin System in Eastern Tianshan. *Acta Petrologica Sinica*. 35, 3161–3188. [in Chinese with English abstract]
- Long, L. L., Wang, J. B., Wang, Y. W., Mao, Q. G., Deng, X. H., Zhao, L. T., et al. (2016). Discussion on the Age of Ore-Hosting Volcanic Strata in Kalatage Ore Concentration Area, Eastern Tianshan, Xinjiang. *Mineral. Exploration*. 7, 31–37. doi:10.3969/j.issn.1674-7801.2016.01.004 [in Chinese with English abstract]
- Lowell, J. D., and Guilbert, J. M. (1970). Lateral and Vertical Alteration-Mineralization Zoning in Porphyry Ore Deposits. *Econ. Geology*. 65, 373–408. doi:10.2113/gsecongeo.65.4.373
- Ma, R. S., Shu, L. S., and Sun, J. (1997). *Tectonic Evolution and Metalogeny of Eastern Tianshan Mountains*. Beijing: Geological Publishing House
- Ma, T. L., Wang, L. Q., Sun, L. Q., and Shu, B. (2003). Application of Magnetic Fabric Analysis to the Ductile Deformation Belt. *Acta Geoscientia Sinica*. 449–452. doi:10.3321/j.issn:1006-3021.2003.05.010 [in Chinese with English abstract]
- MacLean, W. H. (1988). Rare Earth Element Mobility at Constant Inter-REE Ratios in the Alteration Zone at the Phelps Dodge Massive Sulphide deposit, Matagami, Quebec. *Mineral. Deposita*. 23, 231–238. doi:10.1007/bf00206399
- Mao, J. W., Yang, J. M., Qu, W. J., Du, A. D., Wang, Z. L., and Han, C. M. (2002). Re-Os Dating of Cu-Ni Sulfide Ores from Huangshandong deposit in Xinjiang and its Geodynamic Significance. *Mineral. Deposits*. 21, 323–330. doi:10.1007/s11769-002-0037-5
- Mao, Q. G., Fang, T. H., Wang, J. B., Wang, S. L., and Wang, N. (2010). The Geochronology Studies of the Early Paleozoic Honghai Massive Sulfide Deposits and its Geological Significance Kalatage belt, in Eastern Tianshan Mountain, Xinjiang, Northwest China. *Acta Petrologica Sinica*. 26, 3017–3026. [in Chinese with English abstract]
- Mao, Q. G., Wang, J. B., Fang, T. H., Yu, M. J., and Sun, Y. (2017). Discovery of the Middle Devonian Yudai Porphyritic Cu(Au) Deposit in the Kalatage Area of Eastern Tianshan Mountain, Xinjiang and its Geological Prospecting Significance. *Geology Exploration* 53, 1–11. [in Chinese with English abstract]
- Mao, Q. G., Wang, J. B., Fang, T. H., Yu, M. J., Zhu, J. J., Zhuang, R., et al. (2016). Geological Characteristics of Honghai VMS Type deposit of Kalatage Ore belt in the Eastern Tianshan. *Mineral. Exploration*. 7, 17–30. [in Chinese with English abstract]
- Mao, Q. G., Wang, J. B., Yu, M. J., Ao, S. J., and Li, Y. C. (2020). Re-Os and U-Pb Geochronology for the Xiaorequanzi VMS deposit in the Eastern Tianshan, NW China: Constraints on the Timing of Mineralization and Stratigraphy. *Ore Geology. Rev.* 122, 1–14. doi:10.1016/j.oregeorev.2020.103473
- Mao, Q. G., Xiao, W. J., Han, C. M., Sun, M., Yuan, C., Yan, Z., et al. (2006). Zircon U-Pb Age and the Geochemistry of the Baishiquan Mafic-Ultramafic Complex in the Eastern Tianshan, Xinjiang: Constraints on the Closure of the Paleo-Asian Ocean. *Acta Petrologica Sinica* 22, 153–162. doi:10.3321/j.issn:1000-0569.2006.01.016 [in Chinese with English abstract]
- Mao, Q. G., Xiao, W. J., Windley, B. F., yU, M. J., and Zhang, J. E. (2019). Early Permian Subduction-Related Transtension in the Turpan Basin, East Tianshan (NW China): Implications for Accretionary Tectonics of the Southern Altids. *Geol. Mag.*, 1–24.

- Mao, Q., Wang, J., Xiao, W., Fang, T., Yu, M., Ao, S., et al. (2014a). Stratigraphic, U-Pb (Zircon) and Geochemical Constraints on Magmas, Mineralization and Geological Evolution of the Kalatage District, the Central Part of Dananhu Arc in Eastern Tianshan Mountains. *Acta Geologica Sinica - English Edition*. 88, 885–886. [in Chinese with English abstract]. doi:10.1111/1755-6724.12376_11
- Mao, Q., Xiao, W., Fang, T., Windley, B. F., Sun, M., Ao, S., et al. (2014b). Geochronology, Geochemistry and Petrogenesis of Early Permian Alkaline Magmatism in the Eastern Tianshan: Implications for Tectonics of the Southern Altaids. *Lithos*. 190–191, 37–51. doi:10.1016/j.lithos.2013.11.011
- Mao, Q., Yu, M., Xiao, W., Windley, B. F., Li, Y., Wei, X., et al. (2018). Skarn-mineralized Porphyry Adakites in the Harlik Arc at Kalatage, E. Tianshan (NW China): Slab Melting in the Devonian-Early Carboniferous in the Southern Central Asian Orogenic Belt. *J. Asian Earth Sci.* 153, 365–378. doi:10.1016/j.jseas.2017.03.021
- Michard, A., and Albarède, F. (1986). The REE Content of Some Hydrothermal Fluids. *Chem. Geology*. 55, 51–60. doi:10.1016/0009-2541(86)90127-0
- Pan, H. D., Shen, P., Chen, G., Yang, J. T., and Dai, H. W. (2013). Volcanic-plutonic Complex, Ore-Forming Rocks and Their Alterations in Tuwu Porphyry Cu deposit of Xinjiang. *Mineral. Deposits*. 32, 794–808.
- Parsapoor, A., Khalili, M., and Mackizadeh, M. A. (2009). The Behaviour of Trace and Rare Earth Elements (REE) during Hydrothermal Alteration in the Rangan Area (Central Iran). *J. Asian Earth Sci.* 34, 123–134. doi:10.1016/j.jseas.2008.04.005
- Pirajno, F. (2009). *Hydrothermal Processes and Mineral System*. Berlin, Germany: Springer Netherlands
- Pirajno, F. (2013). *The Geology and Tectonic Settings of China's Mineral Deposits*. Berlin, Germany: Springer Netherlands. doi:10.1007/978-94-007-4444-8
- Qin, K.-z., Su, B.-x., Sakyi, P. A., Tang, D.-m., Li, X.-h., Sun, H., et al. (2011). SIMS Zircon U-Pb Geochronology and Sr-Nd Isotopes of Ni-Cu-Bearing Mafic-Ultramafic Intrusions in Eastern Tianshan and Beishan in Correlation with Flood Basalts in Tarim Basin (NW China): Constraints on a Ca. 280 Ma Mantle Plume. *Am. J. Sci.* 311, 237–260. doi:10.2475/03.2011.03
- Qin, Y. S., Zhang, J. C., Ding, K. S., Xu, Y. X., Tang, D. M., Xu, X. W., et al. (2009). Semi-empirical Likelihood Confidence Intervals for the Differences of Quantiles with Missing Data. *Acta Math. Sin.-English Ser.* 25, 845–854. [in Chinese with English abstract]. doi:10.1007/s10114-009-6476-5
- Reed, M. H. (1997). "Hydrothermal Alteration and its Relationship to Ore Fluid Composition," in *Geochemistry of Hydrothermal Ore Deposits*. Editor H. L. Barnes. third ed. (New York: Wiley), 1–29.
- Reich, M., Deditius, A., Chrysosoulis, S., Li, J.-W., Ma, C.-Q., Parada, M. A., et al. (2013). Pyrite as a Record of Hydrothermal Fluid Evolution in a Porphyry Copper System: A SIMS/EMPA Trace Element Study. *Geochimica Et Cosmochimica Acta*. 104, 42–62. doi:10.1016/j.gca.2012.11.006
- Rui, Z. Y., Wang, F. T., Li, H. H., Dong, L. H., Wang, L., Jiang, L. F., et al. (2001). New Progress in the Eastern Tianshan Porphyry Copper belt. *Chin. Geology*. 28, 11–16. doi:10.3969/j.issn.1000-3657.2001.02.003 [in Chinese with English abstract]
- Rui, Z. Y., Wang, L. S., and Wang, Y. T. (2002). Discussion on Metallogenic Epoch of Tuwu and Yandong Porphyry Copper Deposits in Eastern Tianshan Mountains, Xinjiang. *Mineral. Deposits*. 21, 16–22. doi:10.3969/j.issn.0258-7106.2002.01.003 [in Chinese with English abstract]
- Şengör, A. M. C., Natal'in, B. A., and Burtman, U. S. (1993). Evolution of the Altaid tectonic collage and Paleozoic crustal growth in Eurasia. *Nature* 364, 209–304. doi:10.1038/364299a0
- Shen, P., Pan, H. D., Dong, L. H., Yang, J. T., Shen, Y. C., Dai, H. W., et al. (2012). Caldera Complex, Hosted Rocks and Alteration of the Yandong Porphyry Copper deposit in Eastern Tianshan, Xinjiang. *Acta Petrologica Sinica*. 28, 1966–1980. [in Chinese with English abstract]
- Shen, P., Pan, H., and Dong, L. (2014a). Yandong Porphyry Cu deposit, Xinjiang, China-geology, Geochemistry and Sims U-Pb Zircon Geochronology of Host Porphyries and Associated Alteration and Mineralization. *J. Asian Earth Sci.* 80, 197–217. doi:10.1016/j.jseas.2013.11.006
- Shen, P., Pan, H., Zhou, T., and Wang, J. (2014b). Petrography, Geochemistry and Geochronology of the Host Porphyries and Associated Alteration at the Tuwu Cu deposit, NW China: a Case for Increased Depositional Efficiency by Reaction with Mafic Hostrock? *Miner. Deposita*. 49, 709–731. doi:10.1007/s00126-014-0517-4
- Shu, L., Wang, B., Zhu, W., Guo, Z., Charvet, J., and Zhang, Y. (2011). Timing of Initiation of Extension in the Tianshan, Based on Structural, Geochemical and Geochronological Analyses of Bimodal Volcanism and Olistostrome in the Bogda Shan (NW China). *Int. J. Earth Sci. (Geol. Rundsch.)*. 100, 1647–1663. doi:10.1007/s00531-010-0575-5
- Song, B., Li, J. Y., Li, W. P., Wang, K. Z., and Wang, Y. B. (2002). SHRIMP Dating of the Dananhu and Kezirkalasayi Granitoids Batholiths in Southern Margin of Tuha Basin and Their Geological Implication. *Xinjiang Geology*. 20, 332–345. [in Chinese with English abstract]
- Song, X. X., and Zhang, J. K. (1986). *Minor Elements in Pyrite of Various Genetic Types Form China*. Bulletin of the Institute of mineral Deposits, Chinese Academy of Geological Sciences. Beijing: Geological Publishing House
- Sun, G. H., Li, J. Y., Gao, L. M., and Yang, T. N. (2005). Zircon SHRIMP U-Pb Age of a Dioritic Pluton in the Harlik Mountain, Eastern Xinjiang, and its Tectonic Implication. *Geol. Rev.* 51, 463–469. doi:10.3321/j.issn:0371-5736.2005.04.015 [in Chinese with English abstract]
- Sun, Y., Wang, J. B., Li, Y. C., Wang, Y. W., Yu, M. J., Long, L. L., et al. (2017). Recognition of Late Ordovician Yudai Porphyry Cu (Au, Mo) Mineralization in the Kalatag District, Eastern Tianshan Terrane, NW China: Constraints from Geology, Geochronology, and Petrology. *Ore Geology. Rev.* 100, 220–236. doi:10.1016/j.oregeorev.2017.07.011
- Sverjensky, D. A. (1984). Europium Redox Equilibria in Aqueous Solution. *Earth Planet. Sci. Lett.* 67, 70–78. doi:10.1016/0012-821x(84)90039-6
- Tan, W., Han, R. S., Wang, L., Liu, F., Guo, Y. X. Y., Wang, M. Z., et al. (2016). REE Geochemical of Gold-Polymetallic deposit in Beiya, Western Yunnan Province. *J. Chin. Soc. rare earths*. 34, 113–128. [in Chinese with English abstract]
- Tan, W., Han, R. S., Wang, L., Liu, F., Wang, M. Z., and Guo, Y. X. Y. (2018). Iron Source of the Beiya Porphyry-type Au-Polymetallic deposit in Northwestern Yunnan, China. *Geochimica*. 47, 541–553. doi:10.19700/j.0379-1726.2018.05.007 [in Chinese with English abstract]
- Tang, J. H., Gu, L. X., Zheng, Y. C., Fang, T. H., Zhang, Z. Z., Gao, J. H., et al. (2006). Petrology, Geochemistry and Genesis of the Na-Rich Volcanic Rocks of the Kalatag Area, Eastern Tianshan. *Acta Petrologica Sinica*. 22, 1150–1166. doi:10.3321/j.issn:1000-0569.2006.05.008 [in Chinese with English abstract]
- Taylor, S. R., and McLennan, S. M. (1985). The Continental Crust: Its Composition and Evolution. *J. Geology*. 94, 57–72. doi:10.1086/629067
- Terakado, Y., and Fujitani, T. (1998). Behavior of the Rare Earth Elements and Other Trace Elements during Interactions between Acidic Hydrothermal Solutions and Silicic Volcanic Rocks, Southwestern Japan. *Geochimica Et Cosmochimica Acta*. 62, 1903–1917. doi:10.1016/s0016-7037(98)00109-4
- Wang, F. T., Feng, J., Hu, J. W., Wang, L., Jiang, L. F., and Zhang, Z. (2001). The geological characteristics and discovery significance of Tuwu porphyry copper deposit, Xinjiang. *Geology. China* 28, 36–39. doi:10.1007/s00126-018-0859-4 [in Chinese with English abstract]
- Wang, J. B., Wang, Y. W., and He, Z. J. (2006). Ore Deposits as a Guide to the Tectonic Evolution in the East Tianshan Mountains, NW China. *Geology. China*, 461–469. [in Chinese with English abstract]
- Wang, J. R., Li, T. D., Tian, L. P., Yu, M., Wang, H. T., Zhao, Z. X., et al. (2010). Late Paleozoic Tectono-Magmatic Evolution in Bogda Orogenic Belt, Xinjiang: Evidence from Geochemistry of Volcanic Rocks. *Acta Petrologica Sinica* 26, 1103–1115. [in Chinese with English abstract]
- Wang, K. R. (1989). *Genesis Mineralogy of the Earth and Universe*. Hefei, Anhui Education Press
- Wang, Y.-H., Xue, C.-J., Liu, J.-J., Wang, J.-P., Yang, J.-T., Zhang, F.-F., et al. (2015). Early Carboniferous Adakitic Rocks in the Area of the Tuwu deposit, Eastern Tianshan, NW China: Slab Melting and Implications for Porphyry Copper Mineralization. *J. Asian Earth Sci.* 103, 332–349. doi:10.1016/j.jseas.2014.09.032
- Wang, Y., Chen, H., Baker, M. J., Han, J., Xiao, B., Yang, J., et al. (2018). Multiple Mineralization Events of the Paleozoic Tuwu Porphyry Copper deposit, Eastern Tianshan: Evidence from Geology, Fluid Inclusions, Sulfur Isotopes, and Geochronology. *Miner. Deposita*. 54, 1053–1076. doi:10.1007/s00126-018-0859-4
- Wang, Y. F., Chen, H. Y., Xiao, B., Han, J. S., and Yang, J. T. (2016). Porphyritic-overlapped Mineralization of Tuwu and Yandong Copper Deposits in Eastern Tianshan Mountains, Xinjiang. *Mineral. Deposits*. 35, 51–68. doi:10.1611/j.0258-7106.2016.01.004 [in Chinese with English abstract]

- Wang, Y. L., Zhang, Z. W., Zhang, J. W., You, M. X., Li, K., and Wang, B. L. (2016). Mineralogy and Sr-Nd Isotope Characteristics of Baixintan Ni-Cu deposit in Eastern Tianshan Mountains, Xinjiang, and Mineralization Process. *Acta Geologica Sinica*. 90, 2747–2758. [in Chinese with English abstract]
- Wang, Y. H., Xue, C. J., Liu, J. J., Wang, J. P., Yang, J. T., Zhang, F. F., et al. (2014). Geochemistry, Geochronology, Hf Isotope, and Geological Significance of the Tuwu Porphyry Copper deposit in Eastern Tianshan, Xinjiang. *Acta Petrologica Sinica*. 30, 3383–3399. [in Chinese with English abstract]
- Wilkinson, J. J., Chang, Z., Cooke, D. R., Baker, M. J., Wilkinson, C. C., Inglis, S., et al. (2015). The Chlorite Proximito: A New Tool for Detecting Porphyry Ore Deposits. *J. Geochemical Exploration*. 152, 10–26. doi:10.1016/j.gexplo.2015.01.005
- Wu, H., Li, H. Q., Chen, F. W., Lu, Y. F., Deng, G., Mei, Y. P., et al. (2006). Zircon SHRIMP U-Pb Dating of Plagiogranite Porphyry in the Chihu Molybdenum-Copper District, Hami, East Tianshan. *Geol. Bull. China* 25, 549–552. doi:10.3969/j.issn.1671-2552.2006.05.003 [in Chinese with English abstract]
- Xiao, B., Chen, H., Hollings, P., Wang, Y., Yang, J., and Wang, F. (2018). Element Transport and Enrichment during Propylitic Alteration in Paleozoic Porphyry Cu Mineralization Systems: Insights from Chlorite Chemistry. *Ore Geology. Rev.* 102, 437–448. doi:10.1016/j.oregeorev.2018.09.020
- Xiao, B., Chen, H. Y., Wang, Y. F., and Yang, J. T. (2017). Zircon U-Pb and Molybdenite Re-os Dating of the Tuwu–Yandong Cu Deposit Belt of the Eastern Tianshan Mountains and its Geological Significance. *Geotectonica et Metallogenia* 41, 145–156. doi:10.16539/j.ddgzyckx.2016.06.020
- Xiao, W.-J., Zhang, L. C., Qin, K. Z., Sun, S., and Li, J. L. (2004). Paleozoic Accretionary and Collisional Tectonics of the Eastern Tianshan (China): Implications for the continental Growth of central Asia. *Am. J. Sci.* 304, 370–395. doi:10.2475/ajs.304.4.370
- Xiao, W., Windley, B. F., Sun, S., Li, J., Huang, B., Han, C., et al. (2015). A Tale of Amalgamation of Three Permo-Triassic Collage Systems in Central Asia: Oroclines, Sutures, and Terminal Accretion. *Annu. Rev. Earth Planet. Sci.* 43, 477–507. doi:10.1146/annurev-earth-060614-105254
- Yang, K., and Scott, S. D. (1996). Possible Contribution of a Metal-Rich Magmatic Fluid to a Sea-Floor Hydrothermal System. *Nature*. 383, 420–423. doi:10.1038/383420a0
- Yao, F. J. (2006). The Study of Spectral Feature and Extraction of Remote Sensing Alteration Anomalies for Metallic Ore Deposits in Gobi Arid Zone and Application in mineral Resources. Master Thesis. Beijing: Chinese Academy of Geological Sciences.
- Ye, L., Cook, N. J., Ciobanu, C. L., Yiping, L., Qian, Z., Tiegeng, L., et al. (2011). Trace and Minor Elements in Sphalerite from Base Metal Deposits in South China: A LA-ICPMS Study. *Ore Geology. Rev.* 39, 188–217. doi:10.1016/j.oregeorev.2011.03.001
- Yu, M., Wang, Y., Wang, J., Mao, Q., Deng, X., Sun, Y., et al. (2019). The Mineralization of the Kalatage Arc, Eastern Tianshan, NW China: Insights from the Geochronology of the Meiling Cu-Zn(-Au) deposit. *Ore Geology. Rev.* 107, 72–86. doi:10.1016/j.oregeorev.2018.12.009
- Zang, W., and Fyfe, W. S. (1995). Chloritization of the Hydrothermally Altered Bedrock at the Igarapé Bahia Gold deposit, Carajás, Brazil. *Mineralium Deposita*. 30, 30–38. doi:10.1007/bf00208874
- Zhai, Y. S., Yao, S. Z., and Cai, K. Q. (2011). *Ore deposit Science*. Third edition. Beijing: Geological Publishing House. doi:10.1145/2063348.2063363
- Zhang, L., Xiao, W., Qin, K., and Zhang, Q. (2006). The Adakite Connection of the Tuwu-Yandong Copper Porphyry belt, Eastern Tianshan, NW China: Trace Element and Sr-Nd-Pb Isotope Geochemistry. *Miner Deposita*. 41, 188–200. doi:10.1007/s00126-006-0058-6
- Zhang, R., Mao, Q. G., Yu, M. J., Fang, T. H., and Cheng, F. W. (2017). Geochemical Characteristics and Zircon U-Pb Ages of the Magmatite in the Qiongduduke Ag-Pb-Zn Polymetallic deposit of Xinjiang. *Geology. Exploration*. 53, 270–282. [in Chinese with English abstract]
- Zhang, W. D., Wu, X. B., Deng, X. H., Mao, Q. G., Zhang, H. Q., Yang, L. Y., et al. (2018). Fluid Inclusions Constraints on the Origin of the Xiaorequanzi Deposit in Eastern Tianshan. *Diqiu Kexue Zhongguo Dizhi Daxue Xuebao/earth Sci. J. China Univ. Geosciences*. 43, 3036–3048. doi:10.3799/dqkx.2018.150
- Zhang, W., Lentz, D. R., Thorne, K. G., and Massawe, R. J. R. (2020). Late Silurian-Early Devonian Slab Break-Off beneath the Canadian Appalachians: Insights from the Nashuaak Granite, West-central New Brunswick, Canada. *Lithos*. 358–359, 105393. doi:10.1016/j.lithos.2020.105393
- Zhao, Z. N., Wang, Y. H., Wang, J. P., Dong, L. S., Wang, H., Zhang, F. F., et al. (2014). Geochemistry and Geochronology of Diorite Porphyrite of the Tuwu Copper Deposit and its Geological Significance, Eastern Tianshan. *Acta Mineralogica Sinica*. 34, 332–349. doi:10.16461/j.cnki.1000-4734.2014.04.012 [in Chinese with English abstract]
- Zhou, J. Y., Cui, B. F., Xiao, H. L., Chen, S. Z., and Zhu, D. M. (2001). The Kangguertag-Huangshan Collision Zone of Bilateral Subduction and its Metallogenic Model and Programs in Xinjiang, China. *Volcanology Mineral. Resour.* 22, 252–263.
- Zhou, M.-F., Michael Leshner, C., Yang, Z., Li, J., and Sun, M. (2004). Geochemistry and Petrogenesis of 270 Ma Ni-Cu-(PGE) Sulfide-Bearing Mafic Intrusions in the Huangshan District, Eastern Xinjiang, Northwest China: Implications for the Tectonic Evolution of the Central Asian Orogenic belt. *Chem. Geology*. 209, 233–257. doi:10.1016/j.chemgeo.2004.05.005
- Zhou, T. F., Zhang, L. J., Yuan, F., Fan, Y., and David, R. C. (2010). LA-ICP-MS *In Situ* Trace Element of Pyrite from the Xinqiao Cu-Au-S deposit in Tongling, Anhui, and its Constraints on the Ore Genesis. *Earth Sci. Front.* 17, 306–319. [in Chinese with English abstract]

Conflict of Interest: WT, QM, MY, YS, and XL were employed by the company Beijing Institute of Geology for Mineral Resources Co., Ltd., and WT and XL were employed by the company Sino-Zijin Resources Ltd.

Copyright © 2021 Tan, Mao, Yu, Sun and Lv. This is an open-access article distributed under the terms of the Creative Commons Attribution License (CC BY). The use, distribution or reproduction in other forums is permitted, provided the original author(s) and the copyright owner(s) are credited and that the original publication in this journal is cited, in accordance with accepted academic practice. No use, distribution or reproduction is permitted which does not comply with these terms.



Gem-Grade Garnet With Metamorphic Origin in the Tiemurt Orogenic-Type Deposit, Chinese Altay Orogen: Texture, Chemistry, and Physicochemical Condition

Zhaobin Hu¹, Yi Zheng^{1,2,3*}, Pengpeng Yu^{1,2}, Yihan Wu¹ and Chengming Wang^{1,3}

¹Guangdong Provincial Key Lab of Geological Process and Mineral Resources Survey, School of Earth Sciences and Geological Engineering, Sun Yat-Sen University, Guangzhou, China, ²Guangdong Provincial Key Lab of Geodynamic and Geohazards, Sun Yat-Sen University, Guangzhou, China, ³Southern Marine Science and Engineering Guangdong Laboratory, Zhuhai, China

OPEN ACCESS

Edited by:

Xiaohua Deng,
Beijing Institute of Geology for Mineral
Resources, China

Reviewed by:

Yu Zhang,
Central South University, China
Pei Liang,
University of Science and Technology
Beijing, China

*Correspondence:

Yi Zheng
zhengy43@mail.sysu.edu.cn

Specialty section:

This article was submitted to
Economic Geology,
a section of the journal
Frontiers in Earth Science

Received: 20 March 2021

Accepted: 07 June 2021

Published: 01 July 2021

Citation:

Hu Z, Zheng Y, Yu P, Wu Y and
Wang C (2021) Gem-Grade Garnet
With Metamorphic Origin in the Tiemurt
Orogenic-Type Deposit, Chinese Altay
Orogen: Texture, Chemistry, and
Physicochemical Condition.
Front. Earth Sci. 9:683312.
doi: 10.3389/feart.2021.683312

The Chinese Altay Orogen represents an accretionary collage with episodic subduction-related accretion from the Neoproterozoic to Permian, followed by Triassic continent–continent collision. Reddish gem-grade garnet grains are widespread in Au–Cu–Pb–Zn sulfide deposits of the Chinese Altay Orogen, and how their formation links to regional geological processes such as seafloor sedimentation, magmatic hydrothermal metasomatic, or orogenic metamorphism remains unclear. In this context, we present an integrated set of geological occurrences, mineral texture, and major trace elemental geochemistry of six garnet grains from the representative Tiemurt Cu–Pb–Zn(–Au) deposit. Two categories of garnets, Grt1 and Grt2, are identified in terms of distinct mineral assemblages, textures, and geochemistry. The sub- to euhedral biotite inclusion-rich Grt1 with fine grains of less than 0.3 cm in diameter is intergrown with amphibole, chlorite, and biotite. Comparatively, the euhedral mineral inclusion-poor Grt2 with coarse grains of 0.5–5 cm in diameter is paragenetic with quartz, calcite, chlorite, and biotite. Forty-one EMPA analyses show that Grt1 and Grt2 have similar major elemental compositions of SiO₂ (36.2–37.5 wt%), Al₂O₃ (19.9–20.7 wt%), and CaO (5.3–7.8 wt%) but host variable contents of FeO (31.7–35.9 wt% for Grt1 and 23.0–30.0 wt% for Grt2) and MnO (0.8–3.7 wt% for Grt1 and 4.3–12.7 wt% for Grt2). Both Grt1 (with a chemical formula of Alm_{49.3–54.6}Spe_{19.7–24.6}Gro_{14.6–18.4}Pyr_{3.7–4.8}And_{3.5–4.9}) and Grt2 (Alm_{57.4–64.4}Gro_{15.5–18.3}Spe_{9.62–19.8}Pyr_{3.8–5.7}And_{1.1–4.4}) are plotted into the field close to the end-member of almandine (Fe–Al–garnet). Compared to Grt1, Grt2 displays a Fe-enriched and Mn-depleted trend. Additionally, Mn is enriched in the core but Fe is enriched in the rim on the major elemental profile of Grt1. Regarding the trends of trace elements and REEs, Grt2 is believed to be produced during the detriment and replacement of Grt1 by an intense external metal-rich fluid. In combination with previous fluid inclusion research, the garnet-related fluids are characterized by CO₂-rich, mesothermal, mildly acidic, and reduced redox, analogous to metamorphic fluids generated during orogenesis. Collectively, we conclude that the reddish gem-grade garnet crystals in the Chinese Altay Orogen are of metamorphic origin.

Keywords: garnet, metamorphic origin, orogenic-type deposit, Tiemurt Pb–Zn–Cu deposit, Chinese Altay Orogen

INTRODUCTION

Garnet is a widespread silicate mineral in variable geological settings on Earth, for example, mantle transition zone, subducting ocean crust, skarn deposits with magmatic hydrothermal origin, seafloor sedimentary exhalation, and metamorphic rocks (Marco and Donald, 1982; Doyle and Allen, 2003; Meinert et al., 2005). Different garnets host a similar crystal structure of $[\text{SiO}_4]$ tetrahedrons with the chemical formula of $\text{A}_3\text{B}_2(\text{SiO}_4)_3$, in which $\text{A} = \text{Ca}^{2+}$, Fe^{2+} , Mg^{2+} , and/or Mn^{2+} , while $\text{B} = \text{Al}^{3+}$, Fe^{3+} , and/or Cr^{3+} (Menzer, 1926; Bernard et al., 2013; Dietrich, 2020). Two principal categories of garnets with different chemical compositions have been well documented, that is, the Al-rich garnet (represented by pyrope, almandine, and spessartine) and Fe-rich garnet (grossular, uvarovite, and andradite) (Charles, 2016). In particular, the chemical variations of these garnets, coupled with mineral growth zonation, are often used as a sensitive indicator of physicochemical conditions, such as pressure (P), temperature (T), redox state, and acidity (Jamveit et al., 1993; Konrad-Schmolke et al., 2005; Baxter and Scherer, 2013). Linkage of garnet mineral growth and metal accumulation has received much attention in the skarn deposits (Jamveit et al., 1993), owing to the substantial Ca-rich garnet produced by contact replacement of magmatic fluids with host carbonates (Xu et al., 2016; Park et al., 2019). However, garnet geological indicator is rarely used in other genetic-type metal deposits largely because of its scarcity.

An abundance of reddish gem-grade garnet has been discovered in the Au–Cu–Pb–Zn polymetallic ore deposits in the Chinese Altay Orogen, but their origin remains unclear (Chen, 2000; Yang et al., 2018). In fact, ore genesis of these polymetallic ore deposits is also intensively debated as the volcanogenic massive sulfide (VMS), metamorphosed VMS, or orogeny-driven metamorphic hydrothermal (orogenic-type) deposits (Zheng et al., 2013b; Stefanie et al., 2014). These controversies are partially due to most of these polymetallic deposits possessing significant characteristics of textural modification and chemical remobilization during the subsequently magmatic and metamorphic overprinting (Jamveit et al., 1993; Ciobanu and Cook, 2004; Barrie et al., 2010). It is hard to evaluate the contribution of seafloor sedimentation or subsequent orogenesis for these polymetallic deposits in the Chinese Altay Orogen (Yu and Zheng, 2019). Therefore, these garnet grains have great potential to answer the questions of how the metals were enriched up to ores.

The representative Tiemurt Pb–Zn–(Cu–Au) deposit hosts large amounts of garnet grains paragenetic with the chief sulfide ores (Zheng et al., 2013a; Zhang et al., 2017a; Yu and Zheng, 2019). To address the above scientific issue, we conducted an integrated set of paragenetic sequence, internal textures, and their corresponding *in situ* major and minor elemental compositions of the Tiemurt garnet. The growth history and physicochemical condition of garnet is believed to assist to yield much clearer understanding on the ore genesis and regional metallogeny (Konrad-Schmolke et al., 2005). In addition, this research might shed light on the reconstruction of tectonic evolution of the Chinese Altay Orogen and even CAO.

GEOLOGICAL BACKGROUND

Tectonic Settings

The Central Asian Orogenic Belt (CAOB), the largest accretionary orogen on Earth (Jahn, 2004; Xiao et al., 2009; Chen et al., 2012), is located between the Siberia Craton to the north and Tarim–Sinokorea Craton to the south (Figure 1A). An abundance of Paleozoic ophiolites, arc igneous rocks, and Precambrian massifs records a complex accretionary history prior to the Triassic collisions of the Siberian with Tarim–Sinokorea Craton (Xiao et al., 2009).

As an important element of CAO, the Chinese Altay Orogen is an accretionary complexity toward the southern margin of the Siberian Craton and contains four principle tectonic units from north to south (Figure 1B; Chen et al., 2012), including 1) Unit 1: the Late Devonian–Early Carboniferous Nurt volcanic basin developed on a Precambrian crystalline basement; 2) Unit 2: the Paleozoic Keketuohai magmatic arc that contains Precambrian high-grade metamorphic rocks, Neoproterozoic–Earliest Triassic granites, and the giant Keketuohai pegmatite field; 3) Unit 3: the Devonian–Carboniferous volcanic basins developed on the southern margin of the pre-Devonian metamorphic rocks, for example, the Kelan, Ashele, and Maizi basins; and 4) Unit 4: the Armantay–Ertix accretionary terrane and Devonian–Carboniferous fossiliferous sedimentary rocks, intruded by post-orogenic granites.

The basins in Unit 3 of the Chinese Altay Orogen is filled by a package of low-grade metamorphosed volcano-sedimentary rocks comprising the continentally derived turbidites (e.g., Habahe Group), volcanic rocks (e.g., Altay Formation), and volcanic-sedimentary rocks (e.g., Kangbutiebao Formation) (Wang et al., 1998; Goldfarb et al., 2003). It is notable that these basins are metal-fertile and hosting considerable amount of metal deposits. The representative deposits include the giant Ashele Cu–Zn, Keketale Pb–Zn, Mengku Fe deposits (Wang et al., 1998; Wan et al., 2010a, 2010b; Zheng et al., 2013b), and numerous polymetallic lode deposits (Figure 2A; e.g., the Sarekuobu Au, the Wulasigou Cu deposit, and Tiemurt Au–Cu–Pb–Zn deposits (Zhang et al., 2012; Zheng et al., 2012; Yu et al., 2020).

Field Geology of the Kelan Basin

The Kelan Basin is particularly rich in the Au–Cu–Pb–Zn lode deposits that are controlled by a series of complex structures. A huge multiple overturned syncline system, with the axial plane dipping toward northwest, is identified in the Kelan Basin (Figure 2A). The well-developed NW-trending faults are the chief ore-controlled structures and also separate the distinct stratigraphic units, that is, the Keyingong and Hongdun faults separate the Kulumuti Group and the Kangbutiebao Formation, while the Abagong and Altay faults separate the Kangbutiebao and Altay Formations (Figure 2A).

Among the strata, the Silurian Kulumuti Group with lithological composition of migmatite, gneiss, and schist is unconformably overlain by the Devonian Kangbutiebao and Altay formations. The Kangbutiebao Formation consists of a set of felsic lavas, pyroclastic rocks, and siliciclastic

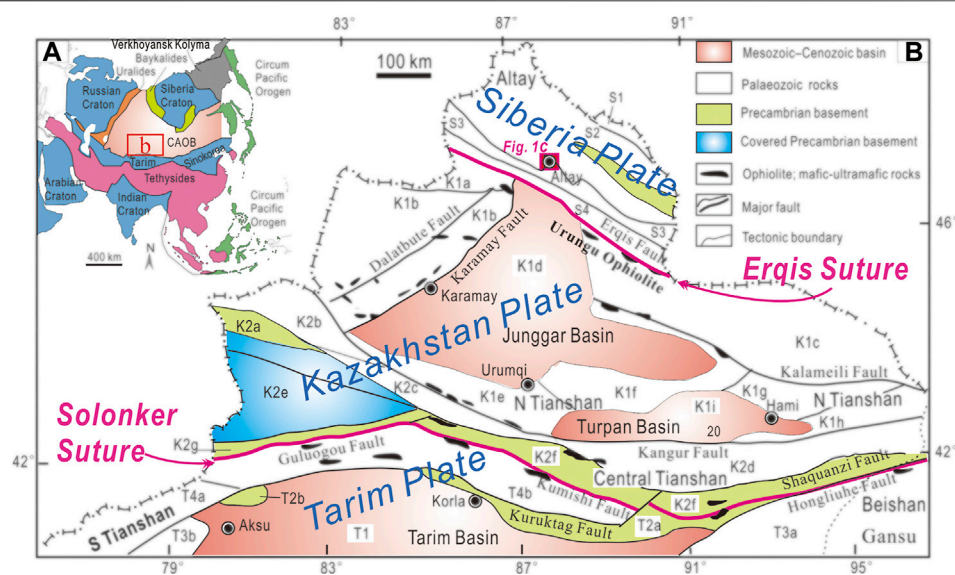


FIGURE 1 | (A) Tectonic framework of the Central Asian Orogenic Belt. **(B)** Geological sketch map showing the tectonic units of North Xinjiang (Chen et al., 2012). Siberia plate: S1, Late Devonian–Early Carboniferous Nurt volcanic basin; S2, Paleozoic Keketuohai magmatic arc; S3, Devonian–Carboniferous Kelan forearc basin; S4, Arantay–Irtysch accretionary wedge. Kazakhstan plate: K1a, Zhama–Sawur island arc; K1b, Western Junggar accretionary complex; K1c, Eastern Junggar accretionary complex; K1d, Mesozoic–Cenozoic Junggar basin; K1e, Late Paleozoic Yelienhabirga backarc basin; K1f, Late Paleozoic Bogada aulacogen; K1g, Paleozoic Harlike island arc; K1h, Dananhu island arc; K1i, Mesozoic–Cenozoic Turpan basin; K2a, Sailimu massif; K2b, Wenquan terrane; K2c, Paleozoic Boloholo arc basin system; K2d, Paleozoic Yamansu–Jueluotag arc basin system; K2e, Carboniferous–Permian Ili rift; K2f, Early Paleozoic central Tianshan island arc with Precambrian fragments; K2g, Nalati massif. Tarim Plate: T1, Mesozoic–Cenozoic Tarim basin; T2a, Precambrian Kuruktag massif; T2b, Muzart massif; T3a, Carboniferous–Permian Beishan aulacogen; T3b, Late Paleozoic Kalatierak passive marginal sediments; T4a, Late Paleozoic Southwest Tianshan fold-thrust belt; T4b, Paleozoic Southern Tianshan (or Kumishi) accretionary complex.

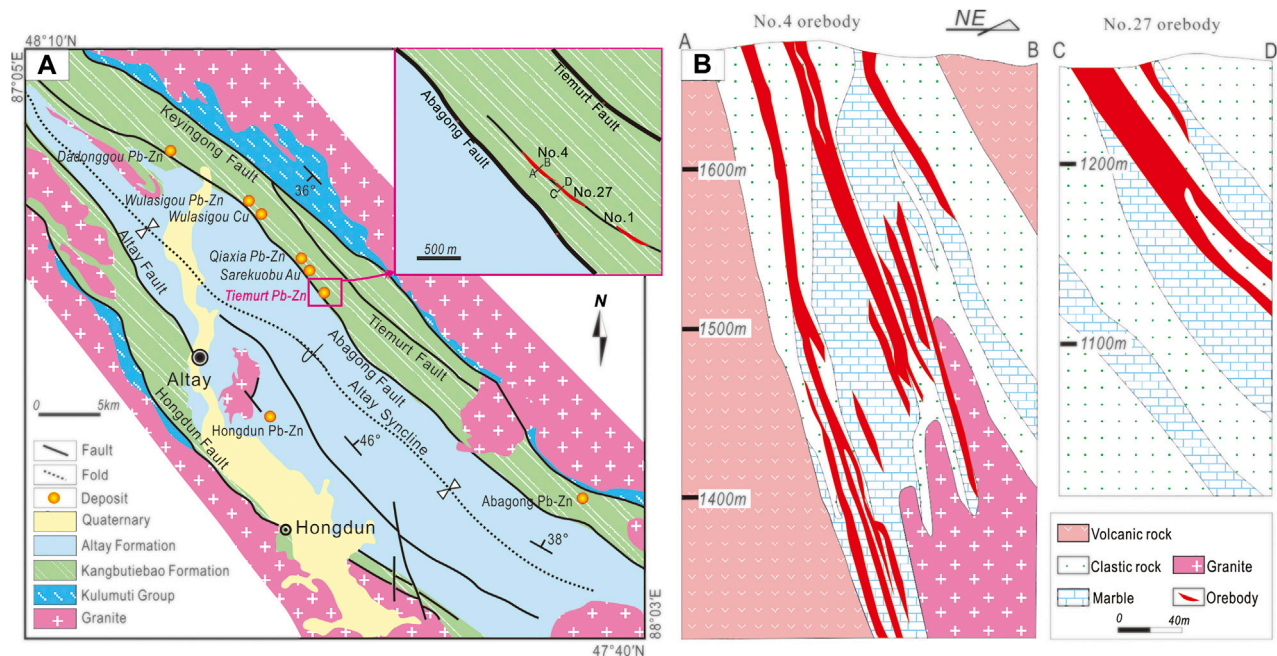


FIGURE 2 | (A) Geological map of the Kelan Basin and ore deposits, and the inserted geological map of the Tiemurt Pb–Zn–Cu deposit (modified after Geological Team 706 of the Xinjiang Bureau of Nonferrous Metals, 2000). **(B)** Geological cross sections of the Tiemurt ore bodies No. 4 and No. 27 (modified after Xinjiang Geological Team 706, 2000).

interlayered with marine carbonates with an eruptive age of ~400 Ma through zircon U–Pb dating (Chai et al., 2009; Zheng et al., 2015). Slate, greywacke, schist, and phyllite are the diagnostic rocks assemblage of the Altay Formation. In addition, all the abovementioned strata suffered regional amphibolite to greenschist-facies metamorphism during the subsequent Permian to Triassic orogenesis (Zhuang, 1994; Laurent et al., 2002). Limited Ordovician–Early Jurassic intermediate to felsic intrusions are exposed in the Kelan Basin (Figure 2A).

Ore Deposit Geology of the Tiemurt

The Tiemurt polymetallic deposit contains a confirmed metal reserve of Pb–Zn (0.29 million tons) and Cu (0.15 million tons), as well as economic Au (8 tons). Three principal lode ore bodies (Nos. 1, 4, and 27) accounted for ~90% of the total reserves. They are controlled by the Abagong Fault and its subordinate faults that trend to NW trending with a highly dipping angle of 49–80° (Figure 2B). Intensive alterations, marked by quartz, calcite, chlorite, epidote, biotite, amphibole, tremolite, and garnet, are widely presented along the ore bodies and ore-controlled faults in the ore-hosting Kangbutiebao Formation.

A majority of metallic minerals, including pyrite, galena, sphalerite, chalcopyrite, and pyrrhotite, present ore fabrics of massive, banded, disseminated, or as veinlets and breccias. Taking into account of paragenesis sequences, two major metallogenic ore-forming stages attributed to metal accumulation are identified, that is, the seafloor sedimentation and regional orogeny-related metamorphic hydrothermal activities (Yu and Zheng, 2019).

SAMPLING AND ANALYTICAL METHODOLOGY

Sampling

A total of six host rock samples that contain visible garnet grains were collected from the Nos. 4 and 27 ore bodies at Tiemurt. These samples can be categorized into two types of sulfides-bearing (mineralized) and -barren (unmineralized) ones, respectively (Figure 3). All samples were polished into thin sections with thickness of 30 μm for petrographic study (Figure 4). After petrographic examination under microscope, three samples (Nos. 10TMZK-49, 10TM-26-1, and 10TM-26-2) were conducted for textural and mineral chemical analyses. Six garnet grains and their paragenetic amphibolite and biotite were analyzed to yield their textural characteristics by scanning electron microscope (SEM), as well as *in situ* major and trace elemental compositions using the coupled electron probe microanalysis (EPMA) and laser ablation–inductively coupled plasma mass spectrometry (LA-ICPMS), respectively. *In situ* LA-ICPMS and EPMA measurements were made at the same area of the minerals.

Internal Textual Analysis by SEM

After the detailed petrographic observation, we use a SIGMA scanning electron microscope (SEM) equipped with an

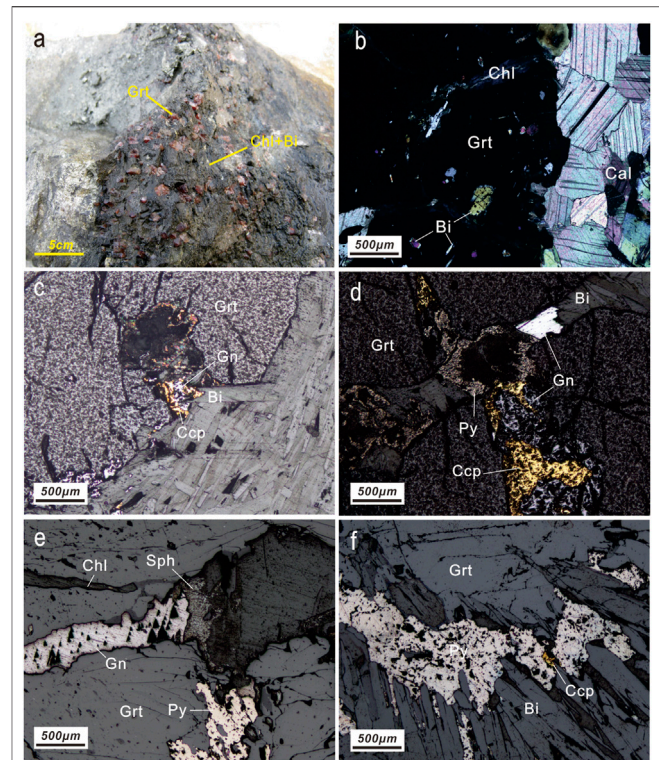


FIGURE 3 | (A) Reddish gem-garnet samples hosted in the greenschist from the Tiemurt deposit. (B) Biotite inclusion-rich Grt1 intergrown with chlorite and calcite. (C) and (D) Garnet1 coexists with chalcopyrite, chlorite, galena, and biotite. (E) and (F) Chalcopyrite, sphalerite, pyrite intergrown with garnet2, biotite, and chlorite.

X-MAX020 energy-dispersive spectrometer (EDS) that is housed at the School of the Earth Science and Geological Engineering, Sun Yat-Sen University (SYSU), to obtain internal textural information of the representative garnet grains. The instrument was operated on a backscattered electron (BSE) mode with an acceleration voltage of 20 Kv, a beam current of 20 nA, and a beam diameter of less than 1 μm.

Major Elements Analysis by EMPA

To yield major element compositions of the six garnet grains and their paragenetic amphibole, we adopted the JXA-8800 R electron probe micro analyzer (EMPA) at SYSU and the JEOL JXA-8100 EPMA at the Guangzhou Institute of Geochemistry, Chinese Academy of Science (GIG, CAS). The similar working conditions were set at an acceleration voltage of 15 kV, a beam current of 20 nA beam, and a beam diameter of 1–2 μm. Each point analysis of major elements contains a 10–20 s background acquisition (gas blank) followed by a 20 s data acquisition of the sample.

Trace Elements Analysis by LA-ICP-MS

To acquire the *in situ* minor and trace elemental compositions of garnet grains coupled with the above textures and major

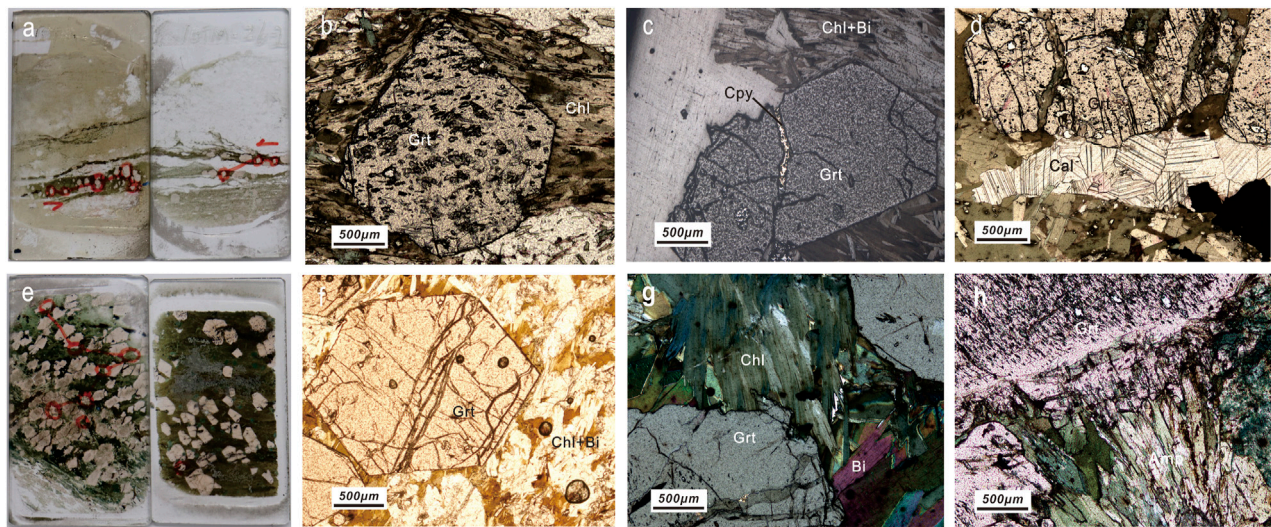


FIGURE 4 | Photographs of the garnets from the Tiemurt Pb-Zn-Cu deposit. **(A)** Thin sections (Nos. 10TM-26-1 and 10TM-26-2). **(B)** Photomicrograph of the sub- to euhedral mineral inclusion-rich Grt1 with chlorite (under the reflected light). **(C)** Photomicrographs of Grt1 garnet intergrown with chlorite and biotite, being cut by chalcopyrite veinlet (under the plane-polarized light). **(D)** Garnet grains in 10TM-26-1 intergrown with chlorite and calcite. **(E)** Thin sections (No. 10TMZK-49). **(F)** Photomicrograph of the mineral poor Grt2 intergrown with chlorite and biotite (under the cross-polarized light). **(G)** Photomicrograph of Grt2 coexisting with chlorite and biotite (under the cross-polarized light). **(H)** Garnet grains in 10TMZK-49 coexist with amphibole. Abbreviations: Amphibole = Amp, Biotite = Bi, Chalcopyrite = Cpy, Chlorite = Chl, Calcite = Cal, Chalcopyrite = Cpy, and Garnet = Grt.

elements, we operated a laser ablation-inductively coupled plasma-mass spectrometry (LA-ICP-MS) at the GIG, CAS. Each ablative spot of garnet grain was performed at the size of 47 µm in diameter, the laser repetition rate of 5 Hz, and the beam energy of ~7.2 J/cm² using helium as the carrier gas. The operation time include a 30 s background and a 60 s elemental information measurement. Thirty-five elements (Sc⁴⁵, V⁴⁹, Cr⁵³, Co⁵⁹, Ni⁶⁰, Cu⁶³, Zn⁶⁶, Ga⁶⁹, Rb⁸⁵, Sr⁸⁸, Y⁸⁹, Zr⁹¹, Nb⁹³, Cs¹³³, Ba¹³⁸, La¹³⁹, Ce¹⁴⁰, Pr¹⁴¹, Nd¹⁴³, Sm¹⁴⁷, Eu¹⁵¹, Gd¹⁵⁵, Tb¹⁵⁹, Dy¹⁶³, Ho¹⁶⁵, Er¹⁶⁶, Tm¹⁶⁹, Yb¹⁷³, Lu¹⁷⁵, Hf¹⁷⁸, Ta¹⁸¹, Pb²⁰⁸, Th²³², and U²³⁸) were measured. Data quantification is used in the united method of the internal standard method (Longerich et al., 1996) and the external standard of zircon 91,500 (Wiedenbeck et al., 1995). To monitor the instrumental drift, we analyzed the standard twice every 1.5 h at the condition of a 100 µm beam and a 10 Hz laser repetition rate.

RESULTS

Textural Characteristics of Garnet Grains

As illustrated in the Table 1 and Figure 3, the garnet grains are commonly intergrown with amphibolite, biotite, chlorite, calcite, chalcopyrite, pyrite, and sphalerite. Most of garnet grains present euhedral to subhedral crystals with a diameter of 0.3–5 cm in diameter (Figure 3A). In combination with their reddish color and good transparency, they can be classified into the gem-grade garnet (Figure 4). No distinctive textural zonation was observed in these garnet grains in microscopic observation and in BSE imaging (Figures 3C–F–F, 4, 5).

A slight difference is identified between these garnet grain samples. The garnet grains in samples 10TM-26-1 and 10TM-26-2 are intergrown with calcite, biotite, chalcopyrite, and chlorite with a smaller grain size of 0.01–3 cm in diameter (Figures 4A–D). In contrast, the garnet grains in sample 10TMZK-49 coexist with chlorite, amphibole, and biotite with a diameter of 0.5–5 cm in diameter (Figures 4E–H).

Major Elemental Compositions

The Supplementary Table S1 shows all the major elemental compositions of 41 spots in six representative garnet grains from three samples, and the Table 2 presents the selected major elements with relatively high contents.

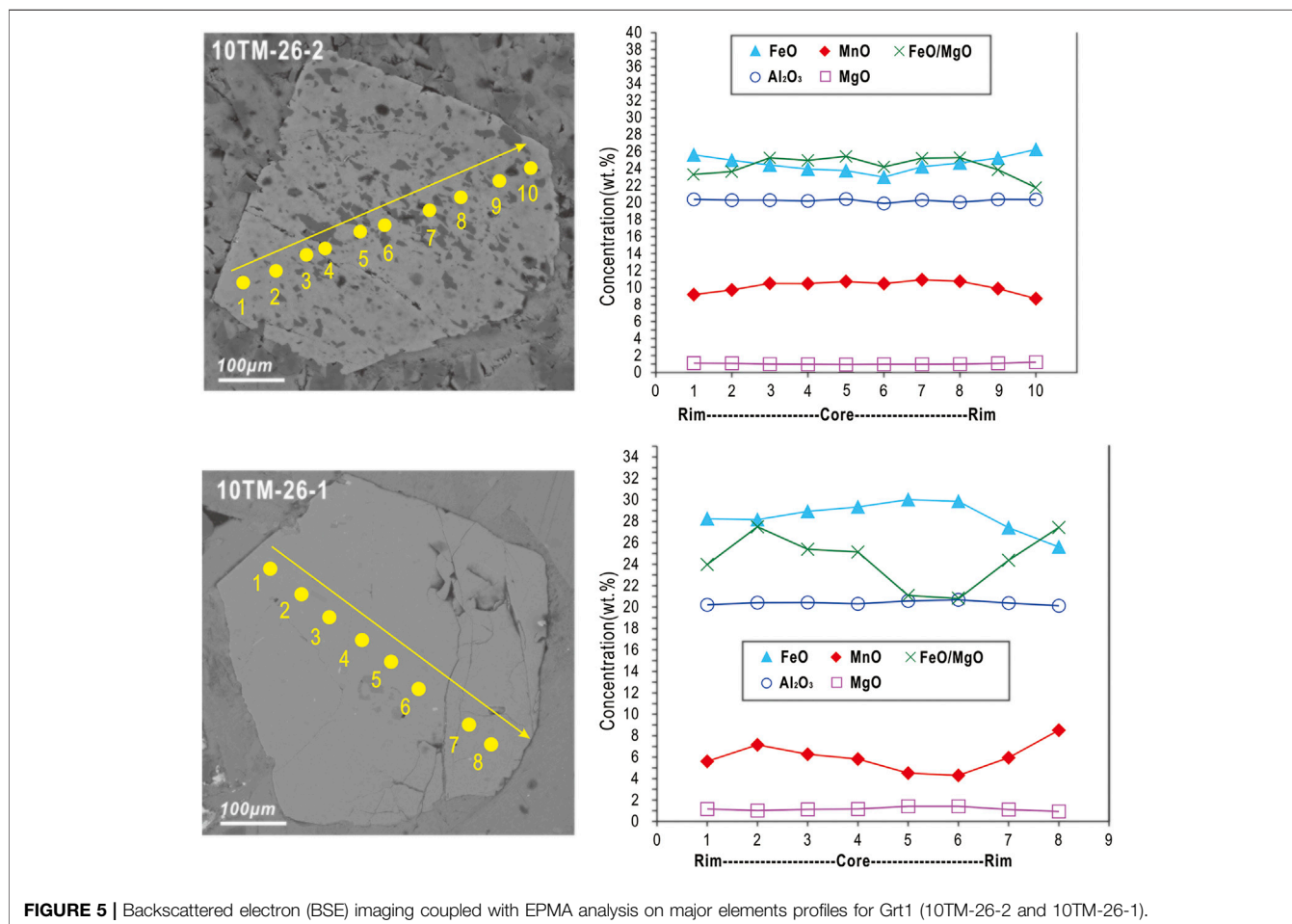
Garnet

A total of 41 EMPA spot analyses were completed on the six garnet grains, including 13 spots on sample 10TMZK-49 and 14 spots each for samples 10TM-26-1 and 10TM-26-2. The results indicate that grains in 10TMZK-49 has SiO₂, MnO, and FeO concentrations of 36.63–37.46 wt%, 0.79–3.65 wt%, and 31.74–35.86 wt%, respectively. The SiO₂, MnO, and FeO concentrations of garnets in 10TM-26-2 vary from 36.36 wt% to 37.22 wt%, 8.68 wt% to 10.90 wt%, and 22.93 to 26.36 wt%, respectively. While the grain in 10TM-26-1 vary from 36.23 wt% to 37.23 wt%, 4.29 wt% to 12.67 wt%, and 23.23 wt% to 30.02 wt %, respectively (Table 2).

As exhibited in the Figure 6, most of the garnet grains are plotted from the spectrum of spandite (spessartite–almandine) with compositions ranging from Alm_{49.31}Gro_{18.42} to Alm_{76.56}Gro₁₁. It is notable that no analysis is plotted in the field of spessartite + andradite + uvarovite.

TABLE 1 | Sampling description of two garnet generations in the Tiemurt deposit.

Sample No.	Position	Mineral assemblage	Size	Shape	Color
10TMZK-49	No. 4 ore body	Garnet, chlorite, biotite, amphibole, chalcopyrite, pyrite, and galena	0.5–5 cm	Euhedral to subhedral	Reddish
10TM-26-2	No. 27 ore body	Garnet, calcite, chlorite, chalcopyrite, sphalerite, and pyrite	0.01–0.3 cm	Euhedral to subhedral	Reddish
10TM-26-1	No. 27 ore body	Garnet, chlorite, calcite, chalcopyrite, sphalerite, and pyrite	0.01–0.3 cm	Euhedral to subhedral	Reddish

**FIGURE 5** | Backscattered electron (BSE) imaging coupled with EPMA analysis on major elements profiles for Grt1 (10TM-26-2 and 10TM-26-1).

Despite homogeneously isotropic textures observed in these garnet grains by BSE imaging (Figure 5), we conduct two profiles of major elements to examine whether they host chemical zonings. As a result, one garnet grain in 10TM-26-2 shows remarkable chemical zoning (Figure 5A). From core to rim, the almandine shows a significant increasing trend (56.30 mole % for rim and 49.31 mole % for core), but spessartine and grossularite show a decreasing trend from rim to core.

Different major elements show different spatial distribution pattern in the major elemental profiles (Figure 5B). Manganese (Mn) element is relatively enriched in the core, but iron (Fe) is enriched in the rim. In contrast, the elements of magnesium (Mg) and aluminum (Al) show no significant compositional variation from core to rim. Furthermore, the

ratios of iron to magnesium (expressed by FeO/MgO) present significantly higher contents from core to rim, which is consistent with the compositional variations of spessartine and andradite.

Notably, the almandine, grossularite, and pyrope components in garnet grains are heterogeneous from core to rim. For 10TM-26-1, the contents of almandine range from 57.39 mole (%) to 64.41 mole (%) that decreases slightly from rim to core, and then decreases from core to rim (Figure 5B, Table 4). By comparison, the spessartine and andradite increase from rim to core, and then decrease from core to rim. The FeO/MnO ratios vary consistently to the almandine, grossularite, and pyrope variations. Moreover, FeO/MgO ratio variations are analogous to spessartine and andradite variations. The contents

TABLE 2 | EMPA geochemical data (wt%) of the Tiemurt garnets.

No.	10TMZK-49-G1						10TMZK-49-G2						
Id	1	2	3	4	5	6	1	2	3	4	5	6	7
SiO ₂	37.46	36.97	37.19	36.80	36.63	36.68	36.96	37.24	37.08	37.02	36.98	37.06	36.92
TiO ₂	0.04	0.03	0.02	0.00	0.00	0.01	0.03	0.04	0.02	0.00	0.00	0.00	0.05
Al ₂ O ₃	20.68	20.52	20.50	20.52	20.37	20.14	20.38	20.59	20.48	20.61	20.70	20.44	20.41
Cr ₂ O ₃	0.00	0.00	0.00	0.01	0.01	0.02	0.00	0.00	0.00	0.00	0.01	0.00	0.00
FeO	33.23	33.34	33.90	33.24	32.22	31.74	33.69	34.25	34.10	35.86	34.23	33.01	33.60
MnO	3.30	2.86	2.93	2.41	3.64	3.65	2.97	1.74	1.39	0.79	1.75	2.99	2.51
MgO	0.92	0.80	0.90	0.83	0.89	0.92	0.88	1.34	1.44	1.73	1.32	0.88	0.85
CaO	6.09	6.53	6.00	6.76	6.21	6.50	6.09	6.00	6.48	5.26	6.26	6.39	6.28
Total	101.73	101.04	101.43	100.58	99.97	99.66	101.00	101.20	100.99	101.27	101.23	100.77	100.61
Si	2.99	2.97	2.98	2.97	2.98	2.99	2.98	2.98	2.97	2.96	2.96	2.99	2.98
Ti	0.00	0.00	0.00	0.00	0.00	0.00	0.00	0.00	0.00	0.00	0.00	0.00	0.00
Al	1.94	1.94	1.94	1.95	1.95	1.93	1.93	1.94	1.93	1.95	1.95	1.94	1.94
Cr	0.00	0.00	0.00	0.00	0.00	0.00	0.00	0.00	0.00	0.00	0.00	0.00	0.00
Fe ³⁺	0.06	0.07	0.08	0.07	0.06	0.08	0.08	0.07	0.08	0.08	0.07	0.07	0.07
Fe ²⁺	2.16	2.17	2.20	2.18	2.12	2.08	2.19	2.22	2.20	2.32	2.22	2.15	2.20
Mn	0.22	0.19	0.20	0.17	0.25	0.25	0.20	0.12	0.09	0.05	0.12	0.20	0.17
Mg	0.11	0.10	0.11	0.10	0.11	0.11	0.11	0.16	0.17	0.21	0.16	0.11	0.10
Ca	0.52	0.56	0.52	0.59	0.54	0.57	0.53	0.51	0.56	0.45	0.54	0.55	0.54
Ura	0.00	0.01	0.00	0.04	0.04	0.06	0.00	0.00	0.00	0.00	0.02	0.00	0.00
And	3.06	3.53	3.77	3.25	3.19	3.80	3.99	3.42	4.09	3.86	3.45	3.44	3.46
Pyr	3.63	3.16	3.55	3.29	3.56	3.69	3.49	5.31	5.67	6.81	5.18	3.49	3.40
Spe	7.42	6.44	6.59	5.45	8.29	8.34	6.70	3.91	3.13	1.77	3.90	6.77	5.70
Gro	14.23	15.06	13.31	16.03	14.65	14.95	13.40	13.64	14.30	11.00	14.22	14.84	14.55
Alm	71.66	71.80	72.78	71.94	70.27	69.15	72.43	73.73	72.80	76.56	73.24	71.46	72.89
Other	0	0	0	0	0	0	0	0	0	0	0	0	0

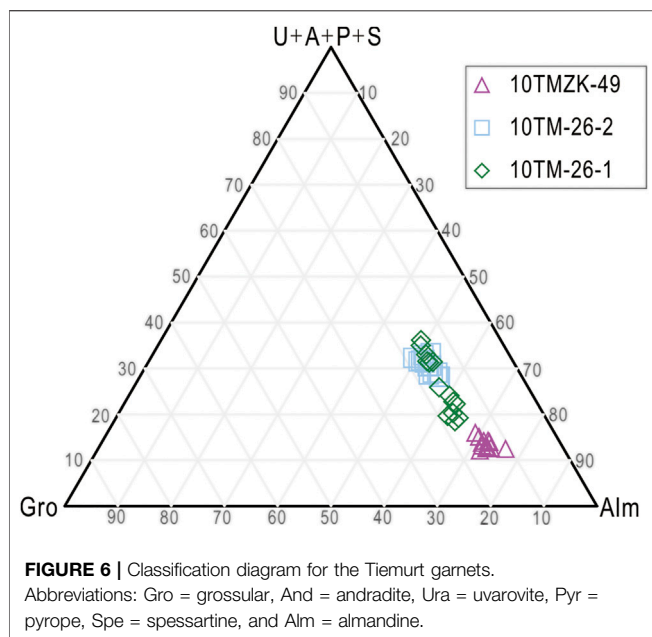
No.	10TM-26-1-G1						10TM-26-2-G1			
Id	1	2	3	4	5	6	1	2	3	4
SiO ₂	37.16	37.23	36.72	36.87	36.73	36.64	37.22	37.02	37.18	36.58
TiO ₂	0.09	0.10	0.08	0.12	0.09	0.08	0.15	0.04	0.07	0.06
Al ₂ O ₃	20.20	20.19	20.21	20.12	20.20	20.57	20.25	20.46	20.40	20.29
Cr ₂ O ₃	0.00	0.00	0.00	0.00	0.00	0.01	0.00	0.02	0.00	0.00
FeO	25.18	23.46	23.23	24.88	24.18	24.95	24.84	26.36	25.52	25.96
MnO	10.27	12.23	12.67	10.39	11.38	11.06	10.06	8.68	8.95	9.03
MgO	0.81	0.67	0.72	0.76	0.71	0.82	0.97	1.20	1.12	1.14
CaO	7.28	7.07	6.85	7.35	6.93	6.45	7.58	6.83	7.51	6.82
Total	101.00	100.94	100.48	100.49	100.22	100.56	101.05	100.60	100.75	99.87
Si	2.98	2.99	2.97	2.98	2.97	2.96	2.98	2.98	2.98	2.97
Ti	0.01	0.01	0.01	0.01	0.01	0.00	0.01	0.00	0.00	0.00
Al	1.91	1.91	1.93	1.91	1.93	1.96	1.91	1.94	1.93	1.94
Cr	0.00	0.00	0.00	0.00	0.00	0.00	0.00	0.00	0.00	0.00
Fe ³⁺	0.10	0.09	0.09	0.10	0.09	0.06	0.10	0.07	0.08	0.08
Fe ²⁺	1.59	1.48	1.48	1.58	1.55	1.62	1.57	1.70	1.63	1.68
Mn	0.70	0.83	0.87	0.71	0.78	0.76	0.68	0.59	0.61	0.62
Mg	0.10	0.08	0.09	0.09	0.09	0.10	0.12	0.14	0.13	0.14
Ca	0.63	0.61	0.59	0.64	0.60	0.56	0.65	0.59	0.64	0.59
Ura	0.00	0.00	0.00	0.00	0.00	0.03	0.00	0.06	0.00	0.00
And	4.87	4.57	4.56	4.88	4.25	3.17	4.86	3.69	4.09	4.01
Pyr	3.20	2.66	2.85	3.04	2.85	3.23	3.83	4.77	4.43	4.56
Spe	23.17	27.68	28.67	23.53	25.85	24.93	22.64	19.56	20.15	20.46
Gro	15.90	15.69	15.04	16.17	15.67	15.20	16.72	15.71	17.30	15.54
Alm	52.84	49.39	48.87	52.37	51.38	53.44	51.96	56.20	54.03	55.43
Other	0	0	0	0	0	0	0	0	0	0

Note: All the calculations are based on 12 oxygens. Abbreviations: Ura-uvarovite, And-andradite, Pyr-pyrope, Spe-spessartine, Gro-grossular, Alm-almandine, and Amp-amphibole. "-": Below the detection limit.

of FeO are higher in core than rim, but its variations from rim to core are different. Distinctively, MnO is weakly zoned in core and it varies consistently to the FeO/MgO variations. While Al₂O₃ and MgO concentrations show no spatial variations from core to rim.

Amphibolite

Somewhat amounts of amphibole grains coexist with garnet grains in 10TMZK-49 (Figure 4), and two analyses of their compositions are listed in Table 3. They contain major compounds of SiO₂, MgO, Al₂O₃, MnO, and



FeO contents up to 40.51–51.94 wt%, 4.67–11.70 wt%, 0.32–15.01 wt %, 0.18–0.73 wt%, and 23.45–33.25 wt%, respectively.

Trace Elemental Compositions

A total of thirty (30) trace elements analyses were conducted on garnet grains in the three samples, including 10 spots in 10TMZK-49, and 20 spots in 10TM-26-1 and 10TM-26-2. The results are listed in the **Table 5**, and the spike diagrams of rare earth elements (REEs) are plotted in the **Figure 7**, and the spike and statistical column diagrams of trace elements are displayed in the **Figure 8**.

The garnet grains in three samples show similar chondrite-normalized REE patterns. High rare-earth elements (HREE) are relatively enriched with the \sum HREE values of 21.43–101.98 ppm (mean = 41.65 ppm). Moreover, the values of \sum LREE/ \sum HREE is extremely low (0.03–0.13, mean = 0.071). The feature of cerium negative anomaly (δ Ce = 0.11–4.17, mean = 0.58) and europium positive anomalies (Eu/Eu* = 1.28–2.57, mean = 1.66) is also identified.

In addition, the large-ion lithophile elements (LILE) are extremely depleted in all garnet grains, with negligible amounts of Rb, Sr, and Ba, much lower than the value of average primitive mantle (Sun and McDonough, 1989; **Figure 8**). By contrast, the high-field elements (HFS), such as Th, Zr, and Y, are relatively enriched in the Tiemurt garnet than the values of average primitive mantle (**Figure 8**). As for the trace elements of P, Sm, and Ti, both the Tiemurt garnet and average primitive mantle show no obvious distinction in concentrations (**Figure 8**).

DISCUSSION

Mineral Growth History and Origin of Garnet

The systematic textural and chemical characteristics provide solid evidence for our discussion on mineral growth history

TABLE 3 | EMPA geochemical data (wt%) of the Tiemurt amphibole.

No. Id	10TMZK-49	
	1	2
K ₂ O	0.44	0.52
Na ₂ O	1.18	1.01
SiO ₂	40.51	41.13
TiO ₂	0.15	0.12
Al ₂ O ₃	15.01	14.13
FeO	23.75	23.45
MgO	4.67	5.46
MnO	0.2	0.18
CaO	11.45	11.43
Total	97.33	97.22

and origin of the Tiemurt gem-grade garnet grains (Vander and Andre, 1991; Zhao et al., 1999; Martin et al., 2011). During the mineral growing, the garnet can grow to geo grade under the conditions of 1) the adequate influx supplying and 2) large enough growth space (Hickmott and Spear, 1992; Baxter et al., 2013). Our garnet displays relatively coarse and euhedral grains (**Figure 3A**), indicative of a well-supplied open space. However, the origin of Tiemurt garnet, such as mantle, ocean crust, skarn metasomatism, sedimentary exhalation, or metamorphism, needs to be discussed in detail (Gemmell et al., 1992; Hoal et al., 1994; Burton et al., 1999).

In the skarn deposit, the magmatic-hydrothermal fluids replace host carbonates to facilitate growth of gem-grade garnet (Jeremy and Hamid, 2013). In this case, the skarn garnet universally hosts some clear occasional zonation because of the relatively low rate of the metasomatic process (Vander and Andre, 1991; Park et al., 2017). In fact, the growth rate also acts as an important factor in controlling the grain size as well as the zonation pattern of garnet (Jamtveit and Hervig, 1994; García-Ruiz and Otálora, 2015). No textural zonation in the Tiemurt garnet implies a relatively high growth rate, which also exclude their possibility of magmatic-hydrothermal origin analogy to skarn (Jamtveit, 1991; Jamtveit et al., 1993; Zang et al., 2019).

The chemical compositions further provide reliable evidences for the garnet origin (Zhai et al., 2014; An et al., 2017). It is consensus that an abundance of Fe and Mn is distributed in the seawater, and therefore the garnet with sedimentary exhalation origin is Fe and Mn rich for their incorporation into the garnet crystal lattices (Gemmell et al., 1992; Burton et al., 1999). For the Tiemurt garnet, the feature of Al and Fe rich but Ca and Mn depleted are not products of seafloor sedimentation (Zheng et al., 2013a). Considering that no rocks related to the mantle transition zone or subducting ocean crust have been reported in the region, the only possible origin for the Tiemurt garnet is metamorphic.

In fact, the variations of geological occurrence, mineral assemblages, mineralogy, textures, and chemistry between Grt1 and Grt2 are just caused by the orogeny-related metamorphism and deformation (Chen et al., 2012; Zheng

TABLE 4 | EMPA geochemical data (wt%) of the two generation garnet profiles.

10TM-26-2-G2										
No.										
Id	1 (Rim)	2	3	4	5 (Core)	6 (Core)	7	8	9	10 (Rim)
SiO ₂	36.84	36.79	36.85	36.82	36.89	36.36	36.83	36.78	36.79	36.78
TiO ₂	0.02	0.06	0.04	0.03	0.04	0.04	0.07	0.09	0.05	0.05
Al ₂ O ₃	20.36	20.27	20.29	20.19	20.42	19.90	20.30	20.02	20.36	20.34
Cr ₂ O ₃	0.03	0.02	0.02	0.00	0.01	0.00	0.00	0.02	0.00	0.00
FeO	25.61	24.96	24.39	23.91	23.74	22.96	24.20	24.64	25.22	26.22
MnO	9.16	9.71	10.47	10.44	10.69	10.45	10.90	10.73	9.86	8.69
MgO	1.10	1.06	0.97	0.96	0.94	0.95	0.96	0.98	1.06	1.20
CaO	7.12	7.31	7.32	7.41	7.46	7.82	7.25	6.81	7.01	6.68
Total	100.24	100.16	100.35	99.76	100.17	98.48	100.52	100.06	100.35	99.97
Si	2.97	2.97	2.97	2.98	2.98	2.98	2.97	2.98	2.97	2.98
Ti	0.00	0.00	0.00	0.00	0.00	0.00	0.00	0.01	0.00	0.00
Al	1.94	1.93	1.93	1.93	1.94	1.92	1.93	1.91	1.94	1.94
Cr	0.00	0.00	0.00	0.00	0.00	0.00	0.00	0.00	0.00	0.00
Fe ³⁺	0.08	0.09	0.09	0.08	0.07	0.09	0.09	0.10	0.08	0.07
Fe ²⁺	1.65	1.60	1.56	1.54	1.53	1.49	1.54	1.57	1.62	1.70
Mn	0.63	0.66	0.72	0.72	0.73	0.73	0.74	0.74	0.67	0.60
Mg	0.13	0.13	0.12	0.12	0.11	0.12	0.12	0.12	0.13	0.15
Ca	0.62	0.63	0.63	0.64	0.64	0.69	0.63	0.59	0.61	0.58
FeO/MgO	23.26	23.68	25.15	24.85	25.31	24.12	25.10	25.17	23.79	21.78
Ura	0.09	0.06	0.05	0.00	0.03	0.01	0.00	0.06	0.00	0.00
And	3.87	4.23	4.29	4.07	3.50	4.35	4.45	4.90	4.06	3.66
Pyr	4.38	4.21	3.86	3.85	3.74	3.86	3.83	3.92	4.21	4.81
Spe	20.70	21.96	23.66	23.77	24.19	24.05	24.57	24.40	22.26	19.71
Gro	16.40	16.62	16.59	17.27	17.82	18.42	16.24	14.63	15.96	15.52
Alm	54.56	52.92	51.56	51.04	50.72	49.31	50.91	52.09	53.50	56.30
Other	0	0	0	0	0	0	0	0	0	0

10TM-26-1-G2								
No.								
Id	1	2	3	4 (Core)	5 (Core)	6	7	8 (Rim)
SiO ₂	36.82	37.05	36.79	36.87	36.98	36.70	36.26	36.23
TiO ₂	0.04	0.06	0.05	0.03	0.03	0.04	0.06	0.09
Al ₂ O ₃	20.22	20.42	20.43	20.31	20.59	20.70	20.39	20.14
Cr ₂ O ₃	0.01	0.02	0.00	0.00	0.00	0.04	0.02	0.00
FeO	28.24	28.15	28.93	29.35	30.02	29.87	27.41	25.61
MnO	5.61	7.15	6.28	5.83	4.52	4.29	5.94	8.51
MgO	1.18	1.02	1.14	1.17	1.42	1.43	1.13	0.93
CaO	6.65	6.82	6.93	6.97	6.96	7.30	6.64	6.45
Total	98.77	100.69	100.56	100.52	100.52	100.37	97.85	97.97
Si	3.01	2.98	2.96	2.97	2.97	2.95	2.99	2.99
Ti	0.00	0.00	0.00	0.00	0.00	0.00	0.00	0.01
Al	1.95	1.94	1.94	1.93	1.95	1.96	1.98	1.96
Cr	0.00	0.00	0.00	0.00	0.00	0.00	0.00	0.00
Fe ³⁺	0.05	0.07	0.08	0.09	0.07	0.06	0.02	0.04
Fe ²⁺	1.88	1.82	1.87	1.89	1.95	1.95	1.87	1.72
Mn	0.39	0.49	0.43	0.40	0.31	0.29	0.41	0.60
Mg	0.14	0.12	0.14	0.14	0.17	0.17	0.14	0.11
Ca	0.58	0.59	0.60	0.60	0.60	0.63	0.59	0.57
FeO/MgO	23.98	27.49	25.40	25.15	21.08	20.84	24.37	27.42
Ura	0.04	0.05	0.00	0.00	0.00	0.11	0.07	0.01
And	2.43	3.71	4.01	4.43	3.37	3.07	1.12	2.19
Pyr	4.79	4.07	4.51	4.63	5.64	5.65	4.60	3.82
Spe	12.96	16.16	14.14	13.13	10.17	9.62	13.80	19.81
Gro	16.96	15.72	15.71	15.45	16.43	17.50	18.33	16.78
Alm	62.82	60.30	61.63	62.36	64.41	64.04	62.09	57.39
Other	0	0	0	0	0	0	0	0

Note: All the calculations are based on 12 oxygens. Abbreviations: Ura-uvarovite, And-andradite, Pyr-pyrope, Spe-spessartine, Gro-grossular, Alm-almadine, and Amp-amphibole. "–": Below the detection limit.

et al., 2013a). In the early stage of orogenesis, the wall rocks are highly foliated to form garnet schists (Grt1). As the orogenesis continues, the ongoing structural development and accompanying large-scale fluid activities cause destruction of Grt1 and Grt2

precipitations in the larger host space. This mineral growth process is recorded by the variations of grain size, micromineral inclusions, and mineral assemblages between Grt1 and Grt2.

Physicochemical Condition Recorded by Garnet

Under the metamorphic environment, we can utilize the contents and variations of Ca, Mn, Fe, and Mg in garnet to evaluate the pressure (P)–temperature (T) condition (Andrew, 1994; Gerya et al., 1997). The principle is that the P-T condition has an impact on cooperation of these cations into crystal structures of garnet in relation with anions' charge and radius (Shannon, 1976; Smith et al., 2004; Xia et al., 2016). For the same (II) charge substituting to the "A" location, the decreasing order of anions radius $\text{Ca}^{2+} > \text{Mn}^{2+} > \text{Fe}^{2+} > \text{Mg}^{2+}$ is sensitive to reflect the fluctuation of the P-T condition (Zhou et al., 2014), that is, Ca-rich garnet formed in low-pressured contact metamorphism, Mn-Al-rich garnet formed in low-grade regional metamorphism, Fe-Al-rich garnet formed in relatively higher regional metamorphism, and Mg-rich garnet formed in high-pressured metamorphism (Yardley et al., 1991; Jamtveit et al., 1993; Crowe et al., 2001; Fernando et al., 2003). Therefore, the Tiemurt Fe-Al-rich garnet is formed in relatively higher regional metamorphism. In consideration of regional geology (Chen et al., 2012), the low-amphibolite to middle-greenschist facies are the preferred window for the Tiemurt garnet.

Amphibole is a common mineral of metabasites from amphibolite to greenschist facies, and its composition changes regularly with metamorphic grade (Triboulet, 1992). The amphibole paragenetic with garnet allows us to calculate more accurate P-T condition (Gerya et al., 1997). Here, we adopt the methodology of Gerya et al. (1997) based on the Gibbs' phase rule at mineral equilibrium (Holland and Blundy, 1994; Gerya et al., 1997). The calculation is based on the following formula derivation, that is,

$$T(K) = \frac{6119 - 28.4P + 114X_{\text{Mg}}^{\text{Hbl}}}{8.181 - R \ln(8.489 - \text{Si}^{\text{Hbl}})}$$

$$P(\text{kbar}) = \left[2543 - 4.744T + 175X_{\text{Mg}}^{\text{Hbl}} + RT \ln(\text{Al}^{\text{Hbl}} + 1.433) \right] \times /148.1,$$

where $P = P$, kbar; $T = T$, K; $X_{\text{Mg}}^{\text{Hbl}} = \text{Mg}/(\text{Fe} + \text{Mg})$, bulk Mg mole fraction of amphibole; and Si^{Hbl} and Al^{Hbl} are Si and Al in amphibole calculated on 13 cations.

The calculated temperature range of 10TMZK-49 is 640–643°C at the pressure of 5,218–5,900 bar (Table 6).

Additionally, we can use the distribution patterns of REE and trace elements to further deduce the acidity and redox condition (Sverjensky, 1984; Bau, 1991). It is suggested that REE fractionation is strongly dependent on the hydrothermal fluid pH (Bau, 1991), HREE enrichment, and LREE depletion with weak negative or no Eu anomalies indicating a nearly neutral environment. Garnet from the Tiemurt is characterized as HREE-rich, LREE-depleted, and weak positive Eu anomaly (Figure 7). Fractionation of HREE against LREE is controlled by the major compositions such as Al and Fe in garnet, and the weak positive Eu anomaly is caused by the metamorphic hydrothermal fluids under mildly acidic condition (Scherer et al., 2000; Pertermann et al., 2004; Schmidt et al., 2011; Cheng et al., 2012). In this case, the REE pattern is chiefly determined by the complex agents (e.g.,

Cl^-) that enhance stability of Eu^{2+} , rather than REE^{3+} , in solution (Geiger et al., 1989; Ballaran et al., 1999), which can produce distinct positive Eu anomalies. The presence of chlorite intergrown with garnet also supports the mildly acidic condition, which facilitates soluble Eu^{2+} transporting and substituting Fe^{2+} in garnet crystal to form distinctly positive Eu anomalies (Smith et al., 2004; Gaspar et al., 2008).

Another evidence is the concentrations of uranium, which is a redox-sensitive element with different valence states of U^{4+} and U^{6+} (Smith et al., 2004; Zhang et al., 2017b). The decrease of $f\text{O}_2$ in the hydrothermal fluids reduces the solubility of U and increases the incorporation of U into Garnet. It means that the higher U contents of garnet may indicate the lower $f\text{O}_2$ of hydrothermal fluids. At the Tiemurt, Grt1 has lower U contents (0.0002–0.19 ppm) than those of Grt2 (0.02–12.5 ppm), which partly indicate that Grt1 hosts higher $f\text{O}_2$.

Additionally, the iron electrovalence ratio ($\text{Fe}^{2+}/\text{Fe}^{3+}$) is also an important oxygen fugacity indicator of garnet (Park et al., 2017; Liang et al., 2021). For the garnet $\text{A}_3\text{B}_2(\text{SiO}_4)_3$ formula, the cations of Fe^{2+} and Fe^{3+} can be accommodated into the crystal structure of A and B, respectively. For the B location, both Al^{3+} and Fe^{3+} can occupy together, and therefore Al-rich chemical composition can reduce the amount of Fe^{3+} (Jamtveit et al., 1993). In the Tiemurt garnet, Grt1 yields a more Al-rich chemical composition that can be calculated into the equal $\text{Fe}^{2+}/\text{Fe}^{3+}$ ratios of 15.9–23.1, distinct from Grt2 with a higher $\text{Fe}^{2+}/\text{Fe}^{3+}$ ratio of 21.1–83.3. Therefore, the variation of $\text{Fe}^{2+}/\text{Fe}^{3+}$ from Grt1 to Grt2 records a significant decreasing trend of oxygen fugacity at the Tiemurt.

Furthermore, the enrichment of Th, Y, and HREE indicates a relatively reduced condition in Grt2 (Gaspar, 2005). Taking the element of Th for an example, the decreasing $f\text{O}_2$ value of the fluid system could reduce Th solubility in solution and in turn increase Th incorporation into garnet (Huang et al., 2014).

Metamorphic Garnet Linking With the Orogenic-Type Deposits in Altay

On the basis of above discussion, the garnets from the Tiemurt deposit are principally crystallized from the metamorphic hydrothermal fluids, and therefore the variations in garnet geochemistry are largely controlled by some external factors such as fluid compositions, fluid–rock interactions, and metasomatism dynamics (Jamtveit, 1991; Ottonello et al., 1996; Ottonello and Moretti, 1998; Gaspar et al., 2008). Grt1 and Grt2 host the similar fluid origin and fluid–rock interaction ratios, and therefore their chemical variations are possibly caused by metasomatism dynamics, that is, diffusive or infiltration metasomatism (Bau, 1991; Gaspar et al., 2008). The diffusive metasomatism will produce fluids with near-neutral pH and alteration products in which REE composition is buffered by the composition of the host rocks due to long pore fluid residence under closed-system conditions (Dziggel et al., 2009; Zhang et al., 2017a; Xiao et al., 2018). While the infiltration metasomatism, associated with an increase in fluid–rock interaction ratios, will produce fluids and mineral assemblages buffered by reduced, mildly acidic, external-derived fluids, where chloride complexes

TABLE 5 | Representative LA-ICP-MS data (ppm) of garnets from the Tiemurt deposit.

No.	GT1									
Id	1	2	3	4	5	6	7	8	9	10
Trace element										
Sr	0.021	0.000	0.000	0.033	0.011	0.000	0.000	0.042	0.025	0.020
Rb	0.000	0.042	0.000	0.000	0.010	0.001	0.025	0.064	0.022	0.000
Ba	0.000	0.000	0.000	0.030	0.028	0.059	0.052	0.000	0.000	0.000
Th	0.000	0.002	0.000	0.014	0.164	0.031	0.028	0.245	0.010	0.000
U	0.012	0.026	0.000	0.591	1.516	0.584	0.375	0.073	0.049	0.023
Ta	0.000	0.010	0.000	0.004	0.000	0.002	0.000	0.009	0.000	0.043
Nb	0.000	0.002	0.000	0.000	0.044	0.052	0.013	0.001	0.000	0.000
P	33.537	40.304	40.537	32.427	34.267	38.722	36.034	36.842	32.796	37.750
Zr	3.578	3.942	3.773	68.137	143.078	42.672	30.271	4.199	4.638	4.172
Hf	0.016	0.040	0.058	1.766	3.072	1.204	0.674	0.102	0.119	0.045
Ti	46.466	55.841	56.164	44.927	47.477	53.649	49.925	51.044	45.438	52.303
Y	94.569	92.279	66.469	77.404	54.408	66.340	54.650	40.667	52.979	80.598
REE										
La	0.000	0.000	0.000	0.000	0.054	0.000	0.031	0.016	0.000	0.000
Ce	0.244	0.010	0.021	0.000	0.050	0.088	0.023	0.060	0.051	0.019
Pr	0.117	0.173	0.230	0.059	0.127	0.000	0.097	0.283	0.189	0.237
Nd	0.739	0.763	0.839	1.008	0.807	0.774	0.275	0.395	0.253	0.379
Sm	9.024	10.390	9.865	10.042	11.036	8.402	11.575	9.710	11.049	10.367
Eu	26.575	29.058	26.545	29.117	26.642	28.363	29.007	29.237	29.933	26.730
Gd	32.409	31.830	29.613	31.123	27.296	29.138	31.245	26.526	30.765	29.781
Tb	36.030	37.053	33.286	33.791	27.393	29.324	28.226	24.437	26.902	36.701
Dy	47.151	46.328	35.571	39.922	26.586	34.811	30.429	24.912	29.826	40.725
Ho	57.155	55.752	38.859	45.130	30.698	38.012	30.829	23.533	29.352	44.864
Er	74.422	67.941	43.026	56.392	34.987	46.962	38.052	27.968	34.977	62.542
Tm	90.430	78.550	46.163	66.192	40.166	53.914	46.190	29.713	35.729	77.801
Yb	102.935	91.637	46.231	76.022	47.549	59.567	55.507	34.404	35.686	91.758
Lu	107.189	93.968	47.398	80.941	47.926	65.647	63.035	34.474	35.072	105.836
ΣREE	584.420	543.452	357.646	469.739	321.316	395.001	364.522	265.668	299.784	527.741
LREE	36.699	40.394	37.501	40.226	38.715	37.627	41.009	39.702	41.475	37.732
HREE	547.721	503.058	320.146	429.513	282.601	357.374	323.514	225.966	258.309	490.008
LREE/HREE	0.067	0.080	0.117	0.094	0.137	0.105	0.127	0.176	0.161	0.077
LaN/YbN	0.000	0.000	0.000	0.000	0.001	0.000	0.000	0.000	0.000	0.000
δEu	4.229	4.497	4.388	4.625	4.482	4.972	4.393	5.236	4.651	4.334
δCe	0.647	0.018	0.029	0.000	0.103	0.590	0.066	0.065	0.084	0.025

No.	GT2									
Id	1	2	3	4	5	6	7	8	9	10
Trace element										
Sr	0.024	0.014	0.046	0.017	0.000	0.010	0.000	0.037	0.000	0.000
Rb	0.034	0.000	0.000	0.000	0.012	0.000	0.053	0.019	0.030	0.013
Ba	0.000	0.042	0.000	0.017	0.000	0.000	0.000	0.013	0.015	0.051
Th	0.289	0.223	0.007	0.006	0.018	0.000	0.588	0.016	0.121	0.012
U	2.241	1.553	0.056	0.037	0.021	0.019	12.527	0.000	1.246	0.000
Ta	0.000	0.000	0.005	0.025	0.009	0.000	0.029	0.002	0.026	0.012
Nb	0.000	0.000	0.012	0.032	0.035	0.025	0.022	0.032	0.015	0.000
P	40.747	32.876	37.976	31.987	38.109	32.096	36.587	36.815	37.197	36.800
Zr	167.055	110.385	4.163	3.830	4.450	6.404	1,350.733	4.528	114.192	3.518
Hf	4.305	2.837	0.000	0.130	0.216	0.088	35.570	0.045	2.872	0.074
Ti	56.455	45.550	52.615	44.317	52.800	44.469	50.691	51.008	51.536	50.986
Y	34.559	62.959	111.729	93.450	150.614	128.534	139.929	102.712	108.036	82.849
REE										
La	0.000	0.031	0.000	0.000	0.021	0.000	0.000	0.111	0.043	0.029
Ce	0.032	0.056	0.000	0.005	0.039	0.061	0.004	0.018	0.037	0.021
Pr	0.225	0.211	0.000	0.000	0.000	0.000	0.025	0.000	0.000	0.028
Nd	0.000	0.378	0.953	0.498	0.452	0.309	0.632	0.000	0.173	0.937
Sm	7.080	5.596	5.367	8.865	9.607	9.118	9.526	6.099	7.795	5.553
Eu	21.915	21.530	22.508	25.412	27.075	28.145	26.841	25.004	24.334	21.353
Gd	19.620	23.900	28.772	28.740	32.100	29.660	30.044	27.967	25.659	27.271
Tb	17.696	28.649	36.197	36.040	42.895	37.396	42.376	36.991	34.451	30.589
Dy	16.733	31.967	50.877	45.802	59.839	52.838	61.972	45.593	46.816	40.309

(Continued on following page)

TABLE 5 | (Continued) Representative LA-ICP-MS data (ppm) of garnets from the Tiemurt deposit.

No.	GT2									
	1	2	3	4	5	6	7	8	9	10
Ho	16.564	32.037	62.313	52.091	82.521	68.587	83.550	55.819	60.413	44.990
Er	23.856	42.635	84.099	65.940	129.771	109.202	115.769	76.993	85.242	64.704
Tm	28.860	50.128	105.204	84.622	179.313	152.400	145.646	99.616	114.065	81.839
Yb	34.537	63.975	131.639	99.817	239.726	205.976	190.661	122.911	156.172	105.187
Lu	39.003	71.522	147.738	113.165	279.686	247.076	223.939	139.362	182.381	122.095
ΣREE	226.121	372.613	675.667	560.998	1,083.044	940.768	930.983	636.485	737.582	544.906
LREE	29.252	27.801	28.828	34.780	37.194	37.633	37.027	31.232	32.383	27.922
HREE	196.869	344.812	646.839	526.218	1,045.850	903.135	893.956	605.253	705.199	516.985
LREE/HREE	0.149	0.081	0.045	0.066	0.036	0.042	0.041	0.052	0.046	0.054
LaN/YbN	0.000	0.000	0.000	0.000	0.000	0.000	0.000	0.001	0.000	0.000
δEu	5.331	4.856	4.433	4.430	4.263	4.759	4.440	4.900	4.773	4.357
δCe	0.044	0.078	-	0.177	0.378	0.778	0.046	0.128	0.366	0.163

No.	GT3									
	1	2	3	4	5	6	7	8	9	10
Trace element										
Sr	0.027	0.009	0.000	0.039	0.000	0.021	0.000	0.000	0.001	0.000
Rb	0.039	0.000	0.036	0.031	0.000	0.000	0.028	0.008	0.000	0.030
Ba	0.032	0.035	0.027	0.000	0.034	0.000	0.000	0.001	0.000	0.000
Th	0.046	0.127	0.381	0.021	0.015	0.156	0.708	0.066	0.000	0.011
U	0.096	1.487	4.145	0.107	0.134	2.505	9.938	0.825	0.087	0.187
Ta	0.009	0.000	0.007	0.000	0.022	0.007	0.034	0.015	0.003	0.012
Nb	0.000	0.002	0.035	0.031	0.031	0.009	0.082	0.035	0.102	0.028
P	34.733	34.420	40.483	44.056	36.789	33.070	38.216	29.967	31.515	36.069
Zr	7.050	148.967	325.363	11.300	11.735	234.233	1,125.763	67.664	5.868	11.284
Hf	0.172	4.166	8.708	0.181	0.293	5.863	29.051	1.799	0.136	0.205
Ti	48.123	47.689	56.090	61.039	50.972	45.818	52.949	41.519	43.664	49.974
Y	43.349	48.502	57.178	46.032	59.583	58.396	59.344	63.203	43.397	46.229
REE										
La	0.004	0.000	0.171	0.001	0.000	0.000	0.000	0.001	0.078	0.088
Ce	0.000	0.000	0.028	0.012	0.000	0.000	0.035	0.045	0.043	0.023
Pr	0.154	0.127	0.168	0.221	0.134	0.070	0.073	0.034	0.088	0.109
Nd	0.889	0.603	0.583	0.371	1.228	0.468	0.462	1.071	0.399	0.000
Sm	7.839	7.455	8.631	6.307	6.746	9.058	7.869	7.877	7.461	7.220
Eu	25.843	27.598	28.016	30.971	31.776	27.403	31.706	29.707	27.020	25.975
Gd	20.512	18.911	19.893	20.635	17.984	17.304	18.565	20.681	18.495	16.513
Tb	18.235	19.282	19.973	18.205	21.001	19.854	21.015	21.913	17.879	18.656
Dy	20.742	21.961	25.614	20.717	24.393	25.567	25.423	26.029	19.038	20.580
Ho	22.719	25.962	29.688	24.018	31.818	32.106	32.044	35.861	23.446	25.675
Er	28.306	35.793	45.119	34.266	52.625	49.464	48.706	54.634	33.124	37.628
Tm	38.475	48.965	57.556	43.967	71.233	66.136	65.387	76.081	45.260	53.363
Yb	45.297	57.665	68.263	52.262	93.460	82.534	82.415	108.278	57.090	65.256
Lu	47.006	69.847	76.029	56.348	108.956	93.387	100.252	126.359	58.463	71.436
ΣREE	276.021	334.170	379.732	308.300	461.354	423.351	433.950	508.573	307.885	342.521
LREE	34.728	35.784	37.597	37.882	39.884	36.999	40.144	38.736	35.091	33.415
HREE	241.293	298.386	342.135	270.418	421.470	386.352	393.806	469.836	272.795	309.107
LREE/HREE	0.144	0.120	0.110	0.140	0.095	0.096	0.102	0.082	0.129	0.108
LaN/YbN	0.000	0.000	0.002	0.000	0.000	0.000	0.000	0.000	0.001	0.001
δEu	5.900	6.761	6.305	7.540	8.326	6.589	7.712	6.734	6.715	7.022
δCe	0.190	0.000	0.037	0.017	0.000	0.000	0.150	0.403	0.112	0.050

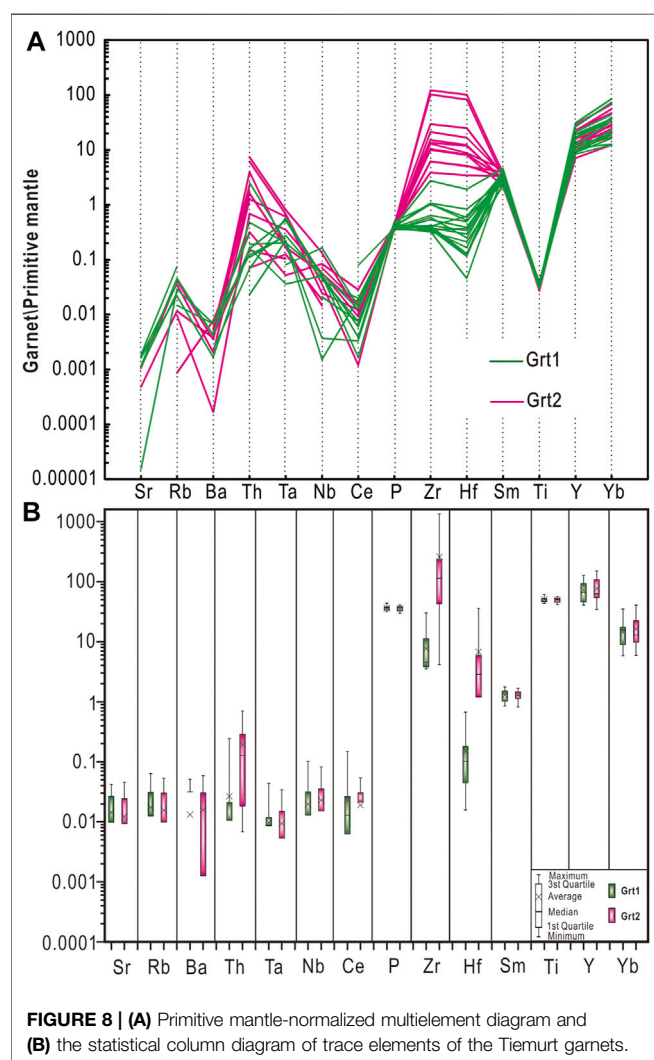
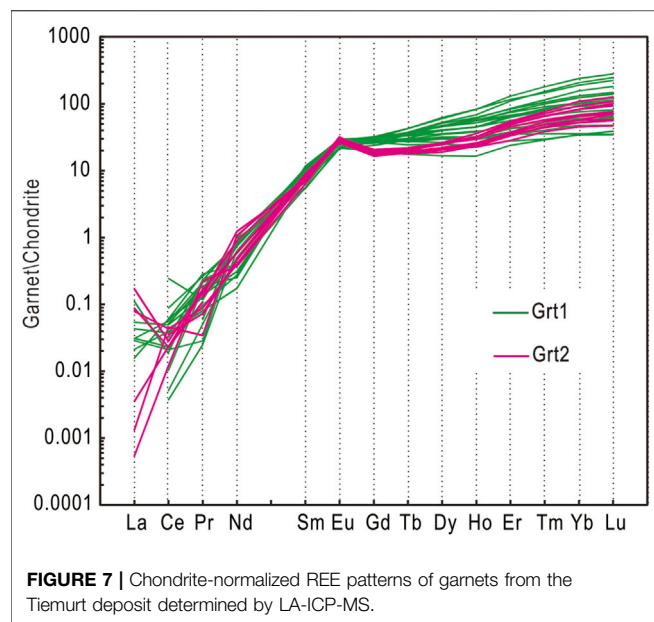
Note: REE normalized to chondrite (Sun and McDonough, 1989). “-”: Below the detection limit.

can be important in Eu^{2+} transport (Bau, 1991; Yardley et al., 1991; Lottermoser, 1992).

Since the Tiemurt garnet formed under mildly acidic and relatively reduced condition, we inferred that they have formed by advective metasomatism (Gaspar, 2005), that is, diffusive metasomatism by fluids equilibrated with the host rocks. In this case, Grt1 and cores of Grt2 are formed by advective

metasomatism, while rims of Grt2 are formed by the episodic inflections between infiltration metasomatism and advective metasomatism (Meinert et al., 2005; Dziggel et al., 2009).

As the Tiemurt garnets are spatially close to the polymetallic ores, their formation has potential to code the ore genesis of the Tiemurt deposit. A diversity of genetic types has been suggested for the ore genesis of the Pb–Zn–Cu–Au deposit in the Chinese

**TABLE 6 |** Calculation results of the amphibole pressure and temperature.

Samples	Input T (°C)	Input P (bar)	T (calc) (°C)	P (calc) (bar)
10TMZK-49	623	5,900	643	5,900
10TMZK-49	640	5,028	640	5,218

Altay Orogen, such as VMS, metamorphosed VMS, and orogenic-type deposits (Xu et al., 2008; Xu et al., 2011; Wan et al., 2010a; Zhang et al., 2012; Zheng et al., 2013b). The key to resolve these disagreements lies in the origin of their ore fluids. The metamorphic garnet supporting the polymetallic deposits are orogenic-type, and therefore the eventual metal accumulation is attributed for the orogeny-related metamorphism and deformation, as well as the metamorphic hydrothermal fluids' activities.

CONCLUSION

- 1) Two categories of almandine (Fe-Al-garnet), Grt1 and Grt2, both have similar major elemental compositions (such as SiO₂, Al₂O₃, and CaO), chondrite-normalized REE patterns (HREE-enriched, LREE-depleted, Ce negative anomaly, and Eu positive anomalies), depleted lithophile elements, and enriched high-field elements.
- 2) The sub- to euhedral mineral inclusion-rich Grt1 is intergrown with amphibolite, chlorite, and biotite; the sub- to euhedral mineral poor Grt2 is paragenetic with quartz, calcite, chlorite, and biotite. Grt1 and Grt2 assembles and trace elements recorded a methosthermal, high-pressured, mildly acidic, and reductive condition.
- 3) Grt1 and cores of Grt2 are formed by advective metasomatism, while rims of Grt2 are formed by the episodic inflections between infiltration metasomatism and advective metasomatism, and their formation linking with orogeny-type regional metamorphism as well as the metamorphic hydrothermal fluids' activities.

DATA AVAILABILITY STATEMENT

The original contributions presented in the study are included in the article/**Supplementary Material**; further inquiries can be directed to the corresponding author.

AUTHOR CONTRIBUTIONS

ZH prepared samples for analysis, performed initial data analysis, and took the lead on writing the manuscript. YZ and PY wrote the final version of the manuscript. ZH was responsible for the statistical treatment of the data. YZ, YW, and CW took part in the fieldwork and developing the original ideas.

FUNDING

This study was jointly funded by the National Natural Science Foundation of China (Nos. U1803115, 41872193,

and 42022020) and Natural Science Foundation of Guangdong Province (Nos. 2018B030306021 and 2016ZT06N331).

ACKNOWLEDGMENTS

Prof Chen YJ (Peking University) is thanked for his field assistance and writing guidance. We also appreciate the editor

and two reviewers for their constructive suggestions and comments.

SUPPLEMENTARY MATERIAL

The Supplementary Material for this article can be found online at: <https://www.frontiersin.org/articles/10.3389/feart.2021.683312/full#supplementary-material>

REFERENCES

- An, Y., Huang, J.-X., Griffin, W. L., Liu, C., and Huang, F. (2017). Isotopic Composition of Mg and Fe in Garnet Peridotites from the Kaapvaal and Siberian Cratons. *Geochimica et Cosmochimica Acta* 200, 167–185. doi:10.1016/j.gca.2016.11.041
- Andrew, A. S. (1994). "Regional Metamorphism within a Creationist Framework: What Garnet Compositions Reveal," in Proceedings of the Third International Conference on Creationism, Pittsburgh, PA, July 18–23, 1994. Editor R. E. Walsh, 485–496.
- Ballaran, T. B., Carpenter, M. A., and Geiger, C. A. (1999). Local Structural Heterogeneity in Garnet Solid Solutions. *Phys. Chem. Miner.* 26, 554–569. doi:10.1007/s002690050219
- Barrie, C. D., Cook, N. J., and Boyle, A. P. (2010). Textural Variation in the Pyrite-Rich Ore Deposits of the Røros District, Trondheim Region, Norway: Implications for Pyrite Deformation Mechanisms. *Miner. Deposita* 45, 51–68. doi:10.1007/s00126-009-0261-3
- Bau, M. (1991). Rare-earth Element Mobility during Hydrothermal and Metamorphic Fluid-Rock Interaction and the Significance of the Oxidation State of Europium. *Chem. Geology* 93, 219–230. doi:10.1016/0009-2541(91)90115-8
- Baxter, E. F., Caddick, M. J., and Ague, J. J. (2013). Garnet: Common Mineral, Uncommonly Useful. *Elements* 9, 415–419. doi:10.2113/gselements.9.6.415
- Baxter, E. F., and Scherer, E. E. (2013). Garnet Geochronology: Timekeeper of Tectonometamorphic Processes. *Elements* 9, 433–438. doi:10.2113/gselements.9.6.433
- Bernard, J. W., Ekaterina, S. K., and Andrew, K. M. (2013). Garnet in the Earth's Mantle. *Elements* 9 (6), 421–426. doi:10.2113/gselements.9.6.421
- Burton, K. W., Bourdon, B., Birck, J.-L., Allègre, C. J., and Hein, J. R. (1999). Osmium Isotope Variations in the Oceans Recorded by FeMn Crusts. *Earth Planet. Sci. Lett.* 171, 185–197. doi:10.1016/S0012-821X(99)00139-9
- Chai, F., Mao, J., Dong, L., Yang, F., Liu, F., Geng, X., et al. (2009). Geochronology of Metarhyolites from the Kangbutiebao Formation in the Kelang basin, Altay Mountains, Xinjiang: Implications for the Tectonic Evolution and Metallogeny. *Gondwana Res.* 16, 189–200. doi:10.1016/j.gr.2009.03.002
- Charles, A. G. (2016). A Tale of Two Garnets: The Role of Solid Solution in the Development toward a Modern Mineralogy. *Am. Mineral.* 101, 1735–1749. doi:10.2138/am-2016-5522
- Chen, Y. J., Pirajno, F., Wu, G., Qi, J. P., and Xiong, X. L. (2012). Epithermal Deposits in North Xinjiang, NW China. *Int. J. Earth Sci. (Geol. Rundsch)* 101, 889–917. doi:10.1007/s00531-011-0689-4
- Chen, Y. J. (2000). Progress in the Study of Central Asia-type Orogenesis-Metallogenesis in Northwest China. *Geol. J. China Univ.* 6, 17–22. (in Chinese with English abstract). doi:10.16108/j.issn1006-7493.2000.01.002
- Cheng, H., Zhang, C., Vervoort, J. D., Lu, H., Wang, C., and Cao, D. (2012). Zircon U-Pb and Garnet Lu-Hf Geochronology of Eclogites from the Lhasa Block, Tibet. *Lithos* 155, 341–359. doi:10.1016/j.lithos.2012.09.011
- Ciobanu, C. L., and Cook, N. J. (2004). Skarn textures and a case study: the Ocna de Fier-Dognecea orefield, Banat, Romania. *Ore Geology. Rev.* 24, 315–370. doi:10.1016/j.oregeorev.2003.04.002
- Crowe, D. E., Riciputi, L. R., Bezenek, S., and Ignatiev, A. (2001). Oxygen Isotope and Trace Element Zoning in Hydrothermal Garnets: Windows into Large-Scale Fluid Flow Behavior. *Geology* 29, 479–482. doi:10.1130/0091-7613(2001)029<0479:OIATEZ>2.0.CO;2
- Dietrich, R. V. (2020). Garnet Encyclopedia Britannica. Available at: <https://www.britannica.com/science/garnet> (Accessed March 5, 2021).
- Doyle, M. G., and Allen, R. L. (2003). Subsea-floor Replacement in Volcanic-Hosted Massive Sulfide Deposits. *Ore Geology. Rev.* 23, 183–222. doi:10.1016/S0169-1368(03)00035-0
- Dziggel, A., Wulff, K., Kolb, J., Meyer, F. M., and Lahaye, Y. (2009). Significance of Oscillatory and bell-shaped Growth Zoning in Hydrothermal Garnet: Evidence from the Navachab Gold deposit, Namibia. *Chem. Geology* 262, 262–276. doi:10.1016/j.chemgeo.2009.01.027
- Fernando, G. W. A. R., Hauzenberger, C. A., Baumgartner, L. P., and Hofmeister, W. (2003). Modeling of Retrograde Diffusion Zoning in Garnet: Evidence for Slow Cooling of Granulites from the Highland Complex of Sri Lanka. *Mineralogy Pet.* 78, 53–71. doi:10.1007/s00710-002-0224-1
- García-Ruiz, J. M., and Otálora, F. (2015). "Crystal Growth in Geology." in *Handbook of Crystal Growth*. Second Edition. Editor T. Nishinaga (Boston: RudolphElsevier), 1–43. doi:10.1016/B978-0-444-63303-3.00001-8
- Gaspar, M., Knaack, C., Meinert, L. D., and Moretti, R. (2008). REE in Skarn Systems: a LA-ICP-MS Study of Garnets from the Crown Jewel Gold deposit. *Geochimica et Cosmochimica Acta* 72, 185–205. doi:10.1016/j.gca.2007.09.033
- Gaspar, M. (2005). The Crown Jewel Gold Skarn deposit. [Ph.D. Thesis]. Washington, DC: State University.
- Geiger, C. A., Winkler, B., and Langer, K. (1989). Infrared Spectra of Synthetic Almandine-Grossular and Almandine-Pyropes Garnet Solid Solutions: Evidence for Equivalent Site Behaviour. *Mineral. Mag.* 53, 231–237. doi:10.1180/minmag.1989.053.370.10
- Gemmell, J. B., Zantop, H., and Meinert, L. D. (1992). Genesis of the Aguilar zinc-lead-silver deposit, Argentina; Contact Metasomatic vs. Sedimentary Exhalative. *Econ. Geol.* 87, 2085–2112. doi:10.2113/gsecongeo.87.8.2085
- Gerya, T. V., Perchuk, L. L., Triboulet, C., Audren, C., and Sez'ko, A. I. (1997). Petrology of the Tumanshet Zonal Metamorphic Complex, Eastern Sayan. *Petrology* 5, 503–533.
- Goldfarb, R. J., Mao, J. W., Hart, C., Wang, D., Anderson, E., and Wang, Z. (2003). "Tectonic and Metallogenic Evolution of the Altay Shan, Northern Xinjiang Uygur Autonomous Region, Northwestern China," in *Tectonic Evolution and Metallogeny of the Chinese Altay and Tianshan*. Editors J. W. Mao, R. J. Goldfarb, R. Seltmann, D. H. Wang, W. J. Xiao, and C. Hart (London: Natural History Museum).
- Hickmott, D., and Spear, F. S. (1992). Major- and Trace-Element Zoning in Garnets from Calcareous Pelites in the NW Shelburne Falls Quadrangle, Massachusetts: Garnet Growth Histories in Retrograded Rocks. *J. Pet.* 33, 965–1005. doi:10.1093/petrology/33.5.965
- Hoal, K. E. O., Hoal, B. G., Erlank, A. J., and Shimizu, N. (1994). Metasomatism of the Mantle Lithosphere Recorded by Rare Earth Elements in Garnets. *Earth Planet. Sci. Lett.* 126, 303–313. doi:10.1016/0012-821X(94)90114-7
- Holland, T., and Blundy, J. (1994). Non-ideal Interactions in Calcic Amphiboles and Their Bearing on Amphibole-Plagioclase Thermometry. *Contr. Mineral. Petrol.* 116, 433–447. doi:10.1007/BF00310910
- Huang, F., He, Z., Schmidt, M. W., and Li, Q. (2014). *The Effect of fO₂ on Partition Coefficients of U and Th between Garnet and Silicate Melt*. America, San Francisco: Agu Fall Meeting/AGU Fall Meeting Abstracts.

- Jahn, B.-M. (2004). The Central Asian Orogenic Belt and Growth of the continental Crust in the Phanerozoic. *Geol. Soc. Lond. Spec. Publications* 226, 73–100. doi:10.1144/GSL.SP.2004.226.01.05
- Jamtveit, B. (1991). Oscillatory Zonation Patterns in Hydrothermal Grossular-Andradite Garnet. Nonlinear Dynamics in Regions of Immiscibility. *Am. Mineral.* 76, 1319–1327.
- Jamtveit, B., and Hervig, R. L. (1994). Constraints on Transport and Kinetics in Hydrothermal Systems From Zoned Garnet Crystals. *Science* 263, 505–508. doi:10.1126/science.263.5146.505
- Jamtveit, B., Wogelius, R. A., and Fraser, D. G. (1993). Zonation Patterns of Skarn Garnets: Records of Hydrothermal System Evolution. *Geology* 21, 113–116. doi:10.1130/0091-7613(1993)021<0113:ZPOSGR>2.3.CO;2
- Jeremy, P. R., and Hamid, M. (2013). Magmatic-hydrothermal Processes within an Evolving Earth: Iron Oxide-Copper-Gold and Porphyry Cu ± Mo ± Au Deposits. *Geology* 41, 767–770. doi:10.1130/G34275.1
- Konrad-Schmolke, M., Handy, M. R., Babist, J., and O'Brien, P. J. (2005). Thermodynamic Modelling of Diffusion-Controlled Garnet Growth. *Contrib. Mineral. Petrol.* 149, 181–195. doi:10.1007/s00410-004-0643-6
- Laurent, S., Charvet, J., Shu, L. S., Ma, R. S., and Lu, H. F. (2002). Paleozoic Late Collisional Strike-Slip Deformations in Tianshan and Altay, Eastern Xinjiang, NW China. *Terra Nova* 14, 249–256. doi:10.1046/j.1365-3121.2002.00417.x
- Liang, P., Zhang, Y., and Xie, Y. (2021). Chemical Composition and Genesis Implication of Garnet from the Laoshankou Fe-Cu-Au Deposit, the Northern Margin of East Junggar, NW China. *Minerals* 11, 334. doi:10.3390/min11030334
- Longerich, H. P., Jackson, S. E., and Günther, D. (1996). Inter-laboratory Note. Laser Ablation Inductively Coupled Plasma Mass Spectrometric Transient Signal Data Acquisition and Analyte Concentration Calculation. *J. Anal. Spectrom.* 11, 899–904. doi:10.1039/ja9961100899
- Lottermoser, B. G. (1992). Rare Earth Elements and Hydrothermal Ore Formation Processes. *Ore Geology. Rev.* 7, 25–41. doi:10.1016/0169-1368(92)90017-F
- Marco, T. E., and Donald, M. B. (1982). Introduction; Terminology, Classification, and Composition of Skarn Deposits. *Econ. Geol.* 77, 745–754. doi:10.2113/gsecongeo.77.4.745
- Martin, L. A. J., Ballèvre, M., Boulvais, P., Halfpenny, A., Vanderhaeghe, O., Duchène, S., et al. (2011). Garnet Re-equilibration by Coupled Dissolution Reprecipitation: Evidence from Textural, Major Element and Oxygen Isotope Zoning of 'cloudy' Garnet. *J. Metamorph. Geol.* 29, 21–231. doi:10.1111/j.1525-1314.2010.00912.x
- Meinert, L. D., Dipple, G. M., and Nicolescu, S. (2005). World Skarn Deposits. *Econ. Geol.* 100, 299–336. doi:10.5382/AV100.11
- Menzer, G. (1926). Die kristallstruktur von granat. *Zeitschrift für Kristallographie*. 63, 157–158.
- Ottoneo, G., Bokreta, M., and Sciuto, P. F. (1996). Parameterization of Energy and Interactions in Garnets; End-Member Properties. *Am. Mineral.* 81, 429–447. doi:10.2138/am-1996-3-417
- Ottoneo, G., and Moretti, R. (1998). On the Significance of Static Interactions in Silicate Garnets. *J. Phys. Chem. Sol.* 59, 893–901. doi:10.1016/S0022-3697(98)00030-4
- Park, C., Park, C., Song, Y., and Choi, S.-G. (2019). Sequential Trace Element Analysis of Zoned Skarn Garnet: Implications for Multi-Stage Fluxing and Flow of Magmatic Fluid into a Skarn System. *Lithos* 350–351, 105213. doi:10.1016/j.lithos.2019.105213
- Park, C., Song, Y., Kang, I.-M., Shim, J., Chung, D., and Park, C.-S. (2017). Metasomatic Changes during Periodic Fluid Flux Recorded in Grandite Garnet from the Weondong W-Skarn deposit, South Korea. *Chem. Geology*. 451, 135–153. doi:10.1016/j.chemgeo.2017.01.011
- Pertermann, M., Hirschmann, M. M., Hametner, K., Günther, D., and Schmidt, M. W. (2004). Experimental Determination of Trace Element Partitioning between Garnet and Silica-Rich Liquid during Anhydrous Partial Melting of MORB-like Eclogite. *Geochem. Geophys. Geosyst.* 5, a-n. doi:10.1029/2003GC000638
- Scherer, E. E., Cameron, K. L., and Blichert-Toft, J. (2000). Lu-Hf Garnet Geochronology: Closure Temperature Relative to the Sm-Nd System and the Effects of Trace mineral Inclusions. *Geochimica et Cosmochimica Acta* 64, 3413–3432. doi:10.1016/S0016-7037(00)00440-3. doi:10.1016/S0016-7037(00)00440-3
- Schmidt, A., Mezger, K., and O'Brien, P. J. (2011). The Time of Eclogite Formation in the Ultrahigh Pressure Rocks of the Sulu Terrane. *Lithos* 125, 743–756. doi:10.1016/j.lithos.2011.04.004
- Shannon, R. D. (1976). Revised Effective Ionic Radii and Systematic Studies of Interatomic Distances in Halides and Chalcogenides. *Acta Cryst. Sect. A*. 32, 751–767. doi:10.1107/S0567739476001551
- Smith, M. P., Henderson, P., Jeffries, T. E. R., Long, J., and Williams, C. T. (2004). The Rare Earth Elements and Uranium in Garnets from the Beinn an Dubhaich Aureole, Skye, Scotland, UK: Constraints on Processes in a Dynamic Hydrothermal System. *J. Pet.* 45, 457–484. doi:10.1093/petrology/egg087
- Stefanie, M. B., Stephen, J. P., Paul, J. S., Stephanie, M., and Larry, P. (2014). Evidence for Syngenetic Precious Metal Enrichment in an Appalachian Volcanogenic Massive Sulfide System: The 1806 Zone, Ming Mine, Newfoundland, Canada. *Econ. Geol.* 109, 1611–1642. doi:10.2113/econgeo.109.6.1611
- Sun, S.-s., and McDonough, W. F. (1989). Chemical and Isotopic Systematics of Oceanic Basalts: Implications for Mantle Composition and Processes. *Geol. Soc.* 42, 313–345. doi:10.1144/GSL.SP.1989.042.01.19
- Sverjensky, D. A. (1984). Europium Redox Equilibria in Aqueous Solution. *Earth Planet. Sci. Lett.* 67, 70–78. doi:10.1016/0012-821X(84)90039-6. doi:10.1016/0012-821X(84)90039-6
- Triboulet, C. (1992). The (Na?Ca)amphibole?albite?chlorite?epidote?quartz Geothermobarometer in the System $Sr_2A_2F_2M_2C_2N_2H_2O$. 1. An Empirical Calibration. *J. Metamorph. Geol.* 10, 545–556. doi:10.1111/j.1525-1314.1992.tb00104.x
- Vander, A. J., and Andre, L. (1991). Trace Elements (REE) and Isotopes (O, C, Sr) to Characterize the Metasomatic Fluid Sources: Evidence from the Skarn deposit (Fe, W, Cu) of Traversella (Ivrea, Italy). *Contrib. Miner. Petrol.* 106, 325–339. doi:10.1007/BF00324561
- Wan, B., Zhang, L., and Xiang, P. (2010a). The Ashele VMS-type Cu-Zn deposit in Xinjiang, NW China Formed in a Rifted Arc Setting. *Resour. Geol.* 60, 150–164. doi:10.1111/j.1751-3928.2010.00122.x
- Wan, B., Zhang, L., and Xiao, W. (2010b). Geological and Geochemical Characteristics and Ore Genesis of the Keketale VMS Pb-Zn deposit, Southern Altai Metallogenic Belt, NW China. *Ore Geology. Rev.* 37, 114–126. doi:10.1016/j.oregeorev.2010.01.002
- Wang, J. B., Qin, K. Z., Wu, Z. L., Hu, J. H., and Deng, J. N. (1998). *Volcanic-exhalative-sedimentary Lead Zinc Deposit in the Southern Margin of the Altai*. Xinjiang Beijing: Geology Publishing House. (in Chinese).
- Wiedenbeck, M., Allé, P., Corfu, F., Griffin, W. L., Meier, M., Oberli, F., et al. (1995). Three Natural Zircon Standards for U-Th-Pb, Lu-Hf, Trace Element and REE Analyses. *Geostand. Newslett.* 19, 1–23. doi:10.1111/j.1751-908X.1995.tb00147
- Xia, Q.-X., Wang, H.-Z., Zhou, L.-G., Gao, X.-Y., Zheng, Y.-F., Van Orman, J. A., et al. (2016). Growth of Metamorphic and Peritectic Garnets in Ultrahigh-Pressure Metagranite during continental Subduction and Exhumation in the Dabie Orogen. *Lithos* 266–267, 158–181. doi:10.1016/j.lithos.2016.08.043
- Xiao, W. J., Windley, B. F., Huang, B. C., Han, C. M., Yuan, C., Chen, H. L., et al. (2009). End-Permian to Mid-Triassic Termination of the Accretionary Processes of the Southern Altaids: Implications for the Geodynamic Evolution, Phanerozoic continental Growth, and Metallogeny of Central Asia. *Int. J. Earth Sci. (Geol. Rundsch)* 98, 1189–1217. doi:10.1007/s00531-008-0407-z
- Xiao, X., Zhou, T.-f., White, N. C., Zhang, L.-j., Fan, Y., Wang, F.-y., et al. (2018). The Formation and Trace Elements of Garnet in the Skarn Zone from the Xinqiao Cu-S-Fe-Au deposit, Tongling Ore District, Anhui Province, Eastern China. *Lithos* 302–303, 467–479. doi:10.1016/j.lithos.2018.01.023
- Xu, J., Ciobanu, C. L., Cook, N. J., Zheng, Y., Sun, X., and Wade, B. P. (2016). Skarn Formation and Trace Elements in Garnet and Associated Minerals from Zhibula Copper deposit, Gangdese Belt, Southern Tibet. *Lithos* 262, 213–231. doi:10.1016/j.lithos.2016.07.010
- Xu, J., Hart, C. J. R., Wang, L., Chu, H., Lin, L., Wei, X., et al. (2011). Carbonic Fluid Overprints in Volcanogenic Massive Sulfide Deposits: Examples from the Kelan Volcanosedimentary Basin, Altaides, China. *Econ. Geology*. 106, 145–155. doi:10.2113/econgeo.106.1.145
- Xu, J. H., Shan, L. H., Ding, R. F., Craig, H., Wang, L. L., and Wei, X. F. (2008). Carbonic Fluid Inclusion Assemblages and Their Geological Significance at the Tiemurte Lead-Zinc Deposit, Altay. *Acta Petrologica Sinica*. 24, 2094–2104. (in Chinese with English abstract)
- Yang, F., Geng, X., Wang, R., Zhang, Z., and Guo, X. (2018). A Synthesis of Mineralization Styles and Geodynamic Settings of the Paleozoic and Mesozoic

- Metallic Ore Deposits in the Altay Mountains, NW China. *J. Asian Earth Sci.* 159, 233–258. doi:10.1016/j.jseas.2017.05.020
- Yardley, B. W. D., Rochelle, C. A., Barnicoat, A. C., and Lloyd, G. E. (1991). Oscillatory Zoning in Metamorphic Minerals: an Indicator of Infiltration Metasomatism. *Mineral. Mag.* 55, 357–365. doi:10.1180/minmag.1991.055.380.06
- Yu, P.-P., Zheng, Y., and Wang, C.-M. (2020). Trace Elemental and Sulfur-lead Isotopic Variations in Metamorphosed Volcanogenic Massive Sulfide (VMS) Mineralization Systems: An Example from the Keketale Pb-Zn(-Ag) deposit, NW China. *Ore Geology. Rev.* 125, 103685. doi:10.1016/j.oregeorev.2020.103685
- Yu, P., and Zheng, Y. (2019). Pb-Zn-Cu Accumulation from Seafloor Sedimentation to Metamorphism: Constraints from Ore Textures Coupled with Elemental and Isotopic Geochemistry of the Tiemurt in Chinese Altay Orogen, NW China. *Gondwana Res.* 72, 65–82. doi:10.1016/j.jgr.2019.02.007
- Zang, Z. J., Dong, L. L., Liu, W., Zhao, H., Wang, X. S., Cai, K. D., et al. (2019). Garnet U-Pb and O Isotopic Determinations Reveal a Shear-Zone Induced Hydrothermal System. *Sci. Rep.* 9, 10382. doi:10.1038/s41598-019-46868-4
- Zhai, D.-G., Liu, J.-J., Zhang, H.-Y., Wang, J.-P., Su, L., Yang, X.-A., et al. (2014). Origin of Oscillatory Zoned Garnets from the Xieertala Fe-Zn Skarn deposit, Northern China: *In Situ* LA-ICP-MS Evidence. *Lithos* 190–191, 279–291. doi:10.1016/j.lithos.2013.12.017
- Zhang, L., Zheng, Y., and Chen, Y. (2012). Ore Geology and Fluid Inclusion Geochemistry of the Tiemurt Pb-Zn-Cu deposit, Altay, Xinjiang, China: A Case Study of Orogenic-type Pb-Zn Systems. *J. Asian Earth Sci.* 49, 69–79. doi:10.1016/j.jseas.2011.11.019
- Zhang, Y., Liu, Q., Shao, Y., and Li, H. (2017a). Fingerprinting the Hydrothermal Fluid Characteristics from LA-ICP-MS Trace Element Geochemistry of Garnet in the Yongping Cu Deposit, SE China. *Minerals* 7, 199. doi:10.3390/min7100199
- Zhang, Y., Shao, Y.-J., Wu, C.-d., and Chen, H.-Y. (2017b). LA-ICP-MS Trace Element Geochemistry of Garnets: Constraints on Hydrothermal Fluid Evolution and Genesis of the Xinqiao Cu-S-Fe-Au deposit, Eastern China. *Ore Geology. Rev.* 86, 426–439. doi:10.1016/j.oregeorev.2017.03.005
- Zhao, B., Zhao, J. S., and Liu, H. C. (1999). REE Geochemical Studies of Whole Rock and Rockforming Minerals in Skarns from Cu (Au), Cu-Fe (Au) and Fe Ore Deposits Distributed along Middle-Lower Reaches of Yangtze River, China. *Geochimica* 28, 113–125. (in Chinese with English abstract) .
- Zheng, Y., Zhang, L., Chen, Y.-j., Hollings, P., and Chen, H.-y. (2013b). Metamorphosed Pb-Zn(-Ag) Ores of the Keketale VMS deposit, NW China: Evidence from Ore Textures, Fluid Inclusions, Geochronology and Pyrite Compositions. *Ore Geology. Rev.* 54, 167–180. doi:10.1016/j.oregeorev.2013.03.009
- Zheng, Y., Zhang, L., Chen, Y.-J., Qin, Y.-J., and Liu, C.-F. (2012). Geology, Fluid Inclusion Geochemistry, and $^{40}\text{Ar}/^{39}\text{Ar}$ Geochronology of the Wulasigou Cu deposit, and Their Implications for Ore Genesis, Altay, Xinjiang, China. *Ore Geology. Rev.* 49, 128–140. doi:10.1016/j.oregeorev.2012.09.005
- Zheng, Y., Zhang, L., and Guo, Z. L. (2013a). Zircon LA-ICP-MS U-Pb and Biotite $^{40}\text{Ar}/^{39}\text{Ar}$ Geochronology of the Tiemurt Pb-Zn-Cu deposit, Xinjiang: Implications for the Ore Genesis. *Acta Petrol. Sin.* 29, 191–204. (in Chinese with English abstract) .
- Zheng, Y., Zhang, L., Li, D.-F., Kapsiotis, A., and Chen, Y.-J. (2015). Genesis of the Dadonggou Pb-Zn deposit in Kelan basin, Altay, NW China: Constraints from Zircon U-Pb and Biotite $^{40}\text{Ar}/^{39}\text{Ar}$ Geochronological Data. *Ore Geology. Rev.* 64, 128–139. doi:10.1016/j.oregeorev.2014.07.002
- Zhou, L.-G., Xia, Q.-X., Zheng, Y.-F., and Hu, Z. (2014). Polyphase Growth of Garnet in Eclogite from the Hong'an Orogen: Constraints from Garnet Zoning and Phase Equilibrium. *Lithos* 206–207, 79–99. doi:10.2113/gselements.9.6.415
- Zhuang, Y. X. (1994). *Tectonothermal Evolution in Space and Time and Orogenic Process of Altaide, China*. Changchun: Jilin Scientific and Technical Press. (in Chinese).

Conflict of Interest: The authors declare that the research was conducted in the absence of any commercial or financial relationships that could be construed as a potential conflict of interest.

Copyright © 2021 Hu, Zheng, Yu, Wu and Wang. This is an open-access article distributed under the terms of the Creative Commons Attribution License (CC BY). The use, distribution or reproduction in other forums is permitted, provided the original author(s) and the copyright owner(s) are credited and that the original publication in this journal is cited, in accordance with accepted academic practice. No use, distribution or reproduction is permitted which does not comply with these terms.



Genesis of the Heiyanshan Tungsten Skarn Deposit in the East Tianshan, NW China: Insights From Geology, Fluid Inclusion, Isotopic Geochemistry and Geochronology

Dong Xue^{1,2}, Xiao-Hua Deng^{2*}, Leon Bagas^{3,4}, Xu-An Chen¹, Yan-Shuang Wu⁵ and Xiao Jiang⁶

¹State Key Laboratory of Geological Processes and Mineral Resources, China University of Geosciences, Beijing, China, ²Beijing Institute of Geology for Mineral Resources Co., Ltd., Beijing, China, ³Centre for Exploration Targeting, The University of Western Australia, Crawley, WA, Australia, ⁴Key Laboratory for the Study of Focused Magmatism and Giant Ore Deposits of the Ministry of Natural Resources, Xi'an Center of China Geological Survey, Xi'an, China, ⁵State Key Laboratory of Desert and Oasis Ecology, Xinjiang Institute of Ecology and Geography, Chinese Academy of Sciences, Urumqi, China, ⁶No.6 Geological Survey Team, Bureau of Xinjiang Geological Exploration, Hami, Urumqi, China

OPEN ACCESS

Edited by:

Ryan Mathur,
Juniata College, United States

Reviewed by:

Youye Zheng,
China University of Geosciences,
China
Fuquan Yang,
Institute of Biophysics (CAS), China
Hendrik Falck,
Northwest Territories Geological
Survey, Canada

*Correspondence:

Xiao-Hua Deng
dxh198411@126.com

Specialty section:

This article was submitted to
Economic Geology,
a section of the journal
Frontiers in Earth Science

Received: 05 February 2021

Accepted: 23 August 2021

Published: 07 September 2021

Citation:

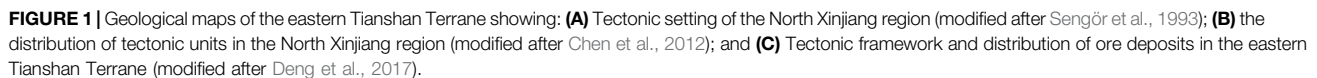
Xue D, Deng X-H, Bagas L, Chen X-A,
Wu Y-S and Jiang X (2021) Genesis of
the Heiyanshan Tungsten Skarn
Deposit in the East Tianshan, NW
China: Insights From Geology, Fluid
Inclusion, Isotopic Geochemistry
and Geochronology.
Front. Earth Sci. 9:664603.
doi: 10.3389/feart.2021.664603

The eastern Tianshan Terrane is a highly prospective zone that contains several porphyry Cu–Mo, VMS Cu–Zn, magmatic Cu–Ni, epithermal and orogenic Au deposits. However, few attention has been paid to tungsten deposits. Of these, the source and evolution of the mineralising fluids related to the skarn W deposits are poorly understood. The Heiyanshan W deposit is hosted by metamorphosed clastic and carbonate beds in the Mesoproterozoic Jianshanzi Formation deposited on a continental margin tectonic setting. The Jianshanzi Formation is intruded by biotite monzogranite that yield weighted ²⁰⁶Pb/²³⁸U age of 326.9 ± 1.6 Ma, which suggest that the Heiyanshan W deposit was formed in the Carboniferous. The mineralisation is hosted by a prograde hydrothermal altered zone represented by a garnet (–pyroxene) skarn, and retrograde skarn characterised by fine-grained scheelite. The paragenesis of the Heiyanshan mineralisation can be subdivided into prograde skarn stage, retrograde skarn stage, quartz-sulphide stage and quartz-calcite vein stage. The types of fluid inclusions recognised in the various minerals in the deposits are liquid-rich aqueous, vapour-rich aqueous, and daughter mineral-bearing. The homogenisation temperatures of fluid inclusions from the Heiyanshan deposit decrease from 290 ± 28°C in garnet, through 232 ± 31°C in scheelite, to 232 ± 36°C in quartz and 158 ± 15°C in non-mineralised calcite, which is typical of W-bearing skarn deposits worldwide. The δ¹⁸O_{water} values from the Heiyanshan deposit range from +4.7 to +6.6‰ in garnet, +1.3 to +1.9‰ in quartz and –6.1 to –4.4‰ in calcite. We have measured δD in fluid inclusions from different minerals, although these bulk analyses are just a mixture of the different FIA's present in the sample. The δD values of fluid inclusions in garnet, quartz, and calcite are from –121 to –71‰, –84 to –75‰ and –101 to –82‰, respectively, also indicative of deep-sourced magmatic fluids mixed with meteoric water. The decrease in the homogenisation temperatures for the fluid inclusions at the Heiyanshan deposit is accompanied by a

Keywords: tianshan, heiyanshan, isotopic geochemistry, fluid inclusion, tungsten skarn

Chinese production of tungsten accounts for over half of the world's supply of the metal. Skarns are one of the most common hosts for the W representing 71% of China's production of W (Chang et al., 2019). Tungsten deposits in China are widely distributed in the South China Block, Kunlun-Qilian-Qinling-Dabie-Sulu orogens, Sanjiang and Himalaya-Tibetan, and

The eastern Tianshan Terrane (ETT) at the southern margin of the CAO, is a highly prospective region containing several major porphyry Cu–Au–Mo, VMS Cu–Zn and magmatic Cu–Ni deposits, as well as orogenic and epithermal gold deposits (Chen



et al., 2012; Deng et al., 2016; Wang et al., 2016, 2018; Wang and Zhang, 2016; Xiao et al., 2017; Wu et al., 2018; Li et al., 2019; Zhang et al., 2019; Chen et al., 2020; He et al., 2020; Muhtar et al., 2020). Several large porphyry Mo and W-(Mo) skarn deposits are also present in the region, including the Donggebi Mo, Baishan Mo, Shadong W-Rb and Xiaobaishitou W-(Mo) deposits (Deng et al., 2017; Wu et al., 2017; Chen et al., 2018; Li et al., 2019b, 2020a). These W skarn deposits contain resources of over 200,000 t WO_3 , with minor molybdenum and rubidium.

The Heiyanshan W skarn deposit located in the central part of the ETT was discovered in 2013 with a pre-mining resource of over 10,000 t WO_3 . Previous studies focused on the geology, geochemistry, geochronology of ore-related granites at W deposits of the ETT (Chen, 2006; Li et al., 2011; Deng et al., 2017; Chen et al., 2018; Li et al., 2019a), but there are few detailed descriptions of fluid inclusions and systematic isotope studies of the major skarn W deposits. The Heiyanshan skarn deposits provide an excellent opportunity to study the source and evolution of mineralised fluids and metals, and how the W mineralisation precipitated in skarns. This study aims to improve our understanding of the major W skarn mineralisation in NW China.

REGIONAL GEOLOGY

The CAO is bounded by the Tarim Block to the south and by the Siberian Craton to the north (Figures 1A–C; Sengör et al., 1993; Windley et al., 2007; Xiao et al., 2013, 2020). The ETT is a significant component of the CAO located between the Kelameli Fault in the north and the Toukexun-Gangou-Xinxingxa Fault in the south (Figure 1B). The ETT is subdivided into the North Tianshan and Central Tianshan Blocks, separated by the Aqikekuduke Fault (Figure 1C; Qin et al., 2002).

The Northern Tianshan Block is subdivided in the Dananhu-Tousuquan and Harlik Belts in the north separated from the Aqishan-Yanmansu Belt in the south by the Kanggur-Huangshan Shear Zone (Gu et al., 2001). The Dananhu-Tousuquan volcanic arc consists of Ordovician to Devonian volcanic and sedimentary rocks hosting VMS Cu–Zn deposits (Deng et al., 2016, 2020) and porphyry Cu deposits (Zhang et al., 2006; Wang et al., 2016, 2018). The Yamansu volcanic arc includes Carboniferous to Permian volcanic-sedimentary rocks hosting several Fe deposits (Zhao et al., 2019). The Kanggur-Huangshan Shear Zone includes Cu–Ni sulphide, porphyry Mo deposits and orogenic Au deposits (Mao et al., 2015; Wu et al., 2018; Muhtar et al., 2020).

The Central Tianshan Block (CTB) includes Meso- to Neoproterozoic greenschist to amphibolite facies metamorphic rocks and minor Palaeozoic volcano-sedimentary rocks (Qin et al., 2002; Lei et al., 2011). The Mesoproterozoic rocks include Jianshanzi Formation in the Kawabulag Group (Lei et al., 2011). The Precambrian units are intruded by Palaeozoic and Mesozoic plutons (Wang et al., 2006), some of which are related to tungsten skarn deposits, such as the Xiaobaishitou and Heiyanshan deposits (Deng et al., 2017). The CTB includes the Weiya V–Ti magnetite, Tianhu Fe, and

the Caixiashan giant-size Pb–Zn deposit, and the Permian mafic-ultramafic complexes present along the northern margin of the area, which hosts the Tianyu and Baishiquan Cu–Ni deposits (Wu et al., 2010; Yu et al., 2018; Li et al., 2019; Tang et al., 2020).

GEOLOGY OF THE HEIYANSHAN DEPOSIT

Geological Background

The host lithologies at Heiyanshan deposit consist of the Mesoproterozoic Jianshanzi Formation of the Kawabulag Group (Figure 2; Hu et al., 2016). The Kawabulag Group is distributed in the southern part of the Heiyanshan district (Figure 2A), with strike near east-west and dip about 50°–70° to the southeast. It is represented by a suite of metamorphic rocks, mainly marble, dolomite marble, metamorphic sandstone, and mica quartz schist, in which marble is the main ore-bearing lithology.

The igneous rocks at the deposit include Carboniferous biotite monzogranite and E-trending dykes of diorite. The Carboniferous biotite monzogranite is distributed in the northern part of the ore district, intruding into the Kawabulag Group. It is grey, medium-grained, and consists of plagioclase (35–40 wt%), K-feldspar (25–33 wt%), quartz (25–30 wt%), biotite (5–8 wt%), and accessory amounts of tourmaline and zircon. The biotite monzogranite is characterized by high silicon and alkali, and plot into high-K calc-alkaline series. The ASI values cluster between 0.91 and 1.02, indicating metaluminous affinity. The residual marble of the Kawabulag Group can be seen in the biotite monzogranite, accompanied by scheelite mineralization.

The structure of the ore district includes faults, folds and contact zone structures, which obviously control the formation and distribution of orebodies.

Orebodies

The Heiyanshan deposit includes 25 scheelite-rich orebodies hosted by skarn in contact of biotite monzogranite and marble, to a minor extent, in fractures in the biotite monzogranite (Jiang, 2016). Three economic W orebodies referred to as the No. XVIII, XX, XIV orebodies grading between 0.12 and 1.06 wt% WO_3 have been delineated at the deposit, which are 100–1,500 m long and 0.5–8 m thick (Figure 2A; Hu et al., 2016).

No. XVIII orebody is located in the southwestern part of the ore district, with the thickness of 4.6 m, and length of 1,186 m and an ore grade of 0.52 wt% WO_3 . The orebody is mainly composed of garnet skarn and diopside skarn, which occurs in the external contact skarn zone along the contact zone structure. The direction of dip of the orebody is 120–170° and the dip angle is 50–90°.

No. XIV orebody is located in the northwest of the ore district, with a thickness of 1.1 m, and a length of 1,194 m and an ore grade of 0.41 wt% WO_3 . The orebody is mainly composed of garnet skarn and diopside skarn and occurs in the external contact skarn zone along the contact zone structure (Figure 3). The direction of dip of the orebody is 350–14° and the dip angle is 40–65°.

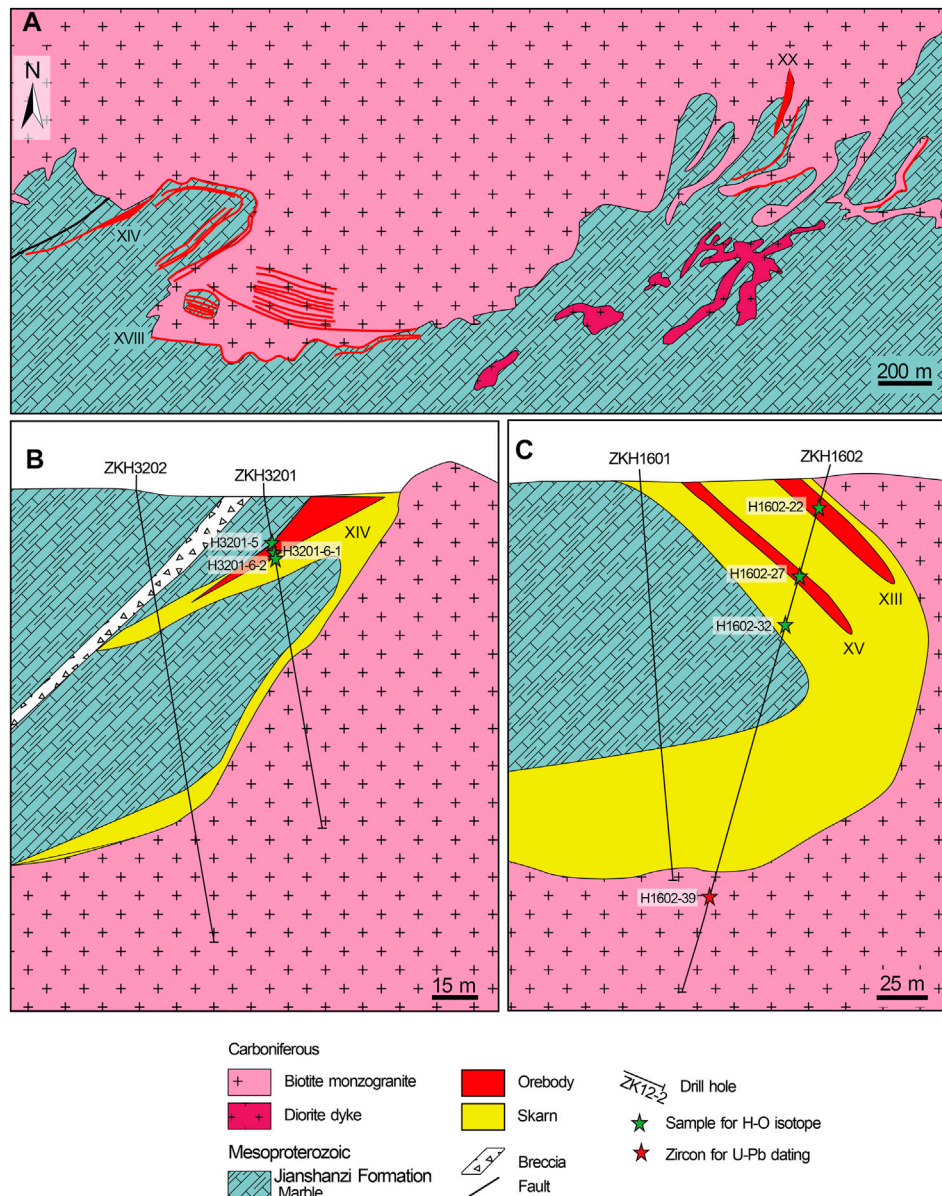


FIGURE 2 | Geological map and profiles of the Heiyanshan deposit (modified after Hu et al., 2016).

No. XX orebody is located in the eastern part of the ore district, with the thickness of 7.2 m, and length of 289 m and an ore grade of 0.31 wt % WO_3 . The orebody occurred as lens between biotite monzogranite and marble, with a dip of 135° and a dip angle is $50\text{--}70^\circ$.

Skarn Mineralogy and Paragenesis

The skarn is zoned with garnet in the inner zone near biotite monzogranite, succeeded by pyroxene in the outer zone (Figure 3). The skarn is composed of garnet and pyroxene, with minor amounts of scheelite, magnetite, quartz, and calcite (Figures 4A,B). The scheelite is disseminated in the skarn and associated with the retrograde skarn alteration, or in quartz veins cut the skarn (Figures 4B,C,E). Based on field investigation and

petrographic observation, the paragenesis of the Heiyanshan mineralisation is subdivided into: 1) prograde skarn stage; 2) retrograde skarn stage; 3) quartz-sulphide vein stage; and 4) quartz-calcite vein stage (Figure 5).

The prograde skarn stage is characterised by large amounts of garnet and pyroxene in banded skarn (Figures 4A,D). The garnet is fine-grained (0.05–0.5 mm), euhedral to subhedral, and is commonly intergrown with pyroxene (Figures 4D,E,G). The EPMA data show that garnet from the Heiyanshan W deposit is essentially grossularite-andradite-pyralspite (Gr-Ad-Py) solid solutions (Table 1; Figure 6A). The composition of garnet is relatively uniform and there are no obvious core and rim structure. In most cases, the garnet are enriched in Fe relative to Al. The composition range of Gr, Ad and

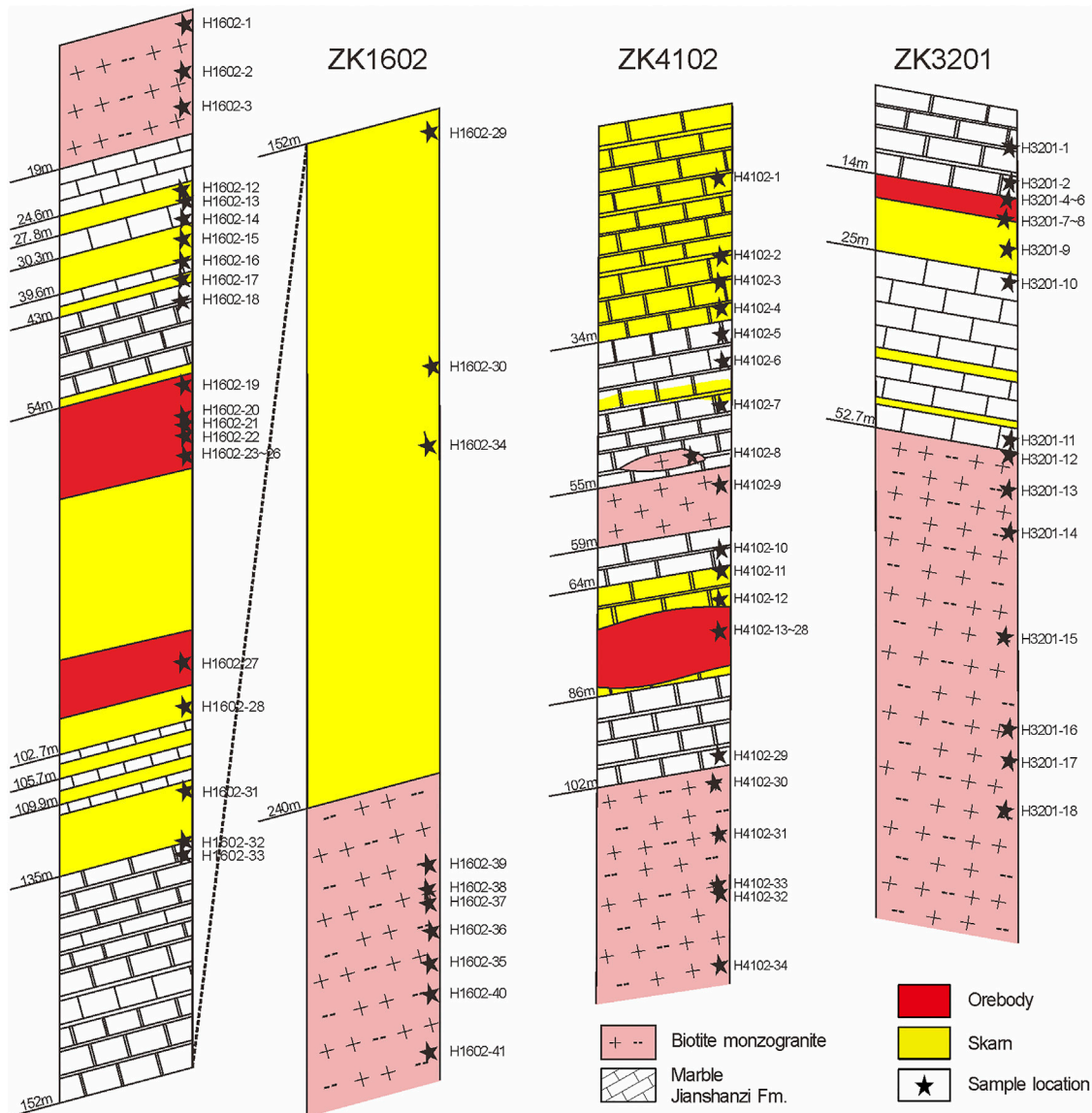


FIGURE 3 | Columnar diagram of drill hole of the Heiyanshan deposit showing the sample location.

Py is 78.43–80.39%, 8.99–11.58%, and 9.99–11.47%, respectively. The pyroxene is green, fine-grained (0.01–0.5 mm), and euhedral to subhedral (**Figure 4H**). The EPMA data show that pyroxene from the Heiyanshan W deposit is essentially diopside-hedenbergite (Di-Hd) solid solutions (**Table 1**; **Figure 6B**). In summary, the garnet in the Heiyanshan W deposit displays characteristics similar to those in most other skarn systems and are compositionally consistent with garnets in W skarns (**Figure 6**; Meinert et al., 2005).

The retrograde skarn stage consists of epidote, tremolite, actinolite, scheelite and quartz, which replace the garnet and pyroxene in the prograde skarn (**Figures 4B,G**). The quartz-sulphide stage is characterised by veins with the mineral assemblages of quartz-scheelite, and quartz-molybdenite-pyrrhotite-chalcopryrite-sphalerite-galena, which cross-cut the earlier stages intrude into the earlier skarn stage ores (**Figures**

4C,E,F). The quartz-calcite stage is represented by calcite veinlets crosscutting the skarn (**Figure 4I**). In addition, the tourmaline occurs as veins in altered granite (**Figures 4C,J**) and has no direct contact with skarn minerals, thus, the relationship between tourmaline and skarn is not clear. However, tourmaline is replaced by quartz + calcite (**Figure 4J**), indicating earlier than the quartz-calcite stage.

SAMPLING AND ANALYTICAL METHODS

Fluid Inclusion Study

All the samples used for fluid inclusions study were collected from drill hole of the Heiyanshan deposit (**Figure 3**). Doubly polished thin sections with a thickness of ~0.20 mm were

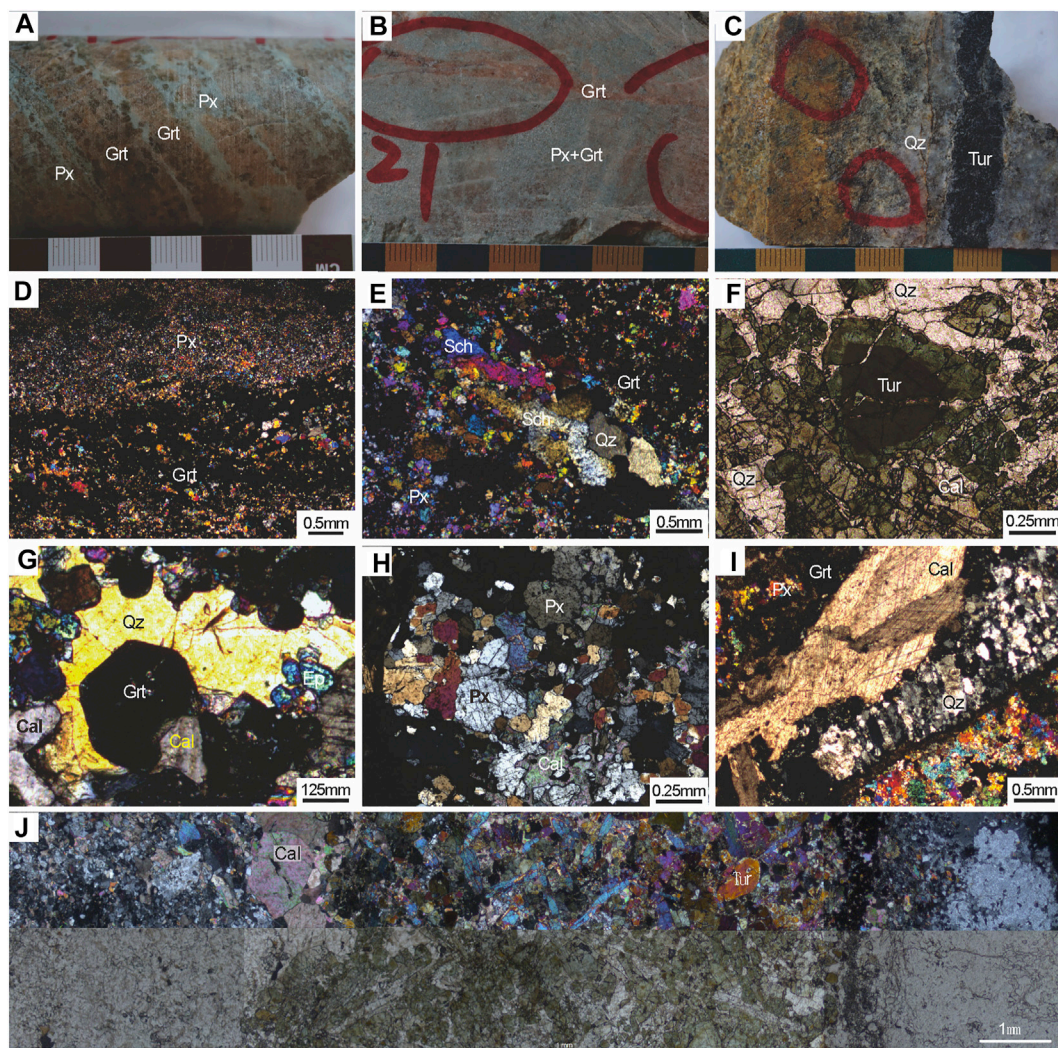


FIGURE 4 | Photographs and photomicrographs of mineralisation at the Heiyanshan deposit: **(A)** garnet and pyroxene in banded skarn; **(B)** disseminated scheelite in the garnet-pyroxene skarn; **(C)** tourmaline occurred as vein in altered biotite monzogranite; **(D)** garnet and pyroxene in banded skarn; **(E)** quartz-scheelite vein cross-cut the garnet-pyroxene skarn; **(F)** tourmaline in altered monzogranite; **(G)** prograde euhedral garnet overgrown by retrograde epidote, quartz, and calcite; **(H)** prograde pyroxene replaced by calcite; and **(I)** prograde garnet and pyroxene cut by a quartz-calcite vein. **(J)** tourmaline occurs as veins in altered granite, and replaced by quartz + calcite.

prepared from garnet, scheelite, quartz, and calcite samples associated with different stages of the Heiyanshan mineralisation. The fluid inclusions were carefully observed to identify their genetic relationships and types, vapour-liquid ratios, and spatial clustering, and to choose representative examples for microthermometric studies. The studies were carried out using a Linkam THMSG600 Heating-Freezing stage at the Fluid inclusion laboratory of the Institute of Geology for Mineral Resources in Beijing. The heating stage is designed to measure temperatures between -196 and 600°C , and it was attached to a Leica DM2700P microscope connected to a television camera and screen. The stage was calibrated using synthetic fluid inclusions at -56.6 , 0.0 , and $+374.1^{\circ}\text{C}$, with a heating/freezing rate of 0.2 – $5.0^{\circ}\text{C}/\text{min}$, which was reduced to $<0.2^{\circ}\text{C}/\text{min}$ near the phase transformation. The uncertainties for

the measurements are $\pm 0.5^{\circ}\text{C}$ for runs in the range from -120 to 30°C , ± 1 for temperatures between 30 and 300°C , and $\pm 2.0^{\circ}\text{C}$ from 300 to 600°C . Ice melting temperatures were observed at a heating rate of less than $0.1^{\circ}\text{C}/\text{min}$, and homogenisation temperatures at a rate of $\leq 1^{\circ}\text{C}/\text{min}$.

All low-temperature phase transitions were measured using a standard procedure starting with rapidly cooling to -120°C . This was followed by progressive heating at a rate of 5 – $10^{\circ}\text{C}/\text{min}$ and reduced to $<0.5^{\circ}\text{C}/\text{min}$ near the phase transformation. Two-phase transitions were observed in the inclusions involving the melting of the ice ($T_{m(\text{ice})}$) and the homogenisation temperature (T_h). All the phase transitions were measured using the cycling method described by Goldstein and Reynolds (1994). Salinities of aqueous inclusions were calculated using the equations of Bodnar (1993).

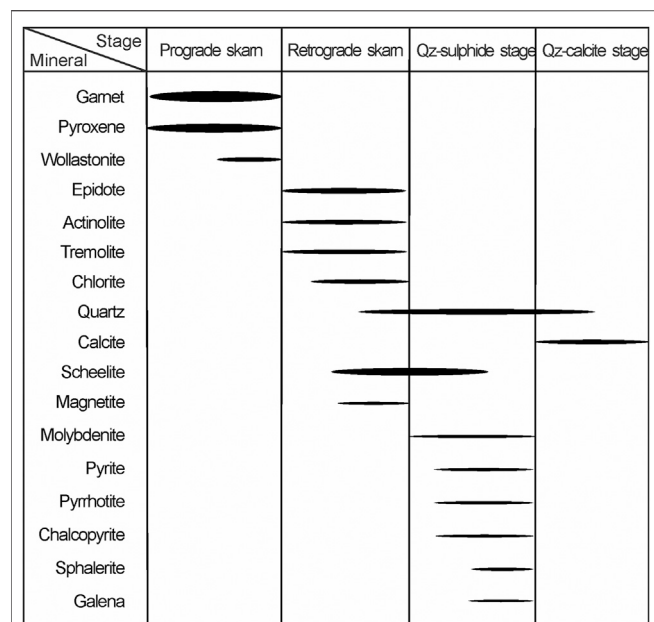


FIGURE 5 | Mineral paragenesis for the Heiyanshan W deposit.

Isotopic Analyses

Ten samples from the Heiyanshan deposit were selected for hydrogen and oxygen isotope studies. The sample location is recorded in **Figure 2** and **Figure 3**. The samples from the Heiyanshan deposit comprise four from garnet in the prograde skarn, three from quartz in the quartz-sulphide stage, and three from calcite in the carbonate stage.

The analytical methods were explained in detail by Ding (1988). Mineral separates were reacted with BrF_5 , followed by total conversion to CO_2 for oxygen isotope analysis. The δD values were measured on water in fluid inclusions decalcified from garnet, quartz, and calcite separates by heating at 600°C for 1 h. The released gases were passed through a CuO bucket at

600°C and frozen with liquid nitrogen to obtain water from which hydrogen gas was released by reduction with zinc.

The oxygen, hydrogen and carbon isotope analyses were conducted using a Finnigan MAT 253 EM mass spectrometer at the Open Laboratory for Isotope Geochemistry, Chinese Academy of Geological Sciences in Beijing. Isotopic data were reported per mil relative to the Vienna SMOW standard for oxygen and hydrogen. The total uncertainties were estimated to be better than $\pm 0.2\text{‰}$ for $\delta^{18}\text{O}$ and $\pm 2.0\text{‰}$ for δD at the σ level.

Zircon LA-ICPMS U-Pb Dating

Zircon sample was collected from unaltered granite (H1602-39). The sample location is recorded in **Figure 2C** and **Figure 3**. The LA-ICP-MS U-Pb dating analyses of zircon was performed at the Key Laboratory of Marine Resources and Coastal Engineering, Sun Yat-sen University. The analyses were performed using a 193 nm ArF excimer laser ablation system (GeoLasPro) coupled with an Agilent 7,700x ICP-MS. A $32\text{ }\mu\text{m}$ spot size was used with an energy density of 5 J/cm^2 and a repetition rate of 5 Hz. Zircon 91500 was used as age standard (1,062 Ma, Wiedenbeck et al., 1995). Analytical methodology is described in detail in Liu et al. (2010). Errors on individual analyses by LA-ICPMS are quoted at 95% (1σ) confidence level.

FLUID INCLUSIONS

Types of Fluid Inclusions

Three types of primary fluid inclusions were identified in different minerals from the Heiyanshan deposits (**Figure 7**). The L-type inclusions are biphasic liquid-rich inclusions with variable proportions of vapour between 5 and 20 vol%. This type of inclusion commonly has a negative crystal shape, elliptic or irregular shapes and range in size from 5 to $20\text{ }\mu\text{m}$, and is the dominant type at the Heiyanshan deposits (about 90% of the total). The V-type inclusions are biphasic inclusions with high vapour proportions containing $>50\%$ vapour/(vapour + liquid).

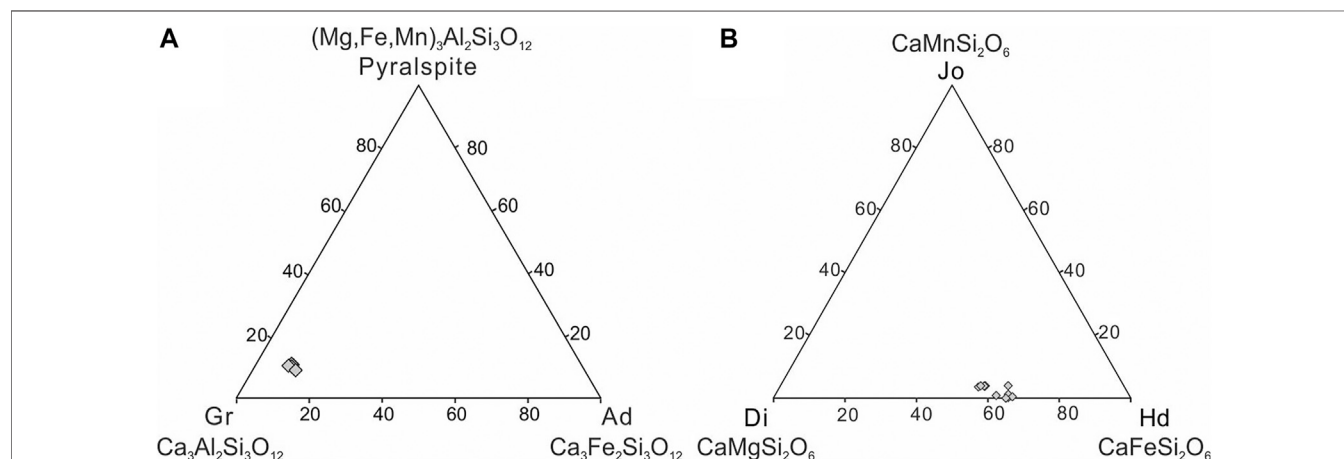


FIGURE 6 | Ternary diagrams summarizing garnet and pyroxene compositions in the Heiyanshan W deposit. Ad = andradite, Gr = grossular, Pyralspite = (pyrope + almandine + spessartine).

TABLE 1 | Representative Electron Microprobe Analyses of garnet from the Heiyanshan deposit.

Sample no	h1602-21-1.1	h1602-21-1.2	h1602-21-2.1	h1602-21-2.2	h1602-21-2.3
Oxide composition (wt%)					
SiO ₂	39.75	39.69	40.17	40.03	39.57
TiO ₂	0.26	0.30	0.11	0.23	0.42
Al ₂ O ₃	20.52	20.49	20.68	20.85	20.24
Cr ₂ O ₃	0.01	0.00	0.00	0.02	0.01
TFe ^a	5.83	5.90	5.73	5.38	6.06
MnO	2.44	2.33	2.35	2.47	2.36
MgO	0.11	0.09	0.10	0.08	0.06
CaO	33.5	33.17	33.91	33.83	34.02
Total	102.42	101.97	103.05	102.89	102.74
Number of ions on the base of 12 atoms of oxygen and 0 OH					
Si	2.972	2.978	2.982	2.975	2.954
Ti	0.015	0.017	0.006	0.013	0.024
Al	1.808	1.812	1.809	1.826	1.781
Cr ³⁺	0.001	0.000	0.000	0.001	0.001
Fe ³⁺	0.201	0.191	0.199	0.181	0.233
Fe ²⁺	0.164	0.179	0.157	0.154	0.145
Mn ²⁺	0.155	0.148	0.148	0.155	0.149
Mg ²⁺	0.012	0.010	0.011	0.009	0.007
Ca ²⁺	2.683	2.667	2.697	2.694	2.721
Total cations	8.011	8.002	8.009	8.008	8.015
End member percentages					
Grossularite	79.01	79.24	79.62	80.39	78.43
Andradite	9.990	9.530	9.910	8.990	11.58
Pyr + Spe + Alm	11.00	11.23	10.47	10.62	9.990

Abbreviation: Alm = almandine, Pyr = pyrope, Sp = Spessartine.

TFe^a = FeO + Fe₂O₃.

TABLE 2 | Microthermometric data for fluid inclusions from the Heiyanshan W deposits.

Mineral	Type	$T_{m(ice)}$ (No.)	T_h (°C)		W (wt% NaCl equiv.)		ρ (g/cm ³)	
			Range (No.)	Mean	Range	Mean	Range	Mean
Garnet	L	−9.4 to −4.8 (33)	228–338 (33)	290 ± 28	7.6–13.3	10.4 ± 1.6	0.7–0.9	0.83 ± 0.04
Scheelite	L	−9.5 to −3.4 (28)	146–296 (28)	232 ± 31	5.6–13.4	9.4 ± 1.9	0.8–1.0	0.90 ± 0.04
Quartz	L	−9.5 to −3.2 (159)	178–393 (159)	232 ± 36	5.3–13.4	9.0 ± 1.7	0.8–1.0	0.89 ± 0.03
Calcite	L	−5.5 to −1.6 (35)	136–186 (35)	158 ± 15	2.7–8.5	5.2 ± 1.3	0.9–1.0	0.95 ± 0.02

These inclusions commonly have negative crystal or ellipse shape and range in size from 5 to 30 μ m.

Entrapment Sequence of Fluid Inclusions

The Microthermometry results of fluid inclusions in the samples of the Heiyanshan W deposit are summarized in **Figure 8**. Although CL image can be successfully used for the interpretation of the entrapment sequence of fluid inclusions in the sample, the entrapment sequence of fluid inclusions was identified in the different skarn minerals. The prograde skarn stage includes garnet and pyroxene, which contain abundant L-type inclusions (**Figure 7A**) and are considered to be primary fluid inclusions (c.f. Goldstein and Reynolds, 1994; Chi et al., 2021). The retrograde skarn stage contains scheelite, which contain primary L-type and V-type inclusions that are scattered or randomly distributed within the host crystals (**Figure 7B**). The sulphide stage includes sulphide and quartz enriched in L- and V-type

inclusions (**Figures 7C–E**). The carbonate stage contains L-type fluid inclusions in calcite (**Figure 7F**).

Microthermometry

In the prograde garnet, 33 of L-type and inclusions have been analyzed (**Table 2**; **Figure 8**). The L-type inclusions with melting of the ice ($T_{m(ice)}$) range from −9.4 to −4.8°C, corresponding to salinity of 7.6–13.3 wt% NaCl equiv (mean = 10.4 ± 1.6 wt% NaCl equiv.). They are homogenized to liquid at 228–338°C, with mean of 290 ± 28°C. The bulk densities range from 0.74 to 0.93 g/cm³.

In the scheelite of quartz-sulphide stage, 28 L-type inclusions have been analyzed (**Table 2**). The L-type inclusions with $T_{m(ice)}$ range from −9.5 to −3.4°C. The estimated salinities range from 5.6 to 13.4 wt % NaCl equiv (mean 9.4 ± 1.9 wt% NaCl equiv.). They are homogenized to liquid at temperatures of 146–296°C (mean = 232 ± 31°C), slightly lower than that of the L-type inclusions in prograde garnet. The bulk densities range from 0.81 to 0.96 g/cm³.

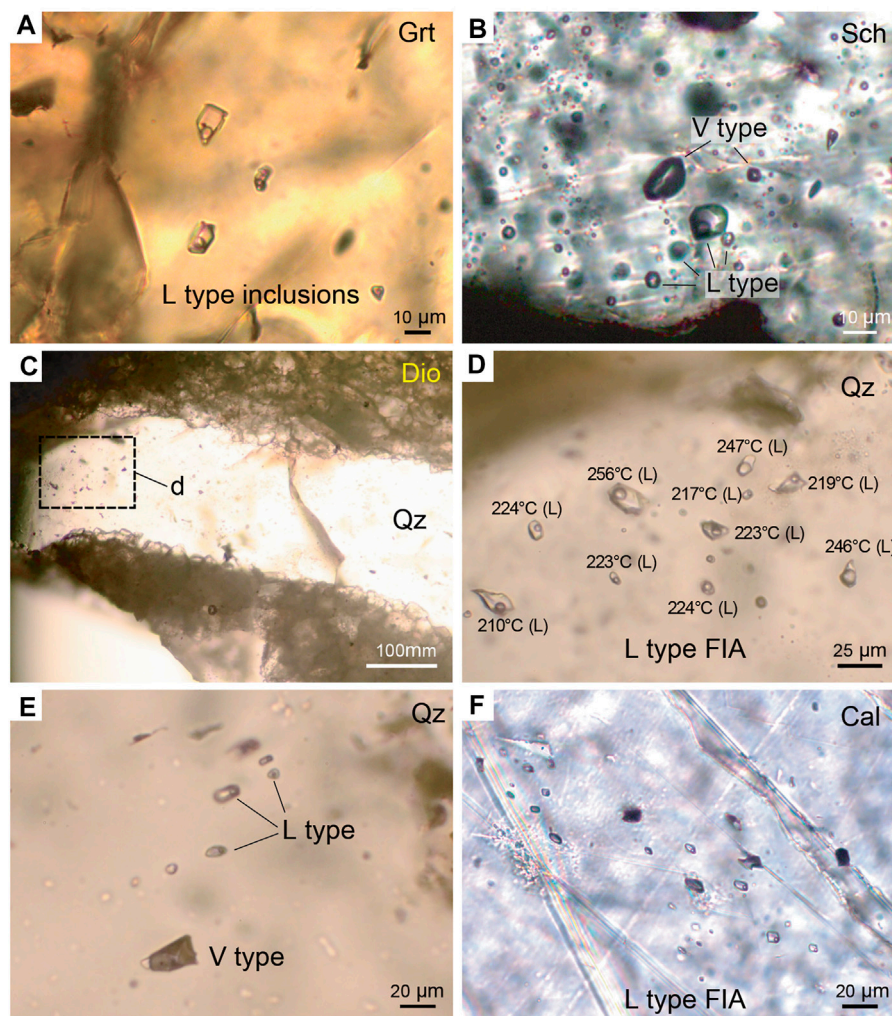


FIGURE 7 | Photomicrographs of fluid inclusions from the Heiyanshan deposit showing: **(A)** scattered two-phase L-type fluid inclusions in garnet from the prograde skarn; **(B)** coexistence of L- and V-type fluid inclusions in scheelite **(C, D)** two-phase L-type fluid inclusions randomly distributed in quartz with similar homogenise temperatures; **(E)** coexisting L- and V-type fluid inclusions in quartz; and **(F)** clusters of two-phase L-type fluid inclusions in calcite.

In the quartz of quartz-sulphide stage, 159 L-type inclusions are analyzed (**Table 2**). The L-type inclusions with $T_{m(ice)}$ range from -9.5 to -3.2°C . The estimated salinities range from 5.3 to 13.4 wt% NaCl equiv (mean = 9.0 ± 1.7 wt% NaCl equiv.). They are homogenized to liquid at temperatures of 178 – 393°C (mean = $232 \pm 36^{\circ}\text{C}$). The bulk densities range from 0.78 to 0.96 g/cm^3 .

In the calcite of carbonate stage, a total of 35 L-type inclusions yield $T_{m(ice)}$ of -5.5 to -1.6°C (**Table 2**), salinities of 2.7–8.5 wt% NaCl equiv (mean = 5.2 ± 1.3 wt% NaCl equiv.), and homogenization to liquid at temperature of 136 – 186°C (mean = $158 \pm 15^{\circ}\text{C}$). The bulk densities range from 0.91 to 0.98 g/cm^3 .

OXYGEN AND HYDROGEN ISOTOPIC SYSTEMATICS

The $\delta^{18}\text{O}$ values for garnet in the prograde skarn at the Heiyanshan W deposit range from $+4.8$ to $+6.7\text{‰}$, and the

$\delta^{18}\text{O}$ values for quartz from the sulphide stage range from $+11.1$ to $+11.7\text{‰}$ (**Table 3**). The $\delta^{18}\text{O}$ values of $+8.7$ to $+10.4\text{‰}$ for calcite from the carbonate stage are similar to those of the sulphide stage. Considering the homogenisation temperatures of the fluid inclusions, the calculated $\delta^{18}\text{O}_{\text{water}}$ values of the mineralising fluid related to the prograde skarn range from $+4.7$ to $+6.6\text{‰}$ (**Table 3**; **Figure 9**). The calculated $\delta^{18}\text{O}_{\text{water}}$ values for quartz from the sulphide stage are between $+1.3$ and $+1.9\text{‰}$, which are obviously lower than those of the skarn. The carbonate stage has $\delta^{18}\text{O}_{\text{water}}$ values between -6.1 and -4.4‰ , lower than those of the sulphide stage and skarn.

The measured δD values of fluids associated with the prograde skarn at the Heiyanshan W deposit are between -121 and -71‰ , and the δD values of quartz from sulphide stage range from -84 to -75‰ (**Table 3**). The carbonate stage has $\delta\text{D}_{\text{water}}$ values between -101 and -82‰ , with are lower than those for the sulphide stage and skarn.

TABLE 3 | Isotopic compositions (‰) of samples from the Heiyanshan W deposit.

Samples	Mineral/Rock	$\delta^{18}\text{O}_{\text{mineral}}$	T (°C)	$\delta^{18}\text{O}_{\text{water}}$	$\delta\text{D}_{\text{water}}$
H1602-27	Garnet	4.8	290	4.7	-83
H1602-32	Garnet	5.4	290	5.3	-71
H4102-25	Garnet	6.6	290	6.5	-121
H4102-28	Garnet	6.7	290	6.6	-119
Average	N = 4	5.9	290	5.7	-99
Median		6	290	5.9	-101
H3201-5	Quartz	11.1	232	1.3	-84
H3201-6-1	Quartz	11.1	232	1.3	-82
H3201-6-2	Quartz	11.7	232	1.9	-75
Average	N = 8	11.3	232	1.5	-80
Median		11.1	232	1.3	-82
H1602-22	Calcite	10.4	158	-4.4	-96
H1602-27	Calcite	8.7	158	-6.1	-101
H1602-32	Calcite	9.7	158	-5.1	-82
Average	N = 3	9.6	158	-5.2	-93
Median		9.7	158	-5.1	-96

The $\delta^{18}\text{O}_{\text{water}}$ values were calculated using equations for garnet–water, quartz–water and calcite–water provided by Bottinga and Javoy, 1975, Zheng, 1993, and O'Neill et al. (1969), respectively.

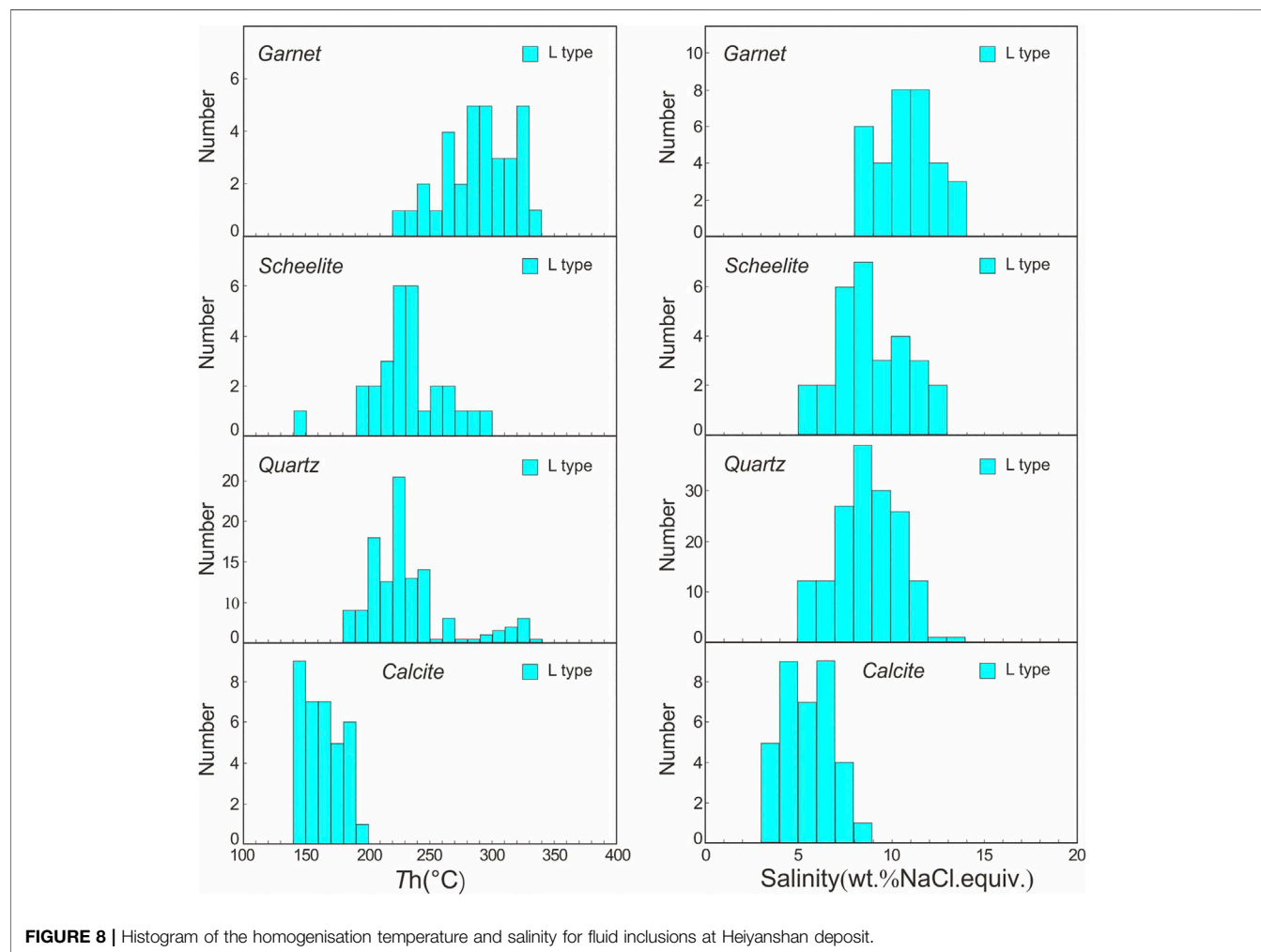
**FIGURE 8** | Histogram of the homogenisation temperature and salinity for fluid inclusions at Heiyanshan deposit.

TABLE 4 | LA-ICP-MS zircon U-Pb dating results of granites from the Heiyanshan W deposit.

Spot	Content (ppm)				Ratios				Error correct				Age (Ma)			
	Pb	Th	U	Th/U	$^{207}\text{Pb}/^{235}\text{U}$	1σ	$^{206}\text{Pb}/^{238}\text{U}$	1σ	$^{207}\text{Pb}/^{206}\text{Pb}$	1σ	$^{207}\text{Pb}/^{235}\text{U}$	1σ	$^{206}\text{Pb}/^{238}\text{U}$	1σ	$^{207}\text{Pb}/^{235}\text{U}$	1σ
1	191	700	3507	0.20	0.38244	0.01037	0.05188	0.00043	0.30615	0.00161	0.05581	0.00161	455.6	60.2	328.8	7.6
2	196	888	3482	0.26	0.38968	0.01063	0.05193	0.00048	0.34133	0.00162	0.05669	0.00162	479.7	63.0	334.1	7.8
3	240	1,011	4,331	0.23	0.38487	0.01003	0.05197	0.00047	0.34760	0.00148	0.05528	0.00148	493.4	61.1	330.6	7.4
4	255	1,015	4,613	0.22	0.36926	0.00913	0.05188	0.00046	0.35662	0.00156	0.05052	0.00156	220.4	70.4	319.1	6.8
5	144	429	2,649	0.16	0.38240	0.01094	0.05219	0.00044	0.29423	0.00170	0.05628	0.00170	464.9	66.7	328.8	8.0
6	214	768	3990	0.19	0.36253	0.00940	0.05196	0.00044	0.33023	0.00160	0.05231	0.00160	298.2	70.4	314.1	7.0
7	305	1,440	5243	0.27	0.38183	0.00990	0.05246	0.00046	0.33822	0.00197	0.05492	0.00197	409.3	79.6	328.4	7.3
8	204	880	3653	0.24	0.35458	0.00885	0.05194	0.00043	0.33495	0.00156	0.04932	0.00156	164.9	74.1	308.2	6.6
9	335	1,540	5987	0.26	0.36604	0.00841	0.05184	0.00046	0.38619	0.00132	0.05312	0.00132	344.5	57.4	316.7	6.3
10	615	2,947	10,654	0.28	0.36784	0.00897	0.05194	0.00051	0.40484	0.00136	0.05227	0.00136	298.2	57.4	318.1	6.7
11	193	778	3396	0.23	0.36740	0.00958	0.05226	0.00048	0.34982	0.00151	0.04838	0.00151	116.8	74.1	317.7	7.1
12	219	909	3831	0.24	0.38326	0.01045	0.05193	0.00049	0.34844	0.00156	0.05458	0.00156	394.5	64.8	329.4	7.7

ZIRCON U-PB DATING

Zircons in sample H1602-39 are colorless and euhedral (**Figure 10A**). The crystals range in length from 100 to 200 μm , with length/width ratios ranging from 2:1 to 4:1. Cathodoluminescence images reveal complex zoning characterized by two major concentric zones, i.e., core and rim (**Figure 10A**). The LA-ICP-MS analyses were concentrated on the zircon rims in an attempt to date the crystallization age of the granite.

Twelve analyses conducted on the rims show they have 2,649–10,654 ppm U, 429–2,947 ppm Th, and Th/U ratios of 0.16–0.28 (**Table 4**). Their $^{206}\text{Pb}/^{238}\text{U}$ ages vary from 325.8 ± 2.8 Ma to 329.6 ± 2.8 Ma (1σ error), with an average of 326.9 ± 1.6 Ma ($n = 12$, MSWD = 0.16; **Figure 10B**), which is interpreted as the crystallization age of the granite.

DISCUSSION

Fluid Evolution in the W-Skarn Deposits

Our studies show that the evolution of hydrothermal fluids related to the Heiyanshan W-skarn deposits involved at least four stages: 1) an early high to moderate temperature of $\sim 290^\circ\text{C}$ during the development of the prograde stage; 2) development of a retrograde skarn hosting W mineralisation; 3) development of a low-temperature ($\sim 230^\circ\text{C}$) quartz-sulphide stage hosting scheelite; and 4) development of a low-temperature (160°C) barren carbonate stage. The temperature of the mineralising fluid decreased from the prograde skarn, through the sulphide stage to the carbonate stage, which is consistent with W-skarns worldwide (**Figure 11**; Pan et al., 2019).

During Carboniferous, the carbonaceous limestone and marble in the Jianshanzi Formation was intruded by the biotite monzogranite in the extensional event associated with the alteration of the limestone into the prograde skarn. Primary fluid inclusions in minerals have long been thought to be relics or residuals of mineralising fluids trapped and preserved in crystals (c.f. Roedder, 1984; Chen et al., 2007; Pirajno, 2009). For example, prograde skarns at the W-skarn deposits in the Tianshan region included high temperature ($>400^\circ\text{C}$), medium pressure (>700 bars), and high salinity ($>45\text{wt}\%$ NaCl equiv.) magmatic-related hydrothermal fluids that exsolved from a crystallising magma (Soloviev, 2011, 2015; Soloviev and Kryazhev, 2017a,b). However, the fluid inclusions at the W-hosted prograde skarns in the ETT have high to moderate homogenisation temperatures of $\sim 300^\circ\text{C}$ and medium to low salinities and are classified as NaCl-H₂O fluids. Furthermore, the tourmaline occurs as veins in altered granite indicates that the magma-related hydrothermal fluid at the deposits contained boron in addition to aqueous solution (**Figure 4F**).

The fluid inclusions in the retrograde skarn at the Heiyanshan W deposit are characterised by their low temperatures ($\sim 230^\circ\text{C}$), moderate to low salinities, and can be classified as a NaCl-H₂O fluid. The H-O isotopes in the quartz at the deposit are indicative of magmatic fluids mixed with meteoric water resulted in the formation of coarse-grained scheelite in quartz veins.

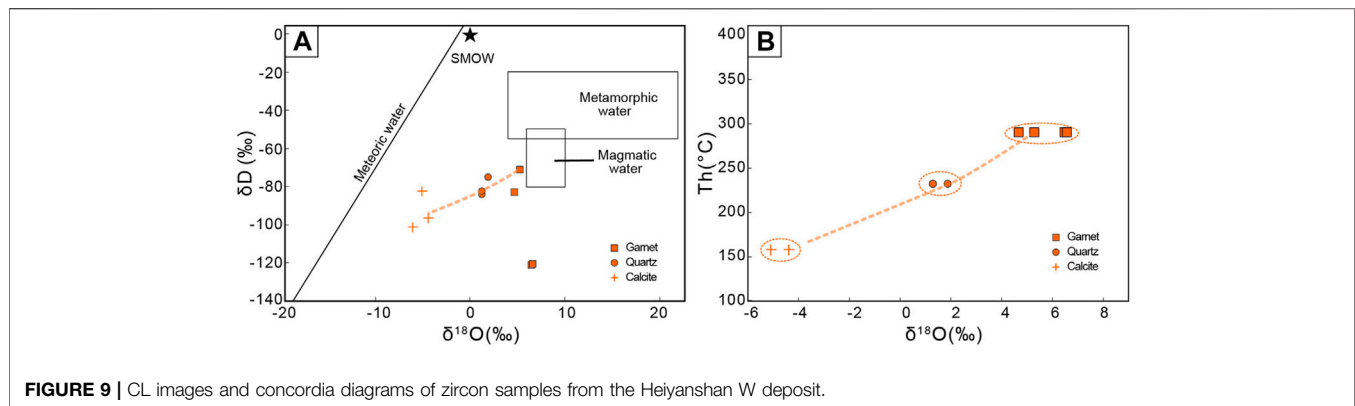


FIGURE 9 | CL images and concordia diagrams of zircon samples from the Heiyanshan W deposit.

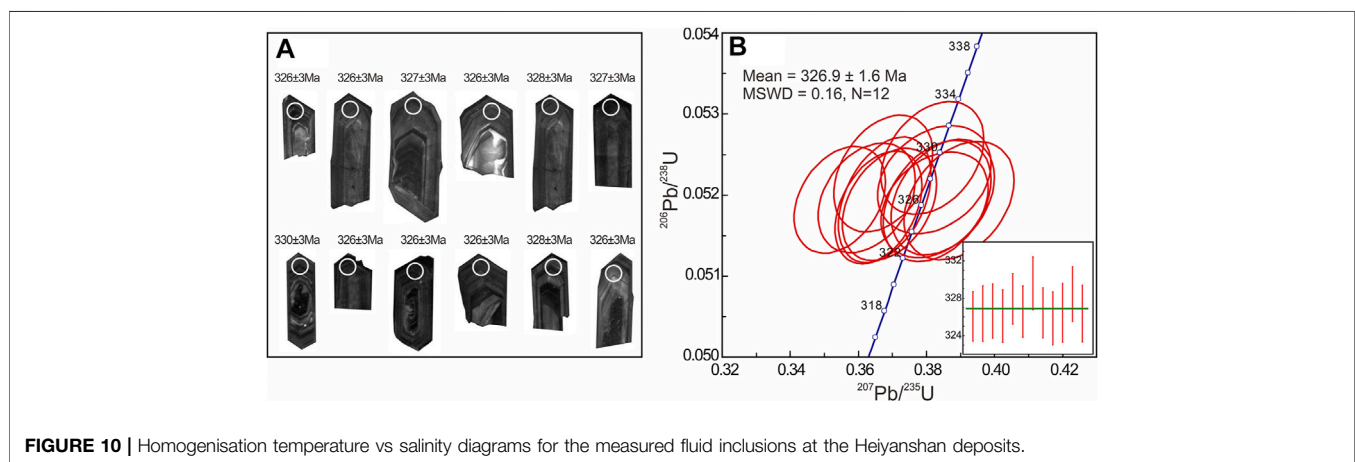


FIGURE 10 | Homogenisation temperature vs salinity diagrams for the measured fluid inclusions at the Heiyanshan deposits.

The fluid inclusions in the carbonate stage have low-temperatures (160°C), low salinities, low pressure, and can be classified as NaCl-H₂O fluids. The δD and $\delta^{18}O$ values point to a meteoric source for the fluid inclusions. Thus, the precipitation of calcite represents the end of the magma-related mineralising hydrothermal fluids.

Fluid Mixing and Precipitation of Tungsten

The precipitation of scheelite can relate to cooling of the carrying fluids resulting in the decrease in W-solubility, fluid mixing, and the buffering of pH levels neutral levels by reaction with carbonate rocks (e.g., Wood and Samson, 2000; Robb, 2005).

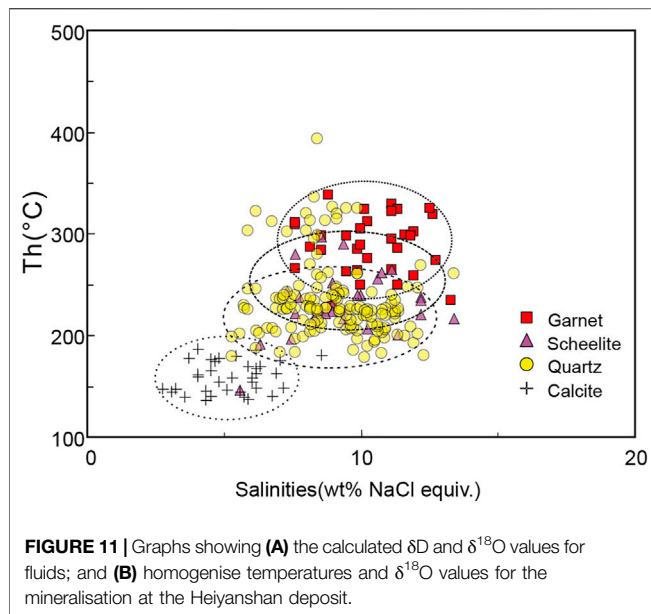
If simple cooling of the mineralised fluids led to tungsten deposition, it would be expected that the fluid's salinity would not change significantly (Ni et al., 2015). However, the salinity decreases from the early prograde skarn to the late carbonate stage at Heiyanshan (Figure 11), which also excludes cooling as a key factor during the mineralising process.

Fluid boiling is also crucial for the deposition of tungsten-bearing minerals because fluid boiling increase pH values that destabilize tungsten complexes, leading to tungsten precipitation (c.f. Jiang et al., 2019). The irregular presence of L- and V-type inclusions in scheelite from the oxide stage and quartz from the sulphide stage are characteristic of fluid boiling (Figures 7B,E).

However, the fluid inclusions homogenizing into different phases (liquid and gas) at similar temperatures is not obvious in the Heiyanshan deposit. Therefore, fluid boiling may not be the major cause to promote tungsten precipitation for the Heiyanshan deposit.

Einaudi et al. (1981) proposed that the key mechanism for precipitating scheelite in skarns is the increase of Ca^{2+}/H^{+} due to reaction of W-rich fluids with Ca-rich lithologies, but this would include changes in the fluid's salinity (c.f. Wilkinson, 2001). The calculated $\delta^{18}O_{water}$ and δD_{water} values for fluid inclusions in the prograde skarn at Heiyanshan plot near the edge of the magmatic box on the δD - $\delta^{18}O$ diagram (Figure 9), which is similar to that of the prograde skarn at Xiaobaishitou (Li et al., 2020b). The calculated $\delta^{18}O_{water}$ and δD_{water} values for the carbonate stage plot closer to the meteoric water line (Figure 9), indicating the possible contribution of meteoric water. The fluids from sulphide stage have $\delta^{18}O_{water}$ and δD_{water} values intermediate between those for the prograde skarn and carbonate stages, indicating a mixing of deep-sourced magmatic fluids with meteoric water.

Therefore, it is proposed that the fluid mixing during its reaction with carbonates are the major factors involved during the precipitation of scheelite at Heiyanshan deposit.



Two Pulse of Tungsten Skarn in East Tianshan

In recent years, several tungsten skarn deposits have been discovered in ETT, and the WO_3 resources of these tungsten skarn deposits are more than 200,000 tons. The tungsten deposit in ETT is mainly distributed in the Central Tianshan Block and the South Tianshan Terrane (Figure 1). The Central Tianshan Block contains Xiaobaishitou W (-Mo), Shadong Rb-W, Heiyanshan W, Jiangshan W, Shadongdong W and Jinshan Au-W deposit. South Tianshan Terrane contains Zhongbao W, Sangshuyuanzi W and Wutonggou W deposits (Figure 1C). The metallogenic ages of these tungsten deposits can be divided into two stages, namely, Late Carboniferous and Early Triassic.

The Zhongbao and Sangshuyuanzi W deposits in Kumush area of South Tianshan Terrane are typical skarn tungsten deposits. The W orebodies occur in the contact zone between quartz schist and marble of the Arpishimaibulag Formation and monzogranite. Chen et al. (2013) reported that LA-ICP-MS zircon U-Pb age of monzogranite from the Zhongbao and Sangshuyuanzi W deposits are 296 ± 4 Ma and 293 ± 3 Ma, respectively, indicating that the tungsten deposits in the Kumush area of South Tianshan were mainly formed in the Late Carboniferous. We have recently discovered the Wutonggou tungsten skarn deposit in the South Tianshan Terrane. The orebody is stratiform and lenticular and occurs in the contact zone between quartz schist and marble of the Arpishimaibulag Formation and monzogranite. The LA-ICP-MS zircon U-Pb age of Wutonggou monzogranite is 313 ± 2 Ma (unpublished data), indicating an important Late Carboniferous tungsten mineralization in Kumush area, South Tianshan Terrane. This paper reports a LA-ICP-MS zircon U-Pb age of 326.9 ± 1.6 Ma for the biotite monzogranite in the Heiyanshan W deposit (Figure 10), which indicate a Late Carboniferous tungsten mineralization in the Central Tianshan Block.

The Xiaobaishitou and Heiyanshan W deposits are typical calcareous skarn deposits in Central Tianshan Block. The orebody is controlled by the contact zone of Mesoproterozoic Jianshanzi Formation of the Kawabulag Group and granite. Although Chen and Wang (1993) have reported whole rock Rb-Sr isochron age of 294 ± 49 Ma for Xiaobaishitou W deposit, the easily disturbed Rb-Sr isotopic systems make these data unreliable. Deng et al. (2017) reported that LA-ICP-MS zircon U-Pb age of biotite granite and Mo-mineralized granite are 242 ± 1.7 Ma and 240.5 ± 2.1 Ma, which constrains the emplacement age of the Xiaobaishitou granite more precisely as 240 Ma. Li et al. (2020b) obtained molybdenite Re-Os isochron age and muscovite $^{40}Ar/^{39}Ar$ plateau age of 253.0 ± 2.7 Ma and 247.6 ± 2.3 Ma, respectively, which consistent with our results. The Shadong W deposit is unique magnesia skarn tungsten deposit in Central Tianshan Block. Tungsten skarn occurs in the contact zone between schist and gneiss of Kawabulag Group and granite. Chen et al. (2018) obtained a LA-ICP-MS zircon U-Pb age of 239 ± 2 Ma, indicating the development of large-scale Early Triassic tungsten mineralization in the Central Tianshan Block.

In a word, ETT contains two pulse of tungsten metallogenic events of Late Carboniferous and Early Triassic. More and more tungsten deposits have been discovered in ETT, indicating that ETT will become an important tungsten metallogenic belt in northwest China.

CONCLUSION

The ore-forming process at the Heiyanshan W deposit in the East Tianshan consists of four stages, namely, prograde skarn stage, retrograde skarn stage, quartz-sulphide vein stage, and quartz-calcite vein stage.

The mineralised magma-related hydrothermal fluids related to the Heiyanshan W deposit progressed with the development of a skarn at moderate to low temperatures and salinities.

The decrease in the fluid's temperatures is probably due to a gradual introduction of meteoric water interacting with the hydrothermal fluid resulting in the deposition of scheelite.

The LA-ICP-MS zircon U-Pb age of 326.9 ± 1.6 Ma for the host biotite monzogranite, demonstrating that the Heiyanshan W system was formed in the Carboniferous, and the eastern Tianshan contains two pulse of tungsten metallogenic events.

DATA AVAILABILITY STATEMENT

The original contributions presented in the study are included in the article/supplementary material, further inquiries can be directed to the corresponding author.

AUTHOR CONTRIBUTIONS

XD and LB led the conception and design of the study. DX, XD, YW and XJ contributed the field work. DX and XC contributed

the experiments of fluid inclusion and H-O isotopic analysis. DX and XD wrote the first draft of the manuscript and interpreted the results with LB, XC, YW, and XJ. All authors contributed to manuscript revision, read and approved it for publication.

FUNDING

This study is supported by the National Key Research and Development Program of China (2018YFC0604006), the National Natural Science Foundation of China (91962214 and

42072106), the Geological Survey Project of China (1212011140056).

ACKNOWLEDGMENTS

We sincerely thank Profs. Yanjing Chen, Lianhui Dong, Xun Qu, Changzhi Wu, Haoshu Tang, Qiugen Li, Jing Zhang, Suwei Yue, Xiheng He assisted us with field investigations. We are grateful to Dengfeng Li for her help on zircon LA-ICP-MS U-Pb analyses. Comments and suggestions from editor and three reviewer greatly improved the quality of the paper.

REFERENCES

- Bodnar, R. J. (1993). Revised Equation and Table for Determining the Freezing point Depression of H₂O-NaCl Solutions. *Geochim. Cosmochim. Acta* 57, 683–684. doi:10.1016/0016-7037(93)90378-a
- Bottinga, Y., and Javoy, M. (1975). Oxygen isotope partitioning among the minerals in igneous and metamorphic rocks. *Rev. Geophys.* 13(2), 401–418. doi:10.1029/RG013i002p00401
- Chang, Z. S., Shu, Q. H., and Meinert, L. D. (2019). Skarn Deposits of China. *Soc. Econ. Geol. Spec. Publ.* 22, 189–234. doi:10.5382/SP.22.06
- Chen, Y. L., and Wang, Z. G. (1993). Geochemical Characteristics of East Tianshan Granitoid Rocks, Xinjiang, China. *Geochimica* 3, 288–302. (in Chinese with English abstract).
- Chen, Y. J., Ni, P., Fan, H. R., Pirajno, F., Lai, Y., Su, W. C., et al. (2007). Diagnostic Fluid Inclusions of Different Types Hydrothermal Gold Deposits. *Acta Petrol. Sin.* 23, 2085–2108. (in Chinese with English abstract).
- Chen, Y. J., Pirajno, F., Wu, G., Qi, J. P., Xiong, X. L., and Zhang, L. (2012). Epithermal Deposits in north Xinjiang, NW China. *Int. J. Earth Sci. (Geol. Rundsch)* 101, 889–917. doi:10.1007/s00531-011-0689-4
- Chen, C., Lu, X. B., Cao, X. F., Wu, C. M., and Zhu, J. (2013). Geochronology, Geochemistry and Geological Significance of Late Carboniferous-Early Permian Grnaites in Kumishi Area, Xinjiang. *Earth Sci.* 38 (2), 218–232. (in Chinese with English abstract).
- Chen, C., Lü, X., Wu, C., Jiang, X., and Mao, C. (2018). Origin and Geodynamic Implications of Concealed Granite in Shadong Tungsten Deposit, Xinjiang, China: Zircon U-Pb Chronology, Geochemistry, and Sr-Nd-Hf Isotope Constraint. *J. Earth Sci.* 29, 114–129. doi:10.1007/s12583-017-0808-7
- Chen, X., Wu, Y. S., Zhao, K., Zhou, K., and Chen, Y. (2020). Age, Sediment Source and Tectonic Setting of the Ore-Hosting Jinwozi Formation at the Jinwozi Gold deposit in Beishan Orogen, NW China: Evidence from Detrital Zircon U-Pb Ages and Lu-Hf Isotopes. *Ore Geology. Rev.* 117, 103296. doi:10.1016/j.oregeorev.2019.103296
- Chen, Y. R. (2006). Geological Characteristics and Ore Genesis of the Xiaobaishitou Tungsten-(Molybdenum) deposit, Xinjiang. *Gansu Metall.* 28, 75–81. (in Chinese with English abstract).
- Chi, G., Diamond, L. W., Lu, H., Lai, J., and Chu, H. (2021). Common Problems and Pitfalls in Fluid Inclusion Study: A Review and Discussion. *Minerals* 11, 7. doi:10.3390/min11010007
- Deng, X.-H., Wang, J.-B., Pirajno, F., Wang, Y.-W., Li, Y.-C., Li, C., et al. (2016). Re-Os Dating of Chalcopyrite from Selected mineral Deposits in the Kalatag District in the Eastern Tianshan Orogen, China. *Ore Geol. Rev.* 77, 72–81. doi:10.1016/j.oregeorev.2016.01.014
- Deng, X.-H., Chen, Y.-J., Santosh, M., Wang, J.-B., Li, C., Yue, S.-W., et al. (2017). U-pb Zircon, Re-os Molybdenite Geochronology and Rb-Sr Geochemistry from the Xiaobaishitou W (-Mo) deposit: Implications for Triassic Tectonic Setting in Eastern Tianshan, NW China. *Ore Geology. Rev.* 80, 332–351. doi:10.1016/j.oregeorev.2016.05.013
- Deng, X.-H., Wang, J.-B., Pirajno, F., Mao, Q.-G., and Long, L.-L. (2020). A Review of Cu-Dominant mineral Systems in the Kalatag District, East Tianshan, China. *Ore Geology. Rev.* 117, 103284. doi:10.1016/j.oregeorev.2019.103284
- Ding, T. P. (1988). *Stable Isotope Studies on Several Typical Deposits in China*. Beijing: Science and Technology Publishing House of Beijing, 21–44.
- Einaudi, M., Meinert, L. D., and Newberry, R. J. (1981). Skarn Deposits. *Econ. Geol. 75th Anniversary Volume*, 317–391. doi:10.5382/av75.11
- Goldstein, R. H., and Reynolds, T. J. (1994). Systematics of Fluid Inclusions in Diagenetic Minerals. *Soc. Sediment. Geol. Short Course* 31. doi:10.2110/scn.94.31
- Gu, L. X., Hu, S. X., Yu, C. S., Zhao, M., Wu, C. Z., and Li, H. Y. (2001). Intrusive Activities during Compression–Extension Tectonic Conversion in the Bogda Intracontinental Orogen. *Acta Petrol. Sin.* 17, 187–198. (in Chinese with English abstract).
- He, X.-H., Deng, X.-H., Bagas, L., Zhang, J., Li, C., and Zhang, W.-D. (2020). Geology, Geochronology, and Fluid Inclusion Studies of the Xiaorequanzi Volcanogenic Massive Sulphide Cu-Zn deposit in the East Tianshan Terrane, China. *Can. J. Earth Sci.* 57 (12), 1392–1410. doi:10.1139/cjes-2019-0067
- Hu, D. Q., Wang, D. K., Li, Y. F., Zhao, X. B., and Lin, L. (2016). The Geological Characteristics and Ore-controlling Factors of the Heiyanshan Tungsten deposit. *West China Prospecting Engineering*, 28 (5), 170–174. (in Chinese with English abstract).
- Jiang, H., Jiang, S.-Y., Li, W.-Q., Peng, N.-J., and Zhao, K.-D. (2019). Fluid Inclusion and Isotopic (C, H, O, S and Pb) Constraints on the Origin of Late Mesozoic Vein-type W Mineralization in Northern Guangdong, South China. *Ore Geology. Rev.* 112, 103007. doi:10.1016/j.oregeorev.2019.103007
- Jiang, X. (2016). *Study on Metallogenic Regularity of Tungsten Deposits and Prospecting Target Optimization in the Area of Shadong in Hami*. Xinjiang, Beijing: China University of Geosciences.
- Lei, R.-X., Wu, C.-Z., Gu, L.-X., Zhang, Z.-Z., Chi, G.-X., and Jiang, Y.-H. (2011). Zircon U-Pb Chronology and Hf Isotope of the Xingxingxia Granodiorite from the Central Tianshan Zone (NW China): Implications for the Tectonic Evolution of the Southern Altids. *Gondwana Res.* 20, 582–593. doi:10.1016/j.gr.2011.02.010
- Li, P., Lv, X. B., Chen, C., Cao, X. F., Ma, Y. L., and Su, Y. Y. (2011). Geochronology and Geochemical Characteristics of the Biotite-Granite in the Xiaobaishitou Tungsten deposit, East Tian Shan Mountains of Xinjiang and Their Geological Implications. *Geol. Expl.* 47, 543–554.
- Li, D. F., Chen, H. Y., Sun, X. M., Fu, Y. M., Liu, Q. F., Xia, X. P., et al. (2019). Coupled Trace Element and SIMS Sulfur Isotope Geochemistry of Sedimentary Pyrite: Implications on Pyrite Growth of Caixiashan Pb-Zn deposit. *Geosci. Front.* 10, 2177–2188. doi:10.1016/j.gsf.2019.05.001
- Li, N., Yang, F., Zhang, Z., and Tang, L. (2019a). Petrogenesis of Early Devonian Granodiorite in the Xiaobaishitou W-(Mo) Ore District of East Tianshan, Northwest China, and Tectonic Implications: U-Pb Geochronological, Geochemical, and Sr-Nd Isotopic Evidence. *Geol. J.* 55 (1), 4302–4323. doi:10.1002/gj.3668
- Li, N., Yang, F., Zhang, Z., and Yang, C. (2019b). Geochemistry and Chronology of the Biotite Granite in the Xiaobaishitou W-(Mo) deposit, Eastern Tianshan, China: Petrogenesis and Tectonic Implications. *Ore Geology. Rev.* 107, 999–1019. doi:10.1016/j.oregeorev.2019.03.027
- Li, N., Yang, F., and Zhang, Z. (2020a). Fluid Inclusions and Isotope (C, H, O, S, He, and Ar) Study of the Xiaobaishitou Skarn W-(Mo) deposit, East Tianshan, NW China. *Ore Geology. Rev.* 122, 103520. doi:10.1016/j.oregeorev.2020.103520
- Li, N., Yang, F., Zhang, Z., and Li, C. (2020b). Dating the Xiaobaishitou Skarn W-(Mo) deposit, Eastern Tianshan, NW China: Constraints from Zircon U-Pb,

- Muscovite 40Ar-39Ar, and Molybdenite Re-os System. *Ore Geology. Rev.* 124, 103637. doi:10.1016/j.oregeorev.2020.103637
- Liu, Y., Hu, Z., Zong, K., Gao, C., Gao, S., Xu, J., et al. (2010). Reappraisal and Refinement of Zircon U-Pb Isotope and Trace Element Analyses by LA-ICP-MS. *Chin. Sci. Bull.* 55 (15), 1535–1546. doi:10.1007/s11434-010-3052-4
- Mao, Y.-J., Qin, K.-Z., Li, C., and Tang, D.-M. (2015). A Modified Genetic Model for the Huangshandong Magmatic Sulfide deposit in the Central Asian Orogenic Belt, Xinjiang, Western China. *Miner. Deposita* 50, 65–82. doi:10.1007/s00126-014-0524-5
- Mao, J. W., Ouyang, H. G., Song, S. W., Santosh, M., Yuan, S. D., Zhou, Z. H., et al. (2019). Geology and Metallogeny of Tungsten and Tin Deposits in China, in Chang, Z., and Goldfarb, R.J., eds., *Mineral Deposits of China. SEG Spec. Publ.* 22, 411–482. doi:10.5382/SP.22.10
- Meinert, L. D., Dipple, G. M., and Nicolescu, S. (2005). World skarn deposits: Economic Geology 100th Anniversary Volume. 299–336.
- Muhtar, M. N., Wu, C.-Z., Brzozowski, M. J., Li, P., Yuan, X.-C., Wang, S.-M., et al. (2020). Geochronology, Geochemistry, and Sr-Nd-Pb-Hf-S Isotopes of the wall Rocks of the Kanggur Gold Polymetallic deposit, Chinese North Tianshan: Implications for Petrogenesis and Sources of Ore-Forming Materials. *Ore Geology. Rev.* 125, 103688. doi:10.1016/j.oregeorev.2020.103688
- Ni, P., Wang, G.-G., Yu, W., Chen, H., Jiang, L.-L., Wang, B.-H., et al. (2015). Evidence of Fluid Inclusions for Two Stages of Fluid Boiling in the Formation of the Giant Shapinggou Porphyry Mo deposit, Dabie Orogen, Central China. *Ore Geology. Rev.* 65, 1078–1094. doi:10.1016/j.oregeorev.2014.09.017
- O'Neil, J. R., Clayton, R.-N., Mayeda, T. K., et al. (1969). Oxygen isotope fractionation in divalent metal carbonates. *J. Chem. Phys.* 51, 5547–5558. doi:10.1063/1.1671982
- Pan, J.-Y., Ni, P., and Wang, R.-C. (2019). Comparison of Fluid Processes in Coexisting Wolframite and Quartz from a Giant Vein-type Tungsten deposit, South China: Insights from Detailed Petrography and LA-ICP-MS Analysis of Fluid Inclusions. *Am. Mineral.* 104, 1092–1116. doi:10.2138/am-2019-6958
- Pirajno, F. (2009). *Hydrothermal Processes and Mineral Systems*. Netherlands: Springer, 1250p. doi:10.1007/978-1-4020-8613-7
- Qin, K. Z., Fang, T. H., and Wang, S. L. (2002). Plate Tectonics Division, Evolution and Metallogenic Settings in Eastern Tianshan Mountains, NW China. *Xinjiang Geol.* 20, 302–308. (in Chinese with English abstract).
- Robb, L. (2005). *Introduction to Ore-Forming Processes*, Blackwell Publishing. 382p., ISBN 0-632-06378-5.
- Roedder, E. (1984). *Fluid Inclusions*. Washington, DC: Mineralogical Society of America, 644.
- Sengör, A. M. C., Natalin, B. A., and Burtman, V. S. (1993). Evolution of the Altaid Tectonic Collage and Paleozoic Crustal Growth in Eurasia. *Nature* 364, 299–307.
- Soloviev, S. G., and Kryazhev, S. (2017a). Geology, Mineralization, and Fluid Inclusion Characteristics of the Chorukh-Dairon W-Mo-Cu Skarn deposit in the Middle Tien Shan, Northern Tajikistan. *Ore Geology. Rev.* 80, 79–102. doi:10.1016/j.oregeorev.2016.06.021
- Soloviev, S. G., and Kryazhev, S. G. (2017b). Geology, Mineralization, and Fluid Inclusion Characteristics of the Skrytoe Reduced-type W Skarn and Stockwork deposit, Sikhote-Alin, Russia. *Miner. Deposita* 52, 903–928. doi:10.1007/s00126-016-0705-5
- Soloviev, S. G. (2011). Geology, Mineralization, and Fluid Inclusion Characteristics of the Kensu W-Mo Skarn and Mo-W-Cu-Au Alkaline Porphyry Deposit, Tien Shan, Kyrgyzstan. *Econ. Geology*. 106, 193–222. doi:10.2113/econgeo.106.2.193
- Soloviev, S. G. (2015). Geology, Mineralization, and Fluid Inclusion Characteristics of the Kumbel Oxidized W-Cu-Mo Skarn and Au-W Stockwork deposit in Kyrgyzstan, Tien Shan. *Miner. Deposita* 50, 187–220. doi:10.1007/s00126-014-0531-6
- Tang, D., Qin, K., Su, B., Mao, Y., Evans, N. J., Niu, Y., et al. (2020). Sulfur and Copper Isotopic Signatures of Chalcopyrite at Kalatongke and Baishiquan: Insights into the Origin of Magmatic Ni-Cu Sulfide Deposits. *Geochim. Cosmochim. Acta* 275, 209–228. doi:10.1016/j.gca.2020.02.015
- Wang, Y.-H., and Zhang, F.-F. (2016). Petrogenesis of Early Silurian Intrusions in the Sanchakou Area of Eastern Tianshan, Northwest China, and Tectonic Implications: Geochronological, Geochemical, and Hf Isotopic Evidence. *Int. Geol. Rev.* 58, 1294–1310. doi:10.1080/00206814.2016.1152516
- Wang, J. B., Wang, Y. W., and He, Z. H. (2006). Ore Deposits as a Guide to the Tectonic Evolution in the East Tianshan Mountains, NW China. *Geol. China* 33, 461–469. (in Chinese with English abstract).
- Wang, Y.-H., Zhang, F.-F., and Liu, J.-J. (2016). The Genesis of the Ores and Intrusions at the Yuhai Cu-Mo deposit in Eastern Tianshan, NW China: Constraints from Geology, Geochronology, Geochemistry, and Hf Isotope Systematics. *Ore Geology. Rev.* 77, 312–331. doi:10.1016/j.oregeorev.2016.03.003
- Wang, Y., Chen, H., Han, J., Chen, S., Huang, B., Li, C., et al. (2018). Paleozoic Tectonic Evolution of the Dananhu-Tousuquan Island Arc belt, Eastern Tianshan: Constraints from the Magmatism of the Yuhai Porphyry Cu deposit, Xinjiang, NW China. *J. Asian Earth Sci.* 153, 282–306. doi:10.1016/j.jseas.2017.05.022
- Wiedenbeck, M., Allé, P., Corfu, F., Griffin, W. L., Meier, M., Oberli, F., et al. (1995). Three Natural Zircon Standards for U-Th-Pb, Lu-Hf, Trace Element and REE Analyses. *Geoanal. Res.* 19, 1–23. doi:10.1111/j.1751-908x.1995.tb00147.x
- Wilkinson, J. J. (2001). Fluid Inclusions in Hydrothermal Ore Deposits. *Lithos* 55, 229–272. doi:10.1016/s0024-4937(00)00047-5
- Windley, B. F., Alexeiev, D., Xiao, W., Kröner, A., and Badarch, G. (2007). Tectonic Models for Accretion of the Central Asian Orogenic Belt. *J. Geol. Soc.* 164, 31–47. doi:10.1144/0016-76492006-022
- Wood, S. A., and Samson, I. M. (2000). The Hydrothermal Geochemistry of Tungsten in Granitoid Environments: I. Relative Solubilities of Ferberite and Scheelite as a Function of T, P, pH, and mNaCl. *Econ. Geol.* 95, 143–182. doi:10.2113/gsecongeo.95.1.143
- Wu, C.-Z., Zhang, Z.-Z., Gu, L.-X., Tang, J.-H., and Lei, R.-X. (2010). Sr, Nd and O Isotopic Characters of Quartz Syenite in the Weiya Magmatic Complex from Eastern Tianshan in NW China: Melting of the Thickened Juvenile Lower Crust. *Geochem. J.* 44, 285–298. doi:10.2343/geochemj.1.0072
- Wu, Y.-S., Zhou, K.-F., Li, N., and Chen, Y.-J. (2017). Zircon U-Pb Dating and Sr-Nd-Pb-Hf Isotopes of the Ore-Associated Porphyry at the Giant Donggebi Mo deposit, Eastern Tianshan, NW China. *Ore Geology. Rev.* 81, 794–807. doi:10.1016/j.oregeorev.2016.02.007
- Wu, C.-Z., Xie, S.-W., Gu, L.-X., Samson, I. M., Yang, T., Lei, R.-X., et al. (2018). Shear Zone-Controlled post-magmatic Ore Formation in the Huangshandong Ni-Cu Sulfide deposit, NW China. *Ore Geology. Rev.* 100, 545–560. doi:10.1016/j.oregeorev.2017.02.015
- Xiao, W., Windley, B. F., Allen, M. B., and Han, C. (2013). Paleozoic Multiple Accretionary and Collisional Tectonics of the Chinese Tianshan Orogenic Collage. *Gondwana Res.* 23, 1316–1341. doi:10.1016/j.gr.2012.01.012
- Xiao, B., Chen, H., Hollings, P., Han, J., Wang, Y., Yang, J., et al. (2017). Magmatic Evolution of the Tuwu-Yandong Porphyry Cu belt, NW China: Constraints from Geochronology, Geochemistry and Sr-Nd-Hf Isotopes. *Gondwana Res.* 43, 74–91. doi:10.1016/j.gr.2015.09.003
- Xiao, W., Song, D., Windley, B. F., Li, J., Han, C., Wan, B., et al. (2020). Accretionary Processes and Metallogenesis of the Central Asian Orogenic Belt: Advances and Perspectives. *Sci. China Earth Sci.* 63, 329–361. doi:10.1007/s11430-019-9524-6
- Yu, P.-P., Zheng, Y., Qian, J.-H., and Lin, Z.-W. (2018). Geological, Geochronological and Geochemical Constraints on the Tianhu Iron deposit, Chinese Tianshan Orogen, NW China: A Modified Algoma-type BIF deposit. *Ore Geology. Rev.* 100, 317–333. doi:10.1016/j.oregeorev.2017.06.004
- Zhang, L., Xiao, W., Qin, K., and Zhang, Q. (2006). The Adakite Connection of the Tuwu-Yandong Copper Porphyry belt, Eastern Tianshan, NW China: Trace Element and Sr-Nd-Pb Isotope Geochemistry. *Miner. Deposita* 41, 188–200. doi:10.1007/s00126-006-0058-6
- Zhang, F.-F., Wang, Y.-H., Xue, C.-J., Liu, J.-j., and Zhang, W. (2019). Fluid Inclusion and Isotope Evidence for Magmatic-Hydrothermal Fluid Evolution in the Tuwu Porphyry Copper deposit, Xinjiang, NW China. *Ore Geology. Rev.* 113, 103078. doi:10.1016/j.oregeorev.2019.103078
- Zhao, L., Chen, H., Hollings, P., and Han, J. (2019). Late Paleozoic Magmatism and Metallogenesis in the Aqishan-Yamansu belt, Eastern Tianshan: Constraints from the Bailingshan Intrusive Complex. *Gondwana Res.* 65, 68–85. doi:10.1016/j.gr.2018.08.004
- Zheng, Y. F. (1993). Calculation of oxygen isotope fractionation in anhydrous silicate minerals. *Geochim. Cosmochim. Acta* 57, 1079–1091. doi:10.1016/0016-7037(93)90042-U

Conflict of Interest: Authors DX and XD were employed by the company Beijing Institute of Geology for Mineral Resources Co., Ltd.

The remaining authors declare that the research was conducted in the absence of any commercial or financial relationships that could be construed as a potential conflict of interest.

The reviewer (YZ) declared a shared affiliation with several of the authors, (DX, JZ, XC, XH), to the handling editor at time of review.

Publisher's Note: All claims expressed in this article are solely those of the authors and do not necessarily represent those of their affiliated organizations, or those of the publisher, the editors and the reviewers. Any product that may be evaluated in

this article, or claim that may be made by its manufacturer, is not guaranteed or endorsed by the publisher.

Copyright © 2021 Xue, Deng, Bagas, Chen, Wu and Jiang. This is an open-access article distributed under the terms of the Creative Commons Attribution License (CC BY). The use, distribution or reproduction in other forums is permitted, provided the original author(s) and the copyright owner(s) are credited and that the original publication in this journal is cited, in accordance with accepted academic practice. No use, distribution or reproduction is permitted which does not comply with these terms.



Petrology, Geochemical Characteristics, Tectonic Setting, and Implications for Chromite and PGE Mineralization of the Hongshishan Alaskan-Type Complex in the Beishan Orogenic Collage, North West China

Zhaolin Wang^{1,2*}, Xiaoming Zheng^{3*}, Guixiang Meng^{1,2}, Hejun Tang^{1,2} and Tonghui Fang³

¹Chinese Academy of Geological Sciences, Beijing, China, ²Deep Exploration Center-SinoProbe Center, China Geological Survey and Chinese Academy of Geological Sciences, Beijing, China, ³China Non-ferrous Metals Resource Geological Survey, Beijing, China

OPEN ACCESS

Edited by:

David R. Lentz,
University of New Brunswick
Fredericton, Canada

Reviewed by:

Yufeng Deng,
Hefei University of Technology, China
Dongmei Tang,
Institute of Geology and
Geophysics(CAS), China

*Correspondence:

Zhaolin Wang
wangzl@cags.ac.cn
Xiaoming Zheng
zxm9981@hotmail.com

Specialty section:

This article was submitted to
Economic Geology,
a section of the journal
Frontiers in Earth Science

Received: 03 February 2021

Accepted: 25 October 2021

Published: 29 November 2021

Citation:

Wang Z, Zheng X, Meng G, Tang H
and Fang T (2021) Petrology,
Geochemical Characteristics, Tectonic
Setting, and Implications for Chromite
and PGE Mineralization of the
Hongshishan Alaskan-Type Complex
in the Beishan Orogenic Collage, North
West China.
Front. Earth Sci. 9:663760.
doi: 10.3389/feart.2021.663760

The Hongshishan mafic-ultramafic complex is situated in the north of the Beishan orogenic collage and the southern part of the Central Asian Orogenic Belt. This paper outlines the petrological, geochemical, and mineralogical data of the Hongshishan ultramafic–mafic complex in the Beishan orogenic collage to constrain its tectonic setting and mineralization. The lithological units of the complex include dunite, clinopyroxene peridotite, pyroxenite, and gabbro. The complex showed concentric zonation, from clinopyroxene peridotite and dunite in the core to pyroxenite and gabbro in the margin. These ultramafic–mafic rocks are characterized by cumulate and layering textures. Field observations, petrography, and significant elemental composition variation, a decreasing sequence of ferromagnesian minerals (Mg#), olivine Fo, and spinel Cr#, all show fractional crystallization trends from dunites through clinopyroxene peridotite and pyroxenite, to gabbros. There are systematic trends among the primary oxides, e.g., CaO, TiO₂, and Al₂O₃, with MgO, suggesting a fractional crystallization trend. SiO₂ and Al₂O₃ increased, which coupled with decreasing MgO, suggested olivine fractionation. The negative correlations of CaO and Al₂O₃ with MgO meant the accumulation of spinel and mafic minerals. The compositions of olivines from the dunite and clinopyroxene peridotite in the Hongshishan plot within the Alaskan Global trend fields displayed a typical fractional crystallization trend similar to olivines in an Alaskan-type complex. The clinopyroxenes in the clinopyroxene peridotite primarily occur as a diopside and appear in the field of an Alaskan-type complex. The absence of orthopyroxene, less hydrous, and free of fluid inclusions in the chrome spinels means the absence of a magmatic origin of chromite-bearing peridotites in hydrous parental melts or scarce hydrous melts. Serpentinization, carbonatization, subduction modification, and enrichment may account for the LILE-enrichment and HFSE-depletion of peridotite rocks. Negative Eu anomalies and REE fractionations of mafic-ultramafic rocks may not be directly attributed to crustal assimilation. Petrological, mineralogical, and geochemical characteristics indicated the Hongshishan complex is not the member compositions of a typical ophiolite. However, it displays many similarities to Alaskan-type mafic-ultramafic

intrusions related to subduction or arc magmas setting at ~366.1 Ma and suffered subduction modification and enrichment. The Hongshishan complex is a unique Ir-Ru-rich chromite deposit in the southern margin of the Altaids orogenic belt. Chromites occur primarily in light yellow dunites, with banded, lenticular, veined, thin-bedded, and brecciated textures. Part of the chromite enrichment in IPGE (Os, Ir, Ru) and the chondrite-normalized spider diagram of PGE showed steep right-facing sloped patterns similar to those of the PGE-rich ophiolitic chromites.

Keywords: Beishan orogenic collage, Hongshishan ophiolite, Alaskan-type complex, petrology, fractional crystallization, chromite and PGE mineralization, subduction tectonic environments

INTRODUCTION

Generally, Alaskan-type complexes show the following characteristics: they are related to the subduction environment and composed of a central dunite body grades outward into wehrlite, clinopyroxenite and gabbroic lithologies, occasionally occurring olivine clinopyroxenite, hornblendite clinopyroxenite, hornblendite, and hornblendite gabbro, characterized by the dominance of olivine, clinopyroxene, hornblende and the absence of orthopyroxene and plagioclase. Pyroxenes in the complexes are almost exclusively clinopyroxenes (mainly diopside in composition) and olivines are occasionally Mg-rich (Irvine 1967; Himmelberg and Loney 1995; Krause et al., 2007; Su et al., 2012, 2014; Habtoor et al., 2016). Magma composition comes from the mantle with no significant crustal contamination (Helmy and El Mahallawi, 2003; Tian et al., 2011). Geochemically, the complex shows a slight LREE enrichment and weak or no Eu anomalies, an elevated LILE, and obvious low high-field strength elements (HFSE) such as Nb, Ta, and Ti (Himmelberg and Loney, 1995; Helmy and El Mahallawi, 2003; Pettigrew and Hattori 2006; Ripley 2009).

Various hypotheses have been suggested to describe the petrogenesis of Alaskan-type complexes such as fractional melting in the mantle (Irvine, 1967; Taylor, 1967), fractional crystallization from magma mixtures (Sha, 1995; Farahat and Helmy, 2006; Habtoor et al., 2016), fractional crystallization from a common hydrous parental magma without significant crustal contamination (Farahat and Helmy, 2006; Tian et al., 2011), depleted mantle metasomatized by subduction-related melts/fluids (Su et al., 2014), and tectonic emplacement of fragments of a pre-existing body (Efimov, 1998). These hypotheses have generated some controversy and contradictions. For example, for fractional melting, Taylor (1967) and Irvine (1967) suggested that petrologic and mineralogical relationships among ultramafic rocks can be interpreted by multiple magmatic intrusion mechanisms; however, this mechanism runs contrary to the diagenetic order of most Alaskan-type complexes. The viewpoint of depleted mantle metasomatized by subduction-related melts/fluids favors multiple magmatic pulses instead of fractional crystallization within a common parental magma (Su et al., 2014).

Alaskan-type complexes generally form in arc-related tectonic environments (Taylor 1967; Irvine, 1974; Helmy and El Mahallawi, 2003; DeBari and Coleman 1989; Brugmann et al.,

1997; Helmy et al., 2014; Saleeby 1992; Foley et al., 1997; Valli et al., 2004; Su et al., 2012, 2014) or at the change from the arc setting to the extensional regime (Tistl et al., 1994; Mues-Schumacher et al., 1996; Chen et al., 2009; Tian et al., 2011; Spandler and Pirard, 2013; Helmy et al., 2015). According to Tistl (Tistl et al., 1994) and Mues-Schumacher (Mues-Schumacher et al., 1996), Alaskan-type intrusions also represent geodynamic setting variations from arc-related convergent systems to a local extension, e.g., reararc-backarc setting or strike-slip system (Spandler and Pirard, 2013; Helmy et al., 2015). However, Alaskan-type candidate complexes formed during an extensional setting are rare and the characteristics of the complexes differ significantly from typical ones, and even some ultramafic rocks, generated during post-collision extension or an intracontinental rift stage, do not belong to Alaskan-type complexes (Su et al., 2013). Alaskan-type complexes are considered as possible mantle plume-related intrusions (Ishiwatari and Ichiyama, 2004; Pirajno, 2004; Farahat and Helmy, 2006). In this hypothesis, plume interaction may account for the superheating required to generate an Alaskan-type intrusion, and similarities with Alaskan-type intrusions are nothing but trace element geochemistry (Farahat and Helmy, 2006). Moreover, the mafic rocks associated with a plume do not possess Alaskan-type intrusion characteristics (Pirajno, 2004).

Based on the above disputes, determining the nature of the mafic-ultramafic intrusions and their tectonic setting is significant to understand the tectonic evolution of the orogenic belts (Helmy and Mogessie, 2001; Helmy, 2004; Helmy, 2005; Su et al., 2012, 2014; Deng et al., 2015a,b; Khedr et al., 2020; Wang et al., 2021). Significantly, chromite mineralization associated with a typical Alaskan-type complex (Garuti et al., 2002, 2003; Krause et al., 2007; Khedr et al., 2020; Wang et al., 2021) and the Gaositai complex in North China Craton (Zhou and Bai, 1992; Chen et al., 2009; Tian et al., 2011) is found in the core of concentrically zoned intrusions. In contrast with high-Al and high-Cr chromites in ophiolites, chromites formed in Alaskan-type complexes are characterized by high Ti, high oxygen fugacity (fO_2), and Fe³⁺ enrichment; furthermore, their sub-economic PGE mineralization draws the attention of geologists (Zhou and Bai, 1992; Tian et al., 2011; Khedr et al., 2020).

The Hongshishan mafic-ultramafic rocks were previously considered as component parts of an ophiolitic mélangé and occur as a suture in the plate of Kazakhstanian-Junggar and

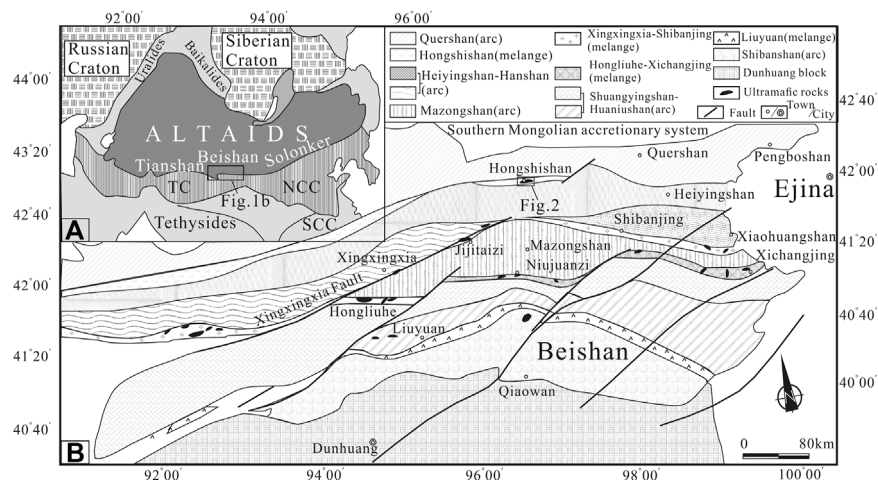


FIGURE 1 | (A) Simplified tectonic sketch map of Asia showing the location of the Beishan orogenic collage. **(B)** Simplified tectonic map of the Beishan orogen showing the tectonic subdivisions and study area (modified after Xiao et al., 2010; Song et al., 2015). TC, Tarim Craton; NCC, North China Craton; SCC, South China Craton.

Siberian (Gong et al., 2003; Huang and Jin, 2006a; Xiao et al., 2010), but absent in the corresponding mantle peridotites and cumulates and contain banded chromites in core dunites from the concentrically zoned complex (Wei, 1978; Yang et al., 2010; Wang et al., 2013; Peng et al., 2016). The Hongshishan complex differs from the SSZ ophiolite but shares many similarities with a Dahanib Alaskan-type complex in the Southern Eastern Desert of Egypt (Khedr and Arai, 2016; Khedr et al., 2020), the Uralian-Alaskan-type complex (Garuti et al., 2002, 2003; Krause et al., 2007), and a series of complexes in Beishan Terrane and Middle Tianshan Terrane (Su et al., 2012, 2013, 2014). But the emplacement mechanism, geochemical composition, and evolution of the Hongshishan complex, especially chromite origins, are poorly understood.

Although much work has been conducted on chronological and geochemical studies of the Hongshishan mafic-ultramafic complex (Wei et al., 2004; Huang and Jin, 2006b; Wang et al., 2014; Shi et al., 2017), very little research has provided evidence for Alaskan-type complexes, thought to have formed above subduction zones, and no attention has been paid to the inherent formation of chromites related to an Alaskan-type complex and may shed light on its metallogenic significance (Khedr and Arai, 2016; Khedr et al., 2020).

In this study, we present new zircon U-Pb isotopic data, silicate chemical compositions, chromian minerals of spinels, olivines, and clinopyroxenes, which should provide new insights and realizations regarding tectonic evolution in the Beishan orogenic collage.

GEOLOGICAL SETTING

The Beishan orogenic collage, between the Kazakhstanian-Junggar plate to the north and the Tarim-North China craton to the south, is framed by the southern Mongolia accretionary system in the north and the Dunhuang block in the south

(Figure 1) (Xiao et al., 2010; Song et al., 2015). It marks the attachment to the Eastern Tianshan orogenic belt by the Xingxingxia ductile left-lateral strike-slip fault, though it is not well defined and covered by the Badain Jaran Desert to the east despite occasional ophiolites (Zuo et al., 1991; Liu and Wang, 1995; Xiao et al., 2010). The development of the Beishan orogenic collage assists the final attachment of the Tarim-North China plate to the southern accretionary orogenic belt of the southern Altai (Ao et al., 2010; Guo et al., 2012; Mao et al., 2012).

Spatially, the Beishan orogenic collage consists of several tectonic units formed by multiple accretionary orogenies, from north to south, Hongshishan mélangé, together with the Shibanjing-Xiaohuangshan, Hongliuhe-Yushishan-Niujuanzi-Xichangjing, and Liuyuan ophiolitic mélangé, separate the Beishan orogenic collage into several discrete terranes units, Quershan, Hanshan, Mazongshan, Shuangyingshan and Shibanshan terranes (Figure 1B).

At the end of the Early Paleozoic, the Hongliuhe-Niujuanzi-Xichangjing ocean closed, followed by attachment and soft collision during the Devonian between the diverse accreted tectonic units formed in the margin of Kazakhstan and the Tarim plate including magmatic arcs, accretionary complexes etc., and formed a uniform continent (He et al., 2005; Song and Pirard., 2013, 2015). During the Early Carboniferous, continental cracking and intense stretching occurred in the Heiyingshan area between the Quershan and the Gongpoquanarc-accretionary system, forming a rift basin along Kangguer, Hongshishan, and Pengboshan (He et al., 2005; Xia et al., 2005; Yang et al., 2010; Peng et al., 2016). The amalgamation and accretion of the above tectonic units gave rise to strong Late Permian to Triassic deformations that included thrust imbrication and strike-slip faulting (Xiao et al., 2010).

Among the mélanges mentioned above, the so-called Hongshishan ophiolitic mélanges lie in the northern part of the orogenic collage and occupy an important position as the

distribution center for the biogeography of Carboniferous North China and South China. Angara floras were distributed north of the Hongshishan suture and Carboniferous marine fauna, the Cathaysia floras were only distributed south of the Duhuang block (Yue et al., 2001), whereas Hongshishan contained no complete ophiolite stratigraphy (Peng et al., 2016; Shi et al., 2018).

Gabbros in Hongshishan used LA-ICP-MS and SHRIMP U-Pb to generate $^{206}\text{Pb}/^{238}\text{U}$ weighted mean ages of 346.6 ± 2.8 and 357 ± 4 Ma respectively (Wang et al., 2014; Shi et al., 2017). The fossils *Leiotrites netiux* *H aequ* *Punctatiporites planus* *H aequ* that occurred in the volcanic-sedimentary rocks that covered the ophiolite suggested the Hongshishan mélange formed during the Early Carboniferous (Wei, 2004). Previous geochemical and Sm/Nd isotope characters indicated that the Hongshishan basic volcanic rocks formed in a MORB tectonic environment (Huang and Jin, 2006a; Wang et al., 2014) and the Hongshishan complex was thought to form during the Carboniferous-Permian and suffered at least three stage structural deformation metamorphisms before returning to terrene by shearing at the Late Permian (Wei et al., 2004; Huang and Jin, 2006b). The thrusts and imbricate structures that occurred in the north and south margins of Hongshishan mélanges indicated a southward translation (Xiao et al., 2010).

GEOLOGICAL AND PETROGRAPHY CHARACTERS OF COMPLEX ROCKS

The fish-shaped Hongshishan complex situated in the north of the Beishan orogenic collage strikes E-W, approximately 7 km long and up to 2 km wide (Figure 2). The mélange contains Carboniferous marine sandstone, sandy slate, chert, chlorite schist, and ultramafic-mafic rocks. The ultramafic and mafic complex intrude in the Carboniferous metamorphic volcanic-sedimentary sequences (Zuo et al., 1990a; Zuo et al., 1990b; Zuo et al., 1991). The complex comprises east and west segments. The west segment constitutes the main structure of the complex, dominated by clinopyroxene peridotite and dunite in the core, with accompanying mafic intrusions that include pyroxenite, gabbro distributed in the ultramafic and mafic rocks as lenticular, banding, and isolated. Grading outward into clinopyroxene peridotite with numerous dunite schlierens in the North-West part. Altered gabbro, pyroxenite, and basaltic schist sit along the north and south rims. The ultramafic and mafic complex inclines steeply or suberect in the south and dips northward in the north margin. The Hongshishan complex contains no harzburgites.

The surrounding stratigraphy of the complex consists of the Lower Carboniferous Lvtiaoshan Formation in the north and the Baishan Formation in the south. The former, formed in a calc-alkaline volcanic environment, consists of sandy slate, metasandstone, quartz sandstone with siliceous rocks, basalt, andesite as intercalated beds and gives rise to a chlorite sericite quartz schist, tuffaceous metasandstone, fused breccia, andesite, and rhyolite (Huang and Jin., 2006c; Peng et al., 2016). Even largely intruded by Permian biotite monzogranite, intermediate-basic dykes and covered by Quaternary

sediments in the middle segment, the complex outlines a concentrically zoned structure and resembles Alaskan-type complexes (Taylor, 1967; Himmelberg and Loney, 1995; Garuti et al., 2002, 2003; Krause et al., 2007; Tian et al., 2011; Khedr et al., 2020).

Dunite

The dunites are situated along the south and north-western margins, in the central part and occasionally scattered as schlieren in the clinopyroxene peridotite of the western border and are divided into two types: light yellow dunites and yellow-green dunites (Figure 2). The light yellow dunites underwent silicification and carbonatation, were exposed to the surface and their color lightened (Figures 3A,D,E; Figures 4A–K). In the outcrop, dunites show small-scale layering features and typical cumulate textures (Figure 3F). These rocks primarily consist of olivine pseudomorphs and chromites with minor altered clinopyroxene relics (<5 vol%) and magnetites. Olivines in light yellow dunite are nearly all altered to antigorite-lizardite-magnetite assemblages exposing mesh textures due to serpentinization. The light yellow dunites comprise most of the chromite orebodies (Figures 4A–G).

Despite undergoing serpentinization, yellow-green dunites with unaltered olivine cores or whole grains are relatively fresh compared to light yellow dunites. Olivines in yellow-green dunites are homogenous, fresh, and free of opaque inclusions, and show crystalized textures of variable size, subeuhedral-euhedral crystals, and angular shapes with variable grain sizes (from 0.3 to 0.8 mm; Figures 5A,B). Dunites are composed of cumulus olivines with varying densities, disseminated chromian spinels, and subordinate Cpxs (<3 vol%). Serpentinite and carbonatite veins cut through a large number of olivine grains. Dunite schlierens in clinopyroxene peridotites are the exclusive metallogenic rocks of chromites. Chromian spinels in yellow-green dunite are generally sparsely disseminated or scattered texture (Figures 5J,L).

Clinopyroxene Peridotite

Clinopyroxene peridotites are widely exposed in the central and east areas and weathered red with nodular appearances (Figures 3G,H). In the southeast of the biotite monzogranite, clinopyroxene peridotites underwent serpentinization, carbonatization, silicification, and turned brown due to abundant iron oxide. The boundary between clinopyroxene peridotites and dunites normally curves and transitions gradually into clinopyroxene dunites. Occasionally, clinopyroxene peridotites alternate with dunite and pyroxenite layers and cut by dunite veins (Figure 3D), indicative of magma differentiation and evolution. Clinopyroxene peridotites consist of olivines, clinopyroxenes, amphiboles, and some altered minerals with olivines (80–85 vol%), Cpxs (5–10 vol%), Cr-spinels (<3 vol%), and opaques (<2 vol%). Olivines are subeuhedral columnar crystals that primarily morph into serpentines. Clinopyroxenes are mainly diopsides and sometimes replaced by neogenic pargasites, edenites, and actinolites at their edges (Figures 5C,G,I). Due to serpentinization and weathering, clinopyroxenes were oriented

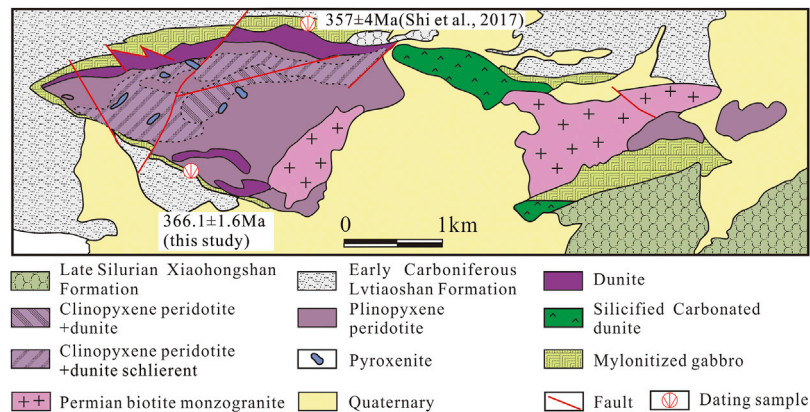


FIGURE 2 | Simplified geological map of the Hongshishan complex (modified after Wei, 1978).

as pseudomorphs in the olivine matrix and were mostly substituted by serpentines, carbonate minerals, tremolites, and magnetites.

Gabbro

Gabbros are exposed on the north and southeast margins of the mafic-ultramafic complex (**Figure 2**). They have equigranular texture and are composed of clinopyroxenes (40–45 vol%), plagioclases (35–45 vol%), hornblendes (<5 vol%), and 3–5% opaque minerals (mostly magnetite). Several outcrops in the field show signs of rhythmic layering of clinopyroxenes and plagioclases (**Figures 3B,C**). Most clinopyroxenes morph into actinolites or tremolites, and plagioclases normally change into zoisites (**Figures 5D,F,H**). Gabbros on the north and southeast margins often show strong foliation with mylonitic textures and sharp tectonic contacts to the peridotites. S-C fabrics and rotational speckles characterize the dextral ductility shear (Huang and Jin, 2006b). Additionally, as a general feature of Alaskan-type complexes, several gabbroic dykes with magmatic layering intrude into dunites and clinopyroxene peridotites (**Figure 3C**). The dykes may form in later-stage residual melts after fractionation rather than the cumulate in ophiolite (Irvine, 1974; Snoke et al., 1981; Himmelberg and Loney, 1995). Unaltered gabbro samples from the southern margin were collected for zircon U–Pb dating and geochemistry analyses.

Chromite

Chromites occur primarily in light yellow dunites, with subordinate Cpx-enriched dunites. Classified by shapes and spatial distributions of the chromite orebodies, the orebodies are labeled as: banded, lenticular, veined, thin-bedded, and brecciated texture (**Figures 4A–G**). Nearly 70–80% of modal chromites in Hongshishan show primary magmatic layering where individual seams involve layers of massive, spotted, schlieren, and banded-texture chromites. Banded chromites, occasionally with crossbedding, are primarily composed of massive and varying degrees of disseminated chromian-spinel grains that interbed alternately with inch-scale thickness of layers

chromian spinels (**Figures 4F,H–L**). Orebodies of the banded subzone are tabular and more extensive laterally. Many bands show small-scale faulting and cataclasis.

Most chromites show weak deformations with polygonal or angular crystal appearances and pull-apart fractures, cataclastic textures (**Figure 4D**), and occasional ductile deformations (such as elongated worm-like shapes), and cluster to form chromite bands or disseminated varieties, though morphologically distinct from podiform chromites in supra subduction zone environments (Zhou et al., 2014). Skeletal textures also occurred in chromites and were interpreted as indicators for rapid crystallization, possibly due to supersaturation processes (Greenbaum, 1977). The chromite textures in Hongshishan showed that disseminated chromites crystallized earlier than the massive chromites.

SAMPLES AND ANALYTICAL TECHNIQUES

Representative samples from the Hongshishan mafic-ultramafic complex, including dunite, clinopyroxene peridotite, pyroxenite, and gabbro came from the western and eastern part of the intrusion. Samples for LA-ICP-MS U–Pb dating were collected from gabbros in the southern margin of the complex. Polished thin sections made from unaltered ultramafic-mafic rocks and chromites ore samples were chosen and analyzed by electron microscopy.

Major, Trace, and Rare-earth Elements

The determination of major, trace, and rare-earth elements was conducted at the Beijing GeoAnalysis Technology Co., Ltd. using X-ray fluorescence (XRF-1800; SHIMADZU) on fused glasses. Inductively coupled plasma mass spectrometry (ICP-MS, 7500; Agilent) was conducted at Beijing Createch Testing Technology Co., Ltd. on samples after acid digestion in Teflon bombs. Loss on ignition was measured after heating to 1,000°C for 3 h in a muffle furnace. The precision of the XRF analyses was within $\pm 2\%$ for oxides with >0.5 wt% and within $\pm 5\%$ for oxides >0.1 wt%. Sample powders (~40 mg) were placed in Teflon bombs and dissolved using a mixture of HF and HNO₃ for 48 h at 190°C. The solution

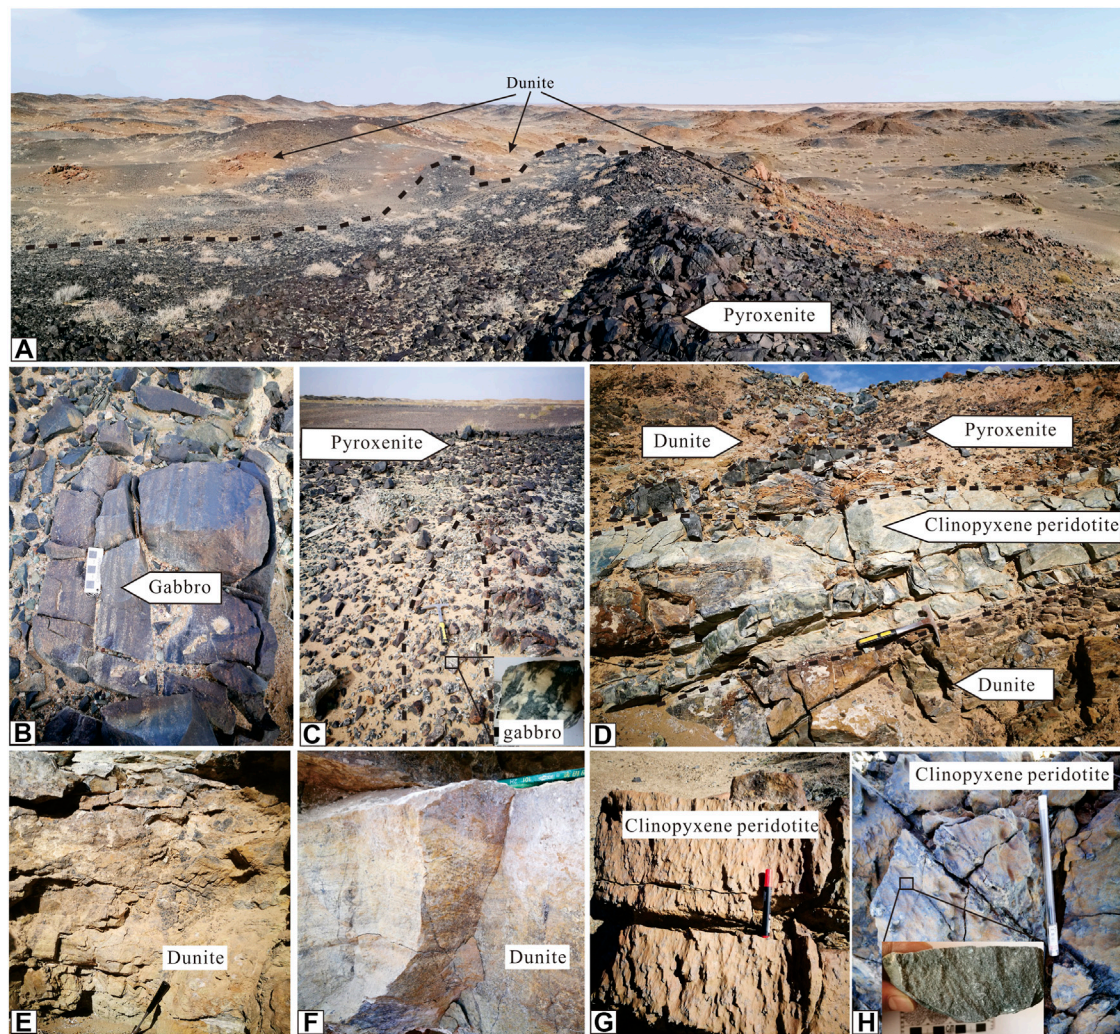


FIGURE 3 | Field photographs of Hongshishan ultramafic-mafic complex. **(A)** Dunites are intruded by pyroxenite; **(B)** Gabbro with the rhythmic layering of clinopyroxene and plagioclase, showing the magmatic fractional crystallization; **(C)** Coarse grain gabbro dyke intruded into pyroxenite; **(D)** Dunite layers alternating with clinopyroxene peridotite, pyroxenite layer; **(E)** The light yellow dunites contain chromites; **(F)** Dunite showing typical cumulate textures and small-scale layering features (0.2–0.6 cm); **(G, H)** Clinopyroxene peridotites were weathered red with nodular appearances.

was evaporated to dryness, re-dissolved using concentrated HNO_3 , and evaporated at 150°C to dispel any fluorides. Samples were diluted to approximately 80 g for analysis after dissolution in 30% HNO_3 overnight. An internal standard solution containing Rh was used to monitor signal drift during the analyses. Results from USGS standards indicated the uncertainty for most elements was $\pm 5\%$.

Mineral Chemistry

The chemistry of unaltered minerals (olivines, pyroxenes, and chrome spinel, etc.) in silicates and oxides was conducted by wavelength-dispersive X-ray analysis using a JEOL electron-probe micro analyzer (EPMA) JXA-8230 at the Institute of Mineral Resources, Chinese Academy of Geological Sciences. We used 15 kV for the acceleration voltage, 20 nA for the beam current, a $5\ \mu\text{m}$ beam diameter, and the counting time was between 20 and 40 s for major elements and 40–60 s for minor elements. SPI mineral standards (USA) were used

for calibration. The precision for all elements analyzed exceeded 98.5%. The Cr- and Mg-numbers ($\text{Cr}^\#$ and $\text{Mg}^\#$) of the chromian spinel were the $\text{Cr}/(\text{Cr} + \text{Al})$ and $\text{Mg}/(\text{Mg} + \text{Fe}^{2+})$ atomic ratios, respectively. We assumed all Fe in silicates was ferrous.

Geochronology

Zircon U-Pb dating was conducted using an LA-ICPMS at Beijing GeoAnalysis Co., Ltd. The Resolution SE model laser ablation system (Applied Spectra, United States) was equipped with an ATL (ATLEX 300) excimer laser and a Two-Volume S155 ablation cell. The laser ablation system was coupled to an Agilent 7900 ICPMS (Agilent, United States). Zircons were mounted in epoxy discs, polished to expose the grains, ultrasonically cleaned in ultrapure water, then cleaned again prior to the analysis using AR grade methanol. Pre-ablation was conducted for each spot analysis using five laser shots ($\sim 0.3\ \mu\text{m}$ in depth) to remove potential surface contamination. The

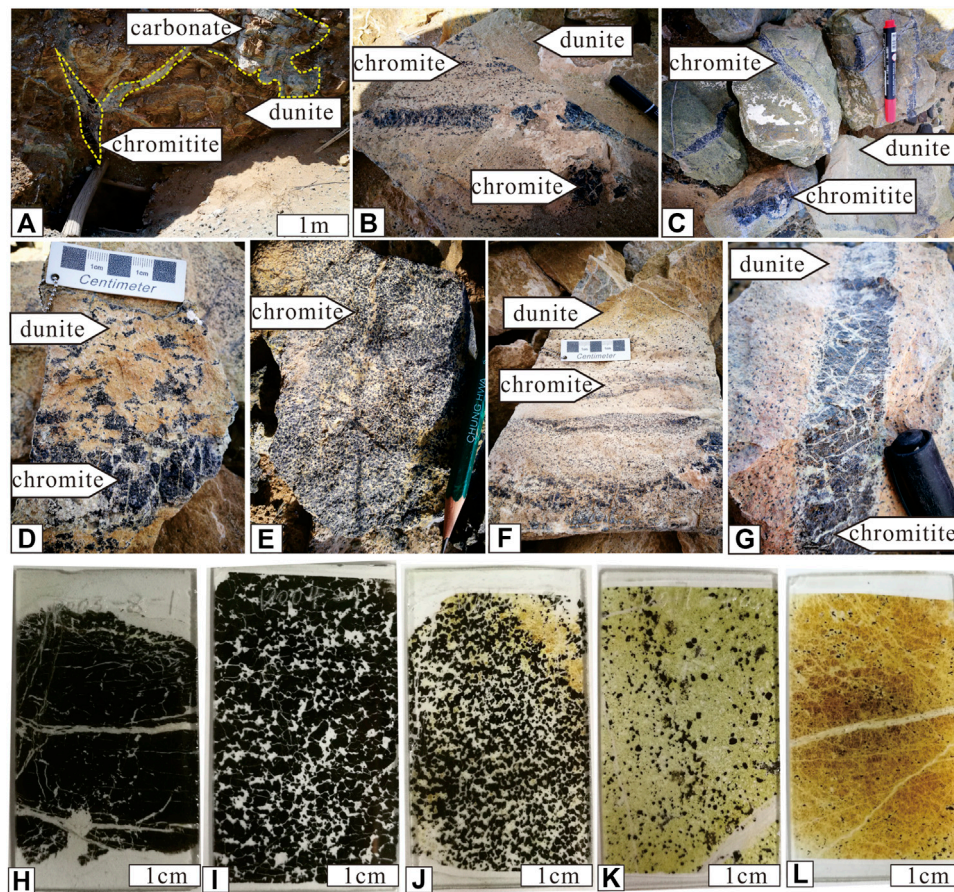


FIGURE 4 | Field and sample photographs of peridotite-hosted chromites in the Hongshishan complex. **(A)** Lenticular chromite orebody in carbonated dunite; **(B)** Banded chromite orebody cut by dunite; **(C)** Veined chromite orebodies in dunite; **(D)** Brecciated chromites; **(E)** Dense disseminated chromites; **(F)** Banded chromite composed of medium density disseminated, sparsely disseminated, and brecciated chromites; **(G)** Veined chromite crosscutting dunite with sparsely disseminated chromites; **(H)** Massive chromites; **(I)** Dense disseminated chromites; **(J)** Medium density disseminated chromites; **(K)** Sparsely disseminated chromites; **(L)** Scattered chromites. **(H–L):** thin-section).

analysis was performed using a 30 μm diameter spot at 5 Hz and a fluence of 2 J/cm².

Zircon 91500 and GJ-1 were used as primary and secondary reference materials, respectively. Zircon 91500 was analyzed twice and GJ-1 was analyzed once every 10–12 analyses. Typically, 35–40 s of the sample signals were acquired after 20 s of gas background measurement. NIST 610 and ⁹¹Zr were used to calibrate the trace element concentrations as the external reference material and the internal standard element, respectively. The ages of the reference materials in the batch are as follows: 91,500 (1061.5 \pm 3.2 Ma, 2 σ), GJ-1 (604 \pm 6 Ma, 2 σ), and agreed with the reference value within definite uncertainty.

RESULTS

Major, Trace, and REE Silicate Geochemical Compositions

Supplement 1 lists the analytical data of major, trace, and REE for samples from each rock unit of the Hongshishan complex.

Disseminated chromian spinels-bearing dunites had high volatile levels (LOI: 9.43–14.83 wt%, except for D002-7 and D003-6). For the dunites, SiO₂ compositions varied from 35.23 to 38.82 wt%, Al₂O₃ from 0.39 to 4.45 wt%, and TiO₂ from 0.00 to 0.07 wt%. While the composition of clinopyroxene peridotites was SiO₂, 29.55–42.61 wt%, Al₂O₃, 0.43–7.97 wt%, TiO₂, 0.00–0.11 wt%, they were nevertheless distinguished from the dunites by much higher Ca concentrations (CaO 1.13–8.68%). Pyroxenite components had the following compositions, SiO₂ from 40.65 to 45.76 wt%, Al₂O₃ from 9.31 to 16.05 wt%, and TiO₂ from 0.07 to 0.14 wt%; gabbros SiO₂ from 42.01 to 49.58 wt%, Al₂O₃ from 12.81 to 22.25 wt% and TiO₂ from 0.02 to 0.30 wt%. These compositions reflect depleted mantle melts as the primary intrusion source.

MgO compositions decreased systematically from the dunites (23.53–43.02 wt%) and clinopyroxene peridotites (29.43–36.23 wt%), followed by pyroxenites (14.75–31.85 wt%) and gabbros (8.46–18.22 wt%). In Harker diagrams (**Figure 6**), these major compositions, e. g. Al₂O₃, CaO, and TiO₂ were lowest in dunites and peridotites cores, increased gradually in pyroxenite and maximized in the marginal gabbros. Most dunites have low

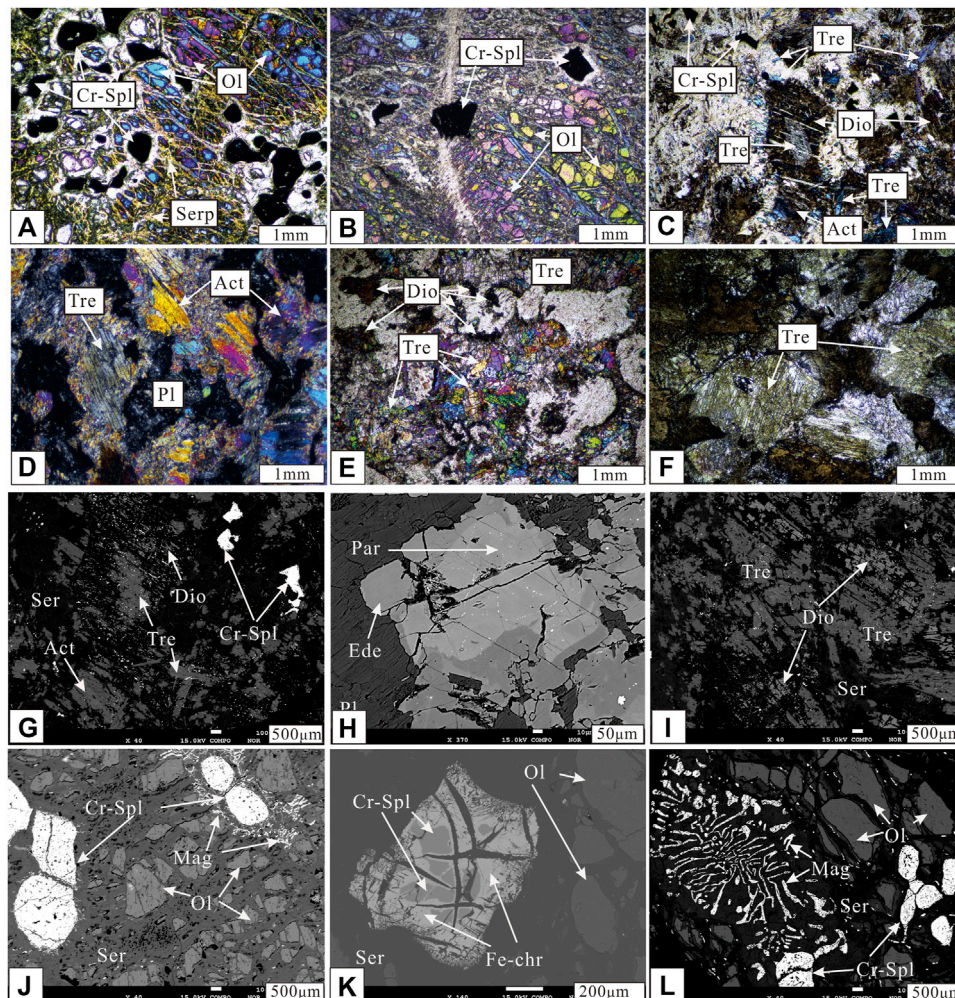


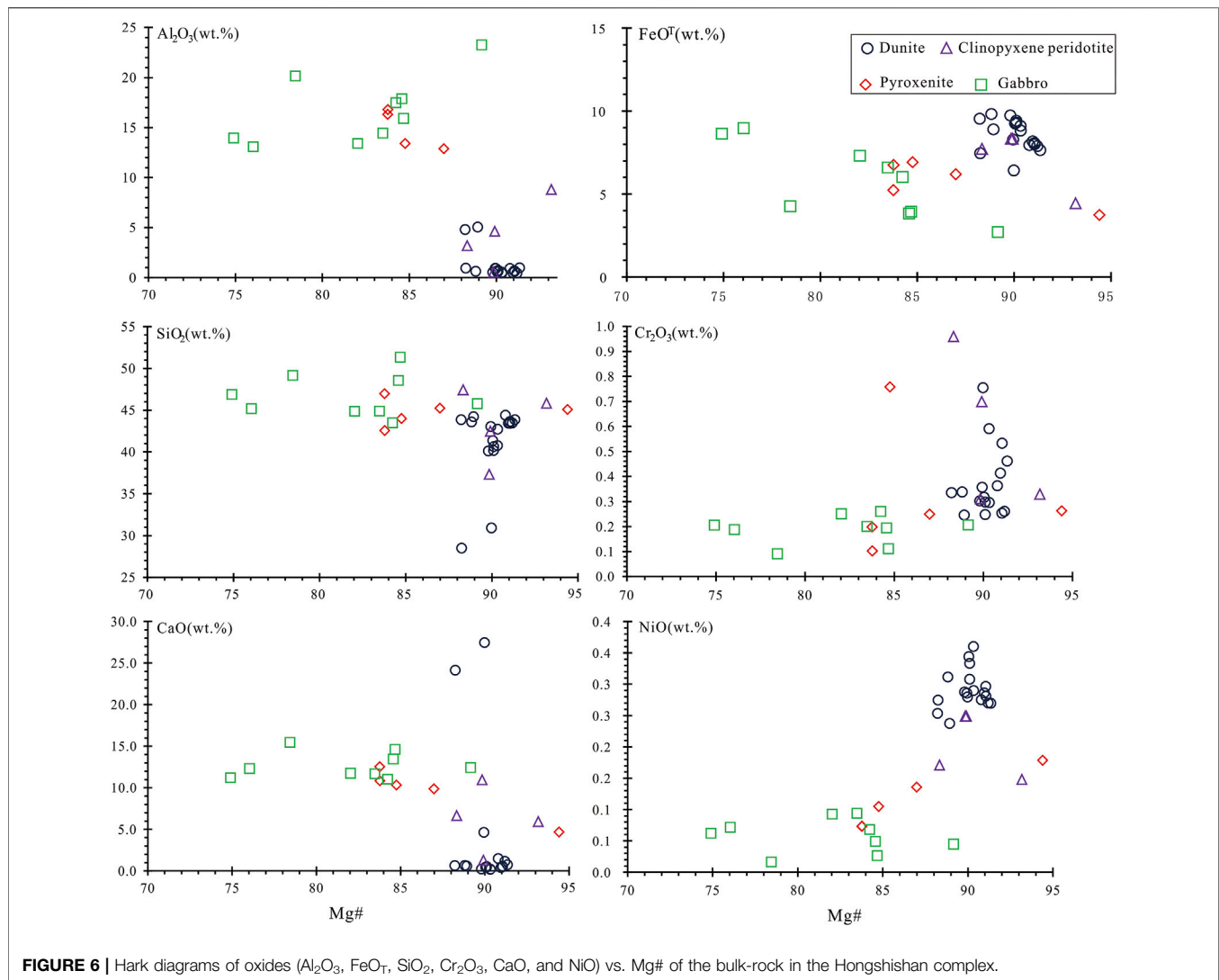
FIGURE 5 | Photomicrographs and backscattered electron (BSE) images of clinopyroxene peridotite and dunite. **(A)** Medium-density disseminated chromites in dunites; **(B)** Scattered chromites in dunites; **(C)** Diopsides in clinopyroxene peridotite are replaced by neogenic tremolite and actinolite; **(D, F)** Diopsides in altered gabbros are altered to actinolite and tremolite, and plagioclases are commonly altered to zoisite; **(E)** Residual diopsides in serpentine and neogenic tremolite; **(G, I)** Neogenic actinolite and tremolite in clinopyroxene peridotite; **(H)** unaltered pargasite and endenite in altered gabbro; **(K)** Chrome spinel (dark gray) with melting corrosion structure, altered to ferritchromite (Fe-chr) (lighter gray) along cracks and margins of Cr-spinel in scattered chromites-bearing dunite; **(J, L)** Medium density disseminated subhedral chromites and skeleton-texture magnetite in dunite. **(A–E)**: cross-polarized light; **F**: plane-polarized light; **G–L**: backscattered electron (BSE) images; Ser—serpentine; Act—actinolite; Dio—diopside; Tre—tremolite; Par—pargasite; Ede—endenite; Ol—olivine; Cr-Spl—chrome spinel; Mag—magnetite; Pl—plagioclase; Fe-chr—ferritchromite).

CaO levels (<1 wt%), whereas clinopyroxene peridotites and pyroxenites had higher CaO concentrations (1.13–8.68 wt% and 4.23–12.21 wt%, respectively). The gabbros had the highest CaO concentrations (10.66–15.06 wt%). TiO₂ levels in the dunites were virtually non-existent, but increased in clinopyroxene peridotites (0.00–0.11 wt%) and pyroxenites (0.07–0.14 wt%), and reached a maximum in the gabbros (0.02–0.30 wt%). The average Mg# (Mg/(Mg + Fe) atomic ratio) accordingly decreased from 0.90 in dunites, 0.90 in clinopyroxene peridotites, followed by 0.87 in pyroxenites to 0.82 in the marginal gabbros (Supplementary Table S1).

In terms of trace elements, dunites contain enriched levels of large-ion lithophile elements (LILE) (like Cs), high field strength

elements (HFSE) (U, Zr, Hf), and Er. Also, significantly negative anomalies in Nb, Ba were observed, and Ti to a lesser extent (Nb/La ratios from 0.12 to 0.19, Th/Yb ratios from 0.39 to 2.78, Ta/La from 0.03 to 0.18 and Nb/Th from 0.01 to 0.55; Supplement 1). The gabbroic rocks shared many geochemical similarities with pyroxenites. They had higher trace element abundances and distinctive Ba, Pb, Cs, and Ti anomalies than the ultramafic rocks, which had lower Rb and Ba levels (Figure 7).

Different from the dunites in the Alaskan complex with identical flat REE patterns (Su et al., 2014; Habtoor et al., 2016), the dunites in Hongshishan display higher REE abundances (average 6.04 ppm) and enriched light REE (LREE) values relative to heavy REE (HREE) with high La_N/



Yb_N ratios (average 4.49; **Supplementary Table S1**), negative Eu anomalies and pronounced positive Er anomalies with a typical V (or U)-shaped pattern (Song and Frey, 1989; Wang et al., 1996). The clinopyroxene peridotites showed negative Eu anomalies and wide compositional HREE variations. Pyroxenites and gabbros showed nearly flat REE patterns and positive Eu, Er anomalies (**Figure 7**). The positive Eu anomalies in the pyroxenites and gabbros indicated the presence of plagioclase in the crystallized rocks, which was in accord with other petrographic investigations. The positive Sr anomalies were consistent with the positive Eu anomalies and implied plagioclase accumulation.

Zircon U–Pb Ages

One gabbro sample collected from the south margin of the mafic-ultramafic complex was selected for zircon U–Pb dating. Zircons separated from the sample ranged from 30 to 100 μm and were generally euhedral, colorless, and transparent. The cathodoluminescence (CL) images with internal growth

zoning indicated a magmatic crystallization origin. (**Figure 8**). Sixteen-grain effective data formed a concordant group in the Concordia diagram with a weighted mean age of 366.1 ± 1.6 Ma (MSWD = 1.17), the age reflects the gabbro emplacement time. This age predates previous gabbro geochronological data and is regarded as an estimate of the Hongshishan complex crystallization age. Supplement 2 gives the analytical data of the Hongshishan gabbro Zircon U–Pb age.

Mineral Chemistry of Chromian Spinel, Olivines, and Clinopyroxenes

The microprobe analysis data for chromian spinels, olivines, clinopyroxenes, hornblendes in the Hongshishan mafic-ultramafic complex are listed in **Supplementary Table S3**.

Chromian spinels in veins and massive chromites have average Al_2O_3 wt% levels of 0.97–25.81 (average 16.6 wt%), Cr_2O_3 (40.52–58.23, average 48.8), Fe_2O_3 (0–2.4, average 4.2), FeO

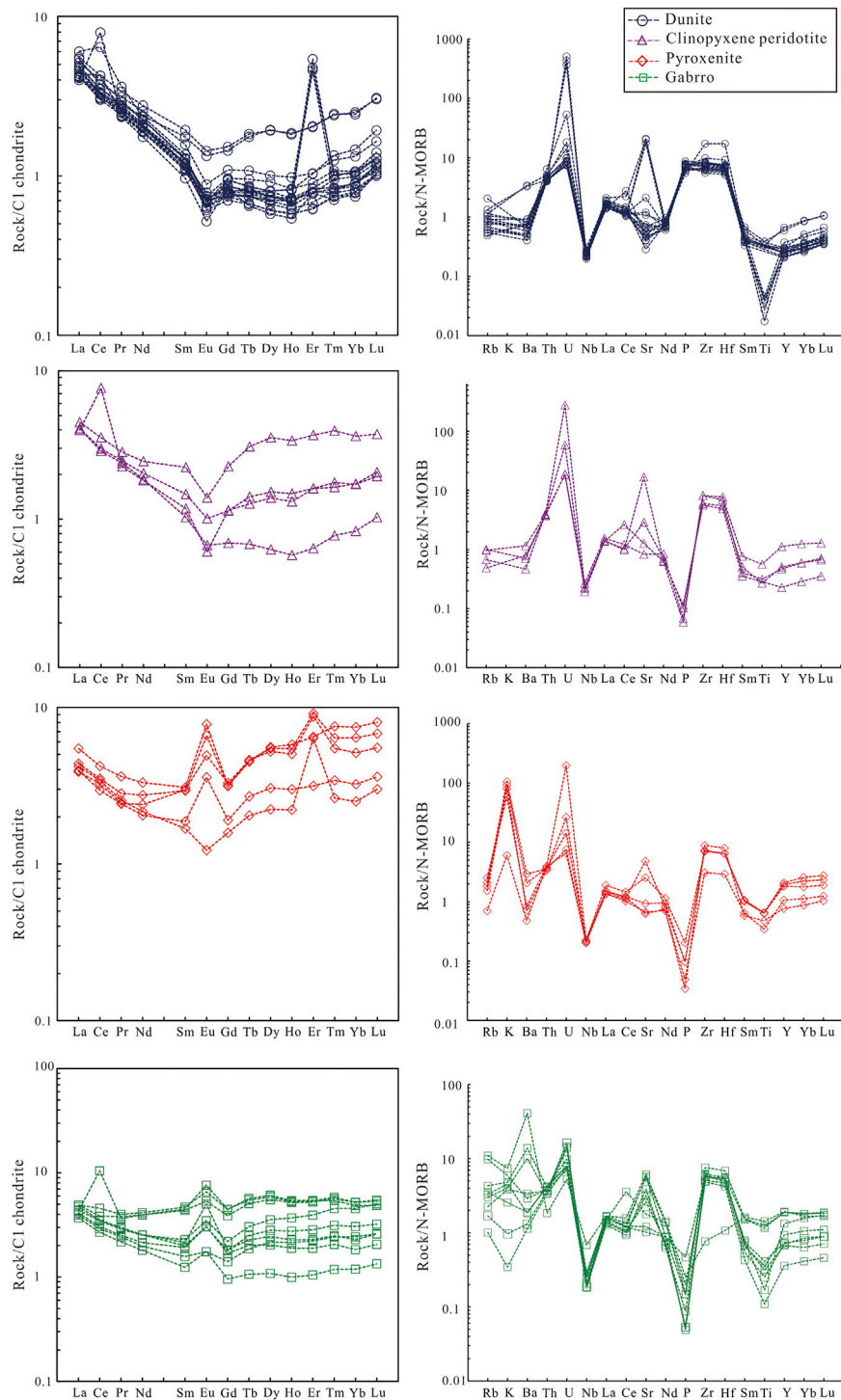


FIGURE 7 | N-MORB normalized spider diagrams and C1 chondrite-normalized REE patterns of the Hongshishan complex. C1 chondrite-normalizing values are from Sun and McDonough (Sun et al., 1989), primitive mantle-normalizing values are from McDonough and Sun (McDonough and Sun., 1995).

(12.97–29.15, average 19.3), TiO_2 (0.06–0.46, average 0.2) and MgO (2.24–14.73, average 9.8), with narrow Cr# ranges (from 0.52 to 1.00; 0.70 on average) and Mg# (0–0.63; 0.38 on average).

Various density degrees of chromian spinels in dunites have wide oxide ranges with Al_2O_3 ranging from 0 to 29.27 wt% (average 10.07 wt%), Cr_2O_3 from 0.20 to 57.74 (average 36.63 wt%), Fe_2O_3

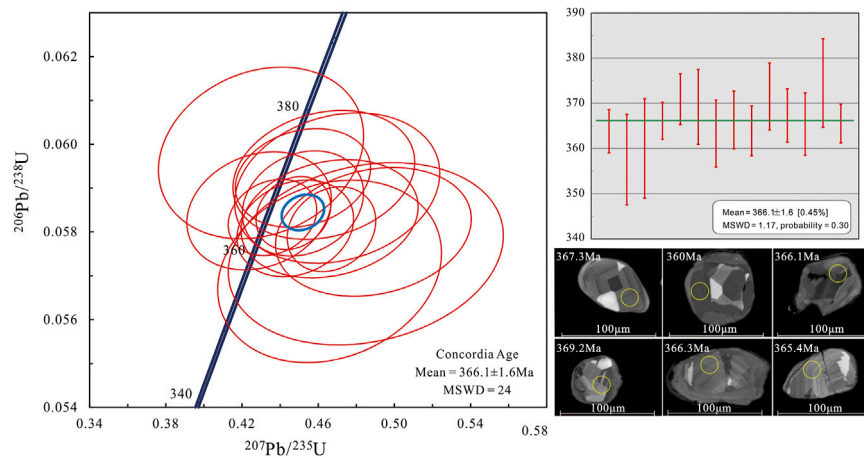


FIGURE 8 | Concordia plot of LA-ICP-MS U-Pb analyses and CL images of zircons from the gabbro in the south margin of Hongshishan intrusion.

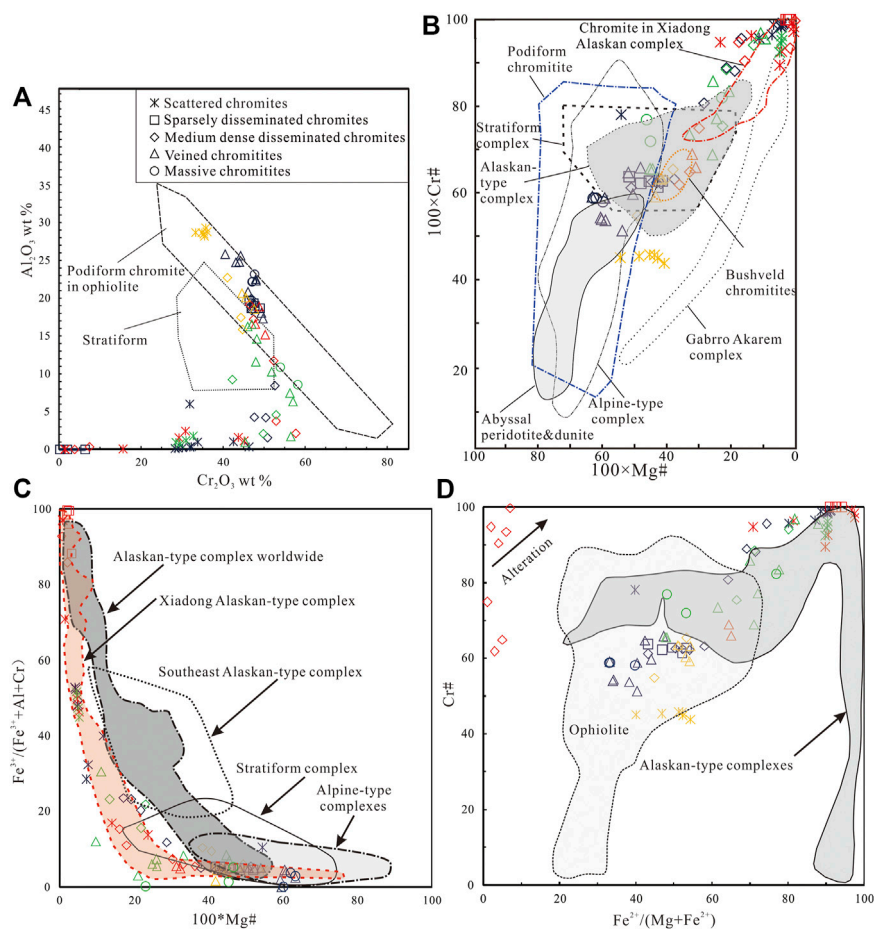


FIGURE 9 | Chromite compositional comparisons of the Hongshishan complex with abyssal peridotites, ophiolites, Alpine-type complex, Bushveld chromites, stratiform complex, and typical Alaskan-type complexes. **(A)** Plot of Al_2O_3 vs. Cr_2O_3 of chromites. Compositional fields of podiform and stratiform chromites are from Bonavia et al. (1993); **(B)** $\text{Cr}\#$ vs. $\text{Mg}\#$ diagram of chromites. Compositional fields of abyssal peridotites and dunites are from (Dick and Bullen, 1984); the fields of podiform, stratiform, Alaskan-type complex, Bushveld chromites and Alpine-type field are from Irvine (1967) and Leblanc and Nicolas (1992); the field of the Gabbro Akarem complexes is from Helmy and El Mahallawi (2003); the field of the Xiadong Alaskan complex is from Su et al. (2012); **(C)** Plot of $\text{Mg}\#$ versus $\text{Fe}^{2+}/(\text{Fe}^{2+} + \text{Al} + \text{Cr})$ of chromites. The field of Alaskan-type complexes worldwide is from Barnes and Roeder (2001); Southeast Alaskan-type complexes, stratiform complexes, and Alpine-type complexes are from Irvine (1967); the Xiadong field is from Su et al. (2012); **(D)** Plot of $\text{Fe}^{2+}/(\text{Mg} + \text{Fe}^{2+})$ vs. $\text{Cr}\#$ of chromites. The fields of Alaskan-type complexes and ophiolite and alteration trend are after Barnes and Roeder (2001). Different symbol colors correspond to different degrees of magnetization or ferritchromite levels.

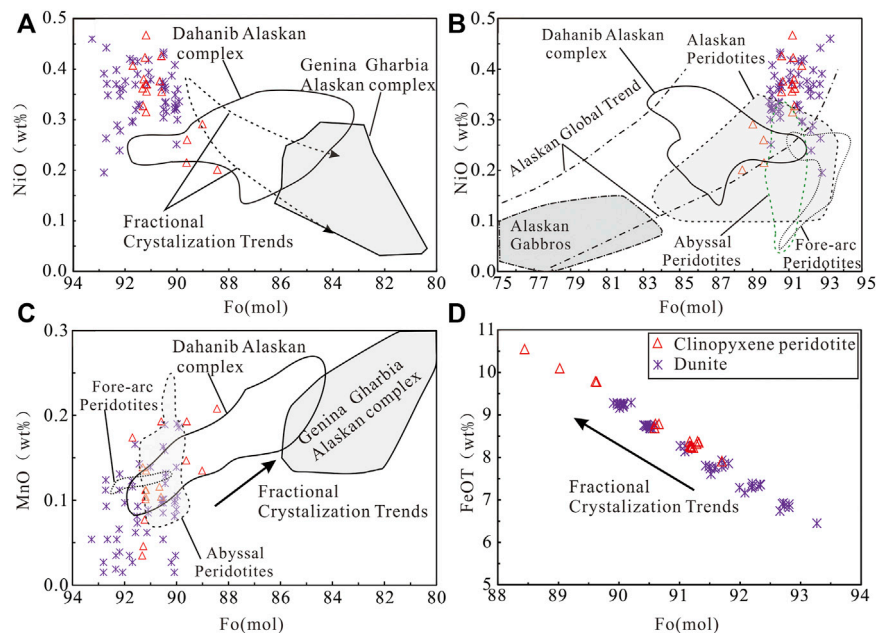


FIGURE 10 | Olivine chemistry of the Hongshishan dunite and clinopyroxene. Plots of Fo versus NiO (wt%), MnO (wt%) showing the olivines following the fractional crystallization trend and Alaskan global trend. The fields of Dahanib and Genina Gharbia are from Khedr et al. (Khedr and Arai, 2016). The fields of the Alaskan global trend and Alaskan gabbros are after Krause et al. (2007), and the fields of Abyssal peridotites and Fore-arc peridotites are from Pagé et al. (2008).

from 2.97 to 70.97 (average 21.72 wt%), FeO from 15.9 to 31.86 (average 23.83 wt%), TiO_2 from 0 to 1.59 (average 0.36 wt%), MgO from 0.27 to 14.73 (average 6.19 wt%), and Cr# from 0.44 to 1.0 (0.79 on average) and Mg# from 0 to 0.55 (0.25 on average). A portion of non-magnetized spinels compositions fell inside the field of ophiolitic podiform chromites (Figures 9A,D), while plots of Mg# vs. $\text{Fe}^{3+}/(\text{Fe}^{3+} + \text{Cr} + \text{Al})$ and Cr# vs. $\text{Fe}^{2+}\#s$ (Figures 9B–D) show that most data approximate the field of the Alaskan-type complex worldwide and nearly approached the field of the Xiadong Alaskan-type complex (Barnes and Roeder, 2001; Habtoor et al., 2006; Su et al., 2012). The chromites of Hongshishan trend towards Fe^{3+} -rich composition (Figure 2), a typical arc-related trend.

Olivines from the dunite are chemically homogeneous, with FeO (average 8.15 wt%), MnO (average 0.09 wt%) and NiO (average 0.35 wt%); they have Forsterite compositions that vary between Fo_{90–93}. Olivines from the clinopyroxene peridotites show slightly higher FeO and MnO levels (average 8.77 and 0.13 wt%, respectively) and the same NiO (average 0.35 wt%). They have Forsterite compositions that vary from Fo_{88–92}, all of which are higher than olivines in Abu Hamamid (Fo_{74–81}), Gabbro-Akarem (Fo_{69–87}), Genina Gharbia (Fo_{80–86}) and Alaskan-type complex (Khedr and Arai, 2016). The Hongshishan olivines plot of NiO, MnO versus Fo falls within in the Alaskan Global trend field but out of the Abyssal peridotite and Fore-arc peridotite fields (Figures 10B,C). A graph of FeO_T vs. Fo shows a systematic negative correlation (Figure 10D), and a typical fractional crystallization trend similar to olivines in the Alaskan-type complex (Figures 10A–C).

The Clinopyroxenes (Cpxs) from the clinopyroxene peridotites are represented by Wo (45–50) and display narrow Mg# (92.4–96.4). The Cpxs contain average amounts of Al_2O_3 (1.07 wt%), Cr_2O_3 (0.31 wt%), FeO (1.99 wt%) and higher amounts of CaO (23.94 wt%). Increased amounts of Al_2O_3 and Na_2O (samples of D01-5-3-1, D01-5-3-2) may be attributed to the neogenic pargasite in diopsides. In the pyroxene classification diagram (Figure 11A), nearly all Hongshishan clinopyroxenes fall within the diopside and show similar compositional variations with those of Poshi complexes and Alaskan-type complexes (Su et al., 2013). In the diagram of Al_2O_3 vs. Mg# (Figure 11B), most clinopyroxenes from Hongshishan complexes that belong to the second Cpx are similar to those in Alaskan-type intrusions (Khedr and Arai, 2016).

Platinum-Group Elements Geochemistry

Table 1 shows PGE concentrations for all rock types. Total chromite PGE concentrations varied from 17.41 to 218.90 ppb. Just like most ophiolitic podiform chromites, which contain Os, Ir and Ru levels between 0.1 and 0.01 times chondritic (Leblanc 1991) and lower concentrations of Pt and Pd, all samples, except Cr9-11, showed an enriched Ir-subgroup (IPGE = Os, Ir, and Ru) and a depleted Pd-subgroup (PPGE = Rh, Pt, and Pd). The (Pd/Ir)_N ratio of the chromites ranged from 0 to 0.06 (except Cr9-11, Pd/Ir = 8.26) and the chondrite-normalized spider diagram showed steep right-facing sloped patterns, mostly similar to those of the PGE-rich chromites of the Wadi Al Hwanet ophiolite in Saudi Arabia (Ahmed et al., 2012) and the chromitites of the Luobusa ophiolite in Tibet (Zhou et al., 1996) (Figure 12).

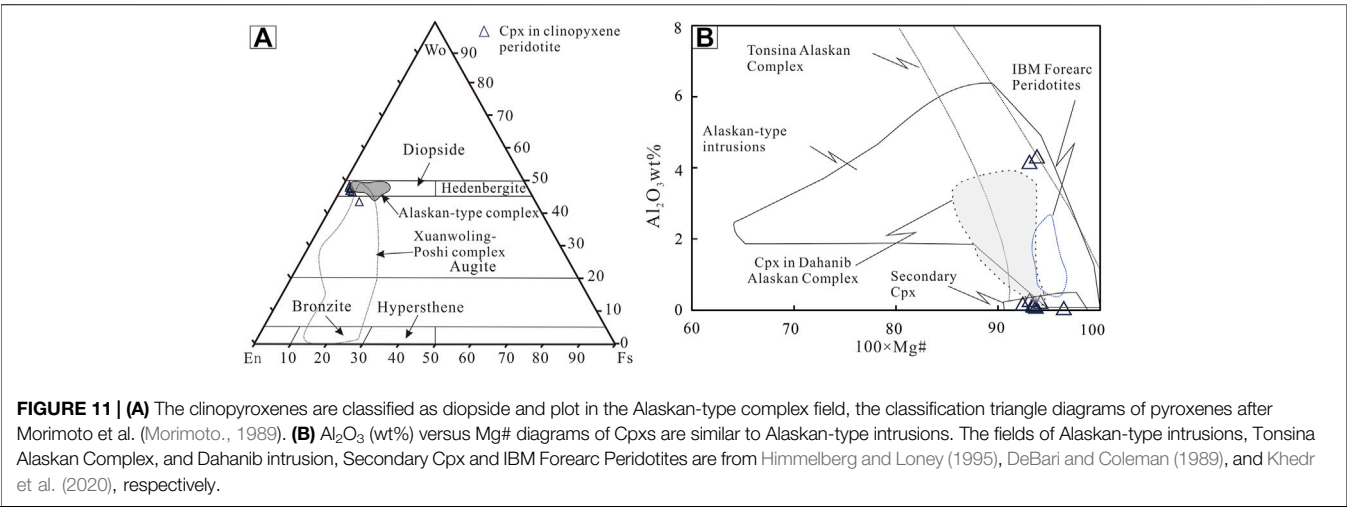
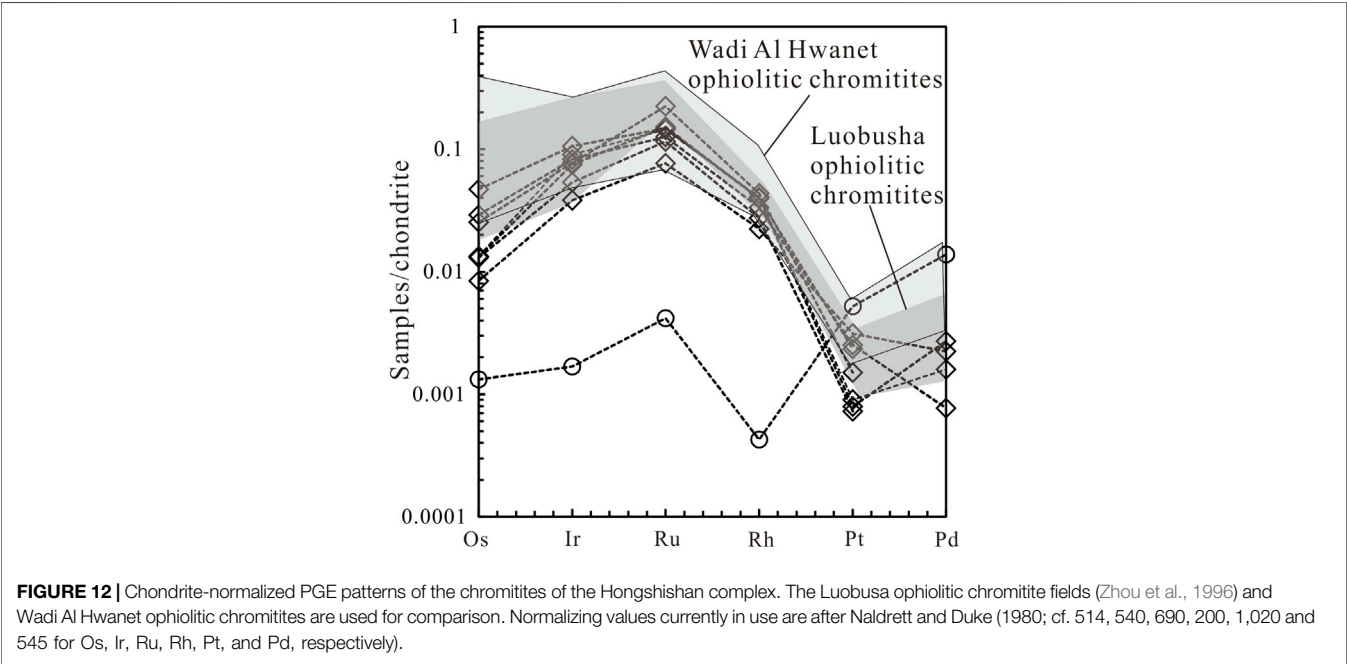


TABLE 1 | PGE compositions of whole-rock samples of chromite-bearing dunites in Hongshishan complex.

Sample	Os (ng/g)	Ir (ng/g)	Ru (ng/g)	Rh (ng/g)	Pt (ng/g)	Pd (ng/g)	Σ	Pd/Ir
Cr27-b3	6.69	28.90	79.70	5.49	0.74	0.00	121.52	0.00
Cr27-b4	6.81	40.50	105.00	7.93	0.81	1.48	162.53	0.04
Cr27-b5	6.84	48.70	99.70	8.14	0.92	0.87	165.17	0.02
Cr9-B2	24.20	57.00	102.00	7.92	2.40	0.00	193.52	0.00
Cr9-b4	15.00	44.50	86.70	6.71	2.58	0.42	155.91	0.01
Cr9w-B2	13.00	41.70	154.00	8.67	1.53	0.00	218.90	0.00
Cr9-11	0.68	0.91	2.88	0.09	5.33	7.52	17.41	8.26
Cr9-13	4.32	20.60	52.80	4.46	3.18	1.22	86.58	0.06



DISCUSSION

Texture, Mineralogy, Geochemistry of the Hongshishan Complex and Fractional Crystallization Trends

Petrologically and mineralogically, the Hongshishan complex shows similarities with the Xiadong complex in the Middle Tianshan Terrane (Su et al., 2012; Su et al., 2014) and the Tuerkubantao intrusion in West Junggar (Deng et al., 2015a; Deng et al., 2015b). The Hongshishan complex contains no cross-cutting and intrusive rock unit relationships with distinct geochemical features, this implied the complex was probably not formed by multiple magmatic pulses (Su et al., 2012, 2014). The zonal textural features demonstrated the dunitic core resulted from crystal mush intrusions of deeper-seated cumulate fractionations (Tisl et al., 1994). In our study, compared with Alaskan-type complexes (Irvine, 1974; Himmelberg and Loney, 1995; Krause et al., 2007; Su et al., 2012), the Hongshishan complex has a concentrically zoned structure characterized predominantly by olivine, chrome spinel, clinopyroxene, and hornblende and an absence of orthopyroxene and plagioclase. Nearly all chrome spinels were less hydrous and were free of fluid inclusions, which implied the absence of a magmatic origin of chromite-bearing peridotite silicates in hydrous parental melts or scarce hydrous melts trapped during spinel growth.

Based on field observations, petrography and major element composition variations, the mineral crystallization sequence of the complex proceeded as follows: early cumulus olivine + chrome spinel formed chromite-bearing dunite, followed by crystallization of olivine + chrome spinel + clinopyroxene in spinel-poor clinopyroxene peridotite, and plagioclase + Cpx crystallized to form gabbro (Green et al., 2004; Krause et al., 2007; Khedr et al., 2020).

Generally, the Mg# values of the silicates indicated a fundamental range that followed normal fractional crystallization trends. Moreover, dunites have the highest levels of Ni, Cr, and Mg as compared to other complex units, and probably represented early magmatic products with olivine fractionation (Himmelberg and Loney, 1995). Significantly, from the ultramafic core to the mafic rim, through pyroxenite and the gabbroic margin, the major oxides of the Hongshishan complex have systematically negative correlation trends between major oxides (Al_2O_3 , SiO_2 , CaO) with Mg# and positive correlations between Mg# with MgO , NiO , and Cr_2O_3 ; these represent an accumulation of spinel and mafic minerals and the change of fractional crystallization degrees from the ultramafic core outwards from a common parental magma chamber of Uralian-Alaskan-type complex (Himmelberg and Loney, 1995; Farahat and Helmy, 2006; Habtoor et al., 2016).

For Uralian-Alaskan-type complexes, decreases in Fo and Cr# in the coexisting chromite helped monitor the early olivine and chromite crystallization stages. Olivine fractionation was significant during the early stage of magma ascension and evolution, as Mg preferentially partitioned into olivine

accumulation instead of coexisting in a melt or other silicate minerals (Green et al., 2004; Teng, 2017). Crystallization of large olivine amounts to form an olivine-rich peridotite enriched the parental melt with Cr, Fe, and Al and triggered the crystallization of Fe, Al-rich chromite to form chromite. Crystallization of the chromite, and vice versa, increased magma Mg levels. High Fo values in olivine and the high Cr/(Cr + Al) in the spinel implied a parental magma rich in MgO but poor in Al_2O_3 (Krause et al., 2007). Additionally, increased Fe and Mn levels in dunite olivines to the one in the spinel-poor clinopyroxene peridotite likely relates to fractional crystallization (Khedr et al., 2020). Diagrams of major oxides versus Fo for olivines in dunite and clinopyroxene peridotite from the Hongshishan complex appeared within the Alaskan Global trend fields and showed a typical fractional crystallization trend similar to olivines in typical Alaskan-type complexes (Figure 10).

The Chondrite-normalized rare Earth element patterns are shown in Figure 7. All samples showed highly variable concentrations of HREE but slight enrichments of total REE levels and other incompatible elements relative to primitive mantle values from the ultramafic core to the marginal gabbroic rocks. The strong positive anomalies of Ba and Sr and the slight positive Eu anomaly from gabbros and pyroxenite whole rock samples supported a cumulative origin, i.e., accumulation of plagioclase. The REE patterns of the peridotites depended on the melting degree and mineralogy involved when the initial residue and enriched melt were formed. Residue composition formed by varying degrees of non-modal fractional melting of the same source. LREE-enriched patterns developed if melting occurred in the spinel stability field. U-shaped REE patterns represent mixing of these residues with different degrees of incipient melts (Song and Frey, 1989). Additionally, serpentinization, carbonation, and hydrous fluid metasomatism by LREE-enriched melts act as primary causes of LREE/HREE fractionation, LREE enrichment in carbonated peridotite rocks (Becker et al., 2001; Tian et al., 2011; Boskabadi et al., 2020), and subduction-related fluid, melts necessarily account for LILE-enrichment and HFSE-depletion of peridotite rocks in this complex.

Our preliminary investigation, combining the current field survey with these new observations, revealed that the petrological and mineralogical features of the Hongshishan complex were comparable with a Ural-Alaskan type complex.

Crustal Contamination

Even though interactions with late interstitial, percolating melts, fluids, and subsolidus equilibration with neighboring grains can modify the elemental concentration in minerals as well as the mineral composition in cumulate rocks (Krause et al., 2007; Murphy, 2013); however, we did not observe any evidence of percolation and melt-rock reactions in the field or on a microscopic scale. Additionally, even though crustal contamination potentially increases Th/Yb ratios and reduces Nb/La, Ta/La, and Nb/Th ratios (Neal et al., 2002; Pearce, 2008), negative Eu anomalies and REE fractionation may imply crustal assimilation. Because the trace and REE element patterns of ultramafic cores and the marginal gabbros have sub-parallel trends, it implied that the different rock types of the Hongshishan complex are comagmatic, and

initially generated by fractional crystallization from a common basaltic melt. The negative Eu anomalies of dunite accompanied by LREE enrichment were interpreted by a disequilibrium melting model, when and where, melting began in the garnet lherzolite facies through the spinel facies and concluded in the plagioclase facies. Phases in the source melted; however, the melt did not equilibrate with residual minerals. The negative Eu anomalies meant that some partial melting occurred in the plagioclase facies. Disequilibrium melting of plagioclase produces a residue with a negative Eu anomaly because of the positive Eu anomaly caused by suppressed crystallization of plagioclase (Prinzhofer and Allègre, 1985; McDonough and Frey, 1989; Wang et al., 1996). In addition, the absence of plagioclase in dunite and clinopyroxene peridotite likely caused the negative Eu anomaly due to low Sr concentrations, and subsequent serpentinization, carbonatization and metasomatism related subduction resulted in the higher total REE abundance, LREE enrichment with negative dunite Eu anomalies.

Cr-spinels in Hongshishan dunites showed $^{187}\text{Os}/^{188}\text{Os}$ isotopic ratios from 0.1251 to 0.1274 and $^{187}\text{Re}/^{188}\text{Os}$ ratios from 0.0066 to 0.0842. The Re/Os isotopic compositions of Cr-spinel samples appeared in the chromite field, which represents a residual peridotites trend. Just like a Gaositai complex with no significant crustal contamination in North China (Tian et al., 2011), the mean $^{187}\text{Os}/^{188}\text{Os}$ ratio for the chromites from Hongshishan showed that magmas originated from the mantle. The radiogenic Os isotopic compositions of the chromites meant the parental magmas of the Hongshishan complex suffered minor contamination coming from crustal components during magma evolution. So crustal assimilation may not be necessary to significantly change the geochemical compositions of the parental magmas (Reiners et al., 1996; Batanova et al., 2005; Burg et al., 2009; Su et al., 2014).

Possible Tectonic Setting of the Hongshishan Alaskan-type Complex

Tectonically, some researchers have proposed that Alaskan-type complexes formed at subduction zones, representing arc magmas (Taylor, 1967; Irvine, 1974; Helmy and El Mahallawi, 2003), arc-root complexes (DeBari and Coleman, 1989; Brugmann et al., 1997; Helmy et al., 2014), at the change from the arc setting to the extensional regime (Tistl et al., 1994; Mues-Schumacher et al., 1996; Chen et al., 2009; Tian et al., 2011; Spandler and Pirard, 2013; Helmy et al., 2015) or even related to mantle plume (Ishiwatari and Ichiyama, 2004; Pirajno, 2004; Farahat and Helmy, 2006).

The Alaskan-type complexes of Xiadong in Central Tianshan and Tuerkubantao in West Junggar are arc-related, and interpreted as the product of partial melting of metasomatized lithospheric mantle triggered by subduction of an oceanic plate or slab window created by the subduction of an oceanic ridge (Xiao et al., 2010; Su et al., 2012; Su et al., 2014; Deng et al., 2015a; Deng et al., 2015b). In the early Carboniferous, Hongshishan, Liutuoshan areas might have evolved into an initial small oceanic basin (Zuo et al., 1990a; Zuo et al., 1990b; Zhao et al.,

1994; Wang et al., 2014), but had not reached the degree of a mature mid-ocean ridge (Gong et al., 2003; Huang and Jin, 2006a; Huang and Jin, 2006b; Shi et al., 2017) because the geochemistries and age data came from basalts and gabbros in the Carboniferous Lvtiaoshan Formation, characterized by the occurrence of the bimodal volcanic rocks and lack of data on the mafic and ultramafic rocks in the complex (Peng et al., 2016). Virtually, the Hongshishan ultramafic-mafic complex lacked mantle peridotite, mafic cumulate, as well as pillow lava, so the ultramafic and mafic rocks were not the member compositions of a typical ophiolite (Yang et al., 2010; Wang et al., 2013; Peng et al., 2016).

We deduced that subduction or an arc magma setting could account for the upwelling of the depleted asthenosphere and rapid ascending magma flow which was less hydrous or free of opaque inclusions. Os isotopic compositions of chromian spinels in chromite suggested minor magma crustal contaminations. Formation of chromite was thought of as related to the evolution and chemical composition change of the parent magma (Tian et al., 2011). We attributed the enriched Fe^{3+} chromite compositions, LILE-enrichment, and HFSE-depletion of peridotite rocks and the neogenic clinopyroxenes in the clinopyroxene peridotites to suffering subduction modification and enrichment.

Chromite and PGE Mineralization

In the Alaskan-type complexes, chromites occurred as bands, seams, massive, veined or disseminated, and were accompanied by cumulate dunites (Himmelberg and Loney, 1995; Garuti et al., 2002; Garuti et al., 2003; Krause et al., 2007; Tian et al., 2011; Khedr et al., 2020). Cumulus olivines in host dunites and banded chromites with varying degrees of disseminated chromian-spinel grains were the typical characters of fractional crystallization (Khedr et al., 2020). Chromites may enter clinopyroxene crystals in an isomorphic form instead of an olivine form and crystallize in a chromian-spinel form during cumulation of olivine, so chromites form in cumulate dunite rather than in clinopyroxene-riched rocks. As the olivines fractionally crystallized, chromite compositions and relatively volatile components concentrated in residual magma. The emergence of high concentrations of volatiles largely delayed melt crystallization times and promoted the formation of ore pulp from ore-forming components as a massive and veined chromite orebody. Thus, those two different processes accounted for chromite formation, where the former crystallized from melting and released chrome-bearing minerals, which accumulated through fractional crystallization. In the latter, ore pulps carried by volatiles cut across the earlier disseminated chromite ores. The textures in Hongshishan chromites show that the disseminated chromite crystallized earlier than the massive and veined chromites. The Uralian-Alaskan-type chromites are characterized by the predominant composition of $\text{Cr}^{3+} \rightarrow \text{Fe}^{3+}$ substitution, which indicated an oxygen fugacity ($f\text{O}_2$) variation during chromite precipitation (Johan, 2006). Crystallization and separation of Alaskan-type magma at high oxygen fugacity promoted transformation of the magma Fe^{2+} components into Fe^{3+} , which impeded the

combination of FeO with MgO and SiO₂ to produce poor a CaO-poor orthopyroxene, which instead occurred as magnetite and dispersed throughout the magma to form an iron-rich cumulatite.

Alaskan-type complexes are well-known as sub-economic Cu-Ni-PGE mineralization hosts, other than chromite deposits (Helmy and Mogessie, 2001; Helmy, 2004). However, the parental magmas of Alaskan-type complexes are water-rich/hydrous with high oxygen fugacities and less crustal assimilation, which might explain the absence of Ni-Cu sulfide mineralization that requires a reducing environment for most Alaskan-type complexes (Pettigrew and Hattori, 2006; Su et al., 2013). The Hongshishan complex contains a unique Ir-Ru-rich chromite deposit along the southern border of the Altaids orogenic belt. The first PGE-bearing sulfides crystallized within the early cumulus olivine and chromian spinels as primary inclusions with variable but generally high levels of PGE (17.41–218.90 ppb). They display similar patterns with IPGE enrichment (Os, Ir, Ru), PPGE depletion (Pt, Pd), and Ni/Cu depletions. Partial melting of the upper mantle controls PGE levels and their distribution in mantle rocks, and the migrating ability of IPGE is significantly weaker than PPGE (Wood, 1987; Zhou et al., 2014). IPGEs are compatible elements in monosulfide solid solutions (MSS), while PPGEs are incompatible with MSS when MSS forms by fractional crystallization of sulfide melts. High levels of IPGEs occurred in MSS whereas PPGE increased in residual sulfide melts, leading to the differentiation of PGE (Mungall et al., 2005; Cui et al., 2020).

PGE-bearing chromite mineralization in addition to the Hongshishan complex has not been reported in a mafic-ultramafic complex along the southern border of the Altaids orogenic belt. The identification of the Hongshishan Alaskan-type complex indicated that this kind of complex has great potential for chrome-PGE prospecting in the Beishan orogenic collage.

CONCLUSION

- 1) The Hongshishan mafic-ultramafic complex shows concentric zonation, from clinopyroxene peridotite and dunite in the core to mafic intrusions, including pyroxenite and gabbro in the margin.
- 2) Systematic trends among the major element oxides and chemical compositions of spinel, olivine, and clinopyroxenes suggested fractional crystallization. The absence of orthopyroxene and the fact that nearly all chrome spinels were less hydrous and free of fluid inclusions meant a magmatic origin of chromite-bearing peridotites was absent in hydrous parental melts or scarce hydrous melts. Subduction modification and enrichment, together with serpentinization and carbonatization, may explain the LILE-enrichment and HFSE-depletion of peridotite rocks in this complex. Crustal

assimilation may not directly explain negative Eu anomalies and REE fractionation of mafic-ultramafic rocks. The complexes share similar petrological, geochemical, and mineralogical features with typical Alaskan-type complexes.

- 3) The Hongshishan complex contains a unique Ir-Ru-rich chromite deposit along the southern border of the Altaids orogenic belt. The chromites are enriched in IPGE and a chondrite-normalized spider diagram showed steep right-facing sloped patterns, which approximated those of PGE-rich ophiolitic chromites.
- 4) Tectonically, the Hongshishan complex is neither an ophiolite remnant nor a stratiform mafic-ultramafic intrusion, but rather an Alaskan-type intrusion related to subduction or arc magmas and approximately 366.1 Ma years old and suffered subduction modification and enrichment.

DATA AVAILABILITY STATEMENT

The original contributions presented in the study are included in the article/**Supplementary Material**, further inquiries can be directed to the corresponding authors.

AUTHOR CONTRIBUTIONS

All authors listed have made a substantial, direct, and intellectual contribution to the work and approved it for publication.

FUNDING

This research was jointly supported by the National Key Research and Development Program of China (No. 2018YFC0604002), China Geological Survey (Nos. DD20190071, DD20190812), and the Basic Science Foundation of CAGS, China (No. JKY21021).

ACKNOWLEDGMENTS

The authors thank the reviewers for their thorough, critical, and constructive reviews and comments. We are also grateful to Prof. Yufeng Deng for their helpful discussions and suggestions.

SUPPLEMENTARY MATERIAL

The Supplementary Material for this article can be found online at: <https://www.frontiersin.org/articles/10.3389/feart.2021.663760/full#supplementary-material>

REFERENCES

Ahmed, A. H., Harbi, H. M., and Habtoor, A. M. (2012). Compositional variations and tectonic settings of podiform chromitites and associated ultramafic rocks of

the Neoproterozoic ophiolite at Wadi Al Hwanet, northwestern Saudi Arabia. *J. Asian Earth Sci.* 56, 118–134.

Ao, S. J., Xiao, W. J., Han, C. M., Mao, Q. G., and Zhang, J. E. (2010). Geochronology and Geochemistry of Early Permian Mafic-Ultramafic Complexes in the Beishan Area, Xinjiang, NW China: Implications for Late

- Paleozoic Tectonic Evolution of the Southern Altai. *Gondwana Res.* 18 (2–3), 466–478. doi:10.1016/j.gr.2010.01.004
- Barnes, S. J., and Roeder, P. L. (2001). The Range of Spinel Compositions in Terrestrial Mafic and Ultramafic Rocks. *J. Pet.* 42, 2279–2302. doi:10.1093/petrology/42.12.2279
- Batanova, V. G., Pertsev, A. N., Kamenetsky, V. S., Ariskin, A. A., Mochalov, A. G., and Sobolev, A. V. (2005). Crustal Evolution of Island-Arc Ultramafic Magma: Galmoenan Pyroxenite-Dunite Plutonic Complex, Koryak Highland (Far East Russia). *J. Pet.* 46, 1345–1366. doi:10.1093/petrology/egi018
- Becker, H., Shirey, S. B., and Carlson, R. W. (2001). Effects of Melt Percolation on the Re-os Systematics of Peridotites from a Paleozoic Convergent Plate Margin. *Earth Planet. Sci. Lett.* 188, 107–121. doi:10.1016/S0012-821X(01)00308-9
- Bonavia, F. F., Diella, V., and Ferrario, A. (1993). Precambrian Podiform Chromites from Kenticha Hill, Southern Ethiopia. *Econ. Geology.* 88, 198–202. doi:10.2113/gsecongeo.88.1.198
- Boskabadi, A., Pitcairn, I. K., Leybourne, M. I., Teagle, D. A. H., Cooper, M. J., Hadizadeh, H., et al. (2020). Carbonation of Ophiolitic Ultramafic Rocks: Listvenite Formation in the Late Cretaceous Ophiolites of Eastern Iran. *Lithos.* 352–353. doi:10.1016/j.lithos.2019.105307
- Brüggmann, G. E., Reischmann, T., Naldrett, A. J., and Sutcliffe, R. H. (1997). Roots of an Archean volcanic arc complex: the Lac des Iles area in Ontario, Canada. *Precambrian Res.* 81, 223–239. doi:10.1016/S0301-9268(96)00036-8
- Burg, J.-P., Bodinier, J.-L., Gerya, T., Bedini, R.-M., Boudier, F., Dautria, J.-M., et al. (2009). Translithospheric Mantle Diapirism: Geological Evidence and Numerical Modelling of the Kondyor Zoned Ultramafic Complex (Russian Far-East). *J. Pet.* 50, 289–321. doi:10.1093/petrology/egn083
- Chen, B., Suzuki, K., Tian, W., Jahn, B. M., and Ireland, T. (2009). Geochemistry and Os-Nd-Sr Isotopes of the Gaositai Alaskan-type Ultramafic Complex from the Northern North China Craton: Implications for Mantle-Crust Interaction. *Contrib. Mineral. Petrol.* 158, 683–702. doi:10.1007/s00410-009-0404-7
- Cui, M. M., Su, B. X., Wang, J., Chen, K. Y., and Gao, D. L. (2020). Alaskan-type Nature and Pge Mineralization of the Wuxing Mafic-Ultramafic Complex in Eastern Part of the central Asian Orogenic belt. *Ore Geo. Rev.* 123, 10356. doi:10.1016/j.oregeorev.2020.103566
- DeBari, S. M., and Coleman, R. G. (1989). Examination of the Deep Levels of an Island Arc: Evidence from the Tonsina Ultramafic-Mafic Assemblage, Tonsina, Alaska. *J. Geophys. Res.* 94, 4373–4391. doi:10.1029/jb094ib04p04373
- Deng, Y.-F., Yuan, F., Zhou, T., White, N. C., Zhang, D., Guo, X., et al. (2015b). Zircon U-Pb Geochronology, Geochemistry, and Sr-Nd Isotopes of the Ural-Alaskan Type Tuerkubantao Mafic-Ultramafic Intrusion in Southern Altai Orogen, China: Petrogenesis and Tectonic Implications. *J. Asian Earth Sci.* 113, 36–50. doi:10.1016/j.jseas.2015.05.007
- Deng, Y., Yuan, F., Zhou, T., Xu, C., Zhang, D., and Guo, X. (2015a). Geochemical Characteristics and Tectonic Setting of the Tuerkubantao Mafic-Ultramafic Intrusion in West Junggar, Xinjiang, China. *Geosci. Front.* 6, 141–152. doi:10.1016/j.gsf.2013.10.003
- Dick, H. J. B., and Bullen, T. (1984). Chromian spinel as a petrogenetic indicator in abyssal and alpine-type peridotites and spatially associated lavas. *Contrib. Mineral. Petrol.* 86, 54–76.
- Efimov, A. A. (1998). The Platinum belt of the Urals: Structure, Petrogenesis, and Correlation with Platiniferous Complexes of the Aldan Shield and Alaska. Abstr 8th Intern Platinum Symp, South Africa, June 29–July 2, 1998, 93–96.
- Farahat, E. S., and Helmy, H. M. (2006). Abu Hamamid Neoproterozoic Alaskan-type Complex, South Eastern Desert, Egypt: Petrogenetic and Geotectonic Implications. *J. Afr. Earth Sci.* 45, 187–197. doi:10.1016/j.jafrearsci.2006.02.003
- Foley, J. P., Light, T. D., Nelson, S. W., and Harris, R. A. (1997). Mineral Occurrences Associated with Mafic-Ultramafic and Related Alkaline Complexes in Alaska. *Econ. Geology.* 9, 396–449.
- Garuti, G., Pushkarev, E. V., Zaccarini, F., Cabella, R., and Anikina, E. (2003). Chromite Composition and Platinum-Group mineral Assemblage in the Uktus Uralian-alaskan-type Complex (Central Urals, Russia). *Can. Mineral.* 38, 312–326. doi:10.1007/s00126-003-0348-1
- Garuti, G., Pushkarev, E. V., and Zaccarini, F. (2002). Composition and Paragenesis of Pt Alloys from Chromites of the Uralian-alaskan-type Kytlym and Uktus Complexes, Northern and central Urals, Russia. *Can. Mineral.* 40, 1127–1146. doi:10.2113/gscanmin.40.4.1127
- Gong, Q. S., Liu, M. Q., and Liang, M. H. (2003). The Tectonic Facies and Tectonic Evolution of Beishan Orogenic belt. *Gansu. Northwest. Geology.* 36 (1), 11–17. (in Chinese with English abstract).
- Green, D. H., Schmidt, M. W., and Hibberson, W. O. (2004). Island-arc Ankarmites: Primitive Melts from Fluxed Refractory Lherzolitic Mantle. *J. Pet.* 45, 391–403. doi:10.1093/petrology/egg101
- Greenbaum, D. (1977). The Chromitiferous Rocks of the Troodos Ophiolite Complex, Cyprus. *Econ. Geology.* 72, 1175–1194. doi:10.2113/gsecongeo.72.7.1175
- Guo, Q., Xiao, W., Windley, B. F., Mao, Q., Han, C., Qu, J., et al. (2012). Provenance and Tectonic Settings of Permian Turbidites from the Beishan Mountains, NW China: Implications for the Late Paleozoic Accretionary Tectonics of the Southern Altai. *J. Asian Earth Sci.* 49, 54–68. doi:10.1016/j.jseas.2011.03.013
- Habtoor, A., Ahmed, A. H., and Harbi, H. (2016). Petrogenesis of the Alaskan-type Mafic-Ultramafic Complex in the Makkah Quadrangle, Western Arabian Shield, Saudi Arabia. *Lithos.* 263, 33–51. doi:10.1016/j.lithos.2016.08.014
- He, S. P., Zhou, H. W., Ren, B. C., Yao, W. G., and Fu, L. P. (2005). Crustal Evolution of Paleozoic in Beishan Area, Gansu and Inner Mongolia, China. *Northwest. Geology.* 38 (3), 6–15. (in Chinese with English abstract).
- Helmy, H. M., Abd El-Rahman, Y. M., Yoshikawa, M., Shibata, T., Arai, S., Tamura, A., et al. (2014). Petrology and Sm-Nd Dating of the Genina Gharbia Alaskan-type Complex (Egypt): Insights into Deep Levels of Neoproterozoic Island Arcs. *Lithos.* 198–199, 263–280. doi:10.1016/j.lithos.2014.03.028
- Helmy, H. M. (2004). Cu Ni PGE Mineralization in the Genina Gharbia Mafic Ultramafic Intrusion, Eastern Desert, Egypt. *The Can. Mineralogist* 42, 351–370. doi:10.2113/gscanmin.42.2.351
- Helmy, H. M., and El Mahallawi, M. M. (2003). Gabbro Akarem Mafic-Ultramafic Complex, Eastern Desert, Egypt: a Late Precambrian Analogue of Alaskan-type Complexes. *Mineralogy Pet.* 77, 85–108. doi:10.1007/s00710-001-0185-9
- Helmy, H. M. (2005). Melonite Group Minerals and Other Tellurides from Three Cu-Ni-PGE Prospects, Eastern Desert, Egypt. *Can. Mineral.* 42, 305–324. doi:10.2113/gscanmin.42.2.351
- Helmy, H. M., and Mogessie, A. (2001). Gabbro Akarem, Eastern Desert, Egypt: Cu-Ni-PGE Mineralization in a Concentrically Zoned Mafic-Ultramafic Complex. *Mineralium Deposita* 36, 58–71. doi:10.1007/s001260050286
- Helmy, H. M., Yoshikawa, M., Shibata, T., Arai, S., and Kagami, H. (2015). Sm-Nd and Rb-Sr Isotope Geochemistry and Petrology of Abu Hamamid Intrusion, Eastern Desert, Egypt: An Alaskan-type Complex in a Backarc Setting. *Precambrian Res.* 258, 234–246. doi:10.1016/j.precamres.2015.01.002
- Himmelberg, G. R., and Loney, R. A. (1995). Characteristics and Petrogenesis of Alaskan-type Ultramafic-Mafic Intrusions, southeastern Alaska. USGS, U.S. Geological Survey Professional Paper 1564.
- Huang, Z. B., and Jin, X. (2006a). Tectonic Environment of Basic Volcanic Rocks in the Hongshishan Ophiolite Melange Zone, Beishan Mountains. *Gansu. Geology in China* 33 (5), 1030–1037. (in Chinese with English abstract).
- Huang, Z. B., and Jin, X. (2006b). Geochemistry Features and Tectonic Setting of the Hongshishan Ophiolite in. *Gansu Province. Chin. J. Geology.* 41 (4), 601–611. (in Chinese with English abstract).
- Huang, Z. B., and Jin, X. (2006c). Geological Characteristics and its Setting for Volcanic Rocks of Baishan Formation in Hongshishan Area of Gansu Province. *Gansu. Geology.* 15, 19–24. (in Chinese with English abstract).
- Irvine, T. N. (1967). Chromian Spinel as a Petrogenetic Indicator. Part II. Petrogenetic Applications. *Can. J. earth Sci.* 11 (4), 71–103. doi:10.1139/e67-004
- Irvine, T. N. (1974). Petrology of the Duke Island ultramafic complex, southeastern Alaska. *Geol. Soc. Amer. Memo.* 138, 1–240.
- Ishiwatari, A., and Ichiyama, Y. (2004). Alaskan-Type Plutons and Ultramafic Lavas in Far East Russia, Northeast China, and Japan. *Int. Geology. Rev.* 46, 316–331. doi:10.2747/0020-6814.46.4.316
- Johan, Z. (2006). Platinum-group Minerals from Placers Related to the Nizhni Tagil (Middle Urals, Russia) Uralian-alaskan-type Ultramafic Complex: Ore-Mineralogy and Study of Silicate Inclusions in (Pt, Fe) Alloys. *Mineralogy Pet.* 87, 1–30. doi:10.1007/s00710-005-0117-1
- Khedr, M. Z., Arai, S., and Morishita, T. (2020). Formation of Banded Chromitites and Associated Sulphides in the Neoproterozoic Subarc Deep-Crustal Magma Inferred from the Alaskan-type Complex, Egypt. *Ore Geology. Rev.* 120, 103410. doi:10.1016/j.oregeorev.2020.103410

- Khedr, M. Z., and Arai, S. (2016). Petrology of a Neoproterozoic Alaskan-type Complex from the Eastern Desert of Egypt: Implications for Mantle Heterogeneity. *Lithos* 263, 15–32. doi:10.1016/j.lithos.2016.07.016
- Krause, J., Brüggmann, G. E., and Pushkarev, E. V. (2007). Accessory and Rock Forming Minerals Monitoring the Evolution of Zoned Mafic-Ultramafic Complexes in the Central Ural Mountains. *Lithos* 95, 19–42. doi:10.1016/j.lithos.2006.07.018
- Leblanc, M., and Nicolas, A. (1992). Ophiolitic Chromitites. *Int. Geology. Rev.* 34, 653–686. doi:10.1080/00206819209465629
- Leblanc, M. (1991). “Platinum-Group Elements and Gold in Ophiolitic Complexes: Distribution and Fractionation from Mantle to Oceanic Floor,” in *Ophiolite Genesis and Evolution of the Oceanic Lithosphere*. Editors T Peters, A. Nicolas, and R. G. Coleman (Dordrecht: Kluwer Academic), 231–260. doi:10.1007/978-94-011-3358-6_13
- Liu, X., and Wang, Q. (1995). Tectonics and Evolution of the Beishan Orogenic belt. West China. *Geol. Res.* 10, 151–165.
- Mao, Q., Xiao, W., Windley, B. F., Han, C., Qu, J., Ao, S., et al. (2012). The Liuyuan Complex in the Beishan, NW China: a Carboniferous-Permian Ophiolitic Fore-Arc Sliver in the Southern Altids. *Geol. Mag.* 149, 483–506. doi:10.1017/s0016756811000811
- McDonough, W. F., and Frey, F. A. (1989). Rare Earth Elements in Upper Mantle Rocks. *Rev. Mineralogy Geochem.* 21, 100–145.
- McDonough, W. F., and Sun, S. S. (1995). The Composition of the Earth. *Chem. Geology*. 120 (3–4), 223–253. doi:10.1016/0009-2541(94)00140-4
- Morimoto, N. (1989). Nomenclature of Pyroxenes. *Can. Mineral.* 27, 143–156. doi:10.2465/minerj.14.198
- Mues-Schumacher, U., Keller, J., Kononova, V. A., and Suddaby, P. J. (1996). Mineral Chemistry and Geochronology of the Potassic Alkaline Ultramafic Inagli Complex, Aldan Shield, Eastern Siberia. *Mineral. Mag.* 60, 711–730. doi:10.1180/minmag.1996.060.402.02
- Mungall, J. E., Andrews, D. R. A., Cabri, L. J., Sylvester, P. J., and Tubrett, M. (2005). Partitioning of Cu, Ni, Au, and Platinum-Group Elements between Monosulfide Solid Solution and Sulfide Melt under Controlled Oxygen and Sulfur Fugacities. *Geochimica et Cosmochimica Acta* 69, 4349–4360. doi:10.1016/j.gca.2004.11.025
- Murphy, J. B. (2013). Appinite Suites: a Record of the Role of Water in the Genesis, Transport, Emplacement and Crystallization of Magma. *Earth-Science Rev.* 119, 35–59. doi:10.1016/j.earscirev.2013.02.002
- Neal, C. R., Mahoney, J. J., and Chazey, W. J., III (2002). Mantle Sources and the Highly Variable Role of Continental Lithosphere in Basalt Petrogenesis of the Kerguelen Plateau and Broken Ridge LIP: Results from ODP Leg 183. *J. Pet.* 43, 1177–1205. doi:10.1093/petrology/43.7.1177
- Pagé, P., Bédard, J. H., Schroetter, J.-M., and Tremblay, A. (2008). Mantle Petrology and Mineralogy of the Theford Mines Ophiolite Complex. *Lithos* 100, 255–292. doi:10.1016/j.lithos.2007.06.017
- Pearce, J. A. (2008). Geochemical Fingerprinting of Oceanic Basalts with Applications to Ophiolite Classification and the Search for Archean Oceanic Crust. *Lithos* 100, 14–48. doi:10.1016/j.lithos.2007.06.016
- Peng, X. P., Chen, G. C., Li, Y. H., Li, J. C., Jiang, T., Shi, J. Z., et al. (2016). Ophiolite Mélange belt Composition and Geologic Significance of Hongshishan in Beishan Area. *Xinjiang Geol.* 34 (2), 184–191. (in Chinese with English abstract).
- Pettigrew, N. T., and Hattori, K. H. (2006). The Quetico Intrusions of Western Superior Province: Neo-Archean Examples of Alaskan/Ural-type Mafic-Ultramafic Intrusions. *Precambrian Res.* 149, 21–42. doi:10.1016/j.precamres.2006.06.004
- Pirajno, F. (2004). Hotspots and Mantle Plumes: Global Intraplate Tectonics, Magmatism and Ore Deposits. *Mineralogy Pet.* 82, 183–216. doi:10.1007/s00710-004-0046-4
- Prinzhofer, A., and Allègre, C. J. (1985). Residual Peridotites and the Mechanisms of Partial Melting. *Earth Planet. Sci. Lett.* 74, 251–265. doi:10.1016/0012-821x(85)90025-1
- Reiners, P. W., Nelson, B. K., and Nelson, S. W. (1996). Evidence for Multiple Mechanisms of Crustal Contamination of Magma from Compositionally Zoned Plutons and Associated Ultramafic Intrusions of the Alaska Range. *J. Pet.* 37, 261–292. doi:10.1093/petrology/37.2.261
- Ripley, E. M. (2009). “Magmatic Sulfide Mineralization in Alaskan-type Complexes,” in *New Development in Magmatic Ni-Cu and PGE Deposits*. 7. Editors C.S. Li and E.M. Ripley (Beijing: Geological Publishing House), 219–228.
- Saleeby, J. B. (1992). Age and Tectonic Setting of the Duke Island Ultramafic Intrusion, Southeast Alaska. *Can. J. Earth Sci.* 29, 506–522. doi:10.1139/e92-044
- Sha, L.-K. (1995). Genesis of Zoned Hydrous Ultramafic/mafic-Silicic Intrusive Complexes: an MHFC Hypothesis. *Earth-Science Rev.* 39, 59–90. doi:10.1016/0012-8252(95)00002-r
- Shi, Y., Li, L., Kröner, A., Ding, J., Zhang, W., Huang, Z., et al. (2017). Carboniferous Alaskan-type Complex along the Sino-Mongolian Boundary, Southern Margin of the Central Asian Orogenic Belt. *Acta Geochim* 36 (2), 276–290. doi:10.1007/s11631-017-0145-7
- Shi, Y., Zhang, W., Kröner, A., Li, L., and Jian, P. (2018). Cambrian Ophiolite Complexes in the Beishan Area, China, Southern Margin of the Central Asian Orogenic Belt. *J. Asian Earth Sci.* 153, 193–205. doi:10.1016/j.jseas.2017.05.021
- Snoke, A. W., Quick, J. E., and Bowman, H. R. (1981). Bear Mountain Igneous Complex, Klamath Mountains, California: an Ultrabasic to Silicic Cale-Alkaline Suite. *J. Pet.* 22, 501–552. doi:10.1093/petrology/22.4.501
- Song, D., Xiao, W., Windley, B. F., Han, C., and Tian, Z. (2015). A Paleozoic Japan-type Subduction-Accretion System in the Beishan Orogenic Collage, Southern Central Asian Orogenic Belt. *Lithos* 224–225, 195–213. doi:10.1016/j.lithos.2015.03.005
- Song, Y., and Frey, F. A. (1989). Geochemistry of Peridotite Xenoliths in basalt from Hannuoba, Eastern china: Implications for Subcontinental Mantle Heterogeneity. *Geochimica et Cosmochimica Acta* 53 (1), 97–113. doi:10.1016/0016-7037(89)90276-7
- Spandler, C., and Pirard, C. (2013). Element Recycling from Subducting Slabs to Arc Crust: a Review. *Lithos* 170–171, 208–223. doi:10.1016/j.lithos.2013.02.016
- Su, B.-X., Qin, K.-Z., Sakya, P. A., Malaviarachchi, S. P. K., Liu, P.-P., Tang, D.-M., et al. (2012). Occurrence of an Alaskan-type Complex in the Middle Tianshan Massif, Central Asian Orogenic Belt: Inferences from Petrological and Mineralogical Studies. 54, 249–269. doi:10.1080/00206814.2010.543009
- Su, B.-X., Qin, K.-Z., Zhou, M.-F., Sakya, P. A., Thakurta, J., Tang, D.-M., et al. (2014). Petrological, Geochemical and Geochronological Constraints on the Origin of the Xiadong Ural-Alaskan Type Complex in NW China and Tectonic Implication for the Evolution of Southern Central Asian Orogenic Belt. *Lithos* 200–201, 226–240. doi:10.1016/j.lithos.2014.05.005
- Su, B. X., Qin, K. Z., Santosh, M., Sun, H., and Tang, D. M. (2013). The Early Permian Mafic-Ultramafic Complexes in the Beishan Terrane, NW China: Alaskan-type Intrusives or Rift Cumulates? *Int. Geology. Rev.* 66, 175–187. doi:10.1016/j.jseas.2012.12.039
- Sun, S. S., and McDonough, W. F. (1989). Chemical and Isotopic Systematics of Oceanic Basalts: Implications for Mantle Composition and Processes. *Geol. Soc. Lond. Spec. Publications* 42 (1), 313–345. doi:10.1144/gsl.sp.1989.042.01.19
- Taylor, H. P. (1967). “The Zoned Ultramafic Complexes of southeastern Alaska, Part 4III,” in *Ultramafic and Related Rocks*. Editor P.J. Wyllie (New York: John Wiley), 96–118. *Geol. Soc. Lond. Spec. Publications*
- Teng, F.-Z. (2017). Magnesium Isotope Geochemistry. *Rev. Mineralogy Geochem.* 82, 219–287. doi:10.2138/rmg.2017.82.7
- Tian, W., Chen, B., Ireland, T. R., Green, D. H., Suzuki, K., and Chu, Z. (2011). Petrology and Geochemistry of Dunites, Chromitites and mineral Inclusions from the Gaositai Alaskan-type Complex, North China Craton: Implications for Mantle Source Characteristics. *Lithos* 127, 165–175. doi:10.1016/j.lithos.2011.08.013
- Tistl, M., Burgath, K. P., Höhndorf, A., Kreuzer, H., Muñoz, R., and Salinas, R. (1994). Origin and Emplacement of Tertiary Ultramafic Complexes in Northwest Colombia: Evidence from Geochemistry and K Ar, Sm Nd and Rb Sr Isotopes. *Earth Planet. Sci. Lett.* 126, 41–59. doi:10.1016/0012-821x(94)90241-0
- Valli, F., Guillot, S., and Hattori, K. H. (2004). Source and Tectono-Metamorphic Evolution of Mafic and Pelitic Metasedimentary Rocks from the central Quetico Metasedimentary belt, Archean Superior Province of Canada. *Precambrian Res.* 132, 155–177. doi:10.1016/j.precamres.2004.03.002
- Wang, G. Q., Li, X. M., Xu, X. Y., Yu, J. Y., and Wu, P. (2014). Ziron U-Pb Chronological Study of the Hongshishan Ophiolite in the Beishan Area and Their Tectonic Significance. *Acta Petrologica Sinica* 30 (6), 1685–1694.
- Wang, X. B., Bao, P. S., and Rong, H. (1996). Rare Erath Elements Geochemistry of the Mantle Peridotite in the Ophiolite Suites of China. *Acta Petrologica Sinica* 11 (Suppl. I), 24–41.

- Wang, X. H., Yang, J. G., Xie, X., and Wang, L. (2013). The Genetic Type and Tectonic Significance of Hongshishan Basic-Ultrabasic Rocks in Beishan, Gansu Province. *Northwest. Geology*. 46 (1), 26–55. (in Chinese with English abstract).
- Wang, Z. L., Meng, G. X., Tang, H. J., Yuan, L. L., Yang, Z. S., and Xiao, Y. D. (2021). Geochemistry of Clinopyroxene and Chrome Spinel in the Zhaheba Peridotite, Eastern Junggar, Xinjiang, China and Its Chromitite Metallogenesis. *Geology in China* 48 (2), 477–494 [in Chinese with English abstract].
- Wei, W. Z. (1978). On the Genesis and Genetic Types of a Chromite deposit in Kansu. *Acta Geologica Sinica* 4, 269–281.
- Wei, Z. J. (2004). *Report of regional geological survey of Hongbaoshi Region, China: No. 4 Geological Team of the Gansu Bureau of Geology and Mineral Deposits, scale 1:250,000*. Beijing: China Geological Survey [in Chinese].
- Wei, Z. J., Huang, Z. B., Jin, X., Sun, Y. J., and Huo, J. C. (2004). Geological Characteristics of Ophiolite Migmatitic Complex of Hongshishan Region. *Gansu. Northwest. Geology*. 37 (2), 13–18. (in Chinese with English abstract).
- Wood, S. A. (1987). Thermodynamic Calculations of the Volatility of the Platinum Group Elements (PGE): The PGE Content of Fluids at Magmatic Temperatures. *Geochimica et Cosmochimica Acta* 51, 3041–3050. doi:10.1016/0016-7037(87)90377-2
- Xia, L. Q., Xia, Z. C., Xu, X. Y., Li, X. M., Ma, Z. P., and Wang, L. S. (2005). Relationships between Basic and Silicic Magmatism in Continental Rift Settings: A Petrogeochemical Study of Carboniferous Post-collisional Rift Silicic Volcanics in Tianshan, NW China. *Acta Geologica Sinica* 79 (5), 633–653. (in Chinese with English abstract).
- Xiao, W. J., Mao, Q. G., Windley, B. F., Han, C. M., Qu, J. F., Zhang, J. E., et al. (2010). Paleozoic Multiple Accretionary and Collisional Processes of the Beishan Orogenic Collage. *Am. J. Sci.* 310, 1553–1594. doi:10.2475/10.2010.12
- Yang, H. Q., Li, Y., Zhao, G. B., Li, W. Y., Wang, X. H., Jiang, H. B., et al. (2010). Character and Structural Attribute of the Beishan Ophiolite. *Northwest. Geol.* 43 (1), 26–36. (in Chinese with English abstract).
- Yue, Y., Liou, J. G., and Graham, S. A. (2001). Tectonic Correlation of Beishan and Inner Mongolia Orogens and its Implications for the Palinspastic Reconstruction of north China. *Memoir Geol. Soc. America*, 101–116. doi:10.1130/0-8137-1194-0.101
- Zhao, R. S., Zhou, Z. H., Mao, J. H., and Zhao, Z. X. (1994). Plate Tectonic Units and Tectonic Evolution in Gansu. *Reg. Geology. China* 13 (1), 28–36.
- Zhou, M. F., and Bai, W. J. (1992). Chromite deposits in China and their origin. *Mineralium Deposita* 27, 192–199.
- Zhou, M.-F., Robinson, P. T., Malpas, J., and Li, Z. (1996). Podiform Chromitites in the Luobusa Ophiolite (Southern Tibet): Implications for Melt-Rock Interaction and Chromite Segregation in the Upper Mantle. *J. Pet.* 37, 3–21. doi:10.1093/petrology/37.1.3
- Zhou, M.-F., Robinson, P. T., Su, B.-X., Gao, J.-F., Li, J.-W., Yang, J.-S., et al. (2014). Compositions of Chromite, Associated Minerals, and Parental Magmas of Podiform Chromite Deposits: the Role of Slab Contamination of Asthenospheric Melts in Suprasubduction Zone Environments. *Gondwana Res.* 26, 262–283. doi:10.1016/j.jgr.2013.12.011
- Zuo, G. C., Zhang, S. L., He, G. Q., and Zhang, Y. (1990a). Early Paleozoic Plate Tectonics in Beishan Area. *Scientia Geologica Sinica* 4, 305–314. (in Chinese with English abstract).
- Zuo, G. C., Zhang, S. L., Wang, X., Jin, S. Q., He, G. Q., Zhang, Y., et al. (1990b). *Plate Tectonics and Metallogenic Regularities in Beishan Region*. Beijing: Peking University Publishing House. (in Chinese with English abstract).
- Zuo, G., Zhang, S., He, G., and Zhang, Y. (1991). Plate Tectonic Characteristics during the Early Paleozoic in Beishan Near the Sino-Mongolian Border Region, China. *Tectonophysics* 188, 385–392. doi:10.1016/0040-1951(91)90466-6

Conflict of Interest: The authors declare that the research was conducted in the absence of any commercial or financial relationships that could be construed as a potential conflict of interest.

Publisher's Note: All claims expressed in this article are solely those of the authors and do not necessarily represent those of their affiliated organizations, or those of the publisher, the editors and the reviewers. Any product that may be evaluated in this article, or claim that may be made by its manufacturer, is not guaranteed or endorsed by the publisher.

Copyright © 2021 Wang, Zheng, Meng, Tang and Fang. This is an open-access article distributed under the terms of the Creative Commons Attribution License (CC BY). The use, distribution or reproduction in other forums is permitted, provided the original author(s) and the copyright owner(s) are credited and that the original publication in this journal is cited, in accordance with accepted academic practice. No use, distribution or reproduction is permitted which does not comply with these terms.

Advantages of publishing in Frontiers



OPEN ACCESS

Articles are free to read
for greatest visibility
and readership



FAST PUBLICATION

Around 90 days
from submission
to decision



HIGH QUALITY PEER-REVIEW

Rigorous, collaborative,
and constructive
peer-review



TRANSPARENT PEER-REVIEW

Editors and reviewers
acknowledged by name
on published articles

Frontiers

Avenue du Tribunal-Fédéral 34
1005 Lausanne | Switzerland

Visit us: www.frontiersin.org

Contact us: frontiersin.org/about/contact



REPRODUCIBILITY OF RESEARCH

Support open data
and methods to enhance
research reproducibility



DIGITAL PUBLISHING

Articles designed
for optimal readership
across devices



FOLLOW US

@frontiersin



IMPACT METRICS

Advanced article metrics
track visibility across
digital media



EXTENSIVE PROMOTION

Marketing
and promotion
of impactful research



LOOP RESEARCH NETWORK

Our network
increases your
article's readership